

Transactions of the ASME®

HEAT TRANSFER DIVISION
Chair, R. A. NELSON
Vice Chair, L. C. WITTE
Past Chair, W. F. FIVELAND
Secretary, Y. BAYAZITOGU
Treasurer, Y. JALURIA
Technical Editor, J. R. HOWELL (2000)

Associate Technical Editors,
C. T. AVEDISIAN (2002)
P. S. AYYASWAMY (2000)
C. BECKERMANN (2001)
F.-B. CHEUNG (2002)
T. Y. CHU (2002)
B. T. F. CHUNG (2001)
R. W. DOUGLASS (2000)
J. P. GORE (2002)
J.-C. HAN (2000)
M. HUNT (2002)
Y. JALURIA (2000)
D. A. KAMINSKI (2001)
R. L. MAHAJAN (2001)
A. MAJUMDAR (2001)
P. MENGUC (2000)
M. F. MODEST (2000)
D. POULIKAKOS (2002)
S. S. SADHAL (2002)
D. A. ZUMBRUNNEN (2001)

BOARD ON COMMUNICATIONS
Chairman and Vice President
R. K. SHAH

OFFICERS OF THE ASME
President, R. E. NICKELL
Executive Director,
D. L. BELDEN
Treasurer,
J. A. MASON

PUBLISHING STAFF
Managing Director, Engineering
CHARLES W. BEARDSLEY
Director, Technical Publishing
PHILIP DI VIETRO
Managing Editor, Technical Publishing
CYNTHIA B. CLARK

Managing Editor, Transactions
CORNELIA MONAHAN
Production Coordinator
JUDITH SIERANT
Production Assistant
MARISOL ANDINO

Transactions of the ASME, Journal of Heat Transfer (ISSN 0022-1481) is published quarterly (Feb., May, Aug., Nov.) for \$250.00 per year by The American Society of Mechanical Engineers, Three Park Avenue, New York, NY 10016. Periodicals postage paid at New York, NY and additional mailing offices. POSTMASTER: Send address changes to Transactions of the ASME, Journal of Heat Transfer, c/o THE AMERICAN SOCIETY OF MECHANICAL ENGINEERS, 22 Law Drive, Box 2300, Fairfield, NJ 07007-2300. CHANGES OF ADDRESS must be received at Society headquarters seven weeks before they are to be effective. Please send old label and new address. PRICES: To members, \$40.00, annually; to nonmembers, \$250.00. Add \$40.00 for postage to countries outside the United States and Canada.

STATEMENT from By-Laws. The Society shall not be responsible for statements or opinions advanced in papers or printed in its publications (B7.1, Para. 3). COPYRIGHT © 1999 by The American Society of Mechanical Engineers. For authorization to photocopy material for internal or personal use under those circumstances not falling within the fair use provisions of the Copyright Act, contact the Copyright Clearance Center (CCC), 222 Rosewood Drive, Danvers, MA 01923, tel: 978-750-8400, www.copyright.com. Request for special permission or bulk copying should be addressed to Reprints/Permission Department. INDEXED by Applied Mechanics Reviews and Engineering Information, Inc. Canadian Goods & Services Tax Registration #126148048.

Journal of Heat Transfer

Published Quarterly by The American Society of Mechanical Engineers

VOLUME 121 • NUMBER 4 • NOVEMBER 1999

769 Editorial

TECHNICAL PAPERS

Special Invited Paper on Opportunities in Heat Transfer

774 Free Drawing and Polymer Coating of Silica Glass Optical Fibers
U. C. Paek

Forced Convection

779 Heat Transfer Enhancement and Vortex Flow Structure Over a Heated Cylinder Oscillating in the Crossflow Direction
C. Gau, J. M. Wu, and C. Y. Liang

796 Coupling Between Heat and Momentum Transfer Mechanisms for Drag-Reducing Polymer and Surfactant Solutions
G. Aguilar, K. Gasljevic, and E. F. Matthys

Jets, Wakes and Impingement

803 The Effect of Drainage Configuration on Heat Transfer Under an Impinging Liquid Jet Array
K. Garrett and B. W. Webb

811 Local Heat Transfer in a Rotating Square Channel With Jet Impingement
S.-S. Hsieh, J.-T. Huang, and C.-F. Liu

Natural and Mixed Convection

819 Effect of Aperture Geometry on Heat Transfer in Tilted Partially Open Cavities
M. M. Elsayed and W. Chakroun

828 Inverse Natural Convection Problem of Estimating Wall Heat Flux Using a Moving Sensor
H. M. Park and O. Y. Chung

837 Mixture Fraction Statistics of Plane Self-Preserving Buoyant Turbulent Adiabatic Wall Plumes
R. Sangras, Z. Dai, and G. M. Faeth

Radiative Transfer

844 Far-Infrared Transmittance and Reflectance of $YBa_2Cu_3O_{7-\delta}$ Films on Si Substrates
A. R. Kumar, Z. M. Zhang, V. A. Boychev, D. B. Tanner, L. R. Vale, and D. A. Rudman

Boiling and Condensation

852 The Role of Bubble Waiting Time in Steady Nucleate Boiling
R. L. Judd

856 Analysis of the Polarity Influence on Nucleate Pool Boiling Under a DC Electric Field
M. C. Zaghoudi and M. Lallemand

865 Pool Boiling Critical Heat Flux in Reduced Gravity
D. P. Shatto and G. P. Peterson

874 Forced Convection Condensation on a Horizontal Tube: Influence of Turbulence in the Vapor and Liquid Phases
D. Homescu and P. K. Panday

(Contents continued on Outside Back Cover)

This journal is printed on acid-free paper, which exceeds the ANSI Z39.48-1992 specification for permanence of paper and library materials. ©™
85% recycled content, including 10% post-consumer fibers.

(Contents continued)

Combustion

- 886 A Heat and Mass Transfer Analysis of the Ignition and Extinction of Solid Char Particles
T. X. Phuoc and K. Annamalai

Phase Change and Multiphase Heat Transfer

- 894 The Leidenfrost Point: Experimental Study and Assessment of Existing Models
J. D. Bernardin and I. Mudawar
- 904 Complete Condensation of Forced Convection Two-Phase Flow in a Miniature Tube
E. Begg, D. Khristalev, and A. Faghri
- 916 Analysis of Coupled Nuclear/Thermal Instabilities of Two-Phase Flows in Parallel Boiling Channels
M. Uehiro, Y. F. Rao, and K. Fukuda
- 924 Experimental Study of Dispersed Droplets in High-Pressure Annular Flows
T. A. Trabold, R. Kumar, and P. F. Vassallo
- 934 On the Prediction of Local Ice Formation in Pipes in the Presence of Natural Convection
A. C. Keary and R. J. Bowen

Micro-Scale Heat Transfer

- 945 Phonon Wave Heat Conduction in Thin Films and Superlattices
G. Chen
- 954 Optical Measurement of Thermal Contact Conductance Between Wafer-Like Thin Solid Samples
Y. Ohson, G. Wu, J. Dryden, F. Zok, and A. Majumdar
- 964 Instability of Ultra-Thin Water Films and the Mechanism of Droplet Formation on Hydrophilic Surfaces
A. Majumdar and I. Mezic
- 972 Heat Transfer Enhancement by Fins in the Microscale Regime
F.-C. Chou, J. R. Lukes, and C.-L. Tien

Porous Media, Particles and Droplets

- 978 A New Method for Evaluation of Heat Transfer Between Solid Material and Fluid in a Porous Medium
K. Ichimiya
- 984 Energy Dissipation in Sheared Granular Flows
A. Karion and M. L. Hunt

Multimode Heat Transfer

- 992 Three-Dimensional Study of Combined Conduction, Radiation, and Natural Convection From Discrete Heat Sources in a Horizontal Narrow-Aspect-Ratio Enclosure
V. H. Adams, Y. Joshi, and D. L. Blackburn
- 1002 Heat Transfer in Discretely Heated Side-Vented Compact Enclosures by Combined Conduction, Natural Convection, and Radiation
E. Yu and Y. K. Joshi

Heat Exchangers

- 1011 Enhanced Heat Transfer Characteristics of Viscous Liquid Flows in a Chevron Plate Heat Exchanger
A. Muley, R. M. Manglik, and H. M. Metwally
- 1018 Performance of Dehumidifying Heat Exchangers With and Without Wetting Coatings
K. Hong and R. L. Webb

Heat Transfer in Manufacturing

- 1027 Turbulent Convection in a Czochralski Silicon Melt
T. Zhang, F. Ladeinde, and V. Prasad
- 1042 Measurement of the Transient Glass Surface Deformation During Laser Heating
T.-R. Shiu, C. P. Grigoropoulos, and R. Greif

(Contents continued on Inside Back Cover)

(Contents continued)

- 1049 **Modeling of Fluid Flow and Heat Transfer in a Hydrothermal Crystal Growth System: Use of Fluid-Superposed Porous Layer Theory**
Q.-S. Chen, V. Prasad, and A. Chatterjee

Heat Transfer Applications

- 1059 **Transient Heat Transfer for Layered Ceramic Insulation and Stainless Foil Fire Barriers**
G. D. Caplinger, W. H. Sutton, R. Spindler, and H. Gohlke

TECHNICAL NOTES

- 1067 **Hysteresis of Thermochromic Liquid Crystal Temperature Measurement Based on Hue**
J. W. Baughn, M. R. Anderson, J. E. Mayhew, and J. D. Wolf
- 1072 **The Time Delay for a Perceptible Thermal Disturbance in a Slab**
M. G. Davies
- 1076 **A Residual-Based Fuzzy Logic Algorithm for Control of Convergence in a Computational Fluid Dynamic Simulation**
J. Ryoo, D. Kaminski, and Z. Dragojlovic
- 1078 **Analytical Solution of the Graetz Problem With Axial Conduction**
J. Lahjomri and A. Oubarra
- 1083 **Nusselt Numbers in Rectangular Ducts With Laminar Viscous Dissipation**
G. L. Morini and M. Spiga
- 1088 **Experimental Investigation of Marangoni Convection in Aqueous LiBr Solution With Additives**
Y. T. Kang, A. Akisawa, and T. Kashiwagi
- 1091 **Transient Free Convection Flow Past an Infinite Vertical Plate With Periodic Temperature Variation**
U. N. Das, R. K. Deka, and V. M. Soundalgekar
- 1094 **Onset of Convection in a Fluid Saturated Porous Layer Overlying a Solid Layer Which is Heated by Constant Flux**
C. Y. Wang

ANNOUNCEMENTS AND SPECIAL NOTES

- 827 **Change of Address Form**
- 843 **Heat Transfer Web Site**
- 915 **Periodicals on ASMENET**
- 1098 **Information for Authors**
- 1099 **Author Index**
- 1109 **Policy Statement on Numerical Accuracy**

At the National Heat Transfer Conference in Albuquerque on August 16, 1999, the Editorial Board of the *Journal of Heat Transfer* considered and unanimously adopted a common symbol list for papers submitted to the Journal. At a meeting later that day, the Editors of 20 journals in the field of heat transfer unanimously adopted the same list, and will be publicizing its use to authors that submit manuscripts to their respective journals.

This action came after almost two years of consideration and revision of the list.

Authors submitting papers to the *Journal of Heat Transfer* should now use the symbols and definitions in the list, which is published in this issue of the Journal and is posted on the JHT web page. *When these symbols are used, they need not be included in the Nomenclature section of the paper.* Only those symbols not included in the common list need be placed in the Nomenclature of a particular paper. Because of the broad range of heat transfer topics covered in the Journal, the Common List cannot cover all

quantities, and the exceptions should be covered as before in the individual Nomenclature definitions.

The Editors hope that the adoption of the Common List will make it easier for future readers of heat transfer literature to interpret paper content because of the common symbols and definitions used across the major journals. For the *Journal of Heat Transfer* in particular, eliminating the duplication of definitions used in the many papers in a single Journal issue allows the limited page count available for the Journal to be put to better use.

We do expect a certain amount of controversy, because every author has particular preferences for nomenclature and symbols. We hope that in the long term, the symbols in the Common List will be adopted across the field, and will provide a basis for more uniform and clear communication in the heat transfer community.

John R. Howell
Technical Editor

NOMENCLATURE

QUANTITY	SYMBOL	COHERENT SI UNIT
Absorptivity (radiation)	α	—
Absorption Coefficient (radiation)	κ	m^{-1}
Activation Energy of a Reaction	ΔE	J/kg
Amount-of-Substance	N	kmol
molar flow rate	\dot{N}	kmol/s
molar 'mass velocity' ($= \dot{N} / A_c$)	\dot{n}	kmol/m ² s
Angle		
plane	$\alpha, \beta, \gamma, \theta, \phi$	rad
solid	Ω, ω	sr
of contact	θ	rad
Area		
cross-sectional	A_c, S	m ²
surface	A, A_s	m ²
Coefficient of Volume Expansion	$\beta = (1/v) (\partial v / \partial T)_p$	K ⁻¹
Compressibility Factor ($= p\bar{v} / RT$)	Z	—
Complex Refractive Index	$m = n - ik$	—
Concentration		
mass ($= M/V$)	c_p, ρ_i	kg/m ³
molar ($= N/V$)	$\bar{c}_i, \bar{\rho}_i$	kmol/m ³
Coordinates		
Cartesian	x, y, z	m, m, m
cylindrical	r, ϕ, z	m, rad, m
spherical	r, θ, ϕ	m, rad, rad
Density		
mass ($= M/V$)	ρ	kg/m ³
molar ($= N/V$)	$\bar{\rho}$	kmol/m ³
Diffusion Coefficient	D	m ² /s
Diffusivity, Thermal ($= k / \rho c_p$)	α	m ² /s
Dryness Fraction (quality) of flow	x x^*	— —
Emissive Power (radiation)	E	W/m ²
Emissivity (radiation)	ϵ	—
Energy		
kinetic	E_k	J = Nm
potential	E_p	J = Nm
transfer per unit time (power)	\dot{W}, \dot{Q}	W = Nm/s = kg m ² /s ³
Enthalpy ($= U + pV$)	H	J
specific, molar	h, \bar{h}	J/kg, J/kmol
of reaction	ΔH^0	J
Entropy		
specific, molar	s, \bar{s}	J/kg K, J/kmol K
Equilibrium (dissociation) constant	K	—
Extinction coefficient	$\beta = \kappa + \sigma_s$	m ⁻¹

Force weight (force of gravity)	F Mg	$N = kg\ m/s^2$ $N = kg\ m/s^2$
Fraction mass, of species i mole, of species i void of volume flow	x_i, y_i \bar{x}_i, \bar{y}_i ε ε'	— — — —
Frequency circular	ν, f ω	$Hz = s^{-1}$ rad/s
Gas Constant molar (universal) specific, of species i	\bar{R} R_i	J/kmol K J/kg K
Gibbs Function ($= H - TS$) specific ($= h - Ts$) molar ($= \bar{h} - T\bar{s}$)	G g \bar{g}	J J/kg J/kmol
Gravitational Acceleration standard	g g_n	m/s^2 m/s^2
Heat quantity of rate (power) flux (\dot{Q}/A) rate per unit volume	Q \dot{Q}, q \dot{q}, q'' \dot{S}, \dot{q}'''	J W = J/s W/m ² W/m ³
Heat Capacity specific (constant ν or p) molar (constant ν or p) ratio c_p/c_v	C c_ν, c_p \bar{c}_ν, \bar{c}_p γ	J/K J/kg K J/kmol K —
Heat Transfer Coefficient	h	W/m ² K
Helmholtz Function ($= U - TS$) specific ($= u - Ts$) molar ($= \bar{u} - T\bar{s}$)	F f \bar{f}	J J/kg J/kmol
Intensity (radiation)	I	W/m ² sr
Internal Energy specific, molar	U u, \bar{u}	J J/kg, J/kmol
Joule - Thomson Coefficient	$\mu_T = (\partial T/\partial p)_h$	K/Pa = m ² K/N
Length width height diameter radius distance along path film thickness thickness	L W H D R s δ δ, Δ	m m m m m m m m
Mass flow rate velocity of flux (flowrate per unit area = \dot{M}/A_c)	M \dot{M} $\dot{m}, \rho u$	kg kg/s kg/m ² s
Mass Transfer Coefficient	h_m, k_m	m/s
Molar Mass	\bar{M}	kg/kmol

Mean Free Path	$\bar{\lambda}, l$	m
Optical Thickness	τ	—
Phase Function (radiation)	Φ	—
Pressure	p	Pa = N/m ²
drop	Δp	Pa
partial	p_i	Pa
Reflectivity (radiation)	ρ	—
Scattering Albedo	$\omega = \sigma_s / (\sigma_s + \kappa)$	—
Scattering Coefficient (radiation)	σ_s	m ⁻¹
Shear Stress	τ	Pa = N/m ² = kg/m s ²
Stoichiometric Coefficient	ν	—
Surface Tension	σ	N/m = kg/s ²
Temperature absolute	T	K
Thermal Conductivity	k	W/mK
Time	t	s
Velocity	u	m/s
components in Cartesian coordinates x, y, z	u, v, w	m/s
View Factor (geometric or configuration factor)	F_v	—
Viscosity dynamic (absolute)	μ	Pa s = N s/m ² = kg/m s
kinematic (= μ/ρ)	ν	m ² /s
Volume	V	m ³
flow rate	\dot{V}	m ³ /s
specific, molar	$\nu, \bar{\nu}$	m ³ /kg, m ³ /kmol
Work	W	J = Nm
rate (power)	\dot{W}	W = J/s = Nm/s
Wavelength	λ	m

SUBSCRIPTS AND SUPERSCRIPTS

QUANTITY	SYMBOL
Bulk	b
Critical State	c
Fluid	f
Gas or Saturated Vapour	g
Liquid or Saturated Liquid	l
Change of Phase fusion	ls
sublimation	sg
evaporation	lg
Mass transfer quantity	m
Solid or Saturated Solid	s
Wall	w
Free-stream	∞
Inlet	in, 1
Outlet	out, 2
At Constant Value of Property	p, ν, T , etc
Molar (per unit of amount-of-substance)	— (overbar)
Stagnation (subscript)	0

DIMENSIONLESS GROUPS*

QUANTITY	SYMBOL
Biot Number	$Bi = hL / k$
Bond Number	$Bo = g(\rho_l - \rho_v)L^2 / \sigma$
Dean Number	$(Re)(r_m/R_{coil})^{1/2}$ (r_m = tube inner radius; R_{coil} = coil mean radius)
Eckert Number	$Ec = u^2/c_p \Delta T$
Euler Number	$Eu = \Delta p / (\frac{1}{2} \rho u^2)$
Fourier Number	$Fo = \alpha t/L^2$
Friction Factor	$f = \tau_w / (\frac{1}{2} \rho u^2)$
Froude Number	$Fr = u^2/gL$
Galileo Number	$Ga = L^3 g/\nu^2$
Grashof Number	$Gr = \frac{\beta g L^3 \Delta T}{\nu^2}$
Graetz Number	$Gz = (Re)(Pr) D/L$
Knudsen Number (λ = mean free path)	$Kn = \lambda / L$
Lewis Number	$Le = (Sc)/(Pr) = \alpha/D$
Mach Number	$M = u / u_{sound}$ $= u / (\gamma \bar{R} T / M)^{1/2}$ for perfect gas
Marangoni Number	$Ma = \frac{\partial \sigma}{\partial T} R \Delta T / (\alpha \mu)$
Nusselt Number	$Nu = hL/k_c$
Péclet Number	$Pe = (Re)(Pr)$
Prandtl Number	$Pr = \frac{\mu c_p}{k}$
Rayleigh Number	$Ra = (Gr)(Pr)$
Reynolds Number	$Re = uL / \nu = \rho u L / \mu = \dot{m} L / \mu$
Schmidt Number	$Sc = \nu/D = \mu/\rho D$
Sherwood Number	$Sh = h_c L/D$
Stanton Number	$St = (Nu)/(Re)(Pr) = h/\rho c_p u$
Stefan or Jakob Number	Ste or $Ja = c_p \Delta T / \Delta h$
Strouhal Number	$Sr = \nu L/u$
Weber Number	$We = u^2 \rho L / \sigma$

* The symbol L in the dimensionless groups stands for a generic length, and is defined according to the particular geometry being described; i.e., it may be diameter, hydraulic diameter, plate length, etc.

PHYSICAL CONSTANTS

QUANTITY	SYMBOL
Avogadro's Number	$N_A = 6.0225 \times 10^{26} \text{ kmol}^{-1}$
Boltzmann's Constant	$k = 1.38066 \times 10^{-23} \text{ J/K}$
Planck's Constant	$h = 6.62608 \times 10^{-34} \text{ Js}$
Stefan-Boltzmann Constant	$\sigma = 5.67051 \times 10^{-8} \text{ W/(m}^2\text{K}^4)$
Speed of Light in Vacuum	$c = 2.99792 \times 10^8 \text{ m/s}$
Universal Gas Constant	$\bar{R} = 8.31441 \times 10^3 \text{ J/kmol}\cdot\text{K}$

Free Drawing and Polymer Coating of Silica Glass Optical Fibers

U. C. Paek

Professor of Department of Information and Communications,
Director, Research Center for Ultrafast Fiber-Optic Networks,
Kwangju Institute of Science and Technology,
Kwangju 506-712, Korea
e-mail: ucpaek@kjst.ac.kr

The paper is primarily to highlight the current issues concerning fiber drawing and coating. The main emphasis is on high-volume production of silica-based optical fibers by using a large preform and a high-speed drawing. The commercial application of these processes has led to increasing the productivity in fiber manufacturing and resulted in a low cost of produced fibers. In order to systematically address the problems associated with the fiber manufacturing process, the fiber drawing system was divided into three major functional sections: heating, cooling, and coating zones. The governing equations at each section were formulated to describe the process mechanics and to identify the key control parameters for drawing and coating. These process parameters are the basic elements of implementing a streamline production system of optical fibers.

1 Introduction

Since the invention of a silica-based optical fiber with the low optical transmission loss (20 dB/km) was first announced by Kapron et al. (1970), research and development efforts for the fiber technology have led to remarkable achievements in every field associated with the lightwave communications applications. Particularly, the manufacturing technology of silica glass optical fibers has advanced rapidly to meet the demand for very large quantities of low cost fibers for many applications such as ocean cable, terrestrial cable, loop, customer premises penetration, etc. It is anticipated that fiber demand in the next century will increase drastically and outpace current world production capacities when an optical fiber network is introduced to the home. Therefore, Paek and Schroeder (1988) investigated a method for high volume mass production that can provide cost-effective manufacturing of optical fibers. The high-volume fiber fabrication basically requires two things: One is to produce a large size of an optical fiber preform (>8 cm in its diameter). The other is to draw a 125- μm diameter fiber from the preform and to coat it simultaneously with polymer materials at a high draw speed, perhaps greater than 20 meters per second. However, this paper will specifically deal with the free drawing technique. Until the late 1970s, the fiber draw speed was typically in the range of 1 ~ 2 m/s. Paek and Schroeder (1981b) first demonstrated the draw and coating speed of 5 m/s, using a UV curable resin. Prior to this work, Paek and Runk (1978) had investigated the neck-down region of a silica glass preform in a furnace during fiber drawing process, using a simplified model to understand the deformation mechanics. Yin and Jaluria (1998) took a rigorous theoretical approach to describe the radiative heat transfer of a large and transparent fiber preform in a graphite furnace. This calculation was based on a three-dimensional model including convection, conduction, and radiation transport between the furnace muffle and the necked preform. The results provide useful information on a large preform drawing, namely, a 10-cm diameter preform drawn into a 125- μm diameter fiber at a draw speed of 15 m/s.

A fiber drawing system is composed of functionally different instruments and apparatus such as a high-temperature furnace, fiber diameter measurement system, coating applicator, centering device, UV curing apparatus, draw tension gauge, and

take-up capstan. In modeling the process, the draw tower that is normally taller than eight meters is divided into three major zones to analyze each section separately, namely the heating zone, fiber cooling zone, and coating zone, as shown in Fig. 1. The heating zone that includes a high-temperature furnace and a precision temperature controller softens a silica-based preform made of transparent (diathermanous) material. In the formulation of the governing equations, the spectral effects of material transparency on the thermal radiation were taken into account. In this case, the typical value of bulk emissivity of silica glass is taken to be 0.91 (Gardon, 1956). However, it must be noted that the emissivity of glass depends not only on the temperature and but also on the thickness of a radiating body. For example, at 1000°C, a 0.5-cm thick silica glass has an emissivity of 0.6 (Petrov and Reznik, 1973). The softening point of silica glass ranges from 1400 to 2350°C. The viscosity of silica glass in the temperature of 1935 to 2322°C varies from $10^{5.86}$ to $10^{4.63}$ poises (Bacon et al., 1960). In order to heat the preform to the softening point and then to pull a fiber, two types of the furnaces are commonly used. They are a zirconia induction furnace and a graphite resistance furnace. The basic configuration of the zirconia furnace is that a silica vicar unit containing either a single or a double-jacketed zirconia susceptor tube surrounded by a thick layer of zirconia grain insulation is placed within an induction coil. For the graphite furnace case, the introduction of an inert gas such as nitrogen or argon into the furnace cavity is needed to protect the graphite heating elements from oxidation. To draw, for example, ~ a 400 km length of fiber from a 8-cm diameter and a 1-m long silica preform, the draw furnace should have a bore diameter larger than 10 cm with a longer heating zone. As shown in Fig. 2, the broad temperature distribution along the furnace wall yields a mild temperature gradient across the preform diameter and thus provides a low-fiber draw tension. On the other hand, the narrow heat zone as indicated by the dotted line in the figure induces an extremely high draw tension in case of drawing a fiber from a large preform. Therefore, to achieve a high-speed draw, a low tension at 1 m/s is essential, because tension is linearly proportional to draw speed. In case of drawing the nominal diameter fiber (125 μm), the tension at the draw speed of 1 m/s should be less than 10 g regardless of a preform size. A high tension induces strength degradation due to the fatigue effect, producing an extremely weak fiber and causing the fiber to break during drawing (Kalish and Tariyal, 1978). Sakaguchi and Kimura (1985a) obtained a draw speed as high as 20 m/s. Later, Kobayashi et al. (1991) achieved ~22 m/s (1300 m/min)

Contributed by the Heat Transfer Division for publication in the JOURNAL OF HEAT TRANSFER. Manuscript received by the Heat Transfer Division, June 18, 1999. Keywords: Coatings, Furnaces, High Temperature, Optical Fiber, Radiation. Associate Technical Editor: Y. Jaluria.

that has been so far known to be the maximum draw speed in a two layer coating on the fiber. Therefore, fiber manufacturers are making every effort to increase draw and coating speed in order to improve their fiber productivity. The current situation of fiber manufacturers is very serious to find a solution that can provide a method of pulling a fiber not only from a large preform but also at a high rate, perhaps exceeding 30 m/s. In addition, note that high tension affects optical and mechanical properties of fiber such as index of refraction, residual stresses, and transmission loss (Bateson, 1958; Krohn and Cooper, 1969; Hanafusa et al., 1985; Bouten et al., 1989).

We have so far discussed primarily the case of bare fiber drawing with no application of polymer in-line coating on the fiber surface. According to the work of Griffith (1920), fine glass fibers were shown to be of high strength due to the flawless condition of their surface. The theoretical strength of silica bare fiber is known to be approximately 70,000 kg/cm² (one million psi) in air, which indicates that silica glass fibers are truly much stronger than piano wires. However, it is easily degraded due to surface damage when a bare fiber comes in contact with a foreign particle or matter. Thus, it is imperative to put a coating material on an optical fiber, to protect their surface from external damage and to preserve the fiber's pristine state strength. In addition to draw tension, there is another crucial factor to be considered in high-speed coating. It is the effect of the temperature T_c that is the temperature of the fiber entering coating material in the coating applicator (Paek and Schroeder, 1981b). This temperature increases as the fiber draw speed increases. Therefore, this temperature must be maintained below a certain point to prevent the coating material from over-heating. Otherwise, it causes burning the material or losing the integrity of material. The maximum allowable T_c value for polymer coating material was found to be $\sim 80^\circ\text{C}$. An important thing to note is that the meniscus formed by the fiber entering the coating

material will collapse when the temperature is higher than that point. Particularly in coating of a fiber with a nonpressurized applicator, the maintenance of this meniscus is absolutely necessary to ensure proper wetting of resin material on the fiber surface and to yield a uniform and smooth coating.

Therefore, the cooling zone defined by region L between the bottom of furnace and the top of coating applicator is an important parameter in determining the maximum draw speed (Fig. 1). One way of maintaining a low T_c is to provide a long distance L . This will allow a fiber to sufficiently be cooled down by surrounding air so that T_c may reach the desirable point before it contacts the coating material. Evidently, this requires very high draw tower in order to implement a high-speed coating. The alternative way is to cool the fiber by blowing pre-dried gas of high thermal conductivity, i.e., helium gas. In this case, a special care must be taken to avoid an excessive flow over the fiber that may abrade the fiber surface, and localized dynamic pressure may also enhance the surface degradation by abrasion or corrosion (fatigue). However, the extremely rapid cooling of a fiber during drawing helps to give a better strength but tends to increase the fiber transmission loss (Bateson, 1958; Anderson, 1958).

Lastly, it is also important to find how high viscous polymer flow in a coating die causes fiber surface damage. In high-speed coating, the shear rate becomes so large that a fiber coated at a high speed often exhibits poor strength. It is suspected that high draw tension and viscous friction on the fiber surface by prepolymer solution in the coating die may contribute to the weak fiber strength. The common practice for reducing a high shear force in fiber manufacturing is to heat the coating applicator to reduce the polymer viscosity. The viscosity level set for coating is normally in the range of 10 poises.

The three zones (preform heating, fiber cooling, and fiber coat-

Nomenclature

a = susceptor bore radius	K = total conductivity ($K_c + K_r$)	q = input radiative heat flux
$B(p)$ = parameter defined by $\partial u^*/\partial \xi _0$	K_c = thermal conductivity	q_i = incoming radiative heat flux arriving at dA'_2
C = P_w/P_t	K_r = radiative conductivity	q_z = heat flux in z direction
C_p = specific heat	L = distance between bottom of furnace and coating applicator	q_0 = radiative heat flux leaving differential area dA'_2
$[c]$ = molar concentration of photoinitiator in monomer	L_f = length of neck-down region	$R(z)$ = neck shape
D = susceptor bore diameter ($2a$)	l = optical path length ($2H_\infty$)	$R\cdot$ = free radical
d = coating die length	\bar{M} = monomer	R_d = radius of coating die
d_1 = preform diameter	$\bar{M}\cdot$ = radical state of monomer	R_g = gas constant
d_2 = fiber diameter	n = refractive index of silica glass	R_0 = radius of coated fiber
dA_1 = differential area in neck-down region of preform	\bar{n} = unit vector normal to neck-down surface	R_1 = preform radius ($d_1/2$)
dA_2, dA'_2 = differential areas on susceptor surface	\bar{n}_r, \bar{n}_z = r component of unit vector \bar{n}	R_2 = fiber radius ($d_2/2$)
$dF_{dA_2-dA_1}$ = differential shape factor between dA_1 and dA_2	\bar{n}_1, \bar{n}_2 = unit vector normal to surface 1 and 2	r = radial direction
dF_{1-2} = view factor between dA_2 and dA'_2	P_c = required UV power to cure coating material	S = distance connecting two differential areas, dA_1 and dA_2
dq_{2-1} = radiative heat flux from differential area 2 to 1	P_t = total power supplied	\bar{S} = photoinitiator
F = fiber draw tension	P_w = power coupled into zirconia susceptor	\bar{S}^* = excited state of photoinitiator
F_c = pulling tension in coating	P_0 = rated lamp power per unit length	S_c = focused spot size
g = acceleration due to gravity	P_λ = spectral power per unit length of lamp	T = temperature
H = dimensionless parameter ($4hd_2/K_c$)	p = pressure	T^* = dimensionless temperature, $(T - T_0)/(T_s - T_0)$
H_c = mean curvature of surface	Q = flow rate	T_f = temperature at the midpoint of furnace
H_∞ = coating thickness	Q_{2-1} = total heat flux area 2 to differential area 1	T_s = softening point of silica glass
h = convective heat transfer coefficient		T_0 = ambient temperature
$h\nu$ = photon		u = velocity component of fluid in z direction
$J(\xi)$ = radiative heat flux along surface 2		u^* = u/V_2
		\bar{V} = velocity vector $\{V_z, V_r\}$
		V_r = velocity component in r direction
		V_z = velocity component in z direction

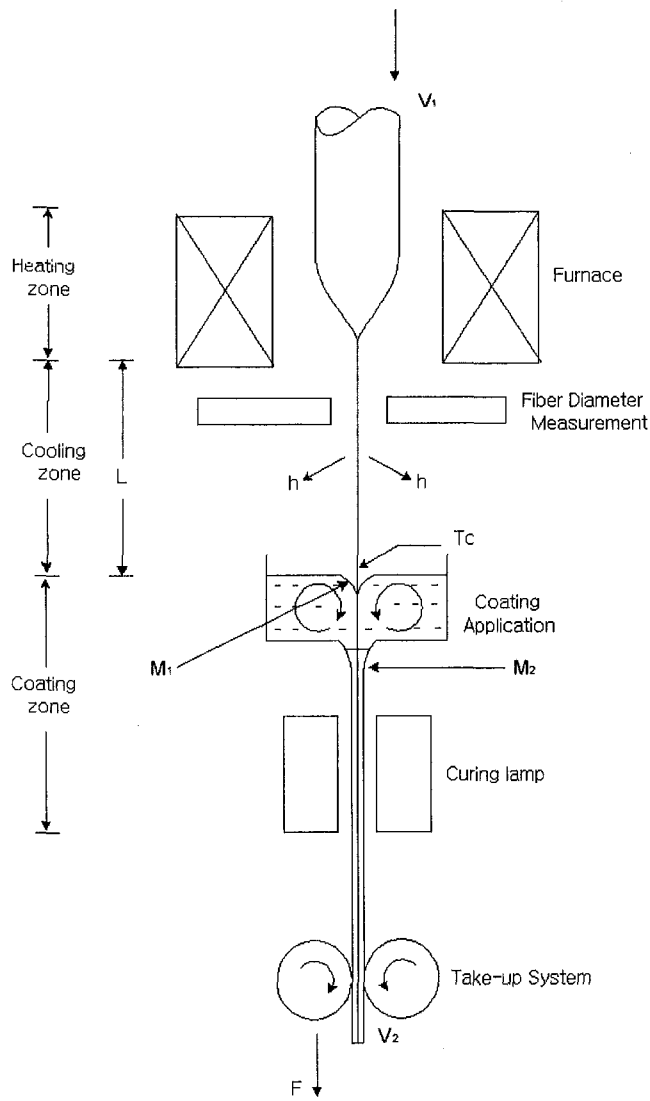


Fig. 1 Schematic of high-speed drawing and coating showing heating zone, fiber cooling zone, and coating zone

ing) of a fiber draw system as shown in Fig. 1 will be systematically described below in detail.

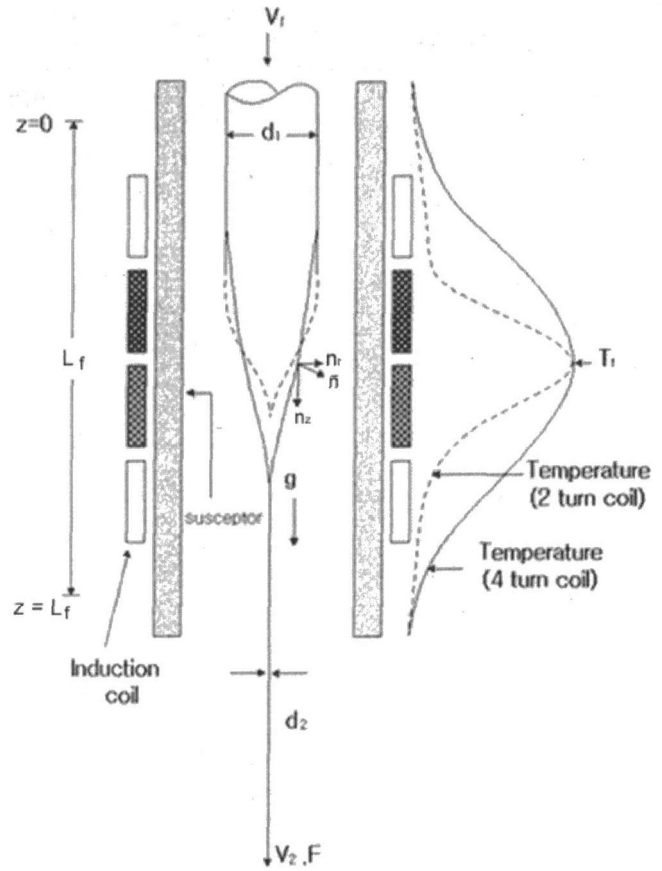


Fig. 2 Furnace configuration with two and four turn coils, and schematic illustration of neck elongation by pulling

2 Fiber Draw Furnace

Silica glass is one of a few high-temperature materials with noncrystalline properties. Its softening point ranges from 1400°C to 2300°C. Thus, a specially designed high-temperature furnace is needed to process this material. Particularly, for the fiber draw application a particle-free environment of furnace cavity is imperative in order to produce a pristine state of fiber surface. This assures high strength of a produced fiber. For fiber drawing applications, two types of electric furnaces are commonly used. They are a graphite furnace and a zirconia furnace. The zirconia induc-

Nomenclature (cont.)

V_1 = preform feed speed
 V_2 = fiber draw speed
 W = total power UV power for fiber coating
 $x = z/D$
 $x' = z'/D$
 z = axial direction
 z^* = dimensionless distance (z/d_2)

Greek Symbols

α = surface tension of silica glass
 α_λ = molar absorption coefficient
 β = a beam divergence angle from lamp
 ΔE = activation energy of silica glass
 ΔE_c = activation energy of photoinitiator
 δ = a beam divergence angle from lamp

ϵ = emissivity of silica
 ϵ_s = emissivity of zirconia susceptor
 ϵ_r = overall efficiency
 ϵ_1 = lamp efficiency
 ϵ_2 = reflector efficiency
 ϵ_3 = UV absorptivity of polymer coating material
 γ = absorption coefficient of silica glass
 $\dot{\gamma}$ = strain rate
 η = silica viscosity
 η_0 = pre-exponential constant
 η_1 = focusing effectiveness of reflector
 η_2 = effective ratio ($2R_0/S_c$)
 κ = thermal diffusivity
 Λ = dimensionless parameter ($V_2 d_2 / \kappa$)

μ = viscosity of polymer coating material
 θ_1, θ_2 = angle with respect to unit vector \bar{n}_1 and \bar{n}_2
 ρ = density of silica
 σ = Stefan-Boltzmann constant
 σ_{ij} = stress component acting on the i direction on the plane perpendicular to the j direction
 σ_{zz} = axial stress component acting on surface normal to z direction
 τ_{rz} = shear stress
 $\Omega = \ln [(T_s - T_0)/(T_c - T_0)]$
 ξ = length measured along susceptor surface
 ζ = dimensionless parameter $(r - R_2)/(R_d - R_2)$

tion or resistance furnace is designed to be operated under atmospheric environment, while the graphite furnace must be operated under a nonoxidation atmosphere sustained by introduction of inert gases (typically argon, nitrogen, and helium) into the furnace cavity. The flow of these inert gases is essential to protecting the graphite muffle from burning. The strength of convection current within the furnace is the sum of forced convection by gas blowing from the furnace bottom and natural convection by high-temperature heating. On the other hand, the zirconia furnace induces only natural convection between the preform and the muffle. Therefore, the heat transfer coefficient around the preform in the zirconia furnace is substantially different from that in the graphite furnace. Within the draw furnace, cooling of an optical fiber preform is predominantly due to convection, but heating is thermal radiation emitting from the furnace wall. In consideration of those complex dynamics, designing of a reliable furnace that can provide not only a long furnace lifetime but also produce a low-loss and high-strength fibers is challenging.

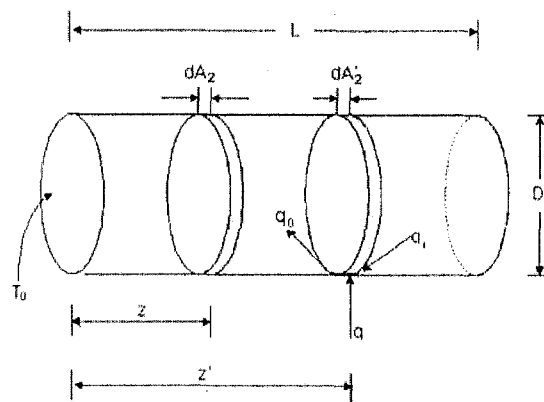
1 Large Bore Zirconia Induction Furnace. For the power calculation, a zirconia induction furnace is considered. Free drawing of optical fibers with a graphite furnace is almost the same as that with a zirconia furnace except for gas flowing inside the furnace cavity. To understand the relationship between draw tension and neck-down shape of the preform in the furnace, we take an elongational and Newtonian flow model. It assumes that $\sigma_{zz} = 3\eta(\partial V_z/\partial z)$ and that V_z is a function of z only, where σ_{zz} is the axial (z) stress component acting on the surface normal to the z direction and V_z is the velocity component in the z direction within the neck-down region in the furnace. This is a valid assumption for a long neck-down region with a high viscosity. η is the silica viscosity and strongly depends on temperature, which may be expressed in terms of activation energy ΔE by the following formula, $\eta = \eta_0 \exp(\Delta E/R_g T)$, where η_0 is pre-exponential constant and R_g the gas constant. When a fiber of its diameter d_2 is pulled in the z direction at a speed of V_2 , draw tension F can be formulated from the above σ_{zz} expression together with the mass conservation $V_2(d_2/2)^2 = V_z(z)R(z)^2$ into the following form (Paek and Runk, 1978):

$$F = -\frac{3}{2} \pi \eta(T) V_2 d_2^2 \left(\frac{1}{R}\right) \frac{dR}{dz}. \quad (1)$$

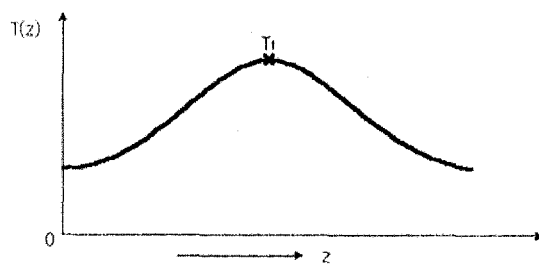
In the above equation, silica viscosity η and neck-shape $R(z)$ are evaluated at the point where the maximum furnace temperature T_f occurs in the furnace (see Fig. 2). A longer neck-shape obtained with a longer heating zone gives a lower value of $(1/R)dR/dz$ and viscosity, thereby reducing the tension F . Figure 2 shows a qualitative description of two neck shapes formed by the two different induction coils presenting a longer neck formation under the broader heat zone. The temperature profiles along the susceptor produced by the two turn and four turn induction coil are also given in the figure, where the dotted curve represents the temperature profile obtained from the two turn coil furnace and the solid line from the four turn coil. The heat zone of four turn coil furnace is twice as large as that of two turn coil furnace (Runk, 1977). The heat zone is determined by the measurement of temperature distribution along the furnace wall (Issa et al., 1996).

2 Power Requirement. In order to calculate the input power P_w (watt) under a steady-state condition, we consider a susceptor cylinder as shown in Fig. 3(a). In the power calculation the effect of a silica glass preform in the furnace cavity is not considered since the maximum power is needed to operate the furnace under the situation that the furnace bore is empty and its both ends are fully opened. Let us define the radiation flux leaving the differential area dA_2' as q_0 and the incoming flux arriving at the same differential area as q_i . The energy balance at dA_2' gives the following relation with the input flux, q (w/cm^2),

$$q(z) = q_0(z) - q_i(z). \quad (2)$$



(a)



(b)

Fig. 3 (a) The coordinate system of the susceptor and geometric relation for radiation exchange between two differential areas in the susceptor; (b) temperature distribution along the susceptor wall

When the outer surface of the tube is assumed insulated, some part of the outgoing flux q_0 will be lost through the two open ends. This will be a major loss of thermal radiation from the system, but a majority of the radiation flux will be confined within the furnace cavity. The open ends are considered black disks at room temperature. To determine the incoming flux q_i , it is necessary to know the view factor dF_{1-2} between differential surfaces, dA_2 and dA_2' . The view factor is given by the reference (Siegel and Howell, 1972),

$$dF_{1-2} = 1 - \frac{(|x' - x|^3 + 1.5|x' - x|)}{[(x' - x)^2 + 1]^{3/2}}, \quad (3)$$

where $x = z/D$, $x' = z'/D$ and D is the susceptor bore diameter. Therefore, the incoming radiative flux q_i can be obtained by summing up all the outgoing flux q_0 over the entire surface that falls upon dA_2 .

$$q_i = \int_0^b q_0 dF_{1-2} dx' \quad (4)$$

Therefore, from Eq. (2) the power P_w coupled into the zirconia susceptor tube can be calculated by integrating q over the entire inner surface of the tube. Namely,

$$P_w = \pi D \int_0^L q_0 dz - \pi D \int_0^L \int_0^b q_0 dF_{1-2} dx' dz, \quad (5)$$

where $b = L/D$. It is seen in Eq. (5) that the power P_w can be obtained when q_0 is known.

The value of q_0 can be determined by measuring temperature

along the susceptor tube wall with an optical pyrometer. The relation between q_0 and the measured temperature is given by $q_0 = \epsilon_s \sigma T^4$, where ϵ_s is the emissivity of the zirconia susceptor and σ the Stefan Boltzmann constant. The emissivity of zirconia susceptor is assumed to be constant and equal to 0.7. The furnace temperature, T_f is the temperature at the midpoint of the furnace, representing the maximum value of the temperature distribution along the wall (Fig. 3(b)). A power generator supplies electromagnetic field to the induction coil around the susceptor tube through a microwave waveguide. The coupling coefficient C is given by $C = P_w/P_t$, where P_w is the power coupled to the susceptor and P_t the total power supplied. In this case, the value of the coupling coefficient C was determined to be 0.47 (Davies and Simpson, 1979), giving the calculated power P_t to be 14.7 kw at $T_f = 2250^\circ\text{C}$ for the two turn coil and 24.8 kw at $T_f = 2100^\circ\text{C}$ for the four turn coil. The measured powers were ~ 15 kw and ~ 24.5 kw, respectively, for the two turn coil and the four turn coil both at an operating temperature of 2100°C . Hence, it can be concluded that at least 30-kw power supply is needed to draw a 125- μm diameter fiber from a 7.5-cm diameter preform with low tension (Paek and Schroeder, 1988). Recently, Rajala et al. (1998) investigated the design of a graphite induction furnace capable of drawing a large preform at high speed. A 44-kw power supply unit was used to operate a furnace susceptor with a 8-cm graphite bore at 2250°C . It is shown that under the same draw conditions the graphite furnace needs more energy than the zirconia furnace since there is the heat loss due to forced cooling by the inert gas flow inside the furnace cavity.

3 Neck-Down Region in Furnace. The main aim of this study is to understand how the neck-down region affects the geometry or the properties of drawn fibers; namely, fiber diameter variations, fiber strength, optical loss, core index change, germanium defect generation, etc. (Hanawa et al., 1987; Scherer, 1979; Scherer, 1980). Lee and Jaluria (1995, 1996) formulated the complicated governing equations with the minimum approximations and assumptions to solve the thermal radiation problem of transparent material in the fiber draw process. Also, Kaminski (1995) studied the heat transfer problem with combined radiation and convection in a fiber draw furnace, using a two-dimensional, axisymmetric energy equation. In this case, the temperature distribution in a glass preform was calculated based on a measured neck shape. However, it must be noted that the accurate prediction of a neck shape in a draw furnace is the main interest of this section and can be achieved by solving the energy and momentum equations simultaneously. The two equations are coupled by the viscosity equation of silica glass that is a strong function of temperature.

Most optical fibers are drawn from a silica preform by peripherally heating as described in Fig. 4. Given the rod feed and fiber draw speeds, the draw-down ratio is determined by the conservation of mass. As a fused silica rod having a diameter d_1 proceeds through the heat zone of the furnace, its temperature and viscosity will vary along its axial direction z due to the furnace heat distribution. The extensional deformation of the preform rod by pulling yields a "neck-down" shape within the heating zone. This neck-down shape described by $R(z)$ is influenced by different drawing conditions and in turn influences the fiber diameter uniformity (Smithgall, 1979; Mulpur and Thompson, 1996). The $R(z)$ is determined by the draw parameters such as furnace temperature, draw tension, draw speed, preform diameter, fiber diameter, etc., and is found by solving the mass, momentum, and energy equations simultaneously. In the drawing process, the viscosity in the viscoelastic flow of silica glass is so high that the Reynolds number of the flow field is small and the inertia terms of the momentum equations can be ignored. Therefore, the momentum equation can be written in the following way (Paek and Runk, 1978):

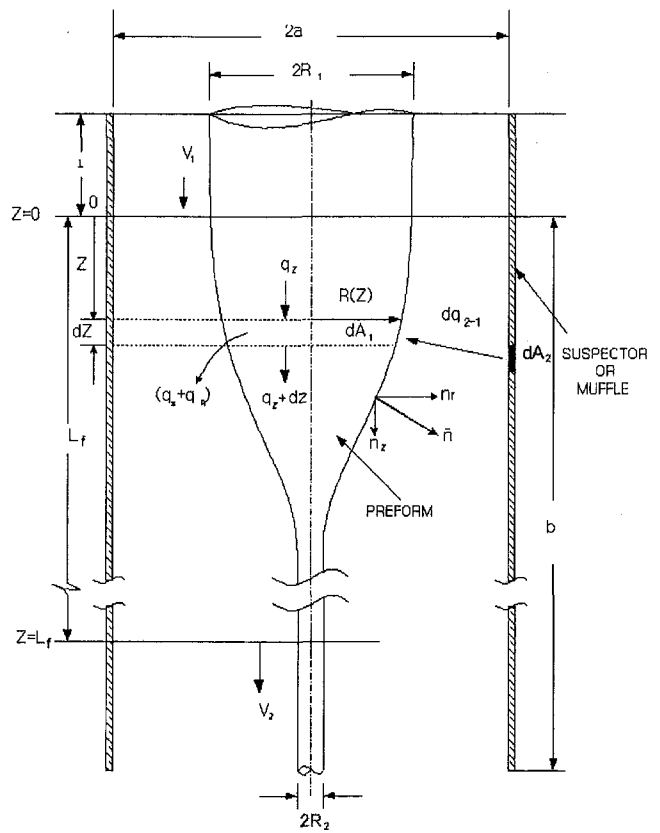


Fig. 4 Physical model and its coordinates system in the furnace drawing of optical fibers

$$\rho g + \frac{\partial \sigma_{zz}}{\partial z} + \frac{1}{r} \frac{\partial}{\partial r} (r \sigma_{rz}) = 0, \quad (6)$$

$$\frac{\partial \sigma_{rr}}{\partial r} + \frac{\partial \sigma_{rz}}{\partial z} + \frac{\sigma_{rr} - \sigma_{\theta\theta}}{r} = 0, \quad (7)$$

where ρ and g are the density of silica glass and the acceleration due to gravity, respectively. The boundary conditions of the neck-down region are

$$\left. \begin{aligned} V_z &= V_1 & \text{at } z &= 0, \\ V_z &= V_2 & \text{at } z &= L_f. \end{aligned} \right\} \quad (8)$$

The boundary conditions are set to be the two points where the deformation of the preform starts and ends. Therefore, the beginning of the neck-down at $z = 0$ maintains the preform size ($R_1 = d_1/2$) at which the feeding speed is V_1 , while its end at $z = L_f$ maintains the fiber size ($R_2 = d_2/2$) at which the draw speed is V_2 , as shown in Fig. 2. The free boundary condition at $r = R(z)$ is given by

$$\sigma_{ij} \bar{n} + 2\alpha H_c \bar{n} = 0, \quad (9)$$

where α is the surface tension, H_c the mean curvature of the surface, and σ_{ij} the stress tensor defined by

$$\sigma_{ij} = \begin{bmatrix} \sigma_{zz} & \sigma_{rz} & 0 \\ \sigma_{rz} & \sigma_{rr} & 0 \\ 0 & 0 & \sigma_{\theta\theta} \end{bmatrix}. \quad (10)$$

Note that the subscripts i and j of σ_{ij} refer to a stress component acting in the i direction on the plane perpendicular to the j direction and $\sigma_{ij} = \sigma_{ji}$. The H can be written by

$$H_c = \frac{1}{2} \left\{ \frac{1}{R} + \frac{1}{R} \left(\frac{dR}{dz} \right)^2 - \frac{d^2 R}{dz^2} \right\} \left\{ 1 + \left(\frac{dR}{dz} \right)^2 \right\}^{-3/2}. \quad (11)$$

From Eq. (11), the free boundary condition can be divided into two equations in terms of z and r components.

$$\sigma_{zz}n_z + \sigma_{rz}n_r + 2\alpha H_c n_z = 0, \quad (12)$$

$$\sigma_{rz}n_z + \sigma_{rr}n_r + 2\alpha H_c n_r = 0. \quad (13)$$

Here, $\bar{n} = n_z\bar{z} + n_r\bar{r}$. The z and r components of the unit vector \bar{n} can be expressed as

$$n_z = -\frac{R'}{(1+R'^2)^{1/2}}, \quad (14)$$

$$n_r = \frac{1}{(1+R'^2)^{1/2}}, \quad (15)$$

where

$$R' = \frac{dR}{dz}.$$

By multiplying Eq. (6) by $2\pi r dr$ and integrating it from 0 to $R(z)$, one obtains

$$\rho g R^2 + 2 \int_0^R r \frac{\partial \sigma_{zz}}{\partial z} dr + 2R\sigma_{rz}(R) = 0. \quad (16)$$

From Eq. (12), the solution of Eq. (16) can be obtained subject to the boundary conditions at the both ends of neck-down region.

$$V_z(z) = C_1 \int_0^z \frac{dz}{\eta R^2} - \frac{\rho g}{3} \int_0^z \frac{1}{\eta R^2} \left(\int_0^z R^2 dz \right) dz - \frac{4\alpha}{3} \int_0^z \frac{1}{\eta R^2} \left(\int_0^z R' R H_c dz \right) dz + V_1, \quad (17)$$

where

$$C_1 = \left\{ (V_2 - V_1) + \frac{\rho g}{3} \int_0^{L_f} \frac{1}{\eta R^2} \left(\int_0^z R^2 dz \right) dz + \frac{4\alpha}{3} \int_0^{L_f} \frac{1}{\eta R^2} \left(\int_0^z R' R H_c dz \right) dz \right\} \cdot \left\{ \int_0^{L_f} \frac{dz}{\eta R^2} \right\}^{-1}$$

The velocity component V_r of $\bar{V} = \{V_z, V_r\}$ can be determined from the equation of continuity, $V_r = -\frac{1}{2}rV'_z$.

Now, let us consider the formulation of energy equation which is coupled with the momentum equation through the viscosity of the material. From Fig. 4, the heat flux leaving differential area dA_2 of the susceptor will be partially absorbed by differential area dA_1 in the neck-down region of the preform. A portion of the absorbed energy will be conducted through the neck-down region while the rest will be lost to the surroundings in the form of thermal radiation and convection. For such a diathermanous or transparent material the radiative transfer within the material is significant, especially at elevated temperatures. The conduction due to radiation contribution must be added to the nonradiative heat conduction. Therefore, the apparent thermal conductivity, K , will be the sum of the nonradiative conductivity, K_c , and radiative conductivity, K_r . The K_r is expressed by

$$K_r = \frac{16n^2\sigma T^3}{3\gamma}, \quad (18)$$

where n is the refractive index of silica glass, σ the Stefan-Boltzmann constant, and γ the absorption coefficient of silica glass. For the value of $\gamma = 0.2 \text{ cm}^{-1}$ the conductivity K_r is calculated to be approximately $0.25 \text{ w/cm}^\circ\text{C}$ in the temperature

Table 1 Material properties of silica (from Paek and Kurkjian, 1975)

Thermal Conductivity K_c (cal/s cm $^\circ\text{C}$)	0.0064
Density ρ (g/cm 3)	2.2
Specific heat C_p (cal/g $^\circ\text{C}$)	0.25
Elastic modulus E (kg/cm 2)	8.25×10^5
Linear expansion coefficient α_c ($^\circ\text{C}^{-1}$)	5.5×10^{-7}
Surface tension α (dyne/cm) at 2000 $^\circ\text{C}$	310

range of 1500 to 2000 $^\circ\text{C}$ and the value of K_c is $\sim 0.05 \text{ w/cm}^\circ\text{C}$. The density and specific heat of fused silica are $\rho = 2.2 \text{ g/cm}^3$ and $C_p = 0.25 \text{ cal/g}^\circ\text{C}$ (Table 1).

When the heat transfer coefficient surrounding the preform in the furnace is defined by h , the Biot number ($hd_1/4K$) is calculated to be less than 0.1. Thus, the temperature gradient across the preform rod with its diameter d_1 can be neglected. If the rod diameter is less than 1.5 cm, the condition can be easily satisfied and the energy equation can be reduced to a one-dimensional problem. However, for a large size preform a modeling requires the formulation of a three-dimensional radiative heat conduction equation. Since the analysis of the neck-down region in a three-dimensional case is extremely complex and beyond the scope of this paper, the one-dimensional coupled radiative heat conduction equations are illustrated to describe the temperature distribution along the elongated silica glass rod. The heat flux q_z and heat conduction in the z direction with a variable cross section ($A = \pi R^2$) can be formulated by the energy balance in the control volume (Fig. 4) as

$$q_z = -K_c \frac{dT}{dz} - K_r(T) \frac{dT}{dz}, \quad (19)$$

$$\rho C_p V_z(z) \frac{dT}{dz} + \frac{d(q_z A)}{Adz} + \frac{2\{\epsilon\sigma(T^4 - T_0^4) + h(T - T_0)\}}{R} = \frac{2Q_{2-1}}{R}, \quad (20)$$

where ϵ is the emissivity of silica glass, and $V_z = R^2 V_1 / R^2$. A detailed expression of Q_{2-1} is given in the Appendix. We need to define two proper boundary conditions within the neck-down region in order to solve the coupled first-order differential equations of Eq. (19) and Eq. (20). The softening point T_s of silica glass is taken at two boundary points, $z = 0$ and $z = L_f$ at which the deformation of the preform is to start and end as mentioned earlier. Thus, the region between these two points will maintain a temperature higher than T_s ($\sim 1600^\circ\text{C}$).

$$\left. \begin{aligned} T &= T_s & \text{at } z &= 0, \\ T &= T_s & \text{at } z &= L_f. \end{aligned} \right\} \quad (21)$$

However, it must be noted that the values of emissivity ϵ and heat transfer coefficient h depend strongly on the thickness of a sample. For example, the emissivity of silica glass changes significantly if the thickness is less than 0.2 cm (Petrov, 1973). Since the dimensional reduction in the neck-down region is so large (1.5 cm to 0.01 cm), the emissivity is taken to be 0.6 in the region where the diameter of the neck-down region is greater than 0.2 cm, while in the fiber region it is assumed to be 0.1. In the intermediate region the two values are smoothly connected with a polynomial. Similarly, the heat transfer coefficient h in the intermediate region defined above is also obtained by smoothly connecting the value of $1.5 \times 10^{-2} \text{ w/cm}^2 \text{ }^\circ\text{C}$ in the bulk region to that of $3 \times 10^{-2} \text{ w/cm}^2 \text{ }^\circ\text{C}$ in the fiber region (Paek and Runk, 1978). Thus, the following iterative computational scheme is used to calculate the temperature distribution $T(z)$ along the neck-down region, velocity $V_z(z)$ and the neck shape:

- (i) an arbitrary neck shape $R(z)$ is assumed for a set of drawing condition (V_2, d_1, d_2, T_f, F).

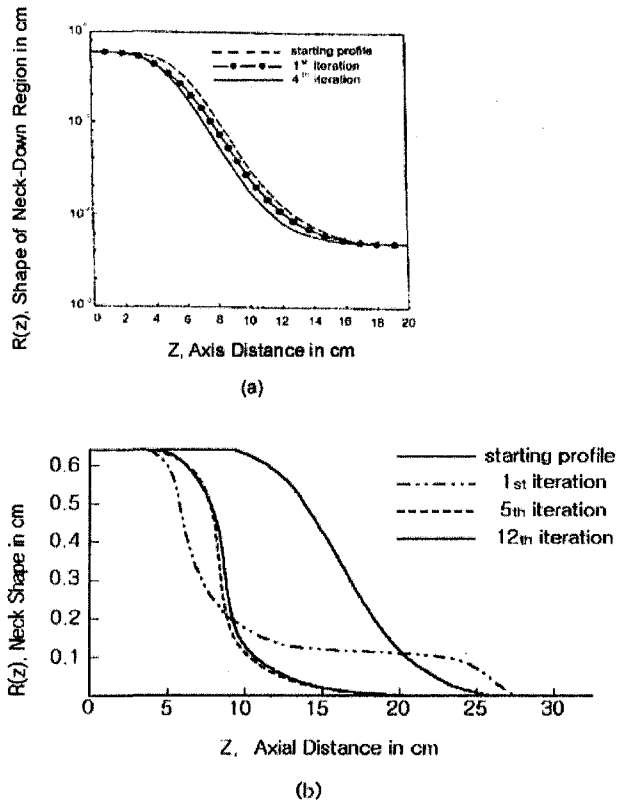


Fig. 5 (a) Neck shapes (solid line: neck shape obtained after the fourth iteration; solid and dotted line: neck shape after the first iteration; broken line: measured neck shape). (b) Neck shapes predicted by Jaluria et al. (1992).

- (ii) The temperature $T(z)$ can be obtained from Eq. (19) and Eq. (20) using the arbitrary neck shape $R(z)$. Then, the viscosity $\eta(T)$ is determined from the relation between the viscosity and the temperature of silica glass, namely, $\eta(T) = \eta_0 \exp(\Delta E/R_g T)$.
- (iii) The viscosity and the assumed neck shape are substituted into Eq. (17) to obtain the velocity $V_z(z)$, which will yield a new neck shape $R(z)$ from the conservation of mass.

$$R(z) = R_1 \sqrt{\frac{V_1}{V_z}} \quad (22)$$

The iterative steps of (i), (ii), and (iii) are repeated until the neck shape is converged. Three or four iterations are sufficient to reach the final solutions (Fig. 5(a)). In order to warrant fast convergence in the iterative scheme, the initial neck shape used for this computation is the measured profile with a linear voltage transducer after the preform is quenched by removing it quickly from the furnace during the fiber draw. Similarly, Choudhury et al. (1995) also developed an analytical and numerical model to calculate the shape of the neck-down region formed during fiber drawing in the furnace. The result is shown in Fig. 5(b). Figure 6 shows the temperature distributions $T(z)$ for three different values of draw speeds. Particularly in this experiment, a 100- μm diameter fiber was drawn from a 1.2-cm diameter fused silica rod at three different drawing speeds ($V_2 = 100 \text{ cm/s}$, $V_2 = 200 \text{ cm/s}$, $V_2 = 300 \text{ cm/s}$). The corresponding draw tensions are measured to be 16, 32, and 48 g, respectively. On the other hand, the tension was calculated from Eq. (1) by using the values of $R(z)$, dR/dz and viscosity at the T_f point. The measured and the calculated tensions are compared and given in Fig. 7(a). The results of this low-speed drawing case indicated that the draw tension was in a linear proportion with the draw speed. Also, Choudhury et al. (1995) modeled rigorously the radiation transport in a fiber draw furnace

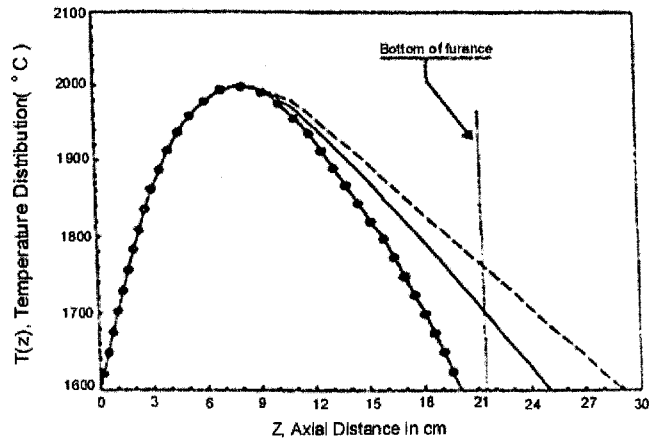


Fig. 6 Temperature distributions along the neck-down region for three different draw speeds

and predicted the tension at the draw speed of 1 m/s to be $\sim 10 \text{ g}$. Rajala et al. (1998) recently reported the experimental results of high-speed drawing. The measured data for draw tension versus

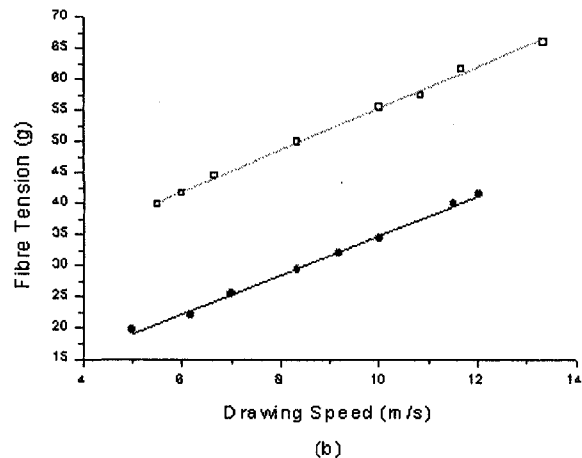
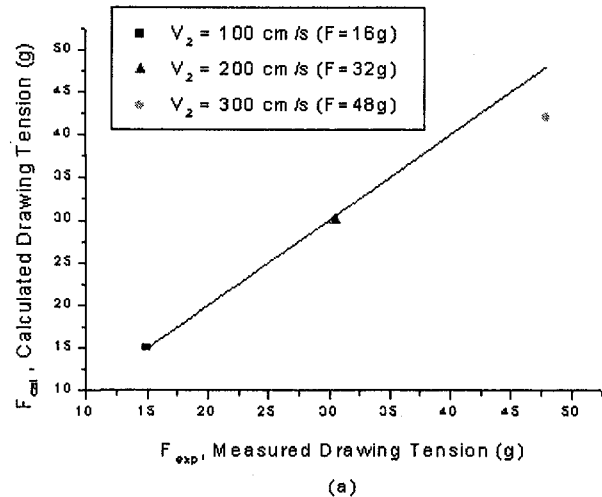


Fig. 7 (a) Comparison of calculated and measured drawing tension. (b) Draw tension versus drawing speed with two furnace input powers: 85 percent (\square) and 90 percent (\bullet) (from Rajala et al., 1998).

drawing speed in high-speed drawing also show a linear relationship as given in Fig. 7(b).

In this low-speed draw cases, the lengths of neck-down region were $L_f = 20, 25,$ and 29 cm, respectively. Recently, Vaidya and Mihalacopoulos (1998) investigated the neck-down profile in high-speed drawing. It was shown from both of low and high-speed drawing cases that the length of neck-down also varies linearly with draw speed.

3 Fiber Cooling

The fiber exiting from the bottom of the furnace by free drawing is cooled rapidly by the surrounding air or by blowing a gas (helium). Most of analyses dealing with fiber cooling were formulated on the basis of an approximated method such as Reynolds' analogy or boundary layer approximations. Generally, the heat transfer coefficient is calculated based on the boundary layer approximations. However, it must be noted that the calculation of fiber cooling based on the boundary layer approximations may not be applicable because the boundary layer thickness is of the same order of magnitude as the fiber diameter. Physically, it seems difficult to imagine how a thin boundary layer can establish along the length of a fiber having a very thin diameter ($125\text{-}\mu\text{m}$ diameter). Therefore, a new novel analysis on the heat transfer problem associated with flow over a needle-like body such as a fiber should be explored, since the fiber cooling time depends mainly on an accuracy of the value of heat transfer coefficient, h (Anderson, 1958; Arridge and Prior, 1964). Paek and Kurkjian (1975) developed a method for calculating the fiber cooling time while a fiber is being drawn. The analysis is applicable to obtaining the cooling rate regardless of convection modes (natural convection or forced convection), provided that the heat transfer coefficient is known. Conversely, using the equation of fiber cooling, one can also obtain accurately the heat transfer coefficient from a measured fiber temperature at a certain position and draw parameters. Importantly, it is worthy to remember that the cooling time is the key factor determining a fiber coating speed.

In the cooling rate calculation, the fiber temperature near the bottom of the furnace is designated as T_s , the softening point. Setting $z = 0$ at the bottom of the furnace as an origin, we can formulate the governing equation along the fiber by taking energy balance (see the cooling zone in Fig. 1). The physical size of the fiber diameter is so small that the emissivity of the silica fiber is also negligibly small (Petrov et al., 1973) and thus, the radiative contribution to cooling can be ignored. The transverse temperature gradient can also be neglected because of smaller dimension of fiber diameter. Therefore, the one-dimensional steady-state heat conduction equation can be formulated based on the energy balance from a local control volume in the fiber cooling zone as (Paek and Schroeder, 1981b),

$$V_2 \frac{dT}{dz} = \kappa \frac{d^2T}{dz^2} - \frac{4h(T - T_0)}{\rho C_p d_2}, \quad (23)$$

where κ is the thermal diffusivity of silica glass. Since the fiber is to cool down to ambient temperature T_0 , the boundary conditions can be set as

$$\left. \begin{aligned} T &= T_s & \text{at } z &= 0, \\ T &= T_0 & \text{at } z &= \infty. \end{aligned} \right\} \quad (24)$$

The following nondimensional variables and parameters are introduced.

$$\begin{aligned} T^* &= (T - T_0)/(T_s - T_0), & z^* &= z/d_2, \\ \Lambda &= V_2 d_2/\kappa, & H &= 4hd_2/K_c. \end{aligned} \quad (25)$$

With Eqs. (24) and (25), Eq. (23) can be rewritten in the following forms:

$$\frac{d^2T^*}{dz^{*2}} - \Lambda \frac{dT^*}{dz^*} - HT^* = 0, \quad (26)$$

$$\left. \begin{aligned} T^* &= 1 & \text{at } z^* &= 0, \\ T^* &= 0 & \text{at } z^* &= \infty. \end{aligned} \right\} \quad (27)$$

Assuming that all material properties remain constant during the drawing period (see Table 1), one can find the solution of Eq. (26). Namely,

$$T^* = \exp\left\{-\frac{1}{2}(\sqrt{\Lambda^2 + 4H} - \Lambda)z^*\right\}. \quad (28)$$

Since a fiber draw speed V_2 is much faster than thermal diffusion speed, Eq. (28) can be further simplified as shown below:

$$\left. \begin{aligned} \Lambda^2 &\gg 4H, \\ \text{or} \\ \left(V_2 \frac{d_2}{\kappa}\right)^2 &\gg \frac{16hd_2}{K_c}. \end{aligned} \right\} \quad (29)$$

Hence, it can be reduced to a simpler form,

$$\frac{T - T_0}{T_s - T_0} = \exp\left(-\frac{4hz}{\rho C_p d_2 V_2}\right). \quad (30)$$

In this drawing experiment, h is found to be 7.2×10^{-3} cal/cm²s °C. T_s and T_0 are chosen to be 1600 and 25°C, respectively (Paek and Schroeder, 1981b). The draw speed V_2 in Eq. (30) can be replaced with z/t , where t is the cooling time. Then, the following expression for fiber cooling is obtained:

$$\frac{T - T_0}{T_s - T_0} = \exp\left(-\frac{4ht}{\rho C_p d_2}\right). \quad (31)$$

Numerous calculations and measurements have been made for the cooling rate of fibers produced at a moderate temperature ($\sim 1250^\circ\text{C}$) (Bateson, 1958; Burgmann, 1970). Glicksman (1968) estimated the Nusselt number by using the boundary layer approximation to calculate the time required for cooling from 1750 to 200 and 100°C. Even though all the properties of materials involved are assumed to be independent of temperature, it is difficult to exactly calculate the heat transfer coefficient h around an extremely thin body like a fiber. For example, Arridge and Prior (1964) measured the cooling rate of silica fibers of different diameters drawn at different speeds. The experimental data are given in Fig. 8(a). The heat transfer coefficient h was calculated from these measured data by using Eq. (31) and its value was obtained to be $\sim 7 \times 10^{-3}$ cal/s cm² °C for the high-temperature region ($T > 100^\circ\text{C}$) and 1×10^{-3} cal/s cm² °C for $t > 300$ ms in the region of $T < 100^\circ\text{C}$. Subsequently, these results were also experimentally confirmed by Kyriacou et al. (1990). Vaskopoulos et al. (1992, 1995), and Choudhury et al. (1994) further studied active cooling of optical fibers. In this study, Vaskopoulos et al. (1992, 1995) designed a cooling apparatus for opposing flow to increase the heat transfer coefficient h . Subsequently, Vaskopoulos et al. (1992) found experimentally that the heat transfer effect is approximately fivefold increased simply by changing nitrogen to helium gas. This is believed to be due to the increase in the thermal conductivity approximately six times. Recently, Gossiaux et al. (1998) studied numerically on fiber cooling by using a water-cooled tube in which a gas is introduced to increase heat transfer. The calculated results are shown in Fig. 8(b).

In addition to the method using Eq. (31), there are two other ways of determining the heat transfer coefficient h accurately by using Eq. (30). The methods are called the one-point measurement technique and the two-point measurement technique, which can be applied to both of natural cooling and forced cooling. In the one-point measurement technique the temperature measurement system is placed at the distance L between the furnace and the coating applicator to measure the fiber temperature, while the draw

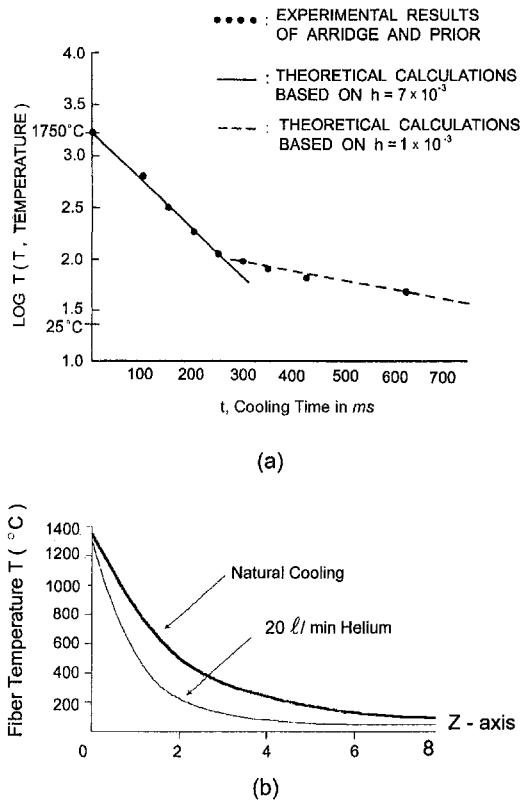


Fig. 8 (a) Comparison of calculated and experimental cooling rates; (b) computed fiber temperature as a function of the cooling conditions (from Gossiaux et al., 1998).

speed is changed (see Fig. 1). For example, when a fiber is drawn at two different speeds of V_2^1 and V_2^2 , the corresponding temperatures, T_1 and T_2 will be recorded by the temperature measurement system. Thus, the substitution of the measured data into Eq. (30) gives the following relation:

$$\frac{T_2 - T_0}{T_1 - T_0} = \exp\left\{-\frac{4hL}{\rho C_p d_2} \left(\frac{1}{V_2^2} - \frac{1}{V_2^1}\right)\right\}. \quad (32)$$

From the above equation, the heat transfer coefficient h can be obtained since all the variables and parameters are known except the coefficient h .

Similarly, the two-point measurement technique can also determine the heat transfer coefficient h by measuring the fiber temperatures T_1 and T_2 at two different locations, L_1 and L_2 , while a fiber is being drawn at a speed of V_1 . The following expression can be obtained from Eq. (30). Namely,

$$\frac{T_1 - T_0}{T_2 - T_0} = \exp\left\{-\frac{4h}{\rho C_p d_2 V_2} (L_1 - L_2)\right\}. \quad (33)$$

Therefore, the heat transfer coefficient h can be found from the above equation. Considering the difficulties of analyzing high-temperature heat transfer and flow problems associated with fiber drawing, we found that the applications of Eq. (30) have led to the convenient and simple ways of determining the heat transfer coefficient h as demonstrated by Eq. (32) and Eq. (33) (Paek and Kurkjian, 1975).

As discussed earlier, let us define the fiber temperature at the entrance of coating applicator as T_c . From Eq. (30), the T_c values for different coating speed V_2 in terms of L are compared with the measured values and shown in Fig. 9. However, at this point it must be noted that a coating speed entirely depends on the temperature T_c . In fact, the value of T_c for polymer coating materials is generally less than 100°C. As mentioned earlier, its value is

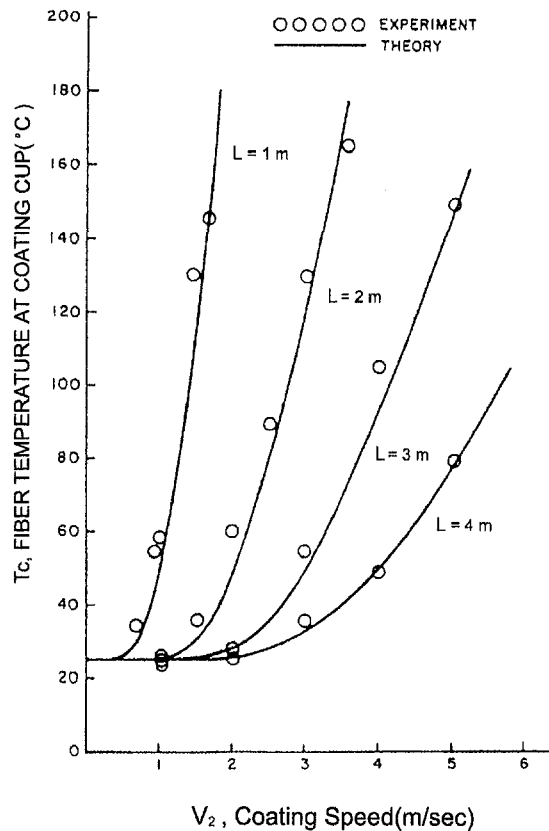


Fig. 9 Fiber temperature T_c versus coating speed V_2 for different locations of coating applicator

taken to be 80°C. Putting $T = T_c$ and $z = L$ into Eq. (30), we can determine the relationship between draw speed V_2 and the distance L . Therefore, the following relation can be obtained:

$$L = \left(\frac{\rho C_p d_2 \Omega}{4h}\right) V_2, \quad (34)$$

where

$$\Omega = \ln\left(\frac{T_s - T_0}{T_c - T_0}\right).$$

The equation shows that distance L is linearly proportional to draw speed. This gives us the important result that the height of a draw tower increases linearly with a draw speed. Thus, this allows us to estimate a draw tower height required for achieving a desired draw speed. Therefore, in designing a high-speed coating system the following considerations must be taken: (1) to provide a sufficient distance between the furnace and coating applicator, and (2) to attach a gas blowing device around the fiber to cool it effectively (Paek and Schroeder, 1979; Vaskopoulos et al., 1992; Gossiaux et al., 1998). Nowadays, it is common to find the draw towers higher than 22 meters in fiber manufacturing plants.

4 Fiber Coating

The application of a thin layer coating on an optical fiber is to provide a protection of its surface and to preserve the pristine state of its strength. Many candidates for coating materials can be grouped into two categories: one includes organic materials; for example, UV curable material (Epoxy Acrylate, Urethane), thermally curable material (silicone), hot melt coating (EVA), etc. The other includes inorganic materials such as, metallic coating, silicon nitride, carbon coating, and so forth. However, all those materials must meet a variety of the stringent coating requirements for

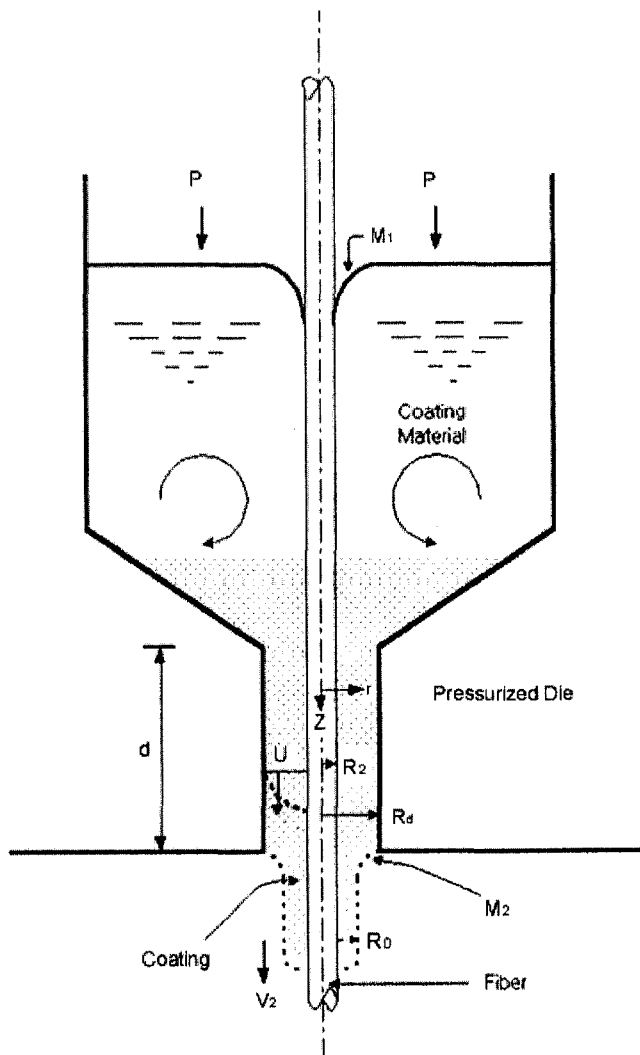


Fig. 10 Schematic diagram of pressurized coating applicator (from Sakaguchi and Kimura, 1985b)

mechanical and optical properties to assure a good performance of coated fibers. To avoid possible contamination and damage on the fiber surface the coating apparatus is in-line with the drawing system so that the fiber can be immediately coated while it is being drawn. Since the UV curable polymer materials are found to be the choice of high-speed coating among different polymerization schemes, nowadays they are exclusively used in fiber manufacturing. In implementing a high-speed fiber coating technology, there are two fundamental drawbacks that limit the draw speed and affect fiber strength as well. One is the fiber cooling rate problem. The other is the high shear rate problem as a draw speed increases. Therefore, this section will only focus on the polymer coating technology practiced in the fiber production.

1 Coating Mechanics. Figure 10 shows a schematic diagram of a pressurized coating applicator. In the pressurized coating die with a length d , the coating material velocity u along the z direction can be expressed as (Sakaguchi and Kimura, 1985b),

$$\frac{\partial^2 u}{\partial r^2} + \frac{1}{r} \frac{\partial u}{\partial r} = \frac{1}{\mu} \frac{\partial p}{\partial z}, \quad (35)$$

where μ is the viscosity of a coating material and p the pressure in the die. The boundary conditions are

$$\left. \begin{aligned} u &= V_2, & \text{at } r &= R_2 \\ u &= 0, & \text{at } r &= R_d \end{aligned} \right\}, \quad (36)$$

where $2R_2$ and $2R_d$ are the diameters of the fiber and die, respectively. From the above equation, the pressure gradient can be obtained. Namely,

$$\frac{\partial p}{\partial z} = \frac{4\mu V_2}{R_2^2 - R_d^2 - 2R_2^2 \ln \frac{R_2}{R_d}} \quad (37)$$

When the pressure gradient is replaced by $\Delta p/d$, it can be noticed that the pressure is directly related to the viscosity and the draw speed. Therefore, for a given viscosity at a set temperature, the optimum pressure can be chosen to coat a fiber at a desired speed. However, we notice that a high shear force damages the fiber surface, resulting in a weak strength of the fiber. To avoid this situation, the coating material is normally heated to reduce its viscosity as mentioned earlier.

From Eqs. (34) and (35) the solution u can be obtained as

$$u = \frac{V_2}{\left(R_2^2 - R_d^2 - 2R_2^2 \ln \frac{R_2}{R_d} \right)} \left(r^2 - R_d^2 - 2R_2^2 \ln \frac{r}{R_d} \right). \quad (38)$$

Therefore, the flow rate Q , which can be obtained from the expression $2\pi \int_{R_2}^{R_d} u r dr$ is needed to determine the coated fiber diameter $2R_0$. From the conservation of mass, the coated fiber diameter $2R_0$ is found to be

$$R_0^2 = \frac{(R_2^2 - R_d^2)^2}{2 \left(R_2^2 - R_d^2 - 2R_2^2 \ln \frac{R_2}{R_d} \right)}. \quad (39)$$

This equation shows that when the pressure is optimized the coated fiber diameter only depends on the sizes of fiber and die (Sakaguchi and Kimura, 1985). The coating thickness defined by $H_\infty = (R_0 - R_2)$ is nominally 50 μm , which must be maintained uniformly on the fiber surface regardless of fiber draw speed. Kobayashi et al. (1991) developed high-speed UV curable resins that were successfully applied for coating a fiber at a rate of 21.7 m/s (1300 m/min). These coated fibers demonstrated the satisfactory results that met the stringent requirements for the mechanical properties and the transmission characteristics. Koizawa et al. (1995) studied the mechanism of the coating diameter decrease due to insufficient cooling, while the pressure was not optimized. The two-layer coating model provides useful information on a concentric geometry of two different viscosities around a fiber moving at a high speed.

2 Shear Force in Coating Application. In coating, it is always observed that two menisci are formed. One is at the free surface where the fiber enters, and the other at the fiber exiting side of the coating die. They are designated by M_1 and M_2 , as shown in Fig. 10. When the fiber drawing speed exceeds a certain point, the meniscus (M_1) at the fiber entrance side collapses due to the T_c rise beyond the tolerable point. The meniscus collapse causes no wetting on the fiber surface, consequently inhibiting fiber coating. The second meniscus (M_2) formed at the exiting side also controls the uniformity of a coating. The stability of the lower meniscus is due largely to the shear induced within the applicator. The applicator die of length d , where the coating thickness is controlled has a thin tube shape with a diameter ($2R_d$). In this case, the flow motion in the coating die is well described by Chida et al. (1982). When the dimensionless variable ζ defined by $(r - R_2)/(R_d - R_2)$, the profiles of normalized velocity $u^* = u/V_2$ are similar along the axis. In the above the r refers to the radial distance measured from the fiber axis and R_2 is the fiber radius. The shear rate $\dot{\gamma}$ acting on the fiber surface can be expressed as (see Fig. 10)

$$\dot{\gamma} = \frac{\partial u}{\partial r} \Big|_{R_2} = \frac{\partial u^*}{\partial \zeta} \Big|_0 \frac{V_2}{(R_d - R_2)}. \quad (40)$$

The value of $\partial u^*/\partial \zeta|_0$ is constant for a given pressure p and designated as $B(p)$.

From Eq. (40), it can be found that the shear rate induced during high-speed coating is also linearly proportional to the fiber draw speed, V_2 . The shear stress τ_{rz} is given by

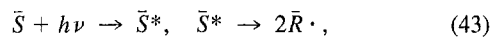
$$\tau_{rz} = \mu \dot{\gamma}. \quad (41)$$

Thus, the pulling tension F_c in coating can be calculated by integrating the shear stress τ_{rz} over the fiber surface ($2\pi R_2 d$) in the die. Finally, the coating tension F_c can be expressed by

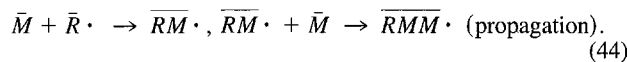
$$F_c = \frac{2\pi R_2 \mu B(p) V_2 d}{(R_d - R_2)}. \quad (42)$$

The above equation explicitly shows the functional relationships among the parameters and variables, helping in understanding the effects of the parameters such as coating speed, fiber radius, viscosity of coating material, and coating die dimensions on the tension F_c (Paek and Schroeder, 1981b). As the draw tension F is a linear dependence on the draw speed, so the coating tension F_c varies linearly with the draw speed. In high-speed coating, this shear must be minimized to produce a desirable coating. According to Eq. (42) there are two ways to lower the value of F_c . One is simply to shorten the die length d . The other is to heat the coating material to effectively reduce its viscosity. However, the heating temperature is normally limited to 60°C because of the gelation problem of polymer. At 50°C the viscosity becomes 9 poises, while it is 60 poises at 25°C. Therefore, the total pulling tension, F_T in coating is the sum of F and F_c . Sakaguchi and Kimura (1985a) demonstrated successfully high-speed coating using the pressurized applicator shown in Fig. 10. They achieved a coating speed as high as 20 m/s with a pressure of $P = 7 \text{ kg/cm}^2$ and $F_T = 120 \text{ g}$. The coating application parameters used were $2R_2 = 125 \text{ }\mu\text{m}$, $2R_d = 0.35 \text{ mm}$, die length $d = 0.2 \text{ mm}$ and $\mu(T) = 9 \text{ poises}$.

3 Photopolymerization of Coating Material. In a prepolymer solution mixed with a photoinitiator, polymerization process can be described in three steps: (1) initiation, (2) propagation, and (3) termination. The first step is that the initiator (\bar{S}) absorbs the photon ($h\nu$) and a sufficient absorption cleaves the chemical bonds of molecules to form the free radicals (Walker et al., 1970; Paek and Schroeder, 1981a; Kokubun et al., 1989). The excitation and fragmentation processes are described in the following way.



where $\bar{R}\cdot$ refers to the free radical. In the subsequent step, these radicals react rapidly with a monomer \bar{M} , and progressively grow the chains to cross-link into the polymer network (Ferington, 1959).



This propagation continues until it is terminated by hydrogen. However, the required UV power is determined by the initial step described by Eq. (43). Let us consider a case of fiber drawing with a speed of V_2 (cm/s). The fiber coated to a thickness by passing through a coating die is immediately cured by UV radiation. The coating thickness H_∞ is defined by $H_\infty = (R_0 - R_2)$ where $2R_0$ is the coated fiber diameter. For a photoinitiator having an activa-

Table 2 Data of photoinitiator (Irgacure 651 from Paek and Schroeder, 1981)

Activation energy ΔE_c (kcal/mole)	70
Density ρ_c (g/cm ³)	1.2
Molecular weight M_w	256
Molar absorption coefficient α_λ (liter/mole cm) at $\lambda = 340 \text{ nm}$	320

Table 3 Radiated power in the effective spectral range (300–400 nm) of 200 w/in. medium pressure mercury arc lamp

Wavelength λ (nm)	Unit Length Radiation P_λ (w/cm)
296.7	0.7874
302.5	1.2598
313.0	2.1654
334.1	0.5512
365.0	4.7638
404.5	2.4015

tion energy ΔE_c (kcal/mole) and molar concentration $[c]$, the required UV power P_c (watt) can be formulated as

$$P_c = \pi \Delta E_c \cdot [c] (R_0^2 - R_2^2) \cdot V_2. \quad (45)$$

The concentration level of photoinitiator added to the prepolymer solution is 3 ~ 5 percent of which 4 percent concentration corresponds to $\sim 2 \times 10^{-4} \text{ mole/cm}^3$ (see Table 2). Thus, the substitution of $2R_0 = 225 \text{ }\mu\text{m}$ and $2R_2 = 125 \text{ }\mu\text{m}$ with $[c]$ and ΔE_c into Eq. (45) gives the following result:

$$P_c = 0.016 V_2. \quad (46)$$

For example, in case of a draw speed of 100 cm/s, the power is calculated to be 1.6 W. However, it must be noted that Eq. (46) is formulated based on the assumption that all the power supplied to the lamp is converted to UV light and then totally absorbed in the coating material. In a real system, there will be the component losses of the system, for example, in spectral power conversion of the lamp, in the reflector unit itself, etc. The total system performance can be expressed in terms of the overall efficiency and will ultimately determine the required power W such as $W = P_c/\epsilon_i$. Therefore, the estimation of overall efficiency ϵ_i is the key to the power calculation. The efficiency is largely dependent on the design of a system, and will be determined by the performance of the unit and chemical characteristics of the prepolymer. The curing unit consists of a mercury arc lamp and a reflector with efficiencies ϵ_1 and ϵ_2 , respectively. Defining the absorptivity of the prepolymer solution, ϵ_3 in percent, one can write $\epsilon_i = \epsilon_1 \epsilon_2 \epsilon_3$. Hence, the evaluation of each efficiency of ϵ_1 , ϵ_2 , and ϵ_3 is required to determine the overall efficiency ϵ_i of the system. The calculation is as follows.

(a) *Lamp Efficiency ϵ_1 .* The medium to high-pressure mercury arc lamps are the most common energy sources for photochemical reactions, but their emission spectra are not continuous. The typical spectral distribution of the power per unit length, P_λ (W/cm) of the medium pressure lamp used in the experiment, is given in Table 3. The absorption of the photoinitiator is most pronounced in the range of 300 to 400 nm. The power outside this range will not contribute to producing the free radicals. Therefore, ϵ_1 can be expressed by

$$\epsilon_1 = \frac{\sum P_\lambda}{P_0}, \quad (47)$$

where P_0 is the rated lamp power per unit length and equal to 78.74 W/cm (200 W/in), and the summation in the above expression runs from 300 nm to 400 nm, yielding $\sim 12 \text{ w/cm}$. Hence, the value of ϵ_1 is calculated to be ~ 0.15 .

(b) *Reflector Efficiency ϵ_2 .* The reflector chamber is composed of two or four cylindroids (elliptic cylinder) of which the efficiency ϵ_2 can be broken into two parts, based on whether the rays are focused or not. As shown in Fig. 11, the UV flux within an angle β is diverging toward the second focal plane. The energy density in the neighborhood of the focal point is much smaller compared to that of the focused beam. Thus, the contribution of the nonfocusing beam to the prepolymer coating on a fiber will be of

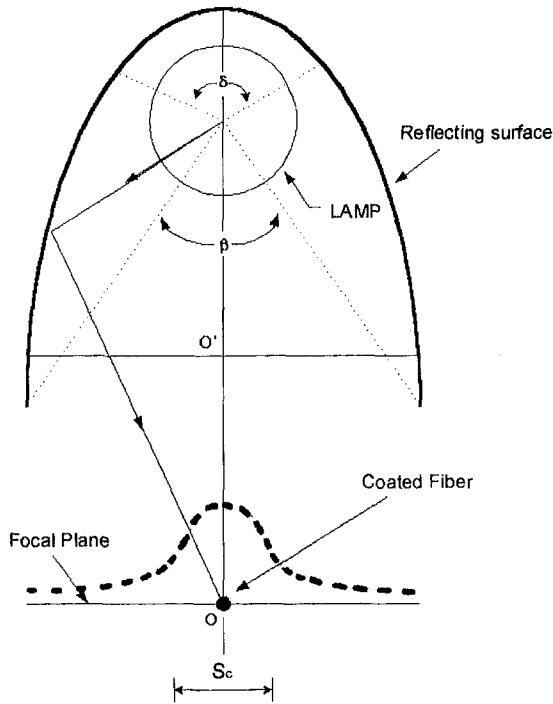


Fig. 11 Cross-sectioned cylindroidal reflector and imaged spot size in the focal plane

little significance. On the other hand, the rays within the angle δ behind the lamp, blocked by its envelope will not contribute to the polymerization process at all. The contributing UV light will be the rays reflected from the portion of reflector surface covered by an angle of $[2\pi - (\beta + \delta)]$. When the effectiveness η_1 of a reflector is defined as the ratio of the focusing rays to the UV light leaving the lamp, it can be written as

$$\eta_1 = \frac{2\pi - (\beta + \delta)}{2\pi} \quad (48)$$

Since the angle $(\beta + \delta)$ is close to π , the value of η_1 is equal to ~ 0.5 .

As shown in Fig. 11, the reflected UV light is focusing to a spot size S_c in the focal plane, where the coated fiber is to be cured by passing through. The spot size is only determined by the lamp diameter and reflector quality. The effective ratio η_2 defined by a ratio of the coated fiber diameter $2R_0$ to the focused spot S_c is expressed by $\eta_2 = 2R_0/S_c$. The value of S_c is determined by measuring the light intensity distribution along the focal plane. For this measurement, an IL 730A digital actinic radiometer and a 1-mm diameter pinhole detector were used with a UV bandpass filter. The value of S_c was measured to be ~ 1.2 cm and η_2 is ~ 0.02 for a $225 \mu\text{m}$ coated fiber. Therefore, the efficiency of the reflector, ϵ_2 is given by $\epsilon_2 = \eta_1\eta_2$ and equal to $\sim 10^{-2}$.

(c) Absorptivity ϵ_3 . The UV radiation incident on an absorbing media decreases exponentially when passing through its thickness. The absorption ϵ_3 of light depends on the molar concentration $[c]$ of a photoinitiator molar absorption coefficient α_λ and coating thickness H_∞ . From the Beer's law, the absorptivity can be written as

$$\epsilon_3 = 1 - \exp\{-\alpha_\lambda[c]l\}, \quad (49)$$

where $l = 2H_\infty$ and $H_\infty = 50 \mu\text{m}$. The molar absorption coefficient α_λ is taken to be 320 liter/mole \cdot cm at the wavelength of 340 nm (Table 2). The four percent initiator by weight in the prepolymer solution amounts to $\sim 2 \times 10^{-4}$ mole/cm³. Thus, the absorptivity ϵ_3 is calculated to be ~ 0.5 for $l = 100 \mu\text{m}$.

Since the values of ϵ_1 , ϵ_2 , and ϵ_3 are known, the overall efficiency ϵ_t can be computed simply by multiplying together.

$$\epsilon_t = 7.5 \times 10^{-4}. \quad (50)$$

Thus, the total required power W can be finally expressed in terms of the draw speed V_2 .

$$W = 21V_2 \quad (51)$$

The fiber coating speed V_2 in the unit of cm/s yields W in watts. Consequently, when considering a coating speed in the range of 4 – 5 m/s, the power required to cure polymer material at that speed will be ~ 10 kW.

5 Discussion

It should be mentioned that fiber cooling and reheating for annealing influence the optical and mechanical characteristics of a fiber such as transmission loss and fiber strength. The lightguiding fiber consists of the core and cladding that are two different kinds of materials. To produce a low-loss and high-strength fiber, it is necessary to fully investigate the draw mechanics and to quantitatively identify the effects on the fiber performance. For example, the effect of draw tension on the fiber strength is directly related to the compositions of the core and cladding materials (Krohn and Cooper, 1969). Certain combinations of the composition materials for core and cladding can change the state of axial component of the residual stresses in the cladding from the tensile stress to compressive stress or vice versa (Paek and Kurkjian, 1975). Many investigators (Anderegg, 1939; Moley et al., 1964) studied the tensile strength of fused silica fibers as a function of fiber diameter. They showed that the finer fibers tend to give higher strength than larger diameter fibers. In absence of gas blowing, the cooling rate is basically determined by the fiber diameter. First, let us examine the effect of fiber cooling rate on the fiber strength with a low draw tension (low draw speed). According to Anderson (1958) a quenching time estimated to be of order of the Maxwell relaxation time $\tau = \eta/G$ inhibits the formation of flaw in glass fibers, where η is the viscosity of glass and G the shear modulus. This implies higher strength value for the fiber than that for bulk glass. Hillig (1961) measured the ultimate strength at liquid nitrogen temperature (-196°C) to be $140,000 \text{ kg/cm}^2$ (2 million psi). In air and at room temperature the maximum strength is approximately $70,000 \text{ kg/cm}^2$ (1 million psi). Griffith (1920) also estimated the theoretical strength of a silica fiber based on the intrinsic bonding forces of molecular structure of a solid. He reached a conclusion that $0.1E$ is a good estimate of a reasonable value for the theoretical limit of the ultimate strength. Here, E is the Young's modulus of silica glass, which is $825,000 \text{ kg/cm}^2$. In fact, the average strength of manufactured optical fibers falls far below this figure. We believe this is primarily due to surface flaws, internal defects, inclusions, or minute bubbles, etc.

Secondly, let us discuss the effect of fiber draw speed (draw tension) on the fiber strength in conjunction with the cooling rate. It was mentioned earlier that as the draw speed increases, the draw tension also increases in a linear fashion. Therefore, in the drawing process stresses are induced in the composite structure of a fiber, which will partially remain as residual stresses when the fiber cools down to room temperature. The residual stresses ultimately influence the fiber strength (Maklad et al., 1979). For example, the compressive state of the residual stress in the fiber cladding is considered to be favorable since it helps prevent a flaw or defect from growing. However, it is worthy of noting that the state of compression and tension of the residual stresses depends upon the composition of fiber structure and the draw conditions (Mohr et al., 1980; Kurkjian and Paek, 1978). Bouten et al. (1989) investigated the strength of fibers with different residual tensile stresses at the surface in order to predict the lifetime of fibers. The strength and lifetime experiment determines the fatigue coefficient that is a key parameter in predicting the survival time of a fiber under a certain

applied tension, when a fiber cable is installed for communications applications.

In addition, it is also important to note that the optical fiber loss is partly influenced by the drawing conditions. Hanawa (1987) studied the optical characteristics of silica-core with fluorine-doped silica cladding to clarify the effect of the drawing conditions on the optical transmission loss. They established the relationship between the draw-induced excess loss at the wavelength of 1.55 μm . The excess loss in silica core fibers decreases rapidly with increasing drawing temperature, reaching its minimum value near 2270°K. But the loss in germania doped silica core fiber varies with drawing temperature. In this case, the increased loss is particularly pronounced in the long wavelength. This indicates that the increase in optical fiber loss depends on the draw tension that is determined by the furnace temperature, draw speed, and preform diameter.

Polymer coatings may not be impervious to moisture (Wang et al., 1979). The moisture that permeates through the polymer coating degrades the fiber strength under a tension over a period of time due to fatigue. Considerable efforts have been given to many different types of hermetic coatings. Particularly, metallic coatings such as copper, tin, silver, aluminum, etc. are attractive for hermetically sealing glass surfaces. An ideal hermetic coating material should be easily applied at a high draw speed and should not introduce any additional optical loss. Metallic coatings have unique advantages: (1) high fatigue parameter, (2) higher strength, (3) high-temperature resistance and (4) solderability (Bubel et al., 1989; Biswas et al., 1995; Simkins et al., 1995; Bogtyrjov et al., 1996). Those advantages of metallic coatings over polymer-based coating are attractive to fiber manufacturers for the unique applications of fiber-based optical devices and components.

6 Summary

We have discussed the calculation of the neck-down shape of preform in the draw furnace and its temperature response, using one-dimensional scheme of the radiative heat conduction in a silica-based glass (transparent material). Those results are applicable to a small diameter silica preform. For a large size preform, it is evident that the formulation of a three-dimensional coupled equations of viscoelastic flow and radiative heat conduction in the neck-down region is needed. The implementation of the high-speed drawing (>20 m/s) for a large size preform has always faced the high draw tension problem. Regardless of how fast a fiber is to be drawn, it is desirable that the draw tension should not exceed 150 g in order to achieve continuous pulling without break during fiber draw operation (Sakaguchi, 1984). Therefore, the tension at 1 m/s draw speed should be as low as possible, perhaps, less than 4 g. To achieve this low tension the viscosity of the silica glass must be uniformly low across the diameter of the preform in the furnace. Thus, fiber manufacturers will be searching a new furnace for a high-volume production.

As explained previously, the high-speed coating requires the installation of a tall draw tower with a helium gas blowing system. The next concern is how to coat a polymer material on the fiber without damaging the glass surface. To minimize the shear force occurring in high-speed coating, many pressurized coating applicators with heating element have been investigated. In addition, it must be pointed out that two-layer coating is applied to reduce the microbending loss that is an added loss due to the stiffness of the coating (Bouten et al., 1989). The inner layer coating is chosen to be a soft material to eliminate the microbending loss while the outer coating is a stiff material needed to protect the fiber from external damage. Finally, the coated fibers should meet the stringent reliability requirements such as strength, fatigue, aging, uniformity, concentricity, durability, etc.

Acknowledgment

This work was supported in part by the Korea Science and Engineering Foundation (KOSEF) through the Ultrafast Fiber-Optic Networks Research Center (UFON) at Kwangju Institute of Science and Technology.

References

- Anderegg, F. O., 1939, "Strength of Glass Fibers," *Industrial Engineering Chemistry*, Vol. 31, pp. 290–298.
- Anderson, O. L., 1958, "Cooling Time of Strong Glass Fibers," *Journal of Applied Physics*, Vol. 29, No. 1, pp. 9–12.
- Arridge, R. G. C., and Prior, K., 1964, "Cooling Time of Silica Fibers," *Nature*, Vol. 203, pp. 386–387.
- Bacon, J. F., Hasapis, A. A., and Wholly, Jr., J. W., 1960, "Viscosity and Density of Molten Silica and High Silica Content Glass," *Physics and Chemistry of Glasses*, Vol. 1, No. 3, pp. 90–98.
- Bateson, S., 1958, "Critical Study of the Optical and Mechanical Properties of Glass Fibers," *Journal of Applied Physics*, Vol. 29, No. 1, pp. 13–21.
- Biswas, D. R., Kurkjian, C. R., and Yuce, H. H., 1995, "Hermetic Coating for Optical Glass Fibers," *Int. Wire & Cable Symposium Proceedings*, pp. 317–324.
- Bogatyryov, V. A., Cheremisin, I. I., Dianov, E. M., Golant, K. M., and Tomashuk, A. L., 1996, "Super-High-Strength Metal-Coated Low-Hydroxyl Low-Chlorine All-Silica Optical Fibers," *IEEE Trans. Nuclear Science*, Vol. 43, No. 3, pp. 1057–1060.
- Bouten, P. C. P., Broer, D. J., Jochem, C. M. G., Meeuwssen, T. P. M., and Timmermans, H. J. M., 1989a, "Doubly Coated Optical Fibers with a Low Sensitivity to Temperature and Microbending," *Journal of Lightwave Technology*, Vol. 7, No. 4, pp. 680–686.
- Bouten, P. C. P., Hermann, W., Jochem, C. M. G., and Wiechert, D. U., 1989b, "Drawing Influence on the Lifetime of Optical Fibers," *IEEE Journal of Lightwave Technology*, Vol. 7, No. 3, pp. 555–559.
- Bubel, G. M., Krause, J. T., Bickta, B. J., and Ku, R. T., 1989, "Mechanical Reliability of Metallized Optical Fiber for Hermetic Terminations," *IEEE Journal of Lightwave Technology*, Vol. 7, No. 10, pp. 1488–1493.
- Burgmann, A., 1970, "Liquid Glass Jets in the Forming of Continuous Glass Fibers," *Glass Technology*, Vol. 11, No. 4, pp. 110–116.
- Chida, K., Sakaguchi, S., Wagatsuma, M., and Kimura, T., 1982, "High-Speed Coating of Optical Fibers With Thermally Curable Silicon Resin Using a Pressure Die," *Electron Letters*, Vol. 18, No. 16, pp. 713–715.
- Choudhury, S. R., Jaluria, Y., Vaskopoulos, T., and Polymeropoulos, C. E., 1994, "Forced Convective Cooling of Optical Fiber During Drawing Process," *ASME JOURNAL OF HEAT TRANSFER*, Vol. 116, pp. 790–794.
- Choudhury, S. R., Jaluria, Y., Lee, S. H.-K., 1995, "Generation of Neck-Down Profile for Furnace Drawing of Optical Fiber," National Heat transfer Conference, ASME HTD-Vol. 306, pp. 23–32.
- Davies, J., and Simpson, P., 1979, *Induction Heating Handbook*, McGraw-Hill, New York.
- Ferington, T., 1959, "Kinetics of Polymer Formation by Free Radical Mechanism," *Vol. 36, No. 4*, pp. 174–181.
- Gardon, R., 1956, "The Emissivity of Transparent Materials," *Journal of American Ceramic Society*, Vol. 39, No. 8, pp. 278–289.
- Glicksman, L. G., 1968, "The Cooling of Glass Fibers," *Glass Technology*, Vol. 9, No. 5, pp. 131–138.
- Gossiaux, M.-G., Bourhis, J.-F., Orce, G., 1998, "Numerical Simulation of Optical Fiber Cooling During the Fiber Drawing Process," *Int. Wire and Cable Symposium Proceedings 1998*, pp. 81–84.
- Griffith, A. A., 1920, "The Phenomena of Rapture and Flow in Solids," *Philosophical Transactions of Royal Society, London*, Vol. A221, pp. 163–198.
- Hanafusa, H., Hibino, Y., and Yamamoto, F., 1985, "Formation Mechanism of Drawing-Induced E' Centers in Silica Optical Fibers," *Journal of Applied Physics*, Vol. 58, No. 3, pp. 1356–1361.
- Hanawa, F., Hibino, Y., Shimizu, M., Sudo, H., and Horiguchi, M., 1987, "Influences of the Drawing Conditions on Optical Characteristics in Undoped-Silica-Core Single-Mode Fibers," *Optics Letters*, Vol. 12, pp. 617–618.
- Hillig, W. B., 1961, "Strength of Bulk Fused Quartz," *Journal of Applied Physics*, Vol. 32, pp. 741–741.
- Issa, J., Yin, Z., Polymeropoulos, C. E., and Jaluria, Y., 1996, "Temperature Distribution in an Optical Fiber Draw Tower Furnace," *Journal of Material Processing & Manufacturing Science*, Vol. 4, pp. 221–232.
- Kalish, D., and Tariyal, B. K., 1978, "Static and Dynamic Fatigue of a Polymer-Coated Fused Silica Optical Fiber," *Journal of American Ceramic Society*, Vol. 61, No. 11–12, pp. 518–523.
- Kaminski, D. A., 1995, "Thermal Transport in Optical Fiber Manufacturing," *Proceedings of the First International Symposium on Radiation Transfer*, pp. 667–681.
- Kapron, F. P., Keck, D. B., and Maurer, R. D., 1970, "Radiation Losses in Glass Optical Waveguide," *Applied Physics Letters*, Vol. 17, pp. 423–425.
- Koizawa, H., Orita, N., Kamiya, T., 1995, "Study of Coating Diameter at High Speed Drawing of Optical Fiber With UV Curable Resin," *Tech. Digest of IOOC'95, FA1-2*, Vol. 4, pp. 4–5.
- Kobayashi, K., Tsurusaki, K., Sato, Y., and Araki, S., 1991, "High-Speed Coating of Optical Fibers With UV Curable Resins," *Int. Wire and Cable Symposium Proceedings 1991*, pp. 126–133.
- Kokubun, T., Katsuyama, Y., Hogari, K., and Hatano, S., 1989, "Resin Selection

and High-Speed Coating of Optical Fibers With UV-Curable Materials," *IEEE Journal of Lightwave Technology*, Vol. 7, No. 5, pp. 824–828.

Krohn, D. A., and Cooper, A. R., 1969, "Strengthening of Glass Fibers; I. Cladding," *Journal of American Ceramic Society*, Vol. 52, No. 12, pp. 661–664.

Kurkjian, C. R., and Paek, U. C., 1978, "Effect of Drawing Tension on Residual Stresses in Clad Glass Fibers," *Journal of American Ceramic Society*, Vol. 61, No. 3–4, pp. 137–138.

Lee, S. H.-K., and Jaluria, Y., 1995, "The Effect of Geometry and Temperature Variations on the Radiative Transport During Optical Fiber Drawing," *Journal of Material Processing & Manufacturing Science*, Vol. 3, pp. 317–331.

Lee, S. H.-K., and Jaluria, Y., 1996, "Effects of Variable Properties and Viscous Dissipation During Optical Fiber Drawing," *ASME JOURNAL OF HEAT TRANSFER*, Vol. 118, pp. 350–358.

Maklad, M. S., Asam, A. R., and Akers, F. I., 1979, "Recent Advances in High Strength Optical Fibers Having Surface Compression," *Int. Wire and Cable Symposium Proceedings 1979*, pp. 340–343.

Mohr, R. K., El-Bayoumi, O. H., and Ingel, R. P., 1980, "Static Fatigue in Glass Optical Fibers Having Surface Compression," *American Ceramic Society Bulletin*, Vol. 59, No. 11, pp. 1145–1150.

Moley, J. G., Andrew, P. A., and Whitney, I., 1964, "Strength of Fused Silica," *Physical Chemistry and Glass*, Vol. 5, pp. 1–10.

Mulpur, A., and Thompson, C., 1996, "Nonlinear Control of Optical Fiber Diameter Variation," *IEEE Control System Technology*, Vol. 4, No. 2, pp. 152–162.

Paek, U. C., and Kurkjian, C. R., 1975, "Calculation of Cooling Rate and Induced Stresses in Drawing of Optical Fibers," *Journal of American Ceramic Society*, Vol. 58, No. 7–8, pp. 330–335.

Paek, U. C., and Runk, R. B., 1978, "Physical Behavior of the Neck-Down Region during Furnace Drawing of Silica Fibers," *Journal of Applied Physics*, Vol. 49, No. 8, pp. 4417–4422.

Paek, U. C., and Schroeder, C. M., 1979, "Forced Convective Cooling of Optical Fibers in High-Speed Coating," *Journal of Applied Physics*, Vol. 50, No. 10, pp. 6144–6148.

Paek, U. C., and Schroeder, C. M., 1981a, "Calculation of Photopolymerization Energy Required for Optical Fiber Coating," *Applied Optics*, Vol. 20, No. 7, pp. 1230–1233.

Paek, U. C., and Schroeder, C. M., 1981b, "High Speed Coating of Optical Fibers With UV Curable Materials at a Rate of Greater than 5 m/s," *Applied Optics*, Vol. 20, No. 23, pp. 4028–4034.

Paek, U. C., and Schroeder, C. M., 1988, "Fiber Drawing From 7.5 cm Diameter Preform at High Speed," *Technical Digest of OFC/FS'88*, New Orleans, LA, Paper PD-3.

Petrov, V. A., and Reznik, V. Yu., 1973, "The Effect of Thickness and Temperature Upon the Total Emissivity of Quartz Glass," *Proceedings of 6th Symposium on Thermophysical Properties*, pp. 301–304.

Rajala, M., Asikkala, K., Maekinen, M., Tuormala, T., and Peltoluhta, E., 1998, "Combination Furnace for Drawing Large Optical Fiber Preforms at High Speed," *Int. Wire and Cable Symposium Proceedings 1998*, pp. 483–488.

Runk, R. B., 1977, "A Zirconia Furnace for Precision Silica Waveguides," *Digest of Topical Meeting on Optical Fiber Transmission*, Williamsburg, VA, Paper TuB5-1.

Sakaguchi, S., 1984, "Drawing of High-Strength Long-Length Optical Fibers for Submarine Cables," *IEEE Journal of Lightwave Technology*, Vol. LT-2, No. 6, pp. 808–815.

Sakaguchi, S., and Kimura, T., 1985a, "A 1200 m/min Speed Drawing of Optical Fibers With Pressurized Coating," *Technical Digest of OFC'85*, San Diego, CA, Paper MG2.

Sakaguchi, S., and Kimura, T., 1985b, "High-Speed Drawing of Optical Fibers With Pressurized Coating," *IEEE Journal of Lightwave Technology*, Vol. LT-3, No. 3, pp. 669–673.

Scherer, G., 1979, "Thermal Stresses in a Cylinder: Application to Optical Waveguide Blanks," *Journal of Non-Crystalline Solids*, Vol. 34, pp. 223–238.

Scherer, G., 1980, "Stress-Induced Index Profile Distortion in Optical Waveguides," *Applied Optics*, Vol. 19, No. 12, pp. 2000–2006.

Siegel, R., and Howell, J. R., 1972, *Thermal Radiation Heat Transfer*, McGraw-Hill, New York.

Simkins, P. G., Kurkjian, C. R., and Schroeder, 1995, "Aluminum-Coated Silica Fibers: Strength and Solderability," *Electronics Letters*, Vol. 31, No. 9, pp. 747–749.

Smithgall, D. H., 1979, "Application of Optimization Theory to the Control of the Optical Fiber Drawing Process," *Bell System Technical Journal*, Vol. 58, pp. 1425–1435.

Vaidya, D. S., Mihalacopoulos, G. D., 1998, "Characterization of Meltdown Profile During Fiber Draw," *Int. Wire and Cable Symposium Proceedings 1998*, pp. 73–80.

Vaskopoulos, T., Polymeropoulos, C. E., and Zebib, A., 1992, "Heat Transfer From Optical Fiber During the Draw Process," *Int. Conference of Transport Phenomena in Processing*, Honolulu, HI, pp. 1–10.

Vaskopoulos, T., Polymeropoulos, C. E., and Zebib, A., 1995, "Cooling of Optical Fiber in Aiding and Opposing Forced Gas Flow," *Int. J. Heat Mass Transfer*, Vol. 18, No. 11, pp. 1933–1944.

Walker, P., Webers, V. J., and Thommes, G. A., 1970, "Photopolymerizable Reproduction Systems—Chemistry and Applications," *Journal of Photographic Science*, Vol. 18, pp. 150–157.

Wang, T. T., Varzirani, H. N., Schonhorn, H., and Zupko, H. M., 1979, "Effects of Water and Moisture on Strength of Optical Glass (Silica) Fibers Coated With a UV-Cured Epoxy Acrylate," *Journal of Applied Polymer Science*, Vol. 23, pp. 887–892.

Yin, Z., and Jaluria, Y., 1998, "Thermal Transport and Material Flow in High Speed Optical Fiber Drawing," *ASME JOURNAL OF HEAT TRANSFER*, to appear.

APPENDIX

The explicit expression of Q_{2-1} in Eq. (20) is obtained from the shape factor between two surfaces, 1 and 2. From Fig. 12, drawing a line to connect two differential dA_1 and dA_2 whose distance is denoted by S yields the angles θ_1 and θ_2 with respect to the unit vector \bar{n}_1 and \bar{n}_2 normal to surface 1 and 2, respectively. dq_{2-1} defined as a radiative flux leaving the differential area dA_2 that arrives at dA_1 , can be expressed by

$$dq_{2-1} = \epsilon(z)J(\xi)dA_2dF_{dA_2-dA_1}, \quad (A1)$$

where $J(\xi)$ is the radiative flux along surface 2.

The differential shape factor is given by

$$dF_{dA_2-dA_1} = \frac{\cos \theta_2 \cos \theta_1 dA_1}{\pi S^2}. \quad (A2)$$

Now, it is necessary to perform an integration over area A_2 to obtain the total contribution due to surface 2. Therefore, the expression for Q_{2-1} is written as

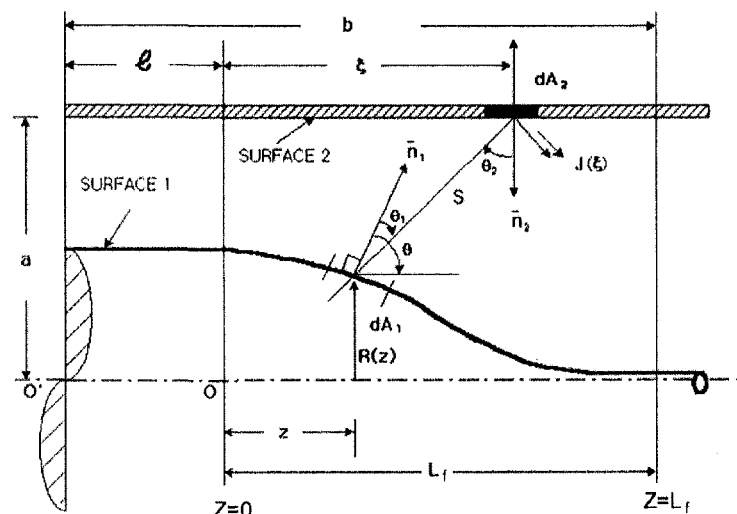


Fig. 12 Coordinate system of the elongated preform in the furnace and geometric relation between preform surface 1 and susceptor surface 2

$$Q_{2-1} = \epsilon(z) \int_{A_2} \frac{J(\xi) \cos \theta_1 \cos \theta_2}{\pi S^2} dA_2. \quad (\text{A3})$$

From the geometric relation among the angles θ_1 , θ_2 , and θ , Eq. (A3) can be rewritten as

$$Q_{2-1} = \frac{2\epsilon(z)(a-R)a}{(1+R'^2)^{1/2}} \int_{-1}^{b-1} \frac{J(\xi)[-R'(\xi-z) + (a-R)]d\xi}{[(\xi-z)^2 + (a-R)^2]^2}, \quad (\text{A4})$$

where

$$S^2 = (\xi - z)^2 + (a - R)^2, \quad \cos \theta_1 = \cos \left[\theta - \left(\frac{1}{2} \pi - \theta_2 \right) \right],$$

$$\cos \theta_2 = \frac{(a - R)}{S}, \quad \sin \theta_2 = \frac{(\xi - z)}{S},$$

$$\cos \theta = -\frac{R'}{(1 + R'^2)^{1/2}}, \quad \sin \theta = \frac{1}{(1 + R'^2)^{1/2}}.$$

From Eq. (A4), Q_{2-1} can be determined when the flux $J(\xi)$ is provided.

Heat Transfer Enhancement and Vortex Flow Structure Over a Heated Cylinder Oscillating in the Crossflow Direction

C. Gau
Professor

J. M. Wu
Graduate Student

C. Y. Liang
Graduate Student

Institute of Aeronautics and Astronautics,
National Cheng Kung University,
Tainan 70101, Taiwan, R.O.C.

Experiments are performed to study the flow structure and heat transfer over a heated oscillating cylinder. Both flow visualization using a smoke wire and local heat transfer measurements around the cylinder were made. The excitation frequencies of the cylinder are selected at $F_c/F_n = 0, 0.5, 1, 1.5, 2, 2.5,$ and 3 . These include excitations at harmonic, subharmonic, superharmonic, and nonharmonic frequencies. Synchronization of vortex shedding with the cylinder excitation occurs not only at $F_c/F_n = 1$ but also at $F_c/F_n = 3$, which can greatly enhance the heat transfer. The simultaneous enhancement of heat transfer at the stagnation point, its downstream region, and the wake region of the flow suggests that different modes of instabilities occurring in the shear layer of the near wake are actually initiated and amplified far upstream in the stagnation point, which were suppressed in the accelerated flow region and re-amplified in the decelerated flow region. As long as the dominant mode of the instability is amplified by the excitation of cylinder, enhancement of heat transfer can be obtained. During the experiments, the Reynolds numbers vary from 1600 to 4800, the ratios of oscillation amplitude to diameter of the cylinder from 0.064 to 0.016.

Introduction

Any thermal device during its normal operation will encounter some degree of vibration. The vibration may be generated from the flow itself and/or other components in motion. These kinds of vibrations usually have small amplitudes and relatively high or low frequency. In practical design of a thermal system, vibrations under this small amplitude are not considered and their effects on the wall heat transfer are neglected. This paper takes an example to show that even vibration at a very small amplitude, in the order of 0~2 mm (A/D less than 0.1), may have a significant effect on both the flow and the heat transfer. The example selected is the flow over a heated cylinder oscillating in a direction transverse to the mean flow.

In the past, most of the work on heat transfer from an oscillating cylinder has been performed under vigorous oscillation, i.e., with large amplitude (in the order from 1 to 4 cm, i.e., $A/D = 0.2$ to 2) and relatively high frequencies (in the order from 0.5 to 2 Hz). A significant enhancement in the heat transfer has been found (Leung et al., 1981). Kezios and Prasanna (1966) reported a 20 percent increase in the average heat transfer from transverse oscillation of a cylinder. Saxena and Laird (1978) observed that local heat transfer can be enhanced up to 60 percent higher for a cylinder oscillating transversely to the mean water flow. Takahashi and Endoh (1990) found a significant increase in heat transfer for a streamwise oscillating cylinder. The increase in heat transfer is attributed to vibration which gives rise to turbulence in the case of laminar boundary layer flow. However, there are other works (Sreenivasan and Ramachandran, 1961; Mori and Tokuda, 1966) that found no appreciable effects of vibration on the heat transfer. In general, it has been recognized that rapid, small amplitude oscillations of approximately 2 mm ($A/D = 0.1$ or less) at 30 Hz would cause no significant increase in heat transfer.

For numerical studies, only a few works are found. Karanth et

al. (1994) solved the vorticity transport and energy equations at a low Reynolds number, $Re = 200$, and found that the heat transfer rate from the cylinder oscillating both in the transverse and the streamwise direction increases with increase in velocity amplitude.

In the field of fluid mechanics, there are numerous reports either numerical (Hurlbut et al., 1982; Lecoite and Piquet, 1989; Chang and Sa, 1992; Liu et al., 1992) or experimental (Koopmann, 1967; Griffin and Votaw, 1972; Griffin and Ramberg, 1974 and 1976; Tanida et al., 1973; Ongoren and Rockwell, 1988a,b) studies of flow structure over a cylinder vibrating either in the direction transverse or in line to the mean flow. Good review articles can be found in other references (Berger and Wille, 1972; Sarpkaya, 1979; Bearman, 1984). Of particular interest in these reports are the significant variations in the vortex flow structure near the back of the cylinder and the significant increase in the average drag force for vibration in the lock-in frequency. From the relationship of the Reynolds analogy, significant increase in the average drag over the cylinder, which is mainly due to the viscous force effect, implies that a significant increase in heat transfer can be expected, especially for vibration in the lock-in frequency. This is the condition when the cylinder excitation synchronizes with vortex shedding. When the lock-in phenomenon occurs, the amplitude need not be large. In theory (Blevins, 1990), the amplitude can be significantly less than a few tenth or hundredth millimeters (i.e., hundredth A/D ratios). These conclusions further stimulate our interest to study the flow and heat transfer over a cylinder oscillating at small amplitude.

The present paper presents an experimental study of the flow structure and heat transfer of air moving over a heated cylinder oscillating at small amplitudes, in the direction transverse to the mean flow. The excitation frequency of the cylinder versus the shedding frequency of the vortex ranges from 0 to 3. The Reynolds number ranges from 1600 to 4800. Both flow visualization and local heat transfer measurements around the cylinder are made and compared with published results for a stationary cylinder. Flow visualization is made by smoke generation, which is facilitated upstream of the cylinder by a thin, electrically heated wire coated with oil. The temperature distributions around the cylinder wall are

Contributed by the Heat Transfer Division for publication in the JOURNAL OF HEAT TRANSFER. Manuscript received by the Heat Transfer Division, May 10, 1998; revision received, June 15, 1999. Keywords: Cylinder, External, Heat Transfer, Vibrating, Vortex. Associate Technical Editor: J. Han.

measured with K-type thermocouples, which are used to obtain the heat transfer data. The variation of the flow structure and the heat transfer with the oscillating amplitudes and frequencies of the cylinder will be systematically discussed.

Experimental Apparatus and Procedures

The cylinder is 50 cm long and is made of 0.3-cm thick Bakelite tube which has outside diameter of 3 cm. The purpose for selecting a thin Bakelite tube is first to reduce both the radial and the circumferential conduction of heat, second to reduce the vibration load of the cylinder and third to maintain a certain kind of rigidity which causes no deformation during vibration. To further reduce the circumferential conduction of heat, a 0.05-cm thick rubber tube is used to cover the cylinder. This makes the outside diameter of the cylinder 3.1 cm. A thin 0.015-mm thin stainless steel foil is glued on the tube. After passing electric current through the foil, the cylinder surface can be heated uniformly at desired heat flux conditions. The tube ends are sealed with rubber for insulation. The total heat loss to the ambient, which includes the conduction loss along the cylinder wall and the radiation loss directly from the steel foil, is estimated to be less than two percent.

The cylinder is placed horizontally in the test section of the wind tunnel which has a cross section of 30 cm × 30 cm. The wind tunnel can provide an uniform air flow over the cylinder with a turbulence intensity less than 0.7 percent. The wall of the test section is made of Plexiglas to allow for flow visualization. A vertical slot 3.5 cm wide is cut on both the side walls of the wind tunnel to allow the cylinder to oscillate in the vertical direction. The cylinder is held by an aluminum frame which is connected to a vibration exciter (Type 4809, made by B&K). Two ball bearings fixed on the side walls of the wind tunnel are used to allow the frame of the cylinder to oscillate in the direction transverse to the mean flow but prevent from oscillating in the streamwise direction. The vibration signals (sinusoidal) with controlled frequency are initiated from a function generator, then amplified with a power amplifier (Type 2706, made by B&K) and finally are sent to the exciter. An accelerometer is attached to the cylinder wall to acquire and monitor the amplitude of the vibration.

To measure the circumferential temperature distribution around the cylinder wall, a total of 30 thermocouples are inserted individually into equally spaced small holes drilled in the tube wall in such a way that the thermocouple junctions can be attached to the heated steel foil. All the thermocouples used have a very small diameter $d = 0.05$ mm. This can further reduce the vibration load of the cylinder. To check the axial conduction loss along the cylinder wall, some additional thermocouples are embedded in the tube wall close to the ends. All the temperature signals are acquired with a data logger and sent into a PC for data processing and plotting. Before the experiments, all the thermocouples are calibrated in a constant temperature bath to ensure a measurement accuracy of $\pm 0.1^\circ\text{C}$.

To ensure that the stainless steel foil is heated uniformly, the

entire foil is cut into a number of long strips that are axial. Each strip is heated individually with an equal amount of DC power. With the desired voltage, V , and current, I , passing through the thin strip, the heat flux along the surface can be calculated and is equal to VI/A , where A is the area of the strip. The local heat transfer coefficient can be determined with the following equation:

$$h = q/(T_w - T_o). \quad (1)$$

The uncertainty of the experimental data obtained in the present system is determined according to the procedure outlined by Kline and McClintock (1953). It is found that the maximum uncertainty in the local Nusselt number is 3.47 percent, and the Reynolds number is 5.67 percent.

From the correlations listed in the references (Roshko, 1954; Zdravkovich, 1986), the Strouhal number of the vortex shedding in the current experimental range of the Reynolds numbers covered was $F_n D/u_o = 0.194$. Therefore, the shedding frequency of the vortex can be calculated at a given flow speed and a known size of cylinder. The calculated shedding frequencies agree well with the ones obtained from our experimental observations. Therefore, the previous correlation was adopted to find the shedding frequencies of the vortex in the present work.

During the experiments, the excitation frequencies of the cylinder are selected at 0.5, 1, 1.5, 2, 2.5, and 3 times the formation frequency of the vortex. In this way, one could examine the effect of the cylinder excitation on the flow and heat transfer at subharmonic frequencies $F_e/F_n = 0.5$, synchronization $F_e/F_n = 1$, superharmonic frequencies $F_e/F_n = 2, 3$, and nonharmonic frequencies $F_e/F_n = 1.5, 2.5$.

Results and Discussions

1 Flow Visualizations. The flow visualization experiments performed by Koopmann (1967), Griffin and Votaw (1972), and Griffin and Ramberg (1974) are at very low Reynolds numbers ($Re \leq 200$). In addition, the wake structures obtained by Zdravkovich (1982) and Ongoren and Rockwell (1988) are for water, which may not be used for air. In addition, the excitation frequencies of the cylinder versus the vortex shedding frequency made before are all less than 1.17, which does not cover the current experimental ranges. Therefore, flow visualization is still required to provide a better understanding of the phenomenon.

In general, the flow visualization results indicate that although the vortex structure may vary significantly as the cylinder oscillates at different frequencies and amplitudes selected in the present experimental conditions, the vortex shedding frequency does not change. Therefore, the complete duration for the initiation, the growth and the breakdown of vortex will not be affected by the different frequencies and amplitudes of the cylinder excitation. In the following presentation, instead of the complete cycle of the vortex formation, only the vortex structure at two particular instants, i.e., $t/Te = 0.33$ and 0.66 , are presented and compared with each other at different excitation frequencies.

Nomenclature

A = amplitude of oscillating cylinder
 D = diameter of cylinder
 F_e = frequency of oscillating cylinder
 F_n = vortex shedding frequency
 h = convective heat transfer coefficient
 I = electric current
 h_{ave} = average heat transfer coefficient
 k = thermal conductivity of air
 Nu = local Nusselt number, hD/k

Nu_{ave} = average Nusselt number, $h_{ave}D/k$
 q = heat flux
 Re = Reynolds number, $u_o D/\nu$
 St = Strouhal number
 t = time
 Te = the period for complete cycle of vortex formation, $1/F_n$
 T = temperature
 u = velocity
 V = voltage

Greek Symbols

ν = kinematic viscosity
 θ = angle measured from the stagnation point

Subscripts

ave = refers to average
 o = refers to freestream
stag = refers to stagnation
 w = refers to the wall of cylinder

Figure 1(a) shows the vortex formation process in the wake region when the cylinder is stationary. In general, it can be seen that the vortex formation length is relatively long and it decreases with increasing the Reynolds number (in the current experimental range). This finding agrees with Unal and Rockwell (1988) and Ongoren and Rockwell (1988). One can expect that the formation of vortices and their intense mixing with the wake flow have little effect on the heat transfer in the back side of the cylinder, even when the Reynolds number is higher and the mixing activities become more intense. The formation of the vortex is apparently due to exponential growth of small disturbances where the dominant mode (fundamental) of frequency is the vortex shedding frequency F_n . The small disturbances also include superharmonics of F_n and the small-scale instability found by others (Gerrard, 1978). However, it was found (Unal and Rockwell, 1988) that the spectral energy at these frequencies is relatively small as compared with the fundamental frequency. The formation length is primarily affected by the instability at the fundamental frequency F_n .

When the cylinder oscillates at the shedding frequency of the vortex, i.e., cylinder oscillation synchronizes with vortex shedding, the small disturbance at the fundamental frequency can be greatly amplified, which greatly shortens the formation length of the vortex, as shown in Fig. 1(b). The vortex that appears at $t/Te = 0.33$ or 0.66 is much stronger and closer to the cylinder than the case when the cylinder is stationary. The synchronization occurring for cylinder oscillation at F_n has been found by many investigators listed in the references. One can expect that the intense vortex activity in the close vicinity of the cylinder can greatly enhance the wall heat transfer in that region.

For the case when $F_e/F_n = 3$, the vortex formation and growth process, as shown in Fig. 1(c), is very much similar to the case when $F_e/F_n = 1$. It appears that the cylinder oscillation synchronizes in every three cycles with the vortex shedding. The explanation for the occurrence of synchronization is given in Figs. 2(a)–2(c). When the cylinder is stationary, the vortex is shed alternatively at upper and lower side of the cylinder. The solid dots represent the occurrence of vortex formation. At $F_e/F_n = 1$, the phase of vortex shedding is completely locked-in with the phase of cylinder displacement. The excitation energy of the cylinder can be readily transmitted into the small disturbance of the shear layer and cause the amplification. This also occurs for the case when $F_e/F_n = 3$. In other words, the lock-in frequencies occur at both $F_e/F_n = 1$ and 3 .

For excitation at another superharmonic frequency, i.e., $F_e/F_n = 2$, the synchronization of vortex shedding with the cylinder oscillation does not occur, as shown in Fig. 1(d). However, the vortex formation and growth is stronger and closer to the cylinder than the case when the cylinder is stationary, but is not so stronger and closer as the case when synchronization occurs. Similar situations occur for cylinder excitation at $F_e/F_n = 2.5$ and 0.5 , as shown in Figs. 1(e) and 1(f). As explained in Figs. 2(d), 2(e), and 2(f), only one side (either upper or lower side) of the vortex shedding can be synchronized with the cylinder excitation. For the case when $F_e/F_n = 2.5$ or 0.5 , the synchronization of vortex shedding occurs every four of the vortex formation. One can expect that the vortex is weaker and farther away from the cylinder than the case when $F_e/F_n = 2$ and synchronization of vortex shedding occurs at every two of the vortex formation. However, it appears that the vortex structure for $F_e/F_n = 2.5$ is slightly stronger and is able to generate more turbulent mixing than the case for $F_e/F_n = 0.5$. At $F_e/F_n = 1.5$, the vortex shedding is completely out of phase with the cylinder excitation, as shown in Fig. 2(g). The vortex structure is more irregular which generates turbulent mixing with the wake flow, shown in Fig. 1(g). The irregular vortex structure is attributed to the nonharmonic oscillation of the cylinder which amplifies the small disturbance of nonharmonic frequency in the shear layer. This is expected to enhance the heat transfer in the back of the cylinder.

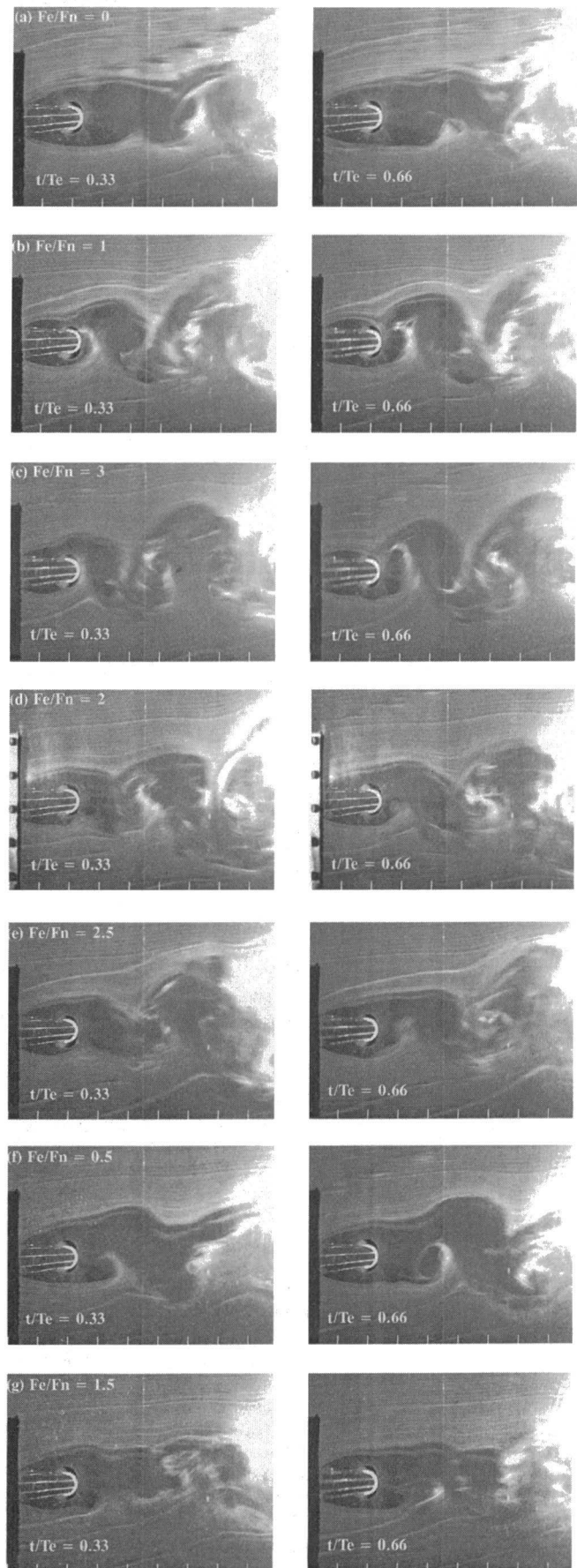


Fig. 1 Vortex structure at $t/Te = 0.33$ and 0.66 for $Re = 1600$, $A/D = 0.064$ and (a) $F_e/F_n = 0$, (b) $F_e/F_n = 1$, (c) $F_e/F_n = 3$, (d) $F_e/F_n = 2$, (e) $F_e/F_n = 2.5$, (f) $F_e/F_n = 0.5$ and (g) $F_e/F_n = 1.5$

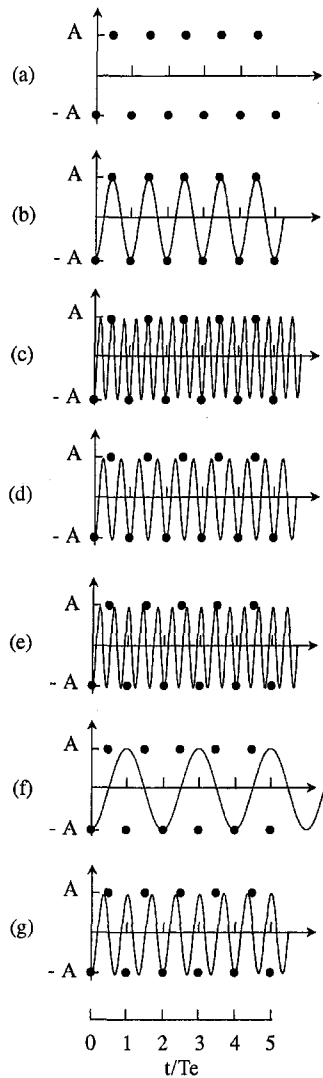


Fig. 2 Phase of vortex shedding (dots) relative to phase of cylinder displacement (sin curve) as function of time for (a) $F_e/F_n = 0$, (b) $F_e/F_n = 1$, (c) $F_e/F_n = 3$, (d) $F_e/F_n = 2$, (e) $F_e/F_n = 2.5$, (f) $F_e/F_n = 0.5$, and (g) $F_e/F_n = 1.5$

2 Heat Transfer. Let's consider the case when the cylinder is stationary. The forward stagnation point has the maximum heat transfer while the rear stagnation point has the minimum heat transfer, as shown in Fig. 3. The significantly higher heat transfer is attributed to the occurrence of three dimensional counter rotating vortices at the forward stagnation point (Gau and Chung, 1991). This unstable flow can significantly enhance the heat transfer. As the flow moves downstream, the acceleration of the flow by the convex surface has an effect to stabilize the flow and suppress the instability generated at the stagnation point. This effect reduces the heat transfer. One suspects that this instability of the flow can be reinitiated as the flow moves across the maximum velocity point and becomes decelerated. This will be discussed later. The deceleration of flow can amplify the instability while the adverse pressure gradient causing the deceleration can make the boundary layer flow separate from the wall and cause the occurrence of wake flow. As the vortex shedding as a result from amplification of the instability grows slowly and does not generate much turbulence, the heat transfer in the wake region will be relatively low, as shown in Fig. 3. This is the case, which is covered in the range of current experiments, when the Reynolds number is low. As the Reynolds number become higher, a rapid growth of vortices and their intense interaction with the wake flow can occur which may lead to generation of turbulence. This can significantly enhance the

heat transfer in the back side of the cylinder, shown in Fig. 3 for $Re = 9600$ (Liang, 1996). The separation point of flow which can be inferred from the minimum in the heat transfer data occurs at $\theta = 80$ deg. This trend agrees with the results of Giedt (1949), except the minimum heat transfer is lower. Therefore, one can expect that the flow in the front of the cylinder is laminar. This is also confirmed in the previous flow visualization.

In general, all the data in the front side of the cylinder in the region of $\theta < 80$ deg or $\theta > 280$ deg agree very well with the Frossling solution. However, in the back side of the cylinder there are some discrepancies between different works. One can expect that the discrepancies are attributed to the different size of cylinders used in different works which result in different types of flow and lead to different levels in the enhancement of the heat transfer. In the work of Krall and Eckert, the cylinder used is very small which had a diameter of 4.73 mm. To achieve the same Reynolds number as in the current work, the flow velocity has to be much higher (about seven times greater) than that of the current work. This can lead to a turbulent boundary layer in the front side and a delay in the occurrence in the separation point. The occurrence of flow separation at a later stage, i.e., at $\theta = 110$ deg as indicated by the minimum in heat transfer of Krall and Eckert in Fig. 3 confirms this point. In addition, this turbulence in flow can significantly shorten the formation length of the vortex and enhance the heat transfer in the back of the cylinder, as shown in Fig. 3. The significant reduction in the formation length at a higher velocity is also found in other work (Unal and Rockwell, 1988).

When the cylinder oscillates with an amplitude of $A/D = 0.064$, the heat transfer can be significantly enhanced, as shown in Fig. 4. When synchronization of cylinder oscillation with the vortex shedding occurs, the heat transfer results are much greater than the case at desynchronization. In addition, the heat transfer for the synchronization at $F_e/F_n = 3$ is greater than the case at $F_e/F_n = 1$. It appears that the occurrence of synchronization at a higher oscillation frequency can generate a higher heat transfer rate. This is also occurred in the case at desynchronization, as shown in Fig. 4 for $F_e/F_n = 2.5$ and $F_e/F_n = 0.5$ where instability of flow can still be amplified as explained in Figs. 2(e) and 2(f). The heat transfer in the former is higher than in the latter. One can conclude from these observations that as long as the instability of the flow can be amplified by the cylinder excitation, the heat transfer at a higher frequency oscillation is higher than at a low-frequency oscillation. It appears that the higher frequency oscillation can provide more energy to disturb the flow and enhance the heat transfer at a higher rate. At synchronizations, the

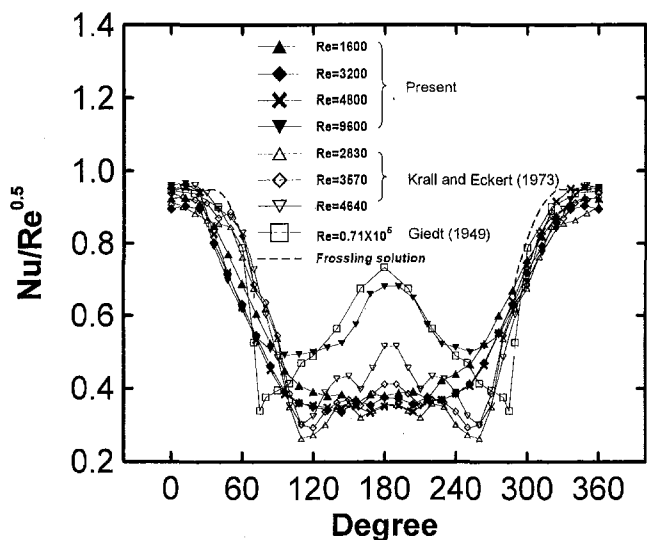


Fig. 3 Comparison of the Nusselt number distributions between the current measurements and the published reports when the cylinder is stationary

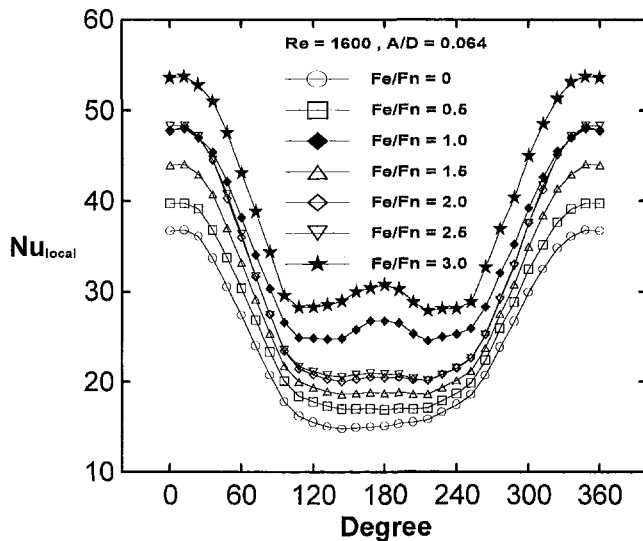


Fig. 4 The Nusselt number distributions around the cylinder at different excitation frequencies for $Re = 1600$, $A/D = 0.064$

enhancement of the heat transfer in the wake region is due to the rapid growth of vortices and their intense interaction with the wake flow.

Notice that the heat transfer in the other regions, especially in forward stagnation point, is also significantly enhanced. Since the intense activity of the vortices in the wake region could not possibly affect the flow in the upstream, especially in the forward stagnation point. One can readily conclude this point from flow visualization experiments. It appears that the cylinder excitations not only amplify the instability occurring in the shear layer of the near wake but also the instability occurring at the stagnation point and its downstream region. The only chance that the dominant mode of instability in these regions can be amplified simultaneously by the cylinder excitation is that the dominant modes of instability, i.e., the fundamental frequencies, in these regions are the same. Therefore, one confirms the former suspicion discussed in the first paragraph of this section, i.e., the instability occurring in the shear layer of the near wake is actually generated far upstream in the stagnation point region.

At $F_e/F_n = 2$, which is the case when either the upper or the lower side of vortices can be amplified, the heat transfer is significantly lower than the case at synchronization. However, the heat transfer at $F_e/F_n = 2$ is very close to the case at a higher frequency, i.e., $F_e/F_n = 2.5$, where amplification of the vortex by the excitation occurs only in one side and once every other vortex. It appears that the heat transfer enhancement due to a more intense amplification of the vortex at $F_e/F_n = 2$ as discussed in the previous section of flow visualization is counterbalanced by the heat transfer enhancement due to a higher frequency excitation at $F_e/F_n = 2.5$. Note that at $F_e/F_n = 1.5$ when none of the vortices can be amplified by the cylinder excitation, the heat transfer results are even higher than the case at $F_e/F_n = 0.5$, where every other vortex in either upper or lower side of the cylinder can be amplified. It appears that from previous flow visualization for $F_e/F_n = 1.5$ other modes of the instability in the vortex can be amplified which can greatly disturb the vortex structure and lead to intense mixing of the vortex with the mainflow. In addition, the heat transfer at the stagnation point and its downstream region is also enhanced greatly. This suggests that the other mode of the instability in these regions is also amplified. It appears that not only the fundamental mode but also the other modes of the instability occurring in the near wake are actually initiated far upstream at the stagnation point.

When the Reynolds number is higher, the shedding frequency of vortex increases significantly. Due to the limitation of the current

experimental facility, the maximum frequency of excitation one can reach is $F_e/F_n = 1.5$ for $Re = 3200$ and $F_e/F_n = 1.0$ for $Re = 4800$. The synchronization of cylinder oscillation with vortex shedding can still significantly enhance the heat transfer as shown in Figs. 5(a) and 5(b). However, the percentage of the heat transfer enhancement at higher Reynolds number is lower than at a lower Reynolds number. This is attributed to the fact that at a higher Reynolds number the amplification of disturbance by the cylinder excitations is not so efficient as the amplification of disturbance by the flow itself. Therefore, one can expect that to get the same percentage of heat transfer enhancement, the excitation energy, i.e., the excitation amplitude, provided must be greater. Note that the heat transfer at $F_e/F_n = 1.5$ is still higher than the case at $F_e/F_n = 0.5$.

At a lower amplitude excitation of the cylinder, as shown in Figs. 6(a) and 6(b), the heat transfer enhancement is greatly reduced. In other words, the excitation energy provided is not enough to disturb or amplify the instability and enhance the heat transfer. Even at synchronization for $F_e/F_n = 1$, the heat transfer enhancement is not so significant and is less than the case when the cylinder oscillates at a higher frequency, which can provide more

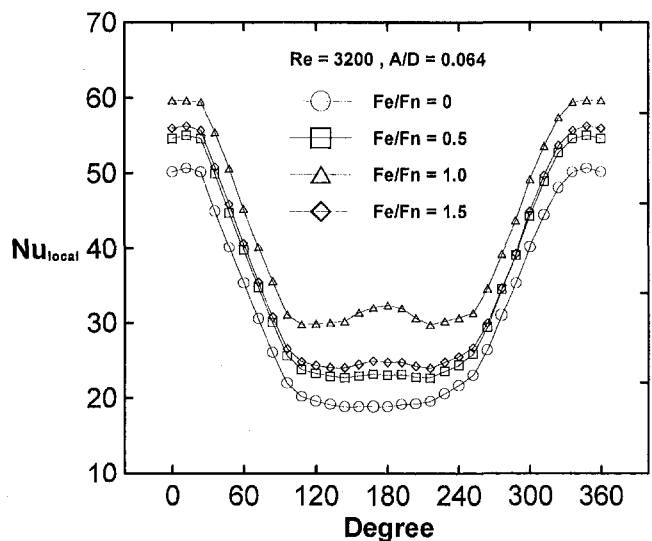


Fig. 5(a)

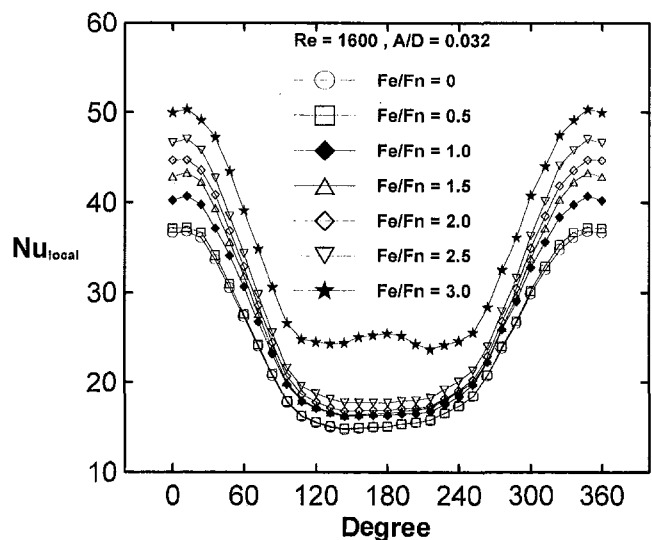


Fig. 5(b)

Fig. 5 The Nusselt number distributions around the cylinder at different excitation frequencies for $A/D = 0.064$ and (a) $Re = 3200$ and (b) $Re = 4800$

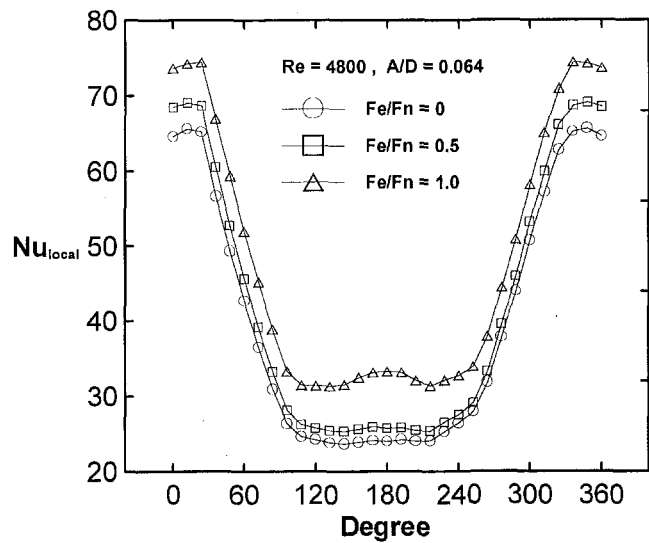


Fig. 6(a)

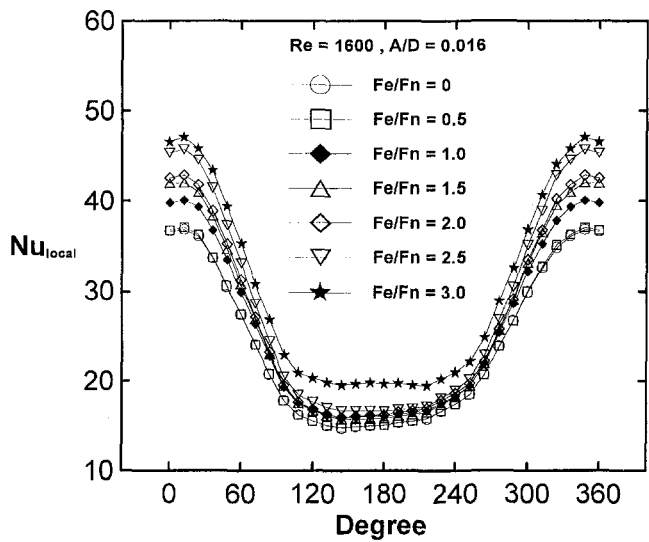


Fig. 6(b)

Fig. 6 The Nusselt number distributions around the cylinder at different excitation frequencies for $Re = 1600$ and (a) $A/D = 0.032$ and (b) $A/D = 0.016$

energy to disturb the flow. The enhancement in the heat transfer is almost proportional to the magnitude of the excitation frequency. However, for synchronization at a higher frequency, i.e., $F_e/F_n = 3$, significant enhancement in the heat transfer is still observed. Similar trend as discussed previously can be observed in Fig. 7 for the stagnation point heat transfer and Fig. 8 for the average heat transfer. In the experimental ranges covered for the Reynolds number from 1600 to 4800 and A/D from 0.016 to 0.064, in general, the increase in the Reynolds number or the decrease in the excitation amplitude of the cylinder leads to a less enhancement of heat transfer. To obtain a higher heat transfer enhancement at small-amplitude oscillation, the excitation frequencies must be large.

Conclusions

Flow visualization has provided a clear vortex structure which grows more rapidly as the dominant mode of the instability in the shear layer can be amplified by the excitation. Synchronization of the vortex shedding with the cylinder oscillation occurs not only at

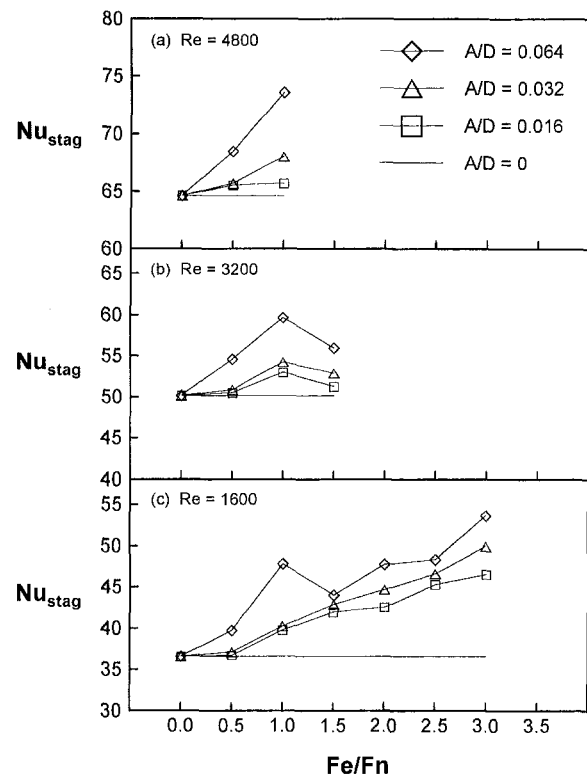


Fig. 7 The stagnation point Nusselt number for cylinder excitation at different frequencies and amplitudes with (a) $Re = 4800$, (b) $Re = 3200$, and (c) $Re = 1600$

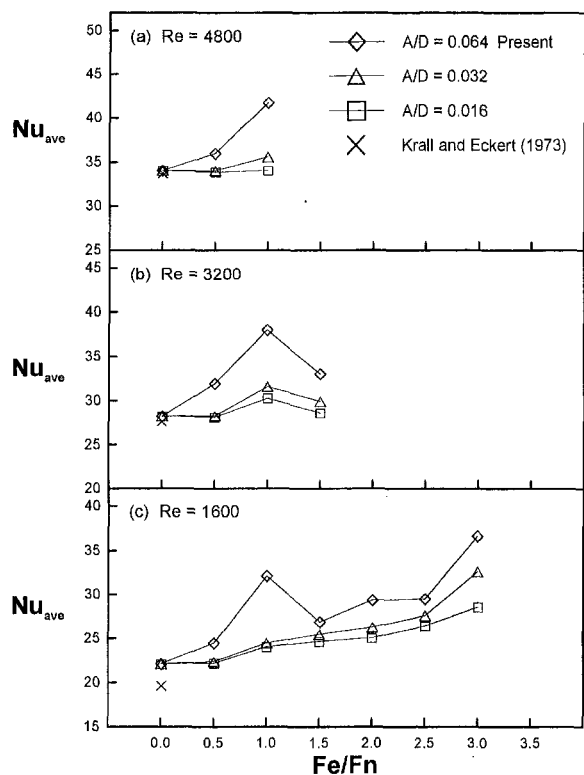


Fig. 8 The average Nusselt number for cylinder excitation at different frequencies and amplitudes with (a) $Re = 4800$, (b) $Re = 3200$, and (c) $Re = 1600$

$F_o/F_n = 1$ but also at $F_o/F_n = 3$, which can greatly enhance the heat transfer in the wake region. The accompanying enhancement of the heat transfer in both the stagnation point and its downstream region suggests that the dominant mode of the instability occurring in the wake region is actually initiated far upstream at the stagnation point. This is also the case for other modes of instability occurring in the wake region. As long as the instability mode in the wake or in the stagnation point region is amplified, heat transfer enhancement can be expected. In addition, the enhancement in the heat transfer is proportional to the magnitude of the excitation frequency. However, at a higher Reynolds number or a smaller amplitude of cylinder excitation, the enhancement in the heat transfer become less.

Acknowledgments

This research was sponsored by the National Science Council of Taiwan under contract No. NSC 86-2212-E-006-046.

References

- Bearman, P. W., 1984, "Vortex Shedding from Oscillating Bluff Bodies," *Annual Review of Fluid Mechanics*, Vol. 16, pp. 195–222.
- Bearman, P. W., and Graham, J. M. R., 1980, "Vortex Shedding from Bluff Bodies in Oscillatory Flow: A Report on Euromech 119," *Journal of Fluid Mechanics*, Vol. 99, pp. 225–245.
- Berger, E. W., and Wille, R., 1972, "Periodic Flow Phenomena," *Annual Review of Fluid Mechanics*, Vol. 4, pp. 313–340.
- Blevins, D. R., 1990, *Flow-Induced Vibration*, 2nd Ed., John Wiley and Sons, New York, pp. 54–58.
- Chang, Keun-Shik, and Sa, Jong-Youb, 1992, "Patterns of Vortex Shedding from an Oscillating Circular Cylinder," *AIAA Journal*, Vol. 10, No. 5, pp. 1331–1336.
- Gau, C., and Chung, C. M., 1991, "Surface Curvature Effect on Slot-Air-Jet Impingement Cooling Flow and Heat Transfer Process," *ASME JOURNAL OF HEAT TRANSFER*, Vol. 113, pp. 858–864.
- Gerrard, J. H., 1978, "The Wake of Cylindrical Bluff Body at Low Reynolds Number," *Philosophical Transaction Royal Society of London*, Vol. A288, No. 1354, pp. 351–382.
- Giedt, W. H., 1949, *Fundamentals of Heat and Mass Transfer*, 4th Ed., Incropera and DeWitt, eds., John Wiley and Sons, New York, 1996, p. 369.
- Griffin, O. M., and Votaw, C. W., 1972, "The Vortex Street in the Wake of a Vibrating Cylinder," *Journal of Fluid Mechanics*, Vol. 51, Part 1, pp. 31–48.
- Griffin, O. M., and Ramberg, S. E., 1974, "The Vortex-Street Wakes of Vibrating Cylinder," *Journal of Fluid Mechanics*, Vol. 66, Part 3, pp. 553–576.
- Hurlbut, S. E., Spaulding, M. L., and White, F. M., 1982, "Numerical Solution for Laminar Two Dimensional Flow about a Cylinder Oscillating in a Uniform Stream," *ASME Journal of Fluids Engineering*, Vol. 104, pp. 214–222.
- Karant, D., Rankin, G. W., and Sridhar, K., 1994, "A Finite Difference Calculation of Forced Convective Heat Transfer from an Oscillating Cylinder," *International Journal of Heat and Mass Transfer*, Vol. 37, No. 11, pp. 1619–1630.
- Kezios, S. P., and Prasanna, K. V., 1966, "Effect of Vibration on Heat Transfer from a Cylinder in Normal Flow," *ASME Paper No. 66-WA/HT-43*.
- Kline, S. J., and McClintock, F. A., 1953, "Describing Uncertainties in Single-Sample Experiments," *Mechanical Engineering*, Vol. 75, No. 1, pp. 3–12.
- Koopmann, G. H., 1967, "The Vortex Wakes of Vibrating Cylinders at Low Reynolds Numbers," *Journal of Fluid Mechanics*, Vol. 28, Part 3, pp. 501–512.
- Krall, K. M., and Eckert, E. R. G., 1973, "Local Heat Transfer Around Cylinder at Low Reynolds Number," *ASME JOURNAL OF HEAT TRANSFER*, Vol. 94, No. 2, pp. 273–274.
- Lecoite, Y., and Piquet, J., 1989, "Flow Structure in the Wake of an Oscillating Cylinder," *ASME Journal of Fluids Engineering*, Vol. 111, pp. 139–148.
- Leung, C. T., Ko, N. W. M., and Ma, K. H., 1981, "Heat Transfer From a Vibrating Cylinder," *Journal of Sound and Vibration*, Vol. 75, No. 4, pp. 581–582.
- Liang, C. Y., 1996, "Convective Heat Transfer from a Heated Oscillating Cylinder," M.S. thesis, National Cheng-Kung University, Tainan, Taiwan, ROC.
- Mori, Y., and Tokuda, S., 1966, "The Effect of Oscillation on Instantaneous Local Heat Transfer in Forced Convection from a Cylinder," *Proceedings of Third International Heat Transfer Conference*, Vol. III, Chicago, Aug., pp. 49–56.
- Ongoren, A., and Rockwell, D., 1988a, "Flow Structure from an Oscillating Cylinder, Part 1. Mechanisms of Phase Shift and Recovery in the Near Wake," *Journal of Fluid Mechanics*, Vol. 191, pp. 197–223.
- Ongoren, A., and Rockwell, D., 1988b, "Flow Structure from a Oscillating Cylinder, Part 2. Mode Competition in the Near Wake," *Journal of Fluid Mechanics*, Vol. 191, pp. 225–245.
- Roshko, A., 1954, "On the Drag and Shedding Frequency of Two-Dimensional Bluff Bodies," *NACA Technical Note*, p. 3169.
- Sarpkaya, T., 1979, "Vortex-Induced Vibrations: A Selective Review," *ASME JOURNAL OF APPLIED MECHANICS*, Vol. 39, pp. 883–890.
- Saxena, U. C., and Laird, A. D. K., 1978, "Heat Transfer From a Cylinder Oscillating in a Cross-Flow," *ASME JOURNAL OF HEAT TRANSFER*, Vol. 100, pp. 684–689.
- Sreenivasan, K., and Ramachandran, A., 1961, "Effect of Vibration on Heat Transfer from a Horizontal Cylinder to a Normal Air Stream," *International Journal of Heat Mass Transfer*, Vol. 3, pp. 60–67.
- Takahashi, K., and Endoh, K., 1990, "A New Correlation Method for the Effect of Vibration on Forced Convection Heat Transfer," *Journal of Chemical Engineering of Japan*, Vol. 23, No. 1, pp. 45–50.
- Unal, M. F., and Rockwell, D., 1988, "On Vortex Formation From a Cylinder, Part 1. The Initial Instability," *Journal of Fluid Mechanics*, Vol. 190, pp. 491–512.
- Wu, J. M., 1997, "Low Reynolds Number Flow and Convective Heat Transfer from an Oscillating Cylinder," M.S. thesis, National Cheng Kung University, Taiwan.
- Zdravkovich, M. M., 1982, "Modulation of Vortex Shedding in the Synchronization Range," *ASME Journal of Fluids Engineering*, Vol. 104, pp. 513–517.

Coupling Between Heat and Momentum Transfer Mechanisms for Drag-Reducing Polymer and Surfactant Solutions

G. Aguilar

K. Gasljevic

E. F. Matthys¹

Department of Mechanical and Environmental Engineering,
University of California,
Santa Barbara, CA 93106

Drag-reducing solutions exhibit simultaneous friction and heat transfer reductions, yet it has been widely believed that there is no direct coupling between the two. In this work, we have conducted a study to re-examine this issue, using measurements of friction and heat transfer over a wide range of flow conditions from onset to asymptotic, various pipe diameters, and several polymer and surfactant solutions. Contrary to some earlier suggestions, our tests show that no decoupling of the momentum and heat transfer mechanisms was seen at the onset of drag reduction, nor upon departure from the asymptotes, but rather that the friction and heat transfer reductions change simultaneously in those regions. For asymptotic surfactant and polymer solutions, the ratio of heat transfer and drag reductions was seen to be constant over a large range of Reynolds numbers, if modified definitions of the reduction parameters are used. In the nonasymptotic region, however, the ratio of heat transfer to drag reductions is higher and is a function of the reduction level, but is approximately the same for polymer and surfactant solutions. This variation is consistent with the concept of a direct coupling through a nonunity constant Pr_t , as also suggested by our local measurements of temperature and velocity profiles. We also saw that our diameter scaling technique for friction applies equally well to heat transfer. These findings allow us to predict directly the heat transfer from friction measurements or vice versa for these drag-reducing fluids, and also suggest that a strong coupling exists between the heat and momentum transfer mechanisms.

1 Introduction

It has been shown repeatedly that small amounts of polymers or surfactant additives lead to reduced turbulent friction and heat transfer coefficients compared to those of water. Early analyses implied that the drag reduction characteristics have a direct equivalent in the heat transfer reduction; for example, that the maximum drag reduction asymptote (MDRA) has an equivalent maximum heat transfer reduction asymptote (MHTRA). This could also mean that the Reynolds analogy suggesting that the turbulent Prandtl number (Pr_t) is equal to 1, is as much applicable for these fluids as it is for water (Poreh and Paz, 1968; Kale, 1977; Smith and Edwards, 1981). It was later suggested, however, by Cho and Hartnett (1982) and others, that this assumption is not proper because the percentage reductions corresponding to the MHTRA are always significantly larger than those for the MDRA. In addition, for nonasymptotic fluids, the percentage of heat transfer reduction (HTR) is normally higher than the percentage of drag reduction (DR) at the same Reynolds number (Re). (The definitions we use here for DR and HTR are

$$DR = \frac{(C_{Fw,T} - C_F)}{C_{Fw,T}} \times 100; \quad HTR = \frac{(Nu_{w,T} - Nu)}{Nu_{w,T}} \times 100$$

where “W, T” stands for turbulent flow of water at the same Reynolds number.)

¹To whom correspondence should be addressed.

Contributed by the Heat Transfer Division for publication in the JOURNAL OF HEAT TRANSFER and presented at 1998 ASME IMECE, Anaheim. Manuscript received by the Heat Transfer Division, Mar. 30, 1998; revision received, May 5, 1999. Keywords: Convection, Fluids, Heat Transfer, Non-Newtonian, Turbulent. Associate Technical Editor: M. Kaviany.

This difference in the reduction levels may indicate that a direct coupling between the heat and momentum transfers through a Pr_t of about 1, does not hold for this type of fluids. Indeed, various eddy diffusivity models were developed, most of them predicting a Pr_t much greater than one (e.g., Kale, 1977; Mizushima et al., 1975; Yoon and Ghajar, 1987). Roethig and Matthys (1988), for example, estimated values of Pr_t on the order of 10–15 for asymptotic conditions. Such a large difference between the eddy diffusivities is a striking concept, and it is indeed a very interesting issue worth looking at carefully because of the fundamental implications that it may have.

Other consequences of this apparently increased Pr_t is a difference between heat and momentum developing lengths and a difference between the velocity and temperature profiles. With respect to the entry lengths, Ng et al. (1980) observed that the thermal development region was at least three times longer than that for friction for the fluids they studied, and that many of the experimental setups used previously did not have the minimum length needed for the development of the temperature profile. Toh and Ghajar (1988) and Matthys (1991) also observed thermally developing flow even after 600 D , with little or no effect of the Reynolds number after appropriate nondimensionalization, whereas it was generally believed that the momentum entrance length was only about 100 diameters. Recently, however, we have revisited the problem of the relationship between HTR and DR within the developing region for surfactant solutions (Gasljevic and Matthys, 1997) and we have seen that—contrary to what was believed to be the case for most polymer solutions—the friction and heat transfer coefficients for cationic surfactants were still changing at the same rate 300 D downstream of the entrance, when nondimensionalized by the “fully developed” values measured at more than 650 D downstream. This finding could imply that the Pr_t

is not as large as that predicted by some earlier studies, at least for surfactant solutions. This notion is also supported by some of our recent studies on turbulent temperature profiles (to be presented elsewhere).

Besides the possibility of higher Pr_t , there was also a possibility of complete decoupling of the two exchange mechanisms in some limited regions. For instance, previous experimental evidence seemed to suggest that there are different onsets for drag and heat transfer reductions. To complicate the matter further, it was shown (Ng and Hartnett, 1979; Matthys, 1991) that in the process of degrading an asymptotic polymer solution, the HTR begins to decrease from its asymptotic level before the DR does, suggesting that in this region the DR and HTR are decoupled. We decided therefore to investigate this latter issue further, and to look in more detail at the relationship between DR and HTR close to the asymptotic regimes.

Finally, we have recently studied the diameter effect on friction, and we have developed a simple correlation based on bulk velocity that allows us to scale readily DR up or down with diameter. If a fixed relationship between DR and HTR does not exist, the HTR would likely not be well represented by the correlation applicable to the DR. On the other hand, if a fixed relationship does exist, the diameter effect on heat transfer should be the same as that for DR. This issue still had to be resolved prior to the present study.

To address the problem of relationship between the two transfer mechanisms, we rely in this work on global measurements of the friction coefficient and Nusselt number. Although local measurements of velocity and temperature profiles (which we will address elsewhere) are best suited for direct determination of the Pr_t , the global measurements can contribute greatly as well to the discussion, and particularly so in the region at and close to onset, where profile measurements become inaccurate because of the smaller velocity and temperature gradients. Global measurements are also the best tool for resolving the problem of possible decoupling during departure from the asymptotes by dilution or degradation. The aim of the present work was therefore to analyze the relationship between the DR and HTR by performing measurements of both, under wide experimental conditions and for various drag-reducing fluids.

2 Experimental Setup and Procedure

The experimental setup consists of four stainless steel tubes of 2, 5, 10, and 20-mm inner diameters. These tubes are fed from a pressurized tank by a distribution line. The pipes are 1000 diameters long each, except for the largest pipe which is 680 diameters long. This setup was previously used for studies of the diameter effect on friction (for details on this setup see Gasljevic (1990) and Aguilar (1995), and only additional instrumentation was needed for the heat transfer measurements.

The pipes were fitted with temperature sensors (miniature 100 Ω , 10×2 mm RTDs), cemented on top of the outer wall at 860 and 960 diameters downstream of the entrance, and at 634 and 675 diameters for the 20-mm pipe. Another RTD (100 Ω) was placed

in the supply manifold of the pipes for bulk temperature measurements. This shielded probe was inserted perpendicular to the flow at the pipe entrance. The three RTDs for each pipe were connected to a precision multimeter (Keithley 199 DMM/Scanner). Errors in the measurements were reduced by noise rejection and averaging techniques. A near-uniform wall heat flux condition was provided by two 20 kW DC power supplies connected directly to each pipe by means of customized copper clamps providing very good electrical contact (in order to prevent contact heating). The heat transfer measurement technique is described in more detail in Gasljevic and Matthys (1997). For better comparison, we controlled the heating in such a way that for each experiment the bulk temperature was about the same at the location where both DR and HTR are measured. All these experiments were carried out in a once-through mode to avoid unintentional flow perturbations and fluid degradation, and the flow rate was measured continuously by discharging the fluid into instrumented calibrated tanks.

The equipment was calibrated for friction and heat transfer measurements by running tests with tap water. The results were successfully compared with some of the better correlations for Newtonian fluids for friction coefficients (Blasius, 1913; Filomenko, 1954; Petukov, 1970); and for heat transfer coefficients (Kays, 1966; Petukov, 1970; Sleicher and Rouse, 1975). The accuracy of the flow rate measurement is about one to two percent (Gasljevic, 1990). Altogether, the uncertainty of our experimental data for water is estimated to be about five percent for the friction measurements, and eight to ten percent for the Nusselt number over most of the velocities covered, and somewhat higher—between seven to eight percent for friction and 12 to 15 percent for heat—for low velocities. The expected uncertainty is lower for the drag-reducing solutions where the temperature differences between the wall and bulk temperatures are bigger and the uncertainty becomes proportionally smaller. The uncertainty in the calculation of the relative drag and heat transfer reductions is also about half of those for C_f and Nu because the errors in some of the parameters cancel out when the HTR and DR ratios are calculated.

We used three different drag-reducing fluids, one polymer and two surfactant solutions, each in a number of concentrations: Separan AP-273, a hydrolized high-molecular weight polymer by Dow chemicals; SPE 95285, a nonionic surfactant developed in collaboration with Dr. M. Hellsten at Akzo Nobel Chemicals; and Ethoquad T13-27, a cationic surfactant by Akzo Nobel Chemicals. The water used as solvent was deionized or tap water, and in the case of the 50 ppm Separan solution small amounts of NaCl were added to the tap water in order to illustrate the effect of salts on the drag-reducing ability of the fluid. We have also examined data from other authors.

When working with drag-reducing fluids, it is often critical to measure and take properly into account the viscosity if we want to avoid large errors. We have therefore systematically measured the viscosity of the fluids either with Couette or high-shear capillary systems. For the polymer solutions with concentrations of 50 ppm or less, the viscosity was found to be very close to that of water at

Nomenclature

$C_f = 2\tau_w/\rho V^2$ = friction coefficient
 D = pipe diameter (mm)
 $h = q''/\Delta T_{w-b}$ = heat transfer coefficient (W/m² K)
 k_f = fluids thermal conductivity (W/mK)
 $Nu = hD/k_f$ = Nusselt number
 $Pr = \nu/\alpha$ = Prandtl number
 $Pr_t = \epsilon_M/\epsilon_H$ = turbulent Prandtl number
 $Re = VD/\nu$ = Reynolds number

$u^* = \sqrt{\tau_w/\rho}$ = shear velocity (m/s)
 V = bulk velocity (m/s)
Greek Letters
 $\alpha = k/\rho C$ = thermal diffusivity (m²/s)
 ϵ = eddy diffusivity (m²/s)
 ΔT_{w-b} = wall to bulk temperature difference (°C)
 ν = kinematic viscosity (m²/s)

ρ = density (kg/m³)
 τ_w = shear stress at the wall (N/m²)
Subscripts
 H = relative to heat
 L = relative to laminar flow
 M = relative to momentum
 T = relative to turbulent flow
 W = relative to the solvent (water)

shear rates comparable to those encountered in the pipe runs; for polymer concentrations of 100 ppm, the apparent wall viscosity was used to compute the Reynolds number and the corresponding DR and HTR values. For the 4000 ppm nonionic surfactant solution, the viscosity at room temperature was about twice as high as water, but at the temperature used in the tests (33–35°C), the viscosity was also found to be close to that of water. To most of the Ethoquad T13-27 solutions, we added 3 mM/l of copper hydroxide $\text{Cu}(\text{OH})_2$ in order to increase the stability of the fluid and to reduce the viscosity to the water level as well. When this approach was not followed, the apparent wall viscosity of the surfactant solution was used to compute the Reynolds number, DR and HTR values (as in Figs. 7 and 8). Except for the test with the 4000 ppm nonionic surfactant, all the other fluids were tested at room temperature (approx. 20°C.) Unless otherwise indicated, all fluids exhibited a molecular Prandtl number of about 6 during these tests.

3 Results and Discussion

3.1 Diameter Effect on Drag and Heat Transfer Reduction.

We have recently conducted a study of the diameter effect on polymeric drag-reducing fluids (Gasljevic et al., 1999). According to our results, the DR data measured in various pipe diameters for these fluids can be represented by a single curve if plotted as a function of the bulk velocity. It was then decided to investigate the diameter effect on the heat transfer, and to verify the validity of the same correlation for heat transfer reduction. For this purpose we performed simultaneous measurements of DR and HTR under various conditions. Figure 1 shows our results for a nonasymptotic 20-ppm polyacrylamide (Separan AP-273) solution measured in four pipes of 2, 5, 10, and 20-mm inner diameter. As can be seen in the upper graph, the HTR scales with bulk velocity just as well as DR does, which means that the ratio between HTR and DR does not depend on the pipe diameter in this representation. The ratio does, however, depend on the flow velocity, as seen in the lower graph, with a ratio tending to about 1.15 at high DR levels. In a previous article (Aguilar et al., 1998), the data scatter at low velocities was attributed to the difficulty in conducting these measurements in that region, but it was later observed that this scatter was more likely due to viscosity and buoyancy effects, as discussed below.

This independence of the HTR/DR ratio on the pipe diameter suggests that the diameter effect on heat transfer is the same as that on friction, essentially eliminating the diameter effect on heat

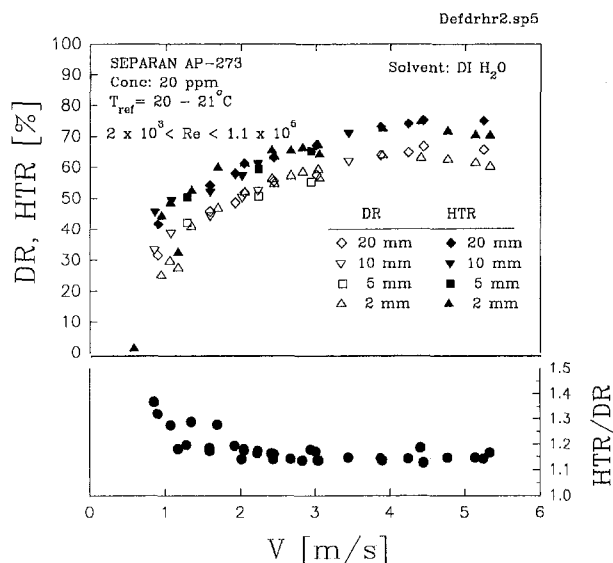


Fig. 1 Diameter and velocity effects on DR, HTR, and the HTR/DR ratio for a polymer solution

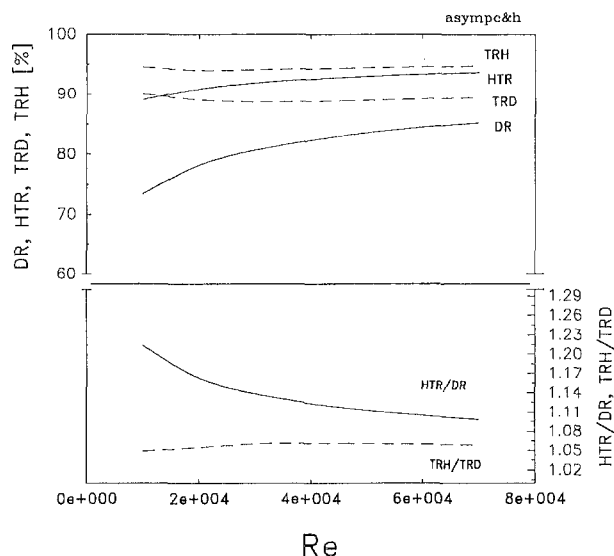


Fig. 2 Maximum drag reduction asymptote (MDRA) and maximum heat transfer asymptote (MHTRA) from Cho and Hartnett (1982) plotted as DR, TRD, HTR, and TRH versus Reynolds number. The ratios between the corresponding heat transfer and friction parameters are also shown in the lower graph.

transfer as a separate problem. In addition to its usefulness for predictions, this finding has theoretical implications in that it suggests that a strong coupling does exist between the heat and momentum transfer mechanisms. The dependence of the HTR/DR ratio on velocity indicates that this coupling may not be a simple relationship, however.

3.2 Maximum Drag and Heat Transfer Reductions (Asymptotic Regime).

Figure 2 shows the maximum drag and heat transfer asymptotes (MDRA and MHTRA) proposed by Cho and Hartnett (1982) for polymer solutions. The asymptotes are presented in two ways; on the one hand in terms of the usual DR and HTR (solid lines), and on the other hand, in terms of the parameters that we have recently referred to as “turbulence reduction-drag” (TRD) and “turbulence reduction-heat” (TRH) (the dashed lines). These latter quantities are defined as follows:

$$\text{TRD} = \frac{(C_{F_{w,T}} - C_F)}{(C_{F_{w,T}} - C_{F_{w,L}})} \times 100;$$

$$\text{TRH} = \frac{(\text{Nu}_{w,T} - \text{Nu})}{(\text{Nu}_{w,T} - \text{Nu}_{w,L})} \times 100$$

where the subscript T stands for turbulent flow, L for laminar flow, and W for the solvent (water).

(Regarding the second representation, similar parameters have been proposed in earlier studies as an alternative to the percentage reduction parameters (DR and HTR). The former are indeed physically more meaningful since they reflect the degree of turbulence reduction with respect to full laminarization rather than to an artificial zero-viscosity fluid (Astarita et al., 1969; Schmitt, 1988). They were disregarded early on, though, because they incorporate an additional parameter (the laminar friction coefficient) and because the difference between these and the DR and HTR parameters is in some cases small. We have recently shown (Gasljevic and Matthys, 1999), however, that although both representations are equally useful in providing information in some cases, in some others the TRH and TRD definitions may indeed be much better than DR and HTR.)

The ratio of the two reductions is calculated for both presentations and shown in the lower graph of Fig. 2. We can see that the ratio between HTR and DR is dependent on the Reynolds number, whereas TRH/TRD is about independent of the Reynolds number

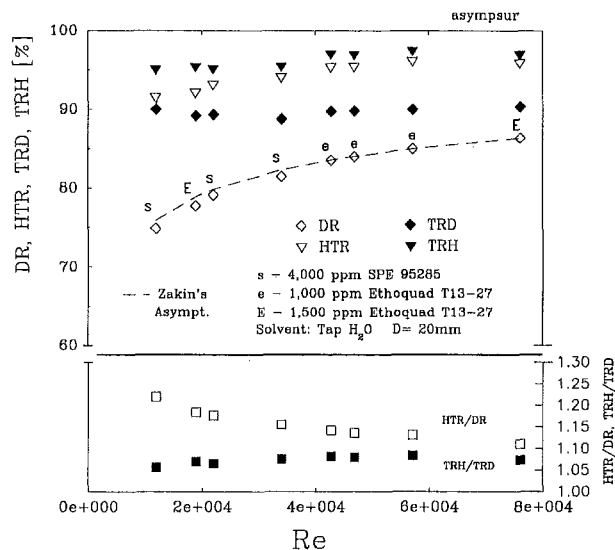


Fig. 3 Asymptotic values of drag and heat transfer plotted as DR, TRD, HTR, and TRH versus Reynolds number for various surfactant concentrations. The MDRA proposed by Zakin et al. (1996) is shown for comparison (dashed line). The ratios between the corresponding heat and friction parameters are also shown in the lower graph. All solutions showed water-like viscosity under the test conditions (solvent: tap water, pipe ID = 20 mm).

(since both TRD and TRH are as well), and is about 1.06. (If Virk's asymptote is used for friction instead of Cho and Hartnett's, a slightly higher value in the ratio is obtained, i.e., about 1.12). The HTR/DR ratio decreases here from about 1.2 to 1.1 as the Reynolds number increases, in good agreement with Fig. 1.

Figure 3 (top) shows data for asymptotic friction and heat expressed both in terms of DR and HTR (hollow symbols) and in terms of TRD and TRH (solid symbols) for various asymptotic surfactant solutions. The HTR/DR and TRH/TRD ratios are also shown (bottom). As it has been frequently observed, higher levels of reductions are achieved with surfactant than with polymer solutions. It is also seen that the power-law asymptotic correlation proposed by Zakin et al. (1996) fits our data reasonably well. The TRH/TRD ratio is again practically independent on Re, showing a value of approximately 1.07, very close to that for the polymer solution asymptotes (1.06). This difference between the ratios obtained for the surfactant and polymer solutions may be considered to be well within the limits of experimental error.

3.3 Intermediate Drag and Heat Transfer Reductions (Nonasymptotic Regime). We have seen above that a constant ratio between the reductions in heat and drag holds for asymptotic drag reduction if our "turbulence reduction parameters" (TRH and TRD) are used. However, in the nonasymptotic regime, the HTR/DR ratio clearly depends on velocity (as does the HTR/DR ratio for any asymptotic reductions—although much less as seen in Fig. 2). We decided then to examine the generality of the ratio between TRH and TRD (or HTR and DR) for nonasymptotic fluids, including both polymers and surfactants. Figure 4 (top) shows results of simultaneous heat transfer and friction measurements for polymer solutions, presented as TRH versus TRD. The TRH/TRD ratio (which was independent of Reynolds number for asymptotic conditions) is also shown (bottom) as a function of TRD. This is a convenient representation because it allows us to see easily the relative variation of TRH with TRD, and it is also independent of the fluid drag-reducing ability.

Data from three sources are presented: Various polyacrylamide (Separan AP-273) solutions of different concentrations prepared in our laboratory; a 20 ppm Separan AP-273 solution used by Matthys (1991) at three different levels of degradation; and two polyethylene oxide solutions (Polyox) used by Yoon and Ghajar

(1987). The results of Matthys and of Yoon show a practically constant TRH/TRD, whereas our data show an increased ratio at low levels of TRD. The difference in results is likely not due to different solutions, because Matthys' and ours were the same type of polymer. In an earlier article (Aguilar et al., 1998), we plotted all these results together and considered TRH/TRD to be approximately constant with Re, although with a relatively large scatter at low reduction levels. However, after a detailed analysis, we decided to distinguish the two groups of results, and it is seen here that all our solutions show a stronger variation of the ratio compared to the measurements of Yoon and Ghajar or Matthys, which show more constant values. The reason for this discrepancy is not yet fully known, but it is likely that it originated in the variations of the experimental conditions, including differences in the quality of the solvents.

Our measurements of temperature profiles for fluids which are believed to be well represented by Virk's three-layers velocity profile model, such as these low concentration Separan solutions, indicate that the Pr_t is about constant and equal to 5 or 6 across the region of the pipe radius where drag-reducing effects occur (the elastic layer, according to Virk's three-layers model). Based on this finding, we have made use of a simple mathematical model to calculate the TRH and TRD using Virk's three-layer velocity profile, a constant $Pr_t = 5$, and the assumption of equal thickness for the momentum and thermal elastic layers. The results of these calculations are shown as the upper dashed line on Fig. 4 (top), indicating that TRH should increase faster than TRD with increasing level of reduction right after the onset. The values of TRH/TRD computed with this model are also plotted as a dashed line in the lower portion of Fig. 4 showing a reasonably good fit with our data. (The difference between the modeled and the measured values could be reduced or eliminated if the thickness of the thermal elastic layer is reduced relative to the thickness of the momentum elastic layer in the model, or if the Pr_t is somewhat reduced in the region closer to the wall. For our purposes here, however, the point was not to improve the model (e.g., by tuning Pr_t), but rather simply to show that the variation of TRH/TRD which we measured is reasonable.) As expected, TRH/TRD at high

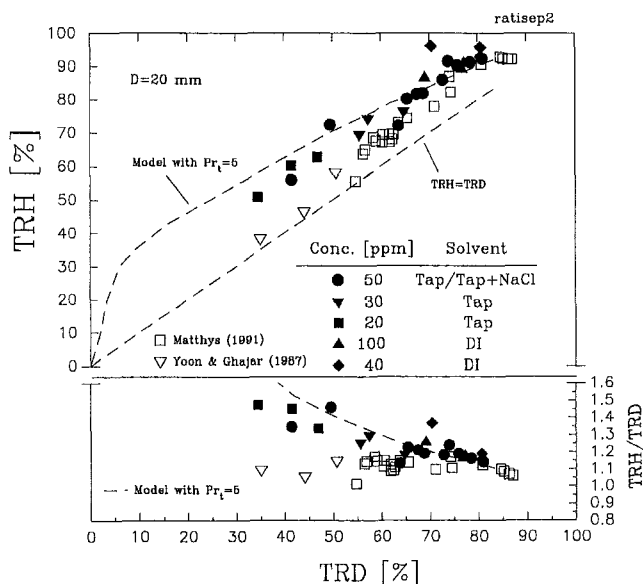


Fig. 4 TRH versus TRD for various polyacrylamide (Separan AP-273) concentrations (solid symbols). Data from Matthys (1991) for a 20 ppm AP-273 Separan solution at various degradation levels and data from Yoon and Ghajar (1987) for a 50 and 100 ppm Polyethylene oxide (Polyox) solutions are also shown (hollow symbols). The upper dashed line represents the TRH predicted by a three-layers temperature profile model assuming a constant $Pr_t = 5$. The TRH/TRD ratio is shown in the lower graph for experimental data (symbols) and the model predictions (dashed line) (pipe ID = 20 mm).

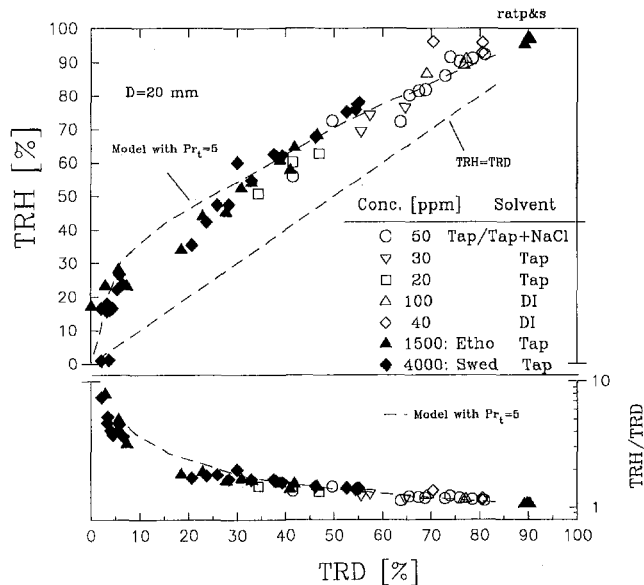


Fig. 5 TRH versus TRD for two surfactant solutions: Ethoquad T13-27 and SPE 95285 (solid symbols) and for the polymer solution data shown in Fig. 4 (hollow symbols). The upper dashed line shows the predicted TRH based on a three-layers temperature profile model assuming a constant $Pr_t = 5$. The TRH/TRD ratio is shown at the bottom for the experimental data (symbols) and the model predictions (dashed line) (pipe ID = 20 mm).

levels of TRD approaches the constant value measured for asymptotic conditions (about 1.06).

Figure 5 shows results for surfactant solutions, including data close to onset, together with our data for the polymer solutions shown in Fig. 4. The results for surfactants are close to those for polymer solutions. Both surfactant solutions used in these experiments had water-like viscosity (see Section 2), which we endeavored to achieve to eliminate the effect of strong viscosity dependence on the shear rate in the calculations of friction and heat transfer coefficients. In this case the fluids were found to show a Pr_t of approximately 5. We also see that TRH/TRD increases significantly at very low levels of drag reduction. (It should be noted, however, that the measurement uncertainty is larger in this region.) As we see, for both polymer and surfactants, a Pr_t of about 5 in the mathematical model gives predictions that fit well the experimental data. For the surfactants, it was possible to obtain measurements closer to the onset, which show a sharper increase in TRH than in TRD, as was indeed predicted by the model. Since the surfactants used for these tests had water-like viscosity, a practical advantage of knowing this ratio is that it can also be used to determine whether or not other more viscous solutions are in reality asymptotic. Viscosity affects TRD and TRH in opposite directions, which means that the fluid might have a high viscosity if the expected TRH/TRD ratio is not obtained in simultaneous drag and heat transfer tests.

Overall, these results suggest that although TRH/TRD seems to be a function of the level of drag-reducing effects (TRD), there is indeed a strong coupling between the heat transfer and friction reductions for these fluids through a constant, or approximately constant, nonunity Pr_t . In addition, it appears that both surfactant and polymer solutions exhibit very similar TRH/TRD ratios.

(A word of caution is appropriate here, however. All our results reported here, except for those shown in Figs. 7 and 8, correspond to fluids with a molecular Prandtl number of about 6 around ambient temperature. Some later tests conducted with fluids exhibiting significantly higher Pr_t (e.g., 40 to 60 for some surfactant solutions) showed a somewhat higher TRH/TRD ratio at low Re , however. We are presently investigating further this issue through direct measurements of the temperature profiles and the preliminary findings suggest that the viscous layer may be significantly

thickened for some fluids, which would indeed cause the molecular Prandtl number to affect the TRH/TRD ratio. These results will be published elsewhere.)

3.4 Onset of Heat Transfer and Friction Reduction Phenomena. A possible decoupling between heat transfer and friction has been thought to take place at the onset of drag and/or heat transfer reductions, each of which could conceivably occur at a different shear stress. Different onsets means that there would be some drag reduction without heat transfer reduction, or vice versa. This was apparently observed in some previous studies (Mizushima and Usui, 1977; Kwack et al., 1982). This concept is puzzling, however, if one thinks in terms of the physical flow/fluid interaction mechanisms behind turbulent viscoelastic drag reduction, and one might think it rather unlikely. Accordingly, we undertook investigations to reexamine this issue. In these experiments, the heat transfer and friction coefficients were measured in pipes of various diameters and with various flow velocities. The velocity was lowered systematically, so that the TRD for all pipes was reduced until Newtonian turbulent friction coefficients were detected (i.e., $DR = TRD = 0$ percent).

Some data for a surfactant solution are shown in Fig. 6, where we plot TRD (hollow symbols) and TRH (solid symbols) as a function of shear velocity, i.e., of shear stress. Data for both a 10-mm and a 20-mm pipes are shown. The TRD data are as measured, but the TRH data have been corrected by a constant Nusselt number multiplier coefficient (different for each pipe) to remove a small positive constant offset (ten percent or less, i.e., within the limits of uncertainty for that region) in TRH observed in the data before onset. This is not necessary for the purpose of estimating the onset of drag and heat transfer reductions, but it makes the figure much clearer and we have therefore decided to include it here for better illustration of the onset effect. (Practically speaking, this correction only shifts the curves vertically in this graph.) This offset may result from buoyancy effects (described elsewhere) or from instrumentation calibration errors, but its constancy before onset over a wide range of velocities clearly suggests that it is indeed purely a measurement offset rather than a true viscoelastic reduction effect, and is therefore not affecting our onset evaluation.

The data for both pipes are seen to be very similar, as expected

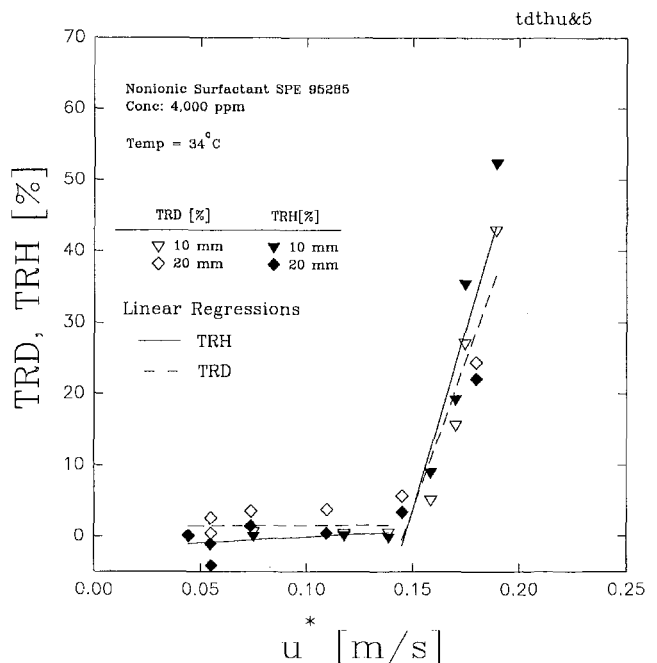


Fig. 6 TRH (corrected) and TRD: onset of drag and heat transfer reductions (solvent: tap water)

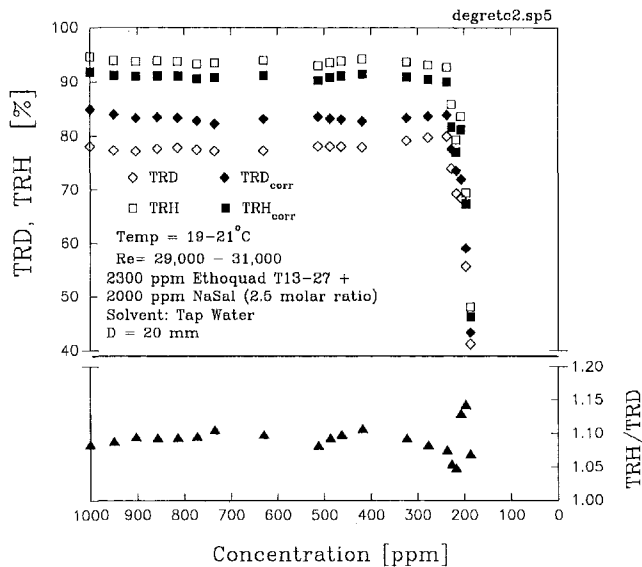


Fig. 7 Relationship between TRH and TRD in the asymptotic and non-asymptotic regions: effect of a decrease in concentration for a surfactant solution. (TRH_{corr} and TRD_{corr} are calculated by using the solution apparent viscosity at the wall, rather than the solvent viscosity as used for TRH and TRD) (pipe ID = 20 mm).

in this representation. To quantify better the onsets, we show calculated linear regressions through both pipe data, both before and after the sharp increase in TRH and TRD. Whereas such a procedure is approximate, we nevertheless clearly see through the extrapolated intersections of the regressions that the onsets for both friction and heat transfer reductions take place at about the same shear stress (corresponding to about $u^* = 0.15$ m/s in this case) i.e., simultaneously. This is in sharp contrast to the concept that heat transfer and friction might depart from Newtonian behavior under different flow conditions, as some have suggested. It is also interesting to see that the data confirm that the onsets take place at the same shear stress for both pipe diameters.

3.5 Departure From Asymptotic Behavior. Another apparent contradiction with the idea of coupling through constant Pr, is an observation reported by some authors (Ng and Hartnett, 1979; Matthys, 1991) that HTR departs from its asymptotic value sooner than DR during the process of degradation. If this is indeed the case, then the momentum and heat transfer mechanisms would not be coupled in this region. It appears that relatively small uncertainties in viscosity estimations might account for the apparent initial decrease in the friction and the apparent rapid increase in heat transfer after the start of degradation shown in Ng and Hartnett (1979). Once compensated for, this viscosity effect would indeed lead to data consistent with simultaneous departure of heat transfer and friction coefficients from their asymptotic values. This viscosity effect would not explain the data in Matthys (1991), but it is possible that the latter may have been affected by buoyancy effects as described above. In an attempt to clarify these issues, we conducted dedicated experiments with the same polymer solution (Separan AP-273) and with a surfactant solution (Ethoquad T13-27). In both cases we started out with a fluid showing asymptotic TRD and TRH, but the procedure by which we departed gradually from the asymptotic conditions was different. Figure 7 shows the experimental data for the surfactant solution, which was gradually diluted until a clear decrease of TRD and TRH occurred. This sudden change results from the critical shear stress for micellar breakup becoming smaller at that reduced concentration than the actual shear stress in the pipe. Samples of each concentration were taken in order to measure the viscosity in a capillary pipe viscometer at the same apparent shear stress as the flow in the pipe. The corresponding molecular Prandtl number ranged from about 15 at

high concentration to about 6 at low concentration (and similar numbers for the polymer solution discussed in Fig. 8 at no and high degradation, respectively.) The TRD and TRH values with no correction for viscosity are shown in Fig. 7 as the hollow symbols (assuming a constant viscosity equal to that of the solvent), whereas the solid ones are calculated with the actual solution viscosity. It should be noted that the viscosity corrections affect heat transfer and friction in opposite directions. The effect is not large here, because we have used a fluid with a viscosity close to that of water, which is advantageous if we want to reduce the possible errors due to the complex issue of appropriate choice of viscosity. Throughout all levels of dilution we see a constant ratio of approximately 1.07 again (with larger scatter after the sudden drop because of calculation uncertainties there). It is also apparent that both heat transfer and friction drop off suddenly at the same concentration, suggesting again that they are coupled in the near-asymptote region and that departure from asymptotic conditions takes place simultaneously for drag and heat transfer.

Figure 8 shows the data for the polymer solution experiment. A relatively high concentration of Separan AP-273 (100 ppm) was used to provide enough resistance to mechanical degradation, resulting in a noticeable increase of the fluid viscosity. In this case the fluid was gradually degraded by recirculation in a loop including a near-closed valve generating high shear stresses. Simultaneous TRD and TRH measurements in the loop were conducted at various times. As with the surfactant solution, samples of fluid were taken at every stage and their viscosity was measured with a capillary viscometer at approximately the same apparent shear stress as in the pipe. Again, the TRD and TRH values with and without correction for viscosity are shown. We see that the departure from asymptotic conditions occurs at the same time for friction and heat transfer, and that further decreases appear to occur in parallel. The TRH/TRD ratio is indeed again remarkably constant throughout the whole range of degradation levels and again remains at a value very close to 1.07. These data again reinforce the notion that a strong coupling exists between heat and friction under asymptotic and near-asymptotic conditions. These results for both polymer and surfactant solutions all do indeed appear to be contradicting the notion suggested in some earlier studies that heat transfer reduction may depart earlier from its asymptote than the friction.

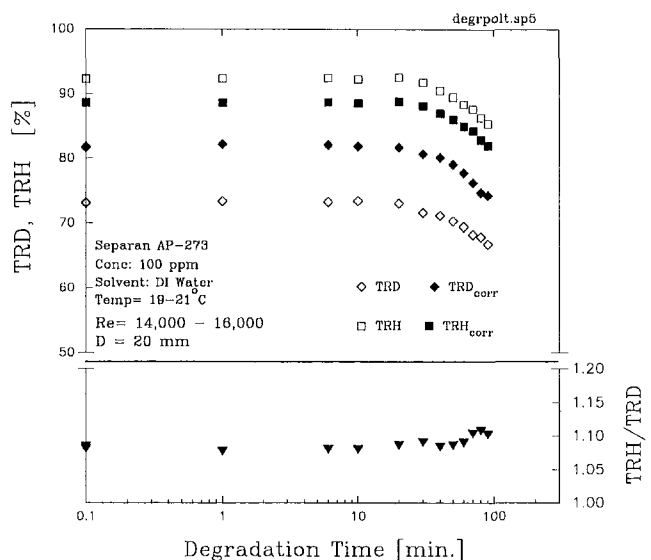


Fig. 8 Relationship between TRH and TRD in the asymptotic and non-asymptotic regions: effect of mechanical degradation for a polymer solution. (TRH_{corr} and TRD_{corr} are calculated by using the solution apparent viscosity at the wall, rather than the solvent viscosity as used for TRH and TRD) (pipe ID = 20 mm).

4 Summary and Conclusions

In this work we investigated the coupling between drag and heat transfer reductions for polymer and surfactant solutions through the use of global flow parameters (friction and heat transfer coefficients).

In the asymptotic regime an approximately constant value of the TRH/TRD ratio is found if modified definitions of the level of reductions are used. The ratio of these modified reduction definitions, which we referred as turbulence reduction-heat (TRH) and turbulence reduction-drag (TRD) was found to be about 1.06 for polymer and surfactant solutions.

In the nonasymptotic regime, however, TRH/TRD is a function of the level of drag reduction. At high levels of TRD the ratio is equal to its value measured for asymptotic regime, whereas it increases with decreasing TRD. The reason for this behavior is likely that TRH increases much faster than TRD with increasing velocity after the onset.

A simple mathematical model based on a three-layers velocity profile model, on our measurements of temperature profiles for the same fluids (showing a Pr_t of about 5 or 6 within the elastic layer), and on the assumption of the same thickness for both thermal and momentum elastic layers, would predict the same type of behavior. Altogether, a strong coupling between the heat and momentum exchange mechanisms is indeed suggested, although certainly not as simple as the Newtonian Reynolds analogy of a unity turbulent Prandtl number.

Decoupling of the two exchange mechanisms was also suggested by some authors in the region close to the onset and in the vicinity of asymptotes. Our tests with both surfactant and polymer solutions in both regions showed the opposite, i.e., a strong coupling of the two exchange mechanisms: In simultaneous measurements of heat transfer and friction at increasing flow velocity, drag and heat transfer reductions appeared to begin to take place at the same onset shear stress. In tests in a circulation loop with asymptotic fluids, the first signs of departure from the asymptotes due to either mechanical degradation or dilution appeared at the same time for drag and heat transfer.

On the theoretical side these results are very interesting in that they suggest a much stronger coupling between heat and momentum transfer than was generally believed recently, but yet not the full physical coupling ($Pr_t \approx 1$) seen for Newtonian fluids.

On the practical side, these findings are also very useful. As the ratio TRH/TRD appeared to be a unique function of TRD even for very different fluids such as polymer and surfactant solutions, one can readily predict the heat reduction based on measurements of drag reduction, or vice versa. This may also be particularly useful for surfactant solutions which exhibit a strong dependence of the viscosity on shear rate. For example, if simultaneous measurements of friction and heat transfer reductions are made, one could easily check if the viscosity used in evaluating both friction and heat transfer coefficients is appropriate by testing for the expected ratio of reductions. This is particularly convenient for the asymptotic regime, for which the ratio is a constant.

Our study of the diameter effect on heat transfer for drag-reducing fluids showed that the scaling procedure proposed for friction holds just as well for heat transfer; i.e., that the ratio between heat transfer and drag reduction does not depend on pipe diameter.

Finally, the observation that the same ratio holds for both the surfactant and polymer solutions does support the notion that the drag reduction phenomenon involves similar physical mechanisms for both type of solutions.

Acknowledgments

We acknowledge gratefully the financial support of the California Energy Commission (contract No. 490260 to EFM) and the

generous supply of surfactants by Drs. S. Shapiro and M. Hellsten (AKZO-Nobel Chemicals). GA also wishes to acknowledge the Universidad Nacional Autonoma de Mexico, and especially the DGAPA and the IIM for support granted through the scholarship program.

References

- Aguilar, G., 1995, "Study of the Diameter Effect and Scaling Procedures for Drag-Reducing Surfactant and Polymer Solutions," M.Sc. thesis, University of California, Santa Barbara, CA.
- Aguilar, G., Gasljevic, K., and Matthys, E. F., 1998, "On the Relationship Between Heat Transfer and Drag Reductions for Polymer and Surfactant Solutions," *Heat Transfer in Flowing Systems*, ASME, New York, pp. 139–146.
- Astaria, G., Greco, Jr., G., and Nicodemo, L., 1969, "A Phenomenological Interpretation and Correlation of Drag Reduction," *AIChE J.*, Vol. 14, No. 4, pp. 564–567.
- Blasius, H., 1913, "Das Ahnlichkeitsgesetz bei Reibungsvorgängen in Flüssigkeiten," *Forsch. Ing.-Wes.*, No. 134, Berlin.
- Cho, Y. I., and Hartnett, J. P., 1982, "Non-Newtonian Fluids in Circular Pipe Flows," *Advances in Heat Transfer*, Vol. 15, Academic Press, San Diego, CA, pp. 60–141.
- Filomenko, G. K., 1954, *Hydraulic Resistance in Pipes*, Vol. 1, No. 4, pp. 40–44.
- Gasljevic, K., 1990, "Design and Construction of an Experimental Installation for the Investigation of Heat Transfer and Drag Reductions in Turbulent Flow of Viscoelastic Fluids," M.Sc. thesis, University of California, Santa Barbara, CA.
- Gasljevic, K., Aguilar, G., and Matthys, E. F., 1999, "An Improved Diameter Scaling Correlation for Turbulent Flow of Drag-Reducing Polymer Solutions," *J. of Non-Newtonian Fluid Mechanics*, Vol. 84, No. 3, pp. 131–148.
- Gasljevic, K., and Matthys, E. F., 1997, "Experimental Investigation of Thermal and Hydrodynamic Development Regions for Drag-Reducing Surfactant Solutions," *ASME JOURNAL OF HEAT TRANSFER*, Vol. 119, pp. 80–88.
- Gasljevic, K., and Matthys, E. F., 1999, "Improved Quantification of the Drag Reduction Phenomenon Through Turbulence Reduction Parameters," *J. of Non-Newtonian Fluid Mechanics*, Vol. 84, No. 3, pp. 123–130.
- Kale, D. D., 1997, "An Analysis of Heat Transfer to Turbulent Flow of Drag-Reducing Fluids," *Int. J. of Heat and Mass Transfer*, Vol. 20, pp. 1077–1081.
- Kays, W. M., 1966, *Convective Heat and Mass Transfer*, McGraw-Hill, New York.
- Kwack, E. Y., Hartnett, J. P., and Cho, Y. I., 1982, "Turbulent Heat Transfer in Circular Tube Flows of Viscoelastic Fluids," *Wärme und Stoffübertragung*, Vol. 16, pp. 34–55.
- Matthys, E. F., 1991, "Heat Transfer, Drag Reduction, and Fluid Characterization for Turbulent Flow in Polymer Solutions; Recent Results and Research Needs," *J. of Non-Newtonian Fluid Mechanics*, Vol. 38, pp. 313–342.
- Mizushima, T., and Usui, H., 1997, "Reduction of Eddy Diffusion for Momentum and Heat in Viscoelastic Fluid Flow in a Circular Tube," *Phys. Fluids*, Vol. 20, pp. S100–S108.
- Mizushima, T., Usui, H., and Yamamoto, T., 1975, "Turbulent Heat Transfer of Viscoelastic Fluid Flow in Pipes," *Letters in Heat and Mass Transfer*, Vol. 2, pp. 19–26.
- Ng, K. S., Cho, Y. I., and Hartnett, J. P., 1980, "Heat Transfer Performance of Concentrated Polyethylene Oxide and Polyacrylamide Solutions," *AIChE Symposium Series* (19th National Heat Transfer Conference), Vol. 76, No. 199, pp. 250–256.
- Ng, K. S., and Hartnett, J. P., 1979, "Effects of Mechanical Degradation on Pressure Drop and Heat Transfer Performance of Polyacrylamide Solutions in Turbulent Pipe Flow," *Studies in Heat Transfer*, T. F. Irvine, Jr., et al., eds., McGraw-Hill, New York, pp. 297–307.
- Petukov, B. S., 1970, "Heat Transfer and Friction in Turbulent Pipe Flow With Variable Physical Properties," *Advances in Heat Transfer*, Vol. 6, pp. 503–564.
- Poreh, M., and Paz, U., 1968, "Turbulent Heat Transfer to Dilute Polymer Solutions," *Int. J. Heat and Mass Transfer*, Vol. 11, pp. 805–810.
- Roethig, T. R., and Matthys, E. F., 1988, "Eddy Diffusivities for Non-Isothermal Tube Flow of Drag-Reducing Polymer Solutions," *Proceedings of the 10th International Congress on Rheology*, Vol. 2, P. Uhlherr, ed., ASR, Sydney, Australia, pp. 227–229.
- Schmitt, K., Brunn, P. O., and Durst, F., 1988, "Scaling-Up Correlations for Drag Reducing Surfactants," *Progress and Trends in Rheology II*, pp. 249–252.
- Sleicher, C. A., and Rouse, M. W., 1975, "A Convenient Correlation for Heat Transfer to Constant and Variable Property Fluids in Turbulent Pipe Flow," *Int. J. of Heat and Mass Transfer*, Vol. 18, pp. 677–683.
- Smith, R., and Edwards, M., 1981, "Heat Transfer to non-Newtonian and Drag-Reducing Fluids in Turbulent Pipe Flow," *Int. J. Heat Mass Transfer*, Vol. 24, pp. 1059–1069.
- Toh, K. H., and Ghajar, A. J., 1998, "Heat Transfer in the Thermal Entrance Region for Viscoelastic Fluids in Turbulent Pipe Flow," *Int. J. Heat and Mass Transfer*, Vol. 31, No. 6, pp. 1261–1267.
- Yoon, H. K., and Ghajar, A. J., 1987, "A Heat Transfer Correlation for Viscoelastic Turbulent Pipe Flows Under Constant Wall Heat Flux," *Proceedings of the 1987 ASME/AIChE National Heat Transfer Conference*, Pittsburgh, PA, Aug. 9–12, ASME New York, pp. 1–7.
- Zakin, J. L., Myska, J., and Chara, Z., 1996, "New Limiting Drag Reduction and Velocity Profile Asymptotes for Non-polymeric Additives Systems," *AIChE Journal*, Vol. 42, No. 12, pp. 3544–3546.

The Effect of Drainage Configuration on Heat Transfer Under an Impinging Liquid Jet Array

K. Garrett

B. W. Webb

Mechanical Engineering Department,
435 CTB,
Brigham Young University,
Provo, UT 84602

The heat transfer characteristics of single and dual-exit drainage configurations for arrays of liquid jets impinging normal to a heated isoflux plate has been studied experimentally. The interaction of drainage channel crossflow from upstream jets and the stagnation jets and its impact on heat transfer was the focus of the investigation. Infrared thermography was used to measure the local temperature distribution on the heated plate, from which local heat transfer coefficients were determined. A single jet diameter was used, and jet arrays with jet-to-jet spacings of 4.8, 6, 8, and 12 jet diameters were studied. Average jet Reynolds numbers in the range 400–5000 were investigated for jet nozzle-to-impingement plate spacings of 1, 2, and 4 jet diameters for fully flooded (submerged) drainage flow. A single jet-to-plate spacing large enough to yield free-surface jets was also studied. The data reveal a complex dependence of local and average Nusselt numbers on the geometric parameters which describe the problem configuration.

Introduction

Impinging jets provide high transport coefficients which make them attractive for use in applications such as paper drying, quenching of metals, turbine blade cooling, and thermal control of a variety of high heat flux devices (electronics, X-ray optics, etc.). Impinging liquid jets provide particularly high heat/mass transfer. Although such jets yield very high heat transfer coefficients in the stagnation zone, the transport drops quite rapidly as the fluid transits from impingement at the jet stagnation point to parallel flow. For this reason jets are often used in arrays in industrial practice. There has been considerable recent work investigating the fundamental transport behavior of single liquid jets. There is a considerable body of literature dealing with crossflow effects on heat transfer under arrays of air jets (Florschuetz et al., 1980; Florschuetz et al., 1981; Hollworth and Berry, 1978; Huang et al., 1998; Kercher and Tabakoff, 1970; Obot and Trabold, 1987; Van Treuren et al., 1994). These studies have thoroughly investigated the influence of crossflow of spent air on heat transfer over a wide range of relevant problem parameters. Recent reviews surveying the literature on liquid jets (Lienhard, 1995; Webb and Ma, 1995) reveal few investigations characterizing the behavior of liquid jet arrays. More recent studies include those of Pan and Webb (1995), Lienhard et al. (1996), and Oh et al. (1998). These investigations have focused largely on arrays for which cross-flow effects, which potentially degrade the high stagnation heat transfer associated with impinging jets, are designed to be minimal.

This study deals with the effect of drainage configuration on the transport behavior of liquid jet arrays in confined channels. Heat transfer phenomena are studied for both flooding (submerged) and free-surface jet arrays conditions.

Experimental Apparatus and Procedure

The apparatus for study of the effects of drainage configuration on heat transfer under an array of impinging liquid jets consisted of the liquid delivery and metering system, the heater plate, and the

local temperature measurement system. These will now be described in detail, followed by the experimental procedure.

Flow Delivery System. The flow delivery system is shown schematically in Fig. 1. House supply water at 517 kPa (75 psi) was delivered to two vertically mounted rotameters which were configured in parallel. The two flowmeters provided two different ranges (maxima $1.3 \times 10^{-4} \text{ m}^3/\text{s}$ and $9.5 \times 10^{-4} \text{ m}^3/\text{s}$, respectively) for optimal control of the water flow rate and metering. After passing through the flowmeters the water was directed to the top of a plenum 100 mm square by 130 mm high. Inside the walled Plexiglas plenum the water passed through two baffle plates before entering a 9.5-mm thick jet orifice plate attached to the bottom of the plenum. The plenum was designed to accommodate one of four such orifice plates, each with a different nozzle array configuration (5×5 , 7×7 , 9×9 , and 11×11 jet arrays corresponding, respectively, to dimensionless jet-to-jet spacings of $s/d = 12$, 8, 6, and 4.8 in a square jet array pattern). The jet orifice diameter was maintained constant among all plates at $d = 1.6$ mm. Plenum-side orifice entrances were countersunk at 45-deg angles to provide smooth inlets. After passing through the orifice plate the water impinged against a heated plate of area $90 \text{ mm} \times 100 \text{ mm}$. The spent fluid flowed in a rectangular channel bounded by the jet orifice plate on top, the heated impingement plate on bottom, and copper electrical bus bars which formed the side walls. Single and dual-exit configurations were studied, which permitted channel drainage from one or both ends of the channel, respectively, as seen in the lower panel of Fig. 1. The orifice plate was positioned at a desired distance z from the impingement plate using precision-machined spacer rods, after which the bus bars were pressed firmly against the plenum/orifice plate assembly to form a water-tight seal. No leakage was observed between the copper bus bars and the vertical walls of the plenum.

Four different nozzle-to-plate spacings were investigated in the study corresponding to $z/d = 1$, 2, 4, and a final spacing which would ensure free-surface flow for all jets in the array (typically 15 diameters). The spacing chosen for the free-surface jets insured that jet acceleration and necking due to gravity was less than five percent of the jet exit values, with the exception of the very low Reynolds number experiments where it reached as high as ten percent.

Contributed by the Heat Transfer Division for publication in the JOURNAL OF HEAT TRANSFER. Manuscript received by the Heat Transfer Division, Dec. 1, 1998; revision received, July 26, 1999. Keywords: Experimental, Heat Transfer, Jets. Associate Technical Editor: J.-C. Han.

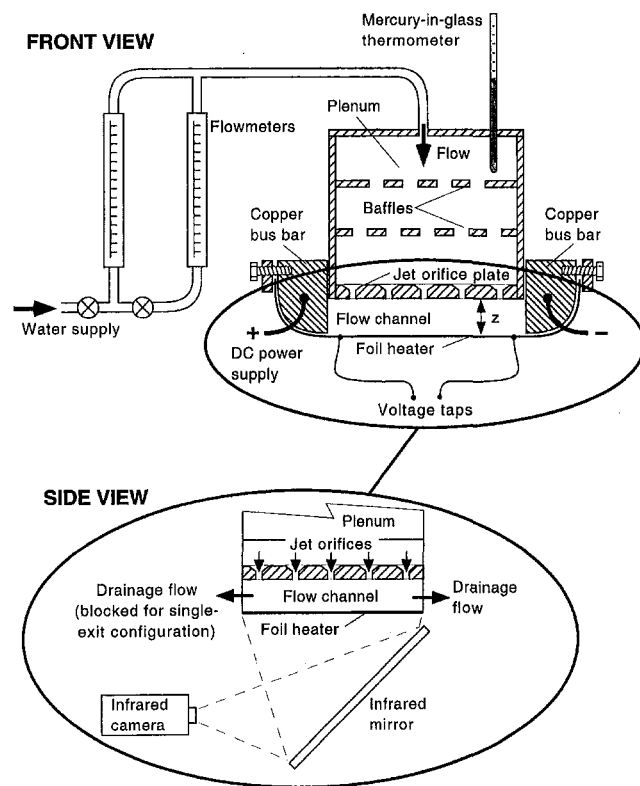


Fig. 1 Schematic illustration of the experimental apparatus

A jet-average Reynolds number was calculated from the total metered water flow rate from the relation

$$Re = \frac{4G}{n\pi d\nu} \quad (1)$$

where G is the total flow rate through all orifices and n is the total number of jets in the array.

To evaluate the differences in jet velocity due to drainage channel streamwise variations in pressure the apparatus was modified to permit the collection of pressure data in the channel. Pressure difference data were taken for the $s/d = 4.8$ orifice plate for the single-exit flow condition, since the heat transfer data for this experimental condition showed the greatest influence of jet velocity variations in the streamwise direction. The bus bars which formed the side walls of the flow channel were replaced in the pressure measurement experiments by Plexiglas plates. Pressure taps were drilled in one of the Plexiglas side walls at five equispaced locations along the channel. These holes were used to measure the pressure difference between the plenum directly above the jet orifice plate and the flow channel at the five streamwise locations. The taps were located in the side wall of the flow

channel so as to measure the difference between plenum pressure and static pressure in the channel. Data were taken for four different operating conditions: $z/d = 1$ and 4 at representative low and high flow rates. The acquired pressure difference data permitted the estimate of the distribution of flow rates among jets in the array along the streamwise direction.

Heated Impingement Plate. The impingement plate was composed of a 0.025-mm thick sheet of stainless steel shim stock which was connected to two large copper bus bars (see Fig. 1). The bus bars were contoured along one edge so as to provide good contact area with the metal foil heater, in a design similar to that used previously (Pan et al., 1992). The metallic foil heater was stretched tightly to prevent deflection by the impinging force of the jets. This was accomplished by systematically tightening threaded rods connected to, but electrically insulated from the bus bars. Measurements of impingement plate displacement under the jet array revealed a maximum deflection of less than 0.04 mm (0.0015 in.). The bus bars provided not only uniform distribution of the electrical power to the heater foil, but also served as the bounding side walls in the channel flow following impingement of the jets. The bus bars were attached by welding cable to two DC power supplies connected in parallel, with a maximum total amperage capacity of 240 amps.

The total power dissipated in the foil heater was calculated by the product of the voltage drop and the current drawn. The power supplies provided accurate digital readout of the total current drawn by the foil heater during heating. Since considerable voltage drop can occur in the contact between the copper bus bars and the foil heater, voltage taps were attached directly to one edge of the heater foil at a known distance along the direction of current flow. The total power was then determined by the product of the sum of the current from the two power supplies, and the measured voltage drop across the heater. The heat flux imposed was then calculated as the ratio of the Ohmic dissipation to the area defined by the heater width and the heater length between voltage taps.

Temperature Measurement. The local temperature of the heated impingement plate was measured using a two-dimensional infrared imaging camera. The unwetted underside of the heated foil was painted flat black (to maximize emission and minimize reflections), and was imaged through an infrared, front-surface mirror by the thermal imaging camera. The infrared image was recorded on a conventional video cassette recorder for subsequent playback and analysis using commercial frame grabber hardware and image manipulation software. The optical configuration used in this study yielded spatial temperature resolution on the heated plate of the order of 0.3 mm. During the experimentation, the liquid jet temperature T_j was measured radiometrically by imaging the unheated foil exposed to jet impingement. A precision liquid-in-glass thermometer positioned in the plenum provided a reference measurement for comparison. The local heated plate temperature T_p was measured after electrical current was applied to the heater and under the cooling effects of the impinging jet array. The local heat transfer coefficient was calculated from the heat flux

Nomenclature

A = impingement plate area
 d = inside diameter of jet
 G = total volumetric flow through jet array
 h = heat transfer coefficient
 \bar{h} = plate-average heat transfer coefficient
 \bar{h}_r = row-average heat transfer coefficient
 k = thermal conductivity

L = plate length
 n = number of jets in the array
 Nu = local Nusselt number, hd/k
 \bar{Nu} = plate-average Nusselt number, $\bar{h}d/k$
 \bar{Nu}_r = row-average Nusselt number, $\bar{h}_r d/k$
 q'' = plate heat flux

Re = jet-average Reynolds number
 s = jet-to-jet spacing (center-to-center)
 T_j = jet temperature
 T_p = local impingement plate temperature
 \bar{T}_p = average plate temperature
 \bar{T}_r = average temperature below jet row
 z = nozzle-to-plate spacing
 ν = kinematic viscosity

imposed at the heater foil and the measured liquid jet and local plate temperatures from Newton's law of cooling:

$$h = q''/(T_p - T_j). \quad (2)$$

The registration of positions in the infrared images and the physical location on the heated plate was accomplished by matching drastic changes in the emissivity of the imaged system with known physical components and their positions.

The infrared thermography system was calibrated using the procedure outlined by Pan et al. (1992), and described in detail by Garrett (1998). While the plate was unheated electrically, heated water was directed through the array and the infrared image of the plate was acquired. The water temperature was measured using the precision mercury-in-glass thermometer. With such high heat transfer coefficients ($h > 20,000 \text{ W/m}^2\text{K}$) the plate assumed the impinging jet water temperature. The measured plate radiance was then related to the known plate (jet water) temperature independent of the radiative properties on the imaged side of the impingement plate. This procedure was followed for 15 different water temperatures spanning the plate temperature range observed in the experiments, and a calibration table was developed. This procedure yields accuracy in measured plate temperature of $\pm 0.1^\circ\text{C}$.

The two-dimensional infrared images associated with the jet array cooling were extracted from the recorded images using the frame grabber hardware and software. Local Nusselt numbers were calculated for the array from the heat transfer coefficient determined according to Eq. (2) and from the definition of Nu used here, which is based on the jet orifice diameter. Row-average Nusselt numbers were determined from plate temperature data in areas on the heated plate defined by a row of jets perpendicular to the crossflow direction according to the relation

$$\overline{\text{Nu}}_r = \frac{q'' d}{(\bar{T}_r - T_j)k} \quad (3)$$

where \bar{T}_r is the average heated surface temperature under the jet row in question. The plate-average Nusselt number was determined for the full heated plate per the relation

$$\overline{\text{Nu}} = \frac{q'' d}{(\bar{T}_p - T_j)k} \quad (4)$$

where \bar{T}_p is the average plate temperature. Note that the jet orifice diameter d is the characteristic length used in the definitions of local and average Nusselt number. The row-average and plate-average temperatures used in Eqs. (3) and (4), respectively, were calculated by area-averaging the local impingement surface temperature data measured. The side columns of jets (column parallel to drainage flow and adjacent to the bounding side walls) and exit row jets were not used in the determination of the plate-average Nusselt number in order to eliminate end effects and anomalous exit row phenomena.

An uncertainty analysis was performed by the method outlined in Beckwith et al. (1982), and full details of the analysis may be found in Garrett (1998). The calibrated infrared imaging system yielded measured temperature differences ($T_p - T_j$) conservatively accurate to 0.3°C . Voltage and current for the heated impingement plate were measured to 0.02 V and 0.3 A, respectively. Water flow rates were measured to 2.5 percent of flowmeter full scale. These were the dominant contributions to uncertainty in dimensionless quantities. The uncertainty in average jet Reynolds number was found to be 3.9 percent and 10.8 percent for $\text{Re} = 3600$ and 820, respectively. Corresponding uncertainties in Nusselt number were 4.6 percent and 8.3 percent, respectively.

Results and Discussion

Jet Flow Distribution. An understanding of the flow rate distribution among jets in the orifice plate is critical to the understanding of the local and average heat transfer phenomena. Using

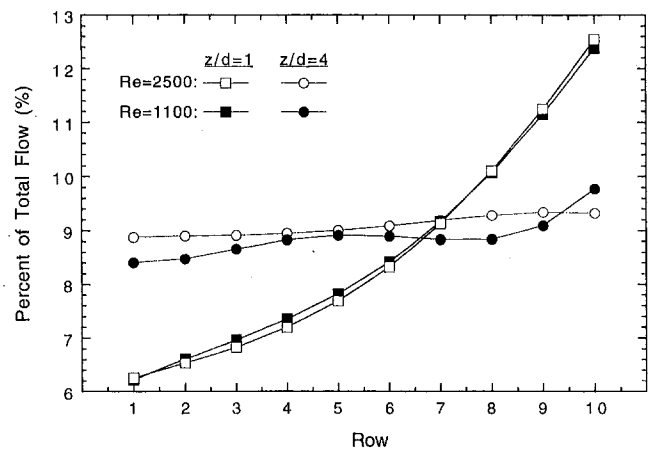


Fig. 2 Distribution of flow through each jet row for the $s/d = 4.8$ array configuration

the measured pressure differences between plenum and drainage channel, the fluid flow rate through each row of jet orifices was calculated from the energy equation (Gerhart and Gross, 1985). All pressure losses were included in the analysis. Since the pressure difference was measured at only five streamwise locations, the data were interpolated to determine the flow rate through each of the jet rows in the array. Velocities in each of the jet rows were determined with the constraint that the sum of jet flows from all rows matched the metered total flow rate. The predicted distributions are shown in Fig. 2 as a percentage of total flow through each row of jets for nominal Reynolds numbers 1100 and 2500 for $s/d = 4.8$ (11×11 array), $z/d = 1$ and 4, with the single-exit drainage configuration. The final row of jets did not impinge completely on the impingement plate, so it is not included here. However, its contribution to the total flow was included in the calculation.

Figure 2 reveals that the larger nozzle-to-plate spacing results in more uniform flow rate distribution among jet rows. There is little variation in the percent of total flow among the rows of jets for $z/d = 4$ for both Reynolds numbers studied. However, there is significant variation in the distribution for $z/d = 1$; the fraction of total array flow through each row of orifices varies from slightly over six percent in the upstream-most row (row 1) to 12.5 percent in the final row of holes. This is due to the fact that pressures in the upstream region of the drainage channel are higher than those downstream near the exit. Resulting pressure differences are lower upstream than near the exit with correspondingly lower jet velocities. This has been observed previously in air jet arrays with confined crossflow (Kercher and Tabakoff, 1970; Florschuetz et al., 1981; Van Treuren et al., 1994). This nonuniform flow distribution among jets in the array cannot be avoided if the orifices are fed from a common plenum. As will be seen in sections to follow, the nonuniform flow distribution will impact the local and row-average Nusselt number distribution along the impingement plate. It is expected that the flow rate distribution would be uniform through the array for free-surface jet conditions, since the orifice exit pressure is identical for all jets along the length of the flow channel for this condition.

Plate-Average Nusselt Number. The variation in plate-average Nusselt number with Reynolds number is shown in Fig. 3 for the $z/d = 4$ configuration for all jet-to-jet spacings studied. Nusselt numbers have been normalized by $\text{Pr}^{1/3}$ to facilitate later comparison with air jet array studies. All properties were determined at the average film temperature. The solid and dashed lines are least-squares fits of the dual-exit and single-exit drainage configuration data, respectively. The empirical correlations will be presented and discussed later. The general trends in these data are representative of those for other nozzle-to-plate spacings studied.

Figure 3 reveals that the dual-exit configuration results in higher

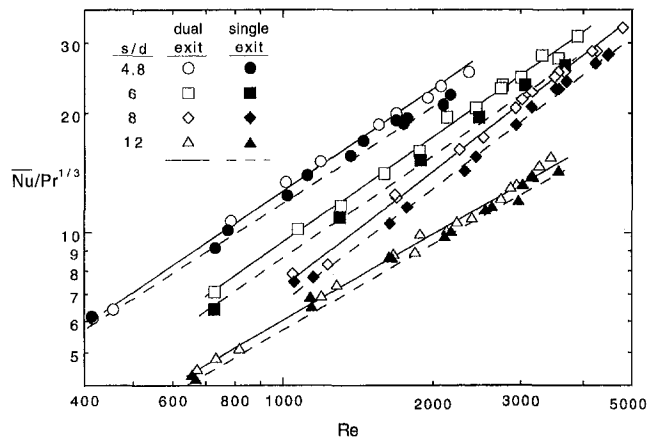


Fig. 3 Variation of plate-average Nusselt number with Reynolds number for the $z/d = 4$ nozzle-to-plate spacing

average Nusselt number than the single-exit system. The difference in \overline{Nu} between the two drainage modes is modest, but consistent. Recall that the spent fluid is free to exit on both sides of the bounding channel in the dual-exit configuration, whereas the crossflow accumulates entirely in one direction for single-exit drainage. The dual exit configuration thus minimizes the influence of crossflow. Therefore, stagnation flow heat transfer has more influence on overall heat transfer from the heated plate than the channel flow heat transfer resulting from increased crossflow. This is consistent with the intuitive observation that well-drained arrays yield higher average heat transfer than those for which drainage is somehow inhibited and where the resulting parallel flow momentum interrupts the stagnation flow. A comparison of data from this study with the empirical correlation developed for the well-drained square array configuration of Pan and Webb (1995) showed average square-array module Nusselt numbers to be between 20 percent and 30 percent higher than for the confined exit flow results presented here (Garrett, 1998).

Finally, the data of Fig. 3 reveal that the plate-average Nusselt number is higher for lower jet-to-jet spacings (i.e., more dense jet arrays). A higher density of jets yields stagnation flow with its associated higher transport over greater area on the impingement plate. Further, it is consistent with prior air jet array studies (e.g., Kercher and Tabakoff, 1970; Hollworth and Berry, 1978; Florschuetz et al., 1981). It is also true that, for the same average Reynolds number as defined here, denser jet arrays have higher overall mass flow rate, which would produce more intense crossflow heat transfer as well. The plate-average heat transfer coefficient \overline{h} for the different jet array configurations is compared on the basis of overall array mass flow rate G in Fig. 4 for the single-exit drainage configuration and the two extremes in nozzle-to-plate spacing studied, $z/d = 1$ and free-surface jets. A higher plate-average heat transfer coefficient indicates more effective cooling with resulting lower average plate temperature for the isoflux boundary condition. The figure shows that on the basis of identical total mass flow rate through the jet array, the higher jet-to-jet spacing (less populated array) yields a higher plate-average heat transfer coefficient. This was also observed by Hollworth and Berry (1978) and Obot and Trabold (1987) for air jet arrays. Using the total fluid delivered to the heated plate as the basis for comparison, the sparse array has the overall thermal advantage. However, it will be shown later that sparse arrays yield considerable more variation in local heat transfer.

Single submerged impinging jets exhibit a maximum in Nusselt number as a function of the nozzle-to-plate spacing in the range $z/d = 5 - 8$ (Martin, 1977). This spacing corresponds to the end of the jet potential core where the jet velocity is still substantially equal to the nozzle exit velocity, and the turbulence due to shear between jet and ambient fluid is a maximum. To investigate this

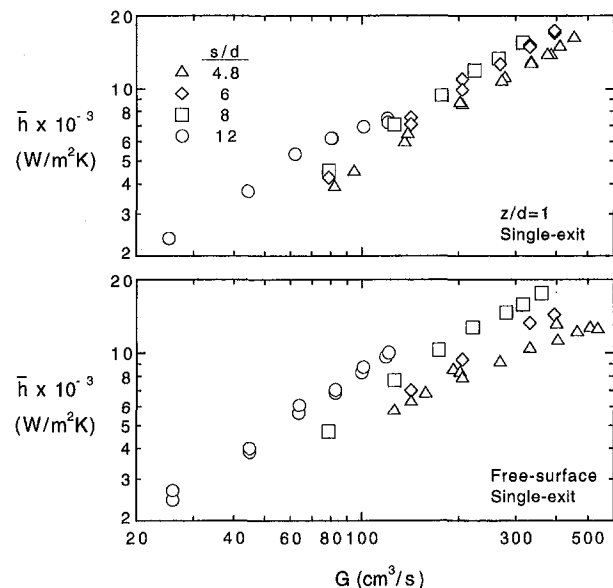


Fig. 4 Variation of plate-average heat transfer coefficient with total array flow rate for the $z/d = 1$ and free-surface jet conditions

phenomenon for liquid jet arrays with crossflow, the influence of nozzle-to-plate spacing on plate-average Nusselt number was carefully studied for two Reynolds numbers with the $s/d = 4.8$ jet array, single-exit configuration. The results are shown in Fig. 5 where the plate-average Nusselt number is plotted as a function of the nozzle-to-plate spacing. As z/d is increased the flow character changes from a flooded channel/submerged jet flow to free-surface jets. The free-surface jet regime is characterized by distinct free-surface jets issuing from each orifice in the array, subsequently forming a layer of liquid along the heated plate whose local thickness depends on s/d and Re . There is a transition regime which separates the fully flooded (submerged) channel flow from the free-surface jet flow. This transition regime is characterized by an upstream portion of the channel being flooded and the remaining portion near the channel exit being free-surface; the "interface" between flooded and free-surface portions is displaced upstream as Re is reduced or z/d is increased. The filled symbols in Fig. 5 indicate the fully flooded regime, the open symbols denote the free-surface regime, and the shaded symbols reflect z/d values where transition between the two occurs. It appears that the tran-

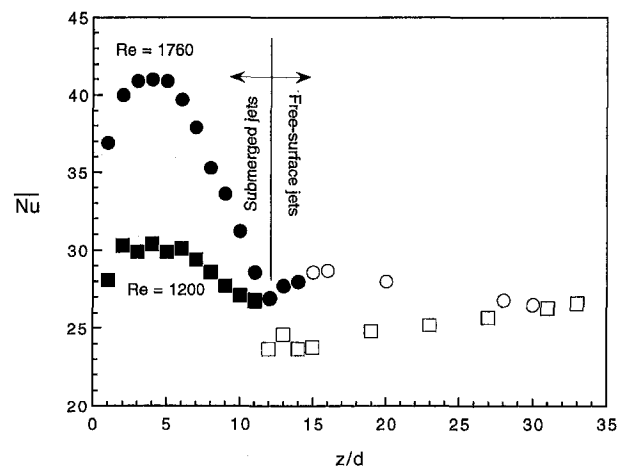


Fig. 5 Variation of plate-average Nusselt number with nozzle-to-plate spacing for the $s/d = 4.8$ array. Filled symbols denote fully flooded channel flow, open symbols indicate free-surface jets, and the shaded symbols reflect transition between the flooded and free-surface regimes.

Table 1 Constants for the empirical correlation of Eq. (5) for the $z/d = 4$ configuration

s/d	Single-exit drainage		Dual-exit drainage	
	A	m	A	m
4.8	0.042	0.82	0.041	0.84
6	0.019	0.88	0.022	0.88
8	0.0099	0.95	0.0089	0.97
12	0.048	0.70	0.041	0.73

sition occurs at or near $z/d = 12$ for both Reynolds numbers explored. The Nusselt number maximum observed previously for single submerged jets is also exhibited in the jet flow/crossflow configuration. Further, the maximum is found for $z/d \approx 4$, which is perhaps lower than the $z/d = 5-8$ range published for single submerged jets. This reduction in the z/d corresponding to maximum heat transfer has been observed in some previous studies of air jet arrays with crossflow (Hollworth and Berry, 1978; some suggestion of maximum in Obot and Trabold, 1987). The average Nusselt number at values of z/d above the transition jet-to-plate spacing ($z/d \approx 12$) is nearly constant.

Figure 5 shows clearly that free-surface jet arrays exhibit lower transport characteristics than the submerged jet arrays. This general observation is typical of all experimental data in the study. The difference can be quite dramatic; the $Re = 1760$ data reveal a 25–40 percent drop in \overline{Nu} between the maximum in the flooded jet array at $z/d \approx 4$ and the values found in the free-surface regime ($z/d > 12$). The reason for the reduced heat transfer in the free-surface regime will be discussed later where the row-average Nusselt number data are explored.

As revealed by the data of Fig. 5, the \overline{Nu} versus Re data of Fig. 3 for $z/d = 4$ represent the optimum spacing for plate-average heat transfer coefficient. Given this optimum heat transfer condition, the data for $z/d = 4$ were correlated empirically for both the single-exit and dual-exit configurations, for all jet-to-jet spacings studied over the range of Reynolds number in the investigation. The form of the correlation used is

$$\overline{Nu}/Pr^{1/3} = A Re^m \quad (5)$$

where A and m are constants determined from the least-squares correlation of the measurements. The correlation results are summarized in Table 1. It is seen that the exponent m varies between 0.70 and 0.97. With the exception of the $s/d = 12$ array, the exponent m increases with increasing s/d , as was observed by Kercher and Tabakoff (1970) for air jet arrays with crossflow. The exponent for turbulent channel flow would be expected to be $m \approx 0.8$, as opposed to $m \approx 0.5$ characteristic of stagnation flow (Pan et al., 1992; Gabour and Lienhard, 1993). It is clear that the superposition of stagnation flow and crossflow in the channel yields heat transfer characteristics different from either mechanism. Even the most sparse array ($s/d = 12$), for which the crossflow is a minimum and the jets act rather independently, exhibits average heat transfer behavior somewhat different from single submerged liquid jets.

The correlated plate-average Nusselt number for submerged jets from the present study (in the single-exit configuration) is compared to previously published correlations for air jet arrays in Fig. 6. Unless noted otherwise in the figure (as in the case of limits in the experimental conditions studied) the correlation data shown were generated for $s/d = 6$ and $z/d = 4$. As a rule, previous correlations suggest that \overline{Nu} is proportional to Re^m , where m is approximately 0.8. Kercher and Tabakoff found that the Reynolds number exponent m increased from 0.6 to 0.95 for jet-to-jet spacing increasing from $s/d = 3$ and 12. Obot and Trabold (1987) presented three different correlations depending on the nature of the crossflow configuration (minimum, intermediate, and maximum crossflow), with greater crossflow effect reducing the plate-

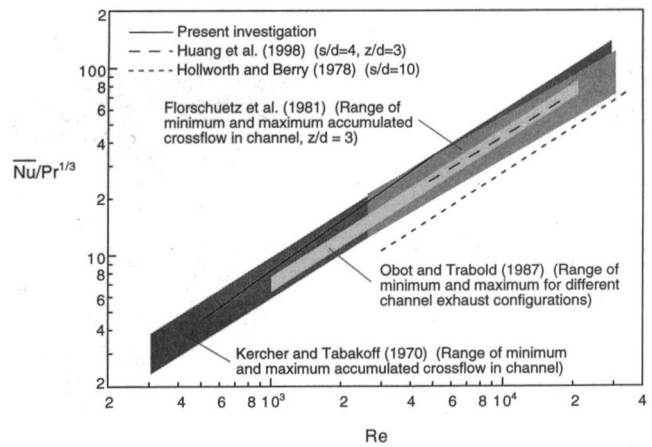


Fig. 6 Comparison of present study with previous results for air jet arrays with crossflow

average Nusselt number. The range of plate-average Nusselt number bounded by minimum and maximum crossflow configurations from that study is shown in Fig. 6. The investigations of Kercher and Tabakoff (1970) and Florschuetz et al. (1981) adopted an empirical correlation of the general form $\overline{Nu}/Pr^{1/3} = \phi Re^m f(s/d, z/d)$, where the function $f(s/d, z/d)$ accounts for the influence of jet-to-jet and nozzle-to-plate spacing on average heat transfer, and ϕ is a heat transfer degradation factor accounting for the influence of local crossflow. Both $f(s/d, z/d)$ and ϕ were presented graphically. Ranges in average Nusselt number given by their correlations are shown in Fig. 6, with maximum crossflow reducing the minimum-crossflow \overline{Nu} by approximately 60 percent in both cases.

As seen in Fig. 6, differences exist in the magnitudes of correlated average Nusselt number among the studies. The results of this study lie within the range of all investigations. The differences in correlated Nusselt number may possibly be explained by variations in plenum and jet orifice design (with associated differences in jet velocity distribution and turbulence level), heated impingement plate length, etc. It has been previously shown that impinging jet heat transfer is significantly affected by the jet velocity distribution (Pan and Webb, 1992; Obot et al., 1979) and the turbulence level (Hoogendoorn, 1977; Kestin and Wood, 1971).

Row-Average Nusselt Number. The row-average Nusselt number is shown as a function of jet row in the array for the $s/d = 8$, dual-exit configuration in Fig. 7. Figure 7(a) displays the influence of Reynolds number, while Fig. 7(b) reveals the dependence on z/d . The general symmetry expected for dual-exit drainage is seen in the data about the channel centerline. The row-average Nusselt number clearly rises with Reynolds number. Further, it may be seen that \overline{Nu} displays greater dependence on row number as Reynolds number is increased; the $Re = 700$ data in Fig. 7(a) are nearly uniform over the channel length, while there is considerably more variation in \overline{Nu} , for $Re = 3570$.

Figure 7(b) shows interesting behavior as z/d increases. \overline{Nu} increases with increasing nozzle-to-plate spacing from $z/d = 1$ to 4, then falls as z/d is further increased to the free-surface jet regime. This behavior was previously observed in the plate-average Nusselt number data of Fig. 5. For identical Reynolds number, Fig. 7(b) shows that the shape of the \overline{Nu} profile changes as the flow makes its transition from the fully flooded regime to the free-surface jet regime. The flooded regime features a local maximum in \overline{Nu} , at the channel center, whereas local maxima occur at the channel exits for the free-surface jet regime. For the fully flooded case, the heated plate near the channel center is exposed largely to stagnation flow with its associated high local heat transfer, while the impinging jets downstream (on either side of the channel center for the dual-exit configuration) are weakened by the accumulated crossflow of upstream mass flow. In the free-surface

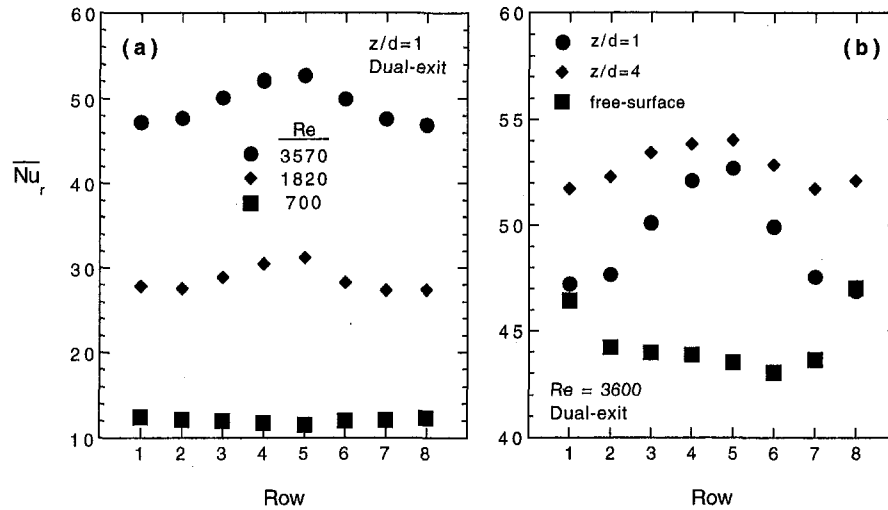


Fig. 7 Variation of row-average Nusselt number with location (row) for the $s/d = 8$ array configuration: (a) dependence on Reynolds number and (b) dependence on nozzle-to-plate spacing

regime puddling occurs in the flow channel, with pockets of air and liquid separated by a free-surface interface. A two-dimensional depiction of the observed puddling and resulting stratification of the free surface profile along the channel length for the dual-exit configuration is illustrated qualitatively in Fig. 8. Near the center of the channel the puddling was deepest, with successively thinner layers proceeding toward the channel exits on both sides. Thus, the impinging jets in this free-surface regime were forced to penetrate a thick turbulent liquid layer near the channel center, which is speculated to have reduced the jet stagnation momentum and associated stagnation heat transfer of the impinging jets there. The result, seen in Fig. 7(b), is row-average Nusselt numbers lower than that seen for the flooded cases at $z/d = 1$ and 4, particularly near the center of the channel. The accumulated drainage flow exits the channel in a thin fast-moving layer, which results in relatively intense film heat transfer in those regions (rows 1 and 8 in Fig. 7(b)). Thus, local maxima in \overline{Nu}_r are observed at the exits of the channel. Overall, the result is lower row-average heat transfer coefficients throughout most of the channel in the free-surface regime, with corresponding lower plate-average heat transfer.

The row-average Nusselt number for the single-exit configuration is shown in Fig. 9 for all jet-to-jet spacings studied at $z/d = 1$ for Reynolds numbers which are nearly the same. Comparison at identical Re was not possible, but the conclusions drawn are not sensitive to Reynolds number. The data have been plotted as a function of normalized channel position, x/L , where L is the streamwise length of the heated plate, and x is defined such that $x = 0$ is the upstream channel boundary and $x = L$ coincides with

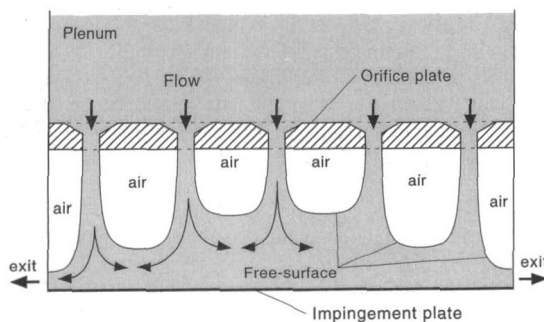


Fig. 8 Two-dimensional illustration of puddling and free-surface stratification for the free-surface jet regime in the dual-exit channel configuration

the downstream location of the (single) exit. These data are generally representative of profiles for other z/d investigated in the fully flooded regime. There is a general decreasing trend in \overline{Nu}_r with increasing x/L for the $s/d = 6, 8,$ and 12 arrays. However, there is a local minimum in the \overline{Nu}_r behavior for the $s/d = 4.8$ data near $x/L = 0.5$. Channel flow heat transfer is characteristically less effective than stagnation flow, so the decreasing trend in \overline{Nu}_r with x/L is seen where the crossflow momentum may disrupt the impinging jets. Additionally, recall that for the same average Reynolds number, the total mass flow rate increases with decreasing s/d (increasing total number of jets in a given array area). Smaller jet-to-jet spacing with associated higher mass flow may result in increasingly higher crossflow intensity for downstream jets (at identical z/d). As s/d is reduced (at constant z/d), the combination of accumulated mass flow from upstream and the increasing jet flow rate in downstream jets (with associated strong stagnation transport) produces intense heat transfer. This yields a local minimum in \overline{Nu}_r at $x/L \approx 0.5$ with increasing magnitudes thereafter. Monotonic decreases in the row-average Nusselt number profile for jet-to-jet spacings of $s/d = 6, 8,$ and 12 were observed for all z/d investigated with the exception of the $s/d = 6, z/d = 4$ configuration where a local minimum in \overline{Nu}_r was seen very near the channel exit (Garrett, 1998).

The local minimum in \overline{Nu}_r for the $s/d = 4.8$ array configuration observed in Fig. 9 for $z/d = 1$ was displaced downstream as z/d was increased. This is illustrated in Fig. 10, where profiles of \overline{Nu}_r

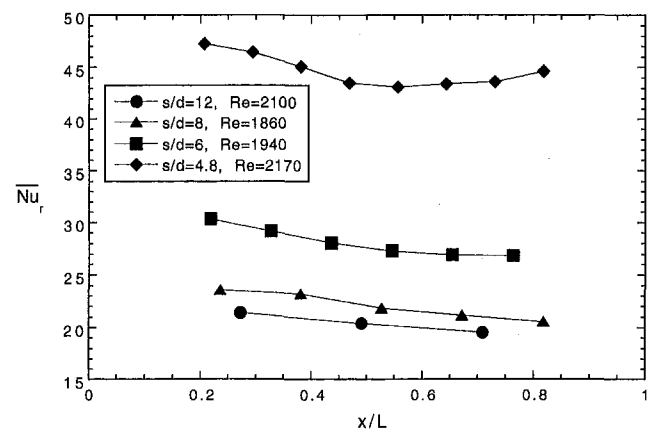


Fig. 9 Variation of row-average Nusselt number with streamwise position along the heated plate for the $z/d = 1$ condition

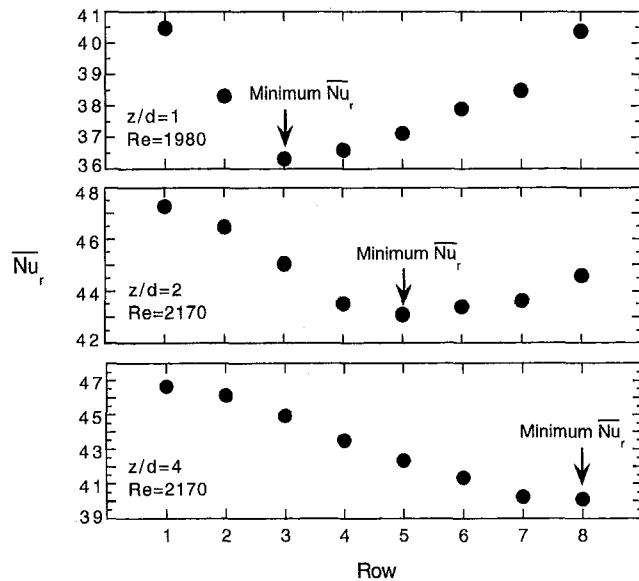


Fig. 10 Illustration of streamwise displacement of the local minimum in row-average Nusselt number as the nozzle-to-plate spacing is increased for $s/d = 4.8$

are plotted as a function of position in the channel (jet row) for $z/d = 1, 2,$ and 4 at a nominal Reynolds number of $Re = 2100$. The location of the local minimum in the row-average Nusselt number is clearly evident (shown by the arrows). It is seen that the local minimum in Nu_r moves downstream with increasing nozzle-to-plate spacing. Recall that higher jet mass flow rates were observed for downstream jets at low z/d (see Fig. 2). The local increase in Nu_r at downstream locations is perhaps the result of more intense stagnation flow here due to higher jet velocities. The suggestion is that the position where improved jet stagnation flow heat transfer commences moves as the channel becomes restricted (reduced z/d). Although not verified here, it may be speculated that this complex phenomenon would also be observed for less dense arrays (higher s/d) at Reynolds numbers higher than those investigated here. It may be concluded that nonmonotonic row-wise heat transfer is experienced as s/d and/or z/d are decreased. The phenomenon is quite complex and the local Nusselt number behavior would be difficult to correlate.

Local Heat Transfer. Local Nusselt number data are displayed in two forms, with the objective of illustrating and drawing qualitative conclusions in support of those made previously with regard to average Nusselt number behavior. Gray-scale contour information is shown in Fig. 11 showing several streamwise columns of heated impingement plate area for the single-exit configuration at $z/d = 1$. These data are local Nusselt number contours calculated directly from the infrared images. The jet stagnation areas are distinguishable clearly as locally high Nusselt number regions (lighter gray shades), with areas of lower transport between jet stagnation zones (darker gray shades). At extreme upstream locations in the channel these high transport regions are near-concentric circles with highest Nu in the center. Downstream, the crossflow disrupts the impinging jets, deflecting the jet slightly downstream. The local heat transfer then becomes a superposition of stagnation flow and accumulated channel flow. The elongation of locally higher Nusselt number distributions under the jets is particularly evident near the exit. These trends are similar to those reported by Huang et al. (1998) for local heat transfer under air jet arrays.

The local Nu contours of Fig. 11 suggest that the stagnation zones may be less affected by crossflow for increasing jet-to-jet spacing. This is evidenced by more concentric impingement heat transfer zones even for jets downstream near the channel exit (see,

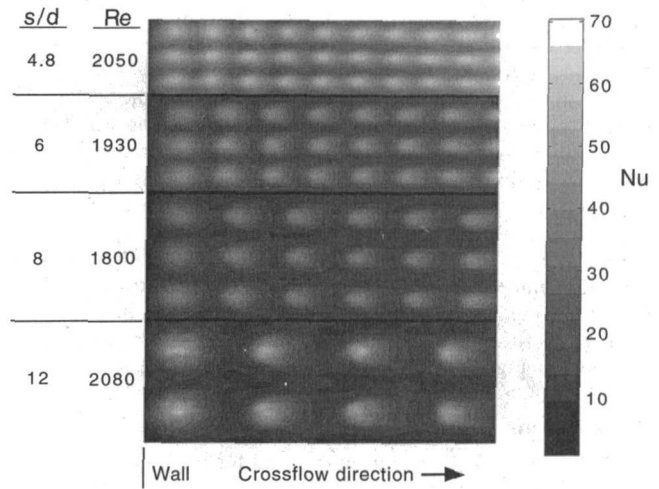


Fig. 11 Gray-scale contours of local Nusselt number for the four jet-to-jet spacings investigated at $z/d = 1$

e.g., $s/d = 12$). It would seem that with sparsely populated jet arrays there is ample drainage flow area between jets, permitting channel flow with reduced disturbance of the impinging jets themselves. The radial drainage from adjacent jets in the cross-stream direction influences jet heat transfer more dramatically for smaller s/d ; the elliptical shape of the stagnation region at $s/d = 4.8$ is evident even at extreme upstream jet rows, where neighboring jets in the same row “squeeze” the otherwise concentric impingement zone below jets in the array, similar to that observed by Van Treuren et al. (1994) for confined air jet arrays.

Figure 12 illustrates profiles of the local Nusselt number distribution along a streamwise line joining jet centers, and a streamwise line midway between jet centers for $z/d = 1, Re = 2070$, at $s/d = 6$ and 12 . For the profiles along lines connecting jet centers, the oscillatory nature of the Nu profiles illustrates the regions of high and low transport directly beneath and between the jets, respectively. Although the peak local Nusselt numbers are nearly the same for the two jet-to-jet spacings shown, the average along the line is considerably lower for the $s/d = 12$ data profiles (corresponding to lower minima in Nu). This is consistent with the plate-average and row-average Nusselt number data presented previously, which showed lower average Nusselt numbers for sparse jet arrays. The Nu profiles corresponding to locations midway between the jets exhibit variation only in the extreme upstream regions where crossflow effects are minimal. They are otherwise nearly constant with denser jet arrays yielding higher Nu

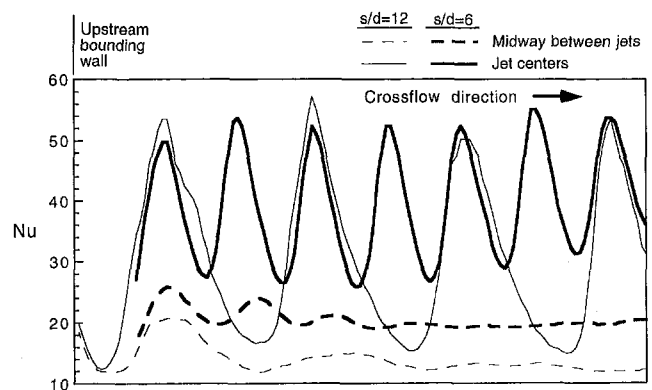


Fig. 12 Streamwise profiles of the local Nusselt number along a streamwise line joining jet centers (solid line) and a streamwise line midway between jet centers (dashed line) for two jet-to-jet spacings, $z/d = 1, Re = 2070$

along the line. Such strong oscillations in local Nusselt number have been observed previously in air jet arrays with crossflow (Florschuetz et al., 1980; Huang et al., 1998).

All other experimental parameters remaining the same, the impact of crossflow appears to increase for decreasing s/d . This is due to the combined effects of greater proximity among jets and greater total flow rate in the array (with resulting higher accumulation of fluid to be drained from the channel). Figures 11 and 12 suggest that the local heat transfer at the stagnation point is not significantly affected by crossflow; the magnitude of maximum Nusselt number is nearly the same for both jet-to-jet spacings shown in Fig. 12. However, there is a reduction in local heat transfer coefficient in the area between jets, evidenced in both the contours of Fig. 11 and the between-jet data of Fig. 12.

Conclusions

Heat transfer data have been reported for impinging liquid jets issuing into a channel whose drainage is confined. Free-surface and flooded jets were studied for four different jet-to-jet spacings and four different nozzle-to-plate spacings. The results reveal that the plate-average heat transfer coefficient increases for decreasing jet-to-jet spacing. However, on the basis of identical total array flow rate, the average heat transfer coefficient is highest for the sparse array. A maximum in plate-average Nusselt number was observed for $z/d \approx 4$, with reduced heat transfer for configurations at z/d below and above this value. As the nozzle-to-plate spacing is increased to approximately 12 diameters, the channel flow makes a transition from flooded (submerged) flow to distinct free-surface jets with a liquid layer blanketing the heated plate. Free-surface jet array heat transfer is found to be considerably lower than that for the fully flooded regime, believed due to the ineffective penetration by jets of the puddling and resulting liquid layer along the plate. There is substantial variation in the local heat transfer on the heated impingement plate with highest values directly beneath the impinging jets and lowest values along a streamwise line midway between the jets. Crossflow and the presence of close neighboring jets has the effect of rendering normally concentric heat transfer zones around the stagnation point elliptical with some slight deflection of the jet's effect downstream.

References

Beckwith, T. G., Buck, N. L., and Marangoni, R. D., 1982, *Mechanical Measurements*, 3rd Ed., Addison-Wesley, Reading, MA.

Florschuetz, L. W., Berry, R. A., and Metzger, D. E., 1980, "Periodic Streamwise Variations of Heat Transfer Coefficients for In-line and Staggered Arrays of Circular

Jets With Crossflow of Spent Air," *ASME JOURNAL OF HEAT TRANSFER*, Vol. 102, pp. 132–137.

Florschuetz, L. W., Truman, C. R., and Metzger, D. E., 1981, "Streamwise Flow and Heat Transfer Distributions for Jet Array Impingement With Crossflow," *ASME JOURNAL OF HEAT TRANSFER*, Vol. 103, pp. 337–342.

Gabour, L. A., and Lienhard, J. H. V., 1993, "Wall Roughness Effects on Stagnation-Point Heat Transfer Beneath an Impinging Jet," *ASME Heat Transfer Division HTD-Vol. 249*, pp. 35–43.

Garrett, K., 1998, "The Effect of Drainage Configuration on Heat Transfer under an Impinging Liquid Jet Array," M.S. thesis, Brigham Young University, Provo, UT.

Gerhart, P. M., and Gross, R. J., 1985, *Fundamentals of Fluid Mechanics*, Addison-Wesley, Reading, MA.

Hollworth, B. R., and Berry, R. D., 1978, "Heat Transfer From Arrays of Impinging Jets With Large Jet-to-Jet Spacing," *ASME JOURNAL OF HEAT TRANSFER*, Vol. 100, pp. 352–357.

Hoogendoorn, C. J., 1977, "The Effect of Turbulence on Heat Transfer at a Stagnation Point," *Int. J. Heat Mass Transfer*, Vol. 20, pp. 1333–1338.

Huang, Y., Ekkad, S. V., and Han, J.-C., 1998, "Detailed Heat Transfer Distributions Under an Array of Orthogonal Impinging Jets," *AIAA J. Thermophysics Heat Transfer*, Vol. 12, pp. 73–79.

Kercher, D. M., and Tabakoff, W., 1970, "Heat Transfer by a Square Array of Round Air Jets Impinging Perpendicular to a Flat Surface Including the Effect of Spent Air," *ASME Journal of Engineering for Power*, Vol. 92, pp. 73–82.

Kestin, J., and Wood, R., 1971, "The Influence of Turbulence on Mass Transfer from Cylinders," *ASME JOURNAL OF HEAT TRANSFER*, Vol. 93, pp. 321–327.

Lienhard, V. J. H., 1995, "Liquid Jet Impingement," *Annual Review of Heat Transfer*, Vol. 6, C. L. Tien, ed., Begell House, New York, pp. 199–270.

Lienhard, V. J. H., Dahbura, R. S., Younis, H. F., and Oh, C. H., 1997, "Experiments on Jet-Array Cooling Modules With High Heat Flux Removal," *High Heat Flux and Sychrontron Radiation Beamlines*, SPIE Vol. 3151, pp. 6–17.

Martin, H., 1977, "Heat and Mass Transfer Between Impinging Gas Jets and Solid Surfaces," *Advances in Heat Transfer*, Vol. 13, pp. 1–60.

Obot, N. T., and Trabold, T. A., 1987, "Impingement Heat Transfer Within Arrays of Circular Jets: Part 1—Effects of Minimum, Intermediate, and Complete Crossflow for Small and Large Spacings," *ASME JOURNAL OF HEAT TRANSFER*, Vol. 109, pp. 872–879.

Obot, N. T., Majumdar, A. A., and Douglas, W. J. M., 1979, "The Effects of Nozzle Geometry on Impingement Heat Transfer Under a Round Turbulent Jet," *ASME Paper No. 79-WA/HT-53*.

Oh, C. H., Lienhard, V. J. H., Younis, H. F., Dahbura, R. S., and Michels, D., 1998, "Liquid Jet-Array Cooling Modules for High Heat Fluxes," *AIChE Journal*, Vol. 44, pp. 769–779.

Pan, Y., and Webb, B. W., 1995, "Heat Transfer Characteristics of Arrays of Free-Surface Liquid Jets," *ASME JOURNAL OF HEAT TRANSFER*, Vol. 117, pp. 878–883.

Pan, Y., Stevens, J., and Webb, B. W., 1992, "Effect of Nozzle Configuration on Transport in the Stagnation Zone of Axisymmetric, Impinging Free-Surface Liquid Jets: Part 2—Local Heat Transfer," *ASME JOURNAL OF HEAT TRANSFER*, Vol. 114, pp. 880–886.

Van Treuren, K. W., Wang, Z., Ireland, P. T., and Jones, T. V., 1994, "Detailed Measurements of Local Heat Transfer Coefficient and Adiabatic Wall Temperature Beneath an Array of Impinging Jets," *ASME Journal of Turbomachinery*, Vol. 116, pp. 369–374.

Webb, B. W., and Ma, C.-F., 1995, "Single-Phase Liquid Jet Impingement Heat Transfer," *Advances in Heat Transfer*, Vol. 26, pp. 105–217.

Local Heat Transfer in a Rotating Square Channel With Jet Impingement

S.-S. Hsieh

Sun Yat-Sen Professor of
Mechanical Engineering,
Dean of Engineering,
Fellow ASME

J.-T. Huang

Graduate Student,
Department of Mechanical Engineering

C.-F. Liu

Graduate Student,
Department of Mechanical Engineering

National Sun Yat-Sen University,
Kaohsiung 80424, Taiwan, R.O.C.

The influence of rotation and jet mass flow rate on the local heat transfer coefficient for a single confined impinging round jet with a fixed jet-to-wall spacing of $H/d = 5$ was studied for the jet Reynolds number from 6500 to 26,000 and the rotational Reynolds number from 0 to 112,000. The local heat transfer coefficient along the surface is measured and the effect of the rotation on the stagnation (peak) point, local and average Nusselt number, is presented and discussed. Furthermore, a correlation was developed for the average Nusselt number in terms of the parameters of Re_j and Re_Ω . In general, the combined jet impingement and rotation effect are shown to affect the heat transfer response. Rotation decreases the average Nusselt number values from 15 to 25 percent in outward and inward radial flow, respectively. Finally, comparisons of the present data with existing results for multijets with rotation were also made.

Introduction

Jet impingement cooling has long been an area of active research, and with an ever-increasing scope of applications, the field continues to attract plenty of attention. Extensive reviews of flow and heat transfer between impinging jets and a flat plate have been reported by Becko (1976) and Martin (1977). Impingement jets can be applied to the locations of interest and produce very high local heat transfer rates with minimal consumption of fluid. In addition, heat transfer on rotating disks is also a commonly occurring topic in convection heat transfer, especially in rotating machinery. This process is particularly important to protect the local hot spots such as occur near the stagnation region of gas turbine blades. A number of investigators have studied the flow phenomena and heat transfer characteristics for a circular impinging jet onto a flat plate. These are including the local heat transfer and the correlations of the average Nusselt number in terms of relevant parameters (Gardon and Cobonpue, 1962; Gardon and Akfirat, 1966). However, the impingement cooling studied in the past was forced on a flat plate.

Recently, Gau and Chung (1991) experimentally studied the surface curvature effect on the slot air jet impingement cooling flow and heat transfer process. Data for the stagnation point and the average Nusselt number over the curved surface were extensively extracted. Jambunathan et al. (1992) studied the impingement cooling of a single air jet and correlated the local convective heat transfer coefficient as a function of Re , z/d , x/d , and Pr . Huber and Viskanta (1994) reported the results of the effect of jet-to-wall spacing on convective heat transfer in a confined impinging jet. More recently, Garimella and Rice (1995) experimentally investigated the local heat transfer from a small heat source to a perpendicular injection of a confined liquid jet.

Several papers related to a rotating free (unenclosed) disk in an impinging round jet were reported by Metzger and Grochowsky (1977) and Popiel and Boguslawski (1986), respectively. The study done by Metzger and Grochowsky (1977) concerns measurements of the average convective heat transfer characteristics on the jet-side disk face. Popiel and Boguslawski (1986) measured the distributions of the local heat transfer coefficient versus the rotational Reynolds number. Identification of flow conditions at

which impinging jets provide effective intensification of convective processes on rotating disks was achieved. Moreover, when impingement is not on the axis of the rotation, the rotating disk induces on its surface an axisymmetric wall jet which interacts with the impinging jet to produce a cross flow effect, affecting the jet trajectories and consequently affecting the distribution of impingement heat transfer rates. Metzger et al. (1991) developed an experimental method applied to the measurement of local heat transfer on a rotating disk, with flow between the disk and a closely spaced stator disk provided by jet impingement onto the disk from a single jet nozzle in the stator.

In spite of the foregoing discussion, it is found that the studies of confined impingement coolings on a flat wall with rotation with applications to gas turbines are relatively scarce. Bunker et al. (1992a, b) experimentally studied local heat transfer in turbine disk cavities in rotor and stator cooling with hub and radial location injection of a coolant. The effect of channel rotation on jet impingement cooling by arrays of circular jets in two channels was studied by Parsons et al. (1998) and Parsons and Han (1998).

Based on the literature review with rotation, it is found that, in addition to the aspect ratio, the ratio of wall temperature to local fluid temperature, and which wall is heated, the local Nusselt number in the flow direction of the impingement of a confined air jet on a constant heat flux smooth flat plate is a function of following variables and it can be written in the following form:

$$Nu = Nu(Re_j, Re_\Omega, H/d, x/d, q) \quad (1)$$

in which H/d is jet-to-wall spacing, q stands for surface heat flux, x is the flow direction, and d is jet hole diameter. Re_j is the jet Reynolds number based on nozzle diameter, $v_j d / \nu$ and Re_Ω is the rotational Reynolds number based on the rotational speed Ω and the rotating radius R .

In this work an experimental study of the heat transfer of a single circular air jet on a heated flat rotating wall was studied for Re_j from 6500 to 26,000, $H/d = 5$, and Re_Ω from 16,000 to 112,000 with a constant heat flux level of 6890 W/m^2 . Temperature measurements for the target were made to quantitatively determine the local heat transfer coefficients under various Re_j and Re_Ω . The heat transfer results were correlated in terms of the relevant parameters such as Re_j and Re_Ω to provide a thermal design basis for related applications. Table 1 gives the relevant parameters of the present study. The objectives of the study are threefold: (1) to apply the experimental method developed to the acquisition of local data for heat transfer between a rotating channel and impinging jet, (2) to explore the effects of Re_j and

Contributed by the Heat Transfer Division for publication in the JOURNAL OF HEAT TRANSFER. Manuscript received by the Heat Transfer Division, Aug. 24, 1997; revision received, June 15, 1999. Keywords: Heat Transfer, Impingement, Jets, Rotating, Turbines. Associate Technical Editor: J. Han.

Table 1 Nozzle geometries and operating conditions in the channel under study

geometries	W (mm)	H(mm)	AR(H/W)	L(mm)	d(mm)	L _n (mm)	r _Ω (mm)	L _n /D	(H/d)
	10	10	1	170	2	9	150	4.5	5
relevant parameters	Re _j (Jet Reynolds number)			Re _Ω = $\frac{\Omega R^2}{\nu}$ (Rotational Reynolds number) (R = 1 + r _Ω)					
	6500~26000			0~112000					
test section boundary conditions	Q = constant heat flux (6980 W/m ²) T ₂ = T ₃ = T ₄ = isothermal(25 °C)								

Re_Ω on stagnation and local heat transfer characteristics in a single circular confined jet with rotation, and (3) to broaden our fundamental understanding of the confined circular jet with rotation.

Experimental Apparatus and Procedure

The experimental setup and details for temperature measurement are shown in Fig. 1 and Fig. 2, respectively. The facility is mainly comprised of a heated section, compressor, a motor, a heat source, two slip ring assemblies, and a data logger (see Fig. 1 for details). The hollow rotating shaft is driven by 1 HP DC motor with a toothed belt drive pulley system through a frequency-controlled motor controller with a maximum rotating speed of 1600 rpm. The rotation speed is measured by a digital photo tachometer and varies up to 420 rpm. The rotating shaft and supporting bearing system are horizontally mounted on a rigid, heavy steel plate. The rotating channel is connected perpendicularly to the rotating shaft. The impinging air jet with average jet exit horizontally about 50 to 250 m/s issuing from the nozzle is supplied with a high-pressure compressor (5 HP motor driven) system. The air pressure in the compressor tank is in the range of 6 ~ 8 kg/cm². Air is compressed and stored in a 200 L air tank at a specified pressure for eliminating air surge. Air flow rate is controlled and measured by a precise pressure regulator (model FCK-500). To obtain the accurate flow rate, the measured flow rate

should be compensated due to the temperature effect with a factor of 0.3%/°C which was suggested by the manufacturer. A flexible tube at the end of the air supply system is connected to the air jet chamber, which is composed of two air plena. The upper plenum is made of 12-mm thick plexiglas which is 170 mm long and the internal cross section is 10 × 10 mm. The lower plenum is designed and constructed for the flexibility in interchanging different circular nozzle configurations. The details of the test section assembly are also presented in Fig. 2.

The main part was a strip of 0.1-mm thick copper plate with a heating section of nominal 110 × 12-mm etched thin-foil heater with a thickness of 0.1 mm exposed to the coolant to warrant a nearly uniform heat flux hold. The test section consisted of a square channel with a cross section of 10 × 10 mm mounted on a shaft supported by two bearings. The rotating shaft speed is measured by a digital photo tachometer. The air jet generated from the air jet chamber normally impinges onto the center of a heated impingement block. The size of the heated impingement block is 110 mm long, 12 mm wide, and 12.2 mm thick. The heated impingement plate composed of three layers is also shown in Fig. 2 (see, section A-A for details). The first layer is the heated impingement surface, made of a 0.1-mm thick copper sheet with a size of 110 × 12 mm. It is polished to minimize the surface roughness and emissivity. Therefore, it reduces radiative heat

Nomenclature

A = area of heated surface
d = jet hole diameter (=2 mm)
h = convective heat transfer coefficient, $q/(T_{w,x} - T_j)$
k = thermal conductivity of air
L = test section length (=170 mm)
ℓ = downstream (lateral) length (=85 mm)
L_n = jet hole length (=9 mm)
Nu = local Nusselt number, hd/k
Nu_r = local Nusselt number with rotation
Nu_s = local Nusselt number without rotation
Nu_o = stagnation (peak) Nusselt number, $h_o d/k$
q = surface heat flux, Q_{cv}/A
R = rotating radius (=r_Ω + ℓ)

Re_j = jet Reynolds number, $v_j d/\nu$
Re_Ω = rotational Reynolds number based on the rotating radius, $\Omega R^2/\nu$
r_Ω = the distance from the center of rotating axis to the end of test section indicated in Table 1 (=150 mm)
S = dimensionless distance between the stagnations point (stationary) to the peak point
T_j = jet exit temperature
T_{w,x} = local wall temperature
v_j = average jet exit velocity
x = lateral distance from the midpoint of the test section
x/d = dimensionless lateral distance
H = jet-to-wall spacing (=10 mm)
H/d = dimensionless jet-to-wall spacing

Greek Symbols

ν = kinematic viscosity at T_j
Ω = rotational speed

Subscripts

aw = adiabatic wall
b, x = local bulk mean fluid temperature
j = jet
r, o = stagnation point with rotation
x = local downstream position
w = wall/surface
w, x = local wall temperature
0 = stagnation point
- = average
Ω = rotation

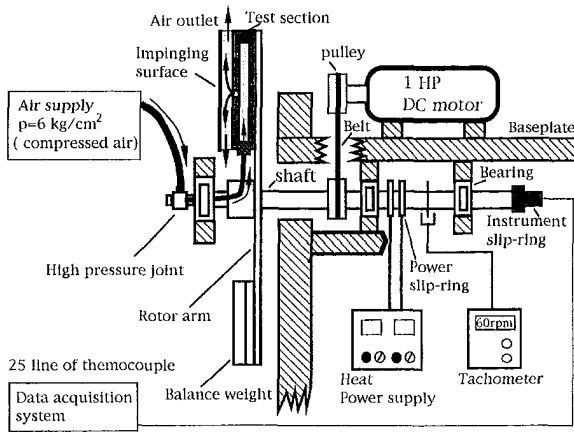


Fig. 1 Experimental setup and instrumentation details of temperature measurement (side view)

losses. The second layer is a 110×12 -mm etched thin-foil heater with a thickness of 0.1 mm, cemented on the inner surface of the first layer. The etched thin-foil heater, which can be applied to a voltage range of 0–60 V, is used for heating the copper plate. The third layer (i.e., outer layer) is a 12-mm thick plexiglas, which is adhered to the backside of the film heater to prevent conductive heat losses from the heaters. It is so designed that the maximum heat flux can be reached to 0.15 MW/m^2 . The temperature of the center of the inner surface (exposed to the flow) of the heater was measured by 23-gage 40 Fe-Cn thermocouples which were electrically insulated from the thin-foil heater. The spacing of any two neighboring thermocouples is 5 mm. The thermocouples were spring-loaded against the copper surface and a silicone paste (cement) was applied to each thermocouple bead to provide electrical isolation with good thermal contact. The test plate is designed to provide a known heat flux and allow measurement of the wall temperature at various locations. Temperatures measured at the bottom surface of the heated impingement plate were used with a solution of the two-dimensional heat equation to obtain the temperature field within the plate and the distribution of the convection heat transfer coefficient along the impingement surface. A two-dimensional conduction model was used to provide wall temperature correction estimates for the measurements.

The strip on either side of the active section was connected to

plexiglas bus blocks, which were in turn connected to power leads. The jet nozzle is stuck on a balsa wood plate with a jet hole length to jet diameter of $L_n/d = 4.5$ served as a jet plate which has a thickness of 38 mm. The jet direction relative to rotation axis is in parallel, but exit flow (wall jet) direction is perpendicular to the rotation axis. To reduce the heat loss from the jet plate, it is also covered with 12-mm thickness plexiglas, which ensures that the impingement plate and the jet plate are insulated. The assembly was fixed in a stainless steel frame with a screwed flange. The source of power for the circuit was an autotransformer, supplied from a standard 110 V, 60 Hz AC wall outlet. For the present study, the transformer was designed for a load output of 20, 40, and 60 V with a maximum current of 3 amps. The supplied power to the heating foils is measured by an accurate digital power meter. Two additional thermocouples are used to measure the bulk flow temperature of working fluid at the inlet/exit. All the temperature signals are acquired with a data logger (YEW Model 3088) and sent into a 486 PC for data processing and plotting.

Data Reduction

For estimating the convective heat flux dissipated from the heated impingement plate, based on the energy balance, it is proposed that at steady state, the total heat generated by the thin-foil heater Q_i is converted into the following heat transfer modes during the experiments: (1) conductive heat loss, Q_c ; (2) radiative heat loss, Q_r ; and (3) convective heat dissipated from the impingement plate, Q_{cv} . That is,

$$Q_{cv} = Q_i - Q_c - Q_r \quad (2)$$

This energy balance of Eq. (2) calculates the net convective heat, Q_{cv} , dissipated from the impingement plate to the air jet in the confinement. Heat loss measurements were obtained with no coolant flow (i.e., no jet impingement) with the channel ends sealed and the internal recirculation was restricted as well and constant electrical power was supplied under steady-state conditions with rotation. The total power input to heater is Q_i which equals $I^2 R$. Here I is the electric current of the AC power supply and R is the resistance of the thin-foil heater. It was verified in preliminary tests that the variation of resistance with temperature could be neglected (less than ± 0.2 percent), as the heater temperature variation was less than 40 K in the present study and the variation in resistivity with temperature is extremely small. Q_r is the radiative heat loss from the copper surface to its surroundings.

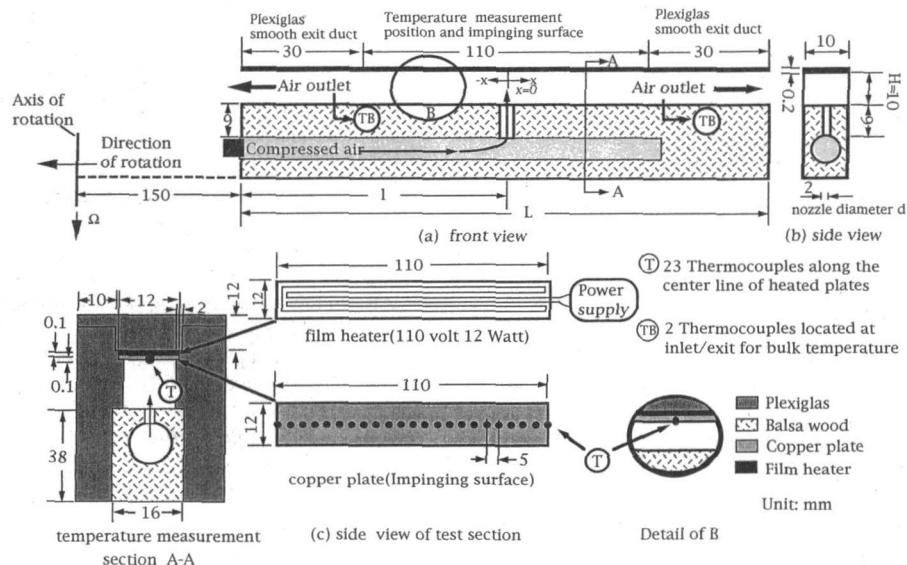


Fig. 2 Detailed dimensions of the test section

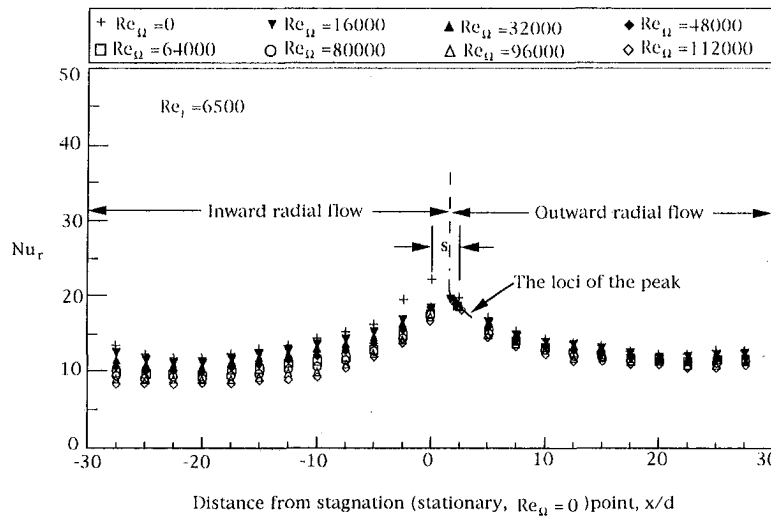


Fig. 3 Effect of rotational Reynolds number on the axial variation of local Nusselt number or $Re_j = 6500$

It is calculated using thermal diffuse gray-body networks. Based on the above analysis, the maximum radiative heat loss is less than five percent of the total power input for all the cases under study. Q_c is the conductive heat loss to the copper plate and balsa block and was calculated using a two-dimensional conduction mode and, eventually, to the room through the plexiglas. It is found that Q_c value varies from 5–20 percent of the total input power.

Before the experiments, all the thermocouples are calibrated in a constant temperature bath to ensure the measurement accuracy of $\pm 0.1^\circ\text{C}$. In each test run, the mass flow rate is adjusted to give the desired Reynolds number. After steady state is reached, the temperature distribution on the test plate is measured. It usually takes 30 minutes to reach steady state except for the first data set. To get the local Nusselt number, one uses the following equation:

$$h_x = \frac{Q_{cv}}{A(T_{w,x} - T_{b,x})} \quad (3)$$

The area A of the heated surface was carefully measured for each test section. The value of $T_{b,x}$ is obtained by an energy balance.

Consequently, based on Eq. (3), an average heat transfer coefficient (Gardon and Akfirt, 1966) for the surface can be secured as follows:

$$\bar{h} = \frac{\left(\frac{1}{\ell}\right) \sum_{i=1}^n h_x(T_{w,x} - T_j)\Delta x}{\frac{1}{\ell} \sum_{i=1}^n (T_{w,x} - T_j)\Delta x} \quad (4)$$

where n stands for a half-number of temperature measurement points (=11 for this study), i is the i th measurement point, and Δx is the distance between two consecutive measurement points. Experimental data were taken in both rotating and stationary channels. Rotational speeds of 60, 120, 180, 240, 300, 360, and 420 rpm were set in a clockwise direction.

Uncertainty Analysis

The uncertainty in the measurement can be categorized into two parts. The first is from the mass flow rate, the second is due to the convective heat transfer coefficient. The former is caused by the flow meter. The jet temperatures were measured just upstream of the nozzle inlet and were maintained at $25 \pm 0.1^\circ\text{C}$ throughout the experiments. Jet flow rates were measured upstream of the plenum using a floating meter (HC Model P-23-41G) which was accurate

to within one percent of full-scale (0.5 l/s). The inlet Prandtl number was $0.7 (\pm 0.5 \text{ percent})$ based on the jet exit temperature. The flow rates were used to determine mean nozzle discharge velocities from which impingement velocities were calculated. The uncertainty in Nusselt number was influenced primarily by the determination of heat flux and wall temperature. The heat flux was corrected, followed by Eq. (2). The determination of the heated impingement wall temperature was related to the thermal resistance of the adhesive layer ($\sim 0.1 \text{ mm}$) between the thermocouple bead and bottom wall of the copper plate. Since the thermal resistance of the adhesive layer is extremely small (typical value; $7 \times 10^{-10} \text{ m}^2\text{KW}^{-1}$), the uncertainty was determined to be negligible ($4.9 \times 10^{-6}^\circ\text{C}$). The uncertainty in Reynolds number was affected by measurement of the flow rate and the nozzle exit area. Based on the above uncertainty estimate, the uncertainty in Re_j was 6.2 percent and the Nusselt number was found to be less than 16 percent.

Results and Discussion

Based on the previous studies (Parsons and Han, 1998; Parsons et al., 1998), the Nusselt number inside a rotating square channel with jet impingement is governed by the rotating mean radius, jet flow rate, rotational speed, duct length, jet-to-wall spacing, wall heat flux and flow direction (radial outward/or radial inward flow). For a duct of fixed length, jet-to-wall spacing, and rotating mean radius, the Nusselt number can be expressed as a function of Re_j , Re_Ω , x/d , and q . Moreover, the average Nusselt number is found as a function of Re_j and Re_Ω .

Effect of Rotation on Local Nusselt Number. Streamwise (axial) variation of local heat transfer was measured as a function of axial distance from the stagnation (peak) point and rotational Reynolds number. Figure 3 shows local Nusselt number obtained at jet Reynolds number = 6500. In all aspects except the peak location, conditions are virtually identical to those of previous studies for confined jets. Again, the streamwise range of the results acquired has been extended by marking seven separate tests for different Re_Ω . As is evident, little additional information was acquired as compared to the stationary channel except for the magnitude of Nu and the peak point shift toward the radially outward due to rotation. It can be observed that the Nu decreases as Re_Ω increases. In addition, the near-symmetric distribution of heat transfer radially outward from the peak point strongly suggests that the rotation has little effect on the heat transfer near the impingement location. Figure 4 presents similar results for $Re_j =$

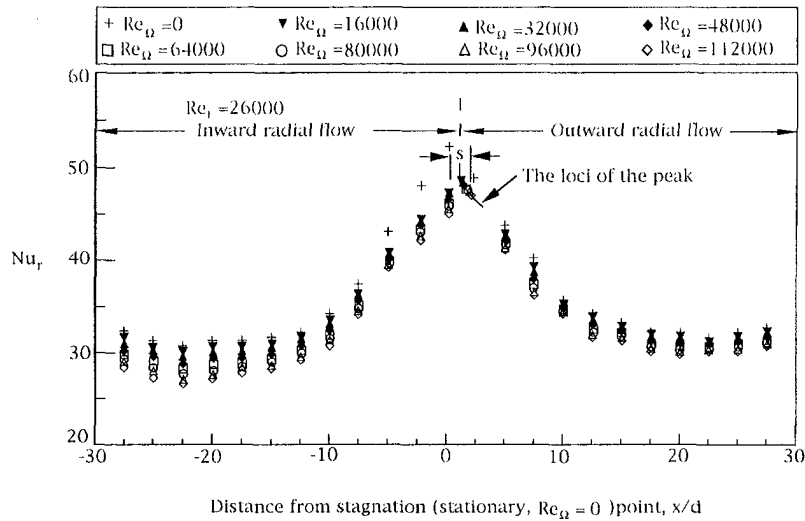


Fig. 4 Effect of rotational Reynolds number on the axial variation of local Nusselt number for $Re_j = 26,000$

26,000. The preceding discussion of Fig. 3 applies equally well to all the curves shown in Fig. 4. Comparison of the results of Fig. 4 with those of Fig. 3 shows that for the same rotational speed the heat transfer rates are greater than 2.5 times of their level. However, the radially outward effect (positive x direction) due to rotation seems much smaller at $Re_j = 26,000$ as the loci of the peak shows. This also means that the center thermocouple is not always the stagnation point. Detailed shifts under different Re_Ω for different jet flow rates are tabulated in Table 2 and were also plotted against Re_Ω as shown in Fig. 5. In addition, the observation regarding the character of the results of Figs. 3 and 4 is that the streamwise (axial) heat transfer distribution is essentially dominated by the impingement character of the flow. Furthermore, the fact that the flow rate is provided at the center of rotating channel and forced outward radially through the channel with minor rotation effect. This is because the present jet velocity is parallel to the rotation vector. There is no Coriolis force due to the jet. However, there is Coriolis force in the lateral (spanwise) direction due to exit jet flow which generated the secondary flow in the cross section of the channel perpendicular to the radially out/inward flow. Moreover, the centrifugal force is now in the radially outward direction. Such effect decreases as Re_j increases (e.g., $Re_j = 26,000$). As a result, the heat transfer coefficients are high on/or near the center region of the channel, where the forced velocities are large, and then decrease gradually in the axial direction. This behavior is quite similar to that of Metzger et al. (1991). Near the exit of the outward/inward radial channel, large velocity gradients near the target wall were produced; therefore, high Nusselt number values

were observed. Furthermore, Nusselt number values in the radially outward channel were higher when compared with those in radially inward channel. The distance (S) between the stagnation ($Re_\Omega = 0$) to the loci of the peak shown in Fig. 5 strongly suggests that a radially outward flow was induced with rotation. The shift S was increased as Re_Ω increases. However, this effect is not significant at higher jet flow rates until Re_j gets small ($\leq 13,000$). This is quite expected since the rotating channel induces on the channel surface a symmetric wall jet. Also included in Fig. 5 is a composite correlation made for Re_j , Re_Ω , and S for further examination. It is again found the shift would increase as Re_Ω increases. However, it decreases as Re_j increases. The moderate power dependence on each Re_Ω ($=0.329$) and Re_j ($=0.275$) seems roughly equal in the magnitude but the trend is opposite.

Effect of Re_j and Re_Ω on \bar{Nu} , and $Nu_{r,o}$ Figure 6 shows the variation of average Nusselt number calculated from Eq. (4) and $Nu_{r,o}$ with two different Re_Ω for seven different jet Reynolds numbers. The effect of Re_j in this study is clearly observed. It is seen that the value of Nu , increases with an increase in Re_j . Nu , in outward radial flow was about ten percent higher when compared to that in inward radial flow at the corresponding Re_j . Moreover, there seems no differences in Nu values with nonrotation cases in which the outward/inward radial flow have the same Nu values for different Re_j as expected. Figure 7 shows the effect of rotation on the Nusselt number distribution at two different Re_j . The trend showed that rotation did not significantly change Nusselt number distribution, but decreased Nusselt number values slightly. This is perhaps because the rotation-induced centrifugal force causes the jets to bend and deflect away from the target walls which results in a lower velocity gradient near the target walls and, consequently, reduces the impingement effect on target walls. It is speculated that the bending and deflection jets due to rotation induced centrifugal force would result in a lower impingement effect on the target walls. Therefore, lower heat transfer values were recorded with rotation as shown in Fig. 7.

It has been found that for planar air jets (Gardon and Akfirt, 1966) the axial variation of stagnation point heat transfer is affected by two factors: one is arrival jet velocity at the centerline and the other is the turbulent intensity. Since the present $H/d = 5$ is within the so-called potential core, the jet velocity at centerline remains unchanged. As to turbulence, the present results show that it significantly enhances the impingement heat transfer. Stagnation point heat transfer rates were measured and collected as a function of jet exit velocity and rotational speed. The results are also exhibited in Figs. 6 and 7. Figure 6 depicts the variation of

Table 2 Distance between stagnation (stationary, $Re_\Omega = 0$) to the peak point

$\frac{Re_j}{Re_\Omega}$	6500	9750	13000	16250	19500	22750	26000
0	0	0	0	0	0	0	0
16000	1.54	1.46	1.29	1.19	1.09	1.04	1.02
32000	1.67	1.57	1.44	1.32	1.21	1.15	1.13
48000	1.81	1.67	1.55	1.47	1.35	1.30	1.27
64000	2.05	1.94	1.83	1.67	1.54	1.51	1.46
80000	2.46	2.25	2.05	1.90	1.75	1.65	1.61
96000	2.49	2.45	2.37	2.14	1.94	1.84	1.81
112000	2.51	2.47	2.44	2.35	2.19	2.12	2.07

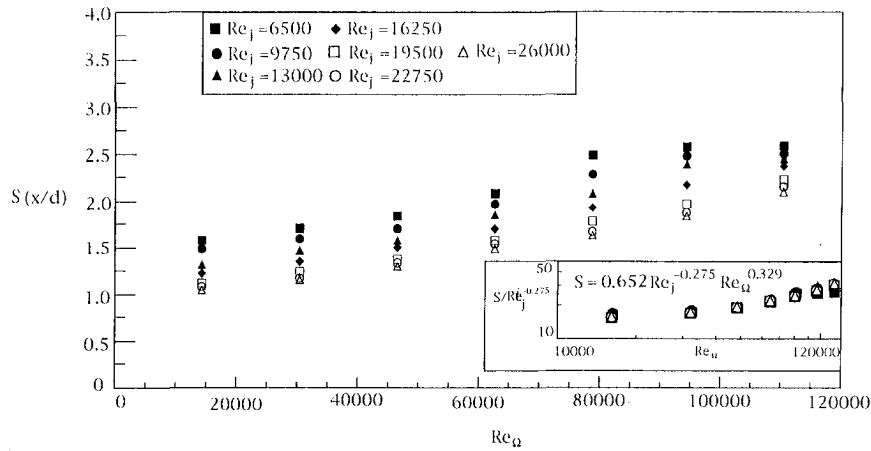


Fig. 5 Distance from stagnation (stationary, $Re_{\Omega} = 0$) to the loci of the peak

stagnation point Nusselt number with rotational speeds for seven jet Reynolds numbers, while Fig. 7 illustrates the variation of $Nu_{r,o}$ with jet Reynolds number for eight rotational speeds. As shown in Fig. 7, there is a distinct rotational speed dependence as compared to the corresponding distribution of Fig. 6 in the functional relationship of stagnation point Nusselt number with jet Reynolds number. Lower stagnation point heat transfer rates were observed for higher Re_{Ω} as one would expect due to the reasons stated above. This observation is consistent with the corresponding results of Fig. 6. The rotational speed dependence was ascribed to decay of the turbulence for initially turbulent jets as stated in the work of Gardon and Akfirat (1966). It is speculated that this effect of initial turbulence would be reduced for impingement with rotation in the present study. This would be expected because the turbulence intensity may be reduced as the formation of counter/corotating vortices of the secondary flow occur due to Coriolis forces with exit jet flow and centrifugal force. The present result was also shown that the strength of the aforementioned secondary flow gets stronger as Re_j increases and weaker as Re_{Ω} increases.

Heat Transfer Reduction and Correlation of \overline{Nu}_r with Parameter (Re_j, Re_{Ω}). Figure 8 presents the axial distributions of the Nusselt number ratio, Nu_r/Nu_s under different rotating condition. The influence due to the rotation is clearly noted and the reduction due to rotation seems much higher at lower Re_j (e.g. 40 percent reduction (max. value) at $Re_j = 6500$) than that at a higher Re_j (e.g. 25 percent reduction (max. value) at $Re_j = 26,000$) at the maximum rotational speed (i.e., $Re_{\Omega} = 112,000$). In general, Fig. 8 shows that the Nusselt number ratio is dependent upon the axial positions. For the results shown in Figs. 3 and 4 at $Re_{\Omega} = 0$, the heat transfer rates exhibit a bell-shape-like curve as

those of rotating channels except the different positions for stagnation (peak) point located. Namely, for a fixed Re_{Ω} the heat transfer rate also decreases as the axial distance increases. However, the decreasing rate seems a little different. It is found that the decrease with streamwise distance variation in the heat transfer rate in a rotating channel with jet impingement is quicker than that in a stationary channel. Based on the reasons stated above, it is therefore that the curves of Nu ratios shown in Fig. 8 show a weak dependence on axial distance and exhibit a moderate decrease as the axial distance increases. The maximum Nu ratios were found at about $x/d \approx 2.5$, as Fig. 8 shows.

Figure 9 shows the outward/inward radial flow channel averaged Nusselt number values for various rotational speeds and jet Reynolds numbers. Correlations were developed for the radially outward and inward flow, respectively, and have the form of $Nu_r \sim Re_j^{0.503}$ (see Fig. 9(a)) and $Nu_r \sim Re_j^{0.498}$ (see Fig. 9(b)). Nusselt number values obtained with those in the outward radial flow channel were a little bit higher when compared with those in the inward flow. This is because of rotation-induced centrifugal forces, which cause the exit jet flow (wall jet) accelerating (outward radial flow)/or decelerating (inward radial flow). Taking further inspection examination of Fig. 9 at a fixed rotational speed, rotation again decreased the average Nusselt number values 15 to 25 percent (below nonrotating values) at $Re_j = 26,000$ and 6500 , respectively. The figure also indicates that the average Nusselt number decreased with an increase in rotational speeds. Correlations were also developed and have the form of $Nu_r \sim Re_{\Omega}^{-0.052}$ (see Fig. 9(a)) and $Nu_r \sim Re_{\Omega}^{-0.054}$ (see Fig. 9(b)) for the radial outward and inward channel, respectively. Based on the relationship of Re_j and

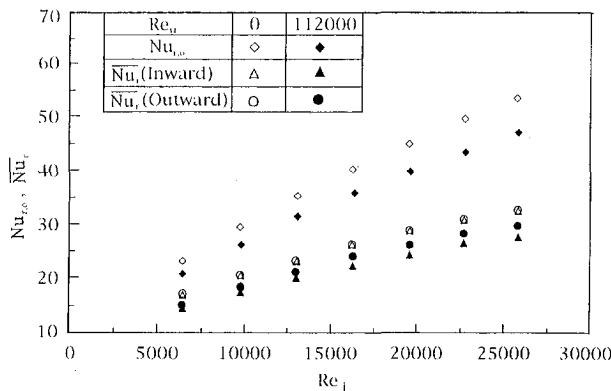


Fig. 6 $Nu_{r,o}$ and \overline{Nu}_r versus Re_j at different Re_{Ω}

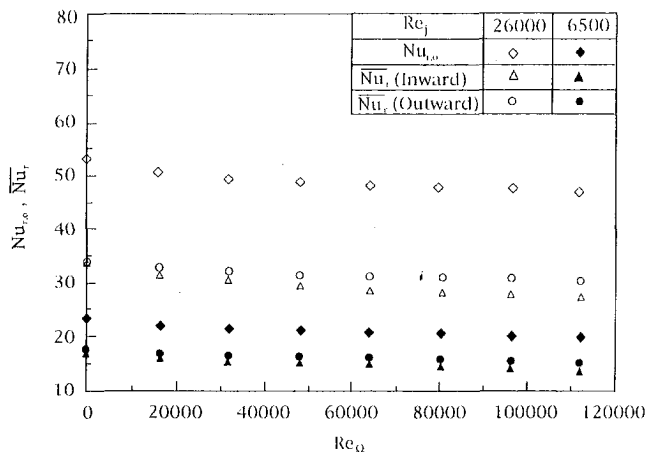


Fig. 7 $Nu_{r,o}$ and \overline{Nu}_r versus Re_{Ω} at different Re_j

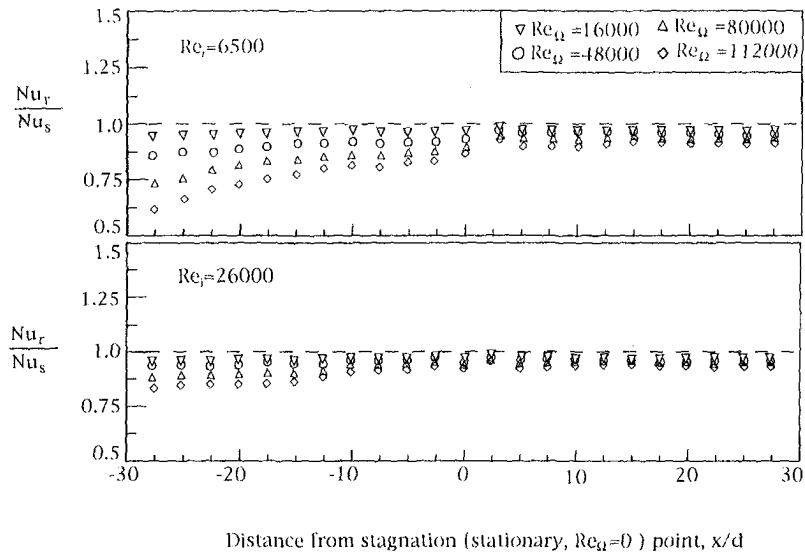


Fig. 8 Effect of rotational Reynolds number on the axial variation of Nu_r/Nu_s for $Re_j = 6500$ and $Re_j = 26,000$

Re_Ω with \overline{Nu}_r , found before, the composite correlations were thus developed for both the radially outward and inward channel in the following from:

$$\overline{Nu}_r = 0.329 Re_j^{0.503} Re_\Omega^{-0.052} \quad (\text{outward radial flow})$$

$$\overline{Nu}_r = 0.327 Re_j^{0.498} Re_\Omega^{-0.054} \quad (\text{inward radial flow})$$

for $6500 \leq Re_j \leq 26,000$

and $16,000 \leq Re_\Omega \leq 112,000$. (5)

Each power dependence on the parameter strongly suggests that the average Nusselt number \overline{Nu}_r of the present study is mainly affected by these parameters.

Comparisons of the present results with those of Akella and Han (1998) was made as also shown in Fig. 9 in which channel-averaged impingement heat transfer from rotating two-pass rectangular channels with multijets was reported. The power dependence of Re_j on Nu in Akella and Han (1998) was found to be 0.56 (first channel) to 0.57 (second channel), while it is 0.503 (outward) and 0.498 (inward), respectively, in different channels for this study. Therefore, the influ-

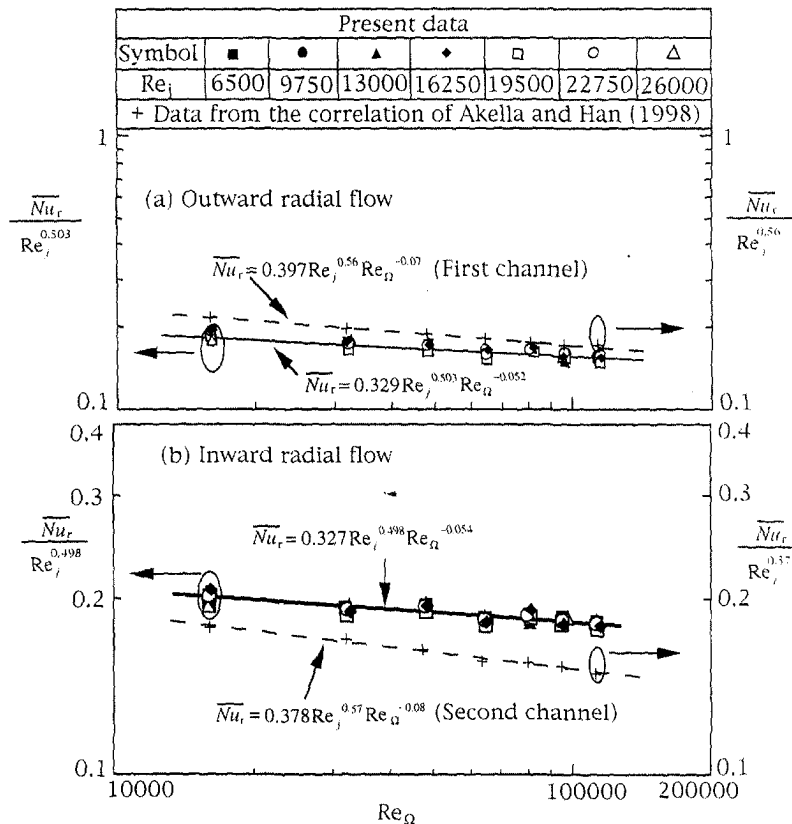


Fig. 9 The relationship between \overline{Nu}_r and Re_Ω at different Re_j for (a) outward radial flow and (b) inward radial flow and comparison with other investigations

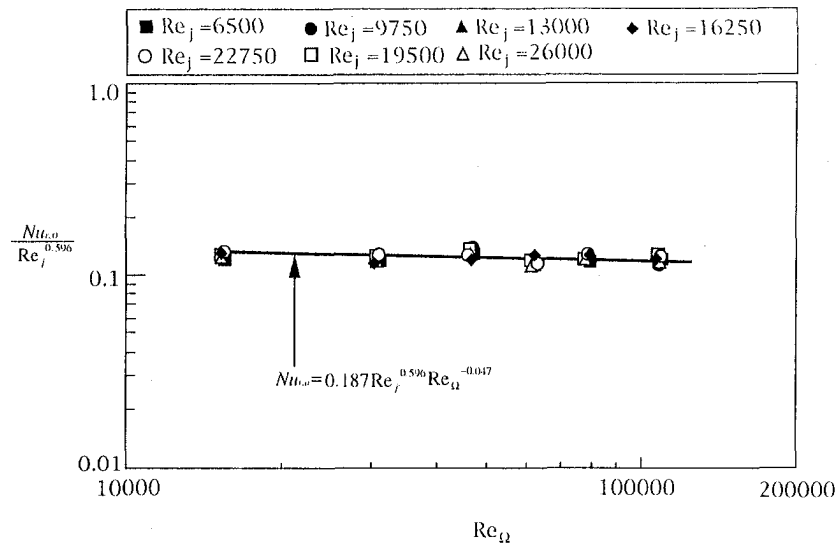


Fig. 10 The relationship between $Nu_{r,o}$ and Re_{Ω} at different Re_j

ence of Re_j on \overline{Nu} , looks similar based on the magnitude of the power dependence of Re_j . In fact, in general, for impingement heat transfer, the target wall local Nusselt number is proportional to Re_j^m where $0.5 < m < 0.8$ (Parsons et al., 1998). The present data of \overline{Nu} , and $Nu_{r,o}$ follow the same trend for the entire Re_j with the $Nu_{r,o}$ the highest. Figure 10 shows the similar results of Figs. 9 for the correlations of the stagnation point heat transfer on Re_j and Re_{Ω} . The results are shown in the following form:

$$Nu_{r,o} = 0.187 Re_j^{0.596} Re_{\Omega}^{-0.047}$$

for $6500 \leq Re_j \leq 26,000$

$$\text{and } 16,000 \leq Re_{\Omega} \leq 112,000. \quad (6)$$

Again, Re_j and Re_{Ω} have also some influences on $Nu_{r,o}$.

Concluding Remarks

A study of the measured distribution of the local heat transfer coefficients along a rotating channel surface with a single round jet impingement has made it possible to examine, for the first time, the effect of a number of parameters. The combined influence of the jet Reynolds number and rotational Reynolds number was examined and discussed. Nusselt number values in the radially outward channel were about ten percent higher when compared to those at the corresponding location in the radially inward channel at the corresponding Re_j ($6500 \leq Re_j \leq 26,000$). It was found that the increase in rotational speed results in a decrease in streamwise (axial) heat transfer distribution along the channel surface and, consequently, it also results in an average Nusselt number decrease of about 15–25 percent, depending on the magnitude of Re_j . The heat reduction rate seems consistent with those of the previous studies of Akella and Han (1998) and Mattern and Hennecke (1996) for multijets.

Acknowledgment

This work was supported by a research grant (NSC 87-2212-E-110-026) from the National Science Council, Taiwan, R.O.C.

References

Becko, Y., 1976, "Impingement Cooling—A Review," Von Karman Institute for Fluid Dynamics, Lecture Series 83.

- Bunker, R. S., Metzger, D. E., and Wittig, S., 1992a, "Local Heat Transfer in Turbine Disk Cavities: Part I—Rotor and Stator Cooling with Hub Injection of Coolant," *ASME Journal of Turbomachinery*, Vol. 144, pp. 211–220.
- Bunker, R. S., Metzger, D. E., and Wittig, S., 1992b, "Local Heat Transfer in Turbine Disk Cavities: Part II—Rotor Cooling with Radial Location Injection of Coolant," *ASME Journal of Turbomachinery*, Vol. 114, pp. 221–228.
- Dutta, S., Andrews, M. J., and Han, J. C., 1996, "Prediction of Turbulent Heat Transfer in Rotating Smooth Square Ducts," *International Journal of Heat and Mass Transfer*, Vol. 39, No. 12, pp. 2505–2514.
- Garimella, S. V., and Rice, R. A., 1995, "Confined and Submerged Liquid Jet Impingement Heat Transfer," *ASME JOURNAL OF HEAT TRANSFER*, Vol. 117, pp. 871–877.
- Gardon, R., and Cobonpue, J., 1962, "Heat Transfer Between a Flow Plate and Jets of Air Impinging on It," *Proceedings of the 2nd International Heat Transfer Conference*, ASME, New York, pp. 454–460.
- Gardon, R., and Akfirt, J., 1966, "Heat Transfer Characteristics of Impinging Two-dimensional Air Jet," *ASME JOURNAL OF HEAT TRANSFER*, Vol. 118, pp. 103–108.
- Gau, C., and Chung, C. M., 1991, "Surface Convective Effect on Slot Air-Jet Impingement Cooling Flow and Heat Transfer Process," *ASME JOURNAL OF HEAT TRANSFER*, Vol. 113, pp. 858–864.
- Huber, A. M., and Viskanta, R., 1994, "Effect of Jet-Jet Spacing on Convective Heat Transfer to Confined Impinging Arrays of Axisymmetric Air Jets," *International Journal of Heat and Mass Transfer*, Vol. 37, pp. 2859–2869.
- Jambunathan, K., Lai, E. A., and Button, B. L., 1992, "Review of Heat Transfer Data for Circular Jet Impingement," *International Journal of Heat and Fluid Flow*, Vol. 13, pp. 337–344.
- Martin, H., 1977, "Heat and Mass Transfer between Impinging Gas Jets and Solid Surfaces," *Advances in Heat Transfer*, J. Irvine, Jr., ed., Vol. 13, pp. 1–60.
- Mattern, C., and Hennecke, D. K., 1996, "The Influence of Rotation on Impingement Cooling," Turbo Expo, ASME, Paper No. 96-GT-161, Birmingham, England, UK.
- Metzger, D. E., and Grochowsky, L. D., 1977, "Heat Transfer between an Impinging Jet and Rotating Disk," *ASME JOURNAL OF HEAT TRANSFER*, Vol. 99, pp. 663–667.
- Metzger, D. E., Bunker, R. S., and Bosch, G., 1991, "Transient Liquid Crystal Measurement of Local Heat Transfer on a Rotating Disk With Jet Impingement," *ASME Journal of Turbomachinery*, Vol. 113, pp. 52–59.
- Parsons, J. A., Han, J. C., and Lee, C. P., 1998, "Rotation Effect on Jet Impingement Heat Transfer in Smooth Rectangular Channels With Four Heated Walls and Radially Outward Crossflow," *ASME Journal of Turbomachinery*, Vol. 120, pp. 79–85.
- Parsons, J. A., and Han, J. C., 1998, "Rotation Effect on Jet Impingement Heat Transfer in Smooth Rectangular Channels with Heated Target Walls and Radially Outward Crossflow," *International Journal of Heat and Mass Transfer*, Vol. 41, No. 13, pp. 2059–2071.
- Popiel, C. O., and Boguslawski, L., 1986, "Local Heat Transfer from a Rotating Disk in on Impinging Round Jet," *ASME JOURNAL OF HEAT TRANSFER*, Vol. 108, pp. 357–364.

Effect of Aperture Geometry on Heat Transfer in Tilted Partially Open Cavities

M. M. Elsayed

e-mail: mustafa@kuc01.kuniv.edu.kw
Mem. ASME

W. Chakroun

chakroun@kuc01.kuniv.edu.kw

Mechanical Engineering Department,
Kuwait University,
P.O. Box 5969,
Safat 13060, Kuwait

Free convection from a square, tilted partially open cavity was investigated experimentally. The experiment was carried out to study the effect of the aperture geometry on the heat transfer between the cavity and the surrounding air. Four different geometrical arrangements for the opening were investigated: (1) high wall slit, (2) low wall slit, (3) centered wall slit, and (4) uniform wall slots. Each opening arrangement was studied at opening ratios (i.e., ratio of opening height to cavity height) of 0.25, 0.5, and 0.75. The average heat transfer coefficient between the cavity and the surrounding air was estimated for each geometrical arrangement for tilt angles ranging from -90 deg to $+90$ deg with increments of 15 deg and at a constant heat flux Grashof number of 5.5×10^8 . The results showed that for tilt angles between 90 and 75 deg, the heat transfer coefficient has a small value that is independent of the geometrical arrangement of the opening. The value of the heat transfer coefficient increases sharply with decreasing tilt angle until an angle value of zero degrees is reached. The increase in the heat transfer coefficient continues in the negative range of tilt angle but not in the same rate as in the positive range of the tilt angle. The uniform slot arrangement gave in general higher heat transfer coefficient than the other three arrangements of the opening. Large differences in the heat transfer coefficient were observed between the high and the low wall slits where the high wall slit is found to transfer more heat to the surroundings than the low wall slit. Correlations were developed to predict the average Nusselt number of the cavity in terms of the opening ratio and the cavity tilt angle for cavities with high wall slit, low wall slit, centered wall slit, and the uniform wall slots.

1 Introduction

Heat transfer in cavities is receiving increasing attention because of the various applications in engineering; e.g., passive solar heating, energy conservation in buildings, solar concentrating receivers, and electronic equipment. The present experiment adds some information in the area of open cavity design where heat transfer by natural convection is the main mechanism of heat transfer.

Many investigations have been carried out previously to study heat transfer in cavities by natural convection. Experimental as well as numerical works have been reported for cavities with various fluids. Cavities, in general, are classified to be either closed or opened (where one side is open to surroundings). Figure 1 presents the general geometry of a tilted partially open cavity. The tilt of the cavity is identified by the angle α between wall number 1 and the vertical axis, with α taken positive in the clockwise direction as shown in the figure. The geometrical parameters that affect the heat transfer between the cavity and the surroundings are: the aspect ratio ($AR = H/B$), opening ratio ($OR = a/H$), the opening displacement ratio ($DR = d/H$), and the tilt angle α . Grashof and Prandtl numbers are also important parameters in the determination of heat transfer in cavities.

One of the early works that was reported for heat transfer from open cavities is that of Le Quere et al. (1981). In this work a fully open square cavity with isothermal walls was studied numerically. Tilt angles of 0 , 20 , and 45 deg were considered for Grashof numbers Gr_H ranging between 10^4 and

10^7 . The effect of changing the aspect ratio from 1 to 0.5 or 2 was studied for cavities with $\alpha = 0$ deg and $Gr_H = 10^7$. The authors found that the flow field within the cavity and in the aperture plane is determined mainly by local heat transfer effects. They also showed that changes in cavity orientation produce striking variations in cavity flow patterns due to the interchanging heat transfer roles of the walls as the cavity is inclined. Thermal losses from the cavity decreased as α increased due to the stable stratification of the flow.

Several other investigators studied heat transfer by natural convection from open cavities. Some of these studies focused on the effect of varying the aspect ratio and/or the opening ratio of the cavity on the flow pattern and on the heat transfer from the cavity. Other studies investigated the effect of varying the tilt angle of the cavity and/or the conditions of its walls on heat transfer.

Table 1 summarizes some of the previous work on fully/partially open cavities. Four types of boundary conditions are included in the review. The explanation of the various types of boundary conditions on the walls of the cavity is given in Table 2. A cavity is considered fully open when the opening ratio is equal to 1 ($OR = 1$), and partially open when $OR < 1$. In Table 1, two forms of the Grashof number are used, one when the cavity has isothermal wall(s) and the other when the cavity has constant heat flux on the wall(s). The Grashof number for a cavity with isothermal walls is defined as follows:

$$Gr_L = g\beta \frac{|T_w - T_\infty| L^3}{\nu^2}$$

where L is a characteristic length of the cavity (either B or H) and T_w is the temperature of the wall. The Grashof number for cavities with walls having constant heat flux is defined as follows:

Contributed by the Heat Transfer Division for publication in the JOURNAL OF HEAT TRANSFER. Manuscript received by the Heat Transfer Division, Jan. 14, 1998; revision received Sept. 22, 1998. Keywords: Cavities, Convection, Experimental, Heat Transfer, Natural Convection. Associate Technical Editor: R. Dougllass.

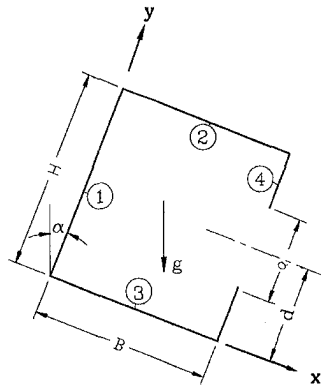


Fig. 1 Geometry of a partially open cavity

$$Gr_L^* = g\beta \frac{q''L^4}{k\nu^2}$$

where q'' is the heat flux to the wall.

A common feature for all the cavity studies listed in Table 1 is that $DR = 0.5$, i.e., the aperture is at the center of wall 4. None of these studies have covered the case when the aperture is located off the center of wall 4, i.e., when $DR < 0.5$ or $DR > 0.5$. Of special interest are cavities with an aperture having $DR = 0.5 OR$ and $DR = 1 - 0.5OR$, i.e., when the cavity has a slit at the bottom and at the top of wall 4, respectively. These geometries are of special importance in solar and air conditioning applications. A third geometry which is of special interest in electronic equipment is when wall 4 has a uniformly distributed longitudinal slots. Here, the opening ratio is defined as $OR = na/H$ where n is the number of slots and a is the height of each slot. Heat transfer data for the above three geometries; cavity with high wall slit, cavity with low wall slit, and cavity with

Table 1 Review of previous work on fully/partially open cavities

Reference	Geometry			B.C.*	α	Pr	Gr or Ra
	AR	OR	DR				
LeQuere et al.	1981	1	1	0.5	A	0, 20, 45	$10^4 \leq Gr_H \leq 10^7$
		0.5, 2	1	0.5	A	0	$Gr_H = 10^7$
Penot	1982	1	1	0.5	A	0, ± 45 , 90	$10^5 \leq Gr_H \leq 10^7$
Miyamoto et al.	1989	1	0.5, 1	0.5	A	$-45 \leq \alpha \leq 80$	$7 \times 10^3 \leq Ra_B \leq 7 \times 10^4$
		1	0.5, 1	0.5	A	0	$1 \leq Ra_B \leq 7 \times 10^5$
Showole and Tarasuk	1993	0.25, 0.5, 1	1	0.5	A	$-90 \leq \alpha \leq -30$	$10^4 < Ra_H < 5 \times 10^5$
		1	1	0.5	A	$-90, -45$	$10^3 < Ra_H < 5 \times 10^5$
Angirasa et al.	1995	1	1	0.5	A	0	$10^4 \leq Gr_H \leq 10^7$
Sernas and Kyriakides	1982	1	1	0.5	B	0	$Gr_H = 10^7$
Hess and Henze	1984	1	0.5, 1	0.5	C	0	$3 \times 10^{10} \leq Ra_H \leq 2 \times 10^{11}$
Chan and Tien	1985	1, 0.143	1	0.5	C	0	$10^3 \leq Ra_H \leq 10^7$
Chan and Tien	1986	0.143	1	0.5	C	0	$10^6 \leq Ra_H \leq 10^8$
Angirasa et al.	1992	1	1	0.5	C	0	$10^2 \leq Ra_H \leq 10^8$
Lin and Xin	1992	1	1	0.5	C	0	$Ra_H = 10^{10}, 10^{11}$
Mohamad	1995	0.5, 2, 1	1	0.5	C	$-80 \leq \alpha \leq 0$	$10^3 \leq Ra_H \leq 10^7$
Chakroun et al.	1997	0.25, 0.5, 1	0.25, 0.5, 1	0.5	E	$-90 \leq \alpha \leq 90$	$Gr_H^* = 5.5 \times 10^8$
Elsayed et al.	1998	1	1	0.5	C	$-60 \leq \alpha \leq 90$	$10^2 \leq Gr_H \leq 10^5$
Elsayed	1998	1	1	0.5	D	0	$Gr_H = 10^2, 10^7, 10^{10}$
present		1	0.25, 0.5, 0.75	**	E	$-90 \leq \alpha \leq 90$	$Gr_H^* = 5.5 \times 10^8$

* see table 2 for explanation

** $0 < DR < 1$, and uniform slots

Nomenclature

a = height of aperture
 AR = cavity aspect ratio, $= H/B$
 B = width of the cavity
 d = distance from the centerline of the opening to the base of the cavity
 DR = opening displacement ratio, $= d/H$
 F_{pa} = configuration factor between hot wall and aperture
 Gr_L = Grashof number for cavity with isothermal wall(s)
 Gr_L^* = Grashof number for cavity with wall(s) having constant heat flux
 h = local value of heat transfer coefficient
 \bar{h} = average convective heat transfer coefficient
 H = width of the cavity
 I = electric current
 k = thermal conductivity of air
 k_w = thermal conductivity of the Plexiglas walls

L = characteristic length of the cavity, also the length of the cavity
 \bar{Nu} = average Nusselt number
 $\Delta \bar{Nu}$ = uncertainty in \bar{Nu}
 $(\Delta \bar{Nu})_p$ = precision limit error in \bar{Nu}
 $(\Delta \bar{Nu})_b$ = bias limit error in the variable \bar{Nu}
 OR = opening ratio, $= a/H$
 q'' = convective heat transfer rate per unit area of the wall, also constant heat flux to a wall
 q_c'' = conductive heat loss rate per unit area of the hot wall
 q_r'' = radiative heat loss rate per unit area of the hot wall
 s = distance along a wall
 T = temperature
 \bar{T}_p = average temperature of hot plate

T_{pi} = strip surface temperature of the hot wall
 T_∞ = ambient temperature
 t = thickness of Plexiglas walls
 V = voltage
 x = one of the variables used in the determination of \bar{Nu}
 Δx_{bi} = bias limit error in the variable x_i
 Δx_{pi} = precision limit error in the variable x_i
 α = tilt angle of cavity, positive direction in clock wise direction, see Fig. 1
 β = coefficient of thermal expansion of air
 ϵ = emissivity of the heated wall (aluminum plate)
 ν = kinematic viscosity of air
 σ = Stefan-Boltzmann constant

Table 2 Explanation for the types of boundary conditions given in Table 1

B.C. type	Boundary condition on walls			
	1	2	3	4
A	T_h	T_h	T_h	T_h
B	T_h	T_h	T_∞	N/A
C	T_h	a	a	a
D	T_c	a	a	a
E	q''	a	a	a

Notes: $T_c < T_\infty < T_h$, a = adiabatic, N/A not applicable, and q'' = constant heat flux on the wall

uniform wall slots are not available in the literature to the best of the author's knowledge. The results of these geometries will be very useful for several engineering applications.

In the present work, three different geometrical arrangements of the opening slit were studied; high wall slit, low wall slit, and uniform wall slots. For each arrangement, three different opening ratios were examined; i.e., at $OR = 0.25, 0.5,$ and 0.75 . The results of the centered wall slit and fully open cavity were obtained from Chakroun et al. (1997) for comparison purpose. Geometries of the cavities that are considered in the present work are shown in Fig. 2. For all these arrangements, the variation of the Nusselt number with the tilt angle is presented for tilt angles ranging from -90 deg to $+90$ deg with an increment of 15 deg, and at $Gr_H^* = 5.5 \times 10^8$.

2 Experimental Setup and Procedure

The experimental setup is shown in Fig. 3. A brief description of the apparatus is given below. A more detailed discussion can be found in Chakroun et al. (1997).

The setup consists of a rectangular cavity with $H = B = 14.85$ cm and $L = 91.45$ cm. The cavity is mounted on rotatable frame which can vary the tilt angle. The angle of rotation is measured with respect to the vertical axis (see Fig. 1) and can be read from a protractor.

Figure 4 shows a cross-sectional view of the cavity. The side of the cavity which faces the aperture (heated surface) is made of an aluminum plate (14.85 cm \times 91.45 cm and 0.6 cm thick) and the other sides are made of Plexiglas (1.0 cm thick). The heating system consists of flexible heating pads which affix to the aluminum plate. The heating pads provide a constant heat flux to the plate. A total of 18 heaters (each is 7.5 cm \times 10 cm) were used. A thick piece of hard Plexiglas insulation is

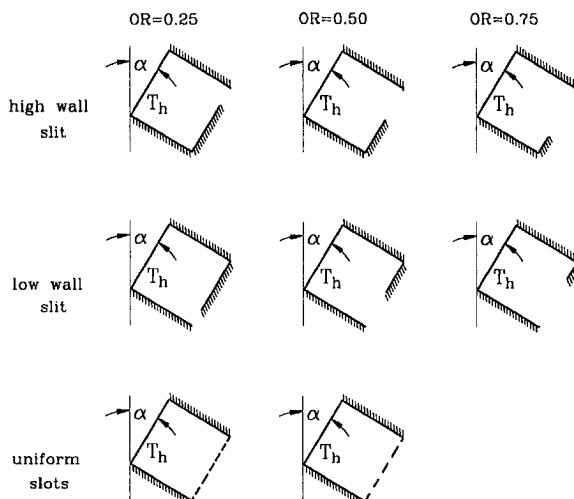


Fig. 2 Geometries of cavities that are considered in the present work

pressed against the pads to ensure that the heaters are in good contact with the aluminum plate. All pads are connected in parallel, hence they receive the same power. The heat input to the pads is controlled by an electric circuit composed of a 240 V power supply and a voltage regulator. The voltage and the current applied to the heaters are measured continuously by a digital voltmeter and an ammeter with accuracy of 0.025 percent, plus two least-significant digits, respectively. All sides of the cavity, including the plate, are insulated with a 5-cm thick glass wool to minimize heat loss from the cavity.

The surface temperature of the aluminum plate is monitored using five thermocouples, equally spaced, across the width of the plate (see Fig. 4). In addition, surface thermocouples were fixed on the inside and outside of the side walls. Also, to estimate the heat loss from behind the pads, a Plexiglas plate was fixed behind the aluminum plate, and thermocouples were installed on both surfaces of the plate. The ambient temperature outside the opening of the cavity is measured by a separate thermocouple. All 25 thermocouples (shown in Fig. 4) were connected to a digital recorder to record the temperature once steady-state was achieved. The steady-state condition was considered to be achieved when the differences in the wall temperatures were not changing by more than 0.2°C within 15 minutes. For a given opening ratio, the cavity was rotated by an increment of 15 deg between -90 deg and $+90$ deg around the vertical axis. A total of 12 runs were carried out for each opening arrangement.

3 Nusselt Number Data Reduction Equation

The average Nusselt number from the cavity is defined as

$$\overline{\text{Nu}} = \frac{\bar{h}B}{k} \quad (1)$$

where \bar{h} is the average heat transfer coefficient between the cavity and the surroundings, B is the width of the cavity, and k is the thermal conductivity of the air in the cavity. In terms of the local heat transfer coefficient h , Eq. (1) is rewritten in the following form:

$$\overline{\text{Nu}} = \frac{1}{k} \frac{B}{H} \int_0^H h dy \quad (2)$$

where y and H are as defined in Fig. 1. When wall 1 is heated at constant heat flux q'' , the local heat transfer coefficient is given by the equation

$$h = \frac{q''}{(T_p - T_\infty)} \quad (3)$$

where T_p is the local temperature of the wall. Dividing the wall into five equal sections, Eqs. (2) and (3) are combined to give

$$\overline{\text{Nu}} = \frac{B}{5k} \sum_{i=1}^5 \frac{q''}{(T_{pi} - T_\infty)} \quad (4)$$

where i is the order of the various sections on the heated plate.

To calculate q'' , an energy balance for the heated plate gives

$$IV = HL(q'' + q_c'' + q_r'') \quad (5)$$

where I and V are the current and the voltage to the heating elements, q_c'' is the heat lost through all walls of the cavity to the ambient, and q_r'' is the heat transferred by radiation from the hot wall to the surroundings as seen through the aperture. The double primes indicate that the heat transfer term is per unit area of the hot wall. Using Eq. (5), Eq. (4) becomes

$$\overline{\text{Nu}} = \frac{B}{5k} \sum_{i=1}^5 \left\{ \left(\frac{IV}{HL} - q_c'' - q_r'' \right) / (T_{pi} - T_\infty) \right\} \quad (6)$$

The radiation heat loss q_r'' from the hot wall is estimated as follows:

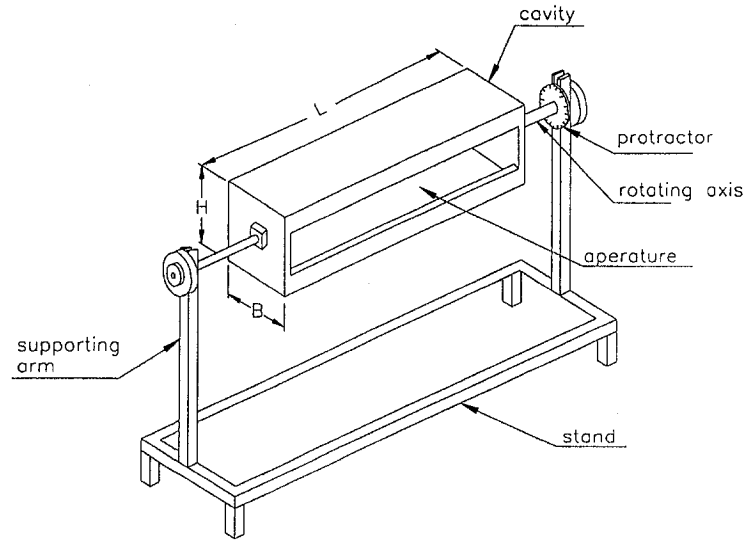


Fig. 3 Main features of the experimental setup

$$q_r'' = \sigma[(\bar{T}_p + 273)^4 - (T_\infty + 273)^4] / \left(\frac{1 - \epsilon}{\epsilon} + \frac{1}{F_{pa}} \right) \quad (7)$$

where \bar{T}_p is the average temperature of the hot wall, ϵ is its emissivity and F_{pa} is the configuration factor between the plate and the aperture. In Eq. (7) it is assumed that the surrounding is a black body at temperature T_∞ . The configuration factor F_{pa} is calculated from the analytical expression given by Gross et al. (1981).

The conduction heat loss q_c'' in Eq. (6) is the sum of the heat loss through walls 2, 3, 4 and 5 (see Fig. 4). This is expressed as follows:

$$q_c'' = \frac{k_w}{H} \sum_{j=2}^5 \int_0^{s_j} (T_{j,i} - T_{j,o}) \frac{ds}{t_j} \quad (8)$$

where j is the wall identification number, k_w is the thermal conductivity of the Plexiglas walls, t is the thickness of the Plexiglas walls, s is the distance along the walls, and $T_{j,i}$ and $T_{j,o}$ are the local temperatures on the inner and outer surfaces of the j th wall, respectively (see Fig. 4). The temperature distribution on the inner and outer surfaces of walls 2 through 5 is found to fit linear relations. These relations are used to deter-

mine the local surface temperatures in Eq. (7). Using Eqs. (7) and (8), the expression of Nu given by Eq. (6) yields

$$\bar{Nu} = \frac{B}{5k} \sum_{i=1}^5 \left\{ \frac{IV}{HL} - \frac{k_w}{H} \sum_{j=2}^5 \int_0^{s_j} (T_{j,i} - T_{j,o}) \frac{ds}{t_j} - \sigma[(\bar{T}_p + 273)^4 - (T_\infty + 273)^4] / \left(\frac{1 - \epsilon}{\epsilon} + \frac{1}{F_{pa}} \right) \right\} \quad (9)$$

The above expression shows explicitly all the variables involved in the experimental determination of Nu.

The uncertainty in the experimentally determined Nusselt number was estimated based on the ANSI/ASME Standard on Measurement Uncertainty (1986) following the procedure of Coleman and Steele (1989). The uncertainty ΔNu in the value of Nu is expressed as follows:

$$\Delta \bar{Nu} = \sqrt{(\Delta \bar{Nu})_b^2 + (\Delta \bar{Nu})_p^2} \quad (10)$$

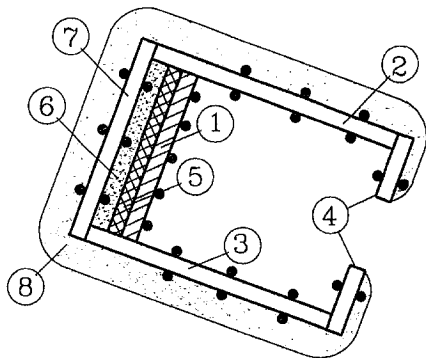
where the subscripts b and p refer, respectively, to the bias and precision limit errors. Now, Eq. (9) is rewritten in the following form:

$$\bar{Nu} = \bar{Nu}(x_1, x_2, \dots, x_m) \quad (11)$$

where x_1 to x_m are the variables that affect the determination of Nu. The values of $(\Delta \bar{Nu})_p$ and $(\Delta \bar{Nu})_b$ are then determined as follows:

$$(\Delta \bar{Nu})_p^2 = \sum_{i=1}^m \left(\frac{\partial \bar{Nu}}{\partial x_i} \Delta x_{pi} \right)^2 \quad (12)$$

$$(\Delta \bar{Nu})_b^2 = \sum_{i=1}^m \left(\frac{\partial \bar{Nu}}{\partial x_i} \Delta x_{bi} \right)^2 + 2 \left(\frac{\partial \bar{Nu}}{\partial x_1} \right) \left(\frac{\partial \bar{Nu}}{\partial x_2} \right) \overline{\Delta x_{b1} \Delta x_{b2}} + \dots \quad (13)$$



- | | |
|-------------------|-------------------------|
| 1 aluminum plate | 6 hard insulation |
| 2 plexiglass wall | 7 plexiglass back wall |
| 3 plexiglass wall | 8 glasswool insulation |
| 4 plexiglass wall | ● thermocouple junction |
| 5 heating pads | |

Fig. 4 Cross-sectional view of the cavity with thermocouple locations

Δx_{bi} is the bias limit error in the variable x_i , and $\overline{\Delta x_{bi} \Delta x_{bj}}$ is the correlated bias limit error for variables x_i and x_j .

A computer program was prepared to determine \bar{Nu} and $\Delta \bar{Nu}$ using Eqs. (9) and (10), respectively. Central differencing was used to determine the partial derivatives $\partial \bar{Nu} / \partial x_i$. The

Table 3 Precision and bias limit errors for the variables used to determine \overline{Nu}

Variable, x	Δx_p	Δx_b
electric current, I	0.23%	0.2%
electric volt, V	0.5%	0.3%
temperature (any), T	0.1°C	0.23°C
distance (any)	0	0.03 mm
thermal conductivity of air	0	0.5%
thermal conductivity of Plexiglas	3%	3%
emissivity of aluminum	0	10%

values of Δx_{pi} and Δx_{bi} of the various variables used in the determination of \overline{Nu} are given in Table 3. Only the bias limit errors of temperature readings are correlated with each other since the same thermocouple wires were used to measure all the temperatures. The value of $\Delta x_{bi}/\Delta x_{bj}$ for all temperatures was taken equal to 0.18°C.

It was found that the uncertainty $\Delta \overline{Nu}$ —for the data of \overline{Nu} which will be reported later in the following section—ranges from four percent to ten percent depending on the values of OR , DR , and α .

4 Results and Discussions

4.1 Presentation of Results. As discussed earlier, the experimental work was performed to study the effect of the aperture geometry of a tilted, partially open cavity on the rate of heat transfer between the cavity and the surrounding air. For each run, the heat transfer coefficient was obtained for tilt angles ranging between -90 to 90 deg with increments of 15 deg, with the aspect ratio of the cavity taken to be one and in a controlled temperature environment ($T_\infty = 22^\circ\text{C}$). In all experiments, the heated wall was found to be isothermal within $\pm 0.3^\circ\text{C}$ under constant heat flux condition. Therefore the stratification in the present cases was relatively mild. The average temperature of the heated wall was found to be dependent on the tilt angle of the cavity and the dimension and geometry of the aperture of the cavity. Figures 5 to 11 include the variation of \overline{Nu} for various aperture geometry and at different values of OR . The figures also include the variation of \overline{Nu} with α as predicted by the correlations developed later in Section 4.2.

Figure 5 presents the variation of average temperature of the heated wall and the average Nusselt number with the tilt angle of the cavity for the case of the centered wall slit. Data for opening ratios of 0.25, 0.5, and 1.0 are presented. As shown in the figure, the average wall temperature \overline{T}_p increases with the increase of the tilt angle of the cavity and/or with the decrease of the opening ratio. The figure also shows that the average Nusselt number decreases as the opening ratio decreases and/or as the tilt angle increases. When the opening ratio decreases, the circulation motion of air inside the cavity becomes slower thus resulting in a decrease in the rate of heat transfer to the surroundings. For opening ratios of 1 and 0.5, the difference in the rate of heat transfer is seen only between angles of -30 and 60 where the values of Nusselt numbers for $OR = 0.5$ are slightly less than those of $OR = 1$. For $OR = 0.25$, the effect is found in almost all the tilt angles. At zero tilt angle, a cavity with an opening ratio of 1.0 has a larger Nusselt number than that with an opening ratio of 0.5 and 0.25 by 8.4 percent and 39.2 percent, respectively.

Figure 6 presents the results for a cavity with a high wall slit. The data are presented for opening ratios of 0.25, 0.5, and 0.75. As shown in the figure, the opening ratio of 0.75 gives the minimum values of the average wall temperature and the maximum values of Nusselt number for all the tilt angles. Not much difference is seen between OR of 0.75 and 0.5 because the difference is within the uncertainty of the measurements. For $OR = 0.25$, the values of Nusselt number show an appreciable

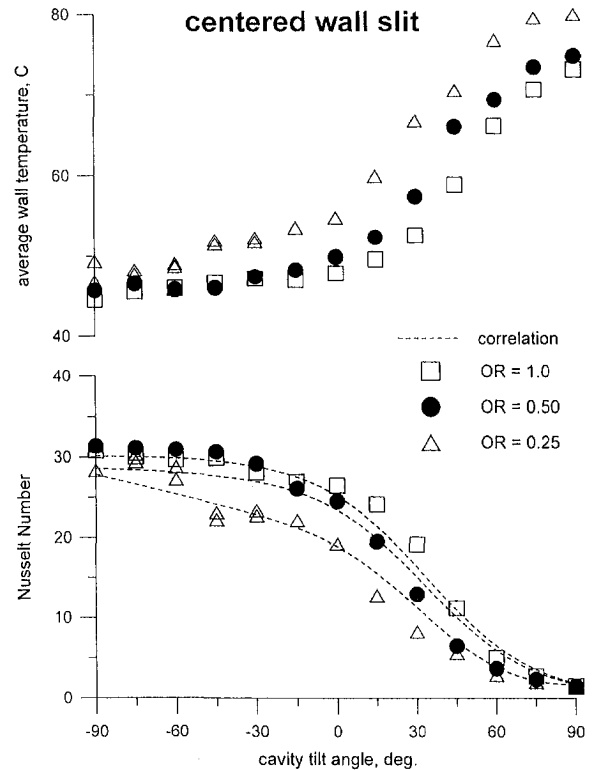


Fig. 5 Variation of average wall temperature and Nusselt number with cavity tilt angle for centered wall slit (all data were taken from Chakroun et al., 1997)

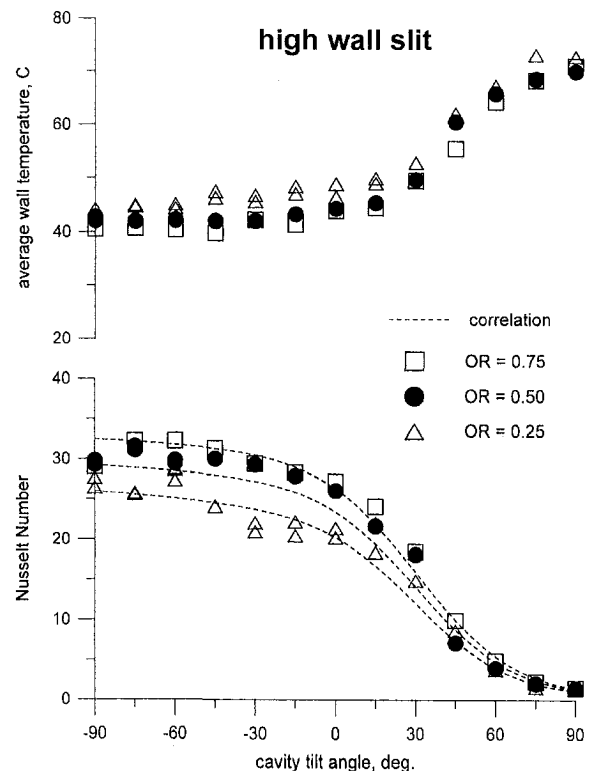


Fig. 6 Variation of average wall temperature and Nusselt number with cavity tilt angle for high wall slit

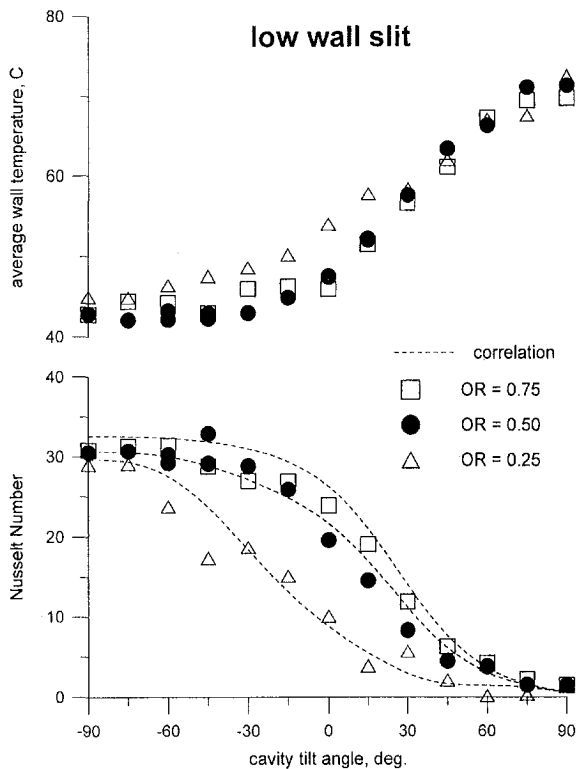


Fig. 7 Variation of average wall temperature and Nusselt number with cavity tilt angle for low wall slit

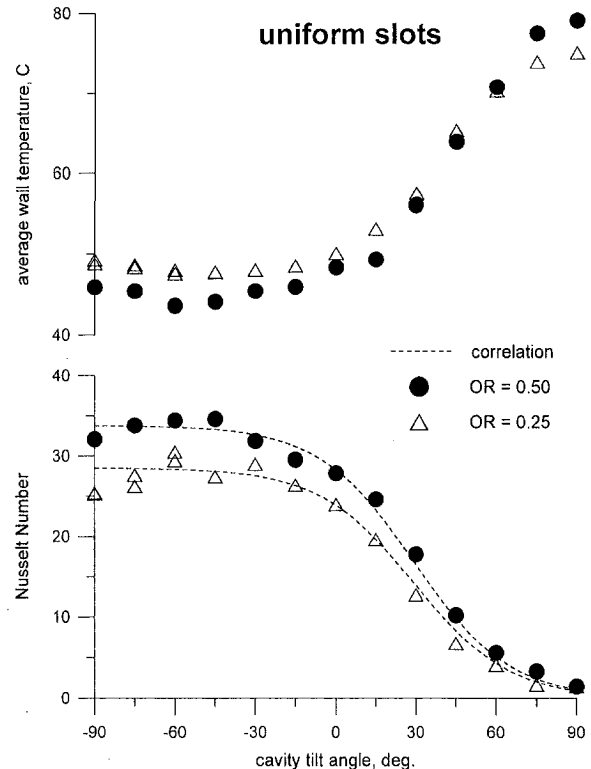


Fig. 8 Variation of average wall temperature and Nusselt number with cavity tilt angle for uniform slots

decrease and an increase in \bar{T}_p in comparison to those of $OR = 0.5$ or $OR = 0.75$ for tilt angle less than 30. At zero tilt angle, a cavity with an opening ratio of 0.75 has a larger Nusselt number than opening ratios of 0.5 and 0.25 by 3.5 percent and 32.3 percent, respectively.

Figure 7 presents the results for the low wall slit. The trend of the variation of the wall average temperature and the average Nusselt number with the tilt angle of the cavity and the opening ratio is the same as that for the case of the high wall slit. At zero tilt angle, an opening ratio of 0.75 has a larger Nusselt number than opening ratios of 0.5 and 0.25 by 21.9 percent and 136 percent, respectively.

Figure 8 presents the data for uniformly distributed wall slits. The data is presented for opening ratios of 0.25 and 0.5. Heat transfer for an opening ratio of 0.5 gives values of Nusselt number greater than those for opening ratio of 0.25 for all the tilt angles. The Nusselt number for $OR = 0.5$ is larger than that of 0.25 by 17 percent and 26 percent at tilt angle of zero and -90 , respectively.

For a given arrangement and at a certain value of OR , the effect of changing the tilt angle α on Nu depends on the range over which α is changed. Two zones are identified: $\alpha < 0$ deg and $\alpha > 0$ deg. The case with $\alpha < 0$ deg represents all cavities with heat flow in the upward direction. Here, heat is transferred in the same direction with the buoyancy force. Within this zone a change in α has a negligible effect of Nu . The case with $\alpha > 0$ deg, however, behaves differently. This is the case when heat is transferred in a downward direction, i.e., in the opposite direction to the buoyancy force. Here, as α is increased, the buoyancy component that opposes the flow of heat increases and thus convection is suppressed. On the limiting case when $\alpha = 90$ deg, heat is transferred only by conduction through the air in the cavity, since this air becomes fully stratified. Therefore, as α approaches 90 deg, Nu approaches 1.0 as shown in the figures.

Figure 9 shows the variation of the Nusselt number with the cavity tilt angle for opening ratio of 0.25 and for all four

arrangements; centered, high, low, and uniformly distributed wall slits. It is clear from the results in the figure that no trend can be predicted for the effect of the opening geometry on the rate of heat transfer at $\alpha < -60$ deg. At $\alpha \geq -60$ deg it is clear that cavities with low wall slit give the least amount of heat transfer in comparison with other cases. Other than the low wall slit, one cannot derive conclusions on the preference of one opening geometry over the other with respect to the rate of heat transfer.

Figure 10 presents similar results when opening ratio of 0.5 is used. It is clear here that the uniformly distributed wall slits

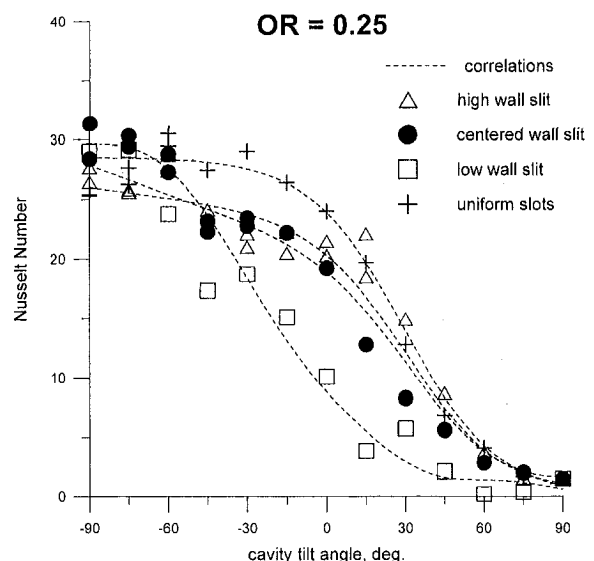


Fig. 9 Variation of Nusselt number with cavity tilt angles for four types of cavities at $OR = 0.25$

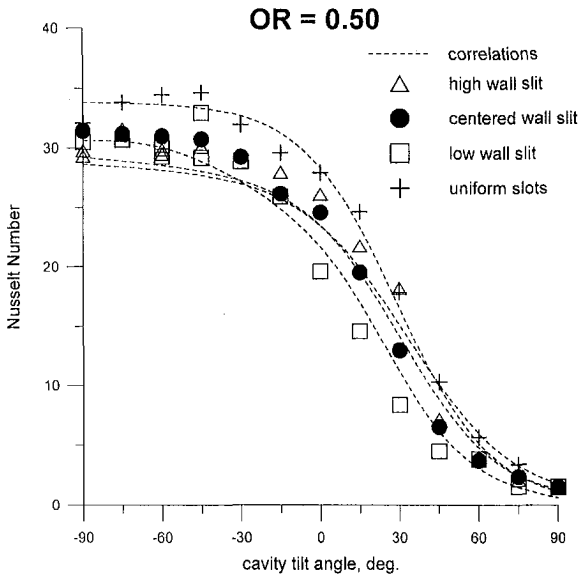


Fig. 10 Variation of Nusselt number with cavity tilt angles for four types of cavities at $OR = 0.50$

have the highest values of Nusselt number for all the tilt angles. The low wall slit arrangement gives the lowest values of Nusselt number for all tilt angles. At a tilt angle of zero degrees the uniformly distributed wall slots have a higher Nusselt number than the high, centered, and low wall slits by 6.87 percent, 15.7 percent, and 42.43 percent, respectively.

Figure 11 shows the variation of Nusselt number with the cavity tilt angle for the high and low wall slits of opening ratio of 0.75. The high wall slit always has a higher value of Nusselt number than that of the low wall slit for all tilt angles. At a tilt angle of zero deg, the high wall slit has a higher Nusselt number than the low wall slit by 14.3 percent.

4.2 Empirical Correlations. Four empirical correlations were developed to fit the experimental data in Figs. 5 to 11. The expressions for these correlations are as follows:

A centered wall slit ($0.25 \leq OR \leq 1.0$)

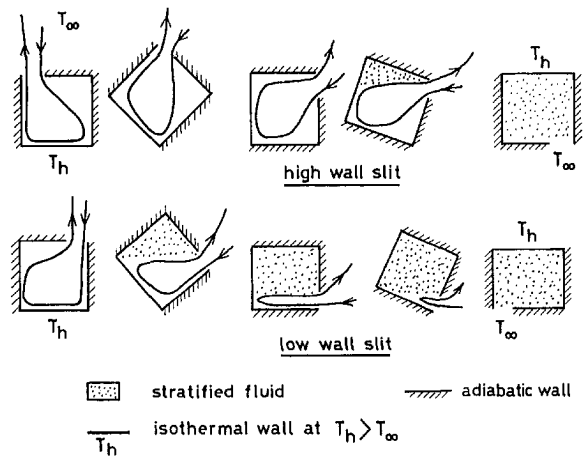


Fig. 12 Effect of tilt angle and position of opening on the heat transfer from a cavity

$$\overline{Nu} = \frac{154(0.9 + 0.1OR)}{5.1 + \exp(2.78\alpha)} - \frac{0.07}{OR^3} \cos \alpha \quad (14)$$

B high wall slit ($0.25 \leq OR \leq 0.75$)

$$\overline{Nu} = \frac{154(0.755 + 0.43OR)}{5.1 + \exp(3\alpha)} - \frac{0.75}{\sqrt{OR}} \cos \alpha \quad (15)$$

C low wall slit ($0.25 \leq OR \leq 0.75$)

$$\overline{Nu} = \frac{154(0.95 + 0.13OR)}{5.1 + \exp(3.5\alpha)} - \frac{1}{OR^2} \cos^3 \alpha \quad (16)$$

D uniformly distributed wall slots ($0.25 \leq OR \leq 0.5$)

$$\overline{Nu} = \frac{154(0.77 + 0.7OR)}{5.1 + \exp(3.2\alpha)} \quad (17)$$

In the above correlations α is the tilt angle of the cavity (in radians). The correlations are valid for cavities of $AR = 1$, with type E boundary conditions (see Table 2) and at $Gr_{\beta}^* = 5.5 \times 10^8$. Figures 5 to 8 depict comparisons between these correlations and the experimental data. The agreement between these correlations and their corresponding data is within the experimental uncertainty of the experiments. These correlations cannot be used at different Grashof's number, therefore their usefulness is limited. More experimentation is needed to cover wider range of Grashof's numbers.

4.3 Heat Transfer Mechanism. The results in Figs. 5 to 11 together with the previous discussion on these figures can now be used to understand the dependence of the average Nusselt number on both the tilt angle of the cavity and the geometry of its opening. For this purpose, consider cases of the high wall slit and the low wall slit with various tilt angles as shown in Fig. 12. In these cavities heat is transferred by the buoyancy driven flow. Starting with a tilt angle equal to -90 deg, both the high wall slit and the low wall slit have the same flow pattern and temperature distribution, thus resulting in the same value of Nu (see Figs. 9, 10, and 11). As the tilt angle increases to approach zero tilt angle (i.e., vertical cavity), a stagnant zone of air starts to exist in the low wall slit cavity as a result of stratification. This may lead to using only a fraction of the surface area of the heated wall to derive the flow through the cavity (see Fig. 12). The conclusion is that the low wall slit cavity has a lower value of Nu than that of the high wall slit cavity. When the tilt angle reaches zero, i.e., the cavity becomes vertical, a sizable zone in the low wall slit cavity becomes stratified, thus causing an appreciable drop in the value of Nu in comparison with that given by the high wall slit cavity. Notice

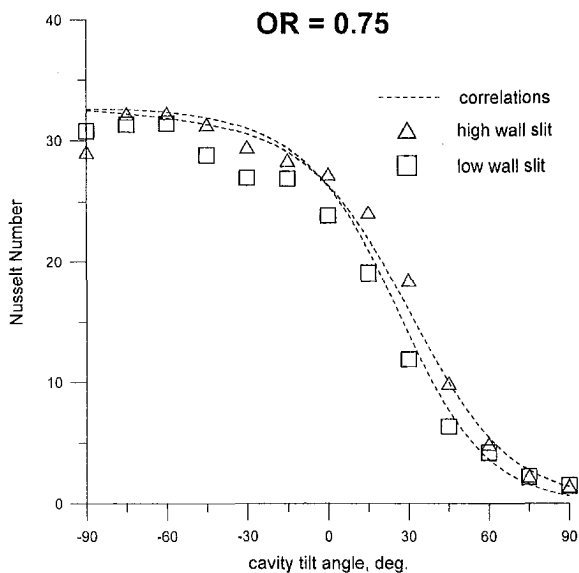


Fig. 11 Variation of Nusselt number with cavity tilt angles for two types of cavities at $OR = 0.75$

Table 4 Comparison of values of \overline{Nu} from square cavities ($AR = 1$) as obtained from present work and literature

α	Ra	OR	DR	Nu	B.C. type	Reference
0	7.6×10^6	1	0.5	24.5	E	present, Chakroun et al. (1997)
		1	0.5	26.4*	C	Mohamad (1995)
		1	0.5	27.9*	C	Chan and Tien (1985)
		flat	plate	27.7		Churchill and Chu (1975)
0	6.7×10^6	0.5	0.75	26.1	E	present work
		0.5	0.25	25.9	D	Elsayed (1998), cold walls, i.e., $T_h < T_c$
		flat	plate	26.8		Churchill and Chu (1975)
		1	0.5	28.1	E	present, Chakroun et al. (1997)
-30	7.7×10^6	1	0.5	30.6	A	Showole and Tarasuk (1993)

* by interpolation of available data using the relation $\overline{Nu} = c_1 Ra^{c_2}$

here the effect of the height of the slit which indicates that reducing the opening ratio increases the difference in the values of \overline{Nu} for the high and low wall slits (see Figs. 9 to 12). An increase in the tilt angle beyond 0 deg causes the development of a stratified zone in the high wall slit cavity and increases the size of the stratified zone in the low wall slit cavity, as shown in Fig. 12. This causes the decrease of the value of \overline{Nu} in both geometries. As the cavity reaches a tilt angle of 90 deg the air within the cavity becomes fully stratified and heat transfer in this case takes place by conduction only, since convection is suppressed. At this position \overline{Nu} becomes 1 in both geometries (see Figs. 9 to 11). Another interesting phenomenon is observed in the analysis of the results. Referring to Fig. 9 for cavities with $OR = 0.25$, one finds a sudden change in the trend of variation of \overline{Nu} with α for tilt angles between -30 deg to -60 deg. This sudden change in the value of \overline{Nu} is more pronounced in the low wall slit than in the high wall slit. This is may be related to dependence of the geometry of the stratified zone and the point of flow separation on the heated surface on the value of the tilt angle and the position and size of the opening of the cavity. The previous observation needs to be further investigated numerically and/or experimentally at different Grashof numbers.

Le Quere et al. (1981) showed that flow unsteadiness arises for values of $Gr > 10^6$ in open cavities. Vafai and Ettfagh (1990a, b) investigated further this phenomenon in vertical open cavities. They found that there is an oscillation in the value of the Nusselt number from the cavity and there is a one to one relationship between the frequency of the periodic oscillations in \overline{Nu} and the central vortex's oscillations and location inside the cavity. They also showed that the frequency of the oscillations of \overline{Nu} increases linearly as Ra increases. Also, Angirasa et al. (1995) showed that steady flow can not be reached in a vertical square cavity with isothermal walls when Gr_H is increased to 10^7 (same range of the present work). The authors showed that there is an instability that begins at the lower corner and then spreads along the vertical wall to the top corner. This leads to oscillation in the value of the Nusselt numbers from the cavity and from the bottom, vertical and the top sides as well. They also showed that the oscillation in the value of \overline{Nu} is more pronounced for the bottom and for the vertical sides of the cavity than that for the top side. These oscillation behaviors of \overline{Nu} cannot be detected in the present work because the recorded temperatures were collected for a long term time average.

4.4 Comparison With Literature. Comparison of the present work with that in the literature is not an easy task. One of the reasons is that the present work was carried out at boundary conditions different from those available in literature (see Tables 1 and 2). Another reason is that there is no work available in the literature for the present geometry under the present range of Ra and α . It was possible, however, to compare few cases in the present work with some previous work from literature. Table 4 shows comparison of the values of \overline{Nu} from a cavity

with $\alpha = 0$, $Ra = 7.6 \times 10^6$, $OR = 1$ and $DR = 0.5$. Here it should be mentioned that in the determination of \overline{Nu} from the work of Mohamad (1995) and Chan and Tien (1985), a relation in the form

$$\overline{Nu} = c_1 Ra^{c_2}$$

was used to fit the available data around $Ra = 7.6 \times 10^6$. The value of \overline{Nu} from a vertical flat plate with isothermal surface is also included in the table. Table 4 also compares the value of \overline{Nu} for a cavity with $\alpha = 0$, $Ra = 6.7 \times 10^6$, $OR = 0.5$, $DR = 0.75$ (i.e., high wall slit) with the numerical work of Elsayed (1998) at the same conditions except for the position of the opening and the type of the boundary condition. It should be noticed that a cold cavity with low wall slit is equivalent to a warm cavity with high wall slit according to the heat transfer mechanism given in the previous section.

The third case of comparison in Table 4 is for the case of a cavity with $\alpha = -30$ deg, $Ra = 7.7 \times 10^6$, $OR = 1$, and $DR = 1$. Notice here that a cavity of type A boundary conditions gives higher value of \overline{Nu} than that obtained from a cavity with type E boundary conditions since Type A uses larger heating surface than that of type E.

Conclusions

Free convection heat transfer from rectangular, tilted partially open cavities has been investigated experimentally. Four different geometrical arrangements for the opening were presented; opening in the center, top, bottom, and opening in the form of slots distributed uniformly along the wall facing the heated surface. Conduction and radiation losses are taken into account in the determination of average Nusselt number of the cavity. For the centered wall slit, the heat transfer decreases as the opening ratio decreases and/or the tilt angle increases. The heat transfer for the low wall slit cavity is smaller in all the test cases than that of the high wall slit cavity. For an opening ratio of 0.5, the uniformly distributed wall slot have the highest heat transfer for all values of tilt angle than the center, high, and low wall slit. For 0.25 opening ratio, no definite trend can be seen when the heat transfer for the four different arrangements are compared together.

Acknowledgment

This work was carried out for Project EPM 106 sponsored by the Research Administration of Kuwait University.

References

- Angirasa, D., Pourquie, M. J. B. M., and Nieuwstadt, F. T. M., 1992, "Numerical study of transient and steady laminar buoyancy-driven flows heat transfer in a square open cavity." *Numerical Heat Transfer, Part A*, Vol. 22, pp. 223-239.
- Angirasa, D., Eggels, I. G., and Nieuwstadt, F. T. M., 1995, "Numerical simulation of transient natural convection from an isothermal cavity open on a side," *Numerical Heat Transfer, Part A*, Vol. 28, pp. 755-768.
- ASME, 1986, "Measurement Uncertainty," ASNI/ASME PTC 19.1-1985, Part 1.

- Chakroun, W., Elsayed, M. M., and Al-Fahed, S. F., 1997, "Experimental Measurements of Heat Transfer Coefficient in a Partially/Fully Opened Tilted Cavity," *ASME Journal of Solar Energy Engineering*, Vol. 119, pp. 298–303.
- Chan, Y. L., and Tien, C. L., 1985, "A numerical study of two-dimensional laminar natural convection in shallow open cavities," *Int. J. Heat Mass Transfer*, Vol. 28, pp. 603–612.
- Chan, Y. L., and Tien, C. L., 1986, "Laminar Natural Convection in Shallow Open Cavities," *ASME JOURNAL OF HEAT TRANSFER*, Vol. 108, pp. 305–309.
- Churchill, S. W., and Chu, H. H. S., 1975, "Correlating equations for laminar and turbulent free convection from a vertical plate," *Int. J. Heat Mass Transfer*, Vol. 18, pp. 1323–1329.
- Coleman, H. W., and Steele, W. G., 1989, *Experimental and Uncertainty Analysis for Engineers*, John Wiley and Sons, New York.
- Elsayed, M. M., 1998, "Infiltration load in cold rooms," *HVAC&R Research*, Vol. 4, No. 2, pp. 179–202.
- Elsayed, M. M., Al-Najem, N. M., El-Refaei, M. M., and Noor, A. A., 1998, "Numerical study of natural convection in fully open tilted cavities," *Heat Transfer Engineering*, accepted for publication.
- Gross, U., Spindler, R., and Hahne, E., 1981, "Shape-factor equations for radiation heat transfer between plane rectangular boundaries," letter in *Heat Transfer*, Vol. 8, pp. 219–227; reported in J. R. Howell, 1982, *Catalog of Radiation Configuration Factor*, Howell, J. R., 1982, McGraw-Hill, New York, p. 97.
- Hess, C. F., and Henze, R. H., 1984, "Experimental Investigation of Natural Convection Losses From Open Cavities," *ASME JOURNAL OF HEAT TRANSFER*, Vol. 106, pp. 333–338.
- Le Quere, P., Humphrey, J. A. C., and Sherman, F. S., 1981, "Numerical calculation of thermally driven two-dimensional unsteady laminar flow in cavities of rectangular cross section," *Numerical Heat Transfer*, Vol. 4, pp. 249–283.
- Lin, C. X., and Xin, M. D., 1992, "Transient turbulent free convection in an open cavity," *Institution of Chemical Engineers Symposium Series*, Vol. 1, pp. 515–521.
- Miyamoto, M., Keuhn, T. H., Goldstein, R. J., and Katoh, Y., 1989, "Two-dimensional laminar natural convection heat transfer from a fully or partially open square cavity," *Numerical Heat Transfer, Part A*, Vol. 15, pp. 411–430.
- Mohamad, A. A., 1995, "Natural convection in open cavities, and slots," *Numerical Heat Transfer, Part A*, Vol. 27, pp. 705–716.
- Penot, F., 1982, "Numerical calculation of two-dimensional natural convection in isothermal open cavities," *Numerical Heat Transfer*, Vol. 5, pp. 421–437.
- Sernas, V., and Kyriakides, I., 1982, "Natural convection in an open cavity," *Proceedings of the Seventh International Heat Transfer Conference*, Munchen, Germany, Vol. 2, pp. 275–280.
- Showole, R. A., and Tarasuk, J. D., 1993, "Experimental and Numerical Studies of Natural Convection With Flow Separation in Upward-Facing Inclined Open Cavities," *ASME JOURNAL OF HEAT TRANSFER*, Vol. 115, pp. 592–605.
- Vafai, K., and Eftefagh, J., 1990A, "The effects of sharp corners on buoyancy-driven flows with particular emphasis on outer boundaries," *Int. J. Heat Mass Transfer*, Vol. 33, No. 10, pp. 2311–2328.
- Vafai, K., and Eftefagh, J., 1990A, "Thermal and fluid flow instabilities in buoyancy-driven flows in open-ended cavities," *Int. J. Heat Mass Transfer*, Vol. 33, No. 10, pp. 2329–2344.

Inverse Natural Convection Problem of Estimating Wall Heat Flux Using a Moving Sensor

H. M. Park¹

O. Y. Chung

Department of Chemical Engineering,
Sogang University,
Shinsoo-Dong, Mapo-Gu,
Seoul, Korea

The inverse problem of determining heat flux at the bottom wall of a two-dimensional cavity from temperature measurement in the domain is considered. The Boussinesq equation is used to model the natural convection induced by the wall heat flux. The inverse natural convection problem is posed as a minimization problem of the performance function, which is the sum of square residuals between calculated and observed temperature, by means of a conjugate gradient method. Instead of employing several fixed sensors, a single sensor is used which is moving at a given frequency over the bottom wall. The present method solves the inverse natural convection problem accurately without a priori information about the unknown function to be estimated.

1 Introduction

Inverse heat transfer problems have many applications in various branches of science and engineering. Contrary to the direct problem which consists of computing the consequences of given causes, the inverse problem is associated with the reversal of the cause-effect sequence and consists of finding the unknown causes of known consequences. In many situations, the direct measurement of the cause is impossible or not practical and one is forced to estimate the cause from the observation of the effect. Specific examples are the determination of the outer surface condition during the re-entry of a space vehicle; temperature measurement in glass manufacturing; determination of the heat transfer coefficient when the measurement of surface temperature is extremely difficult due to a hostile environment such as high temperature, erosion, or surface sublimation; and so forth. The solution of these inverse problems is not straightforward due to their ill-posedness in the sense of Hadamard: Small perturbations in the observed functions may result in large changes in the corresponding solutions (Beck and Arnold, 1977). The ill-posed nature renders many algorithms used for direct problems inapplicable to inverse problems, and special numerical techniques must be employed to stabilize the calculation results. One commonly adopted technique is the regularization that imposes additional restrictions on the admissible solution. Recently, conjugate gradient methods, where the regularization is inherently built in the iterative procedure, have been employed in the solution of inverse heat conduction problems (IHCP) and found to be very efficient (Jarny et al., 1991).

There are many engineering devices and processes where natural convection occurs and has significant influences on heat transfer rates. Examples of large scale are the liquid metal nuclear reactor at the shutdown stage and many crystal growth processes such as the Czochralski process and the Bridgman process. Examples of smaller scale are modern electronic devices. In those processes and devices, natural convection is induced by a heat source or a heat flux at the boundary. In many situations it is very difficult or even impossible to measure the strength of the heat source or the magnitude of the heat flux directly. Therefore, it is very important to develop techniques of inverse natural convection

problems which are as rigorous and as efficient as those for the IHCP. Contrary to the IHCP, inverse convection problems have not been frequently addressed partly due to their mathematical complexity as compared to the inverse heat conduction. Convective heat transfer is governed by a set of nonlinear partial differential equations including the continuity equation, the Navier-Stokes equation, and the energy equation. Therefore convection problems are difficult to solve and very few papers devoted to inverse convection have been published so far. Moutsoglou (1980) investigated a steady two-dimensional laminar free-convection flow in a vertical channel. The governing equations are simplified by neglecting the axial diffusion of momentum and heat and further by decoupling the longitudinal and lateral pressure gradients, through which the governing equations are parabolized. He considers the case when the heat flux at one wall is unknown and the temperature for the other insulated wall can be measured. To circumvent the ill-posedness of the problem, the sequential function specification method is adopted, which is well suited for parabolic problems. Huang and Özisik (1992) considers an inverse problem of linear forced convection in the fully developed channel flow. Since the velocity profile is assumed, they deal only with the energy equation to determine the unknown wall heat flux from some temperature measurements at certain locations in the channel. They employ the conjugate gradient method, which consists of the sensitivity problem and the adjoint problem as well as the direct problem. Prud'homme and Nguen (1997) considers an inverse natural convection problem employing a conjugate gradient method. They adopt the stream function-vorticity formulation to describe the flow field and use the adjoint variable method to determine the conjugate direction.

In the present work we consider an inverse convection problem of determining the wall heat flux from the temperature measurement within the flow. The natural convection governing equation, the Boussinesq equation, is employed without any simplification to determine the velocity and temperature fields. The inverse problem is posed as an optimization problem which is solved by a conjugate gradient method, employing the adjoint equation to obtain the descent direction. The advantage of the present algorithm adopted is that no a priori information is needed on the shape of the unknown function, since the solution automatically determines the functional form over the domain. Because the governing equation is not simplified in the present analysis of the inverse natural convection problem, this method can be applied to many different inverse convection problems to

¹ To whom correspondence should be addressed.

Contributed by the Heat Transfer Division for publication in the JOURNAL OF HEAT TRANSFER. Manuscript received by the Heat Transfer Division, Jan. 21, 1999; revision received, June 25, 1999. Keywords: Heat Transfer, Inverse, Natural Convection, Numerical Methods. Associate Technical Editor: C. Beckermann.

yield rigorous results. Another important feature of the present investigation is the employment of one moving sensor instead of several fixed sensors for the determination of the distribution of the wall heat flux. It is obvious that we need several fixed sensors to resolve the spatial variation of the wall heat flux, the number of sensors required increasing according to the spatial complexity of wall heat flux function. But it shall be shown that a single moving sensor can detect complicated functions of the wall heat flux efficiently.

2 The System and Governing Equations

We consider a two-dimensional rectangular cavity filled with a Boussinesq fluid. At the bottom wall an unknown function of heat flux is imposed. The side walls are kept adiabatic while the top boundary is maintained at a constant temperature. Due to the heat flux through the bottom wall, convection is induced inside the cavity. The flow pattern and magnitude are determined by the shape of the heat flux function $f(x)$ imposed at the bottom. Since the temperature field inside the cavity is decided mainly by the fluid flow in the cavity, we try to determine the unknown function of space-dependent wall heat flux from the unsteady readings of a moving temperature sensor located in the cavity. This rather simple flow geometry facilitates the demonstration of the present algorithm for the inverse natural convection problems.

We use superscript asterisk to denote dimensional quantities, and introduce the following dimensionless variables:

$$x = \frac{x^*}{d_x}, \quad y = \frac{y^*}{d_y}, \quad t = \frac{\kappa t^*}{d_x^2}, \quad \mathbf{v} = \frac{d_y \mathbf{v}^*}{\kappa},$$

$$T = \frac{T^* - T_{\text{cold}}^*}{T_{\text{hot}}^* - T_{\text{cold}}^*}, \quad P' = \frac{d_y^2 P^*}{\rho \kappa^2} \quad (1)$$

where T^* is the temperature, T_{cold}^* is the temperature at the upper wall, T_{hot}^* is the nominal bottom temperature of the system, t^* is time, \mathbf{v}^* is the velocity field, P^* is the pressure field, κ is the thermal diffusivity, ρ is the density, d_x is the half-width of the cavity and d_y is the half-depth of the cavity. Then the set of governing equations in dimensionless variables are

$$\nabla \cdot \mathbf{v} = 0 \quad (2)$$

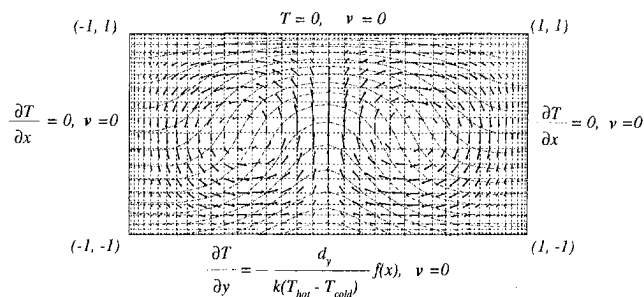


Fig. 1 The system domain and the initial velocity and temperature fields. The grid system (40 × 20) employed in the Chebyshev pseudospectral method is also depicted.

$$\frac{\partial \mathbf{v}}{\partial t} + \mathbf{v} \cdot \nabla \mathbf{v} = -\nabla P + \text{Pr} \nabla^2 \mathbf{v} + \text{R Pr} T \mathbf{j} \quad (3)$$

$$\frac{\partial T}{\partial t} + \mathbf{v} \cdot \nabla T = \nabla^2 T \quad (4)$$

where P is the modified pressure given by

$$P = P' - (T_{\text{cold}}^* - T_{\text{ref}}^*) \frac{d_y^3}{\kappa} \alpha g y, \quad (5)$$

α is the thermal expansion coefficient, \mathbf{j} is the unit vector in the y -direction, and g is the gravitational constant. The reference temperature T_{ref}^* is determined by

$$T_{\text{ref}}^* = \frac{1}{2} (T_{\text{hot}}^* + T_{\text{cold}}^*). \quad (6)$$

The dimensionless group R is the Rayleigh number and Pr is the Prandtl number defined as follows:

$$\text{R} = \alpha g \frac{(T_{\text{hot}}^* - T_{\text{cold}}^*) d_y^3}{\kappa \nu} \quad (7)$$

$$\text{Pr} = \frac{\nu}{\kappa} \quad (8)$$

Nomenclature

$d^i(x)$ = conjugate direction, Eq. (29)
 d_x = half-width of the system domain
 d_y = half-depth of the system domain
 $f(x)$ = heat flux function
 δf = variation of the heat flux function
 g = gravitational constant
 $\widehat{\mathbf{GX}}^{(1)}$ = matrix defined in Eq. (59)
 $\widehat{\mathbf{GX}}^{(2)}$ = matrix defined in Eq. (60)
 $\widehat{\mathbf{GY}}^{(1)}$ = matrix defined in Eq. (61)
 $\widehat{\mathbf{GY}}^{(2)}$ = matrix defined in Eq. (62)
 J = performance function, Eq. (13)
 δJ = variation of the performance function J
 ∇J = gradient of the performance function
 k = thermal conductivity
 NX = number of cells in the x -direction in the Chebyshev pseudospectral method

NY = number of cells in the y -direction in the Chebyshev pseudospectral method
 P = pressure
 Pr = Prandtl number
 δP = variation of the pressure field
 q = adjoint pressure field
 r = optimal step length in the conjugate gradient method, Eq. (35)
 R = Rayleigh number
 T = temperature field
 T_{cold}^* = temperature at the boundary
 T_{hot}^* = nominal bottom temperature
 T_{ref}^* = reference temperature of the system
 δT = variation of the temperature field
 t = time
 t_f = final time
 \mathbf{v} = velocity field
 $\delta \mathbf{v}$ = variation of the velocity field

Greek Symbols

α = thermal expansion coefficient
 γ^i = parameter defined in Eq. (30)
 $\delta(x)$ = Dirac delta function
 η = adjoint temperature field
 κ = thermal diffusivity
 ν = kinematic viscosity
 ξ = adjoint velocity field
 ξ_x = the x -component of ξ
 ξ_y = the y -component of ξ
 ρ = density
 $\tau = t_f - t$
 ω = sweeping frequency of the moving sensor (Eq. (14))

Superscripts

* = dimensional quantities
 \dagger = measured variable

Subscripts

m = measurement point

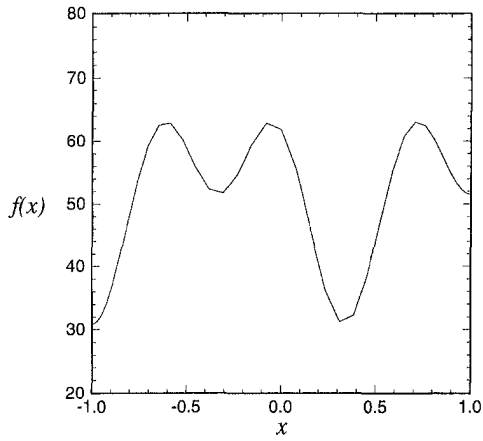


Fig. 2 A heat flux function of arbitrary shape

where ν is the kinematic viscosity. The relevant initial and boundary conditions are

$$t = 0, \quad \mathbf{v} = \mathbf{v}_0(x, y), \quad T = T_0(x, y) \quad (9)$$

$$x = \pm 1, \quad \mathbf{v} = 0, \quad \frac{\partial T}{\partial x} = 0 \quad (10)$$

$$y = +1, \quad \mathbf{v} = 0, \quad T = 0 \quad (11)$$

$$y = -1, \quad \mathbf{v} = 0, \quad \frac{\partial T}{\partial y} = -\frac{d_y}{k(T_{\text{hot}}^* - T_{\text{cold}}^*)} f(x) \quad (12)$$

where the initial velocity and temperature fields, \mathbf{v}_0 and T_0 , are the steady fields with $f(x) = 77.25$ (constant). Here, k is the thermal conductivity of the fluid. Figure 1 depicts the system with the grids (40×20) employed in the numerical computation. Also plotted is the initial velocity field \mathbf{v}_0 and the isotherms for the initial temperature field T_0 .

3 The Inverse Natural Convection Problem

The temperature field inside the domain, which can be easily measured at various locations, is determined by the heat flux function $f(x)$. Therefore, $f(x)$ can be estimated by using the measured values of the temperature field at certain locations. The performance function for the identification of $f(x)$ is expressed by the sum of square residuals between the calculated and observed temperature as follows:

$$J = \frac{1}{2} \int_0^t [T(x_m(t), y_m(t), t) - T^+(x_m(t), y_m(t), t)]^2 dt \quad (13)$$

where $T(x_m(t), y_m(t), t)$ is the calculated temperature, and $T^+(x_m(t), y_m(t), t)$ is the observed temperature at the moving observation location $(x_m(t), y_m(t))$. The measurement point $x_m = (x_m(t), y_m(t))$ is moving according to

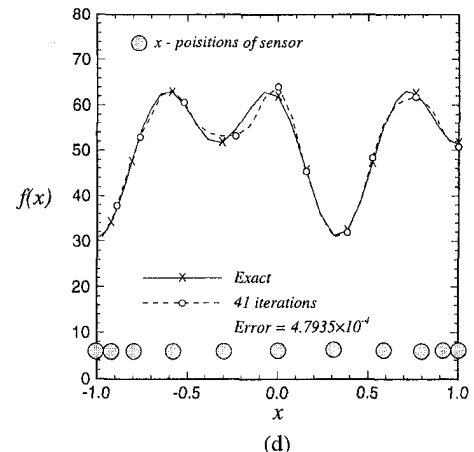
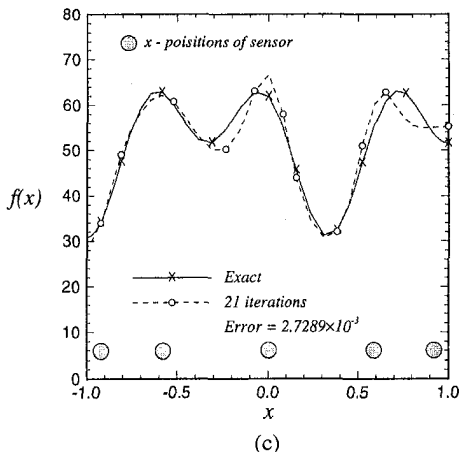
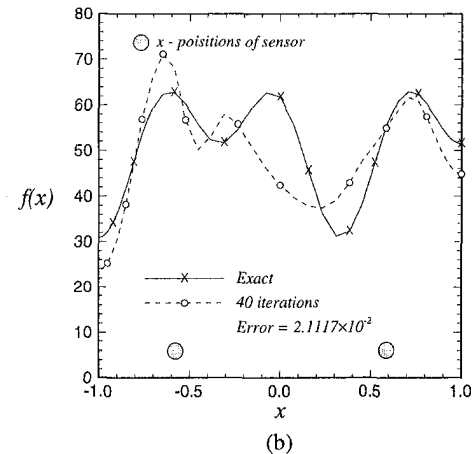
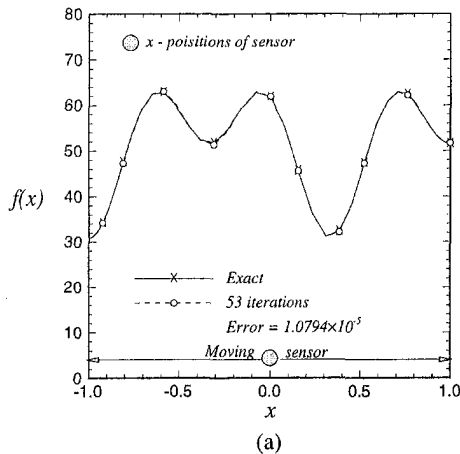


Fig. 3 The estimated heat flux functions for the case of Fig. 2; (a) with a single moving sensor with $\omega = 2$, (b) with 2 fixed sensors, (c) with 5 fixed sensors, (d) with 11 fixed sensors

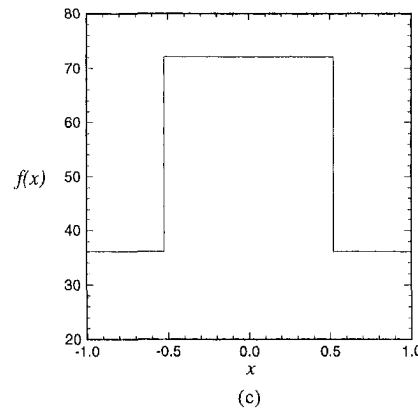
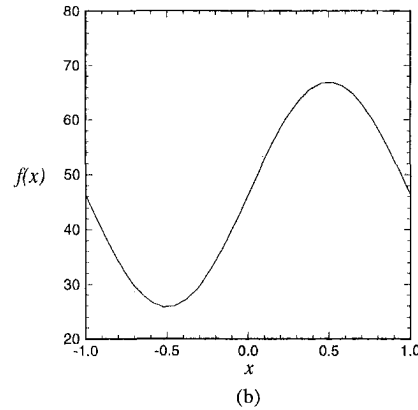
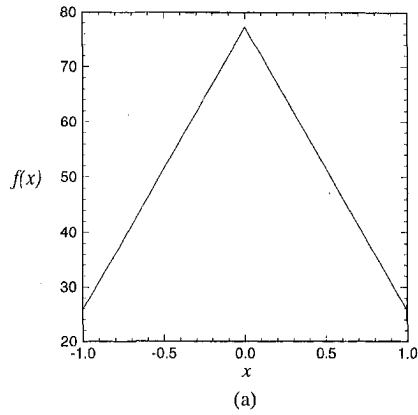


Fig. 4 Some standard shapes of heat flux functions $f(x)$ considered in the present investigation; (a) case I, (b) case II, (c) case III

$$\mathbf{x}_m = \begin{bmatrix} x_m(t) \\ y_m(t) \end{bmatrix} = \begin{bmatrix} a \sin \left[\frac{2\pi\omega t}{t_f} \right] \\ y_m^\dagger \end{bmatrix} \quad (14)$$

where $a = 1.0$, ω is the frequency and t_f is the duration of measurement. Here, it is assumed that the sensor is moving only horizontally at a fixed vertical location, y_m^\dagger . To minimize the performance function (13), we need the gradient of J , ∇J , which is defined by

$$\delta J(f) \equiv J(f + \delta f) - J(f) = \langle \nabla J, \delta f \rangle = \int_{x=-1}^1 \nabla J(x) \delta f(x) dx \quad (15)$$

where t_f , the final time, is 1.5. The function ∇J can be obtained by introducing the adjoint variables ξ , q , and η such that the performance function can be rewritten as follows:

$$J(f) = \frac{1}{2} \int_0^{t_f} [T(x_m, y_m, t) - T^\dagger(x_m, y_m, t)]^2 dt - \int_0^{t_f} \int_\Omega \xi \cdot \left[\frac{\partial \mathbf{v}}{\partial t} + \mathbf{v} \cdot \nabla \mathbf{v} + \nabla P - \text{Pr} \nabla^2 \mathbf{v} - \text{R Pr} T_j \right] d\Omega dt + \int_0^{t_f} \int_\Omega q [\nabla \cdot \mathbf{v}] d\Omega dt - \int_0^{t_f} \int_\Omega \eta \left[\frac{\partial T}{\partial t} + \mathbf{v} \cdot \nabla T - \nabla^2 \delta T \right] d\Omega dt. \quad (16)$$

In fact, the adjoint variables ξ , q , and η are the Lagrange multipliers usually employed in the constrained optimization. The variation of J , δJ , is then given by the following equation:

$$\delta J = \int_0^{t_f} [T(x_m, y_m, t) - T^\dagger(x_m, y_m, t)] \delta T(x_m, y_m, t) dt - \int_0^{t_f} \int_\Omega \xi \cdot \left[\frac{\partial \delta \mathbf{v}}{\partial t} + \delta \mathbf{v} \cdot \nabla \mathbf{v} + \mathbf{v} \cdot \nabla \delta \mathbf{v} + \nabla \delta P - \text{Pr} \nabla^2 \delta \mathbf{v} - \text{R Pr} \delta T_j \right] d\Omega dt + \int_0^{t_f} \int_\Omega q [\nabla \cdot \delta \mathbf{v}] d\Omega dt - \int_0^{t_f} \int_\Omega \eta \left[\frac{\partial}{\partial t} \delta T + \delta \mathbf{v} \cdot \nabla T + \mathbf{v} \cdot \nabla \delta T - \nabla^2 \delta T \right] d\Omega dt. \quad (17)$$

Integrating δJ by parts both in space and time, and exploiting the boundary conditions for \mathbf{v} , $\delta \mathbf{v}$, T and δT , the gradient of J , ∇J , defined in Eq. (15) is found to be the following:

$$\nabla J = \int_0^{t_f} \eta \left. \frac{d_y}{k(T_{\text{hot}}^* - T_{\text{cold}}^*)} \right|_{y=-1} dt \quad (18)$$

while the adjoint variables ξ , q , and η must satisfy

$$\frac{\partial \xi}{\partial t} + \mathbf{v} \cdot \nabla \xi = \nabla q - \text{Pr} \nabla^2 \xi + \xi \cdot (\nabla \mathbf{v})^T + \eta \nabla T \quad (19)$$

$$\nabla \cdot \xi = 0 \quad (20)$$

$$\frac{\partial \eta}{\partial t} + \mathbf{v} \cdot \nabla \eta = -\nabla^2 \eta - \text{R Pr} \xi^y - [T(x, y, t) - T^\dagger(x, y, t)] \delta(x - x_m) \delta(y - y_m) \quad (21)$$

where $\delta(x)$ is the Dirac delta function, superscript T in Eq. (19) means the transpose, and $\xi = (\xi^x, \xi^y)$. The relevant boundary conditions are

$$x = \pm 1, \quad \xi = 0, \quad \frac{\partial \eta}{\partial x} = 0 \quad (22)$$

$$y = -1, \quad \xi = 0, \quad \frac{\partial \eta}{\partial y} = 0 \quad (23)$$

$$y = +1, \quad \xi = 0, \quad \eta = 0. \quad (24)$$

The starting conditions are

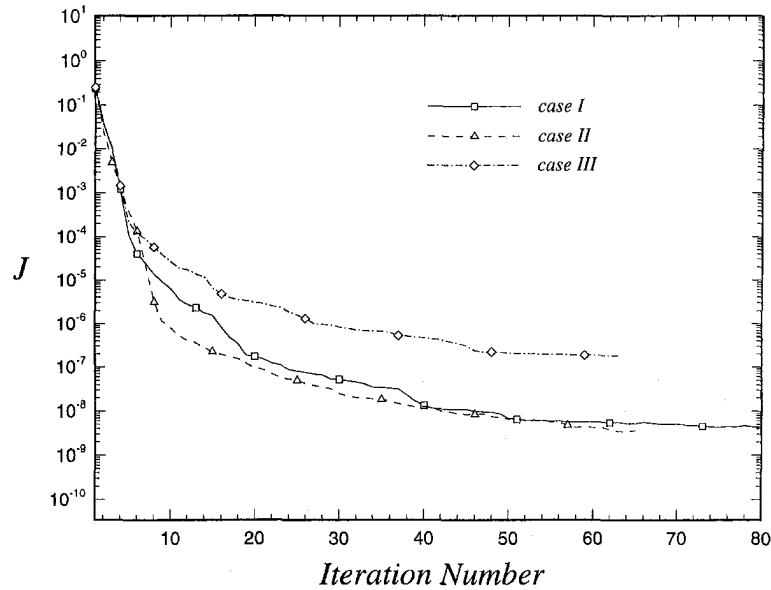


Fig. 5 Convergence rate of the conjugate gradient iteration for the three cases of Fig. 4

$$\xi(\mathbf{x}, t = t_f) = 0, \quad \eta(\mathbf{x}, t = t_f) = 0. \quad (25)$$

For the convenience of numerical integration, we change the time variable and rewrite Eqs. (19) and (21) as follows:

$$\frac{\partial \xi}{\partial \tau} - \mathbf{v} \cdot \nabla \xi = -\nabla q + \text{Pr} \nabla^2 \xi - \xi \cdot (\nabla \mathbf{v})^T - \eta \nabla T \quad (26)$$

$$\frac{\partial \eta}{\partial \tau} - \mathbf{v} \cdot \nabla \eta = +\nabla^2 \eta + \text{R Pr} \xi^y + [T(x, y, t) - T^\dagger(x, y, t)] \delta(x - x_m) \delta(y - y_m) \quad (27)$$

where $\tau \equiv t_f - t$ and t_f is the final time.

The Fletcher-Reeves method (Fletcher and Reeves, 1964), which is one of the conjugate gradient methods, is successfully applied to the minimization of the performance function, using the gradient of J determined by Eq. (18). The search direction or the conjugate direction at the first step is determined by

$$d^0(x) = \nabla J(x) = \int_0^{t_f} \eta \left. \frac{d_y}{k(T_{\text{hot}}^* - T_{\text{cold}}^*)} \right|_{y=-l} dt. \quad (28)$$

Beginning the second iteration step, the conjugate direction is given by

$$d^i(x) = \nabla J^i(x) + \gamma^i d^{i-1}(x) \quad (29)$$

where

$$\gamma^i = \frac{\int_{x=-1}^{x=1} (\nabla J^i(x))^2 dx}{\int_{x=-1}^{x=1} (\nabla J^{i-1}(x))^2 dx} \quad (30)$$

and i is the iteration number. Once the conjugate direction is obtained, the heat flux function $f(x)$ is updated in that direction.

$$f^{i+1}(x) = f^i(x) - r d^i(x) \quad (31)$$

The optimal step length r in the direction $d^i(x)$ is obtained by minimizing $J(f^i - r d^i)$ with respect to r . Formally, $J(f^i - r d^i)$ is expressed as

$$J(f^i - r d^i) = \frac{1}{2} \int_0^{t_f} [T(x_m, y_m; f^i - r d^i) - T^\dagger(x_m, y_m, t)]^2 dt. \quad (32)$$

The directional derivative of T at $f(x)$ in the direction of $d(x)$, denoted as δT , is defined by

$$\delta T = \lim_{\epsilon \rightarrow 0} \frac{T(f + \epsilon d) - T(f)}{\epsilon}. \quad (33)$$

Then, the term $T(x_m, y_m; f^i - r d^i)$ in Eq. (32) is approximated by

$$T(x_m, y_m; f^i - r d^i) = T(x_m, y_m; f^i) - \delta T(x_m, y_m, t) r. \quad (34)$$

Substituting Eq. (34) into Eq. (32), partially differentiating it with respect to r and setting the resulting equation equal to zero, the value of r that minimizes $J(f^i - r d^i)$ is obtained as

$$r = \frac{\delta J^i}{K^i} \quad (35)$$

where

$$K^i = \int_0^{t_f} [\delta T(x_m, y_m, t)]^2 dt \quad (36)$$

and

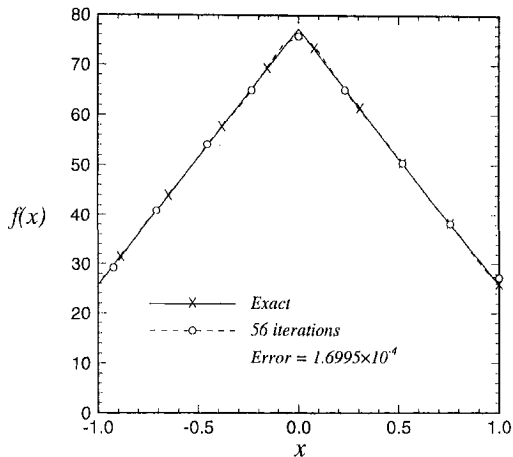
$$\delta J^i = \int_0^{t_f} [T(x_m, y_m, t) - T^\dagger(x_m, y_m, t)] \delta T(x_m, y_m, t) dt. \quad (37)$$

The sensitivity equations which determine δT is given by the following set of equations.

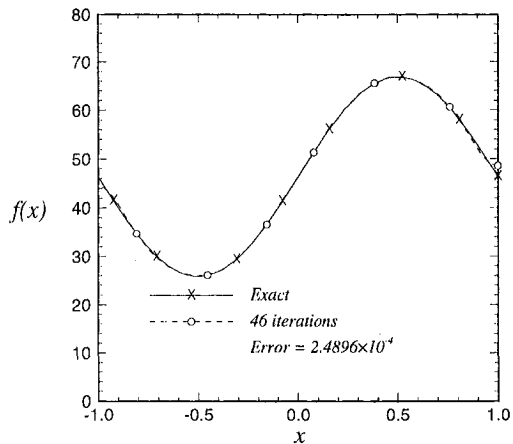
$$\nabla \cdot \delta \mathbf{v} = 0 \quad (38)$$

$$\frac{\partial}{\partial t} \delta \mathbf{v} + \delta \mathbf{v} \cdot \nabla \mathbf{v} + \mathbf{v} \cdot \nabla \delta \mathbf{v} = -\nabla \delta P + \text{Pr} \nabla^2 \delta \mathbf{v} + \text{R Pr} \delta T \mathbf{j} \quad (39)$$

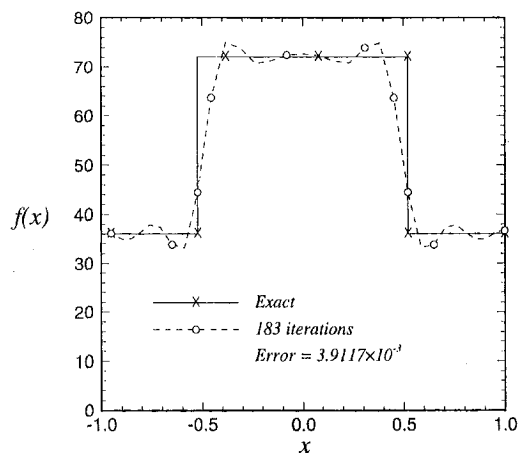
$$\frac{\partial}{\partial t} \delta T + \delta \mathbf{v} \cdot \nabla T + \mathbf{v} \cdot \nabla \delta T = \nabla^2 \delta T \quad (40)$$



(b)



(c)



(c)

Fig. 6 The estimated profiles of heat flux function $f(x)$ for the three cases of Fig. 4 when the sweeping frequency $\omega = 5$

The relevant initial and boundary conditions for the set of sensitivity equations are

$$t = 0, \quad \delta \mathbf{v}(x, y, t = 0) = 0, \quad \delta T(x, y, t = 0) = 0 \quad (41)$$

$$x = \pm 1, \quad \delta \mathbf{v} = 0, \quad \frac{\partial}{\partial x} \delta T = 0 \quad (42)$$

$$y = +1, \quad \delta \mathbf{v} = 0, \quad \delta T = 0 \quad (43)$$

$$y = -1, \quad \delta \mathbf{v} = 0, \quad \frac{\partial}{\partial y} \delta T = -\frac{d_y}{k(T_{\text{hot}}^* - T_{\text{cold}}^*)} d(x). \quad (44)$$

The present algorithm of the conjugate gradient method is summarized as follows.

- 1 Assume the heat flux function $f(x)$ and calculate the velocity and temperature fields by solving Eqs. (2)~(12).
- 2 Solve the adjoint Eqs. (20), (22)~(27) from $\tau = 0$ to $\tau = t_f$.
- 3 ∇J is determined by Eq. (18).
- 4 The conjugate direction $d^l(x)$ is given by Eq. (29) with γ^l determined by Eq. (30).
- 5 Solve the sensitivity Eqs. (38)~(44).
- 6 The optimal step length in the conjugate direction $d^l(x)$ is determined by Eq. (35).
- 7 The heat flux function $f(x)$ is updated according to Eq. (31).
- 8 Repeat the above procedure until convergence.

4 The Chebyshev Pseudospectral Method

The sets of equations governing the present problem of inverse natural convection, i.e., the set of Eqs. (2)~(12) for the direct problem, the set of Eqs. (20), (22)~(27) for the adjoint problem and the set of Eqs. (38)~(44) for the sensitivity problem, are solved by employing the following time splitting scheme to impose the solenoidal conditions, Eqs. (2), (20), and (38), implicitly:

Direct Problem.

Prediction Step.

$$\frac{\mathbf{v}^* - \mathbf{v}^n}{\Delta t} = -\mathbf{v}^n \cdot \nabla \mathbf{v}^n + \text{Pr} \nabla^2 \mathbf{v}^n + \text{R Pr} T^n \mathbf{j} \quad (45)$$

Pressure Equation.

$$\nabla^2 P^{n+1} = \frac{1}{\Delta t} \nabla \cdot \mathbf{v}^* \quad (46)$$

Correction Step.

$$\frac{\mathbf{v}^{n+1} - \mathbf{v}^*}{\Delta t} = -\nabla P^{n+1} \quad (47)$$

Energy Equation.

$$\frac{T^{n+1} - T^n}{\Delta t} = -\mathbf{v}^{n+1} \cdot \nabla T^{n+1} + \nabla^2 T^{n+1} \quad (48)$$

Adjoint Equation.

Prediction Step.

$$\frac{\xi^* - \xi^l}{\Delta \tau} = \mathbf{v}^l \cdot \nabla \xi^l + \text{Pr} \nabla^2 \xi^l - \xi^l \cdot (\nabla \mathbf{v}^l)^T - \eta \nabla T^l \quad (49)$$

Pressure Equation.

$$\nabla^2 q^{l+1} = \frac{1}{\Delta \tau} \nabla \cdot \xi^* \quad (50)$$

Correction Step.

$$\frac{\xi^{l+1} - \xi^*}{\Delta \tau} = -\nabla q^{l+1} \quad (51)$$

Energy Adjoint Equation.

$$\frac{\eta^{l+1} - \eta^l}{\Delta \tau} = \mathbf{v}^{l+1} \cdot \nabla \eta^{l+1} + \nabla^2 \eta^{l+1} + \text{R Pr} (\xi^y)^{l+1} + [T^{l+1} - (T^l)^{l+1}] \delta(x - x_m) \delta(y - y_m) \quad (52)$$

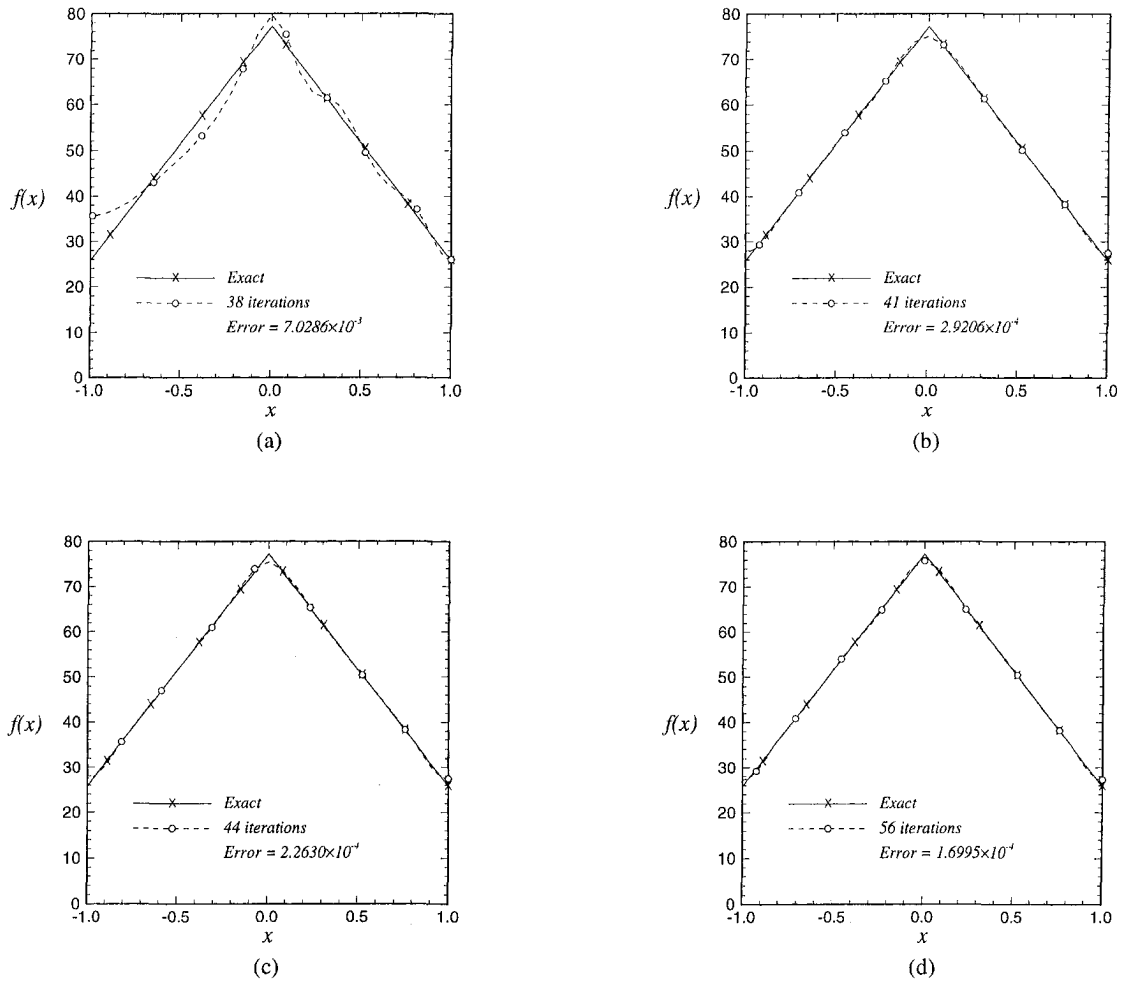


Fig. 7 The effect of the sweeping frequency of the moving sensor on the accuracy of the estimation; (a) $\omega = 0.5$, (b) $\omega = 1.0$, (c) $\omega = 2.0$, (d) $\omega = 5.0$

Sensitivity Equation.

Prediction Step.

$$\frac{\delta \mathbf{v}^* - \delta \mathbf{v}^n}{\Delta t} = -\delta \mathbf{v}^n \cdot \nabla \mathbf{v}^n - \mathbf{v}^n \cdot \nabla \delta \mathbf{v}^n + \text{Pr} \nabla^2 \delta \mathbf{v}^n + \text{R Pr} \delta T^n \mathbf{j} \quad (53)$$

Pressure Equation.

$$\nabla^2 \delta P^{n+1} = \frac{1}{\Delta t} \nabla \cdot \delta \mathbf{v}^* \quad (54)$$

Correction Step.

$$\frac{\delta \mathbf{v}^{n+1} - \delta \mathbf{v}^*}{\Delta t} = -\nabla \delta P^{n+1} \quad (55)$$

Energy Sensitivity Equation.

$$\frac{\delta T^{n+1} - \delta T^n}{\Delta t} = -\delta \mathbf{v}^{n+1} \cdot \nabla T^{n+1} - \mathbf{v}^{n+1} \cdot \nabla \delta T^{n+1} + \nabla^2 \delta T^{n+1} \quad (56)$$

The discretization of the spatial derivatives in Eqs. (45)~(56) is performed by using the Chebyshev pseudospectral method (Ku et al., 1987). Adoption of this technique allows one to approximate the differentiation of a function with matrix multiplication. According to the Chebyshev pseudospectral method the collocation points are selected as

$$x_i = \cos \left[\frac{\pi(i-1)}{NX} \right] \quad (1 \leq i \leq NX+1) \quad (57)$$

$$y_j = \cos \left[\frac{\pi(j-1)}{NY} \right] \quad (1 \leq j \leq NY+1) \quad (58)$$

where NX and NY are the number of computational cells in the x and y -direction, respectively. Then the first and second partial derivatives of a function $u(x, y)$, defined for $-1 \leq x \leq 1$ and $-1 \leq y \leq 1$, can be approximated by

$$\frac{\partial u}{\partial x}(x_i, y_j) = \sum_{l=1}^{NX+1} \widehat{\mathbf{G}\mathbf{X}}_{il}^{(1)} u(x_l, y_j) \quad (59)$$

$$\frac{\partial^2 u}{\partial x^2}(x_i, y_j) = \sum_{l=1}^{NX+1} \widehat{\mathbf{G}\mathbf{X}}_{il}^{(2)} u(x_l, y_j) \quad (60)$$

$$\frac{\partial u}{\partial y}(x_i, y_j) = \sum_{l=1}^{NY+1} \widehat{\mathbf{G}\mathbf{Y}}_{jl}^{(1)} u(x_i, y_l) \quad (61)$$

$$\frac{\partial^2 u}{\partial y^2}(x_i, y_j) = \sum_{l=1}^{NY+1} \widehat{\mathbf{G}\mathbf{Y}}_{jl}^{(2)} u(x_i, y_l) \quad (62)$$

The detailed expression for the matrices $\widehat{\mathbf{G}\mathbf{X}}^{(1)}$, $\widehat{\mathbf{G}\mathbf{X}}^{(2)}$, $\widehat{\mathbf{G}\mathbf{Y}}^{(1)}$, and $\widehat{\mathbf{G}\mathbf{Y}}^{(2)}$ are given in Ku et al. (1987). Numerical inversion of

large matrices arising in Eqs. (46), (48), (50), (52), (54), and (56) has been done by the tensor-product method.

5 Result

We examine the efficiency and accuracy of the present inverse analysis for estimating the spatially varying function of an unknown wall heat flux $f(x)$ at the bottom of the domain. Several test cases have been run with simulated measurements $T^{\dagger}(x_m(t))$, $y_m(t)$, and the estimated heat flux is compared with the exact one. The grid system adopted is (40×20) , which is found to be sufficient to resolve the flow and temperature fields when $d_x = 1$ cm, $d_y = 0.5$ cm, thermal diffusivity $\kappa = 2.06 \times 10^{-5}$ m²/s, thermal conductivity $k = 0.02575$ W/m · K, the measurement duration $t_f = 1.5$ and the Prandtl number $Pr = 0.72$. The dimensionless vertical distance of the sensor from the bottom wall, as given by y_m^{\dagger} in Eq. (14), is assumed to be 0.04775 if not specified otherwise. In the following, the accuracy of the estimation is quantified by the following definition of estimation error:

$$\text{Error} = \frac{\|f_{\text{estimated}} - f_{\text{exact}}\|_{L_2}^2}{\|f_{\text{exact}}\|_{L_2}^2} \quad (63)$$

where $\|\cdot\|_{L_2}$ is the usual L_2 -norm. The simulated measurements containing measurement errors are generated by adding random errors to the computed exact temperatures as follows:

$$T_{\text{measured}} (= T^{\dagger}) = T_{\text{exact}} + \omega \sigma \quad (64)$$

where σ determines the noise level, which takes values of 0.0, 0.1, 0.5, and ω is a random number between $-2.576 \leq \omega \leq 2.576$. In fact, σ is the standard deviation of the measurement errors which is assumed to be the same for all measurements, and ω is the Gaussian distributed random error. The above range of ω value corresponds to 99 percent confidence bound for the temperature measurement. Specifically, $\sigma = 0.1$ corresponds to about two percent relative measurement error and $\sigma = 0.5$ induces about ten percent relative measurement error.

To demonstrate the efficiency of a single moving sensor as compared to the fixed sensors for solving the inverse natural convection problem at hand, we first consider a heat flux function of arbitrary shape as depicted in Fig. 2. We try to estimate this function using a moving sensor and several fixed sensors, respectively, assuming there is no measurement error, i.e., $\sigma = 0$. The estimated heat flux function employing a single moving sensor with the sweeping frequency $\omega = 2$ (cf. Eq. (14)) is given in Fig. 3(a), while the estimated functions using 2, 5, and 11 fixed sensors are shown in Fig. 3(b), 3(c), and 3(d), respectively. In these figures, the location of the sensors and the estimation errors are also indicated. It is obvious that we need more than 11 fixed sensors to estimate with reasonable accuracy the heat flux function of Fig. 2, while a single moving sensor with $\omega = 2$ could estimate the heat flux profile very accurately.

Figures 4(a)~4(c) show some well-defined functions of heat flux $f(x)$ which are employed in the investigation of the present algorithm of inverse natural convection problem using a moving sensor. The equation of $f(x)$ for the three cases shown in Fig. 4 are as follows.

$$\text{(Case I)} \quad f(x) = 51.5x + 77.25 \quad (-1 \leq x \leq 0)$$

$$f(x) = -51.5x + 77.25 \quad (0 \leq x \leq 1) \quad (65)$$

$$\text{(Case II)} \quad f(x) = 20.6 \sin \pi x + 46.35 \quad (-1 \leq x \leq 1) \quad (66)$$

$$\text{(Case III)} \quad f(x) = 36.05 \quad (-1 \leq x < -0.5; 0.5 < x \leq 1)$$

$$f(x) = 72.1 \quad (-0.5 \leq x \leq 0.5) \quad (67)$$

When there is no measurement error, the convergence rate of the conjugate gradient procedure employing a single moving sensor with $\omega = 5.0$ is shown in Fig. 5 for the above three cases (Eqs.

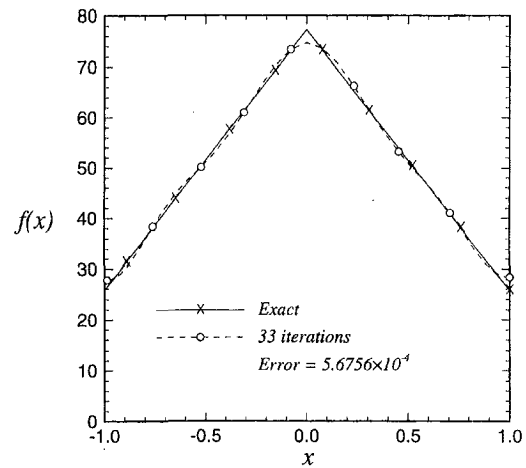


Fig. 8(a)

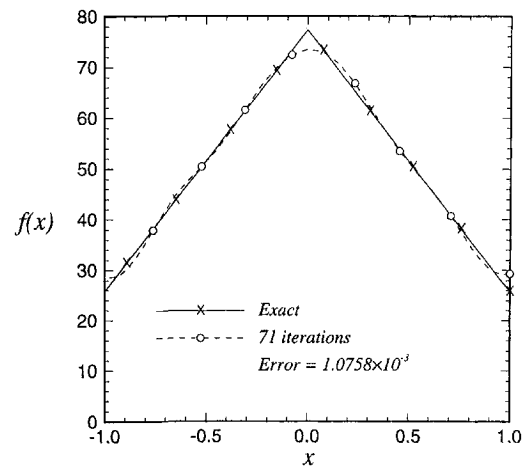


Fig. 8(b)

Fig. 8 The effect of vertical location of sensor, y_m^{\dagger} , on the accuracy of the estimated heat flux profiles; (a) the vertical distance (dimensionless) from the bottom wall is 0.0732; (b) the vertical distance (dimensionless) from the bottom wall is 0.1031

(65)~(67)). The resulting converged estimations of the heat flux function $f(x)$ for the above three cases are plotted in Fig. 6(a)~6(c). Figure 6(a) is the converged estimation of $f(x)$ for the case I after 56 iterations with the estimation error of 1.6995×10^{-4} . Figures 6(b) and 6(c) are the converged estimations for the case II and the case III, respectively, with the corresponding estimation errors of 2.4896×10^{-4} and 4.9069×10^{-3} .

The next consideration is the effect of the sweeping frequency of the moving sensor, ω , on the accuracy of the estimation. The heat flux function for the case I of Fig. 4 is estimated using a single moving sensor with $\omega = 0.5, 1.0, 2.0$, and 5.0 , respectively, when there is no measurement error. Figures 7(a)~7(d) are the resulting estimation with the corresponding estimation errors indicated. Generally, the estimation error decreases as the sweeping frequency ω increases. When ω is 0.5 (cf. Fig. 7(a)), the sensor moves starting from $x = 0$ to $x = 1$ and then returns to $x = 0$ for the duration of measurement t_f . Therefore, the left half of the domain, $-1 \leq x \leq 0$, is not scanned by the sensor and, as expected, the estimation of $f(x)$ for $-1 \leq x \leq 0$ is much less accurate than that for $0 \leq x \leq 1$. When ω value is larger than 1.0, the sensor scans the domain horizontally at least two times, and the estimation is quite accurate over the whole range (Fig. 7(b)~7(d)). If the sensor adopted has slow response time and causes troubles in temperature measurement, we can increase the dimensionless measurement duration t_f . The value of t_f is taken to be 1.5 to save the CPU time

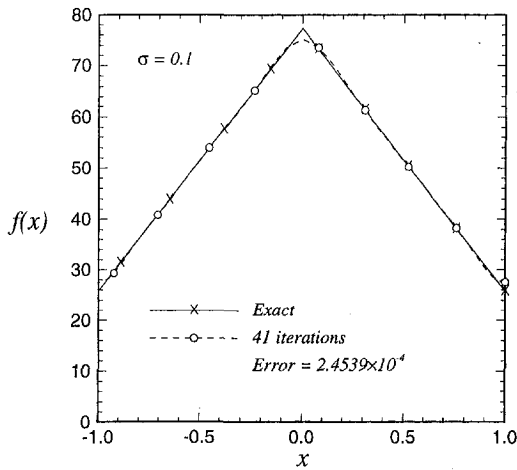


Fig. 9(a)

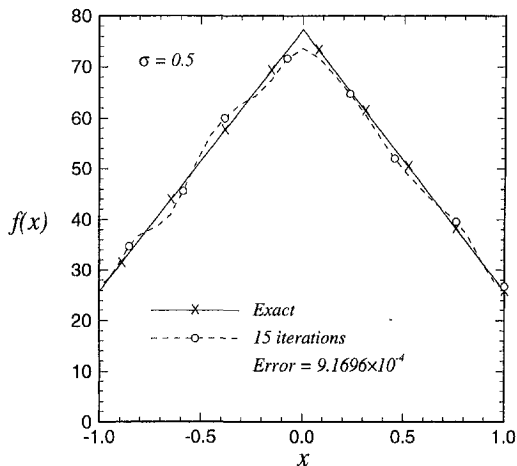


Fig. 9(b)

Fig. 9 The effect of noise level σ on the accuracy of the estimated heat flux function; (a) $\sigma = 0.1$, (b) $\sigma = 0.5$

of the numerical computation. If we increase t_f , not only the experimental measurement will become easier but also the numerical algorithm will yield better results.

Figures 8(a)~8(b) show the effect of vertical location of the moving sensor, y_m^+ , on the accuracy of the estimated heat flux profile for the case I, when there is no measurement error and the sweeping frequency $\omega = 5.0$. The default distance dimensionless has been 0.04775 (cf. Fig. 6(a)), and Fig. 8(a) is for the dimensionless distance of 0.0732 and Fig. 8(b) is for the dimensionless vertical distance of 0.1031. Comparing results of Figs. 8(a)~8(b) with that of Fig. 6(a) we find that as the vertical location of the moving sensor approaches the bottom wall where the heat flux is imposed, the accuracy improves, since the sensitivity of the temperature field with respect to the imposed wall heat flux increases as y_m^+ decreases.

Finally, the effect of noise level on the accuracy of the estimated heat flux function $f(x)$ is investigated. In all practical experimental situations it is expected that some errors will be induced into measurements. For the case of employing a moving sensor, the measurement error includes the uncertainty in sensor location as well. The following discrepancy principle is adopted as the stopping criterion of the iterative procedure of the conjugate gradient method when there are measurement errors (Alifanov, 1972; Huang et al., 1992). Assume the measurement errors be the same for all horizontal locations, i.e.,

$$T(x_m, y_m) - T^\dagger(x_m, y_m) \approx \sigma. \quad (68)$$

Introducing this result into Eq. (13), we find

$$J \approx \frac{1}{2} \int_0^{t_f} \sigma^2 dt = \frac{1}{2} \sigma^2 t_f. \quad (69)$$

Then the discrepancy principle for the stopping criterion is taken as

$$J < \epsilon^2. \quad (70)$$

If the functional J has a minimum value that is larger than ϵ^2 the following criterion is used to stop the iteration:

$$J(f^{(i+1)}) - J(f^{(i)}) < \epsilon_1 \quad (71)$$

where ϵ_1 is a prescribed small number. Figures 9(a)~9(b) show the estimated heat flux functions for the case I of Fig. 4 for various values of the noise level σ when $\omega = 5.0$. Comparing results of Figs. 9(a)~9(b) with that of Fig. 6(a) where there is no measurement error, it is revealed that accuracy of estimation deteriorates as the noise level increases.

6 Conclusion

The inverse natural convection problem of estimating wall heat flux from the temperature measurement within the flow is investigated by employing the conjugate gradient method. The gradient of the performance function needed in the conjugate gradient iteration is obtained by solving the adjoint equation. The conjugate gradient method, where the regularization is built in implicitly, could alleviate the ill-posedness symptoms of the inverse natural convection problems. One interesting facet of the present investigation is the employment of a single moving sensor instead of several fixed sensors to estimate the spatially varying heat flux $f(x)$. In certain situations the implementation of a moving sensor may be more difficult than the implementation of several fixed sensors, but for many other situations the employment of a single moving sensor is quite feasible and economical especially when using modern optical diagnostic techniques. The present method is found to solve the inverse natural convection problem accurately without a priori information about the unknown function to be estimated. The effects of sweeping frequency of the moving sensor, the vertical location of the moving sensor and the measurement noise level on the accuracy of the estimation are investigated.

Contrary to the previous works on inverse natural convection problems, the present method employs the exact Boussinesq equation without any simplifications, and therefore can be applied to many different problems of inverse natural convection to yield rigorous results.

References

- Alifanov, O. M., 1972, "Application of the Regularization Principle to the Formulation of Approximate Solution of Inverse Heat Conduction Problem," *J. Engng Phys.*, Vol. 23, pp. 1566-1571.
- Beck, J. V., and Arnold, K. J., 1977, *Parameter Estimation in Engineering and Science*, John Wiley and Sons, New York.
- Fletcher, R., and Reeves, R. M., 1964, "Function Minimization by Conjugate Gradients," *The Computer Journal*, Vol. 7, pp. 149-154.
- Huang, C. H., and Özisik, M. N., 1992, "Inverse Problem of Determining Unknown Wall Flux in Laminar Flow Through a Parallel Plate Duct," *Num. Heat Transfer, Part A*, Vol. 21, pp. 55-70.
- Jarny, Y., Özisik, M. N., and Bardon, J. P., 1991, "A General Optimization Method Using Adjoint Equation for Solving Multidimensional Inverse Heat Conduction," *Int. J. Heat Mass Transfer*, Vol. 34, pp. 2911-2919.
- Ku, H. C., Taylor, T. D., and Hirsh, R. S., 1987, "Pseudospectral Methods for Solution of the Incompressible Navier-Stokes Equations," *Computer & Fluids*, Vol. 15, pp. 195-214.
- Moutsoglou, A., 1989, "An Inverse Convection Problem," *ASME JOURNAL OF HEAT TRANSFER*, Vol. 221, pp. 37-43.
- Prud'homme, M., and Nguyen, T. H., 1997, "Whole Time-Domain Approach to the Inverse Natural Convection Problem," *Num. Heat Transfer, Part A*, Vol. 32, pp. 169-186.

Mixture Fraction Statistics of Plane Self-Preserving Buoyant Turbulent Adiabatic Wall Plumes

R. Sangras

Z. Dai

G. M. Faeth¹

e-mail: gmfaeth@umich.edu

Department of Aerospace Engineering,
The University of Michigan,
Ann Arbor, MI 48109-2140

Measurements of the mixture fraction properties of plane buoyant turbulent adiabatic wall plumes (adiabatic wall plumes) are described, emphasizing conditions far from the source where self-preserving behavior is approximated. The experiments involved helium/air mixtures rising along a smooth, plane and vertical wall. Mean and fluctuating mixture fractions were measured using laser-induced iodine fluorescence. Self-preserving behavior was observed 92–155 source widths above the source, yielding smaller normalized plume widths and near-wall mean mixture fractions than earlier measurements. Self-preserving adiabatic wall plumes mix slower than comparable free line plumes (which have 58 percent larger normalized widths) because the wall prevents mixing on one side and inhibits large-scale turbulent motion. Measurements of probability density functions, temporal power spectra, and temporal integral scales of mixture fraction fluctuations are also reported.

Introduction

Plane turbulent wall plumes are caused by line sources of buoyancy along the base of flat walls. These flows are of interest because they are a classical buoyant turbulent flow with numerous applications for confined natural convection processes and unwanted fires. Thus, the objective of the present investigation was to extend recent measurements of turbulent round and free line plumes (Dai and Faeth, 1996; Dai et al., 1994, 1995a, b; Sangras et al., 1998) to consider plane turbulent wall plumes using similar methods. Present observations were limited to turbulent wall plumes along smooth plane vertical surfaces for conditions where the streamwise buoyancy flux is conserved, which corresponds to flow along an adiabatic wall for a thermal plume.

Present measurements emphasize fully developed conditions far from the source where effects of source disturbances and momentum have been lost. Free line plumes become self-preserving at these conditions which simplifies reporting and interpreting measurements of their properties (Tennekes and Lumley, 1972). Adiabatic wall plumes never formally approach self-preserving behavior, however, because the streamwise growth rates of the near-wall boundary layer and the outer plume-like region are not the same. Nevertheless, the outer plume-like region grows more rapidly than the near-wall boundary layer and eventually dominates wall plumes far from the source, where wall plumes approximate self-preserving behavior with scaling similar to free line plumes (Grella and Faeth, 1975; Liburdy and Faeth, 1978). Thus, self-preserving behavior of adiabatic wall plumes was sought in this approximate sense during the present investigation.

Ellison and Turner (1959) and Turner (1973) describe some of the earliest studies of wall plumes, considering adiabatic wall plumes consisting of saline solutions in still water. The entrainment rates that they observed for wall plumes were much smaller than those observed for turbulent free line plumes by Rouse et al.

(1952) and Lee and Emmons (1961). This behavior was attributed to the wall both preventing mixing on one side and inhibiting the cross stream turbulent motion needed for effective mixing.

Grella and Faeth (1975) report hot-wire probe measurements of velocities and temperatures in weakly buoyant turbulent adiabatic wall plumes along smooth vertical surfaces. A linear array of small flames was used for the buoyant source; therefore, source dimensions are hard to define and plume buoyancy fluxes are difficult to quantify due to near-source heat losses. The measurements suggest that approximate self-preserving behavior was approached but could not be achieved due to the limited dynamic range of hot-wire probes. Ljuboja and Rodi (1981) subsequently predicted the properties of these flows using a turbulence model that included effects of buoyancy/turbulence interactions. The agreement between predictions and measurements was reasonably good for conditions farthest from the source which best approached approximate self-preserving behavior.

Lai et al. (1986) and Lai and Faeth (1987) reported laser velocimetry (LV) and laser-induced fluorescence (LIF) measurements of mean and fluctuating velocities and concentrations in weakly buoyant adiabatic wall plumes. Gas mixtures leaving a slot provided the buoyancy source so that uncertainties of source sizes and heat losses were absent and source dimensions and buoyancy fluxes were well defined. These measurements were used to evaluate predictions based on simplified mixing length and turbulence models, finding good predictions of mean properties but relatively ineffective predictions of turbulence properties. These measurements were limited to flow development at near-source conditions, $0 \leq (x - x_o)/b \leq 37.5$, so that self-preserving behavior was not achieved. This behavior is consistent with recent measurements of turbulent free line plumes where self-preserving behavior was only observed for $(x - x_o)/b > 76$ (Sangras et al., 1998).

In addition to large values of $(x - x_o)/b$ to avoid effects of source disturbances, approximate self-preserving behavior also requires large values of $(x - x_o)/l_M$ to avoid effects of source momentum (Turner, 1973). Noting that plume behavior dominates adiabatic wall plumes at self-preserving conditions, l_M can be defined by analogy to free line plumes having uniform source properties, as follows (List, 1982):

$$l_M/b = (\rho_o/\rho_\infty)u_o^2/(bu_o g|\rho_o - \rho_\infty|/\rho_\infty)^{2/3} \quad (1)$$

¹ To whom correspondence should be addressed.

Contributed by the Heat Transfer Division for publication in the JOURNAL OF HEAT TRANSFER and presented at the 1999 ASME/JSME Joint Thermal Engineering Conference, San Diego. Manuscript received by the Heat Transfer Division, Sept. 8, 1998; revision received, May 21, 1999. Keywords: Heat Transfer, Natural Convection, Nonintrusive Diagnostics, Plumes, Turbulence. Associate Technical Editor: R. Dougllass.

where the absolute value of the initial density difference is used to account for both rising and falling plumes. A related parameter used to characterize source momentum properties is the source Froude number, Fr_o , defined for adiabatic wall plumes by analogy to free line plumes, as follows:

$$Fr_o^2 = \rho_o u_o^2 / (2bg|\rho_\infty - \rho_o|). \quad (2)$$

Using these parameters, the measurements of Lai et al. (1986) and Lai and Faeth (1987) were limited to $(x - x_o)/l_M \leq 5$ which is small compared to the values on the order of 10 required for buoyancy-dominated self-preserving behavior for free line plumes (Sangras et al., 1998).

In view of these observations, the objective of the present investigation was to measure the mean and fluctuating scalar properties of adiabatic wall plumes, emphasizing conditions within the approximate self-preserving region far from the source. The experiments consisted of helium/air source flows, along a smooth plane and vertical wall in still air at standard temperature and pressure, which provides straightforward specifications of source dimensions and plume buoyancy fluxes. Scalar properties were characterized by mixture fractions, defined as the mass fraction of source gas in a sample (Sangras et al., 1998). Measurements of mixture fractions were carried out using iodine vapor LIF in order to provide the large dynamic range needed to reach approximate self-preserving conditions.

Experimental Methods

Apparatus. Experimental methods were similar to the free line plume study of Sangras et al. (1998). The plumes were observed in an enclosure (3400 × 2000 × 3600 mm high) that had porous side walls (parallel to the source) and a porous ceiling made of filter material. This approach controlled room disturbances and ambient light leakage into the test enclosure while allowing free inflow of entrained air and free exhaust of the plume. The source slot (876 mm long × 9.4 mm wide) was mounted flush to a flat floor (876 mm long × 610 mm wide) with the vertical wall mounted adjacent to one edge of the slot. The floor/slot/wall assembly was mounted in turn normal to end walls (2440 mm high × 610 mm wide). A screen array (2 screens, 16 mesh × 0.20 mm wire diameter, separated by a distance of 38 mm) was installed across the outer edge of the end walls (facing the vertical wall) to

further control room disturbances, following Gutmark and Wygnanski (1976), Sangras et al. (1998) and references cited therein. The entire floor/slot/wall assembly was traversed to accommodate rigid optical instruments in the same manner as Sangras et al. (1998).

Gas supplies to the source were metered and measured using critical flow orifices in conjunction with pressure regulators. These flow rates were calibrated using either wet test or turbine flow meters. After mixing, the source flows passed through beds of iodine flakes and feed lines having length-to-diameter ratios of 1200 to ensure uniformly seeded mixtures. Uniform source flow properties were provided by a bed of beads, a filter and a 3.4:1 contraction at the slot exit.

Instrumentation. The LIF signal was produced by an argon-ion laser operating at 514.5 nm (measuring volume diameter at e^{-2} points of 0.16 mm with a maximum optical power of 1800 mW). The laser beam was horizontal and directed normal to the wall. The beam passed through an opening in the wall and was captured by a horn trap. Laser power was monitored to correct for power fluctuations. Absorption of the laser beam in the flow was less than one percent, and was even smaller for fluorescence emissions, so that it was not necessary to account for effects of absorption when data was processed.

LIF observations were made through windows (457 mm wide × 203 mm high) mounted flush to the inner surface of the end walls and centered on the laser beam height. Collecting optics were f5.1 with a diameter of 100 mm. The LIF signal was separated from light scattered at the laser line using long-pass optical filters having a cutoff wavelength of 530 nm. The detector aperture provided a measuring volume length of 2 mm. Signal detection, processing, and calibration were the same as Sangras et al. (1998).

Effects of differential diffusion of helium and iodine vapor were small, less than 0.1 percent, based on binary diffusivity estimates from Bird et al. (1960) and the analysis of Stárner and Bilger (1983). Gradient broadening errors were also small, less than one percent. Experimental uncertainties (95 percent confidence) were found following Moffat (1982) as discussed by Sangras et al. (1998), yielding maximum experimental uncertainties of the flow properties, as follows: 6 percent for $F(y/(x - x_o))$, 10 percent for $F'(y/(x - x_o))$, 10 percent for PDF(f), 40 percent for the low-frequency region of $E_f(n)/(\tau_f f'^2)$, and 35 percent for $B_o^{1/3} \tau_f$

Nomenclature

b = source width	n = frequency	z = normalized distance parallel to slot source, measured from its midplane location
B_o = source buoyancy flux	PDF(f) = probability density function of mixture fraction	Z = source length
d = source diameter	Re_c = characteristic plume Reynolds number, Eq. (9)	ν = kinematic viscosity
$E_f(n)$ = temporal power spectral density of f	Re_o = source Reynolds number, $2\bar{u}_o b / \nu_o$	ρ = density
f = mixture fraction	u = streamwise velocity	τ_f = temporal integral scale of mixture fraction fluctuations
$F(y/(x - x_o))$ = normalized self-preserving cross stream distribution of \bar{f}	$U(y/(x - x_o))$ = normalized self-preserving cross stream distribution of \bar{u}	
$F'(y/(x - x_o))$ = normalized self-preserving cross stream distributions of \bar{f}'	x = vertical streamwise distance above source	Subscripts
Fr_o = source Froude number, Eq. (2)	y = cross stream distance normal to wall surface	max = condition where the property reaches a maximum value
g = acceleration of gravity		o = initial value or virtual origin location
l_f = characteristic plume width based on \bar{f} , Eq. (5)		∞ = ambient value
l_M = Morton length scale, Eq. (1)		Superscripts
l_u = characteristic plume width based on \bar{u} , Eq. (8)		$(\bar{\quad})$ = time-averaged mean value
		$(\overline{\quad})'$ = root-mean-squared fluctuating value

Table 1 Summary of plane buoyant turbulent adiabatic wall plume test conditions^a

Source properties	Case 1	Case 2
Helium concentration (percent by volume)	29.0	52.3
Density (kg/m ³)	0.871	0.639
Kinematic viscosity (mm ² /s)	22.1	31.3
Average velocity (mm/s)	868	1240
Buoyancy flux, B_o (m ³ /s ²)	0.0200	0.0514
Density ratio, ρ_o/ρ_∞	0.750	0.550
Reynolds number, Re_o	740	745
Froude number, Fr_o	3.50	3.20
Morton length scale, l_M/b	7.7	6.1

^a Helium/air sources directed vertically upward at the base of a vertical smooth plane wall in still air with an ambient pressure of 99 ± 0.5 kPa and temperature of 297 ± 0.5 K. Pure gas properties as follows: air density of 1.161 kg/m³, air kinematic viscosity of 15.9 mm²/s, helium density of 0.163 kg/m³, and helium kinematic viscosity of 122.5 mm²/s. Source slot width and length of 9.4 and 876 mm. Virtual origin based on \bar{f} of $x_o/b = 0$ determined from present measurements in the range $(x - x_o)/b = 92-155$ and $(x - x_o)/l_M = 12-21$.

$(x - x_o)$. These uncertainties were maintained down to half the maximum value of each measured parameter (excluding the spike region of the PDF) but increased at smaller values roughly inversely proportional to the value of the parameter.

Test Conditions. The test conditions are summarized in Table 1. Two source flows were considered in order to test scaling of source properties in the region of self-preserving behavior. Approximate self-preserving behavior for adiabatic wall plumes was only observed relatively far from the source at $(x - x_o)/b \geq 92$; therefore, the locations of the virtual origin could not be distinguished from $x_o/b = 0$ within present experimental uncertainties.

Self-Preserving Scaling

The state relationship for density as a function of mixture fraction, assuming an ideal gas mixture, can be found in Dai et al. (1994). Far from the source where the flow becomes self-preserving, this expression can be approximated as follows:

$$\rho = \rho_\infty + f\rho_o(1 - \rho_\infty/\rho_o), f \ll 1. \quad (3)$$

Assuming approximate self-preserving behavior for adiabatic wall plumes, in the sense discussed earlier, mean and fluctuating mixture fractions can be scaled in terms of self-preserving variables, as follows (List, 1982):

$$F(y/(x - x_o)) \quad \text{or} \quad F'(y/(x - x_o)) \\ = (\bar{f} \text{ or } \bar{f}')gB_o^{-2/3}(x - x_o)|1 - \rho_\infty/\rho_o| \quad (4)$$

where $F(y/(x - x_o))$ and $F'(y/(x - x_o))$ are appropriately scaled cross stream profile functions of mean and fluctuating mixture fractions, which approximate universal functions far from the source where Eq. (3) applies. A characteristic plume width, l_f , based on \bar{f} is also defined, similar to turbulent free line plumes, as follows (Dai et al., 1994):

$$F(l_f/(x - x_o))/F(0) = e^{-1}. \quad (5)$$

For plane turbulent adiabatic wall plumes, F decreases monotonically as y increases and there is only one location where Eq. (5) is satisfied. The source buoyancy flux, B_o , is a conserved scalar of the flow which can be found as follows for plane plumes having uniform source properties (List, 1982):

$$B_o = bu_o g|\rho_o - \rho_\infty|/\rho_\infty. \quad (6)$$

The corresponding approximate self-preserving relationship for mean streamwise velocities was not studied here but these properties are useful for defining the turbulence properties of the wall plumes. Thus, mean streamwise velocities within approximate

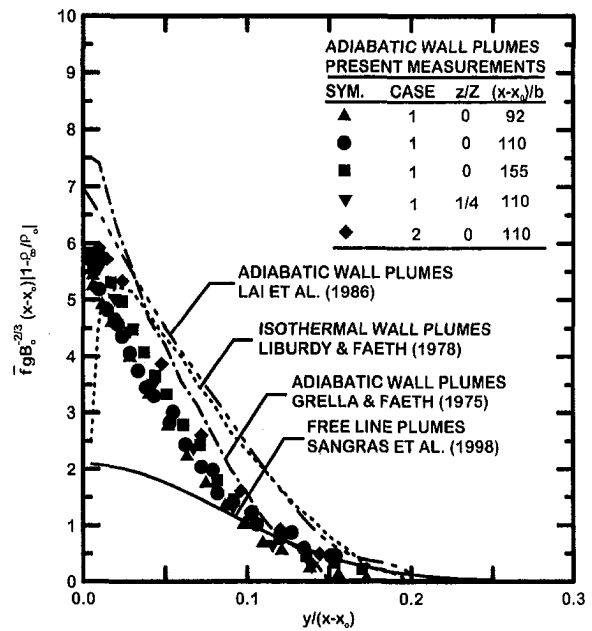


Fig. 1 Cross stream distributions of mean mixture fractions in plane buoyant turbulent plumes. Measurements of Grella and Faeth (1975), Lai and Faeth (1987), and the present investigation for adiabatic wall plumes; measurements of Liburdy and Faeth (1978) for isothermal wall plumes; and measurements of Sangras et al. (1998) for free line plumes. Results from Grella and Faeth (1975), Liburdy and Faeth (1978), and Lai and Faeth (1987) are for their largest distances from the source.

self-preserving turbulent adiabatic wall plumes can be scaled in terms of self-preserving variables, as follows (List, 1982):

$$U(y/(x - x_o)) = \bar{u}/B_o^{1/3} \quad (7)$$

where $U(y/(x - x_o))$ is an appropriately scaled cross stream profile function. A characteristic plume width based on \bar{u} , l_u , is also defined, similar to turbulent free line plumes, as follows (Dai et al., 1995a):

$$U(l_u/(x - x_o))/U_{max} = e^{-1} \quad (8)$$

where l_u is the largest value of cross stream distance where Eq. (8) is satisfied, noting that U is a double-valued function of y . The corresponding characteristic plume Reynolds number can be written as follows for approximate self-preserving conditions (Sangras et al., 1998):

$$Re_c = \bar{u}_{max} l_u / \nu_\infty = U_{max} B_o^{1/3} l_u / \nu_\infty. \quad (9)$$

For present purposes, values of U_{max} and l_u were taken as averages of the measurements farthest from the source reported by Grella and Faeth (1975).

Results and Discussion

Mean Mixture Fractions. Distributions of mean mixture fractions in the approximate self-preserving region of the flow will be considered first. Present measurements of cross stream distributions of mean mixture fractions for the two sources are illustrated in Fig. 1. The scaling parameters of Eq. (4) have been used when plotting the figure so that the value of the ordinate is $F(y/(x - x_o))$. Results for $z/Z = 0$ and $1/4$ (where z is measured from a position halfway between the end walls), are in good agreement with each other which confirms the two-dimensionality of the flow. The present measurements also yield universal distributions within experimental uncertainties for $92 \leq (x - x_o)/b \leq 155$ and $12 \leq (x - x_o)/l_M \leq 21$ with flow aspect ratios of $Z/l_f \geq 7.9$, as required for self-preserving flow. Present conditions within the self-preserving region of the flow correspond to $3800 \leq$

Table 2 Development of plane turbulent adiabatic wall plumes^a

Source	$(x - x_o)/b$	$l_f/(x - x_o)$
Lai et al. (1986)	10.0	0.173
	20.0	0.118
	37.5	0.093
Present (self-preserving region)	92–155	0.076

^a Plane turbulent adiabatic wall plumes in still and unstratified environments.

$Re_c \leq 6700$ which is comparable to conditions within the self-preserving region of round and plane free turbulent plumes of $2500 \leq Re_c \leq 7500$ observed by Dai et al. (1994, 1995a,b) and Sangras et al. (1998). These are reasonably large values of characteristic Reynolds numbers for turbulent plume-like flows. For example, this range is comparable to the largest values of Re_c where measurements of turbulent wake properties have been reported, while turbulent wakes exhibit self-preserving turbulence properties at values of Re_c as small as 70 (Wu and Faeth, 1993).

Measurements of F for a variety of plane turbulent plumes have been plotted in Fig. 1 for comparison with the present measurements, as follows: results for adiabatic wall plumes from Grella and Faeth (1975) and Lai and Faeth (1987), results for isothermal wall plumes from Liburdy and Faeth (1978), and results for free line plumes from Sangras et al. (1998). The measurements of Grella and Faeth (1975), Lai and Faeth (1987), and Liburdy and Faeth (1978) all exhibit streamwise variations of mean mixture fractions scaled for approximate self-preserving behavior; thus, the distributions plotted in Fig. 1 for these measurements are for conditions farthest from the source. The remaining results from Sangras et al. (1998) and the present study represent scaled mean mixture fractions averaged over the self-preserving portions of the plumes.

Considering the three adiabatic wall plume results in Fig. 1, it is evident that the measurements of Lai and Faeth (1987) are considerably broader than the present results (22 percent broader at the e^{-1} points of the distributions) and that the values of F for both Grella and Faeth (1975), and Lai and Faeth (1987) are considerably larger than the present results near the wall (up to 31 percent larger). The larger scaled widths of the mean mixture fraction distributions of the earlier adiabatic wall plumes are typical of conditions in the developing plume region before self-preserving behavior is achieved. Developing flow was especially evident for the measurements of Lai and Faeth (1987) which were limited to $(x - x_o)/b \leq 37.5$ while self-preserving behavior was only observed much farther from the source $(x - x_o)/b \geq 92$, during the present investigation. This behavior is illustrated by the values of $l_f/(x - x_o)$ summarized in Table 2 for the measurements of Lai et al. (1986) and the present investigation. The progressive reduction of $l_f/(x - x_o)$ with increasing distance from the source, tending toward the value observed during the present investigation, is quite evident. The corresponding streamwise locations of the measurements of Grella and Faeth (1975) cannot be stated in terms of $(x - x_o)/b$ because their source dimensions are not well defined; nevertheless, it is encouraging that the characteristic width of these measurements at the largest distance from the source is in good agreement with the present measurements.

Differences between the magnitudes of the scaled mean mixture fraction measurements of Grella and Faeth (1975) and the present investigation can be attributed to problems of specifying the buoyancy flux, B_o , for the measurements of Grella and Faeth (1975). In particular, B_o was accurately prescribed by the gas mixture at the source exit for the present study but B_o had to be obtained from measurements of plume velocity and temperature properties for the study of Grella and Faeth (1975) due to the difficulties of determining energy losses from thermal plumes near the source. This approach introduces significant uncertainties in B_o , particularly because a significant portion of B_o is transported by streamwise

turbulent motion, e.g., Dai et al. (1995b) and George et al. (1977) find that streamwise turbulent transport contributes 15–16 percent of B_o for round buoyant turbulent plumes with similar levels anticipated for plane turbulent plumes. The streamwise transport contribution to B_o was not measured by Grella and Faeth (1975) and had to be ignored so that the corresponding underestimation of B_o tends to increase values of F compared to present results as seen in Fig. 1.

The comparison between the distributions of F for adiabatic wall plumes and free line plumes, plotted in Fig. 1, is also of interest. Both sets of results represent self-preserving behavior and have the same buoyancy flux. Comparing the two flows, it is evident that the adiabatic wall plumes spread much slower than the free line plumes. For example, the characteristic widths, l_f , are 58 percent larger for the free line plumes than for the adiabatic wall plumes whereas the maximum scaled mean mixture fraction, $F(0)$, is 2.7 times larger for adiabatic wall plumes than for the free line plumes. This behavior has unfortunate implications for the environment of unwanted fires within structures where the reduced mixing rates of fire plumes along surfaces allow heated regions to extend much farther from the source than would be the case for unconfined fires; this behavior tends to enhance fire spread rates. These effects also tend to reduce dilution rates of pollutants and other hazardous substances within buoyant flows along surfaces compared to unconfined buoyant flows.

Reduced rates of mixing of adiabatic wall plumes compared to free line plumes can be attributed to reduced access to the ambient environment, the direct effects of wall friction and inhibition of turbulent mixing by the presence of the wall. The reduced access to the ambient environment comes about because adiabatic wall plumes can only mix on one side while free line plumes can mix on both sides. This effect might be expected to increase the maximum scaled mean mixture fraction, $F(0)$, by a factor of 2; instead, $F(0)$ increases even more, by a factor of 2.7, which suggests that other effects are influencing mixing rates as well. The direct effect of wall friction, however, does not explain any significant tendency to retard mixing rates for adiabatic wall plumes. For example, earlier studies of adiabatic wall plumes show the direct effects of wall friction on plume structure are small because the wall boundary layer is much thinner than the outer plume-like region as self-preserving conditions are approached (Grella and Faeth, 1975; Lai et al., 1986; Lai and Faeth, 1987). Thus, the presence of the wall must reduce mixing in its own right, probably by inhibiting cross stream turbulent motion at the largest scales that significantly contribute to the mixing of free line plumes.

Results for isothermal wall plumes due to Liburdy and Faeth (1978) plotted in Fig. 1 also support the idea that the main functions of the wall are to limit mixing to just one side of the plume and to inhibit turbulent motion at the largest scales which tends to reduce mixing rates. In particular, Liburdy and Faeth (1978) find little effect of direct transport to the wall on reducing values of F as self-preserving conditions are approached (although wall heat losses near the source are very important for these thermal plumes). On the other hand, wall heat losses shift the maximum value of F away from the wall, tending to increase the thickness of the flow. This increased thickness accommodates larger scales of turbulence which increases mixing rates as evidenced by the smaller F_{max} for isothermal wall plumes than for adiabatic wall plumes.

The differences between the various flows plotted in Fig. 1 are quantified in Table 3, where the aspect ratio of the slot, Z/b , the range of streamwise distances studied $(x - x_o)/b$, the smallest flow aspect ratios, $(Z/l_f)_{min}$, the streamwise distance in terms of Morton length scale, $(x - x_o)/l_M$, and the corresponding values of $l_f/(x - x_o)$, F_{max} and $\bar{f}'_{max}/\bar{f}'_{max}$ are summarized to the extent they are known for adiabatic wall plumes, isothermal wall plumes, and free line plumes. Earlier results for wall plumes exhibit some evolution of F with distance from the source over the range of the measurements; therefore, only findings farthest from the source are shown in the table in these cases. The measurements of Grella and

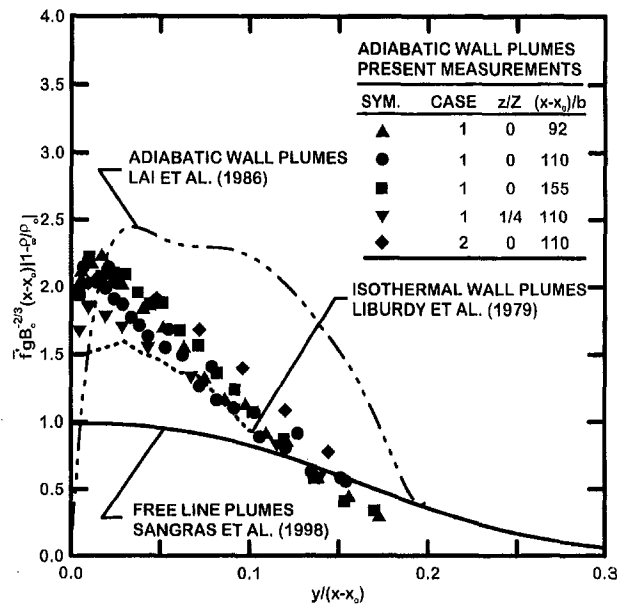


Fig. 2 Cross stream distributions of rms mixture fraction fluctuations in plane buoyant turbulent plumes. Measurements of Lai and Faeth (1987) and the present investigation for adiabatic wall plumes; measurements of Liburdy and Faeth (1978) for isothermal wall plumes; and measurements of Sangras et al. (1998) for free line plumes. Results from Liburdy and Faeth (1978) and Lai and Faeth (1987) are for their largest distances from the source.

Faeth (1975), Liburdy and Faeth (1978) and Liburdy et al. (1979) employed linear arrays of small flames as thermal sources for the plumes so that source dimensions cannot be prescribed for these results. Variations of flow widths and values of F between the various flows have already been discussed in connection with Fig. 1; the properties of mixture fraction fluctuations will be taken up next.

Mixture Fraction Fluctuations. Measurements of cross stream distributions of mixture fraction fluctuations are plotted in Fig. 2. In addition to the present measurements for the same conditions as \bar{f} in Fig. 1, other measurements have been plotted in the figure, as follows: adiabatic wall plumes from Lai and Faeth (1987), isothermal wall plumes from Liburdy and Faeth (1978), and free line plumes from Sangras et al. (1998). As before, the measurements of Lai and Faeth (1987) and Liburdy and Faeth (1978) do not extend to fully self-preserving conditions so that only their results farthest from the source are shown. The remaining results from Sangras et al. (1998) and the present study represent scaled mixture fraction fluctuations in the self-preserving portions of the flow.

Present measurements of F' exhibit self-preserving behavior within experimental uncertainties over the test range. F' becomes small as the wall and the free stream are approached and reaches a maximum near $y/(x-x_0) = 0.02$. The values of \bar{f}' are actually larger for adiabatic wall plumes near this maximum than the values observed in free line plumes at similar conditions because the values of \bar{f} in this region are larger for adiabatic wall plumes than for free line plumes. The values of mixture fraction fluctuation intensities near the maximum \bar{f} condition, however, are actually smaller for adiabatic wall plumes than for free line plumes, e.g., 37 percent as opposed to 47 percent, see Table 3, which is consistent with the wall stabilizing large-scale turbulent motion, and thus turbulent mixing. The adiabatic wall plume results of Lai and Faeth (1987) are similar to present results in terms of magnitudes, e.g., the values of $\bar{f}'_{max}/\bar{f}'_{min}$ for the two studies are 34 and 37 percent, respectively. The distribution of F' is considerably broader for the measurements of Lai and Faeth (1987) than the present study, however, which follows because self-preserving

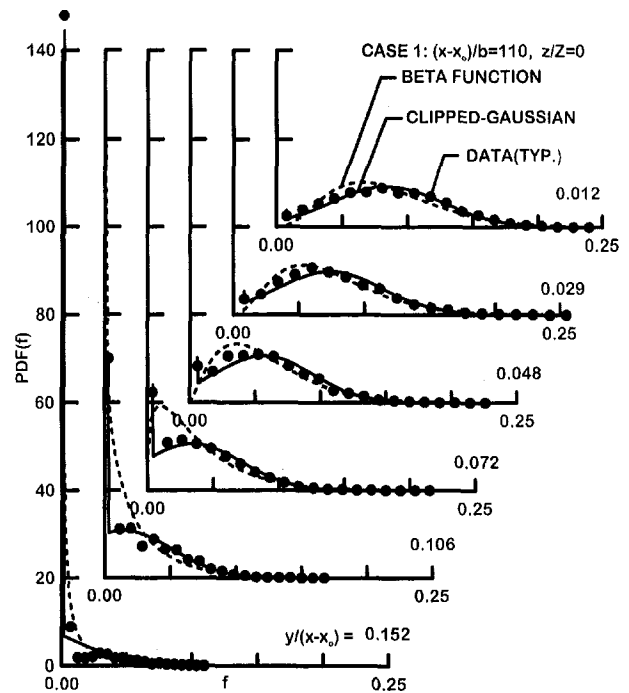


Fig. 3 Typical probability density functions in plane self-preserving buoyant turbulent adiabatic wall plumes: Case 1 flow at $(x-x_0)/b = 110$

conditions were not reached, as noted earlier. The measurements of Liburdy et al. (1979) for isothermal wall plumes are considerably smaller than the other wall plumes for reasons that have yet to be explained; values of $\bar{f}'_{max}/\bar{f}'_{min}$ for this flow are also lower than for all the other plumes, e.g., 25 percent, see Table 3.

Probability Density Functions. The measured PDF(f) are illustrated in Fig. 3 for self-preserving adiabatic wall plumes. These results are for the Case 1 source at various cross stream distances and $(x-x_0)/b = 110$ but results at other self-preserving conditions were similar. The measurements are compared with predictions of clipped-Gaussian and beta function distributions which frequently are used to represent PDF(f) for modeling purposes (Lockwood and Naguib, 1975). These distributions are prescribed by the values of f and f' at each position.

The PDF(f) illustrated in Fig. 3 exhibit progressively increasing spikes at $f = 0$ as $y/(x-x_0)$ increases, representative of increasing time periods spent in ambient fluid as the outer edge of the flow is approached. Both distributions provide a reasonably good representation of the measured PDF's. All these properties are similar to earlier findings for free line plumes (Sangras et al., 1998).

Temporal Power Spectral Densities. Typical temporal power spectra are illustrated in Fig. 4 for self-preserving adiabatic wall plumes. These results are for $92 \leq (x-x_0)/b \leq 155$ with the Case 1 plume but results for other self-preserving conditions are similar. These measurements are normalized by local turbulence properties as described by Hinze (1975).

These spectra are qualitatively similar to earlier results for round plumes reported by Dai et al. (1994) and for free line plumes reported by Sangras et al. (1998). The normalized spectra are relatively independent of cross stream position at each streamwise location. The spectra exhibit a prominent $-5/3$ power decay in an inertial-convective subrange for scalar property fluctuations where effects of molecular diffusion are small (Tennekes and Lumley, 1972) followed by a prominent -3 power decay in an inertial-diffusion subrange for scalar property fluctuations where effects of molecular diffusion are significant (Papanicolaou and List, 1987). The latter region is not observed in nonbuoyant flows and represents an important buoyancy/turbulence interaction.

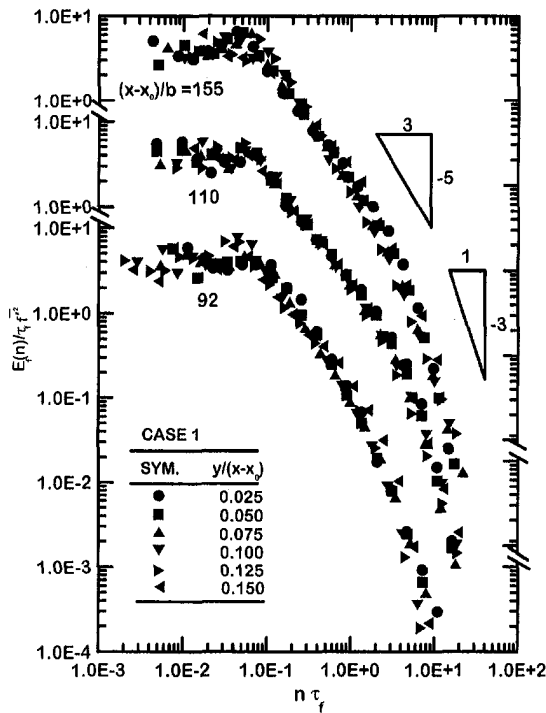


Fig. 4 Typical temporal power spectral densities of mixture fraction fluctuations in plane self-preserving buoyant turbulent adiabatic wall plumes: Case 1 flow at $(x - x_o)/b = 92, 110,$ and 155

Temporal Integral Scales. The properties of the temporal power spectra are completed by temporal integral scales, which are plotted as a function of cross stream distance in Fig. 5. These measurements are limited to the case 1 source for $92 \leq (x - x_o)/b \leq 155$, however, results at other self-preserving conditions are similar. The correlation for the temporal integral scales of self-preserving free line plumes from Sangras et al. (1998) is also shown in the plot for comparison with the present results. The present results provide a scattered correlation when plotted in the manner of Fig. 5; nevertheless, these results agree with the free line plume results within experimental uncertainties in spite of increased width of free line plumes. The shape of the plot generally agrees with expectations for temporal integral scales based on Taylor's hypothesis, as discussed by Sangras et al. (1998).

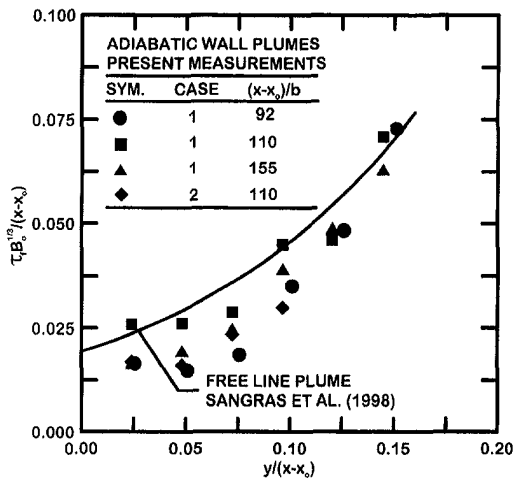


Fig. 5 Cross stream distributions of temporal integral scales of mixture fraction fluctuations in plane self-preserving buoyant turbulent plumes. Measurements of the present investigation for adiabatic wall plumes; measurements of Sangras et al. (1998) for free line plumes.

Conclusions

Mixture fraction statistics were measured in plane turbulent adiabatic wall plumes rising along flat smooth vertical walls in still air. Conditions far from the source were emphasized where effects of source disturbances are lost and the outer plume-like region of the flow approximates self-preserving behavior with scaling similar to self-preserving free line plumes. The test conditions consisted of buoyant jet sources of helium and air to obtain the source properties summarized in Table 1 with measurements involving $(x - x_o)/b$ in the range 92–155 and $(x - x_o)/l_M$ in the range 12–21. The major conclusions of the study are as follows:

1 The present measurements yielded distributions of mean mixture fractions that approximated self-preserving behavior in the outer plume-like region of the flow for $(x - x_o)/b \geq 92$. In this region distributions of mean mixture fractions were up to 22 percent narrower, with scaled values at the wall up to 31 percent smaller than earlier results using buoyant jet sources in the literature. These differences were caused by past difficulties in achieving adequate distances from the source to reach self-preserving conditions and accurately determining the value of the buoyancy flux needed to scale self-preserving properties during the earlier studies.

2 Self-preserving turbulent adiabatic wall plumes mix much slower than comparable free line plumes with characteristic plume widths 58 percent larger and scaled maximum mean mixture fractions 2.7 times smaller for free line plumes than for comparable adiabatic wall plumes mainly because the wall limits mixing to one side of the flow and inhibits the large-scale turbulent motion that is mainly responsible for mixing.

3 Cross stream distributions of mixture fraction fluctuations exhibit reduced values near the wall as expected. The stabilizing effect of the wall also reduces maximum mean mixture fraction fluctuation intensities in self-preserving plane turbulent adiabatic wall plumes compared to corresponding turbulent free line plumes, e.g., the maximum intensities for the two flows are 37 and 47 percent, respectively.

4 The probability density functions of mixture fractions in self-preserving adiabatic wall plumes are approximated reasonably well by either clipped Gaussian or beta function distributions similar to corresponding free line plumes.

5 The low-frequency portion of the spectra of mixture fraction fluctuations scale in a relatively universal manner while the spectra exhibit $-5/3$ power inertial-convective and -3 power inertial-diffusive decay regions. This behavior is typical of other turbulent plumes with the prominent -3 power inertial-diffusive decay region being a characteristic of buoyant flows that is not seen in nonbuoyant flows.

6 Temporal integral scales could be correlated in a relatively universal manner in terms of self-preserving parameters, with results for adiabatic wall plumes in qualitative agreement with the behavior of corresponding free line plumes.

Acknowledgments

This research was supported by the United States Department of Commerce, National Institute of Standards and Technology, Grant No. 60NANB4D1696, with H. R. Baum of the Building and Fire Research Laboratory serving as Scientific Officer.

References

- Bird, R. B., Stewart, W. E., and Lightfoot, E. N., 1960, *Transport Phenomena*, John Wiley and Sons, New York, pp. 502–513.
- Dai, Z., and Faeth, G. M., 1996, "Measurements of the Structure of Self-Preserving Round Buoyant Turbulent Plumes," *ASME JOURNAL OF HEAT TRANSFER*, Vol. 118, pp. 493–495.
- Dai, Z., Tseng, L.-K., and Faeth, G. M., 1994, "Structure of Round, Fully-Developed, Buoyant Turbulent Plumes," *ASME JOURNAL OF HEAT TRANSFER*, Vol. 116, pp. 409–417.
- Dai, Z., Tseng, L.-K., and Faeth, G. M., 1995a, "Velocity Statistics of Round, Fully-Developed Buoyant Turbulent Plumes," *ASME JOURNAL OF HEAT TRANSFER*, Vol. 117, pp. 138–145.

- Dai, Z., Tseng, L.-K., and Faeth, G. M., 1995b, "Velocity/Mixture-Fraction Statistics of Round, Self-Preserving Buoyant Turbulent Plumes," *ASME JOURNAL OF HEAT TRANSFER*, Vol. 117, pp. 918-926.
- Ellison, T. H., and Turner, J. S., 1959, "Turbulent Entrainment in Stratified Flows," *J. Fluid Mech.*, Vol. 6, pp. 423-448.
- George, W. K., Jr., Alpert, R. L., and Tamanini, F., 1977, "Turbulence Measurements in an Axisymmetric Buoyant Plume," *Int. J. Heat Mass Transfer*, Vol. 20, pp. 1145-1154.
- Grella, J. J., and Faeth, G. M., 1975, "Measurements in a Two-Dimensional Thermal Plume Along a Vertical Adiabatic Wall," *J. Fluid Mech.*, Vol. 71, pp. 701-710.
- Gutmark, E., and Wygnanski, I., 1976, "The Plane Turbulent Jet," *J. Fluid Mech.*, Vol. 73, pp. 465-495.
- Hinze, J. O., 1975, *Turbulence*, 2nd Ed., McGraw-Hill, New York, pp. 175-319.
- Lai, M.-C., and Faeth, G. M., 1987, "Turbulence Structure of Vertical Adiabatic Wall Plumes," *ASME JOURNAL OF HEAT TRANSFER*, Vol. 109, pp. 663-670.
- Lai, M.-C., Jeng, S.-M., and Faeth, G. M., 1986, "Structure of Turbulent Adiabatic Wall Plumes," *ASME JOURNAL OF HEAT TRANSFER*, Vol. 108, pp. 827-834.
- Lee, S. L., and Emmons, H. W., 1961, "A Study of Natural Convection Above a Line Fire," *J. Fluid Mech.*, Vol. 11, pp. 353-368.
- Liburdy, J. A., and Faeth, G. M., 1978, "Heat Transfer and Mean Structure of a Turbulent Thermal Plume Along Vertical Isothermal Walls," *ASME JOURNAL OF HEAT TRANSFER*, Vol. 100, pp. 177-183.
- Liburdy, J. A., Groff, E. G., and Faeth, G. M., 1979, "Structure of a Turbulent Thermal Plume Rising Along an Isothermal Wall," *ASME JOURNAL OF HEAT TRANSFER*, Vol. 101, pp. 299-355.
- List, E. J., 1982, "Turbulent Jets and Plumes," *Ann. Rev. Fluid Mech.*, Vol. 14, pp. 189-212.
- Ljuboja, M., and Rodi, W., 1981, "Prediction of Horizontal and Vertical Turbulent Buoyant Wall Jets," *ASME JOURNAL OF HEAT TRANSFER*, Vol. 103, pp. 343-349.
- Lockwood, F. C., and Naguib, A. S., 1975, "The Prediction of Fluctuations in the Properties of Free, Round-Jet Turbulent Diffusion Flames," *Combust. Flame*, Vol. 24, pp. 109-124.
- Moffat, R. J., 1982, "Contribution to the Theory of Single-Sample Uncertainty Analysis," *J. Fluids Engr.*, Vol. 104, pp. 250-258.
- Papanicolaou, P. N., and List, E. J., 1987, "Statistical and Spectral Properties of Tracer Concentration in Round Buoyant Jets," *Int. J. Heat Mass Trans.*, Vol. 30, pp. 2059-2071.
- Rouse, H., Yih, C. S., and Humphreys, H. W., 1952, "Gravitational Convection from a Boundary Source," *Tellus*, Vol. 4, pp. 201-210.
- Sangras, R., Dai, Z., and Faeth, G. M., "Mixing Structure of Plane Self-Preserving Buoyant Turbulent Plumes," *ASME JOURNAL OF HEAT TRANSFER*, Vol. 120, pp. 1033-1041.
- Stärner, S. H., and Bilger, R. W., 1983, "Differential Diffusion Effects on Measurements in Turbulent Diffusion Flames by the Mie Scattering Technique," *Prog. Astro. and Aero.*, Vol. 88, pp. 81-104.
- Tennekes, H., and Lumley, J. L., 1972, *A First Course in Turbulence*, MIT Press, Cambridge, MA, pp. 113-124.
- Turner, J. S., 1973, *Buoyancy Effects in Fluids*, Cambridge University Press, Cambridge, UK, pp. 165ff.
- Wu, J.-S., and Faeth, G. M., 1993, "Sphere Wakes in Still Surroundings at Intermediate Reynolds Numbers," *AIAA J.*, Vol. 31, pp. 1448-1455.

A. R. Kumar

Z. M. Zhang¹

Department of Mechanical Engineering

V. A. Boychev

D. B. Tanner

Department of Physics
University of Florida,
Gainesville, FL 32611

L. R. Vale

D. A. Rudman

Electromagnetic Technology Division,
National Institute of Standards and Technology,
Boulder, CO 80303

Far-Infrared Transmittance and Reflectance of $\text{YBa}_2\text{Cu}_3\text{O}_{7-\delta}$ Films on Si Substrates

The transmittance and reflectance of superconductive $\text{YBa}_2\text{Cu}_3\text{O}_{7-\delta}$ (YBCO) thin films deposited on Si substrates have been measured in the far-infrared frequency region from 10 to 100 cm^{-1} (wavelength from 1000 to 100 μm) at temperatures between 10 and 300 K. The effects of interference, optical resonance, and antireflection on the radiative properties of high-temperature superconducting (HTSC) films are observed and quantitatively analyzed. Furthermore, we have measured the reflectance of the HTSC film-substrate composites for radiation incident on the substrate side (backside reflectance) for the first time. The backside reflectance increases significantly from the normal state to the superconducting state at certain frequencies; this experimentally demonstrates that HTSC films can be used to build far-infrared intensity modulators. The complex refractive index of the YBCO films is determined from the measured transmittance using the Drude model in the normal state and a two-fluid model in the superconducting state. The complex refractive index obtained from this study is useful for various applications of YBCO films, including radiation modulators, detectors, and Fabry-Perot resonators.

1 Introduction

The radiative properties of high-temperature superconducting (HTSC) films change rapidly from the normal state to the superconducting state in the far-infrared region. This distinguishing characteristic of HTSC films may be used in designing thermo-optoelectronic devices such as infrared detectors, intensity and phase modulators, and radiation shields (Zhang and Frenkel, 1994; Zhang, 1998). Additionally, the reflectance of HTSC thin films differs significantly for radiation incident on the substrate side of the film-substrate composite (also called backside illumination) as compared to radiation incident on the film side. Recently, Zhang (1998) presented a design analysis of far-infrared intensity modulators using $\text{YBa}_2\text{Cu}_3\text{O}_{7-\delta}$ (YBCO) films by evaluating the reflectance for various design structures in both the superconducting and normal states. This work predicted large differences in the backside reflectance between the superconducting and normal states. To date, the reflectance of HTSC films has been measured only for radiation incident on the film side (Renk, 1992; Tanner and Timusk, 1992; Zhang et al., 1994). In order to confirm the features associated with the backside illumination, there is a need for measurements of the radiative properties of HTSC films for radiation incident on the substrate.

For the development of HTSC applications, the choice of the substrate material is an important issue. Substrates commonly used for growing HTSC films include MgO, SrTiO_3 , LaAlO_3 , yttria-stabilized zirconia (YSZ), and sapphire (Chen et al., 1995; Phillips, 1996). Several promising far-infrared applications of HTSC films, such as bolometers, modulators, and resonators, demand that the substrate be transparent in the spectral region of interest. Fenner et al. (1993) presented transmittance measurements for various substrates, NdGaO_3 , LaAlO_3 , MgO, YSZ, and Si, in the mid and far-infrared regions. This study showed that the transmittance of Si

is generally higher than that of the other substrates in the measured spectral region. (The transmittance of pure Si is slightly greater than 0.5 at wavelengths longer than 20 μm .) The higher transmittance of Si in a broad spectral region allows new optical designs such as backside-illuminated HTSC microbolometers (Rice et al., 1994). At present, Si substrates have received significant attention from the electronics industry due to the feasibility of lithographically patterning HTSC films and the potential integration of semiconductor and superconducting electronics (Phillips, 1996). High-quality YBCO films have been successfully grown on Si substrates using pulsed laser ablation (Fork et al., 1991; Mechin et al., 1996) but very few measurements have been done to determine the radiative properties of such films. Berberich et al. (1993) measured the transmittance and reflectance of imperfect YBCO films deposited on Si substrates. These films were of poor quality because they were deposited on Si substrates without buffer layers, and the reflectance was measured only at room temperature. Karrai et al. (1992) studied the transmittance of YBCO thin films on Si substrates with and without a magnetic field. However, the substrates were intentionally wedged to avoid interference effects. Most of the reported radiative properties of HTSC superconductors were for opaque samples or thin films on thick substrates (Tanner and Timusk, 1992; Zhang et al., 1994). For transmittance measurements, the interference effects associated with the substrate were often neglected by either averaging over a free spectral range or using wedged substrates (Gao et al., 1991; Karrai et al., 1992; Zhang et al., 1992; Cunsolo et al., 1993). Knowledge of the radiative properties of thin YBCO films deposited on thin substrates is essential for designing optoelectronic devices including radiation modulators and Fabry-Perot resonators (Renk et al., 1990; Genzel et al., 1992; Malone et al., 1993; Zhang, 1998).

The transmittance and reflectance of thin films on transparent substrates typically oscillate periodically as the optical frequency changes, as a result of multiple reflections inside the substrate. This oscillation is particularly prevalent in the far infrared because the wavelength is comparable with the substrate thickness. Hadni et al. (1995) measured the far-infrared transmittance of several YBCO films deposited on MgO substrates. The interference features associated with the substrate were clearly seen in their study

¹ To whom correspondence should be addressed.

Contributed by the Heat Transfer Division for publication in the JOURNAL OF HEAT TRANSFER and presented at 1998 ASME IMECE, Anaheim. Manuscript received by the Heat Transfer Division, Sept. 8, 1998; revision received, May 5, 1999. Keywords: Experimental, Heat Transfer, Interferometry, Radiation, Thin Films. Associate Technical Editor: P. Menguc.

at frequencies from 10 to 40 cm^{-1} . In the present study, several infrared spectrometers have been used to measure both the transmittance and reflectance of YBCO films ($\approx 35\text{-nm}$ thick) deposited on Si substrates ($\approx 200\text{-}\mu\text{m}$ thick), in the frequency region from 10 cm^{-1} to 100 cm^{-1} (wavelength from 1000 to 100 μm) from room temperature down to 10 K. The transmittance was measured with radiation incident on the film side and the reflectance was measured for radiation incident both on the film and on the substrate. The transmittance of the film-substrate composite is the same for radiation incident on the film side and the substrate side. The spectral resolution is chosen high enough to measure the effects of interference associated with the substrate.

Accurate assessments of the potential of YBCO films in optoelectronic applications require the determination of the frequency-dependent radiative properties. Knowledge of the complex dielectric function of the YBCO film facilitates the computation of radiative properties in desired spectral regions (Phelan et al., 1991; 1992). Due to their complicated crystalline structures, the refractive index of the HTSC materials may vary significantly depending on the method of preparation, oxygen content, thickness, and microstructure (Choi et al., 1992; Renk, 1992; Tanner and Timusk, 1992; Flik et al., 1992). In the present study, the measured transmittance spectra are used to determine the complex dielectric function $\epsilon(\omega)$ of YBCO films deposited on Si substrates. In the normal state, a two-component model, consisting of a temperature-dependent free-carrier absorption term (the Drude term) and a temperature-independent mid-infrared term (the Lorentz term), is used for computing $\epsilon(\omega)$. In the superconducting state, the conventional two-fluid model is used for computing $\epsilon(\omega)$ (Tanner and Timusk, 1992). The spectral transmittance and reflectance are calculated with the transfer-matrix method using the refractive indices and thicknesses of the film and the substrate. The dielectric functions are determined at different temperatures by comparing model predictions with measured results. Our measurements demonstrate the feasibility of using thin HTSC films deposited on transparent substrates as radiation modulators. The frequency and temperature-dependent refractive index of the HTSC films obtained from the present study will facilitate future design of potential far-infrared devices based on YBCO films on Si substrates.

2 Experiments

2.1 YBCO Film Preparation. The YBCO films were deposited by pulsed laser ablation using an excimer laser operated at a wavelength of 248 nm. A single-crystal (100) Si wafer, polished on both sides with a thickness of approximately 200 μm and a diameter of 76 mm, was used as the substrate. The wafer is slightly boron-doped and has an electric resistivity of $\approx 1000 \Omega\text{-cm}$. The Si wafer, was cut into approximately $12 \times 12 \text{ mm}^2$ pieces for the deposition of the YBCO. Ag paste was used to mount the substrate onto a substrate holder in the deposition chamber. At high temperatures, Ag may diffuse into the Si substrate. Therefore, a 320-nm thick SiO_2 layer was deposited by chemical vapor depo-

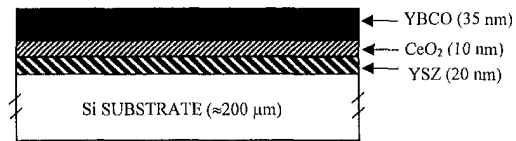


Fig. 1 Structure of the film-substrate composite (the lateral dimensions are $\approx 12 \times 12 \text{ mm}^2$)

sition (CVD) on the backside of the Si substrate before the application of the Ag paste. The substrate was heated to 1063 K for the deposition of a 20-nm thick YSZ layer and then a 10-nm thick CeO_2 layer on the Si substrate. These buffer layers are required for growing high-quality superconducting films (Mechin et al., 1996). A YBCO film of 35 nm was deposited on the top of the buffer layers at 1043 K in an optimized O_2 environment (Rice et al., 1994). The thicknesses of the thin films were determined by calibrations of the rate of deposition. The YBCO films formed this way are a - b plane oriented (c -axis is parallel to the surface normal) with a critical temperature (T_c) between 86 and 88 K.

Several steps were followed to remove the Ag paste and the SiO_2 layer. First, the YBCO film was covered by a photoresist. Second, nitric acid (HNO_3) was used to remove Ag paste and then hydrofluoric acid (HF) was used to etch off the SiO_2 layer. Third, the photoresist was removed using acetone. Finally the film was rinsed with isopropanol. The structure of the film is shown in Fig. 1. Some damage to the film may have taken place during this stripping process since the critical temperature of several films dropped to 80 to 82 K after the removal of the photoresist. However, scanning electron microscopic (SEM) images showed no evidence of microcracks or other surface damage.

2.2 Transmittance and Reflection Measurements. The transmittance spectra of the films were measured using a slow-scan Michelson interferometer with a Hg-arc lamp as the source (Gao, 1992). The entire interferometer chamber is evacuated to eliminate the absorption by atmospheric gases. The source radiation is modulated by a rotating chopper inside the chamber to allow lock-in detection. This procedure allows only in-phase modulated radiation to be detected and thus minimizes the effect of external noise. The radiation is guided by mirrors and light pipes to the sample and thence to the detector. Polyethylene windows, which are transparent in the far-infrared region, are used to seal the cryostat. The detection system consists of a 4.2 K He-cooled Si bolometer. A preamplifier and lock-in electronics are used to measure the detector output signal.

The sample holder consists of two identical copper plates with equally sized apertures in the middle. The copper plates are mounted at a right angle. One aperture is covered by the specimen and the other is left blank for the reference measurement. The sample holder is mounted on the cold finger of the cryostat. The cold finger is kept in high vacuum and cooled by flowing liquid He

Nomenclature

c_0 = speed of light in vacuum, $2.9979 \times 10^8 \text{ m/s}$
 d = thickness, m
 f_s = fraction of superconducting electrons
 $i = (-1)^{1/2}$
 k = imaginary part of refractive index
 N = complex refractive index
 n = real part of the refractive index
 n_e = electron number density, m^{-3}
 r = reflection coefficient
 T = transmittance
 T_c = critical temperature, K

y = dimensionless admittance of the film
 δ = phase change
 $\Delta\omega$ = free spectral range, m^{-1}
 γ_e = damping constant in the Lorentz term, rad/s ; ($1 \text{ rad/s} = 5.3089 \times 10^{-12} \text{ cm}^{-1}$)
 ϵ = dielectric function
 ϵ_0 = electric permittivity of free space, $8.8542 \times 10^{-12} \text{ C} \cdot \text{V}^{-1} \cdot \text{m}^{-1}$
 ϵ_∞ = high-frequency dielectric constant
 λ = wavelength in vacuum, m

$1/\tau$ = electron scattering rate, rad/s
 σ_{DC} = DC conductivity, $(\Omega \cdot \text{m})^{-1}$
 ω = angular frequency, rad/s
 ω_e = center frequency, rad/s
 ω_p = plasma frequency, rad/s
 ω_{pe} = plasma frequency in the Lorentz term, rad/s

Subscripts

f = film
 Si = silicon

at 4.2 K, which results in conductive cooling of the specimen. A diffusion pump is used to achieve a vacuum of 10^{-2} Pa inside the cryostat before cooling; the actual pressure should be much lower due to cryopumping. The liquid He is transferred from a liquid-helium tank via an evacuated transfer line. The specimen temperature is measured using a Si diode. An automatic temperature controller was used to adjust the temperature of the specimen using a proportional-integral-derivative (PID) control scheme and an electric heater wrapped around the cold finger. The temperature variation was within 0.5 K of the set temperature for measurements above 100 K. During the measurements at 10 K and 50 K, the variation of temperature was about 1 K from the set temperature.

The cryostat, along with the sample holder, is introduced vertically into the interferometer chamber. The cryostat can be rotated so that either the blank aperture or the specimen is in the beam path of the far-infrared radiation. For the transmittance measurement, the spectrum obtained with the blank is taken as the background spectrum. The cryostat is then rotated by 90 degrees to introduce the specimen in the beam path. The exact position of the cryostat for the blank aperture or for the specimen is determined by gently rotating the cryostat until the signal is maximum. The transmitted spectrum of the specimen is divided by the background spectrum to obtain the transmittance. The spectral resolution is approximately 0.5 cm^{-1} .

The reflectance was measured using a commercial fast-scan Fourier transform spectrometer. The spectrum is averaged over 128 scans and the resolution is $\approx 1 \text{ cm}^{-1}$. Here, the far-infrared beam is directed to either the specimen or a Au mirror by a combination of plane and elliptical mirrors. The angle of incidence in the reflectance measurement is ≈ 7.5 deg with a beam divergence of 7.5 deg. The Au mirror is used as the reference for the reflectance measurements at all temperatures. In the far-infrared region, the reflectance of the gold is greater than 0.995 at room temperature and increases at lower temperatures. Hence, the reflectivity of the Au mirror is taken to be 1.

The transmittance and reflectance of bare Si substrates were measured at different temperatures to evaluate the measurement uncertainty. The refractive index of single-crystal Si has been well documented (Loewenstein et al., 1973). The use of the high-resistivity single-crystal Si has essentially eliminated absorption in the substrate. The measured transmittance shows interference patterns with T_{max} about 1, T_{min} about 0.3, and a free spectral range $\Delta\omega$ (the wave number interval between two interference maxima) about 7 cm^{-1} . Even a small variation in the substrate thickness (d_{Si}) or its refractive index (n_{Si}) can affect $\Delta\omega$, since $\Delta\omega = (2n_{\text{Si}}d_{\text{Si}})^{-1}$. The Si thickness is determined from the free spectral range by assuming that $n_{\text{Si}} = 3.42$ at frequencies from 10 to 100 cm^{-1} (Loewenstein et al., 1973). The actual angles of incidence in the transmittance measurement have a spread up to 18 degrees as a result of the beam divergence in the light pipe. The effect of inclined incidence on $\Delta\omega$ (and hence d_{Si}) is less than 0.5 percent since the angle of refraction inside the silicon is small. The transmittance extrema shift toward higher frequencies as the temperature decreases, indicating a decrease of the refractive index since the thickness change can be neglected (Loewenstein et al., 1973). The measured transmittance is compared with the calculated transmittance to determine the refractive index at different temperatures. The results are $n_{\text{Si}} \approx 3.405$ at 200 K, 3.395 at 100 K, and 3.39 at 50 K and 10 K. For the same Si wafer, the transmittance maxima become the reflectance minima at all temperatures.

Although the interference patterns in the measured transmittance and reflectance of the Si substrate match theoretical predictions, the radiometric accuracy is not as high. The maximum transmittance often varies between 0.95 and 1.05 or more near the spectral cutoffs. The reflectance minimum is always greater than zero, which may be caused by the insufficient spectral resolution. The root-mean-square difference between the measured and the calculated values shows a standard uncertainty of ≈ 0.05 in both the transmittance and reflectance. Hence, the expanded uncertainty (95 percent confidence) is estimated to be 0.1 for all measure-

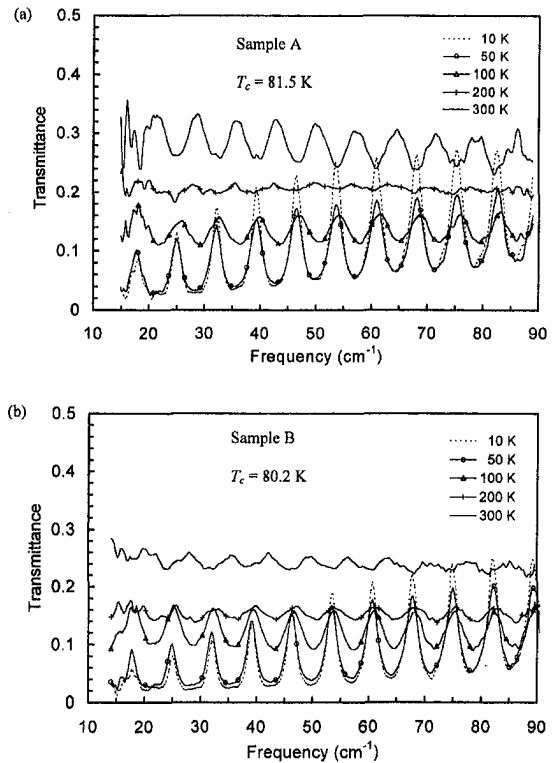


Fig. 2 Measured transmittance of YBCO films on Si substrates at various temperatures

ments. This uncertainty is large compared with the measurements without sharp interference fringes, which could be caused by many parameters, such as detector nonlinearity, misalignment, phase error, and multiple reflections between the sample, windows, and the beam splitter (Griffiths and de Haseth, 1986; Zhang et al., 1996).

Figure 2 shows the measured transmittance of two specimens, identified as Sample A and Sample B, at various temperatures. The transmittance spectra oscillate periodically due to interference effects inside the substrate with $\Delta\omega$ slightly higher than 7 cm^{-1} . In the normal state, the fringe-averaged transmittance, defined as $\bar{T}(\omega) = (1/\Delta\omega) \int_{\omega-\Delta\omega/2}^{\omega+\Delta\omega/2} T(\omega') d\omega'$, is nearly uniform for all the measured frequencies at any given temperature but decreases gradually as the temperature is lowered. This decrease is expected because the electrical conductivity of the YBCO film increases as temperature decreases. The interference pattern is quite periodic over the studied wave number range at any given temperature, but varies significantly as the temperature is changed from 300 K to 100 K. Not only do the peak locations vary with temperature but also the fringe contrast (the relative amplitude of oscillation) changes significantly. There is a phase shift of π rad between the 300 K and 100 K data; that is, the transmittance maxima at one temperature correspond to the transmittance minima at the other. Furthermore, the spectrum at 200 K for Sample A has no discernible interference fringes, which can be attributed to an antireflection effect of the YBCO film. In the superconducting state, the fringe-averaged transmittance is lower at smaller frequencies and increases toward higher frequencies. The peak transmittance is higher at lower temperatures. This is caused by the optical resonance effect in the film-substrate composite and by decreasing losses in the film. The antireflection effect on the interference pattern at 200 K and the effect of optical resonance on the peak transmittance in the superconducting state are discussed in Section 5.

The measured reflectance spectra of Sample A are shown in Fig. 3 for radiation incident on the substrate. The fringe-averaged

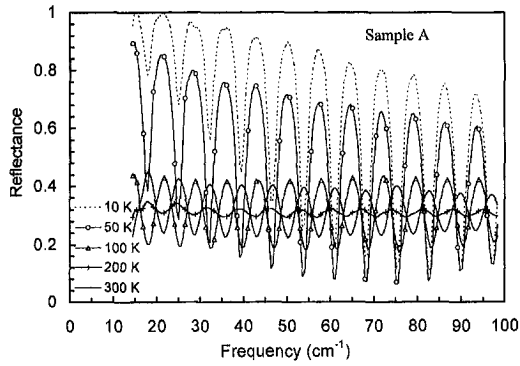


Fig. 3 Measured reflectance for radiation incident on the substrate (backside)

reflectance is nearly independent of wave number in the normal state, but increases toward smaller frequencies in the superconducting state. The reflectance increases sharply as the temperature is reduced to below the critical temperature and increases slightly as the temperature is further reduced. The fringe contrast is much higher in the superconducting state than in the normal state. In a way similar to the transmittance, the fringe contrast is much smaller at 200 K than at 300 K and 100 K. At frequencies where the transmittance is maximum, the reflectance for radiation incident on the substrate decreases to minimum values. The large change in the reflectance of YBCO films at particular frequencies, from the superconducting to the normal state, experimentally demonstrate that HTSC films can be used to construct far-infrared intensity modulators as proposed by Zhang (1998).

Using suitable dielectric function models, the complex refractive index of the YBCO film is determined by fitting the measured transmittance data because the transmittance measurement has a better spectral resolution, which is especially important in the region where sharp interference extrema occur. Comparison is also made between the calculated and measured reflectance whenever the data are available. Detailed discussions are given below.

3 Analysis

3.1 Dielectric Function Models for the Superconductor YBCO. The optical properties of superconducting YBCO change abruptly from the normal state to the superconducting state. Hence, different dielectric function models are used in the normal and superconducting states (Tanner and Timusk, 1992). In the normal state, the frequency-dependent complex dielectric function can be modeled as a sum of the Drude term (ϵ_{Drude}), the Lorentz term ($\epsilon_{\text{Lorentz}}$), and a high-frequency constant ($\epsilon_{\infty} \approx 5$):

$$\epsilon(\omega) = \epsilon_{\text{Drude}} + \epsilon_{\text{Lorentz}} + \epsilon_{\infty}. \quad (1)$$

The Drude term describes the electronic behavior in the infrared region by assuming that free electrons (or holes) are accelerated in the presence of an electric field and that collisions result in a damping force. Thus, the Drude term can be expressed as

$$\epsilon_{\text{Drude}} = -\frac{\omega_p^2}{\omega(\omega + i/\tau)} \quad (2)$$

where ω is the angular frequency, ω_p is the plasma frequency, and $1/\tau$ is the electron scattering rate. The plasma frequency is defined as $\omega_p^2 = n_e e^2 / m \epsilon_0$, where n_e , e , and m are the electron number density, charge, and effective mass, and ϵ_0 is the electric permittivity of free space. The plasma frequency, the scattering rate, and the DC electrical conductivity σ_{DC} are related by

$$\omega_p^2 = \frac{\sigma_{\text{DC}}}{\epsilon_0 \tau}. \quad (3)$$

From Eqs. (2) and (3), only σ_{DC} and $1/\tau$ are needed to calculate ϵ_{Drude} .

The Lorentz term can be derived by assuming that the electrons are bound to their nuclei by harmonic forces and are subjected to damping forces. Lorentz terms are also commonly used to model infrared active phonons. The phonon contributions, however, can be neglected compared to the electronic contributions (Choi et al., 1992). This neglect is particularly valid in the far infrared because the resonant frequencies of most phonons are in the mid-infrared region. For HTSC materials, however, there is a broadband mid-infrared electronic absorption, which is typically modeled with a Lorentz term (Tanner and Timusk, 1992). This contribution is therefore expressed as

$$\epsilon_{\text{Lorentz}} = \frac{\omega_{pe}^2}{\omega_e^2 - \omega^2 - i\omega\gamma_e} \quad (4)$$

where ω_{pe} , ω_e , and γ_e are, respectively, the plasma frequency, center frequency, and damping constant of the mid-infrared band. Due to the relatively weak effect of the Lorentz term in the far infrared, a single oscillator is used with the parameters fixed to those recommended by Zhang et al. (1994), i.e., $\omega_e = 1800 \text{ cm}^{-1}$, $\omega_{pe} = 18000 \text{ cm}^{-1}$, and $\gamma_e = 5400 \text{ cm}^{-1}$. The effect of the mid-infrared band on the radiative properties of the film is very weak at frequencies between 10 and 100 cm^{-1} , because $\epsilon_{\text{Lorentz}}$ is essentially a real constant, $\approx (\omega_{pe}/\omega_e)^2$ in the far infrared. Calculations using different Lorentz parameters, such as $\omega_e = 1800 \text{ cm}^{-1}$, $\omega_{pe} = 24150 \text{ cm}^{-1}$, $\gamma_e = 7500 \text{ cm}^{-1}$ (Flik et al., 1992), do not modify significantly the transmittance and reflectance of the film-substrate composite.

Below the critical temperature T_c , the free-carrier part of the dielectric function is described by a two-fluid model. In this model, only a fraction of electrons (f_s) are assumed to be in the condensed phase (or superconducting state) and the remaining electrons are in the normal state. The superconducting electrons move without any scattering, and the value of f_s is assumed temperature-dependent. The contribution of the superconducting electrons to the dielectric function is

$$\epsilon_{\text{sup}} = -\frac{\omega_p^2}{\omega^2}. \quad (5)$$

The Drude term remains due to the presence of normal electrons with a number density of $(1 - f_s)n_e$. The dielectric function in the superconducting state is therefore modeled as

$$\epsilon(\omega) = f_s \epsilon_{\text{sup}} + (1 - f_s) \epsilon_{\text{Drude}} + \epsilon_{\text{Lorentz}} + \epsilon_{\infty}. \quad (6)$$

3.2 Fitting Procedure. The transfer-matrix method, described by Zhang and Flik (1993), is used to compute the transmittance and reflectance of the film-substrate composite shown in Fig. 1. The Si substrate is assumed to be nonabsorbing and to have the temperature-dependent refractive index described in Section 2.2. The effective thickness of the Si substrate is determined by matching the interference patterns between the calculated and measured spectra. The angle of incidence has little effect except for a slight shift in the frequencies of the interference fringes, which has already been accounted for using the effective thickness of the Si substrate. Hence, the angle of incidence is assumed to be normal in all calculations.

The absorption of dielectric materials, such as YSZ and CeO_2 , is very weak in the far-infrared region, especially for thickness less than 20 nm. The dielectric constant of YSZ is 25 and that of CeO_2 is 17 in the far-infrared and microwave regions (Grischkowsky and Keiding, 1990; Phillips, 1996). In all cases, the addition of the YSZ and CeO_2 layers has essentially no effect on the calculated transmittance and reflectance. Therefore, the YSZ and CeO_2 layers are omitted in the calculations and not discussed further.

The real part $n_r(\omega)$ and imaginary part $k_f(\omega)$ of the complex refractive index of the YBCO film are related to the dielectric function by

Table 1 Fitting parameters, where the expanded uncertainties are estimated to be ten percent in $1/\sigma_{DC}$, 20 percent in $1/\tau$, and 20 percent in f_s

Temp. (K)	Sample A ($T_c = 81.5$)			Sample B ($T_c = 80.2$)		
	$1/\sigma_{DC}$ ($\mu\Omega\text{-cm}$)	f_s	$1/\tau$ (cm^{-1})	$1/\sigma_{DC}$ ($\mu\Omega\text{-cm}$)	f_s	$1/\tau$ (cm^{-1})
300	800	-	600	700	-	600
200	538	-	400	460	-	440
100	306	-	230	290	-	275
50	-	0.25	150	-	0.30	180
10	-	0.35	190	-	0.40	220

$$(n_f + ik_f)^2 = \epsilon(\omega) \quad (7)$$

where $\epsilon(\omega)$ is calculated from Eq. (1) and Eq. (6) for the normal and superconducting states, respectively. The refractive index of YBCO is used to calculate the transmittance and reflectance of the film-substrate composite.

In the normal state, σ_{DC} and $1/\tau$ are taken as adjustable parameters. Their values are determined by fitting the calculated transmittance to the measured transmittance. The best fit is obtained when the root-mean-square difference is the smallest. In some cases, the differences in the fringe-averaged transmittance and the peak transmittance are also used to determine the best fit when the root-mean-square difference is not so sensitive to the parameters. Our calculations show that the radiative properties depend strongly on σ_{DC} but weakly on $1/\tau$, suggesting a larger uncertainty in $1/\tau$. The fitted values of σ_{DC} and $1/\tau$ at room temperature are used to compute the plasma frequency from Eq. (3). The plasma frequency is proportional to the total electron density and is typically constant over temperature (Kamarás et al., 1990; Tanner and Timusk, 1992). Hence, at other temperatures in the normal state, the scattering rate is the only adjustable parameter. Both the superconducting-electron fraction f_s and the scattering rate $1/\tau$ are considered to be adjustable parameters in computing the dielectric function of YBCO in the superconducting state.

4 Results

The fitting parameters for both specimens are shown in Table 1 (Kumar, 1999). The difference in the fitted values may be caused by the slight variation in the film deposition conditions. Figure 4 compares the fitted and measured transmittance of Sample A. The fitted and measured values agree well with a root-mean-square difference of less than 0.03 in most cases. At temperatures greater than T_c , both the scattering rate and the resistivity drop almost linearly with decreasing temperature. At these temperatures, the scattering rate is dominated by the temperature-dependent electronic scattering, which governs the linear dependence of resistivity on the temperature. At low temperatures, below T_c , the temperature-dependent scattering ceases to exist, and the remaining scattering is mainly due to impurities and lattice defects, which should be temperature-independent (Flik et al., 1992). This scattering rate should be constant at low temperatures. However, the best agreement between the measured and calculated transmittance at 10 K was achieved with a scattering rate higher than that for 50 K. This unexpected higher scattering rate at lower temperatures needs further investigation, although it could simply be caused by the experimental uncertainty. Bonn et al. (1992) showed that the scattering rate of YBCO decreases drastically as the temperature is reduced below T_c , due to the rapid reduction of the density of thermally activated quasi-particles. Their results, however, were

for a single-crystal $\text{YBa}_2\text{Cu}_3\text{O}_7$ of extremely high quality with $f_s \approx 1$ at very low temperatures.

Even at very low temperatures, there is a large fraction $(1 - f_s)$ of normal-state electrons in the thin YBCO films. For conventional superconductors, f_s should be zero at temperatures much lower than T_c . The definition of f_s for HTSC materials is rather ambiguous. Some researchers obtained higher values of f_s by assuming that a portion of the YBCO film is not superconductive, also known as "dead layer" (Renk, 1992; Hadni et al., 1995). In the present study, the superconducting fraction is calculated without assuming any dead layer, and this may account for the small values of f_s obtained in this study. Another reason may be the higher DC resistivity ($1/\sigma_{DC}$) of our YBCO films in the normal state. The DC resistivity is strongly affected by the choice of the substrate and buffer layers, by their thicknesses, as well as by the thickness of the YBCO film (Mechin et al., 1996). The damage caused by the stripping process as mentioned in Section 2.1 may have reduced f_s , as well. Although the critical temperature of Sample A is slightly higher than that of sample B, the fraction of superconducting electrons of Sample A is less than that of sample B. This may be explained by the fact that Sample A has a higher electrical resistivity and scattering rate.

The real and imaginary parts of the refractive index of YBCO calculated from Eq. (7) using the fitting parameters for Sample A are shown in Fig. 5. Both n_f and k_f increase as the wave number decreases at all temperatures. In the normal state, $n_f \approx k_f$, as

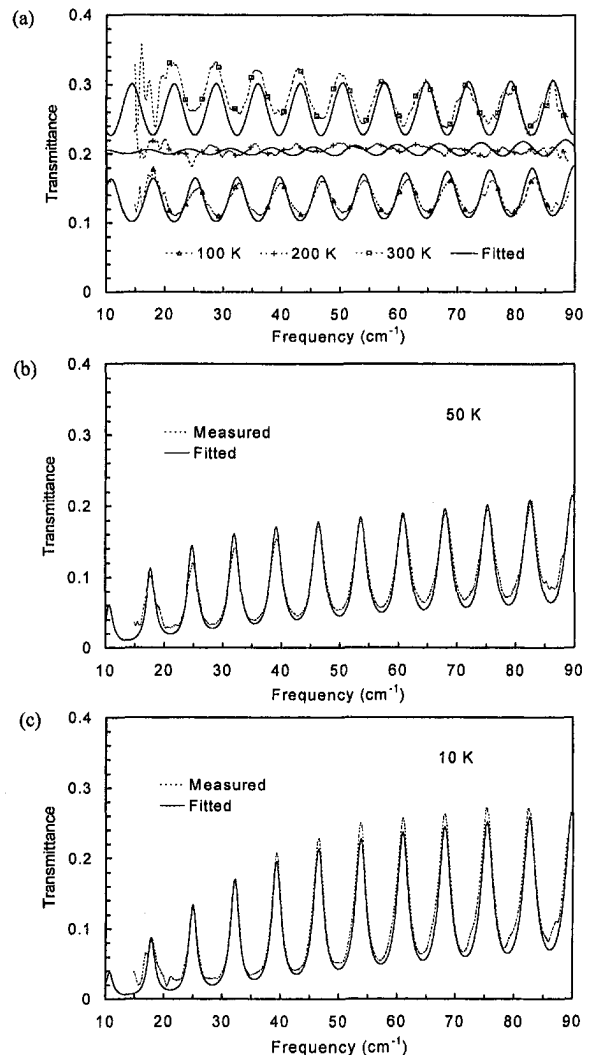


Fig. 4 Comparison between the measured and fitted transmittance for Sample A: (a) normal state; (b) 50 K; (c) 10 K

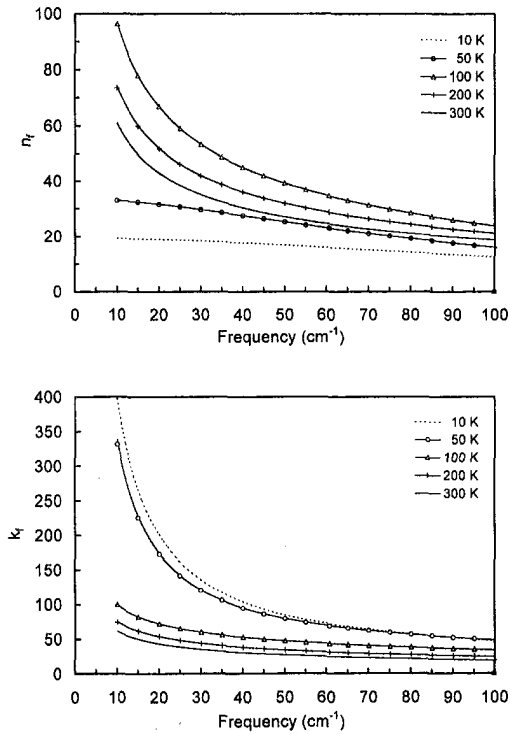


Fig. 5 Complex refractive index of the YBCO film (Sample A)

expected for a metallic film, and both n_f and k_f increase with decreasing temperature. As the film becomes superconducting, n_f drops suddenly but k_f exhibits an abrupt increase, especially at low frequencies. As the temperature is further reduced from 50 K to 10 K, n_f continues to decrease whereas k_f continues to increase. Below T_c , $k_f \gg n_f$, because the film is largely inductive in its optical response. The refractive index of Sample B has a similar trend (Kumar, 1999), but now in the superconducting state the imaginary part is even greater and the real part is even smaller due to a slightly larger fraction of superconducting electrons (see Table 1). The expanded uncertainty in the real and imaginary parts of the refractive index is estimated to be ten percent.

Figure 6 compares the measured with the calculated reflectance at 50 K and 10 K for radiation incident on the substrate. The measured and calculated reflectance is in reasonable agreement. At the reflectance minima, the calculated values are much lower than those measured, which may be caused by insufficient resolution in the measured reflectance or by the beam divergence. Further improvements in radiometric accuracy and spectral resolution are required in order to resolve the discrepancy between the measured and calculated reflectance.

5 Discussion

5.1 The Antireflection Effect. For Sample A, measurements reveal that the minima in the transmittance at 300 K approximately correspond to the maxima at 100 K, 50 K, and 10 K (see Fig. 2(a)). The measured transmittance at 200 K has no discernible interference fringes. This interesting change in the interference pattern is analyzed below by considering the radiation incident from the substrate and reflected by the film. The reflection coefficient at the substrate-film interface is the ratio of the reflected to the incident electric waves (Heavens, 1965):

$$r = \frac{-r_{23} + r_{21} e^{i2\delta_f}}{1 - r_{23} r_{21} e^{i2\delta_f}} \quad (8)$$

where, for normal incidence, $r_{21} = (N_2 - N_1)/(N_2 + N_1)$ and $r_{23} = (N_2 - N_3)/(N_2 + N_3)$, and $\delta_f = \omega d_f N_2 / c_0$ is the complex

phase change in the film. Note that $N_1 = 1$, $N_2 = N_f$, and $N_3 = n_{\text{Si}}$ correspond to the refractive indices of the air, film, and the substrate, respectively, and c_0 is speed of light in vacuum. If $|2i\delta_f| \ll 1$, which is satisfied for the thin YBCO film in the normal state, then $\exp(2i\delta_f) \approx 1 + 2i\delta_f$. The requirement of $|2i\delta_f| \ll 1$ is equivalent to (1) $d_f \ll \lambda/4\pi k_f$ (the film thickness is much smaller than the radiation penetration depth), where λ is the wavelength in vacuum, and (2) $d_f \ll \lambda/4\pi n_f$. After some manipulation, Eq. (8) becomes

$$r \approx \frac{N_3 - N_1 + i\delta_f N_2 (1 + N_3/N_2)(1 - N_1/N_2)}{N_3 + N_1 - i\delta_f N_2 (1 - N_3/N_2)(1 - N_1/N_2)} \quad (9)$$

Assume $|N_1/N_2| \ll 1$ and $|N_3/N_2| \ll 1$, which are also valid since the refractive index and extinction coefficient of metallic films (such as YBCO in the normal state) are generally much greater than the refractive index of dielectric materials (such as the Si substrate used here). Then,

$$r \approx \frac{N_3 - N_1 + i\delta_f N_2}{N_3 + N_1 - i\delta_f N_2} \quad (10)$$

Equation (10) is the same as that derived by McKnight et al. (1987), but here it is obtained directly from Maxwell's equations without assuming that the film is infinitely thin. It is convenient to define a dimensionless admittance, $y = -i\delta_f(N_f)$, which in general is a complex quantity. As discussed above, the dielectric function of YBCO in the normal state is dominated by the Drude term, which becomes purely imaginary at frequencies much smaller than the scattering rate ($\omega\tau \ll 1$); hence, $\epsilon(\omega) \approx i\sigma_{\text{DC}}/\omega\epsilon_0$. From the definitions of y and δ_f , $y \approx \sigma_{\text{DC}}d_f/c_0\epsilon_0$ is a real positive constant in the very far infrared. When $y = n_{\text{Si}} - 1$, the reflection coefficient given by Eq. (10) becomes zero for incidence on the substrate. For $N_3 = n_{\text{Si}} \approx 3.4$, the required DC resistivity ($1/\sigma_{\text{DC}}$) is $\approx 550 \mu\Omega\text{-cm}$ for $d_f = 35 \text{ nm}$. The DC resistivity obtained by fitting the transmittance at 200 K of $538 \mu\Omega\text{-cm}$ is very close to

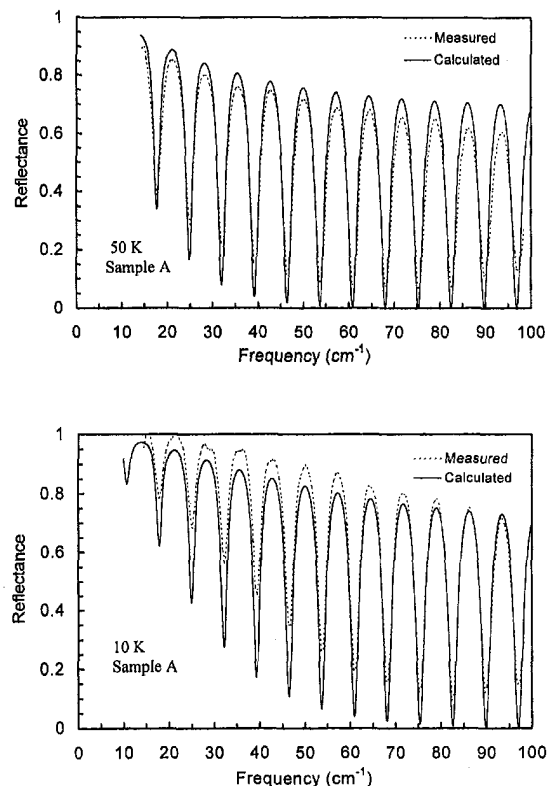


Fig. 6 Measured and calculated backside reflectance for Sample A at 50 K and 10 K

this value. However, because the scattering rate is only 400 cm^{-1} at 200 K (see Table 1), there are residual interference fringes. Because of all the assumptions made earlier, interference fringes persist in the calculated transmittance even with $1/\sigma_{\text{DC}} \approx 550 \mu\Omega\text{-cm}$. McKnight et al. (1987) analyzed and experimentally demonstrated the effect of antireflection coating (also called impedance-matched coating) on the transmittance of a Si wafer coated with a Ni-Cr film. In that work, the scattering rate was much greater than 100 cm^{-1} , and the fringe contrast in the measured transmittance was much smaller.

The change from transmittance maxima at 300 K to transmittance minima at 100 K at fixed wave number can be explained by the sign change of the reflection coefficient given by Eq. (10) as the DC resistivity passes $\approx 550 \mu\Omega\text{-cm}$. The change in the sign of this coefficient, combined with the interference effect inside the Si substrate, will result in a phase shift of π rad in the interference pattern and thus causing the transmittance to change from maxima to minima and vice versa. The calculated transmittance and reflectance agree extremely well in terms of the interference patterns at all temperatures except for Sample A at 200 K. The actual phase at 200 K is very complicated because the assumptions used in deriving Eq. (10) are not perfectly met. The discrepancy in the phase between the calculated and the measured transmittance at 200 K suggests that the scattering rate is complex and may depend on the wave number. Modified Drude models with a complex and frequency-dependent scattering rate have been used for the study of HTSC materials (Varma et al., 1989; Virosztek and Ruvalds 1990; Renk, 1992; Quinlan et al., 1996). Further studies are needed to investigate the applicability of these models to thin YBCO films on Si substrates.

The fringe patterns of Sample B differs from those of Sample A, because their characteristics are different. From Fig. 2(b) and Table 1, we can estimate that the interference contrast for Sample B would be the smallest at a temperature somewhere between 300 K and 200 K, where its DC electric resistivity is near $550 \mu\Omega\text{-cm}$. The condition for impedance matching with the Si substrate is that $(\sigma_{\text{DC}}d)^{-1} \approx 157 \Omega$. Hence, it is possible to construct antireflection coatings with a YBCO film on Si substrate at room temperature by increasing the film thickness. The practical applications of the antireflection effect using HTSC films need further exploration.

5.2 The Effect of Optical Resonance. The measured spectra for both specimens at 10 K and 50 K have sharper transmittance maxima and reflectance minima than the spectra obtained above the critical temperature (see Figs. 2 and 3). In addition, the peak transmittance at 10 K is even higher than that at 50 K. The transmittance is expected to decrease as the temperature is lowered since the YBCO material becomes more and more conductive. The unexpected higher transmittance at lower temperatures in certain spectral bands is the result of optical resonance in the film-substrate composite. A simple optical resonator is a dielectric layer coated with highly reflecting films on both sides. By varying the reflection coefficient of one or both coatings, the transmittance of the resonator can be altered significantly. This resonance effect will result in very high transmittance values at particular frequencies (Klein and Furtak, 1986). In the present study, the specimen is analogous to an optical resonator made of a thin YBCO film coated on only one side of the Si substrate. As the temperature is reduced to below the critical temperature, the reflection coefficient of the YBCO film increases sharply. The large reflection coefficient, coupled with the interference effects in the substrate, can significantly increase the measured transmittance at certain frequencies. The observed resonance effects demonstrate that YBCO films deposited on Si substrates have the potential for construction of Fabry-Perot resonators (Renk et al., 1990; Genzel et al., 1992; Malone et al., 1993). Further studies are needed to construct resonance structures using two identical films facing each other to optimize the performance of such resonators. The calculated minimum transmittance is slightly lower at 10 K than at 50 K. This is consistent with the measured values for Sample B. The measured

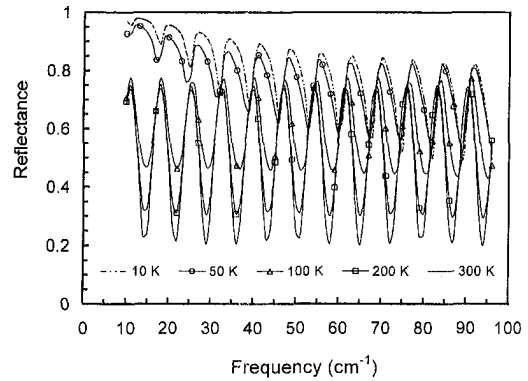


Fig. 7 Calculated film side reflectance for Sample A

minimum transmittance for Sample A is nearly the same at 10 K and 50 K at large frequencies. However, the expected difference is smaller than the experimental uncertainty.

5.3 The Film Side Reflectance. The film side reflectance for Sample A is calculated using the fitted parameters and is shown in Fig. 7. In the normal state, the peak locations of the interference fringes remain at the same frequency. The film side reflectance shows a higher fringe contrast in the normal state and a lower fringe contrast in the superconducting state when compared to the substrate side reflectance. The reflectance measurements on several sample films for the film side incidence agree well with the above-mentioned pattern (Kumar, 1999).

6 Conclusions

We have measured the transmittance and reflectance of thin YBCO films deposited on transparent Si substrates in the far-infrared region at temperatures from 10 K to 300 K. The measurements show fringes caused by interference effects within the Si substrate. The change in the DC conductivity of the YBCO film with temperature causes a change in the reflection coefficient at the substrate-film interface, which results in a variation of the interference pattern. Matching of the admittance of the YBCO film with the refractive index of the Si substrate will yield a zero reflection coefficient at the substrate-film interface and thus eliminate the fringes in the measured transmittance. A change in the sign of the reflection coefficient results in a phase change of π rad in the interference pattern.

Sharp increases in the transmittance maxima in the superconducting state indicate that optical resonance has occurred within the film-substrate composite. The reflectance for radiation incident on the substrate increases significantly upon switching from the normal state to the superconducting state. These phenomena demonstrate that the HTSC thin films on transparent substrates can be used to build far-infrared devices, such as optical resonators and radiation modulators.

The transmittance and reflectance are calculated using the Drude model in the normal state and the two-fluid model in the superconducting state. The predicted values agree closely with the measured values using only a few adjustable parameters. The complex refractive index of the YBCO films is thus obtained at different temperatures. The imaginary part increases steeply as the superconducting state is reached but the real part shows a sudden decrease. The refractive index of YBCO films obtained from this study is important for the design of promising devices using HTSC thin films. Future research is needed to improve the quality of the YBCO films on Si substrates as well as the reproducibility of the deposition process. Methods for improving the radiometric accuracy in the spectrometric measurements with sharp interference fringes need to be further investigated.

Acknowledgments

This research was partially supported by the University of Florida through an Interdisciplinary Research Initiative (IRI) award, and the National Science Foundation through grants DMR-9705108 and CTS-9812027.

References

- Berberich, B., Chiusuri, M., Cunsolo, S., Dore, P., Kinder, H., and Varsamis, C. P., 1993, "Far-Infrared Spectra of Imperfect YBaCuO Films on Si Substrates," *Infrared Physics*, Vol. 34, pp. 269–279.
- Bonn, D. A., Dosanjh, P., Liang, R., and Hardy, W. N., 1992, "Evidence for Rapid Suppression of Quasiparticle Scattering below T_c in YBa₂Cu₃O_{7.8}," *Phys. Rev. Lett.*, Vol. 68, pp. 2390–2393.
- Chen, R. C., Wu, J. P., and Chu, H. S., 1995, "Bolometric Response of High- T_c Superconducting Detectors to Optical Pulses and Continuous Waves," *ASME JOURNAL OF HEAT TRANSFER*, Vol. 117, pp. 366–372.
- Choi, B. C., Zhang, Z. M., Flik, M. I., and Siegrist, T., 1992, "Radiative Properties of Y-Ba-Cu-O Films With Variable Oxygen Content," *ASME JOURNAL OF HEAT TRANSFER*, Vol. 114, pp. 958–964.
- Cunsolo, S., Dore, P., Lupi, S., Trippetti, R., Varsamis, C. P., and Sherman, A., 1993, "Infrared Conductivity of YBCO from Transmittance and Reflectance Spectra of Thin Films," *Physica C*, Vol. 211, pp. 22–28.
- Fenner, D. B., Li, Q., Hamblen, W. D., Johansson, M. E., Hamblen, D. G., and Lynds, L., 1993, "Optical and Thermal Performance Advantages for Silicon Substrates in YBCO Bolometer Devices," *IEEE Trans. Appl. Supercond.*, Vol. 3, pp. 2104–2106.
- Flik, M. I., Zhang, Z. M., Goodson, K. E., Siegal, M. P., and Phillips, J. M., 1992, "Electron Scattering Rate in Epitaxial YBa₂Cu₃O₇ Superconducting Films," *Phys. Rev. B*, Vol. 46, pp. 5606–5614.
- Fork, D. K., Fenner, D. B., Barrera, A., Phillips, J. M., Geballe, T. H., Connell, G. A. N., and Boyce, J. B., 1991, "Buffer Layers for High-Quality Epitaxial YBCO Films on Si," *IEEE Trans. Appl. Supercond.*, Vol. 1, pp. 67–73.
- Gao, F., Carr, G. L., Porter, C. D., Tanner, D. B., Etemad, S., Venkatesan, T., Inam, A., Dutta, B., Wu, X. D., Williams, G. P., and Hirschmugl, C. J., 1991, "Far-Infrared Transmittance and Reflectance Studies of Oriented Thin Films," *Phys. Rev. B*, Vol. 43, pp. 10,383–10,389.
- Gao, F., 1992, "Temperature Dependence of Infrared and Optical Properties of High Temperature Superconductors," Ph.D. dissertation, Department of Physics, University of Florida, Gainesville, FL.
- Genzel, I., Bauer, M., Yoder, R., and Habermeier, H.-U., 1992, "Far-Infrared Investigations on YBa₂Cu₃O₇ Films with the Use of a Reflection Fabry-Perot Interferometer," *Solid State Communications*, Vol. 81, pp. 589–592.
- Griffiths, P. R., and de Haseth, J., 1986, *Fourier Transform Infrared Spectrometry*, John Wiley and Sons, New York, Chapter 1.
- Grischkowsky, D., and Keiding, S., 1990, "THz Time-Domain Spectroscopy of High T_c Substrates," *Appl. Phys. Lett.*, Vol. 57, pp. 1055–1057.
- Hadni, A., Gerbaux, X., Cudraz, H. M., Tazawa, M., Mage, J. C., Marcilhac, B., Mercandalli, and Mansart, D., 1995, "Residual Losses of Superconducting Thin Films of YBa₂Cu₃O_{7.8} in the Far Infrared and Microwaves: Applications," *Physica C*, Vol. 245, pp. 219–230.
- Heavens, O. S., 1965, *Optical Properties of Thin Solid Films*, Dover, New York, Chapter 4.
- Kamarás, K., Herr, S. L., Porter, C. D., Tache, N., Tanner, D. B., Etemad, S., Venkatesan, T., Chase, E., Inam, A., Wu, X. D., Hegde, M. S., and Dutta, B., 1990, "In a Clean High- T_c Superconductor You Do Not See the Gap," *Phys. Rev. Lett.*, Vol. 64, pp. 84–87.
- Karrai, K., Choi, E., Dunmore, F., Liu, S., Ying, X., Li, Q., Venkatesan, T., Drew, H. D., Li, Q., and Fenner, D. B., 1992, "Far-Infrared Magneto-Optical Activity in Type-II Superconductors," *Phys. Rev. Lett.*, Vol. 69, pp. 355–358.
- Klein, M. V., and Furtak, T. E., 1986, *Optics*, 2nd Ed., John Wiley and Sons, New York, Chapter 5.
- Kumar, A. R., 1999, "Far-Infrared Radiative Properties of Superconducting YBCO Films Deposited on Silicon Substrates," Ph.D. dissertation, Department of Mechanical Engineering, University of Florida, Gainesville, FL.
- Loewenstein, E. V., Smith, D. R., and Morgan, R. L., 1973, "Optical Constants of Far-Infrared Materials, 2: Crystalline Solids," *Appl. Opt.*, Vol. 12, pp. 398–406.
- Malone, C. G., Zhang, Z. M., Flik, M. I., and Cravalho, E. G., 1993, "Optimized Design of Far-Infrared Fabry-Perot Resonators Fabricated from YBa₂Cu₃O₇," *IEEE Trans. Appl. Supercond.*, Vol. 3, pp. 2852–2855.
- Mechin, L., Villegier, J. C., Rolland, G., and Laugier, F., 1996, "Double CeO₂/YSZ Buffer Layer for the Epitaxial Growth of YBa₂Cu₃O_{7.8} Films on Si (001) Substrates," *Physica C*, Vol. 269, pp. 124–130.
- McKnight, S. W., Stewart, K. P., Drew, H. D., and Moorjani, K., 1987, "Wavelength-Independent Anti-Interference Coating for the Far-Infrared," *Infrared Physics*, Vol. 27, pp. 327–333.
- Phelan, P. E., Flik, M. I., and Tien, C. L., 1991, "Radiative Properties of Superconducting Y-Ba-Cu-O Thin Films," *ASME JOURNAL OF HEAT TRANSFER*, Vol. 113, pp. 487–493.
- Phelan, P. E., Chen, G., and Tien, C. L., 1992, "Thickness-Dependent Radiative Properties of Y-Ba-Cu-O Thin Films," *ASME JOURNAL OF HEAT TRANSFER*, Vol. 114, pp. 227–233.
- Phillips, J. M., 1996, "Substrate Selection for High-Temperature Superconducting Thin Films," *Journal of Applied Physics*, Vol. 79, pp. 1829–1848.
- Quinlan, S. M., Hirschfeld, P. J., and Scalapino, D. J., 1996, "Infrared Conductivity of $d_{x^2-y^2}$ -Wave Superconductor with Impurity and Spin-Fluctuation Scattering," *Phys. Rev. B*, Vol. 53, pp. 8575–8582.
- Renk, K. F., Betz, J., Schützmann, J., Prückl, A., Brunner, B., and Lengfellner, H., 1990, "Use of High T_c Superconductors for Far-Infrared Fabry-Perot Resonators," *Appl. Phys. Lett.*, Vol. 57, pp. 2148–2149.
- Renk, K. F., 1992, "Far-Infrared Spectroscopy of High Temperature Superconductors," *Studies of High Temperature Superconductors*, A. V. Narlikar, ed., Nova Science Publishers, New York, Vol. 10, pp. 25–62.
- Rice, J. P., Grossman, E. N., and Rudman, D. A., 1994, "Antenna-Coupled High- T_c Air-Bridge Microbolometer on Silicon," *Appl. Phys. Lett.*, Vol. 65, pp. 773–775.
- Tanner, D. B., and Timusk, T., 1992, "Optical Properties of High-Temperature Superconductors," *Physical Properties of High-Temperature Superconductors*, D. M. Ginsberg, ed., World Scientific Publishing Co., Singapore, Vol. 3, pp. 363–469.
- Varma, C. M., Littlewood, P. B., Schmitt-Rink, S., Abrahams, E., and Ruckenstein, A. E., 1989, "Phenomenology of the Normal State of Cu-O High-Temperature Superconductors," *Phys. Rev. Lett.*, Vol. 63, pp. 1996–1999.
- Virosztek, A., and Ruvalds, J., 1990, "Nested-Fermi-Liquid Theory," *Phys. Rev. B*, Vol. 42, pp. 4064–4072.
- Zhang, Z. M., Choi, B. I., Le, T. A., Flik, M. I., Siegel, M. P., and Phillips, J. M., 1992, "Infrared Refractive Index of Thin YBa₂Cu₃O₇ Superconducting Films," *ASME JOURNAL OF HEAT TRANSFER*, Vol. 114, pp. 644–652.
- Zhang, Z. M., and Flik, M. I., 1993, "Predicted Absorptance of YBa₂Cu₃O₇/YSZ/Si Multilayer Structures for Infrared Detectors," *IEEE Trans. Appl. Supercond.*, Vol. 3, pp. 1604–1607.
- Zhang, Z. M., and Frenkel, A., 1994, "Thermal and Nonequilibrium Responses of Superconductors for Radiation Detectors," *Journal of Superconductivity*, Vol. 7, pp. 871–884.
- Zhang, Z. M., Le, T. A., Flik, M. I., and Cravalho, E. G., 1994, "Infrared Optical Constants of the High- T_c Superconductor YBa₂Cu₃O₇," *ASME JOURNAL OF HEAT TRANSFER*, Vol. 116, pp. 253–257.
- Zhang, Z. M., Hanssen, L. M., Datla, R. U., and Drew, H. D., 1996, "An Apparatus for Infrared Transmittance and Reflectance Measurements at Cryogenic Temperatures," *International Journal of Thermophysics*, Vol. 17, pp. 1441–1454.
- Zhang, Z. M., 1998, "Far-Infrared Radiation Modulators Using High- T_c Superconductors," *ASME JOURNAL OF HEAT TRANSFER*, Vol. 120, pp. 24–29.

The Role of Bubble Waiting Time in Steady Nucleate Boiling

R. L. Judd

Department of Mechanical Engineering,
McMaster University,
Hamilton, Ontario L8S 4L7, Canada,
Mem. ASME

Experimental results previously reported by Ibrahim and Judd were examined in order to determine the role of bubble waiting time in steady nucleate boiling. The analysis identified that the time elapsed between the formation of bubbles at a nucleation site is the time required for the liquid which replaced the previous bubble to acquire sufficient energy to sustain the growth of the subsequent bubble, and not the time required to establish the conditions required to enable the nucleus, which formed at the nucleation site, to commence growing into a bubble.

Introduction

From the very earliest attempts to quantify nucleate boiling heat transfer, the importance of being able to predict the frequency of bubble formation at the boiling surface was recognized. When it was believed that the bubbles acted in isolation to promote the transfer of energy from the boiling surface, it was thought that the boiling heat flux was simply related to the product of the frequency of bubble formation, the number of active boiling sites per unit area, and the energy transferred by a single bubble as it moved away from the boiling surface. Subsequent research has revealed that this model of nucleate boiling heat transfer is overly simplistic in as much as bubbles interact in directions both parallel and perpendicular to the boiling surface to form vapor agglomerations, but it is still held that the frequency of bubble formation determines the rate at which bubbles promote the movement of energy away from the boiling surface.

The various theoretical heat transfer models, founded upon different perspectives of the nucleate boiling phenomenon, all require knowledge of the frequency of bubble formation. The bubble period, the inverse of the bubble frequency, is comprised of a growing period during which the bubble size increases and/or decreases until it departs from or collapses at the surface and a waiting period which it has been traditionally thought was determined by the necessity of reestablishing the conditions required for the initiation of the nucleus which appeared at the nucleation cavity after the departure or collapse of the preceding bubble.

$$f = 1/(t_g + t_w) \quad (1)$$

While there are a number of relationships capable of reliably predicting bubble growth and/or collapse for specified thermophysical properties, superheat, and subcooling such that the prediction of bubble growing period is not a problem, the prediction of bubble waiting period is a different matter.

Theoretical relationships capable of predicting the waiting period as a function of cavity radius, superheat, and subcooling based upon the thermodynamic conditions that have to be established in order to upset the stability of the nucleus can be derived from the theories of Hsu (1962) and Han and Griffith (1965).

Hatton and Hall (1966) published the results of an investigation that they performed into the frequency of bubble emission as a function of cavity radius obtained by boiling water on a stainless steel surface containing artificial nucleation cavities. Their experimental results showed that the frequency of bubble emission decreased markedly with increasing cavity radius. Good agreement was obtained between their predictions and results.

Singh, Mikic, and Rohsenow (1976) advanced a nucleation

model capable of predicting the waiting period as a function of cavity radius and superheat based upon the rate at which heat transferred from the surface surrounding the nucleation cavity to the liquid flowing into it after the departure of the preceding bubble would be able to convert the liquid to vapor. The waiting period was deemed to have ended when the rate of vapor generation caused the liquid penetrating the nucleation cavity to reverse direction. Experiments were performed in water boiling on a copper surface that contained artificial nucleation cavities drilled by a laser beam to test this model but poor agreement was observed.

The predictions of these relationships have been found to greatly underestimate the values of waiting time observed experimentally.

Effect of Subcooling on Bubble Growing and Waiting Time

Ibrahim and Judd (1985) presented the results of an experiment to investigate the growing and waiting time of bubbles forming in water boiling on a copper surface. The growth and departure or collapse of bubbles forming at seven different naturally occurring nucleation sites was studied in detail for different combinations of heat flux and subcooling. For each experiment performed, a conductance probe capable of sensing the presence of vapor or liquid at the location of the tip was located a small distance above the surface, and the signals corresponding to the growing and waiting times of 5000 successive bubbles were stored in a computer. The results of the analysis of the results obtained at nucleation site E at a heat flux of 166 kW/m² and various levels of subcooling ranging from 0 to 20°C is presented in Fig. 1.

The most curious aspect of the results is the manner in which the waiting time results varied with subcooling. Similar variations were found in the waiting time results obtained at the different nucleation sites under different combinations of heat flux and subcooling. As indicated in the figure, the variation of the growing time results with subcooling is in excellent agreement with the predictions of a theoretical model represented by Eq. (6) in that paper, but the variation of waiting time with subcooling was most unusual. The initial increase in waiting time with increasing subcooling is consistent with classical nucleation theory in as much as it is apparent that longer waiting times would be required to heat the liquid in the vicinity of a nucleation site to the condition at which a nucleation could occur. However, it was not possible to explain the apparent decrease in waiting time with increasing subcooling at the time that the paper was published.

Subsequent study of the experimental results presented by Ibrahim and Judd (1985) led to the conclusion that nucleation could not be the mechanism responsible for the initial increase in waiting time with increasing subcooling as had been claimed. As seen in Fig. 2, the waiting time measurements obtained during the formation of bubbles at Site E were almost independent of heat flux under nearly saturated boiling conditions. Nucleation theory would

Contributed by the Heat Transfer Division for publication in the JOURNAL OF HEAT TRANSFER. Manuscript received by the Heat Transfer Division, Aug. 12, 1998; revision received, June 30, 1999. Keywords: Boiling, Heat Transfer, Instrumentation, Two-Phase. Associate Technical Editor: P. S. Ayyaswamy.

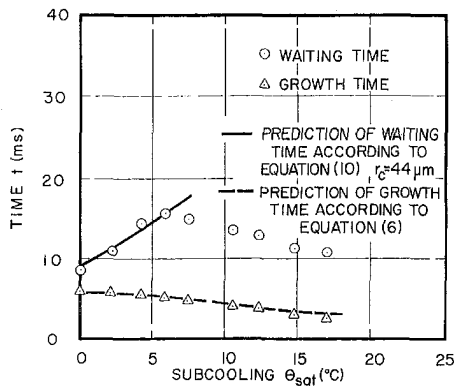


Fig. 1 Variation of waiting and growing times with subcooling for bubbles forming at Site E according to Ibrahim and Judd (1985)

have predicted that the bubble waiting time at the higher level of heat flux should have been much less than that at the lower level of heat flux in as much as the temperature of the liquid which replaced the previous departing bubble should have increased much more rapidly at the higher heat flux than at the lower heat flux and the conditions required for a nucleus to begin to grow into a bubble should have been established in a shorter period of time. Obviously, something other than nucleation theory is required to explain both the “upgoing” and “downgoing” waiting time results.

Interpretation of the Waiting Time Measurements

The waiting time measurements, and the growing time measurements, were obtained from analysis of the signals generated by a conductance probe located above an active nucleation site on the boiling surface. The process is depicted schematically in Fig. 3 along with a voltage signal typical of that produced by the conductance probe as a function of elapsed time. The sensing element was 0.020-in. diameter varnished copper magnet wire supported within a small stainless steel capillary tube which in turn was coaxially located in the conical tip of the conductance probe. The conductance probe was mounted on an X-Y stage capable of moving the sensing element over the boiling surface and positioning it at the locations where the formation of bubbles was the greatest which were deemed to be the nucleation sites.

The distance δ at which the tip of the sensing element was located above the boiling surface could be adjusted as well, but little control was exerted over this variable. From time to time, the varnish would chip off the magnet wire, requiring the sensing element to be repaired. Each time that this occurred, additional magnet wire was withdrawn from the conductance probe. The conductance probe was placed in a jig so that the wire could be cut with a sharp blade, such that the tip would be located no more than 1 mm above the boiling surface. It was thought that the voltage signal generated at this location would differ very little from that which would have been generated if the tip had been located right at the surface, so that the exact distance at which the tip of the

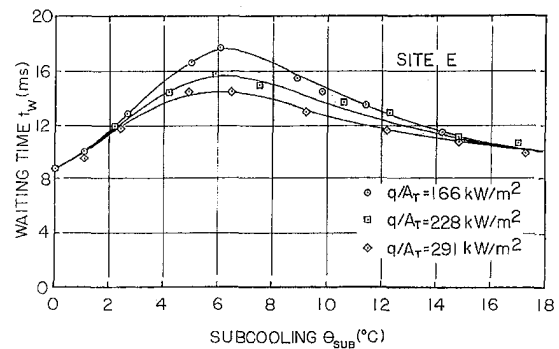


Fig. 2 Superposition of the waiting time measurements for bubbles forming at Site E for all levels of heat flux investigated

sensing element was located above the surface would not be important. This assumption turned out to be responsible for the incorrect interpretation of the experimental results reported previously in Ibrahim and Judd (1985) as will be explained below.

As depicted in Fig. 3, the voltage signal was high whenever liquid occupied the gap between the tip of the sensing element and the boiling surface and the voltage signal was low whenever vapor occupied the gap between the tip of the sensing element and the boiling surface. A voltage level was set in the manner indicated in the illustration to discriminate between these two states. A counter within the computer, which was started whenever the voltage signal went below the Schmitt trigger level, was zeroed and started again whenever the voltage signal went above the Schmitt trigger level. The number of counts accumulated while the signal was above or below the Schmitt trigger level, which is proportional to the waiting or growing times, respectively, was then transferred into memory. The process described was allowed to continue until stable average values of waiting and growing times had been obtained. These values were the results presented in Ibrahim and Judd (1985).

The proper interpretation of the results can only be realized with the help of a bubble growth model such as that of Mikic, Rohsenow and Griffith (1970) which is capable of predicting bubble radius as a function of growing time, waiting time and subcooling. Figure 4 depicts the variation of bubble radius $R(t)$ with elapsed time t for $\Theta_{sub} = 0^\circ\text{C}$, 2.7°C , 6.1°C , 11.4°C and 14.2°C at $q/A = 166 \text{ kW/m}^2$ and clearly distinguishes the bubbles which grow to departure size from those which collapse in place. While there is very little difference in the growing times at $\Theta_{sub} = 6.1^\circ\text{C}$ and $\Theta_{sub} = 8.9^\circ\text{C}$, the bubbles forming under these conditions end entirely differently. Failure to understand the way in which subcooling affects bubble growth was responsible for the incorrect interpretation of the values of bubble growing and waiting time reported in Ibrahim and Judd (1985).

The relationship between the variation of bubble radius and time and the apparent and actual growing and waiting times is shown schematically in Fig. 5. The uppermost diagram relates to bubbles that grew to departure size and the lowermost diagram relates to

Nomenclature

C_l = specific heat of the liquid
 f = frequency of bubble formation
 h_{fg} = latent heat of vapourization
 k_l = thermal conductivity of the liquid
 q/A_T = heat flux
 R = radius of a bubble
 t = elapsed time
 t_g = actual growing time
 t_p = time at which growth relationship peaks

t_w = actual waiting time
 t_1 = time at which bubble makes contact with probe
 t_2 = time at which bubble breaks contact with probe
 T_w = temperature of the boiling surface
 T_{sat} = saturation temperature
 T_∞ = temperature of the boiling liquid
 α_l = thermal diffusivity of the liquid

δ = distance of probe tip from boiling surface
 Θ_{sub} = liquid subcooling $\Theta_{sub} = T_{sat} - T_\infty$
 Θ_{sup} = liquid superheat $\Theta_{sup} = T_w - T_{sat}$
 ρ_l = density of the liquid
 ρ_v = density of the vapor
 τ_g = apparent (measured) growing time
 τ_w = apparent (measured) waiting time

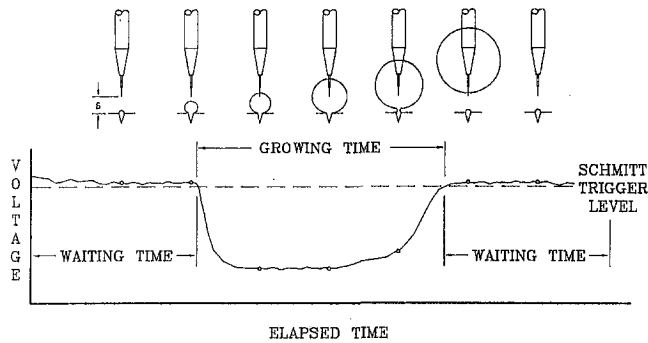


Fig. 3 Schematic representation of the operation of the conductance probe illustrating the variation of the voltage signal

bubbles that grew and collapsed in place. The dashed horizontal line represents the location of the tip of the sensing element of the conductance probe. For those bubbles that grew to departure size, the apparent growing and waiting times τ_g and τ_w are only slightly different than the actual growing and waiting times t_g and t_w , but for those bubbles that collapsed in place, the apparent growing and waiting times τ_g and τ_w are completely different than the actual growing and waiting times t_g and t_w .

The Physical Model

It is implicitly assumed in the theory underlying the Mikic, Rohsenow, and Griffith (1970) model that a nucleus, upon growing into a bubble, lifts the superheated liquid layer that formed at the boiling surface during the waiting period and pushes it ahead of it. The energy required for the bubble to continue to grow is derived from the superheated layer, and the rate at which the bubble grows is governed by the rate of energy transfer occurring at the liquid/vapor interface. So long as energy flows toward the liquid/vapor interface, the bubble will increase in size until it ultimately departs from the surface. However, if at any time energy should flow away from the liquid/vapor interface, the bubble will decrease in size until it ultimately collapses at the surface. Whether or not a reversal in the direction of energy flow at the liquid/vapor interface occurs before the bubble attains departure size will determine which course a bubble will take.

MIKIC ROHSENOW AND GRIFFITH SOLUTION SITE E

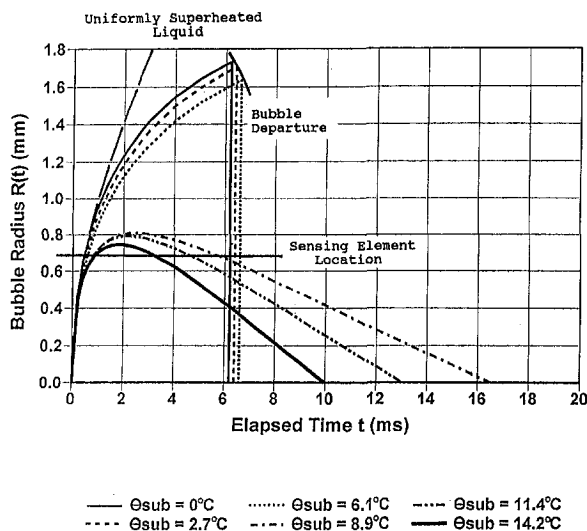


Fig. 4 Variation of bubble radius with time according to Mikic, Rohsenow, and Griffith (1970) for bubbles forming at Site E

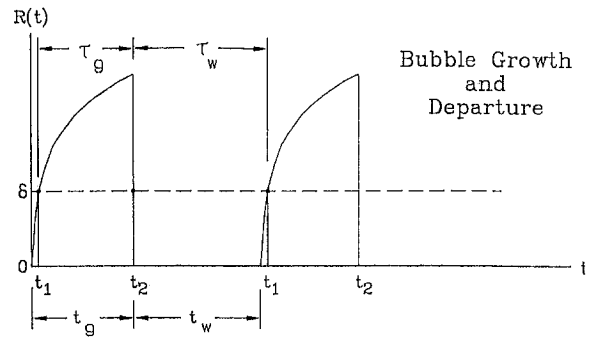


Fig. 5 Schematic representation of bubbles that departed from the surface and bubbles that collapsed at the surface

The following relationship was presented in Mikic, Rohsenow, and Griffith (1970) to predict the energy flow between the superheated liquid layer and the vapor/liquid interface per unit surface area

$$\frac{q(t)}{A} = \sqrt{3}k_l \left[\frac{\Theta_{sup}}{\sqrt{\pi\alpha_l t}} - \frac{\Theta_w}{\sqrt{\pi\alpha_l(t+t_w)}} \right] \quad (2)$$

Accordingly, it is apparent that the flow of energy between the superheated liquid layer and the vapor/liquid interface would reverse and the growing bubble would begin to collapse whenever

$$\left[\frac{\Theta_{sup}}{\sqrt{\pi\alpha_l t_p}} - \frac{\Theta_w}{\sqrt{\pi\alpha_l(t_p+t_w)}} \right] = 0 \quad (3)$$

$$\left(\frac{t_w}{t_p} \right) = \left(\frac{\Theta_w}{\Theta_{sup}} \right)^2 - 1 \quad (4)$$

The radius at which energy flow reversal occurs is predicted by

$$R(t_p) = 2 \sqrt{\frac{3}{\pi}} \frac{\rho_l C_l \Theta_{sup}}{\rho_v h_{fg}} \sqrt{\alpha_l t_p} \left\{ 1 - \frac{\Theta_w}{\Theta_{sup}} \left[\sqrt{1 + \frac{t_w}{t_p}} - \sqrt{\frac{t_w}{t_p}} \right] \right\} \quad (5)$$

according to the Mikic, Rohsenow, and Griffith (1970) relationship.

If the energy flow from the boiling surface to the superheated layer during the waiting time is exactly that required by the bubble to attain the radius at which the energy flow reversal occurs, then t_w/t_p will be equal to unity. As a consequence, whether or not a bubble ultimately grows to departure size or collapses to the size of a nucleus will be determined by the relationship

$$\Theta_w/\Theta_{sup} = \sqrt{2} \quad (6)$$

The dimensionless subcooling which distinguishes the conditions under which bubbles depart from the surface from those under which bubbles collapse is given by the relationship

$$\Theta_{sub}/\Theta_w = (\Theta_w - \Theta_{sup})/\Theta_w = 1 - 1/\sqrt{2} = 0.293 \quad (7)$$

DIMENSIONLESS WAITING TIME CORRELATION

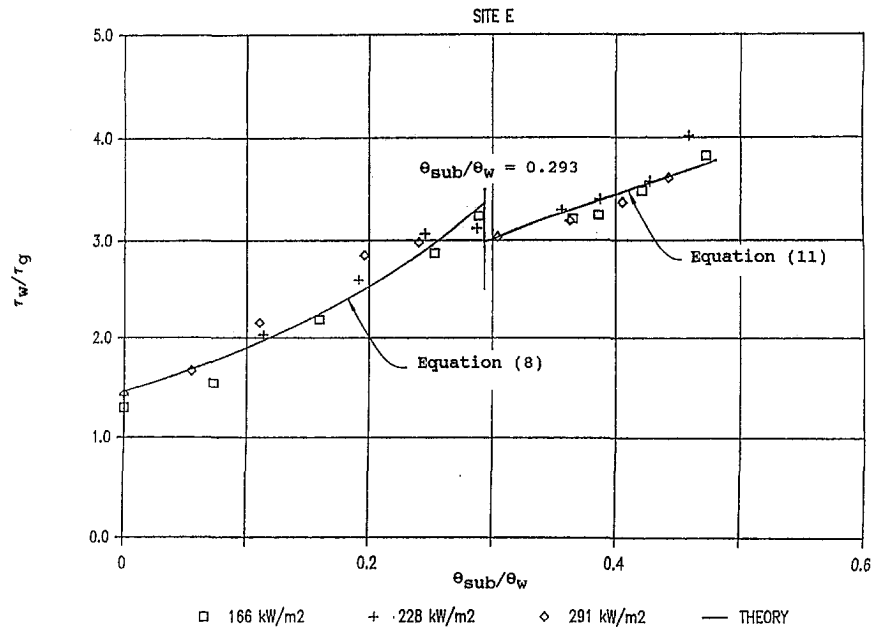


Fig. 6 Comparison of theoretical prediction of τ_w/τ_g as a function of θ_{sub}/θ_w with Ibrahim and Judd's (1985) experimental results

The remainder of the paper is devoted to demonstrating that this simple relationship is in fact substantiated by the results of Ibrahim and Judd (1985) in which it was observed that the apparent waiting time τ_w first increased and then decreased with increasing subcooling Θ_{sub} at constant heat flux q/A .

For those conditions under which the bubbles departed from the surface, the superheat Θ_{sup} and the time t at which the bubble made/broke contact with the tip of the sensing element at distance δ from the boiling surface combined together in such a way that $\Theta_{sup} \sqrt{t_1/\delta} = 15.165$ and $\Theta_{sup} \sqrt{t_2/\delta} = 21.382$. The apparent values of growing time and waiting time τ_g and τ_w , respectively, are related to (t_1/t_w) and (t_2/t_w) according to

$$\frac{\tau_w}{\tau_g} = \frac{t_w + t_1}{t_2 - t_1} = \frac{(t_w/t_w) + (t_1/t_w)}{(t_2/t_w) - (t_1/t_w)} = \frac{1 + (t_1/t_w)}{(t_2/t_w) - (t_1/t_w)} \quad (8)$$

where, in accordance with the Mikic, Rohsenow, and Griffith theory,

$$\left(\frac{t_1}{t_w}\right) = \tan \left[2 \arctan \left[0.122 \left(1 - \frac{\Theta_{sub}}{\Theta_w} \right) \right] \right]^2 \quad (9)$$

$$\left(\frac{t_2}{t_w}\right) = \tan \left[2 \arctan \left[0.377 \left(1 - \frac{\Theta_{sub}}{\Theta_w} \right) \right] \right]^2 \quad (10)$$

For those test conditions under which the bubbles collapsed at the surface, the relationship $(t_2 - t_1)/t_w = 0.0914(\Theta_{sub}/\Theta_w)^{-2.630}$ correlated the difference in the times at which the bubble made/broke contact with the tip of the sensing element $(t_2 - t_1)/t_w$ with the ratio Θ_{sub}/Θ_w . The apparent values of growing time and waiting time τ_g and τ_w are related to $(t_2 - t_1)/t_w$ according to

$$\frac{\tau_w}{\tau_g} = \frac{(t_w + t_g) - (t_2 - t_1)}{(t_2 - t_1)} = \frac{1 + (t_g/t_w)}{(t_2 - t_1)/t_w} - 1 \quad (11)$$

where, in accordance with the Mikic, Rohsenow, and Griffith theory,

$$\left(\frac{t_g}{t_w}\right) = \tan \left[2 \arctan \left[\left(1 - \frac{\Theta_{sub}}{\Theta_w} \right) \right] \right]^2 \quad (12)$$

The curves superimposed on the experimental results presented in Fig. 6 in the form of a plot of τ_w/τ_g versus θ_{sub}/θ_w for bubble formation at Site E are predicted by Eq. (8) and Eq. (11), respectively. The

favorable agreement between the experimental results and the predicted curves is corroboration of the validity of the analysis performed.

Concluding Remarks

The Mikic, Rohsenow, and Griffith (1970) bubble growth model assumes implicitly that the conditions for a nucleus to commence growing into a bubble have been satisfied. In the model, the waiting time is the time required for the liquid which replaced the previous bubble to acquire sufficient energy to sustain the growth of the subsequent bubble to be formed at this location. If in fact all bubble formation, growth, and departure or collapse in pool boiling behaved in this way as the analysis described above suggests, it must be concluded that bubble nucleation theory does not play a significant role in determining the frequency of bubble formation.

This conclusion does not infer that bubble nucleation theory is invalid because it is self-evident that there must be conditions that have to be satisfied for the nucleus that formed at the mouth of the nucleation cavity after the departure or collapse of the preceding bubble to commence growing. However, the implication is that the time required to satisfy these conditions is small with respect to the time required to create a superheated liquid layer containing sufficient energy to sustain the next cycle of bubble formation, growth, and departure or collapse. All of the existing nucleate boiling heat transfer models that depend upon the prediction of the frequency of bubble formation should be reviewed in the context of this new understanding of the phenomenon.

References

- Han, C. Y., and Griffith, P., 1965, "The Mechanisms of Heat Transfer in Nucleate Boiling—The Heat Flux Temperature Difference Relationship," *Int. J. Heat Mass Trans.*, Vol. 8, pp. 905–914.
- Hsu, Y. Y., 1962, "On the Size Range of Active Nucleation Cavities on a Heating Surface," *Transactions of the ASME*, Vol. 84, pp. 207–216.
- Ibrahim, E. A., and Judd, R. L., 1985, "An Experimental Investigation of the Effect of Subcooling on Bubble Growth and Waiting Time in Nucleate Boiling," *ASME JOURNAL OF HEAT TRANSFER*, Vol. 107, pp. 168–174.
- Mikic, B. B., Rohsenow, W. H., and Griffith, P., 1970, "On Bubble Growth Rates," *Int. J. Heat Mass Trans.*, Vol. 13, pp. 657–666.
- Singh, A., Mikic, B. B., and Rohsenow, W. M., 1976, "Effect of Superheat and Cavity Size on Frequency of Bubble Departure," *Transactions of the ASME*, Vol. 99, pp. 246–249.

Analysis of the Polarity Influence on Nucleate Pool Boiling Under a DC Electric Field

M. C. Zaghdoudi

Postdoctoral Fellow,
e-mail: chaker@cethil.insa-lyon.fr

M. Lallemand

Professor,
e-mail: m.lal@cethil.insa-lyon.fr

Centre de Thermique,
UPRESA CNRS 5008,
Institut National des Sciences Appliquées,
20 Av. Albert Einstein,
69621 Villeurbanne, France

An experimental study of the action of an intense electric field on the pool boiling of n-pentane is presented. By the application of a 25 kV/cm electric field strength, a threefold heat transfer enhancement is obtained. The effect of the electric field polarity has been researched. In nucleate boiling, the negative polarity allows to obtain a heat transfer enhancement, which is better than the one obtained in positive polarity. However, in natural convection and near the critical heat flux, the polarity of the electric field has a low influence on the heat transfer. The interpretations of the observed results are based on the action of the electric field on the boiling phenomenon and more particularly on the analysis of the electric field distribution between the electrodes. The influence of the space charge injection and the effect of the temperature on the electric field distribution have been investigated. The results obtained in the two cases of polarity are discussed in terms of effects of electrical and thermal phenomena on the distribution of the electric field between the electrodes.

1 Introduction

In many experiments on boiling heat transfer, a great enhancement of heat transfer has been observed by the application of an electric field. It is known that numerous mechanisms are responsible for this enhancement which depends on different parameters. This complex phenomenon depends on the electrical fluid properties such as the dielectric permittivity and the electrical conductivity. It also depends on electrical parameters such as the electric field strength, the electric field uniformity, which is determined by the geometry of the electrodes generating the electric field, the voltage period for AC electric fields or the polarity for DC electric fields.

The effect of the electric field polarity was outlined in some works. Olinger et al. (1971) reported the voltage polarity influence on the water boiling. For a negative voltage, they found that, for nucleate boiling, the overall effect of the applied voltage is always a decrease of the heated surface temperature. For a positive voltage, this effect depends on the quantity of current passing through the boiling water. For the film boiling regime, the results reveal that a negative applied voltage is much more effective for the destabilization of the vapor film than a positive voltage. According to Olinger, these phenomena are mainly due to a significant change in the surface wettability and to the charge accumulation in the vicinity of the surface that tends to counteract the dipole alignment of molecules and, thus, to destroy the nonwetting condition at the heated surface.

Schnurmann et al. (1972) studied heat transfer by convection for a thin wire in a liquid. They shown that the electric field polarity affects the magnitude of the heat flux enhancement in polar liquids but has no influence in ion-free liquids. The observed polarity effects, in presence of a minute concentration of ions, suggest that this could be an ion wind. Kawahira et al. (1990) reported experiments on the electric field polarity effects concerning boiling heat transfer of R-11. They found that a negative DC source is better for R-11 boiling. However, a positive DC source is preferable for a refrigerant-oil mixture. For cooling small heating elements, Hi-

jikata et al. (1994) found that the heat transfer enhancement is larger for negative than for positive applied voltages for a R-113-ethanol mixture but no polarity effects are observed for FC-72. The authors attribute the polarity effects to convection induced by ions exchange within the mixture. Takahashi et al. (1994) studied the enhancement of R-123 pool boiling heat transfer by utilizing electric fields. The polarity effects were studied for large and small electrical conductivities. For R-123, the enhancement effects of applying negative high voltages are negligible for nucleate boiling and are large near the critical heat flux.

Instead of many experimental results on polarity effects on boiling phenomenon, no quantified detailed explanations of these effects have been reported. In this paper, the effect of DC electric field polarity on the nucleate heat transfer is particularly analyzed in order to clarify the mechanisms governing these phenomena.

2 Experimental Apparatus

The experimental apparatus (Zaghdoudi, 1996) shown in Fig. 1 consists of a cylindrical glass tank closed at both ends by circular nylon flanges. The working fluid, chosen for the experimental investigation is the n-pentane, because of its dielectric properties and low toxicity. It is a nonpolar fluid which has a low relative dielectric permittivity ($\epsilon = 1.8$) and an electrical conductivity σ_e equal to $6.7 \cdot 10^{-9} \Omega^{-1} \cdot m^{-1}$. The horizontal heat transfer surface is the end of a copper rod of 3 cm in diameter and of 9 cm in length. It is polished with an emery paper No. 600 (30- μm roughness). Heat is supplied to the heat transfer surface by two electric resistances so that a heat flux of up to 115 W/cm² can be reached. A water-cooled condenser condenses the vapor generated from the boiling surface and the condensate naturally returns to the liquid pool by gravity. A heating coil wound around the glass enclosure is used to adjust the temperature of the working fluid. The electric field is applied by means of a high voltage DC power supply that provides voltages of up to 30 kV and DC currents of up to 5 mA. In order to have a uniform field, a flat-plane electrode configuration is used. The heating element used as one electrode is electrically grounded. The high-voltage electrode of either positive or negative polarity is made of a brass mesh (0.5-mm wire diameter, 2.5-mm width openings); its void percentage is about of 54 percent. The grid (6-cm diameter) can be moved up and down vertically by moving a supporting rod. Spacing between the electrodes

Contributed by the Heat Transfer Division for publication in the JOURNAL OF HEAT TRANSFER. Manuscript received by the Heat Transfer Division, Jan. 6, 1997; revision received, June 8, 1999. Keywords: Boiling, Electric Fields, Heat Transfer, Phase Change. Associate Technical Editor: J. Howell.

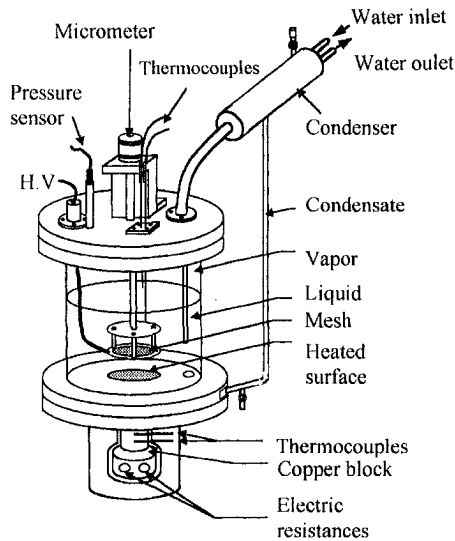


Fig. 1 Experimental apparatus

varies from 0.5 cm to 3 cm so the electric field strength can vary for an applied voltage. The accuracy on the high voltage is about ± 1 percent. Two thermocouples measure, respectively, the vapor and liquid temperatures. The liquid thermocouple is placed so that its measure is always the same as the vapor one. The copper block contains four thermocouples at different depth locations along its central axis providing temperature measurements for the wall temperature (by extrapolation of the linear curve until the heated surface) and the heat flux (deduced from the temperature variation slope). A numerical simulation achieved by finite element method shows that the temperature and the heat flux are uniform on the heated surface, so the heat transfer coefficient is almost constant for the whole surface. The heat transfer coefficient h is calculated using

$$h = \frac{q}{A \Delta T_{\text{sat}}} \quad (1)$$

where A is the heated surface area.

The 95 percent confidence uncertainty in the experimental result is given by the following equation:

$$\frac{\delta h}{h} = \sqrt{\left(\frac{\delta q}{q}\right)^2 + \left(\frac{\delta A}{A}\right)^2 + \left(\frac{\delta \Delta T_{\text{sat}}}{\Delta T_{\text{sat}}}\right)^2}$$

First, the absolute error on ΔT_{sat} is evaluated as follows:

$$\begin{aligned} \delta \Delta T_{\text{sat}} &= \sqrt{\left(\frac{\partial \Delta T_{\text{sat}}}{\partial T_w} \delta T_w\right)^2 + \left(\frac{\partial \Delta T_{\text{sat}}}{\partial T_{\text{sat}}} \delta T_{\text{sat}}\right)^2} \\ &= \sqrt{(\delta T_w)^2 + (\delta T_{\text{sat}})^2}. \end{aligned}$$

The absolute error on T_{sat} is $\delta T_{\text{sat}} = 0.4 + 0.0043|T|$ where T is the measured temperature. For n -pentane, at $P = 1$ bar which corresponds to $T_{\text{sat}} = 36^\circ\text{C}$, the absolute error is $\delta T_{\text{sat}} = \pm 0.5$ K. The absolute error on T_w can be evaluated from the measured temperatures inside the copper block. It depends on the temperature levels during the tests, so for low heat flux $\delta T_w = \pm 2$ K and for high heat flux $\delta T_w = \pm 1.5$ K.

The uncertainty of q , determined by a same manner, is ± 2 percent. The uncertainty on the surface area is ± 1 percent. Then, the uncertainty on the heat transfer coefficient is approximately ± 7 percent for high heat fluxes and ± 23 percent for the lower ones.

3 Experimental Results

Experimental tests have been carried out with saturated n -pentane (95 percent purity) at an average pressure of 1 bar, which corresponds to a saturation temperature of 36°C . The vessel is filled with n -pentane until the liquid-vapor interface is 9 cm above the heat transfer surface. Before starting experiments the fluid is degassed by boiling allowing the noncondensable gases to vent through the condenser. For each test run, the surface is heated sufficiently (95 percent of the critical heat flux) to degas the heating surface and the working fluid. The experiments are carried out as the high voltage is applied, after that the boiling curves are obtained for decreasing heat fluxes, starting at a value near the critical condition. Data, including current and voltage measurements, thermocouples readings and the vessel pressure, are recorded after the achievement of steady state.

3.1 Positive Polarity. The polarity of the upper electrode is positive with the heated surface electrically grounded. Boiling curves obtained, according to this polarity, are shown in Fig. 2 (Zaghdoudi, 1995). As the electric field strength is increased, the wall temperature decreases and the curves $q = f(\Delta T_{\text{sat}})$ are shifted towards the higher heat flux densities. For example, in nucleate boiling regime, with a 24 K superheat, a threefold increase in the heat transfer coefficient is obtained for 25 kV. The visual observations of the boiling phenomenon highlight three flow boiling regimes according to the applied high voltage. In zero-electric field conditions, isolated bubbles appear on the wall for a heat flux equal to approximately 5 W/cm^2 . Natural convection has still a major effect on heat transfer. For applied voltages lower than 10 kV ($E_o < 10 \text{ kV/cm}$), bubbles are weakly influenced by the electric field and the boiling phenomenon is similar to what is observed

Nomenclature

$a = (1/\sigma_e) \partial \sigma_e / \partial T, \text{ K}^{-1}$
 $b = (1/\epsilon) \partial \epsilon / \partial T, \text{ K}^{-1}$
 $d = \text{electrode gap, m}$
 $D = \text{electric induction, } \text{F} \cdot \text{V} \cdot \text{m}^{-2}$
 $E = \text{electric field, } \text{V} \cdot \text{m}^{-1}$
 $E_o = \text{applied electric field, } \text{V} \cdot \text{m}^{-1}$
 $f_v = \text{electric force, } \text{N} \cdot \text{m}^{-3}$
 $h = \text{heat transfer coefficient, } \text{W} \cdot \text{m}^{-2} \cdot \text{K}^{-1}$
 $j = \text{current density, } \text{A} \cdot \text{m}^{-2}$
 $q = \text{heat flux, } \text{W} \cdot \text{m}^{-2}$
 $q_v = \text{electric charge density, } \text{C} \cdot \text{m}^{-3}$
 $T = \text{temperature, K}$
 $T_o = \text{reference temperature, K}$
 $V = \text{voltage, V}$
 $V_o = \text{applied voltage, V}$

$z = \text{ascendant axis, m}$
Greek Symbols
 $\beta = \text{isobaric expansion coefficient, } \text{K}^{-1}$
 $\Delta T_{\text{sat}} = T_w - T_{\text{sat}}, \text{ K}$
 $\epsilon = \text{absolute dielectric permittivity, } \text{F} \cdot \text{m}^{-1}$
 $\epsilon_r = \text{relative dielectric permittivity}$
 $\epsilon_o = \text{vacuum dielectric permittivity, } \text{F} \cdot \text{m}^{-1}$
 $\delta = \text{thermal boundary layer thickness, m}$
 $\sigma_e = \text{electrical conductivity, } \Omega^{-1} \cdot \text{m}^{-1}$
 $\mu_e = \text{electrical charge mobility, } \text{m}^2 \cdot \text{V}^{-1} \cdot \text{s}^{-1}$

$\tau_e = \text{relaxation time, s}$
 $\tau_o = \text{relaxation time at } T_o, \text{ s}$
 $\rho = \text{density, } \text{kg} \cdot \text{m}^{-3}$
 $\xi = E(z=0)/E_o$
 $\psi = j/j_{\text{max}}$

Subscripts

$c = \text{collecting}$
 $C = \text{Coulomb}$
 $d = \text{dielectrophoretic}$
 $e = \text{electric}$
 $el = \text{electrostrictive}$
 $i = \text{injecting}$
 $w = \text{heated wall}$
 $\text{sat} = \text{saturation}$

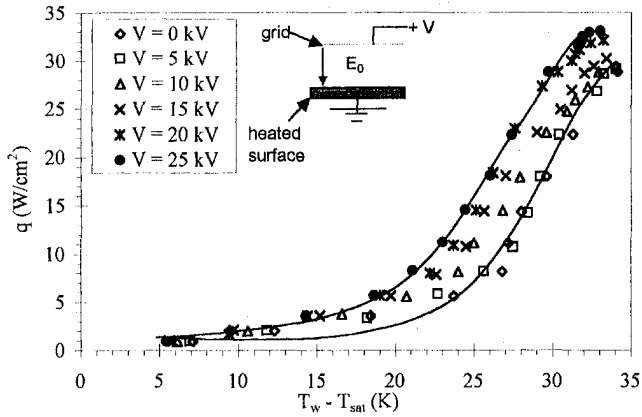


Fig. 2 EHD enhancement of boiling *n*-pentane (positive polarity)

without electric field. At high voltages, larger than 10 kV, the bubbles become smaller, their number increases and the convection due to their departure is higher.

3.2 Negative Polarity. During all these tests, the heated wall is still grounded and the mesh is connected to a negative potential so that the electric field direction is inverted, being oriented from the heated wall to the brass mesh. In Fig. 3 are shown the boiling curves obtained for a negative polarity for different high voltages equal to -5 , -10 , -15 , and -20 kV, respectively. From an overview of the data in Fig. 3, it is seen that the negative high voltages increase nucleate heat transfer. The shift of the boiling curves is greater for the lower voltages than that for the stronger ones. Figure 4 depicts the comparison of the critical heat fluxes obtained for positive and negative polarities. It appears that the critical heat flux increases with the applied voltage and the augmentation is nearly the same for both positive and negative polarities, as it will be explained later. Figure 5 shows the heat transfer coefficients as a function of the applied voltage for different heat fluxes. The asymmetry of the curves in comparison with zero-field conditions shows that the heat transfer coefficients obtained for a negative polarity are greater than those obtained for the positive one. In Fig. 6(a) and 6(b) are shown the ratio $h(V)/h(0)$ of heat transfer coefficients with and without electric field as a function of the applied voltage. At low heat fluxes, the heat transfer enhancement is almost the same for both polarities. In nucleate boiling regime, for example, $q = 14.4$ W/cm², the ratio increase is about 24 percent for $V = -20$ kV and 12 percent for $V = +20$ kV. The enhancement obtained for a negative polarity is then twice higher than for a positive polarity. For $q = 27$ W/cm², the enhancement for $V = -20$ kV is about 16 percent and 12 percent for $V = +20$

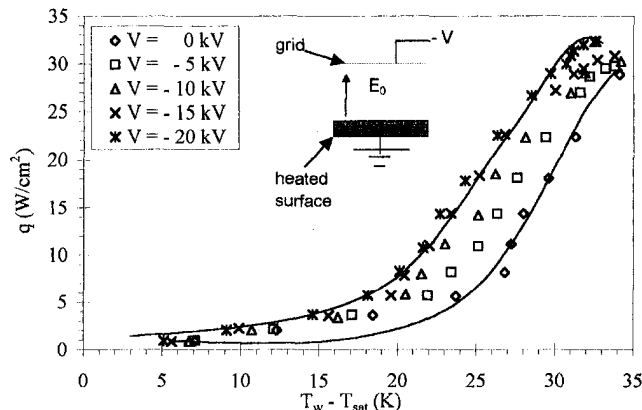


Fig. 3 EHD enhancement of boiling *n*-pentane (negative polarity)

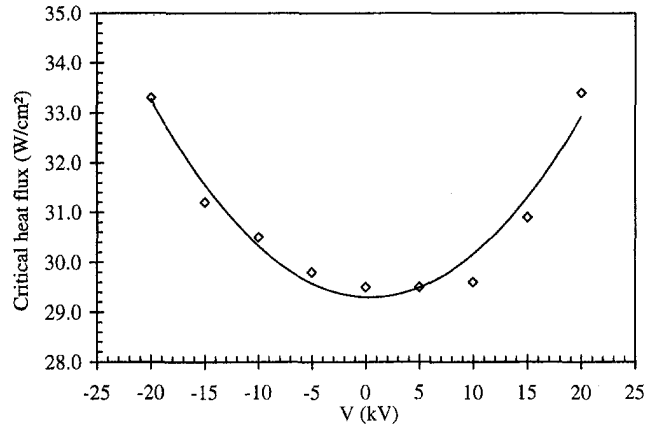


Fig. 4 Polarity effects on critical heat flux

kV. In both cases, the enhancement heat transfer ratio decreases when heat flux increases.

4 Analysis of the Experimental Results

The heat transfer enhancement is due, on one hand, to the electric volume forces in the bulk fluid, on the other hand, to the interfacial electric forces at the bubble interface. In this section, the electric volume forces effect is particularly analyzed. The electric forces within the dielectric fluid are given by

$$f_v = q_v E - \frac{1}{2} E^2 \text{grad } \epsilon + \frac{1}{2} \text{grad} \left(\rho \frac{d\epsilon}{d\rho} E^2 \right). \quad (2)$$

The first term is the Coulomb force exerted on the space electric charges in the dielectric fluid. The second term is the dielectrophoretic force due to the spatial gradient of the dielectric permittivity in the fluid. Physically, this force acts on polarization charges appearing in the dielectric medium under the electric field effect. The third term is the electrostrictive force caused on one hand, by the variation of the dielectric permittivity as a function of the density, on the other hand, by the nonuniformity of electric field in the medium. The analysis of the effect of f_v on the heat transfer rates requires the knowledge of the electric field distribution at the heat transfer surface. This distribution depends on the temperature gradient near the heated surface and on the electrical conduction, which is mainly due to electric charge injection from the electrodes.

4.1 Electric Field Distribution Between the Electrodes.

Space Charge Injection Effect on the Electric Field Distribution. For isothermal dielectric liquids of low electrical conductivity, the process of electric charge generation is referred as an injection

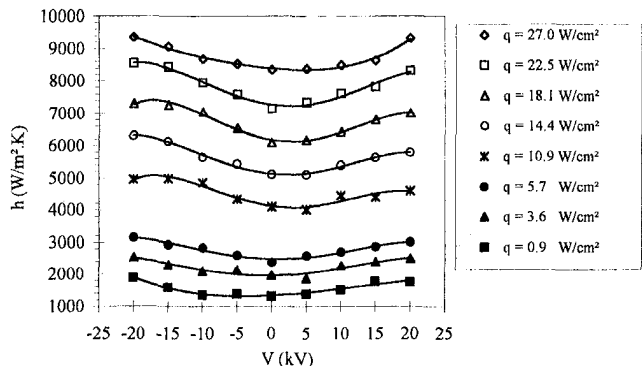


Fig. 5 Heat transfer coefficient versus the applied voltage for various heat fluxes

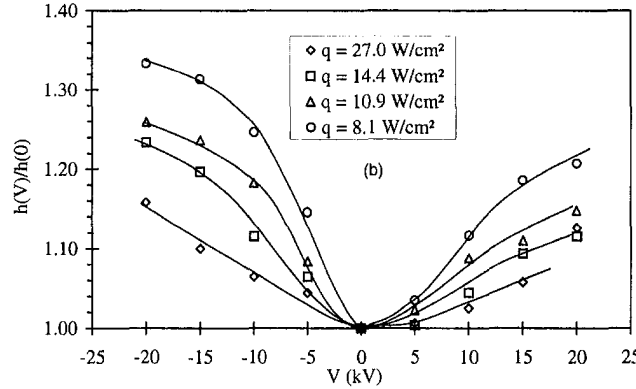
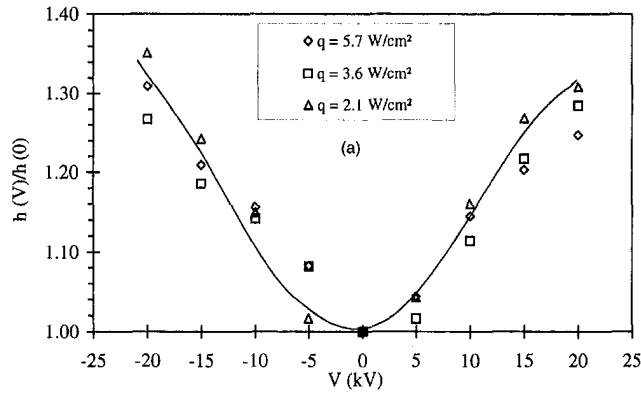


Fig. 6 Heat transfer coefficient ratios as a function of the applied voltage; (a) low heat fluxes, (b) high heat fluxes

phenomenon. This phenomenon does not result of any injection process at the electrodes but is due to the heterocharges appearing in the vicinity of the electrodes (MacCluskey et al., 1991). It results in an increase of the electric conduction within the liquid at strong electric fields and depends greatly on the liquid-electrodes system and on the electric field polarity. Indeed, in the case of a positive polarity, the heated surface is referred to the injecting electrode and the mesh to the collecting electrode (Fig. 7(a)). However, in the case of a negative polarity, the role of the electrodes is opposite (Fig. 7(b)). In an isothermal dielectric medium, the electric field is not uniform between the injecting and collecting electrodes. The electric field distributions between the electrodes for a positive polarity is given by

$$j = \sigma_e E + \mu_e q_v E$$

$$\text{div } \mathbf{j} = 0$$

$$\text{div } \mathbf{D} = \text{div } (\epsilon \mathbf{E}) = q_v. \quad (3)$$

Combining the set of Eqs. (3) yields

$$j = \frac{\mu_e \epsilon}{2} \frac{dE^2}{dz}. \quad (4)$$

Since μ_e and ϵ are constants for an isothermal medium and since the current density is constant (current conservation), Eq. (4) is a linear first-order differential equation with respect to z which can be solved analytically. So, the electric field distribution is

$$E = \left(\frac{2j}{\mu_e \epsilon} \right)^{1/2} (z + A)^{1/2}. \quad (5)$$

The constant A is determined by the following boundary condition:

$$\int_0^d E dz = E_0 d = V_0. \quad (6)$$

Equation (6) yields to an expression of the form

$$E_0 = \left(\frac{8jd}{9\mu_e \epsilon} \right)^{1/2} \left[\left(1 + \frac{A}{d} \right)^{3/2} - \left(\frac{A}{d} \right)^{3/2} \right]. \quad (7)$$

A is determined by a complete knowledge of E_0 , j and the electrical properties μ_e and ϵ of the dielectric medium. A particular case is $A = 0$ for which the electric field strength at the injecting electrode is zero. For this case, the current density reaches its highest value and is expressed by

$$j_{\max} = \frac{9}{8} \mu_e \epsilon \frac{E_0^2}{d} \quad (8)$$

By introducing the injection ratio $\Psi = j/j_{\max}$ and the ratio $\xi = E(z=0)/E_0$, Eqs. (5) and (7) can be written as

$$\frac{E}{E_0} = \left[\frac{3}{4} \psi(z/d) + \xi^2 \right]^{1/2}$$

$$\psi = (\psi + 4/9 \xi^2)^{3/2} - (4/9 \xi^2)^{3/2}. \quad (9)$$

By integration of Eq. (9), the electric potential is found to be

$$\frac{V}{V_0} = \frac{1}{\psi} \left\{ \left(\psi(z/d) + \frac{4\xi^2}{9} \right)^{3/2} - \left(\frac{4\xi^2}{9} \right)^{3/2} \right\}. \quad (10)$$

For a negative polarity, the boundary condition given by Eq. (6) is modified and the electric field distribution is given by

$$\frac{E}{E_0} = \left[\frac{3}{4} \psi(1 - (z/d)) + \xi^2 \right]^{1/2}. \quad (11)$$

The dimensionless electric field variations $E(z)/E_0$ are plotted in Fig. 8 as a function of the dimensionless electrode gap z/d for a positive polarity (Fig. 8(a)) and a negative polarity (Fig. 8(b)) corresponding to different injection ratios ψ . For both polarities, it can be seen that when the injection ratio increases the electric field near the injecting electrode decreases and becomes lower than the applied electric field E_0 , whereas near the collecting electrode the electric field is higher than E_0 . So, for a positive polarity, the electric field strength near the grounded wall is weaker than E_0 and, for a negative polarity, the electric field strength is weaker near the mesh. It can be also noticed that when the negative injected space charges in the dielectric increase ($\psi = 1$), the electric field approaches zero at the injecting electrode whereas at the collecting electrode the electric field is $1.5 E_0$.

Experimental results concerning the electrical potential distributions between two electrodes (electrode gap $d = 5$ mm) for a positive polarity have been obtained by Yabe et al. (1994) (Fig. 9). The electrical potential measurements in an isothermal dielectric medium (R-123) are deduced from the voltage-current characteristics of an electrostatic probe. The deviation from the uniform electric fields (dashed lines) depends on the applied voltage. Yabe et al. have suggested that negative charges are generated at the cathode and the area where the negative charges exist would be

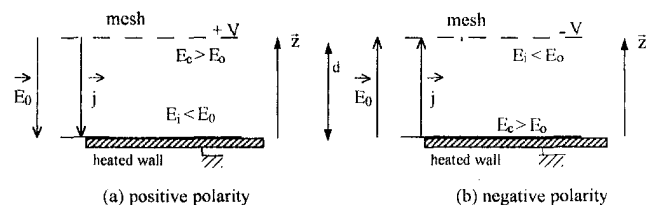


Fig. 7 Injection phenomenon in both positive and negative polarities

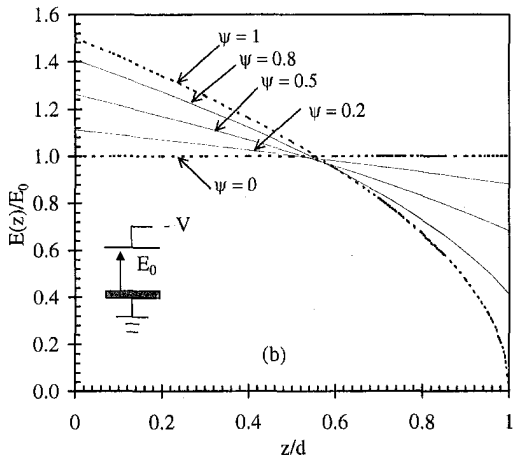
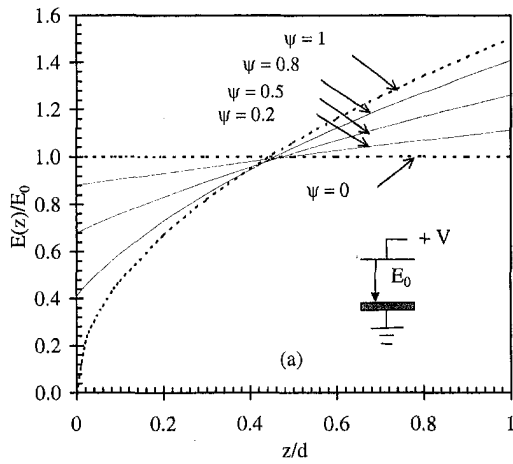


Fig. 8 Injection phenomenon effect on the electric field distribution

spread according to the injection phenomenon. Figures 10(a) and 10(b) compare the electrical potential variations between the electrodes determined by Eq. (10) to those determined experimentally by Yabe et al., for $V = 3$ kV and $V = 5$ kV, respectively. The injection ratios which are considered in the model are equal to 0.2 for $V = 3$ kV and 0.4 for $V = 5$ kV. As shown in Fig. 10, our results agree very well with those of Yabe et al.

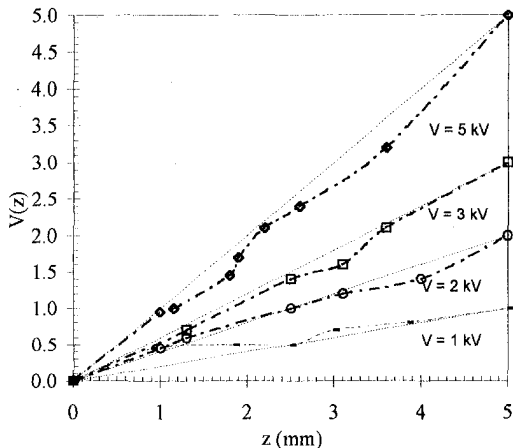


Fig. 9 Potential distribution in R-123 for positive polarity (Yabe et al., 1994)

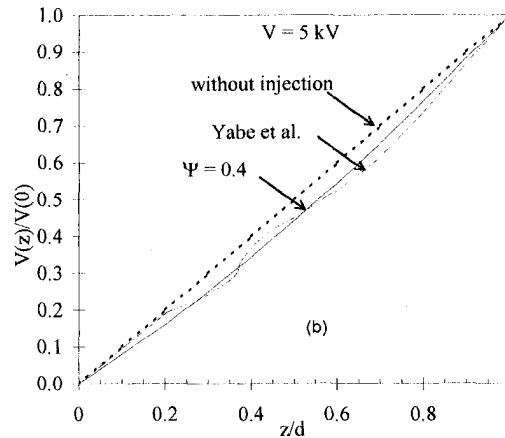
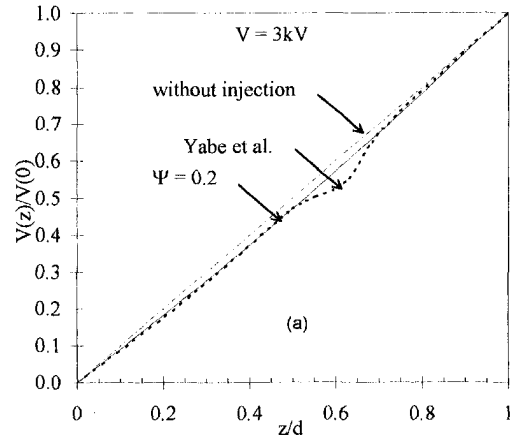


Fig. 10 Comparison between the theoretical results (Eq. (10)) and the experimental results (positive polarity) of Yabe et al. (1994)

The Temperature Gradient Effect on the Electric Field Distribution. For nonisothermal conditions, a thermal boundary layer appears near the heated wall and, far away from the heat transfer surface, the liquid is in saturation conditions. When an electric field is applied, a density of electric charges q_v appears within the thermal boundary layer. This charge depends on the dielectric permittivity and the electrical conductivity gradients due to the spatial temperature gradient. q_v is given by (Appendix A, Eq. (A2)):

$$q_v = \sigma_e \mathbf{E} \cdot \text{grad } \tau_e = \frac{1}{\tau_e} \mathbf{D} \cdot \text{grad } \tau_e \quad (12)$$

τ_e , the relaxation time of electric charges, is the ratio between the dielectric permittivity and the electrical conductivity. By assuming linear variations of σ_e with T , the relaxation time variations with temperature can be expressed as follows:

$$\tau_e = \frac{\epsilon}{\sigma_e} = \frac{\epsilon_0}{\sigma_{e0}} \frac{1 - b(T - T_0)}{1 + a(T - T_0)} = \tau_{e0} \frac{1 - b(T - T_0)}{1 + a(T - T_0)} \quad (13)$$

τ_{e0} is the relaxation time at the reference temperature T_0 . The electric charge density, which appears in the thermal boundary layer, is given by the following expression:

$$q_v = \frac{\epsilon}{\tau_e} \frac{d\tau_e}{dT} \frac{dT}{dz} (\mathbf{E} \cdot \mathbf{z}) = \frac{-(b+a)}{(1+a(T-T_0))(1-b(T-T_0))} \frac{dT}{dz} (\mathbf{E} \cdot \mathbf{z}) \quad (14)$$

For a positive polarity, q_v is negative (Fig. 11(a)) and it is positive for a negative polarity (Fig. 11(b)).

For a nonpolar dielectric liquid, the electric charges appearing in the thermal boundary layer result essentially from the electrical conductivity variations with the temperature because the dielectric permittivity gradient is negligible. These charges modify the distribution of electric field near the wall because the electric current must be constant. If a linear temperature profile within the thermal boundary layer is assumed, the electric field distribution between the electrodes is expressed by (Appendix A):

$$0 \leq z \leq \delta, \quad \frac{E}{E_o} = \frac{d}{\frac{1}{A_2} \ln \left(\frac{A_1}{A_1 - A_2 \delta} \right) + \frac{d - \delta}{A_1 - A_2} A_2 z} \quad (15)$$

$$z \geq \delta, \quad \frac{E}{E_o} = \frac{E(\delta)}{E_o}$$

δ is the thermal boundary layer thickness. A_1 and A_2 are defined by the following expressions:

$$A_1 = 1 - a(T_p - T_o)$$

$$A_2 = \frac{a \Delta T_{sat}}{\delta} \quad (16)$$

Plots of the dimensionless electric field variations E/E_o against the dimensionless electrode gap z/d for two values of the a/b ratio are shown in Figs. 12(a) and 12(b), respectively. The thermal boundary layer thickness is equal to $0.05 d$ (the electrode gap is 1 cm). For n -pentane, the dielectric permittivity coefficient b is equal to $0.16 \cdot 10^{-2} \text{ K}^{-1}$. According to these figures, the electric field strength decreases in the thermal boundary layer as the superheat ΔT_{sat} increases. Indeed, for $a/b = 5$, the electric field strength at the heated wall ($z = 0$) is equal to $0.88 E_o$ for a 20 K superheat. On the high voltage electrode mesh ($z = d$), the electric field strength is a little higher than the applied electric field strength E_o . For a/b equal to 10, the decrease of the electric field strength is higher than in the previous case. Since the dielectric permittivity coefficient is fixed, these results evidence the effect of the electrical conductivity coefficient that depends greatly on the purity of the working fluid. So, for a given superheat ΔT_{sat} , the electric field decrease is a result of an increase of the electrical conductivity coefficient a . These results do not depend on the electric field polarity, but only on the temperature gradient near the heated surface.

In conclusion, the electric field gradient between the electrodes can be explained in terms of electrical effects (injection phenomenon) and thermal effects. For a positive polarity, these two effects lead to a decrease of the electric field near the heat transfer surface. For a negative polarity, the thermal effects tend to decrease the

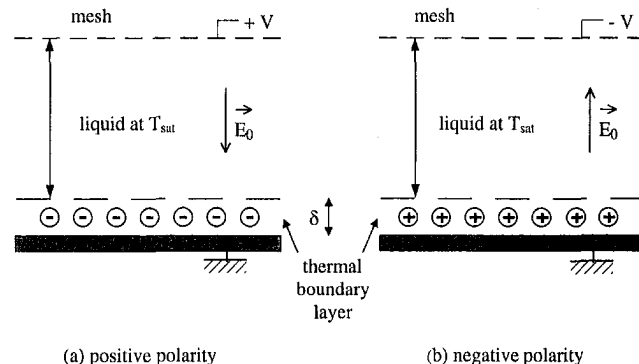


Fig. 11 Electric charge generation due to the temperature gradient within the thermal boundary layer

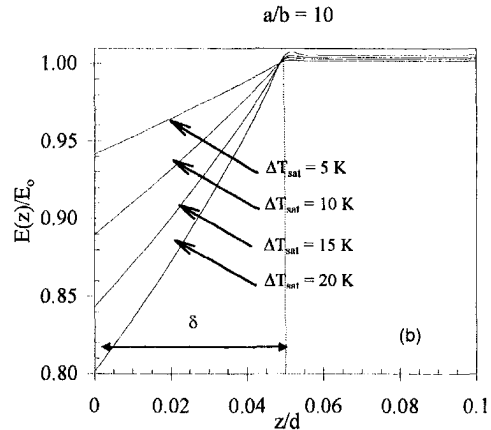
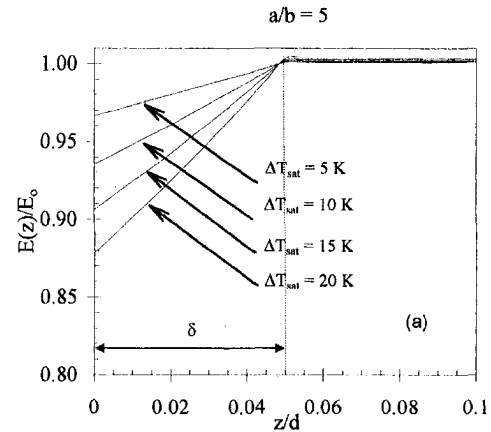


Fig. 12 $E(z)/E_o$ variations as a function of z/d for different superheats (positive polarity)

electric field strength near the wall whereas the electrical effects tend to improve it.

4.2 Study of the Electric Forces. Substituting Eq. (14) into the Coulomb term in Eq. (2) yields

$$\mathbf{f}_c = \frac{\epsilon E^2}{\tau_e} \frac{d\tau_e}{dT} \frac{dT}{dz} \mathbf{z} \quad (17)$$

This force is directed from the heat transfer surface to the fluid for both polarities. However, its intensity is higher for a negative polarity than for a positive polarity because the electric field strength is weaker for the positive polarity than for the negative one.

The sum of the dielectrophoretic and electrostrictive forces can be expressed as

$$\mathbf{f}_d + \mathbf{f}_{el} = -\frac{2(\epsilon - \epsilon_o)}{3\epsilon} E^2 \mathbf{grad} \epsilon + \frac{(\epsilon - \epsilon_o)(\epsilon + 2\epsilon_o)}{6\epsilon_o \epsilon^2} \mathbf{grad} D^2 \quad (18)$$

The first term on the right-hand side of Eq. (18) is a force \mathbf{f}_e depending on the dielectric permittivity variations with temperature and the second term is a force \mathbf{f}_D depending on the spatial electric field variations between the electrodes. In this equation, the dielectric permittivity gradient is written as follows:

$$\mathbf{grad} \epsilon = \left(\frac{\partial \epsilon}{\partial T} \right)_p \mathbf{grad} T + \left(\frac{\partial \epsilon}{\partial \rho} \right)_T \mathbf{grad} \rho \quad (19)$$

Using the temperature density variations ($\rho = \rho_o(1 - \beta(T - T_o))$) and the Clausius-Mossotti relation ($\rho \partial \epsilon / \partial \rho = (\epsilon - \epsilon_o)(\epsilon + 2\epsilon_o)/3\epsilon_o$), valid for nonpolar dielectric liquids whose the dielectric permittivity depends only on density and not on temperature, Eq. (19) can be expressed as

$$\text{grad } \epsilon = \left[\left(\frac{\partial \epsilon}{\partial T} \right)_\rho - \frac{\beta(\epsilon - \epsilon_o)(\epsilon + 2\epsilon_o)}{3\epsilon_o} \right] \frac{dT}{dz} \mathbf{z}. \quad (20)$$

Consequently, the components of the total force can be written as follows:

$$\mathbf{f}_\epsilon = \frac{2(\epsilon - \epsilon_o)}{3\epsilon} \left[- \left(\frac{\partial \epsilon}{\partial T} \right)_\rho + \frac{\beta(\epsilon - \epsilon_o)(\epsilon + 2\epsilon_o)}{3\epsilon_o} \right] E^2 \frac{dT}{dz} \mathbf{z} \quad (21)$$

$$\mathbf{f}_D = \frac{(\epsilon - \epsilon_o)(\epsilon + 2\epsilon_o)}{6\epsilon_o \epsilon^2} \frac{dD^2(z)}{dz} \mathbf{z} \quad (22)$$

Since the dielectric permittivity decreases when the temperature increases, the term between brackets of Eq. (21) is positive and consequently \mathbf{f}_ϵ is directed from the liquid to the boiling surface. As \mathbf{f}_D is a function of the electric induction gradient, it is a function of the applied electric field polarity. Indeed, if the polarity is positive, \mathbf{f}_D is directed from the heated surface to the fluid. For a negative polarity, the \mathbf{f}_D direction is opposite. So, for a negative polarity, \mathbf{f}_D and \mathbf{f}_ϵ directions are the same towards the heated surface. In Fig. 13 are shown the dimensionless electric forces

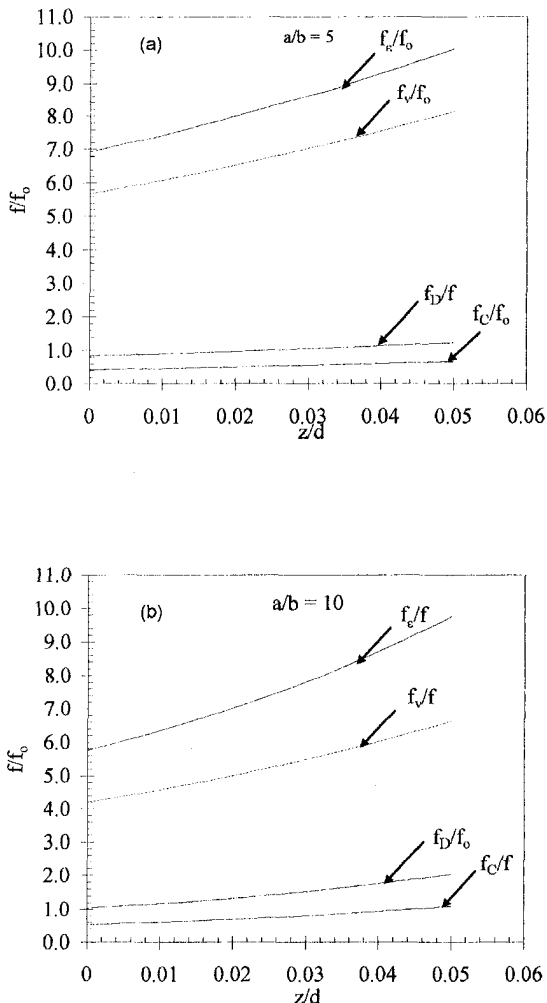


Fig. 13 Electric forces components as a function of z/d ($\Delta T_{\text{sat}} = 20 \text{ K}$)

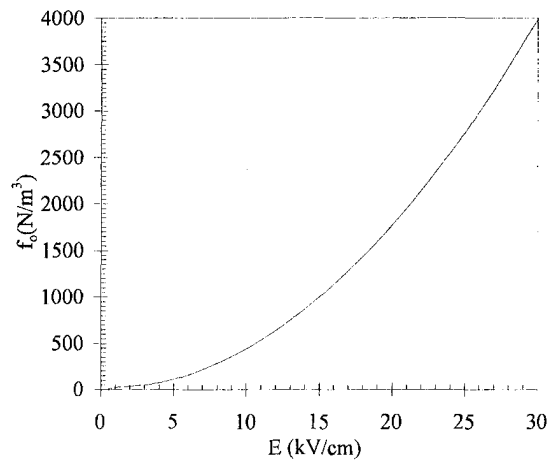


Fig. 14 f_o variations as a function of the applied electric field strength E_o

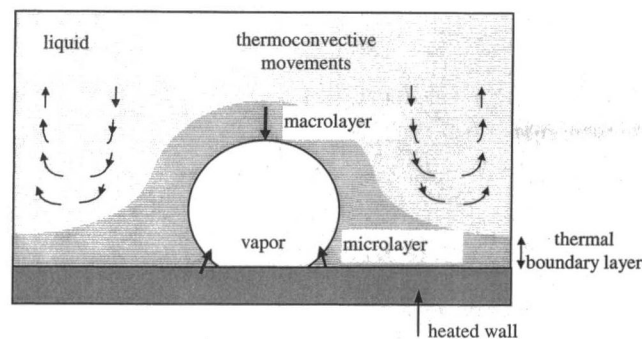
components f_c/f_o , f_e/f_o , and f_D/f_o as a function of the dimensionless electrode gap (z/d) for two a/b ratios equal to 5 and 10, respectively. The force f_o expressed by $\epsilon_o E_o^2/2d$ is the electric force exerted between the electrodes in the vacuum submitted to a uniform electric field. For a given a/b ratio, the different components are stronger far away from the heated wall. However, \mathbf{f}_ϵ decreases as the electrical conductivity coefficient increases whereas \mathbf{f}_c and \mathbf{f}_D strengths increase. Figure 14 shows the f_o variations versus the applied electric field E_o . For $E_o = 30 \text{ kV/cm}$, f_o is equal to 4000 N/m^3 . So, for a 20 K superheat, \mathbf{f}_ϵ is approximately equal to $28\,000 \text{ N/m}^3$ for $a/b = 5$ and about $24\,000 \text{ N/m}^3$ for $a/b = 10$.

4.3 The Effect of the Electric Forces on the Heat Transfer.

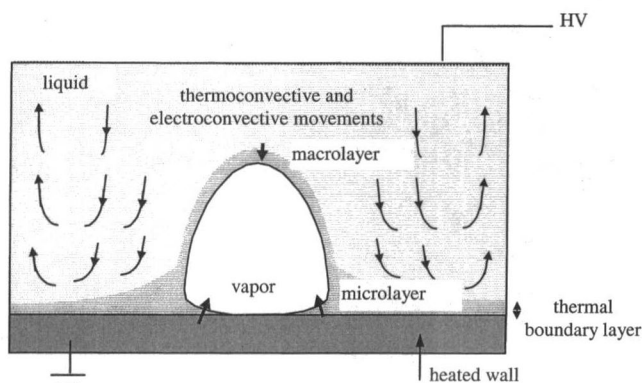
Case of a Positive Polarity. At low heat fluxes, the heat transfer mechanisms are governed by those of the natural convection. When an electric field is applied, the electric forces appearing within the thermal boundary layer have opposite effects. The Coulomb forces are directed from the heated surface towards the fluid and the sum of the dielectrophoretic and electrostrictive forces is directed towards the heated surface because the \mathbf{f}_ϵ strength is higher than the \mathbf{f}_D one. Moreover, the electric forces within the thermal boundary layer are weaker than those appearing far away from the heated surface due to a weaker electric field strength within the thermal boundary layer. This force difference induces an electroconvective movement, thus the thermal boundary layer is decreased and consequently the wall temperature too, when heat flux is imposed.

In nucleate boiling, the bubble growth is governed by the thermal conduction through the macrolayer surrounding the bubble and the evaporation of the microlayer lying between the bottom of the bubble and the heated surface (Fig. 15(a)). When an electric field is applied, the electroconvective movements appear not only between two bubbles but also around the bubble. Due to the electroconvective movements, the macrolayer thickness decreases and the heat transfer within the macrolayer is increased. The interfacial stresses acting on the bubble involve a deformation of its shape. The bubble shape becomes elongated along the direction of the electric field and is very close to that of a prolate spheroid. Due to the electric forces, the bubbles are pressed against the heat transfer surface, the effect of which is an intense evaporation of the microlayer (Fig. 15(b)). Consequently, the heat transfer enhancement through both macrolayer and microlayer causes a faster bubble growth, increasing their departure frequency. Thus, convective movements are more important and result in bubbles, which carry the heat away from the surface.

Case of a Negative Polarity. For a negative polarity, \mathbf{f}_D and \mathbf{f}_ϵ directions are the same, that is towards the heated surface. They



(a)



(b)

Fig. 15 Schematic of the heat transfer mechanisms; (a) without electric field; (b) with electric field

tend to press the bubbles against the heated surface, which results in a better evaporation of the microlayer located between the bubble base and the wall and leads to a faster growth of the bubble.

This analysis also explains the results obtained for low heat fluxes (natural convection) and high heat fluxes. Indeed, for the natural convection, the Coulomb forces are predominating. These forces, which are greater for a negative polarity than for a positive one, enable an increase of the electroconvective movements and consequently an improvement of heat transfer rates. For high heat fluxes, the bubbles coalesce to form large amounts of vapor. However, the rapid growth of the bubbles is limited by interfacial effects. Indeed, the liquid-vapor interface becomes unstable under the action of inertia and surface tension forces (Helmoltz instability). The presence of an electric field drastically modifies the liquid-vapor interface stability and the disturbance wavelength, which depends on the square of the applied electric field, decreases. So, the thermal performance obtained for a negative polarity and for a positive polarity are the same.

5 Conclusion

The purpose of this study was to investigate the effect of a uniform electric field on natural convection and boiling heat transfer for *n*-pentane. The experiments carried out on pool boiling heat transfer on a horizontal surface allow for a threefold heat transfer enhancement. The heat transfer enhancement is greater for natural convection heat transfer than for nucleate boiling. Moreover, it was found that the heat transfer coefficient enhancement decreases when heat flux approaches the critical condition. The polarity of the applied voltage affects the boiling heat transfer. For a negative polarity, the heat transfer enhancement is higher than the one

obtained for a positive polarity. The experimental result analysis is based on the study of the electric force effects. This has led to the analysis of the electric field distribution between the electrodes. It is shown that the electric field is affected by both the injection phenomenon (electrical effect) and the temperature gradient (thermal effect). Indeed, the electric field near the injecting electrode decreases when the injection ratio increases. The results obtained by the model agree with the experimental results of Yabe et al. (1994). The electric field strength decreases when the heated surface temperature increases. This decrease in the electric field strength depends greatly on the electrical conductivity variations with temperature.

References

- Hijkata, K., Kaneko, H., Ogawa, K., 1994, "Micro-scale Heat Transfer Augmentation by Applying Electric Field," *10th International Heat Transfer Conference*, Vol. 6, Brighton, UK, pp. 43–48.
- Kawahira, H., Kubo, Y., Yokoyama, T., Ogata, J., 1990, "The Effect of an Electric Field on Boiling Heat Transfer of Refrigerant 11—Boiling on a Single Tube," *IEEE Transactions on Industry Applications*, Vol. 26, No. 2, pp. 359–365.
- McCluskey, F. M. J., and Atten, P., 1991, "Heat Transfer Enhancement by Electroconvection Resulting From an Injected Space Charge Between Parallel Plates," *Int. J. Heat Mass Transfer*, Vol. 34, No. 9, pp. 2237–2250.
- Olinger, J. L., 1968, "A Study of Electrofluidmechanical Interactions in Boiling Heat Transfer," Ph.D. thesis, The University of Oklahoma.
- Schnurmann, R., and Lardge, M. G. C., 1973, "Enhanced Heat Flux in Non-uniform Electric Fields," *Proc. R. Soc. Lond.*, Vol. A334, pp. 71–82.
- Takahashi, K., Yabe, A., and Maki, H., 1994, "Electrohydrodynamical (EHD) Research of Saturated Pool Boiling Heat Transfer—Critical Heat Flux on Small Scale Surface and Measurement by Capacitance Probe," *10th International Heat Transfer Conference*, Vol. 5, Brighton, U.K., pp. 153–158.
- Yabe, A., Adachi, M., Katayama, T., and Nariai, H., 1994, "Augmentation Mechanism of Forced-Convection Heat Transfer by Applying Electric Fields in the Restricted Region Near the Wall," *10th International Heat Transfer Conference*, Vol. 5, Brighton, U.K., pp. 135–140.
- Zaghdoudi, M. C., Cioulachtjian, S., and Lallemand, M., 1995, "EHD Enhancement of Pool Boiling of Pentane on a Horizontal Copper Surface," *Two-phase Flow Modelling and Experimentation 1995*, Vol. 2, G. P. Celata and R. K. Shah, Ed. ETS, Rome, Italy, pp. 1075–1082.
- Zaghdoudi, M. C., 1996, "Amélioration des transferts de chaleur en ébullition sous l'action d'un champ électrique," Thèse de doctorat, INSA de Lyon, France.

APPENDIX

Temperature Gradient Influence on the Electric Field Distribution

From the current continuity and the electric induction equations (set of Eqs. (3)), we can write

$$\sigma_e \operatorname{div} \mathbf{E} + \mathbf{E} \cdot \operatorname{grad} \sigma_e = 0$$

$$\epsilon \operatorname{div} \mathbf{E} + \mathbf{E} \cdot \operatorname{grad} \epsilon = q_v. \quad (\text{A1})$$

From these equations, we obtain the following expression of q_v :

$$q_v = \frac{\sigma_e}{\epsilon} \mathbf{D} \cdot \left(\frac{1}{\sigma_e} \operatorname{grad} \epsilon - \frac{\epsilon}{\sigma_e^2} \operatorname{grad} \sigma_e \right) = \frac{1}{\tau_e} (\mathbf{D} \cdot \operatorname{grad} \tau_e). \quad (\text{A2})$$

By considering the ϵ and σ_e variations with temperature, Eq. (A2) can be written as

$$\begin{aligned} q_v &= \mp \frac{D}{\tau_e} \frac{d\tau_e}{dT} \frac{dT}{dz} \\ &= \mp \frac{(b+a)D}{(1+a(T-T_o))(1+b(T-T_o))} \frac{dT}{dz}. \end{aligned} \quad (\text{A3})$$

The sign (–) corresponds to the positive polarity and the sign (+) to the negative polarity.

The second equation in the set (A1) yields an expression of the form

$$\frac{\partial D}{\partial z} = \mp q_v = \frac{(b+a)D}{(1+a(T-T_o))(1+b(T-T_o))} \frac{dT}{dz}. \quad (\text{A4})$$

The following first-order ordinary differential equation is then obtained (case of a positive polarity):

$$\frac{\partial D}{D} = - \left(\frac{a}{1 + a(T - T_o)} + \frac{b}{1 - b(T - T_o)} \right) \frac{dT}{dz} dz. \quad (A5)$$

If a linear temperature profile is used, on the form

$$T = T_p - \frac{\Delta T_{\text{sat}}}{\delta} z, \quad (A6)$$

the following differential equation is obtained:

$$\frac{dD}{D} = - \left(\frac{-A_2}{A_1 - A_2 z} + \frac{B_2}{B_1 - B_2 z} \right) dz \quad (A7)$$

where

$$\begin{aligned} A_1 &= 1 + a(T_p - T_o) & B_1 &= 1 + b(T_p - T_o) \\ A_2 &= \frac{a \Delta T_{\text{sat}}}{\delta} & B_2 &= \frac{b \Delta T_{\text{sat}}}{\delta} \end{aligned}$$

Integrating Eq. (A7) yields an expression of the form

$$D = K \frac{B_1 - B_2 z}{A_1 - A_2 z}.$$

K is determined by the following boundary condition:

$$\begin{aligned} V_o &= E_o d = \int_0^d E dz = \int_0^d \frac{D}{\epsilon} dz \\ &= \int_0^\delta \frac{D}{\epsilon} dz + \int_\delta^d \frac{D(z = \delta)}{\epsilon(z = \delta)} dz. \end{aligned}$$

Thus, K is expressed as

$$K = \frac{\epsilon(T_o) E_o d}{(1/A_2) \ln(A_1/(A_1 - A_2 \delta)) + (d - \delta)/(A_1 - A_2 \delta)}$$

and the electric field variations between the electrodes are expressed in the following form:

$$\frac{E}{E_o} = \frac{K}{A_1 - A_2 z}.$$

Pool Boiling Critical Heat Flux in Reduced Gravity

D. P. Shatto

Exxon Production Research Company,
Houston, TX

G. P. Peterson¹

Associate Vice Chancellor and
Executive Associate Dean,
Engineering Program Office,
301 Wisenbaker Engineering Research Center,
Texas A&M University,
College Station, TX 77843-3126

An experimental investigation has been conducted to measure pool boiling critical heat fluxes in reduced gravity. A horizontal cylindrical cartridge heater immersed in water at reduced pressures during parabolic flights on NASA's KC-135 resulted in boiling on the heater surface. Visual observations and qualitative data trends indicate that the conventional Taylor-Helmholtz instability model still governs the critical heat flux mechanism over the range of gravitational accelerations of the current study, which range from $0.0005 < g/g_o < 0.044$. Using data from more than 40 individual tests, two semi-empirical correlations have been developed to account for the effect of thermocapillary flow, which tends to decrease the critical heat flux below the predictions of previous correlations.

Introduction

Two-phase heat transfer mechanisms in reduced gravity are of considerable practical interest in a number of space applications, including the design of spacecraft thermal control systems incorporating heat pipes or capillary-pumped loops, or the development of cryogenic storage and transport systems. In addition, future chemical and materials processing in microgravity environments may involve distillation or quenching, both of which employ gravity-dependent two-phase heat transfer processes. Though much has been learned from recent reduced-gravity experiments, which have examined nucleate pool boiling at low heat fluxes, as recently noted by Oka et al. (1992), we currently have no reliable means to predict critical heat flux (CHF) under microgravity conditions.

In addition to providing a means for accurately predicting CHF, studies in reduced gravity also provide information regarding the fundamental mechanisms of boiling, which may improve our understanding of two-phase heat transfer in terrestrial applications. Most models of boiling heat transfer and critical heat flux yield correlations that include gravity as a parameter. Predictions of pool boiling heat transfer coefficients which have exhibited the greatest versatility in terrestrial applications typically fail to accurately predict the relatively insensitive nature of heat transfer coefficients to variations in the local gravitational acceleration. Critical heat flux predictions, however, seem to predict the correct trends as the CHF decreases with decreasing gravity. Prior to the current investigation, the amount of reduced-gravity CHF data available has been insufficient to draw firm conclusions regarding the applicability of the current models. It has been assumed that the momentum and thermocapillary effects will overtake buoyancy as governing mechanisms in CHF as the local gravitational acceleration is reduced, but the relative significance of the gravity-dependence has not previously been adequately quantified.

The current experimental study seeks to add significantly to the available reduced-gravity critical heat flux data. Forty individual measurements of CHF conditions have been obtained using a horizontal cylindrical heater immersed in water at reduced pressure over a range of $0.0005 < g/g_o < 0.044$ obtained in parabolic flights aboard NASA's KC-135 aircraft. Although the data in this range of gravitational accelerations may not be directly applicable to the design of equipment for use in Martian or Lunar environments, comparison of these data with previous theoretical

CHF predictions will help elucidate the relative significance of thermocapillary flow and buoyancy in reduced gravity and will significantly enhance the general understanding of the factors that govern the critical heat flux mechanisms.

Hydrodynamic CHF Theory

The most widely accepted theoretical model for predicting critical heat flux in pool boiling is based on hydrodynamic instability between the liquid and vapor flowing in the vicinity of the heated surface. These fluid motions are driven by buoyancy, so the local gravitational acceleration appears as a parameter in CHF predictive correlations.

Figure 1 illustrates the idealized Taylor-Helmholtz instability mechanism associated with pool boiling critical heat flux on a horizontal flat plate. Columns of vapor rise from the heated surface at equally spaced nodes corresponding to the "most dangerous" wavelength of Taylor instability, λ_D . The radius of the vapor columns is assumed to be equal to one fourth of the Taylor node spacing. CHF occurs when the vapor jets become Helmholtz unstable at the wavelength λ_H which is assumed to be the same order of magnitude as λ_D . Growth of these waves on the liquid-vapor interface blocks liquid flow to the heated surface resulting in dryout and subsequent film boiling.

Zuber derived an expression for predicting the critical heat flux on infinite flat-plate heaters based on the limiting vapor flux required to trigger Helmholtz instability in the vapor columns:

$$\dot{q}_z'' = \frac{\pi}{24} \sqrt{\rho_v} \cdot h_{fg} [\sigma g (\rho_L - \rho_v)]^{1/4} \quad (1)$$

Lienhard and Dhir (1973) extended this predictive method to other finite geometries, such as cylinders and spheres, by imposing the requirement that the velocity in the vapor film at the onset of film boiling must match the velocity in the column of vapor in which the Helmholtz instability occurs. This analysis resulted in predictive correlations in which the ratio of the characteristic physical dimension of the heater (i.e., radius) to the bubble length scale (sometimes called the Laplace coefficient) appears as a nondimensional parameter. This term, R' , serves to account for the effects of changes in heater size:

$$R' \equiv R \sqrt{\frac{g(\rho_L - \rho_v)}{\sigma}} \quad (2)$$

For small cylinders ($R' < 1.0$):

$$\frac{\dot{q}_{1,D}''}{\dot{q}_z''} = \frac{0.94}{(R')^{1/4}} \quad (3)$$

¹To whom all correspondence should be addressed.

Contributed by the Heat Transfer Division for publication in the JOURNAL OF HEAT TRANSFER. Manuscript received by the Heat Transfer Division, Sept. 3, 1997; revision received, May 5, 1999. Keywords: Boiling, Bubble Growth, Microgravity, Two-Phase, Vaporization. Associate Technical Editor: M. Kaviany.

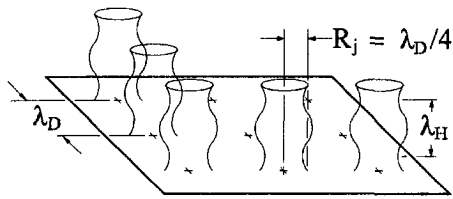


Fig. 1 Vapor columns on a heated surface

and for small spheres ($R' < 4.0$):

$$\frac{\dot{q}_{LD}''}{\dot{q}_Z''} = \frac{1.734}{\sqrt{R'}} \quad (4)$$

while for large spheres ($R' > 4.0$):

$$\frac{\dot{q}_{LD}''}{\dot{q}_Z''} = 0.84 \quad (5)$$

Upon application of this criterion to the original Zuber correlation and comparison with a broader range of data, Lienhard and Dhir also suggested a minor modification for the prediction of CHF on infinite flat-plate heaters:

$$\frac{\dot{q}_{LD}''}{\dot{q}_Z''} = 1.14 \quad (6)$$

Based on the available experimental data, these equations have been found to accurately correlate CHF down to $R' = 0.02$ (Straub et al., 1990).

The characteristic bubble dimension used in Eq. (2) is inversely proportional to the square root of the gravitational acceleration, and is intended to serve as an indicator of the relative size of the bubbles upon departure from the heated surface. In counter-weighted drop tower experiments, Siegel and Keshock (1964) found that the bubble departure diameter varied in proportion to $g^{-1/2}$. It seems appropriate then to treat the bubble length scale in the CHF correlations as a parameter which changes with variations in the local gravitational acceleration.

If the correlations by Lienhard and Dhir (1973) correctly predict the gravitational dependence of the critical heat flux, the CHF should be proportional to $g^{1/4}$ for flat plates and large spheres. Similarly, considering Eq. (1)–Eq. (4), the CHF should be proportional to $g^{1/8}$ for small cylinders, and should be independent of gravity for small spheres.

Previous Studies

Although there have been numerous studies of pool boiling in reduced gravity, the majority have not attained CHF due to the relatively limited power available from the test facilities. Table 1 lists the previous experiments which have measured and/or ob-

served critical heat flux conditions along with the test fluids, heater geometries, and means of obtaining the reduced-gravity environment. The range of conditions considered in previous studies is fairly broad, yet the total amount of data available is rather sparse. Several of these experiments obtained only one or two CHF values due to the limited scope typically associated with such studies. In addition, most recent studies have emphasized measurements of two-phase heat transfer coefficients at low heat fluxes and very low gravity levels (such as those attained in orbital flights or shielded drop towers) rather than critical heat flux mechanisms at intermediate gravity levels, which are the focus of the current study.

As noted in Table 1, various means of attaining a reduced-gravity environment have been employed in previous studies. Orbital or ballistic rocket flights offer true microgravity conditions for a lengthy duration, but are many times more expensive to design and operate than other techniques. A significant advantage of drop towers is their ability to produce steady, fractional-gravity conditions through the use of counterweights, as employed by Usiskin and Siegel (1961). Also, the gravitational field can be measured by observing the rate of descent, eliminating the need for accelerometers. Recent experiments by Abe et al. (1994) and Tokura et al. (1994) used the JAMIC 710 m drop shaft facility in Hokkaido, Japan which provides approximately 10.0 seconds of microgravity ($g/g_o = 10^{-5}$). Parabolic flights can provide microgravity conditions for approximately ten seconds if the apparatus can float freely in the aircraft. Fixed experiments such as the current study, can experience a broad range of gravitational accelerations lasting 25 seconds or longer, depending on the type of parabola flown. Parabolic flights generally have more electrical power available than the other reduced-gravity environments, and also allow researchers to directly observe and accompany experiments rather than to observe them remotely.

Figure 2 illustrates a plot of the ratio of the CHF measured in reduced gravity to that measured (or in some cases predicted) in a terrestrial gravitational environment using the same heater and test conditions. These data were obtained from the references listed in Table 1 and are classified according to the heater geometry. Lines corresponding to the $g^{1/8}$ and $g^{1/4}$ dependence of CHF associated with the Lienhard and Dhir (1973) predictions are also illustrated for clarification.

As illustrated, most of the previous cylinder CHF data closely follow the $g^{1/8}$ line, generally falling slightly below the trend predicted by Eq. (3). Similarly, the data obtained for large spheres tend to fall slightly below the $g^{1/4}$ trend. The sphere data at lower gravitational accelerations qualify as small spheres ($R' \leq 4.0$), and as expected, are not affected as much by variations in the local gravitational acceleration.

There are several possible explanations why the flat-plate data fall mostly above the predicted $g^{1/4}$ trend: First, the heaters used in all of the previous reduced gravity pool boiling CHF experiments do not qualify as “infinite” flat plates. To approximate an infinite flat plate experimentally, one must employ a plate with dimensions

Nomenclature

c, c_1 = dimensionless empirical constants
 E = energy (J)
 g = local gravitational acceleration (m/s^2)
 g_o = Earth gravitational acceleration ($9.81 m/s^2$)
 h_{fg} = enthalpy of vaporization (J/kg)
 k = thermal conductivity ($W/m \cdot K$)
 q'' = heat flux (W/m^2)
 R = heater radius (m)
 R' = dimensionless radius defined by Eq. (2)

T = temperature (K)
 z = distance from heated surface (m)

Greek

λ_D = “most dangerous” wavelength of Taylor instability (m)
 λ_H = wavelength of Helmholtz instability (m)
 Π_1 = dimensionless parameter defined by Eq. (19)
 ρ = density (kg/m^3)
 σ = surface tension (N/m)

Subscripts

CHF = critical heat flux
 g = associated with buoyancy
 L = liquid
LD = Lienhard and Dhir (1973) CHF prediction
tot = total
 v = vapor
 Z = Zuber CHF prediction
 σ = associated with thermocapillary forces

Table 1 Summary of reduced-gravity CHF studies

Study	Fluid	Heater Geometry	Reduced-g Test Platform
Usiskin and Siegel (1961)	water	horizontal wire	drop tower, 1.0 sec.
Merte and Clark (1964)	nitrogen	copper spheres	drop tower, 1.4 sec.
Zell et al. (1989)	R-12	wires	KC-135 parabolic flight
Merte (1990)	hydrogen	copper sphere	drop tower, 1.4 sec.
Straub et al. (1990)	R-113	wire & flat plate	TEXUS ballistic rocket
Abe et al. (1994)	water-ethanol mixture	flat plate	drop tower, 10.0 sec.
Tokura et al. (1994)	methanol	horizontal wires	drop tower, 10.0 sec.
Oka et al. (1995)	<i>n</i> -pentane, R-113	flat plate	Caravelle parabolic flight
Straub et al. (1996)	R-11	sphere (0.26 mm)	Space Shuttle (Spacelab)
Lee et al. (1997)	R-113	flat plate	Space Shuttle (GAS)
Current study	water	horizontal cylinder	KC-135 parabolic flight

significantly larger than λ_D with vertical side walls at the edge of the heater to prevent horizontal in-flow of liquid (Lienhard and Dhir, 1973). Smaller unconfined plates will exhibit higher critical heat fluxes than predicted by the infinite plate correlation. Also, at very low gravitational levels, the wavelength of Helmholtz instability may exceed the extent of the liquid pool, thereby disrupting the hydrodynamic mechanisms of CHF and invalidating the conventional model. Second, these data were obtained in environments in which the direction of the gravitational acceleration varies randomly. The conventional model assumes that the plate is pointing upward with gravity pulling bubbles directly away from the plate, whereas lateral accelerations may have significantly affected the previous reduced-gravity studies. Third, in the previous flat-plate experiments, gravity is so low that its effects may be virtually negligible compared to other forces. Straub (1993) proposed a "micro-wedge" model of pool boiling heat transfer in micro-gravity or zero-gravity fields in which thermocapillary convection, liquid momentum, and interfacial curvature effects combine to govern transient bubble growth and eventual dryout. Such considerations are probably relevant to the previous flat-plate data. Despite ongoing research which has successfully described some aspects of bubble behavior, the micro-wedge model has not yet been shown capable of accurate prediction of the critical heat flux.

Current Experimental Investigation

The Two-Phase Heat Transfer Laboratory at Texas A&M University has conducted an experimental investigation to measure and visually observe critical heat fluxes at reduced gravity environments. The experiments were performed aboard the KC-135 aircraft (NASA 931) operated by NASA Johnson Space Center's Reduced-Gravity Program at Ellington Field in Houston, Texas.

Experimental Apparatus. Figure 3 illustrates the experimental test chamber used in the current study. The test fluid (distilled water) was contained in a rectangular enclosure with a width of 203 mm, height of 152 mm, and internal depth of 76 mm. The top, bottom and sides were stainless steel, and the front and back were constructed of 12.7-mm-thick clear polycarbonate (Lexan) to allow visual observation of the boiling process. The critical heat flux experiments were performed with the cylindrical cartridge heater located approximately 60 mm above the center of the lower plate. A sheathed T-type thermocouple monitored the bulk liquid temperature at a location approximately 40 mm below the center of the upper plate. An absolute pressure transducer measured the fluid pressure at the same elevation as the heater.

The upper plate consisted of a hollow structure formed by stainless steel and copper plates bolted together with a porous

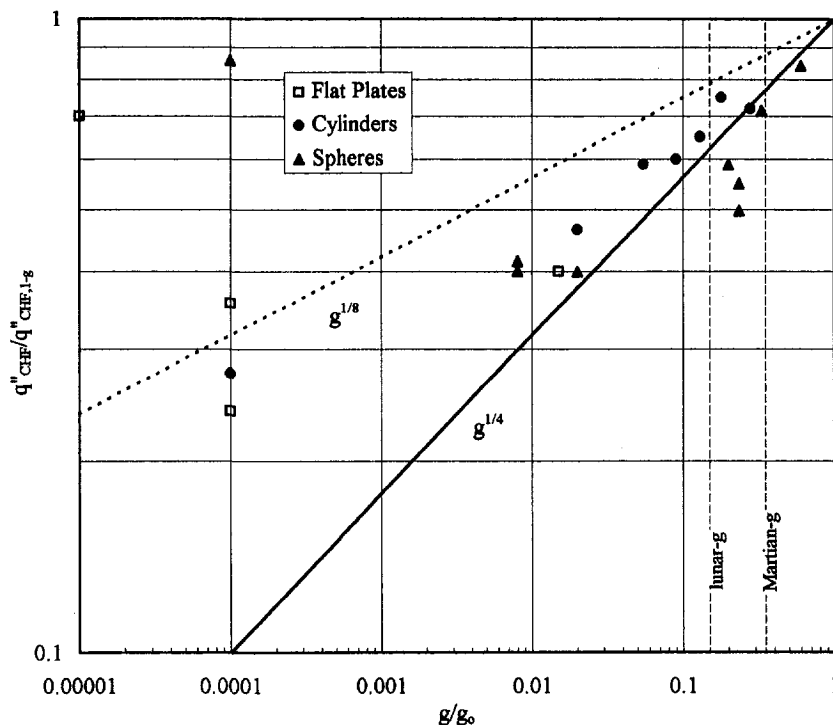


Fig. 2 Previous CHF data

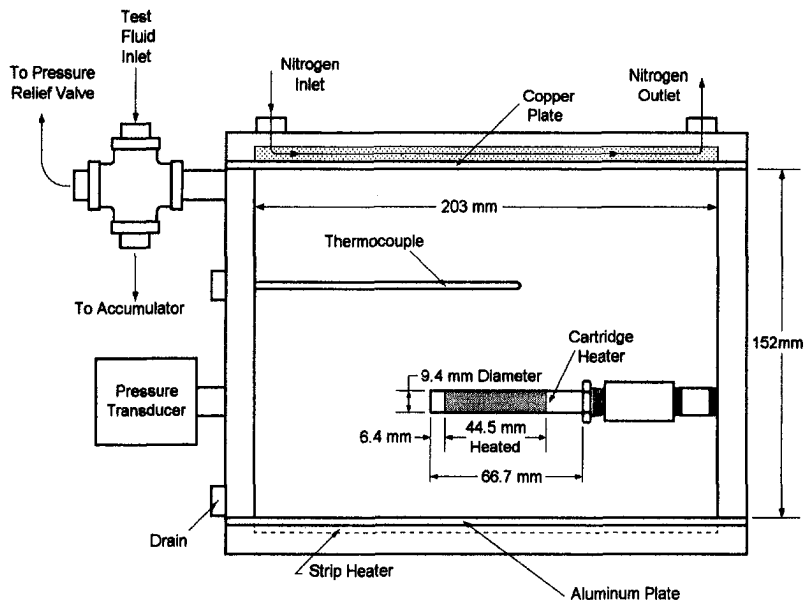


Fig. 3 Test chamber

copper medium sandwiched between them. This allowed the test apparatus to be cooled by passing liquid nitrogen through the upper plate assembly. The flow rate of the liquid nitrogen was adjusted manually to maintain the desired bulk fluid temperature. The test fluid was connected to a piston accumulator, which was in turn connected to a vacuum ejector powered by compressed air. This system maintained the test fluid at reduced pressures, and therefore reduced saturation temperatures, to meet NASA's safety requirements regarding the maximum allowable external surface temperature. The strip heater at the base of the test chamber was used in a previous reduced-gravity study (Shatto et al., 1996) which measured boiling heat transfer coefficients on the flat plate heater at heat fluxes near the onset of nucleate boiling.

The 500 Watt cartridge heater was used in the current CHF experiments. The heater consists of a Nichrome wire wound around a ceramic core covered with an Inconel-800 sheath. At the center of the heated section, a K-type thermocouple monitors the temperature of the ceramic core. This thermocouple is connected to a controller programmed to turn off the electric power to the heater if it exceeds a certain temperature.

The test chamber was mounted in an instrument rack and surrounded by digital panel meters that displayed the gravitational acceleration (as measured by the KC-135's accelerometer), temperatures of the cartridge heater and bulk liquid, pressure, and voltage applied to the cartridge heater. These data were recorded along with the visual observations of the boiling process by filming the front panel with an 8-mm video camera. This data acquisition method insured accurate temporal coordination between the visual observations and measured parameters.

Experimental Procedures. Critical heat flux experiments were conducted on three separate flights consisting of 40 to 45 parabolas each. The test apparatus was attached to the floor of the aircraft. The heater was turned on at 50 percent of its maximum power for approximately 20 minutes preceding the first parabola to heat the fluid to near the saturation temperature. Before the first parabola, the heater power was decreased to approximately two percent of full power. The heat flux was maintained at a constant level during each parabola, and CHF was obtained by gradual reduction of the gravitational acceleration. The voltage was then increased during each "pull-out" maneuver. Smaller power adjustments were made above the lowest heat flux at which CHF occurred, to measure the effect of gravity on the CHF.

The KC-135 normally flies in a trajectory which involves an

abrupt decrease in gravitational acceleration at the beginning of each reduced-gravity portion of the flight. In the current study, the aircraft entered each parabola gradually, so that the transition from the high-gravity "pull-in" maneuver to the desired reduced-gravity condition occurred over a time period of several seconds. Though this technique would result in less time for freely floating experiments, this slow gravity transient was beneficial to the current study, because it reduced the effects of residual buoyant convection and allowed a more precise measurement of the gravitational acceleration at which CHF occurred. CHF was detected visually as an abrupt transition from individual bubble departure to the formation of a thick, stable vapor film on the heater. The temperature excursion of the heater, though noticeable, did not occur rapidly enough to discern the precise conditions under which dryout began.

During some parabolas, the slow changes in gravitational acceleration during the middle portion of the parabola were large enough to cause rewetting of the heater surface. As the pilots corrected this gravitational "jitter" the CHF would occur again, thereby allowing the measurement of two CHF conditions in a single parabola. No systematic difference was noted between these data and the data associated with the pull-in transient. This indicates that the residual natural convection from the high-gravity pull-in maneuver did not significantly affect the measured values of CHF.

Results

Visual Observations. In the current experimental study, heat fluxes below the CHF resulted in the formation of individual bubbles on the cartridge heater which sprang from the surface in all radial directions, with the bubbles departure rate from the surface occurring at higher frequency as the heat flux was increased. Straub et al. (1996) referred to this phenomenon as "sparkling boiling." Tokura et al. (1994) also reported a very similar phenomenon.

Upon reaching the CHF the boiling process changed suddenly and dramatically. A thick, pulsating vapor film completely enveloped the heated portion of the cartridge heater, and visible observation of the radial ejection of small bubbles appeared to cease immediately. The CHF always occurred simultaneously over the entire heated portion of the cartridge heater. At high heat fluxes (above 200 kW/m²), where CHF occurred at relatively high grav-

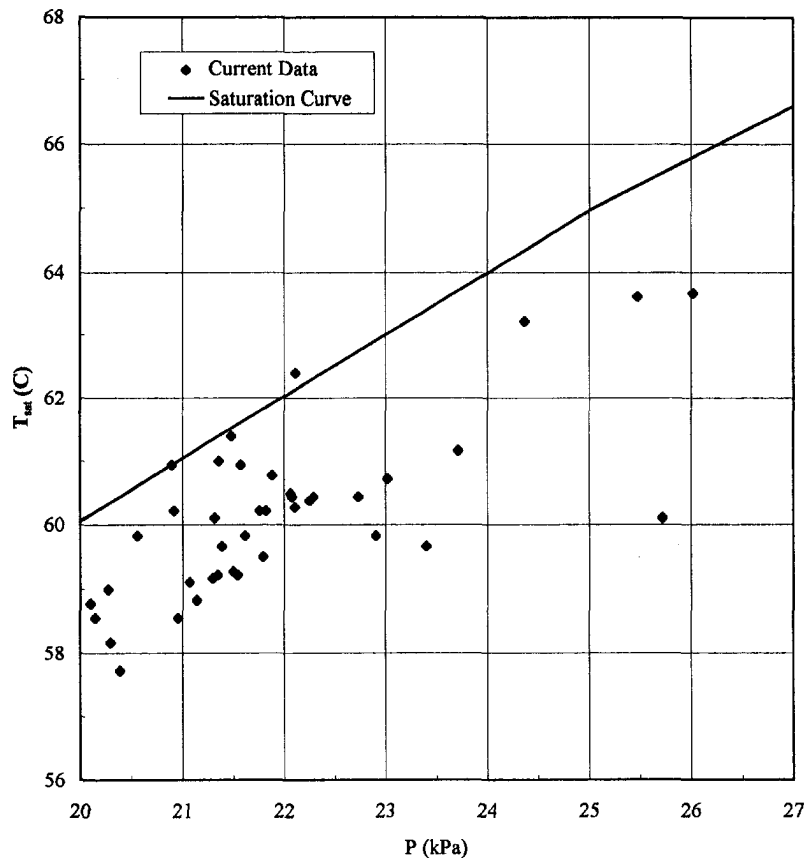


Fig. 4 Saturation state of data from the current experimental study

itational accelerations, the vapor film ejected columns of vapor at regular intervals, in keeping with the physical model of Taylor instabilities. The spacing between bubble departure nodes in stable film boiling is predicted by the "most dangerous" wavelength, λ_D , of Taylor instability, which is inversely proportional to the gravitational acceleration (as described below). Therefore, at lower gravitational accelerations, the interval between vapor columns would have been longer than the heater, so only one cohesive vapor bubble was observed. These observations agree with those of previous researchers, such as Tokura et al. (1994), who observed that at high heat flux, bubbles grew large and spherical and enveloped the wire. Usiskin and Siegel (1961) also found that the physical appearance of the film boiling regime was the same in reduced gravity as in terrestrial gravity, noting that the formation of bubbles at alternately spaced locations persisted for low-gravity fields. Similarly, in their parabolic flight experiments with a flat plate heater, Oka et al. (1995) noticed no difference in physical process toward the critical heat flux between $g/g_0 = 10^{-2}$ and terrestrial gravity. These observations tend to support the conclusion that the Taylor-Helmholtz instability model continues, to some extent, to govern the CHF at gravitational accelerations well below those of terrestrial conditions.

Saturation State. Forty individual instances of departure from nucleate boiling were recorded during the current experimental investigation. The measured pressures and bulk liquid temperatures associated with each CHF occurrence are plotted in Fig. 4 along with the saturation curve for water. Most of these data exhibit subcooling of less than 2.0 K. Considering these relatively low levels of measured subcooling and the proximity of the bulk temperature measurement to the upper cooling surface, it is reasonable to assume that the effects of liquid subcooling were negligible.

Gravitational Field Effects. In Fig. 5, the CHF values measured in the current study are plotted as a function of the local

gravitational acceleration. Also shown in this plot is the CHF prediction by Lienhard and Dhir (1973) for small cylinders evaluated for water at an average pressure of 22.0 kPa. (For the heater used in the current study $R' < 0.4$.) Though 40 CHF measurements were recorded, only 14 data points are shown in Fig. 5. For several heat flux levels, CHF values were obtained multiple times through repeated tests. As illustrated in Fig. 5 some points represent the average of several data at a single heat flux level. The horizontal error bars represent the scatter in these averaged data added to the $\pm 0.0005 \cdot g_0$ uncertainty of the accelerometer measurements. The vertical error bars represent the ± 2.8 percent uncertainty in the measured heat flux.

It is evident from Fig. 5 that the correlation by Lienhard and Dhir (1973) overpredicts the CHF with an average error of approximately 40 percent over the entire range of gravitational acceleration considered in the current study. This is consistent with most of the results from previous experimental studies, as shown in Fig. 2. Though the amount by which the Taylor-Helmholtz instability models overpredict the data is not alarming in light of the data scatter typically found in experimental two-phase heat transfer studies, the observation that this overprediction occurs consistently in several studies leads one to consider and identify other factors that may play a significant role in reduced gravity pool boiling.

Effects of Thermocapillary Flow

The reduction in CHF below the values predicted by conventional models, which has been observed in most experimental studies in reduced gravity fields, may be attributable to thermocapillary flow. The current study seeks a means of quantifying the relative effects of convection driven by surface tension gradients and buoyancy-driven convection.

Basic Mechanisms. A tangential force may be exerted at a liquid-vapor interface if the surface tension varies from point to

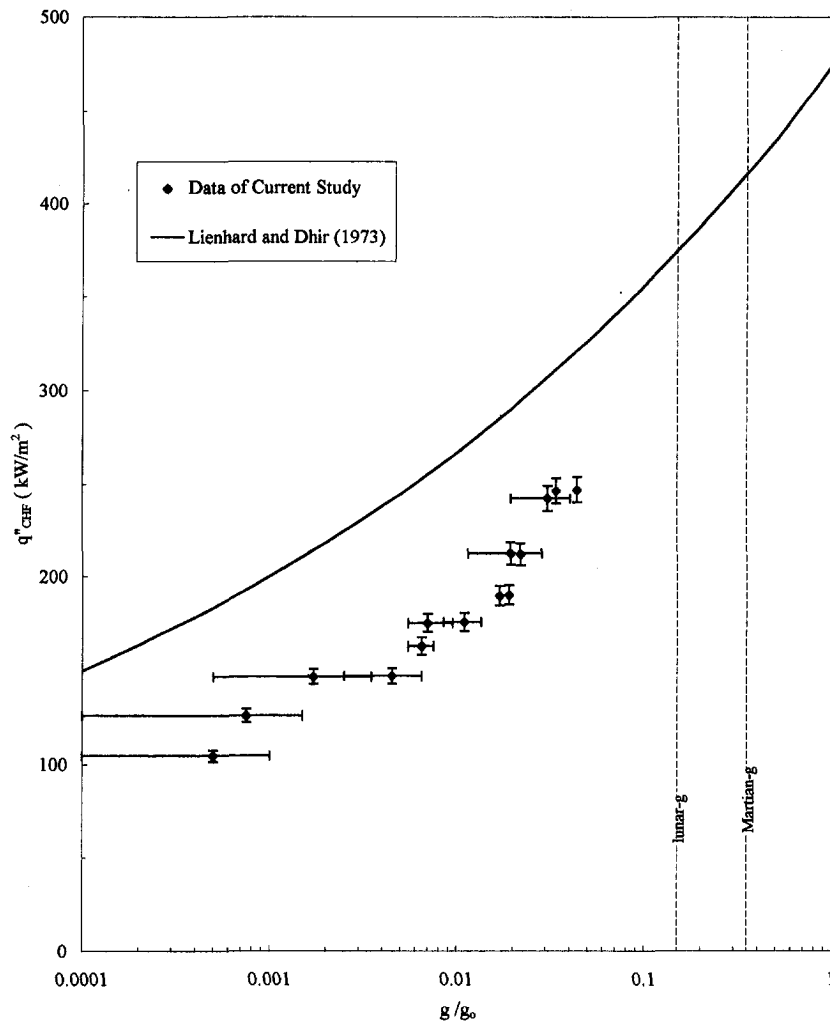


Fig. 5 Data of the current study

point. The magnitude of this force is proportional to the surface tension gradient and causes the fluid at the interface to move in the direction of increasing surface tension. For pure fluids surface tension decreases with increasing temperature, except for some liquid crystals and some metals (Legros et al., 1990). Abrupt temperature gradients associated with high heat fluxes can cause these thermocapillary forces to be quite large.

The qualitative effect of thermocapillary flow on the critical heat flux can be understood by considering a vapor bubble adjacent to a heated surface. Close to the surface, the high liquid temperature will result in a relatively low surface tension. The portion of the bubble's liquid-vapor interface that is most distant from the heated surface will encounter the lowest fluid temperature, and therefore will exhibit the highest surface tension. The fluid at the interface will be pulled toward the region of high surface tension, that is, away from the wall. Because the liquid has a much higher viscosity than the vapor, it has a greater tendency to move with the fluid at the interface. By pushing liquid away from the heated surface, the vapor bubble tends to be impelled toward the heated region. This force tends to counteract the bubble departure mechanisms, and would therefore reduce the CHF value.

Several researchers have alluded to the possible significance of thermocapillary flow in reduced-gravity boiling. Straub et al. (1990) observed that at low gravity levels surface tension and thermocapillary convection dominate the boiling mechanism. The same researchers also observed very strong thermocapillary convection around bubbles which enabled them, in terrestrial tests

with a flat plate oriented downward, to pump hot liquid from the boundary layer against the buoyancy force.

The Marangoni Effect in Mixtures. In many fluid mixtures, the surface tension is very sensitive to the relative concentration of the components. When a fluid mixture boils, the concentration varies along the liquid-vapor interface. The concentration of the more volatile component in the bulk liquid is greater than that near the heated surface. In many mixtures, the surface tension of the more volatile component is less than that of the less volatile component. This is sometimes called a "positive" mixture. In that case, the surface tension gradient pulls the liquid toward the heated wall.

It has long been known that the critical heat flux for "positive" mixtures may significantly exceed that for either pure component. Surface tension gradients due to composition gradients cause shear stresses that can enhance the flow and significantly affect the CHF. In a study seeking to quantify this effect, McGillis and Carey (1996) noted that gradients in temperature may also be expected to influence the CHF in an analogous manner. The qualitative effect of thermocapillary flow on CHF in most pure fluids would be the opposite of that exhibited by positive mixtures, but the means of quantifying these effects should be similar.

This enhancement of the CHF in binary mixtures has even been observed experimentally in reduced gravity. In experiments with mixtures of ethanol and water, Abe et al. (1994) noted that bubbles in mixtures detached immediately from the surface. The liquid layer was prevented from thinning by the liquid supplied to the

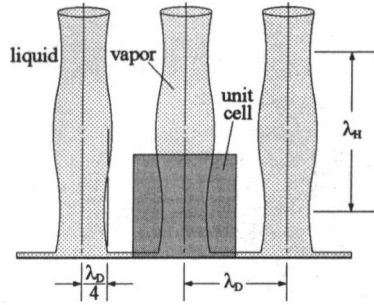


Fig. 6 Unit cell

bottom of the bubble, which was promoted by the Marangoni effect. The microgravity reduction in CHF in binary mixtures (20–40 percent) was considerably smaller than in pure fluids (50–85 percent).

Analysis of Thermocapillary Effects on Reduced-Gravity CHF. The theoretical development presented in the current study is analogous to the work of McGillis and Carey (1996) which quantified the influence of the Marangoni effect on CHF of binary mixtures in terrestrial conditions.

Figure 6 presents a side view of the vapor columns associated with the Taylor-Helmholtz instability CHF model. As in Fig. 1, the centers of the vapor columns are situated at the Taylor nodes spaced evenly at a distance of λ_D , and the column radii are one fourth of this interval. The current analysis considers the balance of gravitational potential energy, E_g , and energy associated with thermocapillary forces, E_σ , acting within the cubic unit cell control volume shown in Fig. 6, which has dimensions λ_D on each side, where

$$\lambda_D = 2\pi \left[\frac{3\sigma}{g(\rho_L - \rho_v)} \right]^{1/2} \quad (7)$$

The gravitational potential energy available within the unit cell to remove vapor from the heated surface can be expressed as

$$E_g = g(\rho_L - \rho_v) \cdot (\text{volume of vapor in unit cell}) \times \left(\frac{1}{2} \text{height of unit cell} \right).$$

Considering the unit cell and vapor column dimensions in Fig. 6, this becomes

$$E_g = g(\rho_L - \rho_v) \left(\frac{\pi \lambda_D^3}{16} \right) \left(\frac{\lambda_D}{2} \right). \quad (8)$$

If one assumes, as a rough approximation, a uniform temperature gradient within the unit cell, the potential energy associated with the thermocapillary stress at the liquid-vapor interface can be expressed as

$$E_\sigma = \frac{d\sigma}{dT} \cdot \frac{dT}{dz} \cdot (\text{cell height}) \cdot (\text{column surface area}).$$

Again, considering the unit cell dimensions in Fig. 6, this becomes

$$E_\sigma = \frac{d\sigma}{dT} \cdot \frac{dT}{dz} \cdot \lambda_D \cdot \left(\frac{\pi \lambda_D^2}{2} \right). \quad (9)$$

Applying an additional assumption that the heat transfer due to conduction in the liquid will be some constant fraction of the total heat flux, the temperature gradient can be approximated as

$$\frac{dT}{dz} = \frac{-c\dot{q}''}{k_L}. \quad (10)$$

The energy per unit cell associated with surface tension then becomes

$$E_\sigma = - \left(\frac{c\pi\lambda_D^3}{2} \right) \frac{d\sigma}{dT} \cdot \frac{\dot{q}''}{k_L}. \quad (11)$$

The forces associated with gravity and surface tension work against each other, so

$$E_{\text{tot}} = E_g - E_\sigma = \frac{\pi\lambda_D^4}{32} g(\rho_L - \rho_v) + \frac{c\pi\lambda_D^3}{2} \cdot \frac{d\sigma}{dT} \cdot \frac{\dot{q}''}{k_L}. \quad (12)$$

Expressing the conventional CHF prediction by Zuber from Eq. (1) in terms of the gravitational potential energy defined in Eq. (8) yields

$$\dot{q}''_Z = \frac{\pi}{24} \rho_v h_{fg} \left[\frac{32\sigma E_g}{\pi \rho_v^2 \lambda_D^4} \right]^{1/4}. \quad (13)$$

In the current model, to consider the effects of thermocapillary flow, E_{tot} from Eq. (12) replaces E_g in Eq. (13). Performing this substitution and expanding the terms yields

$$\dot{q}''_{\text{CHF}} = \frac{\pi}{24} \rho_v h_{fg} \left[\frac{\sigma g(\rho_L - \rho_v)}{\rho_v^2} + \frac{16c\sigma}{\rho_v^2 \lambda_D} \cdot \frac{d\sigma}{dT} \cdot \frac{\dot{q}''}{k_L} \right]^{1/4}. \quad (14)$$

Factoring out the left-hand term in the brackets gives

$$\dot{q}''_{\text{CHF}} = \frac{\pi}{24} \rho_v h_{fg} \left[\frac{\sigma g(\rho_L - \rho_v)}{\rho_v^2} \right]^{1/4} \times \left[1 + \frac{16c}{g(\rho_L - \rho_v)\lambda_D} \cdot \frac{d\sigma}{dT} \cdot \frac{\dot{q}''}{k_L} \right]^{1/4}. \quad (15)$$

Recognizing the Zuber CHF prediction in Eq. (15) and rearranging the definition of λ_D

$$g(\rho_L - \rho_v) = 3\sigma \left(\frac{2\pi}{\lambda_D} \right)^2 \quad (16)$$

to substitute into Eq. (15) yields

$$\frac{\dot{q}''_{\text{CHF}}}{\dot{q}''_Z} = \left[1 + \frac{4c\lambda_D}{3\pi^2\sigma} \cdot \frac{d\sigma}{dT} \cdot \frac{\dot{q}''}{k_L} \right]^{1/4}. \quad (17)$$

Following the recommendation of McGillis and Carey (1996) it is proposed here that this equation can be applied to other geometries such as cylinders and spheres if the appropriate correlation from Lienhard and Dhir (1973) replaces the Zuber CHF prediction. Also, to avoid a cumbersome or iterative solution, the heat flux appearing on the right-hand side of Eq. (17) can be estimated using the Lienhard and Dhir correlations, so Eq. (17) becomes

$$\frac{\dot{q}''_{\text{CHF}}}{\dot{q}''_{\text{LD}}} = \left[1 + \frac{4c\lambda_D}{3\pi^2\sigma} \cdot \frac{d\sigma}{dT} \cdot \frac{\dot{q}''_{\text{LD}}}{k_L} \right]^{1/4}. \quad (18)$$

To express this and subsequent expressions succinctly, a new empirical constant ($c_1 = 4c/3\pi^2$) can be defined, and the positive nondimensional parameter

$$\Pi_1 \equiv \frac{-\lambda_D}{\sigma} \cdot \frac{d\sigma}{dT} \cdot \frac{\dot{q}''_{\text{LD}}}{k_L} \quad (19)$$

developed. The parameter Π_1 is similar to the “dynamic Bond number” which governs the qualitative behavior of drops and bubbles subjected to thermocapillary stresses in fluids with uniform temperature gradients (Wei and Subramanian, 1995).

Equation (18) can now be expressed as

$$\frac{\dot{q}''_{\text{CHF}}}{\dot{q}''_{\text{LD}}} = [1 - c_1 \Pi_1]^{1/4}. \quad (20)$$

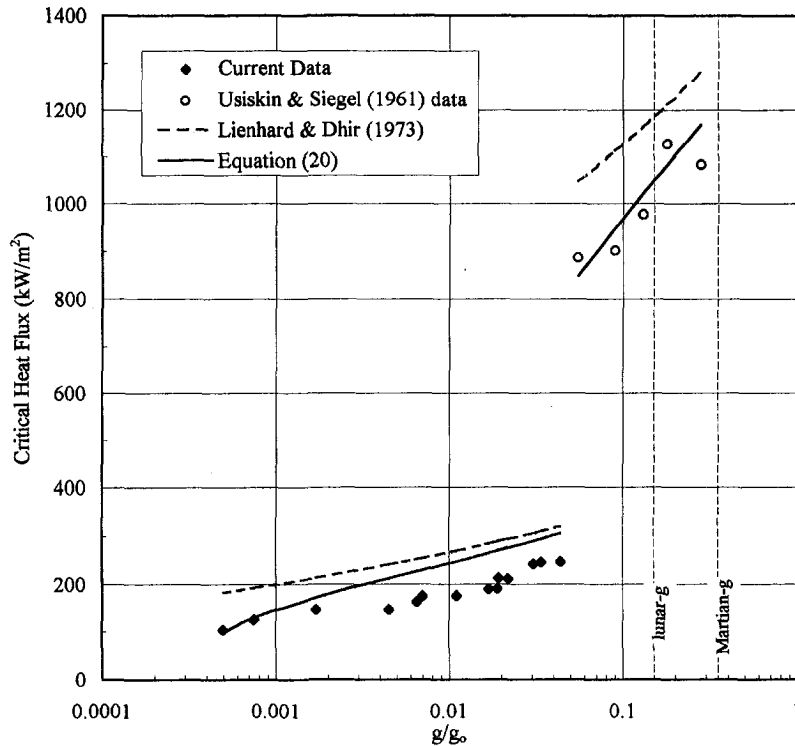


Fig. 7 Comparison of Eq. (20) with the data

This new model has been applied to the data from the current experimental study along with data from the drop tower experiments with water boiling on a horizontal wire performed by Usiskin and Siegel (1961). The results are shown in Fig. 7, where the gravitational variation of CHF as predicted by the current model is compared with the predictions of Lienhard and Dhir

(1973). The constant c_1 was set equal to 0.001, which yields the lowest average absolute error. This correlation tends to overpredict most of the data of the current study. Higher values of the empirical constant c_1 yield better results at higher values of g/g_0 but result in nonreal results at lower gravitational accelerations. One may be inclined to interpret this as an indicator of the lower limit

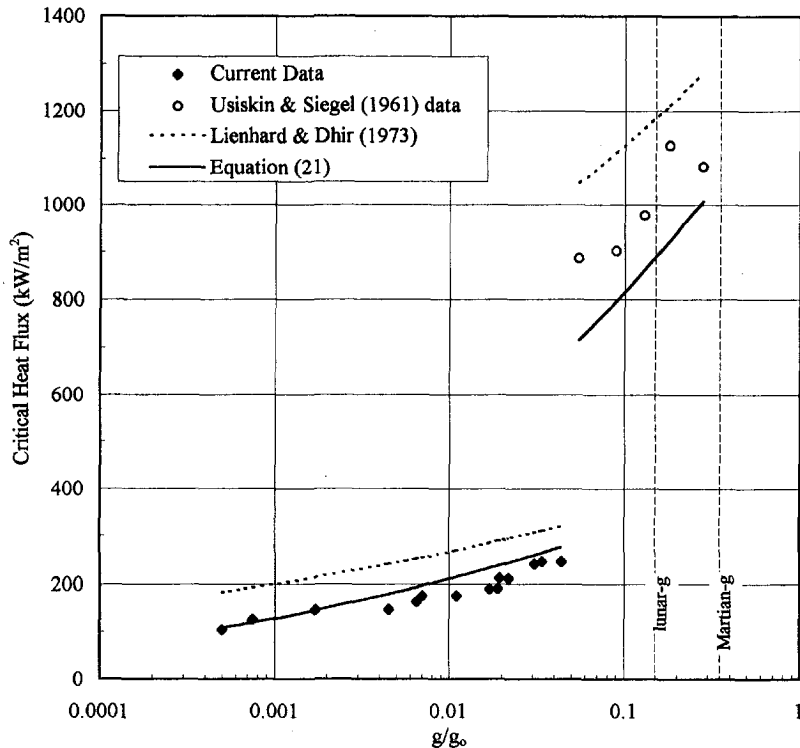


Fig. 8 Comparison of Eq. (21) with the CHF data

Table 2 Error summary

Correlation	Average Error	R.M.S. Error
Lienhard and Dhir (1973)	39 percent	41 percent
Eq. (20)	18 percent	25 percent
Eq. (21)	4 percent	15 percent

of gravitational accelerations for which the model is valid, with gravitational effects becoming negligible below this range. However, Eq. (20) may also yield nonreal results for fluids other than water, even at gravitational levels where the conventional Taylor-Helmholtz CHF model is known to accurately predict the CHF, indicating that the constant $c_1 = 0.001$ is not universal. This may lead one to seek a correlation with more favorable asymptotic behavior.

Treating the $\frac{1}{2}$ exponent in Eq. (20) as an empirical constant along with c_1 and applying nonlinear regression to fit the resulting correlation to the experimental data from the current study and the data from Usiskin and Siegel (1961) yields the following empirical correlation:

$$\frac{\dot{q}_{CHF}''}{\dot{q}_{LD}''} = \frac{1}{\sqrt{1 + \frac{\Pi_1}{500}}} \quad (21)$$

In Fig. 8 the correlation obtained through nonlinear regression, Eq. (21), is compared with the same data used in Fig. 7. Though this correlation tends to underpredict the Siegel and Usiskin (1961) data by an average of 14 percent, it provides a better correlation of both the trend and magnitude of the data from the current study. Also, this correlation provides reasonable CHF predictions for a broader range of conditions, as it does not suffer from the problem of yielding imaginary values at lower levels of gravitational acceleration. Usiskin and Siegel noted that their CHF measurements may be higher than the actual CHF by approximately 25 percent due to the very short duration of their drop tower experiments (1.0 second). The nonlinear regression then correlates this data to within the experimental limits of uncertainty.

Table 2 presents the average percentage error and R.M.S. error associated with the three correlations considered as applied to the data from the current experimental investigation and the data from Usiskin and Siegel (1961).

Conclusions

The current experimental investigation has measured 40 individual values of critical heat flux during reduced-gravity parabolic flights aboard the KC-135 aircraft. For water boiling on a cylindrical heater in the range $0.0005 < g/g_o < 0.044$, the CHF was found to decrease continuously with decreasing gravity. Both the visual observations of this and previous experiments and the qualitative trends of CHF as a function of gravitational acceleration support the view that the conventional Taylor-Helmholtz stability criterion continues to govern the CHF mechanism down to at least $g/g_o = 0.001$.

The reduction in the CHF values below the predictions of previous correlations has been attributed to thermocapillary forces which tend to inhibit the flow of vapor away from the heated surface. The current study has developed a method to quantify the opposing thermocapillary and buoyancy forces at the liquid-vapor interface. In addition to providing a means of identifying situations in which thermocapillary effects may be significant, this study furthers understanding of the relevant mechanisms in reduced gravity boiling.

Previous researchers have observed the effects of thermocapillary flow on pool boiling CHF of binary mixtures, both in reduced

gravity and terrestrial gravity conditions. These results raise the possibility of using "positive" binary mixtures to accommodate large heat fluxes in true microgravity or zero-gravity environments.

Two semi-empirical equations have been developed to correlate CHF data in reduced gravity. The correlation based on nonlinear regression yields a better fit to the data, but has a weaker theoretical foundation than Eq. (20). Additional experimental data would be useful in testing the relative merits of these two correlations.

Acknowledgment

Reduced-gravity parabolic flights on NASA's KC-135 for the current experimental study were provided by the Texas Space Grant Consortium, with additional support provided by a grant from the Texas Higher Education Coordinating Board. Experiments were conducted with the valuable assistance of Texas A&M University undergraduate students J. W. Aaron, K. I. Renzi, and T. K. Morris.

References

- Abe, Y., Oka, T., Mori, Y. H., and Nagashima, A., 1994, "Pool Boiling of a Non-azeotropic Binary Mixture under Microgravity," *International Journal of Heat and Mass Transfer*, Vol. 37, No. 16, pp. 2405-2413.
- Lec, H. S., Merte, H., and Chiamonte, F., 1997, "Pool Boiling Curve in Microgravity," *Journal of Thermophysics and Heat Transfer*, Vol. 11, No. 2, pp. 216-222.
- Legros, J. C., Dupont, O., Queeckers, P., Van Vaerenbergh, S., and Schwabe, D., 1990, "Thermohydrodynamic Instabilities and Capillary Flows," *Low Gravity Fluid Dynamics and Transport Phenomena*, J. N. Koster and R. L. Sani, eds., Progress in Astronautics and Aeronautics, Vol. 130, AIAA, Washington, pp. 207-239.
- Lienhard, J. H., and Dhir, V. K., 1973, "Hydrodynamic Prediction of Peak Pool Boiling Heat Fluxes From Finite Bodies," *ASME JOURNAL OF HEAT TRANSFER*, Vol. 95, pp. 152-158.
- McGillis, W. R., and Carey, V. P., 1996, "On the Role of Marangoni Effects on the Critical Heat Flux for Pool Boiling of Binary Mixtures," *ASME JOURNAL OF HEAT TRANSFER*, Vol. 118, pp. 103-109.
- Merte, H., 1990, "Nucleate Pool Boiling in Variable Gravity," *Low Gravity Fluid Dynamics and Transport Phenomena*, J. N. Koster and R. L. Sani, eds., Progress in Astronautics and Aeronautics, Vol. 130, AIAA, Washington, pp. 15-69.
- Merte, H., and Clark, J. A., 1964, "Boiling Heat Transfer With Cryogenic Fluids at Standard, Fractional, and Near-Zero Gravity," *ASME JOURNAL OF HEAT TRANSFER*, Vol. 86, No. 3, pp. 351-359.
- Oka, T., Abe, Y., Mori, Y. H., and Nagashima, A., 1995, "Pool Boiling of n-Pentane, CFC-113, and Water Under Reduced Gravity: Parabolic Flight Experiments With a Transparent Heater," *ASME JOURNAL OF HEAT TRANSFER*, Vol. 117, pp. 408-417.
- Oka, T., Abe, Y., Tanaka, K., Mori, Y. H., and Nagashima, A., 1992, "Observational Study of Pool Boiling under Microgravity," *JSME International Journal*, Vol. 35, No. 2, pp. 280-286.
- Shatto, D. P., Renzi, K. R., Peterson, G. P., Morris, T. K., and Aaron, J. W., 1996, "An Experimental Study of Pool Boiling Heat Transfer in Reduced Gravity," *Heat Transfer—Houston 1996*, M. S. El-Genk, ed., AIChE Symposium Series 310, Vol. 92, AIChE, New York, pp. 52-59.
- Siegel, R., and Keshock, E. G., 1964, "Effects of Reduced Gravity on Nucleate Boiling Bubble Dynamics in Saturated Water," *AIChE Journal*, Vol. 10, No. 4, pp. 509-517.
- Straub, J., 1993, "The Role of Surface Tension for Two-Phase Heat and Mass Transfer in the Absence of Gravity," *Proceedings of the Third World Conference on Experimental Heat Transfer, Fluid Mechanics and Thermodynamics, Honolulu*, Vol. 1, M. D. Kelleher, R. K. Shah, K. R. Sreenivasan, and Y. Joshi, eds., Elsevier, New York, pp. 103-125.
- Straub, J., Winter, J., Picker, G., and Zell, M., 1996, "Cooling of Small Electronic Devices by Boiling Under Microgravity," *Dynamics of Multiphase Flows Across Interfaces*, A. Steinchen, ed., Springer-Verlag, Berlin, pp. 134-149.
- Straub, J., Zell, M., and Vogel, B., 1990, "Pool Boiling in a Reduced Gravity Field," *Heat Transfer 1990: Proceedings of the Ninth International Heat Transfer Conference, Jerusalem, Israel*, Vol. 1, G. Hetsroni, ed., Hemisphere, New York, pp. 91-112.
- Tokura, I., Hanaoka, Y., Suzuki, H., Hirata, H., and Yoneta, M., 1994, "An Experimental Study of Subcooled Boiling from Wires in Micro-Gravity," *Proceedings of the Nineteenth International Symposium on Space Technology and Science, Yokohama*, M. Hinada, ed., ASME, New York, Paper No. 94-H-7, pp. 629-633.
- Usiskin, M., and Siegel, R., 1961, "An Experimental Study of Boiling in Reduced and Zero Gravity Fields," *ASME JOURNAL OF HEAT TRANSFER*, Vol. 83, pp. 243-253.
- Wei, H., and Subramanian, R. S., 1995, "Migration of a Pair of Bubbles under the Combined Action of Gravity and Thermocapillarity," *Journal of Colloid and Interface Science*, Vol. 172, pp. 395-406.
- Zell, M., Straub, J., and Vogel, B., 1989, "Pool Boiling under Microgravity," *Physicochemical Hydrodynamics*, Vol. 11, No. 5, pp. 813-823.

Forced Convection Condensation on a Horizontal Tube: Influence of Turbulence in the Vapor and Liquid Phases

D. Homescu
Research Student

P. K. Panday
Professor,
Mem. ASME

Universite de Franche Comté,
Institut de Génie Energetique,
2, avenue Jean Moulin,
90000 Belfort, France

An implicit finite difference scheme is used to solve the problem of condensation of pure vapors flowing vertically downwards around a horizontal tube. The incompressible flow equations coupled at the interface for the liquid and vapor phases are solved. The pressure gradient, inertia, and enthalpy convection terms are retained in this analysis, and the influence of turbulence in the two phases is considered. The calculated results for laminar flow and those from different mixing length turbulence models are compared with experimental results for condensation of steam and R113. The results presented show that the average condensation heat transfer coefficients obtained using Kato's turbulence model in the condensate film and Pletcher's model in the vapor phase, are in good agreement with the experimental data.

1 Introduction

Laminar filmwise condensation on a horizontal cylinder placed in quiescent vapor was solved by Nusselt (1916) with simplifying assumptions. The boundary layer equations of the condensate film, by taking into account the inertia and convection terms, were solved by Sparrow and Gregg (1959) using similarity transformation. For forced convection condensation on a cylinder, Shekrladze and Gomelaury (1966) assumed that the shear stress at the liquid vapor interface is equal to the loss of momentum flux of condensing vapor. They used a Nusselt-type analysis for condensate film in laminar flow and proposed Eq. (1), which gave fairly good agreement with experimental data for low vapor velocities ($A > 1$) but did not give satisfactory results for high-vapor velocities ($A < 1$).

$$\text{Nu}(\text{Re})^{-0.5} = 0.64 \cdot (1 + (1 + 1.69 \cdot A)^{0.5})^{0.5} \quad (1)$$

Rose (1984) analyzed the effect of pressure gradient on the heat transfer coefficient using the Shekrladze and Gomelaury (1966) asymptotic shear stress expression. He assumed that the contribution to heat transfer for high-velocity vapor flow is negligible for the lower region of the tube surface where condensate accumulates to give a thick liquid film. For laminar flow of condensate film, the following equations are proposed by Rose (1984):

$$P > A/8 \quad \text{Nu}(\text{Re})^{-0.5} = \frac{0.9 \cdot (1 + G^{-1})^{0.3} + 0.728 \cdot A^{0.5}}{(1 + 3.44 \cdot A^{0.5} + A)^{0.25}} \quad (2)$$

$$P < A/8 \quad \text{Nu}(\text{Re})^{-0.5} = \frac{0.64 \cdot (1 + 1.81 \cdot P)^{0.209} \cdot (1 + G^{-1})^{0.3} + 0.728 \cdot A^{0.5}}{(1 + 3.51 \cdot A^{0.53} + A)^{0.25}} \quad (3)$$

Memory et al. (1993) and Hsu and Yang (1999) have extended this analysis to take into account temperature variation around the tube surface. An explicit finite difference scheme was used by Panday (1988) to analyze the effects of inertia and convection

terms in the condensate flow using the Shekrladze and Gomelaury hypothesis. Fujii et al. (1972) used an integral analysis to solve two-phase equations for flow without pressure gradient and assuming a parabolic velocity profile in the vapor boundary layer. Thus, the vapor boundary layer separation was not taken into account in their analysis. Neglecting inertia and convection terms in condensate film, they proposed the following equation:

$$\text{Nu}(\text{Re})^{-0.5} = 0.9(1 + G^{-1})^{0.3} \left(1 + \frac{0.276 \cdot A}{(0.9 \cdot (1 + G^{-1})^{0.3})^4} \right)^{0.25} \quad (4)$$

The coupled boundary layer equations for laminar film condensation on a cylinder have been solved by Gaddis (1979) using series solutions and potential flow in the vapor phase. An implicit scheme (Keller's box method) has been used by Di Marzo and Casarella (1985) to obtain numerical solutions of coupled boundary layer equations for laminar flow by using scaling laws for low-velocity and high-velocity flows. They defined a critical Froude number, which allows a distinction between the two solution domains. Two-phase flow equations for laminar filmwise condensation on a bundle of tubes have been solved using an implicit procedure by Asbik et al. (1994). Assuming potential flow in the vapor phase, they introduced local acceleration of vapor velocity due to nonuniform passage between tubes.

In the above-mentioned analyses, the cylinder surface is assumed isothermal. None of these investigations could successfully correlate experimental data for high-vapor velocities ($A < 1$). The differences in the theoretical and experimental results for high-vapor velocities has often been assigned to turbulence in the liquid film and the formation of ripples at the surface of the liquid film due to vapor shear. Kutateladze and Gogonin (1985) have presented experimental results for R21 and R12. Accurate measurements of the condensation of steam flowing over a horizontal cylinder have been obtained Michael et al. (1989). Experimental results for the condensation of R-113 have been reported by Lee et al. (1984) and by Honda et al. (1986). Cavallini et al. (1986) have presented results for the condensation of R11. Precise measurements of the condensation of ethylene glycol have been reported by Memory and Rose (1986). The difference between the experimental results and those obtained from theoretical analysis is attributed to the following causes:

Contributed by the Heat Transfer Division for publication in the JOURNAL OF HEAT TRANSFER. Manuscript received by the Heat Transfer Division, Aug. 7, 1997; revision received, June 25, 1999. Keywords: Condensation, Cylinder, Forced Convection, Heat Transfer, Turbulent. Associate Technical Editor: B. Chung.

- On the one hand the temperature distribution of the tube surface is nonisothermal (Memory and Rose, 1991; Zhou and Rose, 1996). Conjugate heat transfer analysis made by Honda and Fujii (1984) shows that the circumferential condensate surface would develop an approximately sinusoidal temperature distribution. In addition, they showed that the overall heat transfer would be influenced particularly at high vapor velocities and for tubes with low thermal conductivities. Recent investigations of Morrison et al. (1998) confirm this analysis.
- On the other hand Michael et al. (1989) suggested that for high vapor velocities the condensate film can be under turbulent regime. Sarma et al. (1998) have analyzed the influence of turbulence in the condensate film using Colburn analogy for the definition of interfacial shear at the liquid vapor interface and Kato's expression of eddy diffusivity for turbulence. Their results based on the assumption that the friction coefficient in condensing flows is identical to that in single-phase flows show fair agreement with the experimental data.

To the authors' knowledge the solution of the coupled boundary layer equations of the condensate film and vapor flow taking into account the turbulence in the two phases have not been presented so far for condensation on a cylinder. The case of condensing flow between parallel plates has been treated by Louahlia and Panday (1996). The present article investigates the influence of turbulence on film condensation of pure saturated vapor flowing in the direction of gravity perpendicular to a horizontal isothermal cylinder. The governing equations of the liquid and vapor phases coupled at the liquid vapor interface are solved numerically using an implicit finite difference marching method. Different mixing length turbulence models are applied in the liquid and vapor phases and their results are compared with available experimental data.

Though Bellinghausen and Renz (1992), have reported good agreement with their experimental results for condensing flows inside a vertical tube using $k-\epsilon$ model, only mixing length models are chosen for this study as they require less computational effort and give satisfactory results with only a few arbitrary constants.

2 Analysis

2.1 Physical Model. The physical model and the coordinate system is shown in Fig. 1. Dry saturated vapor with temperature T_s ,

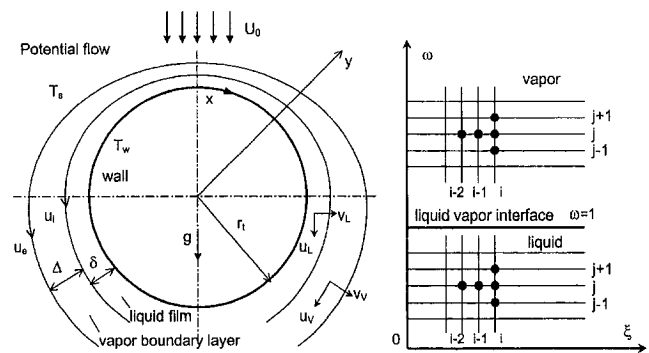


Fig. 1 Physical model and numerical grid

and oncoming velocity U_0 flows perpendicularly downwards across an infinitely long horizontal cylinder. The cylinder wall temperature is lower than the vapor saturation temperature. A thin condensate film is formed and flows under the influence of gravity, the pressure gradient, and interfacial shear. The x -coordinate is taken along the cylinder surface with its origin at the upper intersection between the surface and the axis of symmetry. The y -coordinate is taken along the outward normal to the wall.

To solve the problem the following simplifying assumptions have been made: (i) The wall temperature is constant. (ii) All physical properties are constant. (iii) Surface tension effect is negligible. (iv) The thickness of the condensate film and that of the vapor boundary layer are much smaller than the tube radius. (v) The vapor is saturated and dry. (vi) The heat exchange downward of the vapor separation point is negligible. (vii) Vapor flow outside the vapor boundary layer is potential.

A brief justification for these assumptions is given here. As most of the theoretical analyses and experimental results on condensation are reported for constant wall temperature and constant physical properties we have retained these assumptions to simplify the calculations and to facilitate comparison with other works however the calculation procedure can be used for variable wall temperature case.

As regards the flow of the condensate, surface waves have been

Nomenclature

A = nondimensional number $Pr/(Fr Ja)$
 B = coefficient in Eq. (56)
 C_p = specific heat
 C_f = friction coefficient
 Fr = Froude number $U_0^2/2 \cdot r_i \cdot g$
 g = acceleration due to gravity
 G = dimensionless $[\Delta T \cdot (k/\mu_L \cdot h_{fr})(\mu_L \rho_L / \mu_V \rho_V)^{1/2}]$
 h_{fr} = latent heat
 h = condensation heat transfer coefficient
 Ja = Jakob number $C_p \Delta T / h_{fr}$
 k = thermal conductivity
 L_m = mixing length
 \dot{m} = condensation mass flux
 Nu = Nusselt number
 P = dimensionless $h_{fr}(\rho_V / \rho_L) \cdot (\mu_L / \Delta T \cdot k)$
 p = absolute pressure
 p^+ = dimensionless pressure
 $p_L^+ = (\mu_L / \rho_L^2 \cdot u_{\tau L}^3)(dp/dx)$
 $p_V^+ = (\mu_V / \rho_V^2 \cdot u_{\tau V}^3)(dp/dx)$
 Pr = Prandtl number $\mu_L \cdot C_p / k_L$
 q = heat flux
 r_i = radius of cylinder

Re = Reynolds number $\rho_L \cdot U_0 \cdot 2r_i / \mu_L$
 S = suction parameter $S = (q/h_{fr}) \cdot (2 \cdot r_i / \rho_V \mu_V U_0)^{1/2}$
 T = temperature
 T_s = saturation temperature of vapor
 T_w = wall temperature
 $\Delta T = T_s - T_w$
 u = longitudinal velocity
 U_0 = freestream vapor velocity
 u_{τ} = friction velocity $\sqrt{\tau_w / \rho_L}; \sqrt{\tau_{int} / \rho_V}$
 u^+ = dimensionless velocity u/u_{τ}
 u_e = tangential velocity at vapor boundary
 u_{int} = velocity at liquid-vapor interface
 v = transverse velocity
 v^+ = dimensionless velocity v/u_{τ}
 x = longitudinal coordinate
 y = transverse coordinate
 y^+ = dimensionless coordinate
 $y_L^+ = \rho_L y u_{\tau L} / \mu_L$
 $y_V^+ = \rho_V (y - \delta) u_{\tau V} / \mu_V$

Greek Symbols

δ = condensate film thickness
 Δ = vapor boundary layer thickness

δ^+ = dimensionless thickness
 $\delta_L^+ = (\rho_L \delta \cdot u_{\tau L} / \mu_L)$
 $\delta_V^+ = (\rho_V \Delta \cdot u_{\tau V} / \mu_V)$
 θ = angle measured from the vertical
 θ_c = angular position for separation
 Λ = boundary layer thickness
 μ = dynamic viscosity
 ξ = transformed longitudinal coordinate
 ρ = density
 τ = shear stress
 τ_{fr} = shear stress at $y^+ = 26$
 $\tau_{fr} = \tau_{w,int}(1 + v^+ u^+ + p^+ y^+)$
 ω = transformed transverse coordinate

Subscripts

ft = fully turbulent
 int = interface
 L = liquid phase
 t = turbulent
 V = vapor phase
 w = wall
 x = local value

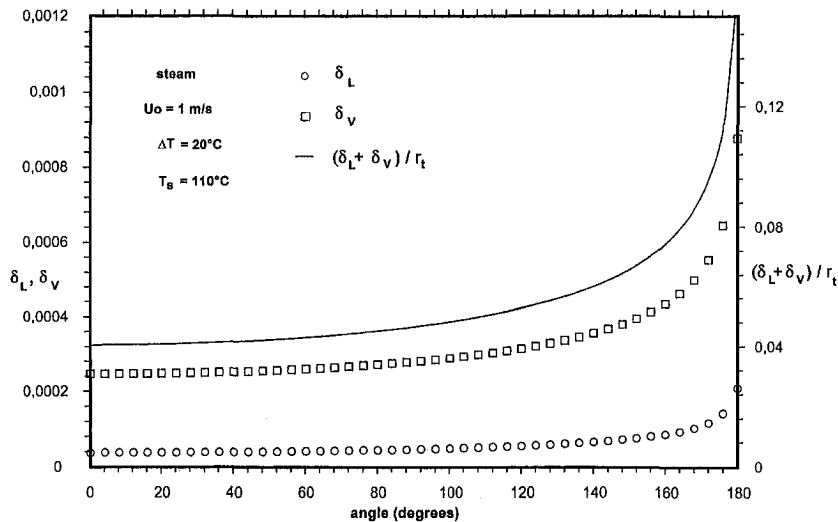


Fig. 2 Combined thickness of condensate film and vapor boundary layer

observed and empirical formulas for mean heat transfer coefficients have been suggested (Kutateladze and Gogonin, 1979). Increased mass transfer for wavy air-water interface have also been reported (Cohen, 1983). Various authors have analyzed the stability of flowing liquid films (Ünsal, 1983) but the influence of the waves on heat transfer coefficients is not clearly understood. Ünsal (1983) has shown that the gravity has a destabilizing effect and the condensation has a stabilizing effect. Hung et al. (1996) have shown that the condensate film flow is more stable compared to an isothermal flow. Ünsal (1988) has shown that surface tension has little effect on film stability and Chou and Chen (1997) have found that the variation of the surface tension with temperature stabilizes the condensate film. Jayanti and Hewitt (1997) have analyzed the influence of waves of given shape on heat transfer in condensation in the absence of shear stress at the interface. Their work shows that the heat transfer is mainly due to conduction through the liquid film and that the mean velocity of the liquid flow is higher in the presence of waves.

The resolution of coupled equations of condensation for the time-dependent interactions between flowing vapor and moving waves with changing shape is a formidable problem and is beyond the scope of this paper. For gas liquid stratified flow in a tube the presence of waves leads to increased turbulence and secondary flows due to coupling between turbulent fluctuations and wave motion (Liné et al., 1991). The measurements of stratified air-water flows show that the wave structure behaves as a rough wall (Toba, 1988) and the mean velocity profiles remain logarithmic though the slope changes (Cheung and Street, 1988). Speck et al. (1997) did not observe surface waves in their visualization study of air water flow on a cylinder of 18-mm diameter but found that the separation angle is modified. We have therefore assumed that the vapor-liquid interface is without waves allowing the turbulence models to take care of the increased turbulence induced by the presence of waves, if any. Smooth interface assumption is also usually made for stratified gas-liquid flows (Lombardi et al., 1996), assuming the interface without waves allows the neglect of time-dependent pressure gradients related to the variation of the local curvature of the liquid-vapor interface and surface tension.

For single-phase flows on a cylinder, the turbulent intensity has an important effect on heat and mass transfer coefficients even at the stagnation point (Morgan, 1975; Mizushima, 1972). Recent work by Scholten and Murray (1998) shows that the whole flow field pulsates due to detachment of vortices and the shape of the local heat transfer coefficient curve is strongly dependent on the turbulent intensity of the freestream flow. Transition to turbulence in their work with single-phase air flow on a cylinder is reported

for the product of turbulence intensity (Tu) times the Reynolds number (Re) of around 1500.

In condensing flows the detachment of liquid drops at the bottom of the tube is a source of further complication. Detailed measurements of pressure distribution and local velocity profiles of the condensate film and the vapor flow for condensing flows are not reported in the literature and only the mean heat transfer coefficients are generally measured.

Due to lack of information on local flow structure and transition to turbulent flow we have assumed in this analysis that the flow is turbulent over the whole circumference. For single-phase air flow on a cylinder, the numerical solution is dependent on boundary conditions used (Paolino et al., 1986; Song and Yuan, 1990). The potential flow is often used for these calculations (Karabulut and Ataer, 1998) as the measured pressure distribution up to the separation point is close to that theoretically obtained (Mizushima et al., 1972). Single-phase high Reynolds number turbulent flows on a cylinder are difficult to simulate numerically and require the vorticity boundary condition at the surface which poses the problem for condensing flows with moving liquid-vapor interface.

In the absence of measured pressure distribution profiles for condensing flows on a cylinder we have assumed potential flow in the vapor phase outside the vapor boundary layer. Condensate film thickness is of the order of a few hundredths of a millimeter (Gadis, 1979; Panday, 1988). Results of present calculations show (see Fig. 2) that the combined thickness of the condensate film and the vapor boundary layer just before separation is negligible compared to the cylinder radius.

2.2 Governing Equations. Based on the above-mentioned assumptions the conservation equations are written as follows: For the vapor boundary layer:

$$\frac{\partial u_v}{\partial x} + \frac{\partial v_v}{\partial y} = 0 \quad (\text{continuity}) \quad (5)$$

$$\rho_v \cdot \left(u_v \frac{\partial u_v}{\partial x} + v_v \frac{\partial u_v}{\partial y} \right) = -\frac{\partial p}{\partial x} + \frac{\partial}{\partial y} \left[(\mu + \mu_t)_v \frac{\partial u_v}{\partial y} \right] \quad (\text{momentum}). \quad (6)$$

For the liquid film:

$$\frac{\partial u_L}{\partial x} + \frac{\partial v_L}{\partial y} = 0 \quad (\text{continuity}) \quad (7)$$

$$\rho_L \cdot \left(u_L \frac{\partial u_L}{\partial x} + v_L \frac{\partial u_L}{\partial y} \right) = g \sin \theta - \frac{\partial p}{\partial x} + \frac{\partial}{\partial y} \left[(\mu + \mu_t)_L \frac{\partial u_L}{\partial y} \right] \quad (\text{momentum}) \quad (8)$$

$$u_L \frac{\partial T}{\partial x} + v_L \frac{\partial T}{\partial y} = \frac{1}{\rho_L \cdot C_p} \cdot \frac{\partial}{\partial y} \left[(k + k_t)_L \frac{\partial T}{\partial y} \right] \quad (\text{energy}). \quad (9)$$

The pressure gradient and the tangential velocity at the edge of the vapor boundary layer are obtained from potential flow as follows:

$$u_e = 2 \cdot U_0 \cdot \sin \theta \quad (10)$$

$$\frac{\partial p}{\partial x} = -u_e \cdot \rho_v \cdot \frac{\partial u_e}{\partial x} = \frac{-2 \cdot \rho_v \cdot U_0^2}{r_t} \sin(2\theta). \quad (11)$$

2.3 Boundary and Compatibility Conditions.

- At the wall ($y = 0$):

$$u_L = v_L = 0 \quad \text{and} \quad T = T_w = \text{const.} \quad (12)$$

At the liquid vapor interface ($y = \delta$):

$$u_L = u_v \quad \text{and} \quad T = T_s \quad (13)$$

$$(\mu + \mu_t)_L \frac{\partial u_L}{\partial y} = (\mu + \mu_t)_v \frac{\partial u_v}{\partial y} \quad (14)$$

$$\rho_L \cdot \left(v_L - u_L \frac{\partial \delta}{\partial x} \right) = \rho_v \cdot \left(v_v - u_v \frac{\partial \delta}{\partial x} \right). \quad (15)$$

At the edge of the vapor boundary ($y = \delta + \Delta$):

$$u_v = 2 \cdot U_0 \cdot \sin \theta. \quad (16)$$

The thickness of the liquid film is determined by a heat balance stating that the heat transferred at the body surface is equal to the heat released at the liquid vapor interface by the condensation process minus the heat that is convected away by the liquid film. Along with the boundary layer approximation, this balance can be written as

$$k_L \left(\frac{\partial T}{\partial y} \right)_{y=0} = \frac{\partial}{\partial x} \left[\int_0^\delta \rho_L \cdot u_L \cdot (h_{fg} + C_p(T_s - T)) \cdot dy \right]. \quad (17)$$

Thus, the thickness of the liquid layer links the momentum and energy equations through the heat balance on the condensate film.

3 Turbulence Models

Various turbulence models based on the knowledge of single-phase flow have been proposed in the literature. k - ϵ type turbulence models were not retained for this analysis as detailed experimental results regarding velocity profiles and turbulent kinetic energy for condensing flows of vapors are not available to justify the coefficients in these models. A brief description of the models used in this study is given herewith. In order to compare different turbulence models we have voluntarily refrained from tuning the coefficients to fit the data.

The mixing length concept was introduced by Prandtl and successfully applied to the study of single-phase turbulent flow (Schlichting, 1979). Using Prandtl's mixing length hypothesis, turbulent viscosity is expressed as

$$\mu_t = \rho_L \cdot L_m^2 \cdot \left| \frac{\partial u}{\partial y} \right|. \quad (18)$$

Turbulent conductivity is expressed using the analogy between heat flux and momentum transfer. The usual assumption is that the turbulent Prandtl number is in the range of 0.9–1.0 for commonly used fluids in turbulent boundary layers and that it has little effect for air and high Prandtl number fluids (Bremhorst and Krebs, 1993). Kays (1994) shows that close to the wall the turbulent

Prandtl number approaches 1.00 and gradually falls to 0.85 in the log region. He suggests a value of 1.07 for $0 < y^+ < 5$. As the local heat transfer depends on near wall characteristics turbulent Prandtl number of 1.00 is used for present calculations:

$$k_t = \frac{C_p \cdot \mu_t}{Pr_t}. \quad (19)$$

3.1 Van Driest Model. Van Driest (1956) proposed the use of an exponential damping coefficient, which forces the mixing length to zero at the wall:

$$L_m = 0.4 \cdot y \left[1 - \exp\left(-\frac{y^+}{26}\right) \right]. \quad (20)$$

3.3 Pletcher Model. Various modifications to the Van Driest model have been proposed in the literature (Mudawwar and El-Masri, 1986; Granville, 1990). Pletcher (1974) suggests a generalization of Van Driest's type damping function for flows with transpiration and pressure gradients. The boundary layer for this model is divided into two regions.

For the internal region ($L_m < 0.089\Lambda$) it is assumed that

$$L_m = 0.41 \cdot y \left[1 - \exp\left(-\frac{y^+}{26} \sqrt{1 + v^+ u^+ + p^+ y^+} \sqrt{\tau_f/\tau}\right) \right] \quad (21)$$

For the external region ($L_m > 0.089\Lambda$) where turbulent transport is dominant, the mixing length is supposed constant,

$$L_m = 0.089\Lambda, \quad (22)$$

where Λ is the boundary layer thickness ($\Lambda = \delta$ in the liquid phase and $\Lambda = \Delta$ in the vapor phase).

3.2 Von Karman Similarity Hypothesis. Von Karman (1939) proposed a rule that allows establishing the dependence of mixing length on space coordinates. He assumed that the turbulent fluctuations are similar at all point of the field of flow and that they differ from point to point only by time and length scale factors.

For the velocity distribution, he supposed the existence of three different regions in the vicinity of a solid wall:

- laminar sublayer $0 < y^+ < 5 \quad \frac{\mu_t}{\mu} = 0 \quad (23)$

- transition layer $5 < y^+ < 30 \quad \frac{\mu_t}{\mu} = \frac{y^+}{5} - 1 \quad (24)$

- fully turbulent layer $30 < y^+ < \delta^+ \quad \frac{\mu_t}{\mu} = \frac{y^+}{2.5} - 1. \quad (25)$

3.4 Kato Model. Kato et al. (1967) proposed a criterion for transition from laminar to turbulent flow, which gives the ratio of energy of mean flow and that dissipated near the wall. They suggested the following expression for turbulent viscosity for both free and forced convection flow:

$$\frac{\mu_t}{\mu} = 0.4 \cdot y^+ [1 - \exp(-0.0017 \cdot (y^+)^2)]. \quad (26)$$

4 Calculation Procedure

In order to solve the system of equations the curvilinear integration domain, x - y is transformed in a rectangular one using a new system of coordinates ξ - ω as follows:

$$\xi = x = r_t \cdot \theta \quad 0 \leq \xi \leq \pi \cdot r_t \quad (27)$$

$$\omega = \frac{y}{\delta} \quad \begin{array}{l} 0 \leq \omega \leq 1 \quad \text{in the liquid phase} \\ 1 \leq \omega \leq 6 \quad \text{in the vapor phase.} \end{array} \quad (28)$$

To guarantee that the edge of the vapor boundary layer does not exceed the ξ - ω plane the value of the maximum ω is set to 6.

4.1 Transformed Equations. In the new system of coordinates the equations to be solved for the vapor boundary layer are

$$\delta \cdot \frac{\partial u_v}{\partial \xi} - \omega \cdot \frac{\partial \delta}{\partial \xi} \cdot \frac{\partial u_v}{\partial \omega} + \frac{\partial v_v}{\partial \omega} = 0 \quad (29)$$

$$u_v \cdot \left(\frac{\partial u_v}{\partial \xi} - \frac{\omega}{\delta} \cdot \frac{\partial \delta}{\partial \xi} \cdot \frac{\partial u_v}{\partial \omega} \right) + \frac{v_v}{\delta} \cdot \frac{\partial u_v}{\partial \omega} = -\frac{1}{\rho_v} \cdot \frac{\partial p}{\partial \xi} + \frac{1}{\rho_v \delta^2} \cdot \frac{\partial}{\partial \omega} \left[(\mu + \mu_t)_v \frac{\partial u_v}{\partial \omega} \right] \quad (30)$$

and for the liquid film flow the equations become

$$\delta \cdot \frac{\partial u_L}{\partial \xi} - \omega \cdot \frac{\partial \delta}{\partial \xi} \cdot \frac{\partial u_L}{\partial \omega} + \frac{\partial v_L}{\partial \omega} = 0 \quad (31)$$

$$u_L \cdot \left(\frac{\partial u_L}{\partial \xi} - \frac{\omega}{\delta} \cdot \frac{\partial \delta}{\partial \xi} \cdot \frac{\partial u_L}{\partial \omega} \right) + \frac{v_L}{\delta} \cdot \frac{\partial u_L}{\partial \omega} = g \cdot \sin \left(\frac{x}{r_i} \right) - \frac{1}{\rho_L} \cdot \frac{\partial p}{\partial \xi} + \frac{1}{\rho_L \delta^2} \cdot \frac{\partial}{\partial \omega} \left[(\mu + \mu_t)_L \frac{\partial u_L}{\partial \omega} \right] \quad (32)$$

$$u_L \cdot \left(\frac{\partial T}{\partial \xi} - \frac{\omega}{\delta} \cdot \frac{\partial \delta}{\partial \xi} \cdot \frac{\partial T}{\partial \omega} \right) + \frac{v_L}{\delta} \cdot \frac{\partial T}{\partial \omega} = \frac{1}{\rho_L \cdot C_p \cdot \delta^2} \cdot \frac{\partial}{\partial \omega} \left[(k + k_t)_L \frac{\partial T}{\partial \omega} \right]. \quad (33)$$

The transformed boundary and compatibility conditions are

- at the wall ($\omega = 0$):
 $u_L = v_L = 0$ and $T = T_w = \text{const.}$ (34)

- at the liquid vapor interface ($\omega = 1$):
 $u_L = u_v$ and $T = T_s.$ (35)

$$\frac{(\mu + \mu_t)_L}{\delta} \frac{\partial u_L}{\partial \omega} = \frac{(\mu + \mu_t)_v}{\delta} \frac{\partial u_v}{\partial \omega} \quad (36)$$

$$\rho_L \cdot \left(v_L - u_L \frac{\partial \delta}{\partial \xi} \right) = \rho_v \cdot \left(v_v - u_v \frac{\partial \delta}{\partial \xi} \right) \quad (37)$$

at the edge of the vapor boundary:

$$u_v = 2 \cdot U_0 \cdot \sin \left(\frac{\xi}{r_i} \right). \quad (38)$$

The enthalpy balance in the liquid film gives

$$\frac{k_L}{\delta} \cdot \left(\frac{\partial T}{\partial \omega} \right)_{\omega=0} = \frac{\partial}{\partial \xi} \left[\delta \cdot \int_0^1 \rho_L \cdot u_L \cdot (h_{fg} + C_p(T_s - T)) \cdot d\omega \right]. \quad (39)$$

4.2 Finite Difference Scheme. The integration domain in the ξ - ω plane is divided into cells of dimensions $\Delta \xi$ and $\Delta \omega$ and indexed by integers i and j . Linearized form of equations are used where any variable f (general function used in the place of u_L, u_v, T) appearing in the equations is lagged and the derivatives of the variable f are evaluated by central differences as follows:

$$\left| \frac{\partial f}{\partial \xi} \right|_{ij} = \frac{3f_{ij} - 4f_{i-1,j} + f_{i-2,j}}{2\Delta \xi} \quad \left| \frac{\partial f}{\partial \omega} \right|_{ij} = \frac{f_{i,j+1} - f_{i,j-1}}{2 \cdot \Delta \omega} \quad \left| \frac{\partial^2 f}{\partial \omega^2} \right|_{ij} = \frac{f_{i,j+1} - 2 \cdot f_{i,j} + f_{i,j-1}}{\Delta \omega^2}. \quad (40)$$

The method of resolution requires the values of different variables for all grid points in ($i-1$) and ($i-2$) planes. The details of the calculation procedure are given by Louahlia and Panday (1996), and will not be repeated in detail. A summary of the calculation procedure is given below.

The momentum equations (Eqs. (30) and (32)) for the vapor and liquid phases and the boundary conditions are written in a matrix form $[A][u_{i,j}] = [B]$ and solved using Gaussian elimination to obtain longitudinal velocity ($u_{i,j}$) at different grid points. The continuity equations (Eqs. (29) and (31)) in both phases are then solved using backward differences in the ξ -direction and central differences in the ω -direction for a fictive node ($i, j + 1/2$). The energy Eq. (33) for the liquid layer written in matrix form is then solved using Gaussian elimination. The calculated temperature and velocity profiles are then substituted in the heat balance equation and the error in the enthalpy balance is calculated using Simpson's method for evaluating the integral. This procedure is repeated for two arbitrarily chosen values of liquid film thickness δ .

$$E_r = \frac{k_L}{\delta_i} \cdot \left(\frac{\partial T}{\partial \omega} \right)_{i,j=1} - \frac{\partial}{\partial \xi} \left[\delta \cdot \int_0^1 \rho_L \cdot u_L \cdot (h_{fg} + C_p(T_s - T)) \cdot d\omega \right]_{i,j} \quad (41)$$

If the heat balance is not satisfied, a new value for the liquid film thickness is assumed and the calculation procedure is repeated. The new value of δ at n th iteration is obtained using the secant method:

$$\delta^{n+1} = \delta^n - (\delta^n - \delta^{n-1}) \frac{E_r^n}{E_r^n - E_r^{n-1}}. \quad (42)$$

Iterations are continued until a satisfactory value of δ is obtained.

The convergence is reached after six to seven iterations. Once the heat balance equation is satisfied within an accuracy of 10^{-6} , the solution is advanced one step and downstream locations are computed. The ω value corresponding to the edge (Δ) of the vapor boundary layer is determined by observing the velocity profile in the vapor boundary layer. The value of ω where $u_v/u_s \geq 0.98$ is reached is considered to be the limit of the vapor boundary layer. The calculation procedure is continued until separation occurs and the boundary layer model becomes invalid. Vapor boundary layer separation is obtained from a test on the velocity gradients. Calculations are stopped when velocity gradient at the liquid-vapor interface becomes zero.

4.4 Calculation of the Heat Transfer Coefficient. At each grid plane (i) the heat flux density exchanged at the wall and the local condensation heat transfer coefficient (h_i) are estimated using Fourier's conduction law:

$$q_{i,1} = \frac{k_L}{\delta_i} \frac{\partial T}{\partial \omega} \Big|_{i,1} = \frac{k_L}{\delta_i} \cdot \frac{-3 \cdot T_{i,1} + 4 \cdot T_{i,2} - T_{i,3}}{\Delta \omega} \quad h_i = \frac{q_{i,1}}{T_s - T_w}. \quad (43)$$

The mean condensation heat transfer coefficient is obtained by numerical integration of the local values using trapezoidal method:

$$h = \frac{1}{\pi \cdot r_i} \int_0^{\theta_{cr,i}} h_x dx = \frac{1}{\pi \cdot r_i} \sum_{x=0}^{\theta_{cr,i}} \frac{h_i + h_{i-1}}{2} (x_i - x_{i-1}). \quad (44)$$

4.3 Starting Procedure. To start the calculations, velocity and temperature profiles are required for all the grid points at $i = 1$ and $i = 2$ planes. These are obtained by neglecting inertia and convection terms in the condensate film and using the power series expansion given by Fujii et al. (1972). Neglecting pressure gradient terms and assuming

Table 1(a) Influence of grid size on numerical results for laminar and turbulent flow (Kato's model in liquid phase, Pletcher's model in vapor phase) condensation

Steam $U_0 = 10$ m/s $G = 4,16$ $\Delta T = 20^\circ\text{C}$ $T_s = 110^\circ\text{C}$		
Grid size (x, y)	$NuRe^{-0.5}$ laminar	$NuRe^{-0.5}$ turbulent
541 x 45	0,64084	1,3919
541 x 49	0,64321	1,3966
541 x 51	0,64924	1,4010
401 x 51	0,65134	1,3998
471 x 51	0,65042	1,4000
541 x 51	0,64924	1,4010

Table 1(b) Comparison of numerical results for laminar flow condensation with Eq. (3) for two different freestream velocities

Vapor velocity U_0 (m/s)	1	10
Number of grid points (x, y)	541 x 51	541 x 51
Computed $Nu Re^{-0.5}$	1,2952	0,64924
Rose - equation (3)	1,2536	0,75069

$$\delta^2 = A_0 + A_2\chi^2 + \dots \quad (45)$$

$$u_{int} = B_1\chi + B_3\chi^3 + \dots \quad (46)$$

Fujii et al. obtained the following equations for A_0 , B_1 , A_2 , and Δ/δ :

$$\begin{aligned} & \{F^3\}A_0^6 + \{6F^3\}A_0^5 + \{-36F^2(8F + H) + 30R^2F^2(H + 4)\}A_0^4 \\ & + \{-144 \cdot F^2(18F + H) + 360R^2F^2H\}A_0^3 \\ & + \{432FH(8F + H) - 90R^2FH(5H + 8)\}A_0^2 \\ & + \{864FH^2 - 1080R^2FH^2\}A_0 \\ & + \{-1728H^2 + 1080R^2H^2(H + 1)\} = 0 \quad (47) \end{aligned}$$

$$R = \left(\frac{\rho_L \mu_L}{\rho_V \mu_V} \right)^{1/2}$$

$$B_1 = \frac{2H}{A_0} - \frac{F}{6} A_0 \quad \text{and} \quad A_2 = \frac{F^3 A_0^3}{24 \cdot B_1 + 10 \cdot F \cdot A_0} \quad (48)$$

and

$$\frac{\Delta}{\delta} = \frac{4 \cdot \mu_V (u_e - u_{int})}{\mu_L \left(2 \cdot u_{int} - \delta^2 \left(\frac{\rho_V}{\rho_L} \cdot u_e \frac{du_e}{dx} - \sin(F \cdot \chi) \right) \right)} \quad (49)$$

where

$$\chi = \frac{\theta}{F} \quad F = \frac{U_0^2}{g \cdot r_i} \quad H = \frac{C_{pL} \Delta T}{Pr \cdot h_{fr}} \quad (50)$$

Among two real and positive roots of Eq. (50) the smaller one is adopted. The film thickness and velocities at planes $i = 1$ and $i = 2$ are calculated using Eq. (45) and (46) to start the calculations.

5 Results and Discussion

This study represents an attempt to predict the average values of the heat transfer coefficients with the assumption that the liquid film flow and the vapor flow are turbulent. Several models are used to evaluate turbulent heat transfer coefficients. In the liquid film, Van Driest, Von Karman, Pletcher, and Kato expressions for turbulent viscosity are used. As for the vapor flow, Pletcher's mixing length model was adopted with the assumption that vapor condensation at the interface can be assimilated with boundary layer suction.

The influence of the grid for condensation of steam is shown in Table 1(a). The condensate film thickness is of the order of a few hundredths of a millimeter (Figs. 2 and 3) and the truncation error increases for a number of grid points in the liquid film beyond a certain limit. The same is true for the heat balance on the cylinder periphery. The best results are obtained for 50 intervals in the liquid film and 540 intervals on the cylinder periphery. For the vapor flow the interval in the y -direction is 1.5 times that in the liquid. A total of 200 intervals in the vapor film are used to guarantee that the vapor boundary layer thickness does not transgress the dimensions of the numerical grid.

The average Nusselt number in laminar regime at 1 m/s and 10 m/s vapor velocities are compared with Eq. (3) proposed by Rose in Table 1(b). The slight difference obtained is logical as the present calculations take into account inertia and enthalpy convection terms which are ignored in the analysis by Rose. The calculations have been carried out on a PC equipped with a 200 MHz Pentium microprocessor and for one value of oncoming vapor velocity the average computation time was of the order of two minutes.

5.1 Numerical Results. Numerical results presented herewith have been obtained using a uniform 541×51 grid in the

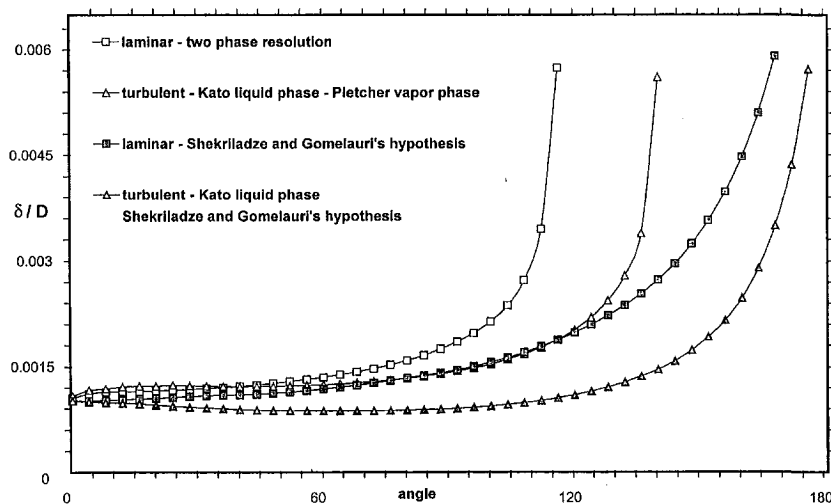


Fig. 3 Condensate film thickness (steam - $U_0 = 10$ m/s; $T_s = 110^\circ\text{C}$; $T_s - T_w = 20^\circ\text{C}$)

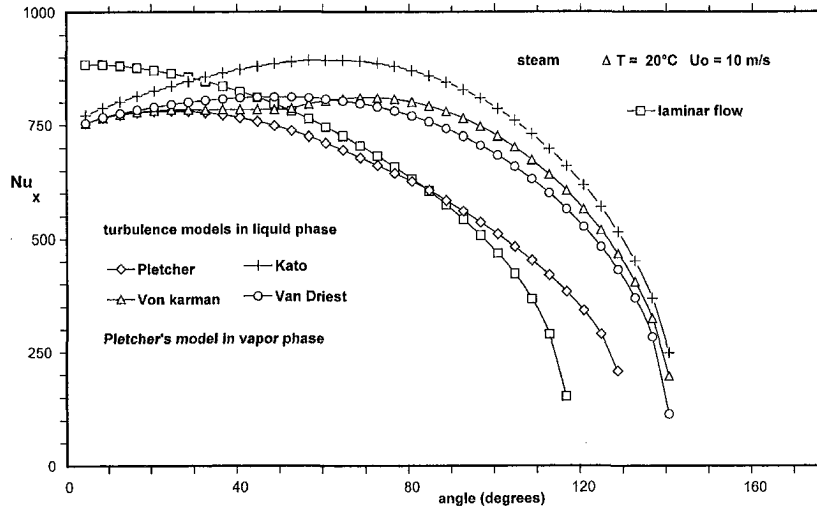


Fig. 4 Variation of local Nusselt number for condensation of steam on 14-mm diameter tube

liquid film. The thickness of the liquid film and vapor boundary layer for the laminar filmwise condensation of steam on a 14-mm diameter tube with an oncoming vapor velocity of 1 m/s

($T_s = 110^\circ\text{C}$; $T_s - T_w = 20^\circ\text{C}$) is shown in Fig. 2. The nondimensional condensate film thickness (δ/D) from the upper stagnation point to the lower stagnation point for the same case

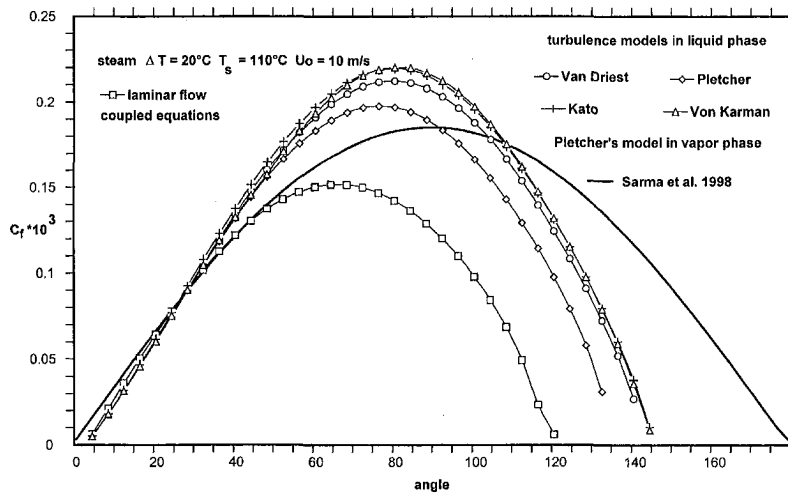


Fig. 5(a) Variation of local friction coefficient for $U_0 = 10$ m/s

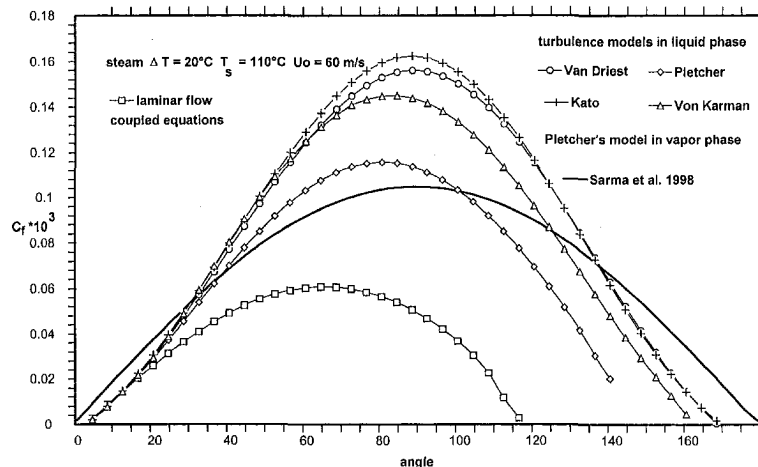


Fig. 5(b) Variation of local friction coefficient for $U_0 = 60$ m/s

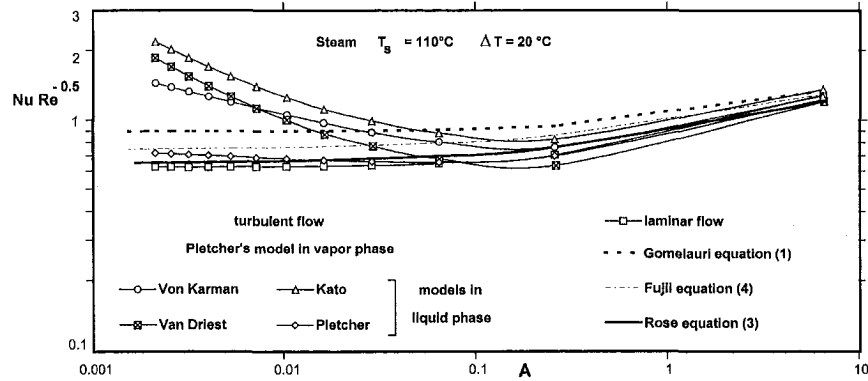


Fig. 6 Comparison of numerical results with different equations for the variation of the mean heat transfer coefficients

is shown in Fig. 3 for a vapor velocity of 10 m/s. The different cases represented are:

- laminar regime for liquid and vapor flow with equality of shear stress at interface,
- laminar flow of condensate with Shekrladze and Gomelaury's hypothesis (vapor flow equations not solved),
- turbulent flow regime (Kato's model in the liquid phase and Pletcher's model in the vapor phase), and
- turbulent flow regime with Shekrladze and Gomelaury's hypothesis (Kato's model in the liquid phase).

The variation of the film thickness is found to be monotonically increasing. The condensate film thickness obtained from the solution of coupled equations for laminar flow are different from those calculated with the Shekrladze and Gomelaury hypothesis. It is seen that the condensate thickness decreases in turbulent regime and reaches a minimum around $\theta = 90$ deg when the Shekrladze and Gomelaury hypothesis is used along with the turbulence model of Kato in the liquid film. The variation of the liquid film thickness obtained by solving the coupled equations in the liquid and vapor phases for turbulent flow differs considerably from that obtained by the asymptotic shear stress model of Shekrladze and Gomelaury in which the vapor phase equations are not solved.

The variation of local Nusselt number for the condensation of steam ($T_s = 110^\circ\text{C}$; $T_s - T_w = 20^\circ\text{C}$; 14 mm. tube diameter and $U_0 = 10$ m/s.) is presented in Fig. 4 for different turbulence models. The solution of the coupled equations for laminar flow are also presented in Fig. 4. It can be seen that when the liquid film is assumed turbulent there is an important modification in the local Nusselt number compared to laminar flow results with a maximum occurring around 80 deg. It is observed that the Kato model in the liquid phase gives the highest value of local Nusselt numbers.

The friction coefficients at the liquid vapor interface, obtained by solving the coupled liquid-vapor phase equations with different turbulence models in the liquid phase, are compared in Figs. 5(a) and 5(b) with those assumed by Sarma et al. (1998) using Colburn's analogy. In their analysis the interfacial shear is obtained from the following equations where C and n are coefficients depending on vapor Reynolds number: local friction coefficient

$$C_f(\theta) = C \cdot \pi \cdot \text{Re}_v^{n-1} \sin \theta \quad (51)$$

$$\tau_{\text{int}} = (1/2 \cdot \rho_v \cdot 4U_0^2 \sin^2 \theta) \cdot C_f(\theta). \quad (52)$$

The variation of local friction coefficient for high freestream vapor velocities reveals that the use of friction coefficient in the analysis of Sarma et al. (1998) evaluated from heat transfer measurements in single phase flows:

- overestimates the shear stress at the liquid vapor interface for laminar flow, and

- underestimates the shear stress at the liquid vapor interface for turbulent flow.

The present results for the average heat transfer, for both laminar and turbulent flow conditions, are compared in Fig. 6 with the Eqs. (1), (3), and (4), for the condensation of steam. At low vapor velocities and for laminar flow conditions the present calculations are in good agreement with equations. At increasing vapor velocities the results of the present calculations give higher average Nusselt numbers. Figure 7 shows the angular position θ_c , which corresponds to the separation in vapor boundary layer for different values of the Froude number and for various condensation rate parameters G , where

$$G = \frac{\Delta T \cdot k}{\mu_L \cdot h_{fg}} \left(\frac{\mu_L \rho_L}{\mu_V \rho_V} \right)^{1/2} \quad (53)$$

It is noted that for turbulent flow, the separation occurs further downstream and a higher condensation rate delays the flow reversal or separation. This is due to the suction effect caused by the condensation process, which is enhanced by the introduction of turbulence. This remark is in agreement with the visual observations reported by Memory and Rose (1995).

Rose (1984) approximated the angle of separation for laminar film condensation as function of suction parameter S by

$$\theta_c = 1.76 + 0.164 \cdot S + 0.00869 \cdot S^2. \quad (54)$$

In Fig. 8 the angle of separation for laminar and turbulent (Pletcher's model in vapor phase and Kato's model in liquid phase) flow is compared with Eq. (54) for condensation rate parameter $G = 4.17$. Figure 8 confirms that turbulent flow delays separation and, the results for laminar flow are in fair agreement with Eq. (54). Karabulut and Ataer (1998) have obtained the following separation positions for single-phase laminar convective heat transfer, from and to an isolated cylinder in crossflow:

- at 110 deg for 300 K surface temperature and 900 K freestream temperature.
- at 99 deg for 900 K surface temperature and 300 K freestream temperature.

It is interesting to note that the present calculations for coupled laminar flow of liquid and vapor and for low condensation rate (thin liquid film) gives the position of the separation point at around 115 deg. For higher condensation rate in laminar flow, the position of separation is located around 125 deg. This shows that the presence of a thin liquid film delays separation to a lower position downstream (Speck et al., 1997).

5.2 Comparison With Experimental Results. In order to check the validity of different turbulence models and accuracy of the computational method, present numerical results are compared

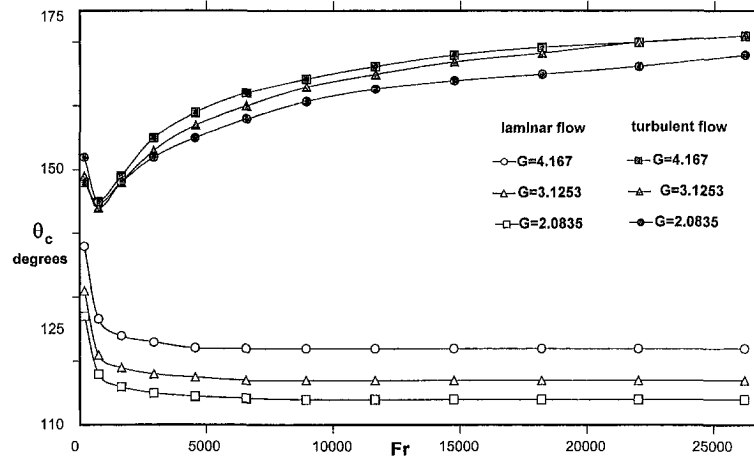


Fig. 7 Angular position of separation in the vapor boundary layer

with those obtained experimentally. Measured values of local heat transfer for condensing flows on a cylinder are not available so only mean heat transfer coefficients are compared.

In Fig. 9, the experimental data of Michael et al. (1989) for saturated steam at 110°C condensing near atmospheric pressure on a tube of 14-mm diameter, are compared with the numerical results for vapor velocities in the range 5 to 60 m/s. The predictions from the present calculations using Kato's turbulence model in the liquid phase and Pletcher's model in the vapor phase seem to be in reasonably good agreement with experimental data. Figure 10 shows the dependence of heat transfer coefficients on the mean temperature drop for different turbulence models at 50 m/s vapor velocity in comparison with data of Michael et al. (1989). It can be seen that for low condensation rate (low temperature drop) there is no major influence of the turbulence models on the heat transfer (the liquid film is thin and turbulent effects are negligible). Figure 10 confirms Michael's suggestion, that the heat transfer increasing with ΔT at high vapor velocities could be associated with effects of turbulence in the condensate film (the shear stress at the liquid vapor interface increases with increasing condensation rate).

The experimental data of Honda et al. (1986) for the condensation of R-113, on a 19 mm diameter tube is compared in Fig. 11 with the calculated values based on average heat transfer coefficients for vapor velocities in the range of 1 to 8 m/s. Honda et al. noticed that the measured values of Nusselt number (Nu) are greater compared to theoretical predictions and the difference

increases as U_0 increases. They explained this enhancement by the turbulent mixing in the condensate film and surface waves that they observed by dye tracer visualization. In Fig. 11 it can be seen that the agreement between numerical results and experimental data is fairly good for low A values (which corresponds to high U_0 values) when using Kato's model in liquid phase and Pletcher's model in vapor phase. Numerical results for low temperature drop ($\Delta T = 4^\circ\text{C}$) were irrelevant as to the influence of turbulence on the average heat transfer.

5.3 Equation for Mean Heat Transfer Coefficient. Figures 12(a) and (b) show the numerical results for the laminar flow condensation and those obtained by using Kato's turbulence model in the liquid phase and Pletcher's turbulence model in the vapor phase. A linear regression using Mathematica software was used to obtain equations representing calculated values. The case of laminar flow of condensate and vapor assuming a dependence of $\text{Nu} \cdot \text{Re}^{-0.5}$ as a function of the parameter A lead to the following equation for $A < 49$:

$$\text{Nu} \cdot \text{Re}^{-0.5} = 0.703(1 + 0.25A^{0.25})^{1.5}. \quad (55)$$

The experimental results show a deviation from laminar theory for $A < 1$ (Panday, 1988). Therefore, for turbulent flows of vapor and condensate an equation was obtained to represent numerical results for $A < 1$:

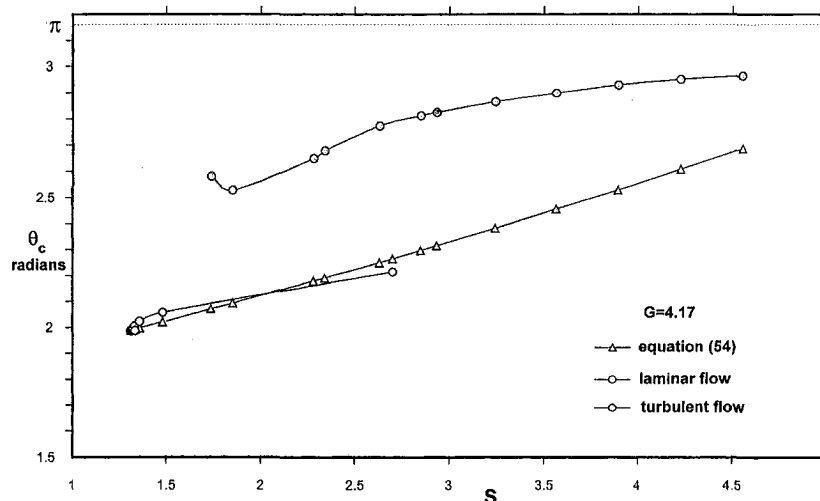


Fig. 8 Comparison of separation angle for laminar and turbulent condensation

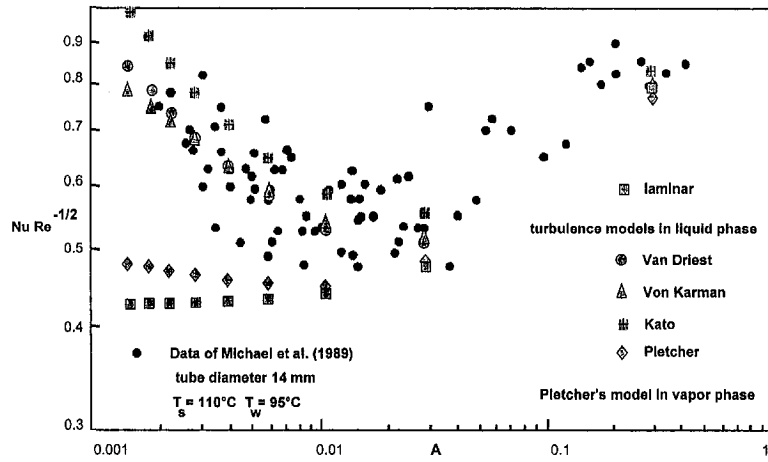


Fig. 9 Condensation of steam. Comparison with experimental data of Michael et al. (1989).

$$Nu_t \cdot Re^{-0.5} = B \left[\frac{(1 + 0.8A)^{0.5}}{(0.25A^{0.5} + 1.75A)^{0.25}} \right]^{1.5} \quad (56)$$

Different values of the coefficient B were obtained for different fluids; $B = 0.44$ for steam, $B = 1.09$ for R113, and $B = 0.72$ for R11. The dependence on parameter G has been analyzed by Rose (1989) for laminar flow condensation on a flat plate. For the present case of condensation on a cylinder we have adopted the dependence on parameter G as suggested by Fuji (1972) and used by Rose (1984). To represent numerical results in turbulent regime

for all the values of the parameter A used in our calculations the following equation for the average Nusselt number is then obtained by combining the dependence on the parameter A for the laminar and turbulent condensation:

$$Nu_t \cdot Re^{-0.5} = 0.291 \left[0.75 \cdot \left(1 + \frac{1}{G} \right)^{1/3} + 0.25 \cdot A^{0.25} + \frac{(1 + 0.8 \cdot A)^{0.5}}{(0.25 \cdot A^{0.5} + 1.75 \cdot A)^{0.25}} \right]^{1.5} \quad (57)$$

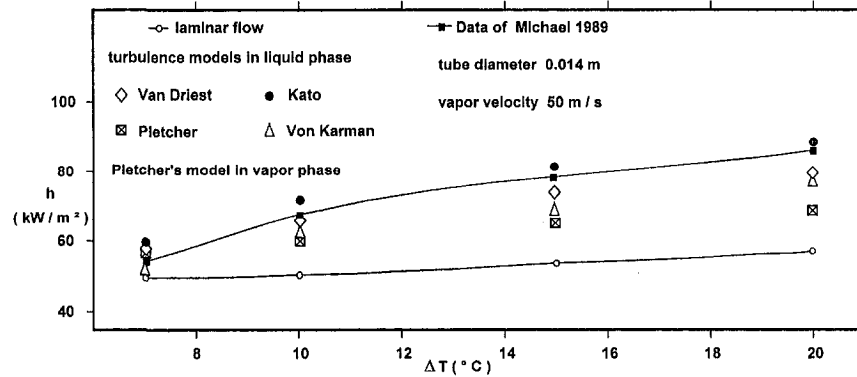


Fig. 10 Average heat transfer coefficients. Comparison with data of Michael et al. (1989).

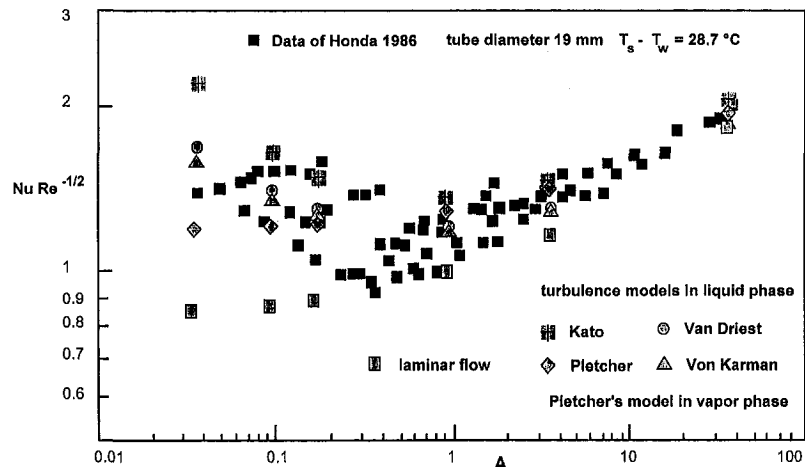


Fig. 11 Condensation of R-113. Comparison with experimental data of Honda et al. (1986).

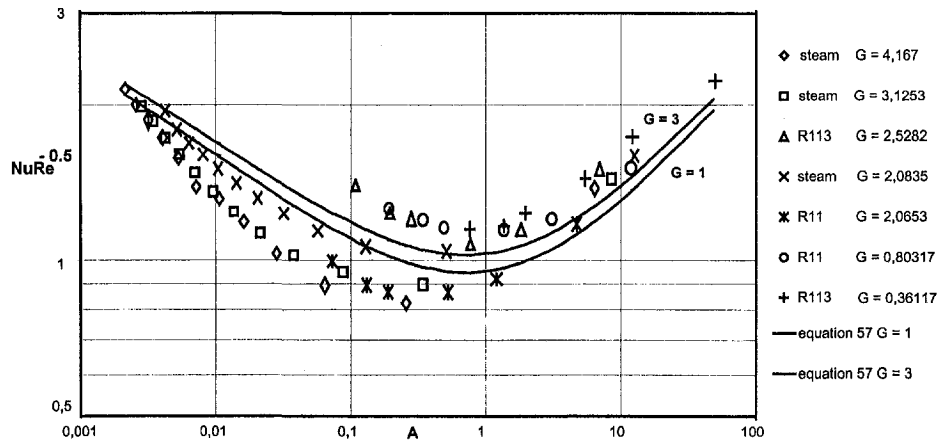


Fig. 12(a) Comparison of numerical results for turbulent flow with Eq. (57)

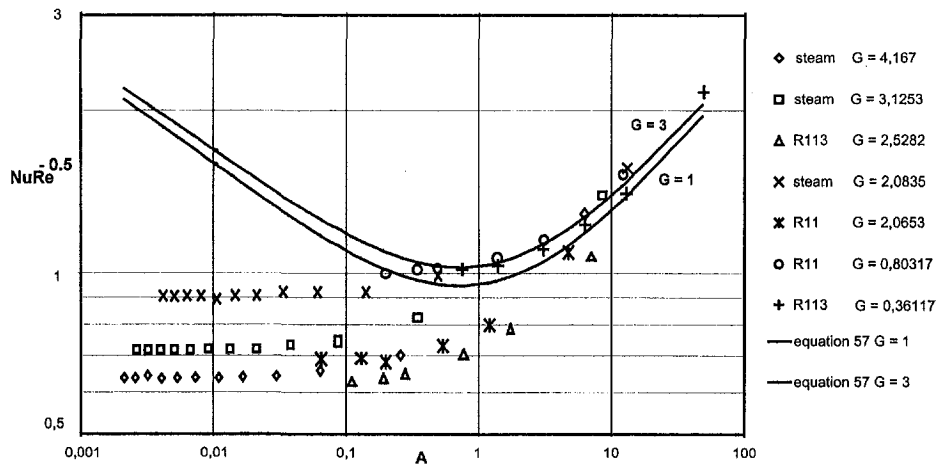


Fig. 12(b) Comparison of numerical results for laminar flow with Eq. (57)

The scatter of the numerical data compared to Eq. (57) is seen in Figures 12(a) and (b). The maximum error is about 26 percent. The proposed equation is compared in Fig. 13, with the experimental data of Honda et al. (1986) for R-113, Eq. (4) of Fujii et al. (1972) and with the numerical results of Sarma et al. (1998). For each case, two lines corresponding to the smallest and the largest value of ΔT are plotted. Equation (57) correlates the experimental data with reasonable accuracy.

6 Concluding Remarks

The film condensation of pure saturated vapor flowing in the direction of gravity perpendicular to a horizontal cylinder is studied by solving the coupled boundary layer equations using an implicit finite difference scheme and the assumption of potential flow in the vapor phase. These equations are coupled at the liquid vapor interface by equality of shear stress, longitudinal velocity, and mass flux.

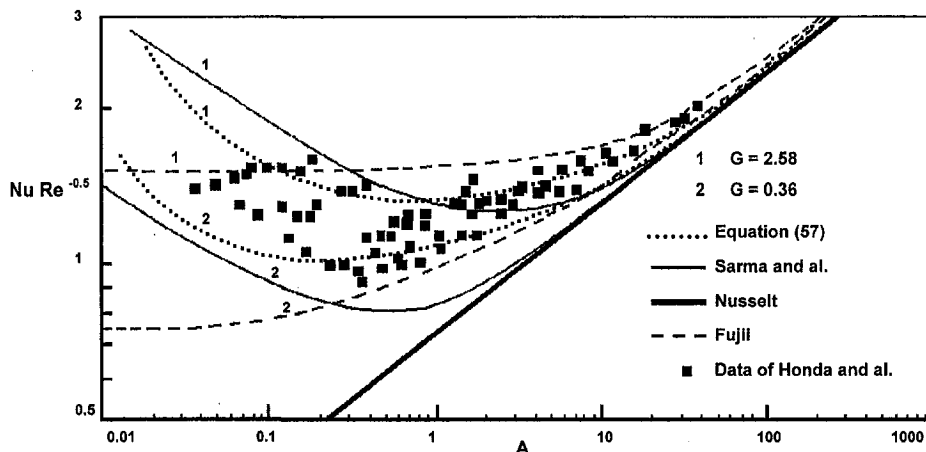


Fig. 13 Comparison of present analysis with theory and experimental data

Different mixing length turbulence models are applied both in the liquid and vapor phase and the results are compared with available experimental data. The conclusions are as follows:

- The comparison of present results with the previous experimental and theoretical results shows that the present analysis is satisfactory for predicting condensation characteristics for steam and refrigerants with the assumption of turbulent regime during film condensation. The flow and heat transfer characteristics are considerably affected when the turbulent regime is considered.
- It is found that the estimation of average heat transfer coefficients, by applying Kato's turbulence model in the liquid phase and Pletcher's turbulence model in the vapor phase, are in good agreement with the experimental data of Michael et al. (1989) for steam and with those of Honda et al. (1986) for refrigerant R-113.
- An equation representing numerical results is proposed for the average heat transfer coefficient. Equation (57) is found to agree satisfactorily for condensation of vapors. Application of mixing length turbulence models is validated for the study of turbulent condensate films on a tube with external flow of vapor.

References

- Asbik, M., Daif, A., and Panday, P. K., 1994, "Condensation of Downward Flowing Vapor on a Single Horizontal Cylinder or a Bank of Tubes With and Without Inundation," *Proc. First ISHMT-ASME Heat Mass Transfer Conference*, Bombay, India, ASME, New York.
- Bellinghausen, R., and Renz, U., 1992, "Heat Transfer and Film Condensation During Condensation of Steam Flowing at High Velocity in a Vertical Pipe," *Int. J. Heat Mass Transfer*, Vol. 35, No. 3, pp. 683-689.
- Bremhorst, K., and Krebs, L., 1993, "Eddy Diffusivity Base Comparisons of Turbulent Prandtl Number for Boundary Layer and Free Jet Flows With Reference to Fluids of Very Low Prandtl Number," *ASME JOURNAL OF HEAT TRANSFER*, Vol. 115, pp. 549-552.
- Cavallini, A., Frizzerin, S., and Rossetto, L., 1986, "Condensation of R-11 Vapor Flowing Downward Outside a Horizontal Tube Bundle," *Proc. of the 8th Int. Heat Transfer Conference*, San Francisco, ASME, New York, pp. 1707-1712.
- Cheung, T. K., and Street, R. L., 1988, "The Turbulent Layer in the Water at an Air-Water Interface," *J. Fluid Mechanics*, Vol. 194, pp. 133-151.
- Chou, G., and Chen, J., 1997, "Linear Stability Study of Waviness Effect on Film Condensation With Non Uniform Surface Tension," *Int. J. Heat Mass Transfer*, Vol. 40, No. 10, pp. 2477-2482.
- Cohen, Y., 1983, "Mass Transfer Across a Sheared Wavy Air-Water Interface," *Int. J. Heat Mass Transfer*, Vol. 26, No. 9, pp. 1289-1297.
- Di Marzo, M., and Casarella, M. J., 1985, "Film Condensation Over a Horizontal Cylinder for Combined Gravity and Forced Flow," *ASME JOURNAL OF HEAT TRANSFER*, Vol. 107, pp. 687-695.
- Fujii, T., Uehara, H., and Kurata, C., 1972, "Laminar Filmwise Condensation of Flowing Vapour on a Horizontal Cylinder," *Int. J. Heat Mass Transfer*, Vol. 15, pp. 235-246.
- Gaddis, E. S., 1979, "Solution of the Two Phase Boundary Layer Equations for Laminar Film Condensation of Vapour Flowing Perpendicular to a Horizontal Cylinder," *Int. J. Heat Mass Transfer*, Vol. 22, pp. 371-382.
- Granville, P. S., 1990, "A Near Wall Eddy Viscosity Formula for Turbulent Boundary Layers in Pressure Gradients Suitable for Momentum, Heat, or Mass Transfer," *ASME Journal of Fluids Engineering*, Vol. 112, pp. 240-243.
- Honda, H., Nozu, S., Uchima, B., and Fujii, T., 1986, "Effect of Vapor Velocity on Film Condensation of R-113 on Horizontal Tubes in a Crossflow," *Int. J. Heat Mass Transfer*, Vol. 29, pp. 429-438.
- Honda, H., and Fujii, T., 1984, "Condensation of Flowing Vapor on a Horizontal Tube: Numerical Analysis as a Conjugate Heat Transfer Problem," *ASME JOURNAL OF HEAT TRANSFER*, Vol. 106, pp. 841-848.
- Hsu, C. H., and Yang, S. A., 1999, "Pressure Gradient and Variable Wall Temperature Effects During Filmwise Condensation From Downward Flowing Vapors Onto a Horizontal Tube," *Int. J. Heat Mass Transfer*, Vol. 42, pp. 2419-2426.
- Hung, C., Chen, C., and Tsai, J., 1996, "Weakly Nonlinear Stability Analysis of Condensate Film Flow Down a Vertical Cylinder," *Int. J. Heat Mass Transfer*, Vol. 39, No. 13, pp. 2821-2829.
- Jayanti, S., and Hewitt, G. F., 1997, "Hydrodynamics and Heat Transfer of Wavy Thin Film Flow," *Int. J. Heat Mass Transfer*, Vol. 40, No. 1, pp. 179-190.
- Karabulut, H., and Ataer, Ö. E., 1998, "Numerical Solution of Boundary Layer Equations in Compressible Cross-Flow to a Cylinder," *Int. J. Heat Mass Transfer*, Vol. 41, No. 17, pp. 2677-2685.
- Kato, H., Nishiwaki, N., and Hirata, M., 1967, "On the Turbulent Heat Transfer by Free Convection From a Vertical Plate," *Int. J. Heat Mass Transfer*, Vol. 11, pp. 1117-1125.
- Kays, W. M., 1994, "Turbulent Prandtl Number—Where Are We?," *ASME JOURNAL OF HEAT TRANSFER*, Vol. 116, pp. 284-295.
- Kutateladze, S. S., and Gogonin, I. I., 1979, "Heat Transfer in Film Condensation of Slowly Moving Vapor," *Int. J. Heat Mass Transfer*, Vol. 22, pp. 1593-1599.
- Kutateladze, S. S., and Gogonin, I. I., 1985, "Heat Transfer in Condensation of Flowing Vapor on a Horizontal Cylinder," *Int. J. Heat Mass Transfer*, Vol. 28, No. 5, pp. 1019-1030.
- Lee, W. C., Rahbar, S., and Rose, J. W., 1984, "Film Condensation of Refrigerant 113 and Ethandiol on a Horizontal Tube—Effect of Vapor Velocity," *ASME JOURNAL OF HEAT TRANSFER*, Vol. 106, pp. 524-530.
- Liné, A., Masbernat, L., Miré, A., and Soualmia, A., 1991, "Analysis of the Local Structure of Co-current Stratified Two-Phase Flow," *European Two Phase Flow Group Meeting*, Rome, May 27-29.
- Lombardi, P., De Angelis, V., and Banerjee, S., 1996, "Direct Numerical Solution of Stratified Gas-Liquid Flow," *Int. Conf. Nuclear Eng.*, Vol. 1—Part A, pp. 101-109.
- Louahlia, H., and Panday, P. K., 1996, "Transfert Thermique pour la Condensation du R123, du R134a et de leurs Mélanges, en Écoulement Forcé Entre Deux Plaques Planes Horizontales-Etude Numérique," *Rev. Gén. Ther.*, Vol. 35, pp. 615-624.
- Memory, S. B., and Rose, J. W., 1986, "Film Condensation of Ethylene Glycol on a Horizontal Tube at High Vapor Velocity," *Proc. of the 8th Int. Heat Transfer Conference*, San Francisco, ASME, New York, pp. 1607-1612.
- Memory, S. B., and Rose, J. W., 1991, "Free Convection Laminar Film Condensation on a Horizontal Tube With Variable Wall Temperature," *Int. J. Heat Mass Transfer*, Vol. 34, No. 11, pp. 2775-2778.
- Memory, S. B., Lee, W. C., and Rose, J. W., 1993, "Forced Convection Film Condensation on a Horizontal Tube-Effect of Surface Temperature Variation," *Int. J. Heat Mass Transfer*, Vol. 36, No. 6, pp. 1671-1676.
- Memory, S. B., and Rose, J. W., 1995, "Forced Convection Film Condensation on a Horizontal Tube—Influence of Vapor Boundary Layer Separation," *ASME JOURNAL OF HEAT TRANSFER*, Vol. 117, pp. 529-533.
- Michael, A. G., Rose, J. W., and Daniels, L. C., 1989, "Forced Convection Condensation on a Horizontal Tube: Experiments With Vertical Downflow of Steam," *ASME JOURNAL OF HEAT TRANSFER*, Vol. 111, pp. 792-797.
- Mizushima, T., Ueda, H., and Umemiya, N., 1972, "Effect of Free Stream Turbulence on Mass Transfer From a Circular Cylinder in Cross Flow," *Int. J. Heat Mass Transfer*, Vol. 15, pp. 769-780.
- Morgan, V. T., 1975, "The Overall Convective Heat Transfer From Smooth Circular Cylinders," *Advances in Heat Transfer*, Vol. 11, pp. 199-264.
- Morrison, J., Deans, J., and McFeaters, J., 1998, "Condensation of Steam on a Thick-Walled Horizontal Tube," *Heat Transfer Engineering*, Vol. 19, No. 1, pp. 17-24.
- Mudawwar, I. A., and El-Masri, M. A., 1986, "Momentum and Heat Transfer Across Freely Falling Turbulent Liquid Films," *Int. J. Multiphase Flow*, Vol. 12, No. 5, pp. 771-790.
- Nusselt, W., 1916, "Die Oberflächkondensation des Wasserdampfes," *Z. Ver. Deut. Ing.*, Vol. 60, pp. 541-546.
- Panday, P. K., 1988, "Condensation of Downward Flowing Vapor on a Horizontal Cylinder," *ASME Proc. Nat. Heat Transfer Conf.*, Vol. 2, ASME, New York, pp. 613-619.
- Paolini, M. A., Kinney, R. B., and Ceruti, E. A., 1986, "Numerical Analysis of the Unsteady Flow and Heat Transfer to a Cylinder in Cross Flow," *ASME JOURNAL OF HEAT TRANSFER*, Vol. 108, pp. 742-748.
- Pletcher, R. H., 1974, "Prediction of Transpired Turbulent Boundary Layers," *ASME JOURNAL OF HEAT TRANSFER*, pp. 89-94.
- Rose, J. W., 1984, "Effect of Pressure Gradient in Forced Convection Film Condensation on a Horizontal Tube," *Int. J. Heat Mass Transfer*, Vol. 27, pp. 39-34.
- Rose, J. W., 1989, "A New Interpolation Formula for Forced Convection Condensation on a Horizontal Surface," *ASME JOURNAL OF HEAT TRANSFER*, Vol. 111, pp. 818-819.
- Sarma, P. K., Vijayalakshmi, B., Mayinger, F., and Kakac, S., 1998, "Turbulent Film Condensation on a Horizontal Tube With External Flow of Pure Vapors," *Int. J. Heat Mass Transfer*, Vol. 41, pp. 537-545.
- Scholten, J. W., and Murray, D. B., 1998, "Unsteady Heat Transfer and Velocity of a Cylinder in Cross Flow—I. Low Free Stream Turbulence," *Int. J. Heat Mass Transfer*, Vol. 41, No. 10, pp. 1139-1148.
- Scholten, J. W., and Murray, D. B., 1998, "Unsteady Heat Transfer and Velocity of a Cylinder in Cross Flow—II. High Free Stream Turbulence," *Int. J. Heat Mass Transfer*, Vol. 41, No. 10, pp. 1149-1156.
- Shekrlidze, I. J., and Gomelauri, V. I., 1966, "Theoretical Study of Laminar Film Condensation of Flowing Vapor," *Int. J. Heat Mass Transfer*, Vol. 9, pp. 581-589.
- Song, C. C. S., and Yuan, M., 1990, "Simulation of Vortex-Shedding Flow About a Circular Cylinder at High Reynolds Numbers," *ASME Journal of Fluids Eng.*, pp. 155-163.
- Sparrow, E. M., and Gregg, J. L., 1959, "Laminar Condensation Heat Transfer on a Horizontal Cylinder," *ASME JOURNAL OF HEAT TRANSFER*, Vol. 81, pp. 291-296.
- Speck, P., Desevaux, P., Panday, P. K., and Prenel, J. P., 1997, "Etude optique du ruissellement d'un film liquide sur un tube lisse horizontal en présence d'un écoulement d'air vertical," *Comptes Rendus de 7^{ème} Colloque Nationale de Visualisation et Traitement d'Images*, St. Louis, France, TEKNEA, Toulouse, France, pp. 281-286.
- Toba, Y., 1988, "Similarity Laws of the Wind Wave and the Coupling Process of the Air and Water Turbulent Boundary Layers," *Fluid Dynamics Research*, Vol. 2, pp. 263-279.
- Ünsal, M., 1983, "A Linearized Stability Analysis of Forced Vapor Flow Condensation," *NATO ASI Series*, Series E, pp. 725-743.
- Ünsal, M., 1988, "Effect of Waves on Nusselt Condensation," *Int. J. Heat Mass Transfer*, Vol. 31, No. 9, pp. 1944-1947.
- Van Driest, E. R., 1956, "On Turbulent Flow Near a Wall," *Journal of Aeronautical Sciences*, Vol. 23, pp. 1011-1036.
- Von Karman, T., 1939, "The Analogy Between Fluid Friction and Heat Transfer," *ASME JOURNAL OF HEAT TRANSFER*, Vol. 61, pp. 705-710.
- Zhou, Y. Q., and Rose, J. W., 1996, "Effect of Two-Dimensional Conduction in the Condensate Film on Laminar Film Condensation on a Horizontal Tube With Variable Wall Temperature," *Int. J. Heat Mass Transfer*, Vol. 39, No. 15, pp. 3187-3191.

A Heat and Mass Transfer Analysis of the Ignition and Extinction of Solid Char Particles

T. X. Phuoc

U.S. Department of Energy,
Federal Energy Technology Center,
P.O. Box 10904,
Pittsburgh, PA 15236
e-mail: tran@fetec.doe.gov

K. Annamalai

Department of Mechanical Engineering,
Texas A&M University,
College Station, TX 77843-3123
e-mail: Kannamalai@mengr.tamu.edu

The present work studies the ignition and extinction of a spherical solid fuel particle exposed to a quiescent, hot, oxygen-containing environment. Using particle sizes and ambient temperature and oxygen concentration as parameters, the ignition, burning, and extinction of particles were parametrically analyzed by studying the relative heat production and heat-loss rates. For a given ambient condition, the results showed that it is possible that both large and small particles might not ignite at all. When a particle burns, its size decreases with time and its combustion characteristics are altered. The extinction condition may be reached due solely to the diminishing size of the particle. The particle extinction diameter was calculated. It strongly depends on the ambient condition and the reaction rate, but not on the initial particle size.

Introduction

Ignition, combustion, and extinction of a solid fuel particle when it is exposed to a hot and oxygen-content environment are the phenomena that involve many physical and chemical processes. Physical processes are mainly the heat and mass transport between the particle and its surrounding, and chemical processes are particle oxidation, devolatilization, and oxidation of volatile gases in the gas phase. These processes are transient, coupled with each other, and depend strongly on the fuel's physical and chemical properties. Among these properties, the particle size has been recognized as a dominant parameter that strongly affects the mechanisms of the ignition and combustion of single, solid fuel particles.

Ubhayakar (1976) presented a theoretical model to analyze the combustion characteristics of a spherical carbon particle. He showed that when a particle is burning quasi-steadily, the particle size decreases with time. Therefore, the combustion mechanism is altered and the extinction condition may be reached due solely to the diminishing size of the burning particle.

Annamalai and Durbetaki (1977) analyzed the ignition of coal particles assuming heterogeneous reactions in the absence of homogeneous reactions and homogeneous reactions in the absence of heterogeneous reactions. They reported that, for a given oxygen concentration, the minimum gas temperature required for the particle to ignite decreases as the particle size increases for both homogeneous ignition and heterogeneous ignition. Similar results were reported by Brooks and Essenhigh (1986) who studied the variation of ignition temperatures of anthracite, bituminous, and char particles. Their predicted and experimental results indicate that the minimum ignition temperature decreases as particle diameter and oxygen concentration increase. Gururajan et al. (1990) developed a detailed model for the steady-state combustion of a coal particle. The model accounted for both surface oxidation and volatile combustion in the gas phase. They showed that the gas-phase ignition temperature is inversely proportional to the particle size and oxygen concentration. They also reported that surface oxidation influences the ignition temperature only for small particles or at high oxygen concentration.

Two ignition mechanisms for coal particles have been reported (Karcz et al., 1980; Gomer and Vastola, 1985; Du and Annamalai, 1994; Kharbat et al., 1995). Whether a particle is ignited heterogeneously or homogeneously depends on the relative rates of the heating of particle surface, the evolution of the volatile gases, the surface oxidation reactions, and the oxidation of the volatile gases in the gas phase. These rates are essentially particle-size dependent. Karcz et al. (1980) studied the ignition of a bituminous coal, an anthracite, and a char produced from bituminous coal. Using the heterogeneous ignition model, they concluded that the coal particles ignited heterogeneously for smaller-particle diameters and homogeneously for larger-particle diameters. Gomez and Vastola (1985), using gas analysis and light intensity techniques, studied the ignition of Wyoming subbituminous coal in air. Single coal particles of diameters from 850 to 1000 μm and gas temperatures from 928 to 1283 K were used. Both heterogeneous and homogeneous mechanisms were observed and the transition from heterogeneous ignition to homogeneous ignition occurred when the gas temperature increased. Du and Annamalai (1994) and Kharbat et al. (1995) reported that when an isolated particle is injected into a hot gas, the mechanism by which the particle ignites depends on the gas temperature, the volatile content, the fixed carbon, and the particle size. For a gas temperature lower than 900 K, particles smaller than 50 μm cannot be ignited either by the homogeneous or heterogeneous mode. For gas temperatures from 1000 K to 1100 K, heterogeneous ignition is expected for most coal sizes smaller 900 μm and homogeneous ignition is expected to occur only for larger ($>900 \mu\text{m}$) and high-volatile coals when the gas temperature exceeds 1100 K.

Effects of the particle size on the temperature distribution in the interior of a coal particle was also reported (Gat, 1986). Phuoc and Mathur (1991) developed a theoretical model to calculate the intra-particle heat transfer behavior of a coal particle when it is undergoing heating and devolatilization. They reported that the temperature field of the interior of a coal particle is not uniform and it depends strongly on the particle size, the heating rate, and the particle thermal conductivity. For a given condition of thermal conductivity and heating rate, a particle of larger size has a large-temperature gradient in its interior. Due to such a temperature gradient, the devolatilization process might proceed in the form of a devolatilization front, which is initiated from the particle surface and moves inward into the center of the particle. Hertzberg et al. (1988) analyzed existing data and their data on mass loss and

Contributed by the Heat Transfer Division for publication in the JOURNAL OF HEAT TRANSFER. Manuscript received by the Heat Transfer Division, Jan. 1, 1999; revision received, July 12, 1999. Key words: Combustion, Flame, Heat Transfer. Associate Technical Editor: J. Gore.

devolatilization time for various coal particles using radiant flux from a CO₂ laser beam. They concluded that devolatilization proceeds at a rate determined by the heat transport rate. The devolatilization front is driven through the particle by the heat source flux, leaving a hotter char zone on the decomposed side in the wake of the devolatilization front, and a cooler unreacted coal zone ahead of the devolatilization front. Thus, for fine coal particles, the devolatilization time is short, the particle is totally devolatilized and the flame propagation process is associated entirely with the hydrocarbon volatiles emitted during the devolatilization process. For coarse particles, the devolatilization time is long and the particle can no longer be totally devolatilized, and only the regions close to the particle surface can contribute volatiles to the flame. The heat transport-driven devolatilization front was also observed by Phuoc and Maloney (1988), who measured the coal devolatilization times using an electrodynamic balance with two coal particle sizes of 60 μm and 120 μm which were subjected to laser radiation intensities varying from 500 to 2500 W/cm². They reported that the time required for complete devolatilization depends strongly on particle size and heat flux.

It is clear that particle size is an important parameter that can alter the mechanisms of ignition, combustion, and extinction of a solid fuel. Its effect can be simply explained in terms of the heat and mass interaction between the particle and the gas phase. According to the thermal ignition theory, ignition occurs when heat loss is counterbalanced by heat generation. Since heat loss becomes large when the particle is small, and the oxygen concentration at the particle surface decreases when the particle is large, this condition is difficult to meet for both small and large particles. It will be shown later that there exist an upper and lower limits of the particle size by which ignition is impossible. And, as the particle is burning, its size is decreasing, heat loss is increasing and the combustion process is altered from diffusion to a kinetically controlled regime. As a result, extinction condition may be reached due solely to the diminishing size of the particle. Such a lower limit of the particle size has been reported by Annamalai (1979), Du and Annamalai (1994), and Kharbat et al. (1995). However the upper size limit, as resulted by the increase in radiation loss coupled with decreased oxygen concentration, has not been discussed by the early work which we will discuss in detail.

The Theoretical Model

The present work considers a spherical solid carbon particle of initial radius $r_{s,i}$, and uniform temperature, T_s , being exposed to a hot, quiescent air of temperature T_e and oxygen concentration $Y_{O_2,e}$. The particle is heated and its temperature increases. As the particle temperature increases, oxidation reactions at the particle surface ensue. Oxygen is assumed to diffuse toward the particle surface. It reacts with the particle to form gaseous products, which

diffuse outward into the gas phase where homogeneous combustion might occur. In this case, oxygen concentration reaching the surface is reduced and so is the heat loss. Compensating effects are present. Since this work analyzes the ignition and extinction of a particle based only on the competition between heat generation and heat loss, such compensating effects will not alter the physics of the problem. The gas-phase oxidation is, therefore, neglected by the present analysis. Combustion and ignition of such a particle depends on reaction rates, heat and mass transport at the particle surface, and the particle size. Thus, by simply analyzing these processes as a function of the particle size, the burning characteristics of the particle, along with its ignition and extinction phenomena, can be investigated. In so doing, the following assumptions are made:

- (i) the process is quasi-steady for the gas phase;
- (ii) the hot air behaves like an ideal gas and has a constant temperature T_e , pressure, and oxygen mass fraction Y_{O_2} ;
- (iii) $\rho_g D$ and $\lambda_g/c_{p,g}$ are constant and the Lewis Number is unity;
- (iv) the particle temperature is initially uniform at its surface temperature T_s ;
- (v) particle thermal properties and physical properties are constant, intra-particle heat and mass transfer are neglected;
- (vi) the surface reaction is exothermic, first order in oxygen concentration; and
- (vii) the following reaction is assumed for the carbon reaction: $C + O_2 = CO_2$, and the rate is expressed in terms of an Arrhenius equation.

The gas-phase conservation equations are
Mass:

$$m = 4\pi r_s^2 w_s \quad (1)$$

Species:

$$m \frac{dY_i}{dr} - \frac{d}{dr} 4\pi r^2 \rho_g D \frac{dY_i}{dr} = 0 \quad (2)$$

where i is O₂, CO₂, and N₂.

Temperature:

$$m \frac{dT_g}{dr} - \frac{d}{dr} 4\pi r^2 \rho_g D \frac{dT_g}{dr} = 0 \quad (3)$$

where T_g is the gas temperature (K), Y_i is the mass fraction of species i , ρ_g is the gas density (g/cm³), m is the mass flow rate (g/s), and D is the diffusivity (cm²/s). The equation of state is

Nomenclature

A = frequency factor (cm/s)	r = r -coordinate (cm)	σ = Stefan-Boltzmann constant (1.356×10^{-12} cal/cm ² -s-K ⁴)
c_p = specific heat (cal/g-K)	r_s = particle radius (cm)	τ = dimensionless time
C_{cp} = specific heat ratio	T = temperature (K)	
D = diffusion coefficient (cm ² /s)	t = time (s)	
$D_{2,s}$ = the dimensionless reaction heat constant	w_s = reaction time (g/cm ² -s)	
$D_{1,s}$ = the dimensionless reaction number	Y_i = species concentration	
D_r = the dimensionless radiation number	ϵ = the emissivity	
E = activation energy (cal/gmole)	θ = the dimensionless temperature	
m = mass flow rate (g/s)	λ = thermal conductivity (cal/cm ² -s-K)	
m^* = the dimensionless mass flow rate	ν = stoichiometric ratio	
q = heat of reaction (cal/g)	ξ = dimensionless particle size	
R = gas constant (cal/gmole-K)	ρ = density (g/cm ³)	
		Subscripts
		CO ₂ = carbon dioxide
		E = extinction
		e = ambient condition
		g = gas phase
		i = species, initial
		I = ignition
		N ₂ = nitrogen
		O ₂ = oxygen
		s = particle

$$\rho_g T_g = \rho_{\text{ref}} T_{\text{ref}} \quad (4)$$

where ρ_{ref} and T_{ref} are the reference density and temperature, respectively. The reaction rate w_s (g of carbon/cm²-s) is expressed in terms of an Arrhenius equation as

$$w_s = \rho_{g,s} Y_{\text{O}_2,s} A e^{-E/RT_s} \quad (5)$$

where A is the frequency factor (cm/s); E is the activation energy (cal/gmole); $\rho_{g,s}$ is the gas density at the particle surface (g/cm³); R is the gas constant (cal/gmole-K); and T_s is the particle temperature (K).

Boundary Conditions:

At $r = r_\infty$:

$$T_g = T_e; \quad Y_i = Y_{i,e}; \quad Y_{\text{CO}_2,e} = 0.0 \quad (6)$$

$$\frac{dT_g}{dr} = \frac{dY_i}{dr} = 0 \quad (7)$$

with $i = \text{O}_s, \text{N}_2$, and CO_2 .

At $r = r_s$:

$$T_g = T_s; \quad Y_i = Y_{i,s} \quad (8)$$

with $i = \text{O}_2, \text{N}_2$, and CO_2 .

$$mY_{\text{O}_2,s} - 4\pi r_s^2 \rho_g D \left(\frac{dY_{\text{O}_2}}{dr} \right)_{r_s} = -\nu_{\text{O}_2} m \quad (9)$$

$$mY_{\text{CO}_2,s} - 4\pi r_s^2 \rho_g D \left(\frac{dY_{\text{CO}_2}}{dr} \right)_{r_s} = \nu_{\text{CO}_2} m \quad (10)$$

$$mY_{\text{N}_2,s} - 4\pi r_s^2 \rho_g D \left(\frac{dY_{\text{N}_2}}{dr} \right)_{r_s} = 0 \quad (11)$$

where ν is the stoichiometric ratio ($\nu_{\text{O}_2} = 32/12$; $\nu_{\text{CO}_2} = 44/12$).

The time rate of change of the particle temperature is given as

$$\frac{dT_s}{dt} = \frac{3[g'(t) - f'(t)]}{4\pi r_s^3 \rho_s c_{p,s}} \quad (12)$$

where the heat loss $f'(t)$, and the heat generation $g'(t)$ are given as

$$g'(t) = m(q - c_{p,g} T_s + c_{p,s} T_s) \quad (13)$$

$$f'(t) = 4\pi r_s^2 \left[-\lambda_g \left(\frac{dT_g}{dr} \right)_{r_s} + \sigma \epsilon (T_s^4 - T_e^4) \right] \quad (14)$$

and the changing particle size is given

$$\frac{dr_s}{dt} = \frac{-m}{4\pi r_s^2 \rho_s} \quad (15)$$

where q (cal/g) is the heat of reaction, $c_{p,g}$ (cal/g-K) is the specific heat of the gas, $c_{p,s}$ (cal/g-K) is the specific heat of the solid, λ_g (cal/cm²-s-K) is the gas thermal conductivity, σ (1.356×10^{-12} cal/cm²-s-K⁴) is the Stefan-Boltzmann constant, and ϵ is the solid emissivity. In Eq. (13), $mc_{p,g} T_s$ represents the heat transported by the combustion products, and $mc_{p,s} T_s$, which is resulted from the time derivative of the particle energy, $d(4\pi r_s^3 \rho_s c_{p,s} T_s)/3dt$, represents the heat contributed by the receding surface. For fuels such that $c_{p,s} \approx c_{p,g}$, $m(c_{p,s} - c_{p,g}) T_s$ might be probably small compared with the combustion heat, and it might be negligible.

Thus, the solutions for T_g and Y_i ; ($i = \text{O}_2, \text{N}_2$, and CO_2) are

$$Y_i = Y_{i,e} + (Y_{i,s} - Y_{i,e}) \frac{1 - e^{-m/4\pi r_s \rho_g D}}{1 - e^{-m/4\pi r_\infty \rho_g D}} \quad (16)$$

$$T_g = T_e + (T_s - T_e) \frac{1 - e^{-m/4\pi r_s \rho_g D}}{1 - e^{-m/4\pi r_\infty \rho_g D}} \quad (17)$$

and $Y_{\text{O}_2,s}$; $Y_{\text{CO}_2,s}$ are given as

$$Y_{\text{O}_2,s} = (Y_{\text{O}_2,e} + \nu_{\text{O}_2}) e^{-m/4\pi r_s \rho_g D} - \nu_{\text{O}_2} \quad (18)$$

$$Y_{\text{CO}_2,s} = \nu_{\text{CO}_2} (1 - e^{-m/4\pi r_s \rho_g D}). \quad (19)$$

In addition, we have

$$\left(\frac{dT_g}{dr} \right)_s = \frac{-m(T_s - T_e)}{4\pi r_s^2 \rho_g D} \left(\frac{e^{-m/4\pi r_s \rho_g D}}{1 - e^{-m/4\pi r_\infty \rho_g D}} \right) \quad (20)$$

$$m = 4\pi r_s \rho_g D \ln \left[\frac{Y_{\text{O}_2,e} + \nu_{\text{O}_2}}{Y_{\text{O}_2,s} + \nu_{\text{O}_2}} \right] \quad (21)$$

or

$$m = \frac{4\pi r_s \lambda_g}{c_{p,g}} \ln \left[1 - \frac{mc_{p,g}(T_s - T_e)}{4\pi r_s^2 \lambda_g \left(\frac{dT_g}{dr} \right)_s} \right] \quad (22)$$

To simplify the above equations, we define the following dimensionless constants:

$$D_{1,s} \equiv \frac{\rho_{\text{ref}} T_{\text{ref}} R A r_s}{E \rho_g D} \quad (23)$$

$$D_{2,s} \equiv \frac{qR}{E c_{p,s}}; \quad C_{cp} \equiv \frac{c_{p,g}}{c_{p,s}} \quad (24)$$

$$D_\sigma \equiv \frac{\sigma \epsilon}{\rho_{\text{ref}} T_{\text{ref}} A c_{p,s}} \left(\frac{E}{R} \right)^4 \quad (25)$$

$$\tau \equiv \frac{3\rho_g D t}{\rho_s r_{s,i}^2}; \quad \xi \equiv \frac{r_s}{r_{s,i}} \quad (26)$$

$$m^* \equiv \frac{m}{4\pi r_s \rho_g D}; \quad \theta \equiv \frac{RT}{E} \quad (27)$$

where $D_{1,s}$ is the dimensionless reaction number, $D_{2,s}$ is the dimensionless reaction heat, D_σ is the dimensionless radiation number, τ is the dimensionless time, ξ is the dimensionless particle size, θ is the dimensionless temperature, C_{cp} is the ratio of the specific heat, and m^* is the dimensionless mass flow rate.

The dimensionless temperature of the particle is

$$\frac{d\theta_s}{d\tau} = \frac{1}{\xi^2} [g(t) - f(t)] \quad (28)$$

where $f(t)$ and $g(t)$ are the dimensionless heat loss and heat generation, respectively,

$$g(t) = (D_{2,s} - C_{cp}\theta_s + \theta_s) \frac{D_{1,s} Y_{\text{O}_2,s} e^{-1/\theta_s}}{\theta_s} \quad (29)$$

$$f(t) = C_{cp} m^* (\theta_s - \theta_e) \left(\frac{e^{-m^*}}{1 - e^{-m^*}} \right) + D_\sigma D_{1,s} (\theta_s^4 - \theta_e^4). \quad (30)$$

The dimensionless particle size becomes

$$\frac{d\xi}{d\tau} = \frac{-D_{1,s} Y_{\text{O}_2,s} e^{-1/\theta_s}}{3\xi \theta_s} \quad (31)$$

and the dimensionless mass flow rate is

$$m^* = \ln \left[\frac{Y_{\text{O}_2,e} + \nu_{\text{O}_2}}{Y_{\text{O}_2,s} + \nu_{\text{O}_2}} \right] = D_{1,s} \frac{Y_{\text{O}_2,s} e^{-1/\theta_s}}{\theta_s}$$

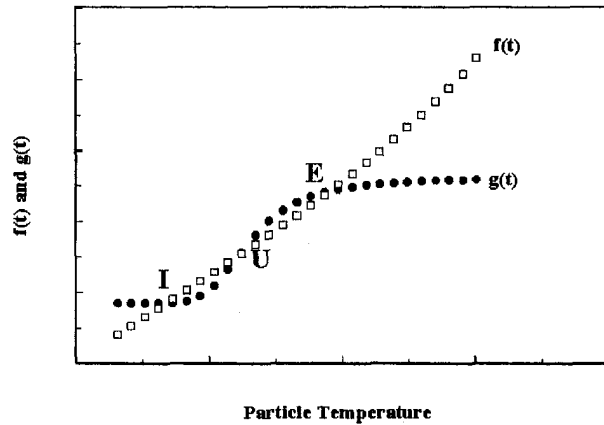


Fig. 1 Diagrammatic plot of the heat loss and the heat generation at the particle surface

$$= \ln \left[1 - \frac{m^*(\theta_s - \theta_e)}{\xi \frac{d\theta}{d\xi}} \right] \quad (32)$$

Ignition and Extinction Conditions. The thermal theory of ignition states that when a particle is dropped into an environment of temperature T_e , ignition occurs when heat generation is equal to heat loss from the particle, ($d\theta_s/d\tau = 0$), and the rate of change of heat generation with the particle temperature is equal to the rate of change of heat loss with the particle temperature. Figure 1 shows the diagrammatic plot of $f(t)$ and $g(t)$ as a function of the particle temperature to illustrate such an ignition condition. The curves show the intersections of $f(t)$ and $g(t)$ at I, U, and E. The intersections at I and E correspond to two stable solutions and the intersection at U corresponds to an unstable solution, which can jump up and down to the two stable solutions at I and E depending on the particle heating conditions. When U coincides with I, $f(t)$ becomes equal and tangential to $g(t)$ at I, ($f(t) = g(t)$ and $dg(t)/d\theta_s = df(t)/d\theta_s$ at I). Thus, ignition occurs at $\theta_{s,i}$ and the particle continues to burn stably to $\theta_{s,E}$. When U coincides with E, $f(t)$ becomes equal and tangential to $g(t)$ at E. The heat generation, $g(t)$, is no longer sufficient to counterbalance the heat loss, $f(t)$. Extinction is said to occur at $\theta_{s,E}$ and the particle temperature drops rapidly to $\theta_{s,i}$.

This condition provides information on the minimum ambient temperature, ($\theta_{e,i}$), required to ignite the particle irrespective of any time limitation. However, when the environment temperature, θ_e , is higher than the required minimum ignition temperature the particle will ignite at some time, and $d\theta_s/d\tau$ is not equal to zero. Du and Annamalai (1994) showed that if the ambient temperature is equal to the required minimum ignition temperature, $\theta_{e,i}$, then $d^2\theta_s/d\tau^2 = 0$ and $d\theta_s/d\tau = 0$ at ignition. If $\theta_e > \theta_{e,i}$ then $d^2\theta_s/d\tau^2 = 0$ and $d\theta_s/d\tau > 0$ at ignition. Thus, the ignition and extinction conditions are evaluated as follows.

Ignition:

$$\frac{d^2\theta_s}{d\tau^2} = 0.0; \quad \frac{d\theta_s}{d\tau} > 0.0. \quad (33)$$

Extinction:

$$\frac{d^2\theta_s}{d\tau^2} = 0.0; \quad \frac{d\theta_s}{d\tau} < 0.0. \quad (34)$$

The determination of $d^2\theta_s/d\tau^2$ requires storage of particle temperatures for three time steps. An alternate procedure is used to estimate the ignition condition and the particle ignition temperature. From Eq. (28), $d^2\theta_s/d\tau^2$ is calculated as

$$\frac{d^2\theta_s}{d\tau^2} = \left(\frac{dg}{d\theta_s} - \frac{df}{d\theta_s} \right) \frac{1}{\xi^2} \frac{d\theta_s}{d\tau} - \frac{2}{\xi} \frac{d\xi}{d\tau} \frac{d\theta_s}{d\tau}. \quad (35)$$

For small m^* , $e^{-m^*/(1-e^{-m^*})} \rightarrow 1/m^*$. Then $Y_{O_{2,s}}$ can be calculated from Eqs. (18), and (32) as

$$Y_{O_{2,s}} = \frac{Y_{O_{2,e}}}{1 + (Y_{O_{2,e}} + \nu_{O_2})D_{1,s} \frac{e^{-1/\theta_s}}{\theta_s}} \quad (36)$$

and the heat loss $f(t)$ reduces to

$$f(t) = C_{cp}(\theta_s - \theta_e) + D_{\sigma}D_{1,s}(\theta_s^4 - \theta_e^4). \quad (37)$$

It is assumed that $d\xi/d\tau$ is small before ignition, and for $d^2\theta_s/d\tau^2 = 0.0$ and $d\theta_s/d\tau > 0$, it is required that

$$\frac{dg}{d\theta_s} = \frac{df}{d\theta_s}. \quad (38)$$

By differentiating $g(t)$, $f(t)$, m^* , and $Y_{O_{2,s}}$ with respect to θ_s and using condition $dg/d\theta_s = df/d\theta_s$ given by Eq. (38), the ignition condition and the particle ignition temperature can be calculated by the following equations:

$$\Pi_1 = \frac{(\Pi_2 + \Pi_3)Y_{O_{2,e}}D_{1,s} \frac{e^{-1/\theta_{s,i}}}{\theta_{s,i}}}{1 + (Y_{O_{2,e}} + \nu_{O_2})D_{1,s} \frac{e^{-1/\theta_{s,i}}}{\theta_{s,i}}} \quad (39)$$

where

$$\Pi_1 = C_{cp} + 4D_{\sigma}D_{1,s}\theta_{s,i}^3 \quad (40)$$

$$\Pi_2 = 1 - C_{cp} \quad (41)$$

$$\Pi_3 = \frac{(D_{2,s} - C_{cp}\theta_{s,i} + \theta_{s,i})(1 - \theta_{s,i})}{\theta_{s,i}^2 \left[1 + (Y_{O_{2,e}} + \nu_{O_2})D_{1,s} \frac{e^{-1/\theta_{s,i}}}{\theta_{s,i}} \right]} \quad (42)$$

The solutions of the above equations with respect to θ_e , $D_{1,s}$, $D_{2,s}$, D_{σ} , and ξ determine the burning characteristics of a solid fuel particle. The heat loss, $f(t)$, strongly depends on ξ , and the heat generation, $g(t)$, is directly proportional to the reaction rate, which is large when the reaction is diffusion-controlled and small when the reaction is kinetically controlled.

To calculate the rate, Eq. (21) is usable only when the combustion rate is totally dependent on the inward diffusion of the oxygen toward the particle surface, and the oxygen concentration must lie in the range $0 \leq Y_{O_{2,s}} < Y_{O_{2,e}}$. Equation (21), however, is no longer valid for the combustion rate calculation when $Y_{O_{2,s}}$ is equal to $Y_{O_{2,e}}$. In this case, the rate must be determined by the Arrhenius equation given by Eq. (5), which essentially depends on the kinetic parameters and the particle temperature. Thus, it is clear that when $Y_{O_{2,s}}$ approaches $Y_{O_{2,e}}$, the particle burns under the kinetically controlled regime, and when $Y_{O_{2,s}}$ is close to zero, the combustion is under the diffusion-controlled regime. Figure 2 shows the variation of $Y_{O_{2,s}}$ with the particle size for $Y_{O_{2,e}} = 0.232$ and $\theta_s = 0.099, 0.115, \text{ and } 0.132$. It is clear that $Y_{O_{2,s}}$ depends strongly on the particle temperature and the particle size. For small particles, $Y_{O_{2,s}}$ was close to $Y_{O_{2,e}}$ and dropped drastically as the particle size increased. Thus, these two combustion regimes are dictated by the particle size. The diffusion-controlled regime exists for very large particles and the kinetic-controlled regime exists for very small particles. For most practical cases, however, the burning is in the kinetic-diffusive regime (Fu and Zhang, 1993, Zeng and Fu, 1996).

From Eqs. (28) and (31), one can write an equation describing the change of the particle temperature with respect to the receding surface as follows:

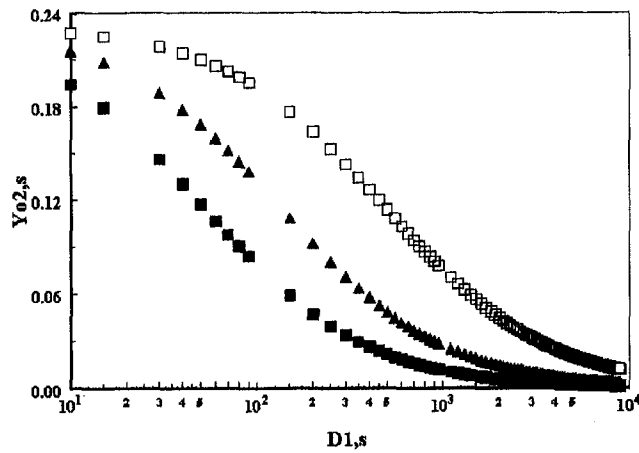


Fig. 2 Oxygen concentration at the particle surface as a function of the particle size ($D_{1,s}$); ($Y_{O_{2,e}} = 0.232$; $\theta_s = 0.082$; $D_\sigma = 0.925$; \square : $\theta_s = 0.1$; \blacktriangle : $\theta_s = 0.115$; \blacksquare : $\theta_s = 0.132$)

$$\frac{d\theta_s}{d\xi} = \frac{-3\theta_s [g(t) - f(t)]}{\xi D_{1,s} Y_{O_{2,s}}} e^{1/\theta_s} \quad (43)$$

Letting $C_{cp} = 1$, $d\theta_s/d\xi$ can be approximated as

$$\frac{d\theta_s}{d\xi} = \frac{-3\theta_s}{\xi} \left[\frac{D_{2,s}}{\theta_s} - \frac{(\theta_s - \theta_e)e^{1/\theta_s}}{D_{1,s} Y_{O_{2,s}}} - \frac{D_\sigma(\theta_s^4 - \theta_e^4)e^{1/\theta_s}}{Y_{O_{2,s}}} \right] \quad (44)$$

The first term in the bracket represents the heat generation, the second and third terms are for the heat loss by conduction and radiation, respectively. From Eq. (36), $D_{1,s} Y_{O_{2,s}}$, and $D_\sigma/Y_{O_{2,s}}$ are given as

$$D_{1,s} Y_{O_{2,s}} = \frac{Y_{O_{2,e}}}{[1/D_{1,s} + (Y_{O_{2,e}} + \nu_{O_2})e^{-1/\theta_s/\theta_s}] \quad (45)$$

$$\frac{D_\sigma}{Y_{O_{2,s}}} = \frac{D_\sigma [1 + (Y_{O_{2,e}} + \nu_{O_2})D_{1,s}e^{-1/\theta_s/\theta_s}]}{Y_{O_{2,e}}} \quad (46)$$

Thus, for large particles, the radiative heat loss becomes dominant while the conductive heat loss approaches a finite value, which is equal to $(1 - \theta_e/\theta_s)(Y_{O_{2,e}} + \nu_{O_2})/Y_{O_{2,e}}$. This might lead to the existence of a critical particle size, beyond which the radiative heat loss is able to counterbalance the combustion heat, and particle extinction occurs. For a particle whose size is below such a critical value, the burning is continued, and its size decreases with time. Since $D_{1,s} Y_{O_{2,s}} \rightarrow 0$, and $D_\sigma/Y_{O_{2,s}} \rightarrow D_\sigma/Y_{O_{2,e}}$, as the particle size becomes small, the heat loss from conduction becomes dominant. The combustion heat generation, $g(t)$, is getting smaller because the combustion regime is altered from the diffusion to the kinetically controlled regime. Eventually, the heat generation is no longer able to counterbalance the heat loss and the extinction condition may be reached due to the diminishing size of the burning particle. Figure 3 shows the plot of $f(t)$ and $g(t)$ as a function of the particle temperature for two different values of $D_{1,s}$. Figure 3(a) shows that $f(t)$ was tangential to $g(t)$ at the stable solution I when $D_{1,s} = 174.7$. Thus, ignition occurs at $\theta_{s,i}$ and the particle continues to burn stably to $\theta_{s,E}$ and $g(t)$ is always higher than $f(t)$. As particle size decreases, both curves shift to the right. The heat loss, $f(t)$, became tangential to $g(t)$ at the stable solution E as shown in Fig. 3(b) where $D_{1,s} = 27.95$. The heat generation, $g(t)$, was no longer sufficient to counterbalance the heat loss, $f(t)$. Thus, extinction occurred at $\theta_{s,E}$. Since $\theta_{s,E}$ is very much higher than $\theta_{s,i}$, the particle will continue to burn, and its temperature will rapidly drop. The combustion has completely ceased when the particle temperature drops below $\theta_{s,i}$.

Thus, by using a simple analysis of heat and mass transfer processes associated with the combustion of a solid fuel particle,

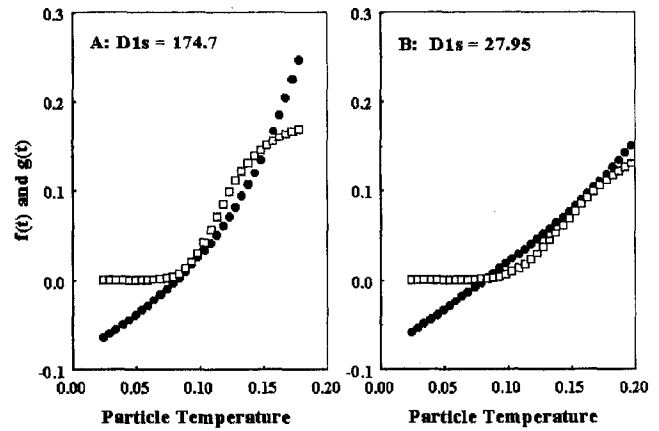


Fig. 3 Heat loss and heat generation as a function of the particle dimensionless temperature, θ_s ; ($Y_{O_{2,e}} = 0.232$; $\theta_e = 0.082$; $D_\sigma = 0.925$)

effects of the particle size on the particle ignition, extinction, and carbon burnout, etc., can be studied. These effects will be discussed in the next section.

Results and Discussions

Using the numerical procedures developed by Phuoc and Mathur (1991), the above equations were calculated numerically with θ_s , $D_{1,s}$, $D_{2,s}$, D_σ , etc., as parameters. Since the chemical reaction rate associated with the equations proceeds at different temperature with very different rates whose time scales can be different by several orders of magnitude, solving these equations requires variable time steps. Explicit methods are not stable when a time step is larger than any characteristic time scale (Cohen et al., 1975) and not suitable for solving these equations. Implicit methods then are preferred because they are stable for any time step. Table 1 lists the physical and chemical constants used in the present calculations. These data were used by Du and Annamalai (1994) in their investigation on the transient ignition of an isolated coal particle. Since these constants are used as reference data for evaluating the base values for θ_s , $D_{1,s}$, $D_{2,s}$, D_σ , etc., the accuracy of these data is, therefore, not critical for the current study.

Particle ignition temperatures, $\theta_{s,i}$, as a function of the particle size, $r_{s,i}$, with radiation effect, with $D_\sigma = 0.925$, and without radiation effect, when $D_\sigma = 0$, are shown in Fig. 4. Other parameters were kept constant at values calculated using the physical and chemical properties in Table 1. The ambient oxygen concentration, and dimensionless temperature were kept constant at 0.232 and 0.089, respectively. The curves obtained with the radiation effect showed that, as the particle size increased, the particle ignition temperature decreased. After it reached a minimum value, the particle ignition temperature started increasing as the particle size increased further. Information given in Fig. 2 shows that $Y_{O_{2,s}}$ was close to $Y_{O_{2,e}}$ for small particles, and close to zero for large particles. Thus, to overcome the lack of sufficient oxygen reaching its surface, a large particle requires a higher ignition temperature to generate sufficient heat for ignition. For a

Table 1 Physical and chemical properties

A	3020.75 m/s
E	100.9 MJ/kmole
q	32819 kJ/kg
$\rho_g D$	0.5×10^{-4} kg/m-s
$c_{p,g}$	1.18 kJ/kg-K
ρ_{ref}	1170 kg/m ³
T_{ref}	300 K
$c_{p,s}$	1.25 kJ/kg-K
ρ_s	1200 kg/m ³
ϵ	0.8

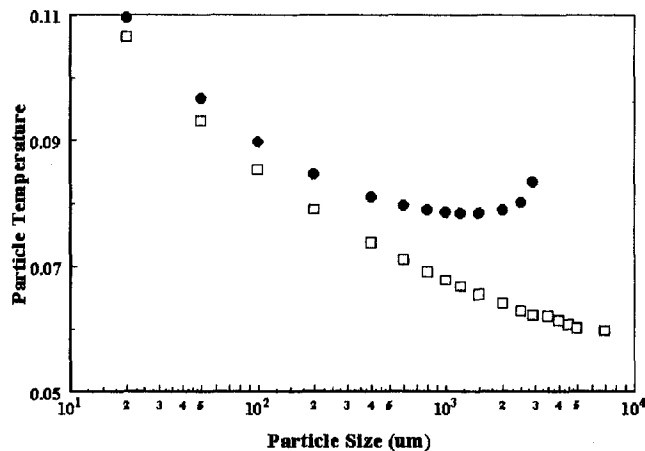


Fig. 4 Particle ignition temperature ($\theta_{s,i}$) as a function of the particle size; ($\theta_e = 0.082$; $Y_{O_2,e} = 0.232$; \bullet : $D_\sigma = 0.925$; \square : $D_\sigma = 0$)

small particle, the rate of heat loss, which inversely depends on particle size, becomes significant. Although oxygen is available at its surface, the particle temperature must be high enough for the heat release to overcome such a significant heat loss.

When radiation was neglected, the particle ignition temperature was lower than that when radiation was included. The significant effect, however, is the difference in the behavior of the particle ignition temperature with respect to the increase of the particle size. The minimum value of the particle ignition temperature does not exist in this case. In fact, the particle ignition temperature was found to monotonically decrease when the particle size increased. This result is attributed to the fact that the rate of change of the heat loss with respect to the particle temperature depends only on λ_g/r_s . Thus, the ignition condition now requires that $dg(t)/d\theta_s$ is proportional to λ_g/r_s , which monotonically decreases as the particle size increases.

Ignition and Nonignition Domains. The effect of the particle size on the particle ignition temperature shown above indicates that, for a given ambient condition, it is possible that both very small and very large particles do not ignite at all. Figure 5 shows the required size (in terms of $D_{1,s}$) of a fuel particle for ignition to occur at a given ambient condition. The ambient temperature was 0.082 and the ambient oxygen concentration was varied up to 1.0. Calculations were done with radiation and without radiation. The curves divided the plot into two regions: the region to the right of the curves was designated as the ignition region and the one to the left of the curves was designated as the no-ignition region.

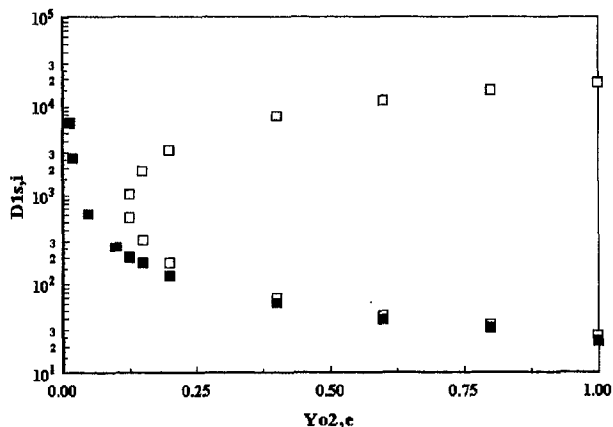


Fig. 5 Particle size required for ignition at a given ambient condition showing the ignition and no-ignition domain ($\theta_e = 0.082$; \square : calculated with $D_\sigma = 0.925$; \blacksquare : calculated with $D_\sigma = 0.0$)

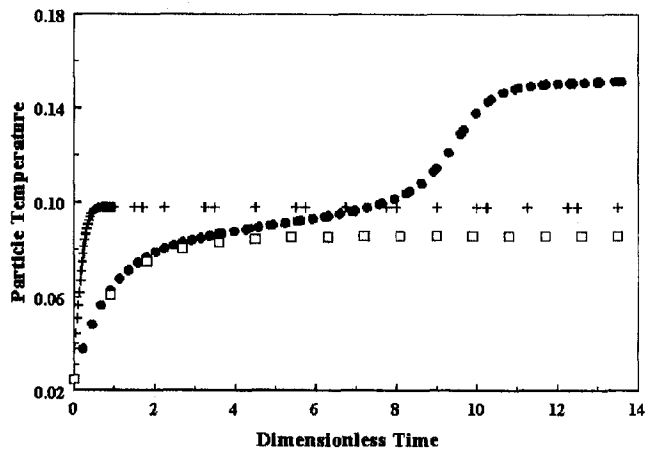


Fig. 6 Particle dimensionless temperature (θ_s) as a function of the dimensionless time (τ) showing the effect of the particle size ($\theta_e = 0.082$; $Y_{O_2,e} = 0.232$; solid circle: $D_{1,s} = 174.7$; plus sign: $D_{1,s} = 5242$; empty square: $D_{1,s} = 87.36$)

When radiation was not included, $D_{1,s}$ at ignition increased as the ambient oxygen concentration decreased. In this case, the ignition region was not bounded but extended to infinity. When radiation was included, the result was very different. It was observed that no ignition was possible regardless of the particle size for $Y_{O_2,e}$ less than 0.125. For $Y_{O_2,e}$ higher than 0.125, however, there were two solutions for $D_{1,s}$ for every value of $Y_{O_2,e}$. As a result, the ignition domain was bounded by the upper and lower limits of $D_{1,s}$. This means that ignition will prevail only for a particle of any size that lies within these limits. And, for particle sizes that are outside these limits, no ignition can occur.

To demonstrate this result the particle temperatures as a function of time were plotted in Fig. 6 showing that both small and large particles could not ignite. The ambient temperature and oxygen concentration were 0.082 and 0.232, respectively. The inflection point was obtained only for 100 μm particle, ($D_{1,s} = 174.73$), and it occurred when τ was about 4.6 and θ_s was about 0.09, indicating that the particle ignited. After ignition, its temperature sharply increased and the particle burned steadily at temperature θ_s , which was approximately 1.66, ($T_s = 2025$ K). As the particle size reduced to about 30 μm , ($D_{1,s} = 52.5$), particle extinction occurred. For 50 μm , ($D_{1,s} = 83.68$), and 3000 μm , ($D_{1,s} = 5242$) particles, no inflection point was obtained, and the temperature curves leveled off at $\theta_s = 0.086$ and $\theta_s = 0.098$, respectively.

These no-ignition and ignition domains were obtained by keeping the ambient oxygen concentration at a fixed value and using the ambient temperature as a parameter. The results are shown in Fig. 7 for $Y_{O_2,e} = 0.232$. Similar to the results shown in Fig. 5, the curves divided the plot into two regions: the ignition region and the noignition region. When $D_\sigma = 0$, the curve extended to infinity as the ambient temperature decreased. When D_σ was not equal to zero, ignition was not possible for θ_e less than 0.070. For θ_e higher than 0.070, however, there exist two solutions for $D_{1,s}$ for every value of θ_e . When θ_e was higher than 0.078, the upper bound of $D_{1,s}$ became constant at 5093 while the lower bound of $D_{1,s}$ decreased.

Using the ignition/extinction conditions described above, the shape of the curves in Figs. 5 and 7 can be theoretically constructed. To do so, we let $d\theta_s/d\xi$ in Eq. (44) be equal to zero, and with Eqs. (45) and (46) we obtain the following theoretical equation:

$$\frac{D_{2,s} D_{1,s} Y_{O_2,e}}{[\theta_s + (Y_{O_2,e} + \nu_{O_2}) D_{1,s} e^{-1/\theta_s}]} = (\theta_s - \theta_e) e^{1/\theta_s} + D_\sigma D_{1,s} (\theta_s^4 - \theta_e^4) e. \quad (47)$$

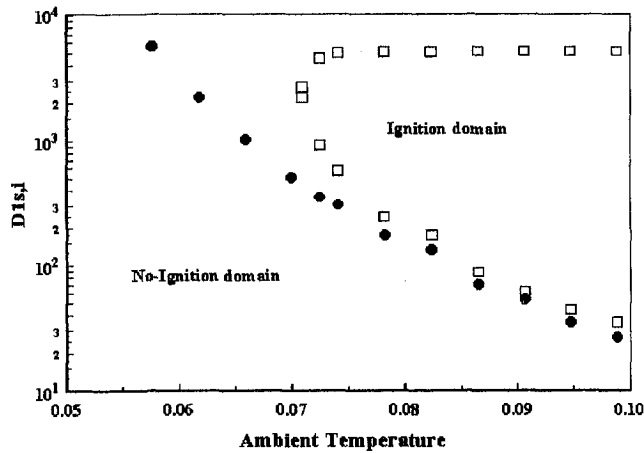


Fig. 7 Variation of $D_{1,s}$ with the ambient dimensionless temperature θ_e showing the ignition and no-ignition domains ($Y_{O_2,e} = 0.232$; \square : calculated with $D_\sigma = 0.925$; \bullet : calculated with $D_\sigma = 0$)

Here the RHS represents the heat loss $f(t)$ and the LHS represents the heat generation $g(t)$. Equation (47), therefore, describes the ignition/extinction conditions at I and E shown in Fig. 3. For a given condition of $Y_{O_2,e}$, and θ_e and with $D_\sigma > 0$ there must exist two corresponding values of $D_{1,s}$ representing the upper and lower bounds of the curves in Figs. 5 and 7. When $D_\sigma = 0$ the heat loss caused by radiation drops out, the upper bound disappears, and $D_{1,s}$ simply extends to infinity when $Y_{O_2,e}$ decreases as described by the following equation:

$$D_{1,s} = \frac{\theta_s(\theta_s - \theta_e)e^{1/\theta_s}}{D_{2,s}Y_{O_2,e} - (\theta_s - \theta_e)(Y_{O_2,e} + \nu_{O_2})} \quad (48)$$

It is important to note that, the solutions for Eqs. (47) and (48) are plausible only in the range $\theta_e \leq \theta_s \leq \theta_{s,max}$, and $D_{2,s}Y_{O_2,e} \geq (\theta_s - \theta_e)(Y_{O_2,e} + \nu_{O_2}) + D_\sigma(\theta_s^4 - \theta_e^4)e^{1/\theta_s}$. Where $\theta_{s,max}$ is the maximum particle burning temperature, which can be calculated by letting $Y_{O_2,s}$ in Eq. (32) be equal to zero. The condition imposed on $Y_{O_2,e}$ indicates that there must be a minimum value of $Y_{O_2,e}$ below which ignition is impossible. Such a minimum value was shown in Fig. 5.

When a solid particle is dropped into an environment at a specified temperature and oxygen concentration, it is heated, its temperature increases, and its size decreases. The reduction of the particle size during this period is caused by the effect of the Arrhenius rate equation, which always has a finite value at any particle temperature. If its initial size is smaller than the lower limit of the ignition domain, ignition cannot occur regardless how long the particle is heated. If its initial size is larger than the upper limit, ignition will not occur until its size reaches the upper limit of the ignition domain. After ignition, the particle continues to burn, and its size continues to decrease. As the particle size is reduced, heat loss is increased, and the combustion is switching to the kinetically controlled regime producing less heat. Thus, the extinction condition is reached when the particle size reduces to a critical value at which combustion heat is not sufficient to overcome heat loss. Since the particle temperature still remains higher than the ignition temperature after extinction, the particle will continue to burn with a rapid temperature drop. The combustion ceases completely when the particle temperature becomes lower than its ignition temperature. Using the conditions described above, such critical sizes ($r_{s,c}$) were calculated, and the results were shown in Fig. 8. It was clear that $r_{s,c}$ existed for every combustion condition, and it did not depend on the initial particle size, but depended strongly on the ambient temperature and the oxygen concentration. For example, as the initial size increased from 30 μm to 500 μm , $r_{s,c}$ remained the same for a given combustion condition but it decreased from 15.89 μm to 2.39 μm when $Y_{O_2,e}$ increased from 0.232 to 0.6.

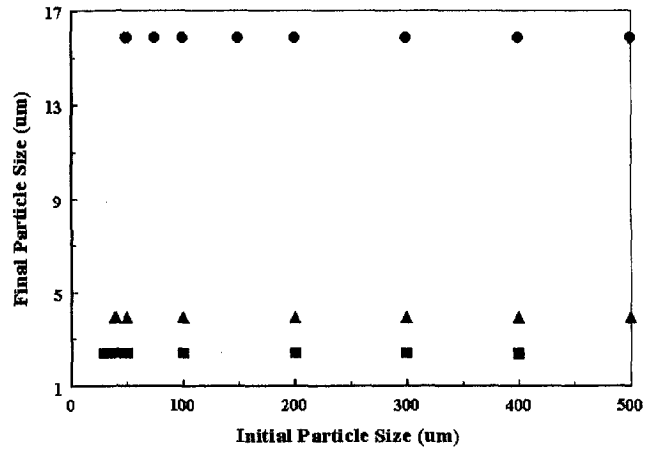


Fig. 8 Final particle sizes as a function of initial particle sizes showing the effect of the ambient oxygen concentration; ($\theta_e = 0.082$; $D_\sigma = 0.925$; \blacksquare : $Y_{O_2,e} = 0.6$; \blacktriangle : $Y_{O_2,e} = 0.4$; \bullet : $Y_{O_2,e} = 0.232$)

Thus, the existence of such a critical size is an unavoidable physical fact.

If ξ_f is the particle size remaining after burn, the combustion efficiency of a solid fuel particle is defined as

$$\phi = \frac{\xi_i - \xi_f}{\xi_i} \quad (49)$$

Figures 9 to 11 show the burning efficiency ϕ for various conditions of ambient temperature, ambient oxygen concentration and initial particle size. It is clear that the burning efficiency can be improved by increasing initial particle size, ambient temperature, and oxygen concentration. For example, as the initial size increased from 30 μm to 400 μm , the burning efficiency increased from 68 percent to 96 percent for $Y_{O_2,e} = 0.232$, from 90 percent to 99 percent for $Y_{O_2,e} = 0.4$, and from 92 percent to 99.4 percent for $Y_{O_2,e} = 0.6$.

Conclusions

A simple one-dimensional model for ignition and extinction of a solid fuel particle was carried out. By using the heat and mass transfer at the particle surface, the model was able to investigate the effects of the particle size and the combustion environment on the particle ignition, extinction, and burnout.

By keeping the ambient oxygen concentration fixed and using the ambient temperature as a parameter, the model showed the

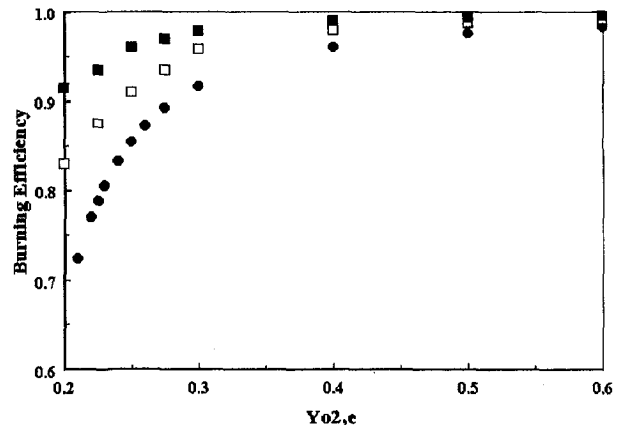


Fig. 9 Burning efficiency as a function of the ambient oxygen concentration; showing the effect of the initial particle size ($\theta_e = 0.082$; $D_\sigma = 0.925$; \blacksquare : $r_{s,i} = 400 \mu\text{m}$; \square : $r_{s,i} = 200 \mu\text{m}$; \bullet : $r_{s,i} = 100 \mu\text{m}$)

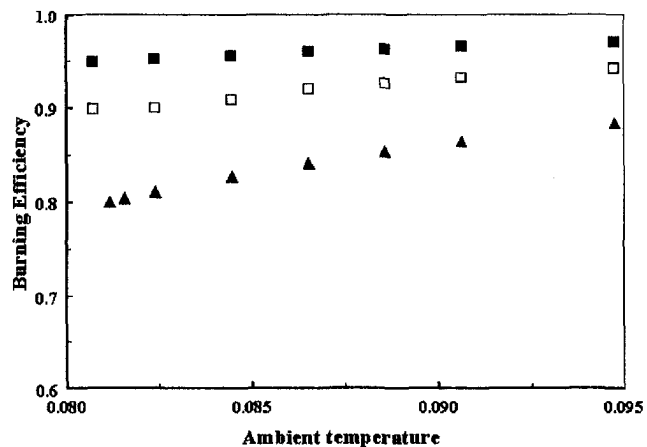


Fig. 10 Burning efficiency as a function of the ambient temperature (θ_a) showing the effect of the initial particle size ($Y_{O_2,o} = 0.232$; $D_v = 0.925$; ■: $r_{s,i} = 400 \mu\text{m}$; □: $r_{s,i} = 200 \mu\text{m}$; ▲: $r_{s,i} = 100 \mu\text{m}$)

existence of the ignition and nonignition domains. Thus, for a given condition, it is possible that both large and small particles could not ignite. When a particle is burning, its size decreases with time. The extinction condition is reached when its size reduces below a critical value. Such a critical size was found to depend on the combustion environment but not on the particle initial size.

The lower limit of the particle size discussed here are similar to the reports by Annamalai (1979), Annamalai and Ryan (1993), Du and Annamalai (1994), and Kharbat et al. (1995). However, there are no existing experimental data on the upper size limit. Anna-

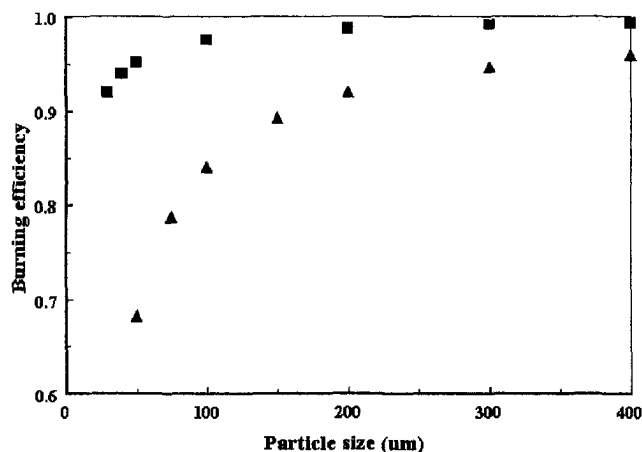


Fig. 11 Burning efficiency as a function of the initial particle size ($\theta_a = 0.082$; $D_v = 0.925$; ■: $Y_{O_2,o} = 0.6$; ▲: $Y_{O_2,o} = 0.232$)

malai and Ryan (1993) reviewed a large amount of recent studies showing that most of the experimental data is limited to particle size of 0.6 mm and the existence of the upper limit of the particle size is caused by the increase in radiation loss coupled with the decrease in oxygen concentration.

The burning efficiency of a fuel particle was defined and it depends on both the combustion environment and the initial particle size. It has been known that other factors such as fuel physical/chemical structure, fuel properties, etc., strongly affect the burning efficiency. These factors, however, were not studied here.

The assumptions of uniform particle temperature and one-dimensional flow for the gas phase might not be justified when the particle size becomes large because buoyancy effect and intraparticle temperature gradient might be significant for large particles. Therefore, the results reported here on large particles are only for model demonstration purposes, and must be used with care.

References

- Annamalai, K., and Durbetaki, P., 1977, "A Theory on Transient of Ignition Phase of Coal Particles," *Combustion and Flame*, Vol. 29, pp. 193–208.
- Annamalai, K., 1979, "Critical Regimes of Coal Ignition," *ASME Journal of Engineering for Power*, Vol. 101, pp. 576–583.
- Annamalai, K., and Ryan, W., 1993, "Interactive Processes in Gasification and Combustion—II: Isolated Carbon/coal and Porous Char Particles," *Journal of the Progress in Energy and Combustion Science*, Invited Review, Vol. 19, pp. 383–446.
- Brooks, P. J., and Essenhigh, R. H., 1986, "Variation of Ignition Temperatures of Fuel Particles in Vitiated Oxygen Atmospheres: Determination of Reaction Mechanism," *Twenty-First Symposium (International) on Combustion*, The Combustion Institute, Pittsburgh, pp. 293–302.
- Cohen, L. M., Short, J. M., and Oppenheim, K., 1975, "A Computational Techniques For The Evaluation of Dynamic Effects of Exothermic Reactions," *Combustion and Flame*, Vol. 24, pp. 319–334.
- Du, X., and Annamalai, K., 1994, "The Transient Ignition of Isolated Coal Particles," *Combustion and Flame*, Vol. 97, pp. 339–354.
- Fu, W., and Zhang, B., 1993, "A Simple and General Method for Calculating the Burning Rate of Coal Char/Carbon Particles in Air," *Comb. Sci. Tech.*, Vol. 89, pp. 405–412.
- Gat, N., 1986, "On Internal Temperature Gradients in a Pyrolyzing Coal Particle," *Combust. Sci. and Tech.*, Vol. 49, pp. 297–303.
- Gomez, C. O., and Vastola, F. J., 1985, "Ignition and Combustion of Single Coal and Char Particles," *Fuel*, Vol. 64, pp. 558–563.
- Gururajan, S. V., Wall, T. F., Gupta, R. F., and Truelove, J. S., 1990, "Mechanisms for the Ignition of Pulverized Coal Particles," *Combustion and Flame*, Vol. 81, pp. 119–132.
- Hertzberg, M., Zlochower, I. A., and Edwards, J. C., 1988, "Coal Particles Pyrolysis Mechanisms and Temperatures," Report of Investigations, RI 9169, Bureau of Mines.
- Karcz, H., Kordylewski, W., and Rybak, W., 1980, "Evaluation of Kinetic Parameters of Coal Ignition," *Fuel*, Vol. 59, pp. 799–802.
- Kharbat, E., Annamalai, K., and Gopalakrishnan, C., 1995, "Ignition and Combustion of Isolated and Binary Array of Coal Particles," *Combustion and Flame*, Vol. 100, pp. 413–421.
- Phuoc, X. T., and Mathur, M. P., 1991, "Transient Heating of a Coal Particle Undergoing Pyrolysis," *Combustion and Flame*, Vol. 85, pp. 380–388.
- Phuoc, T. X., and Maloney, D. J., 1988, "Laser Pyrolysis of Single Coal Particles in an Electrodynamic Balance," *22nd International Symposium on Combustion*, The Combustion Institute, pp. 125–134.
- Ubhayakar, S. K., 1976, "Burning Characteristics of a Spherical Particles Reacting With Ambient Oxidizing Gas at its Surface," *Combustion and Flame*, Vol. 26, pp. 23–34.
- Zeng, T. F., and Fu, W. B., 1996, "The Ratio CO/CO₂ of Oxidation on a Burning Carbon Surface," *Combustion and Flame*, Vol. 107, pp. 197–210.

The Leidenfrost Point: Experimental Study and Assessment of Existing Models

J. D. Bernardin

Research Engineer,
Los Alamos National Laboratory

I. Mudawar

Professor and Director

Boiling and Two-Phase Flow Laboratory,
School of Mechanical Engineering,
Purdue University,
West Lafayette, IN 47907

This study presents a detailed and thorough parametric study of the Leidenfrost point (LFP), which serves as the temperature boundary between the transition and film boiling regimes. Sessile drop evaporation experiments were conducted with acetone, benzene, FC-72, and water on heated aluminum surfaces with either polished, particle blasted, or rough sanded finishes to observe the influential effects of fluid properties, surface roughness, and surface contamination on the LFP. A weak relationship between surface energies and the LFP was observed by performing droplet evaporation experiments with water on polished copper, nickel, and silver surfaces. Additional parameters which were investigated and found to have negligible influence on the LFP included liquid subcooling, liquid degassing, surface roughness on the polished level, and the presence of polishing paste residues. The accumulated LFP data of this study was used to assess several existing models which attempt to identify the mechanisms which govern the LFP. The disagreement between the experimental LFP values and those predicted by the various models suggests that an accurate and robust theoretical model which effectively captures the LFP mechanisms is currently unavailable.

1 Introduction

Recent demands for superior material properties and more efficient use of materials and production time are forcing manufacturers to develop intelligent processing techniques for enhanced process control in order to better dictate the end product. In the heat treatment and processing of metallic alloys, the desire to obtain parts of enhanced and uniform mechanical properties is requiring increased control over heat removal rates and enhanced temperature control. In particular, spray quenching has been shown (Bernardin and Mudawar, 1995) to be an effective means to control and enhance the cooling rates of heat treatable aluminum alloys. Rapid quenching is required to obtain high material strength, while uniform temperature control is necessary to reduce warping and deformation. In addition, the quench rate and material properties of aluminum alloys following solution heat treatment are dictated mainly by low heat flux, high-temperature film boiling spray heat transfer, and the Leidenfrost point (LFP) which forms the lower temperature limit of the film boiling regime (Bernardin, 1993). Thus, when quenching most aluminum alloys, it is desirable to traverse through the film boiling temperature range and get below the LFP as quickly as possible. Consequently, accurate knowledge of the Leidenfrost temperature is necessary if accurate and enhanced control of the quenching process and resulting material properties is desired.

A common technique used for determining the Leidenfrost temperature requires measuring evaporation times of liquid sessile droplets of a given initial volume over a range of surface temperatures to produce a droplet evaporation curve as shown in Fig. 1(b). The curve displays droplet evaporation lifetime versus surface temperature and exhibits the four distinct heat transfer regimes shown on the traditional pool boiling curve of Fig. 1(a). In the single-phase regime, characterized by long evaporation times, heat from the surface is conducted through the liquid film and is dissipated by evaporation at the liquid-gas interface. In the nucleate boiling regime, vapor bubble production and the corresponding

heat flux increase dramatically, thus decreasing the droplet lifetime. The upper limit of the nucleate boiling regime, known as critical heat flux (CHF), corresponds to a maximum heat flux and minimum drop lifetime. In the transition regime, a noncontinuous, insulating vapor layer develops beneath portions of the droplet, leading to reduced evaporation rates and increased drop lifetime. At the upper end of the transition boiling regime, referred to as the LFP, the vapor layer grows substantially to prevent any significant contact between the drop and surface and the droplet evaporation time reaches a maximum. At surface temperatures above the LFP, the droplet remains separated from the surface by a thin vapor layer through which heat is conducted.

Literature Review and Focus of Current Study. Table 1 displays the large variations in the Leidenfrost temperature for water which have been reported in the literature. The discrepancies in these reported values arise from differences in size of the liquid mass, method of liquid deposition, amount of liquid subcooling, solid thermal properties, surface material and finish, pressure, and presence of impurities. These parameters and their observed effects on the LFP are summarized in Table 2 along with the corresponding references.

While many of the LFP investigations have been qualitative in nature, several studies have reported various correlations for predicting the Leidenfrost temperature. One of the correlations most frequently referred to is a semi-empirical expression developed by Baumeister and Simon (1973). Adapting the superheat limit model of Spiegler et al. (1963), Baumeister and Simon included corrections to account for the thermal properties of the heated surface and wetting characteristics of the liquid-solid system, and arrived at the following semi-empirical expression:

$$T_{\text{leid, meas}} = T_f + \frac{0.844T_c \left\{ 1 - \exp \left(-0.016 \left[\frac{\left(\frac{\rho_s}{\sigma_f} \right)^{1.33}}{\sigma_f} \right]^{0.5} \right) \right\} - T_f}{\exp(3.066 \times 10^6 \beta) \operatorname{erfc}(1758 \sqrt{\beta})}, \quad (1)$$

where

Contributed by the Heat Transfer Division for publication in the JOURNAL OF HEAT TRANSFER. Manuscript received by the Heat Transfer Division, Feb. 2, 1998; revision received, Mar. 18, 1999. Keywords: Boiling, Droplet, Evaporation, Film, Heat Transfer, Two-Phase. Associate Technical Editor: D. Kaminski.

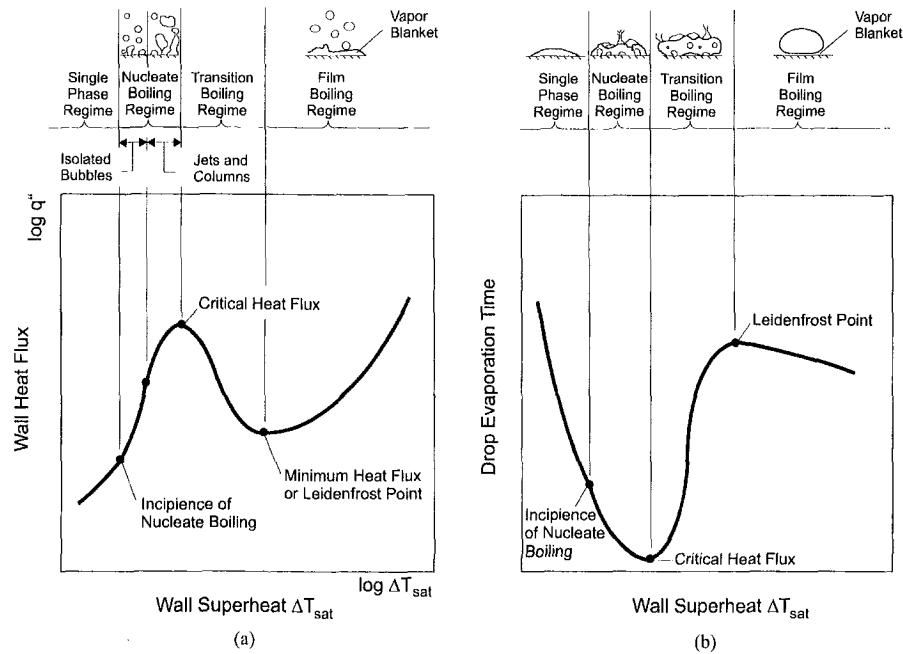


Fig. 1 (a) Boiling curve for a hot surface in a stagnant bath of liquid at saturation temperature and (b) sessile drop evaporation curve

$$\beta = \frac{1}{k_s \rho_s c_{p,s}} \quad (2)$$

The temperature generally measured and reported as the LFP corresponds to that of the solid in the near vicinity of the surface. To be more precise, it is better practice to associate the LFP with the temperature of the liquid-solid interface, which is often several degrees less than that measured within the solid. It is commonly accepted that during the initial stages of droplet-surface contact, the interface temperature between the liquid and solid is dictated by the thermal properties of the liquid and solid as well as by their initial temperatures. This interface temperature, T_i , is given by the solution to the one-dimensional energy equation with semi-infinite body boundary conditions (Eckert and Drake, 1972)

$$T_i = \frac{(k\rho c_p)_s^{0.5} T_{s,o} + (k\rho c_p)_f^{0.5} T_{f,o}}{(k\rho c_p)_s^{0.5} + (k\rho c_p)_f^{0.5}} \quad (3)$$

Nomenclature

A_t = atomic weight of surface material
 c_p = specific heat with constant pressure
 d = droplet diameter
 g = gravitational constant
 h = enthalpy
 h'_{fg} = modified latent heat of vaporization = $c_p(T_f - T_{sat}) + h_{fg}$
 J = vapor embryo formation rate per unit volume of liquid
 k = thermal conductivity
 k_b = Boltzmann constant
 M = molecular weight, constant
 m = mass of a single molecule
 N = number of liquid molecules per unit volume
 Na = Avogadro's number
 P = pressure

Q_a = heat of adsorption
 R = particular gas constant, drop, film, or bubble radius
 T = temperature
 u = droplet velocity
 v = specific volume, velocity

Greek Symbols

β = surface thermal parameter $(k\rho c_p)^{-1}$
 Γ = number of monolayer surface adsorption sites
 η = parameter for embryo formation rate equation
 λ = wavelength
 μ = dynamic viscosity
 θ = contact angle
 ρ = density
 σ = surface tension

τ_o = molecule residence time on surface

Subscripts

c = critical
 f = liquid
 fg = difference between liquid and vapor
 g = vapor
 i = interface
 $leid$ = Leidenfrost point
 $mfbo$ = minimum film boiling point
 o = initial
 r = reduced property
 s = surface, wall
 sat = saturation
 thn = thermodynamic homogeneous nucleation limit

The first objective of this study is to present previously developed models that attempt to describe the governing LFP mechanisms. Next, experimental LFP data for several different liquid-solid systems from the current study will be used to assess these models to display their weaknesses. Based upon lack of experimental validation and sound scientific arguments, a need for a correct and robust theoretical model that correctly captures the LFP mechanisms will be identified.

2 Previous LFP Models

This section discusses several of the most commonly proposed mechanisms for the LFP for droplets and the minimum film boiling point for pools of liquid. Table 3 contains a pictorial summary and corresponding correlations associated with the various models.

Hydrodynamic Instability Hypotheses. Several authors (Zuber, 1958; Berenson, 1961; Hosler and Westwater, 1962; Yao and

Table 1 Summary of Leidenfrost temperatures for water ($P = 101.3$ kPa) as reported in the literature

Reference	T_{leid} (°C)	Surface Material	Notes
Blazkowska and Zakrzewka (1930)	157	Silver	
Borishansky and Kutateladze (1947) [†]	310 255	Graphite	$T_f = 20$ °C $T_f = 85$ °C
Borishansky (1953) [†]	222 194 250 237	Brass Brass Copper Copper	$T_f = 19$ °C $T_f = 89$ °C $T_f = 20$ °C $T_f = 85$ °C $d_o = 4.5$ mm
Tamura and Tanasawa (1959)	302	Stainless steel	
Gottfried (1962) [†]	285	Stainless steel	$T_f = 25$ °C $3.7 < d_o < 4.3$
Betta (1963) ^{††}	245	Not given	$4.6 < d_o$
Lee (1965) ^{††}	280	Not given	$7.8 < d_o$
Godleski and Bell (1966)	320	Stainless steel	$T_{leid} = 264$ °C for extended liquid masses and 161 °C for transient technique
Gottfried <i>et al.</i> (1966)	280	Stainless steel	
Kutateladze and Borishanski (1966)	250	Not given	
Patel and Bell (1966)	305	Stainless steel	$0.05 < V < 10$ ml extended masses
Baumeister <i>et al.</i> (1970)	515 305, 325 230, 235 >200 235 155 265 <184	Pyrex (3-4 rms) Stainless steel (3-4 rms) Brass (3-4 rms) Brass fresh polish (3-4 rms) Aluminum (3-4 rms) Alum. fresh pol. (3-4 rms) Aluminum (25 rms) Gold fresh polish	$d_o = 0.39$ mm $d_o = 0.39$ & 2.25 mm $d_o = 0.39$ & 2.25 mm $d_o = 2.25$ mm $d_o = 0.39$ & 2.25 mm $d_o = 0.39$ mm $d_o = 2.25$ mm $d_o = 2.25$ mm
Emmerson (1975)	282 316 284	Stainless steel Monel Brass	LFP also given for pressures of 210, 315, 420, and 525 kPa
Xiong and Yuen (1991)	280-310	Stainless steel	

[†] As referenced from Patel and Bell (1966), ^{††} As referenced from Testa and Nicotra (1986)

Henry, 1978) have used a hydrodynamic stability theory by Taylor (1950) to describe the minimum film boiling temperature for pool boiling. Assuming potential flow and a sinusoidal disturbance between two fluids of different densities (the more dense on top), Taylor (1950) used a first-order perturbation analysis to show that gravity induced interfacial disturbances with wavelengths given by the following expression will be most likely to grow and disrupt the smooth horizontal interface:

$$\lambda_d = 2\pi \left[\frac{3\sigma_f}{g(\rho_f - \rho_g)} \right]^{1/2} \quad (4)$$

Berenson (1961) showed that the bubble spacing in film boiling was hydrodynamically controlled by a Taylor-type instability and that the presence of the corresponding vapor layer and bubble departure supported film boiling by keeping the liquid from contacting the heated surface. Berenson's analytical expression, Eq. (5), to predict the minimum film pool boiling temperature, T_{mfb} , coincides with the point at which vapor is not generated rapidly enough to sustain the Taylor waves at the liquid-vapor interface.

$$T_{mfb} = T_{sat} + 0.127 \frac{\rho_g h_{fg}}{k_g} \left[\frac{g(\rho_f - \rho_g)}{\rho_f + \rho_g} \right]^{2/3} \times \left[\frac{\sigma}{g(\rho_f - \rho_g)} \right]^{1/2} \left[\frac{\mu_g}{g(\rho_f - \rho_g)} \right]^{1/3} \quad (5)$$

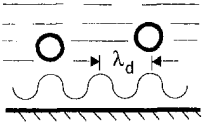
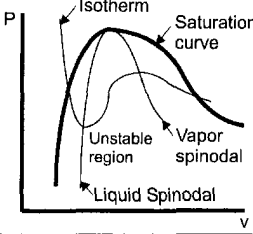
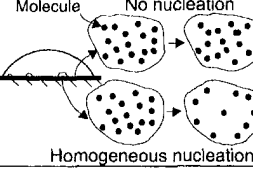
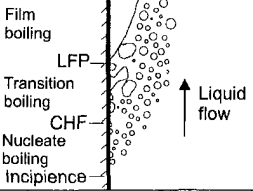
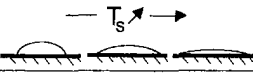
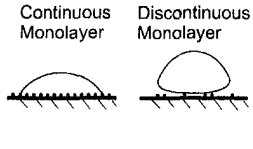
Sakurai *et al.* (1982) and Groenveld (1982) showed that Berenson's model was only fair in predicting their minimum film boiling temperature data at low pressures and was in extreme error at high pressures.

Metastable Liquid—Homogeneous and Heterogeneous Nucleation Hypotheses. Yao and Henry (1978) and Sakurai *et al.* (1982) proposed that spontaneous bubble nucleation at the liquid-solid interface is the mechanism for the minimum pool film boiling point. Bubble nucleation can be either heterogeneous, in which the vapor bubbles are produced within cavities at a solid-liquid inter-

Table 2 Summary of the Influential LFP parameters

Parameter	Observations/References
Size of liquid mass	<ul style="list-style-type: none"> LFP independent of liquid mass size (Gottfried <i>et al.</i> 1966 and Patel and Bell, 1966). LFP increased with droplet volume (Nishio and Hirata, 1978).
Method of liquid deposition	<ul style="list-style-type: none"> LFP differed between steady state drop size technique using a pipet and the transient sessile drop technique (Godleski and Bell, 1966). LFP increased with droplet velocity (Patel and Bell, 1966; Yao and Cai, 1988; Klünzing <i>et al.</i>, 1993; and Labeish, 1994). LFP did not differ between sessile and impinging drops ($u_o < 5$ m/s) (Bell, 1967 and Nishio and Hirata, 1978).
Liquid subcooling	<ul style="list-style-type: none"> Liquid subcooling had little effect on LFP for water on polished aluminum, brass, and stainless steel, but did cause an increased LFP on Pyrex (Baumeister <i>et al.</i> 1970). Subcooling increased drop lifetime but did not influence the LFP (Hiroyasu <i>et al.</i>, 1974). Subcooling raised the LFP for water and other fluids at high pressures where both sensible and latent heat exchange are significant (Emmerson and Snock, 1978).
Solid thermal properties	<ul style="list-style-type: none"> LFP increases as solid thermal capacitance decreases (Patel and Bell, 1966; Baumeister <i>et al.</i>, 1970; and Nishio and Harata, 1978). Baumeister and Simon (1973) developed a LFP correlation accounts for solid thermal properties. LFP independent of solid thermal diffusivity (Bell, 1967 and Emmerson, 1975).
Surface conditions	<ul style="list-style-type: none"> Gottfried <i>et al.</i> (1966) estimated that the vapor layer beneath a film boiling sessile water drop was on the order of 10 μm, which is on the same length scale as surface asperities on machine finished surfaces (Bernardin, 1993). Thus, rough surfaces in comparison to polished surfaces would be expected to require a higher LFP to support a thicker vapor layer to avoid liquid-solid contact for a sessile drop (Bradfield 1966). LFP increased as surface roughness and fouling increased (Baumeister <i>et al.</i>, 1970; Baumeister and Simon, 1973; and Nishio and Hirata, 1978). In contrast, Bell (1967) claimed that surface oxide films had a negligible effect on the LFP for droplets. LFP increased with increasing surface porosity (Avedisian and Koplik, 1987). LFP decreased with increased advancing contact angle in pool boiling (Kovalev, 1966; Unal <i>et al.</i>, 1992; and Labeish, 1994 and Ramilison and Lienhard, 1987).
Pressure	<ul style="list-style-type: none"> LFP increased with pressure for various fluids (Nikolayev <i>et al.</i>, 1974; Hiroyasu <i>et al.</i>, 1974; and Emmerson, 1975; Emmerson and Snock, 1978) $(T_{leid} - T_{sat})$ found to remain constant for various pressures (Hiroyasu <i>et al.</i>, Emmerson, Nishio and Hirata, 1978, and Testa and Nicotra, 1986). Rhodes and Bell (1978) observed $(T_{leid} - T_{sat})$ for Freon-114 to be constant over a reduced pressure range of 0.125 to 0.350 and found it to decrease with increasing pressure above this range. Klimentko and Snytin (1990) reported similar findings for four inorganic fluids.

Table 3 Summary of proposed LFP models

Model	Pictorial Description	Relevant Correlations
Hydrodynamic Instability		Most dangerous wavelength: $\lambda_d = 2\pi \left[\frac{3\sigma_f}{g(\rho_f - \rho_g)} \right]^{1/2}$
Metastable liquid-mechanical stability		Mechanical stability condition: $\left(\frac{\partial P}{\partial v} \right)_T = 0$ Spinodal or liquid superheat limit: (using Van der Waals eqn.) $T_{thn} = 0.844 T_c$
Metastable liquid-kinetic stability		Homogeneous nucleation limit: $J = N_f \left(\frac{3\sigma}{\pi m} \right)^{0.5} \exp \left\{ \frac{-16\pi \sigma^3}{3k_b T_f [\eta P_{sat}(T_f) - P_f]^2} \right\}$ $\eta = \exp \left[\frac{v_f [P_f - P_{sat}(T_f)]}{R T_f} \right]$
Thermo-mechanical effect		Implicit energy balance for LFP: $h_g(T_g) - h_f(T_{leid}) = 0.5 \left[v_g(T_g) - v_f(T_{leid}) \right] \left[P_{sat}(T_{leid}) - P_{sat}(T_g) \right]$
Wettability - contact angle		Contact angle temperature dependence $\cos(\theta) = 1 + C(T_{co} - T)^{\frac{a}{1-a}}$
Wettability - surface adsorption		Monolayer molecular surface coverage temperature dependence: $\frac{\Gamma}{\Gamma_o} = \frac{\exp\left(\frac{Q_a}{RT_f}\right)}{\left(\frac{2\pi MRT}{Na P_o}\right)^{0.5} \Gamma_o + \exp\left(\frac{Q_a}{RT_f}\right)}$

face as a result of the imperfect wetting of the liquid, or homogeneous, where the bubble nuclei are formed completely within the liquid due to density fluctuations over a duration of 10^{-9} to 10^{-8} s (Skrupov et al., 1980).

In the discussion that follows, the metastable state and related physics of homogeneous and heterogeneous nucleation are briefly presented. A more detailed and lengthier discussion of the subject can be found in Skripov (1974) and Carey (1992).

In classical thermodynamics, phase transitions for simple compressible substances are treated as quasi-equilibrium events at conditions corresponding to the saturation state. Between the saturated liquid and saturated vapor states exists a two-phase region where liquid and vapor coexist. Within this region, the temperature and pressure of the two phases must be constant, and the Gibbs function, chemical potential, and fugacity of each phase must be equal. In real-phase transformations, deviations from classical thermodynamics occur under nonequilibrium conditions, such as the superheating of a liquid above its boiling point. These non-equilibrium or metastable states are of practical interest and are important in determining limits or boundaries of real systems.

Shown on the pressure-volume diagram in the pictorial of Table 3 are the superheated liquid and supercooled vapor regions separated by an unstable region. The lines separating these regions are referred to as the liquid and vapor spinodals, which represent the maximum superheating and supercooling limits.

Two different approaches have been used in the literature to predict the superheat limit. The first, based on a mechanical stability condition described by Eberhart and Schnyders (1973) and Carey (1992) for a closed system containing a pure substance which is not in thermodynamic equilibrium, is given as

$$\left(\frac{\partial P}{\partial v} \right)_T < 0. \tag{6}$$

Along the portion of the isotherm between the spinodal lines of Fig. 2, the inequality $\partial p/\partial v > 0$ violates the mechanical stability criterion given by Eq. (6). For this reason, this area is referred to as the unstable region. In the metastable and stable regions, where $\partial p/\partial v < 0$, the liquid or vapor may remain in its form indefinitely. The spinodal limit, at which $\partial p/\partial v = 0$, represents the onset of instability.

Cubic equations of state such as Van der Waals (Spiegler et al., 1963), Himpan (Lienhard and Karimi, 1981), and Berthelot (Blander and Katz, 1975) possess the type of behavior within the vapor dome as discussed above and thus can be used to predict the spinodal limit. Van der Waals equation in terms of the reduced variables $P_r = P/P_c$, $T_r = T/T_c$, and $v_r = v/v_c$, which have been nondimensionalized with the corresponding critical point variables, can be written as

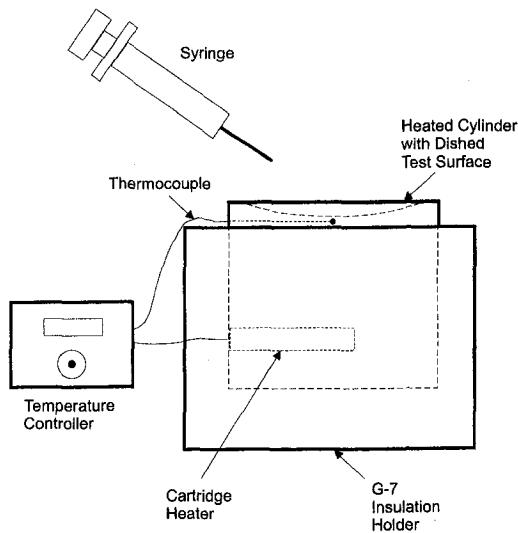


Fig. 2 Schematic diagram of sessile drop experimental apparatus

$$P_r = \frac{8T_r}{3v_r - 1} - \frac{3}{v_r^2} \quad (7)$$

Using this form of Van der Waals equation of state, the condition of mechanical stability given by Eq. (6), and the fact that $P_r \ll 1$ for most fluids at atmospheric conditions, the thermodynamic homogeneous nucleation temperature limit, T_{thn} , can be derived as (Spiegler et al., 1963)

$$T_{\text{thn}} = 0.844T_c, \quad (8)$$

where absolute temperature quantities are used. Modified forms of Eq. (8) using other equations of state and the success of these models in predicting the superheat limits of liquids are discussed in Carey (1992).

For fluids at higher pressures up to the critical point, Lienhard (1976) offered the following maximum superheat correlation:

$$T_{\text{thn}} = T_c \left[0.905 + 0.095 \left(\frac{T_{\text{sat}}}{T_c} \right)^8 \right], \quad (9)$$

where absolute temperatures are implied.

The second approach to describing the maximum liquid superheat temperature is referred to as the kinetic homogeneous nucleation theory, which bases the temperature and pressure dependence of bubble nucleation on molecular fluctuation probability. At and above saturation conditions, molecular fluctuations occur in such a way to cause a localized decrease in the liquid density, leading to the formation of vapor embryos. The fluctuation probability increases with temperature, and at the superheat temperature limit, the probability of a high bubble embryo formation rate is sufficient to transform the liquid to vapor.

By using conventional bubble nucleation theory, Carey showed how Eq. (10) could be derived to describe the rate of critical-size embryo formation, J , for a superheated liquid

$$J = N_f \left(\frac{3\sigma}{\pi m} \right)^{0.5} \exp \left\{ \frac{-16\pi\sigma^3}{3k_b T_f [\eta P_{\text{sat}}(T_f) - P_f]^2} \right\}, \quad (10)$$

where

$$\eta = \exp \left\{ \frac{v_f [P_f - P_{\text{sat}}(T_f)]}{RT_f} \right\}. \quad (11)$$

Slightly different assumptions have led to minor variations of Eq. (10) by several authors (Skripov, 1974; Blander and Katz, 1975; and Lienhard and Karimi, 1981).

The embryo formation rate given by Eq. (10) increases contin-

uously with temperature. However, because the exponential term has such a strong dependence on the liquid equilibrium temperature, T_f , there exists a small temperature range over which the embryo formation rate begins to increase in a drastic manner. It is within this temperature range that the critical embryo formation rate required to initiate homogeneous nucleation is defined with a corresponding value of T_f equal to the maximum superheat or kinetic homogeneous nucleation temperature. From experimental superheat data for a large variety of fluids at atmospheric pressure, Blander and Katz (1975) obtained a threshold value of $10^{12} \text{ m}^{-3} \text{ s}^{-1}$. Using this value for J , Eq. (10) can be solved iteratively for the maximum superheat temperature of a given liquid.

Carey (1992) showed how the development of Eq. (10) can be modified to account for the liquid contact angle, θ , and thus describe the heterogeneous nucleation rate of a liquid at a perfectly smooth surface:

$$J = \frac{N_f^{2/3} (1 + \cos \theta) \left(\frac{3F\sigma}{\pi m} \right)^{1/2} \exp \left\{ \frac{-16\pi F\sigma^3}{3k_b T_f [\eta P_{\text{sat}}(T_f) - P_f]^2} \right\}}{2F}, \quad (12)$$

where

$$F = \frac{2 + 3 \cos \theta - \cos^3 \theta}{4}. \quad (13)$$

The principle factor which is not accounted for in the homogeneous and heterogeneous nucleation models is the influence on the molecular interactions caused by the presence of the solid-liquid interface. Surface energies become influential and continuum fluid theories are not necessarily valid within 50 Å of the interface. Gerwick and Yadigaroglu (1992) recognized that liquid molecular interactions at an interface will be quite different from the bulk liquid. Using statistical mechanics, they developed a modified equation of state for the liquid which was a function of the distance from the solid surface. This equation of state was used to predict the superheat limit of the liquid and thus the rewetting or Leidenfrost temperature of the surface.

Thermomechanical Effect Hypothesis. Schroeder-Richter and Bartsch (1990) refuted the superheated metastable hypothesis of Spiegler et al. (1963) and proposed that the liquid and vapor near the solid surface are in saturated states at different pressures. The authors used a nonequilibrium flow boiling model with conservation equations and appropriate boundary conditions across the liquid-vapor interface, along with assumptions that the liquid immediately in front of the interface is at the Leidenfrost temperature, and that the change in enthalpy during the evaporation is supplied solely by the mechanical energy of the depressurizing liquid to establish the following implicit equation for the Leidenfrost temperature:

$$h_g(T_g) - h_f(T_{\text{leid}}) = 0.5 [v_g(T_g) - v_f(T_{\text{leid}})] [p_{\text{sat}}(T_{\text{leid}}) - p_{\text{sat}}(T_g)]. \quad (14)$$

Using saturation tables and an iterative procedure, Eq. (14) can be solved for the LFP.

Wettability Hypotheses. It has been speculated by several researchers that the temperature dependence of the contact angle is influential in controlling the Leidenfrost phenomenon. In a fundamental study by Adamson (1972), a theoretical model was developed that related the molecular surface adsorption of a solid to the liquid-solid contact angle:

$$\cos \theta = 1 + C(T_{co} - T)^{b/(a-b)}, \quad (15)$$

where T_{co} represents a pseudo-critical temperature, or the temperature at which the contact angle goes to zero, C is an integration constant, and b and a are temperature-independent coefficients from a molecular force balance expression given by Adamson. It

is evident from Eq. (15) that the contact angle decreases with increasing temperature, a trend consistent with experimental findings.

Based upon the work of Adamson, Olek et al. (1988) presented a semi-theoretical analysis which suggests that the rewetting temperature or LFP corresponds to a zero contact angle or perfect wetting. The authors suggested that at the temperature, T_{co} , where the contact angle goes to zero, the liquid drop spreads into a sufficiently thin film such that enough vapor can be generated to disjoin the film from the surface. Olek et al. were only able to provide experimental data for two water-nonmetallic solid systems with which to evaluate their model. Their comparison showed fair agreement between the predicted and measured temperature-dependent contact angle trends. However, they failed to provide Leidenfrost temperature data for the two surfaces.

Segev and Bankoff (1980) offered a more plausible explanation of the Leidenfrost phenomenon based on wetting characteristics. They proposed that wetting of a hot solid surface by a liquid is controlled by a microscopic precursor film which advances in front of the much thicker spreading liquid film. The presence of the thin film, which is required for the advancing and wetting of the remainder of the liquid, is controlled by the temperature-dependent surface adsorption characteristics. The precursor film thickness decreases with increasing temperature and drops off sharply as the temperature threshold (the LFP) is reached. Above this temperature, adsorption of the liquid molecules beyond a monolayer is no longer possible, and surface wetting cannot occur.

Segev and Bankoff based their model on the Langmuir adsorption isotherm

$$\frac{\Gamma}{\Gamma_o} = \frac{\exp\left(\frac{Q_a}{RT_i}\right)}{\left(\frac{(2\pi MRT)^{0.5}\Gamma_o}{N_a P \tau_o}\right) + \exp\left(\frac{Q_a}{RT_i}\right)} \quad (16)$$

which describes the fraction of total monolayer surface adsorption sites, Γ_o , occupied by foreign molecules in terms of the liquid-solid interface temperature, T_i , heat of adsorption, Q_a , and residence time of a molecule in the adsorbed state, τ_o . Segev and Bankoff claimed that the LFP corresponds to a surface monolayer coverage fraction of 0.9, and by using $\Gamma_o = 10^{19}$ molecules/m² and $\tau_o = 10^{-13}$ s, Eq. (16) can be solved explicitly for the surface temperature if the heat of adsorption of the fluid's vapor on the solid is known.

3 Experimental Apparatus and Procedure

The sessile drop apparatus shown in Fig. 2 was used to study the evaporation characteristics of droplets on a heated surface. In particular, the liquid/solid interface temperature corresponding to the Leidenfrost point was determined from droplet evaporation curves for a variety of operating conditions. The sessile drop facility consisted of an instrumented test heater module, temperature controller, and a syringe. The various working fluids included acetone, benzene, FC-72, an inert fluorocarbon produced by the 3M corporation, and distilled water. Several test heater modules were fabricated from either a solid aluminum or copper cylinder with a shallow concave surface designed to contain the liquid droplets during states of transition and film boiling. To investigate surface material effects on the LFP, several copper heater modules were also electroplated with either silver or nickel to a thickness of 0.025 mm. The heater module was mounted in an insulating shell formed from G-7 phenolic, which is capable of withstanding surface temperatures of 300°C for short durations. An Ogden Type 33 temperature controller, a Watlow 150 Watt cartridge heater, and a calibrated Chromel-Alumel (type K) thermocouple (calibrated accuracy = $\pm 0.2^\circ\text{C}$) located 2.5 mm beneath the center of the test surface were used to monitor and control the surface temperature. A finite element analysis and several thermocouple

measurements near the edge of the module were used to verify that the temperature distribution across the plane just beneath the surface was uniform and representative of the surface temperature. Three different surface finishes including polished, particle blasted, and rough sanded, with arithmetic average surface roughness values of 97, 970, and 2960 nm, respectively, were used in the study. A glass syringe with a 24-gauge hypodermic needle having a 0.58-mm (0.023-in.) outer diameter, was used to slowly dispense droplets of uniform diameter onto the test heater. A static force balance between gravity and surface tension dictated the nearly consistent droplet diameter for a given fluid. A high-speed Ektapro motion analyzer was used to verify that the slow droplet generation technique produced uniformly sized droplets within an error band of ten percent. Preliminary tests, performed with water and different diameter needles, revealed no dependence of the LFP on initial droplet size. This is consistent with findings reported by Gaotfried et al. (1966) and Patel and Bell (1966). Consequently, only one initial droplet diameter (fluid dependent) was used in this study.

For each test, single droplet evaporation times were recorded versus surface temperature over a temperature range encompassing the entire boiling spectrum for each particular fluid. The experiments began by dispensing a single drop from a syringe onto the center of the test surface at a temperature well within the film boiling regime from an approximate height of 1 cm. A manual digital stopwatch was used to record the time to the nearest tenth of a second for complete visual evaporation of the drop. To minimize timer (± 0.1 s) and initial droplet size (± 10 percent) errors, five evaporation times were recorded for each temperature increment and then averaged together. This procedure was performed for ten-degree centigrade surface temperature increments from a temperature within the fluid's film boiling regime down to the boiling incipience temperature, with finer two degree centigrade increments being made around the LFP. Each set of droplet evaporation data was used to generate a droplet evaporation curve, similar to the one displayed in Fig. 1(b), from which the LFP was identified by interpolation. The Leidenfrost temperature, or droplet/solid interface temperature corresponding to the LFP, was then determined with Eq. (3), using the measured surface temperature corresponding to the LFP.

The sources of experimental error in determining the Leidenfrost temperature included uncertainties in initial droplet size (± 10 percent), droplet evaporation time (± 0.1 s), and surface temperature measurement ($\pm 0.2^\circ\text{C}$). An additional error was imposed by the graphical LFP interpolation uncertainty caused by the 2°C gap between data points near the LFP on the droplet evaporation plots. The uncertainty in droplet evaporation time was deemed minimal since the accuracy of the timer was nearly two orders of magnitude smaller than typical droplet evaporation times near the LFP. The uncertainty in droplet size was minimized by taking the average evaporation time of five droplets at each data point. The temperature measurement uncertainty combined with the graphical LFP interpolation error created by the 2°C gap between data points, resulted in a total experimental uncertainty of 4.4°C . This was found to be consistent with reproducibility tests that revealed the LFP measurements were repeatable within $\pm 5^\circ\text{C}$.

An extensive database was required for identifying key influential parameters and to assess several analytical and theoretical models. Consequently, the experimental procedure was performed for four different test fluids with and without degassing, various degrees of liquid subcooling, four different surface materials, a variety of surface finishes, and different forms of surface contamination. To investigate the effect of surface impurities left behind from previous drops, two different tests were performed. In one case, the surface was wiped clean with a fine tissue between successive drops, and in the other case, the surface was left as is. More detailed operating conditions for the various tests are discussed with the experimental results.

Table 4 Leidenfrost temperatures for various fluids and aluminum surface conditions

Fluid	T_{leid} (°C)		
	Surface Finish		
	Polished	Particle Blasted	Rough Sanded
Acetone (wiped)	135 [130, 140, 133]	155 [160, 150]	160 [160, 160]
Acetone (unwiped)	185 [185, 183]	200 [195, 203]	178 [180, 173]
Benzene (wiped)	175	220	218
Benzene (unwiped)	180	215	215
FC-72 (wiped)	90	110	120
FC-72 (unwiped)	115	110	120
Water (wiped)	171 [175, 180, 160, 170]	250 [250, 250]	263 [260, 263]
Water (unwiped)	225 [220, 230]	280 [280, 280]	263 [260, 263]

4 Experimental Results and Discussion

In the discussions that follow, the reported empirical Leidenfrost temperatures correspond to measured surface temperatures at the LFP. However, in the evaluations of the LFP models (Table 6), both the empirical Leidenfrost temperatures and adjusted LFP values (using Eq. (3) to account for the liquid/solid interface) are presented.

Table 4 presents the LFP data for acetone, benzene, FC-72, and distilled water on three different aluminum surface finishes for both wiped and unwiped conditions between successive drops. The average LFP values are displayed with large text in Table 4 while the small text in brackets indicates Leidenfrost temperatures from individual runs when more than one test was performed for a single set of operating conditions. The focus of this experimental data was to study the effects of fluid properties, surface roughness, and surface contamination on the LFP.

The Leidenfrost temperature data of Table 4 indicate the following general trends:

Effect of Surface Roughness: For all test fluids, polished surfaces had significantly lower Leidenfrost temperatures than particle blasted and rough sanded surfaces. The surface roughness dependence of the Leidenfrost temperature is speculated to be related to intermittent liquid-solid contact caused by surface aspirates poking through the thin vapor layer, which, as reported by Labeish (1994), is on the order of 1 μm . As the surface roughness increases, a thicker vapor layer, and hence a higher surface temperature, is required to keep the liquid separated from the solid surface. This effect would be expected to taper off as surface roughness increases, which is observed in the similar Leidenfrost temperatures for the particle blasted and rough sanded surfaces.

Effect of Surface Contamination: A wiped surface generally had a considerably lower Leidenfrost temperature than an unwiped surface. This was most evident for the polished surface and to a lesser degree for the particle blasted and rough sanded surfaces.

The surface deposits left from previous drops tended to serve as vapor bubble nucleation sources when making contact with newly deposited drops, much in the same way as the surface aspirates acted on the rougher surfaces. With deposits present, a higher surface temperature was required to sustain film boiling. This finding is consistent with those of Baumeister et al. (1970) who found that the Leidenfrost temperature for water on a freshly polished aluminum surface was 155°C, 70°C less than that of a conventional contaminated surface. It is intuitively obvious that surface contamination from previous drops will act to increase the roughness on a polished surface to a much larger degree than for an initially much rougher surface. This explains why the Leidenfrost temperature for a polished surface is highly influenced by deposits while the rougher surfaces are not.

Table 5 presents Leidenfrost temperature data for water and a variety of polished surface materials. The numbers in large text indicate average LFP temperature values while the numbers in small text and brackets indicate single experimental data points. The accuracy and sensitivity of the measurements resulted in a $\pm 15^\circ\text{C}$ band around the average Leidenfrost temperatures tabulated herein. The focus of this portion of the study was to investigate the influences of surface material, surface contamination from polishing pastes, surface roughness on the polished level, liquid subcooling, and liquid degassing on the LFP.

Effect of Surface Material and Polishing Paste Residue: Leidenfrost temperature values were obtained for water on polished aluminum, silver, nickel, and copper. The average Leidenfrost temperature is nearly identical for the aluminum, silver, and nickel surfaces but is significantly higher for the copper surface. The higher LFP value of the copper surface is speculated to be the result of surface roughening which accompanied large amounts of surface oxidation during heating. Jeschar et al. (1984) also reported a higher Leidenfrost temperature for copper compared to nickel and, as in this study, attributed this to roughening of the copper test piece by heavy oxidation. Labeish (1994) reported

Table 5 Measured Leidenfrost temperatures for water on polished surfaces

Surface	T_{leid} (°C)	Notes
Aluminum	170 [170]	• Study: material effect • Surface: polished with 45, 30, 15, 9, 6, & 3 micron diamond paste and chemically cleaned
Silver	176 [185 170 / 190 166]	• Study: material effect • Surface: polished with 45, 30, 15, 9, 6, & 3 micron diamond paste, silver plated, polished with Simichrome, wiped with acetone, oxidized upon heating
Nickel	173 [173 / 170]	• Study: material effect • Surface: polished with 45, 30, 15, 9, 6, & 3 micron diamond paste, nickel plated, wiped with acetone, no apparent oxidation
Copper	198 [185 200 / 210]	• Study: material effect • Surface: polished with 45, 30, 15, 9, 6, & 3 micron diamond paste and chemically cleaned, heavy oxidation upon heating surface
Nickel	181 [180 190 / 175 190 / 170]	• Study: material effect • Surface: polished with Simichrome, nickel plated, wiped with acetone, no apparent oxidation
Copper	193 [193 / 190]	• Study: material effect • Surface: polished with Simichrome paste, heavy oxidation upon heating surface
Aluminum	175 [170 173 / 180]	• Study: roughness effect • Surface Prep.: polished with 45 micron paste
Aluminum	181 [190 180 / 190 165]	• Study: roughness effect • Surface: polished with 45, 30, & 15 micron diamond paste
Aluminum	185 [180 / 190]	• Study: roughness effect • Surface: polished with 45, 30, 15, 9, 6, & 3 micron diamond paste
Aluminum	171 [175 160 / 180 170]	• Study: roughness effect • Surface: polished w/ 45, 30, 15, 9, 6, & 3 micron diamond paste then with Simichrome paste
Aluminum	178 [190 / 165]	• Study: degassing effects (water degassed) • Surface: polished with 9, 6, & 3 micron diamond paste and chemically cleaned
Aluminum	175	• Study: subcooling effect ($T_f = 90$ °C) • Surface: polished with 45, 30, 15, 9, 6, & 3 micron diamond paste and chemically cleaned
Aluminum	170	• Study: subcooling effect ($T_f = 60$ °C) • Surface: polished with 45, 30, 15, 9, 6, & 3 micron diamond paste and chemically cleaned
Aluminum	160	• Study: polishing paste effect • Surface: polished with Simichrome, then soaked & wiped with acetone

theoretical rewetting wall temperatures for smooth surfaces of different materials wetted by water drops. Accounting for surface thermal properties and neglecting surface effects, nearly identical rewetting temperatures of 270, 282, and 292°C were predicted for copper, nickel, and carbon steel, respectively. These predictions, while higher in absolute value than those reported in this study, indicate a relative insensitivity of the LFP to surface chemistry effects.

As the data of Table 5 indicates, no significant difference was observed in the Leidenfrost temperatures of polished aluminum

samples with the following surface finish preparations: polished with Simichrome paste; polished with Simichrome paste followed by soaking and wiping with acetone to remove the paste residue; and, polished with an array of diamond compounds followed by an acid bath chemical cleaning. The lack of variability in the LFP values for these three surfaces suggests that the polishing paste residue has little influence on the LFP.

Effect of Surface Roughness on the Polished Level: Average Leidenfrost temperatures for water on aluminum surfaces polished with different grades of diamond polishing compound all fell within a 15°C band, thus indicating no significant dependence of the LFP on surface roughness on the polished level.

Effect of Liquid Subcooling: For identical surface conditions, water liquid subcoolings of 10, 40, and 80°C resulted in Leidenfrost temperatures of 170, 170, and 175°C, respectively. The lack of sensitivity of the LFP on liquid subcooling results because the small amount of liquid contained in a single droplet, regardless of initial temperature, is rapidly heated to near saturated conditions when placed on the surface. This finding was also reported by Hiroyasu et al. (1974) and Grissom and Wierum (1981).

Effect of Liquid Degassing: Table 5 lists average Leidenfrost temperatures of 170°C and 178°C for nondegassed and degassed water, respectively, on a polished aluminum surface. Negligible differences of less than five percent were observed between nondegassed and degassed Leidenfrost temperatures for acetone and FC-72 on polished aluminum as well. Clearly, the effect of air and other non-condensable gases within the liquid on the LFP is minimal.

5 Assessment of Models

As mentioned previously, the temperature generally measured and reported as the LFP corresponds to that of the solid in the near vicinity of the surface. However, boiling is an interfacial phenomenon, and thus it is better practice to associate the LFP with the temperature of the liquid-solid interface. In the model assessments that follow, both the empirical Leidenfrost temperatures measured within the solid, and adjusted LFP values (using Eq. (3) to account for the liquid/solid interface) are presented in Table 6 for comparison.

Evaluation of Instability Models. To investigate whether or not a Taylor-type instability could control the Leidenfrost phenomenon, a length scale comparison can be made between the droplet diameter and the Taylor most dangerous interfacial wavelength, λ_d . For Benzene, FC-72, and water the corresponding values of λ_d are 17.7, 8.4, and 27.3 mm, respectively. These wavelengths are of the same order or larger than typical droplet diameters, which indicates that the Taylor interfacial instability, while possibly suitable for pool boiling analysis, does not lend itself to isolated

Table 6 Comparison of various Leidenfrost temperature (°C) models to experimental data for a polished aluminum surface

Fluid	Measured Leidenfrost temperature (°C)	Corrected liquid/solid interface Leidenfrost temperature (eqn. (3))	Berenson (1961) hydrodynamic model	Thermodynamic homogen. nucleation limit temperature	Kinetic homogen. nucleation limit temperature	Baumister and Simon (1973) correlation	Schroeder-Richter and Bartsch (1990) thermo-mechanical model
Acetone	134	132	152	156	198	130	‡
Benzene	175	172	140	201	239	171	180
Water	170	162	152	273	310	156	221
FC-72	90	89	‡	106	144	102	116

‡ Fluid properties unavailable to evaluate model.

boiling drops. Table 6 compares predictions for T_{leid} , using Berenson's (1961) model for T_{mb} (Eq. (5)) to experimentally measured sessile drop Leidenfrost temperatures for several of the fluids used in this study. The predictions show significant error for acetone and benzene and give only satisfactory results for water.

Evaluation of Metastable Liquid Models. Two theoretical models, the thermodynamic or mechanical stability model and the kinetic homogeneous nucleation model, have been developed using entirely different approaches to predict the maximum superheat temperature of liquids. However, attempting to use these models to predict the Leidenfrost temperature for sessile drops has not met reasonable success.

The Leidenfrost point correlation of Baumeister and Simon (1973) contains two sources of concern. First, in developing a conduction model to account for a decrease in the surface temperature at liquid-solid contact, the authors fail to explain how they arrived at the chosen value of an average heat transfer coefficient. Second and most importantly, Baumeister and Simon introduce a surface energy correction factor to the superheat model of Spiegler et al. While this factor leads to a correlation which successfully fits the data, the results may be deceiving in that they suggest that homogeneous nucleation, around which the correlation is constructed, is the mechanism governing the Leidenfrost phenomenon, when in fact, it may not be.

Experimental Leidenfrost temperatures for various liquids on a polished aluminum surface from the current study are compared to thermodynamic and kinetic superheat limits as well as the correlation of Baumeister and Simon (1973) in Table 6. All predictions were made with absolute temperature quantities and then converted to degrees Celsius. For the theoretical metastable liquid models, the superheat limits are considerably higher than the measured Leidenfrost temperatures for all fluids tested, consistent with the results of Spiegler et al. (1963). The semi-empirical correlation by Baumeister and Simon agrees quite well with the experimental data of the present study, but as previously mentioned, it fails to accurately model the physics governing the process. Obviously, superheat criteria alone do not accurately describe the Leidenfrost phenomenon for sessile drops on a heated surface.

While elegant, the modified equation of state and homogeneous nucleation model of Gerwick and Yadigaroglu (1992) involved several assumptions which severely limit its applicability and accuracy. First, a simple hard-sphere potential interaction model using London dispersion forces was used to describe the molecular interactions. This limits the model's applicability to nonpolar liquids, since liquids such as water, with highly polar hydrogen bonding forces, would not lend themselves to such modeling with any high degree of accuracy. Second, a parameter describing the strength of the wall-fluid interactions was stated to be unknown for most practical applications. Consequently, a simplified model which related this parameter to the contact angle was employed. The major argument against this simplification is that the contact angle is typically measured over a distance which is at least six orders of magnitude larger than the thickness of the fluid layer influenced by the presence of the solid surface. In fact, Adamson (1982) has hypothesized that the microscopic contact angle at the leading edge of the liquid film, which is on the order of several molecular diameters in thickness, is significantly smaller than the macroscopic contact angle commonly reported. In addition, the contact angle is highly influenced by surface roughness and impurities (Miller and Neogi, 1985; Bernardin et al., 1997), making it a highly undefined variable.

Evaluation of Nonequilibrium Model. Table 6 compares Leidenfrost temperatures predicted by Eq. (14) to experimentally measured values for several different fluids. The prediction for Benzene is quite good, while that for FC-72 is satisfactory, and the estimate for water is extremely poor.

Several problems exist in the development of Eq. (14) and its application to predicting the Leidenfrost temperature for droplets. First, the original model was constructed to emulate a vertical

dry-out flow boiling situation, a condition far from that of a sessile or impinging droplet. Next, and more importantly, the concept of saturated states at different pressures for the liquid and vapor rather than metastable superheating of the liquid at constant pressure is unsupported. Metastable states for fluids have been frequently observed (Avedisian, 1982; Shepherd and Sturtevant, 1982; McCann et al., 1989) and the physics of such nonequilibrium states have been well documented (Eberhart and Schnyders, 1973; Skripov, 1974; Lienhard and Karimi, 1978; Carey, 1992). In fact, liquid superheating forms the entire well established basis for bubble nucleation theory in boiling (Han and Griffith, 1965; Blander et al., 1971).

Evaluation of Wettability Models. The reasoning behind the contact angle model of Olek et al. (1988) appears unrealistic. In addition, the implicit equation for the LFP is difficult to verify since the required coefficients are only available for a few liquid-solid systems for which no Leidenfrost temperature data exists. The temperature-dependent contact angle measurements found by Bernardin and Mudawar (1997) for water on aluminum show little indication of a zero contact angle condition acting as the Leidenfrost point mechanism. Also in contrast to the model of Olek et al., nearly identical Leidenfrost temperatures were obtained in this study for two identically polished aluminum surfaces, one of which was left with a polishing paste residue, and the other which was chemically cleaned. Also, nearly identical Leidenfrost temperatures were obtained for aluminum, silver, and nickel surfaces, all of which have different wetting characteristics. The contact angle depends to such a large extent on the surface conditions (roughness, contamination, adsorption), as well as on liquid velocity and direction, it is a difficult parameter to characterize and effectively utilize. Thus it can be concluded that while surface wetting, as measured by the contact angle, may play a role in boiling heat transfer, it is not the controlling LFP mechanism.

The surface adsorption hypothesis of Segev and Bankoff (1980) is very difficult to verify for a liquid-surface combination because it requires the corresponding heat of adsorption of the fluid's vapor on the solid surface. Correct knowledge of the chemical makeup of a solid surface is very difficult to obtain. The presence of oxide layers or adsorbed layers of grease and other impurities changes the surface chemistry considerably. In addition, the experimental data of this study tends to disprove the hypothesis proposed by Segev and Bankoff. Using heat of adsorption for water vapor on aluminum oxide (McCormick and Westwater, 1965) and nickel oxide (Matsuda et al., 1992), Eq. (16) predicts Leidenfrost temperatures of 162 and 425°C for saturated water on aluminum and nickel, respectively. The predicted LFP value for the aluminum surface agrees reasonably well with the corresponding experimental value of 170°C, however, the model fails miserably for the nickel surface which had an experimental Leidenfrost temperature of 175°C. Segev and Bankoff's model suggests that the LFP for an aluminum surface possessing a polishing paste residue would be significantly different from an identically polished surface without the residue, a trend not observed in the experimental data of this study.

6 Conclusions

Sessile drop evaporation experiments were performed for a wide variety of operating conditions to establish a large LFP data base for identifying key influential parameters and assessing existing LFP models. From the experimental results, several key conclusions concerning the influential LFP parameters can be drawn.

- Liquid subcooling, the presence of dissolved gasses, and surface roughness on the polished level do not significantly influence the Leidenfrost temperature.
- Surface thermal properties will act to control the interface and hence Leidenfrost temperature. However, aside from thermal properties, the LFP is relatively insensitive to surface material as far as surface energies and wetting characteristics are concerned.
- Surface roughness, beyond that on the polished level, appears to

be a dominant parameter in controlling the Leidenfrost behavior. The data indicate, that for a given fluid, a polished surface possesses a relatively low Leidenfrost temperature in comparison to a particle blasted or rough sanded surface. In addition, surface impurities or deposits act to increase the relative surface roughness and the corresponding Leidenfrost temperature.

Sound arguments supported by experimental data were used to assess several hypothetical models of the LFP mechanism. These models were shown to lack robustness and were ineffective in predicting the Leidenfrost temperature. A model which successfully captures the Leidenfrost mechanism is currently being developed to account for several parameters which were found to actively influence the LFP in both previous investigations and the current study. These parameters include thermal properties of the solid, thermal and thermodynamic properties of the liquid, solid surface structure, pressure, and droplet impact velocity.

References

- Adamson, A. W., 1972, "Potential Distortion Model for Contact Angle and Spreading II. Temperature Dependent Effects," *J. Colloid Interface Sci.*, Vol. 44, pp. 273–281.
- Adamson, A. W., 1982, *Physical Chemistry of Surfaces*, John Wiley and Sons, Inc., New York.
- Avedisian, C. T., 1982, "Effect of Pressure on Bubble Growth Within Liquid Droplets at the Superheat Limit," *ASME JOURNAL OF HEAT TRANSFER*, Vol. 104, pp. 750–757.
- Avedisian, C. T., and Koplik, J., 1987, "Leidenfrost Boiling of Methanol Droplets on Hot Porous Ceramic Surfaces," *Int. J. Heat Mass Transfer*, Vol. 30, pp. 379–393.
- Baumeister, K. J., Henry, R. E., and Simon, F. F., 1970, "Role of the Surface in the Measurement of the Leidenfrost Temperature," *Augmentation of Convective Heat and Mass Transfer*, A. E. Bergles and R. L. Webb, eds., ASME, New York, pp. 91–101.
- Baumeister, K. J., and Simon, F. F., 1973, "Leidenfrost Temperature—Its Correlation for Liquid Metals, Cryogenics, Hydrocarbons, and Water," *ASME JOURNAL OF HEAT TRANSFER*, Vol. 95, pp. 166–173.
- Bell, K. J., 1967, "The Leidenfrost Phenomenon: A Survey," *Chem. Eng. Prog. Symposium Series*, Vol. 63, AIChE, New York, pp. 73–82.
- Berenson, P. J., 1961, "Film Boiling Heat Transfer from a Horizontal Surface," *ASME JOURNAL OF HEAT TRANSFER*, Vol. 83, pp. 351–358.
- Bernardin, J. D., 1993, *Intelligent Heat Treatment of Aluminum Alloys: Material, Surface Roughness, and Droplet-Surface Interaction Characteristics*, Masters thesis, Purdue University, West Lafayette, Indiana, IN.
- Bernardin, J. D., and Mudawar, I., 1995, "Validation of the Quench Factor Technique in Predicting Hardness in Heat Treatable Aluminum Alloys," *Int. J. Heat Mass Transfer*, Vol. 38, pp. 863–873.
- Bernardin, J. D., Mudawar, I., and Franses, E. I., 1997, "Contact Angle Temperature Dependence for Water Droplets on Practical Aluminum Surfaces," *Int. J. Heat Mass Transfer*, Vol. 40, pp. 1017–1033.
- Blander, M., Hengstenberg, D., and Katz, J. L., 1971, "Bubble Nucleation in *n*-Pentane, *n*-Hexane, *n*-Heptane + Hexadecane Mixtures, and Water," *J. Phys. Chem.*, Vol. 75, pp. 3613–3619.
- Blander, M., and Katz, J. L., 1975, "Bubble Nucleation in Liquids," *Amer. Inst. Chem. Eng. J.*, Vol. 21, pp. 833–848.
- Blaszkowska-Zakrzewska, H., 1930, "Rate of Evaporation of Liquids from a Heated Metallic Surface," *Bulletin International de l'Academie Polonaise*, Vol. 4a–5a, pp. 188–190.
- Bradfield, W. S., 1966, "Liquid-Solid Contact in Stable Film Boiling," *I & E C Fundamentals*, Vol. 5, pp. 200–204.
- Carey, V. P., 1992, *Liquid-Vapor Phase Change Phenomena: An Introduction to the Thermophysics of Vaporization and Condensation Processes in Heat Transfer Equipment*, Hemisphere, New York.
- Eberhart, J. G., and Schnyders, H. C., 1973, "Application of the Mechanical Stability Condition to the Prediction of the Limit of Superheat for Normal Alkanes, Ether, and Water," *J. Phys. Chem.*, Vol. 77, pp. 2730–2736.
- Eckert, E. R. G., and Drake, Jr., R. M., 1972, *Analysis of Heat and Mass Transfer*, McGraw-Hill, New York.
- Emmerson, G. S., 1975, "The Effect of Pressure and Surface Material on the Leidenfrost Point of Discrete Drops of Water," *Int. J. Heat Mass Transfer*, Vol. 18, pp. 381–386.
- Emmerson, G. S., and Snoek, C. W., 1978, "The Effect of Pressure on the Leidenfrost Point of Discrete Drops of Water and Freon on a Brass Surface," *Int. J. Heat Mass Transfer*, Vol. 21, pp. 1081–1086.
- Gerweck, V., and Yadigaroglu, G., 1992, "A Local Equation of State for a Fluid in the Presence of a Wall and its Application to Rewetting," *Int. J. Heat Mass Transfer*, Vol. 35, pp. 1823–1832.
- Godleski, E. S., and Bell, K. J., 1966, "The Leidenfrost Phenomenon for Binary Liquid Solutions," *Third International Heat Transfer Conference*, Vol. 4, Chicago, IL, AIChE, New York, pp. 51–58.
- Gottfried, B. S., Lee, C. J., and Bell, K. J., 1966, "The Leidenfrost Phenomenon: Film Boiling of Liquid Droplets on a Flat Plate," *Int. J. Heat Mass Transfer*, Vol. 9, pp. 1167–1187.
- Grissom, W. M., and Wierum, F. A., 1981, "Liquid Spray Cooling of a Heated Surface," *Int. J. Heat Mass Transfer*, Vol. 24, pp. 261–271.
- Han, C. Y., and Griffith, P., 1965, "The Mechanism of Heat Transfer in Nucleate Pool Boiling—Part I," *Int. J. Heat Mass Transfer*, Vol. 8, pp. 887–904.
- Hiroyasu, H., Kadota, T., and Senda, T., 1974, "Droplet Evaporation on a Hot Surface in Pressurized and Heated Ambient Gas," *Bulletin of the JSME*, Vol. 17, pp. 1081–1087.
- Hosler, E. R., and Westwater, J. W., 1962, "Film Boiling on a Horizontal Plate," *ARS J.*, Vol. 32, pp. 553–558.
- Jeschar, R., Scholz, R., and Reiners, U., 1984, "Warmeübergang bei der zweiphasigen spritzwasserkühlung," *Gas-Warme Int.*, Vol. 33, p. 6.
- Klimenko, V. V., and Snytin, S. Y., 1990, "Film Boiling Crisis on a Submerged Heating Surface," *Exp. Thermal Fluid Sci.*, Vol. 3, pp. 467–479.
- Klinzing, W. P., Rozzi, J. C., and Mudawar, I., 1992, "Film and Transition Boiling Correlations for Quenching of Hot Surfaces with Water Sprays," *J. Heat Treating*, Vol. 9, pp. 91–103.
- Kovalev, S. A., 1966, "An Investigation of Minimum Heat Fluxes in Pool Boiling of Water," *Int. J. Heat Mass Transfer*, Vol. 9, pp. 1219–1226.
- Labeish, V. G., 1994, "Thermohydrodynamic Study of a Drop Impact Against a Heated Surface," *Exp. Thermal Fluid Sci.*, Vol. 8, pp. 181–194.
- Lienhard, J. H., 1976, "Correlation for the Limiting Liquid Superheat," *Chem. Eng. Sci.*, Vol. 31, pp. 847–849.
- Lienhard, J. H., and Karimi, A. H., 1978, "Corresponding States Correlations of the Extreme Liquid Superheat and Vapor Subcooling," *ASME JOURNAL OF HEAT TRANSFER*, Vol. 100, pp. 492–495.
- Matsuda, T., Taguchi, H., and Nagao, M., 1992, "Energetic Properties of NiO Surface Examined by Heat-of-Adsorption Measurement," *J. Thermal Analysis*, Vol. 38, pp. 1835–1845.
- McCann, H., Clarke, L. J., and Masters, A. P., 1989, "An Experimental Study of Vapor Growth at the Superheat Limit Temperature," *Int. J. Heat Mass Transfer*, Vol. 32, pp. 1077–1093.
- McCormick, J. L., and Westwater, J. W., 1965, "Nucleation Sites for Dropwise Condensation," *Chem. Eng. Sci.*, Vol. 20, pp. 1021–1036.
- Miller, C. A., and Neogi, P., 1985, *Interfacial Phenomena*, Marcel Dekker, New York.
- Nikolayev, G. P., Bychenkov, V. V., and Skripov, V. P., 1974, "Saturated Heat Transfer to Evaporating Droplets from a Hot Wall at Different Pressures," *Heat Transfer—Soviet Research*, Vol. 6, pp. 128–132.
- Nishio, S., and Hirata, M., 1978, "Direct Contact Phenomenon between a Liquid Droplet and High Temperature Solid Surface," *Sixth International Heat Transfer Conference*, Vol. 1, Toronto, Canada, Hemisphere, New York, pp. 245–250.
- Olek, S., Zvirin, Y., and Elias, E., 1988, "The Relation between the Rewetting Temperature and the Liquid-Solid Contact Angle," *Int. J. Heat Mass Transfer*, Vol. 31, pp. 898–902.
- Patel, B. M., and Bell, K. J., 1966, "The Leidenfrost Phenomenon for Extended Liquid Masses," *Chem. Eng. Progress Symposium Series*, Vol. 62, pp. 62–71.
- Ramilison, J. M., and Lienhard, J. H., 1987, "Transition Boiling Heat Transfer and the Film Transition Regime," *ASME JOURNAL OF HEAT TRANSFER*, Vol. 109, pp. 746–752.
- Rhodes, T. R., and Bell, K. J., 1978, "The Leidenfrost Phenomenon at Pressures up to the Critical," *Sixth International Heat Transfer Conference*, Vol. 1, Toronto, Canada, Hemisphere, New York, pp. 251–255.
- Sakurai, A., Shiotsu, M., and Hata, K., 1982, "Steady and Unsteady Film Boiling Heat Transfer at Subatmospheric and Elevated Pressures," *Heat Transfer in Nuclear Reactor Safety*, S. G. Bankoff and N. H. Afgan eds., Hemisphere New York, pp. 301–312.
- Schroeder-Richter, D., and Bartsch, G., 1990, "The Leidenfrost Phenomenon caused by a Thermo-Mechanical effect of Transition Boiling: A Revisited Problem of Non-Equilibrium Thermodynamics," *Fundamentals of Phase Change: Boiling and Condensation*, ASME, New York, pp. 13–20.
- Segev, A., and Bankoff, S. G., 1980, "The Role of Adsorption in Determining the Minimum Film Boiling Temperature," *Int. J. Heat Mass Transfer*, Vol. 23, pp. 637–642.
- Shepherd, J. E., and Sturtevant, B., 1982, "Rapid Evaporation at the Superheat Limit," *J. Fluid Mechanics*, Vol. 121, pp. 379–402.
- Skripov, V. P., 1974, *Metastable Liquids*, John Wiley and Sons, New York.
- Skripov, V. P., Sinityn, E. N., and Pavlov, P. A., 1980, *Thermal and Physical Properties of Liquids in the Metastable State*, Atomizdat, Moscow.
- Spiegler, P., Hopenfeld, J., Silberberg, M., Bumpus, Jr., C. F., and Norman, A., 1963, "Onset of Stable Film Boiling and the Foam Limit," *Int. J. Heat Mass Transfer*, Vol. 6, pp. 987–994.
- Taylor, G. I., 1950, "The Instability of Liquid Surfaces when Accelerated in a Direction Perpendicular to their Plane, I," *Proc. Royal Society of London*, Vol. A201, p. 192.
- Testa, P., and Nicotra, L., 1986, "Influence of Pressure on the Leidenfrost Temperature and on Extracted Heat Fluxes in the Transient Mode and Low Pressure," *Transactions of the ASME*, Vol. 108, pp. 916–921.
- Unal, C., Daw, V., and Nelson, R. A., 1992, "Unifying the Controlling Mechanisms for the Critical Heat Flux and Quenching: The Ability of Liquid to Contact the Hot Surface," *ASME JOURNAL OF HEAT TRANSFER*, Vol. 114, pp. 972–982.
- Xiong, T. Y., and Yeun, M. C., 1990, "Evaporation of a Liquid Droplet on a Hot Plate," *Int. J. Heat Mass Trans.*, Vol. 34, pp. 1881–1894.
- Yao, S. C., and Henry, R. E., 1978, "An Investigation of the Minimum Film Boiling Temperature on Horizontal Surfaces," *Transactions of the ASME*, Vol. 100, pp. 263–266.
- Yao, S. C., and Cai, K. Y., 1988, "The Dynamics and Leidenfrost Temperature of Drops Impacting on a Hot Surface at Small Angles," *Exp. Thermal Fluid Sci.*, Vol. 1, pp. 363–371.
- Zuber, N., 1958, "On the Stability of Boiling Heat Transfer," *Transactions of the ASME*, pp. 711–720.

Complete Condensation of Forced Convection Two-Phase Flow in a Miniature Tube

E. Begg

D. Khrustalev¹

A. Faghri
Mem. ASME

Department of Mechanical Engineering,
University of Connecticut,
Storrs, CT 06269

A physical and mathematical model of annular film condensation in a miniature tube has been developed. In the model the liquid flow has been coupled with the vapor flow along the liquid-vapor interface through the interfacial temperature, heat flux, shear stress, and pressure jump conditions due to surface tension effects. The model predicts the shape of the liquid-vapor interface along the condenser and the length of the two-phase flow region. The numerical results show that complete condensation of the incoming vapor is possible at comparatively low heat loads. Observations from a flow visualization experiment of water vapor condensing in a horizontal glass tube confirm the existence and qualitative features of annular film condensation leading to the complete condensation phenomenon in small diameter ($d < 3.5$ mm) circular tubes.

Introduction

The need for reliable, high performance, price competitive electronic devices, most notably electronic chips, has created demand for comparably small heat transfer devices capable of removing the required heat load within a known and preferably limited temperature range. Closed two-phase devices such as heat pipes and thermosyphons have been and are being used successfully for this application. Typically, these use a spreading strategy and have a large number of small circular channels arranged in parallel rows in a rectangular body. Whatever configuration is used, the heat energy removed at the chip is transported away and rejected from the system by condensation at a remote location. A fundamental understanding of the condensation process in small diameter channels is necessary to optimize design configurations.

In a review of the operating limitations of micro/miniature devices for possible use in electronic cooling applications Cao and Faghri (1994) describe several experimental studies some of which included visualization of circular tube heat pipes and thermosyphons with inside diameters in the range of 3.6–1.0 mm. Li et al. (1992) performed experiments on cylindrical tube heat pipes with inner diameters of 1.2 mm and 2.5 mm. One particular observation from their results was that circular miniature heat pipes were much more sensitive to amount of fill than conventional size heat pipes. Lee et al. (1992) studied the two-phase flow and heat transfer characteristics of thermosyphons with and without concentric wire inserts. The inside diameters of the thermosyphons were 3.6 mm–1.0 mm. They found that for a thermosyphon of less than 2.3-mm ID, wire inserts were necessary to achieve normal operation as a heat transfer device. Chen et al. (1992) conducted flow visualization experiments on a 2-mm ID glass heat pipe. Four basic flow patterns were observed over the range of operating conditions that included liquid projectile flow, slug flow, suspended liquid column, and annular flow. In retrospect it may be seen that observations cited in the three studies above are most likely a result of the effects of surface tension. Unlike conventional size passages in which surface tension effects are limited, surface tension in miniature size channels can have a significant role on the overall hydrodynamics and in particular on the thin films that are believed to be the dominant mechanism controlling the heat transfer characteristics.

For miniature circular tubes the flow regime maps for condensation in conventional size tubes may not be relevant because of the role of surface tension in the hydrodynamics. Presently, very limited data are available concerning the basic flow patterns for two-phase flow with or without heat transfer in miniature circular tubes. It follows that little is known about the mechanisms associated with transition in these flows.

Condensation in conventional size circular tubes comprises a well-defined body of work. Much of the early work was motivated by the power and chemical process industries. Collier and Thome (1994) present a generally accepted description of the two-phase flow patterns during forced convection condensation in conventional size horizontal tubes with co-current flow. In order of increasing velocity, the flow is found to be stratified, slug, plug or wavy, and annular. The stratified flow pattern is found when there are small vapor velocities and low interfacial shear forces. It is assumed that a laminar film of condensate runs down the inner circumferential surface of the tube and collects in the lower portion of the tube. Slug, plug, and wavy flow patterns are essentially stratified flows where vapor shear forces are becoming significant. At much higher total mass flow rates annular flow is found. Shear forces are large in this regime and the effect of gravity is negligible. It is important to note that in conventional size horizontal tubes this flow regime is believed to have a significant fraction of liquid droplets entrained in the vapor core.

Baker (1954) presented one of the earliest regime maps for two-phase flow patterns based on a collection of experimental data for adiabatic gas-liquid flows in pipes from 25.4–101.6 mm inside diameter. Although the axes of his plot were dimensional, the content of Baker's map became a well accepted standard for predicting flow regime. An important paper by Bell et al. (1970) established a link between the various empirical correlations for heat transfer coefficient and their proper interpretation in terms of flow regime. After an extensive review of the available correlations it was demonstrated that determination of the proper flow regime was necessary in order to choose the proper correlation. Also, the specific limits of validity for each of the condensation correlations were stated. The results presented in this paper may seem obvious now but, at the time, research work in condensation lacked this perspective.

The earliest flow visualization on a condensing two-phase flow with heat transfer reported by Soliman and Azer (1971) used R-12 condensing in a 12.7-mm inside diameter horizontal tube. Their concern was that the majority of two phase flow studies were biased towards boiling and that the flow regime maps available in the literature might not be applicable to condensation. Experiments

¹ Presently at Thermocore, Inc., Lancaster, PA 17601.

Contributed by the Heat Transfer Division for publication in the JOURNAL OF HEAT TRANSFER. Manuscript received by the Heat Transfer Division, July 7, 1998; revision received, June 1, 1999. Keywords: Condensation, Heat Transfer, Microgravity, Microscale, Phase Change. Associate Technical Editor: P. Ayyaswamy.

were conducted over a wide range of conditions including mass flux rates of 25.6–301.9 kg/m² s, quality at the exit 0–0.95, as well as various superheats and coolant flow rates. Six major flow patterns were identified (plug, slug, wavy, semiannular, annular, and spray) in addition to three transitional ones (annular-wavy, semiannular-wavy, spray-annular). They concluded that the flow map of Baker was inadequate for representation of the flow patterns existing in horizontal tubes during the condensation process.

Traviss and Rohsenow (1973) also performed a similar study of condensing flow with the same purpose—to determine if any of the existing flow maps were valid for condensing flows in horizontal tubes. Using R-12 in an 8.0-mm inside diameter tube over a wide range of operating conditions, four flow patterns were observed—dispersed, annular, semiannular, and slug. Results from their observations as well as the Soliman and Azer (1971) data were plotted on a number of flow maps including the standard Baker map. They concluded that adiabatic two-phase flow could be used to predict flow regimes for condensation with the qualification that for tube diameters of less than 25.4 mm, the flow regime boundaries given by Baker could not be considered distinct lines and required a modified interpretation to be successfully applied. It is interesting to note that neither of the R-12 visual studies mentioned above observed a bubble flow pattern.

Taitel and Dukler (1976) developed an analytical method for prediction of flow regime transition between five basic flow patterns. Their approach was based on the analysis of each of the phases, separately, in an adiabatic stratified flow. Then based on a postulation of the physical process by which transition can occur (from one specified flow pattern to another), a criteria is determined by nondimensionalization of the equations derived in their analysis. The results are plotted on a generalized flow regime map as lines marking the boundary of the flow regimes. Three different sets of axes are used for the suggested generalized flow map; however, all use the Martinelli parameter as the abscissa. A comparison to experimental data for air water flows on the superficial liquid and vapor velocity axes for horizontal tubes of 13–50 mm inside diameter and show very satisfactory agreement. This work was a significant contribution to the study of condensation in horizontal tubes because it presented an a priori determination of flow regime regardless of mass flow rate, tube diameter and substance based on an analysis free of specific empirical two phase flow correlations.

Breber et al. (1980), using an extensive collection of data from

the literature, demonstrated the method of Taitel and Dukler (1976) to be specifically applicable to condensation in horizontal tubes. Experimental data from more than 700 condensation flow regime observations in the literature which included water, R-12 and R-113, tube inside diameters of 4.8–50.8 mm, and a wide range of operating parameters were used for the comparison. No adiabatic data were used. With the exception of data from the smallest inside diameter tube (4.8 mm), agreement with the flow regime transition boundaries as predicted by Taitel and Dukler was good. A simplified criterion is suggested for determining the transition boundaries. Sardesai et al. (1981) provided a detailed examination of the transition from annular to stratified/wavy flow during condensation in a horizontal tube. Experiments were conducted for local heat transfer coefficients during condensation of a pure vapor. Approximately 800 measurements of local heat transfer coefficients were made for the condensation of five different substances (R-113, propanol, methanol, n-pentane, water) covering a wide range of mass flow rates. The transition from annular to stratified/wavy flow was found to be close to that recommended by Taitel and Dukler and distinct, i.e., not a region or area about a curve.

Analysis of condensation in a horizontal tube is limited to a particular flow pattern. The stratified flow problem was considered by Chaddock (1957) and Chato (1962) for stagnant vapor and for the case of pressure gradient in the tube by Rufer and Kezios (1966).

The methods of analysis for condensation in a vertical tube have been found to be applicable to the annular flow pattern in both horizontal tube condensation and a reduced gravity environment. Because of the symmetry in both upward and downward flow the analysis of condensation in a vertical tube is a problem that has been treated extensively. Many of the studies use the same type of one-dimensional analysis as the classic Nusselt approach which has been modified to account for pressure drop in the vapor due to both friction at the liquid/vapor interface and momentum exchange between the vapor and liquid due to the condensation mass flux. This approach was used by Seban and Hodgson (1982) with the assumptions of downward laminar flow of liquid and a linear temperature distribution in the liquid film. The vapor flow is considered one-dimensional and a friction coefficient based on both a modified empirical correlation for pipe flow and a term to account for the flux of momentum normal to the vapor at the liquid surface, is used. One of the practical limits of vertical tube con-

Nomenclature

c_p = specific heat at constant pressure, J/(kg-K)
 $f_{i,v}$ = interfacial friction factor
 f_v = vapor friction factor
 h_{fg} = latent heat of vaporization, J/kg
 h_o = outer surface convective heat transfer coefficient, W/(m² K)
 k = thermal conductivity, W/(m-K)
 L_δ = length of the liquid film to the point of complete condensation (Fig. 1), m
 K = curvature, m⁻¹
 \dot{m} = mass flow rate, kg/s
 \dot{m}_t = total mass flow rate, kg/s
 $\dot{m}_{i,in}$ = liquid mass flow rate at $z = 0$, kg/s
 \dot{m}'' = total mass flux, kg/m² s
 $Ma = \bar{w}_v / \sqrt{\gamma_0 R_g T_v}$, Mach number
 p = pressure, Pa
 p_d = disjoining pressure, Pa
 q = heat flux, W/m²

$Q = \dot{Q} = 2\pi R \int_0^z q_w dz - (c_{p,l} \dot{m}_l \bar{T}_l - c_{p,i,in} \dot{m}_{i,in} \bar{T}_{i,in})$, axial heat flow due to phase change, W
 $Q_{in} = \dot{Q}_{in} = \dot{m}_{v,in} h_{fg}$, input heat flow rate, W
 r = radial coordinate, m
 R = inner radius of the channel, m
 R_g = gas constant, J/(kg-K)
 $Re = 2\bar{w}_v (R - \delta) \rho_v / \mu_v$, axial vapor Reynolds number
 $Re_r = 2v_{v,\delta} (R - \delta) \rho_v / \mu_v$, radial vapor Reynolds number
 T = temperature, K
 v = radial velocity, m/s
 w = axial velocity, m/s
 \bar{w} = area-averaged axial velocity, m/s
 z = axial coordinate, m

$\Delta = d\delta/dz$
 δ = liquid film thickness, m
 μ = dynamic viscosity, Pa-s
 ρ = density, kg/m³
 σ = surface tension, N/m
 φ = inclination angle

Subscripts

ent = entrance
in = at $z = 0$
l = liquid
men = meniscus
sat = saturation
v = vapor
w = wall
 δ = liquid film free surface

Greek Symbols

α = accommodation coefficient
 β = momentum flux coefficient
 $\gamma_0 = c_p / c_v$, ratio of specific heats

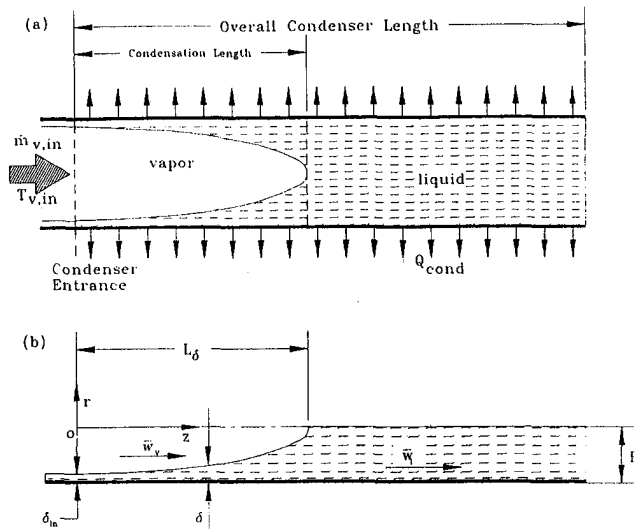


Fig. 1 Description of the physical model for annular film condensation in a miniature tube; (a) structure of two-phase flow for complete condensation, (b) coordinate system and conventions for film condensation model

condensation, known as flooding, was predicted by Seban and Faghri (1984). This occurs in a vertical tube with an upward flow of vapor and a downward flow of liquid and results in a condition of nonstationary blocking of the vapor flow by liquid near the entrance to the tube and a resultant large rise in pressure drop. Another case of shear-dominated condensing flow is presented by Faghri and Chow (1988) for a micro-gravity environment with condensate being removed by suction at the wall.

The objective of this work is to model annular film condensation in miniature circular cylinder tubes where capillary phenomena can conceivably result in blocking of the tube cross section with liquid at some distance from the condenser entrance. A simple flow visualization experiment was conducted to provide a means for verifying the phenomenon associated with complete condensation at low mass fluxes and to gain an understanding of the important qualitative features of the problem. A physical description is illustrated in Fig. 1(a). Vapor condenses inside a tube forming a

stationary liquid-vapor interface. At some point downstream of the inlet, all the incoming vapor is condensed and only liquid flows in the tube cross section. This can occur due to surface tension effects that are usually neglected in film condensation models for tubes with larger diameters. This problem seems to be of practical use, since two-phase heat transfer in miniature channels is under extensive study.

Flow Visualization in Miniature Tubes

A simple flow visualization experiment was performed to allow observation of the condensation flow pattern over the entire region of two-phase flow in a horizontal glass tube. Three tubes of diameters 3.4, 2.3, and 1.6 mm were used. Each small-diameter tube was arranged to be the horizontal leg in a glass loop thermosyphon. Water was used for all experiments. Condensation could be directly observed in the glass tube test section through a transparent cooling water jacket. The total mass flow rate of vapor to the tube was controlled by the heating rate. Cooling on the external wall of the glass tube test section was provided by using forced circulation of water from a commercial constant temperature bath.

The loop thermosyphon shown in Fig. 2, fabricated from borosilicate (commonly known as "Pyrex") was used to perform the flow visualization on small diameter tubes. Two 20-mm diameter vertically oriented tubes acted as reservoirs, one for heating of the liquid forming the vapor reservoir and one for collecting condensate. The test section was a small horizontal diameter tube of the chosen diameter which connected the two reservoirs near the top. A larger diameter (10-mm) horizontal tube connecting the reservoirs near the bottom served as a return line for the condensate to the heater reservoir. A single opening on the upper portion of the condensate reservoir allowed for filling and deaeration. The entire outer surface of the loop was insulated except for the region of heat removal at the condenser. A flexible foil heater, with a nominal resistance of 21.98 ohm, was in direct contact with the outer wall of the heater reservoir. Thermal insulation was placed outside the heater and was continuous with the insulation for the entire device, therefore minimizing heat loss to the surroundings. Forced circulation of water from a commercial constant temperature bath provided the means of cooling on the outer wall of the test section tube. A 16-mm outside diameter, 1.0-mm wall thickness, circular glass tube concentric with the test section was used as a cooling jacket. The initial portion of the test section was insulated to allow

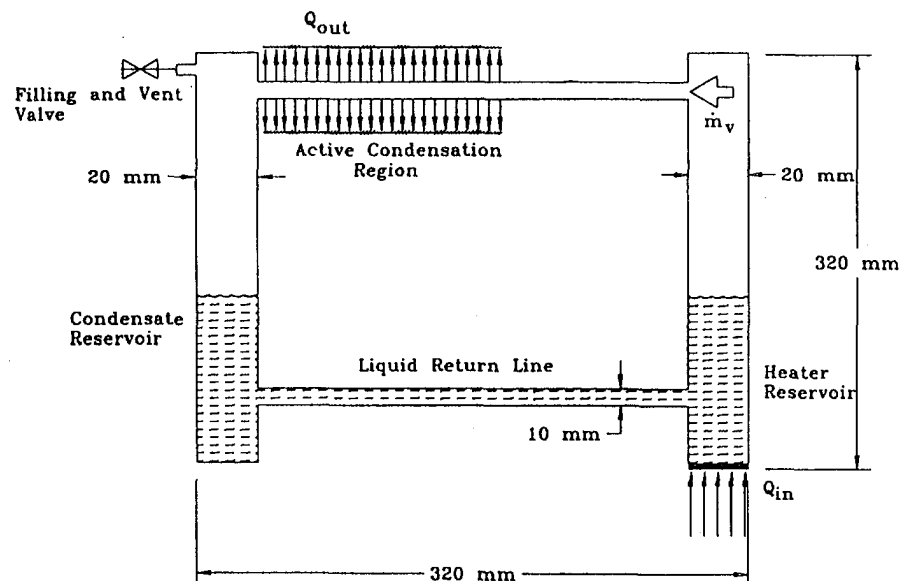


Fig. 2 Schematic of loop thermosyphon used for flow visualization of complete condensation in a horizontal miniature glass tube

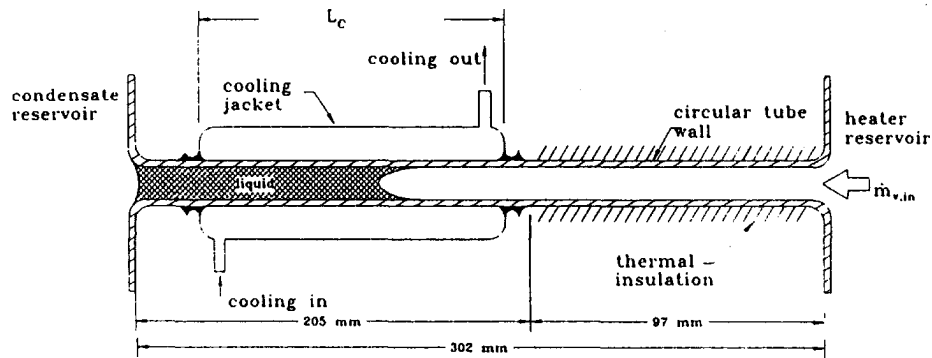


Fig. 3 Schematic of test section for condensation flow visualization experiments

for flow development of the incoming vapor. A schematic of the test section is seen in Fig. 3. The internal surfaces of the loop device were cleaned by filling with methanol and using an ultrasonic bath for agitation. After being blown with grade 5 nitrogen gas, the internal volume was rinsed several times with experimental grade water. The system was deaerated initially by completely filling the internal volume with liquid and then heating to create vapor which was boiled off through the filling/vent valve. The volume of triply distilled HPLC grade water contained in the loop during testing was typically 80–100 ml. Periodic boiling off of vapor prior to operation for experiments was done to insure the removal of any possible air from leaks. Repeatability of the operating conditions for complete condensation proved to be a good indicator of the presence of noncondensable gases in the system. Starting of the system required at least two hours to reach an initial steady-state operation.

Temperature of the vapor in the heater reservoir and the vapor in the condensate reservoir were measured. These are assumed to be the (uniform) saturation temperature in each respective reservoir volume. A variable autotransformer (Variac) with 120 VAC input controlled the supply of power to the flexible foil heater. Power was measured using an ammeter and voltmeter. Thus, mass flow rate of the vapor from the heater reservoir to the tube was controlled by the heating rate.

Black and white photography using a 35-mm camera with either a 100 mm or a 200 mm micro-Nikkor lens was the primary source of documentation. In addition, video recordings were made demonstrating the transition between steady-state conditions.

Photographic Results. Flow patterns are reported for three different diameter tubes at heat loads into the tube which correspond to relatively low mass flux rates. The mass flow rate of vapor into the test section, which is the same as the total mass flow rate, is $\dot{m} = Q_i/h_{fg}$ where Q_i (W) is referred to as the heat load into the tube and is found from the power to the heater on the loop thermosyphon vapor generator reservoir minus the heating rate loss to the surroundings. The latent heat, h_{fg} , is found as a function of the inlet vapor temperature. The total mass flux at the inlet is then $\dot{m}'' = \dot{m}/A$ where A is the flow cross-sectional area of the tube. In this work the inlet conditions are referred to by the heat load into the tube. Table 1 provides the equivalent mass fluxes for the experimental results presented. The range of inlet saturation pressure for water tested was $6.324 \text{ kPa} < p_{\text{sat,in}} < 6.858 \text{ kPa}$.

Photographs of the two-phase flow region for low-pressure water condensing in a horizontal 3.4-mm diameter tube are shown in Fig. 4(a). The flow direction is right to left with only vapor entering the tube. The entire region of two-phase flow is seen in the photographs. A liquid film forms on the tube wall about the vapor flow. The film thickness at the bottom is seen to be thicker than on the top wall over most of the axial length for which two-phase flow exists. At the end of the two-phase flow region the meniscus-like shape of the liquid-vapor interface can be seen. In the first photograph the heat load into the condenser is $Q_i = 3.06 \text{ W}$, resulting

in complete condensation at a length of 10 mm. The next four photographs show the flow pattern for larger heat loads. As the heat load increases the film thickness on the bottom of the tube is seen to increase. The draining of the liquid film under the influence of gravity results in a greater liquid film thickness in the bottom portion of the tube. In conventional-size tubes this effect is referred to as stratification. However, stratification in these small-diameter tubes does not result in a horizontal surface for the liquid in the bottom portion of the tube. Note that the film thickness on the bottom wall decreases prior to the termination of the two-phase flow region. For all results presented the flow field is observed to be steady, i.e., the instantaneous values of the condensation length and local film thickness do not change with time.

Figures 4(b) and 4(c) present close up photographs of low pressure water condensing in horizontal tubes of 2.3 and 1.6-mm diameter, respectively. The entire region of two-phase flow is not seen in either set of pictures because of the relatively long lengths for complete condensation relative to the tube diameter. These pictures are included to show the qualitative similarity in the flow pattern for the three different diameter tubes. Because of stratification an unsymmetric liquid film exists over most of the two-phase flow region in all tubes tested. As the tube diameter becomes smaller, the stratification effect is lessened. In all tubes, as the mass flux rate increases to and approaches the limit for which steady complete condensation will occur, the stratification effect produces a significant difference in film thickness between the top and the bottom of the tube and results in a collection of liquid near the end of the annular film region. For the higher heat load cases in Fig. 4(b) this phenomenon is seen very clearly. This is a result of the interaction of shear and capillary forces with the liquid inventory from stratification. At the end of the two-phase flow, i.e., the location where vapor flow ceases and only liquid occupies the tube cross-sectional area, a meniscus-like interface is formed. The film thickness never appears to achieve a significant dimension of the tube diameter, except near the end of the two-phase flow region.

Table 1 Experimental data for complete condensation of water in three horizontal, miniature Pyrex tubes from loop thermosyphon experiments

d=3.4 mm				
Q (W)	T _v (C)	\dot{m} (kg/s) x 10 ⁻⁶	\dot{m}'' (kg/m ² s)	L _i (mm)
3.06	38.6	1.270	0.140	10
5.29	38.4	2.192	0.241	18
8.87	37.9	3.679	0.405	24
12.06	37.8	5.003	0.551	38
d=2.3 mm				
1.71	24.6	0.701	0.169	23
3.89	25.0	1.593	0.383	60
9.04	22.9	3.696	0.890	162
11.98	24.9	4.906	1.181	190
d=1.6 mm				
2.12	29.8	0.876	0.435	21
5.09	32.7	2.101	1.045	41
8.68	29.9	3.572	1.777	50

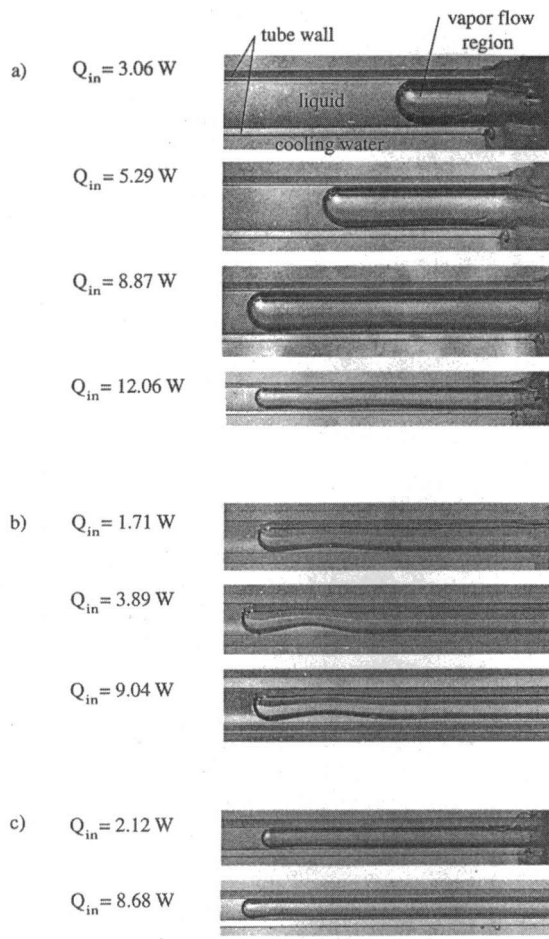


Fig. 4 Photographs of the steady flow pattern during complete condensation of low-pressure water vapor in three miniature horizontal tubes; (a) 3.4-mm inside tube diameter, (b) 2.3-mm inside tube diameter, (c) 1.6-mm inside tube diameter

The change of sign of surface curvature of the film thickness occurs regardless of the degree of stratification. Clearly the capillary force plays a role in the terminal region of the two-phase flow.

Unsteady Condensation. The primary purpose of the flow visualization was to provide a means to verify the steady complete condensation process. However, some observations about the condensation flow pattern at heat loads, and hence mass fluxes, greater than those seen in the pictures may be of interest. Specific comments will be limited to the 3.4-mm tube, but in all three tubes similar flow behaviors were observed. Eventually the steady flow pattern ceases to exist. At $Q_i = 14.47$ W the flow field appears as it is described above, except the instantaneous length of the two-phase region is no longer steady. It varies slowly about an average location. This is the same type of behavior that is observed when increasing or decreasing heat loads in the low heat load range. It appears to be a quasi-steady response. The unsteadiness is believed to be caused by the local unsteadiness of the cooling water in the cooling water jacket. At $Q_i = 33.1$ W slug flow begins. The slug formation is very well behaved. It occurs at the same relative location in the two-phase flow region and with a very precise period corresponding to heat load. The slug always forms at the location near the end of the two-phase flow region where the liquid collection creates a relatively large film thickness on the bottom wall. Thus, when the slug forms it travels a very short distance (approximately two tube diameters) before merging with the liquid. The formation of the slug, its travel downstream and its merging with the liquid all occur within a fraction of a second. The build up of the liquid film thickness at the location of formation may take several seconds, again, depending on the heat load.

Effect of Noncondensable Gases. Extensive testing of the three loop thermosyphons was conducted to establish repeatability of the observed results. As a result of this experience, it became apparent that the presence of air in the system had a significant effect on the observed flow pattern associated with a prescribed heat load. The condensation length was always much greater if air was present. The film thickness profile on the bottom wall is noticeably different. Transition phenomena are effected. When air is present the heat load at transition is significantly different from those measured when a pure vapor was present. Each of the transition flow patterns were affected. For transition from steady complete condensation, the quasi-steady change of the condensation length began at much lower heat loads. During slug formation the period became very irregular and bubbles would be formed as a result of the slug event. Although this investigation was not intended to be a systematic investigation of noncondensable gas effect on condensation, these observations are important in understanding experimental results of condensation small-diameter tubes.

Mathematical Formulation

A steady-state mathematical model of condensation, which leads to complete condensation is developed, which includes coupled vapor and liquid flows with shear stresses at the liquid free surface due to the vapor-liquid frictional interaction and surface tension gradient. The model is based on the following simplifying assumptions:

- 1 The vapor is saturated and there is no temperature gradient in the vapor in the radial direction.
- 2 Heat transport in the thin liquid film is due to conduction in the radial direction only.
- 3 Inertia terms can be neglected for the viscous flow in the liquid films with low Reynolds numbers.
- 4 Force on liquid due to surface tension is much greater than the gravitational force and the gravitational body force is neglected. Therefore the liquid is distributed onto the walls in an axisymmetric film.
- 5 The solid tube wall is infinitely thin so that its thermal resistance in the radial direction can be neglected as well as the axial heat conduction.

This model is different from traditional models for film condensation in tubes due to the following features:

- 1 The liquid momentum conservation equation in cylindrical coordinates is utilized and the corresponding expression for the shear stress at the liquid-vapor interface is used.
- 2 For extremely small channels and film thickness, the disjoining pressure and the interfacial resistance can affect both the liquid and vapor flow, therefore the terms containing the disjoining pressure and interfacial resistance are included in the model.
- 3 The effect of the surface tension on the fluid flow is included in the model and the two principal radii of the liquid-vapor interface curvature are used in the Laplace-Young equation.
- 4 Liquid subcooling is accounted for in the model, since it can result in a significant variation of the wall temperature under convective cooling conditions.

The cylindrical coordinate system used is shown in Fig. 1(b). Both the vapor and liquid flow along the z -coordinate. The physical situation should be described taking into consideration the vapor compressibility and the vapor temperature variation along the channel. Also the second principal radius of curvature of the liquid-vapor interface should be accounted for while it is usually neglected in modeling of film flows in tubes of larger diameters. Within the assumptions considered above, the mass and energy balances for the liquid film shown in Fig. 1(a) yield

$$\int_{R-\delta}^R r w_l(r) dr = \frac{1}{2\pi\rho_l} \left(\dot{m}_{l,in} - \frac{Q(z)}{h_{fg}} \right). \quad (1)$$

$\dot{m}_{l,in}$ is the liquid mass flow rate at the condenser inlet and $Q(z)$ is the rate of heat through a given cross section due to phase change for $z > 0$ and is defined as follows:

$$Q(z) = 2\pi R \int_0^z q_w dz - (c_{p,l} \dot{m}_l \bar{T}_l - c_{p,l,in} \dot{m}_{l,in} \bar{T}_{l,in}). \quad (2)$$

$q_w(z)$ is the heat flux at the solid-liquid interface due to heat conduction through a cylindrical film with a thickness of δ balanced with the liquid enthalpy change. Note that $T_\delta > T_w$ and therefore $Q(z)$ in Eq. (1) will be a negative quantity. The heat flux at the wall is

$$q_w = k_l \frac{T_w - T_\delta}{R \ln [R/(R - \delta)]} \quad (3)$$

where T_δ is the local temperature of the liquid-vapor interface. From Eqs. (2) and (3) we obtain the following equation for the heat rate rejected per unit axial length of the tube:

$$\frac{dQ}{dz} = 2\pi k_l \frac{T_w - T_\delta}{\ln [R/(R - \delta)]} - \frac{d}{dz} (c_{p,l} \dot{m}_l \bar{T}_l) \quad (4)$$

where \bar{T}_l is the area-averaged liquid temperature for a given z location. For consideration of subcooling in the condensed liquid, \bar{T}_l is found from an area average given by

$$\bar{T}_l = \frac{2 \int_{R-\delta}^R r T_l(r) dr}{[R^2 - (R - \delta)^2]} \quad (5)$$

where $T_l(r)$ is the assumed liquid film temperature profile given by the temperature distribution in a cylindrical wall.

$$T_l(r) = T_\delta + \frac{T_w - T_\delta}{R} \ln \frac{r}{R - \delta} \quad (6)$$

Substituting Eq. (6) into Eq. (5) and integrating results in an expression for \bar{T}_l . The derivative of \bar{T}_l in the axial is approximated by

$$\frac{d\bar{T}_l}{dz} = \frac{dT_\delta}{dz} + \left(\frac{dT_w}{dz} - \frac{dT_\delta}{dz} \right) \left[\ln \frac{R - \delta}{R} \right]^{-1} \frac{2}{[R^2 - (R - \delta)^2]} \times \left[\left(\ln \frac{R}{R - \delta} - \frac{1}{2} \right) \frac{R^2}{2} + \frac{(R - \delta)^2}{4} \right] \quad (7)$$

where the change of film thickness in the axial direction is assumed to be negligibly small. This assumption may need to be reconsidered; however, the reduction in mathematical complexity of the formulation resulting from its use is significant.

The axial momentum conservation for viscous flow in a liquid film in which the inertia terms are assumed to be negligible is

$$\frac{1}{r} \frac{\partial}{\partial r} \left(r \frac{\partial w_l}{\partial r} \right) = \frac{1}{\mu_l} \left(\frac{dp_l}{dz} + \rho_l g \sin \varphi \right). \quad (8)$$

The boundary conditions for the last equation are the no-slip condition at $r = R$ and shear stresses at the liquid-vapor interface due to the frictional liquid-vapor interaction, $\tau_{l,v}$, and the surface tension gradient related to the interfacial temperature gradient along the channel.

$$w_l|_{r=R} = 0 \quad (9)$$

$$\left. \frac{\partial w_l}{\partial r} \right|_{(r=R-\delta)} = \frac{1}{\mu_l} \left[-\tau_{l,v} - \frac{d\sigma}{dT} \frac{dT_\delta}{dz} \right] \equiv E \quad (10)$$

where T_δ is the local liquid-vapor interface temperature and the term with $d\sigma/dT$ is due to the Marangoni effect.

Taking into account the effect of the condensation process on the shear stress term, an expression from Munoz-Cobol et al. (1996) for annular filmwise condensation in vertical tubes with noncondensable gases is used for $\tau_{l,v}$.

$$\tau_{l,v} = \tau_{l,v,0} a' / [\exp(a') - 1], \quad (11)$$

where $\tau_{l,v,0}$ is defined as the interfacial shear stress in the absence of phase change and is given by

$$\tau_{l,v,0} = 0.5 f_{l,v} \rho_v (\bar{w}_v - w_{l,\delta})^2 \quad (12)$$

and a' is the ratio of the local condensation mass flow rate to the vapor mass flux rebounding from the interface which is approximated by

$$a' = - \frac{dQ}{dz} / [\pi R h_{fg} \rho_v f_{l,v} (\bar{w}_v - w_{l,\delta})] \quad (13)$$

$$f_{l,v} = f_v \left(1 + 360 \frac{\delta}{2R} \right) \quad (14)$$

and $f_{l,v}$ is the interfacial friction factor from Wallis (1969). From an experimental study for a simulated change of phase the vapor friction factor, f_v , is given as follows (Bowman and Hitchcock, 1988; Jang et al., 1991):

$$f_v = 16 [1.2337 - 0.2337 \exp(-0.0363 \text{Re}_v)] \times [\exp(1.2 \text{Ma}) / \text{Re}_v] \quad (15)$$

Re_v is found using the vapor suction velocity at the liquid-vapor interface due to condensation, $v_{v,\delta}$, which is defined through the condensing mass flux.

$$v_{v,\delta} = \frac{dQ}{dz} \frac{1}{2\pi(R - \delta) h_{fg} \rho_v} \quad (16)$$

Solving Eqs. (8)–(10), the velocity profile is expressed as follows:

$$w_l = - \frac{1}{\mu_l} \frac{dp_l}{dz} \left[\frac{1}{4} (R^2 - r^2) + \frac{(R - \delta)^2}{2} \ln \frac{r}{R} \right] + E(R - \delta) \ln \frac{r}{R}. \quad (17)$$

Substituting Eq. (17) into Eq. (1), we obtain the following equation for the axial pressure gradient in the liquid:

$$\frac{dp_l}{dz} = \rho_l g \sin \varphi + \mu_l \left[\frac{1}{2\pi\rho_l} \left(\frac{Q}{h_{fg}} - \dot{m}_{l,in} \right) + E(R - \delta)F \right] \times \left[\frac{R^4}{16} + \frac{(R - \delta)^2}{2} \left(F + \frac{(R - \delta)^2}{8} - \frac{R^2}{4} \right) \right]^{-1} \quad (18)$$

where

$$F = \frac{(R - \delta)^2}{2} \left(\ln \frac{R}{R - \delta} + \frac{1}{2} \right) - \frac{R^2}{4}. \quad (19)$$

The pressure difference between the vapor and liquid phases is due to capillary effects (Faghri, 1995).

$$p_v - p_l = \sigma \left\{ \frac{d^2\delta}{dz^2} \left[1 + \left(\frac{d\delta}{dz} \right)^2 \right]^{-3/2} + \frac{1}{R - \delta} \cos \left(\text{atan} \frac{d\delta}{dz} \right) \right\} - p_d \quad (20)$$

The term with cosine on the right-hand side of this equation is due to the second principal radius of interfacial curvature. Introducing an additional variable

$$d\delta/dz = \Delta, \quad (21)$$

Eq. (20) can be rewritten as follows:

$$\frac{d\Delta}{dz} = [1 + (\Delta)^2]^{3/2} \left(\frac{p_v - p_l + p_d}{\sigma} - \frac{\cos(\text{atan } \Delta)}{R - \delta} \right). \quad (22)$$

The integral equations of mass conservation for the vapor and liquid flows take the following form:

$$\rho_v A_v \bar{w}_v(z) = \bar{w}_{v,\text{in}} \rho_{v,\text{in}} A_{v,\text{in}} + Q(z)/h_{fg} \quad (23)$$

$$\rho_l A_l \bar{w}_l(z) = \bar{w}_{l,\text{in}} \rho_{l,\text{in}} A_{l,\text{in}} - Q(z)/h_{fg} \quad (24)$$

$A_v = \pi(R - \delta)^2$ is the cross-sectional area of the vapor channel. $\bar{w}_{v,\text{in}}$ is the average vapor velocity at $z = 0$.

The compressible quasi-one-dimensional momentum equation for the vapor flow in the form suggested by Bankston and Smith (1973) is modified to account for nonuniformity of the vapor cross-sectional area of the liquid-vapor interface following Faghri (1995).

$$\frac{dp_v}{dz} = \rho_v g \sin \varphi + \frac{1}{A_v} \left[\frac{d}{dz} (-\beta_v \rho_v \bar{w}_v^2 A_v) - f_v \rho_v \bar{w}_v^2 \pi(R - \delta) + 2\pi(R - \delta) \rho_v v_{v,\delta}^2 \sin(\text{atan } \Delta) \right] \quad (25)$$

with $\beta_v = 1.33$ for small radial Reynolds numbers.

The perfect gas law is employed to account for the compressibility of the vapor flow,

$$\rho_v = \frac{p_v}{R_g T_v}. \quad (26)$$

Therefore,

$$\frac{dp_v}{dz} = \frac{1}{R_g} \left(\frac{dp_v}{dz} \frac{1}{T_v} - \frac{p_v}{T_v^2} \frac{dT_v}{dz} \right). \quad (27)$$

The saturated vapor temperature and pressure are related by the Clausius-Clapeyron equation which can be written in the following form:

$$\frac{dT_v}{dz} = \frac{dp_v}{dz} \frac{R_g T_v^2}{p_v h_{fg}}. \quad (28)$$

The seven first-order differential equations, Eqs. (4), (18), (21), (22), (25), (27), and (28), include the following seven variables: δ , Δ , p_l , Q , p_v , ρ_v , and T_v . Therefore, seven boundary conditions are set forth at $z = 0$:

$$\delta = \delta_{\text{in}} \quad (29)$$

$$\Delta = 0 \quad (30)$$

$$p_l = p_{v,\text{in}} - \frac{2\sigma}{R - \delta_{\text{in}}} + p_d \quad (31)$$

$$Q = 0 \quad (32)$$

$$p_v = p_{v,\text{in}} = p_{v,\text{sat}}(T_{v,\text{in}}) \quad (33)$$

$$\rho_{v,\text{in}} = \frac{p_{v,\text{in}}}{R_g T_{v,\text{in}}} \quad (34)$$

$$T_v = T_{v,\text{in}}. \quad (35)$$

In the boundary condition given by Eq. (29), δ_{in} is defined from the condition that in the adiabatic zone just prior to the entrance of the

condenser the liquid and vapor pressure gradients should be equal. To find δ_{in} , Eqs. (18) and (25) should be solved for the case of $Q = 0$, $v_{v,\delta} = 0$, $dA_v/dz = 0$ and $dT_\delta/dz = 0$. The boundary condition, Eq. (32), directly follows from Eq. (2). There are also parameters $\dot{m}_{l,\text{in}}$ and $\bar{w}_{v,\text{in}}$ and an additional variable T_δ involved in this problem. They will be considered using additional algebraic equations. The parameter $\dot{m}_{l,\text{in}}$ should be found using a constitutive condition at the entrance of the condenser

$$\dot{m}_{l,\text{in}} = \dot{m}_l - Q_{\text{in}}/h_{fg} \quad (36)$$

where Q_{in} is the total heat load into the condenser. Also $\bar{w}_{v,\text{in}} = Q_{\text{in}}/(h_{fg} \rho_v A_{v,\text{in}})$.

The liquid-vapor interface temperature, T_δ , differs from the saturated bulk vapor temperature because of the interfacial resistance and effects of curvature on saturation pressure over liquid films. The interfacial resistance is defined as (Faghri, 1995)

$$q_\delta = - \left(\frac{2\alpha}{2 - \alpha} \right) \frac{h_{fg}}{\sqrt{2\pi R_g}} \left[\frac{p_v}{\sqrt{T_v}} - \frac{(p_{\text{sat}})_\delta}{\sqrt{T_\delta}} \right] \quad (37)$$

where p_v and $(p_{\text{sat}})_\delta$ are the saturation pressures corresponding to T_v and T_δ , the temperatures associated with the thin liquid film interface, respectively. The following two algebraic equations should be solved to determine T_δ for every point along the z -direction. The relation between the saturation vapor pressure over the thin condensing film, $(p_{\text{sat}})_\delta$, affected by the surface tension, and the normal saturation pressure corresponding to T_δ , $p_{\text{sat}}(T_\delta)$, is given by the extended Kelvin equation (Faghri, 1995)

$$(p_{\text{sat}})_\delta = p_{\text{sat}}(T_\delta) \exp \left[\frac{(p_{\text{sat}})_\delta - p_{\text{sat}}(T_\delta) - \sigma K + p_d}{\rho_l R_g T_\delta} \right] \quad (38)$$

where K is the local curvature of the liquid-vapor interface defined by the term in outer brackets in Eq. (20). Notice that under steady conditions, q_δ is due to heat conduction through the liquid film. It follows from Eqs. (3) and (37)

$$T_\delta = T_w + \frac{R}{k_l(R - \delta)} \ln \frac{R}{R - \delta} \left(\frac{2\alpha}{2 - \alpha} \right) \times \frac{h_{fg}}{\sqrt{2\pi R_g}} \left[\frac{p_v}{\sqrt{T_v}} - \frac{(p_{\text{sat}})_\delta}{\sqrt{T_\delta}} \right]. \quad (39)$$

Equations (38) and (39) determine the interfacial temperature, T_δ , and pressure, $(p_{\text{sat}})_\delta$, for a given vapor pressure, $p_v = p_{v,\text{sat}}(T_v)$, temperature of the solid-liquid interface, T_w , and the liquid film thickness, δ . Note that T_w is the local temperature of the wall and can vary along the condenser depending on the cooling conditions.

For the case of variable wall temperature T_w becomes an additional variable. If the convective heat transfer coefficient at the outer tube wall, h_o , and the cooling liquid temperature, T_∞ , are known, the local wall temperature can be defined using an energy balance

$$h_o(T_w - T_\infty) = \frac{1}{2\pi R} \frac{dQ}{dz}. \quad (40)$$

To solve this problem, the first-order ordinary differential equation, Eq. (40), must be added to the seven previously specified. The additional boundary condition is given by

$$z = 0, \quad T_w = T_{w,\text{in}}. \quad (41)$$

Numerical Procedure

Equations (4), (18), (21), (22), (25), (27), and (28) with corresponding boundary conditions have been solved using the standard Runge-Kutta procedure. Algebraic Eqs. (38) and (39) with two unknowns, $(p_{\text{sat}})_\delta$ and T_δ , have been solved numerically for every point on z using Wegstein's iteration method. All the unknown variables were found with the accuracy of 0.0005 percent. During

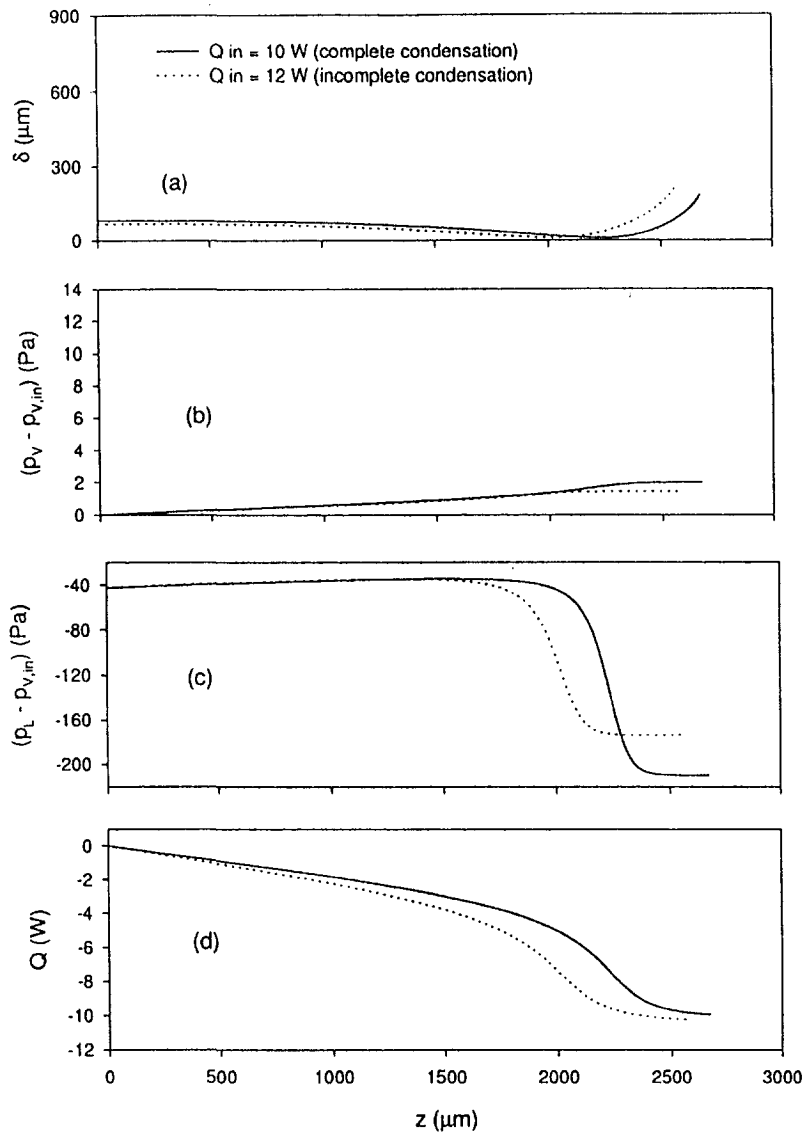


Fig. 5 Annular film condensation in a circular tube with constant wall temperature boundary condition. $R = 1.5$ mm, $T_w = 340$ K, $T_v = 363$ K, $\dot{m} = 0.01$ g/s. (a) Film thickness versus position, (b) vapor pressure versus position, (c) liquid pressure versus position, (d) cumulative heat rejected versus position.

the numerical procedure the interval $0 \leq z \leq L_\delta$ was divided into at least 500 parts, and the thermophysical properties of the saturated vapor and liquid were recalculated for each of the parts at the corresponding vapor temperature $T_v(z)$.

The length of the two-phase zone is given by the numerical solution. At the end of the two-phase zone $d\Delta/dz$ became infinitely large and the film thickness increased dramatically causing the solution to breakdown.

Results and Discussion

Numerical solutions for steady-state axisymmetric annular film condensation of water in a tube with constant wall temperature and convective boundary conditions are presented. Two cases of heat-load-in are presented, one representing complete condensation and the other incomplete condensation. Complete condensation is defined as the condensation of all incoming vapor in a filmwise manner in which the vapor flow terminates at a well-defined location forming a steady meniscus-like interface. The condition of complete condensation requires the overall energy balance to be satisfied. Thus, the energy convected into the tube, or heat-load-in, Q_{in} (W), must be equal to the cumulative heat rate rejected from

the condensing vapor in the tube, referred to simply as Q (W). This occurs over a distance from the inlet to the tube known as the condensation length, L_δ (m). Incomplete condensation is said to exist for a heat-load-in greater than Q_{in} (W) for complete condensation.

Parametric studies of the surface tension and tube diameter demonstrate that complete condensation occurs for a range of conditions for annular film condensation in small diameter tubes.

Figure 5(a) shows variation of the liquid film thickness along the condenser with a vapor inlet temperature of 363 K and a constant wall temperature of 340 K for two cases of heat-load-in, $Q_{in} = 10$ W and $Q_{in} = 12$ W. The total mass flow rate of $\dot{m}_t = 1.00 \times 10^{-6}$ (kg/s) is the same for both cases. The film thickness decreases in the downstream direction before converging due to the capillary forces acting at the liquid-vapor interface. Condensation is more intensive in the region where the film thickness is at the minimum. The values of δ_{in} will be different for each case of heat-load-in even though the total mass flow rate and thermal boundary conditions are the same. At the inlet, the mass flow rates of liquid and vapor adjust themselves to satisfy the energy balance. The vapor pressure drop across the condensation length is insignificant.

nificant compared to the liquid pressure drop as shown in Figs. 5(b, c).

Figure 5(d) shows the cumulative sum of the heat removed from the vapor by condensation. For the case of $Q_{in} = 10$ W, representing complete condensation, all the incoming vapor is condensed and a location is calculated for the beginning of single phase (liquid) flow in the tube. Thus all the heat transfer and associated pressure drop occurs upstream of this location. Although the incomplete condensation case represents a valid numerical solution of the equations modeling axisymmetric film condensation, it must be considered with reference to an overall energy balance to provide a meaningful physical interpretation. For the case of incomplete condensation, $Q_{in} = 12$ W, not all of the heat-load-in to the tube is rejected at the termination of the calculation. At the termination of the calculation the final value of Q at $z = L_{\delta}$ is seen to be less than Q_{in} . Thus the overall energy balance is not satisfied.

During complete condensation the values of the dependent variables (δ_{in} , p_l , p_v , Q) are the steady field solution of the two-phase flow and independent of time as calculated and as interpreted physically. The simple physical interpretation is that the calculated liquid film profile is in fact stationary and goes to the radius of the tube at L_{δ} . Obviously the vapor mass flow rate becomes zero at this point also. However, during incomplete condensation, the numerical solution is interpreted as representing a time-averaged steady-state two-phase flow field where the vapor mass flow rate does not terminate at the calculated condensation length. For values of Q_{in} greater than but close to the maximum heat-load-in, the incomplete condensation solution predicts that two-phase flow will exist downstream of the point calculated for L_{δ} . By implication, the flow field will no longer be steady in an instantaneous sense.

In Fig. 6 results are presented for a significantly lower vapor inlet and wall temperatures, although the total mass flow rate is the same and the vapor-wall temperature difference remains 23 K. The trends for film thickness, pressure in the vapor, pressure in the liquid, and cumulative heat removed shown in Figs. 6(a, b, c, d) are similar to the previous results; however, the value of heat-load-in for complete condensation, Q_{in} , is lower.

The influence of the wall temperature on the computed value of condensation length, L_{δ} , and the parameter heat-load-in, Q_{in} , for two mass flow rates of 1.00×10^{-6} and 3.00×10^{-6} (kg/s) is shown in Fig. 7. All results are for a fixed value of the vapor temperature at the inlet of $T_{v,in} = 323$ K. Obviously, for very small vapor-wall temperature differences the condensation length increases and the heat rate rejected becomes very small. Figure 7(c) shows the change in the value of the film thickness at the inlet to the condenser as a function of wall temperature.

Results obtained for the convective cooling boundary condition are shown in Fig. 8. A significant increase in the wall temperature just prior to the point of complete condensation, coincident with the thinning of the liquid film, is seen in Fig. 8(d). A decrease of the outer wall convective heat transfer coefficient, h_o , from 20,000 to 15,000 W/m² K resulted in an increase of the wall temperature along the length of the condenser, an increase in the maximum wall temperature, and a longer condensation length as shown in Fig. 8(a, d).

Summary of the Complete Condensation Phenomenon.

Features of complete condensation in the annular film regime include an instantaneous steady flow field characterized by the segregation of liquid and vapor into distinct regions within the tube, the confluence of the liquid film at the termination of cocurrent two-phase flow, and the beginning of single-phase (liquid) flow. This forms a well-defined location marking the transition to single-phase (liquid) flow. The axial distance from the inlet of the condenser tube at $z = 0$ to the location at which the entire cross section is filled with liquid, is defined as L_{δ} , the condensation length. Downstream of the meniscus-like surface at the confluence of the liquid film, the entire cross section of the tube is occupied

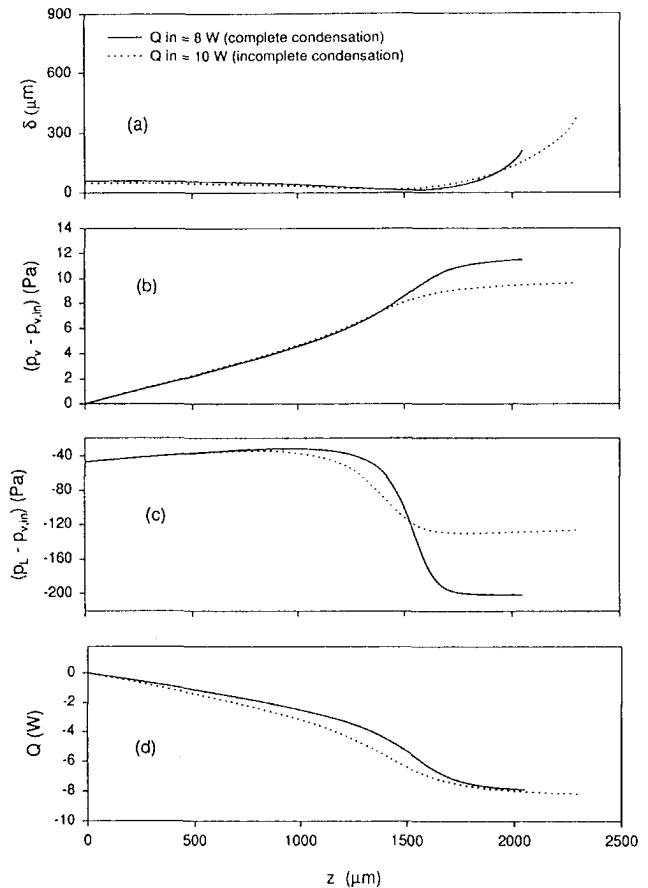


Fig. 6 Annular film condensation in a circular tube with constant wall temperature boundary condition. $R = 1.5$ mm, $T_w = 300$ K, $T_v = 323$ K, $\dot{m} = 0.01$ g/s. (a) Film thickness versus position, (b) vapor pressure versus position, (c) liquid pressure versus position, (d) cumulative heat rejected versus position.

by liquid. Any additional heat removal downstream of this location results only in subcooling of the liquid.

For a given total mass flow rate and tube wall temperature (or convective heat transfer coefficient, h_o , and ambient temperature, T_{∞}) the condensation length changes with heat-load-in, Q_{in} . As the heat load is increased, the limit for complete condensation is reached. Beyond this limit the steady state flow pattern characteristic of the complete condensation phenomenon breaks down and condensation is said to be incomplete. The flow pattern changes to one that is no longer strictly steady. It is presumed for incomplete condensation that a more general two-phase bubbly-type flow exists.

Parametric Study of Surface Tension. The effect of surface tension on annular film condensation in a $R = 1.5$ -mm tube is demonstrated with results from a constant wall temperature example. A reference case is used as a basis of comparison. This reference case is the complete condensation condition with a constant wall temperature of 300 K, as previously presented. The conditions for the reference case are $T_w = 300$ K, $T_{v,in} = 323$ K, $\dot{m}_i = 1.00 \times 10^{-6}$ (kg/s), $Q_{in} = 8$ W and $\sigma = \sigma_{norm}$. This last condition states that the surface tension of water is the normal value as specified in the material property reference (Faghri, 1995). Results are given for two cases in which the surface tension property value has been changed but the same total mass flow rate, wall temperature, and vapor inlet temperature as the reference case are used. These are shown as 2σ , for an increase by a factor of two in the value of surface tension, and $\frac{1}{2}\sigma$, for a decrease by one half in the value of surface tension.

Figure 9 presents the results for δ , the film thickness, $p_v - p_{v,in}$,

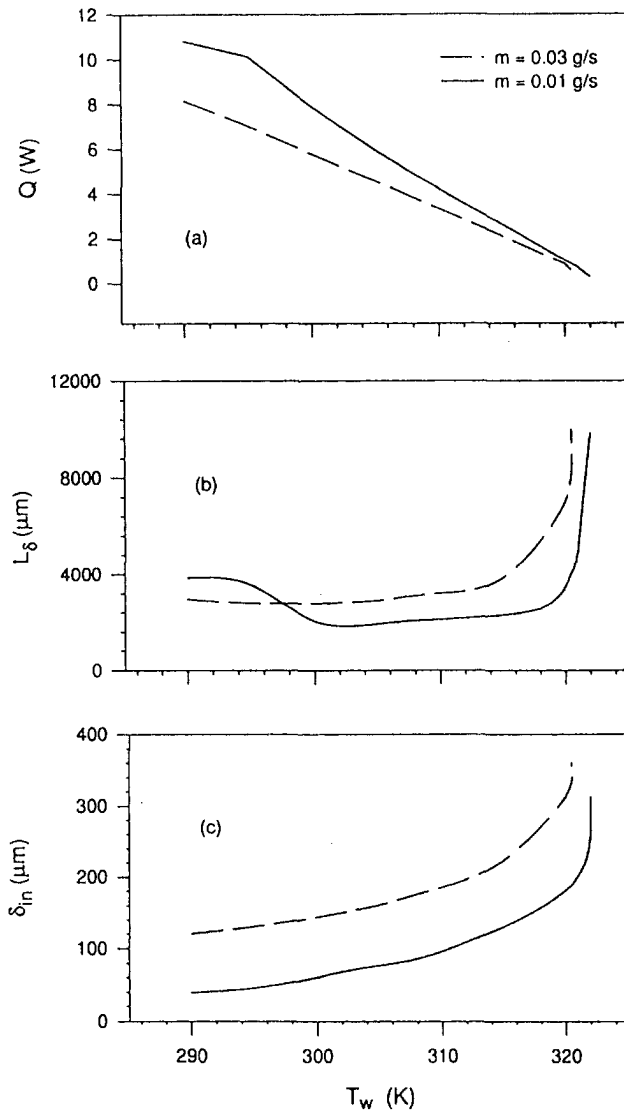


Fig. 7 Parameters of annular film condensation as a function of wall temperature for in a circular tube for the constant temperature boundary condition. $R = 1.5$ mm, $T_v = 323$ K. (a) Cumulative heat load rejected versus wall temperature, (b) condensation length versus wall temperature, (c) inlet film thickness versus wall temperature.

the pressure in the vapor, $p_l - p_{v,in}$, the liquid pressure, and Q , the cumulative heat removed. Previously, it was seen that for the reference conditions ($\sigma = \sigma_{norm}$) complete condensation is achieved. For the case of $\frac{1}{2}\sigma$, seen in Fig. 9(d), only 6.2 W are rejected from the condenser and incomplete condensation results. At this location approximately 1,500 μm downstream from the entrance, the calculation terminates. Note the terminal length of the calculation for this case of reduced surface tension is significantly less than that for the complete condensation case with a normal value of surface tension. The pressure change in the vapor, shown in Fig. 9(b), is greater when considered up to the terminal point, than the case with normal surface tension. Figure 9(c) shows a greater pressure drop in the liquid up to the terminal length.

For a doubling of the value of surface tension, complete condensation occurs at less than the maximum condition. This fact is only uncovered by further calculations and is not revealed directly by any of the results presented here. For the case of 2σ , complete condensation occurs at a heat-load-in greater than 9 W.

Results of computations for three different values of surface tension, the normal value, twice the normal value, and one half the normal value demonstrate that for an increasing value of surface

tension, the maximum heat rate removed at complete condensation increases, with all other inputs fixed.

Parametric Study of Radius. Results are presented for miniature tubes of three different diameters of $R = 1.5$, 1.0, and 0.5 mm. The same constant wall temperature reference case is used were $R = 1.5$ -mm tube, $T_w = 300$ K, $T_{v,in} = 323$ K, $\dot{m}_i = 1.00 \times 10^{-6}$ (kg/s), and $Q_{in} = 8$ W. This case represents complete condensation at the specified total mass flow rate. A comparison is made based on the condition that the mass flux, \dot{m}'' ($\text{kg}/\text{m}^2 \text{ s}$), is constant. The reference case is used to determine the constant value for mass flux of $\dot{m}'' = 1.41$ $\text{kg}/\text{m}^2 \text{ s}$. Figure 10 presents the results for δ , the film thickness, $p_v - p_{v,in}$, the pressure in the vapor, $p_l - p_{v,in}$, the liquid pressure, and Q , the cumulative heat removed. The axial film profile is qualitatively different in the smaller diameter tubes. As the capillary force becomes larger due to both principal radii of curvature becoming smaller, it plays a larger role in the liquid film dynamics. In Fig. 10(a) the liquid film profile for $R = 1.0$ mm, $Q_{in} = 6.2$ W, the film thickness increases along the length of the tube before decreasing to a minimum value of 12.7 μm . This is a case of complete condensation at a value of Q_{in} well below the maximum value. The pressure drop in the vapor for the $R = 1.0$ -mm tube in Fig. 10(b) is seen, after an initial

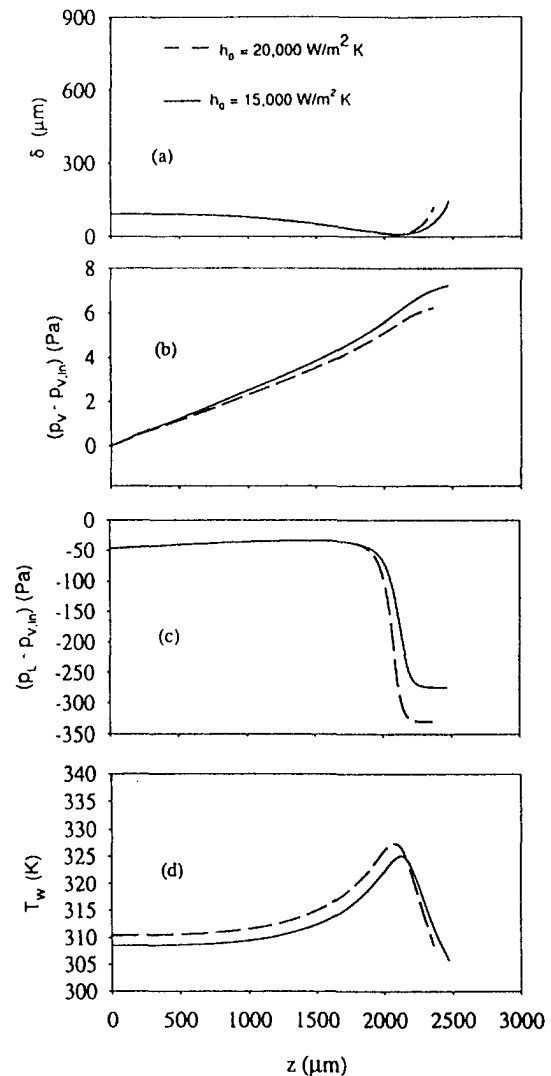


Fig. 8 Annular film condensation in a circular tube with convective cooling boundary condition. $R = 1.5$ mm, $T_v = 333$ K, $\dot{m} = 0.01$ g/s, $Q_{in} = 5.83$ W. (a) Film thickness versus position, (b) vapor pressure versus position, (c) liquid pressure versus position, (d) wall temperature versus position.

change to be nearly zero over a significant portion of the passage length. At the smallest radius, $R = 0.5$ mm, there is significant pressure recovery in the vapor.

Both smaller radii, $R = 1.0$ and 0.5 mm, represent complete condensation at values of Q_{in} well below the maximum value possible for the given parameters of total mass flow rate, wall temperature, and vapor inlet temperature. It is interesting to note that a simple calculation based on Q , the cumulative heat load removed, in Fig. 10(d) demonstrates a considerable increase in the average wall heat flux removed (W/m^2) for condensation in smaller diameter tubes.

Conclusions

Based on the numerical results and visual observations, the following conclusions have been made.

1 Length of film condensation in miniature tubes is very restricted due to surface tension effects that result in liquid blocking a short distance from the condenser inlet. Therefore, condensation in miniature tubes differs from that in larger diameter tubes.

2 The complete condensation length is a nonlinear function of the vapor-wall temperature difference, increasing with the temperature difference approaching zero.

3 Pressure drop in the vapor phase was usually insignificant compared to the pressure drop in liquid. Consequently, the vapor temperature variation along the condenser was infinitesimal.

4 The film thickness decreases significantly just prior to the location of complete condensation.

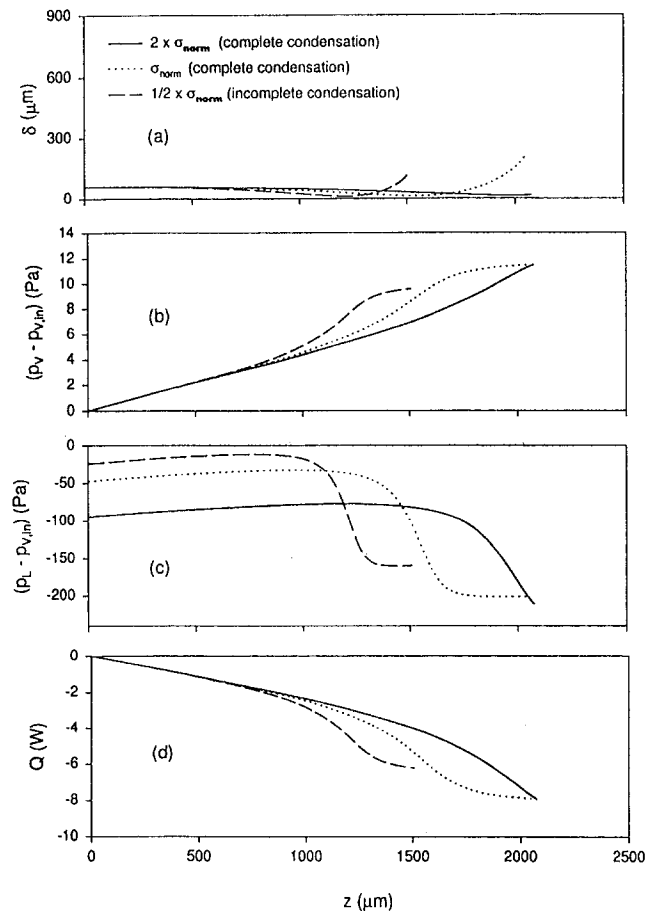


Fig. 9 Parametric study of surface tension for annular film condensation in a circular tube with a constant temperature boundary condition. $R = 1.5$ mm, $T_w = 300$ K, $T_v = 323$ K, $\dot{m} = 0.01$ g/s. (a) Film thickness versus position, (b) vapor pressure versus position, (c) liquid pressure versus position, (d) heat load rejected versus position.

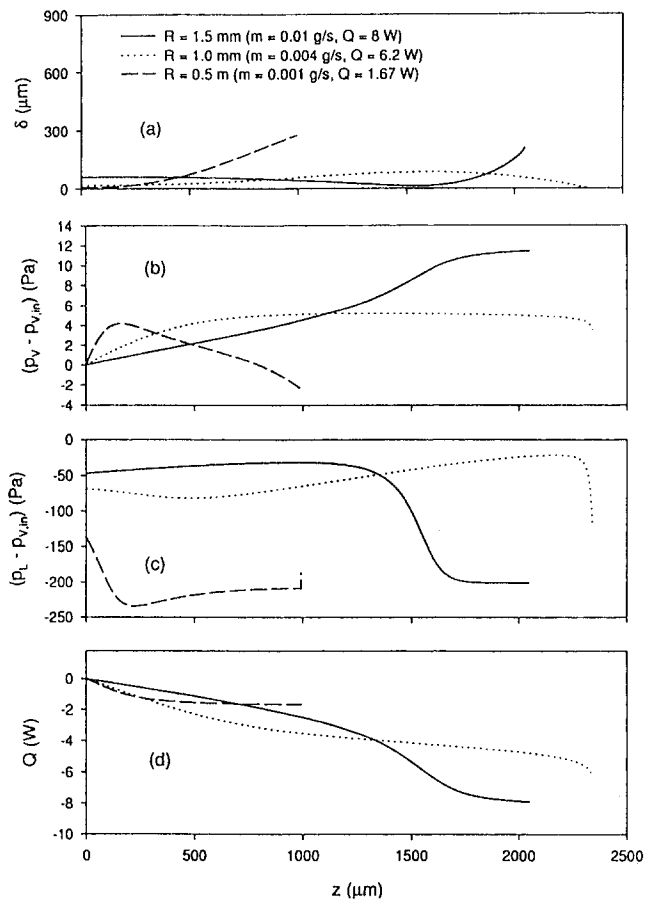


Fig. 10 Parametric study of radius for annular film condensation in a circular tube with a constant temperature boundary condition. Mass flux at the inlet is constant ($\dot{m}'' = 1.41$ kg/m² s) based on the reference case of $R = 1.5$ mm, $T_w = 300$ K, $T_v = 323$ K, $\dot{m} = 0.01$ g/s. (a) Film thickness versus position, (b) vapor pressure versus position, (c) liquid pressure versus position, (d) heat load rejected versus position.

5 Variation of the wall temperature can be significant for convective cooling boundary conditions.

6 Complete condensation in small diameter tubes is a truly steady phenomenon.

7 A very distinct transition is anticipated between the steady phenomenon of complete condensation and the next two-phase flow regime, which is referred to here as incomplete condensation.

References

- Baker, O., 1954, "Simultaneous Flow of Oil and Gas," *Oil and Gas Journal*, Vol. 53, pp. 185-195.
- Bankston, C. A., and Smith, H. J., 1973, "Vapor Flow in Cylindrical Heat Pipes," *ASME JOURNAL OF HEAT TRANSFER*, Vol. 95, pp. 371-376.
- Bell, E., Taborek, J., and Fenoglio, F., 1970, "Interpretation of Horizontal In-Tube Condensation Heat Transfer Correlations Using a Two-Phase Flow Regime Map," *CEP Symposium Series*, Vol. 66, No. 102, pp. 150-163.
- Bowman, W. J., and Hitchcock, J. E., 1988, "Transient, Compressible Heat Pipe Vapor Dynamics," *Proc. ASME National Heat Transfer Conference*, Vol. 1, Houston, TX, ASME, New York, pp. 329-338.
- Breber, G., Palen, J. W., and Taborek, J., 1980, "Prediction of Horizontal Tubeside Condensation of Pure Components Using Flow Regime Criteria," *ASME JOURNAL OF HEAT TRANSFER*, Vol. 102, pp. 471-476.
- Cao, Y., and Faghri, A., 1984, "Micro/Miniature Heat Pipes and Operating Limitations," *Enhanced Heat Transfer*, Vol. 1, No. 3, pp. 265-274.
- Chen, H., Groll, M., and Rosler, S., 1992, "Micro Heat Pipes: Experimental Investigation and Theoretical Modelling," *Proc. 8th Int. Heat Pipe Conf.*, Beijing, China.
- Collier, J. G., and Thome, J. R., 1994, *Convective Boiling and Condensation*, 3rd Ed., Oxford University Press, New York.
- Faghri, A., 1995, *Heat Pipe Science and Technology*, Taylor and Francis, Washington, DC.
- Faghri, A., and Chow, L. C., 1988, "Forced Condensation in a Tube With Suction

at the Wall for Microgravitational Applications," *ASME JOURNAL OF HEAT TRANSFER*, Vol. 110, pp. 982-985.

Jang, J. H., Faghri, A., and Chang, W. S., 1991, "Analysis of the Transient Compressible Vapor Flow in Heat Pipes," *Int. J. Heat Mass Transfer*, Vol. 34, pp. 2029-2037.

Lee, Y. S., Lee, Y. P., and Lee, Y., 1992, "An Experiment Study on Micro Two-Phase Closed Thermosyphons With Inserts," *Proc. 8th Int. Heat Pipe Conf.*, Beijing, China.

Li, T., Cao, L., and Xiang, L., 1992, "Research and Application for the Heat Transfer Performance of Small Heat Pipes," *Proc. 8th Int. Heat Pipe Conf.*, Beijing, China.

Munoz-Cobo, J. L., Herranz, L., Sancho, J., Tkachenko, I., and Verdu, G., 1996, "Turbulent Vapor Condensation With Noncondensable Gases in Vertical Tubes," *Int. J. Heat Mass Transfer*, Vol. 39, No. 15, pp. 3249-3260.

Sardesai, R. G., Owen, R. G., and Pulling, D. J., 1981, "Flow Regimes for Condensation of a Vapour Inside a Horizontal Tube," *Chem. Engr. Science*, Vol. 36, pp. 1173-1180.

Seban, R. A., and Faghri, A., 1984, "Film Condensation in a Vertical Tube With a Closed Top," *Int. J. Heat Mass Transfer*, Vol. 27, No. 6, pp. 944-948.

Seban, R. A., and Hodgson, J., 1982, "Laminar Film Condensation in a Tube With Upward Vapor Flow," *Int. J. Heat Mass Transfer*, Vol. 25, No. 9, pp. 1291-1299.

Soliman, H. M., and Azer, N. Z., 1971, "Flow Patterns During Condensation Inside a Horizontal Tube," *ASHRAE Transactions*, Vol. 77, Part 1, pp. 210-244.

Taitel, Y., and Dukler, A. E., 1976, "A Model for Predicting Flow Regime Transitions in Horizontal and Near Horizontal Gas-Liquid Flow," *AIChE Journal*, Vol. 22, No. 1, pp. 47-55.

Traviss, D. P., and Rohsenow, W. M., 1973, "Flow Regimes in Horizontal Two-Phase Flow With Condensation," *ASHRAE Transactions*, Vol. 79, Part 2, pp. 31-39.

Wallis, G. B., 1969, *One-Dimensional Two-Phase Flow*, McGraw-Hill, New York.

Analysis of Coupled Nuclear/Thermal Instabilities of Two-Phase Flows in Parallel Boiling Channels

M. Uehiro¹

Y. F. Rao²
Mem. ASME

K. Fukuda³

Department of Nuclear Engineering,
Faculty of Engineering,
Kyushu University,
Fukuoka 812, Japan

An analytical model is proposed to study the two-phase flow instabilities of in-phase and out-of-phase modes in parallel boiling channels. This model takes into consideration the interaction between channels with different void fraction variations by modeling the diffusion of neutrons. Linear stability analysis in the frequency domain is performed to obtain stability boundaries and flow oscillation modes. In the case of parallel two channels, two types of stability boundaries are found to exist on the stability map; one for the instability of the in-phase mode and the other for that of the out-of-phase mode respectively. For a certain range of the void-reactivity coefficient, the void-reactivity feedback loop is found to be unstable in a certain region on the stability map, which has an effect on the stability of the in-phase mode. The interaction between channels affects the instability of the out-of-phase mode. The results are also obtained for the case of three and four channels. It is found that the channels having stronger interaction between them are more likely to oscillate in-phase with each other, while those having weaker interaction are more likely to oscillate out-of-phase with each other.

Introduction

The flow instability in boiling water reactors is one of the most important problems for reactor control, design, and safety. The instability was observed in boiling water type test reactors, as well as in early power reactors that were cooled by natural circulation. This subject is receiving renewed interest because of the two representative instability events encountered in the commercial BWRs. One was the well-published event that occurred in LaSalle 2, USA (U.S. NRC, 1988), in which severe oscillations of the neutron flux and the core flow rate eventually caused the reactor scrambling. This event was a core-wide instability, in which the neutron flux, the flow rate, and the void fraction oscillated almost in-phase at every point in the core. The other was the oscillation observed in Caorso, Italy during its dynamic tests (Gialdi et al., 1985). This was an out-of-phase oscillation with a 180-degree phase difference between one half of the core and the other half. This instability was later referred as the regional instability. The regional instability has characteristics similar to those of the parallel channel instability, although it involves the spatial dependence of neutron dynamics. It was considered that the fundamental mechanisms of core-wide and regional instabilities are almost the same; the thermal-hydraulic instability known as the density wave instability coupled with the neutron dynamics by the void-reactivity feedback loop.

For the analysis of the BWR instabilities, a few time-domain computer codes with the space-dependent neutron dynamics model have been developed in recent years. Several numerical simulations of the core-wide in-phase and the regional out-of-phase instabilities have been performed with these codes, and have

produced excellent results (Enomoto et al., 1986; Takigawa et al., 1987; Muto et al., 1990; Valtonen, 1990; Takeuchi and Takigawa, 1994). Araya et al. (1992) tried to estimate the stability boundary by the time-domain transient analysis code RETRAN, and obtained good results about the instability of the in-phase mode. The time-domain numerical simulation is advantageous in analyzing phenomena including nonlinearities, such as the transient events and limit-cycle oscillations. It is, however, less efficient in determining the stability boundaries because of possible dependence of the results on a specific time-integration scheme, and because of long CPU time. Therefore, the frequency-domain linear analysis, which requires very short CPU time, has been performed to obtain many suggestive results (Boure et al., 1973; Lahey, 1986; Blakeman and March-Leuba, 1989). These analysis codes, so far presented, usually adopted the point reactor dynamics model. Therefore, the object of such codes was limited to analyze only the instability of the in-phase mode. March-Leuba and Blakeman (1991) studied the instability of the subcritical neutronic mode, and obtained the stability boundaries for the out-of-phase mode on the power-flow map using the frequency-domain code LAPUR.

In this paper, a frequency-domain analytical model is proposed to study the instabilities of the in-phase and the out-of-phase modes in parallel boiling channels. The nuclear and thermal-hydraulic dynamics are coupled with the void-reactivity feedback. Also, the point reactor dynamics model is modified to take into account the effect of mutual interaction between channels having different void fraction variations. The stability boundaries and the oscillation modes are obtained, and the mechanisms of the two-phase flow instability are discussed.

Analytical Model

Figure 1 shows the analytical model, which consists of parallel boiling channels. Each channel with a uniformly heated section is assumed to correspond to one of the divided regions or subcores of a BWR core. Due to the void-reactivity feedback, heating rate changes as the void fraction changes. In this model, the point kinetics equation is applied to each channel with the assumption that each subcore behaves like an independent core. However, each subcore in the actual BWRs interacts with the others. If the

¹ Presently at the Thermal Power Design Department, Babcock-Hitachi at Kure, Hiroshima, Japan.

² Presently at the R&D Center, Mitsubishi Heavy Industries, Takasago, Hyogo, Japan.

³ To whom correspondence should be addressed.

Contributed by the Heat Transfer Division for publication in the JOURNAL OF HEAT TRANSFER and presented at ICONE-4, New Orleans, Mar. 1996. Manuscript received by the Heat Transfer Division, July 25, 1996; revision received, June 2, 1999. Keywords: Computer Codes, Flow Instability, Multiphase Flows. Associate Technical Editor: D. Zumbrennen.

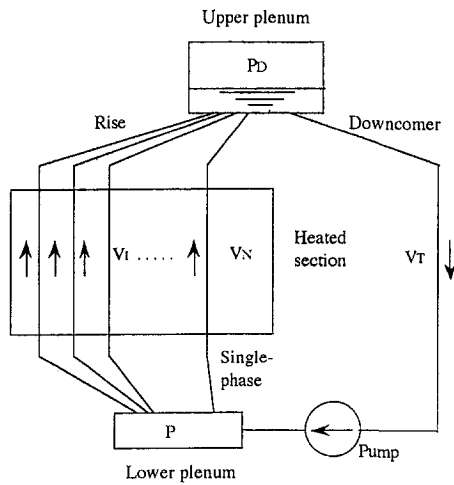


Fig. 1 Analytical model

void fraction varies in a certain subcore, other subcores will be affected due to the neutron diffusion. An analytical model, which is schematically shown in Fig. 2, is thus proposed. The neutron flux variation in subcore 1 is mostly produced by the void-reactivity variation due to the void fraction variation in subcore 1. However, it is assumed that a part of it is caused by neutron diffusion from subcores 2 and 3. Similarly, the void-reactivity variation in subcore 1 leads to the power disturbances in subcores 2 and 3 due to the neutron diffusion. To take into account the interaction between subcores, a coefficient H_{IJ} is introduced, whose physical meaning will be elaborated later. With the coefficient, the power disturbance in subcore 1 is assumed to be given as the summation of contributions from every subcore, i.e., the power

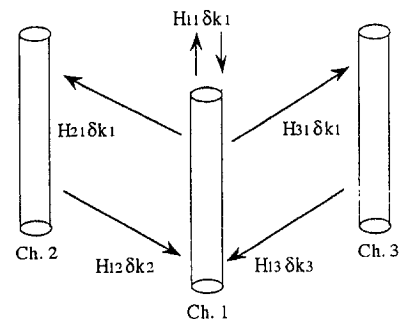


Fig. 2 Analytical model for the channel-to-channel interaction due to the void-reactivity feedback

disturbances in subcore J multiplied by the coefficient H_{IJ} . In the case of a three-channel system as shown in Fig. 2, where the abbreviation Ch stands for "Channel," the power disturbance of subcore 1 is given by

$$\frac{\delta \hat{Q}_1'''}{Q_1'''} = \frac{\delta \hat{n}_1}{n_1} = H_{11} G_{R,1} \delta \hat{k}_1 + H_{12} G_{R,2} \delta \hat{k}_2 + H_{13} G_{R,3} \delta \hat{k}_3 \quad (1)$$

where $G_{R,J}$ is the transfer function of subcore J derived from its neutron dynamics equations, and δk_J is the reactivity perturbation of subcore J . The power disturbance of each subcore is thus governed by the interaction between subcores.

In the thermodynamic analysis, the following assumptions are adopted.

- 1 The two-phase flow is one-dimensional, incompressible, and homogeneous flow.
- 2 The properties of the fluid are constant.
- 3 The heat flux of the heated section is axially uniform.

Nomenclature

A = cross-sectional area (m^2)
 A_f = cross-sectional area of the fuel rod (m^2)
 A_0 = cross-sectional area of the channel (m^2)
 C_i = number density of delayed neutron precursor for group i
 C_α = void-reactivity coefficient, defined in (22)
 F = loop transfer function
 Fr = Froude number
 g = gravitational acceleration (ms^{-2})
 G = loop transfer function
 H_{IJ} = coefficient of the interaction between channels, defined in Eq. (23)
 h = specific enthalpy ($\text{Jkg}^{-1}\text{s}^{-1}$)
 h_f = specific enthalpy of the coolant at saturated state ($\text{Jkg}^{-1}\text{s}^{-1}$)
 h_{fg} = latent heat ($\text{Jkg}^{-1}\text{s}^{-1}$)
 Ja = Jacob or subcooling number
 j = imaginary number, $=(-1)^{1/2}$
 k = effective multiplication factor
 K = pressure loss coefficient
 l = prompt neutron life time
 L = length of a section (m)
 L_n = neutron number migration length
 n = neutron density
 N = number of subcores

Np = phase-change number
 P_h = perimeter of the heated section (m)
 ΔP = pressure drop (Pa)
 q'' = heat flux from the fuel wall to the coolant ($\text{Jm}^{-2}\text{s}^{-1}$)
 q''' = equivalent volumetric heating rate to the coolant ($\text{Jm}^{-3}\text{s}^{-1}$)
 Q''' = nuclear heat generation rate in the fuel rod ($\text{Jm}^{-3}\text{s}^{-1}$)
 R = frictional pressure drop, $K\rho V^2$ (Pam^{-1})
 r_1 = position of subcore
 R_l = ratio of amplitude
 s = Laplace transformation parameter
 t = time (s)
 T = temperature (K)
 $v_e = V_{e0}/V_{i0}$, defined in Eq. (16)
 V = flow velocity (ms^{-1})
 W = mass flow rate (Kgs-l)
 ΔX_{sub} = degree of subcooling at the channel inlet, $(h_f - h_i)/h_{fg}$
 z = axial position (m)

Greek Letter

α = void fraction
 α_f = heat transfer coefficient ($\text{Jm}^{-2}\text{s}^{-1}\text{K}^{-1}$)

β_i = delayed neutron fraction of group i
 $\Gamma = (\rho_l - \rho_g)/h_{fg}\rho_g\rho_l$
 δ = perturbed variable
 ϵ_{IJ} = defined in Eq. (24)
 θ_{IJ} = phase difference
 λ_i = decay constant of delayed neutron precursor of group i
 ρ = density (kgm^{-3})
 τ_M = time constant of the fuel (s)

Subscripts and Superscripts

AV = average along the heated section
 B = boiling boundary
 e = outlet of the heated section
 f = fuel
 g = saturated gas phase
 H = heated section
 i = inlet of the heated section
 I = channel number
 IJ = between J th and I th subcore
 J = subcore number
 l = saturated liquid phase
 R = riser section
 SP = single-phase section
 T = downcomer section
 TP = two-phase section
 $\hat{\quad}$ = Laplace transformed variable, which is a function of the parameter s

4 The subcooled boiling is neglected.

In actual BWRs, pressure and power spatial distributions, various flow patterns of two-phase flow and three-dimensional neutron diffusion effects exist. Therefore, the simplification due to the above assumptions may lead to quantitative errors. They are, however, sufficient to give qualitatively correct results, since the purpose of the present study is to develop a new model to study the basic mechanism of the instabilities, not to develop a general-purpose computer code for real BWRs.

Mathematical Formulation

Basic Equations for the Two-Phase and Single-Phase Flows in Subcores. The conservation equations of mass, energy, and momentum for the one-dimensional homogeneous two-phase flow are given as

$$\frac{\partial \rho}{\partial t} + V \frac{\partial \rho}{\partial z} + \rho \frac{\partial V}{\partial z} = 0 \quad (2)$$

$$\frac{\partial}{\partial t} \{ \rho_g h_g \alpha + \rho_l h_l (1 - \alpha) \} + \frac{\partial}{\partial z} \{ \rho_g h_g \alpha + \rho_l h_l (1 - \alpha) \} V = q''' \quad (3)$$

$$\rho \left(\frac{\partial V}{\partial t} + V \frac{\partial V}{\partial z} \right) + \rho g + \frac{\partial P}{\partial z} + R = 0 \quad (4)$$

where α denotes the void fraction, q''' is the heating rate per unit volume. The linear stability analysis procedure is used to transform the governing equations in the time domain into those of small perturbations in the frequency domain; details of the procedure are referred to in Fukuda and Kobori (1978), Lahey and Moody (1993) and any standard textbook on elementary control theory. Perturbing, Laplace transforming, and integrating over the channel length Eqs. (2)–(4), the transfer functions G_{TP0} and G_{SP} for the two-phase and the single-phase section, respectively, in a subcore (or a channel) between lower and upper plena can be obtained (Rao et al., 1995).

$$\frac{\delta \Delta \hat{P}_{TP}}{\rho_l V_{i0}^2} + G_{TP0} \left(\frac{\delta \hat{V}_i}{V_{i0}} - \frac{\delta \hat{q}'''}{q''_0} \right) + F_q \frac{\delta \hat{q}'''}{q''_0} = 0 \quad (5)$$

$$\frac{\delta \Delta \hat{P}_{SP}}{\rho_l V_{i0}^2} + G_{SP} \frac{\delta \hat{V}_i}{V_{i0}} = 0 \quad (6)$$

where

$$G_{TP0} = G_{TP0}^{(1)} + G_{TP0}^{(2)} \quad (7)$$

$$G_{TP0}^{(1)} = \frac{G_2}{NpFr} + (s' + 1) \ln v_e G_V + G_1 + \frac{K_H}{2Np} \{ 2(v_e - 1)G_V + G_0 \} \quad (8)$$

$$G_{TP0}^{(2)} = \left\{ \frac{NpL'_R}{v_e} s' + K_R + K_{out} \right\} G_V + \left[\left\{ \frac{1}{NpFr v_e} + \frac{K_R v_e}{2NpL'_R} \right\} \frac{1 - e^{-\tau_R s}}{s'} + \frac{K_{out}}{2} \right] G_{\rho,e} \quad (9)$$

$$G_V = 1 - \frac{1 - \exp(-Jas')}{s'} \quad (10)$$

$$G_n = \frac{G_V}{s' - 1} \left\{ \frac{v_e^{1-n} - 1}{1 - n} - \frac{s'}{2 - s' - n} (v_e^{2-s'-n} - 1) \right\} + \frac{v_e^{2-s'-n} - 1}{2 - s' - n} \quad (n = 0, 1, 2) \quad (11)$$

$$G_{\rho,e} = (1 - G_V) v_e^{1-s'} + \frac{1 - v_e^{1-s'}}{s' - 1} G_V \quad (12)$$

$$F_q = (s' + 2)(v_e - 1) + \frac{K_H}{2Np} (v_e^2 - 1) + \left\{ \frac{NpL'_R}{v_e} s' + K_R + K_{out} \right\} v_e \quad (13)$$

$$G_{SP} = (NpL'_{SP} + Ja)s' + K_{SP} \left(1 + \frac{Ja}{NpL'_{SP}} \right) + K_{in} \quad (14)$$

$$\Delta P_{TP} = P_D - P_B; \quad \Delta P_{SP} = P_B - P \quad (15)$$

$$L'_R = \frac{L_R}{L_H}; \quad L'_{SP} = \frac{L_{SP}}{L_H}; \quad v_e = \frac{V_{e0}}{V_{i0}} \quad (16)$$

The Jacob number Ja , phase-change number Np , and Froude number Fr are defined as follows (Ishii and Zuber, 1971):

$$Ja = \Delta X_{sub} \left(\frac{\rho_l}{\rho_g} - 1 \right); \quad Np = \frac{\Gamma q''' L_H}{V_{i0}}; \quad Fr = \frac{V_{i0}^2}{gL_H} \quad (17)$$

where L_{SP} , L_H , and L_R are the lengths of single-phase section, heated section, and riser section, respectively. K_{in} , K_{SP} , K_H , K_R , and K_{out} are the pressure-loss coefficients for the inlet of the subcore, the single-phase section, the heated section, the riser section, and the outlet of the subcore. Γ and ΔX_{sub} are defined in the Nomenclature. The subscript 0 denotes values at steady-state. F_q is the added term introduced through consideration of the coupled nuclear-thermal effect. Thus, this term does not appear in the case of constant heating rate (or without the void-reactivity feedback).

Neutron and Fuel Dynamics. To obtain the transfer functions for perturbed values of inlet velocity $\delta V_i/V_{i0}$ and pressure drop $\delta \Delta P/\rho_l V_{i0}^2$ in Eqs. (5) and (6), we need a relationship between the perturbation of the heating rate $\delta q'''/q''_0$ and that of the inlet velocity $\delta V_i/V_{i0}$, which is obtained as follows:

The point-reactor dynamics equations are given by

$$\frac{dn}{dt} = \frac{k(1 - \beta) - 1}{l} n + \sum_{i=1}^6 \lambda_i C_i \quad (18)$$

$$\frac{dC_i}{dt} = \frac{k\beta_i}{l} n + \lambda_i C_i \quad (i = 1, \dots, 6) \quad (19)$$

where n is the neutron density, k is the effective multiplication factor, l is the prompt neutron life time, β is the delayed neutron fraction, λ_i is the decay constant of delayed neutron precursor of group i , and C_i is the delayed neutron precursor density of group i . Perturbing and Laplace transforming Eq. (18) and (19) yields the perturbation of the nuclear heat generation rate as

$$\frac{\delta \hat{Q}'''}{Q''_0} = \frac{\delta \hat{n}}{n_0} = G_R \delta \hat{k} \quad (20)$$

where

$$G_R = \left\{ s \left(l + \sum_{i=1}^6 \frac{\beta_i}{s + \lambda_i} \right) \right\}^{-1} \quad (21)$$

The void-reactivity coefficient C_α is defined by

$$\delta \hat{k} = C_\alpha \delta \alpha_{AV} \quad (22)$$

where α_{AV} is the average void fraction in a heated section.

The coefficient $H_{J,I}$, which reflects the degree of interaction from subcore J to I , is assumed to be

$$H_{IJ} = \frac{\exp(-\epsilon_{IJ})}{\sum_{J=1}^N \exp(-\epsilon_{IJ})} \quad (23)$$

$$\epsilon_{IJ} = \frac{|r_I - r_J|}{L_n} \quad (24)$$

where $r_I - r_J$ is the distance between subcore I and J , and L_n is the neutron diffusion length.

The coefficient H_{IJ} given in the above equations is a simple model; it indicates the fraction of the power variation of the subcore I due to the void-reactivity variation in the subcore J . It is based on the assumption that the neutron diffusion between subcores is mainly responsible for the subcore-to-subcore interaction due to the void-reactivity feedback. Therefore, the coefficient is assumed to have an exponential form, with the ratio of the subcore-to-subcore distance ($r_I - r_J$) to the neutron diffusion length (L_n) as the parameter; this can most reflect the diffusion-like feature. Furthermore, the coefficient takes a normalized form, i.e., $\sum H_{IJ} = 1$. This guarantees that the multichannel model will produce the same results as the single-channel model for the instability of the in-phase mode. As will be reported in another paper by the authors, further study of the channel-to-channel interaction is under way, which would support the similar relationship of $\sum H_{IJ} = 1$. It should be noted, however, that the model of H_{IJ} is rather rough, and further study is needed for correct quantitative estimation of the channel-to-channel interaction. Nevertheless, the simple model should serve well for the purpose of studying the mechanism of the instabilities. In subsequent studies, the authors have further developed a more rigid but more complex model called the "Multi-Point Reactor Model," in which basic ideas of the present model (called the "Subcore Model") have been inherited, while the effect of neutron migration between subcores is directly taken into consideration in the stage of establishing the neutron dynamics equation for a subcore. (Uehiro et al., 1997; Fukuda et al., 1998) The comparison between results with the present simple model and those with the more advanced "Multi-Point Reactor Model" showed that the conclusions drawn in the present paper remain unchanged.

As described before, the power disturbance for subcore I is therefore given as a summation of contributions from all subcores (including subcore I itself). Combining Eqs. (20), (22), and (23) yields

$$\begin{aligned} \left[\frac{\delta \dot{Q}''}{Q_0''} \right]_I &= \sum_{J=1}^N (H_{IJ} G_{R,J} C_{\alpha,J} \delta \hat{\alpha}_{AV,J}) \\ &= \sum_{J=1}^N (H_{IJ} G_{R,J} C_{\alpha,J} G_{\alpha AV,J}) \left[\frac{\delta \hat{V}_i}{V_{i0}} - \frac{\delta \dot{q}''}{q_0''} \right]_J \end{aligned} \quad (25)$$

where $G_{\alpha AV}$ is the transfer function for the average void fraction in the heated section given by (Rao et al., 1995)

$$\delta \hat{\alpha}_{AV} = G_{\alpha AV} \left(\frac{\delta \hat{V}_i}{V_{i0}} - \frac{\delta \dot{q}''}{q_0''} \right) \quad (26)$$

$$G_{\alpha AV} = -\frac{\rho_l}{N p \rho_{gl}} \left(\frac{v_e^{-s'} - v_e^{-1}}{s' - 1} - \frac{1 - v_e^{-s'}}{s'} \right). \quad (27)$$

The energy conservation equation for a fuel rod is given by

$$\rho_f C_p A_f \frac{dT_f}{dt} = A_f Q'' - P_h q'' \quad (28)$$

$$P_h q'' = A_0 q''' \quad (29)$$

$$q'' = \alpha_f (T_f - T_s) \quad (30)$$

where T_f , ρ_f , and C_p are the temperature, density, and specific heat of the fuel rod, respectively; P_h and A_f are the perimeter and cross-sectional area of the fuel rod, q'' is the heat flux from the surface of fuel to the coolant, q''' is the volumetric heating rate to the coolant, A_0 is the cross-sectional area of the flow channel, T_s is the saturated temperature, and α_f is the heat transfer coefficient on the surface of the fuel. Perturbing, Laplace transforming, and combining Eqs. (28)–(30) yields

$$\left[\frac{\delta \dot{q}''}{q_0''} \right]_I = \left[\frac{1}{1 + \tau_M s} \frac{\delta \dot{Q}''}{Q_0''} \right]_I \quad (31)$$

where τ_M is the fuel time constant defined by

$$\tau_M = \frac{\rho_f C_p A_f}{\alpha_f P_h}. \quad (32)$$

Eliminating $\delta \dot{Q}''/Q_0''$ from Eqs. (25) and (31), we obtain the coupled nuclear-thermal equation.

$$\left[\frac{\delta \dot{q}''}{q_0''} \right]_I = \sum_{J=1}^N \frac{G_{q,IJ}}{\delta_{IJ} + G_{q,IJ}} \left[\frac{\delta \hat{V}_i}{V_{i0}} \right]_J \begin{cases} \delta_{IJ} = 1 & (I = J) \\ \delta_{IJ} = 0 & (I \neq J) \end{cases} \quad (33)$$

where

$$G_{q,IJ} = \frac{H_{IJ} C_{\alpha,J}}{1 + \tau_M s} G_{R,J} G_{\alpha AV,J}. \quad (34)$$

Substituting Eq. (33) into Eq. (5) and combining with Eq. (6), we obtain the transfer function G_{IJ} between total pressure drop in the subcore and inlet velocity.

$$\left[\frac{\delta \Delta \hat{P}}{\rho_l V_{i0}^2} \right]_I = \sum_{J=1}^N G_{IJ} \left[\frac{\delta \hat{V}_i}{V_{i0}} \right]_J \quad (35)$$

where

$$G_{IJ} = [G_{TP0} + G_{SP}]_I \delta_{IJ} + [F_q - G_{TP0}]_I \frac{G_{q,IJ}}{\delta_{IJ} + G_{q,IJ}}. \quad (36)$$

Characteristic Equation and Oscillation Mode. The pressure drop perturbation in the downcomer is derived from the momentum equation, and is given by

$$\delta \hat{P}_D - \delta \hat{P} = G_T \delta \hat{W}_T \quad (37)$$

where

$$G_T = K_T V_{T0} + L_T s \quad (38)$$

$$W_T = \rho_l A_T V_T \quad (39)$$

where G_T is the transfer function, W_T the flow rate, K_T the frictional pressure drop coefficient, V_T the velocity, L_T the length, and A_T the cross-sectional area of the downcomer. The pressure drop perturbation in the subcore is written from Eq. (35).

$$\delta \hat{P} - \delta \hat{P}_D = \sum_{J=1}^N G_{IJ} \delta \hat{W}_J \quad (40)$$

where

$$W_{i0} = \rho_l A_I V_{i0,I}. \quad (41)$$

Total pressure drop perturbation over the whole circulation loop is zero. Therefore, combining Eq. (37) and Eq. (40), and then utilizing the relation of the total flow rate $W_T = \sum W_i$, yields

$$\sum_{J=1}^N F_{IJ} \delta \hat{W}_J = 0 \quad (42)$$

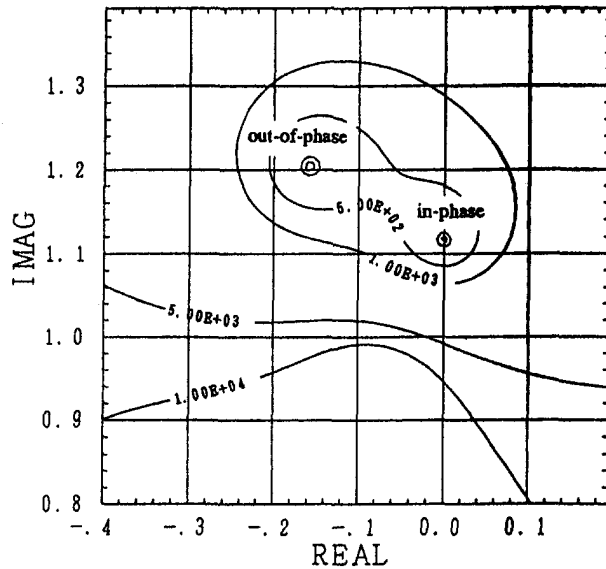


Fig. 3 A contour map showing the existence of two roots of characteristic equation corresponding to the in-phase and the out-of-phase mode, respectively; $Ja = 1.5$, $Np = 4.627$, $Fr = 0.0125$

where

$$F_{IJ} = G_{IJ} + G_T \quad (43)$$

or, if written as a matrix,

$$\begin{bmatrix} F_{11} & F_{12} & F_{1N} \\ F_{21} & F_{22} & \vdots \\ \vdots & O & \vdots \\ F_{N1} & F_{NN} & \vdots \end{bmatrix} \begin{bmatrix} \delta \dot{W}_1 \\ \delta \dot{W}_2 \\ \vdots \\ \delta \dot{W}_N \end{bmatrix} = 0 \quad (44)$$

The characteristic equation of the system is then given by

$$|[F_{IJ}]| = 0 \quad (45)$$

Equation (44) is a set of N simultaneous equations, which can be solved for each root of Eq. (45), to obtain the flow oscillation mode as

$$\delta \dot{W}_1 : \delta \dot{W}_2 : \dots : \delta \dot{W}_N = 1 : R_2 e^{j\theta_2} : \dots : R_N e^{j\theta_N} \quad (46)$$

where R_i is the ratio of the amplitude, and θ_i is the phase difference.

Results and Discussion

Calculation Procedure. In this paper, the Nyquist's method (Hetrick, 1971) is adopted to determine the stability boundary. Substituting $j\omega$ into the Laplace parameter s in the characteristic equation of the system (Eq. (45)), if the Nyquist locus turns right around the origin on the complex $F(s)$ -plane as ω is changed from 0 to ∞ , we recognize that the system is unstable. When the locus passes just on the origin, the system is in a state of marginal stability. The problem arises, however, when for some parameters, the characteristic equation possesses poles in the right half domain on the complex s -plane so that the Nyquist's method is difficult to apply. In that case, we multiply Eq. (45) with the term that possesses the poles to eliminate the poles from the characteristic equation, and then use the new equation to draw a Nyquist locus. The validity of this procedure is proved by drawing the contour map for $f = |F(s)|$ on the complex s -plane to directly obtain roots of the original characteristic equations, and comparing the stability result determined by the roots and that by the Nyquist locus from the modified characteristic equation. In the case of parallel subcores, the system can have as many stability boundaries or corre-

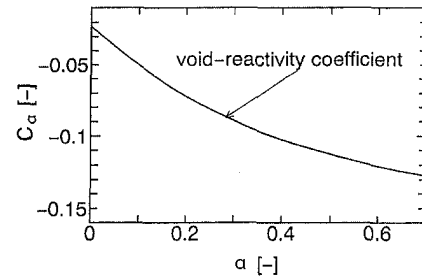


Fig. 4 Void-reactivity coefficient C_α as a function of the average void fraction

sponding fundamental oscillation modes as the number of the subcores. By substituting into Eq. (46) the root of the characteristic equation that is associated with a specific stability boundary, we can find the oscillation mode for that stability boundary. Figure 3 shows an example of the contour map on the complex s -plane, where we can find two roots which correspond to different oscillation modes. This contour map provides supplement for determining the stability boundary with the Nyquist's method.

Case of Two Subcores. The regional instability observed in the commercial BWRs was the out-of-phase mode oscillations with a 180-deg phase difference between one half of a core and the other half; the coolant flow and the neutron distribution in a core behaved as if the core was composed of two subcores. To analyze this phenomenon, the stability analysis is first performed for the case of parallel two subcores. The parameters of the system are taken from the LaSalle 2 data (Commonwealth Edition Co., 1977). The length of adiabatic riser is, however, assumed to be zero for simplicity. The fuel time constant τ_M , which varies with the structure of the core, the operational condition and the degree of the fuel burnup, is set at a value of 6 sec, according to the LaSalle 2 data (Commonwealth Edition Co., 1977) of 5–7 sec. The void-reactivity coefficient is given as a function of the void fraction, as shown in Fig. 4.

Stability Boundary for Each Instability Mode. Figure 5 shows the stability boundaries of the system on the Ja - Np plane (Ishii and Zuber, 1970). The two solid lines display the stability boundaries of the system, one corresponding to the in-phase mode, and the other to the out-of-phase mode. The broken line is the out-of-phase mode stability boundary without including the void-reactivity feedback. In the figure, letter *A* shows a region where only the in-phase mode is unstable; *B*: both modes are unstable; *C*: only the out-of-phase mode is unstable; *D*: both modes are stable. In the case of without the void-reactivity feedback, only the stability boundary of the out-of-phase mode appears, while the in-phase mode is stable everywhere in the map. This agrees with the results in the literature (Fukuda and Kobori, 1978); (Fukuda et al., 1982) that suggest that the in-phase mode oscillation was rarely observed in the system of hydrodynamic parallel boiling channels.

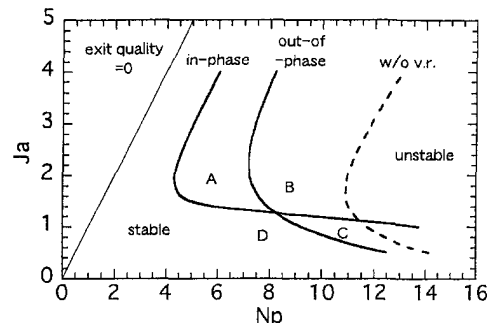
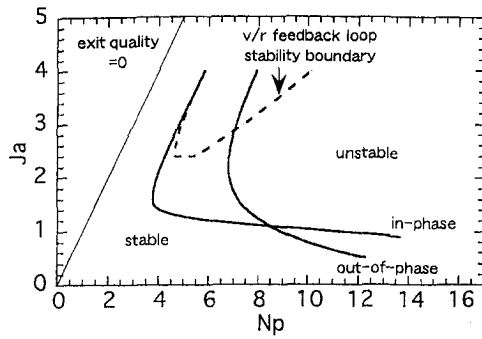
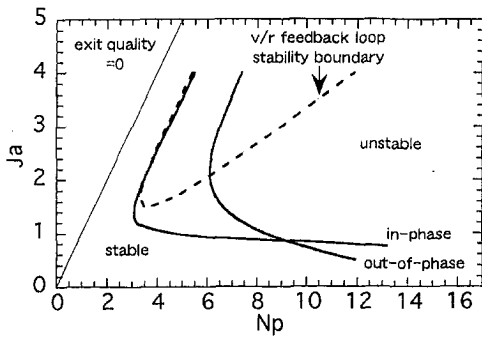


Fig. 5 Stability boundary of the system on the Ja - Np plane, $Fr = 0.0125$



(a) $C_\alpha \times 1.1$



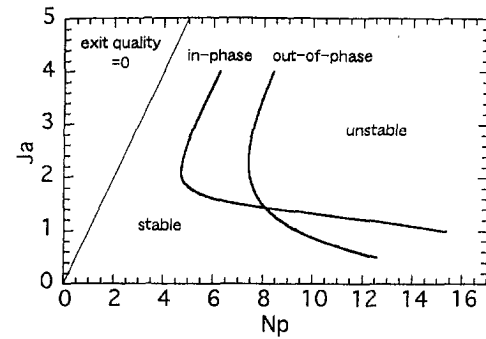
(b) $C_\alpha \times 1.3$

Fig. 6 Effect of the void-reactivity coefficient C_α on the stability boundary, $Fr = 0.0125$

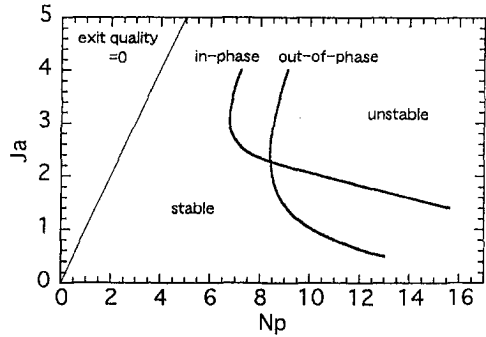
On the other hand, in the case of with the void-reactivity feedback included, not only the in-phase mode unstable region appears on the stability map, but also the out-of-phase mode unstable region is widened compared to that in the case of without void-reactivity feedback. The result shows that the void-reactivity feedback effect makes the system more unstable. Also the shape and the tendency of these stability boundaries are similar to those by March-Leuba and Blakeman (1991). Quantitative comparison is not possible because the present analysis does not include structural details of a BWR. Nevertheless, the result shows that the analysis in this paper is valid for study of the stability mechanism.

Effect of the Void-Reactivity Coefficient. The void-reactivity coefficient represents the degree of the void-reactivity feedback effect, which is one of the governing factors causing the instability of the system. Figure 6 shows the stability boundaries for various void-reactivity coefficients that were modified by multiplying the coefficients shown in Fig. 4 with a constant. The solid lines are the stability boundaries of the system. Inside the broken line is the region in which the poles of the characteristic equation (Eq. (45)), or the roots of $[\delta_{II} + G_{q,II}] = 0$ in Eq. (36), have positive real parts. Since this equation corresponds to the characteristic equation for the closed-loop $\delta V_i - \delta q'''$ transfer function given in Eq. (33), the broken line can be recognized as the stability boundary for the void-reactivity feedback loop (Rao et al., 1995). It was found that as the void-reactivity coefficient becomes larger (or the effect of the void-reactivity feedback becomes stronger), both modes become less stable, and the region where the void-reactivity feedback loop is unstable expands. It is noted that part of the stability boundary of the in-phase mode coincides with part of the stability boundary for the void-reactivity feedback loop; this indicates that the void-reactivity feedback strongly affects the instability of the in-phase mode.

Effect of Froude Number. Figure 7 shows the effect of Froude number on the stability boundaries. It is found that the



(a) $Fr=0.015$



(b) $Fr=0.03$

Fig. 7 Effect of Froude number on the stability boundary

system becomes less stable as Fr decreases. The stability boundary of the in-phase mode shifts toward lower Ja area, while that of the out-of-phase mode shifts toward lower Np area as Fr is decreased. Also, the stability boundary of the in-phase mode is more sensitive to the change in Fr than that of the out-of-phase mode, suggesting that the in-phase mode instability is affected to a larger extent by the inertial force and/or the gravitational force.

Effect of the Interaction between Subcores Through the Void-Reactivity Relation. The parameter ϵ_{II} in Eq. (23) is defined as the ratio of the channel-to-channel distance to the neutron diffusion length, which indicates the degree of the interaction between subcores. Figure 8 shows stability boundaries for various values of ϵ_{12} , where the interaction between subcores is stronger for a smaller ϵ_{12} . It is found that the stability boundary of the in-phase mode is unchanged regardless of the value of ϵ_{12} . However, the stability boundary of the out-of-phase mode changes as the value of ϵ_{12} changes; the out-of-phase mode becomes more unstable as ϵ_{12} increases resulting in a weaker interaction between

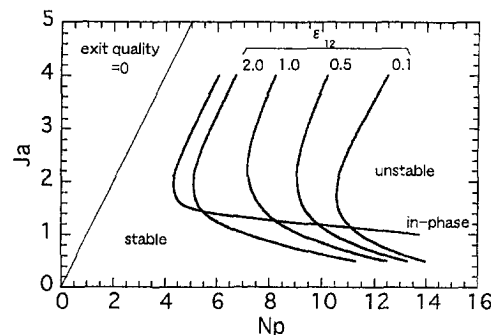


Fig. 8 Effect of parameter ϵ_{II} on the stability boundary of the out-of-phase mode, $Fr = 0.0125$

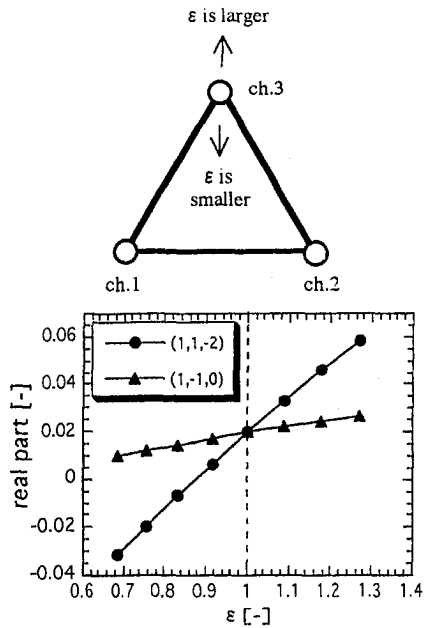


Fig. 9 Case A for the case of 3 subcores; $\epsilon = \epsilon_{13} = \epsilon_{23}$ ($0.68 < \epsilon < 1.27$), $\epsilon_{12} = 1$, $Np = 10$, $Ja = 1$, $Fr = 0.0125$

subcores. On the other hand, for the limiting case of $\epsilon_{12} = 0$, the out-of-phase mode stability boundary was found to be numerically in complete agreement with the stability boundary in the case of without void-reactivity feedback. This interesting result requires further study. The interaction between subcores makes the out-of-phase mode more stable because of the effect of averaging the power disturbances in all subcores. These results seem to suggest that the out-of-phase mode is more influenced by the thermal-hydraulic effect, while the in-phase mode is more influenced by the void-reactivity feedback effect.

Modes in the Case of Three and Four Subcores. In the case of 3 and 4 subcores, the number of the out-of-phase modes increases in comparison with the case of 2 subcores. The characteristic roots associated with the out-of-phase mode are double roots if all subcores are completely at the same condition (geometric, thermal-hydraulic, etc.). The double roots separate into two when the condition of a subcore is a little different from the others. In this section, the effect of subcore interaction on various out-of-phase modes is revealed for the case of 3 and 4 subcores. The degree of this interaction depends on the distance between subcores as modeled by Eqs. (23) and (24). The interaction between subcores can be varied by shifting the position of one of the subcores. Figures 9–11 show patterns of the relationships of the subcores, which are selected to study the basic mechanism, and the variations of the out-of-phase modes for each pattern. In Figs. 9 and 10, the out-of-phase modes are examined when one of the three subcores is shifted. Figure 11 shows state of the out-of-phase modes when the distance between two couples of subcores is changed. In Figs. 9–11, the horizontal axis is the parameter ϵ of the interaction between subcores assumed by Eq. (24). The vertical axis is the real part of characteristic root for each mode. A mode becomes less stable (or more unstable) as its real part becomes larger. Also, the mode is stable when the real part of the characteristic root is negative according to general control theory. A group of numbers within parentheses indicates a specific oscillation mode. Each number is the relative oscillation amplitude of a corresponding subcore. The positive and negative signs represent a phase difference of 180 deg. For example, the mode (1, 1, -2) indicates that the subcores 1 and 2 oscillate in-phase with each other (with a phase difference of 0 deg) and have equivalent oscillation amplitude, while the subcore 3 oscillates out-of-phase

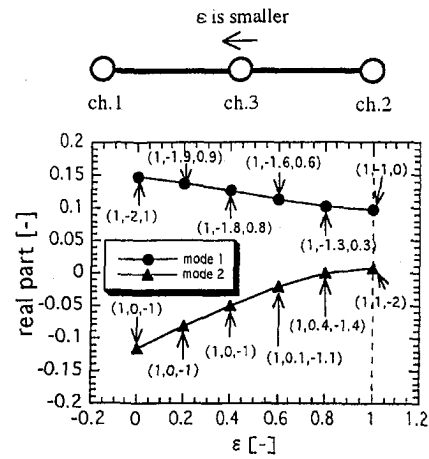


Fig. 10 Case B for the case of three subcores; $\epsilon = \epsilon_{13}$ ($0 < \epsilon < 1$), $\epsilon_{12} = 2$, $Np = 10$, $Ja = 1$, $Fr = 0.0125$

with subcores 1 and 2 (with a phase difference of 180 deg) and has an oscillation amplitude twice as large. Figure 9 shows variation of two modes (1, -1, 0) and (1, 1, -2) with ϵ , which is the relative distance or the strength of interaction between subcore 3 and subcores 1 and 2. For $\epsilon < 1$, the mode (1, -1, 0) is more dominant (having a larger real part) than the mode (1, 1, -2), while for $\epsilon > 1$, the mode (1, 1, -2) is more dominant. Figure 10 shows variations of the two modes when the subcore 3 shifts between subcore 1 and 2 as shown schematically in the figure. When subcore 3 lies just at the center of the subcores 1 and 2, i.e., $\epsilon = 1$, there are two modes (1, -1, 0) and (1, 1, -2), with the former being more dominant than the latter. This dominant mode changes as subcore 3 approaches subcore 1, showing that subcore 3 will oscillate in-phase with subcore 1 to which it has a stronger interaction. Finally, these two modes become (1, -2, 1) and (1, 0, -1) when subcores 3 and 1 are completely at the same position (i.e., $\epsilon = 0$), with the mode (1, -2, 1) much more dominant. Similarly, in the case of four subcores as shown in Fig. 11, three modes exist. The mode (1, 1, -1, -1) becomes more dominant than the others when the distance or interaction between couple 2 (the subcores 3 and 4) and couple 1 (the subcores 1 and 2) is larger than that

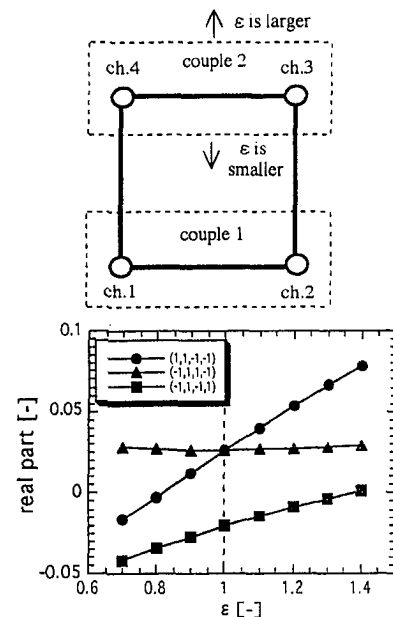


Fig. 11 Case C for the case of four subcores; $\epsilon = \epsilon_{14} = \epsilon_{23}$ ($0.7 < \epsilon < 1.4$), $\epsilon_{12} = \epsilon_{34} = 1$, $Np = 10$, $Ja = 1$, $Fr = 0.0125$

between the two cores in a couple, i.e., $\epsilon > 1$. When $\epsilon < 1$, the mode $(-1, 1, 1, -1)$ is more dominant. These results again confirmed that a subcore is more apt to oscillate in-phase with a subcore of stronger interaction and out-of-phase with a subcore of weaker interaction. These results show that the two-dimensional nuclear interaction between regions in a reactor core plays an influential role in determining the unstable oscillation modes.

In our previous paper (Rao et al., 1995) dealing with only instabilities of the in-phase mode, qualitative comparison was made between the result by the present frequency-domain code and that by a time-domain code. In the present paper, however, qualitative comparison of the results with those by other studies or with experimental data has not been performed. This is partly due to the lack of experimental data on the stability boundary of the out-of-phase mode—some limited transient results cannot be used to compare with the results by a frequency-domain model, which only give stability boundaries not the transient responses. Also, the interaction coefficient between subcores (H_{ij}) need to be evaluated before the present model can be applied to a real BWR. However, the authors believe that the idea presented in this paper will cast a new light on making use of the frequency-domain method to study the out-of-phase instabilities in BWRs.

Conclusion

An analytical model was proposed to study regional instabilities in BWRs. The model consists of parallel boiling channels with coupled nuclear and thermal-hydraulic feedbacks, and is capable of taking into consideration the interaction between subcores. Linear stability analysis was performed to reveal dominant factors affecting the two-phase flow instabilities of the in-phase and the out-of-phase modes. It was found that the void-reactivity feedback plays an important role in initiating the instability of the in-phase mode. The instability of the in-phase mode is more sensitive to the Froude number effect than that of the out-of-phase mode. The interaction between subcores makes the instability of the out-of-phase mode less unstable. A subcore is easier to oscillate in-phase with a subcore to which it has a stronger interaction and out-of-phase with a subcore to which it has a weaker interaction.

References

- Araya, F., Hirano, M., Yoshida, K., Matsumoto, K., Yokobayashi, M., and Kohsaka, A., 1992, "Development of Method to Determine Instability Threshold with RETRAN Code," *J. At. Energy Soc. Jpn.*, Vol. 34, No. 9, pp. 83–92.
- Blakeman, E. D., and March-Leuba, J., 1989, "A Parametric Analysis of Decay

Ratio Calculations in a Boiling Water Reactor," CONF-890555-4, *Proceedings of the 7th Power Plant Dynamics, Control, and Testing Symposium*, American Nuclear Society, LaGrange Park, IL.

Boure, J. A., Bergles, A. E., and Tong, L. S., 1973, "Review of Two-Phase Flow Instability," *Nucl. Eng. Des.*, Vol. 25, pp. 165–192.

Commonwealth Edition Co., 1977, "LaSalle County Station Unit 1 and 2 License Application," Docket-50373-175.

Enomoto, T., Muto, S., Yoshimoto, S., Yokomizo, O., Chuman, K., 1986, "Three Dimensional Stability Analysis of BWR Core," *2nd International Topical Meeting on Nucl. Power Plant Thermal Hydraulics and Operations*, Vol. 2, pp. 15–22.

Fukuda, K., and Kobori, T., 1978, "Two-Phase Flow Instability in Parallel Channels," *Proc. 6th Int. Heat Transfer Conf.*, Vol. B17, Hemisphere, New York, pp. 369–374.

Fukuda, K., Kage, K., and Hasegawa, S., 1982, "Analysis on Two-Phase Flow Oscillation Mode in Parallel Multi-Channels," *Memoirs of the Faculty of Eng. Kyushu Univ.*, Vol. 42, No. 3, pp. 163–175.

Fukuda, K., Rao, Y. F., and Uehiro, M., 1998, "A Multi-Point Kinetic Model and Its Application to Analyses and Experiments of the Regional Instabilities in BWR's," *Proc. 6th Int. Conf. on Nuclear Engineering*, San Diego, CA, ASME, New York, Paper No. 6113.

Gialdi, E., Grifoni, S., Parmeggiani, C., and Tricoli, C., 1985, "Core Stability in Operating BWR: Operational Experience," *Progress in Nucl. Energy*, Vol. 15, pp. 447–459.

Hetrick, D. L., 1971, *Dynamics of Nuclear Reactors*, University of Chicago Press, Chicago, pp. 260–275.

Ishii, M., and Zuber, N., 1970, "Thermally Induced Flow Instabilities in Two-Phase Mixture," *Proc. 4th Int. Heat Transfer Conf.*, Vol. B5, Hemisphere, New York, pp. 11–7.

Lahey, R. T., 1986, "Advances in the Analytical Modeling of Linear and Nonlinear Density-Wave Instability Modes," *Nucl. Eng. Des.*, Vol. 95, pp. 5–34.

Lahey, R. T., Jr., and Moody, F. J., 1993, *The Thermo-Hydraulics of a Boiling Water Nuclear Reactor*, 2nd Ed., American Nuclear Society, LaGrange Park, IL.

March-Leuba, J., and Blakeman, E. D., 1991, "A Mechanism for Out-of-phase Power Instabilities in Boiling Water Reactor," *Nucl. Sci. Eng.*, Vol. 107, pp. 173–179.

Muto, S., Yokomizo, O., Yoshimoto, Y., Fukahori, T., and Ebata, S., 1990, "Space-Dependent Analysis of BWR Core Nuclear Thermal Hydraulic Instability and Thermal Margin," *Nucl. Eng. Des.*, Vol. 120, pp. 227–239.

Rao, Y. F., Fukuda, K., and Kaneshima, R., 1995, "Analytical Study of Coupled Neutronic and Thermodynamic Instabilities in a Boiling Channel," *Nucl. Eng. Des.*, Vol. 154, pp. 133–144.

Takeuchi, Y., and Takigawa, Y., 1994, "TRACG Transient Analysis Code—Three-Dimensional Kinetics Model Implementation and Application for Space-Dependent Analysis," *Nucl. Tech.*, Vol. 105, pp. 162–183.

Takigawa, Y., Ebata, S., Chan, K. C., and Tricoli, C., 1987, "CAORSO Limit Cycle Oscillation Analysis with Three-Dimensional Transient Code TOSDIN-2," *Nucl. Tech.*, Vol. 79, pp. 210–227.

U.S. NRC, 1988, "Augmented Inspection Team Report," NRC Report No. 50-373/88008.

Valtonen, K., 1990, "BWR Stability Analysis," STUK-A88.

Uehiro, M., Rao, Y. F., and Fukuda, K., 1997, "Multi-Channel Modeling Based on a Multi-Point Reactor Model for the Regional Instability in BWRs," *Proc. 8th Int. Topical Meeting on Nuclear Reactor Thermal-Hydraulics*, (Nureth-8), Vol. 1, Kyoto, Japan, American Nuclear Society, LaGrange, IL, pp. 375–384.

Experimental Study of Dispersed Droplets in High-Pressure Annular Flows

T. A. Trabold

R. Kumar
Mem. ASME

P. F. Vassallo

Lockheed Martin Corporation,
Schenectady, NY 12301

Local measurements were made in a droplet-laden vapor core in upward R-134a annular flow in a high aspect ratio vertical duct. These detailed measurements are unique in that they were performed at high pressures and low liquid-to-vapor density ratios. Using a gamma densitometer, hot-film anemometer and laser Doppler velocimeter, profiles of void fraction, liquid droplet frequency, and droplet velocity were acquired across the narrow test section dimension. At relatively high flows, the measured void fraction was highest near the wall, due to the thinning of the liquid film. The dip in the void fraction in the vapor core at these flows suggests significant droplet entrainment. The entrainment fractions for these refrigerant flows fall in the range measured for pressurized steam-water systems. The average drop size, calculated from direct measurements of void fraction, droplet velocity, and frequency, compares favorably with previous experimental results from the literature. These data are useful for developing an improved understanding of practical two-phase flows, and for assessment of advanced two-fluid computer codes.

Introduction

Application of two-fluid model computer codes for prediction of gas-liquid flows relies on the availability of an experimental database from which an understanding of fundamental physical phenomena can be developed. Such a database is also required to rigorously assess a code's predictive capability. Most of the experimental data in the open literature apply to air-water flows through circular geometries at atmospheric conditions. Detailed two-phase flow data for different fluids, in particular for low liquid-to-gas density ratios through noncircular geometries at elevated temperature and pressure conditions, are seriously lacking.

Annular two-phase flow usually occurs through a transition from the slug/churn-turbulent flow regime at high average void fractions. In such flows, the liquid phase is transported in both a film along the walls and as droplets entrained in the central gas core. The ratio of the liquid phase in the film to that in droplet form varies according to a number of parameters, including the fluid flow rates and the liquid-to-gas density ratio. The interface between the liquid film and the vapor core is characterized by disturbance (or roll) waves. These waves often have heights which are several times larger than the mean liquid film thickness, and can travel relative to the liquid film at significant velocities. At high gas velocities, the roll wave crests are sheared off, forming droplets that entrain into a highly turbulent vapor core. Droplets can also be formed by the disintegration of the liquid bridges in the churn-turbulent regime. The droplets thus formed are transferred and redeposited on the film.

Hewitt and Hall-Taylor (1970) state that droplet size is important in determining the mass and heat transfer behavior of the system, and for determining the velocity of the droplets with respect to the gas phase. The droplet size and velocity are usually not simultaneously measured. Indeed, measurements of both droplet size and droplet velocity profiles in annular flow have been reported in only a few publications (Hadded et al., 1985; Tayali et al., 1990; Azzopardi and Teixeira, 1994a, b). These previous

measurements were made in air-water flows for a wide range of flow rates using laser-based velocity and sizing techniques.

Ueda (1979) provided a droplet size correlation based on data obtained in air-water, various aqueous solutions, and low liquid-to-gas density ratio refrigerant flows. There have also been mechanistic models and correlations based on shearing of roll waves (e.g., Tatterson et al., 1977; Kataoka et al., 1983; Lopes and Dukler, 1986) which were developed primarily from air-water data at atmospheric conditions. These models tend to deviate from the experimental data for low liquid-to-gas density ratios. Kocamustafaogullari et al. (1994) developed a droplet size model accounting for the breakup of the droplets in addition to the shearing of the roll waves. Their model has not been tested against detailed local measurements of droplet size in heated systems, especially in geometries other than circular cross sections. As pointed out by Lopes and Dukler (1986), the location at which droplet sampling is made in the vapor core is critical for validating different models.

Few local measurements of droplet size, droplet velocity, and void fraction are available for heated systems with low liquid-to-gas density ratios. In addition, the majority of open literature information involves circular pipes. The present study was undertaken to acquire local data in two-phase flows through a vertical duct geometry, at pressures significantly above atmospheric. This study expands upon earlier work (Trabold et al., 1997) by concentrating attention on upward annular flow phenomena through the application of a variety of instrumentation techniques. The working fluid for all the experiments was R-134a,¹ one of the relatively new class of nonchlorinated refrigerant fluids which does not deplete the ozone layer. This fluid is widely used in heat exchangers, air conditioning, and refrigeration systems, and is recommended as a replacement for R-113 and R-114. Aside from its practical importance, R-134a is also of scientific interest because of its very low liquid-to-vapor density ratio and low surface tension (7.3 and 0.0021 N/m, respectively, at 2.4 MPa).

The specific objectives of this study are to: (1) extend the annular flow database to refrigerant flows through a vertical duct at pressures much higher than atmospheric pressure; (2) provide liquid droplet velocity and size measurements in the vapor core at liquid-to-gas density ratios comparable to steam-water at high

Contributed by the Heat Transfer Division for publication in the JOURNAL OF HEAT TRANSFER. Manuscript received by the Heat Transfer Division, July 12, 1998; revision received, Apr. 23, 1999. Keywords: Annular Flow, Droplet, Entrainment, Sensors, Two-Phase. Associate Technical Editor: M. S. Sohal.

¹ 1,1,1,2-tetrafluoroethane

pressure; and (3) understand the new data for void fraction, droplet frequency, velocity and size, and to gain insight into the complex physical phenomena characteristic of annular two-phase flows.

Experimental Facility and Instrumentation

Flow Loop and Test Section. Key components of the experimental R-134a loop are a chiller and pressurizer to maintain the liquid phase at the inlet of a circulating canned rotor pump, a large CO₂ heat exchanger, loop heaters, high/low range throttle valves, flow meters, and a vertical test section. Loop conditions are set by programmed logic controllers; acquired data include mass flow rate, temperature, pressure, heater power, and test section pressure drop. The loop design pressure ranges from 0.4 to 2.5 MPa, and temperature ranges from 0° to 80°C. The test section, illustrated schematically in Fig. 1, has a hydraulic diameter of 4.85 mm and an aspect ratio of approximately 20. Optical access to the flow is provided by four pairs of fused silica windows. The center of the window width forms the transverse (*Y*) dimension of the flow passage. In the side of the test section between the pairs of windows are 2.5-cm diameter ports which permit access to the flow for various instruments. For these experiments, rakes of nine thermocouples were located in Ports #1 and 5. Three pressure taps were located within each window, as well as at the top and bottom of the test section length.

An instrument scanning mechanism positions the gamma densitometer system (GDS) and laser Doppler velocimeter (LDV) instrumentation along three axes. To measure void distributions in either the thickness (*Z*) or the width (*Y*) directions, the gamma densitometer is rotated 90 degrees about the test section (*X*-axis). Both gamma beam and laser tests have shown that the GDS and LDV positioning accuracy is approximately ±0.03 mm. An offset, usually less than ±0.05 mm in the measurement position introduced by thermal expansion of the test section, was corrected for as necessary.

The inlet to the test section is comprised of three independent flow zones which enable the introduction of different flow rates and/or fluid enthalpies. This feature permits the investigation of flows with nonuniform inlet boundary conditions. For all experiments documented in this paper, the inlet flow was introduced either entirely through the center zone, or evenly divided among the three zones. In the latter case, the fluid enthalpy was not varied across the test section inlet. The experimental results indicate that the manner in which the flow enters the test section has no discernible effect on measurements taken at downstream locations.

Gamma Densitometer System (GDS). The gamma densitometer provides a direct measurement of the density of a two-phase mixture in the path of a gamma beam through the following relationship:

$$\rho_{2\phi} = \frac{\ln\left(\frac{I_o}{I}\right)}{\mu t} \quad (1)$$

where I_o and μt are calibration constants obtained from gamma count measurements at each desired measurement position, with an empty test section and a subcooled liquid-filled test section. I is the count rate measured for the two-phase test condition. The two-phase density is related to the void fraction and vapor and liquid densities through the following relationship:

$$\rho_{2\phi} = (1 - \alpha)\rho_l + \alpha\rho_g \quad (2)$$

where α is the void fraction, ρ_l is the density of the liquid phase, and ρ_g is the density of the vapor phase. Solving for α yields

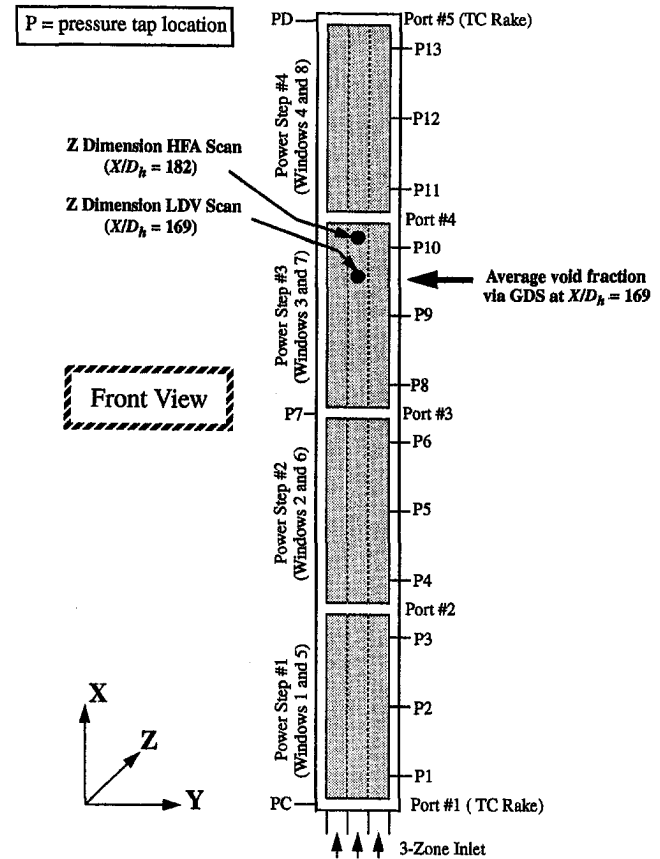


Fig. 1 Test section and measurement locations

Nomenclature

A = aspect ratio (width/thickness)
B = bias
D_h = duct hydraulic diameter, mm
d_d = droplet diameter, μm
d_{sm} = Sauter mean droplet diameter, μm
f_d = droplet frequency, Hz
G = mass flux, kg/hr/m²
P = pressure, MPa
Re = Reynolds number
t = duct thickness, mm

V = HFA output voltage
V_d = droplet velocity, m/s
V_T = threshold voltage for HFA probe signal analysis
W = duct width, mm
We_m = modified Weber number
w = mass flow rate, kg/hr
X = streamwise (length) dimension
Y = width dimension
Z = thickness dimension

Greek Symbols

α = void fraction
 $\Delta\rho$ = density difference, kg/m³
 μ = dynamic viscosity, kg/hr-m
 ρ = density, kg/m³
 σ = surface tension, N/m

Subscripts

d = droplet
g = gas phase
l = liquid phase
 2ϕ = two-phase (mixture)

$$\alpha = \frac{\rho_l - \rho_{2\phi}}{\rho_l - \rho_g} \quad (3)$$

The liquid and vapor-phase densities were determined based on saturation properties at the measured test section exit temperature.

The GDS currently being used in the R-134a test facility features a 9 curie Cesium-137 gamma source and a NaI detector. Typically, eight line-average void fraction measurements were made across the Z dimension of the test section. Another type of gamma densitometer measurement is the wide beam measurement through the Z-axis. These measurements were performed at the centerline of the duct width (Y dimension), about 6.3 cm below the hot-film anemometer probe. The effective gamma beam width at the test section is 4.2 mm. This line-average void fraction measurement provided a means of assessing the accuracy of local void fraction measurements, through comparison to the integrated average of hot-film anemometer data. All three types of GDS data were obtained at a streamwise position of $X/D_h = 169$.

Hot-Film Anemometer (HFA). The constant temperature hot-film anemometer technique was used previously for various two-phase flow measurements in R-114 and R-134a and is described in detail by Trabold et al. (1994, 1997, 1998). The single-sensor HFA probes used in this previous work afforded measurements of both local void fraction and interfacial frequency profiles. For the present testing program, a dual-sensor probe was installed at $X/D_h = 182$ and the center of the Y dimension (Fig. 1). The HFA probe is comprised of two active sensing elements which are separated in the streamwise (X) dimension by a known distance. The probe used in the present tests had platinum film sensors with a 25- μm diameter and 254- μm active length, and a measured sensor separation distance of 1.44 ± 0.01 mm.

The use of two sensors permits acquisition of interfacial velocity measurements based on the cross-correlation between two output voltage signals. The peak in the cross-correlation versus time plot corresponds to the most probable time required for a gas-liquid interface to travel between the HFA sensors, from which the mean interfacial velocity may be calculated. The measurement position ranges from 0.15 mm from the wall to about the duct centerline.

The combined slope and level thresholding method of Carvalho and Bergles (1992) was used to analyze the HFA output voltage signals for determination of local vapor volume fraction. A level threshold was set at the midpoint between the vapor and liquid parts of the output voltage signal, with slope thresholding additionally applied to account for the finite time for gas-liquid interfaces to pass the HFA sensor. A typical output voltage sample histogram associated with a dispersed liquid/continuous vapor waveform is shown in Fig. 2. The large peak represents the baseline vapor phase voltage. Samples in voltage bins to the right of this peak correspond to discrete samples of the liquid droplet pulses. Depending on the magnitude of the dispersed liquid volume fraction, a smaller peak may also be visible at the high end of the output voltage range. The threshold voltage is then taken as the midpoint between the highest and lowest voltage bins after the elimination process. The integrated averages of various HFA Z scan data profiles obtained were found to be in good agreement with line-average gamma densitometer measurements.

In addition to the local void fraction, the data analysis program also provided a measurement of local liquid droplet frequency by counting the number of positive pulses in a known measurement time. More details of eccentric droplet impaction on the sensor are provided by Trabold et al. (1998).

Laser Doppler Velocimeter (LDV). Laser Doppler velocimetry is a well-established instrument for velocity measurements in single-phase gas and liquid flows. This technique has also been used to simultaneously measure vapor and liquid velocities in bubbly flow (e.g., Vassallo et al., 1993). In the present experiments, two focused laser beams were transmitted through a quartz window, to intersect inside the test section at $X/D_h = 169$ (Fig. 1).

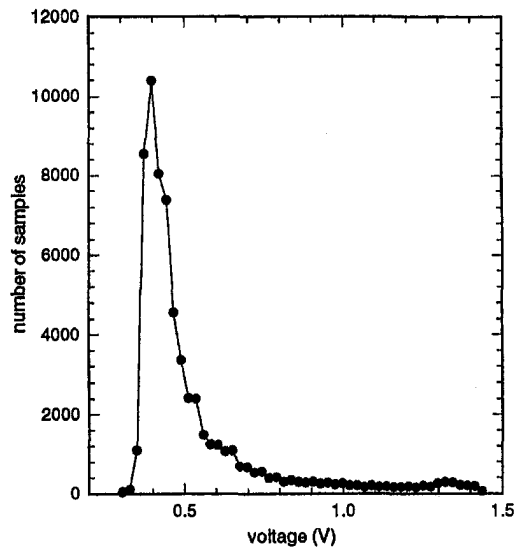


Fig. 2 Hot-film anemometer signal voltage histogram

This intersection point defines the measurement location within the droplet field. At high void fractions and high flow rates, the liquid film is relatively thin, and LDV droplet measurements are possible along most of the Z-axis. As the void fraction or flow rate decreases, the film gets thicker and wavier, and the LDV measurements are more difficult to attain. This is because the true samples in the velocity histogram are masked by a high-frequency noise component (as the gain is increased) occurring near zero velocity. At some moderate void fractions and flow rates, measurements of droplet velocity are only possible near the central plane of the test section, where the noise contribution from the film is reduced. At low void fractions (less than 0.7), the irregularities and thickness of the film make it impossible to obtain any droplet measurements.

A backscatter fiber optic LDV probe was used to acquire the droplet velocity measurements. The probe was equipped with a short focal length lens (122 mm) to produce a measurement volume about 0.25 mm long. The probe was mounted on a traversing slide to enable motion in the Z-axis. The near-wall (closest to the probe) measurement location was determined by moving the probe forward toward the test section and noting the position at which Doppler signals first appeared. Measurements were taken across the test section thickness dimension with a positioning uncertainty of about ± 0.13 mm.

The Doppler signals were analyzed for velocity using a counter-timer signal processor. Input signals must first pass a voltage threshold; if a signal is greater than a minimum amplitude, it is processed for velocity. However, if the processor gain is set too high, noise may be misinterpreted as a valid signal. To ensure that the gain was not excessive during the experiments, a comparison check was employed to assess the repeatability of the time for each cycle within a given Doppler burst. Also, an additional data quality check was performed by occasionally blocking one of the LDV beams to confirm that the data rate fell to zero. If noise appeared in the velocity histograms (usually in the form of stray velocity samples clearly separated from the main peak) it was removed using the data analysis software. These samples usually accounted for less than ten percent of the total number of samples.

Typical data rates for the velocity measurements were between 2 and 20 Hz, depending on the measurement location inside the test section. Between 500 and 1000 velocity samples were obtained at each measurement location over a period of two to five minutes. LDV measurements were only taken across the near half of the test section Z dimension because of the difficulty in obtaining a reasonable data rate as the beams penetrated further into the test section.

Table 1 Experimental parameters and measurement uncertainties

Measurement	Uncertainty Sources Considered	Uncertainty Band
test section absolute pressure	<ul style="list-style-type: none"> transducer accuracy biases: transducer stability, static pressure effect, ambient temperature, data acquisition system accuracy 	±0.02 MPa
mass flow rate	<ul style="list-style-type: none"> same as above venturi calibration 	±3.2 kg/hr
cross-sectional average void fraction (GDS)	<ul style="list-style-type: none"> gamma count repeatability liquid and vapor density variations during calibration and measurement 	±0.017
line-average void fraction (GDS through Z dimension)	<ul style="list-style-type: none"> same as cross-sectional average void fraction 	±0.108
local void fraction (HFA)	<ul style="list-style-type: none"> repeatability based on pooled standard deviation biases: threshold voltage, small droplets, position, sampling time 	±0.025
local droplet frequency (HFA)	<ul style="list-style-type: none"> same as void fraction also, droplet impaction bias 	-79 to +90 Hz at $w = 106$ kg/hr -321 to +652 Hz at $w = 532$ kg/hr
local droplet velocity (HFA)	<ul style="list-style-type: none"> repeatability biases: velocity sampling, droplet size, cross-correlation, sensor spacing, position 	-7.5% to +7.0% (near wall) -7.0% to +6.4% (far wall)
local droplet velocity (LDV)	<ul style="list-style-type: none"> precision based on rms of mean velocity biases: velocity sampling, random noise, position 	-16.2% to +15.2% (near wall) -8.4% to +6.2% (far wall)

Measurement Uncertainty. The measurement uncertainty for all test section instrumentation was calculated based on the root-sum-square uncertainty interval for 95 percent confidence:

$$U = \pm[B^2 + (t_{95}S_{\bar{x}})^2]^{1/2} \quad (4)$$

where B is the bias limit (systematic error) and $t_{95}S_{\bar{x}}$ is the precision limit (random error). The ranges of experimental parameters investigated, and the associated uncertainty are summarized in Table 1.

Results and Discussion

The experimental results discussed in this section were obtained with a fixed nominal system pressure of 2.4 MPa. The two operating variables were mass flow rate (nominally 106, 266, and 532 kg/hr) and cross-sectional average void fraction (nominally 0.75, 0.85, and 0.94). After establishing the pressure and flow conditions, heaters immediately upstream of the test section were used to generate the desired void fraction, as measured with the gamma densitometer. Detailed local data in the narrow (Z) dimension were acquired with both the hot-film anemometer and laser Doppler velocimeter.

Local Void Fraction. As a means of assessing the validity of the local HFA void fraction measurements, simultaneous GDS line-averaged void fraction data were obtained for selected test runs, and compared (not shown here). The two data sets agreed within an average difference of 0.033 in void fraction, with a maximum difference of 0.066. Any difference in the results may also be attributed to the presence of the liquid film near the edges, which is traversed through by the gamma beam.

The local void fraction results are presented in Fig. 3. For each mass flow rate condition, data are plotted for the three nominal average void fractions investigated. The shape of the local void fraction variation is clearly a function of both mass flow rate (w) and cross-sectional average void fraction (α). For $\alpha = 0.94$, the local void fraction profiles are nearly flat over the duct cross section, regardless of the magnitude of w . At $\alpha = 0.85$, void fraction is maximum at the duct centerline for $w = 106$ kg/hr (Fig. 3(a)). As the flow rate is increased to 266 kg/hr (Fig. 3(b)), a distinct change in the local void fraction variation is observed. The maximum in the profile exists around $Z/t = 0.15$, and the minimum void fraction (i.e., largest liquid volume fraction) is measured at the duct centerline. At $w = 532$ kg/hr (Fig. 3(c)), the peak void fraction is measured at the near-wall measurement position, with a local minimum again measured at the center of the flow field. For $\alpha = 0.75$, the void fraction profile is center peaked at $w = 106$ kg/hr and 266 kg/hr (Figs. 3(a) and 3(b)), but again displays a near-wall maximum for the highest mass flow ($w = 532$ kg/hr; Fig. 3(c)). This void inversion results from the apparent thinning of the liquid film with increasing mass flow, as observed on the high-speed video record. With a very thin liquid film and small-amplitude interfacial wave structure, the local void fraction depends solely on the transport of the dispersed liquid droplet field. It is pertinent to note that for $\alpha = 0.75$, the measured centerline dispersed liquid droplet velocity changes from about 1 to 4 m/s with a mass flow rate increase from 106 to 532 kg/hr. The apparent inversion in the void fraction profile with increasing mass flow rate is related to this increase in velocity and measured droplet frequency.

The void fraction data for $\alpha = 0.75$ and 0.85 at $w = 532$ kg/hr are interesting because the profiles indicate the presence of a thin liquid film, with a significant fraction of the liquid phase transported in the dispersed droplet field. The entrainment fraction (E), defined as the ratio of liquid mass flow rate in the entrained (droplet) phase to the total liquid mass flow rate, has been previously investigated. Recently, Lopez de Bertodano et al. (1995) proposed a simple entrainment fraction correlation:

$$E = \frac{1}{3845 \left(1 + \frac{1}{We_c}\right)} \quad (5)$$

where

$$We_c = \text{gas core Weber number} = \frac{\rho_{gc} j_g^2 D}{\sigma} \quad (6)$$

with ρ_{gc} being the mixture density in the gas core. Equation (5) was demonstrated to reasonably represent both low-pressure air-water data (Cousins and Hewitt, 1968), as well as high-pressure steam-water data (Keeys et al., 1970; Wurtz, 1978). Using this expression, E for the three test runs at $w = 532$ kg/hr (Fig. 3(c)) was calculated to be 0.54, 0.58, and 0.73 for $\alpha = 0.75, 0.85,$ and 0.94, respectively. These values are significant because most of the low-pressure air-water data for entrainment fraction fall in the $0.05 < E < 0.3$ range, while the high-pressure data extend over the $0.4 < E < 0.9$ range. The entrainment fractions associated with R-134a at high mass flow rate appear to be more in line with those measured for high-pressure systems. This is likely due to the fact that gas phase density and surface tension for R-134a (130.5 kg/m³ and 0.0021 N/m, respectively, at 2.4 MPa) are much different than for air-water flows; both properties act to increase the value of the gas core Weber number.

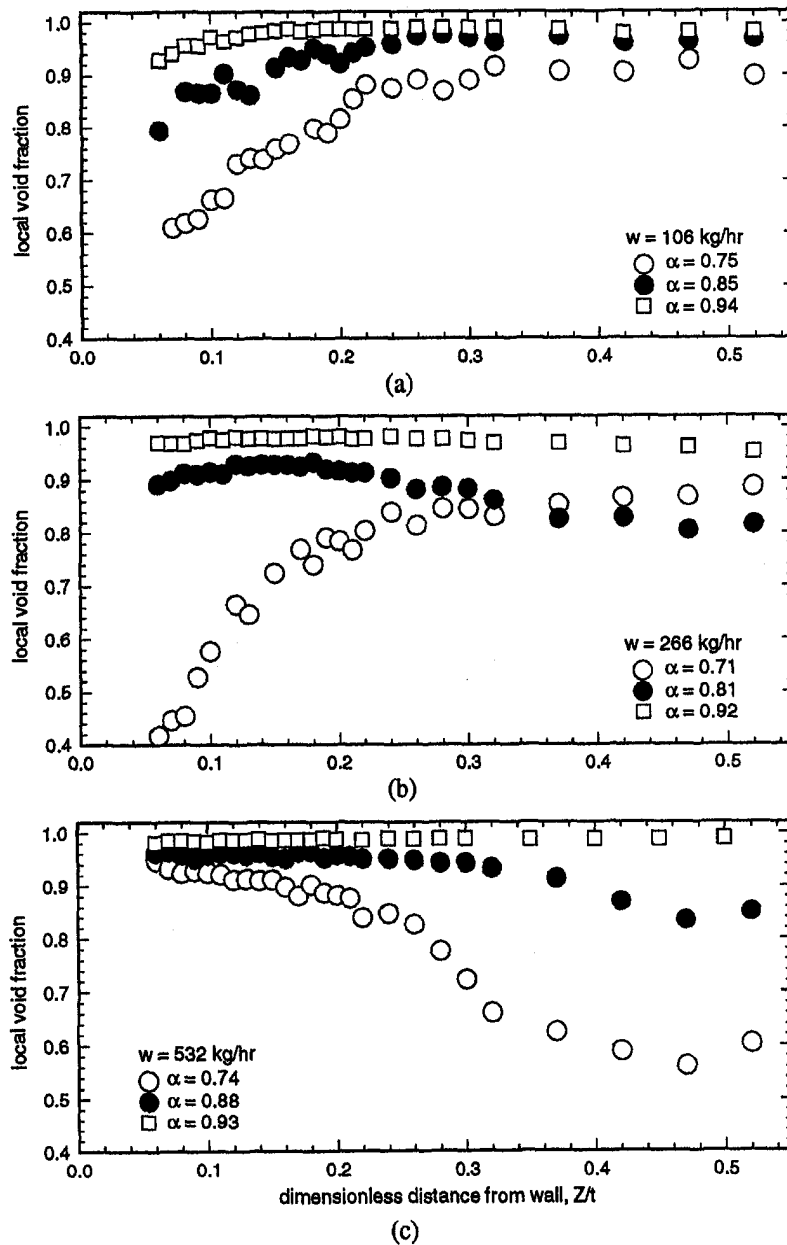


Fig. 3 Hot-film anemometer void fraction profiles for (a) 106 kg/hr, (b) 266 kg/hr, (c) 532 kg/hr

Droplet Frequency. A separate threshold voltage (V_T) was used for measurement of liquid droplet frequency, based on an assumed Gaussian distribution of continuous vapor-phase voltage samples. A faster digitizing rate of 50 kHz of the HFA output voltage signal was required to accurately measure the droplet frequency, f_d , particularly for $w = 532$ kg/hr. This digitizing rate was obtained based on a sensitivity study of different rates from 10 to 100 kHz.

The droplet frequency measurement is complicated by the variable amplitude of the "pulses" in the output voltage signal. Large droplets which strike the HFA sensor directly produce large-amplitude pulses, while small droplets (some of which have a size close to that of the 25- μm diameter sensor) or "glancing" interactions of large droplets produce smaller voltage signals. These smaller signals are more difficult to resolve because of the random fluctuations in the baseline voltage associated with the continuous vapor phase, and due to the inherent noise of the data acquisition system. Goldschmidt (1965) used a hot-wire probe to measure liquid particle concentration in a two-phase jet. He found that

under some conditions the "impaction coefficient" (defined as the ratio of particles counted per time to the particles flowing per time through an area equal to that of the wire facing the stream) was less than unity. Later, Goldschmidt and Eskinazi (1966) determined that the impaction coefficient is independent of both local velocity and particle size distribution. In the present experiments, it is reasonable to expect that not all liquid droplets striking the HFA sensor produce countable pulses. Additionally, large droplets are less likely to produce such signals than are small droplets.

The droplet frequency data are presented in Fig. 4 for mass flow rates of 106, 266, and 532 kg/hr, and nominal cross-sectional average void fractions of 0.75, 0.85, and 0.94. Measured frequencies may be somewhat less than the actual droplet concentration in the flow, and calculation of derived quantities (i.e., droplet diameter) may involve some bias toward larger droplets. The influence of this bias is discussed further below. For $w = 106$ kg/hr, the droplet frequencies in Fig. 4(a) are at least an order of magnitude lower than for the two higher mass flow rates, and nearly constant across the duct spacing dimension. A slight increase in f_d is

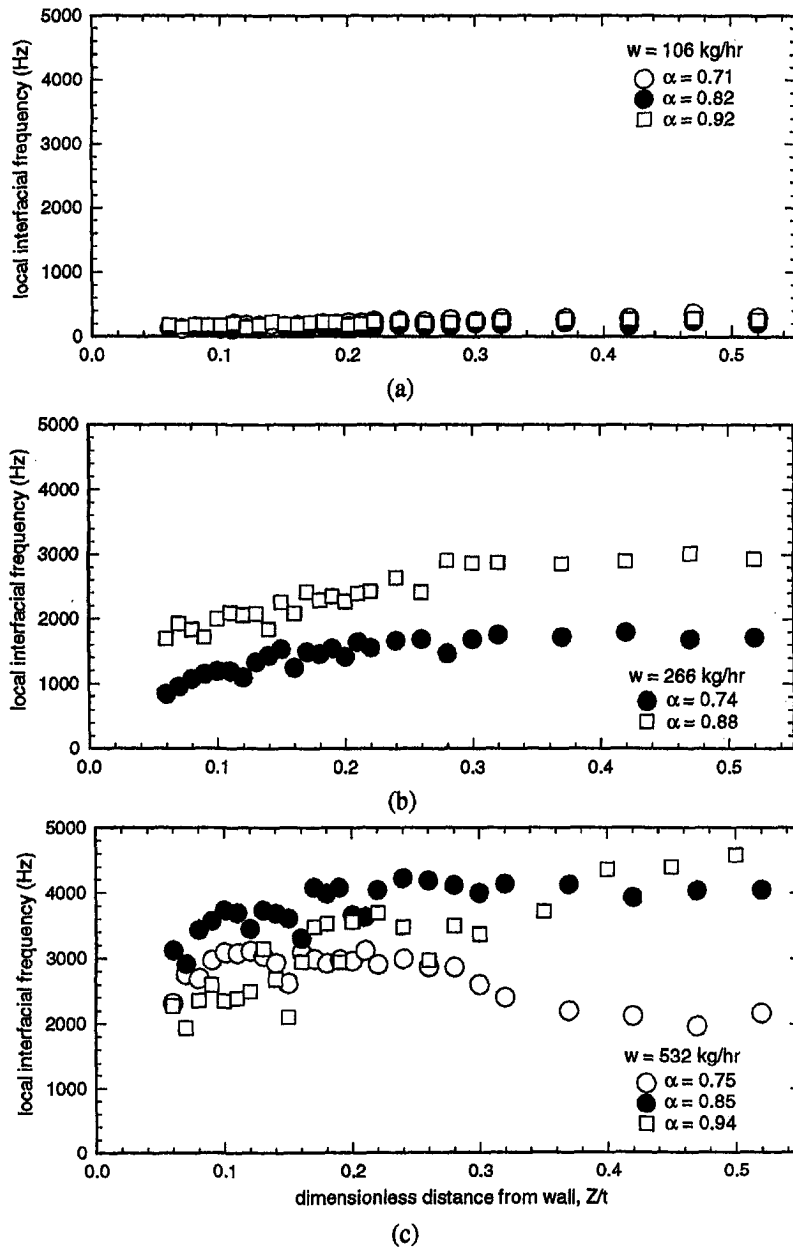


Fig. 4 Hot-film anemometer interfacial frequency profiles for (a) 106 kg/hr, (b) 266 kg/hr, (c) 532 kg/hr

consistently observed upon moving from the near-wall region toward the duct centerline. Additionally, for $w = 106$ kg/hr, it appears that the data for all three average void fractions could be well represented by similar functions. For $w = 266$ kg/hr, the droplet frequency profiles for $\alpha = 0.85$ and 0.94 (Fig. 4(b)) are nonlinear with the frequency doubling for the higher void fraction. For $\alpha = 0.75$, only a 10 kHz HFA digitizing rate was used. Therefore, droplet frequency data were not obtained for this condition.

For the highest mass flow rate test condition (532 kg/hr), the situation becomes more complex because the shapes of the droplet frequency profiles are more dependent on the magnitude of the average void fraction. For $\alpha = 0.85$ (Fig. 4(c)), the f_d trend is similar to that observed for the lower flows. Upon increasing the average void fraction to 0.94, a steady increase is seen in the droplet frequency from the wall to the duct centerline, with no apparent flattening of the profile. Over most of the duct cross section, the measured droplet frequency is less than that for $\alpha =$

0.85, with approximately a 15 percent increase in frequency at the duct centerline for the higher void fraction conditions. For $\alpha = 0.75$, a maximum in f_d is observed at about $Z/t = 0.15$, with a monotonic decrease measured upon moving toward the duct centerline. This result seems contradictory to the void fraction "inversion" observed for this case (Fig. 3(c)), because of the supposition that a lower droplet frequency implies a greater vapor volume fraction. However, as discussed later, the decrease in both void fraction and droplet frequency may be associated with a different droplet generation mechanism which produces relatively large diameter droplets.

Droplet Velocity. Droplet velocity profiles measured across half the test section thickness dimension, using the dual-sensor HFA and LDV techniques, are provided in Fig. 5 for all mass flow rates tested. For $\alpha = 0.85$, only LDV velocity data were obtained. For all experiments conducted with $\alpha = 0.75$ and 0.94, there is good agreement between the two sets of data,

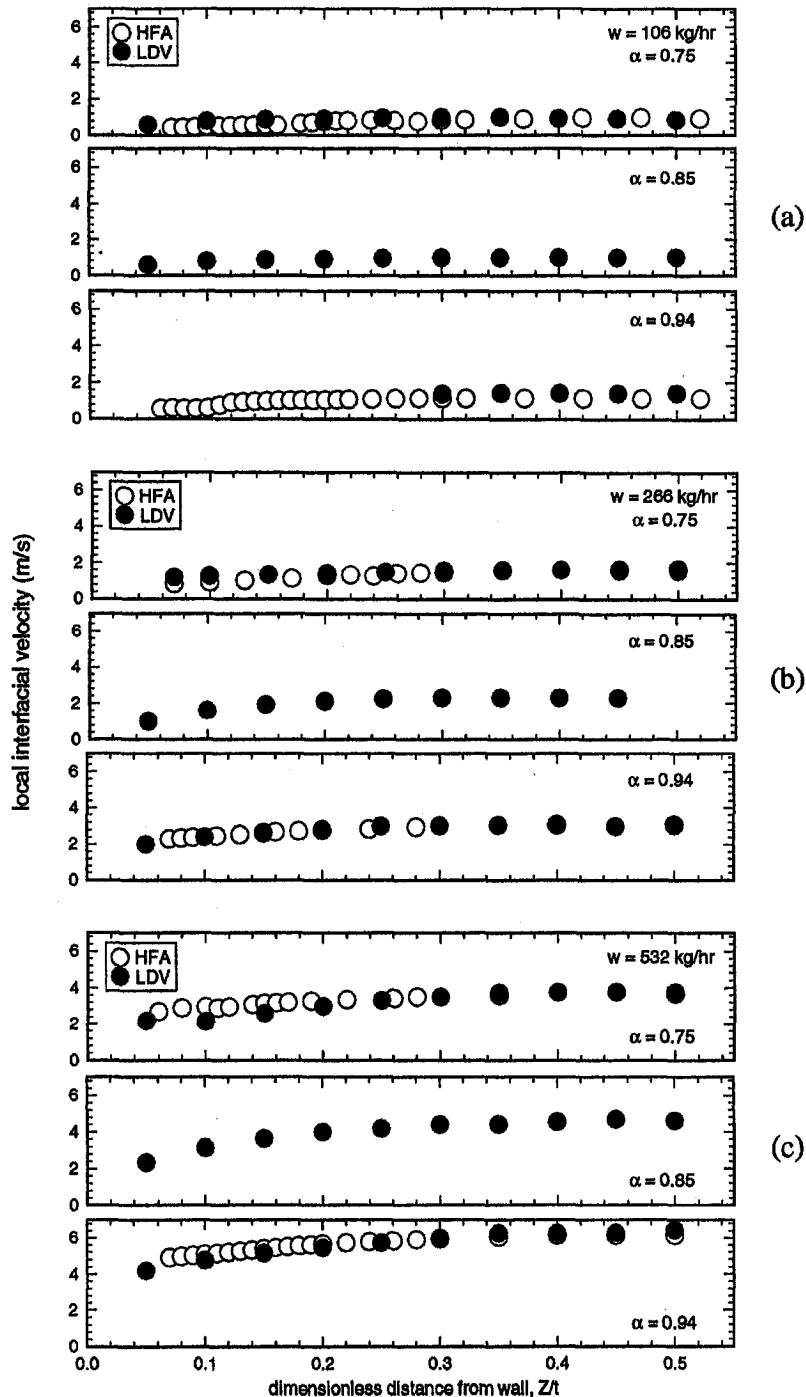


Fig. 5 Hot-film anemometer and laser Doppler velocimeter interfacial velocity profiles for (a) 106 kg/hr, (b) 266 kg/hr, (c) 532 kg/hr

especially near the duct centerline ($Z/t = 0.5$). In the near-wall region ($Z/t < 0.2$), the data sets differ somewhat, with the HFA data being the higher velocity in all cases except for the two lowest mass flow rates at $\alpha = 0.75$ (Fig. 5(a)). These variations may be attributed to inherent differences in the two measurement techniques. The effective size of the measurement volume in the Z dimension (approximately 0.25 mm for LDV and 0.03 mm for HFA) can influence the measurement of mean velocity, especially in a region of large-velocity gradient. Additionally, because the LDV measurement is spatially averaged over 0.25 mm, about one-tenth of the duct spacing dimension, it is possible that in the near-wall region both liquid droplets and slower interfacial waves are measured, thereby causing a negative bias

in the mean velocity. For the experiments with $\alpha = 0.94$, where the wall-bounded liquid film is thinner, the LDV and HFA data are in closer agreement.

From the outset, it was assumed that the annular flows investigated are two-dimensional because of the high width/thickness aspect ratio, and the measurements made in the duct center are representative of the droplet core measurements. To confirm the two-dimensionality, LDV measurements were taken at $Z/t = 0.5$ across the width (Y dimension) for selected conditions (not shown). The droplet velocity profiles are essentially flat across the width, except close to the edges where a thicker film and possibly bigger droplet size lower the droplet velocity.

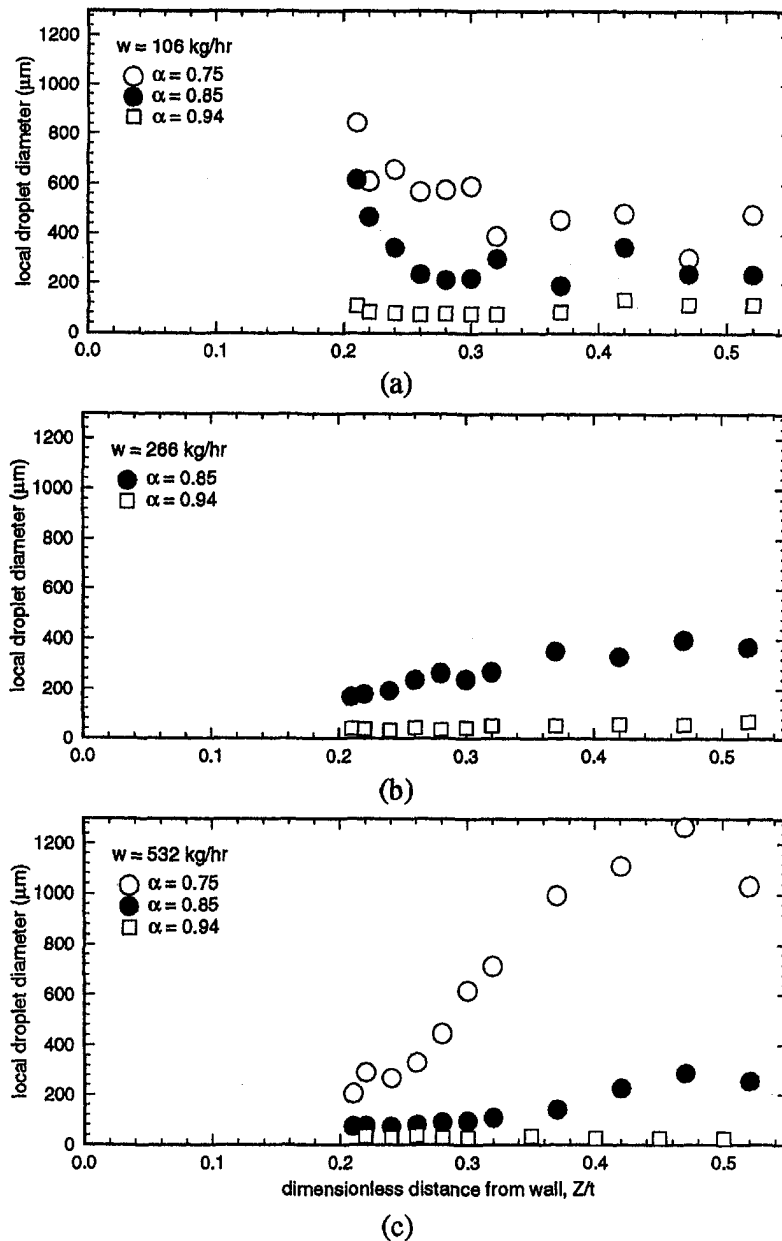


Fig. 6 Droplet diameter profiles for (a) 106 kg/hr, (b) 266 kg/hr, (c) 532 kg/hr

Droplet Size. As shown by previous investigators (Spindler et al., 1988; Trabold et al., 1994), the characteristic size of the dispersed droplet field can be estimated from local measurements of void fraction, velocity, and frequency through the relation

$$d_d = 1.5 \frac{V_d(1 - \alpha)}{f_d} \quad (7)$$

A similar relation was obtained experimentally by Lim and Agarwal (1990) and can also be obtained analytically using a method based on Galaup's (1976) work. Equation (7) is based on the following assumptions: (1) All droplets are spherical. (2) The droplets are randomly distributed about the HFA probe. This assumption strictly applies when the measured droplets are quite small. Once the droplets reach the size of approximately half the test section thickness, this assumption is no longer valid. (3) The nonsteamwise vapor velocity components are negligible. This is a reasonable assumption for most experimental conditions along the Z-axis since the HFA probe should not be exposed to any cir-

culating flow regions. Droplet size calculations are not reported for spacing positions where the presence of the wall and liquid film may have influenced the random motion of the droplet field.

The dispersed liquid droplet diameter data for three mass flow rates at $\alpha = 0.75, 0.85,$ and $0.94,$ are illustrated in Fig. 6. The most obvious trend is that the droplet diameter generally decreases with increasing average void fraction. Also, because d_d varies as $(1 - \alpha),$ the shape of the drop size profiles tends to follow a trend which is the inverse of that observed for the local void fraction, as in most cases the gradients in measured droplet frequency and velocity are small for $Z/t > 0.2.$

For the cases at $w = 106$ kg/hr with $\alpha = 0.75$ and 0.85 where center-peaked void fraction profiles were observed, the droplets appear to be larger in the vicinity of the co-flowing liquid film and smaller near the duct centerline (Fig. 6(a)). The droplets are likely generated near the interface between liquid film and continuous vapor, due to the shearing of the roll waves. As discussed by Kocamustafaogullari et al. (1994), droplet size is controlled by the

interaction between the droplet and the surrounding turbulent gas stream. Hence, newly entrained droplets measured near the liquid film are larger, while droplets at the duct centerline are subjected to turbulent breakup and would, on average, be smaller. Conversely, for test conditions where wall-peaked void profiles were measured, the corresponding mean droplet diameter is significantly larger near $Z/t = 0.5$ (Figs. 6(b), 6(c)).

Several researchers (e.g., Tayali et al., 1990; Azzopardi and Teixeira, 1994a) have reported that droplet sizes measured in circular pipes increase upon moving from the pipe wall to the centerline. For the present experiments, this trend may be the result of physical processes which are characteristic of the duct cross section. For void fractions of 0.75 and 0.85 at mass flow rates of 266 and 532 kg/hr, the flow may be in the late stages of transition to annular flow, with liquid bridges extending across the narrow test section dimension. As these bridges are shattered by the high-velocity vapor, relatively large droplets are produced away from the liquid films on the test section walls. Because the liquid film at the wall is thinner in the middle of the duct width, it is also possible that droplets emanate from the edges where the film is considerably thicker. Consequently, larger droplets emerge from the roll waves at the edges than those arising from the thinner films on the wide walls of the test section. At $\alpha = 0.94$ for all three flow rates, the annular flow is fully developed and the droplet size is fairly constant across the duct.

A recent correlation for mean droplet size in annular flows has been developed by Kocamustafaogullari et al. (1994). His expression for the Sauter mean droplet diameter, considering the maximum stable droplet size in the turbulent vapor core, is given by

$$\frac{d_{sm}}{D_h} = 0.65 C_w^{-(4/15)} We_m^{-(3/5)} \left(\frac{Re_g^4}{Re_l} \right)^{1/15} \times \left[\left(\frac{\rho_g}{\rho_l} \right) \left(\frac{\mu_g}{\mu_l} \right) \right]^{4/15} \left(\frac{\Delta\rho}{\rho_l} \right)^{-(3/5)} = 0.65 K \quad (8)$$

where

$$C_w = \frac{1}{35.34 N\mu^{0.8}} \quad \text{for } N\mu \leq \frac{1}{15} \quad (9)$$

$$N\mu = \text{viscosity number} = \frac{\mu_f}{\left[\rho_l \sigma \left(\frac{\sigma}{g \Delta\rho} \right)^{1/2} \right]^{1/2}} \quad (10)$$

It is instructive to compare the present R-134a data with other open literature results as well as the relation of Kocamustafaogullari et al. (Eq. (8)), because the latter has been demonstrated to reasonably predict droplet diameters in a variety of flows having wide ranges of physical properties. In order to apply Eq. (8) for fluids having small vapor-to-liquid density ratios, such as refrigerant fluids, the term $(\Delta\rho/\rho_l)^{-3/5}$ has been added to the right-hand side. This dimensionless parameter was omitted by Kocamustafaogullari et al. from the development of Eq. (8), based on the assumption that $\rho_l \gg \rho_g$. However, for R-134a at 2.4 MPa, the vapor and liquid densities are 130 and 953.1 kg/m³, respectively, so it is appropriate to include $(\Delta\rho/\rho_l)^{-3/5}$ in the droplet diameter expression. This term increases by 9.2 percent the calculated mean diameters for R-134a, but has no significant effect on these calculations for air-water and other similar systems.

As discussed above, the present droplet size data are calculated from measurements of void fraction, velocity, and droplet frequency. The void fraction and velocity results were confirmed by simultaneous measurements with a gamma densitometer and laser Doppler velocimeter, respectively. However, no such concomitant measurement exists for droplet frequency. If all droplets striking the HFA sensor were counted, the droplet diameter from Eq. (7) would be an arithmetic mean. Based on the work of Goldschmidt (1965) and others, it is reasonable to expect that some droplet impactions do not result in countable voltage pulses. Hence, the

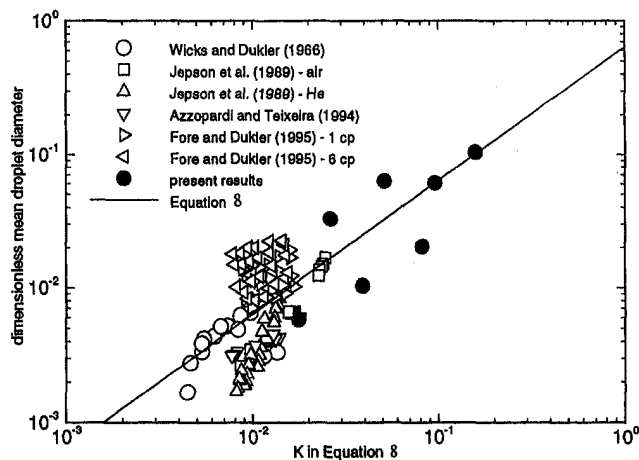


Fig. 7 Comparison of mean droplet size data to relation of Kocamustafaogullari et al. (1994) (see Table 2)

calculated mean droplet size is biased toward larger droplets. As will be seen next, this bias may account for the generally good comparison between the calculated mean diameter and the predicted Sauter mean diameter of other investigators.

A comparison among the average R-134a droplet diameter measurements, other open literature measurements, and the relation proposed by Kocamustafaogullari et al. is illustrated in Fig. 7. The parameter K (Eq. (8)) was calculated using R-134a physical properties at a saturation pressure of 2.4 MPa. The present data correspond to the integrated average of measurements obtained at spacing measurement positions $Z/t > 0.020$; data obtained at near-wall positions were omitted due to the potential for bias associated with the presence of the wall-bounded liquid film or nonrandom droplet motion. The calculated mean droplet size for the test run conducted at $w = 532$ kg/hr with $\alpha = 0.75$ is not included in Fig. 7. As mentioned previously, for this condition the significantly higher droplet size near the duct centerline is most likely the result of a different mechanism for droplet formation. Therefore, it is not reasonable to compare this data point with results for fully developed annular flows that exist at high void fractions.

The data plotted in Fig. 7, from both the present R-134a experiments and previous tests, show an appreciable amount of scatter about the line representing Eq. (8), but this relation reasonably describes the overall trend in the data. This is significant because of the wide variety of fluid physical properties, gas and liquid flow rates, and duct geometries investigated, and the various measurement techniques employed (Table 2). Perhaps the most encouraging aspect of this data comparison is that the liquid-to-gas density ratio varied from 7.3 for R-134a to 3700 in the helium-water experiments of Jepsen et al. (1989). These results suggest that the relation developed by Kocamustafaogullari et al. (1994) can be used to estimate the mean droplet size in various practical two-phase flow systems, in particular pressurized steam-water flows which have physical properties similar to those of R-134a.

Conclusions

Local data for void fraction, droplet frequency, and droplet velocity were obtained for upward annular flows of R-134a in a high aspect ratio vertical duct. The void fraction and velocity measurements acquired using the dual-sensor hot-film anemometer method were confirmed through simultaneous measurements with nonintrusive gamma densitometer and laser Doppler velocimeter systems. It was observed that the shapes of the void fraction and frequency distributions are strongly influenced by mass flow rate. Notably, at relatively high flows, the measured void fraction was highest near the wall, due to the thinning of the liquid film and

Table 2 Summary of mean droplet size experiments

Reference	Fluids	Hydraulic Diameter (mm)	We_m	ρ_l/ρ_g	μ_l/μ_g
Wicks and Dukler (1966)	air-water	33.7	320 - 4100	750	54
Jepson <i>et al.</i> (1989)	air-water	10.3	125 - 1130	555	54
Jepson <i>et al.</i> (1989)	helium-water	10.3	75-218	3700	52
Azzopardi and Teixeira (1994)	air-water	32.0	220 - 1180	830	57
Fore and Dukler (1995)	air-water	50.8	240 - 1110	847	57
Fore and Dukler (1995)	air-50% glycerin & water	50.8	340 - 1050	794	327
present work	R-134a	4.85	94 - 8950	7.3	6.5

significant droplet entrainment. Based on data available in the literature, at relatively high mass flows R-134a appears to have entrainment fractions which fall in the range measured for pressurized steam-water systems. The local diameter of liquid droplets dispersed in the vapor core was calculated from measurements of void fraction, frequency, and velocity. Despite the low liquid-to-vapor density ratio and low liquid surface tension, the relationship derived by Kocamustafaogullari *et al.* (1994) is reasonably accurate for prediction of the present mean droplet diameter results. The local measurements reported in this paper are useful for modeling high-pressure two-phase flows, and for assessment of two-fluid model computer codes.

Acknowledgments

The authors acknowledge the valuable contributions of Messrs. D. M. Considine, W. O. Morris, L. Jandzio, C. W. Zarnofsky, and E. Hurd in the operation of the test facility, and data acquisition and analysis. Dr. G. J. Kirouac is acknowledged for his overall direction of the R-134a experimental program.

References

Azzopardi, B. J., and Teixeira, J. C. F., 1994a, "Detailed Measurements of Vertical Annular Two-Phase Flow—Part I: Drop Velocities and Sizes," *ASME Journal of Fluids Engineering*, Vol. 116, pp. 792–795.

Azzopardi, B. J., and Teixeira, J. C. F., 1994b, "Detailed Measurements of Vertical Annular Two-Phase Flow—Part II: Gas Core Turbulence," *ASME Journal of Fluids Engineering*, Vol. 116, pp. 796–800.

Carvalho, R., and Bergles, A. E., 1992, "The Pool Nucleate Boiling and Critical Heat Flux of Vertically Oriented, Small Heaters Boiling on One Side," Rensselaer Polytechnic Institute, Heat Transfer Laboratory Report HTL-12, Aug.

Cousins, L. B., and Hewitt, G. F., 1968, "Liquid Phase Mass Transfer in Annular Two-Phase Flow: Droplet Deposition and Liquid Entrainment," UKAEA Report AERE-R5657.

Fore, L. B., and Dukler, A. E., 1995, "The Distribution of Drop Size and Velocity in Gas-Liquid Annular Flow," *Int. J. Multiphase Flow*, Vol. 21, pp. 137–149.

Galaup, J. P., 1976, "Contribution to the Study of Methods for Measuring Two-Phase Flow," Centre D'Etudes Nuclearires de Grenoble, Report No. 136.

Goldschmidt, V. W., 1965, "Measurement of Aerosol Concentrations with a Hot Wire Anemometer," *J. Colloid Sci.*, Vol. 20, pp. 617–634.

Goldschmidt, V. W., and Eskinazi, S., 1966, "Two-Phase Turbulent Flow in a Plane Jet," *ASME Journal of Applied Mechanics*, Vol. 33, pp. 735–747.

Hadded, O., Bates, C. J., and Yeoman, M. L., 1985, "Simultaneous Two-Phase Flow Measurement of Droplet Size and Velocity in a 32 mm Diameter Pipe," *International Symposium on Laser Anemometry*, FED-Vol. 33, ASME, New York, pp. 103–109.

Hewitt, G. F., and Hall-Taylor, N. S., 1970, *Annular Two-Phase Flow*, Pergamon Press, Tarrytown, NY.

Jepson, D. M., Azzopardi, B. J., and Whalley, P. B., 1989, "The Effect of Gas Properties on Drops in Annular Flow," *Int. J. Multiphase Flow*, Vol. 15, pp. 327–339.

Kataoka, I., Ishii, M., and Mishima, K., 1983, "Generation and Size Distribution of Droplets in Annular Two-Phase Flow," *ASME Journal of Fluids Engineering*, Vol. 105, pp. 230–238.

Keays, R. K. F., Ralph, J. C., and Roberts, D., 1970, "Liquid Entrainment in Adiabatic Steam-Water Flow at 500 and 1000 p.s.i.a.," AERE-R629.

Kocamustafaogullari, G., Smits, S. R., and Razi, J., 1994, "Maximum and Mean Droplet Sizes in Annular Two-Phase Flow," *Int. J. Heat Mass Transfer*, Vol. 37, pp. 955–965.

Lim, K. S., and Agarwal, P. K., 1990, "Conversion of pierced lengths measured at a probe to bubble size measures: An assessment of the geometrical probability approach and bubble shape models," *Powder Technology*, Vol. 63, pp. 205–219.

Lopes, J. C. B., and Dukler, A. E., 1986, "Droplet Entrainment in Vertical Annular Flow and its Contribution to Momentum Transfer," *AICHE J.*, Vol. 32, p. 1500.

Lopez de Bertodano, M. A., Jan, C.-S., and Beus, S. G., 1995, "Droplet Entrainment Correlation for High Pressure Annular Two-Phase Flow," *ANS Proceedings, National Heat Transfer Conference*, Vol. 8, pp. 3–10.

Spindler, K., Bierer, M., Lorenz, G., Erhard, A., and Hahne, E., 1988, "Measurements in Vertical Gas Liquid Two-Phase Flows Using an Optical Fiber Probe," *Experimental Heat Transfer, Fluid Mechanics and Thermodynamics*, Elsevier, New York, pp. 348–357.

Tattersson, D. C., Dallman, J. C., and Hanratty, T. J., 1977, "Drop Sizes in Annular Gas-Liquid Flows," *AICHE J.*, Vol. 23, pp. 68–76.

Tayali, N. E., Bates, C. J., and Yeoman, M. L., 1990, "Drop Size and Velocity Measurements in Vertical Developing Annular Two-Phase Flow," *Laser Anemometry—Proceedings of the 3rd International Conference*, J. T. Turner, ed., Springer-Verlag, New York, pp. 431–440.

Trabold, T. A., Moore, W. E., Morris, W. O., Symolon, P. D., Vassallo, P. F., and Kirouac, G. J., 1994, "Two Phase Flow of Freon in a Vertical Rectangular Duct, Part II: Local Void Fraction and Bubble Size Measurements," *Experimental and Computational Aspects of Validation of Multiphase Flow CFD Codes*, I. Celik *et al.*, ed., FED-Vol. 180, ASME, New York, pp. 67–76.

Trabold, T. A., Moore, W. E., and Morris, W. O., 1977, "Hot-Film Anemometer Measurements in Adiabatic Two-Phase Refrigerant Flow through a Vertical Duct," *ASME Fluids Engineering Division Summer Meeting, Vancouver, B.C.*, Paper FEDSM97-3518.

Trabold, T. A., Kumar, R., and Vassallo, P. F., 1998, "Annular Flow of R-134a in a Vertical Duct: Local Void Fraction, Droplet Velocity and Droplet Size Measurements," *ASME IMECE*, Nov., Anaheim.

Ueda, T., 1979, "Entrainment Rate and Size of Entrained Droplets in Annular Two-Phase Flow," *Bull. JSME*, Vol. 22, pp. 1258–1265.

Vassallo, P. F., Trabold, T. A., Moore, W. E., and Kirouac, G. J., 1993, "Measurement of Velocities in Gas-Liquid Two-Phase Flow Using Laser Doppler Velocimetry," *Experiments in Fluids*, Vol. 15, pp. 227–230.

Wicks, M., and Dukler, A. E., 1966, "In Situ Measurements of Drop Size Distribution in Two-Phase Flow—A New Method for Electrically Conducting Liquids," *Proc. of the 3rd Int. Heat Transfer Conf.*, Vol. 5, pp. 39–49.

Wurtz, J., 1978, "An Experimental and Theoretical Investigation of Annular Steam-Water Flow in Tubes and Annuli at 30 to 90 bar," RISO Report No. 371.

On the Prediction of Local Ice Formation in Pipes in the Presence of Natural Convection

A. C. Keary

Research Fellow,
e-mail: aky@mech.soton.ac.uk

R. J. Bowen

Senior Lecturer,
e-mail: rjb5@mech.soton.ac.uk

Department of Mechanical Engineering,
University of Southampton,
SO17 1BJ, UK

Pipe freezing is a pipeline maintenance technique which is used to isolate sections of a liquid-filled pipeline by freezing the contents to form a solid pressure-resistant plug. This paper describes the development of a numerical model of natural convection and solidification in a vertical water-filled pipe. The natural convection-driven flows are examined in detail and the interaction with the forming ice plug is studied. The results are compared with experimental data. The numerical approach is contrasted with a simpler one-dimensional analytical method and criteria are proposed to aid the choice of modeling technique under different conditions.

1 Introduction

Pipe freezing is a technique used to effect a temporary pipe blockage by deliberately creating a solid plug inside the pipe. A jacket, typically two or three pipe diameters long, is placed around the pipe and filled with a cryogen, such as liquid nitrogen. This cools the fluid in the pipe causing it to freeze and form a plug. Repeating this at another point isolates the section in between which can then be opened in order to carry out a repair or to add, for instance, a valve or junction. Using pipe freezing can eliminate the need to decommission a large section of the plant and it is less expensive than other plugging techniques which also require more complex equipment and more space around the pipe. Although pipe freezing appears to be a simple technique, the processes taking place inside the pipe as the plug grows can be complex. It is difficult to assess what is happening inside a pipe during a freeze and to determine when the plug has completely sealed the pipe. Convection in the liquid can influence the rate at which the plug freezes; even with no pressure-driven flow in the pipe, the temperature of the liquid may be sufficient to cause significant natural convection which transports heat into the freezing zone, slowing or stopping freezing. In practice it is desirable to know in advance whether a freeze isolation is possible and the expected duration of the process. The work described in this paper aims to provide a model which will address these requirements.

In many cases, the pipe freezing problem may be fully three-dimensional, however, under the conditions considered for this work, namely laminar natural convection in a vertical pipe, it is predominantly two-dimensional. The particular problem considered here is of freezing a water-filled pipe using liquid nitrogen. The problem is transient and includes phase change (water-ice), heat conduction in the ice and pipe wall, natural convection in the water, and heat transfer to the boiling nitrogen on the outside surface of the pipe.

2 Experimental Results

Previous experimental research at Southampton has studied the role of natural convection during freezing. The results from these experiments, carried out in vertical pipes, are reported by Burton (1986), Bowen and Burton (1988), and Tavner (1992). Their findings are summarized in the following points.

Contributed by the Heat Transfer Division for publication in the JOURNAL OF HEAT TRANSFER. Manuscript received by the Heat Transfer Division, Aug. 2, 1998; revision received, July 8, 1999. Keywords: Heat Transfer, Modeling, Natural Convection, Phase Change, Solidification. Associate Technical Editor: C. Beckermann.

2.1 Effect of Pipe Size and Initial Temperature on Freezing.

Experiments were carried out using static water in vertical pipes for varying initial temperatures in four different pipe sizes (100-mm, 150-mm, 200-mm, and 250-mm diameter). At low temperatures, convection is negligible and the freezing time was found to be determined by the rate at which the latent and sensible heats can be removed from the water and ice. This is roughly proportional to the cross-sectional area of the pipe and increases almost linearly with initial temperature. At higher temperatures, convection becomes more significant, increasing the heat flux from the water to the freezing front and extending the freezing time. Increasing the initial temperature further reaches a limiting temperature where the heat flow to the freezing front from the water exceeds that conducted away through the ice, and a complete solid plug will not form. The limiting temperature is lower for larger diameter pipes.

The values of limiting temperature lie on a line of constant Grashof number (2.1×10^9 , based on the jacket length). The dependence on Grashof number suggests that the limiting behaviour is linked to the transition to turbulent convection.

2.2 Interaction Between Convection and Plug Formation.

Burton (1986) examined the effect of varying the volume of water below the freezing zone in a vertical pipe and found it had a significant effect on the shape of the plug. With the pipe closed two diameters below the freezing zone, the plug "closed off" near the axial center of the plug. The bulk temperature of the water in the pipe decayed steadily throughout the freeze and the initial temperature had little effect on the shape of the ice plug. When a large tank of water was placed below the freezing zone (to simulate a long length of pipe) the bulk temperature remained constant. The neck position migrated up the plug during freezing, finally closing off above the axial center of the plug; this vertical asymmetry increased with increasing water temperature.

The neck migration was attributed to interference between the downward boundary layer and the upward core flow at the plug neck when the ice reaches a critical thickness. The water above the neck is trapped and cools rapidly, increasing the local ice growth with the result that the neck moves up the plug. Tavner (1992) noted that the critical ice thickness at the neck decreased with increasing initial water temperature.

2.3 Variation of Bulk Temperature Inside the Freezing Zone.

Burton's experiments show that as the freeze progresses there is a decline in the temperature of the water in the freezing zone when the initial temperature is less than 20°C but very little decline at temperatures above 20°C. During experiments using a longer distance between the freeze and the tank (Tavner), temperature decay was noted at initial temperatures up to 30°C. The

temperature decay can be attributed to the formation of a mixing zone below the freeze in which the cold downward flowing boundary layer cools the upward core flow. These results suggest that as the initial water temperature increases the bottom of the mixing zone moves down the pipe. Once this reaches a change of section of sufficient size, such as a tank, the mixing process is destroyed. The water in the freezing zone is no longer thermally isolated from the main body of water in the pipe and the temperature in the freezing zone is maintained at the initial temperature.

3 Analytical Model

The accuracy and usefulness of a simplified analytical model was investigated as part of this study. This combined previous models for freezing in a pipe (London and Seban, 1943; Lannoy, 1980) with the method of predicting the heat transfer by convection obtained by Bejan (1984) and is described in more detail by Keary (1995) and Keary and Bowen (1998). It was assumed that there was no axial conduction and that a steady temperature distribution existed in the ice.

The rate at which the freezing front moves is governed by the rate at which heat arrives at the interface due to convection in the liquid and the rate at which it is removed by conduction through the forming solid. In the case of one-dimensional solidification, the velocity of the solid/liquid interface is given in Eq. (1).

$$\frac{dR_i}{dt} = \frac{1}{\rho(L + c_i(T_b - T_i))} \left[h(T_b - T_i) + \frac{T_c - T_i}{R_i \left(I + \frac{1}{k_s} \ln \frac{R_w}{R_i} \right)} \right] \quad (1)$$

$$I = \frac{1}{R_w^0 h_c} + \frac{1}{k_w} \ln \frac{R_w^0}{R_i^0}$$

The separate parts of the impedance term, I , are, in order, the impedance of heat transfer to the coolant and the impedance due to the pipe wall. For the case where liquid nitrogen is used as the coolant, the heat transfer coefficient, h_c , depends on the temperature of the pipe wall and varies from around 10–60 W/m²K. This gives a maximum impedance of around 4×10^{-3} mK/W, in a 50-mm diameter pipe. The pipe wall thicknesses are typically between three percent to ten percent of the pipe diameter, giving a maximum impedance of around 4×10^{-3} mK/W. The impedance offered by a growing plug increases then decreases as the plug forms, reaching a maximum value when its radius is given in Eq. (2).

$$R_i = R_w^i e^{-1+k_s} \quad (2) \quad \text{where}$$

The maximum total impedance of coolant, wall, and ice is the reciprocal of the conductivity of ice (approximately 0.45 mK/W). It is therefore apparent that the impedance offered by the ice is the most significant in the conditions considered here. The impedance of the coolant and pipe wall may be significant in other situations, for example, with pipe walls with lower conductivity.

In this case, Eq. (1) may be approximated as shown in Eq. (3).

$$\frac{dR_i}{dt} = \frac{1}{\rho(L + c_i(T_b - T_i))} \left[h(T_b - T_i) + \frac{k_s(T_c - T_i)}{R_i \ln \frac{R_w}{R_i}} \right] \quad (3)$$

Bejan's integral analysis gives the following expression (Eq. (4)) for the heat transfer coefficient over a vertical flat plate at a constant and uniform temperature T_i in a semi-infinite fluid of temperature T_b .

$$h = \frac{k_l \text{Ra}_z^{0.25}}{fz}$$

$$f = \left(\frac{8(q + 0.5)(q + 1)}{3q(q + 2)} \right)^{0.5}, \quad \text{Pr} = \frac{5}{6} q^2 \frac{q + \frac{1}{2}}{q + 2} \quad (4)$$

The heat transfer coefficient includes a vertical distance, z , in both the denominator and the Rayleigh number. The heat transfer coefficient therefore decreases as the flow moves downward over the cooled surface. For the case of modeling pipe freezing, this position, z , was taken as the position of the plug neck. Incorporating this into Eq. (3) and converting the Rayleigh number to Ra_R , based on the pipe radius, gives Eq. (5).

$$\frac{dR_i}{dt} = \frac{1}{\rho(L + c_i(T_b - T_i))} \left[\left(\frac{z}{R_w} \right)^{0.75} \frac{k_l \text{Ra}_R^{0.25}}{fz} (T_b - T_i) + \frac{k_s(T_c - T_i)}{R_i \ln \frac{R_w}{R_i}} \right] \quad (5)$$

Rewriting in terms of nondimensional parameters gives Eq. (6).

$$\frac{d\xi_i}{dt} = \frac{\text{Ste}}{1 + \varsigma \text{Su Ste}} \left[\frac{\kappa \text{Su Ra}_R^{0.25}}{f\eta^{0.25}} + \frac{1}{\xi_i \ln \xi_i} \right], \quad (6)$$

Nomenclature

a = coefficient in discretized scheme
 c = specific heat capacity
 f = fraction (of phase, coefficient)
 g = acceleration due to gravity
 h = heat transfer coefficient
 H = enthalpy
 k = conductivity
 L = latent heat capacity
 r = radial coordinate radial dimension
 R = radius
 t = time
 t^* = nondimensionalized time ($k_s t / \rho c_i R_w^2$)
 T = temperature
 u = radial component of velocity
 w = vertical (axial) component of velocity
 z = vertical (axial) coordinate; vertical (axial) direction

Greek Symbols

β = thermal expansion coefficient
 Δ = change in
 μ = viscosity
 ρ = density
 ξ = nondimensionalized radial coordinate (R/R_w)
 η = nondimensionalized vertical (axial) coordinate (z/R_w)

Subscripts

b = bulk
 c = coolant
 i = interface
 s = solid
 l = liquid
 w = wall

N, S, E, W, P = north, south, east, west, grid point
 u = radial velocity

Superscripts

H = enthalpy
 T = temperature

Dimensionless Numbers

Grashof number = $\text{Gr}_z = (\beta g \Delta T \rho^2 z^3 / \mu^2)$
Prandtl number = $\text{Pr} = (\mu c_p / k)$
Stefan number = $\text{Ste} = [c_i(T_i - T_c) / L]$
Superheating number = $\text{Su} = (T_b - T_i) / (T_i - T_c)$

$$\kappa = \frac{k_l}{k_s}, \quad \varsigma = \frac{c_l}{c_s}$$

As noted earlier, the impedance offered to the heat conduction away from the freezing front to the coolant increases then decreases. If the right-hand side of the equation less than zero when the impedance is at a maximum, a complete plug will form. This is condensed into the following relationship (Eq. (7)) which can be applied to determine the maximum bulk temperature.

$$\text{Ra}_R^{0.25} \text{Su} = \left(e \cdot \frac{f}{\kappa} \cdot \eta^{0.25} \right) \quad (7)$$

This expresses the combination of pipe size, jacket length, initial temperature, and fluid properties for which it is just possible to form a plug. The jacket length is included on the right-hand side of the equation (through the definition of η) and parameters f and κ may be affected by temperature. In the case of water, the conductivity of ice varies strongly with temperature, making κ strongly dependent on coolant temperature. The variation in buoyancy coefficient and viscosity of water with temperature also has a significant effect on the Rayleigh number. In order to implement Eq. (7) to model water, it must be rewritten explicitly in terms of the temperature and the analysis loses the generality of the non-dimensional form.

An alternative form of this analysis is described and applied by Keary and Bowen (1998). This uses the dimensional form to specifically model freezing in water-filled pipes. The variation of the properties of water with temperature is incorporated explicitly and the full term for the impedance of the pipe wall and of heat transfer to the coolant is retained. The model was used to model freezing water in different diameter pipes, assuming a jacket length of twice the pipe diameter and using liquid nitrogen, and predicted freezing times and maximum temperatures. Agreement with the measured freezing times was good when the time to fill the jacket with nitrogen was included. In pipes less than 100–150 mm in diameter, the predicted values of limiting temperature were less than those corresponding to a Grashof number of 2.1×10^9 (experimental result for limiting temperatures). It is therefore proposed that two criteria are required to define the limiting temperature; below 100 mm the relationship is controlled by the effect of laminar natural convection whereas above 150 mm it is controlled by turbulent convection.

This model provides a method of scaling the effect of convection on freezing between pipe sizes by considering the ratio of the heat flux convected to the ice/water interface to that conducted away through the ice. This is summarized by the following relationship (Eq. (8)):

$$TD^{0.446} = \text{constant} \Rightarrow \text{constant effect of convection on freezing.} \quad (8)$$

This implies that, for example, the effect of convection on freezing at 20°C in a 100-mm diameter pipe is equivalent to that at 15°C in a 200-mm diameter pipe and at 27°C in a 50-mm pipe. Scaling is only valid under laminar conditions and in situations where there is no significant neck migration.

This analytical model provides a quick estimate of the freeze time and the limiting temperature and can be applied to different pipe sizes, fluid temperatures, jacket lengths, cooling methods, and even to different fluids. The model could be developed further to include an empirical expression for the turbulent heat transfer to the freezing front. However, in order to predict solidification in conditions where convection is important, a more detailed description of the full-transient two-dimensional problem is required. Such as scheme is described below.

4 Numerical Model

A numerical model was developed to predict the flow field and the forming plug in detail. The problem is described by the

transient Navier-Stokes equations combined with phase change. The governing partial differential equations are included below (Eq. (9)).

$$\begin{aligned} \rho \frac{\partial u}{\partial t} + \rho u \frac{\partial u}{\partial r} + \rho w \frac{\partial u}{\partial z} &= \mu \left[\frac{\partial^2 u}{\partial r^2} + \frac{1}{r} \frac{\partial u}{\partial r} + \frac{\partial^2 u}{\partial z^2} - \frac{u}{r^2} \right] - \frac{\partial p}{\partial r} \\ \rho \frac{\partial w}{\partial t} + \rho u \frac{\partial w}{\partial r} + \rho w \frac{\partial w}{\partial z} &= \mu \left[\frac{\partial^2 w}{\partial r^2} + \frac{1}{r} \frac{\partial w}{\partial r} + \frac{\partial^2 w}{\partial z^2} \right] - \frac{\partial p}{\partial z} - \rho g \\ \frac{\partial \rho}{\partial t} + \frac{1}{r} \frac{\partial(\rho u r)}{\partial r} + \frac{\partial(\rho w)}{\partial z} &= 0 \\ \rho \frac{\partial H}{\partial t} + \rho u \frac{\partial H}{\partial r} + \rho w \frac{\partial H}{\partial z} &= k \left[\frac{\partial^2 T}{\partial r^2} + \frac{1}{r} \frac{\partial T}{\partial r} + \frac{\partial^2 T}{\partial z^2} \right] \quad (9) \end{aligned}$$

The finite volume method was used with the well-known SIMPLER algorithm (Patankar, 1980) to predict convection. The Boussinesq approximation was applied, namely that the density can be treated as constant throughout the formulation, with the exception of in the buoyancy source.

Freezing introduces complexities, in particular the release of latent heat and the continuous movement of the boundary between the liquid and solid regions. The methods that have been used to model freezing and melting fall into two categories, depending on the treatment of the solid and liquid regions. The first is a moving grid or boundary immobilisation method in which the location of the interface remains fixed in relation to the grid and the equations are solved separately in the two regions. The alternative method is a fixed grid approach in which the equations are formulated so that they are equally applicable in the solid and liquid phases. While moving grid methods appear more attractive at first sight they become complex when applied to problems such as pipe freezing which involve a high degree of grid distortion.

The fixed grid enthalpy methods proposed by Shamsundar and Sparrow (1975); Voller and co-workers (1981, 1987); and Cao, Faghri, and Chang (1989) were considered for this analysis. Shamsundar and Sparrow retain both the total enthalpy and the temperature as dependent variables in the governing equations and use a point-by-point scheme to obtain consistent values of each variable at each grid point. Voller et al. divide the total enthalpy into the sensible heat, which is continuous throughout the phase-change material, and latent heat contributions, which is treated as a heat source. Cao, Faghri, and Chang include the conductivity in the definition of the relationship between enthalpy and temperature, thus incorporating the three distributions with discontinuities (enthalpy, specific heat capacity, and conductivity) into one enthalpy-dependent function. The resulting equations are formulated with the total enthalpy as the dependent variable and the latent heat release is effectively treated as a source term. The three methods were used to model freezing water in one dimension and the results compared with the analytical solution (Carslaw and Jaeger, 1959) for the Neumann problem (with different values of thermal diffusivity in the liquid and solid phases). The method of Cao et al. was found to be the fastest, however, stability problems were encountered if the interface jumped several control volumes in one time step. The method of Voller was found to be faster than that of Shamsundar et al. only when the correction proposed by Brent (1988) was used. This correction required several attempts to obtain the best value of an under-relaxation factor, which was grid dependent. One major drawback in formulating the governing equations in terms of a single enthalpy variable is the difficulty in incorporating a third material (the steel pipe wall) into the model. This will cause a discontinuity in both the sensible and the total enthalpy distributions, which will complicate the solution and require separate calculations for the water/ice and steel regions. The method of Shamsundar et al. was therefore chosen.

The fundamental energy equation in Eq. (9) was discretized into the finite volume form (for a grid point P surrounded by North,

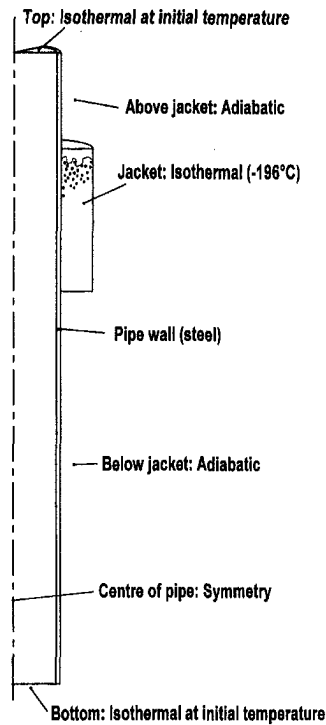


Fig. 1 Model domain and boundary conditions for numerical model ("closed" pipe)

South, East, and West neighbors) in terms of enthalpy and temperature, as shown in Eq. (10).

$$a_p^H H_p + a_p^T T_p = a_E T_E + a_W T_W + a_N T_N + a_S T_S + b \quad (10)$$

The relationship between the enthalpy and temperature is given in Eq. (11), making use of known relationships between the specific heat capacities of ice and water, c_s and c_L , and temperature.

$$H = \int_T^0 c_s(T) dT \quad T, H \leq 0 \quad \text{solid } f_s = 1$$

$$H = L + \int_0^T c_L(T) dT \quad T \geq 0, H \geq L \quad \text{liquid } f_s = 0$$

$$0 < H < L \quad T = 0 \quad \text{solidifying } f_s = 1 - \frac{H}{L} \quad (11)$$

These equations are solved on a point-by-point basis to obtain consistent values of temperature and enthalpy that satisfy Eq. (11)

Table 1 List of properties and parameters

Physical Properties				
Property	Units	Water	Ice	Steel
Density	kg/m ³	Look-up table (constant in continuity equation)	920	7810
Conductivity	W/mK	0.6	2.1725-3.403x10 ⁻³ T+9.085x10 ⁻⁶ T ²	16.0
Specific heat capacity	J/kgK	4200	2117+3.90T	420
Viscosity	kg/ms	Look-up table	-	-
Latent heat	J/kg	333500	-	-
Parameters used in numerical model				
Time step	s	1		
Grid spacing:				
Radial	mm	48x1mm, 4x0.5mm, (wall: 4x1.25mm)		
Vertical		3x5mm, 124x8mm, 3x5mm (convection only)		
		3x5mm, 36x10mm, 88x8mm, 3x5mm ('closed')		
		2x5mm, 48x8mm, 2x5mm ('open')		

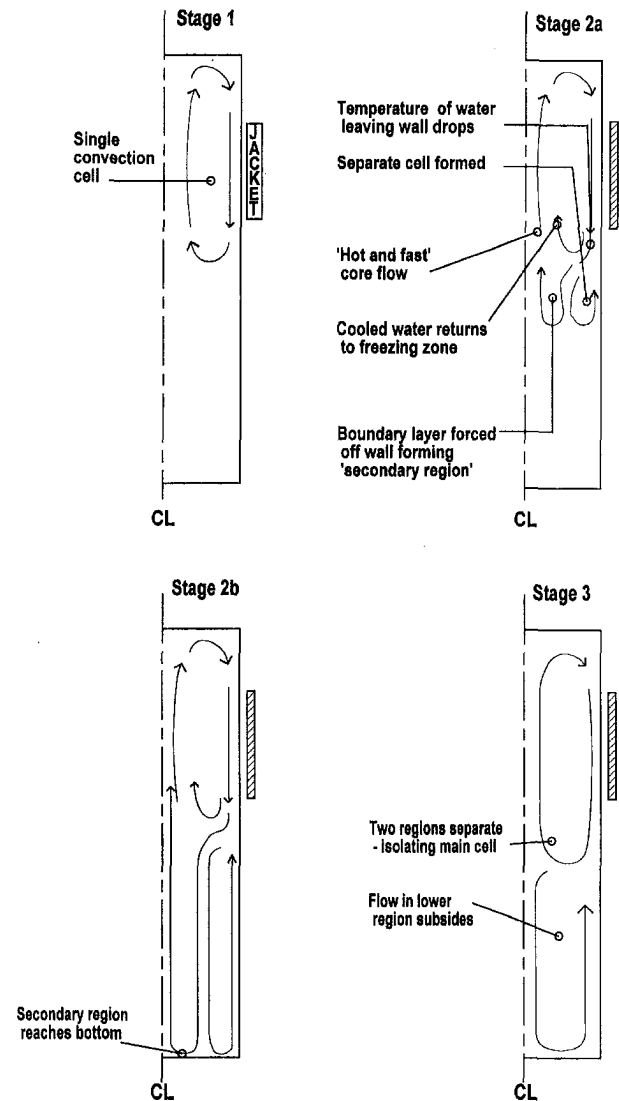


Fig. 2 Sketch of the development of the flow field

at all grid points. Control volumes lying on the solid-liquid boundary have a temperature fixed at the freezing temperature (0°C) and an enthalpy lying between zero and the latent heat of solidification.

The velocity in the solid and solidifying control volumes is forced to zero using the porosity-based approach described by Hibbert (1988). This method results in the inclusion of an extra term in the velocity equation, as shown in Eq. (12).

$$a_p u_p = a_E u_E + a_W u_W + a_N u_N + a_S u_S + b + B_u$$

$$B_u = -f_u (e^{f_s} - 1) u_p$$

$$(a_p + f_u (e^{f_s} - 1)) u_p$$

$$= a_E u_E + a_W u_W + a_N u_N + a_S u_S + b \quad (12)$$

The vertical velocity, w , is treated in the same way.

Thus, as the solid fraction, f_s , of the control volume increases from zero to one, the right-hand side of the equation increases to a level determined by the velocity immobilisation factor, f_u . Using an exponential term in the source term causes a slow initial decrease in velocity as the solid fraction increases from zero, followed by a more rapid decrease as the solid fraction approaches unity. This was found to be more stable than modifying the viscosity of solidifying control volumes. (The choice of value for f_u and f_w is discussed later.)

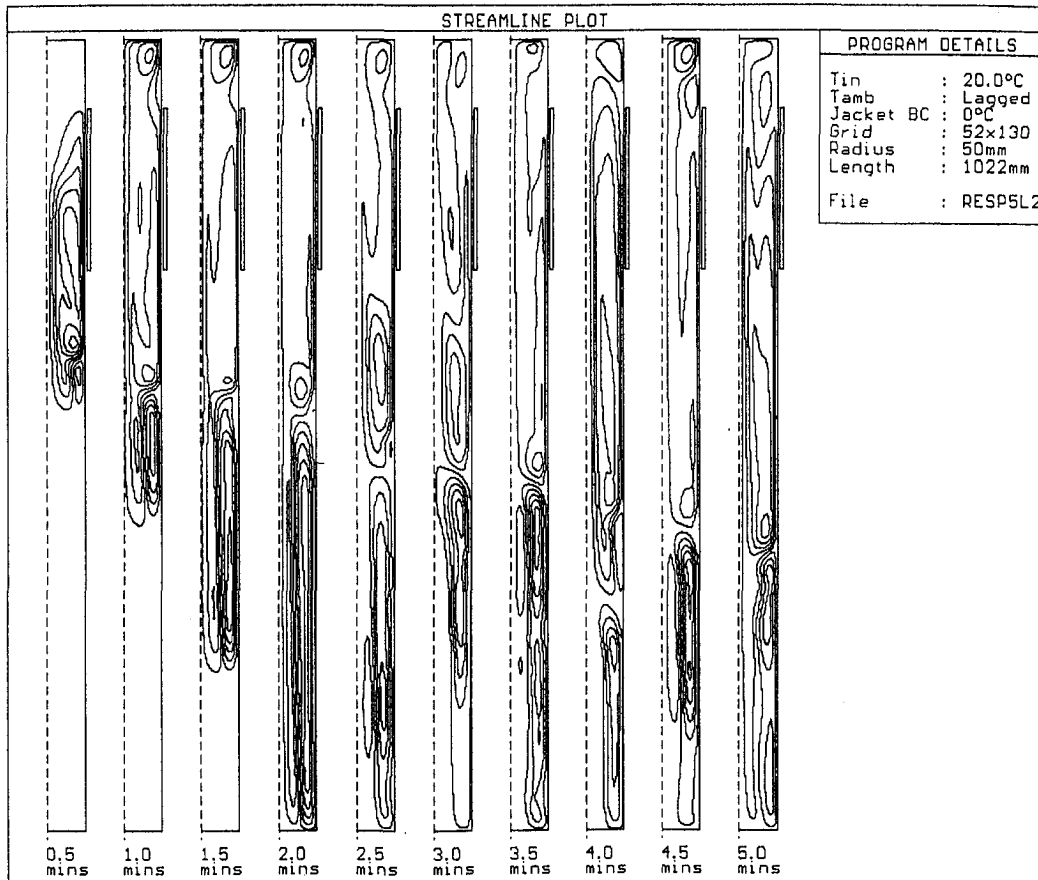


Fig. 3 Predicted flow development (streamlines) in water initially at 20°C, no freezing

A FORTRAN computer program was written specifically for this application and was extensively validated during its development against published benchmark tests. The model was used to predict steady-state natural convection in a square cavity with no freezing for comparison with the benchmark results obtained by de Vahl Davis (1983) and by Markatos and Pericleous (1984). The predicted velocities agreed with the published data from the two studies to within five percent (the average difference was less than three percent) for Rayleigh numbers of 10^3 , 10^4 , and 10^5 . At 10^6 , bordering turbulence, the differences ranged from 2 percent to 12 percent. These differences were comparable with the level of agreement between de Vahl Davis and Markatos and Pericleous. The prediction of natural convection in a cylinder was compared with data published by Huang and Hsieh (1987); comparison of the temperature and velocity distributions showed excellent agreement. The prediction of solidification in the absence of convection was tested using the analytical solution for one-dimensional freezing in a semi-infinite cavity (Carslaw and Jaeger, 1959) and also using published benchmark results (Shamsundar and Rooz, 1988) for transient freezing in a square cavity. For Stefan and Biot Numbers of 0.1, the average differences between these predictions and the published data (in terms of heat flux at a point, surface integrated heat flux, interface position and frozen fraction) at five points in time was less than 1.1 percent. With Stefan and Biot numbers of 1.0, the average difference in surface integrated heat flux and frozen fraction at three points in time was less than one percent.

The convection and solidification solution routines were combined into the final model and tests were carried out to investigate the sensitivity of the model to the grid density. Freezing with natural convection in water initially at 18°C in a 654-mm long, 100-mm diameter, pipe was taken as the test case and the effect of varying the radial grid spacing (0.5 mm, 1 mm and 2 mm) and the vertical grid spacing (5 mm, 8 mm, and 16 mm) was investigated. The predicted flow field was more sensitive to variations in the

radial grid spacing than in the vertical spacing and it was found decreasing the grid spacing below 1 mm in the radial direction and 8 mm in the vertical direction gave no significant changes in the predicted flow field.

Setting a very high value of the velocity immobilization factor, f_u , forces the velocity to near zero in the solid region; however, it may cause instabilities in the solution because it effectively imposes a discontinuous velocity switch-off. A value of 10^6 was initially chosen; this was found through a process of trial and error to be sufficient to force the velocity in the solidified regions to less than 0.05 percent of the velocity in the boundary layer. Further investigations were carried out under the same conditions as the grid sensitivity tests to assess the sensitivity of the solution to this factor. The results obtained with the a value of 10^5 did not look reasonable because they included significant velocities near the interface and a more rapid decay of the bulk temperature away from the ice than expected. The results obtained with values of 10^6 and 10^7 were very similar and therefore the value of 10^6 was chosen because it was the lowest value to give reasonable results.

The predicted solid-liquid interface moves in a "step-wise" manner that is a characteristic of the enthalpy method. Some problems were experienced in obtaining a converged solution for the enthalpy distribution at all time steps and oscillations in the enthalpy-temperature distributions both in the solidifying control volume and in the neighboring control volumes were encountered. The changes in the enthalpy distribution were of the order of ± 1000 J/kg, which is equivalent to an interface movement of ± 3 μ m. The oscillation was maintained when the interface position oscillated from one control volume to another. This was due to the fact that the distribution of conductivity (which changes from around 2.2 W/mK in ice to 0.6 W/mK in water) was recalculated during the solution procedure. The conductivity was therefore only updated at the beginning of a time step; this minimized the oscil-

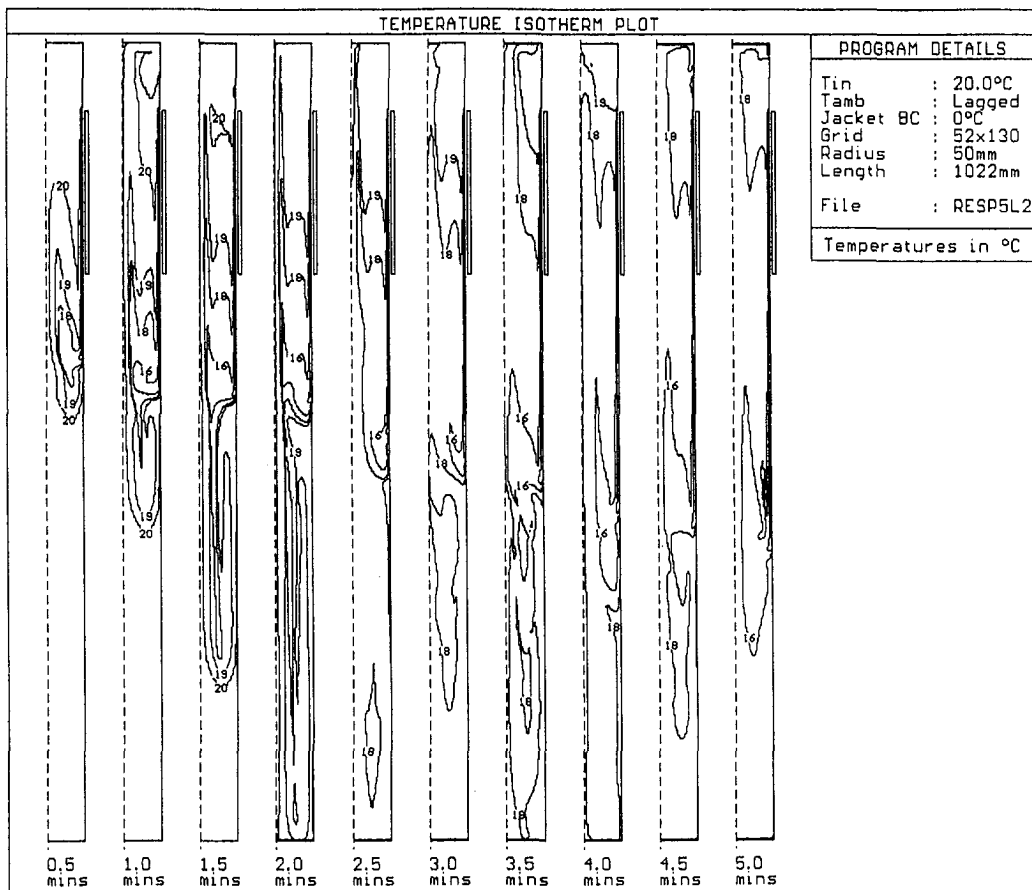


Fig. 4 Temperature field predictions for water initially at 20°C, no freezing

lation, at the cost of introducing a small error in the position of the interface.

The model was used to simulate convection in the absence of freezing in a long vertical pipe with a "closed" bottom and convection with freezing, both in a long "closed" pipe and in a shorter pipe with an "open" lower boundary. For the case of convection with freezing, a 5-mm thick, mild steel wall was included in the domain. In all cases, the water was assumed to be initially static and isothermal. The domain and the boundary conditions are shown in Fig. 1 for the "closed" pipe simulations. The properties and parameters used in these tests are listed in Table 1 and the results from these studies are described below.

4.1 Development of the Flow Field. The model was initially used to investigate the development of the convection driven flow field with no freezing and no pipe wall. A "closed" length of pipe, 100 mm in diameter and 1020 mm long was modeled; convection was driven by a cooled section of wall (set at 0°C) 730 mm from the bottom and 200 mm long. The predictions show that a toroidal convection cell becomes established with water moving downward at the outside of the cell close to the pipe wall and upward at the center of the pipe. As the flow field develops, the results indicate that the temperature of the boundary layer at the point at which it "peels" off the pipe wall to move radially inwards is somewhat lower than that of the surrounding liquid. Following this, a complicated combination of convection cells develops. Close study of the flow development over the first few minutes shows a three-stage process which is sketched in Fig. 2 and described in more detail below.

The down-flowing boundary layer flow is sandwiched between the pipe wall on its outer face and the core flow moving upwards on its inner face. There appears to be a maximum thickness for the boundary layer and the core flow, when an increase in the thick-

ness of one layer will reduce the thickness of the other and force a large increase in velocity to maintain the flow rate thereby increasing the shear between the two flows. The shear at the interface between the boundary layer and the core flow decelerates the boundary layer flow, making the boundary layer "peel" off the wall when it is cooler than the surroundings.

As the temperature at the bottom of the convection cell decreases (Stage 1) a separate recirculation region starts to appear below the original (main) convection cell marking the beginning of Stage 2. This is a result of the cooler liquid at the bottom of the main convection cell cooling the static water immediately below it. This starts a downwards flow approximately halfway between the center of the pipe and the wall and a corresponding up-flow next to the pipe wall which pushes the boundary layer flow off the wall, augmenting the shear effect and acting to support the main cell. As time continues, the temperature at the bottom of the main convection cell decreases further and a secondary region starts to form off the bottom of the main cell, between the center of the pipe and the separate cell. This results in a fast up-flow over a small area at the center of the pipe. Only a portion of the cold water in the main cell joins the secondary region and therefore the bulk temperature within the main cell gradually decreases.

The secondary region stretches gradually (at an approximately constant rate) down the pipe, together with the separate region (Stage 2b) while the height of the bottom of the main convection cell stabilizes and the bulk temperature inside the freezing zone decays. When the secondary region reaches the bottom of the pipe, it breaks off the main region and falls down the pipe, resulting in two separate regions. The lower region slowly stabilizes, stratified, at which point the cooled flow from the main cell starts to extend into the lower region again. There is, therefore, a periodic motion, with the secondary region

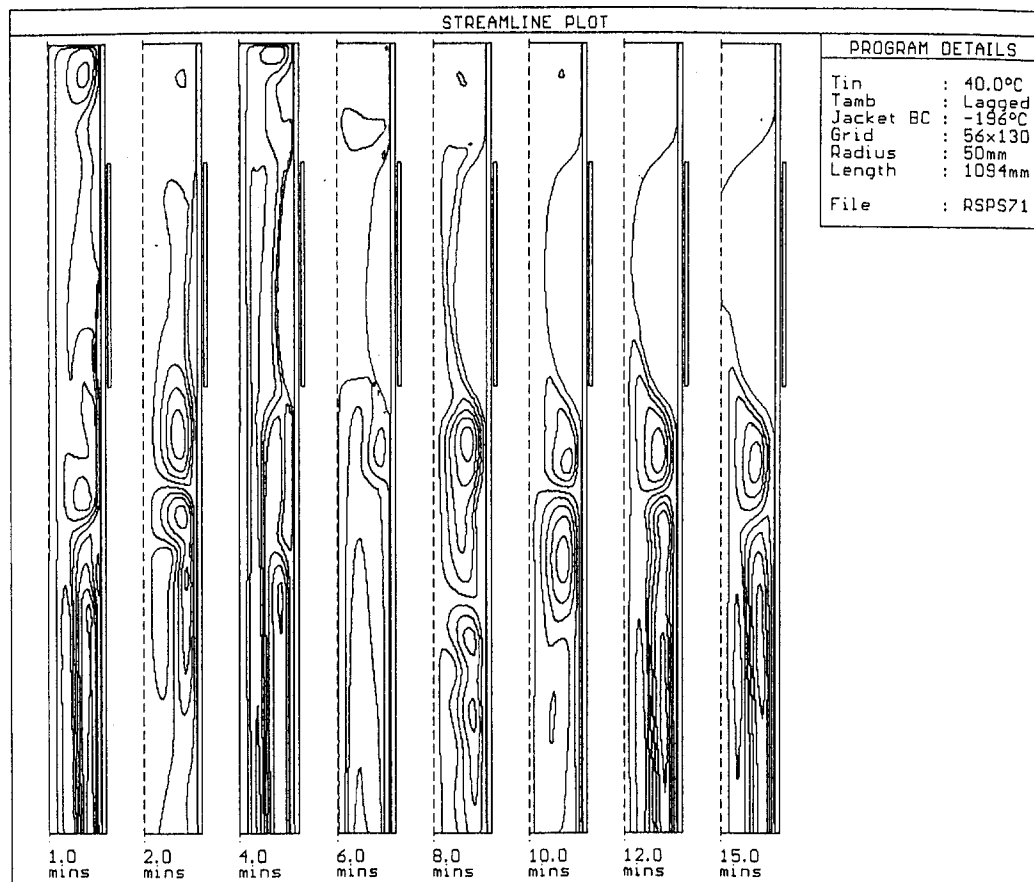


Fig. 5 Predicted flow development (streamlines) in water initially at 40°C with freezing

forming, dropping to the bottom, and breaking off. The height of the bottom of the main cell varies as the flow patterns change, moving upwards when the regions are separate and dropping down as the secondary section reforms.

When the main cell is separate (Stage 3), the rate of bulk temperature decay in the cooled zone increases. When the secondary region reforms the decay rate decreases. Using a "closed" pipe model, the lower region is cooled and so the decay rate is greater than it would be if the pipe were infinitely long.

An example of this is shown in Figs. 3 and 4. Figure 3 shows the growth of the convection cells in a 100-mm diameter pipe, with a cooled wall section (0°C), and initial temperature of 20°C using streamlines (calculated from the velocity distributions); Fig. 4 shows the temperature distribution (using isotherms) at 30-second intervals. The pipe axis is on the left side of each plot and a long thin box indicates the position of the cooled wall section. This shows more detail of the flow development sketched in Fig. 2.

Repeating the simulation with higher temperatures showed that the increase in buoyancy forces cause the main convection cell to drop further down the pipe. Above 30°C, the distance to the bottom of the main cell did not stabilize before the mixing region below reached the bottom of the domain.

The experimental results of Burton (1986) and Tavner (1992) provide some corroboration of this behavior and indicate that when the convection cell extends into a tank the mixing effect is destroyed, halting the decay in bulk temperature. The numerical predictions indicate that the main region would enter the tank for initial temperatures slightly above 20°C in Burton's rig and somewhere between 25°C and 30°C in Tavner's rig. This agrees with the experimental results for the maximum initial temperature at which bulk temperature decay was noted.

The mixing effect decreases with increasing pipe diameter and does not appear to have a significant effect in pipes greater than

200-mm diameter. These predictions give important indications of the effect of the geometry of the surrounding pipe work (for example, branches, junctions onto larger sections) on the flow field and bulk temperature.

Inverted convection cells, in which the cold liquid moves upwards and the warmer liquid moves downwards, were noted in regions where the local temperature was 4°C. These were only noted when the initial temperature was less than 10°C.

4.2 Interaction Between the Forming Plug and the Flow Field. The results obtained from modeling convection without freezing in the "closed" pipe model showed that the bulk temperature within the cooled zone decreases because the entire volume of liquid in the pipe is cooled. Thus, as the freeze progresses, convection decreases and the freezing rate will be artificially increased. The predictions obtained using a "closed" pipe model to simulate situations involving a large bulk of fluid will become less accurate at higher temperatures. It will also be impossible to predict the limiting temperatures above which it is not possible to form a complete plug.

In the following investigations of freezing with convection, two types of geometry were modeled; the first was a "closed" pipe model similar to that used in the flow field investigations. The second type included an "open" lower boundary, 42 mm below the bottom of the freezing zone, across which flow was allowed; a 52×52 nonuniform grid was used. The boundary conditions were specified as constant pressure and zero gradient of radial velocity in the radial direction, the vertical velocity was calculated as part of the solution from the continuity equation. A two-part temperature condition was applied on the lower boundary, with the temperature of the flow entering the domain set at the initial temperature and an adiabatic condition (i.e., zero temperature gradient in the vertical direction) applied to the flow leaving the domain. This

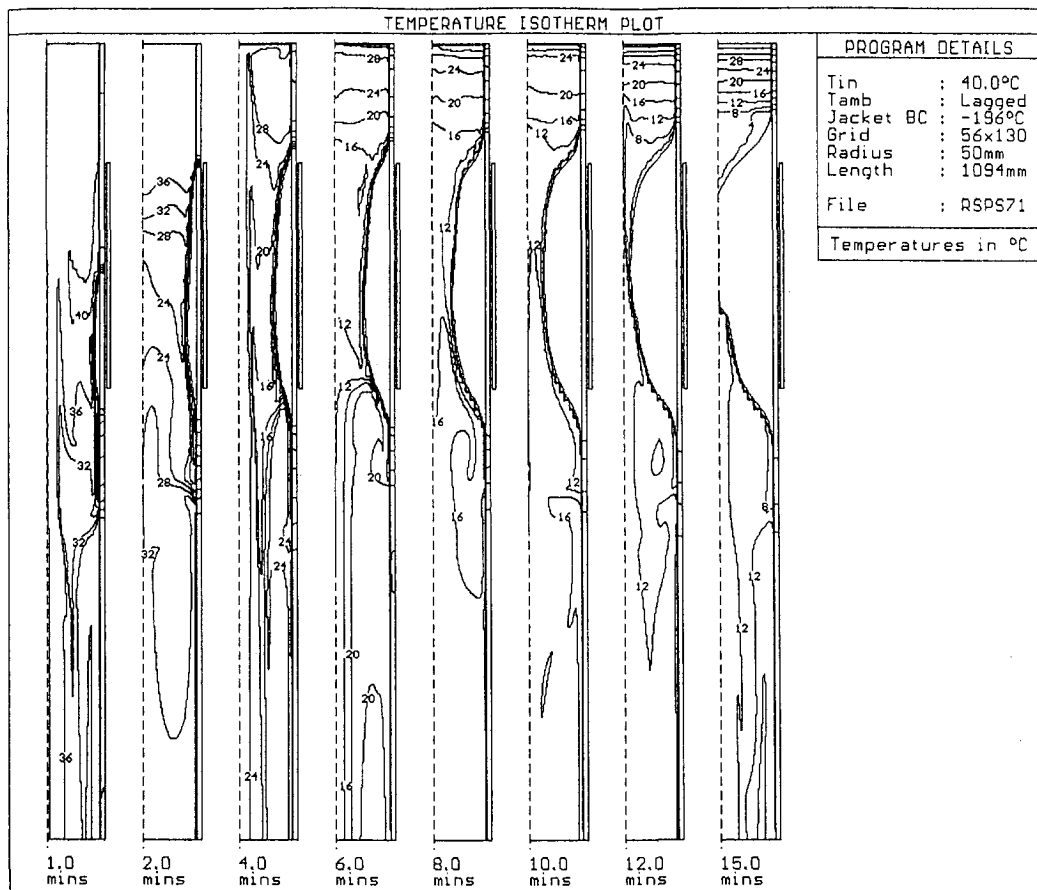


Fig. 6 Temperature field predictions in water initially at 40°C with freezing

combination of boundary conditions could not be used to predict the initial stages of flow development, shown in Figs. 3 and 4, in which the new convection cell stretches down the pipe. In particular, the period during which the bottom of the cell crosses the open boundary could not be modeled. The steady flow field resulting from a cooled isothermal (0°C) "jacket" was calculated as an initial prediction stage. The "open" pipe model neglects the complexities of the flow development and the resulting decay in bulk temperature. It will therefore provide a more conservative estimate of the freezing time and limiting temperature but will be more accurate in larger diameter pipes.

A pipe diameter of 100 mm and jacket length of 200 mm was used with both geometries to allow comparison with experimental results. The effect of varying the initial temperature was investigated. The pipe wall was included in the solution domain for the problem and the boundary condition on the outside of the wall within the freezing jacket was assumed to be isothermal -196°C. The wall was assumed to be perfectly lagged (i.e., adiabatic) above and below the freezing jacket. The length of the cooled section increased from zero to the jacket length over the first two minutes to simulate the process of physically filling the jacket with liquid nitrogen.

Figures 5 and 6 show the results for freezing in the "closed" pipe (diameter 100 mm, domain length 1094 mm) with an initial water temperature of 40°C. The plots are restricted to the top of the computational domain in order to show the detail in the freezing zone and the region immediately below. No streamlines or isotherms are plotted in the ice region which is visible as the clear region growing from the outside of the pipe.

The combination of the heat transfer from the convecting liquid to the plug and the initial coolant filling process results in the plug growing more rapidly near the bottom of the freezing zone. At around ten minutes, interaction between the boundary layer and core flow at the plug neck causes the separation of the regions

above and below the plug neck. The plug neck can then be seen to migrate up the plug.

As expected, the predictions obtained from the "closed" pipe model show that the bulk temperature decreases during the freeze, making convection increasingly insignificant.

Figure 7 shows the predicted freezing times compared with the experimental results obtained by Tavner and by Burton, both in a short closed pipe (no tank) and with a tank below the freezing zone. The predicted freeze times are lower than the measured values; this can be attributed to the assumption of an isothermal -196°C wall temperature inside the jacket. The predicted freezing times increase with initial temperature but show no sign of reaching a limiting value. This behavior was expected as a direct result of modeling a closed pipe and agrees well with the results obtained by Burton for this condition.

The results obtained with the "open" bottom model with an initial water temperature of 20°C and an isothermal, -196°C, boundary condition are shown in Figs. 8 and 9. At four minutes, the generation of a separate recirculation region above the plug neck indicates entrainment of the cooled boundary layer in the core flow in this region. After this, upward core flow becomes increasingly blocked by the plug neck, causing the water above the neck to be isolated from that below the neck. The neck position migrates up the plug and the plug becomes increasingly asymmetric.

The freezing times predicted using the "open" pipe model were much longer than those predicted with the "closed" pipe model, partly because convection decreases during freezing in the latter model. However, the freeze times were much greater than the experimental results and the limiting temperature was much lower. This is discussed in more detail below.

After 15 minutes (not included in Figs. 8 and 9), the solidification rate drops off and the plug and flow field appear to have reached a steady state, implying that it is not possible to freeze

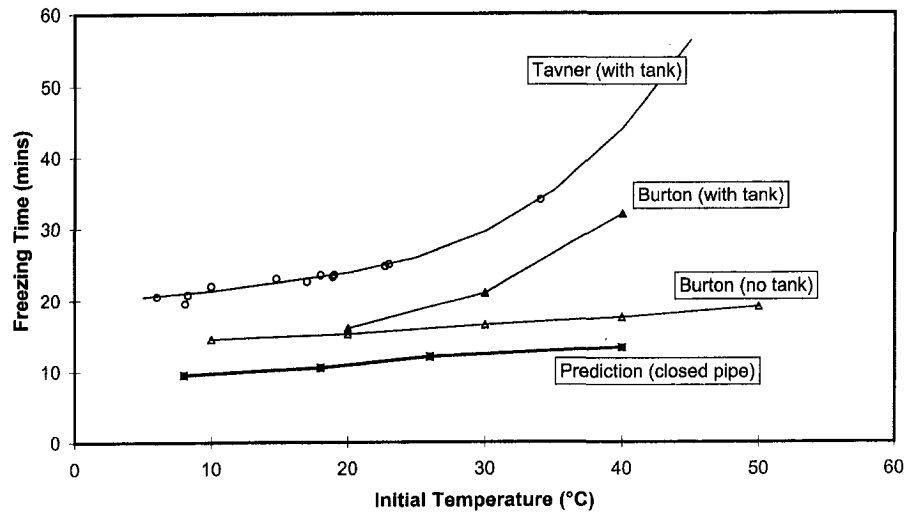


Fig. 7 Comparison between predicted and measured freezing times

water initially at 20°C when there is no bulk temperature decay. This is in contradiction to the experimental results of Burton, who froze water at temperatures up to 45°C while maintaining the bulk temperature by including a tank in the experimental rig. The form of plug development, with neck migration, is similar to that noted in the experiments at higher temperatures. Closer analysis of the predictions reveals that the boundary layer velocities increase as the plug grows, increasing heat transfer to the plug and slowing freezing and leading to a plug form which resembles that found in experiments performed at higher temperatures.

Examination of the temperature distribution in Fig. 9 shows that the boundary layer increases in thickness below the plug, where the flow direction is at an angle to the grid direction. A thicker layer of water is cooled and the velocities increase. This increase in flow is initially fed by pulling more water down over the ice surface. When the ice layer is thicker than the boundary layer (at four minutes), water is "pulled" into the domain across the "open" bottom and an increase in the up-flow immediately below the neck is noted. The "open" bottom therefore includes a positive feedback element in the system that caused the

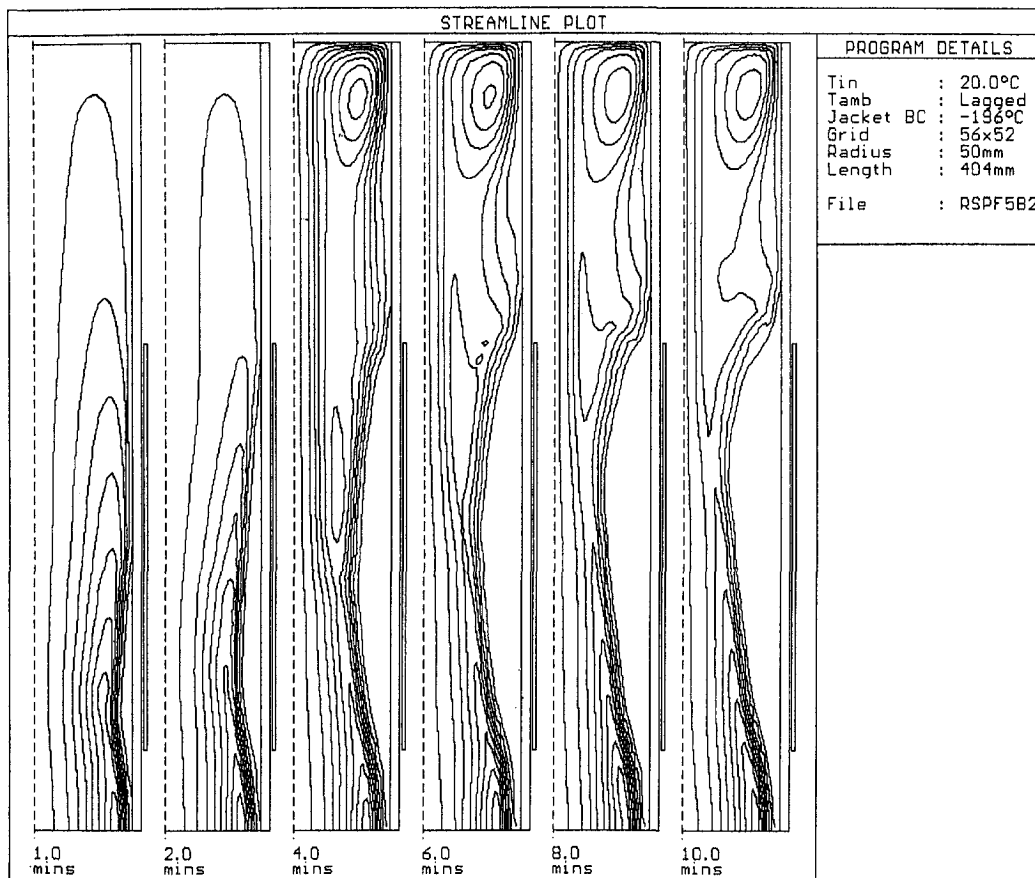


Fig. 8 Predicted flow development (streamlines) in open domain with freezing, initial temperature 20°C

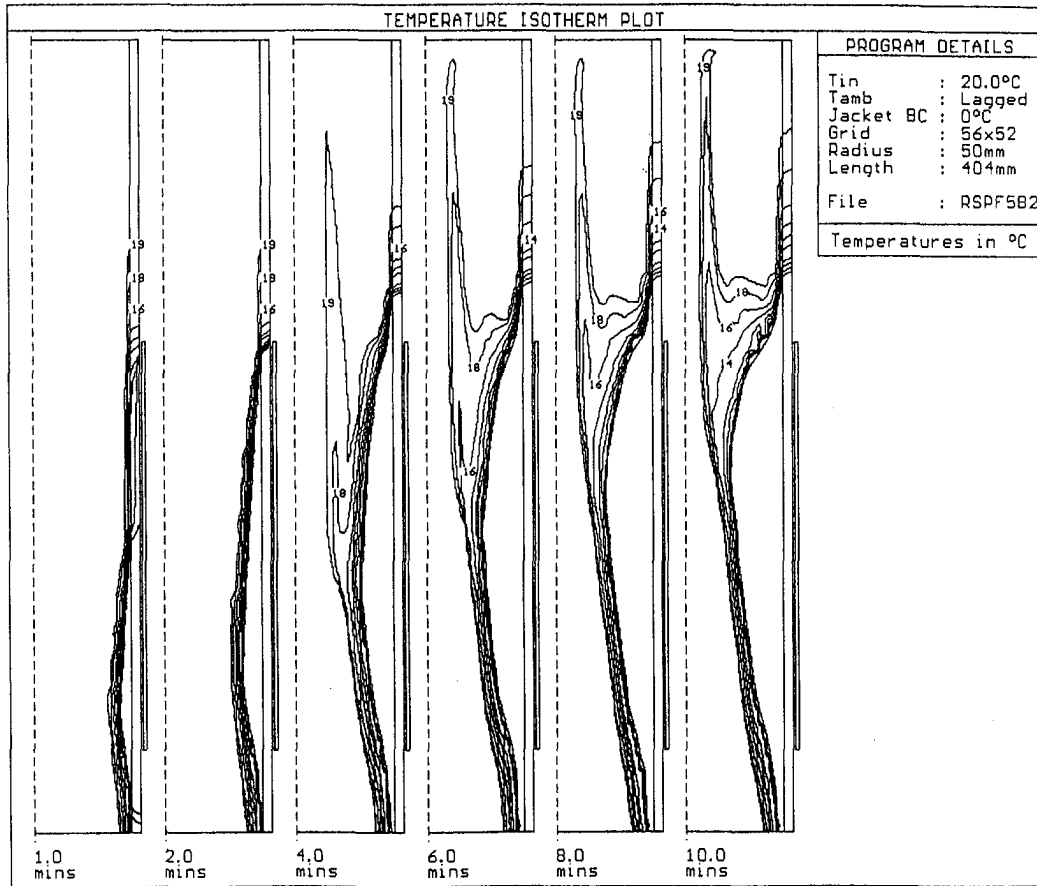


Fig. 9 Temperature field prediction in open domain with freezing, initial temperature 20°C

velocities to increase until the convected heat flux was sufficiently large to melt the plug.

The probable cause of this behavior is false diffusion, causing a local, artificially increased, diffusion coefficient for the dependant variable. This problem originates from the assumption that the flow across the control volume faces is locally one-dimensional; the discretization scheme used in this analysis was a power-law scheme considering the four nearest control volumes. In the case of convection in water, the maximum value of the false diffusion

coefficient is approximately 50×10^{-3} kg/ms (Patankar (1980)); this is an order of magnitude greater than viscosity and two orders of magnitude greater than the thermal diffusivity. A grid spacing of approximately 0.04 mm would be required to reduce the false diffusivity to less than the thermal diffusivity. A possible method of improving the model would be to include a more sophisticated discretisation scheme, for example using the skew upstream scheme proposed by Raithby (1976) or the QUICK scheme proposed by Leonard (1979). This would improve the accuracy of the

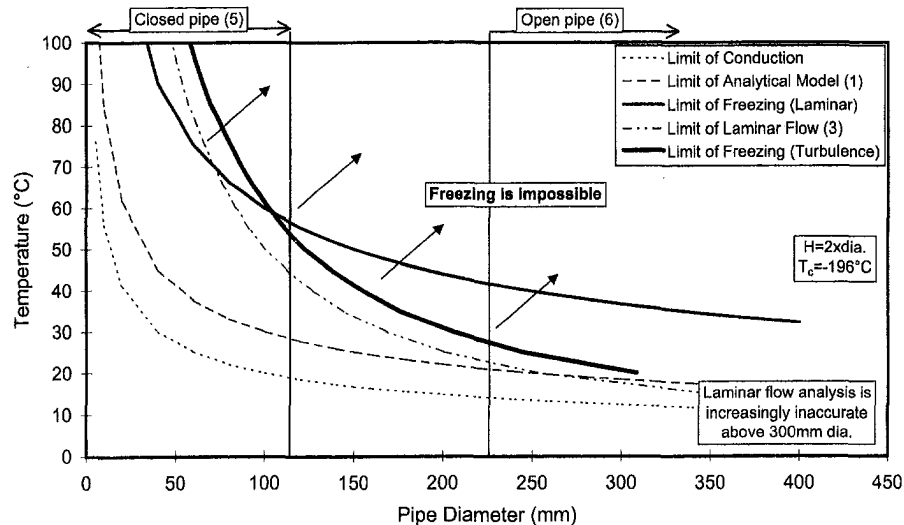


Fig. 10 Guidelines for selecting modeling approach

solution in regions where the flow direction is not aligned with the grid and may also increase the level of detail in the predicted flow field. Danzig (1989) mentions that false diffusion may also be responsible for masking smaller convection cells.

5 Selection of Modeling Method

The choice of modeling method needed to provide accurate predictions of the time to freeze depends on the conditions. The range over which the analytical and numerical models can be applied is described below and illustrated in Fig. 10.

1 If the water temperature is less than a critical temperature which depends on the pipe diameter ($T_{cr} = 7.17 \times D^{-0.446}$) and the flow is still laminar (i.e., Grashof number less than 1.3×10^9), the freezing time can be predicted using either the analytical model or the numerical model (with or without convection).

2 Above the critical temperature, a full numerical model is required to predict the effect of convection on freezing.

3 At and above Grashof numbers of 1.3×10^9 , the numerical model should include turbulence.

4 Convection is important throughout the freeze in water temperatures above 35–40°C in a 100-mm diameter pipe and at decreasing temperatures in larger pipes. For these cases, the numerical model needs further development to solve the problem of false diffusion.

5 The “closed” pipe numerical approach can be applied for pipes less than 100 mm in diameter in which the mixing mechanism will naturally cause a decay in the bulk temperature.

6 The “open” bottom method can be applied to pipes greater than 200 mm in diameter.

7 The intermediate region can either be modelled with a “closed” pipe which would increase the bulk temperature decay and therefore under estimate the freeze time, or using the “open” bottom model which would over estimate the freeze time. A compromise scheme is possible, in which the “open” bottom model is used, together with an estimate of the bulk temperature decay rate which is explicitly incorporated into the model.

6 Conclusions

A numerical model of convection and solidification in a vertical pipe has been developed. This successfully predicts the interaction between the forming ice plug and the flow field and shows good qualitative agreement with the experimental data. The model predicts a complex flow field, which is consistent with experimental results and improves the understanding of the effect of convection during freezing. The model has been developed further to include an open lower boundary which allows greater control of the bulk temperature.

Criteria are defined which take into account the effect of convection, turbulence, and bulk temperature decay and indicate the appropriate modeling approach based on pipe diameter and initial water temperature.

Acknowledgments

The authors acknowledge the financial support of PowerGen for part of the work described in this paper.

References

- Bejan, A., 1984, *Convection Heat Transfer*, John Wiley and Sons, New York.
- Brent, A. D., Voller, V. R., and Reid, K. J., 1988, “Enthalpy-Porosity Technique for Modelling Convection-Diffusion Phase Change—Application to the Melting of a Pure Metal,” *Numerical Heat Transfer*, Vol. 13, pp. 297–318.
- Burton, M. J., 1986, “Experimental and Numerical Study of Plug Formation in Vertical Pipes During Pipe Freezing,” Ph.D. Thesis, Department of Mechanical Engineering, University of Southampton, U.K.
- Burton, M. J., and Bowen, R. J., 1988, “Effect of Convection on Plug Formation During Cryogenic Pipe Freezing,” *Second National Heat Transfer Conference*, Glasgow, UK.
- Carslaw, H. S., and Jaeger, J. C., 1959, *Conduction of Heat in Solids*, Clarendon Press, London.
- Cao, Y., Faghri, A., and Chang, W. S., 1989, “A Numerical-Analysis of Stefan-Problems for Generalised Multi-Dimensional Phase-Change Structures Using the Enthalpy Transforming Model,” *Int. J. Heat and Mass Transfer*, Vol. 32, No. 7, pp. 1289–1298.
- Danzig, J. A., 1989, “Modelling Liquid-Solid Phase Changes With Melt Convection,” *Int. J. Numerical Methods in Engineering*, Vol. 28, pp. 1769–1785.
- Hibbert, S. E., Markatos, N. C., and Voller, V. R., 1988, “Computer Simulation of Moving-Interface, Convective, Phase-Change Processes,” *Int. J. Heat and Mass Transfer*, Vol. 31, No. 8, pp. 1709–1718.
- Huang, D.-Y., and Hsieh, S.-S., 1987, “Analysis of Natural Convection in a Cylindrical Enclosure,” *Numerical Heat Transfer*, Vol. 12, pp. 121–135.
- Keary, A. C., 1995, “A Numerical Study of Solidification and Natural Convection During Cryogenic Pipe Freezing,” Ph.D. Thesis, Department of Mechanical Engineering, University of Southampton, U.K.
- Keary, A. C., and Bowen, R. J., 1998, “Analytical Study of the Effect of Natural Convection on Cryogenic Pipe Freezing,” *Int. J. Heat and Mass Transfer*, Vol. 41, No. 10, pp. 1129–1138.
- Lannoy, A., 1980, “Problèmes thermiques posés par la congélation d’un fluide dans une tuyauterie,” *Revue Général Thermique*, Vol. 220, pp. 311–320, (in French).
- “Thermal Problems Involved in Freezing a Fluid in Pipework,” Translation from: British Library Document Supply Centre DSC 6196.3 1990.
- Leonard, B. P., 1979, “A Stable and Accurate Convective Modeling Procedure Based on Quadratic Upstream Interpolation,” *Computer Methods in Applied Mechanics and Engineering*, Vol. 19, pp. 59–98.
- London, A. L., and Seban, R. A., 1943, “Rate of Ice Formation,” *Trans. ASME*, Vol. 65, pp. 771–778.
- Markatos, N. C., and Pericleous, K. A., 1984, “Laminar and Turbulent Natural Convection in an Enclosed Cavity,” *Int. J. Heat Mass Transfer*, Vol. 27, No. 5, pp. 755–772.
- Patankar, S. V., 1980, *Numerical Heat and Mass Transfer*, Hemisphere, New York.
- Raithby, G. D., 1976, “Skew Upstream Differencing Schemes for Problems Involving Fluid Flow,” *Computer Methods in Applied Mechanics and Engineering*, Vol. 9, pp. 153–164.
- Shamsundar, N., and Rooz, E., 1988, “Numerical Methods for Moving Boundary Problems,” *Handbook of Numerical Heat Transfer*, W. J. Minkowycz, E. M. Sparrow, G. E. Schneider, and R. H. Pletcher, eds., John Wiley and Sons, New York, p. 747.
- Shamsundar, N., and Sparrow, E. M., 1975, “Analysis of Multidimensional Conduction Phase Change via the Enthalpy Method,” *ASME JOURNAL OF HEAT TRANSFER*, Vol. 97, pp. 333–340.
- Tavner, A. C. R., 1992, “An Experimental Study of Ice Formation and Convection During Cryogenic Pipe Freezing,” Ph.D. thesis, Department of Mechanical Engineering, University of Southampton, U.K.
- De Vahl Davis, G., and Jones, I. P., 1983, “Natural Convection of Air in a Square Cavity: A Benchmark Numerical Solution,” *Int. J. Numerical Method Fluids*, Vol. 3, pp. 249–264.
- Voller, V. R., and Cross, M., 1981, “Accurate Solutions of Moving Boundary Problems Using the Enthalpy Method,” *Int. J. Heat and Mass Transfer*, Vol. 24, pp. 545–556.
- Voller, V. R., Cross, M., and Markatos, N. C., 1987, “An Enthalpy Method of Convection/Diffusion Phase Change,” *Int. J. Numerical Methods in Engineering*, Vol. 24, pp. 271–284.

Phonon Wave Heat Conduction in Thin Films and Superlattices

G. Chen

Associate Professor,
Mechanical and Aerospace Engineering
Department,
University of California,
Los Angeles, CA 90095
Mem. ASME

Heat conduction in thin films and superlattices is important for many engineering applications such as thin-film based microelectronic, photonic, thermoelectric, and thermionic devices. Past modeling efforts on the thermal conductivity of thin films were based on solving the Boltzmann transport equation that treats phonons as particles. The effects of phonon interference and tunneling on the heat conduction and the thermal conductivity of thin films and superlattices remain to be explored. In this work, the wave effects on the heat conduction in thin films and superlattices are studied based on the consideration of the acoustic wave propagation in thin film structures and neglecting the internal scattering. A transfer matrix method is used to calculate the phonon transmission and heat conduction through these structures. The effects considered in this work include the phonon interference, tunneling, and confinement. The phonon dispersion is considered by introducing frequency-dependent Lamb constants. A ray-tracing method that treats phonons as particles is also developed for comparison. Sample calculations are performed on double heterojunction structures resembling Ge/Si/Ge and n -period superlattices similar to Ge/Si n (Si/Ge)/Ge. It is found that phonon confinements caused by the phonon spectra mismatch and by the total internal reflection create a dramatic decrease of the overall thermal conductance of thin films. The phonon interference in a single layer does not have a strong effect on its thermal conductance but for superlattice structures, the stop bands created by the interference effects can further reduce the thermal conductance. Tunneling of phonon-waves occurs when the constituent layers are 1–3 monolayer thick and causes a slight recovery in the thermal conductance when compared to thicker layers. The thermal conductance obtained from the ray tracing and the wave methods approaches the same results for a single layer. For superlattices, however, the wave method leads to a finite thermal conductance even for infinitely thick superlattices while the ray tracing method gives a thermal conductance that decreases with increasing number of layers. Implications of these results on explaining the recent thermal conductivity data of superlattices are explored.

Introduction

Phonon thermal conduction in thin film structures has been the focus of some recent theoretical studies (e.g., Chen and Tien, 1993; Majumdar, 1993; Hyldgaard and Mahan, 1995; Goodson, 1996; Chen, 1997a). These studies demonstrated that interfaces, boundaries, and microstructures play important roles in heat conduction through thin film structures. Most of the previous investigations, however, started from the Boltzmann transport equation, which cannot deal with wave effects such as interference and tunneling on heat conduction. Since interference and tunneling of electromagnetic waves were shown to be important for thermal radiative transfer in small gaps (Tien and Cunningham, 1973), similar effects can be anticipated for heat conduction in very thin films (Chen, 1997a, b).

Phonon propagation in thin films, particularly superlattice structures that consist of period layers of thin films, has been an active area of research in solid state physics. Narayanamurti et al. (1979) first observed the phonon interference phenomenon through studying phonon propagation normal to the superlattice film plane. Subsequently, many studies have been devoted to the phonon folding, phonon confinement, and mini-gap formation in superlattices (Colvard et al., 1985). Phonon propagation in oblique directions has also been investigated and the gap formation inside the Brillouin zone was predicted as a result of the phonon mode

conversion at interfaces (Tamura et al., 1989). Those studies, however, are concerned mainly with the phonon spectra modification by superlattices rather than with the thermal transport across superlattices. Several models on the thermal conductivity of superlattices were established based on solving the Boltzmann transport equation (Ren and Dow, 1982; Hyldgaard and Mahan, 1995; Chen, 1997a, 1998; Chen and Neagu, 1997). Hyldgaard and Mahan (1997), and more recently, Tamura et al. (1999) studied heat transfer across superlattices based on calculating the lattice dynamics simulation of the phonon dispersion relation. Their calculation indicates that because of the phonon confinement, the thermal conductivity of superlattices can be one order of magnitude smaller than the results calculated from the Fourier heat conduction theory.

In this work, phonon transport across thin films and superlattices is studied based on the transfer matrix method for the acoustic wave propagation. The thermal conductances of double heterojunction structures and n -period superlattices are calculated as a function of the layer thickness and temperature to explore the phonon interference and tunneling effects on heat conduction. For comparison, a ray-tracing method that treats phonons as particles is also developed for the thermal conductance calculation. Sample calculations are carried out to explore the effects of the layer thickness, the number of periods, temperature on the thermal conductance of the multilayer structures, and the differences between the wave and the particle treatments of phonons.

The Physical Models and Mathematical Formulation

A model structure is shown in Fig. 1(a). It consists of an n -period Si/Ge-like superlattice, a Si-like spacer, and two Ge-like cladding layers. All the inner layers are of equal thickness. When

Contributed by the Heat Transfer Division for publication in the JOURNAL OF HEAT TRANSFER and presented at 1998 AIAA/ASME Joint Thermophysics and Heat Transfer Conference, Albuquerque. Manuscript received by the Heat Transfer Division, Jan. 26, 1998; revision received, May 4, 1999. Keywords: Conduction, Heat Transfer, Microscale, Thermophysical, Thin Films. Associate Technical Editor: D. Zumbrennen.

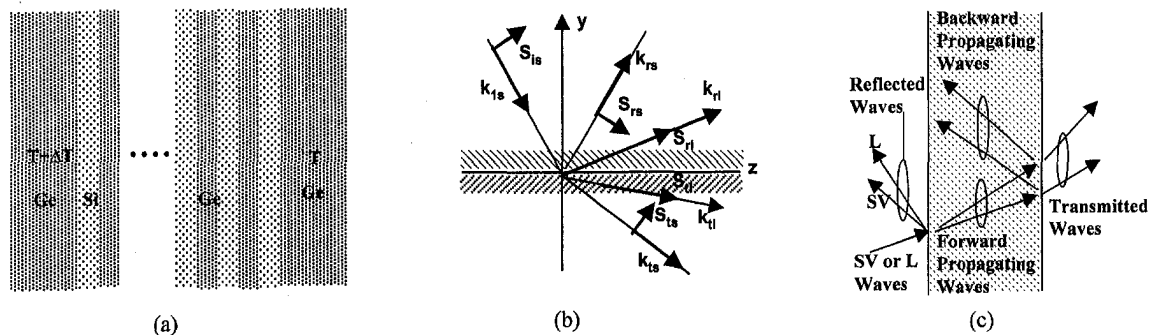


Fig. 1 Schematic of (a) superlattice structure, (b) reflecting and transmission of a SV or a L wave at an interface, showing the mode conversion, and (c) the resultant forward and backward propagating waves inside a film as well as the reflected and transmitted waves

$n = 0$, the structure degenerates into a double heterojunction structure. Both superlattices and double heterojunction structures are often used in semiconductor electronic and photonic devices. More recently, their potential for thermoelectric and thermionic refrigeration and power generation has attracted lots of attentions. The model presented below is based on the following assumptions: (1) each of the two cladding materials is at a uniform temperature, (2) all materials are isotropic, (3) the phonon coherence length is long such that thermal phonons can be represented by plane waves, (4) internal scattering inside all the materials is negligible, and (5) phonon scattering at interfaces is specular and elastic. In the following paragraph, the logic behind these assumptions will be discussed.

The first assumption is made since the focus of the paper is solely on the heat transfer across the thin film and superlattices. Due to the internal scattering, the temperature distributions in the cladding layers (medium 0 and medium 2) are clearly nonuniform. For a single layer, the temperature drop across the cladding materials can easily become larger than that inside the film. For superlattices, however, the two cladding layers can be made thinner (or thermally much more conductive) than the total thickness of the superlattices, and assumption (1) is then reasonable. Regarding to the second assumption, most crystalline materials are anisotropic but an isotropic solid model is a good starting point for exploring the essential aspects of wave effects on heat conduction without the additional complexity of dealing with anisotropic media. Chen (1997a) estimated the phonon coherence length in GaAs to be 10–20 Å at room temperature. This indicates that the third assumption of plane waves with a long coherence length is

unlikely to be valid at room temperature. Due to this conflict, the results of this model can only provide an estimation of the upper limit of the interference effect on heat conduction. On assumption (4), it has been shown before that when a film is much thinner than the phonon mean-free-path (Chen and Neagu, 1997), the internal scattering caused by the three-phonon processes and impurities does not affect the film thermal conductivity. Finally, on the assumption (5), Chen's study (1998) on the cross-plane thermal conductivity of superlattices indicates that interfaces are partially specular and partially diffuse for phonon scattering, and that inelastic scattering of phonon indeed happens at interfaces. On the other hand, in Hyldgaard and Mahan's study (1997) on the cross-plane thermal conductivity of superlattices, it was assumed that the interfaces scatter phonons totally specularly and elastically. The current work makes similar assumptions as used by Hyldgaard and Mahan (1997), since one major objective here is to estimate an upper limit of the wave effects on heat conduction. Diffuse and inelastic scattering will degrade the phonon coherence properties and reduce the impacts of the wave effects discussed in this work.

To calculate the total heat flux, the phonon dispersion in each of the materials must be known. We will first assume linear phonon dispersion relations. This is an approximation that has been often used in the study of phonon propagation in superlattice structures (Colvard et al., 1985; Tamura et al., 1989). Later, we will examine the influence of nonlinear phonon dispersion by introducing the frequency-dependent Lamb constants. It should be emphasized that although the current model starts from the bulk phonon dispersion of the constituent materials, the effective phonon spectrum of the structure will be different from these of its constituent

Nomenclature

A = transfer matrix at an interface for a transverse wave polarized perpendicular to the plane of incidence
 B = transfer matrix at an interface for a transverse wave or a longitudinal wave polarized in the plane of incidence
 D = density of states per unit volume, m^{-3}
 f = Bose-Einstein distribution function
 F = traction force at an interface per unit area, Nm^{-2}
 i = imaginary number, $\sqrt{-1}$
 k = wave vector, m^{-1} ; thermal conductivity, $Wm^{-1}K^{-1}$
 K = thermal conductance, Wm^{-2}
 M = transfer matrix for SH wave
 N = transfer matrix for SV and L wave

P = Poynting vector, Wm^{-2}
 q = heat flux, Wm^{-2}
 S = magnitude of the lattice velocity, ms^{-1}
 S = lattice velocity, ms^{-1}
 r = reflection coefficient
 \mathbf{r} = space vector, m
 R = reflectivity
 t = transmission coefficient
 T = transmissivity; temperature, K
 v = phase velocity, ms^{-1}
 x, y, z = coordinates
 Y = product of acoustic impedance and directional cosine
 Z = acoustic impedance, $kgm^{-2}s^{-1}$
 θ = angle, rad
 λ, μ = Lamé constants
 φ = phase factor

χ = directional cosine
 ω = angular frequency, Hz

Subscripts

0, 1, 2 = medium 0, medium 1, and medium 2
 x, y, z = in the corresponding coordinate direction
 i = incident wave
 L = longitudinal wave
 r = reflected wave
 s = shear wave
 t = transmitted wave
 $+$ = forward propagation direction
 $-$ = backward propagation direction

materials due to the wave effects being studied. This spectrum change is approximately included in the current model since it is caused by the same wave phenomenon. Yet this inclusion is not exact because the atomic level force coupling at the interface cannot be treated exactly under the continuum model.

With a clear understanding of the above assumptions and their limitations, heat transfer across the film structures can be modeled based on the well-established theory in the acoustic wave propagation (e.g., Auld, 1990). Consider a plane wave incident onto the interface between the cladding medium 0 and the film structure with an angle θ_1 from the normal direction, as shown in Fig. 1(b). At the interface, reflection and refraction of the wave occur, similar to those of an electromagnetic wave at an interface (e.g., Knittl, 1976). A fundamental difference, however, exists between the two waves. An electromagnetic wave has only two polarizations oriented perpendicular to the wave propagation direction, while an acoustic wave has three polarizations, i.e., two transverse and one longitudinal waves. Due to the additional longitudinal polarization, the reflection and refraction of acoustic waves at an interface are much more complicated. For a transverse wave polarized perpendicular to the plane of incidence (SH wave), only one reflected and one refracted wave are excited, similar to the excitation of waves by an electromagnetic wave polarized in the same direction. A longitudinal wave (L wave), or a transverse wave polarized in the plane of incidence (SV wave), however, can excite four waves: two reflected waves (L and SV waves) and two refracted waves (L and SV waves) as shown in Fig. 1(b). Mathematical expressions for calculating the reflection and refraction of acoustic waves at an interface are well-documented in the literature (Auld, 1990). The focus of the current model will be on the wave propagation through multilayer structures. The transfer matrix method for acoustic waves (Nayfeh, 1995) will be used to calculate the phonon reflectivity and transmissivity through the structures (Narayanamurti et al., 1979; Tamura et al., 1989). In the following, the transfer matrices for the three wave polarizations will be briefly summarized.

SH Wave. For a SH wave incident from medium 0, the lattice velocity, \mathbf{S} , of various reflected and transmitted waves as marked in Fig. 1(b) has the following form:

$$\mathbf{S}_j = S_j(0) \exp(-i\mathbf{k}_j \cdot \mathbf{r}) \hat{\mathbf{x}} \quad (1)$$

where \mathbf{k} is the wave vector, \mathbf{r} the space vector, $S(0)$ the amplitude of velocity at the interface between medium 0 and the film, and $\hat{\mathbf{x}}$ the unit vector in the x -coordinate direction. The subscript j has the following values and meanings: i and r for the incident and the reflected wave in medium 0, respectively; $+$ and $-$ for the forward and the backward propagating wave in the film, respectively; and t for the transmitted wave in medium 2. In Eq. (1), the time harmonic factor, $e^{i\omega t}$, has been omitted.

For the SH wave, the traction force $\mathbf{F} (= \mathbf{n} \cdot \hat{\mathbf{T}}$, where \mathbf{n} is the unit vector in the direction normal to interface and $\hat{\mathbf{T}}$ the stress tensor) at an interface acts in the x -direction and is equal to the tensor component T_{xy} (Auld, 1990),

$$F_x = T_{xy} = \frac{\mu}{i\omega} \frac{\partial S_x}{\partial y} \quad (2)$$

where μ is one of the two Lamé constants, and ω the angular frequency. The total lattice velocity and traction force acting on a plane parallel to the interface include contributions from all waves passing that plane. At $x = 0$ inside the film, the magnitude of the velocity, $S_1(0)$, and the traction force, $F_x(0)$, are the sum of those induced by the forward propagating and the backward propagating waves inside the film, and can be expressed in terms of the amplitudes of the two waves at $y = 0$ in the following matrix format

$$\begin{pmatrix} S_1(0) \\ F_x(0) \end{pmatrix} = \begin{pmatrix} 1 & 1 \\ -Z_{s1} \cos \theta_{s1} & Z_{s1} \cos \theta_{s1} \end{pmatrix} \begin{pmatrix} S_+(0) \\ S_-(0) \end{pmatrix} \\ = A_1 \begin{pmatrix} S_+(0) \\ S_-(0) \end{pmatrix} \quad (3)$$

where $Z (= \rho v)$ is the acoustic impedance that equals the product of the wave speed, v , and the medium density, ρ ; θ_1 is the angle formed between the direction of the wave propagation inside the film and the norm at the interface. The subscript s represents the properties of the transverse wave. Notation A_1 is used to represent the 2×2 matrix following the first equal sign. A similar relation exists at the other interface,

$$\begin{pmatrix} S_1(d) \\ F_x(d) \end{pmatrix} = A_1 \begin{pmatrix} S_+(d) \\ S_-(d) \end{pmatrix} \quad (4)$$

Inside the film, the magnitudes of the velocities of the forward and the backward propagating waves at $y = 0$ and $y = d$ are related through the following matrix:

$$\begin{pmatrix} S_+(0) \\ S_-(0) \end{pmatrix} = \begin{pmatrix} \exp(i\varphi_{s1}) & 0 \\ 0 & \exp(-i\varphi_{s1}) \end{pmatrix} \begin{pmatrix} S_+(d) \\ S_-(d) \end{pmatrix} \\ = M_i \begin{pmatrix} S_+(d) \\ S_-(d) \end{pmatrix} \quad (5)$$

where $\varphi_{s1} = \omega d \cos \theta_1 / v_{s1}$ and d is the film thickness. Combining Eqs. (3)–(5) leads to

$$\begin{pmatrix} S_1(0) \\ F_{x1}(0) \end{pmatrix} = A_1 M_i A_1^{-1} \begin{pmatrix} S_1(d) \\ F_x(d) \end{pmatrix} = M_1 \begin{pmatrix} S_1(d) \\ F_x(d) \end{pmatrix} \\ = \begin{pmatrix} \cos \varphi_{s1} & i \sin \varphi_{s1} / Y_1 \\ i Y_1 \sin \varphi_{s1} & \cos \varphi_{s1} \end{pmatrix} \begin{pmatrix} S_1(d) \\ F_{x1}(d) \end{pmatrix} \quad (6)$$

where $Y_1 = -Z_{s1} \cos \theta_1$. The transfer matrix M_1 is identical to that for an optical wave polarized in the same direction (Knittl, 1976).

Two equations similar to Eq. (3) can be established to relate the total velocity and the traction force inside medium 0 and medium 2 to the magnitude of the corresponding wave velocities in each medium,

$$\begin{pmatrix} S_0(0) \\ F_{x0}(0) \end{pmatrix} = A_o \begin{pmatrix} S_i(0) \\ S_r(0) \end{pmatrix}, \quad \begin{pmatrix} S_2(d) \\ F_{x2}(d) \end{pmatrix} = A_t \begin{pmatrix} S_t(d) \\ 0 \end{pmatrix} \quad (7)$$

where matrices A_o and A_t are obtained by replacing Z_{s1} and θ_1 in A_1 with the corresponding acoustic impedance and angle in each of the two media. The boundary conditions require that the velocity and the contraction force be continuous at the interfaces. Based on these requirements, the first and the last matrix in Eq. (6) can be replaced by the left-hand sides of the above two equations to yield

$$\begin{pmatrix} 1 \\ r \end{pmatrix} = A_i^{-1} M_1 A_t \begin{pmatrix} t \\ 0 \end{pmatrix} \quad (8)$$

where r and t are the reflection and the transmission coefficients defined as

$$r = S_r(0)/S_i(0) \quad t = S_t(d)/S_i(0) \quad (9)$$

These two coefficients can be obtained by solving Eq. (8).

The advantage of the transfer matrix method is that it can be easily extended to multilayer structures. For the n -period superlattice structure, there are a total of $(2n + 1)$ layers and the phonon reflection and transmission coefficient can be similarly calculated by replacing M_1 in Eq. (8) with the product of the transfer matrix for all the layers in the structure, i.e., $M_1 M_2 \dots M_{2n+1}$. The order of the matrices is the same as the sequence of the layers.

L Wave and SV Wave. Due to the phonon mode conversion, each L or SV incident wave can possibly excite four waves inside a film as shown in Fig. 1(c). Following any standard reference on acoustics (e.g., Auld, 1990), the velocity and traction force components at the first interface can be related to the magnitudes of the velocities of these four waves through the following matrix:

$$\begin{pmatrix} S_y(0) \\ S_z(0) \\ -\omega F_y(0) \\ -\omega F_z(0) \end{pmatrix} = B_1 \begin{pmatrix} S_{+s}(0) \\ S_{+L}(0) \\ S_{-s}(0) \\ S_{-L}(0) \end{pmatrix} \quad (10)$$

where the subscripts y and z represent coordinate directions, and the subscripts s and L represent the SV and the L wave, respectively. The matrix B_1 is given by

$$B_1 = \begin{pmatrix} -\sin \theta_{s1} & \cos \theta_{L1} & \sin \theta_{s1} & -\cos \theta_{L1} \\ \cos \theta_{s1} & \sin \theta_{L1} & \cos \theta_{s1} & \sin \theta_{L1} \\ -\mu_1 k_{s1} \sin 2\theta_{s1} & (\lambda_1 + 2\mu_1 \cos^2 \theta_{L1}) k_{L1} & -\mu_1 k_{s1} \sin 2\theta_{s1} & (\lambda_1 + 2\mu_1 \cos^2 \theta_{L1}) k_{L1} \\ \mu_1 k_{s1} \cos 2\theta_{s1} & \mu_1 k_{L1} \sin 2\theta_{L1} & -\mu_1 k_{s1} \cos 2\theta_{s1} & -\mu_1 k_{L1} \sin 2\theta_{L1} \end{pmatrix} \quad (11)$$

where k ($=\omega/v$) is the magnitude of the wave vector and λ is the other of the two Lamé constants.

A similar derivation as for the SH wave leads to a matrix expression that relates the velocity and contraction force at the two interfaces inside the film,

$$\begin{pmatrix} S_y(0) \\ S_z(0) \\ -\omega F_y(0) \\ -\omega F_z(0) \end{pmatrix} = N_1 \begin{pmatrix} S_y(d) \\ S_z(d) \\ -\omega F_y(d) \\ -\omega F_z(d) \end{pmatrix} \quad (12)$$

where $N_1 = B_1 N_i B_1^{-1}$ and

$$N_i = \begin{pmatrix} e^{i\varphi_{s1}} & 0 & 0 & 0 \\ 0 & e^{i\varphi_{L1}} & 0 & 0 \\ 0 & 0 & e^{-i\varphi_{s1}} & 0 \\ 0 & 0 & 0 & e^{-i\varphi_{L1}} \end{pmatrix} \quad (13)$$

The phase factors in the above matrix are similarly defined as that in Eq. (5).

Based on the continuity requirements on the velocity field and contraction force at the interfaces, the following relation between the incident, reflected, and transmitted velocity fields can be obtained:

$$\begin{pmatrix} S_{si}(0) \\ S_{Li}(0) \\ S_{sr}(0) \\ S_{Lr}(0) \end{pmatrix} = B_i^{-1} N_1 B_i \begin{pmatrix} S_{si}(d) \\ S_{Li}(d) \\ 0 \\ 0 \end{pmatrix} \quad (14)$$

where B_i and B_r are matrices that relate the total velocity and force components to the amplitudes of the velocity fields in medium 0 and in medium 2, respectively. They are obtained by replacing angles and physical properties in Eq. (11) with those in the corresponding media. Equation (14) can be used to calculate the reflection and transmission coefficients for both the L and SV polarized incident waves. For an incident L wave, S_{si} is set to zero, and for an incident SV wave, S_{Li} is set to zero. Compared to the SH wave, the matrix operation becomes more involved and N_1 cannot be easily simplified to a similar form as given in Eq. (6). Equation (14), however, can be solved numerically. For multilayer structures, the product of the transfer matrices for all the layers is again used in lieu of N_1 .

Effective Thermal Conductance and Thermal Conductivity.

The above derivation gives the reflection and the transmission coefficients for single and multilayer structures. The transmissivity and reflectivity can be calculated from these coefficients based on the acoustic Poynting vector (Auld, 1990). For a wave polarized in the p direction ($p = \text{SH, SV, L}$), the energy flux per unit area of the interface is given by the acoustic Poynting vector component in the y -direction,

$$P_{py} = \frac{1}{2} \text{Re}(\cos \theta_p) \cdot Z_p |S_p|^2 = \text{Re}(\cos \theta_p) |P| \quad (15)$$

where $|P|$ is the magnitude of the acoustic Poynting vector. Taking the ratio of the reflected energy flux or the transmitted energy flux to the incident energy flux, the reflectivity (R) or transmissivity (T) can be obtained, respectively. The total heat flux from medium

0 into medium 2 is obtained by summing up phonons of all frequencies, incident angles, and polarizations,

$$q_{0 \rightarrow 2} = \sum_p \int_0^{\omega_{pm}} \left(\int_{2\pi} T_p(\theta, \omega, d) P_{py}(\omega, \theta) d\Omega \right) d\omega \quad (16)$$

where the integration over the solid angle, Ω , covers the half-space, ω_{pm} represents the maximum frequency of p -polarized phonons. The magnitude of the Poynting vector can be related to the medium temperature by equating it to the phonon intensity (Majumdar, 1993; Chen and Tien, 1993)

$$|P| = \frac{1}{4\pi} \hbar \omega f(\omega, T) D(\omega) v_p \quad (17)$$

where D is the phonon density of states, f the Bose-Einstein distribution, and \hbar the Planck constant divided by 2π . Assuming that the temperature difference between media 0 and 2 is small, the net heat transfer rate between medium 0 and medium 2 can be obtained as

$$q = (\Delta T/2) \sum_p \int_0^{\omega_{pm}} \left(\hbar \omega v_p D(\omega) df/dT \int_0^1 T_p(\chi, \omega, d) \chi d\chi \right) d\omega \quad (18)$$

and the effective thermal conductivity of the film can be expressed as

$$k_e = [(2n + 1)d/2] \times \sum_p \int_0^{\omega_{pm}} \left(\hbar \omega v_p D(\omega) df/dT \int_0^1 T_p(\chi, \omega, d) \chi d\chi \right) d\omega \quad (19)$$

where χ ($=\cos \theta$) is the directional cosine and n is the number of periods.

Equation (19) indicates that the thermal conductivity will be linearly proportional to the total thickness of all layers if the phonon transmissivity is thickness independent. This is because internal scattering is assumed to be negligible under the studied cases. A more appropriate property for heat conduction in these

cases is the thermal conductance of the structure, which is defined as

$$K = q/\Delta T$$

$$= (1/2) \sum_p \int_0^{\omega_{pm}} (\hbar \omega v_p D(\omega) df/dT) \int_0^1 T_p(\chi, \omega, d) \chi d\chi d\omega. \quad (20)$$

Ray Tracing. The above model includes wave effects such as tunneling and interference. To examine how large are those effects, the thermal conductance of the film that excludes the wave effects should also be modeled. In this case, the transmissivity and reflectivity of the multilayer structure can be based on the ray tracing method in thermal radiation (Siegel and Howell, 1992). We will first discuss how to deal with single layer of thin films and then extend to the multilayer superlattices.

One Layer Structure. For a single film, the transmissivity of a SH wave from medium 0 to medium 2 is given by

$$T_s = \frac{T_{s01} T_{s12}}{1 - R_{s01} R_{s12}} \quad (21)$$

where T_{sij} and R_{sij} are the transmissivity and reflectivity of phonons from medium i into medium j . They can be calculated from the interface matrix, Eq. (3), or based on well-established formulae (Auld, 1990). For an L or a SV wave, the reflection and transmission can be modeled by replacing the field quantities in Fig. 1(c) with the intensities of the corresponding waves and applying the energy balance at the two interfaces. Assuming that all four waves exist inside the film, the following energy balance equations are obtained for an SV-polarized incident wave:

$$I_{ssr} = R_{ss01} I_{si} + T_{ss10} I_{s-} + T_{Ls10} I_{L-} \quad (22)$$

$$I_{sLr} = R_{sL01} I_{si} + T_{sL10} I_{s-} + T_{LL10} I_{L-} \quad (23)$$

$$I_{ss+} = T_{ss01} I_{si} + R_{ss10} I_{s-} + R_{Ls10} I_{L-} \quad (24)$$

$$I_{sL+} = T_{sL01} I_{si} + R_{sL10} I_{s-} + R_{LL10} I_{L-} \quad (25)$$

$$I_{ss-} = R_{ss12} I_{s+} + R_{Ls12} I_{L+} \quad (26)$$

$$I_{sL-} = R_{sL12} I_{s+} + R_{LL12} I_{L+} \quad (27)$$

$$I_{ssi} = T_{ss12} I_{s+} + T_{Ls12} I_{L+} \quad (28)$$

$$I_{sLi} = T_{sL12} I_{s+} + T_{LL12} I_{L+}. \quad (29)$$

In the above equations, the subscripts in R and T have the following meanings. The first letter represents the polarization of the incident wave and the second letter that of the excited wave. Numbers in the subscripts have similar meaning as for a SH wave. Normalizing all of intensities in the above eight equations by the incident intensity leads to eight unknowns that can be solved to obtain the film reflectivity and transmissivity. The obtained transmissivity can be used in Eqs. (19) and (20) to calculate the effective thermal conductivity and the thermal conductance. By replacing the incident SV wave with an L wave and making corresponding changes in the notations of the above set of equations, the transmissivity for an L incident wave can also be found. It should be cautioned that the above set of equations are estab-

Table 1 Maximum phonon frequency (converted into modal temperature) used in the calculation

	Longitudinal (K)	Transverse (K)
Si Layer	568	183
Ge Layer	335	102

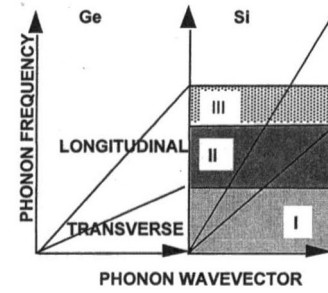


Fig. 2 Frequency integration is divided into three regions. Phonons in region I can transmit through the superlattice without violating the continuity requirements on the traction force and the displacement. Phonons in region II and region III are confined except at normal incidence.

lished for the case when all possible waves are in existence, i.e., four waves inside the film and two excited waves in both medium 0 and medium 2. If the total internal reflection (Auld, 1990) occurs for any of the polarizations, the number of waves in existence will be reduced. Subsequently, some equations and terms should be dropped. These special cases are taking into consideration in the computational results presented in the next section.

Multilayer Structures. The reflectivity and transmissivity of a multilayer structure can be calculated based on the net-radiation method (Siegel and Howell, 1992). This method starts from the last layer, i.e., the $(2n + 1)$ th layer, in the multilayer sequence. The reflectivity and transmissivity of this layer for an SV-polarized phonon beam incident from the $(2n)$ th layer, R_{1ss} , R_{1sL} , T_{1ss} , T_{1sL} , is calculated according to Eqs. (22)–(29). The reflectivity and transmissivity, R_{1Ls} , R_{1LL} , T_{1Ls} , T_{1LL} , of an L wave conjugated to the SV wave through the Snell law is similarly obtained. In the next step, the reflectivity and transmissivity of the $(2n)$ th layer is calculated for a phonon beam incident from the $(2n - 1)$ th layer, again based on Eqs. (22)–(29), by replacing the interface reflectivity and transmissivity, R_{Ls12} , R_{LL12} , T_{Ls12} , T_{LL12} with R_{1Ls} , R_{1LL} , T_{1Ls} , T_{1LL} , i.e., by treating the $(2n + 1)$ th layer at an interface of the $(2n)$ th layer. This recursive procedure is repeated until the reflectivity and transmissivity for the whole structure is obtained. Since the derivation is parallel to the net-radiation method, details of the expressions will be omitted here.

Treatment on the Phonon Dispersion. Strictly speaking, the acoustic wave method we are employing cannot deal with phonon dispersion because the latter results from the discreteness of the lattices. We develop an approximate method to include the phonon dispersion effect by introducing the frequency dependent Lamb constants. We will use a sine function to approximate the phonon dispersion for the transverse and the longitudinal phonons (Chen, 1997),

$$\omega_p = \omega_{mp} \sin(ka/2) \quad (30)$$

where a is the equivalent lattice constant of an isotropic medium. Based on Eq. (30), the phase velocities of the transverse and longitudinal phonons, v_t and v_L , can be calculated for each frequency. The frequency-dependent Lamb constants can be related to the phase velocities of the transverse and longitudinal phonons (Auld, 1990)

$$\lambda = v_t^2, \quad \lambda + 2\mu = v_L^2. \quad (31)$$

With the frequency-dependent Lamb constants, the phonon transmissivity of the thin film structures can be calculated for each frequency as described before. Although the phase velocity is used for the Lamb constants, the phonon group velocity is used in calculating the phonon density of states.

Results and Discussion

The maximum frequencies used for the cladding and the film materials are chosen to resemble those of Si and Ge, as listed in

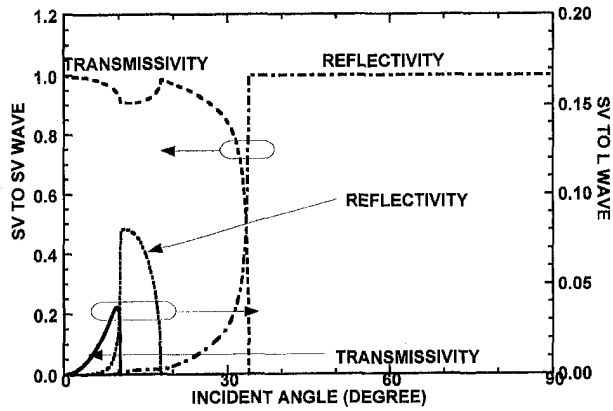


Fig. 3 Reflectivity and transmissivity at one interface as a function of the incident angle for a SV polarized incident wave, showing that both L and SV waves are excited

Table 1. A lattice constant of 2.76 \AA , calculated from the Debye model, is used for both the cladding media and the film. From the given maximum frequencies and the lattice constant, the group and phase velocities of each phonon polarization can be calculated for both the linear dispersion and the nonlinear phonon dispersion that is approximated by sine functions.

Since the phonon spectra are different between the Si and Ge layers, several factors must be considered in carrying out the

integration in Eq. (19) over the frequency. One of the assumptions made in this work is that only elastic scattering occurs at the interface. This dictates that the upper integration limit must be chosen carefully. Because of its lower maximum frequency, all of the transversely polarized phonons in the Ge layer can transmit through the multilayer structure. The integration limit for transverse phonons is thus set at 102 K. Those transverse phonons inside the Si layers that have a modal temperature between 102 K and 183 K are confined inside the layers. The situation for the longitudinal phonons is more complicated and the integration needs to be divided into three regions, as shown in Fig. 2. The region I, from 0 K to 102 K, includes those longitudinal phonons in the Si layers with a frequency less than the maximum of the transverse phonons inside the Ge layer. Phonons in this region can transmit through the film through the normal four-wave excitation process as described in the previous section. The region II, from 102 K to 183 K, is between the maximum transverse phonon frequencies inside the Si and the Ge layers. In this region, both the transverse and longitudinal waves can exist in the Si layers but only longitudinal phonon waves can be excited inside the Ge layers. It can be proven, from the requirements of the continuity of the velocity and the traction force at the interface, that in region II the only case that a longitudinal wave can transmit through the multilayer structure is at the normal incidence. In this case, the longitudinal and the transverse waves are decoupled and only a longitudinal wave is excited inside the film. At an oblique incident angle, the longitudinal wave must be totally reflected to satisfy the continuity requirements on the lattice velocity and the traction force. Region III falls in between the maximum longitudinal fre-

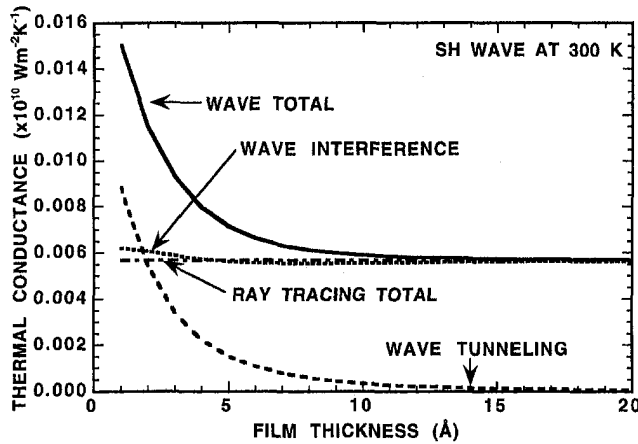


Fig. 4(a)

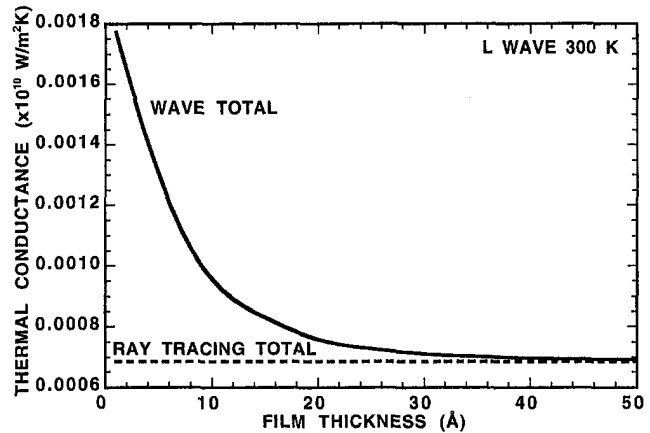


Fig. 4(c)

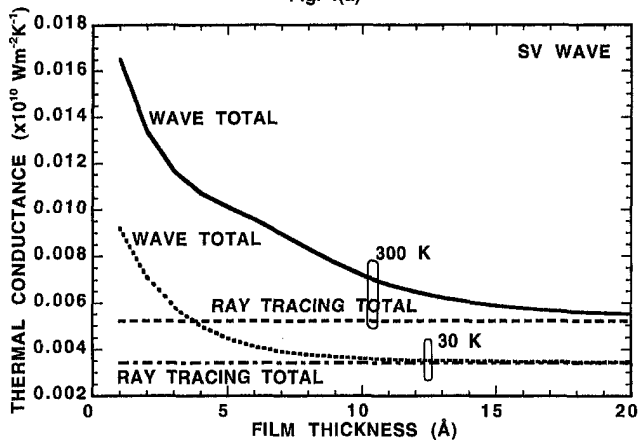


Fig. 4(b)

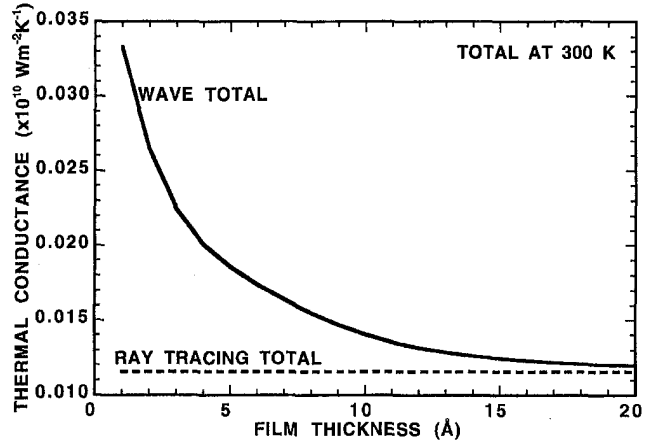


Fig. 4(d)

Fig. 4 Results calculated from the wave approach and the ray tracing approaches for the (a) incident SH wave, (b) incident SV wave, (c) incident L wave, and (d) total of three waves

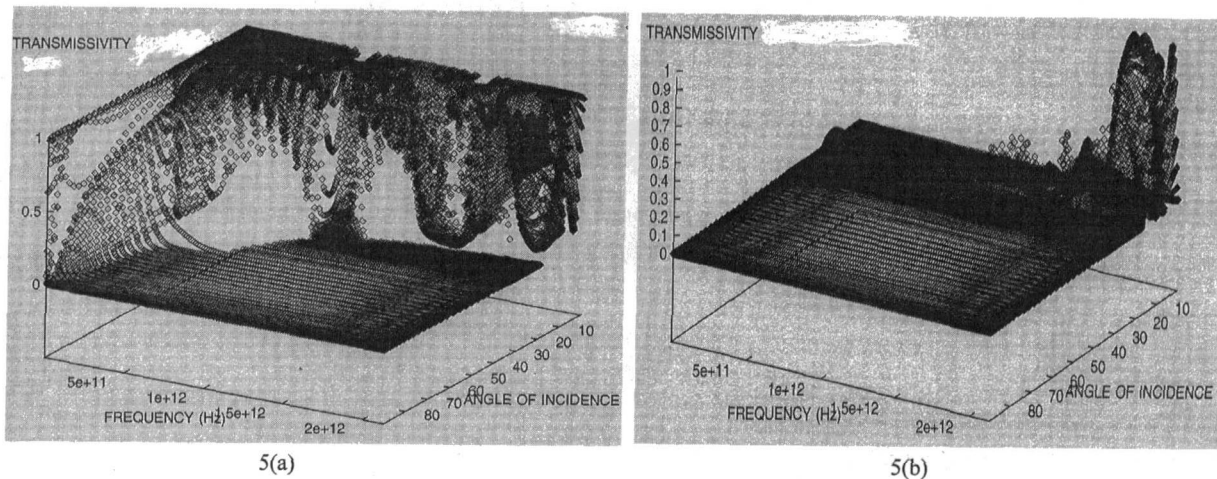


Fig. 5(a-b)

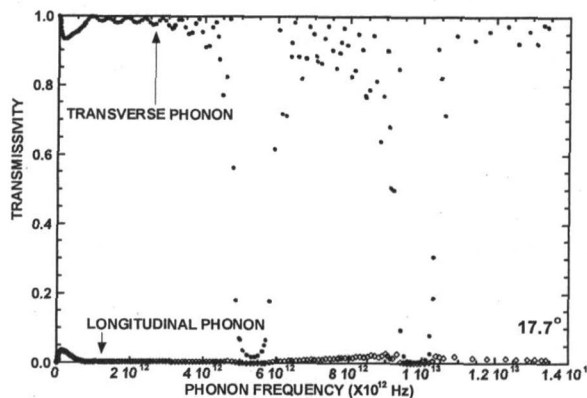


Fig. 5(c)

Fig. 5 Transmissivity of a SV incident wave on a ten-period superlattice (a) three-dimensional plots of SV into SV wave, and (b) three-dimensional plot of a SV into a L wave, and (c) transmissivity as a function of frequency at one specific incident angle

quencies between Si and Ge. Similar to the situation in region II, the transmission of longitudinal wave through the multilayer structure is possible only at the normal incidence. Since the incident energy is assumed to be uniformly distributed in all directions, the energy in the normal direction is small and will be neglected. This means that the longitudinal phonon contribution to the heat conduction comes from phonons in region I only, as does the transverse phonons.

The integration over angle also needs to be divided into sections to take into account different critical angles (Auld, 1990). For a SH incident wave, only one critical angle exists. When the phonon incident angle is larger than the critical angle, the phonon transmissivity from the ray-tracing approach is zero while from the wave approach, it can be nonzero due to the tunneling of phonons. The transmissivity in the latter case can be calculated using the transfer matrix established in the previous section. Integration over the angle for a SH wave is thus divided into two sections: below and above the critical angle. For an incident SV wave, several critical angles exist, one for the reflected/transmitted L wave in the Ge layer, and two for the SV and L excited waves in the Si layer. Correspondingly, integration over the angle for an incident SV wave is divided into four sections as determined by the above described three critical angles. Similarly, for an L incident wave, the integration over angle is divided into three sections since there are generally two critical angles. The matrix formulation established before is valid for all those angles. Special attention needs to be paid to the ray tracing approach because some of terms and equations should be dropped from Eqs. (22)–(29).

Figure 3 shows the phonon reflectivity and transmissivity at one

interface for an SV wave as a function of the incident angle. At a low angle of incidence, most phonons are transmitted. As the incident angle becomes larger than the critical angle, all phonons are reflected. The phonon mode conversion also happens below the critical incident angle. A small fraction of the incident SV wave is converted into the L wave.

Figures 4(a) to 4(d) show the thermal conductance of a one-layer structure ($n = 0$) as a function of the film thickness for waves of different polarizations. For a SH wave as shown in Fig. 4(a), thermal conductance resulted from the normal transmission of phonons (for incidence smaller than the critical angle) and the tunneling of phonons (for incidence larger than the critical angle) are plotted, together with the total thermal conductance calculated from the wave model and the ray tracing model. For a one-monolayer thick film ($\sim 1.4 \text{ \AA}$), tunneling can increase the thermal conductance by a factor of two. As the film becomes thicker than $\sim 10 \text{ \AA}$, tunneling effect is already negligible. The case of a SV wave as shown in Fig. 4(b) is similar. The longitudinal wave (Fig. 4(c)) differs from the transverse waves in two aspects: (1) the thermal conductance is an order of magnitude smaller than those of the transverse waves, and (2) tunneling extends to slightly thicker films. The order of magnitude reduction in the thermal conductance of the longitudinal phonons is caused by the phonon confinement effect. As discussed before, only those longitudinal phonons in region I are possible to transmit through the film if no inelastic scattering occurs at the interface. The specific heat of the longitudinal phonons in region I is small, leading to an order of magnitude reduction in the thermal conductance compared to that of the transverse phonons. In region I, phonons have longer wave-

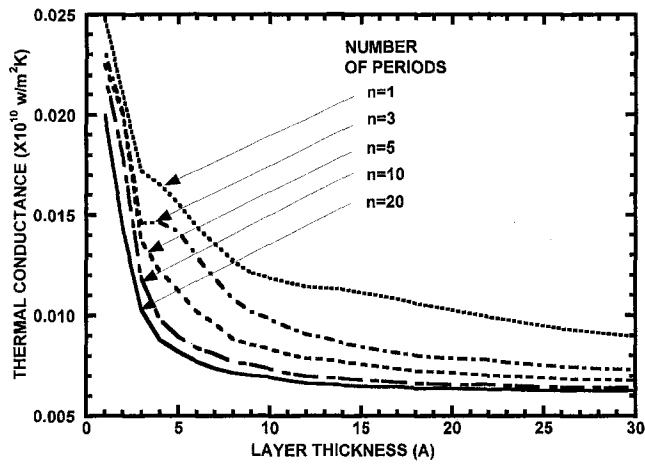


Fig. 6 Thermal conductance as a function of the layer thickness with different periods

lengths than those at the zone boundary and thus can tunnel through thicker films. The total phonon conductance of all three polarizations is given in Fig. 4(d).

The three-dimensional plots of Fig. 5(a) and 5(b) show the phonon transmissivity as a function of the frequency and incident angle for SV-polarized phonons through a 10-period superlattice with 5 Å thick constituting layers. At low angle of incidence and low frequency, the phonon transmission is close to one, indicating that long wavelength phonons do not feel the existence of the interfaces. At higher angle of incidence, total internal reflection occurs and most phonons do not transmit through the interface except in the low frequency region where tunneling effect promotes the transmission of long wavelength phonons. There exist regions where the phonon transmissivity approaches zero even for normal incidence, as shown in Fig. 5(c). In optics, these regions are called the stop bands (Knittl, 1976). These stop bands correspond to the formation of mini-gaps in the phonon spectra of superlattices (Colvard et al., 1985). The existence of these stop bands has been observed experimentally by measuring directly the phonon transmissivity (Narayanamurti et al., 1979) and through Raman spectroscopy of superlattices (Covard et al., 1985). With the calculated transmissivity, values of the thermal conductance of superlattice structures are calculated and the results are given in Fig. 6. It can be seen that the thermal conductance generally increases with decreasing layer thickness, due to the tunneling of phonons above the critical angle. As the layer becomes thicker, the thermal conductance approaches a constant. For small number of periods, the asymptotic values for thick films are different. As the number of periods increases, the thermal conductance for different periods converges to a same value, indicating that the superlattice can be treated as if it has infinite repetition. Figure 6 also shows that the thermal conductance decreases with increasing number of layers, because the formation of stop bands reduces the phonon transmission.

Although Figs. 4(a)–4(d) indicates that the wave and the ray-tracing approaches lead to asymptotically the same results for a single layer structure, the situation is very different for multilayer structures. Figure 7 illustrates the thermal conductance of the superlattice as a function of number of periods, calculated based on the wave approach and the ray-tracing approach. While the thermal conductance from the wave method approaches a constant, the ray-tracing method leads to a thermal conductance of the total structure decreasing with increasing number of periods. This is because under the wave picture, the long wavelength phonons can transmit through the superlattices, as shown in Figs. 5(a)–5(c). Under the ray-tracing method, phonons of all wavelengths will be equally scattered at the interfaces. Thus as the number of interfaces increases, the phonon transmission through the whole structure decreases.

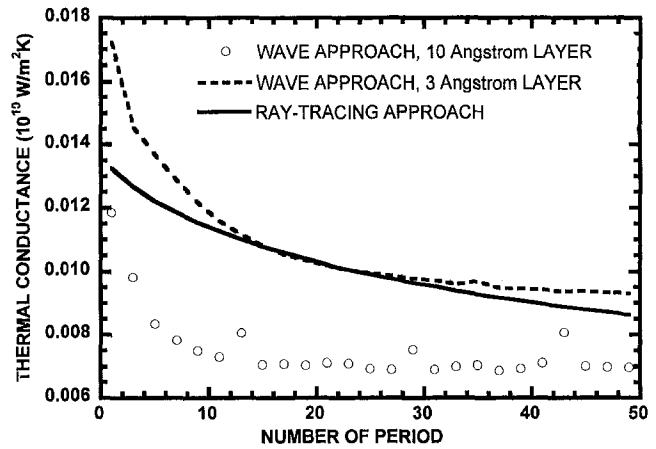


Fig. 7 Comparison of the results from the wave approach and the ray-tracing approach

Figure 8 compares the results of the phonon thermal conductance calculated from linear dispersion and the nonlinear dispersion relations. The product of the thermal conductance and the thickness of one period is also shown. For the Si/Ge structures, the nonlinear dispersion creates a larger mismatch in the phonon acoustic properties (group and phase velocities) and the total thermal conductance is further reduced.

To compare the relative importance of the wave interference and tunneling effects against the effects of the phonon confinement caused by the phonon spectra mismatch and the total internal reflection, the following “bulk” thermal conductance values of the same structure are calculated. These are the values when (1) only elastic scattering is allowed and (2) inelastic scattering is allowed. The transmissivity of all allowable scattering events is set to one. If only elastic scattering is allowed, all phonons in region I as shown in Fig. 2 can transmit through the film and the rest of the longitudinal phonons in the Ge layer cannot go through. In this case, the total thermal conductance is $4.02 \times 10^8 \text{ Wm}^{-2}\text{K}^{-1}$, mainly contributed by the transverse phonons. If inelastic scattering is allowed, all longitudinal phonons in the Ge layer can transmit through the Si film. The total thermal conductance under this circumstance is increased to $10.27 \times 10^8 \text{ Wm}^{-2}\text{K}^{-1}$. In comparison, Fig. 6 and Fig. 8 show that the thermal conductance of Si/Ge superlattices is $\sim 0.6 \times 10^8 \text{ Wm}^{-2}\text{K}^{-1}$ under the linear dispersion approximation and is even smaller under the nonlinear dispersion approximation. These numbers indicate that the reduction in the thin film thermal conductivity caused by the phonon confinement effects is normally much larger than the enhancement

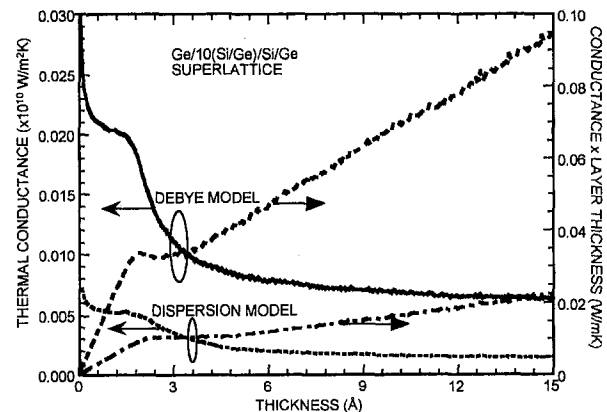


Fig. 8 Comparison of the computational results based on the linear phonon dispersion (named Debye) and the nonlinear (named dispersion) phonon dispersion approximations

of the thermal conductivity caused by the wave tunneling effect. Had we used Si as the cladding materials, the results for the multilayer structures will not be affected, but the basis for comparison, i.e., the "bulk" thermal conductance of the structure will increase, making the contrast between the "bulk" and the actual conductance values even larger.

We will conclude the discussion by comparing the present study with experimental results on the cross-plane thermal conductivity of superlattices on Si/Ge, GaAs/AlAs, and $\text{Bi}_2\text{Te}_3/\text{Sb}_2\text{Te}_3$, and our previous modeling based on the Boltzmann transport equation (Chen and Neagu, 1997; Chen, 1998). Under the presented wave model (which neglected internal scattering), the thermal conductance of a superlattice is approximately a constant, which means that the thermal conductivity is proportional to the total thickness of the superlattices. Existing experimental data, however, suggests, that the thermal conductivity values depend on the thickness of each period rather than on the total thickness of the superlattice. Considering that the calculated conductance is practically independent of the total number of periods if there are more than ten periods in the structure, one expects that the thermal conductivity is independent of the period thickness, in contradiction with existing experimental data. This contradiction, in principle, could be removed if the unklampp scattering of the propagating phonons depends on the period thickness, but reported calculations do not show such a strong dependence (Ren and Dow, 1982). These calculations did not consider the group velocity reduction and the density of states change as is implied in the current model. If these two effects are combined together, perhaps good agreement with experimental data can be reached based on the wave consideration. On the other hand, we modeled the phonon transport in superlattices based on the Boltzmann transport equation (Chen and Neagu, 1997; Chen, 1998), and the model can be fitted to the experimental data on Si/Ge if the inelastic scattering is assumed to occur at the interfaces. It is possible that such inelastic scattering at the interfaces destroys the coherence of phonons so that phonon transport can be practically treated as particles rather than waves. It should be pointed out that many Raman spectroscopy experiments have confirmed the minigap formation in the phonon spectra of superlattices, indicating the coherent nature of phonons. There is little report in literature, however, on how many phonons are really coherent and in which directions are they coherent. Since heat transfer involves all phonons and in all directions, it is plausible that the majority of phonons that contribute to heat conduction are actually incoherent. The presented wave model leads to an increase in the thermal conductance and thus the thermal conductivity when the layer thickness approaches monolayers. Experimental data on the thermal conductivity of $\text{Bi}_2\text{Te}_3/\text{Sb}_2\text{Te}_3$ superlattices indeed shows a similar trend (Venkatasubramanian, 1996). This increment in the thermal conductivity, however, may as well be due to alloying rather than tunneling, depending on the interface sharpness and conditions.

Conclusion

A heat conduction model that includes the effects of phonon interference and tunneling in single-layer and multilayer thin film structures is presented in this work. The model is based on the transfer matrix method for acoustic wave propagation in thin film structures. Calculations were performed for superlattice structures resembling $\text{Ge/Si}_n(\text{Si/Ge})/\text{Ge}$. It is found that a large reduction in

the thermal conductance is created by the phonon confinement phenomena arising from (1) the phonon spectra mismatch and (2) the total internal reflection. The results show that tunneling can cause some recover of the thermal conductance reduction if the constituent layers are within 1–3 monolayers range. For a single layer, the wave effects become negligible for films thicker than $\sim 10 \text{ \AA}$. For multilayer periodic structures, however, the formation of the stop bands can further decrease the thermal conductance. It should be reminded that several assumptions are made on the model developed in this work. Due to these assumptions, the calculated wave effect is considered as an upper limit.

Acknowledgments

This work is supported by a DOD MURI grant on thermoelectrics and a NSF Young Investigator Award.

References

- Auld, B. A., 1990, *Acoustic Fields and Waves in Solids*, 2nd Ed., Krieger, Melbourne, FL, Chapter 9.
- Capinski, W. S., and Maris, H. J., 1996, "Thermal Conductivity of GaAs/AlAs Superlattices," *Physica B*, Vol. 219–220, pp. 699–701.
- Chen, G., 1997a, "Size and Interface Effects on the Thermal Conductivity of Superlattices and Periodic Thin Film Structures," *ASME JOURNAL OF HEAT TRANSFER*, Vol. 119, pp. 220–229.
- Chen, G., 1997b, "Wave Effects on Radiative Transfer in Absorbing and Emitting Thin-Film Structures," *Microscale Thermophysical Engineering*, Vol. 1, pp. 215–224.
- Chen, G., 1998, "Thermal Conductivity and Ballistic Phonon Transport in Cross-Plane Direction of Superlattices," submitted for publication.
- Chen, G., and Neagu, M., 1997, "Thermal Conductivity and Heat Transfer in Superlattices," *Applied Physics Letters*, Vol. 71, pp. 2761–2763.
- Chen, G., and Tien, C. L., 1993, "Thermal Conductivity of Quantum Well Structures," *AIAA Journal of Thermophysics and Heat Transfer*, Vol. 7, pp. 311–318.
- Colvard, C., Gant, T. A., Klein, M. V., Merlin, R., Fisher, R., Morkoc, H., and Gossard, A. C., 1985, "Folded Acoustic and Quantized Optics Phonons in (GaAl)As Superlattices," *Physical Review B*, Vol. 31, pp. 2080–2091.
- Giannozzi, P., de Gironcolo, S., Pavone, P., and Baroni, S., 1991, "Abinitio Calculation of Phonon Dispersions in Semiconductors," *Physical Review B*, Vol. 43, pp. 7231–7242.
- Goodson, K. E., 1996, "Thermal Conduction in Nonhomogeneous CVD Diamond Layers in Electronic Microstructure," *ASME JOURNAL OF HEAT TRANSFER*, Vol. 118, pp. 279–286.
- Hyldgaard, P., and Mahan, G. D., 1995, "Phonon Knudsen Flow in Superlattices," *Thermal Conductivity 23*, Technomic, Lancaster, PA, pp. 172–182.
- Hyldgaard, P., and Mahan, G. D., 1997, "Phonon Superlattice Transport," *Physical Review B*, Vol. 56, pp. 10,754–10,757.
- Knittl, Z., 1976, *Optics of Thin Films*, John Wiley and Sons, New York.
- Lee, S.-M., Cahill, D., and Venkatasubramanian, R., 1997, "Thermal Conductivity of Si-Ge Superlattices," *Applied Physics Letters*, Vol. 70, pp. 2957–2960.
- Majumdar, A., 1993, "Microscale Heat Conduction in Dielectric Thin Films," *ASME JOURNAL OF HEAT TRANSFER*, Vol. 115, pp. 7–16.
- Narayanamurti, V., Stormer, H. L., Chin, M. A., Gossard, A. C., and Wiegmann, W., 1979, "Selective Transmission of High-Frequency Phonons by a Superlattice: the "Dielectric" Phonon Filter," *Physical Review Letters*, Vol. 43, pp. 2012–2016.
- Nayfeh, A. H., 1995, *Wave Propagation in Layered Anisotropic Media*, Elsevier, Amsterdam.
- Ren, S. Y., and Dow, J. D., 1982, "Thermal Conductivity of Superlattice," *Physical Review B*, Vol. 25, pp. 3750–3755.
- Siegel, R., and Howell, J. R., 1992, *Thermal Radiation Heat Transfer*, 3rd Ed., Hemisphere, Washington, DC.
- Tamura, S., Hurley, D. C., and Wolfe, J. P., 1989, "Acoustic-Phonon Propagation in Superlattices," *Physical Review B*, Vol. 38, pp. 1427–1449.
- Tamura, S., Tanaka, Y., and Maris, H. J., 1999, "Phonon Group-Velocity and Thermal Conduction in Superlattices," *Physical Review B*, Vol. 60, pp. 2627–2630.
- Tien, C. L., and Cunningham, G. R., 1973, "Cryogenic Insulation Heat Transfer," *Advances in Heat Transfer*, Vol. 9, pp. 349–417.
- Venkatasubramanian, R., 1996, "Thin-Film Superlattice and Quantum-Well Structures—A New Approach to High-Performance Thermoelectric Materials," *Naval Research Reviews*, Vol. 58, pp. 44–54.

Optical Measurement of Thermal Contact Conductance Between Wafer-Like Thin Solid Samples

Y. Ohsone¹

G. Wu

Department of Mechanical Engineering,
University of California,
Berkeley, CA 94720

J. Dryden

Department of Mechanical and
Materials Engineering,
University of Western Ontario,
London, ON N6A 5B9, Canada

F. Zok

Materials Department,
University of California,
Santa Barbara, CA 93106

A. Majumdar²

Department of Mechanical Engineering,
University of California,
Berkeley, CA 94720
Mem. ASME.

This paper presents a noncontact optical technique for measuring the thermal contact conductance between wafer-like thin solid samples. The technique is based on heating one solid surface by a modulated laser beam and monitoring the corresponding temperature modulation of the other solid surface across the interface using the reflectance of a probe laser beam. The phase lag between the two laser signals is independent of the optical properties of the samples as well as the laser intensities, and can be related to the thermal contact conductance. A detailed theoretical analysis is presented to estimate the thermal contact conductance as well as the thermophysical properties of the solids from the phase lag measured as a function of the modulation frequency. Closed-form solutions in the high-frequency limit are derived in order to provide a simple estimation procedure. The effect of misalignment of the two lasers is studied and the conditions for robust measurements are suggested. As a benchmark for this technique, the thermal conductivity of a single crystal silicon sample was measured to within two percent of reported values. The thermal contact conductance was measured for Al-Si samples, each about 0.22 mm thick, in the pressure range of 0.8–10 MPa. In contrast to traditional contact conductance measurement techniques that require steady-state operation and insertion of thermocouples in thick solid samples, the noncontact dynamic optical technique requires much less time and is particularly well suited for electronic packaging materials that are typically in the thickness range of 0.1–5 mm. In addition, localized conductance measurements are now possible with a spatial resolution of about four times the thickness of the solid and can be used to detect interfacial voids and defects.

1 Introduction

The thermal contact conductance between two solid surfaces depends on a variety of factors such as the structure of surface roughness and waviness, surface hardness and elastic modulus, thermal conductivity, and surface damage of each surface, as well as the type of interstitial gas. Prediction of the thermal contact conductance has been a major challenge in the past, mainly due to the large uncertainty and complexity of surface properties. Although several theories have been developed to predict the thermal contact conductance (Cooper et al., 1969; Mikic, 1974; Fletcher, 1988; Majumdar and Tien, 1991; Nishino et al., 1995; Salgon et al., 1997; Lambert and Fletcher, 1997; Leung et al., 1998) it is rare to have agreement between theory and experiment to within 50 percent. Yet, thermal contact resistance is known to be a significant fraction of the total thermal resistance in electronic packages (Kraus and Bar-Cohen, 1983; Childres and Peterson, 1989). Therefore, its measurement, prediction, and control are critical to the thermal management of electronic and optoelectronic packages. In light of the difficulties in theoretical prediction, one must resort to measuring thermal contact conductance for conditions that are representative of those found in electronic packages. Such measurements can identify the upper and lower bounds for the value of

thermal contact conductance and also provide the opportunity to try different schemes for increasing and controlling the conductance.

The technique that is widely used (Yovanovich, 1987; Seyed-Yagoobi et al., 1992; Williamson and Majumdar, 1992; Maddren and Marschall, 1995; Nishino et al., 1995) for measuring thermal contact conductance is illustrated in Fig. 1. Two solid pieces are brought together under compressive load while being heated on one side and cooled on the other. A series of thermocouples are inserted along the two solids to measure the temperature profile. At steady state, the linear profile is extrapolated to the interface to estimate the temperature jump, ΔT , at the interface. For a known heat flux, q , supplied by the heater and extracted by the cooler, the thermal contact conductance, h , is estimated by the relation, $h = q/\Delta T$. Since the heat flux, q , must be known, the solid pieces should be insulated along the length to reduce heat losses. This is often achieved in a vacuum environment. Although two thermocouples are sufficient to get a temperature gradient, at least four in each solid are usually recommended for accuracy and to ensure that steady state is reached throughout the solid. The time required to reach steady state depends on the size or thermal mass of the system, and is usually about an hour or more for a typical laboratory set-up. Hence, a single data set of conductance versus load containing about eight data points requires at least a day to obtain.

Electronic packages contain solids such as semiconductor wafers as well as ceramic and metal substrates whose thickness range from 0.1 mm to about 5 mm. These are sometimes bonded together or often pressed under compressive load. To measure the contact conductance between such thin samples, the technique described in Fig. 1 cannot be used since it is practically impossible to insert four thermocouples within a distance of 1 mm. In addition, the steady-state technique can be prohibitively time consuming, specially when new control strategies and improvements must be explored.

¹ Visiting scholar from the Mechanical Engineering Research Laboratory, Hitachi, Ltd., 502 Kandatsu, Tsuchiura, Ibaraki 300-0013, Japan. e-mail: ohsone@merl.hitachi.co.jp.

² To whom correspondence should be addressed. e-mail: majumdar@me.berkeley.edu.

Contributed by the Heat Transfer Division for publication in the JOURNAL OF HEAT TRANSFER and presented at the Joint ASME/JSME Thermal Engineering Conference. Manuscript received by the Heat Transfer Division, Oct. 7, 1998; revision received, Mar. 23, 1999. Keywords: Contact Resistance, Experimental, Heat Transfer, Measurement Techniques, Thermophysical. Associate Technical Editor: M. Modest.

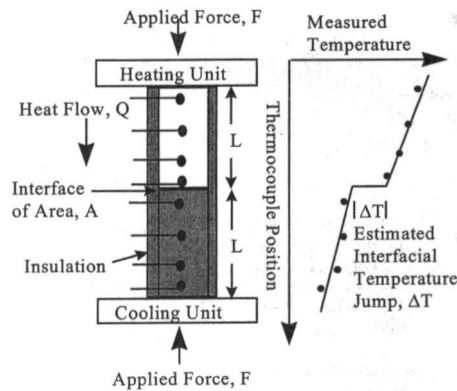


Fig. 1 Schematic diagram illustrating a traditional steady-state technique for measuring the thermal contact conductance between solids. The technique requires a thick solid sample since thermocouples need to be inserted. In addition, it requires a heating unit, a cooling unit, and thermal insulation since the heat flux needs to be precisely measured and should be uniform across the two solids.

To measure the thermal conductance for a thin sample, it is usually sandwiched between two thick samples and measured with the experimental set-up of Fig. 1 where the thermocouples are then inserted in the thick sample (Seyed-Yagoobi et al., 1992; Mohr et al., 1997). However, this generates two interfaces between the thin sample and the surrounding materials. Hence, this technique requires that the thermal conductivity of the thin sample must be known and that the two interfaces must have exactly the same conductance. There is no direct method of measuring the thermal contact conductance of an interface between two thin samples.

In view of the need to measure thermal contact conductance of wafer-like thin samples, a different approach is proposed in this study. This technique relies on photothermal heating and optical temperature measurement and is, therefore, fully noncontact. Although photothermal and photoacoustic techniques have been used to characterize interfaces and their associated thermal boundary resistance (Lepoutre et al., 1985; Tam et al., 1986; Lachaine, 1985), the new technique is based on a different temperature measurement method as described in Section 2. Section 2 explains the principle underlying this technique and describes the experimental apparatus. A theoretical analysis is needed to estimate the thermal contact conductance and thermophysical properties from the measured data, and is described in Section 3. Section 4 presents the experimental results whereas the conclusions are in Section 5.

2 Experiments

2.1 Principle. Figure 2(a) describes the experimental technique used in this study. The intensity of the heating laser is

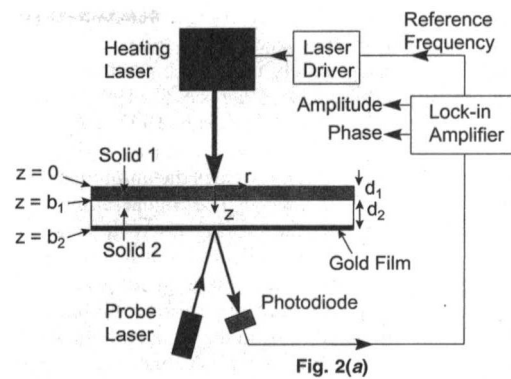


Fig. 2(a)

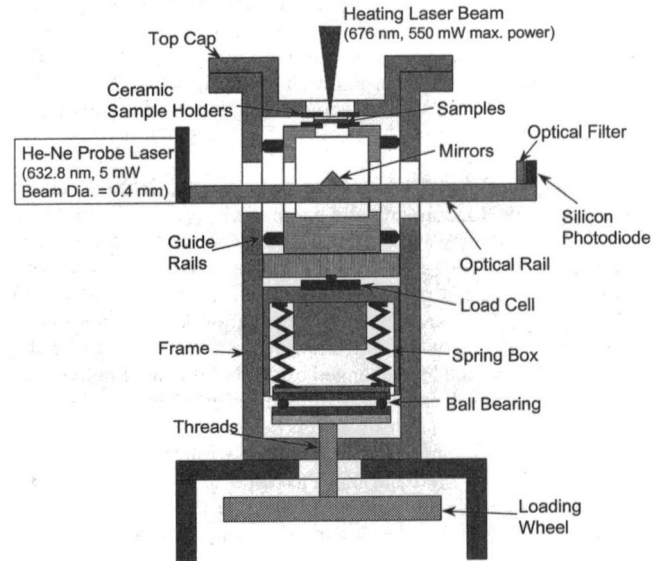


Fig. 2(b)

Fig. 2 (a) Schematic diagram illustrating the principle of the dynamic optical technique; (b) the experimental set-up used for the measurements in this paper

modulated at a frequency, f , and focused on a spot on the top surface of solid 1. Absorption of this laser on the top surface sends out a thermal wave through the bulk and interface of solids 1 and 2. The bottom surface of solid 2 is coated with a gold film of about $0.5 \mu\text{m}$ thickness. A probe laser is used to measure the temperature oscillation at frequency, f , of a spot on the gold surface directly under the heating laser spot through reflectance thermometry (Cardona, 1969; Rosei and Lynch, 1972). This technique is based on

Nomenclature

a = radius of heating laser spot, m
 A = sample surface area, m^2
 b = coordinate along thickness of solid, m
 C = heat capacity, J/kg-K
 C_{TR} = coefficient of thermoreflectance, $1/\text{K}$
 d = thickness of solid, m
 f = frequency, Hz
 F = load, N
 h = thermal contact conductance, $\text{W/m}^2\text{-K}$
 I = probe laser intensity, W
 k = thermal conductivity, W/m-K

P = pressure, N/m^2
 q = heat flux, W/m^2
 Q = heating laser power absorbed, W
 r = radial coordinate, m
 R = reflectivity
 s = Laplace transform variable
 t = time, s
 T = temperature, K
 u = temperature, K
 v = Laplace transform of u
 w = Hankel transform of v
 z = vertical coordinate along thickness of solid, m

α = thermal diffusivity, m^2/s
 β = spectral noise density of intensity, $\text{W}/\sqrt{\text{Hz}}$
 χ = defined in Eq. (14)
 λ = Hankel transform variable
 μ = defined as $l(dh/d\phi)/hl$, $1/\text{rad}$
 ϕ = phase lag, radians
 ρ = density, kg/m^3
 ω = angular frequency, rad/s

Subscripts

1 = solid 1
 2 = solid 2

the temperature dependence of the optical constants of a material which leads to a temperature dependence of its reflectivity. Reflectance thermometry has been widely used for noncontact temperature measurement (Epperlein, 1993; Claeys et al., 1993; Qiu et al., 1993; Quintard et al., 1996; Ju and Goodson, 1997, 1998). A photodiode measures the reflected probe laser intensity and sends the output to a lock-in amplifier, which provides the amplitude and the phase of the signal at frequency, f . The signal amplitude depends on the absorbed power of the heating laser, the heating laser spot size, the coefficient of thermorefectance of gold, as well as the reflectivity of the gold surface. Since these quantities are not always precisely known or require significant effort in calibration, estimation of the thermal conductance from the signal amplitude is difficult. The phase lag, ϕ , between the probe and the heating lasers is, however, immune to these property uncertainties and can be directly related to the thermal conductance. Therefore, this study used the phase lag to estimate the thermal properties of the thermal contact conductance between solids 1 and 2. These estimations require an elaborate theoretical model which is described in section 3.

2.2 Apparatus and Measurements. Figure 2(b) shows the apparatus for the loading unit and the probe laser. The loading unit consisted of a loading wheel that was used to rotate a screw with a thread pitch of 100 μm . The load was applied to a spring box which contained eight parallel compression springs each of 13930 N/m stiffness. The springs were chosen in a way that for a five-degree rotation of the wheel, which was assumed to be the minimum change, the load changed by 5.5 N. The maximum travel of the springs was 1 cm which yielded the maximum load to be 1114.4 N. Since the samples were chosen to be 1 cm \times 1 cm, the corresponding maximum pressure and the minimum change in pressure were 11.1 MPa and 55 kPa, respectively. A ball bearing was used to minimize any torsional load on the unit. The spring box had a sliding fit with the frame of the loading unit. A load cell was used in series to measure the force which was verified with the value calculated from the spring compression. A top cap was screwed on to the frame to provide a reactive force. A cut through the loading unit frame allowed the optical rail of the probe laser system to access the bottom surface of the sample. The samples were placed on ceramic sample holders which provided sufficient rigidity so that a uniform load could be applied on the sample despite the hole at the center used for optical access. When the samples were too thin such that the surface pressure became nonuniform under compressive load, they were placed between two thick glass pieces. The glass pieces provided optical access while ensuring rigidity and uniform load on the sample.

Optical heating was provided by a diode laser emitting at 676-nm wavelength with a maximum power output of 550 mW. The power was modulated using the sinusoidal output from a lock-in amplifier which provided the input for the laser driver. The heating laser beam was focused on to a spot approximately 1 mm \times 1 mm, yielding a flux in the range of 10^2 – 10^9 W/m². To maximize the absorption of the heating laser, a 50-nm carbon coating was applied on the top surface of the top sample. The effect of this very thin film on the phase lag can be expected to be negligible. A HeNe laser with 0.4-mm beam diameter, 5-mW output power at 632.8-nm wavelength, and 1-mrad beam divergence was used as the probe laser. A prism-shaped mirror was used to direct the horizontal incident beam vertical and the vertical reflected beam horizontal and on to a silicon photodiode. A gold film was deposited on the bottom surface as the highly reflective layer. Although the thermorefectance coefficient of Si is higher than that of gold, the gold film was still used for its well-calibrated data and for applications in nonsilicon cases. The photodiode had a noise equivalent power of 2.3×10^{-14} W/ $\sqrt{\text{Hz}}$, a conversion factor of 0.4 A/W at 632.8 nm, and was operated under a reverse bias of 9 V. The photocurrent was passed through a 10 K Ω resistor and the voltage output across the resistor was fed into the lock-in amplifier. Optical filters were used in front of the photodiode to

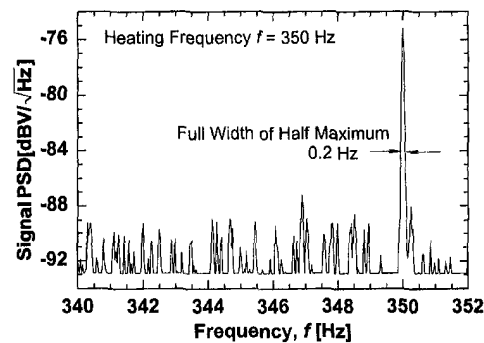


Fig. 3 A frequency spectrum of the photodiode signal showing the peak due to thermorefectance at the heating frequency of 350 Hz with a full-width half maximum of 0.2 Hz

block the heating laser beam at 676 nm and allow only the probe laser beam at 632.8-nm wavelength.

Optical alignment of the system was crucial. Both the heating and the probe lasers were mounted on x - y - z micropositioners. The probe laser beam was aligned onto the photodiode by moving one of the mirrors on the optical rail as well as by translating and rotating the HeNe laser. Before the experiments were started, it was important to ensure that the dc photodiode output was sufficiently high. The heating and the probe laser beams were also aligned, first visually and then by studying the output of the lock-in amplifier for the photodiode signal. Precise alignment of the heating and probing beams is rather difficult in the present experimental setup, but one can circumvent this difficulty as described in Section 3. Although the alignment would be easier if both laser beams are focused on the same side of the sample, it cannot be implemented in this technique since the heating of the sample requires a highly absorptive surface whereas reflectance thermometry requires a highly reflective one. Figure 3 shows a typical scan of the spectrum analyzer indicating the peak at 350 Hz corresponding to the thermorefectance signal. The white-noise floor in this spectrum corresponds to a spectral noise density, $\beta = 6 \times 10^{-9}$ W/ $\sqrt{\text{Hz}}$. The dominant noise source, hence, was not from the photodiode but from another source, perhaps the laser.

The coefficient of thermorefectance, $C_{TR} = (dR/dT)/R$, of gold is on the order of 10^{-5} K⁻¹ at 632.8 nm (Scouler, 1967; Cardona, 1969; Rosei and Lynch, 1972). The temperature resolution, ΔT_{\min} , defined for a signal-to-noise ratio of 2, can be estimated by the relation

$$\Delta T_{\min} = \frac{2\Delta I}{IRC_{TR}} = \frac{2\beta\sqrt{\Delta f}}{IRC_{TR}} \quad (1)$$

where $\Delta I = \beta\sqrt{\Delta f}$ is the noise in the intensity measurement for a bandwidth Δf of the lock-in amplifier, I is the probe laser intensity incident on the photodiode, and R is the reflectivity of the gold film at 632.8-nm wavelength. The typical bandwidth chosen for the measurements was $\Delta f = 7.8$ mHz which led to $\Delta I = 0.53$ nW for the white-noise floor in Fig. 3. A bandwidth of 7.8 mHz corresponds to a time constant of 10 s for the lock-in amplifier. Since it took at least five to ten time constants for the measured phase to be stable, it required one to two minutes to measure the phase lag for a single experimental condition. This is much shorter than 30–60 minutes required for each data point for the steady-state technique illustrated in Fig. 1. Assuming some losses due to reflections from the glass surfaces, $I = 3$ mW for the probe laser. Using $R = 0.95$ and $C_{TR} = 10^{-5}$ K⁻¹ for gold, one can estimate using Eq. (1) the minimum detectable temperature change to be 0.04 K. Although the technique is based on phase measurements, the minimum detectable temperature is an important quantity since, as will be indicated by the theory, it determines the frequency range for the measurements.

The internal resistance of the lock-in amplifier and the capaci-

tance of the photodiode resulted in a time constant which was less than 1 μ s. The phase lag of the system was also experimentally studied by measuring the phase lag between the heating and the probe laser while heating a gold film of 0.5- μ m thickness. The measured phase lag was found to be negligible in the 0–2 kHz frequency range, thus indicating that the system phase lag could be ignored in all measurements.

3 Theoretical Analysis

Consider the geometry in Fig. 2(a). Solid 1 occupies the region $0 < z < b_1$ and has a thickness $d_1 = b_1$, thermal diffusivity α_1 , and thermal conductivity k_1 . Solid 2 occupies the region $b_1 < z < b_2$ with properties α_2 and k_2 and a thickness, $d_2 = b_2 - b_1$. It is assumed that the heating laser is focused to a circular spot of radius, $r = a$, and is absorbed on the top surface of solid 1. The heat conduction equation in cylindrical coordinates is

$$\frac{\partial^2 u_j}{\partial r^2} + \frac{1}{r} \frac{\partial u_j}{\partial r} + \frac{\partial^2 u_j}{\partial z^2} = \frac{1}{\alpha_j} \frac{\partial u_j}{\partial t}; \quad (j = 1, 2) \quad (2)$$

where u_j is the temperature in solid j . It is assumed that most of the heat flow occurs in the r and z directions in the solid and the heat loss to the surrounding air is negligible. The boundary conditions at $z = 0$ are

$$\begin{aligned} -k_1 \left. \frac{\partial u_1}{\partial z} \right|_{z=0} &= \frac{Q}{\pi a^2} e^{-i\omega t} \quad \text{for } r \leq a \\ \left. \frac{\partial u_1}{\partial z} \right|_{z=0} &= 0 \quad \text{for } r > a \end{aligned} \quad (3)$$

where Q is the incident laser power absorbed on the top surface which is modulated at an angular frequency of $\omega = 2\pi f$. At $z = b_2$,

$$\left. \frac{\partial u_2}{\partial z} \right|_{z=b_2} = 0. \quad (4)$$

The energy balance at the interface can be written as

$$k_1 \left. \frac{\partial u_1}{\partial z} \right|_{z=b_1} = k_2 \left. \frac{\partial u_2}{\partial z} \right|_{z=b_1} = h(u_2 - u_1)|_{z=b_1}. \quad (5)$$

Since the periodic steady state is of interest, the starting temperatures are not important and for convenience $u_j(r, z, 0) = 0$ for $j = 1, 2$. It must be noted that a laser beam usually has a Gaussian intensity distribution and does not provide a uniform flux as assumed in Eq. (3). However, one can think of the radius a as an effective radius obtained by averaging over the Gaussian distribution. The agreement between the predictions based on top-hat and Gaussian distributions are good in the high frequency range as illustrated later in Fig. 5.

Details of the method to solve the governing equations in conjunction with the boundary conditions can be found in the Appendix and also partly in Dryden et al. (1998). The solution for the temperature distribution in the two solids are given as

$$\begin{aligned} u_1(r, z, t) &= \frac{Qe^{-i\omega t}}{k_1 \pi a} \times \int_{\lambda=0}^{\infty} \left[\frac{1}{\eta_1} \left\{ -\sinh \eta_1 z + \cosh \eta_1 z \right. \right. \\ &\quad \left. \left. \times \left[\frac{\cosh \eta_1 b_1}{\sinh \eta_1 b_1} - \frac{k_2 \eta_2}{k_1 \eta_1} \frac{\sinh \eta_2 (b_2 - b_1)}{\sinh \eta_1 b_1} \xi(\lambda, s) \right] \right\} \right]_{s=-i\omega} \\ &\quad \times J_1(a\lambda) J_0(r\lambda) d\lambda \quad (6) \end{aligned}$$

$$\begin{aligned} u_2(r, z, t) &= \frac{Qe^{-i\omega t}}{k_1 \pi a} \int_{\lambda=0}^{\infty} \left[\frac{\xi(\lambda, s)}{\eta_1} \cosh \eta_2 (b_2 - z) \right]_{s=-i\omega} \\ &\quad \times J_1(a\lambda) J_0(r\lambda) d\lambda \quad (7) \end{aligned}$$

where λ and s are the variables resulting from the Hankel and Laplace transforms, respectively, J_0 and J_1 are the zeroth and first-order Bessel functions, respectively, and

$$\eta_j = \left(\lambda^2 + \frac{s}{\alpha_j} \right)^{1/2}$$

$$\begin{aligned} \xi(\lambda, s) &= \left[\sinh \eta_1 b_1 \cosh \eta_2 (b_2 - b_1) \right. \\ &\quad \left. + \frac{k_2 \eta_2}{k_1 \eta_1} \cosh \eta_1 b_1 \sinh \eta_2 (b_2 - b_1) \right. \\ &\quad \left. + \frac{k_2 \eta_2}{h} \sinh \eta_1 b_1 \sinh \eta_2 (b_2 - b_1) \right]^{-1}. \quad (8) \end{aligned}$$

Since the measurements with the probe laser were made at $r = 0$ and $z = b_2$, these values can be used to simplify the integrand in Eq. (7). The phase lag at a given position either on the top or the bottom surface can be found from Eqs. (7) and (8). For example, in the expression for u_2 , the integral in Eq. (7) is a complex number which can be written as

$$u_2(r, b_2, t) = |u_2| e^{-i(\omega t - \phi)}. \quad (9)$$

The angle ϕ is the phase lag with respect to the incident radiant flux. This quantity can be used for estimation of the contact conductance as well as the thermophysical properties of the materials.

To establish validity of the conductance measurement technique, it is necessary to compare the measured phase lag with theoretical predictions for a benchmark case. This case was selected to be that of a single material (with no interface) of known thickness and thermal properties. The temperature rise of the bottom surface, $z = b$, at $r = 0$ can be derived (see Appendix) to be

$$u(0, b, t) = \frac{Qe^{-i\omega t}}{k \pi a} \int_{\lambda=0}^{\infty} \left[\frac{1}{\eta} \frac{1}{\sinh \eta b} \right]_{s=-i\omega} J_1(a\lambda) d\lambda. \quad (10)$$

The integral in Eq. (10) was calculated numerically and the phase lag was estimated from this computation. The high-frequency limit of Eq. (10) can be derived analytically and is given as

$$\begin{aligned} u(0, b, t) &= \frac{Q \exp \left[-b \sqrt{\frac{\pi f}{\alpha}} \right]}{\pi a^2 \sqrt{\pi f k \rho C}} \\ &\quad \times \exp \left[-i \left(\omega t - \left(b \sqrt{\frac{\pi f}{\alpha}} + \frac{\pi}{4} \right) \right) \right]. \quad (11) \end{aligned}$$

Therefore, the phase lag in the high-frequency limit can be written as

$$\phi = b \sqrt{\frac{\pi f}{\alpha}} + \frac{\pi}{4}. \quad (12)$$

The phase lag of $\pi/4$ in Eq. (12) results from the inherent phase difference between the heat flux and the temperature at any point. For the two-solid problem that involves contact resistance at the interface, the high-frequency limit of Eq. (7) can be written as

$$\begin{aligned} u_2(0, b_2, t) &= \frac{2\sqrt{2}Q \exp \left[- \left(d_1 \sqrt{\frac{\pi f}{\alpha_1}} + d_2 \sqrt{\frac{\pi f}{\alpha_2}} \right) \right]}{\pi a^2 \sqrt{\pi f (k\rho C)_1}} \\ &\quad \times \frac{\exp \left[-i \left(\omega t - \left(d_1 \sqrt{\frac{\pi f}{\alpha_1}} + d_2 \sqrt{\frac{\pi f}{\alpha_2}} + \frac{\pi}{4} \right) \right) \right]}{\left[1 + \frac{\sqrt{(k\rho C)_2}}{\sqrt{(k\rho C)_1}} + \frac{(1-i)\sqrt{\pi f (k\rho C)_2}}{h} \right]} \quad (13) \end{aligned}$$

where $d_1 = b_1$ is the thickness of solid 1 and $d_2 = b_2 - b_1$ is the thickness of solid 2. The phase lag in the high-frequency limit can be written as

$$\phi = \chi + \tan^{-1} \left[\frac{\left(\frac{\sqrt{\pi f(k\rho C)_2}}{h} \right)}{1 + \sqrt{\frac{(k\rho C)_2}{(k\rho C)_1} + \frac{\sqrt{\pi f(k\rho C)_2}}{h}}} \right];$$

where $\chi = d_1 \sqrt{\frac{\pi f}{\alpha_1}} + d_2 \sqrt{\frac{\pi f}{\alpha_2}} + \frac{\pi}{4}$. (14)

Hence, the thermal contact conductance, h , can be expressed in terms of phase lag as

$$h = \frac{\sqrt{\pi f(k\rho C)_2} [1 - \tan(\phi - \chi)]}{\left[1 + \sqrt{\frac{(k\rho C)_2}{(k\rho C)_1}} \tan(\phi - \chi) \right]}. \quad (15)$$

Note in Eq. (14) that when $h \rightarrow \infty$, i.e., in the absence of an interface, the phase lag reduces to the expression in Eq. (12) except for the fact that the phase lag of the two materials is added. On the other hand, when $h \rightarrow 0$, the additional phase lag from the interface is $\tan^{-1}(1)$ which is $\pi/4$. Hence, the whole range of h corresponds to phase lag range $0 < \phi < \pi/4$. It is also worth noting that if the material subscripts 1 and 2 are switched, the expression in Eq. (15) remains unchanged.

In addition to estimating h from Eq. (15) it is also important to determine the percentage error in h due to error in phase measurement. To facilitate the estimation, the quantity $\mu = |(dh/d\phi)/h|$ can be calculated to be

$$\mu = \left| \frac{1}{h} \left(\frac{dh}{d\phi} \right) \right| = \left| \frac{\tan(\phi - \chi)}{\sin^2(\phi - \chi) [1 - \tan(\phi - \chi)]} \right|. \quad (16)$$

The percentage error in the measured conductance can be expressed as $\Delta h/h = \mu \Delta \phi$ where $\Delta \phi$ is the error in phase measurement.

Figure 4 shows a series of plots of phase lag, ϕ , versus the nondimensional frequency, $b\sqrt{\pi f/\alpha}$, for different values of the ratio, $2a/b$. If the thickness of the material remains constant, variation of $2a/b$ represents changing the spot size of the heating laser. On each graph, $\phi - b\sqrt{\pi f/\alpha}$ curves are plotted for different values of the ratio r/b at the bottom surface. Since $r = 0$ corresponds to the center of the heating laser spot, variation of r/b at the bottom surface attempts to simulate the effect of misalignment of the heating and the probe lasers. It can be clearly seen that if $2a/b < 2$, a slight misalignment of the heating and the probe lasers can lead to large variations in the measured ϕ . Hence, this case is very sensitive to the location of the probe laser and is susceptible to errors. For the range $2a/b > 4$, all the $\phi - b\sqrt{\pi f/\alpha}$ curves for different values of $r/b < 2$ coincide. This makes the dependence of ϕ on r/b negligible which is the preferable condition for conducting experiments. Since the probe laser beam radius was 0.2 mm and the sample thickness ranged from 0.2 mm to 0.5 mm, alignment of the probe laser with the heating laser was possible within $r/b < 2$. On the other hand, the probe laser measured the average temperature and phase lag over a region equal to the probe beam diameter. To ensure that the phase lag over this whole region was almost uniform, it was necessary to satisfy the condition $2a/b > 4$ as suggested by Fig. 4. Increase of the heating laser spot size reduces the incident heat flux and, therefore, can decrease the temperature oscillations below the detectable limit estimated by Eq. (1). Note that although the phase lag, ϕ , starts from zero at low frequencies, it asymptotes to the value $b\sqrt{\pi f/\alpha} + \pi/4$ for higher frequencies, i.e., for $b\sqrt{\pi f/\alpha} > 1.5$, as suggested by Eq. (12). For the experiments results described in the next section, this region of $b\sqrt{\pi f/\alpha}$ was found to be useful for comparing the predictions with measurements.

4 Results

4.1 Single Material. To confirm the accuracy of this technique, it was first necessary to compare the results for a single

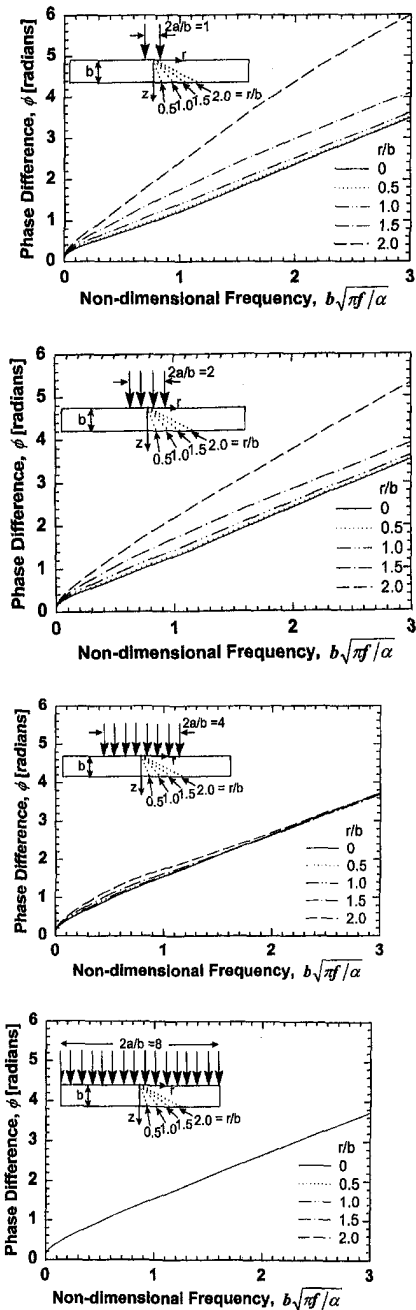


Fig. 4 Effect of the spot size of the heating laser on the top surface and misalignment of the measurement point on the bottom surface on the measured phase lag. The results indicate that if the heating laser spot diameter is more than four times the thickness of the solid then a slight misalignment in the probing point on the bottom leads to only small changes in phase lag.

sample of known thermal properties. Figure 5(a) shows the theoretical prediction and the measurements of the phase lag for a single crystal silicon sample with both surfaces polished. The thickness, b , of the sample was 0.225 mm and the p -doping level was $1.2 \times 10^{16} \text{ cm}^{-3}$. The theoretical prediction of the phase lag as a function of $b\sqrt{\pi f/\alpha}$ resulted in a single curve. To compare the measurements with the theory, it was necessary to guess the thermal diffusivity to normalize the experimental data in terms of the coordinate $b\sqrt{\pi f/\alpha}$. The same experimental data of phase lag is plotted in Fig. 5(a) for three selected values of α . For $b\sqrt{\pi f/\alpha} < 0.8$, there is large disagreement between the predictions and the measurements. It must be noted that $b\sqrt{\pi f/\alpha}$ can also be written as b/δ , where δ is the thermal penetration depth. The results

suggest that when the penetration depth is larger than the material thickness, the predictions do not agree with the measurements. The reason for this is at present unclear, although it may be due to the assumption of insulating boundary conditions at the bottom surface. However, the agreement for $b\sqrt{\pi f/\alpha} > 0.8$ provides a range for using this technique.

The inset in Fig. 5(a) magnifies the results to show the effect of the chosen α on the comparison of the measurements with the theory. The region of $b\sqrt{\pi f/\alpha} > 1.5$ is intentionally chosen because, as indicated before, the phase lag varies as $b\sqrt{\pi f/\alpha} + \pi/4$. It can be seen that the best agreement occurs for $\alpha = (80 \pm 3) \times 10^{-6} \text{ m}^2/\text{s}$. The error margin in the estimation of α was obtained from the error bars in the phase measurements as shown in Fig. 5(a). Using the density and heat capacity of silicon to be 2330 kg/m^3 and 712 J/kg-K (Incropera and Dewitt, 1990), respectively, the thermal conductivity of the silicon sample can be estimated from the measured α to be $k = 132.7 \pm 5 \text{ W/m-K}$. Recent measurements have shown that the thermal conductivity of silicon with both p -doping concentration of $4 \times 10^{14} \text{ cm}^{-3}$ and n -doping concentration of 10^{18} cm^{-3} is 135.1 W/m-K at 300 K (Lee and Cahill, 1997). This is not only within the error margin of the present measurements, the average values are within two percent of each other. The close agreement provides a benchmark test for the optical measurement technique.

Figure 5(b) shows the similar data set for an Al(6061 alloy) sample that was 0.223 mm thick. The inset shows that the best fit between the experiments and theory occurred for thermal diffusivity $\alpha = (73 \pm 3) \times 10^{-6} \text{ m}^2/\text{s}$. Using density $\rho = 2700 \text{ kg/m}^3$ and heat capacity $C = 896 \text{ J/kg-K}$ (Boyer et al., 1985), the thermal conductivity of the Al sample was found to be $176.6 \pm 7.3 \text{ W/m-K}$. The reported values of thermal diffusivity and conductivity of Al6061 are $74.4 \text{ m}^2/\text{s}$ and 180 W/m-K (Boyer et al., 1985), respectively, which are within the error margin of the present measurements and the average values are within two percent. The fact that the errors between reported and measured values are within two percent for both Si and Al samples suggests that the technique is quite accurate and reliable.

It is important to note that when the penetration depth is smaller than the material thickness, $b/\delta > 1$, the temperature oscillations at the bottom surface varies as $\exp(-b\sqrt{\pi f/\alpha})$ (see Eq. (11)). As the frequency is increased, the temperature oscillations decrease. The minimum detectable temperature, as estimated by Eq. (1), provides an upper limit to the frequency. This, for the results presented here, is typically in the range of 2–4 kHz. A small systematic deviation from the theoretical analysis in the high-frequency limit may be due to a larger system phase lag. To make measurements in the high-frequency regime, i.e., $f > 500 \text{ Hz}$, it was impossible to use wire thermocouples since the smallest time constant of commercially available ones are typically on the order of 10 ms. It is for this reason that an optical temperature measurement technique was adopted. In the present work, the maximum frequency for reflectance thermometry was not limited by the sensor response time or the lock-in amplifier bandwidth (which was 100 kHz), but by the minimum detectable temperature as explained above.

4.2 Two Solids With Contact Conductance. It is clear from Eq. (14) that the phase lag, ϕ , in the high-frequency limit can be plotted against the quantity $d_1\sqrt{\pi f/\alpha_1} + d_2\sqrt{\pi f/\alpha_2}$ since under the limiting condition of $h \rightarrow \infty$, the phase lag should vary as $d_1\sqrt{\pi f/\alpha_1} + d_2\sqrt{\pi f/\alpha_2} + \pi/4$. Figure 6 shows a such a plot for the Al-Si contact conductance measurements. The Al and Si samples were exactly the same as the ones used for single material measurements described in Section 4.1, and the measured values of α_1 and α_2 were used for data analysis. The RMS roughness of the contacting surfaces of Al and Si samples were $8.58 \mu\text{m}$ and 3.2 nm , respectively. Under compressive load $F = 1000 \text{ N}$ the phase lag was measured over a wide frequency range and shown as filled circles in Fig. 6. The plot shows that for $d_1\sqrt{\pi f/\alpha_1} + d_2\sqrt{\pi f/\alpha_2} > 1.5$, the high-frequency behavior is observed. In this regime,

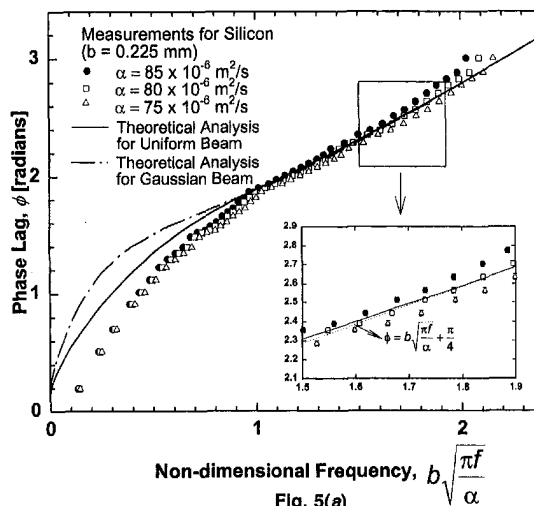


Fig. 5(a)

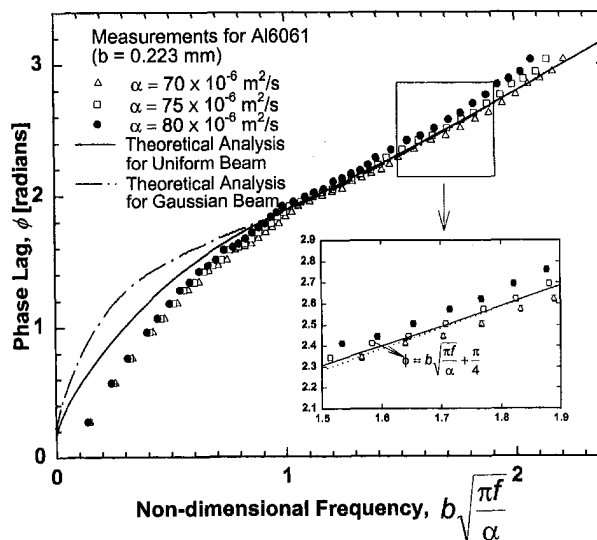


Fig. 5(b)

Fig. 5 (a) Plot of the phase lag as a function of nondimensional frequency for the silicon sample. The frequency is nondimensionalized by choosing the value of thermal diffusivity which gives the closest fit to the predictions (solid line). The inset shows details of the effect of the thermal diffusivity on the agreement between theory and experiments. (b) Similar plot of phase lag versus nondimensional frequency for the aluminum sample.

Eq. (15) could be applied to estimate the contact conductance. The modulation frequency $f = 350 \text{ Hz}$ was chosen so that it fell in the high-frequency regime, and then the load was reduced to 80 N . It can be observed that the phase lag increased as the load was decreased. This is expected since the decrease in load results in a decrease of the real area of contact and thereby a reduction in thermal contact conductance. Also shown are the predictions for the phase lag as a function $d_1\sqrt{\pi f/\alpha_1} + d_2\sqrt{\pi f/\alpha_2}$ for variation of h over two orders of magnitude. Although one could try to fit the predictions to each data at different loads, the closed-form solution in Eq. (15) provides a simple method to estimate the contact conductance from the measured phase lag in the high-frequency regime.

The estimated contact conductance data as a function of load and pressure, $P = F/A$, are shown in Fig. 7. Using the values of ϕ and χ from Fig. 6, the value of μ was calculated using Eq. (16) and found to vary between 6 and 9 rad^{-1} . Although the lock-in amplifier had an intrinsic phase error of about 10^{-5} radians, the actual phase error, $\Delta\phi$, measured during the experiments was typically about 10^{-2} radians. From the relation,

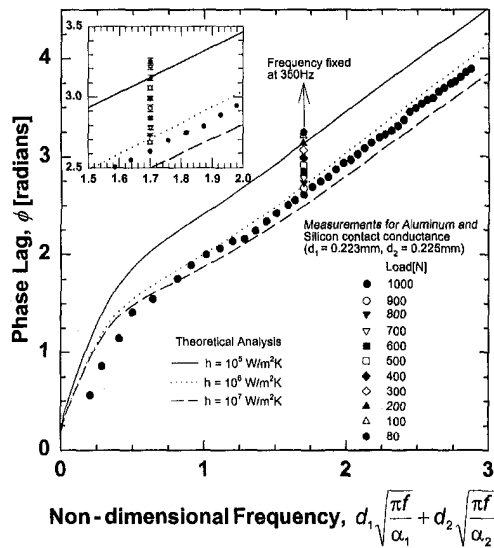


Fig. 6 Plot of phase lag as a function of nondimensional frequency for the Al and Si sample in contact with each other. A frequency was carried out for the load of 1000 N. Then the frequency was fixed at 350 Hz and the load was reduced to 80 N while the phase lag was measured. The inset shows details of how the phase lag changes with load.

$\Delta h/h = \mu \Delta \phi$, the percentage error in the estimated conductance varied between six and nine percent. The phase error and the percentage conductance error for each value of load is shown in Figs. 6 and 7, respectively.

The inset in Fig. 7 shows the conductance-pressure data in a log-log plot. The plot indicates that the conductance varied with pressure as $h \propto P^{1.76}$. It should be noted that previous experimental studies have shown the load exponent to be in the range of 0.6–1.0 and theoretical studies have attempted to explain the origin of the exponent by various means. To the best of our knowledge, an exponent of 1.76 is higher than most observed and predicted values. The reason for this high value is at present unclear. However, it is important to note a significant difference between previous measurements and the present one. Previous measurements based on the technique illustrated in Fig. 1 have all measured the average contact conductance over the whole contact interface which were typically about 1–2 cm in characteristic length. These measurements averaged the conductance over local roughness or surface waviness. In contrast, the present technique measured the local contact conductance over a region that was typically about 2 mm in diameter whereas the samples were 1 cm \times 1 cm in size. Hence, if the surface contained any waviness with wavelengths greater than or equal to 2 mm, then the present measurements would certainly be affected by it. If this is true, then these measurements cannot be compared with those of previous ones since the average conductance was not measured. In addition, it would be difficult to compare with previous theories since they are all based on a nominally flat surface. However, it is unclear at present whether local surface waviness led to such a high exponent value, but it is certainly a possibility. On the other hand, the nonuniform distribution of load across the sample could be another possibility.

5 Conclusions

This paper presents a fully noncontact optical technique for the measurement of thermal contact conductance of wafer-like thin solid samples. The technique is based on heating one exposed solid surface using a modulated high-power laser beam, and the simultaneous measurement of the corresponding temperature modulation on the other exposed solid surface by monitoring the reflectance of a low-power probe laser beam. Because the phase lag

between the probe laser signal and the heating laser is independent of the optical properties of the solid and the laser intensities, it was used to estimate the thermal contact conductance of the interface between the two solids.

A detailed theoretical analysis was developed to estimate the thermal contact conductance as well as the thermophysical properties of the solids from the measured phase lag as a function of the modulation frequency and thickness of the solids. The analysis showed that if the heating laser beam spot is small compared to the thickness of the solid, a slight misalignment between the heating and probe laser beams can lead to large errors in the measured phase lags. The analysis provided the conditions for robust measurement so that slight misalignments do not lead to changes in phase lags. Closed-form solutions were also obtained in the high-frequency limit which provided a simple procedure to estimate thermophysical properties solids as well as the thermal contact conductance of interfaces.

As a benchmark for this technique, the phase lag was measured as a function of modulation frequency for a single crystal silicon wafer that was 0.225 mm thick. Although the low-frequency data did not agree well with the theory, agreement was excellent in the high-frequency range, i.e., when the sample thickness was larger than the thermal penetration depth. Comparison of theory and measurements in the high-frequency range was used to estimate the thermal conductivity of the silicon sample, which was found to be within two percent of previously reported data. Measurements of thermal contact conductance as a function of pressure were successfully made for Al-Si samples that were each about 0.225 mm thick.

In conclusion, it is important to note the differences between the optical technique presented here and the traditional techniques that are widely used for measuring thermal contact conductance. Each data point in the dynamic optical technique requires about one to two minutes whereas it can take about one hour for the traditional techniques since they are based on steady-state measurements. The traditional techniques require thick samples since thermocouples need to be inserted to measure temperature gradients in the solids. In contrast, the optical technique is fully noncontact and can be used for thin solids samples. This is particularly suited for electronic packaging materials which are typically 0.1–5 mm thick. Previous steady-state techniques need precise measurement of heat flux and temperature thereby requiring a well calibrated heater, a controlled steady-state cooling unit, and thermal insulation around the sample. In contrast, because the optical technique is based on phase lag data, temperature and heat flux need not be measured precisely. In addition, the solids do not have to be insulated. Finally, whereas the traditional techniques measure

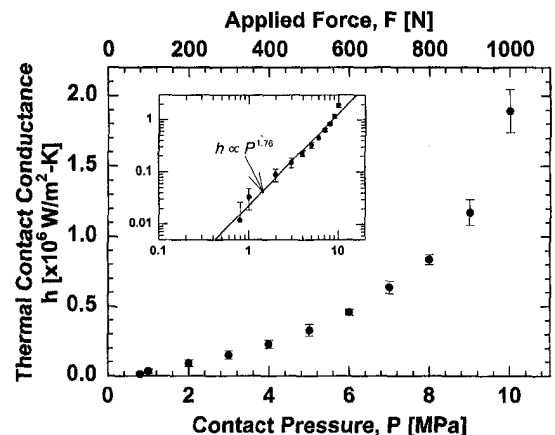


Fig. 7 Plot of thermal contact conductance estimated from the phase lag measurements as a function of compressive load for the Al-Si interface

average thermal contact conductance between the two solids, the optical technique can measure local conductance to a resolution of about four times thickness of the solid. Hence, by moving the laser spot, variations of contact conductance induced by surface waviness, property variations, and interface voids can be measured.

Acknowledgments

This work was partly supported by a grant from Hitachi. Our thanks to Dr. Shigeki Hirasawa of Hitachi Mechanical Engineering Research Laboratory for his interest and support of this work. We take this opportunity to express our deepest gratitude and respect for late Prof. Kunio Hijikata who helped initiate this collaboration. GW and AM were supported by the U.S. National Science Foundation through grant CTS-9796166.

References

- Boyer, H. E., and Gall, T. L., 1985, *Metals Handbook*, Vol. 2, 9th Ed., Am. Soc. Metals, pp. 115–116.
- Cardona, M., 1969, "Modulation spectroscopy," *Solid State Physics*, Suppl. 11, F. Seitz, D. Turnbull, and H. Ehrenreich, eds., Academic Press, New York.
- Childres, W. S., and Peterson, G. P., 1989, "Quantification of thermal contact conductance in electronic packages," *IEEE Trans. Components, Hybrids, & Manufacturing Technol.*, Vol. 12, pp. 717–723.
- Claeys, W., Dilhaire, S., Quintard, V., Dom, J. P., and Danto, Y., 1993, "Thermoreflectance optical test probe for the measurement of current-induced temperature changes in microelectronic components," *Quality & Reliability Eng. Int.*, Vol. 9, pp. 303–308.
- Cooper, M. G., Mikic, B. B., and Yovanovich, M. M., 1969, "Thermal contact conductance," *Int. J. Heat Mass Transfer*, Vol. 12, pp. 279–300.
- Dryden, J. R., McDonald, K. R., Majumdar, A., and Zok, F. W., 1998, "A photothermal technique for the determination of the thermal conductance of interfaces and cracks," submitted for publication.
- Epperlein, P. W., 1993, "Micro-temperature measurements on semiconductor laser mirrors by reflectance modulation: A newly developed technique for laser characterization," *Jpn. J. Appl. Phys.*, Vol. 32, pp. 5514–5522.
- Fletcher, L. S., 1988, "Recent Developments on Contact Conductance Heat Transfer," ASME JOURNAL OF HEAT TRANSFER, Vol. 110, pp. 1059–1070.
- Incropera, F. P., and DeWitt, D. P., 1990, *Fundamentals of Heat and Mass Transfer*, 3rd Ed., John Wiley and Sons, New York.
- Ju, Y. S., and Goodson, K. E., 1997, "Short-timescale thermal mapping of interconnects," *IEEE Proc. Int. Reliab. Phys. Symp.*, Denver, CO, pp. 320–324.
- Ju, Y. S., and Goodson, K. E., 1998, "Short-Time-Scale Thermal Mapping of Microdevices Using Scanning Thermoreflectance Technique," ASME JOURNAL OF HEAT TRANSFER, Vol. 120, pp. 306–313.
- Kraus, A. D., and Bar-Cohen, A., 1983, *Thermal Analysis and Control of Electronic Equipment*, Hemisphere, New York.
- Lachaine, A., 1985, "Thermal analysis by photoacoustic phase measurements: Effect of sample thickness," *J. Appl. Phys.*, Vol. 57, pp. 5075–5077.
- Lambert, M. A., and Fletcher, L. S., 1997, "Review of models for thermal contact conductance of metals," *J. Thermophysics and Heat Transfer*, Vol. 11, pp. 129–140.
- Lee, S. M., and Cahill, D. G., 1997, "Heat transport in thin dielectric films," *J. Appl. Phys.*, Vol. 81, pp. 2590–2595.
- Lepoutre, F., Fournier, D., and Boccara, A. C., 1985, "Nondestructive control of weldings using the mirage detection," *J. Appl. Phys.*, Vol. 57, pp. 1009–1015.
- Leung, M., Hsieh, C. K., and Goswami, D. Y., 1998, "Prediction of Thermal Contact Conductance in Vacuum by Statistical Mechanics," ASME JOURNAL OF HEAT TRANSFER, Vol. 120, pp. 51–57.
- Maddren, J., and Marschall, E., 1995, "Predicting thermal contact resistance at cryogenic temperatures for spacecraft applications," *J. Spacecraft and Rockets*, Vol. 32, pp. 469–474.
- Majumdar, A., and Tien, C. L., 1991, "Fractal Network Model of Contact Conductance," ASME JOURNAL OF HEAT TRANSFER, Vol. 113, pp. 516–525.
- Mikic, B. B., 1974, "Thermal contact conductance: theoretical considerations," *Int. J. Heat Mass Transfer*, Vol. 17, pp. 205–214.
- Mohr, J. W., Seyed-Yagoobi, J., and Price, D. C., 1997, "Thermal Contact Conductance of a Paper/Elastomer Interface," ASME JOURNAL OF HEAT TRANSFER, Vol. 119, pp. 363–366.
- Nishino, K., Yamashita, S., and Torii, K., 1995, "Thermal contact conductance under low applied load in vacuum environment," *Experimental Thermal and Fluid Science*, Vol. 10, pp. 258–271.
- Qiu, T. Q., Grigoropoulos, C. P., and Tien, C. L., 1993, "Novel technique for non-contact and microscale temperature measurements," *Experimental Heat Transfer*, Vol. 6, pp. 231–241.
- Quintard, V., Deboy, G., Dilhaire, Lewis, D., Phan, T., and Claeys, W., 1996, "Laser beam thermography of circuits in the particular case of passivated semiconductors," *Microelectronic Engineering*, Vol. 31, pp. 291–298.
- Rosei, R., and Lynch, D. W., 1972, "Thermomodulation spectra of Al, Au, and Cu," *Phys. Rev. B*, Vol. 5, pp. 3883–3893.
- Salgon, J. J., Robbe-Valloire, F., Blouet, J., and Bransier, J., 1997, "A mechanical

and geometrical approach to thermal contact resistance," *Int. J. Heat Mass Transfer*, Vol. 40, pp. 1121–1129.

Scouler, W. J., 1967, "Temperature-modulated reflectance of gold from 2 to 10 eV," *Phys. Rev. Lett.*, Vol. 18, pp. 445–448.

Seyed-Yagoobi, J., Ng, K. H., Fletcher, L. S., 1992, "Thermal Contact Conductance of a Bone-Dry Paper Handsheet/Metal Interface," ASME JOURNAL OF HEAT TRANSFER, Vol. 114, pp. 326–330.

Tam, A. C., and Sontag, H., 1986, "Measurement of air gap thickness underneath an opaque film by pulsed photothermal radiometry," *Appl. Phys. Lett.*, Vol. 49, pp. 1761–1763.

Williamson, M., and Majumdar, A., 1992, "Effect of Surface Deformations on Contact Conductance," ASME JOURNAL OF HEAT TRANSFER, Vol. 114, pp. 802–810.

Yovanovich, M. M., 1987, "Theory and applications of constriction and spreading resistance concepts for microelectronic thermal management," *Proceedings of the International Symposium on Cooling Technology for Electronic Equipment*, Honolulu, HI.

APPENDIX

Let $v_j(r, z, s)$ be the Laplace transform of $u_j(r, z, t)$ so that

$$v_j(r, z, s) = \int_{t=0}^{\infty} e^{-st} u_j(r, z, t) dt \quad (A1)$$

and let $w_j(\lambda, z, s)$ be the Hankel transform of $v_j(r, z, s)$ so that

$$w_j(\lambda, z, s) = \int_{r=0}^{\infty} v_j(r, z, s) r J_0(\lambda r) dr \quad (A2)$$

where J_0 is the Bessel function of zeroth order.

Laplace transform of Eqs. (2)–(5):

$$\begin{aligned} \frac{\partial^2}{\partial r^2} \int_{t=0}^{\infty} u_j e^{-st} dt + \frac{1}{r} \frac{\partial}{\partial r} \int_{t=0}^{\infty} u_j e^{-st} dt \\ + \frac{\partial^2}{\partial z^2} \int_{t=0}^{\infty} u_j e^{-st} dt - \frac{1}{\alpha_j} \int_{t=0}^{\infty} \frac{\partial u_j}{\partial t} e^{-st} dt = 0 \end{aligned}$$

$$\frac{\partial^2 v_j}{\partial r^2} + \frac{1}{r} \frac{\partial v_j}{\partial r} + \frac{\partial^2 v_j}{\partial z^2} - \frac{1}{\alpha_j} \left([u_j e^{-st}]_{t=0}^{\infty} + s \int_{t=0}^{\infty} u_j e^{-st} dt \right) = 0$$

$$\frac{\partial^2 v_j}{\partial r^2} + \frac{1}{r} \frac{\partial v_j}{\partial r} + \frac{\partial^2 v_j}{\partial z^2} - \frac{s}{\alpha_j} v_j = 0 \quad (A3)$$

$$\begin{aligned} \int_{t=0}^{\infty} k_1 \left. \frac{\partial u_1}{\partial z} \right|_{z=0} e^{-st} dt = k_1 \left. \frac{\partial v_1}{\partial z} \right|_{z=0} \\ = -q_0 f(r) \int_{t=0}^{\infty} e^{-i\omega t} e^{-st} dt = q_0 f(r) \frac{1}{(s + i\omega)} \end{aligned}$$

$$k_1 \left. \frac{\partial v_1}{\partial z} \right|_{z=0} = -q_0 f(r) \frac{1}{(s + i\omega)} \quad 0 < r < \infty \quad (A4)$$

where, for a Gaussian beam, $f(r) = e^{-r^2/a^2}$; for a uniform beam, $f(r) = 1$, $0 < r < a$, otherwise, $f(r) = 0$. In this paper, uniform beam simplification was used. This simplification was carefully studied and compared with the case of Gaussian beam. Some of the results were shown in Fig. 5. The coincidence in the high-frequency range ($b\sqrt{\pi f l \alpha} > 1$) was clearly shown. Since only high-frequency range is of interest, the uniform beam simplification was confirmed to be correct and useful in the high frequency range.

$$\left. \frac{\partial v_2}{\partial z} \right|_{z=b_2} = 0 \quad (A5)$$

$$k_1 \frac{\partial v_1}{\partial z} \Big|_{z=b_1} = k_2 \frac{\partial v_2}{\partial z} \Big|_{z=b_1} = h(v_2 - v_1) \Big|_{z=b_1} \quad (\text{A6})$$

Note that

$$r \frac{\partial^2 v_j}{\partial r^2} + \frac{\partial v_j}{\partial r} = \frac{\partial}{\partial r} \left(r \frac{\partial v_j}{\partial r} \right),$$

$$\lim_{x \rightarrow \infty} J_\nu(x) = 0,$$

$$\frac{d}{dr} J_0(\lambda r) = -\lambda J_1(\lambda r),$$

$$\frac{d}{dr} [r J_1(\lambda r)] = \lambda r J_0(\lambda r).$$

The Hankel transforms of Eqs. (A3)–(A6) are

$$\int_{r=0}^{\infty} \left(r \frac{\partial^2 v_j}{\partial r^2} + \frac{\partial v_j}{\partial r} \right) J_0(\lambda r) dr + \int_{r=0}^{\infty} \frac{\partial^2 v_j}{\partial z^2} r J_0(\lambda r) dr - \frac{s}{\alpha_j} \int_{r=0}^{\infty} v_j r J_0(\lambda r) dr = 0$$

$$\int_{r=0}^{\infty} \frac{\partial}{\partial r} \left(r \frac{\partial v_j}{\partial r} \right) J_0(\lambda r) dr + \frac{\partial^2}{\partial z^2} \int_{r=0}^{\infty} v_j r J_0(\lambda r) dr - \frac{s}{\alpha_j} \int_{r=0}^{\infty} v_j r J_0(\lambda r) dr = 0$$

$$\left[r \frac{\partial v_j}{\partial r} J_0(\lambda r) \right]_{r=0}^{\infty} - \int_{r=0}^{\infty} r \frac{\partial v_j}{\partial r} (-\lambda) J_1(\lambda r) dr + \frac{\partial^2 w_j}{\partial z^2} - \frac{s}{\alpha_j} w_j = 0$$

$$\lambda \int_{r=0}^{\infty} \frac{\partial v_j}{\partial r} r J_1(\lambda r) dr + \frac{\partial^2 w_j}{\partial z^2} - \frac{s}{\alpha_j} w_j = 0$$

$$\lambda [v_j r J_1(\lambda r)]_{r=0}^{\infty} - \lambda \int_{r=0}^{\infty} v_j \lambda r J_0(\lambda r) dr + \frac{\partial^2 w_j}{\partial z^2} - \frac{s}{\alpha_j} w_j = 0$$

$$-\lambda^2 w_j + \frac{\partial^2 w_j}{\partial z^2} - \frac{s}{\alpha_j} w_j = 0.$$

So

$$\frac{\partial^2 w_j}{\partial z^2} - \left(\lambda^2 + \frac{s}{\alpha_j} \right) w_j = 0 \quad (\text{A7})$$

$$\int_{r=0}^{\infty} \frac{\partial v_1}{\partial z} \Big|_{z=0} r J_0(\lambda r) dr = \frac{\partial w_1}{\partial z} \Big|_{z=0}$$

$$= -\frac{q_0}{k_1} \frac{1}{(s + i\omega)} \int_{r=0}^{\infty} f(r) r J_0(\lambda r) dr$$

$$\frac{\partial w_1}{\partial z} \Big|_{z=0} = -\frac{q_0}{k_1} \frac{1}{(s + i\omega)} \int_{r=0}^{\infty} f(r) r J_0(\lambda r) dr \quad (\text{A8})$$

$$\frac{\partial w_2}{\partial z} \Big|_{z=b_2} = 0 \quad (\text{A9})$$

$$k_1 \frac{\partial w_1}{\partial z} \Big|_{z=b_1} = k_2 \frac{\partial w_2}{\partial z} \Big|_{z=b_1} = h(w_2 - w_1) \Big|_{z=b_1}. \quad (\text{A10})$$

Solution of the differential Eq. (A7) can be written as

$$w_j = A_j \sinh \eta_j z + B_j \cosh \eta_j z$$

$$\eta_j = \left(\lambda^2 + \frac{s}{\alpha_j} \right)^{1/2}. \quad (\text{A11})$$

Using the boundary condition at $z = b_2$, the solution for w_2 is

$$w_2 = C_2 \cosh \eta_2 (z - b_2). \quad (\text{A12})$$

Using the boundary conditions at $z = 0$ and $z = b_1$, the solution for w_1 is

$$w_1 = A_1 \sinh \eta_1 z + B_1 \cosh \eta_1 z \quad (\text{A13})$$

where

$$A_1 = -\frac{q_0}{k_1} \frac{1}{(s + i\omega)} \psi(\lambda, s)$$

$$B_1 = -A_1 \left[\frac{\cosh \eta_1 b_1}{\sinh \eta_1 b_1} - \frac{k_2 \eta_2}{k_1 \eta_1} \frac{\sinh \eta_2 (b_2 - b_1)}{\sinh \eta_1 b_1} \xi(\lambda, s) \right]$$

$$C_2 = -A_1 \xi(\lambda, s) \quad (\text{A14})$$

and

$$\psi(\lambda, s) = \frac{1}{\eta_1} \int_{r=0}^{\infty} f(r) r J_0(\lambda r) dr$$

$\xi(\lambda, s)$

$$= \left[\begin{array}{c} \sinh \eta_1 b_1 \cosh \eta_2 (b_2 - b_1) + \frac{k_2 \eta_2}{k_1 \eta_1} \cosh \eta_1 b_1 \\ \sinh \eta_2 (b_2 - b_1) + \frac{k_2 \eta_2}{h} \sinh \eta_1 b_1 \sinh \eta_2 (b_2 - b_1) \end{array} \right]^{-1}. \quad (\text{A15})$$

The steady periodic behavior of temperature in each material is given by inverting the Hankel and Laplace transforms. The Hankel inverse transform is given as

$$v_j(r, z, s) = \int_{\lambda=0}^{\infty} w_j(\lambda, z, s) \lambda J_0(r\lambda) d\lambda \quad (\text{A16})$$

so one can find that

$$v_1(r, z, s) = \frac{q_0}{k_1} \frac{1}{(s + i\omega)} \int_{\lambda=0}^{\infty} \psi(\lambda, s) \times \left\{ -\sinh \eta_1 z + \cosh \eta_1 z \left[\frac{\cosh \eta_1 b_1}{\sinh \eta_1 b_1} - \frac{k_2 \eta_2}{k_1 \eta_1} \frac{\sinh \eta_2 (b_2 - b_1)}{\sinh \eta_1 b_1} \xi(\lambda, s) \right] \right\} \lambda J_0(r\lambda) d\lambda \quad (\text{A17})$$

$$v_2(r, z, s) = \frac{q_0}{k_1} \frac{1}{(s + i\omega)} \int_{\lambda=0}^{\infty} \psi(\lambda, s) \xi(\lambda, s) \times \cosh \eta_2 (b_2 - z) \lambda J_0(r\lambda) d\lambda. \quad (\text{A18})$$

The Laplace inverse transform can be used to determine the temperature distribution. This follows as

$$u_1(r, z, t) = \frac{q_0 e^{-i\omega t}}{k_1} \times \int_{\lambda=0}^{\infty} \left[\psi(\lambda, s) \left\{ -\sinh \eta_1 z + \cosh \eta_1 z \left[\frac{\cosh \eta_1 b_1}{\sinh \eta_1 b_1} - \frac{k_2 \eta_2 \sinh \eta_2 (b_2 - b_1)}{k_1 \eta_1 \sinh \eta_1 b_1} \xi(\lambda, s) \right] \right\} \right]_{s=-i\omega} \lambda J_0(r\lambda) d\lambda \quad (\text{A19})$$

$$u_2(r, z, t) = \frac{q_0 e^{-i\omega t}}{k_1} \times \int_{\lambda=0}^{\infty} [\xi(\lambda, s) \cosh \eta_2 (b_2 - z) \psi(\lambda, s)]_{s=-i\omega} \lambda J_0(r\lambda) d\lambda. \quad (\text{A20})$$

The temperature rise on bottom surface of the specimen at $r = 0$ is

$$u_2(0, b_2, t) = \frac{q_0 e^{-i\omega t}}{k_1} \int_{\lambda=0}^{\infty} [\xi(\lambda, s) \psi(\lambda, s)]_{s=-i\omega} \lambda d\lambda. \quad (\text{A21})$$

Now consider a special case for determining the thermal diffusivity of a single material of thickness, b . The absence of an interface in this case can be represented as $1/h \rightarrow 0$. The temperature distribution in the single material can be derived to be

$$u(r, z, t) = \frac{q_0 e^{-i\omega t}}{k} \int_{\lambda=0}^{\infty} \left[\frac{1 \cosh \eta (b - z)}{\eta \sinh \eta b} \right]_{s=-i\omega} \times \left(\int_{r'=0}^{\infty} f(r') r' J_0(\lambda r') dr' \right) \lambda J_0(r\lambda) d\lambda. \quad (\text{A22})$$

Hence, the temperature rise on the bottom surface, $z = b$ at $r = 0$ is

$$u(0, b, t) = \frac{Q e^{-i\omega t}}{k \pi a} \int_{\lambda=0}^{\infty} \left[\frac{1}{\eta \sinh \eta b} \right]_{s=-i\omega} \times \left(\int_{r'=0}^{\infty} f(r') r' J_0(\lambda r') dr' \right) \lambda d\lambda. \quad (\text{A23})$$

Instability of Ultra-Thin Water Films and the Mechanism of Droplet Formation on Hydrophilic Surfaces

A. Majumdar

Department of Mechanical Engineering,
University of California,
Berkeley, CA 94720

I. Mezić

Department of Mechanical Engineering,
University of California,
Santa Barbara, CA 93106

This paper presents a new theory of droplet formation during condensation of water on a hydrophilic surface. The theory uses hydration, electrostatic, van der Waals, and elastic strain interactions between a hydrophilic solid surface and a water film, and shows that contributions to the disjoining pressure are dominated by hydration forces for films thinner than 3 nm. The equilibrium film thickness is found to remain almost constant at about 0.5 nm for a wide range of relative humidity, although it increases sharply as the relative humidity approaches unity. The competition between strain energy on one hand, and hydration, van der Waals, and liquid-vapor surface tension on the other, induces instability for films thicker than a critical value. The critical wavelength of instability, L_{cr} , is also predicted as a function of film thickness. The theory proposes that as the relative humidity increases, nucleation initially occurs in monolayer fashion due to strong hydration forces. Using nucleation thermodynamics it predicts a critical nucleus size, d^ , and internuclei spacing, l , as a function of subcooling, ΔT , of the solid surface and shows that both length scales decrease with increasing subcooling. Since these monolayer nuclei are formed on the adsorbed water film, it is shown that when the internuclei spacing is larger than the critical wavelength, $l > L_{cr}$, instability occurs in the film resulting in droplet formation. The theory predicts that beyond a certain value of subcooling, the interdroplet spacing is "choked" and cannot decrease further.*

1 Introduction

Formation of droplets during condensation is a well-known phenomenon. Dropwise condensation provides some of the highest known heat transfer coefficients ($\approx 10^4 - 10^5$ W/m²-K) and is critical for many applications of technological importance such as heat exchangers. The normal procedure to promote dropwise condensation is to coat the surface with a hydrophobic or nonwetting material. However, dropwise condensation is not limited to nonwetting surfaces and has often been observed on hydrophilic or wetting surfaces. A common example is the fogging of glasses when one enters a warm room from a cooler exterior or when one breathes on a cold glass surface. Despite the wide use and observations of dropwise condensation, the underlying physics of droplet formation at the molecular scales is not well understood. A deeper understanding could lead to surfaces whose chemistry is tailored for controlled dropwise condensation.

Several theories have been proposed which can be grouped in two categories. Jakob (1936) first proposed that condensation initially occurs in a film-wise manner. On reaching a critical thickness, the film ruptures and the liquid is drawn into droplets by surface tension. The experimental observations of Baer and McKelvey (1958), Welch and Westwater (1961), and Sugawara and Katsuta (1966) seem to confirm this school of thought. A different theory was proposed by Eucken (1937) who suggested that droplet formation is fundamentally a heterogeneous nucleation process of a liquid on a bare solid surface. When vapor molecules adsorb on a solid surface, they diffuse and form a critical nucleus that grows in time due to further condensation. The size of the critical nucleus depends on the liquid surface tension, the contact angle between the solid, and the liquid droplet as well as the Gibbs free-energy

change during condensation. Experiments by Umur and Griffith (1965) and Erb and Thelen (1965) tend to support this theory. Although droplet formation has been a topic of study for over six decades, its origin has remained a topic of debate. Recent experiments on the nature of liquids in contact with solid surfaces have led to several key insights about the underlying intermolecular forces. These insights were not available when the first theories of dropwise condensation were proposed and have not yet been used to understand or explain the phenomenon. The purpose of this paper is to use this new knowledge of intermolecular forces and develop a new theory of droplet formation.

Insight about droplet formation can be obtained from studying the growth of solid films deposited on a solid surface. Three types of growth have been observed (Vook, 1982; Ohring, 1992). First is *island formation* due to heterogeneous nucleation of droplets. This occurs when the attractive forces between the adsorbed atoms and the substrate is less than that between two adsorbed atoms, and when the adsorbed atoms are sufficiently mobile to form nuclei. This is analogous to the Eucken theory of water droplet formation. Second is *epitaxial* growth of solid films which happens when the adsorbed atoms are highly mobile and when the attractive forces between adsorbed atoms and the substrate are very strong. Third is *Stranski-Krastanov* growth in which the film initially grows epitaxially, but on reaching a critical thickness buckles into islands through instability in the film. The instability is induced by competition between elastic strain energy in the film caused by a mismatch in lattice constants, and the surface energy of the film surface which tries to reduce the film surface area (Srolovitz, 1989; Spencer et al., 1991). Beyond a critical thickness, elastic strain overwhelms surface tension resulting in film instability. Since strain energy depends on the film volume and surface energy depends on the surface area, their ratio produces a length scale, which is the critical thickness of the film. It will be shown here that droplet formation in water films on a hydrophilic solid surface is similar to Stranski-Krastanov growth of solid films. However,

Contributed by the Heat Transfer Division for publication in the JOURNAL OF HEAT TRANSFER. Manuscript received by the Heat Transfer Division, Dec. 1, 1998; revision received, May 6, 1999. Keywords: Condensation, Droplet, Heat Transfer, Instability, Interface, Nanoscale. Associate Technical Editor: M. Modest.

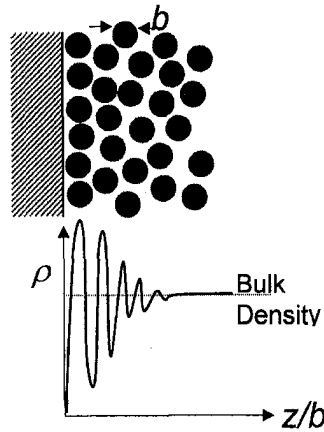


Fig. 1 Schematic diagram of water structure near a crystalline hydrophilic surface

since the behavior of liquids is quite different from that of solids, there are several new aspects that will be presented here.

The paper will rely only on thermodynamic arguments leaving kinetics to a later study. The discussion will concentrate on condensation of water on a hydrophilic surface such as glass, although it can be extended to other types of surfaces as well, including hydrophobic ones. To simplify matters and to concentrate on the effect surface chemistry, it is assumed that the surface is atomically flat such that surface roughness effects can be neglected. Such a situation can be experimentally obtained on a mica surface.

2 Intermolecular Forces at Liquid-Solid Interfaces

There are four types of intermolecular forces that exist between a solid hydrophilic surface and an adsorbed water film—hydration, electrostatic, van der Waals forces, and elastic strain. They operate at different length scales. To appreciate the role of all the forces, one must understand their nature in order to develop a model of water condensation from the molecular level.

2.1 Hydration Forces. Solid surfaces such as silica, mica, or any other oxides or hydrocarbons that contain a polar group, are hydrophilic and form hydrogen bonds with water. The H-bond strength between water molecules and the surface can be so strong that the first few layers of water completely wet the surface and are

often highly structured. This is described qualitatively in Fig. 1, which shows the oscillating density profile near a rigid surface. Such density profiles have been theoretically predicted or obtained by computer simulations (Marcelja et al., 1976; Marcelja and Radic, 1976; Abraham, 1978; Snook and van Meegen, 1979; Jonsson, 1981; Xia and Berkowitz, 1995). The H-bonding network is quite extensive in range and the interfacial force between the hydrophilic surface and the water layer can be long range (Stanley and Teixeira, 1980).

Experimental evidence of such highly ordered two-dimensional phase of water has been obtained by several investigators. Israelachvili and Pashley (1983) used the surface force apparatus (SFA) to bring into contact two cylindrical pieces of mica with the cylinder axes perpendicular to each other. The force between the two cylinders was measured as a function of the distance between them. Figure 2(a) shows a plot of the force-distance diagram that clearly exhibits the oscillating hydration forces. The period of oscillation is about 0.25 nm which is roughly equal to the diameter of a water molecule. There is also an exponential decay of the force envelope with a characteristic length, λ , of about 1–2 nm. Therefore, the two-dimensional phase of water near a mica surface can extend 3–10 monolayers.

The oscillatory behavior of the hydration forces is primarily caused due to the crystalline nature of the contacting surfaces. If the surfaces are noncrystalline, such as in glass or fused silica, or if the surfaces are slightly rough, then the oscillatory forces are not observed (Horn et al., 1989) but the strong repulsion between the surfaces and the exponential decay of hydration forces are still detected, as evident in Fig. 2(b). For a film thickness, h , Israelachvili (1992) proposed that the hydration energy can be written as

$$w_{\text{hyd}}(h) = U \exp\left(-\frac{h}{\lambda}\right). \quad (1)$$

Typically, λ is on the order of 1 nm and U ranges from 3–30 mJ/m². Such a relation cannot be derived from first principles but is a close fit to experimental observations. It does not account for the oscillatory nature observed in Fig. 2(a) but provides the average energy characteristic of that observed in Fig. 2(b). However, it should be noted although Eq. (1) suggests that hydration energy asymptotes to a finite value as $h \rightarrow 0$, experimental data show that the hydration energy keeps increasing as the film thickness decreases. In view of this fact, it is proposed here that the hydration energy is

Nomenclature

a = elastic strain at liquid-solid interface	l = internuclei spacing (m)	ψ = relative humidity
A = Hamaker constant (J)	L = length (m)	ρ = ion concentration (m ⁻³)
b = thickness of a water monolayer (m)	P = disjoining pressure (N/m ²)	ϕ_o = surface potential (V)
B = height perturbation in liquid film (m)	P_v = vapor pressure (N/m ²)	χ = surface charge density (C/m ²)
d = radius of a critical water nucleus (m)	R = gas constant for water vapor (J/kg-K)	σ = surface tension (J/m ²)
e = charge of an electron, 1.6×10^{-19} (C)	S = supersaturation	v = volume of a water molecule (m ³)
E = elastic modulus (N/m ²)	T = temperature (K)	
g_v = volumetric Gibb's free energy (J/m ³)	U = free energy parameter in hydration energy (J/m ²)	
G = Gibb's free energy (J)	v = valence	
h = film thickness (m)	w = free energy per unit area (J/m ²)	
h_{fs} = enthalpy of vaporization of water (J/kg)	W = free energy (J)	
k_B = Boltzmann constant, 1.38×10^{-23} (J/K)	ϵ = dielectric constant	
	ϵ_o = permittivity of vacuum, 8.85×10^{-12} (C ² /N-m ²)	
	η = nucleation density (m ⁻²)	
	κ = reciprocal of Debye length (m ⁻¹)	
	λ = length scale parameter in hydration energy (m)	
		Subscripts
		cr = critical
		el = electrostatic
		eq = equilibrium
		hyd = hydration
		lv = liquid-vapor
		s = surface
		sat = saturation
		sr = strain
		v = volume
		vdW = van der Waal

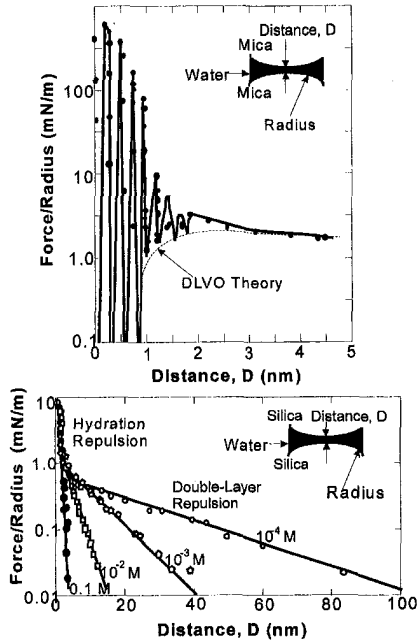


Fig. 2 Repulsive forces measured between two cylinders (a) mica (Israelachvili and Pashley, 1983) and (b) silica (Horn et al., 1989) surfaces in the presence of water in a surface force apparatus. DLVO theory considers van der Waals and electrostatic forces but not the hydration forces.

$$w_{\text{hyd}}(h) = U \left(1 + \frac{\lambda}{h} \right) \exp\left(-\frac{h}{\lambda}\right). \quad (2)$$

This retains the exponential behavior for film thickness on the order of λ but introduces a $1/h$ behavior for thinner films. Note that a generic polynomial, h^{-n} ; $n > 1$, can be chosen but the results of the stability analysis obtained later will not significantly change. Hence, the h^{-1} behavior is chosen for simplicity.

2.2 Electrostatic Forces. Electrostatic forces play a strong role in long-range interactions between water films and a solid surface. A solid surface can be charged in two ways: (i) by ionization or dissociation of a surface group—for example, removal of K^+ ions from a mica surface; (ii) adsorption of ions from solution to a previously uncharged surface—for example, adsorption of Ca^{2+} ions from solution to replace the K^+ ions in mica. Note that even pure water dissociates into an ionic solution of H_3O^+ and OH^- . When a surface is charged, a region of oppositely charged counterions in solution are attracted to the surface. The charge density of counterions decreases with distance from the surface and approaches the bulk value far away. The combination of surface charge and counterions in solution forms a region near the surface called the *electric double layer*. The only reason the ions in the solution do not collapse onto the charged surface is due to rapid thermal motion, which creates a repulsive pressure.

There has been extensive research on quantifying the potential energy of a water film that is electrostatically bound to a solid surface. An excellent description can be found in Israelachvili (1992). The relation between surface charge density, χ , and surface potential, ϕ_o , can be found from the Grahame equation

$$\chi = \sqrt{2\epsilon\epsilon_o k_B T \left(\sum_i \rho_{oi} - \sum_i \rho_{oi} \right)} \quad (3)$$

where ϵ is the dielectric constant of the medium which in our case is water, ϵ_o is the permittivity of vacuum, k_B is the Boltzmann constant, T is the temperature, and ρ_{oi} and ρ_{oi} are the ion concentrations at the surface and far away in solution, respectively, for the i th type of ions. These concentrations are related as

$$\rho_{oi} = \rho_{oi} \exp\left(-\frac{v_i e \phi_o}{k_B T}\right) \quad (4)$$

where v_i is the valence of the ions. Therefore, knowledge of all the bulk ion concentrations in solution, ρ_{oi} , and the surface charge density, χ , can be used to determine the surface potential, ϕ_o . For sufficiently small values of ϕ_o , i.e. $\phi_o < 25$ mV, the Grahame equation reduces to

$$\chi = \epsilon\epsilon_o \kappa \phi_o \quad (5)$$

where $1/\kappa$ is called the Debye length or characteristic thickness of the electric double layer and κ is given as

$$\kappa = \sqrt{\sum_i \frac{\rho_{oi} e^2 v_i^2}{\epsilon\epsilon_o k_B T}}. \quad (6)$$

The potential energy of the system (water film and solid surface) can be derived from these results. Consider a single specie of ions present in the water film. For a film of thickness h , the potential energy density of the system is (Israelachvili, 1992)

$$w_{el}(h) = \frac{64 k_B T \rho_o \gamma^2}{\kappa} \exp(-\kappa h) \quad (7)$$

where ρ_o is the concentration of the solution far away from the surface and γ is given by

$$\gamma = \tan h\left(\frac{e \phi_o}{4 k_B T}\right). \quad (8)$$

Note that the influence of the electrostatic forces depends on the Debye length, $1/\kappa$. For a NaCl solution, this 30.4 nm at 10^{-4} M concentration, 9.6 nm at 1 mM and 0.3 nm at 1 M. For pure water at pH 7, the Debye length is 960 nm or about 1 μm . Therefore, the electrostatic forces can be much longer range than the hydration forces.

2.3 van der Waals Forces. Although not as strong as hydration or electrostatic forces, van der Waals forces are always present whenever a liquid is adsorbed onto a surface. They arise from interactions of induced dipoles between two or more atoms and are typically effective below 10–50 nm. There is extensive literature on van der Waals forces between an adsorbed water film and a surface in the presence of vapor. The interaction energy density is written as

$$w_{vdw}(h) = -\frac{A}{12\pi h^2} \quad (9)$$

where A is the Hamaker constant which depends on the optical properties of the three media—solid surface, water film, and the vapor. Values of the Hamaker constants for several combinations have been calculated and listed in Israelachvili (1992). For example, for a system of water adsorbed on fused quartz in the presence of air, $A = -0.87 \times 10^{-20}$ J. A negative value of A suggests that the energy of the system will reduce if the film grows thicker.

2.4 Elastic Strain. The fact that water molecules are highly ordered in a two-dimensional ice-like structure close to a hydrophilic surface has been established through experiments and molecular dynamic simulations. Therefore, if the lattice constant of the substrate is not exactly equal to that of ice, the bonds between the water molecules will be strained. The fact that strain influences phenomena at the solid-liquid interface has been known for a while. For example, silver iodide (AgI) has been used to nucleate ice and it is commonly believed that it is the lattice match of the crystal structure of AgI and ice that promotes ice nucleation (Hobbs, 1974). Recent experiments have also shown that strain energy can play a significant role in nucleation processes, in particular for heterogeneous nucleation of ice from water on a solid surface (Gavish et al., 1990; Majewski et al., 1993; Popovitz-

Biro et al., 1994). In addition, a recent experiment showed that the first few layers of liquid mercury in contact with a diamond surface form layered structure with the orientation of solid-Hg crystal (Huisman et al., 1997). Hence, if the first few layers are solid-like, there should be some strain due to mismatch in the lattice constants of the solid-like liquid film in contact with the solid substrate. Note, however, that in bulk liquid water, there is no strain between the water molecules. Since the origin of the layered structure lies in hydration forces which decay exponentially, it is proposed here that the strain energy density (per unit volume) at any point in the film is equal to $Ea^2 e^{-h/\lambda}/2$ where E is the elastic modulus of ice which is 17 GN/m^2 (Turnbull and Vonnegut, 1952) and a is the strain of the first monolayer. Values of a typically range between zero and five percent. Hence, total elastic strain energy surface density (per unit film area) of a film of thickness, h , varies as

$$w_{sr} = \frac{E\lambda a^2}{2} \left[1 - \exp\left(-\frac{h}{\lambda}\right) \right]. \quad (10)$$

3 Equilibrium Thickness of Water Films

The total energy density of the system is obtained by adding up the interaction energies as follows:

$$w = w_{hyd} + w_{el} + w_{vdW} + w_{sr}. \quad (11)$$

It should be noted that when only electrostatic and van der Waals forces are considered, the celebrated DLVO theory results, after Derjaguin and Landau (1941) and Verwey and Overbeek (1948). However, the experiments in Fig. 2 clearly show that hydration must be taken into account for films thinner than a 2–3 nm. In previous studies of liquid films undergoing evaporation or condensation or under equilibrium, only the van der Waals interactions were included whereas electrostatic and hydration energies were neglected (Bankoff, 1990; Burelbach et al., 1988; Wayner et al., 1976; Dasgupta et al., 1994). Although these studies concentrated on thicker films for which this may be acceptable, it is not realistic to do so for films in the range of 0–10 nm. This will be demonstrated now.

The disjoining pressure for the water film can be calculated as

$$P(h) = -\frac{dw}{dh} = \frac{Ue^{-h/\lambda}}{\lambda} \left(1 + \frac{h}{\lambda} + \frac{\lambda^2}{h^2} \right) + 64k_B T \rho_w \gamma^2 e^{-\kappa h} - \frac{A}{6\pi h^3} - \frac{E\epsilon_0^2}{2} e^{-h/\lambda} \quad (12)$$

where the four terms on the right side represent the contributions from hydration, electrostatic, van der Waals, and strain interactions. It is important to compare the contribution of the three interactions to the disjoining pressure. This is depicted in Fig. 3 where calculations are presented for $T = 300 \text{ K}$ and some typical parameters are assumed— $\lambda = 1 \text{ nm}$ and $U = 10 \text{ mJ/m}^2$ for hydration; $A = -10^{-20} \text{ J}$ for van der Waals interaction; and for electrostatic interactions four NaCl electrolyte concentrations, 10^{-7} M (pure water), 10^{-4} M , 10^{-2} M and 1 M , are assumed. In addition, it is assumed that the surface potential is $\phi_0 = 100 \text{ mV}$ for an electrolyte solution of NaCl. The Debye length varies as $1/\kappa = 0.304/\sqrt{[\text{NaCl}]}$ nm where $[\text{NaCl}]$ is the molar concentration.

It is clear from Fig. 3 that for pure water (10^{-7} M), hydration interactions dominate for $h < 10 \text{ nm}$ and van der Waals dominate in the range $h > 10 \text{ nm}$. For 10^{-4} M concentration of NaCl, hydration force is the largest for $h < 7 \text{ nm}$ whereas for thicker films, electrostatic forces dominate. van der Waals forces are insignificant for such a condition. For 10^{-2} M , hydration dominates for $h < 3 \text{ nm}$ whereas electrostatic forces dominate for thicker films. For 1 M , though, electrostatic forces decay very quickly and become insignificant making this case similar to that of 10^{-7} M where only hydration and van der Waals forces are important.

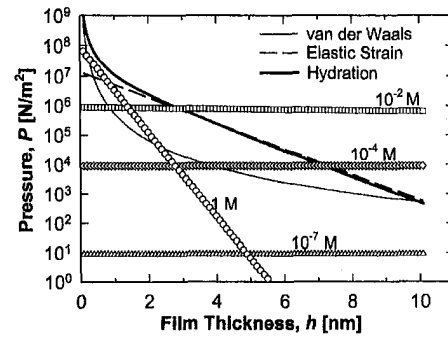


Fig. 3 Comparison of hydration, strain, electrostatic, and van der Waals contributions to the disjoining pressure. The conditions chosen for the calculations were $\lambda = 1 \text{ nm}$ and $U = 10 \text{ mJ/m}^2$ for hydration; $A = -10^{-20} \text{ J}$ for van der Waals interaction; $E = 1.7 \times 10^{10} \text{ N/m}^2$ and $\epsilon_0 = 0.04$ for strain; and for electrostatic interactions four NaCl electrolyte concentrations, 10^{-7} (pure water), 10^{-4} M , 10^{-2} M , and 1 M , with surface potential $\phi_0 = 100 \text{ mV}$.

The disjoining pressure can also be related to the relative humidity, ψ , as follows (Israelachvili, 1992):

$$P(h) = -\frac{dw}{dh} = \frac{k_B T}{v} \ln\left(\frac{1}{\psi}\right). \quad (13)$$

Here v is the volume of a water molecule ($\approx 3 \times 10^{-29} \text{ m}^3$). The disjoining pressure from Eq. (12) can be used in Eq. (13) to establish a relation between the equilibrium film thickness, h_{eq} , and the relative humidity, ψ . Figure 4 shows such a plot. For humidity below 90 percent, h_{eq} is less than 1 nm. In this regime, hydration forces are dominant. This is also clear from Fig. 4, which shows that electrolyte concentrations have negligible effect on h_{eq} . This further emphasizes the point that hydration forces must be included in the analysis of evaporation and condensation of the water film. It is interesting to note that the equilibrium film thickness does not change appreciably over a wide range of relative humidity. The inset in Fig. 4 shows, however, that when the humidity reaches close to 100 percent, the equilibrium film thickness increases sharply. It will be established in Section 4 that during this increase in film thickness, the film becomes unstable and undergoes a transition to droplet formation.

To qualitatively demonstrate the existence of the water film, Fig. 5 presents some results of an experiment performed using an atomic force microscope (AFM). A sharp tip made of silicon nitride was brought in contact with a freshly cleaved mica surface and the cantilever deflection was measured with a laser. Figure 5(a) plots the cantilever deflection as a function of sample position,

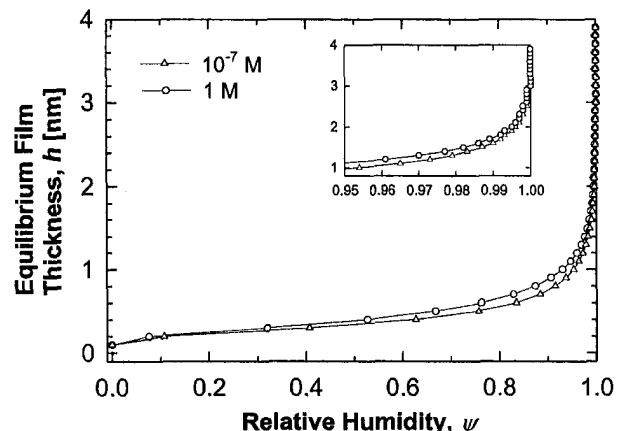


Fig. 4 Equilibrium water film thickness as a function of relative humidity. The conditions were the same as chose for the predictions in Fig. 3.

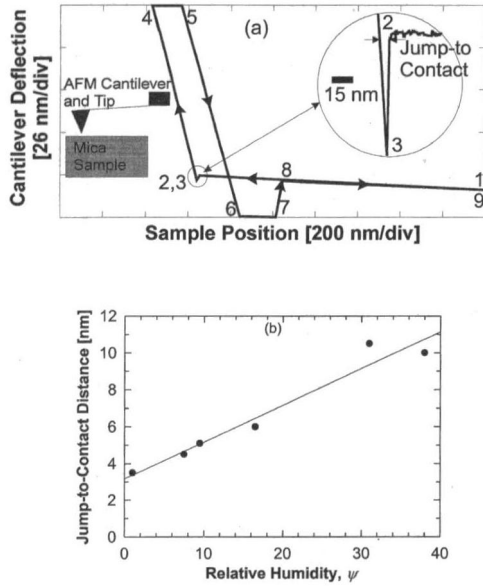


Fig. 5 (a) Deflection of an atomic force microscope (AFM) cantilever tip as a function of sample position during contact with a freshly cleaved mica surface. 1–2 the sample is moved up towards the AFM tip; 2–3 the tip jumps to contact with the surface due to attractive forces; 3–4 sample is moved up pushing the in-contact cantilever tip; 5–6 sample is retracted away although the tip sticks to the surface due to attractive forces; 6–7 tip is still in contact although the signal is out of range; 7–8 cantilever snaps back and out of contact; 8–9 tip is out of contact and remains there as the sample is moved away. (b) Measured jump-to-contact distance as a function of relative humidity.

indicating in the inset the jump-to-contact phenomenon when the tip is within a few nanometers from the surface. This occurs when the attractive force between the two liquid films on the tip and the mica surface exceeds the spring force of the AFM cantilever. When the sample is retracted, notice that the tip sticks to the surface (6–7–8) until the spring force exceeds the force between the water films. Figure 5(b) plots jump-to-contact distance as a function of relative humidity. The fact that this increases with humidity suggests that the water film increases in thickness with humidity. It is difficult to determine the exact film thickness from this experiment, but the data qualitatively demonstrates the presence of the water film and its growth with increasing relative humidity.

4 Onset of Liquid Film Instability

Consider a thin liquid film of thickness, h_o , on a flat surface. A one-dimensional disturbance to film changes the shape to $h(x) = h_o + B \cos(\pi x/L)$ where B is a small perturbation and $2L$ is the wavelength, as shown in Fig. 6. Such a profile conserves mass since

$$\int_0^L h(x) dx = h_o L \quad (14)$$

The total change in the film free energy can be written as

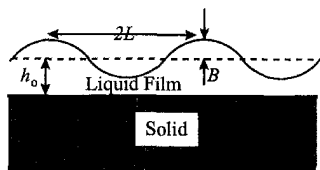


Fig. 6 Perturbation of amplitude B and wavelength $2L$ of a liquid film of nominal thickness h_o

$$\Delta W = \Delta W_v + \Delta W_s \quad (15)$$

where ΔW_v is the volumetric component and ΔW_s is the surface component. The change in volumetric free energy per unit length can be found as

$$\Delta W_v = \int_0^L \left. \frac{dw_v}{dh} \right|_{h_o} (h - h_o) dx + \int_0^L \left. \frac{d^2 w_v}{dh^2} \right|_{h_o} \frac{(h - h_o)^2}{2} dx + \dots \quad (16)$$

Due to mass conservation, the first term on the right side is zero. Using the cosine profile of the film thickness and neglecting terms higher than the second order term, Eq. (16) becomes

$$\Delta W_v = \left. \frac{d^2 w_v}{dh^2} \right|_{h_o} \frac{B^2 L}{4} \quad (17)$$

It will be assumed here that electrostatic forces are negligible. As Fig. 3 indicates, for film thicknesses less than 3 nm, electrostatic forces are not dominant even for surface potential of 100 mV. For lower surface potential, electrostatic forces will be even less. Hence, the volumetric energy density consists of van der Waals, hydration, and strain energy in the liquid film and can be written as

$$w_v = -\frac{A}{12\pi h^2} + U \left(1 + \frac{\lambda}{h} \right) \exp\left(-\frac{h}{\lambda}\right) + \frac{E\lambda\epsilon_o^2}{2} \left[1 - \exp\left(-\frac{h}{\lambda}\right) \right] \quad (18)$$

Thus, the total change in volumetric free energy per unit length of the film can be derived to be

$$\Delta W_v = \frac{B^2 L}{4} \left[-\frac{A}{2\pi h^4} + \frac{U}{\lambda^2} \left(1 + \frac{\lambda}{h} + \frac{2\lambda^2}{h^2} + \frac{2\lambda^3}{h^3} \right) \times \exp\left(-\frac{h}{\lambda}\right) - \frac{E\epsilon_o^2}{2\lambda} \exp\left(-\frac{h}{\lambda}\right) \right] \quad (19)$$

Here, the subscript o has been dropped from the film thickness. To calculate the change in surface energy, it is necessary to calculate the change in surface area. Using the cosine profile, the change ΔL in the surface area is given as

$$\Delta L = \int_0^L \sqrt{1 + \left(\frac{B\pi}{L} \right)^2 \sin^2 \left(\frac{\pi x}{L} \right)} dx - L \quad (20)$$

Assuming that $B \ll L$ (small perturbation), Eq. (20) can be simplified to

$$\Delta L = 2 \left(\frac{B\pi}{L} \right)^2 \int_0^L \sin^2 \left(\frac{\pi x}{L} \right) dx = \frac{(B\pi)^2}{L} \quad (21)$$

Hence, the change in total surface energy due to the perturbation is

$$\Delta W_s = \frac{\sigma_{lv} (B\pi)^2}{L} \quad (22)$$

where σ_{lv} is the surface tension for the liquid-vapor interface. Thus the total change in film free energy can be written as

$$\Delta W = \frac{B^2 L}{4} \left[-\frac{A}{2\pi h^4} + \left\{ \frac{U}{\lambda^2} \left(1 + \frac{\lambda}{h} + \frac{2\lambda^2}{h^2} + \frac{2\lambda^3}{h^3} \right) - \frac{E\epsilon_o^2}{2\lambda} \right\} \times \exp\left(-\frac{h}{\lambda}\right) \right] + \frac{\sigma_{lv} B^2 \pi^2}{L} \quad (23)$$

For the film to be stable, the total change in free energy must be greater than zero, i.e., $\Delta W > 0$. It is clear that if only van der Waals and surface tension forces are considered, as has been done for most previous studies that considered thicker films (Bankoff, 1990; Burelbach et al., 1988; Wayner et al., 1976; Dasgupta et al., 1994), film instability will set in for wavelengths larger than the critical length, L_{cr} , given as

$$L > L_{cr}; \quad L_{cr} = h^2 \sqrt{\frac{8\pi^3\sigma_{lv}}{A}} \quad (24)$$

Short wavelength instabilities are not permitted due to surface tension forces. It is assumed here that the Hamaker constant, A , is positive. This is true in many cases (Israelachvili, 1992), including water on hydrophobic surfaces. In the case of negative Hamaker constant, such as for glass-water-air combination, the film is always stable as suggested by Eq. (23). Hence, for any film-droplet transition for water on glass, other forces must play a role. As observed in Eq. (23), hydration forces alone cannot be responsible since it has a positive coefficient. This suggests that strain energy must play an important role. After considering all the forces, the critical wavelength can be written as

$$L_{cr} = \sqrt{\frac{4\sigma_{lv}\pi^2}{\frac{A}{2\pi h^4} + \left[\frac{E\epsilon^2}{2\lambda} - \frac{U}{\lambda^2} \left(1 + \frac{\lambda}{h} + \frac{2\lambda^2}{h^2} + \frac{2\lambda^3}{h^3} \right) \right] \exp\left(-\frac{h}{\lambda}\right)}} \quad (25)$$

It should be noted that so far there has been no assumption made whether the surface is hydrophobic or hydrophilic. This depends on the constants A and U . The theory developed till now can be used for both cases. As a case study, consider water on a hydrophilic surface such as glass in the presence of water vapor. As previous studies have indicated, U lies between 3–30 mJ/m² and λ is about 1 nm. Hence, the parameters chose for this case study are: $A = -10^{-20}$ J (Israelachvili, 1992); $U = 10$ mJ/m²; $\lambda = 1$ nm; $E = 1.7 \times 10^{10}$ J/m²; $a = 0.04$ (typical strain for lattice mismatch); and $\sigma_{lv} = 72$ mJ/m² (surface energy of liquid-vapor interface for water). Figure 7 plots $1/L_{cr}$ as a function of film thickness and shows the stability boundary. The thickness steps taken for the calculation and represented as filled circles are 0.28 nm which is the size of a water monolayer. It is clear from Fig. 7 that for thickness larger than 3 nm, the film can become unstable. When compared with the plot of film thickness versus humidity in Fig. 4, it becomes apparent that when the relative humidity approaches 100 percent resulting in condensation, the water film becomes unstable.

5 Nucleation Phenomena

The analysis described above shows the stability regimes of thin liquid films. However, it provides no indication as to how the

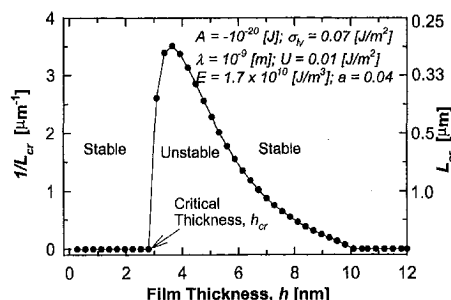


Fig. 7 Stability map of water film in terms of critical wavelength, L_{cr} , as a function of film thickness of the water film

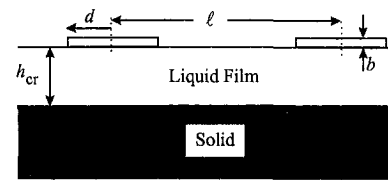


Fig. 8 Schematic diagram showing nuclei of radius d formed as a monolayer of thickness b on a water film of critical thickness, h_{cr} , and separated on an average by a distance, l

instability occurs and the subsequent shape of the liquid film. The following analysis will provide this insight.

Figure 7 shows that for a film of critical thickness, h_{cr} , instability will occur if the wavelength of oscillation, L_{cr} , is extremely large, i.e., $1/L_{cr} \rightarrow 0$. Therefore, for all practical purposes, the film is stable when $h = h_{cr}$. However, if a single monolayer is added to the film, the critical wavelength, $L_{cr}(h_{cr} + b)$, reduces to about 0.4 μm (see Fig. 7). Here, b is the size of a single water monolayer which is about 2.8 \AA . Addition of another monolayer further reduces the critical wavelength to 0.3 μm . Certainly, these wavelengths are possible under most physical conditions.

In light of the experimental evidence that water films form two-dimensional layered structures on a hydrophilic surface due to hydration forces, it is proposed that instability of a water film occurs in the following way. As the relative humidity increases, the equilibrium water film increases in thickness as indicated in Fig. 4. The water film remains stable till the thickness reaches the critical thickness, h_{cr} . If more condensation occurs, it is proposed that the water molecules stick to the water film in a two-dimensional monolayer fashion, as illustrated in Fig. 8. This is based on the recent experimental observations of Hu et al. (1995) who used the atomic force microscope to image condensed water films on a mica surface with nanometer-scale spatial resolution. They observed that water nuclei are formed in two-dimensional monolayer fashion. Thermodynamics requires the existence of a critical nucleus of size, d^* , as will be shown next. Besides this, another length scale is the mean separation between critical nuclei, l . If it so happens that either $d^* > L_{cr}(h_{cr} + b)$ or $l > L_{cr}(h_{cr} + b)$, then the film will undergo an instability since either l or d^* will fall within the unstable region of the stability map of Fig. 7. Since the mean separation between nuclei, l , is larger than the nucleus size, the condition $l > L_{cr}(h_{cr} + b)$ is sufficient for instability.

Consider a two-dimensional circular nucleus of radius, d , formed from a single monolayer of height, b , as shown in Fig. 8. The change in Gibbs free energy for the formation of this nucleus is

$$\Delta G = -\pi d^2 b \left(\Delta g_v - \frac{E\epsilon^2(h_{cr} + b)}{2} \right) + 2\pi d b \sigma_{lv} \quad (26)$$

where Δg_v is the reduction in volumetric Gibbs energy during condensation. The second term in the parenthesis is the strain energy increase for a monolayer at a height, $h_{cr} + b$, above the solid surface. Using $d(\Delta G)/d(d) = 0$, the critical nucleus size can be found to be

$$d^* = \frac{\sigma_{lv}}{\Delta g_v - \frac{E\epsilon^2(h_{cr} + b)}{2}} \quad (27)$$

Using this in Eq. (26), the energy barrier to forming a critical nucleus can be found to be

$$\Delta G^* = \frac{\pi b \sigma_{lv}^2}{\Delta g_v - E\epsilon^2/2} \quad (28)$$

If η_o is the density of possible nucleation sites, the nucleation density, η , can be expressed as

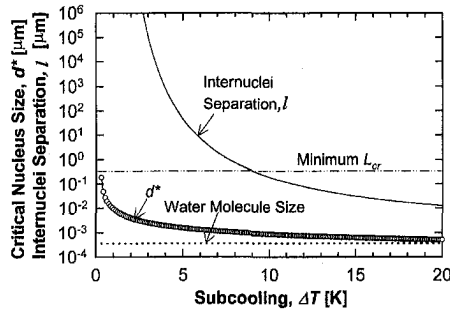


Fig. 9 Prediction of the critical nucleus size and the average internuclei spacing as a function of subcooling for a water film in contact with a hydrophilic surface. The conditions chosen for the hydration, van der Waals, and strain forces are the same as in Fig. 8.

$$\eta = \eta_0 \exp\left(-\frac{\Delta G^*}{k_B T}\right) = \eta_0 \exp\left[-\frac{\pi b \sigma_{lv}^2}{(\Delta g_v - E \epsilon^2/2) k_B T}\right]. \quad (29)$$

Therefore, the mean separation between nuclei follows as

$$l = \frac{1}{\sqrt{\eta}} = b \exp\left[\frac{\pi b \sigma_{lv}^2}{(2 \Delta g_v - E \epsilon^2) k_B T}\right] \quad (30)$$

where it is assumed that $b = 1/\sqrt{\eta_0}$, i.e., the density of possible nucleation sites on the liquid film corresponds to the intermolecular distance.

Consider subcooling of a surface by $\Delta T = T_{\text{sat}}(P_v) - T$, where $T_{\text{sat}}(P_v)$ is the saturation temperature at vapor pressure, P_v , and T is the temperature of the surface on which condensation takes place. Using the Clausius-Clapeyron equation, it can be shown that

$$S = \frac{P_v(T) - P_{\text{sat}}(T)}{P_{\text{sat}}(T)} = \exp\left[\frac{h_{fg}}{R} \left(\frac{1}{T} - \frac{1}{T_{\text{sat}}(P_v)}\right)\right] - 1 \quad (31)$$

where S is called the vapor supersaturation, h_{fg} is the enthalpy of vaporization, and R is the gas constant for water vapor. If the subcooling is small, then S can be expressed as

$$S = \frac{h_{fg}}{RT^2} \Delta T. \quad (32)$$

Using $R = 461.38 \text{ J/kg}\cdot\text{K}$ and $h_{fg} = 2437.6 \text{ kJ/kg}$ at $T = 300 \text{ K}$ for water, one obtains $S = 0.059 \Delta T$. The reduction in volumetric Gibbs free energy can be related to vapor supersaturation as (Ohring, 1992)

$$\Delta g_v = \frac{k_B T}{v} \ln(1 + S) \quad (33)$$

where v is the volume of a water molecule which can be estimated as b^3 or $2.2 \times 10^{-29} \text{ m}^3$.

It is clear from the above analysis that when the subcooling increases, vapor supersaturation (S) increases resulting in an increase in Δg_v . This decreases the size of the critical nucleus, d^* , as well as the internuclei spacing, l . This is quantitatively shown in Fig. 9 which plots both l and d^* for water at a saturation temperature of 300 K. The values of E , a , and λ are the same as used before for Fig. 7. It is interesting to note that for subcooling higher than 1 K, the critical nucleus size does not change appreciably and falls in the range of 1–10 nm. On the other hand, the internuclei separation is a strong function of subcooling and can vary over an order of magnitude for a change in subcooling by 1 K. Two other length scales—size of water molecule and the minimum critical wavelength, $L_{cr,\text{min}}$ —are also shown in Fig. 9. The critical nucleus size approaches the water molecule size as subcooling is increased and is always less than $L_{cr,\text{min}}$. Hence, instability occurs through the condition $l > L_{cr}$ and not through the condition $d^* > L_{cr}$. However, note that when the subcooling

increases above 9 K, the internuclei separation falls below $L_{cr,\text{min}}$. Although this would suggest that instability will not occur, there will always be subharmonics of the internuclei separation, i.e., nl , $n > 1$, which will satisfy the condition that $nl > L_{cr}$. This means that every nuclei will not produce droplets, but those that are separated by internuclei distance of L_{cr} will induce instability and form droplets. Therefore, below subcooling of 9 K, the interdroplet separation will be equal to the internuclei separation since every nuclei will produce a droplet. For subcooling higher than 9 K, the interdroplet separation is “choked” and will not further decrease below $L_{cr,\text{min}}$.

Equation (23) suggests that the total change in film free energy can be written as $\Delta W = \xi(h) B^2$. For an unstable film, $\xi(h) < 0$. The fact that $\Delta W \propto B^2$ suggests that once the instability occurs, the maximum reduction in energy is achieved when the film nuclei grow. Mass conservation demands that this can only happen when the film becomes thinner in internuclei region. This process is essential in the formation of droplets. The shape of the droplet requires further research on the surface energies and the contact angle, which has been left for a later study. In addition, the time it takes for this instability to occur depends on the kinetics of the process that have not been included in this study and, again, has been left for a later study.

It should be noted that since the internuclei spacing is larger than $1 \mu\text{m}$ for subcooling less than 8 K, it would be possible to observe these nuclei under an optical microscope. Hence, an experiment of condensation of water on mica under controlled humidity and temperature conditions is now being planned. Comparison of the measured average internuclei spacing as a function of subcooling with the theoretical predictions in Fig. 9 would verify the theoretical predictions of the instability and nucleation theories presented in this paper.

6 Conclusions

This paper presents a new theory for instability of ultrathin water films on a hydrophilic surface that leads to the formation of droplets during condensation. Previous studies on instability have concentrated only on thicker films and included van der Waals and surface tension forces for analysis. However, previous experimental and theoretical studies have shown that for films thinner than about 3 nm, hydration forces dominate. In addition, electrostatic forces within the double layer as well as elastic strain of the water film near the solid surface are also important. Using all the known intermolecular interactions, the paper calculates the equilibrium film thickness as a function relative humidity and shows that the thickness is about 0.5 nm (2 monolayer) for a wide range of humidity but grows very sharply as the humidity approaches 100 percent. Using purely thermodynamic arguments, the stability theory shows that there exists a critical film thickness on about 3 nm such that thicker films can undergo an instability arising from a competition between strain energy on one hand, and van der Waals, hydration, and surface tension on the other. Once the critical film thickness is reached, further condensation results in the formation of nuclei of a critical size in a monolayer fashion. Based on the thermodynamics of nucleation, the critical nucleus size and the internuclei spacing are predicted as a function of surface subcooling. When the internuclei spacing is larger than the critical wavelength, the resulting instability leads to growth of the critical nuclei to form droplets. The theory predicts that although the inter-droplet spacing decreases with increasing subcooling, the spacing “chokes” beyond a certain subcooling value and remains constant. In summary, the paper proposes a new theory of droplet formation during condensation of water on a hydrophilic surface. The theory has elements of both previous theories which propose either film instability or heterogeneous nucleation as the mechanism for droplet formation.

Acknowledgments

We thank Steve Morris and Van Carey for their insightful comments, and K. Ogawa for performing the AFM experiments. AM would like to thank the NSF for the NYI award under which this study was conducted.

References

- Abraham, F. F., 1978, "The Interfacial Density Profile of a Lennard-Jones Fluid in Contact With a (100) Lennard-Jones Wall and Its Relationship to Idealized Fluid-Wall Systems," *J. Chem. Phys.*, Vol. 68, No. 8, pp. 3713–3716.
- Baer, E., and McKelvey, J. M., 1958, "Heat Transfer in Dropwise Condensation," *Proc. of Symp. On Heat Transfer in Dropwise Condensation*, University of Delaware, Newark, p. 24.
- Bankoff, S. G., 1990, "Dynamics and Stability of Thin Heated Liquid Films," *ASME JOURNAL OF HEAT TRANSFER*, Vol. 112, pp. 538–545.
- Burelbach, J. P., Bankoff, S. G., and Davis, S. H., 1988, "Nonlinear Stability of Evaporating/Condensing Liquid Films," *Journal of Fluid Mechanics*, Vol. 195, pp. 463–494.
- Dasgupta, S., Kim, I. Y., and Wayner, P. C., Jr., 1994, "Use of Kelvin-Clapeyron Equation to Model an Evaporating Curved Microfilm," *ASME JOURNAL OF HEAT TRANSFER*, Vol. 116, pp. 1007–1015.
- Derjaguin, B. V., and Landau, L., 1941, *Acta Physicochim. URSS*, Vol. 14, pp. 633–662.
- Erb, R. A., and Thelen, E., 1965, "Dropwise condensation," 1st Int. Symp on Water Desalination, Washington DC, also Erb, R. A., Ph.D. dissertation, Temple University (1965).
- Eucken, A., 1937, *Naturwissenschaften*, Vol. 25, p. 209.
- Gavish, M., Popovitz-Biro, R., Lahav, M., and Leiserowitz, L., 1990, "Ice Nucleation by Alcohols Arranged in Monolayers at the Surface of Water Drops," *Science*, Vol. 250, pp. 973–975.
- Hobbs, P. V., 1974, *Ice Physics*, Clarendon Press, Oxford.
- Horn, R. G., Smith, D. T., and Haller, W., 1989, "Surface Forces and Viscosity of Water Measured Between Silica Sheets," *Chemical Physics Letters*, Vol. 162, No. 4–5, pp. 404–408.
- Hu, J., Xiao, X. D., Ogletree, D. F., and Salmeron, M., 1995, "Imaging the Condensation and Evaporation of Molecularly Thin Films of Water With Nanometer Resolution," *Science*, Vol. 268, pp. 267–269.
- Huisman, W. J., Peters, J. F., Zwanenburg, M. J., deVries, S. A., Derry, T. E., Abernathy, D., and vanderVeen, J. F., 1997, "Layering of a liquid metal in contact with a hard wall," *Nature*, Vol. 390, No. 6658, pp. 379–381.
- Israelachvili, J. N., 1992, *Intermolecular and Surface Forces*, 2nd Ed., Academic Press, San Diego, CA.
- Israelachvili, J. N., and Pashley, R. M., 1983, "Molecular Layering of Water at Surfaces and Origin of Repulsive Hydration Forces," *Nature*, Vol. 306, pp. 249–250.
- Jakob, M., 1936, "Heat Transfer in Evaporation and Condensation," *Mech. Engr.*, Vol. 58, pp. 729–739.
- Jonsson, B., 1981, "Monte Carlo Simulations of Liquid Water Between Two Rigid Walls," *Chem. Phys. Lett.*, Vol. 82, No. 3, pp. 520–525.
- Majewski, J., Popovitz-Biro, R., Kjaer, K., Als-Neilsen, J., Lahav, M., and Leiserowitz, L., 1994, "Toward a Determination of the Critical Size of Ice Nuclei. A Demonstration by Grazing Incidence X-ray Diffraction of Epitaxial Growth of Ice Under the C₃₁H₆₃OH Monolayer," *J. Phys. Chem.*, Vol. 98, pp. 4087–4093.
- Marcelja, S., and Radic, N., 1976, "Repulsion of Interfaces due to Boundary Water," *Chemical Physics Letters*, Vol. 42, No. 1, pp. 129–130.
- Marcelja, S., Mitchell, D. J., Ninham, B. W., and Sculley, M. J., 1976, "Role of Solvent Structure in Solution Theory," *J. Chem. Soc. Faraday Trans. 2*, Vol. 73, pp. 630–648.
- Ohring, M., 1992, *The Materials Science of Thin Films*, Academic Press, San Diego, CA.
- Popovitz-Biro, P., Wang, J. L., Majewski, J., Shavit, E., Leiserowitz, L., and Lahav, L., 1994, "Induced Freezing of Supercooled Water Into Ice by Self-Assembled Crystalline Monolayers of Amphiphilic Alcohols at the Air-Water Interface," *J. Am. Chem. Soc.*, Vol. 116, pp. 1179–1191.
- Snook, I., and van Megen, W., 1979, "Structure of Dense Liquids at Solid Interfaces," *J. Chem. Phys.*, Vol. 70, No. 6, pp. 3099–3105.
- Spencer, B. J., Voorhees, P. W., and Davis, S. H., 1991, "Morphological Instability in Epitaxially Strained Dislocation-Free Solid Films," *Physical Review Letters*, Vol. 67, No. 26, pp. 3696–3699.
- Srolovitz, D. J., 1989, "On the Stability of Surfaces of Stressed Solids," *Acta Metall.*, Vol. 37, No. 2, pp. 621–625.
- Stanley, H. E., and Teixeira, J., 1980, "Interpretation of the Unusual Behavior of H₂O and D₂O at Low Temperatures: Tests of a Percolation Model," *Journal of Chemical Physics*, Vol. 73, No. 7, pp. 3404–3422.
- Sugawara, S., and Katsuta, K., 1966, "Fundamental Study of Dropwise Condensation," *Proc. 3rd Int. Heat Transfer Conference*, Vol. 2, pp. 354–361.
- Turnbull, D., and Vonnegut, B., 1952, *Ind. Engng. Chem.*, Vol. 44, pp. 1292–1298.
- Umur, A., and Griffith, P., 1965, "Mechanism of Dropwise Condensation," *ASME JOURNAL OF HEAT TRANSFER*, Vol. 87, pp. 275–282.
- Verwey, E. J. W., and Overbeek, J. Th. G., 1948, *Theory of Stability of Lyophobic Colloids*, Elsevier, Amsterdam.
- Vook, R. W., 1982, "Structure and Growth of Thin Films," *International Metals Review*, Vol. 27, No. 4, pp. 209–245.
- Wayner, P. C., Jr., Kao, Y. K., and La Croix, L. V., 1976, "The Interline Heat-Transfer Coefficient of an Evaporating Wetting Film," *Int. J. Heat Mass Transfer*, Vol. 19, pp. 487–492.
- Welch, J. F., and Westwater, J. W., 1961, "Microscopic Study of Dropwise Condensation," *International Developments in Heat Transfer*, Part II, ASME New York.
- Xia, X., and Berkowitz, M. L., 1995, "Electric-Field Induced Restructuring of Water at a Platinum-Water Interface: A Molecular Dynamics Computer Simulation," *Phys. Rev. Lett.*, Vol. 74, No. 16, pp. 3193–3196.

Heat Transfer Enhancement by Fins in the Microscale Regime

F.-C. Chou¹

Department of Mechanical Engineering,
National Central University,
Chung-li, Taiwan 320, R.O.C.
Mem. ASME

J. R. Lukes

C.-L. Tien

e-mail: mariaa@newton.berkeley.edu
Honorary Mem. ASME

Department of Mechanical Engineering,
University of California at Berkeley,
Berkeley, CA 94720

The current literature contains many studies of microchannel and micro-pin-fin heat exchangers, but none of them consider the size effect on the thermal conductivity of channel and fin walls. The present study analyzes the effect of size (i.e., the microscale effect) on the microfin performance, particularly in the cryogenic regime where the microscale effect is often appreciable. The size effect reduces the thermal conductivity of microchannel and microfin walls and thus reduces the heat transfer rate. For this reason, heat transfer enhancement by microfins becomes even more important than for macroscale fins. The need for better understanding of heat transfer enhancement by microfins motivates the current study, which resolves three basic issues. First, it is found that the heat flow choking can occur even in the case of simple plate fins or pin fins in the microscale regime, although choking is usually caused by the accommodation of a cluster of fins at the fin tip. Second, this paper shows that the use of micro-plate-fin arrays yields a higher heat transfer enhancement ratio than the use of the micro-pin-fin arrays due to the stronger reduction of thermal conductivity in micro-pin-fins. The third issue is how the size effect influences the fin thickness optimization. For convenience in design applications, an equation for the optimum fin thickness is established which generalizes the case without the size effect as first reported by Tuckerman and Pease.

Introduction

Fins and microchannels are widely used to enhance heat transfer in heat exchangers. The advent of high-density electronic components has resulted in high energy dissipation and requires more effective heat transfer enhancement techniques. The pioneering work of Tuckerman and Pease (1981) provided a method for cooling a chip by forcing coolant through closed microchannels etched onto the backside of a silicon wafer. Subsequently, many theoretical and experimental investigations of microchannel and micro-pin-fin heat exchangers have been conducted. Some works focused on how to optimize arrays of fins (Harpole and Eninger, 1991; Knight et al., 1992). Silicon and CVD diamond were employed or proposed due to the high thermal conductivity to make microchannel heat exchangers, such as for laser diode array cooling (Munding et al., 1988; Missaggia et al., 1989; Goodson et al., 1997). To meet the requirement of high cooling rate, water (Tuckerman and Pease, 1981) and liquid nitrogen (Choi et al., 1992; Cha et al., 1993; Riddle and Bernhardt, 1992) were used as the working fluids. Numerical analyses of the conjugate heat transfer in the silicon micro-pin-fin arrays and microchannels operating with liquid nitrogen were reported by Yin and Bau (1997a, b).

It should be noted that none of the above works consider the size effect (Flik and Tien, 1990) on the thermal conductivity of channel and fin walls. All of the analyses use the conventional macroscale approach in which only the thermal conductivity for bulk materials is used. The size effect is a phenomenon in which the thermal conductivity of a material is less than the bulk value due to the scattering of the primary carriers of energy by its boundaries. This effect is important for systems that are very small or are at low temperatures. The microscale approach may be needed to study the performance of microchannels and microfins because widths as narrow as 10 μm (Harpole and Eninger, 1991; Cha et al., 1993; Joo et al., 1995) are practical today and cooling at cryogenic temperatures is required for the operations of complementary metal-

oxide-semiconductor (CMOS) devices (Yin and Bau, 1997a, b) and superconducting magnets (Cha et al., 1993).

This paper studies how to effectively enhance the heat transfer by fins in the microscale regime, despite the size effect-induced reduction of the thermal conductivity of microchannel and fin walls. This study resolves three basic issues: (1) heat flow choking in microfins, (2) the effect of size on the heat transfer enhancement ratio, and (3) the effect of size on the fin thickness (or channel wall thickness in microchannel heat exchangers) optimization.

Heat Flow Choking in Microfins

This issue comes from the question: "Is there an upper limit for the heat transfer enhancement?" A quantitative review of some typical existing works will be helpful to answer the question. Tuckerman and Pease (1981) were able to support a chip heat flux up to 790 W/cm^2 , which corresponds to a convective heat transfer coefficient of about $h = 4 \times 10^4 \text{ W}/(\text{m}^2\text{-K})$, by using the microchannel shown in Fig. 1(a) and single phase water cooling. The channel wall width, t_w , ranges from 44 to 57 μm . Copeland (1996) achieved $h = 2.4 - 49.3 \text{ kW}/(\text{m}^2\text{-K})$ for single-phase FC-72 jet impingement cooling of pin fin arrays, and the critical heat flux was about 45–395 $\text{kW}/(\text{m}^2\text{-K})$ for boiling cooling. The size of the smallest copper fin was 0.1 mm. Riddle and Bernhardt (1992) used liquid nitrogen as the working fluid in a heat sink consisting of 50 μm wide and 800 μm deep channels. A thermal resistance as low as $4.6 \times 10^{-6} \text{ K}/(\text{W}/\text{m}^2)$ was achieved.

Considering a plate fin as shown in Fig. 1(b), an estimation of related parameters from existing experimental works is as follows:

$$h = 10^2 - 10^5 \text{ W}/(\text{m}^2\text{-K})$$

$$H = 10^{-4} - 10^{-3} \text{ m}$$

$$k_w = 10^2 - 10^4 \text{ W}/(\text{m-K})$$

where h is the convective heat transfer coefficient, H is the fin height, and k_w is the thermal conductivity of the fin. The heat transfer rate by conduction through the fin base is estimated to be $O\{k_w t_w L(T_0 - T_L)/H\}$ where T_0 and T_L are the temperatures of fin base and fin tip, respectively. The convection heat transfer rate along the fin surface is $O\{2hHL[(T_0 + T_L)/2 - T_f]\}$. Approx-

¹ This work was performed while the author visited the University of California at Berkeley.

Contributed by the Heat Transfer Division for publication in the JOURNAL OF HEAT TRANSFER. Manuscript received by the Heat Transfer Division, Aug. 2, 1998; revision received, Apr. 23, 1999. Keywords: Conjugate, Enhancement, Finned Surfaces, Heat Transfer, Microscale. Associate Technical Editor: T. F. Chung.

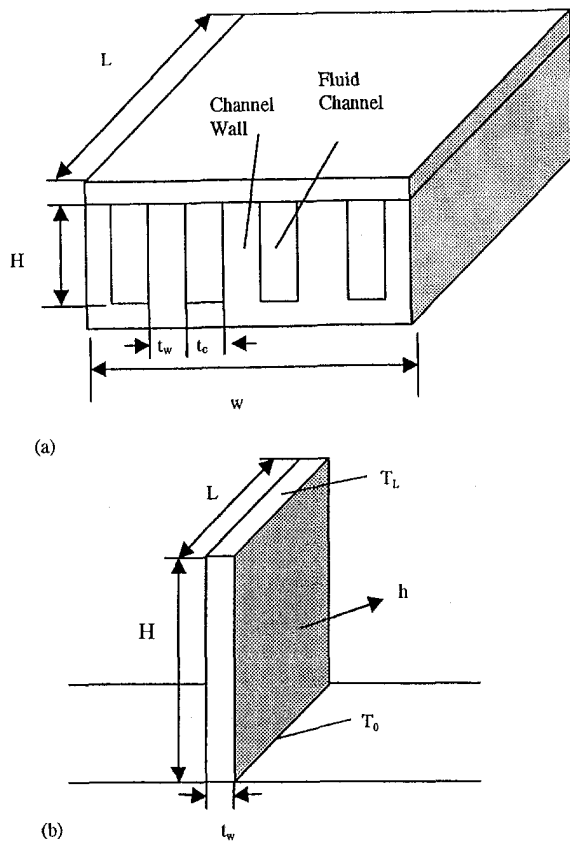


Fig. 1 Schematic of (a) a microchannel heat sink and (b) a plate fin

imations adopted in this order of magnitude estimation are: the temperature distribution from fin base to fin tip is linear, the temperature of fin tip T_L approaches the temperature of fluid T_f , and h is constant along the fin surfaces. To prevent heat flow choking (Kraus and Bar-Cohen, 1985) of the fin, the amount of heat that can be conducted through the fin base, must exceed the amount of convection along the fin surfaces. Otherwise, the per-

formance of the fin may become limited by the heat flow choking. Therefore, the following equation must be satisfied:

$$O[k_w t_w L(T_0 - T_f)/H] > O[hHL(T_0 - T_f)]. \quad (1)$$

The fin thickness to prevent choking is thus

$$t_{wc} > O(hH^2/k_w) = O[(hH/k_w)H] = O(Bi H), \quad (2)$$

where $Bi (= hH/k_w)$ is the Biot number. From the foregoing estimations, Bi is found to range from 1 to 10^{-6} .

The cases of $Bi = 0.14$, 0.1 , and 0.05 are taken as examples, which may correspond to water cooling ($h = 5.36 \times 10^4$, 3.83×10^4 and 1.91×10^4 W/(m²-K)) of a silicon fin ($k_w = 1.34 \times 10^2$ W/(m-K) at 325 K) with fin height $H = 350 \mu\text{m}$. The aforementioned cases are those that might occur in Tuckerman and Pease (1981). Then, Eq. (2) becomes

$$t_{wc} > O(49 \mu\text{m}) \text{ for } Bi = 0.14 \text{ and } H = 350 \mu\text{m}. \quad (3)$$

A regime map for the cases is shown in Fig. 2. Above the horizontal lines at 49, 35, and $17.5 \mu\text{m}$, for the cases of $Bi = 0.14$, 0.1 , and 0.05 and $H = 350 \mu\text{m}$, choking will not occur in plate fins. The curved lines, which delineate the regimes where the size effect on thermal conduction in diamond, silicon, and copper should be considered, are from the results of Flik et al. (1992). It should be noted that the lines are not obtained from the bulk mean free path, λ_b , but from seven times the bulk mean free path, $7\lambda_b$. At temperatures and fin thicknesses below these lines, thermal conductivity will be reduced due to the size effect. This reduction of thermal conductivity will make Bi even higher than that with same h and H but without the size effect. The ranges of fin thickness and working temperature in the work of Tuckerman and Pease (1981) and many other similar works are shown in Fig. 2. Yin and Bau (1997a, b) and Krane et al. (1990) reported that the operation of CMOS devices at cryogenic temperatures, such as those obtained by using neon (24.5–44.5 K) and nitrogen (63–77 K), provides a number of significant benefits such as lower electrical resistance of the conductors, lower leakage currents between conductors, and lower component degradation. The case of working temperature 63–77 K and fin thickness $50 \mu\text{m}$ was studied in the work of Yin and Bau (1997b). A microchannel heat sink with channel wall thickness $10 \mu\text{m}$ was proposed by Cha et al. (1993) for liquid nitrogen cooling of superconducting magnets. Figure 2

Nomenclature

A = fin base area, m²
 A_c = cross-sectional area of rod, m²
 Bi = Biot number, hH/k_w
 c_p = specific heat at constant pressure, J/(kg-K)
 d = diameter of pin fin, m
 D_h = hydraulic diameter of fluid channel, m
 f = flow rate, m³/s
 H = height of fin or microchannel wall, m
 h = convective heat transfer coefficient, W/(m²-K)
 k = thermal conductivity, W/(m-K)
 L = longitudinal length of fin or microchannel, m
 mL = dimensionless parameter for fin, $(hPH^2/k_w A)^{0.5}$
 N = dimensionless parameter related to fin efficiency, $(2h/k_w t_w)^{0.5} H$
 n = exponent of thermal conductivity reduction in Eq. (18)
 Nu = Nusselt number, hD_h/k_f

P = perimeter of fin, m
 p = probability of diffuse phonon scattering at boundary
 Q = heat flow, W
 R = thermal resistance, K/W or K/(W/m²)
 T = temperature, K
 t = thickness of fin or microchannel wall, m
 w = width of microchannel substrate, m
 α = surface multiplication factor, $2H/(t_c + t_w)$
 δ = dimensionless plate fin thickness, t_w/λ_b
 δ_d = dimensionless pin fin diameter, d/λ_b
 η = fin efficiency
 λ = mean free path, m
 λ_c = mean free path for pure diffuse reflection, m
 ρ = fluid density, kg/m³

Subscripts

0 = fin base
 b = quantity for bulk materials
 c = convection by the fluid or fluid channel
 d = pin fin with diameter d
 f = fluid
 h = heating of fluid
 L = fin tip
 r = reference state
 t = plate fin with thickness t_w
 w = wall of fin or microchannel
 wc = wall thickness of fin to prevent choking
 w_o = optimum wall thickness for microchannel
 z = longitudinal direction

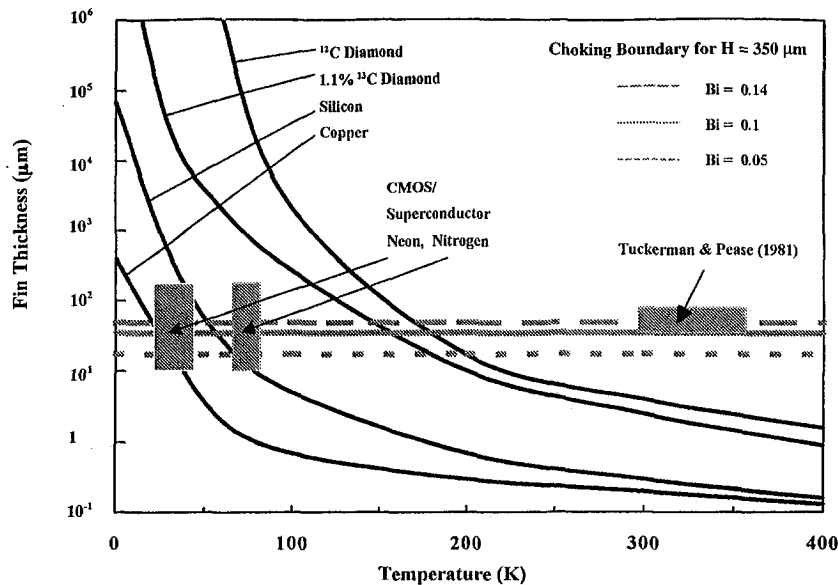


Fig. 2 Regime map for fin heat flow choking and thermal conductivity size effect for diamond, silicon, and copper films (Flik and Tien, 1990)

shows that there is no need to consider the size effect for fins at room temperature. For the nitrogen and neon cooling of CMOS devices and superconducting magnets, however, the consideration of the size effect is absolutely needed.

Figure 2 also shows that the ranges of fin thickness and working temperature in the works of Tuckerman and Pease (1981) and for CMOS/superconducting magnet microchannel cooling are below the choking line for $Bi = 0.14$ and $H = 350 \mu\text{m}$. Of course, the result of Eq. (3) is only an order of magnitude estimation. The utilization of fin thicknesses of $t_w < 49 \mu\text{m}$ may not necessarily induce heat flow choking under the condition of $Bi = 0.14$ and $H = 350 \mu\text{m}$, but a more careful analysis is required to make a definitive determination. It is worth noting that although choking has usually been found to be caused by the accommodation of a cluster of fins at the fin tip (Kraus and Bar-Cohen, 1995), in the microscale regime, choking may occur even in the cases of simple plate and pin fins (without clusters).

For the case of small Biot number, $Bi = 10^{-5}$, which corresponds to air cooling ($h = 10^2 \text{ W}/(\text{m}^2\text{-K})$) of a metal fin ($k_w = 10^3 \text{ W}/(\text{m-K})$) at room temperature) of height $H = 100 \mu\text{m}$, Eq. (2) becomes

$$t_{wc} > O(2 \times 10^{-9} \text{ m}) = O(2 \text{ nm}). \quad (4)$$

This shows that there will be no choking under the condition of small Biot number, regardless of fin thickness.

The Effect of Size on the Heat Transfer Enhancement Ratio

This second section studies how small size influences the effectiveness of heat transfer enhancement by fins. The heat transfer rate Q through the fin base can be found in standard heat transfer texts,

$$Q = k_w A (T_0 - T_f) (h P H^2 / k_w A)^{0.5} \tanh mL \\ = (T_0 - T_f) (h P H^2 k_w A)^{0.5} \tanh mL, \quad (5)$$

where T_0 and T_f are the temperatures of fin base and fluid, respectively, $mL = (h P H^2 / k_w A)^{0.5}$ is a dimensionless parameter for the fin, P is the perimeter of the fin, and A is area of the fin base. The value of mL is not too much greater than unity in a well-designed fin (Lienhard, 1981). To make a reasonable comparison, the fin number is increased but the total fin base area and

fin height are kept fixed. For pin fins, this means that if the fin number increases four times, the diameter of each fin decreases to half of the original one. The convective heat transfer coefficient h is assumed to be unchanged. Then, the heat transfer enhancement ratio can be obtained for pin and plate fins.

Pin Fins. For pin fins, the heat transfer enhancement ratio can be derived as

$$Q_d/Q_r = (k_d/k_r)^{0.5} (d_r/d)^{0.5} \\ \times \tanh [(mL_r)(d/d_r)(k_d/k_r)^{0.5}] / \tanh mL_r, \quad (6)$$

where the subscript "d" denotes the quantities or properties of pin fin with diameter d , and the subscript "r" denotes a reference state which may or may not be in the size effect regime. Concerning the phonon transport along an infinite rod, Ziman (1960) showed that the phonon mean free path, λ , limited by diffuse surface scattering is

$$\lambda = [(2 - p)/p] \lambda_c, \quad (7)$$

where p is the probability of diffuse phonon scattering at boundaries, and λ_c is the mean free path for pure diffuse reflection given as $\lambda_c = 1.12(A_c)^{0.5}$, where A_c is the cross-sectional area of the rod. The value of p depends on the ratio of the phonon wavelength to the characteristic roughness of the surface, but is close to unity for most engineering surfaces at moderate temperatures. Assuming that p is also unity for microfin operation at moderate temperatures, the size effect on thermal conductivity for pin fins can be expressed as $k_d/k_b = \delta_d = d/\lambda_b$, where k_d and k_b are the thermal conductivities for the pin fin with diameter d and for the bulk material. This linear reduction of thermal conductivity with size, however, is only for the case $\delta_d \ll 1$ (Tien et al., 1969). A simple approximate relation: $(k_d/k_b) = \delta_d/(1 + \delta_d)$, which holds for $p = 1$ and all values of δ_d , has been suggested by Nordheim (1934). It shows that k_d/k_b approaches unity for $\delta_d \gg 1$ and becomes a linear reduction with d for $\delta_d \ll 1$. The variation of heat transfer enhancement ratio Q_d/Q_r with diameter ratio d/d_r is shown in Fig. 3 for $mL_r = 1$ and 2 for the cases with and without size effect. The set of curves for $k_d/k_r = 1$ is for the cases without size effect. The reference state for the consideration of size effect shown in Fig. 3 is $d_r = \lambda_b$. For this reference state, $k_r/k_b = 0.5$ and the thermal conductivity ratio k_d/k_r , for the cases with size effect is

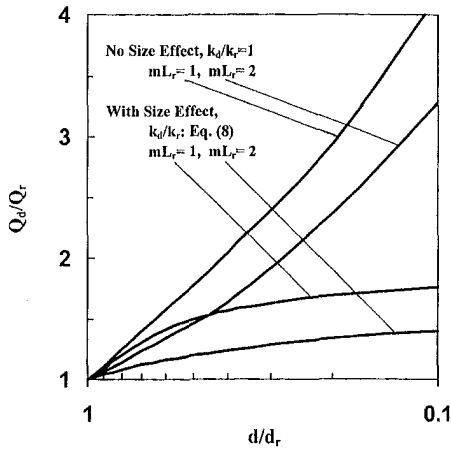


Fig. 3 Pin fin heat transfer enhancement ratio versus diameter ratio

$$(k_d/k_r) = 2(d/d_r)/[1 + (d/d_r)]. \quad (8)$$

A typical reference case for the pin fin is liquid cooling ($h = 2.5 \times 10^4 \text{ W/(m}^2\text{-K)}$) of a CVD diamond fin ($k_w = 10^3 \text{ W/(m-K)}$) around 70 K) of height $H = 2 \times 10^{-3} \text{ m}$ and diameter $d_r = 400 \mu\text{m}$. For this case, $mL_r = 1$. The results for $mL_r = 1$ and 2 with $k_d/k_r = 1$ in Fig. 3 shows that heat transfer will be significantly enhanced by increasing the fin number but keeping the fin base area fixed if the size effect is not accounted for. The results for $mL_r = 1$ and 2 with k_d/k_r , according to Eq. (8) are depicted in Fig. 3 and show that the heat transfer enhancement ratio will be significantly reduced and will rapidly reach a saturated value due to the size effect. From the foregoing comparison, one finds that if fins are not in the size effect regime, there is significant heat transfer enhancement by increasing the number of fins while keeping total fin base area fixed. If fins are in the size effect regime, there is only a small enhancement.

Plate Fins. For plate fins, the heat transfer enhancement ratio can be derived as

$$Q_d/Q_r = (k_d/k_r)^{0.5}(t_r/t)^{0.5} \times \tanh[(mL_r)(t/t_r)^{0.5}(k_r/k_d)^{0.5}]/\tanh mL_r \quad (9)$$

where the subscript "t" denotes the quantities and properties of the plate fin with fin thickness t_w . Again, the subscript "r" denotes a reference state, which may or may not be in the size effect regime. The match solution for the phonon mean free path along the film (Flik and Tien, 1990) is

$$\lambda_z/\lambda_b = 0.5 - (\cos^{-1} \delta)/\pi - (1 - S^3)/(3\delta\pi) + \delta[1 + \exp(-6\delta)] \ln[(1 + \delta + S)/(1 + \delta - S)]/\pi, \quad (10)$$

where λ_z is the mean free path in the longitudinal direction, $\delta = t_w/\lambda_b$ is the dimensionless plate fin thickness, and $S = (1 - \delta^2)^{0.5}$. The solution derived from uniform origination (Flik and Tien, 1990) is

$$\lambda_z/\lambda_b = 0.5 - (\cos^{-1} \delta)/\pi - (1 - S^3)/(3\delta\pi) + \delta \ln[(1 + \delta + S)/(1 + \delta - S)]/\pi, \quad (11)$$

and the reduction of the thermal conductivity (Flik and Tien, 1990) is $k_t/k_b = \lambda_z/(\lambda_b/2)$. The variation of heat transfer enhancement ratio Q_d/Q_r with plate fin thickness ratio t_w/t_r is shown in Fig. 4 for $mL_r = 1$ and 2 for the cases with and without size effect. The set of curves for $k_t/k_r = 1$ is for the cases without size effect. The reference state for the consideration of size effect shown in Fig. 4 is $t_r = \lambda_b$. For this reference state $k_r/k_b = 0.7878$, and the thermal conductivity ratio is

$$k_t/k_r = 2.539\lambda_z/\lambda_b. \quad (12)$$

Figure 4 shows that the reduction of the heat transfer enhancement ratio due to the size effect is much smaller for plate fins than for pin fins. This is caused by the fact that the reduction of thermal conductivity for plate fins described by Eqs. (10)–(12) is smaller than that for pin fins described by Eq. (8). This result shows that, in the microscale regime, the shape effect should be considered in the design of micro heat exchangers as well as the size effect. This result also suggests that plate fins are more desirable than pin fins for heat transfer enhancement.

The Effect of Size on the Optimization of Plate Fin Thickness

Several works on microchannel thickness optimization have been reported by Tuckerman and Pease (1981) and many other investigators. Most results from later investigators compare favorably with the original results of Tuckerman and Pease (1981), although a few studies that do not closely agree. None of these studies, however, consider the size effect. The present analysis of fin thickness optimization basically follows that of Tuckerman and Pease (1981), but includes the size effect. Therefore, it will be described only briefly. Considering the microchannel heat sink shown in Fig. 1(a), the thermal resistance, $R = \Delta T/Q$ where ΔT is the temperature difference, can be divided into the resistances due to convection from the heat sink to the coolant fluid, R_c , and due to heating of the fluid as it absorbs energy passing through the heat exchanger, R_h :

$$R_c = 1/(\alpha h L w) = D_h/(\alpha \text{Nu} k_f L w), \quad \text{and} \quad (13)$$

$$R_h = 1/(\rho c_p f) = [24 \mu L/(\rho c_p w \Delta P)](\alpha^{-1} t_c^{-3}). \quad (14)$$

Here $\alpha = 2H/(t_c + t_w)$ is the surface multiplication factor, L is the channel length in the longitudinal direction, w is the width of the microchannel substrate, $\text{Nu} = h D_h/k_f$ is the Nusselt number, D_h is the hydraulic diameter of the flow channel, k_f is the thermal conductivity of the fluid, c_p is the heat capacity of the fluid, f is the flow rate, and ΔP is the pressure drop. To account for the fin efficiency η , Eq. (13) becomes

$$R_c = D_h/(\alpha \text{Nu} k_f L w \eta) = 2t_c/(\alpha \text{Nu} k_f L w \eta). \quad (15)$$

Approximating D_h as $2t_c$ for a high-aspect ratio channel, the fin efficiency can be obtained by assuming that the heat flow in the channel wall is one-dimensional,

$$\eta = \tanh N/N, \quad (16)$$

where

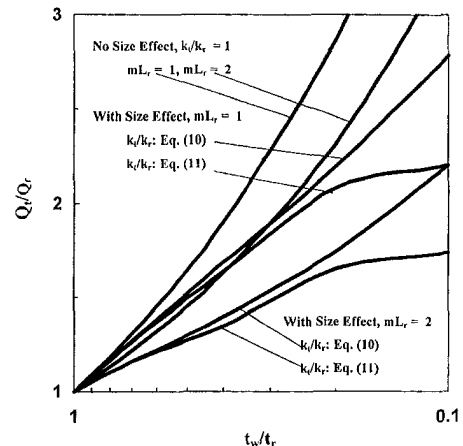


Fig. 4 Plate fin heat transfer enhancement ratio versus fin thickness ratio

$$N = (2h/k_w t_w)^{0.5} H = (Nu k_f/k_w t_c t_w)^{0.5} \alpha (t_c + t_w)/2. \quad (17)$$

From Eqs. (14) and (15), one can see that for any t_c and α , the thermal resistance can be minimized by maximizing η . Since η is a monotonically decreasing function of N , maximizing η can be obtained by minimizing N .

The size effect on the thermal conductivity of plate fin walls is approximated by a power law of fin thickness ratio,

$$k_w = k_b (t_w/\lambda_b)^n. \quad (18)$$

Minimizing N can be obtained from

$$dN/dt_w = d[k_b (t_w/\lambda_b)^n]^{0.5} (t_c t_w)^{0.5} / [\alpha (t_c + t_w)] / dt_w = 0. \quad (19)$$

Then the optimum fin thickness can be obtained as

$$t_{wo} = (0.5 + 0.5n)t_c / (0.5 - 0.5n). \quad (20)$$

The optimum fin thickness can also be obtained by holding H instead of α constant. For this case, it is important to note that an identical result to that of Eq. (20) will be obtained. The result $t_{wo} = t_c$, which was found by Tuckerman and Pease (1981), corresponds to the result without size effect: $n = 0$ in the present result. If k_w linearly decreases with t_w , such as the behavior of pin fins for $\delta_f \ll 1$, $n = 1$ is another special case: a limiting case. Equation (20) shows that there is no realistic optimum value for t_{wo} under the condition of $n \geq 1$. This is illustrated in Fig. 6. For $n = 0.5$, Eq. (20) indicates that $t_{wo} = 3t_c$.

Two methods can be used to calculate the value of n . The first method is to fit the curve of the following effective thermal conductivity variation (Flik and Tien, 1990),

$$\delta > 1 (t_w > \lambda_b)$$

$$k_w/k_b = 1 - 2/(3\delta\pi) \quad (21)$$

$$\delta \leq 1 (t_w \leq \lambda_b)$$

$$k_w/k_b = 1 - 2(\cos^{-1} \delta)/\pi - 2(1 - S^3)/(3\delta\pi) + 2\delta[1 + \exp(-6\delta)] \ln [(1 + \delta + S)/(1 + \delta - S)]/\pi. \quad (22)$$

The results are shown in Fig. 5. One can see that the three segments $n = 0.0352$ for $4 \leq \delta (= t_w/\lambda_b) \leq 10$, $n = 0.133$ for $1 \leq \delta \leq 4$, and $n = 0.35$ for $0.1 \leq \delta \leq 1$ can fit the curve. This result might be easier to use than the second method but is less accurate.

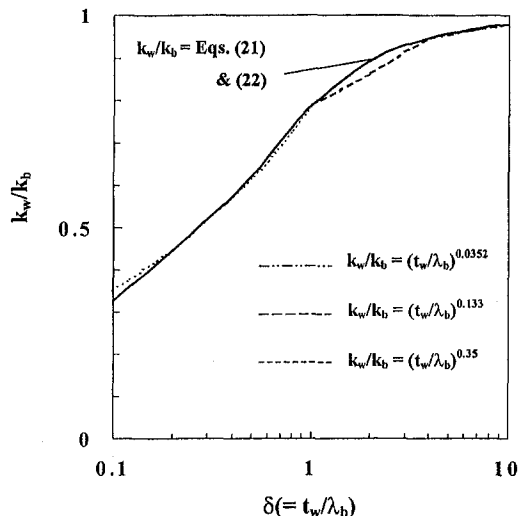


Fig. 5 Curve fitting of the thermal conductivity ratio by the power law of the dimensionless plate fin thickness δ

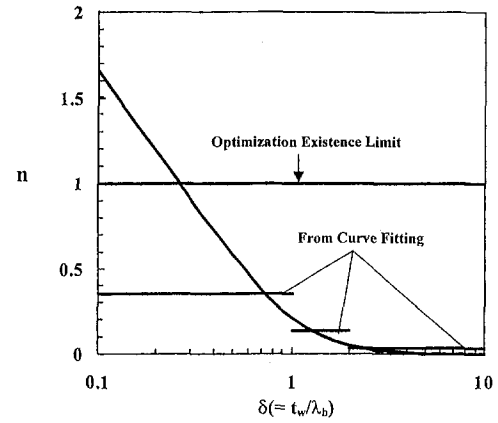


Fig. 6 Variation of the power-law exponent n with the dimensionless plate fin thickness δ

In the second method, by differentiating Eqs. (21) and (22) with respect to δ , one can obtain the n variation as follows:

$$\delta > 1 (t_w > \lambda_b)$$

$$n = 2/(3\delta^2\pi). \quad (23)$$

$$\delta \leq 1 (t_w \leq \lambda_b)$$

$$n = 2/(\pi S) + 2(1 - S^3)/(3\delta^2\pi) - 2S/\pi + 2[1 + \exp(-6\delta)] \ln [(1 + \delta + S)/(1 + \delta - S)]/\pi - 12\delta \exp(6\delta) \ln [(1 + \delta + S)/(1 + \delta - S)]/\pi + 2\delta[1 + \exp(-6\delta)] \{ [1 - (\delta/S)]/(1 + \delta + S) - [1 + (\delta/S)]/(1 + \delta - S) \}/\pi. \quad (24)$$

The following results can be compared with those of the first method: $n = 0.0021$ for $\delta = 10$, $n = 0.012$ for $\delta = 4$, $n = 0.212$ for $\delta = 1$, $n = 0.465$ for $\delta = 0.5$, and $n = 1.656$ for $\delta = 0.1$. The last result, $n = 1.656$ for $\delta = 0.1$, means that for plate fins, there is a regime for δ in which there is no optimum fin thickness. The variation of n with δ for the aforementioned two methods is shown in Fig. 6. The results of the second method are much more accurate than the first method, especially in the regime of low δ .

It is worth noting that an iterative process is required to determine the optimum fin thickness t_{wo} in the size effect regime. Now, some discussions and quantitative examples on t_w and t_c are needed. As discussed in the Introduction, liquid nitrogen was proposed or used as a working fluid by Choi et al. (1992), Cha et al. (1993), and Riddle and Bernhardt (1992). Going back to Fig. 2, one can see that at cryogenic temperatures (below 90 K), there is no optimum fin thickness if ^{12}C diamond is used to fabricate the microchannels. This occurs because the frequently used microfin thicknesses 50–500 μm are far smaller than the bulk mean free path indicated by the curved line shown in Fig. 2, making δ very small and thus yielding $n > 1$ in Fig. 6. The fin thickness optimization may be found in certain ranges for silicon and 1.1 percent ^{13}C diamond. The selection of t_c is mainly based on the allowable pressure drop. Since the viscosity of nitrogen is about one-fifth of water, $t_c = 50 \mu\text{m}$ as used by Tuckerman and Pease (1981) is a reasonable choice. The 1.1 percent ^{13}C diamond is chosen as the material for thickness optimization because it has higher bulk thermal conductivity than silicon at 70 K. From Fig. 2, one can find that λ_b is about 100 μm for 1.1 percent ^{13}C diamond at 70 K. The following procedures for iteration are followed.

- 1 Begin the iteration by assuming $t_w = t_c$, then $\delta = 0.5$ and $n = 0.464$ from Eq. (24).
- 2 From Eq. (20), $t_{wo} = 2.73t_c$, then $\delta = 1.36$ and n is about 0.16 from Eq. (23).

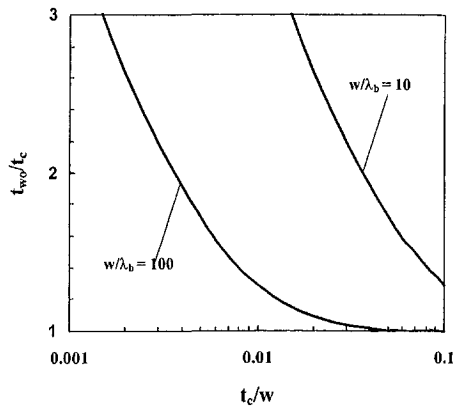


Fig. 7 Optimum wall thickness versus dimensionless fluid channel width for two values of dimensionless substrate width

- 3 From Eq. (20), $t_{wo} = 1.38t_c$, then $\delta = 0.69$ and n is about 0.3 from Eq. (24).

After many more iterations, the result is found to be $t_{wo} = 1.724t_c = 86.2 \mu\text{m}$ for $t_c = 50 \mu\text{m}$ and $\lambda_b = 100 \mu\text{m}$. It should be noted however, that if t_c is relatively small, the iteration will diverge unless a good initial guess for t_w is given. For example, for $t_c = 20 \mu\text{m}$, $n > 1$ will be obtained in the above step 1. Even beginning with $t_w = 2t_c$, a divergent result will be obtained. By beginning with $t_w = 3t_c$, the result $t_{wo} = 2.63t_c = 52.6 \mu\text{m}$ is obtained for $t_c = 20 \mu\text{m}$ and $\lambda_b = 100 \mu\text{m}$.

To assist in the design of microchannels, the foregoing calculation was generalized to obtain the optimum fin thickness. The result is shown in Fig. 7, which depicts the variation of t_{wo}/t_c with the ratio of fluid channel width to width of microchannel substrate t_c/w . This shows that t_{wo}/t_c is almost 1 for $t_c/w = 0.1$ and $w/\lambda_b = 100$. The value of t_{wo}/t_c gradually increases when t_c/w decreases from 0.1 to 0.01. It is worth noting that t_{wo}/t_c increases rapidly when t_c/w approaches 0.001. The curve of $w/\lambda_b = 10$ shows a same trend as that of $w/\lambda_b = 100$ but shifts toward a higher value of t_c/w . Since the number of fluid channels for the microchannel substrate will be less than five when t_c/w is larger than 0.2, it is not practical to show any result for $t_c/w > 0.2$.

Conclusion

This paper studies how to effectively enhance heat transfer by fins in the microscale regime, despite the size effect-induced reduction of the thermal conductivity of microchannel and fin walls. This study resolves three basic issues. The first issue comes from the question: "Is there an upper limit for the heat transfer enhancement?" It is found that although choking is usually observed in fins with clusters at the tip, choking may occur even in the case of simple plate fins or pin fins in the microscale regime.

The second issue considered is how the size effect affects the heat transfer enhancement ratio by increasing the fin number while keeping the total fin base area fixed. For this case, the analysis shows that heat transfer is significantly enhanced if there is no size effect. The heat transfer enhancement ratio is relatively low and will rapidly reach a saturated value if there is a size effect. The heat transfer enhancement ratio for plate fins, however, is significantly higher than that of pin fins. The reason is that the thermal conductivity reduction due to the size effect for plate fins is smaller than that for pin fins. This result shows that, in the microscale regime, the shape effect should be considered in the design of micro heat exchangers as well as the size effect. Plate fins are more desirable than pin fins for heat transfer enhancement.

The third issue considered is how the size effect affects the fin thickness (or channel wall thickness in microchannel heat ex-

changers) optimization. The size effect on the thermal conductivity of plate fins is approximated by a power law of fin thickness ratio, $k_w = k_b(t_w/t_b)^n$. Then the optimum fin thickness can be obtained as

$$t_{wo} = (0.5 + 0.5n)t_c / (0.5 - 0.5n),$$

where t_c is the width of the fluid channel. The result, $t_{wo} = t_c$, which was found by Tuckerman and Pease (1981), corresponds to the case of $n = 0$ in the present result. For convenience in design applications, the variations of t_{wo}/t_c with t_c/w are established to calculate the optimum wall thickness in the size effect regime.

Acknowledgments

The authors gratefully acknowledge the support of the National Science Foundation and the Department of Energy. Fu-Chu Chou thanks the National Science Council of the Republic of China. Jennifer Lukes is supported by a National Science Foundation Fellowship.

References

- Cha, Y. S., Hull, J. R., and Choi, U. S., 1993, "Cryostabilization of High-Temperature Superconducting Magnets with Subcooled Flow in Microchannels," *IEEE Trans. on Applied Superconductivity*, Vol. 3, pp. 172-176.
- Choi, U. S., Rogers, C. S., and Mills, D. M., 1992, "High-Performance Micro-channel Heat Exchanger for Cooling High-Heat-Load X-ray Optical Elements," *Proc. ASME Micro Mechanical Systems*, ASME DSC-40, pp. 83-89.
- Copeland, D., 1996, "Single-Phase and Boiling Cooling of Small Pin Fin Arrays by Multiple Nozzle Jet Impingement," *ASME Journal of Electronic Packaging*, Vol. 118, pp. 21-26.
- Flik, M. I., Choi, B. I., and Goodson, K. E., 1992, "Heat Transfer Regimes in Microstructures," *ASME JOURNAL OF HEAT TRANSFER*, Vol. 114, pp. 666-674.
- Flik, M. I., and Tien, C. L., 1990, "Size Effect on the Thermal Conductivity of High- T_c Thin-Film Superconductors," *ASME JOURNAL OF HEAT TRANSFER*, Vol. 112, pp. 872-881.
- Harpole, G. M., and Eninger, J. E., 1991, "Micro-Channel Heat Exchanger Optimization," *Proc. 7th IEEE SEMI-THERM Symposium*, pp. 59-63.
- Joo, Y., Dieu, K., and Kim, C. J., 1995, "Fabrication of Monolithic Microchannels for IC Chip Cooling," *Proc. IEEE Micro Electro Mechanical Systems 1995*, IEEE, Piscataway, NJ, pp. 362-367.
- Knight, R. W., Hall, D. J., Goodling, J. S., and Jaeger, R. C., 1992, "Heat Sink Optimization With Application to Microchannels," *IEEE Trans. on Components, Hybrids, and Manufacturing Technology*, Vol. 15, pp. 832-842.
- Krane, R. J., Bar-Cohen, A., Jaeger, R. C., and Gaensslen, F. H., 1990, "MOS Electronics and Thermal Control for Cryogenically-Cooled Computer Systems," *Advances in Thermal Modeling of Electronic Components and Systems*, Vol. 2, A. Bar-Cohen and A. D. Kraus, eds., Hemisphere, New York, pp. 185-232.
- Kraus, A. D., and Bar-Cohen, A., 1995, *Design and Analysis of Heat Sinks*, John Wiley and Sons, New York, pp. 154-157.
- Lienhard, J. H., 1981, *A Heat Transfer Textbook*, Prentice-Hall, Englewood Cliffs, NJ, p. 138.
- Majumdar, A., 1993, "Microscale Heat Conduction in Dielectric Thin Films," *ASME JOURNAL OF HEAT TRANSFER*, Vol. 115, pp. 7-16.
- Missaggia, L. J., Walpole, J. N., Liao, Z. L., and Phillips, R. J., 1989, "Micro-channel Heat Sinks for Two-Dimensional High-Power-Density Diode Laser Arrays," *IEEE J. Quantum Electron.*, Vol. 25, pp. 1988-1992.
- Mundinger, D., Beach, R., Bennett, W., Solarz, R., Krupke, W., Staver, R., and Tuckerman, D., 1988, "Demonstration of High-Performance Silicon Microchannel Heat Exchangers for Laser Diode Array Cooling," *Appl. Phys. Lett.*, Vol. 53, pp. 1030-1032.
- Nordheim, L. W., 1934, "Die Theorie der Thermoelektrischen Effekte," *Actes Scientifiques et Industrielles*, No. 131, Herman, Paris.
- Riddle, R. A., and Bernhardt, A. F., 1992, "The Microchannel Heat Sink With Liquid Nitrogen Cooling," Paper No. UCRL-JC-109267, Lawrence Livermore National Laboratory, Livermore, CA.
- Tien, C. L., Armaly, B. F., and Jagannathan, P. S., 1969, "Thermal Conductivity of Thin Metallic Films and Wires at Cryogenic Temperatures," *Proc. of 8th Thermal Conductivity Conference*, Plenum Press, New York, pp. 13-20.
- Tuckerman, D. B., and Pease, R. F. W., 1981, "High Performance Heat Sinking for VLSI," *IEEE Electron Device Lett.*, Vol. EDL-2, pp. 126-129.
- Yin, X., and Bau, H. H., 1997a, "Micro Heat Exchangers Consisting of Pin Arrays," *ASME Journal of Electronic Packaging*, Vol. 119, pp. 51-57.
- Yin, X., and Bau, H. H., 1997b, "Uniform Channel Micro Heat Exchangers," *ASME Journal of Electronic Packaging*, Vol. 119, pp. 89-94.
- Zhuang, Y., Ma, C. F., and Qin, M., 1997, "Experimental Study on Local Heat Transfer With Liquid Impingement Flow in Two-Dimensional Micro-Channels," *Int. J. Heat Mass Transfer*, Vol. 40, pp. 4055-4059.
- Ziman, J. M., 1960, *Electrons and Phonons*, Oxford University Press, Oxford, UK, pp. 466-470.

A New Method for Evaluation of Heat Transfer Between Solid Material and Fluid in a Porous Medium

K. Ichimiya

Department of Mechanical System Engineering,
Yamanashi University,
Takeda-4, Kofu
Yamanashi 400-8511, Japan
e-mail: ichimiya@ccn.yamanashi.ac.jp
Mem. ASME

The author proposes a new method to estimate the heat transfer between fluid gas and solid material in a porous medium. In the first stage, the local Nusselt numbers on the heated wall of a flow passage with a porous medium are numerically obtained in advance for the parameter H_m , including the volumetric heat transfer coefficient, h_m , between the fluid and the solid material in a porous medium. In the second stage, the experimental Nusselt numbers on the heated wall are obtained by measuring wall temperatures and heat flux. The volumetric heat transfer coefficient, h_m , is evaluated by comparing experimental Nusselt numbers with numerical ones. This method also gives the longitudinal characteristics of the heat transfer in a porous medium.

Introduction

Technological applications in which porous materials are utilized include thermal energy storage, geophysical fluid engineering, thermal insulation, heat transfer enhancement, and heat exchangers. Such materials are favored because they produce high thermal performance and low pressure drop. To develop and optimize the design of such advanced devices, it is necessary to know the convective heat transfer coefficient data between a fluid and a solid material in a porous medium. However, there is a dearth of such data because of the technical difficulty of temperature measurements arising from the fact that the material structure is very fine and often complex. Hamaguchi et al. (1983) obtained the average heat transfer coefficient by comparing the experimental temperature behavior of air with the theoretical temperature behavior at the entrance and exit of a porous material after it was heated and then instantly inserted into a cooled section. Kondoh et al. (1987) measured the volumetric heat transfer coefficient by heating two sides of a porous material, measuring the temperatures in the material and the bulk temperature of air, and calculating the net heat flux. The net heat flux was calculated by subtracting the heat loss from the electrically supplied power. Fukuda et al. (1990) also evaluated the volumetric heat transfer coefficient in a fluidized bed filled with glass beads by measuring the particle and air temperatures at its entrance and exit. Golombok et al. (1990) measured the heat flow from high to low temperature gases in wires and fibers, and then evaluated the heat transfer. Younis and Viskanta (1993) carried out experiments on a ceramic foam in a flow passage for high temperature air. The volumetric heat transfer coefficient was obtained by comparing the one-dimensional prediction with the experimental values of the temperature difference between the entrance and exit of ceramic foams. These previous studies illustrate the difficulty of each temperature measurement in a porous material, namely, solid temperature and fluid temperature. Additionally, a one-dimensional system was assumed in estimating the heat transport in a porous medium, so that the average heat transfer along the flow direction was obtained. The result is that the longitudinal behavior, which is important in determining the size of the porous medium used in various heat exchangers, has not yet been clarified.

To determine the heat transfer coefficient between the solid and the fluid, we must take account of thermal nonequilibrium effects. Analyses in which the thermal nonequilibrium was considered have been presented. Dixon and Cresswell (1979) constructed a theory for predicting the effective axial and radial thermal conductivity and the apparent wall heat transfer coefficient for constant wall temperature. The solid and fluid temperatures were found by using the two-phase model equations. However, in the fluid-to-solid Nusselt number, they utilized the empirical correlations (Handley and Heggs, 1968; Miyauchi et al., 1976). Vafai and Sozen (1990) presented the two analyses for the forced convection of vapor through packed bed and for the behavior of a packed bed of phase-change material and condensing flow through it. For the fluid-to-solid heat transfer coefficient, the empirical correlations presented in terms of Colburn-Chilton j factors were utilized. Kuznetsov (1997) analyzed the solution for a rectangular packed bed with constant wall temperatures by using the perturbation technique. In brief, the solid temperature differs from the fluid temperature by a small perturbation. Kuznetsov (1998) also carried out the analyses of thermal nonequilibrium one-dimensional Darcian flow and non-Darcian flow of an incompressible fluid. The fluid-to-solid Nusselt number in these analyses was correlated with the expression presented in Handley and Heggs (1968) and Miyauchi et al. (1976).

In the present research, the author proposes a new method to evaluate the heat transfer between solid and fluid in a porous medium. First, the flow field in a porous medium is analyzed in a two-dimensional system. The results are then applied to the energy equation that includes the heat transfer coefficient, h_m , between solid and fluid. The volumetric heat transfer coefficient, h_m , is obtained by comparing the numerical and experimental values of heat transfer on a heated wall of a flow passage without directly measuring the solid and fluid temperatures in a porous medium.

Description of the Problem

The fine structure of a porous medium is very complex. Therefore, the temperatures of solid and fluid cannot be directly measured with sufficient accuracy. In the present study, a new method that does not include directly measuring the temperatures of solid and fluid is proposed. This method is based on thermally nonequilibrium convection in a porous medium. In brief, there is a temperature difference between solid and fluid in a porous medium. In the first stage, the flow field in a porous medium and the energy equation including the heat transfer parameter between solid and

Contributed by the Heat Transfer Division for publication in the JOURNAL OF HEAT TRANSFER. Manuscript received by the Heat Transfer Division, Jan. 6, 1999; revision received, June 22, 1999. Keywords: Analytical, Convection, Experimental, Heat Transfer, Porous Media. Associate Technical Editor: M. Hunt.

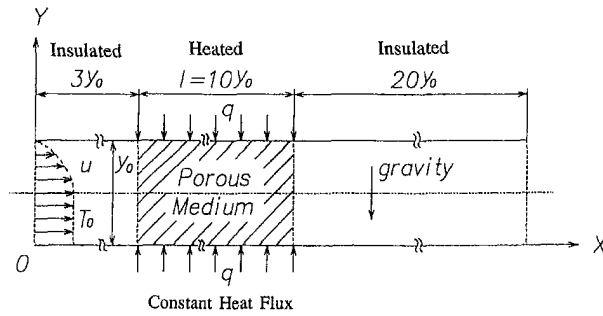


Fig. 1 Two-dimensional model

fluid, $H_a (= h_v y_0^2 / \lambda_a)$ are solved numerically to obtain the Nusselt number on the heated wall of a flow passage. In the next stage, Nusselt numbers on the heated wall are experimentally obtained by measuring the heated wall temperatures. The parameter, H_a , is determined by adjusting H_a so that the numerical Nusselt number becomes equal to the experimental one, and the volumetric heat transfer coefficient, h_v , is evaluated.

Figure 1 shows a two-dimensional model. A parallel plate duct with height, y_0 , is filled with a porous medium of constant porosity along flow direction, $l = 10y_0$ (solid lines in Fig. 1). Both the upper and lower walls of the duct are heated uniformly (heat flux, q). The working fluid (air in the present case) uniform in temperature runs into the flow passage. The velocity at the entrance has a fully developed laminar flow distribution. The fluid is released into the atmosphere after developing a length of $20y_0$ from a porous medium. The heat transfer experiment corresponding to the model is carried out by using air. The Nusselt numbers on the heated wall are then compared with numerical values.

The flow in a porous medium is assumed to be a non-Darcian flow including the Brinkman viscous term and Forchheimer inertia term (Vafai and Tien, 1981; Kaviany, 1991) to apply this method over a wide range. When we apply the method to a Darcy flow, we should neglect both terms in the momentum equation. The fact that the flow velocity is not as high as the velocity of sound and the temperature is not as high as thermal radiation is considered. Therefore, it is assumed that the flow is steady, laminar, and incompressible, and the thermal radiation is neglected.

Numerical Calculation

In the numerical calculation, the governing equations of the flow and the energy can be written in dimensionless form with the following parameters:

$$X = x/y_0, \quad Y = y/y_0, \quad Z = z/y_0, \quad U = u/u_m,$$

$$V = v/u_m, \quad \Psi = \psi/u_m y_0, \quad \Omega = \omega y_0 / u_m$$

$$H_a = h_v y_0^2 / \lambda_a, \quad H_p = h_p y_0^2 / \lambda_p,$$

$$\Theta_{a,p,w} = (T_{a,p,w} - T_0) / (q y_0 / \lambda_a), \quad Re = 2u_m y_0 / \nu$$

$$Pr = Cp \mu_a / \lambda_a, \quad Gr = g \beta y_0^3 (q y_0 / \lambda_a) / \nu^2,$$

$$Nu = 2q y_0 / \{\lambda_a (T_w - T_0)\}, \quad Da = k / y_0^2. \quad (1)$$

Although the porous diameter may be better as a characteristic length, the heat source for convection is the wall of the flow passage. Therefore, the size of the flow passage, y_0 , is used as a characteristic length. The dimensionless parameters H_a and H_p are introduced as parameters of the volumetric heat transfer coefficient. The physical meaning of H_a is a kind of volumetric Nusselt number between solid and fluid (air) in a porous medium. On the other hand, the physical meaning of H_p is a kind of volumetric Biot number for a solid in a porous medium.

The flow equation based on a non-Darcian flow as described in "Description of the Problem" is expressed in Eq. (2).

$$\frac{1}{\epsilon^2} \left(\frac{\partial \Psi}{\partial Y} \frac{\partial \Omega}{\partial X} - \frac{\partial \Psi}{\partial X} \frac{\partial \Omega}{\partial Y} \right) - \frac{2}{\epsilon Re} \left(\frac{\partial^2 \Omega}{\partial Y^2} + \frac{\partial^2 \Omega}{\partial X^2} \right) + \frac{2\Omega}{Da Re} + \frac{C}{Da^{0.5}} \left[\frac{\partial}{\partial X} \left\{ \left| \frac{\partial \Psi}{\partial X} \right| \left(-\frac{\partial \Psi}{\partial X} \right) \right\} - \frac{\partial}{\partial Y} \left\{ \left| \frac{\partial \Psi}{\partial Y} \right| \left(\frac{\partial \Psi}{\partial Y} \right) \right\} \right] - \frac{4 Gr}{Re^2} \frac{\partial \Theta_a}{\partial X} = 0 \quad (2)$$

The coefficient C in Eq. (2) is expressed as the following equation given by Ergun (1952),

$$C = (1.75 / \sqrt{175}) \epsilon^{-1.5}. \quad (3)$$

This constant, obtained on the assumption that a small-particle bed is a porous medium, was applied to $10 < U_m Dp / \{\nu(1 - \epsilon)\} < 2000$ in which Dp is the hydraulic diameter of a particle. The parameter $U_m Dp / \{\nu(1 - \epsilon)\}$ of a porous medium used in the heat transfer experiment is 133 for $Re = 300$. This satisfies the region applicable to Eq. (3).

Energy equations including the heat transfer between fluid and solid material are applied to each fluid and solid material in a porous medium.

For a fluid section,

Nomenclature

C = coefficient (refer to Eq. (3))
 Cp = specific heat of fluid, J/kgK
 d = mean porous diameter, mm or m
 Da = Darcy number (refer to Eq. (1))
 Gr = Grashof number (refer to Eq. (1))
 h_v = volumetric heat transfer coefficient, W/m³K
 H = dimensionless heat transfer coefficient
 k = permeability, m²
 l = length of porous medium, mm or m
 Nu = Nusselt number (refer to Eq. (1))
 Pr = Prandtl number (refer to Eq. (1))
 Re = Reynolds number (refer to Eq. (1))
 Re_d = Reynolds number based on porous diameter ($= u_m d / \nu$)

RRM = ratio of thermal conductivities = λ_p / λ_a
 T = temperature, K or °C
 u = velocity along x -direction, m/s
 v = velocity along y -direction, m/s
 x = coordinate along flow direction
 y = coordinate perpendicular to flow direction
 y_0 = height of a flow passage, mm or m

Greek Symbols

β = volumetric expansion coefficient, 1/K
 ϵ = porosity
 Θ = dimensionless temperature (refer to Eq. (1))

λ = thermal conductivity, W/mK
 μ = viscosity, Pa · s
 ν = kinematic viscosity, m²/s
 ψ = stream function, m²/s
 ω = vorticity, 1/s

Subscripts

a = air
 m = mean
 p = porous medium
 w = wall
 o = entrance

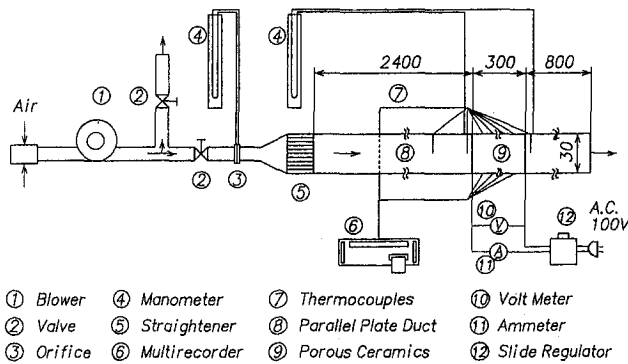


Fig. 2 Experimental apparatus

$$\frac{\partial \Psi}{\partial Y} \frac{\partial \Theta_a}{\partial X} - \frac{\partial \Psi}{\partial X} \frac{\partial \Theta_a}{\partial Y} - \frac{2\epsilon}{\text{Re Pr}} \left(\frac{\partial^2 \Theta_a}{\partial X^2} + \frac{\partial^2 \Theta_a}{\partial Y^2} \right) + \frac{2H_a}{\text{Re Pr}} (\Theta_a - \Theta_p) = 0. \quad (4)$$

For a solid section,

$$(1 - \epsilon) \left(\frac{\partial^2 \Theta_p}{\partial X^2} + \frac{\partial^2 \Theta_p}{\partial Y^2} \right) - H_p (\Theta_a - \Theta_p) = 0. \quad (5)$$

The dimensionless boundary conditions are as follows.

- at the entrance of a flow passage: $U = -6Y^2 + 6Y, V = 0, \Theta_a = 0$
- on the wall: $U = 0, V = 0$
- on the unheated wall: $\partial \Theta_a / \partial Y = 0$
- on the heated wall: $\partial \Theta_a / \partial Y = (\lambda_p / \lambda_a) (\partial \Theta_p / \partial Y) = 1$ or -1
- at the exit of a flow passage:

$$\partial U / \partial X = 0, V = 0, \partial \Theta_a / \partial X = 0$$

at the entrance and exit of a porous medium:

$$\begin{aligned} (\mu_p / \mu_a) \partial V / \partial Y|_p &= \partial V / \partial Y|_a \\ \partial \Theta_a / \partial X|_p &= \partial \Theta_a / \partial X|_a \\ (\lambda_p / \lambda_a) (\partial \Theta_p / \partial X) &= \partial \Theta_a / \partial X \end{aligned} \quad (6)$$

The ratio (μ_p / μ_a) is the ratio of effective viscosity to fluid viscosity, and it depends on porosity ϵ . In the present calculation, (μ_p / μ_a) is 1.2 corresponding to $\epsilon = 0.87$, which Neal and Nader (1974) proposed.

Discrete forms of the governing equations were derived by integrating in a control volume, expressing the conservative form, and applying the upwind method (Patankar, 1980). Conservative algebraic equations were solved by changing the relaxation parameter and using an iteration method. The number of grids were 826 along the flow direction, and 26 perpendicular to the flow, for a total of 21476. The convergence criterion, namely, the absolute maximum change of two terms for each Ψ , Ω , and Θ , is less than 10^{-5} .

Numerical calculations were performed for the following conditions: the Reynolds number, $\text{Re} = 300 \sim 600$; the heat transfer parameter between fluid and solid, $H_a = 100 \sim 50,000$; the thermal conductivity ratio, $\text{RRM} = 154$, which corresponds to the experiment; the Darcy number, $\text{Da} = (2.44 \sim 14.8) \times 10^{-5}$; and porosity, $\epsilon = 0.87$. The numerical result is evaluated with the Nusselt number Nu on the wall of the flow passage defined by

$$\begin{aligned} \text{Nu} &= 2qy_o / [\lambda_a (T_w - T_o)] \\ &= 2 / [(T_w - T_o) / qy_o / \lambda_a] = 2 / \Theta_w. \end{aligned} \quad (7)$$

Heat Transfer Experiment

Figure 2 shows the experimental apparatus corresponding to the

Table 1 Porous medium

	d (mm)	k (m ²) x 10 ⁸	ε (%)	Da x 10 ⁵
Porous Medium 1	1.3	2.193	87.5	2.44
Porous Medium 2	2.0	3.779	87.0	4.20
Porous Medium 3	4.2	13.324	87.3	14.8

model (Fig. 1). The rectangular flow passage whose height and width are 30 mm and 300 mm, respectively, is made of acrylic resin. Air flow as a working fluid is developed in an entrance region whose length is 2400 mm. Air runs into a 300 mm long porous medium and is heated electrically from both the upper and lower walls covered by a stainless steel foil and transparent acrylic plate whose thicknesses are 0.03 mm and 10 mm, respectively. After that, it is released into the atmosphere. Air temperatures at the entrance and exit of a porous medium and the heated wall temperatures along the flow direction were measured by 44 T-type thermocouples calibrated in advance. The heat loss from the heated section was evaluated based on the thermal conduction in a substrate (stainless steel foil and acrylic plate) and by the natural convection from the heated section to the atmosphere. The result was 15 ~ 20 percent of the supplied heat flow. The net heat flux was calculated by subtracting the heat loss from the electric supply (total heat flow). Two-dimensional characteristics were realized across three-fourths of the width in considering the wall temperature distribution. In the experiment, the room temperature of the laboratory was kept within $\pm 1^\circ\text{C}$. The wall temperatures of the flow passage and the inlet temperature were measured continuously and became steady after three to four hours. The heat transfer on the wall of the flow passage was evaluated in a steady condition.

The properties of the porous medium used are listed in Table 1. It was made of alumina-ceramic foam ($2\text{MgO} \cdot 2\text{Al}_2\text{O}_3 \cdot 5\text{SiO}_2$) with various porous diameters, permeabilities and Darcy numbers for almost constant porosity $\epsilon = 0.87$. The complex cell and matrix structure (Fig. 3) caused the difference in the local heat transfer.

In the first stage, it was recognized that the numerical heat transfer without a porous medium (Kays and Crawford, 1993) agreed with experimental values within three percent. In the next stage, the experiment with a porous medium was performed for $\text{Re} = 300$ and 600.

Uncertainties

Experimental Nusselt numbers are composed of the heat flux q , the heated wall temperature T_w , the entrance temperature T_o , the thermal conductivity of air λ_a , and the size of a flow passage y_o . The uncertainty of Nu was evaluated in the representative case of $d = 1.3$ mm and $\text{Re} = 300$ (ANSI/ASME, 1985). The bias limit and precision index are shown in Table 2 for $q = 92.29$ W/m², $T_w = 35.05^\circ\text{C}$, $T_o = 19.77^\circ\text{C}$, $\lambda_a = 0.0219$ W/(m · K) and $y_o = 30$ mm. As a result, a 95 percent relative coverage of uncertainty for the Nusselt number was 2.66 percent.

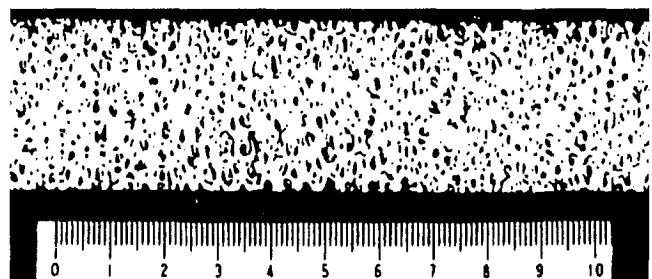


Fig. 3 Photograph of porous medium 3

Table 2 Bias limit and precision index

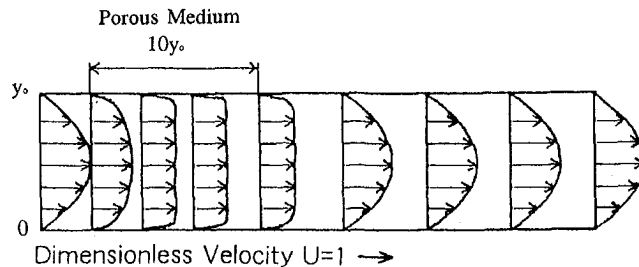
Item	Bias Limit	Precision Index
q 92.29 W/m ²	0.82	0.98
T_w 35.05 °C	0.053	0.11
T_o 19.77 °C	0.05	0.09
λ_s 0.0219 W/mK	3.76×10^{-6}	7.05×10^{-6}
y_o 30 mm	0.05	0

On the other hand, the accuracy of the numerical estimation was previously considered by comparing the numerical values with the final solution of laminar heat transfer for a single flow in a parallel plate duct without a porous medium. It was within 2.3 percent. Consequently, the accuracy of both the experimental and numerical method was within five percent. That accuracy is improved by computing Nu with small intervals of dimensionless parameter H_a .

Results and Discussions

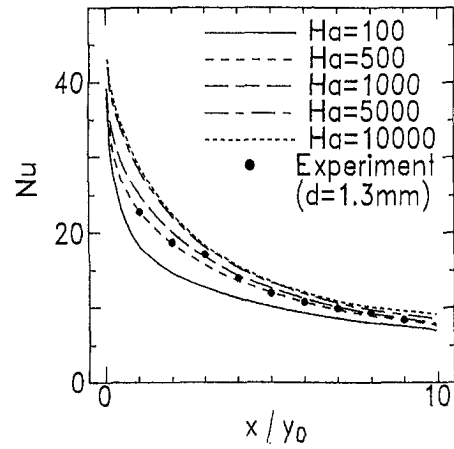
The flow along the longitudinal direction for $Re = 300$ and $Da = 4.2 \times 10^{-5}$ is presented in Fig. 4. The size along the flow direction of this figure is compressed to one-eighth. The velocity distribution becomes flat after having penetrated within about $2y_o$ of a porous medium and recovers to a parabolic distribution after exiting of a porous medium. In this condition, the heat transfer on the heated wall of the flow passage filled with a porous medium is evaluated. Even if the velocity at the entrance is different (for example, uniform velocity), the effect for heat transfer on the wall is not great because the developing region becomes short in the porous medium.

Figures 5(a), (b), and (c), illustrate the numerical Nusselt numbers by solid and broken lines as a parameter of H_a and the experimental values by solid circles. Figure 5(a) presents the Nusselt numbers for $d = 1.3$ mm, $Da = 2.44 \times 10^{-5}$, and $Re = 300$. According to the figure, experimental values agree well with numerical ones for $H_a = 500$ along the flow direction. However, in a higher Reynolds number (Fig. 5(b), $Re = 600$), the experimental values take greater values than the numerical ones at the first half and smaller ones at the latter half compared with Fig. 5(a). The behavior of H_a corresponding to those experimental values is similar to that of the Nusselt numbers described above. When the porous diameter increases (Fig. 5(c), $d = 4.2$ mm), H_a tends to increase at the latter half. It is recognized that Nusselt numbers on the heated wall and H_a have a relation to each other. This means that the physical variation in a porous medium affects the heat transfer on the heated wall of a flow passage. Therefore, the longitudinal variation in the heat transfer between solid and fluid in a porous medium can be evaluated quantitatively corresponding to the local Nusselt numbers on the heated wall. However, the scale of the figure and the experimental accuracy should be improved with an increase in H_a because the variation in Nu for

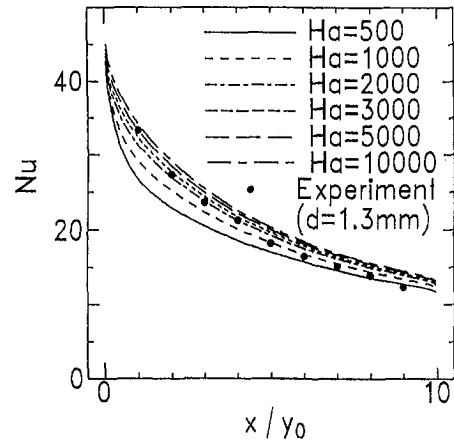


(The size along the flow direction is compressed to one-eighth)

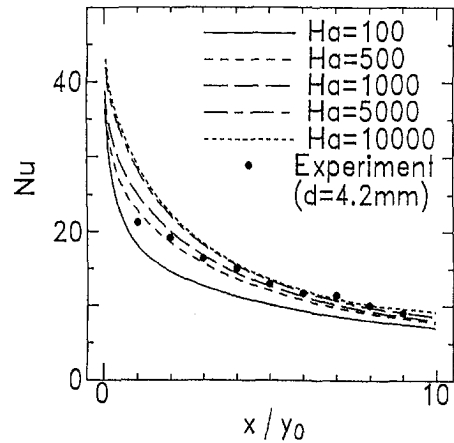
Fig. 4 Longitudinal variation of velocity distribution



(a) $d=1.3$ mm, $Re=300$



(b) $d=1.3$ mm, $Re=600$



(c) $d=4.2$ mm, $Re=300$

Fig. 5 Longitudinal Nusselt number (a) $d = 1.3$ mm, $Re = 300$ (b) $d = 1.3$ mm, $Re = 600$; (c) $d = 4.2$ mm, $Re = 300$

H_a larger than 5000 is small. The accuracy of the correspondence between numerical and experimental Nusselt numbers can be improved by narrowing the numerical interval of H_a . Figure 6 shows H_a along the flow direction for various porous diameters and Reynolds numbers. The fact that experimental Nusselt numbers on the heated wall agree well with numerical ones at a certain H_a means that the average heat transfer between solid and fluid in

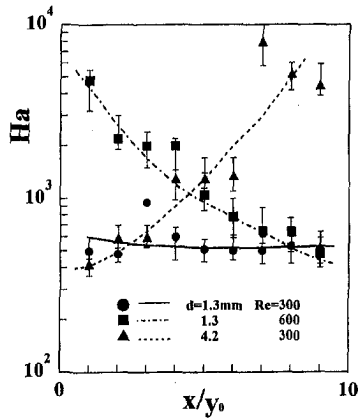


Fig. 6 Dimensionless heat transfer coefficient H_a

a porous medium across the section of a flow passage has the same value along the flow direction (symbol ● in Fig. 6). With an increase in air flow rate, however, H_a increases measurably over the entire range and tends to decrease with x/y_0 (symbol ■ in Fig. 6). This is due to the impinging effect at the entrance of a porous medium by the increase in the flow rate. As a result, the effect approaches the center section. In the latter half, H_a decreases because the stagnant region seem to be generated in a cell. With an increase in porous diameter, H_a increases at the latter half (symbol ▲ in Fig. 6) due to the fact that the inner structure of a porous medium, namely, the roughness effect in a cell, induces turbulence. The volumetric heat transfer coefficient is obtained by H_a , namely,

$$h_v = H_a (\lambda_a / y_0^2). \quad (8)$$

In order to compare with previously reported results, the present local H_a was averaged along the thickness and h_v was obtained. Figure 7 shows the relationship between h_v and Re_d based on the porous diameter as a characteristic length. Present data were presented by symbols ●, ▲, and ■. The dotted region and inclined lines represent the applied regions. In the figure, a large variation in the values of h_v is observed, presumably due to the various structures of porous mediums. The present porous medium is similar to the material which Younis and Viskanta (1993) used.

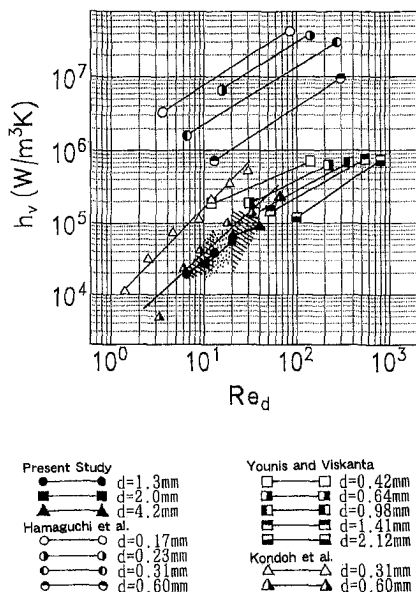


Fig. 7 Volumetric heat transfer coefficient

Therefore, the experimental data exist over a region extrapolated from Younis and Viskanta's data. The Re_d dependency of the volumetric heat transfer coefficient, h_v , in air can be represented as $h_v \sim Re_d^{0.91}$. This behavior accords with the tendency shown by Hamaguchi's (1983) data.

The length of the porous medium used in our present experiment is sufficient to allow for a discussion of the longitudinal behavior in a porous medium. In this connection, Hamaguchi's (1983) test section is 80 mm at most, Younis's (1993) is 15 mm, and Kondoh's (1987) is 10 mm. The volumetric heat transfer coefficient h_v obtained in the present method is not only compared with other data, but also evaluated along the longitudinal direction. However, the effect of a porous diameter does not appear clearly and seems to be depressed because the length, $10y_0$, is too great.

In closing, the basic assumptions underlying the proposed method must be reviewed. In the present analysis, the effect of thermal radiation is not included. This effect appears at temperatures beyond 650 K (Japan Society of Thermophysical Properties, 1990), and a thermal wake may be generated. Therefore, this method should be applied at lower temperatures than 650 K. Additionally, this analysis was performed under the assumption that a porous medium is constituted by small spherical particles. Therefore, models covering structures other than spheres must await future development.

Conclusions

A new method for the evaluation of the heat transfer between solid and fluid in a porous medium was proposed. The major conclusions are as follows.

- 1 This method is derived from the experimental Nusselt numbers on a heated wall of a flow passage and the numerical ones with dimensionless heat transfer parameters, H_a , based on thermal nonequilibrium effect. The volumetric heat transfer coefficient can be obtained by choosing H_a in which the numerical Nusselt number agrees with the experimental values.
- 2 Temperatures of solid and fluid in a porous medium do not need to be measured directly in the experiment.
- 3 Heat transfer on a heated wall of a flow passage includes the structural effect of a porous medium.
- 4 The longitudinal behavior of the volumetric heat transfer coefficient is evaluated for various conditions.

Acknowledgments

The author is grateful to Mr. Takeshi Matsuda of the Yamanashi Prefectural Government, Kofu, for his assistance in the experiment.

References

- ANSI/ASME PTC 19-1, 1985, *Supplement to Performance Test Codes, Instrument and Apparatus, Part 1—Measurement Uncertainty*, ASME, New York.
- Dixon, A. G., and Cresswell, D. L., 1979, "Theoretical Predictions of Effective Heat Transfer Parameters in Packed Beds," *AIChE Journal*, Vol. 25, pp. 663-676.
- Ergun, S., 1952, "Fluid Flow through Packed Columns," *Chem. Eng. Progr.*, Vol. 48, No. 2, pp. 89-94.
- Fukuda, K., Hasegawa, S., and Kondoh, T., 1990, "Study on Heat Transfer Correlation for Porous Media," *Trans. of JSME (Ser. B)*, Vol. 56, No. 529, pp. 2729-2736.
- Golombok, M., Jariwara, H., and Shirvil, L. C., 1990, "Gas-Solid Heat Exchange in a Fibrous Metallic Material Measured by a Heat Generator Technique," *Int. J. Heat Mass Transf.*, Vol. 33, No. 2, pp. 243-252.
- Hamaguchi, K., Takahashi, S., and Miyabe, T., 1983, "Friction Loss and Heat Transfer Performance of Regenerator Matrix (In the Case of Formed Metal)," *Trans. of JSME (Ser. B)*, Vol. 49, No. 445, pp. 1991-1999.
- Handley, D., and Heggs, P. J., 1968, "Momentum and Heat Transfer Mechanism in Regular Shaped Packings," *Trans. Inst. Chem. Engrs.*, Vol. 46, pp. 251-264.
- Japan Society of Thermophysical Properties (ed.), 1990, *Thermophysical Properties Handbook*, 177, Yokendo, Tokyo.
- Kaviany, M., 1991, *Principles of Heat Transfer in Porous Media*, Springer-Verlag, New York, pp. 50-78.
- Kays, W. M., and Crawford, M. E., 1993, *Convective Heat and Mass Transfer*, McGraw-Hill, New York, pp. 136-140.

- Kondoh, T., Fukuda, K., Hasegawa, S., and Nakagawa, K., 1987, "Flow Resistance and Heat Transfer Characteristics of Porous Media," *Bulletin of Interdisciplinary Graduate School of Engineering Science*, Kyushu University, Vol. 9, No. 1, pp. 57-63.
- Kuznetsov, A. V., 1997, "A Perturbation Solution for Heating a Rectangular Sensible Heat Storage Packed Bed with a Constant Temperature at the Walls," *Int. J. Heat Mass Transf.*, Vol. 40, pp. 1001-1006.
- Kuznetsov, A. V., 1998, "Thermal Non-equilibrium Forced Convection in Porous Media," *Transport Phenomena in Porous Media*, D. B. Ingham and I. Pop, eds., Elsevier, Oxford, pp. 103-129.
- Miyauchi, H., Kataoka, H., and Kikuchi, T., 1976, "Gas Film Coefficients of Mass Transfer in Low Peclet Number Region for Sphere Packed Beds," *Chem. Engn. Sci.*, Vol. 31, pp. 9-13.
- Neal, G., and Nader, W., 1974, "Practical Significance of Brinkman's Extension of Darcy's Law (coupled Parallel Flows within a Channel and a Bounding Porous Medium)," *Can. J. Chem. Eng.*, Vol. 52, pp. 475-478.
- Patankar, S. V., 1980, *Numerical Heat Transfer and Fluid Flow*, McGraw-Hill, New York, pp. 79-109.
- Younis, L. B., and Viskanta, R., 1993, "Experimental Determination of the Volumetric Heat Transfer Coefficient Between Stream of Air and Ceramic Foam," *Int. J. Heat Mass Transf.*, Vol. 36, pp. 1425-1434.
- Vafai, K., and Sozen, M., 1990, "Analysis of Energy and Momentum Transport for Fluid Flow through a Porous Bed," *ASME JOURNAL OF HEAT TRANSFER*, Vol. 112, pp. 690-699.
- Vafai, K., and Sozen, M., 1990, "An Investigation of a Latent Heat Storage Porous Bed and Condensing Flow through It," *ASME JOURNAL OF HEAT TRANSFER*, Vol. 112, pp. 1014-1022.
- Vafai, K., and Tien, C. L., 1981, "Boundary and Inertia Effects on Flow and Heat Transfer in Porous Media," *Int. J. Heat Mass Transf.*, Vol. 24, pp. 195-203.
-

Energy Dissipation in Sheared Granular Flows

A. Karion

e-mail: karion@caltech.edu

M. L. Hunt

e-mail: hunt@caltech.edu

Division of Engineering and Applied Sciences,
California Institute of Technology,
Pasadena, CA 91125

Using a two-dimensional discrete element computer simulation of a bounded, gravity-free Couette flow of particles, the heat dissipation rate per unit area is calculated as a function of position in the flow as well as overall solid fraction. The computation results compare favorably with the kinetic theory analysis for rough disks. The heat dissipation rate is also measured for binary mixtures of particles for different small to large solid fraction ratios, and for diameter ratios of ten, five, and two. The dissipation rates increase significantly with overall solid fraction as well as local strain rates and granular temperatures. The thermal energy equation is solved for a Couette flow with one adiabatic wall and one at constant temperature. Solutions use the simulation measurements of the heat dissipation rate, solid fraction, and granular temperature to show that the thermodynamic temperature increases with solid fraction and decreases with particle conductivity. In mixtures, both the dissipation rate and the thermodynamic temperature increase with size ratio and with decreasing ratio of small to large particles.

1 Introduction

Granular material flows describe flows of solid particles in which the interstitial fluid plays a negligible role in the flow mechanics. Examples include the transport of coal, food products, detergents, pharmaceutical tablets, and toner particles in high-speed printers. Much of the recent analytical work on dry granular flows uses dense-gas kinetic theory, assuming that the motion of individual grains in a rapid flow with no viscous drag forces from the interstitial fluid can be modeled as the motion of molecules in a gas with instantaneous, binary collisions. In addition, discrete element simulations have been used to study the behavior of such flows, while neglecting any effects from the interstitial fluid. This current work uses discrete element simulations to investigate the energy dissipation and the resulting thermodynamic temperature rise in Couette flows of granular materials between two infinite parallel plates in the absence of gravity.

Various industrial processes shear granular material in some way. Often, mixers shear particles of different sizes or properties to achieve a uniform product. One such example motivating this research is the mixing of toner and larger carrier particles in an electrophotographic device, such as a high-speed laser printer. The two different kinds of particles are sheared by a screw mixer to electrostatically charge the toner and to mix it with the carrier particles. Frictional heating during this process may cause unwanted melting of the toner in such a device. This study investigates heat generation in a planar Couette flow because it is the simplest kind of shear flow in which there are solid boundaries driving the flow. Previous computer simulation studies of Couette flow include those of Campbell (1993) and Savage and Dai (1993); experimental work on two-dimensional Couette flows between concentric cylinders includes that of Elliot et al. (1998) and Veje et al. (1999).

Energy dissipation in a flow of granular material occurs due to inelastic collisions between particles and between particles and boundaries. A second source of energy loss is the frictional interaction during a collision. The two-dimensional kinetic theory analysis of Jenkins and Richman (1985) provides an analytical representation for the dissipation in a flow of frictional inelastic disks of the same size. Calculations of dissipation in binary mix-

tures currently only exist for smooth particles (Farrell et al., 1986; Jenkins and Mancini, 1987; Jenkins and Mancini, 1989); the dissipation term is only due to inelastic collisions, not friction. Energy dissipation due to friction at the moving boundaries can be very significant in a Couette flow. The dissipation at a flat, frictional boundary calculated by Jenkins (1992) does not account for the dissipation of rotational fluctuation kinetic energy, and numerous boundary dissipation results for boundaries roughened by the attachment of smooth disks (Jenkins and Richman, 1986; Richman and Chou, 1988) do not incorporate friction. For the above reasons, computer simulations can be used to measure frictional dissipation and determine its contribution to the overall thermodynamic temperature rise in a flow.

Computer simulations have been shown to be a powerful tool in the investigation of granular shear flows (Campbell, 1993; Walton, 1984; Savage and Dai, 1993). Soft-particle models (Walton, 1984; Wassgren, 1997) have proven to be effective in modeling dense flows with enduring frictional contacts, such as those presented here. This research utilizes a soft-particle simulation to model both frictional and viscous dissipation in dense, bounded, Couette flows between two infinite plates moving in opposite directions.

2 Computer Simulations

The computer simulation used is a two-dimensional soft particle discrete element simulation (Wassgren, 1997) based on the contact model of Cundall and Strack (1979). The forces on each particle are calculated directly and Newton's second law is integrated to find the acceleration, velocity, and position of each particle at each time step. Only normal and tangential contact forces act on each particle, as these simulations do not include gravity. When two particles (or a particle and a solid boundary) come into contact, they are allowed to overlap slightly. The time step of the simulation is chosen so that this overlap does not exceed one percent of a particle diameter. The normal contacts are modeled by a linear spring and dashpot so that

$$F_n = -k_n \Delta + \nu_n \delta \dot{x}_n, \quad (1)$$

where F_n represents the normal force on the contact, and k_n and ν_n are the normal spring constant and damping coefficient respectively; Δ is the overlap between the two contacting surfaces. The damping coefficient is calculated based on a chosen coefficient of restitution and multiplies the relative normal velocity of the two contacting surfaces, $\delta \dot{x}_n$. Tangential contacts are modeled by a linear spring and frictional slider. The tangential force is first calculated from the spring-displacement law,

Contributed by the Heat Transfer Division for publication in the JOURNAL OF HEAT TRANSFER and presented at 1998 IMECE, Anaheim. Manuscript received by the Heat Transfer Division, Aug. 27, 1998; revision received, Apr. 8, 1999. Keywords: Heat Transfer, Multiphase, Particulate, Shear Flows. Associate Technical Editor: D. Kaminski.

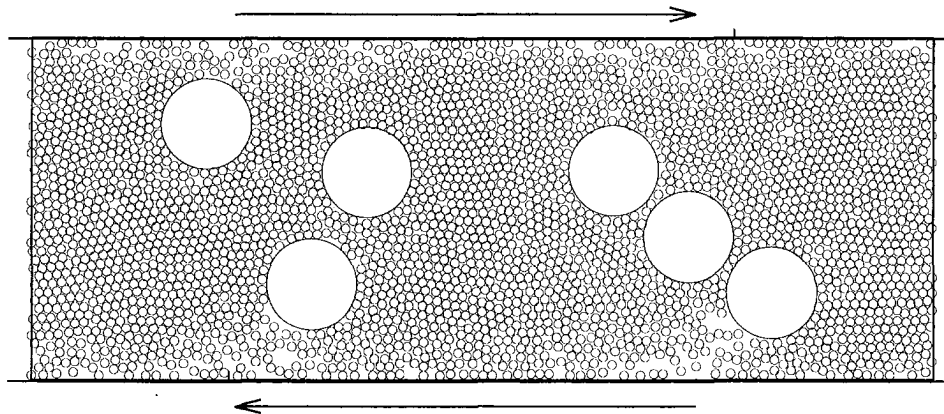


Fig. 1 A snapshot of a simulation with $d_{\text{large}}/d_{\text{small}} = 10$ and $\nu_{\text{small}}/\nu_{\text{large}} = 5$. The upper boundary is traveling to the right and the lower boundary to the left. The right and left boundaries are periodic.

$$F_{s,\text{spring}} = -k_s \delta s, \quad (2)$$

where k_s is the tangential spring constant (in this case equal to k_n), and δs is the tangential displacement between the initial contact points. Then the friction force is calculated using a friction coefficient μ :

$$F_{s,\text{friction}} = \mu F_n. \quad (3)$$

The force used in the simulation is the lesser of these two forces. If the friction force is lower, then it is assumed that the surfaces are slipping against each other. If the spring force is lower, then it is assumed that the two surfaces are "sticking" and there is no energy dissipation. This calculation occurs at each time step of the contact, and each contact usually lasts 40 to 50 time steps. Thus, during a single collision, both sticking and slipping may occur at the contact point.

Using this contact model, the amount of energy dissipated in each collision is calculated directly. The energy dissipated in the inelasticity of the contact is equal to that dissipated in the dashpot of the normal contact model.

$$\Delta E_i = \nu_n (\delta \dot{x}_n)^2 \delta t, \quad (4)$$

where ΔE_i is the energy dissipated in the dashpot in one time step, and δt is the time step. The energy dissipated in the tangential portion of the contact is equal to the tangential force multiplied by the distance the contact slips:

$$\Delta E_f = F_s \delta s. \quad (5)$$

This quantity is only valid when the contact is slipping, so that $F_s = F_{s,\text{friction}}$.

The flows simulated in the current research are Couette flows of particles in the absence of gravity. The upper and lower boundaries are frictional walls moving in opposite directions with velocities $\pm U/2$. Their faces are flat, but they have a constant coefficient of friction μ . The right and left boundaries are periodic: When a particle exits from the right, it enters on the left with the same vertical position and velocity. The distance between the walls, h , is 20 particle diameters in the simulations with same-size particles and 40 small particle diameters in the simulations of mixtures. The width of the same-size particle flows is 50 particle diameters. Flows of mixtures with a diameter ratio of two and five have a width of 75 small particle diameters, and flows of mixtures with a diameter ratio of ten have a width of 100 small particle diameters. The strain rate, U/h , is 250 1/s for all flows. The friction coefficient for interparticle and particle-wall collisions, μ , is 0.5. This value of the friction coefficient was chosen so that it was a reasonable value physically while still being high enough to show a large amount of frictional dissipation. Another reason for a relatively high friction coefficient is that because the walls are flat, the friction between walls and particles is the only force driving the flow; a friction coefficient of 0.5 is high enough to achieve a steady Couette flow with significant shearing at the wall. The coefficient of restitution for all collisions, e , is 0.8. This value of the coefficient of restitution in the normal direction is chosen based on a typical value used by previous researchers (Campbell, 1993; Savage and Dai, 1993) and reasonable for a number of materials.

Nomenclature

c_p = particle specific heat	k_p = particle thermal conductivity	W = rate of work done by boundaries
d = particle diameter	k_{tot} = total effective thermal conductivity	β = particle roughness coefficient
e = coefficient of restitution between particles and between particles and walls	m = particle mass	γ = energy dissipation rate per unit area
ΔE = loss of energy during a collision	Pe = Peclet number	Γ_w = energy dissipation rate at wall
h = height of computational domain	q_h = heat flux	Θ = nondimensional thermodynamic temperature
I = particle moment of inertia	T_r = rotational granular temperature component	μ = coefficient of friction between particles and between particles and walls
k_n = spring constant used in normal contact model of simulations	T_t = translational granular temperature component	ν = solid fraction
k_s = spring constant used in tangential contact model of simulations	\mathcal{T} = thermodynamic temperature	ν_n = damping coefficient used in normal contact model of simulations
k_g = thermal conductivity of gas phase	U = relative velocity of the two boundaries	ρ_p = particle density
k_{kr} = streaming, or kinetic thermal conductivity	u = particle velocity component in flow direction	ω = particle rotational velocity
k_{mc} = molecular effective thermal conductivity	v = particle velocity component perpendicular to flow direction	

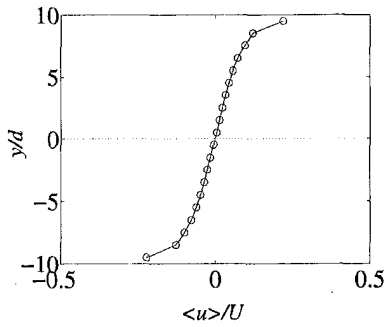


Fig. 2(a) Velocity

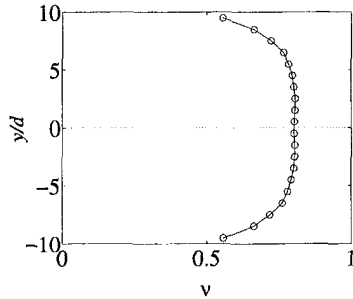


Fig. 2(b) Solid fraction

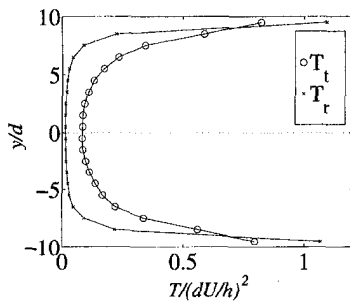


Fig. 2(c) Granular temperature

Fig. 2 Velocity, solid fraction, and granular temperature profiles for Couette flow of same-size particles with overall $\nu = 0.75$

The solid fraction, ν , is defined as the ratio of particle area to the total area. The same-size particle simulations exhibit overall solid fractions ranging from 0.45 to 0.8, and the binary mixture simulations were all conducted for an overall solid fraction of 0.75. The solid fraction ratio in the mixtures, $\nu_{\text{small}}/\nu_{\text{large}}$, ranges from 0.4 to 5. Mixture simulations were conducted for diameter ratios $d_{\text{large}}/d_{\text{small}}$ of two, five, and ten. The number of particles used in the simulations ranges from 580 to 3006. Figure 1 is a snapshot of a simulation of 3006 particles, with a size ratio of ten and a solid fraction ratio of five.

The simulations are two-dimensional so that fewer particles are necessary than in a three-dimensional simulation, decreasing computational time. The particles are not cylindrical rods or disks with a mass proportional to their area, however. Instead, each particle has the mass and moment of inertia of a sphere, and can be thought of as a sphere constricted to move in only two dimensions. Simulations were run until the kinetic energy in the system became approximately constant. After this steady-state was reached, measurements were made over many time steps and were averaged in time and over the length of the domain to gather data about the simulation.

3 Results

Local measurements of flow properties are made by dividing the domain into bins roughly one small particle diameter high. The

velocity, area, and fluctuating velocity of each the particles in each bin are averaged in space and time to determine the properties. Quantities are averaged over periods ranging between 4×10^6 and 1.5×10^7 time steps for different simulations. The number of samples in each average is at least 60. Figure 2 shows typical velocity, solid fraction, and granular temperature profiles for a same-size particle flow. The rotational and translational granular temperatures are defined as follows:

$$T_t \equiv \frac{1}{2} \langle u' u' + v' v' \rangle \quad (6)$$

$$T_r \equiv \frac{1}{2} \left(\frac{I}{m} \right) \langle \omega' \omega' \rangle, \quad (7)$$

where u denotes the velocity component of a particle in the direction parallel to the walls, v is the velocity component in the direction perpendicular to the walls, and ω is the angular velocity. The fluctuating velocities, u' , v' , and ω' are defined as the difference between the particle velocity and the average local velocity. The moment of inertia and mass of each particle are denoted as I and m , respectively. The brackets, $\langle \rangle$, denote an area average for the particular bin. Figure 3 shows velocity, solid fraction, and granular temperature profiles for a binary mixture with a diameter ratio of 10. The solid fraction profiles for the large and small particles are shown separately along with the overall solid fraction. These profiles illustrate the high shear zones nearest

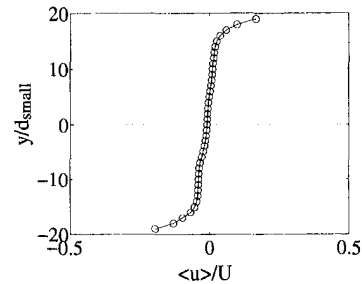


Fig. 3(a) Velocity

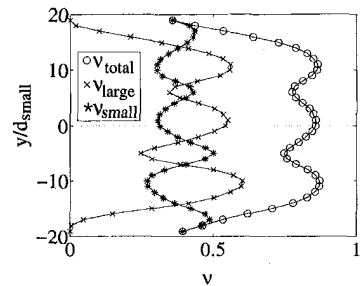


Fig. 3(b) Solid fraction

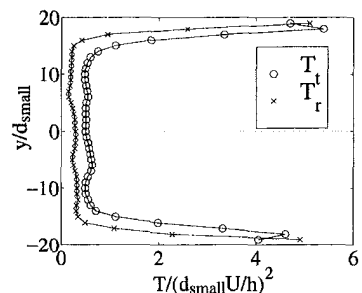


Fig. 3(c) Granular temperature

Fig. 3 Velocity, solid fraction, and granular temperature profiles for Couette flow of a mixture with overall $\nu = 0.75$, $d_{\text{large}}/d_{\text{small}} = 10$, and $\nu_{\text{small}}/\nu_{\text{large}} = 1$

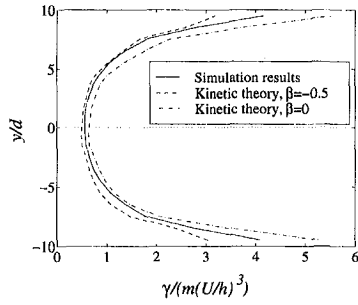


Fig. 4 Energy dissipation rate as a function of vertical position for Couette flow of same-size particles with overall $\nu = 0.75$

the walls, which correspond to low solid fractions and high granular temperatures.

3.1 Dissipation in Same-Size Flows. Analytical expressions for the dissipation term in the energy equation for granular materials have been derived using kinetic theory for many cases, including flows of smooth and rough identical particles (Lun et al., 1984; Jenkins and Richman, 1985; Lun and Savage, 1987; Lun, 1991). The analysis by Jenkins and Richman (1985) most closely resembles the flows in the current simulations, modeling frictional two-dimensional inelastic particles.

Jenkins and Richman (1985) derive dissipation terms from kinetic theory for the loss of both translational and rotational energy (referred to as $-\chi_{\alpha\alpha}$ and $-\chi_{33}$ in their work, but referred to here as γ_t and γ_r) due to interparticle collisions. These terms contain an unknown coefficient of roughness, β , which ranges from 1 to -1 , characterizing disks ranging from perfectly rough (conserving all energy due to tangential rebound) to perfectly smooth. The simplification of the general relations for slightly rough and nearly elastic particles ($\beta \approx -1$, $e \approx 1$) is as follows:

$$\gamma_t = 2 \frac{\alpha T_t}{d^2} \left(\frac{\kappa(1+\beta)}{(1+\kappa)} + 2(1-e) \right) \quad (8)$$

$$\gamma_r = -\frac{\alpha T_t (1+\beta)}{d^2 (1+\kappa)} \left(\frac{\kappa(1+\beta)}{(1+\kappa)} - 4 \frac{T_r}{T_t} \right) \quad (9)$$

where

$$\alpha = \frac{8 m \nu^2}{\pi d} g_0 \left(\frac{T_t}{\pi} \right)^{1/2}$$

$$\kappa = \frac{4I}{m d^2}$$

The translational and rotational granular temperatures are defined in Eqs. (6) and (7). The factor of 4 in the last term of the rotational dissipation is due to a difference in the definition of T_r ; in the original work it is a factor of 2. The radial distribution function for disks in contact is used, so that

$$g_0(\nu) = \frac{16 - 7\nu}{16(1 - \nu^2)}, \quad (10)$$

as suggested by Jenkins and Richman (1985).

If Eqs. (8) and (9) are simplified for smooth disks (the case of $\beta = -1$), the expression for γ_r becomes zero, since perfectly smooth disks will have no rotational (frictional) dissipation; there will only be dissipation due to the inelasticity of collisions. Substituting $\beta = -1$ into the expression for γ_t , a simpler expression for the overall dissipation $\gamma = \gamma_t + \gamma_r$ of smooth disks is

$$\gamma = \frac{32 m \nu^2}{d^3} g_0 (1-e) \left(\frac{T_t}{\pi} \right)^{3/2} \quad (11)$$

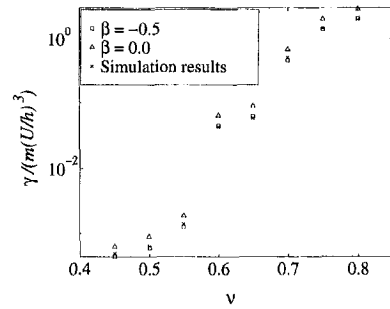


Fig. 5 Energy dissipation rate as a function of overall solid fraction for Couette flow of same-size particles

This expression can be simply derived from the product of the number density, the collision rate, and the energy lost in each collision.

Returning to the more complex expressions of Eqs. (8) and (9) for the more general case of β not equal to -1 , the sum of the two dissipation terms, γ_t and γ_r , can be calculated. This sum is equal to the total dissipation rate due to particle-particle collisions. The theoretical dissipation terms are evaluated at $\beta = 0$ and -0.5 for comparison with simulation results.

Figure 4 presents simulation results for dissipation rate per unit area, γ , as a function of position in the flow for one example of a monodisperse flow. The dissipation rate per unit area is calculated as an average within each bin, whose height is approximately one particle diameter. The curves shown for the kinetic theory are for $\gamma = \gamma_t + \gamma_r$, as defined in Eqs. (8) and (9). These expressions from Jenkins and Richman (1985) are functions of local solid fraction and granular temperature; the solid fractions and temperatures used in the calculation are those measured by the simulation. The dissipation rate is high near the walls, where the granular temperature and strain rate are high as well. Figure 5 shows the mean dissipation rate per unit area for all the same-size particle flows as a function of overall solid fraction. The dissipation rate rises sharply with solid fraction due to higher particle collision rates.

In addition to the energy dissipation rate inside the flow, the energy dissipation rate at the walls due to particle-wall collisions was calculated in the simulations. The rate of dissipation at the walls, Γ_w , is compared to the rate of work done by the walls, W , to determine the amount of work done on the flow inside the boundaries. The fraction of the work that is dissipated at the boundaries, Γ_w/W , is shown in Fig. 6, and indicates that the ratio decreases with overall solid fraction. Figure 7 presents the rate of work done by the boundaries as a function of solid fraction for same-size flows.

Although the interstitial gas (air, in this instance), can generally be neglected in the analysis of the dynamics of the flow, it cannot be neglected in the heat transfer. In order to translate the dissipation rates computed in the simulations into actual thermodynamic

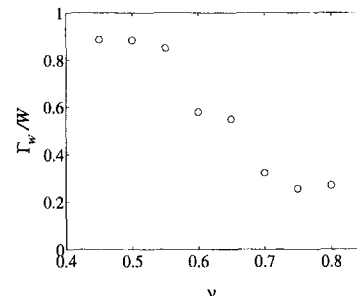


Fig. 6 Ratio of energy dissipation rate at wall to rate of work done by walls as a function of solid fraction for same-size particle flows

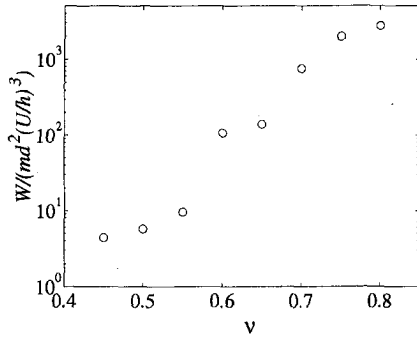


Fig. 7 Rate of work done by moving boundaries as a function of solid fraction for same-size particle flows

temperature changes, a heat transfer analysis is performed on both phases of the system. An energy equation can be solved using the total energy dissipation calculated in the simulations as a heat source to obtain thermodynamic temperature profiles in same-size flows. The general energy equation with a heat source term is expressed as

$$\rho c_p \frac{DT}{Dt} = \nabla \cdot (k_{tot} \nabla T) + \gamma \quad (12)$$

where T is the thermodynamic temperature. The relation $\nu \rho_p c_p + (1 - \nu) \rho_{air} c_{air} \approx \rho c_p$ was used in the above equation, where ρ_p and c_p are the density and heat capacity of the particles, and ρ_{air} and c_{air} are the corresponding values for air. Because this equation is three-dimensional, γ represents the total energy dissipation rate per unit volume (due to both friction and inelasticity of collisions), both within the flow and at the walls. The two-dimensional dissipation rate calculated in the simulation was converted to three dimensions by considering the flow as a monolayer of particles constrained to motion within the plane. The depth of this monolayer is one particle diameter, and so the dissipation per unit volume was calculated based on this depth.

The total conductivity, k_{tot} , is defined as in Natarajan and Hunt (1998), as the sum of the molecular conductivity, k_{mc} and the streaming conductivity, k_{st} . The effective molecular conductivity used in the analysis is that proposed by Gelperin and Einstein (1971):

$$\frac{k_{mc}}{k_g} = 1 + \frac{\nu \left(1 - \frac{k_g}{k_p}\right)}{\frac{k_g}{k_p} + 0.28(1 - \nu)^{0.63} (k_g/k_p)^{-0.18}} \quad (13)$$

In the above expression, k_g and k_p are the conductivities of the gas and solid phases respectively; k_{mc} is the effective molecular conductivity for both phases together. The expression for a streaming conductivity, k_{st} , was derived using gas kinetic theory by Hsiao and Hunt (1993) in three dimensions, and later extended to two dimensions by Hunt (1997) using similar methods:

$$k_{st} = \frac{\pi^{3/2} \rho_p c_p d T_t^{1/2}}{32 g_0(\nu)} \quad (14)$$

This expression assumes perfectly smooth particles, and thus only uses the translational granular temperature term. This streaming conductivity is the conductivity due to energy transfer by particle motion from hotter to colder regions. The kinetic theory-derived expression for k_{st} above also assumes a small particle Biot number for a lumped mass analysis and a small ratio of the time between collisions to the thermal time constant of the particles; it applies to flows of same-size particles only.

A similar conductivity exists to account for the local variations in the fluid velocity, which enhance the energy transport when a

temperature gradient exists. In a packed bed of stationary particles, this enhanced thermal transport is modeled using a dispersion conductivity, which is approximated as $k_d = C \rho_f c_f u_f d$, where C is a constant, ρ_f and c_f are the density and thermal heat capacity of the interstitial fluid, u_f is the average velocity, and d is a particle diameter (Hunt, 1990). Considering this scaling for the dispersion conductivity of a fluid in a packed bed, this contribution to the overall conductivity of the granular system has been neglected in the current analysis, because the density and thermal heat capacity of air are small when compared with those of the solid particles.

Wang et al. (1989) have shown that particle rotation does not affect heat transfer at low particle rotational Peclet numbers, where $Pe = \omega(d/2)^2 / (k_p / \rho_p c_p)$. The flow conditions in the current work have $Pe < 1$, justifying the assumption that rotation does not affect the conductivity of the system significantly.

For two-dimensional steady-state flow with periodic boundaries (i.e., no gradients in the x -direction) and no mean velocity in the vertical (y)-direction, the nondimensional energy equation reduces to

$$\frac{d}{dy} \left(k_{tot}(y) \frac{d\Theta}{dy} \right) = -\gamma(y) \quad (15)$$

The nondimensional thermodynamic temperature is defined as $\Theta = (T - T_0) / (U^2 / c_p)$, where T_0 is the temperature at $y = h$. The total conductivity can be determined from the expressions above using the solid fraction and granular temperature profiles obtained from the simulations. Likewise, the nondimensionalized dissipation term γ is also known from the simulations, and the above equation can be solved by integrating directly for the thermodynamic temperature profile. The dissipation rate, solid fraction, and granular temperature calculated in the simulations are averaged over the width of each bin, that is they are only known at discrete points. The bins are chosen to be one particle diameter wide in order to provide a sensible average for a continuum analysis. The two boundary conditions consist of an adiabatic wall condition at $y = 0$ and a fixed temperature T_0 at the upper wall $y = h$:

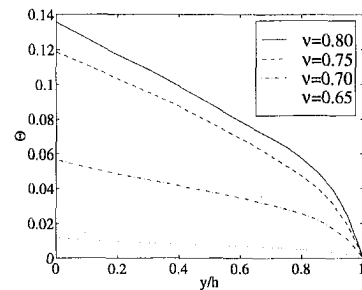


Fig. 8(a) Temperature

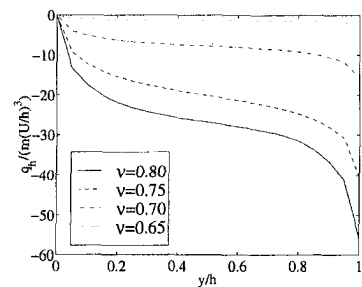


Fig. 8(b) Heat flux

Fig. 8 Nondimensional thermodynamic temperature (θ) and heat flux (q_h) profiles for same-size flows of various overall solid fractions. The conductivity ratio is $k_p/k_g = 23$.

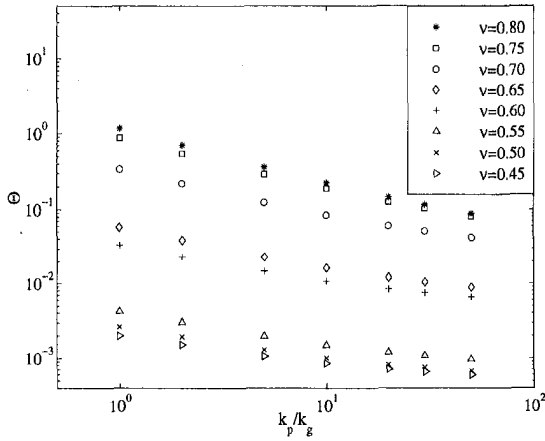


Fig. 9 Nondimensional adiabatic wall temperature as a function of the conductivity ratio, k_p/k_g , for same-size flows of varying overall solid fractions

$$q_h|_{y=0} = k_{tot} \left. \frac{d\Theta}{dy} \right|_{y=0} = 0 \quad (16)$$

$$\Theta|_{y=h} = 0. \quad (17)$$

The solution in this case is

$$\Theta(y) = \int_0^h \frac{1}{k(y)} \left(\int_0^y \gamma(y') dy' \right) dy - \int_0^y \frac{1}{k(y')} \left(\int_0^{y'} \gamma(y'') dy'' \right) dy'. \quad (18)$$

Figure 8 shows the dimensionless thermodynamic temperature as a function of the vertical distance in the flow for various solid fractions at a constant conductivity ratio, $k_p/k_g = 23$, which is approximately that found in the flow of toner in a high-speed laser printer. The temperature increases with solid fraction due to the higher dissipation rate of denser flows. The heat flux is also plotted in this figure, showing that it is equal to zero at the adiabatic wall.

The slope of the temperature profile does not approach zero near the adiabatic wall due to the finite size of the bins over which the integration and properties are calculated (bins are approximately one particle diameter in width). The finite value of the heat flux one bin away from the wall results in a finite value of the derivative of the temperature near the wall as well. Decreasing the size of the bins will not alleviate this issue because of the heat generated at the wall itself, which causes a nonzero value of the heat flux at any finite distance from the wall. The relatively large bin size does not affect results away from the two walls, where there are smaller gradients in heat flux and the curves are smooth.

Figure 9 presents the maximum temperature, which occurs at the adiabatic wall ($y = 0$), as a function of the conductivity ratio of particles to gas. The gas conductivity is constant while the conductivity ratio varies. The molecular conductivity term dominates in all the cases, so increasing the conductivity ratio increases the total conductivity. Higher conductivities decrease the maximum temperature obtained in the flow as the heat generated is conducted through the flow at a higher rate.

3.2 Dissipation in Binary Mixture Flows. Energy dissipation calculations were also conducted for the flows of binary mixtures. Although kinetic theory derivations for binary flows do exist (Farrell et al., 1986; Jenkins and Mancini, 1987; Jenkins and Mancini, 1989), all assume perfectly smooth particles and have not been applied to this flow.

Figure 10 presents results similar to those for same-size particle

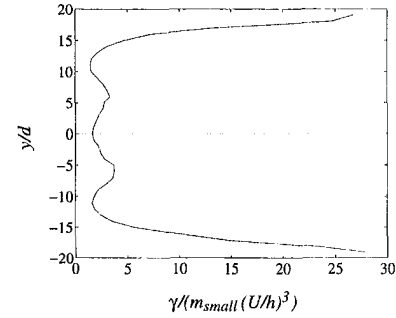


Fig. 10 Energy dissipation rate as a function of position for a Couette flow of a particle mixture. Overall $\nu = 0.75$, $d_{large}/d_{small} = 10$, and $\nu_{small}/\nu_{large} = 1$.

flows for the dissipation rate as a function of vertical position in mixtures; dissipation increases in the high granular temperature and high strain rate regions near the walls. The dissipation rate as a function of solid fraction ratio, ν_{small}/ν_{large} , is presented in Fig. 11 for various diameter ratios. This figure exhibits a trend of lower dissipation rates with higher solid fraction ratios. Thus, for a constant overall solid fraction, when there are more large particles in the flow, the dissipation is greater than when there are relatively few. The trend becomes more apparent at the larger diameter ratios. Collisions of large particles with small particles or with each other dissipate more energy than collisions between two small particles. This phenomenon is explained by the proportionality of the kinetic energy decrease to the mass of the colliding bodies if the coefficient of restitution is held constant. The mass ratio of large to small particles is proportional to the cube of the diameter ratio, and so the flows with larger diameter ratios show more dissipation. At the highest solid fraction ratio, for all three size ratios, the dissipation rate approaches the limit of that for the same-size flow with the same overall solid fraction, which is plotted as a dotted line. Figure 12 indicates that the fraction of work dissipated in a mixture at the boundaries increases slightly with solid fraction ratio. The dotted line shows the value of this ratio for same-size flows with the same overall solid fraction. Only flows with many large particles exhibit a ratio lower than that for the mono-sized system. The rate of work done is shown in Figure 13 as a function of solid fraction ratio for binary mixtures.

The energy equation used for same-size particle flows can also

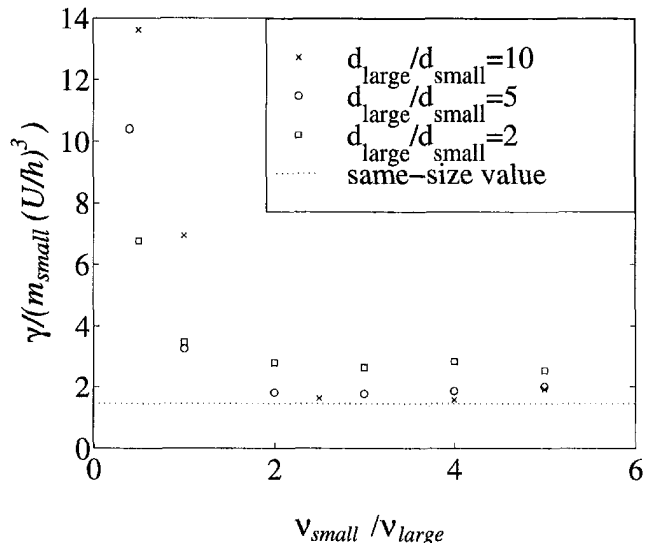


Fig. 11 Energy dissipation rate as a function of solid fraction ratio for Couette flow of mixtures. Overall $\nu = 0.75$.

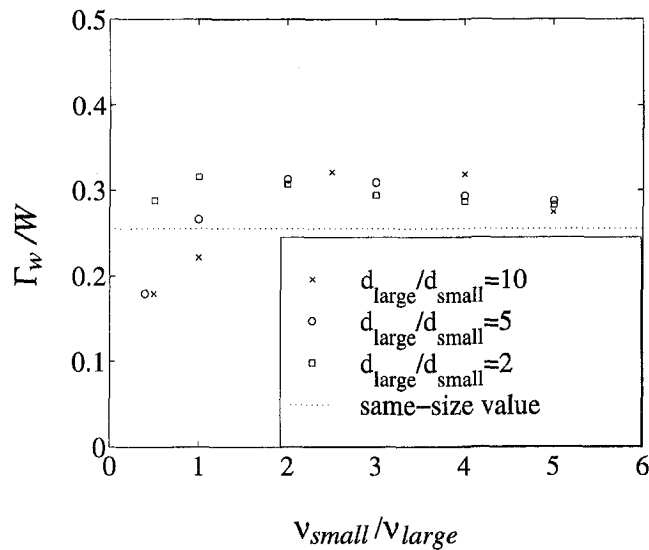


Fig. 12 Ratio of energy dissipation rate at wall to rate of work done by walls as a function of solid fraction ratio for mixture flows with overall $\nu = 0.75$

be applied here for binary mixtures in the same form (Eq. (15)). However, the kinetic theory-derived expression for the kinetic, or streaming, conductivity, k_{st} , does not apply for mixture flows. In the same-size flow calculations, however, this streaming term only accounts for at most three percent of the total conductivity used in the calculation; the molecular conductivity, k_{mc} , is far larger at all solid fractions. Therefore, the analysis is followed in the same manner as in the same-size flows, with the exception of neglecting the contribution of the streaming conductivity, k_{st} so that $k_{tot} = k_{mc}$. The resulting adiabatic wall temperature, $\Theta = (T - T_0)/(U^2/c_p)$ is shown in Fig. 14 as a function of solid fraction ratio for various size ratios. The temperature follows the same trend as the dissipation rate in these flows; flows with many large particles dissipate more energy, resulting in a higher thermodynamic temperature.

4 Conclusion

Simulations of a Couette flow of particles between two parallel plates indicates regions of high granular temperature, high velocity gradient, and low solid fraction near the moving boundaries. Higher dissipation rates are observed in these regions of the flow, due to the higher agitation and collision frequency. The location of the highest dissipation rate (and thus, the most heat generation) is of interest to industry because it may affect the method used to attempt to cool this type of flow. Energy dissipation rates also

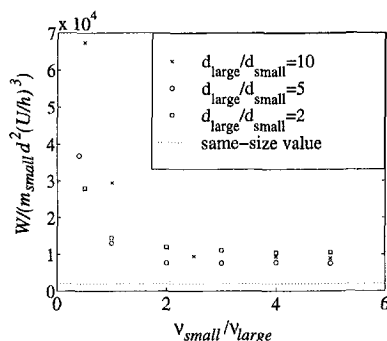


Fig. 13 Rate of work done by moving boundaries as a function of solid fraction ratio for mixture flows with overall $\nu = 0.75$

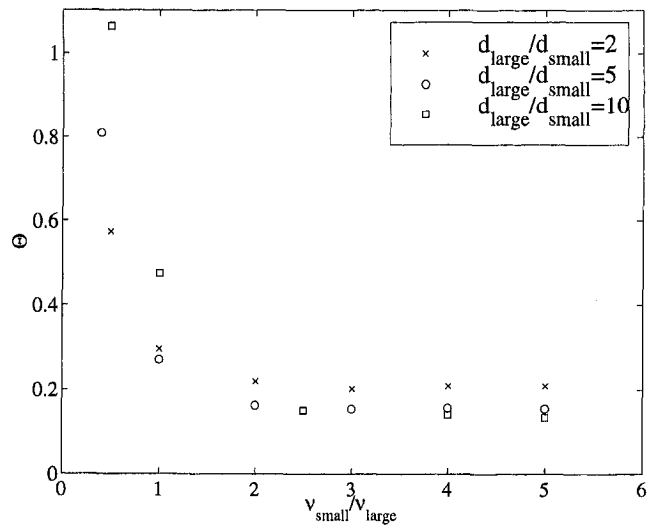


Fig. 14 Nondimensional adiabatic wall temperature as a function of solid fraction ratio for various diameter ratios in mixture flows

increase drastically with overall solid fraction, again due to the larger collision frequency in a dense system.

In binary mixtures, flows with a low solid fraction ratio of small to large particles exhibit higher dissipation rates, due to the larger number of collisions involving large particles in those flows. The energy dissipated, or the kinetic energy change, in a collision is proportional to the mass of the bodies colliding when the coefficient of restitution is held constant. Thus, the low-solid-fraction-ratio flows exhibit more collisions between large particles and between large and small particles than flows with a high solid fraction ratio. The value of dissipation at a solid fraction ratio of two approaches the value for same-size flows.

The dissipation rate at the moving boundaries was also investigated as a fraction of the work done on the flow. For flows of same-size particles, the fraction of work dissipated at the walls is highest for flows with low solid fractions and decreases as the solid fraction increases. For very low solid fraction flows, up to 90 percent of the work done by the walls is dissipated in collisions of particles with the walls themselves, not inside the flow. A similar investigation for flows of mixtures shows that the fraction of work dissipated at the wall is not affected significantly by the solid fraction ratio of the mixture. For most flows the fraction is slightly higher than that of the corresponding same-size flow, but it is lower for flows with diameter ratios of five and ten and solid fraction ratios of 0.5 and 1.

An energy analysis in which the thermal energy equation is solved for the case of one adiabatic wall and one constant temperature wall indicates that higher solid fractions (and thus dissipation rates) lead to higher overall temperatures in the flow. In mixtures, flows with more large particles have higher temperatures due to their greater heat dissipation rate. Increasing the particle to gas conductivity ratio decreases the thermodynamic temperature of the flow.

Simulation results for energy dissipation due to particle-particle collisions within the flow compare well with kinetic theory results for rough identical disks. It is important to note, however, that this result was obtained by using granular temperature and solid fraction profiles from the simulation, not derived by solving the equations of motion using kinetic theory-derived constitutive relations. Existing kinetic theory results for granular flows do not as yet model the frictional dissipation at the wall accurately. Current simulations show that the friction can account for up to 90 percent of the dissipation at the wall. Jenkins' (1992) boundary conditions for a flat frictional wall do not account for rotational fluctuation energy dissipation at the wall. Relations for binary mixtures only exist for smooth particles, as well, which do not account for the

dissipation of rotational fluctuation energy. A purely kinetic theory-based analysis of the current problem would necessarily ignore frictional dissipation and the resulting temperature rise calculated would be low.

Acknowledgments

Partial support for this work is provided by the Hitachi Research Laboratory, Hitachi, Ltd., and by the National Science Foundation under grant CTS-9530357.

References

- Campbell, C. S., 1993, "Boundary Interactions for Two-Dimensional Granular Flows. Part I. Flat Boundaries, Asymmetric Stresses and Couple Stresses," *J. Fluid Mech.*, Vol. 247, pp. 111–136.
- Cundall, P. A., and Strack, O. D. L., 1979, "A Discrete Numerical Model for Granular Assemblies," *Géotechnique*, Vol. 29, pp. 47–65.
- Elliot, K. E., Ahmadi, G., and Kvasnak, W., 1998, "Couette Flows of a Granular Monolayer—An Experimental Study," *J. Non-Newtonian Fluid Mech.*, Vol. 74, pp. 89–111.
- Farrell, M., Lun, C. K. K., and Savage, S. B., 1986, "A Simple Kinetic Theory for Granular Flow of Binary Mixtures of Smooth, Inelastic, Spherical Particles," *Acta Mech.*, Vol. 63, pp. 45–60.
- Gelperin, N. I., and Einstein, V. G., 1971, "Heat Transfer in Fluidized Beds," *Fluidization*, J. F. Davidson and D. Harrison, ed., Academic Press, London and New York, pp. 471–568.
- Hsiau, S. S., and Hunt, M. L., 1993, "Kinetic Theory Analysis of Flow-Induced Particle Diffusion and Thermal Conduction in Granular Material Flows," *ASME JOURNAL OF HEAT TRANSFER*, Vol. 115, pp. 541–548.
- Hunt, M. L., 1990, "Comparison of Convective Heat Transfer in Packed Beds and Granular Flows," *Annual Review of Heat Transfer*, Vol. 3, C. L. Tien, ed., pp. 163–193.
- Hunt, M. L., 1997, "Discrete Element Simulations for Granular Material Flows: Effective Thermal Conductivity and Self-Diffusivity," *Int. J. Heat Mass Transfer*, Vol. 40, pp. 3059–3068.
- Jenkins, J. T., and Richman, R., 1985, "Kinetic Theory for Plane Flows of a Dense Gas of Identical, Rough, Inelastic, Circular Disks," *Phys. Fluids*, Vol. 28, pp. 3485–3494.
- Jenkins, J. T., and Richman, R., 1986, "Boundary Conditions for Plane Flows of Smooth, Nearly Elastic, Circular Disks," *J. Fluid Mech.*, Vol. 171, pp. 53–69.
- Jenkins, J. T., and Mancini, F., 1987, "Balance Laws and Constitutive Relations for Plane Flows of a Dense, Binary Mixture of Smooth, Nearly Elastic, Circular Disks," *ASME JOURNAL OF APPLIED MECHANICS*, Vol. 54, pp. 27–34.
- Jenkins, J. T., and Mancini, F., 1989, "Kinetic Theory for Binary Mixtures of Smooth, Nearly Elastic Spheres," *Phys. Fluids*, Vol. 12, pp. 2050–2057.
- Jenkins, J. T., 1992, "Boundary Conditions for Rapid Granular Flow: Flat, Frictional Walls," *ASME JOURNAL OF APPLIED MECHANICS*, Vol. 59, pp. 120–127.
- Lun, C. K. K., Savage, S. B., Jeffrey, D. J., Chepurmy, N., 1984, "Kinetic Theories for Granular Flow: Inelastic Particles in Couette Flow and Slightly Inelastic Particles in a General Flowfield," *J. Fluid Mech.*, Vol. 140, pp. 223–256.
- Lun, C. K. K., and Savage, S. B., 1987, "A Simple Kinetic Theory for Granular Flow of Rough, Inelastic, Spherical Particles," *ASME JOURNAL OF APPLIED MECHANICS*, Vol. 54, pp. 47–53.
- Lun, C. K. K., 1991, "Kinetic Theory for Granular Flow of Dense, Slightly Inelastic, Slightly Rough Spheres," *J. Fluid Mech.*, Vol. 233, pp. 539–559.
- Natarajan, V. V. R., and Hunt, M. L., 1998, "Kinetic Theory Analysis of Heat Transfer in Granular Flows," *Int. J. Heat Mass Transfer*, Vol. 41, pp. 1929–1944.
- Richman, M. W., and Chou, C. S., 1988, "Boundary Effects on Granular Shear Flows of Smooth Disks," *Z. Angew. Math. Phys.*, Vol. 39, pp. 885–901.
- Savage, S. B., and Dai, R., 1993, "Studies of Granular Shear Flows: Wall Slip Velocities, 'Layering' and Self-Diffusion," *Mech. Mat.*, Vol. 16, pp. 225–238.
- Veje, C. T., Howell, D. W., and Behringer, R. P., 1999, "Kinematics of a Two-Dimensional Granular Couette Experiment at the Transition to Shearing," *Phys. Rev. E*, Vol. 59, No. 1, pp. 739–745.
- Walton, O. R., and Braun, R. L., 1986, "Viscosity, Granular-Temperature, and Stress Calculations for Shearing Assemblies of Inelastic, Frictional Disks," *J. Rheol.*, Vol. 30, pp. 949–980.
- Wang, D. G., Sadhal, S. S., and Campbell, C. S., 1989, "Particle Rotation as a Heat Transfer Mechanism," *Int. J. Heat Mass Transfer*, Vol. 32, pp. 1413–1423.
- Wassgren, C. R., 1997, "Vibration of Granular Materials," Ph.D. thesis, California Institute of Technology, Pasadena, CA.

Three-Dimensional Study of Combined Conduction, Radiation, and Natural Convection From Discrete Heat Sources in a Horizontal Narrow-Aspect-Ratio Enclosure

V. H. Adams

Y. Joshi

Department of Mechanical Engineering,
University of Maryland,
College Park, MD 20742

D. L. Blackburn

Semiconductor Electronics Division,
National Institute of Standards and Technology,
Gaithersburg, MD 20899

Three-dimensional natural convection flow and heat transfer were numerically studied for a three-by-three array of discrete protruding heat sources on a horizontal substrate in an air-filled, rectangular, narrow-aspect-ratio enclosure with length, width, and height ratio of 6:6:1. The governing equations for natural convection in air, coupled with conjugate conduction and radiation within the enclosure were solved using a finite volume method. The study examines the complex thermal interactions between the heat sources, substrate, and enclosure walls as affected by the thermal conductance of the walls and substrate with the intent of determining which physical effects and level of detail are necessary to accurately predict thermal behavior of discretely heated enclosures. The influence of radiation on the overall heat transfer is given particular attention. The three-dimensionality of the problem was evident in the overall flow characteristics and in the convective heat transfer edge effects on the heat source surfaces. Excellent agreement between temperature predictions on the heat sources and substrate and experimental measurements was obtained for modified Rayleigh numbers in the range of 9.7×10^5 to 1.6×10^7 .

Introduction

The trend toward higher power density and larger chip size in electronic packages coupled with temperature limitations on device and package components for reliability and operability purposes has placed increased emphasis on thermal management in electronic enclosures. Natural convection in air is the preferred thermal management technique for hand-held and portable electronic applications. It provides a reliable, low cost, and quiet method of thermal management in electronic enclosures with minimal peripheral power requirements. The portability requirement for systems often dictates that they be narrow-aspect-ratio enclosures in which components are mounted on horizontally oriented printed circuit boards.

Much work has been accomplished toward understanding the physics of natural convection within enclosures. Yang (1988) and Ostrach (1988) provide overviews of studies in this area. The majority of the studies either involve vertical enclosures (heat source mounted on vertical walls), or for horizontal heating, involve the classic Rayleigh-Benard convection problem with fully heated surfaces. Moffat and Ortega (1989) and Peterson and Ortega (1990) provide in-depth reviews of applications involving natural convection in electronic enclosures. However, very few studies have been conducted on natural convection in horizontal enclosures with discrete heat sources.

Torrence and Rockett (1969) and Papanicolaou and Gopalakrishna (1995) conducted numerical studies involving two-dimensional enclosures with flush-mounted discrete heating. Torrence and Rockett (1969) studied laminar natural convection

induced by a discrete isothermal heat source located at the bottom center of a circular cylinder. Excellent qualitative agreement with earlier flow visualization results obtained by Torrence et al. (1969) for the same geometry was obtained over a range of Grashof numbers (Gr_H) from 4×10^4 to 1.2×10^9 . Torrence et al. (1969) also conducted experimental studies on a rectangular enclosure with similar results. Papanicolaou and Gopalakrishna (1995) studied natural convection in an enclosure with a flush-mounted, constant heat flux source. Their numerical analysis was also extended to three side-by-side sources. These studies involved relatively simple geometries consisting of isothermal or isoflux heat sources and neglected enclosure wall thermal conduction and radiative heat transfer.

Meyer et al. (1982), Kim and Viskanta (1984a), and Huang and Aggarwal (1995) numerically investigated the effects of enclosure wall thickness and thermal conductivity on natural convection in a two-dimensional rectangular enclosure with a fully heated, isothermal wall. These studies indicate that the qualitative features of the flow field were not influenced by enclosure wall conductance; however, the quantitative results were significantly affected. In general, including wall conductance reduced the intensity of the flow and the total heat transfer rate from the heated surface. Kim and Viskanta (1984a) also validated their simulations with experimental data.

Larson and Viskanta (1976) numerically examined the effects of radiative heat transfer on natural convection from a high temperature heat source (such as a fire) in a two-dimensional enclosure. They determined that, for their problem, radiative heat transfer was 1 to 2 orders of magnitude larger than natural convection heat transfer. The rapid thermal response of the enclosure walls in conjunction with thermal radiation altered the convective flow problem. ElSherbiny et al. (1982) presented experimental results and a qualitative analysis, which demonstrated the importance of

Contributed by the Heat Transfer Division for publication in the JOURNAL OF HEAT TRANSFER. Manuscript received by the Heat Transfer Division, June 30, 1997; revision received, June 7, 1999. Keywords: Conjugate Heat Transfer, Enclosure Flows, Natural Convection. Associate Technical Editor: R. Douglass.

the effects of boundary conditions including wall conduction and radiation on natural convection in a tilted two-dimensional enclosure. Kim and Viskanta (1984b) numerically studied the effects of wall conduction and radiation in a two-dimensional rectangular enclosure and determined that these effects reduced natural convection heat transfer.

Additional experimental studies involving discrete heating include Kang and Jaluria (1990) and Ortega and Lall (1996). Kang and Jaluria (1990) obtained experimental results for natural circulation over a protruding heat source on horizontal and vertical plates. The experimental setup was configured to approximate a two-dimensional heat source in an extensive environment. They determined that some of the heat was removed from the heat source by conduction through the horizontal substrate, which manifested itself in symmetric isotherms about the source. Ortega and Lall (1996) conducted experiments involving a single, centrally located, flush heat source on a horizontal, low thermal conductivity substrate. The mean Nu_H obtained from experiment was significantly different than those obtained from classical correlations for fully heated plates.

All the geometries studied involve simplified approximations of realistic systems. Numerical studies involve two-dimensional analyses with flush isothermal or isoflux heat sources in enclosures of simple geometry with limited multi-mode heat transfer interaction. Experimental studies typically use foil-type heaters to provide isothermal or isoflux conditions which are in intimate contact with a substrate or enclosure wall. Natural convection in air for modern, compact portable systems involves three-dimensional, conjugate heat transfer with multiple heat sources in varying geometries, and include different materials with widely varying thermophysical properties and length scales.

Previous studies have not looked at a three-dimensional analysis of conjugate heat transfer to evaluate the complex thermal interactions between the heat sources, substrate, and enclosure walls. This three-dimensional study investigates complex thermal interactions in a three-by-three array of protruding heat sources mounted on a horizontal substrate in a narrow-aspect-ratio enclosure. The objective of the study is to determine the impact of each interaction on convective heat transfer from the heat source surface and what level of detail is required in numerical simulations to accurately capture the thermal behavior of the system. Experimental data for selected conditions are presented to benchmark the computations.

Problem Formulation

Experimental Setup and Procedure. Figure 1(a) depicts the geometry and dimensions of the enclosure and the layout of the

heat sources (packages) on the substrate (printed wiring board (PWB)). The $0.1524\text{ m} \times 0.1524\text{ m} \times 0.0318\text{ m}$ inside dimensions enclosure is constructed of 0.0127 m thick Plexiglas side walls, a 0.0063-m thick Plexiglas bottom wall, and a 0.0095-m thick temperature-controlled aluminum top plate. A single metallization layer, $0.1524\text{ m} \times 0.1524\text{ m} \times 0.0015\text{ m}$ fiberglass-reinforced (FR-4) substrate is horizontally located 0.0063 m above the bottom plexiglas plate providing a gap under the substrate through which the connecting power and sense leads, and thermocouple wires are routed out of the enclosure. The placement of the substrate is such that the air space above it has a height of 0.0254 m with a height-to-width aspect ratio of 1:6. A three-by-three array of heat sources is centrally located on the substrate with a center-to-center spacing of 0.0254 m . The outside vertical sides and bottom of the enclosure are insulated with 0.0381-m thick foam, while the top aluminum plate is maintained at a constant temperature 20°C by a liquid-cooled, copper cold plate. The measured spatial variation in temperature across the inside face of the aluminum plate inclusive of numerical uncertainty is less than 0.4°C .

Figure 1(b) shows the details of the heat sources, which are used for modeling purposes. Each heat source is an 88-lead electronic package with overall dimensions of $15.7\text{ mm} \times 15.7\text{ mm} \times 2.1\text{ mm}$, containing a silicon thermal test chip (die). Each die contains a diffused resistive element for power dissipation and a string of five series diodes located in the center. The forward voltage of the diode string is used as the temperature-sensitive parameter (TSP) to measure the die temperature. The electric leads of the heated components are soldered to the substrate to give a standoff distance of 0.2 mm from the PWB substrate.

Separate custom-designed-and-built constant power sources supply power to the resistive elements in each of the packages over the range 0.25 W to 1.5 W . All actual power readings are within 0.8 percent of nominal values, with the largest percentage difference occurring at the lower power settings.

Copper-constantan (Type-T) thermocouples (0.08 mm) are attached to the heat sources, substrate, and enclosure walls using 0.05 mm thick thermally conductive tape. These are located on the top center surface of each of the heat sources, on the bottom side of the substrate directly under the center of each heat source, and at 0.0127-m intervals from the center point of the outer heat sources to the sides of the substrate. Three thermocouples are placed at the center position across one plexiglas side wall and the associated foam insulation to provide temperature measurements from the inside wall to the ambient environment. The thermocouples are connected to a digital voltmeter with a digital thermometer capability via a scanning multiplexer which has an internal reference junction. The thermocouple measurement system is calibrated

Nomenclature

A = area (m^2)
 c_p = specific heat at constant pressure ($\text{J kg}^{-1} \text{K}^{-1}$)
 F_{ij} = radiation view factor (nondimensional)
 g = gravitational acceleration (m s^{-2})
 h = heat transfer coefficient at surface ($\text{W m}^{-2} \text{K}^{-1}$)
 H = fluid region height (m)
 k = thermal conductivity ($\text{W m}^{-1} \text{K}^{-1}$)
 Nu_H = Nusselt number (nondimensional)
 p = pressure (N m^{-2})
 q_{total} = total heat generation rate in enclosure (W)
 q''_{rad} = radiative heat flux (W m^{-2})
 q''' = volumetric heat generation rate (W m^{-3})

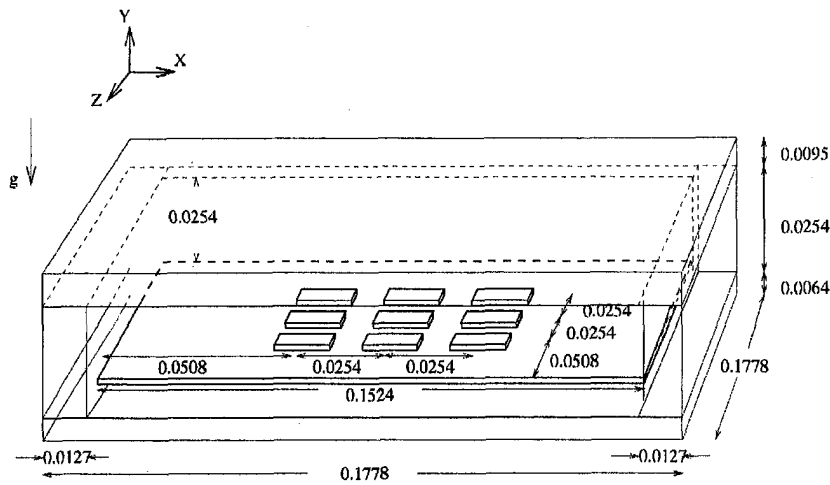
Ra_H^* = modified Rayleigh number (nondimensional)
 Ra_H = temperature-based Rayleigh number (nondimensional)
 t = time (s)
 T = temperature (K)
 T_r = temperature of the top cold plate (heat sink) (K)
 T_{j-a} = heat source to cold plate temperature difference (K)
 T_{b-a} = substrate to cold plate temperature difference (K)
 V = fluid velocity (m s^{-2})
 x, y, z = coordinates (m)
 X_L, Y_L, Z_L = enclosure dimensions (m)

Greek Symbols

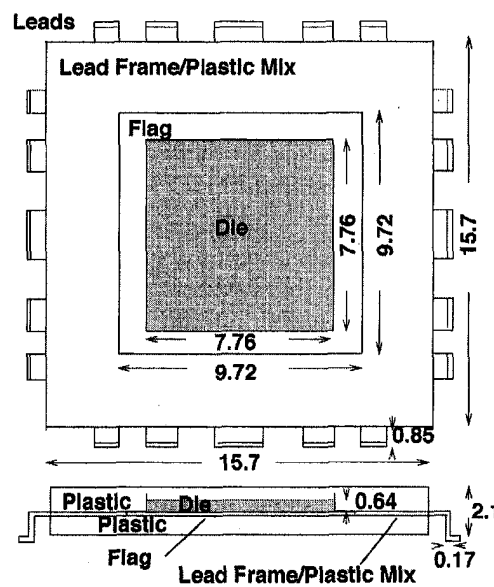
α = thermal diffusivity ($\text{m}^2 \text{s}^{-1}$)
 β = coefficient of thermal expansion (K^{-1})
 ϵ = emissivity (nondimensional)
 μ = kinematic viscosity ($\text{m}^2 \text{s}^{-1}$)
 ν = density (kg m^{-3})
 σ = Stefan-Boltzman constant ($\text{W m}^{-2} \text{K}^{-4}$)

Subscript

f = fluid
 i, j = i th/ j th package
PWB = substrate



(a) enclosure geometry



(b) heat source geometry

Fig. 1 System geometry: (a) enclosure (dimensions in meters) and (b) heat source (package—dimensions in millimeters)

in an ice bath. The overall temperature measurement uncertainty is estimated to be $\pm 0.2^\circ\text{C}$.

The die temperature measurement system is calibrated in a stirred Fluorinert FC 40 bath using the thermocouples located at the top of each of the components to measure their respective surface temperatures. The entire substrate with attached unpowered heat sources is placed in the bath. A quadratic function relating die temperature to diode voltage drop is curve fit to calibration data obtained for each package over a temperature range of 0°C to 100°C . The overall die temperature measurement uncertainty is estimated to be $\pm 0.4^\circ\text{C}$.

Modeling Methodology. The thermophysical properties listed in Table 1 for the materials used in the system and heated components are assumed to be constant and at an ambient temperature of 20°C . A constant temperature of 20°C is specified for the top surface of the enclosure, and adiabatic boundary conditions are specified for all other outer boundaries. Zero air velocities are

specified for the outer boundaries. Heat generation is assumed to be uniform through the entire silicon chip.

The geometric details of the enclosure and electronic packages, as shown in Fig. 1, were included in the numerical model. Effective, uniform, and isotropic properties are used to model the fiberglass composite FR-4 substrate (PWB) with its surface metallization. Measurements (Holometrix, 1996) were used to determine the in-plane thermal conductivity of the bare FR-4 substrate by a thermal wave-based method. The thermal diffusivities obtained from this technique, along with measured values of density and specific heat for the sample, resulted in an in-plane and cross-plane thermal conductivity of 0.52 W/m-K and 0.34 W/m-K , respectively.

To account for the effect of the copper metallization on the in-plane thermal conductivity of the substrate, a simple analytic model of parallel metal and FR-4 conductance is assumed. The thickness and width of the metal lines ($0.03\text{ mm} \times 0.13\text{ mm}$) in a

Table 1 Thermophysical properties used for computations

Materials	Thermal Conductivity (W/m K)	Density (kg/m ³)	Specific Heat (kJ/kg-K)	Dynamic Viscosity (kg-m/s)	Emissivity
Air	0.0263	1.1614	1007.0	1.846x10 ⁻⁷	--
FR-4	0.35	1900.0	930.0	10 ¹⁰	0.9
Copper	401.	8933.0	385.0	10 ¹⁰	--
Die Flag	260.0	8780.0	385.0	10 ¹⁰	--
Encapsulant	0.8	1206.0	1000.0	10 ¹⁰	0.9
Lead Frame Composite	138.5	5750.0	631.0	10 ¹⁰	--
Chip (Si)	148.0	2330.0	712.0	10 ¹⁰	--
Aluminum	--	--	--	--	0.2
Plexiglas	0.195	1180.0	1440.	10 ¹⁰	0.9

unit cell of substrate (1.5 mm × 1.4 mm) is determined. Based on this geometry, a value for in-plane effective substrate thermal conductivity of 1.1 W/m-K is obtained and represents an upper limit. Since the FR-4 cross-plane thermal conductivity is significantly lower compared to the effective in-plane value for the substrate, an effective isotropic value of 0.8 W/m-K is used for the substrate thermal conductivity (k_{PWB}).

Governing Equations. The entire enclosure is solved as a single computational domain. Figure 2 shows a cross section of the computational domain with the thermal boundary conditions applied. Governing conservation equations for continuity, momentum, and energy in the three-dimensional problem, assuming constant properties and the Boussinesq approximation, are developed for a generic control volume and are given by the following:

Continuity.

$$\nabla \cdot \mathbf{V} = 0 \quad (1)$$

Momentum.

$$\rho \left(\frac{\partial \mathbf{V}}{\partial t} + \mathbf{V} \cdot \nabla \mathbf{V} \right) = -\nabla p + \mu \nabla^2 \mathbf{V} + \rho g \beta (T - T_r) \quad (2)$$

Energy.

$$\rho c_p \left(\frac{\partial T}{\partial t} + \mathbf{V} \cdot \nabla T \right) = k \nabla^2 T - \nabla \cdot \mathbf{q}''_{rad} + q''' \quad (3)$$

Boundary conditions at the enclosure walls are as follows:

$$x = 0., \quad \frac{\partial T}{\partial x} = 0., \quad u = v = w = 0.$$

$$x = X_L, \quad \frac{\partial T}{\partial x} = 0., \quad u = v = w = 0.$$

$$z = 0., \quad \frac{\partial T}{\partial z} = 0., \quad u = v = w = 0.$$

$$z = Z_L, \quad \frac{\partial T}{\partial z} = 0., \quad u = v = w = 0.$$

$$y = 0., \quad \frac{\partial T}{\partial y} = 0., \quad u = v = w = 0.$$

$$y = Y_L, \quad T = T_r, \quad u = v = w = 0. \quad (4)$$

Radiative heat transfer is included by using an irradiation/radiosity method which assumes that the air is nonparticipating, the radiating surfaces are opaque, and that radiation exchange between surfaces is gray and diffuse (Incropera and DeWitt, 1980). The net radiative flux from surface i is given by

$$q''_{rad,i} = \frac{\sigma T_i^4 - J_i}{(1 - \epsilon_i)/\epsilon_i A_i} = \sum_{j=1}^N \frac{J_i - J_j}{(A_i F_{ij})^{-1}}, \quad (5)$$

where σ is the Stefan-Boltzmann constant, $q''_{rad,i}$, T_i , J_i , ϵ_i , and A_i are the net radiative heat flux, temperature, radiosity, emissivity, and area of the i th surface, respectively, and F_{ij} is the view factor from the i th to j th surface. An enclosure bounded by the top of the substrate, the sides of the system enclosure, and the aluminum cold plate is used in the radiation computations. Since the heat sources are low in vertical profile, they are treated as flush with the substrate surface of the "radiation" enclosure (only for radiation computations). The radiation enclosure is divided into 23 surfaces. View factors for these surfaces are obtained from Howell (1982). An area-weighted mean temperature is obtained for each surface from the data stored in the computational domain. These temperatures, along with the view factors and emissivities (shown in Table 1), are used to determine the radiosities and net radiative heat fluxes.

Due to the computations involving radiation, the governing equations were solved in their dimensional form. For comparison purposes, some data were reduced to nondimensional form as a Rayleigh (Ra) number or Nusselt (Nu) number. A modified Ra_{Hj}^* is used to represent the total power generation in the enclosure and is defined by

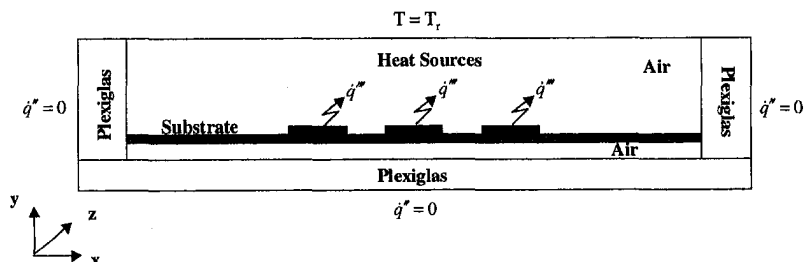


Fig. 2 Cross section through computational domain showing thermal boundary conditions. Heat sources have volumetric heat generation rate, q''' .

$$Ra_H^* = \frac{g \beta_f q_{\text{total}} H^2}{k_f \alpha_f \nu_f} \quad (6)$$

For comparison with Nu values in the literature, a temperature-based Ra_H , defined by

$$Ra_H = \frac{g \beta_f (T_{\text{surf}} - T_r) H^3}{\alpha_f \nu_f} \quad (7)$$

is used. The local Nusselt numbers (Nu_H) on the top surfaces of the heat sources and substrate are determined by

$$Nu_H = \frac{-(\partial T / \partial n)_{\text{surf}} H}{T_{\text{surf}} - T_r} \quad (8)$$

and the mean Nu_H by

$$\overline{Nu}_H = \frac{1}{A_{\text{surf}}} \int_{\text{surf}} \frac{-(\partial T / \partial n)_{\text{surf}} H}{T_{\text{surf}} - T_r} dA_{\text{surf}} \quad (9)$$

Numerical Solution

A finite volume-based single-domain approach using the SIMPLER algorithm described by Patankar (1980) is used to solve the governing equations. The method is fully implicit in time (unconditionally stable) and uses a staggered mesh for velocities and pressure/temperature. Boundary conditions at surfaces (heat flux, temperature, and velocities) within the domain are ensured by using a harmonic mean for the interface diffusivities. In materials that were solid (e.g., chip, substrate, etc.), large values of the viscosity and zero volumetric thermal expansion coefficient (β) are prescribed. The code was designed for transient convection problems; however, in this study, the steady-state problem was solved using one large time-step. No time-dependent behavior was observed for the highest Ra_H considered in this study when the transient code was time stepped using the nominally steady values, previously obtained, as initial conditions.

Convergence criteria were based on the L_1 norm,

$$\|\epsilon\|_1 = \frac{1}{JK} \sum \left| \frac{\phi^{n+1} - \phi^n}{\phi_{\text{max}}^{n+1}} \right| \quad (10)$$

for each of the velocities and temperature. Several conditions are specified to ensure a converged solution. The first is that the normalized residuals of velocities and temperature be less than 1×10^{-5} . The second requirement is that the maximum velocities and package temperatures in the vertical planes passing through the center and outer row of packages change by less than 0.5 percent over an interval of 1000 iterations. The last requirement is that the energy imbalance over the volume encompassing each package be less than 0.5 percent. In addition, an energy balance over the top cold-plate surface is checked. In all cases, this energy imbalance is less than one percent with the majority of cases being less than 0.5 percent of the total heat generated in the enclosure.

Computations were performed for a Ra_H^* range of 9.7×10^5 to 1.6×10^7 which corresponds to individual device heat dissipation requirements of approximately 0.047 W to 0.75 W (total enclosure heat generation of 0.423 W to 6.75 W) in air. For all computations, a very fine mesh was required to capture the details of each heat source. No symmetry was assumed in the computations, though the results obtained showed a twofold symmetry in both the x and z planes about the center of the enclosure. A partial grid refinement study was conducted to determine adequacy of the mesh scheme. Nonuniform grid sizes of $71 \times 71 \times 36$, $81 \times 81 \times 36$, and $71 \times 71 \times 46$ were evaluated. Differences between package temperatures and maximum velocities for the two finer grids and the coarsest grid were less than two percent. Further grid refinement was deemed impractical based on computational time requirements to obtain a converged solution. Based on the grid refinement study, the $71 \times 71 \times 36$ grid size was used for the detailed model

simulation. Details of the packages required $14 \times 5 \times 14$ control volumes for each package. Remaining control volumes were spaced to properly represent velocity boundary layers near the enclosure walls. Under relaxation was required to improve the convergence rate of each case.

The code was validated against a study by Fusegi et al. (1991) involving natural convection in a three-dimensional cubical enclosure with one set of opposite vertical walls heated and cooled. For Ra of 10^3 , 10^4 , and 10^6 , the overall and z -averaged Nusselt numbers at the heated wall and the maximum nondimensional vertical velocity agreed to within two percent with similar velocity patterns and isotherms in the x - y and x - z planes.

Results and Discussions

In order to evaluate the effects of enclosure wall conduction, substrate conduction, and radiation, numerical computations are conducted in a systematic manner starting with the "base" case in which heat conduction in the walls and air gap under the substrate, and radiation are neglected. These assumptions are made based on the relatively low thermal conductivities of the thin air layer under the substrate, the substrate itself, and the enclosure walls. Table 2 defines the specific cases analyzed and provides temperature differences between the chip and ambient (ΔT_{j-a}) and the substrate and ambient (ΔT_{b-a}). Here, the ambient temperature is defined as the cold-plate temperature. Experimental measurements of ΔT_{j-a} and ΔT_{b-a} are made for heat sources uniformly powered at 0.047 W, 0.25 W, 0.5 W, and 0.75 W per heat source.

Table 3 shows the computed mean Nu_H for each package surface, the array treated as one large effective source, and the substrate (excluding regions under the heat sources) for selected cases. Due to the symmetric results, three heat source locations: the center, side, and corner, are representative of the entire array.

The discussions, which follow, are divided into six subsections. The first provides a general description of the temperature and flow field for this problem, followed by a discussion of the effects of enclosure wall conduction, radiation, and substrate thermal conductivity on convective heat transfer in the enclosure. Based on these individual effects, multimode heat dissipation from the heat sources and convective heat transfer in the enclosure are examined. Unless specifically noted, evaluation of system parameters and their impact on natural convection heat transfer are accomplished for a Ra_H^* of 1.0×10^7 (0.5 W per package, 4.5 W total heat generation in the enclosure).

General Description of Flow and Temperature Field. All the cases considered exhibit qualitatively similar flow and temperature characteristics. Figure 3(a-c) shows the velocity vectors in a vertical plane passing through the enclosure centerline ($z = 0.0889$ m), the centerline of an outer row of heat sources ($z = 0.0635$ m), and in the horizontal plane passing just above the heat sources ($y = 0.0155$ m) for Case 7 ($Ra_H^* = 1.0 \times 10^7$). A toroidal-shaped circulation cell forms in the enclosure over the substrate and the outer heat sources (side and corner) of the array. A plume forms over the center heat source and impinges on the top cold plate where it is redirected outward. Also, as the heated air rises over the heat sources, cold air flows inward from the enclosure walls over the top of the substrate and is entrained in the plume. Some of the inward air flow moves through lanes between the side and corner heaters where it is entrained, either over the inside corners and edges of these outer heat sources, or over the center heat source (see Fig. 3(c)). This "lane" flow of relatively cool air results in increased convective heat transfer over the inner corners and edges of the side and corner heat sources as is shown later. The remaining inward directed air flow passes over the outer heat sources of the array where it is heated as it moves toward the center heat source. Air flow along the top cold plate is redirected by the enclosure walls to the substrate completing the cellular flow structure. Additional complex flow structures in the form of inward directed helical flows develop between the corner and side heaters

Table 2 Effect of model assumptions on chip junction-to-ambient and PWB board-to-ambient temperature differences

Case	Configuration	Heater ΔT_{j-a} (°C)			Substrate ΔT_{b-a} (°C)					
		corner	side	center	corner	center	side	Loc. 1	Loc. 2	Loc. 3
exp.	$P_{wr} = 0.5 \text{ W/hr}$ ($Ra_{hi}^* = 1 \times 10^7$)	60.4	67.3	75.7	53.1	67.8	59.4	43.1	23.9	15.1
1	Base = no wall or radiation, $k_{pwb} = 0.35 \text{ W/m-K}$	108.6	115.6	135.7	103.2	130.4	110.7	66.5	31.5	21.2
2	Base + encl. wall and air gap under PWB	92.4	98.7	114.8	83.8	106.3	90.7	54.4	24.7	14.2
3	Base + wall, air gap, and rad. ($\epsilon_{AI} = 0.07$)	77.2	79.7	86.5	69.6	79.2	72.4	45.5	24.1	15.4
4	Base + wall, air gap, and rad. ($\epsilon_{AI} = 0.2$)	76.4	78.9	85.8	68.6	78.2	71.5	43.5	20.6	13.1
5	Base + wall, air gap, and rad. ($\epsilon_{AI} = 0.9$)	68.2	70.7	77.3	60.2	79.6	63.0	34.1	11.0	4.5
6	Base + wall, air gap, rad. ($\epsilon_{AI} = 0.2$), and $k_{pwb} = 0.8 \text{ W/m-K}$	69.7	73.5	81.2	60.2	72.0	64.5	43.0	22.8	14.4
7	Base + wall, air gap, rad. ($\epsilon_{AI} = 0.2$), $k_{pwb} = 0.8 \text{ W/m-K}$, and lead footprint	64.7	69.7	77.7	59.0	72.1	64.2	47.0	23.2	14.2
8	Base + $k_{pwb} = 0.8 \text{ W/m-K}$	101.3	111.4	131.3	94.3	124.1	104.6	64.6	33.3	23.0
9	Case 3 + $k_{pwb} = 0.8 \text{ W/m-K}$	73.2	77.1	84.9	63.7	75.5	68.0	46.4	25.8	17.1
exp	$P = 0.047 \text{ W/hr}$, ($Ra_{hi}^* = 9.7 \times 10^7$)	8.0	8.8	10.0	6.9	9.0	7.8	5.9	3.4	2.3
10	$P = 0.047 \text{ W/hr}$, sim.	8.1	8.9	10.2	7.5	9.6	8.3	6.3	3.2	1.9
exp	$P = 0.25 \text{ W/hr}$, ($Ra_{hi}^* = 5.2 \times 10^7$)	33.3	37.4	42.5	29.5	38.5	33.3	24.4	13.6	8.5
11	$P = 0.25 \text{ W/pkg}$, sim.	36.1	39.3	44.3	33.1	41.3	36.4	26.7	13.3	8.0
exp	$P = 0.75 \text{ W/pkg}$, ($Ra_{hi}^* = 1.6 \times 10^7$)	83.7	92.3	102.9	72.2	90.3	79.9	58.1	33.3	22.1
12	$P = 0.75 \text{ W/pkg}$, sim.	90.9	97.3	107.7	82.7	99.5	89.3	65.4	32.3	19.9

(shown in Fig. 3(b)). This complex flow pattern may be the result of interaction between the cooler, entrained lane flow and the warmer, inward directed air flow over these heat sources.

Limited smoke flow visualization studies show that the major flow characteristics found in the simulation are present in the actual enclosure. For Ra_{hi}^* greater than 1.0×10^7 , some time-dependent oscillation of the plume, which is not present in the simulations, is observed. Temperature measurements on the substrate and in the heat source (die) were found to be steady.

Temperature distributions for Case 7 are shown in Fig. 4(a-c) for the vertical planes passing through the enclosure centerline ($z = 0.0889 \text{ m}$), the centerline of an outer row of heat sources ($z = 0.0635 \text{ m}$), and for the horizontal plane passing through the substrate ($y = 0.0120 \text{ m}$). Simulations show that the temperature rise as a result of the heat sources is concentrated in the buoyant plume over the array of heaters and in the substrate under the packages. Heat spreads radially outward through the substrate. The effectiveness of the heater electrical leads in removing heat is evident in the rippling of the isotherms along the heat source footprint. The toroidal flow pattern results in a "necking" of the isotherms in the plume.

Table 2 contains experimental measurements of ΔT_{j-a} and ΔT_{b-a} for 0.047 W, 0.25 W, 0.5 W, and 0.75 W per heat source for comparison with simulations (Cases 7, 10, 11, and 12) at corresponding heat generation rates. Mean differences between predicted and experimental ΔT_{j-a} and ΔT_{b-a} of 4.4 percent and 8.3

percent, respectively, were observed. The largest difference in substrate temperatures occurred at locations directly under the packages on the bottom side of the substrate where a maximum difference of 14.4 percent was observed. These differences are presumably the result of using a uniform, isotropic k_{pwb} in the simulations, whereas k_{pwb} is actually anisotropic with a lower value in the cross-plane direction. The substrate temperature measurements under each heat source are more strongly influenced by the smaller cross-plane thermal conductivity than by the larger in-plane thermal conductivity. Temperature measurements on the bottom of the substrate, extending outward from the array, are in better agreement (<11 percent maximum difference) since the in-plane thermal conductivity more strongly influences conductive heat transfer in these regions.

Effects of Enclosure Wall Thermal Conductivity. Cases 1 and 2 (see Tables 2 and 3) are analyzed to deduce the effects of wall conduction on the thermal performance of the system. The inclusion of wall conduction in the analysis did not change the qualitative characteristics of the flow and temperature fields previously described; however, the magnitudes of the air velocity and temperature were reduced. Modeling the plexiglas walls and the air gap under the substrate (Case 2) resulted in a 13 to 21 percent decrease in simulated ΔT_{j-a} with respect to the temperatures of Case 1 and a seven percent decrease in the maximum velocity in the plume (from 0.177 m/s for Case 1 to 0.165 m/s for Case 2). Whereas, the only mode of heat removal from the substrate in Case 1 is by convection, allowing for wall conduction in the simulations results in approximately six percent of the total heat generated in the enclosure being conducted from the substrate to the enclosure walls in Case 2. Multimode heat transfer by conduction and convection from the substrate accounts for the increased conduction from the heat source to the substrate.

Effect of Radiation on Natural Convection. Cases 2 through 5 examine the effects of radiation on natural convection in the enclosure. Case 2, without radiation, represents the base for comparison purposes, while the remaining cases look at the effect of cold-plate emissivity (ϵ_{AI}) on thermal interactions in the enclosure. Measurements of ϵ_{AI} using an infrared microscope while controlling the temperature of the plate showed that it was in the range of 0.1 to 0.2 (Cases 3 and 4). Figure 5 shows the mean radiative heat flux from the enclosure walls, cold plate, and the corner regions of

Table 3 Effect of modeling assumptions on package and PWB mean Nu for $P_d = 0.5 \text{ W/hr}$

Case	Package Mean Nu			Array Mean Nu	PWB Mean Nu
	corner	side	center		
1	7.1	7.2	5.5	7.0	1.4
2	7.3	7.4	5.6	7.2	2.8
3	6.6	6.4	4.8	6.3	2.3
4	6.7	6.6	5.0	6.5	2.2
5	7.2	7.0	5.4	6.9	2.2
6	6.3	6.0	4.3	6.0	2.4
7	5.8	5.5	3.8	5.4	2.6
8	7.1	7.1	5.1	6.9	2.8
9	6.3	6.1	4.3	6.0	2.5

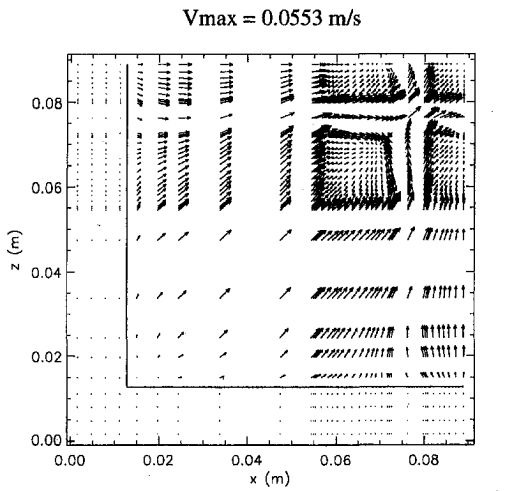
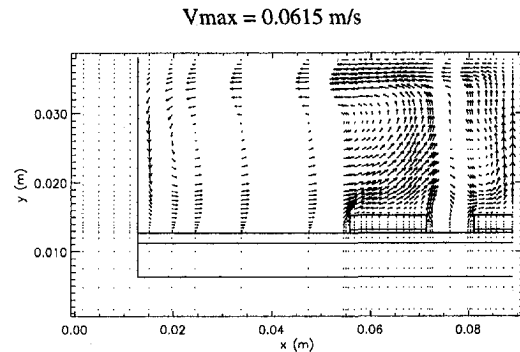
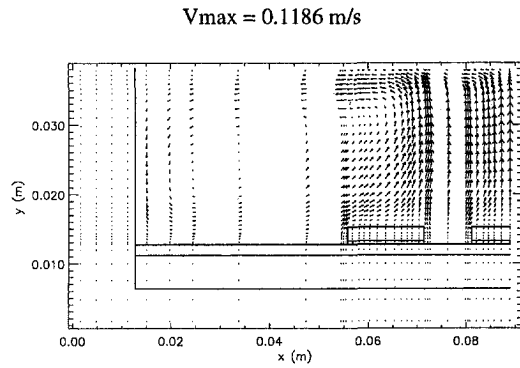


Fig. 3 Velocity vectors through (a) vertical plane, $z = 0.0889$ m, (b) vertical plane, $z = 0.0635$ m, and (c) horizontal plane, $y = 0.0155$ m for case 7

the substrate (bounded by the enclosure walls and lines passing along the outer edges of the heater array) as cold-plate emissivity is varied. Positive values indicate radiative cooling, while, negative values indicate radiative heating of the surfaces. The regions of the substrate excluding the corner regions were radiatively cooled for all values of emissivity. As cold-plate emissivity increases, the amount of reflected irradiation from the cold-plate surface to the enclosure walls and substrate is reduced resulting in less radiative heating. For the substrate, high values of emissivity ($\epsilon_{Al} = 0.9$) result in radiative cooling for the entire board.

Case 4 ($\epsilon_{Al} = 0.2$) represents the best estimate of radiative conditions for the actual enclosure. For this case the ΔT_{j-a} for each heater decreased by 17 to 25 percent and the maximum plume velocity by 21 percent compared to Case 2 (without radiation). Despite the overall decrease of temperatures in the enclosure, the mean temperature of the inside surface of the enclosure walls

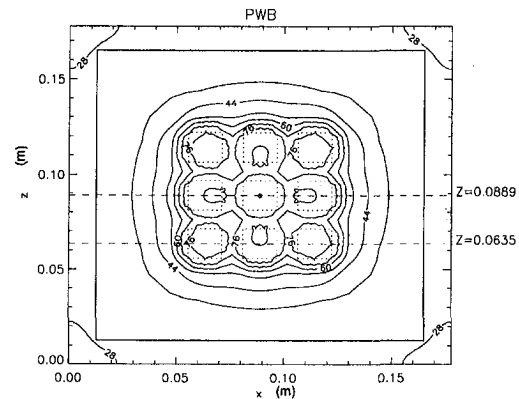
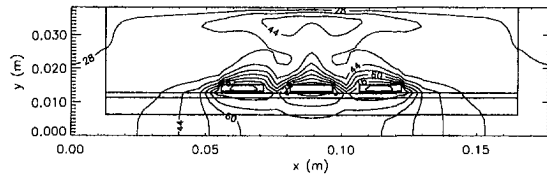
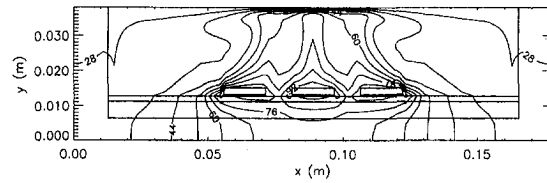


Fig. 4 Temperature contours ($^{\circ}\text{C}$) for (a) enclosure centerline, $z = 0.0889$ m, (b) vertical plane, $z = 0.0635$ m, and (c) horizontal plane through the substrate ($y = 0.0120$ m) for case 7

increased from 23.9°C for Case 2 to 26.4°C for Case 4 due to radiative heating of the wall. Heat is then convected from the walls to the downward flowing air or conducted through the enclosure walls from the substrate to the top cold plate. Radiative heating contributes to reductions in wall conduction from the substrate, from six percent (Case 2) to four percent (Case 4) of the total heat generated in the enclosure.

Further analysis shows that the net radiative heat transfer from the substrate and heat sources increases from 29.7 percent to 49.6 percent of the total power generated in the enclosure for ϵ_{Al} values of 0.2 and 0.9, respectively. Of this fraction, the largest changes in

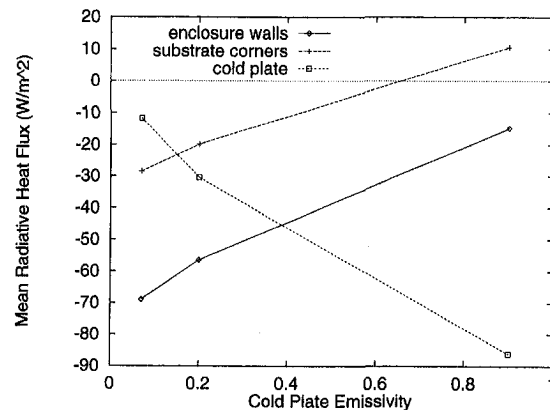


Fig. 5 Mean radiative heat flux to the enclosure walls, substrate corner regions, and top cold plate as a function of top cold-plate emissivity

radiative heat transfer occur on the substrate (7.5 percent to 25.9 percent of the total heat generated). Radiative heat transfer from the top surfaces of the heat sources was relatively insensitive to ϵ_{Al} due to the small size of each package relative to the surface area of the cold plate and radiative view factor considerations. For the range of ϵ_{Al} considered, radiative heat transfer from the heat sources accounted for 22.2 percent to 23.7 percent of the total heat generated.

The influence of radiation is felt at several levels within the system enclosure. Radiation provides another mode of heat transfer, which has a direct effect on the heat source through its surfaces, and an indirect effect by way of the substrate and enclosure walls. Radiative heat transfer from the substrate improves its ability to remove heat via conduction from the heat sources. Radiative heating of the enclosure walls, on the other hand, reduces the substrate's cooling effectiveness by reducing conduction from the substrate to the enclosure walls. The impact of these indirect effects on thermal performance of the heat sources is dependent on the surface emissivity of the cold plate.

Effect of Substrate Thermal Conductivity on Natural Convection. This analysis considers an increase in substrate thermal conductivity (k_{PWB}) from 0.35 W/m-K (based on handbook values for a bare FR-4 board) to 0.8 W/m-K (including the effects of substrate metallization). Because there are important interactions between substrate conduction, convection, and radiation, three comparisons are analyzed: (1) Cases 1 and 8, without enclosure wall conduction and radiation, (2) Cases 3 and 9, with enclosure wall conduction and radiation ($\epsilon_{Al} = 0.07$), and (3) Cases 4 and 6, with enclosure wall conduction and radiation ($\epsilon_{Al} = 0.2$). The comparisons show a varying sensitivity of system thermal performance for a given change in k_{PWB} depending upon the radiative characteristics of the enclosure. For the comparison without radiation, increasing k_{PWB} resulted in a 7.5 to 13 percent decrease in heater ΔT_{j-a} and a six percent decrease in maximum air velocity in the plume with respect to the conditions of Case 8. For the same change in k_{PWB} , but with an ϵ_{Al} of 0.07, the heater ΔT_{j-a} decreased by two to five percent and the maximum air velocity in the plume by two percent. The reduced sensitivity of the system thermal performance to k_{PWB} is the result of radiative heating of the substrate as previously described. Finally, for an ϵ_{Al} of 0.2, the heater ΔT_{j-a} decreased by 8 to 12 percent and the maximum air velocity in the plume by two percent.

The substrate serves as an extended surface whose effectiveness is dependent on its thermal conductivity and the radiative and convective heat transfer from its surface. For enclosures with low-emissivity walls (e.g., $\epsilon_{Al} = 0.07$), radiative heating of the outlying regions of the substrate and the enclosure walls increases the overall temperature of the substrate and reduces the effectiveness of the substrate to conduct heat away from the heat sources. Increasing ϵ_{Al} results in increased radiative heat transfer from the substrate, lower substrate temperatures, and increased heat conduction from the heat sources. Increasing k_{PWB} under these conditions has a greater effect on thermal performance of the enclosure.

Heat Dissipation Balance. The primary means of heat removal from the heat sources are natural convection from the top and side surfaces, radiation from the top surfaces, and conduction to the substrate via the electrical leads and bottom surfaces. Figure 6 shows the percentage of the power generated in the center heat source that is removed by conduction, convection, and radiation as a function of the total power generated in the component. Similar trends were noted for the corner and side heat sources. A substantial fraction of the heat generated in the heat source is conducted to the substrate where it is further convected, radiated, and conducted to the environment via the circulating air and enclosure walls. This indicates that parameters associated with the substrate and the interface between the heat source and substrate will have a significant impact on the thermal performance of the system. As total thermal load on the substrate increases, the substrate temperature increases, which impedes the heat conduction from the

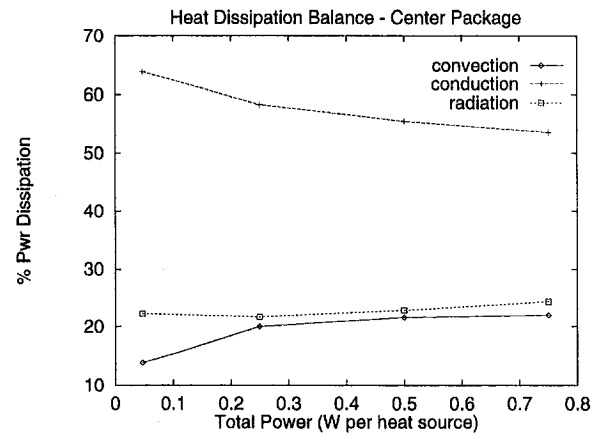


Fig. 6 Heat dissipation balance for the center heat source

individual heaters and results in higher heat source temperatures. A larger fraction of the heat generated is therefore removed by convection and radiation from the heat source top and surfaces.

The effect of wall thermal conduction, in the absence of radiation, is to provide a conduction heat removal mechanism from the substrate. This mechanism improves the effectiveness of the substrate at removing heat from the heat source. The relative distribution of heat removal by the conduction and convection heat transfer modes from the center heat source shifts from 44 percent and 56 percent of the total heat generated for Case 1 (without wall conduction) to 51 percent and 49 percent of the total heat generated for Case 2 (with wall conduction), respectively.

When radiative effects are also considered (Case 4), the distribution of heat dissipation in the center heat source shifted to 42 percent, 32 percent, and 26 percent of the total heat generated for conduction, convection, and radiation, respectively. Consideration of radiation in the simulation had both a direct and indirect effect on heat transfer from the heat sources. Radiation from the surfaces of the heat source directly reduces the heat source temperature, which in turn, reduces the fraction of the total heat dissipated by convection and conduction. Indirectly, radiation from the substrate improves its effectiveness at removing heat from the package, increasing the relative contribution of heat conduction from the heat source. These radiation effects have opposite effects on conduction from the heat sources. Radiation from the heater surfaces tends to reduce the amount of heat transfer by conduction while radiation from the substrate tends to increase conduction from the heat source to the substrate. From a heat source perspective, radiative heat transfer had a larger impact on convection from the source than on conduction. The actual interactions are more complex than this simple description, but it serves to illustrate the trends observed.

Description of Heat Transfer Characteristics. The effect of the flow field on convective heat transfer is seen in Fig. 7. Figure 7 (quarter geometry displayed) shows the local Nu_H for the top surfaces of the heat sources for Case 7. The larger local Nu_H occur for those heaters which have sides along the exterior boundary of the array since these sides are the leading edges of the array to the inward air flow over the substrate (see Fig. 3(c)). As the air flows inward over the heat sources, heating of the air by the heat sources "upstream" reduces convective heat transfer for the heater surfaces "downstream"; thus, the overall trend is a reduction in local Nu_H for locations interior to the array boundaries. This trend is seen in Table 3 where the corner and side heat sources have the largest mean Nu_H compared to the center heat source. The corner heat sources have a larger mean Nu_H than the side heat sources since two of their sides are leading edges to the flow. Enhanced convective heat transfer is evident along the edges of the corner and side package sides interior to the array boundary. This improved

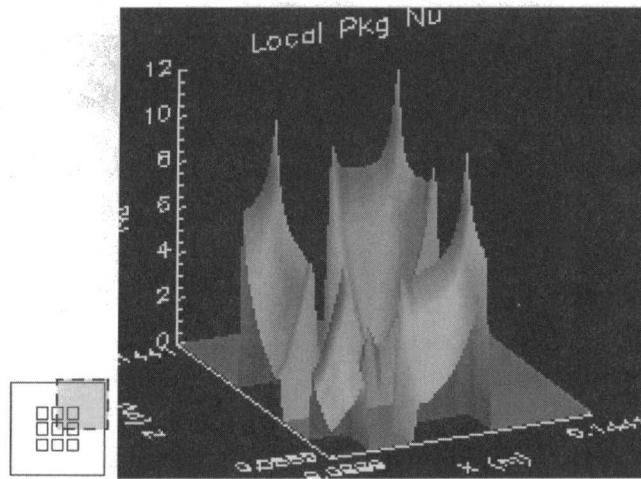


Fig. 7 Local Nu_H over top surface of the heat sources for Case 7 (quarter geometry shown)

heat transfer is primarily due to the entrainment of cooler air from the regions between the heat sources and thermal diffusion from the warmer air over the heat sources to the cooler air in the lanes. For the center heat source, this effect is less pronounced and is due to the re-establishment of the thermal boundary layer, which has partially thinned in the regions of the substrate between the center and surrounding heat sources.

The mean Nu_H for the array, where the top surfaces of the heaters are treated as one effective heat source, is compared to the data from Ortega and Lall (1996), and the classical correlations from Holland et al. (1975) and Globe and Dropkin (1959) in Fig. 8. The classical correlations for natural convection, obtained from low-aspect-ratio horizontal enclosures that are fully heated from below, underpredict the mean Nu_H of the array by approximately 30 percent. Since the relatively larger heated area (with respect to the enclosure dimensions) and higher thermal conductivity substrate of the present study more closely represent the fully heated conditions of the classical correlations than the relatively small, single heat source and low thermal conductivity substrate study of Ortega and Lall (1996), the mean Nu_H for the array compares more favorably to the correlations.

As previously indicated, the effect of cold plate ϵ_{Al} is more significant for the substrate than the heat source surfaces. Figure 9

shows the local Nu_H for the substrate without radiation (Case 2) and with radiation and ϵ_{Al} of 0.2 (Case 4) and 0.9 (Case 5). Large peaks in local Nu_H occur in regions of the substrate surrounding the heat sources where the approaching cool air flow in the lanes between the heaters thermally interacts with the heated substrate. For Case 4 where ϵ_{Al} is low, the corners of the substrate are radiatively heated, resulting in a more uniform temperature distribution compared to the no-radiation case. There is also increased convection in these regions due to higher temperatures. This increased convection is shown in the local peaking of Nu_H in the corners of the substrate (see Fig. 9(b)). For Case 5 ($\epsilon_{Al} = 0.9$), simulations show that the entire substrate radiates heat, resulting in a substantial reduction in its temperatures (see ΔT_{b-a} data in Table 2) and slightly reduced convection. Figure 9(c) shows that very little convection is taking place on regions of the substrate outside of the heater array. From Table 3, as ϵ_{Al} increases, the mean Nu_H of the substrate decreases due to increased radiative heat transfer.

Conclusions

A three-dimensional numerical study was conducted to investigate conjugate transport resulting from a three-by-three array of heated components on a horizontal substrate in a narrow-aspect-ratio enclosure for values of Ra_H^* in the range of 9.7×10^5 to 1.6×10^7 , corresponding to power dissipations of approximately 0.047 W to 0.75 W per heat source. Excellent agreement was obtained between simulated and experimental measurements of substrate and heat source temperatures over the range of power considered when all the physical effects and material parameters were best accounted for. The study showed that fluid flow in the enclosure, particularly in the regions between heat sources, and the resulting edge effects in convective heat transfer were strongly three-dimensional.

The major effects studied were wall conduction, radiation, and substrate thermal conductivity. The effect of wall conduction and radiation was to reduce convective heat transfer from the package surfaces. The qualitative characteristics of the temperature and flow field were not affected. Failure to include wall conduction and radiation in the analysis would result in significant differences between simulated and actual conditions in the enclosure. For this study, the magnitude of these differences were in the range of 80 percent to 90 percent of the actual measured temperature of the device and substrate.

The conjugate nature of heat transfer with natural convection in a horizontal orientation results in complex thermal interactions between the heat source, substrate, and enclosure walls which are

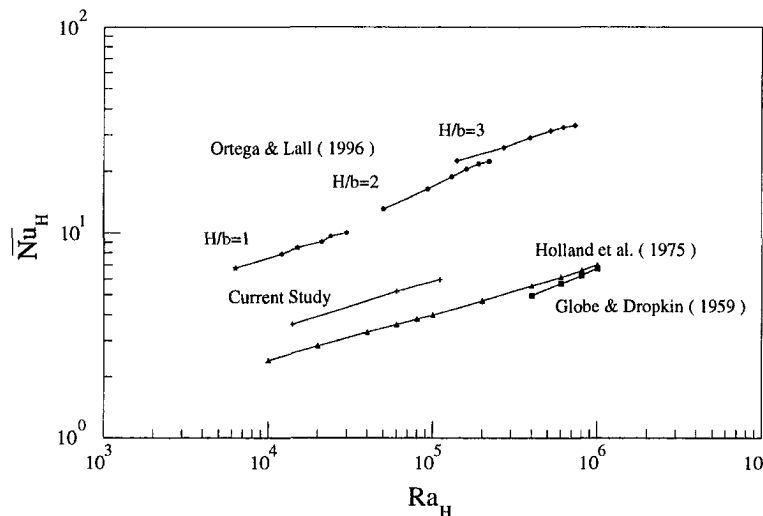


Fig. 8 Comparison of mean Nu_H for heater array treated as one effective heat source with correlations from Holland et al. (1975), Globe and Dropkin (1959), and Ortega and Lall (1996)

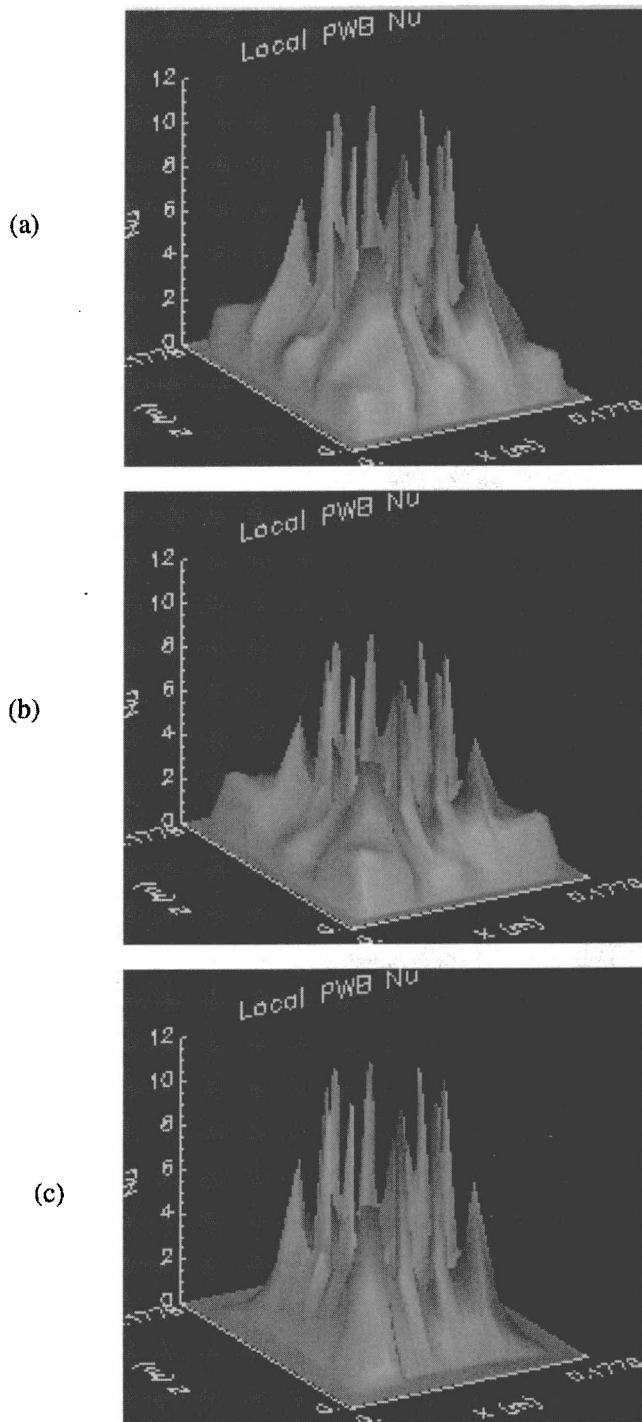


Fig. 9 Local Nu_H over the substrate surface: (a) Case 2 (no radiation), (b) Case 4 ($\epsilon_{AL} = 0.2$), and (c) Case 5 ($\epsilon_{AL} = 0.9$)

difficult to isolate for evaluation. Neglecting the effects of radiation and/or wall thermal conductance to simplify parametric studies of other factors in the enclosure may result in erroneous conclusions being drawn from the data obtained from those studies. An example, in the form of an analysis of the effects of substrate thermal conductivity on natural convection in the enclosure, was provided.

For the geometry and parameters considered in this study, radiative heat transfer was of the same order of magnitude as natural convection heat transfer from the top surfaces of the heat sources. The percentage of total heat generation, radiated from the top surface of the package, was insensitive to variations in emis-

sivity of the top cold plate. The top cold plate had a greater effect on thermal radiation from the substrate, resulting in an increase in radiative heat transfer with increasing cold-plate emissivity.

Acknowledgment

This work was supported by the National Semiconductor Metrology Program and the Semiconductor Electronic Division at the National Institute of Standards and Technology; not subject to copyright. The authors wish to thank Dan Rodkey of Delco Electronics for providing the thermal test packages and Dave Berning from NIST for design and production of the power supplies used in this study.

Certain commercial equipment, instruments, or materials are identified in this paper in order to specify the procedure adequately. Such identification does not imply recommendation or endorsement by the National Institute of Standards and Technology, nor does it imply that the materials or equipment identified are necessarily the best available for the purpose.

References

- El Sherbiny, S. M., Hollands, K. G. T., and Raithby, G. D., 1982, "The Effect of Thermal Boundary Conditions on Natural Convection in Vertical and Inclined Air Layers," *ASME JOURNAL OF HEAT TRANSFER*, Vol. 104, pp. 515-520.
- Fusegi, T., Hyun, J. M., Kuwahara, K., and Farouk, B., 1991, "A Numerical Study of Three-Dimensional Natural Convection in a Differentially Heated Cubical Enclosure," *Int. J. Heat Mass Transf.*, Vol. 34, pp. 1543-1557.
- Globe, S., and Dropkin, D., 1959, "Natural-Convection Heat Transfer in Liquids Confined by Two Horizontal Plates and Heated From Below," *ASME JOURNAL OF HEAT TRANSFER*, Vol. 81, pp. 24-28.
- Holland, K. G. T., Raithby, G. D., and Konicek, L., 1975, "Correlation Equations for Free Convection Heat Transfer in Horizontal Layers of Air and Water," *Int. J. Heat Mass Transf.*, Vol. 18, pp. 879-884.
- Holometrix Product Literature, 1996, Holometrix, Inc., Bedford, MA.
- Howell, J. R., 1982, *A Catalog of Radiation Configuration Factors*, McGraw-Hill, New York.
- Huang, Y. H., and Aggarwal, S. K., 1995, "Effect of Wall Conduction on Natural Convection in an Enclosure With a Central Heat Source," *ASME Journal of Electronic Packaging*, Vol. 117, pp. 301-306.
- Incropera, F. P., 1988, "Convection Heat Transfer in Electronic Equipment Cooling," *ASME JOURNAL OF HEAT TRANSFER*, Vol. 110, pp. 1097-1111.
- Kang, B. H., and Jaluria, Y., 1990, "Natural Convection Heat Transfer Characteristics of a Protruding Thermal Source Located on Horizontal and Vertical Surfaces," *Int. J. Heat Mass Transf.*, Vol. 33, pp. 1347-1357.
- Kim, D. M., and Viskanta, R., 1984a, "Study of the Effects of Wall Conductance on Natural Convection in a Differentially Oriented Square Cavity," *J. Fluid Mech.*, Vol. 144, pp. 153-176.
- Kim, D. M., and Viskanta, R., 1984b, "Effect of Wall Conduction and Radiation on Natural Convection in a Rectangular Cavity," *Num. Heat Transf.*, Vol. 7, pp. 449-470.
- Larson, D. W., and Viskanta, R., 1976, "Transient Combined Laminar Free Convection and Radiation in a Rectangular Enclosure," *J. Fluid Mech.*, Vol. 78, pp. 65-85.
- Meyer, B. A., Mitchell, J. W., and El-Wakil, M. M., 1982, "The Effect of Thermal Wall Properties in Natural Convection in Inclined Rectangular Cells," *ASME JOURNAL OF HEAT TRANSFER*, Vol. 104, pp. 111-117.
- Moffat, R. J., and Ortega, A., 1988, "Direct Air-Cooling of Electronic Components," *Advances in Thermal Modeling of Electronic Components and Systems*, Vol. 1, A. Bar-Cohen and A. D. Kraus, eds., Hemisphere, New York, pp. 129-282.
- Ortega, A., and Lall, B. S., 1996, "Natural Convection Air Cooling of a Discrete Source on a Conducting Board in a Shallow Horizontal Enclosure," *Proc. Twelfth IEEE Semiconductor Thermal Measurement and Management Symposium*, Austin, TX, pp. 201-213.
- Ostrach, S., 1988, "Natural Convection in Enclosures," *ASME JOURNAL OF HEAT TRANSFER*, Vol. 110, pp. 1175-1190.
- Papanicolaou, E., and Gopalakrishna, S., 1993, "Natural Convection in Shallow, Horizontal Air Layers Encountered in Electronic Cooling," *ASME Journal of Electronic Packaging*, Vol. 117, pp. 307-316.
- Patankar, S. V., 1980, *Numerical Heat Transfer and Fluid Flow*, Hemisphere, New York.
- Peterson, G. P., and Ortega, A., 1990, "Thermal Control of Electronic Equipment and Devices," *Advances in Heat Transfer*, Vol. 20 J. P. Hartnett and T. F. Irvine, Jr., eds., Academic Press, San Diego, pp. 181-314.
- Torrence, K. E., and Rockett, J. A., 1969, "Numerical Study of Natural Convection in an Enclosure With Localized Heating from Below—Creeping Flow to the Onset of Laminar Instability," *J. Fluid Mech.*, Vol. 36, pp. 33-54.
- Torrence, K. E., Orloff, L., and Rockett, J. A., 1969, "Experiments on Natural Convection in Enclosures With Localized Heating from Below," *J. Fluid Mech.*, Vol. 36, pp. 21-32.
- Yang, K. T., 1988, "Natural Convection in Enclosures," *Handbook of Single-Phase Convective Heat Transfer*, S. Kakac, R. K. Shah, and W. Aung, eds., John Wiley and Sons, New York, Chapter 13.

Heat Transfer in Discretely Heated Side-Vented Compact Enclosures by Combined Conduction, Natural Convection, and Radiation

E. Yu¹
Mem. ASME

Y. K. Joshi
e-mail: yoji@eng.umd.edu
Mem. ASME

Department of Mechanical Engineering and
CALCE Electronic Products and
Systems Consortium,
University of Maryland,
College Park, MD 20742

A three-dimensional investigation of combined conduction, natural convection, and radiation in a side-vented compact enclosure is carried out. The focus of the study is on the enhancement of overall heat transfer through the opening, and the roles of the various modes in achieving it. A discrete heat source, flush-mounted centrally on a vertical substrate, is placed in the enclosure with a single rectangular opening on the opposite vertical wall. Steady-state computations are carried out for Rayleigh numbers, Ra , at 2.6×10^6 and 2.0×10^7 . The results show that radiation plays a significant role in the overall heat transfer, and the radiative transport is even more pronounced for lower Ra . It is found that natural convection is weakened by radiation, however, contrary to the existing studies on top vented enclosures, the overall heat transfer is enhanced when radiation is included in the computations. Flow recirculation by radiative heating of enclosure walls is predicted, and is also observed experimentally. Heat spreading in the substrate is found to effect both convection and radiation. The numerical solutions on an extended computational domain are found in good agreement with the experimental data, when the conjugate effects are accounted for.

Introduction

Passively cooled, vented enclosures arise in numerous electronics cooling applications driven by requirements of low-cost, high-reliability, low-maintenance, no-noise, and interference-free operation. Examples of these include compact power supplies, portable computers and telecommunications enclosures. A recent summary of the studies on natural convection in electronics enclosures is provided by Lasance and Joshi (1998). Natural convection transport in such systems occurs in conjunction with conduction and radiation, which are often comparable in magnitude. While many investigations have been carried out for natural convection and radiation in complete enclosures (Kassemi (1993), Balaji and Venkatesan (1993, 1994a)), only a handful of studies exist on transport in vented enclosures including combined modes.

Smith et al. (1991) investigated combined conduction, natural convection, and radiation heat transfer in an electronic chassis. A subsystem consisting of three circuit cards was considered. Both one and two-dimensional radiation models were investigated. It was found that when the boards and top/bottom walls had large temperature differences, the two-dimensional model was necessary. One interesting result was that natural convection was not pronounced for a circuit card of large thermal conductivity.

Conjugate transport in partially open enclosures has been considered in a few recent studies. Moutsoglou et al. (1992) investigated the convection-radiation interaction in buoyancy-induced channel flows with and without venting. In their computations, two-dimensional vertical laminar flow was considered. An asymmetric nonuniform heat flux was prescribed on the inside of each of the channel walls. It was found that radiation tended to bring the

temperatures of the two channel walls closer together and enhanced the heat transfer compared to a purely natural convection process.

Lage et al. (1992) numerically studied natural convection and radiation in a two-dimensional top-vented enclosure, with one side-wall heated. A three-surface radiation model was employed. Balaji and Venkateshan (1994b) considered the same configuration and solved for coupled natural convection and radiation. The radiation from the left wall caused a temperature increase on the right wall, resulting in a more vigorous air-flow along this wall. Beckermann et al. (1994) reported a two-dimensional thermal analysis of a vertically oriented multiboard electronic module. Radiation was found to enhance heat transfer over natural convection and three-dimensional effects were found significant.

Dehghan (1994) and Dehghan and Behnia (1996) presented a numerical and experimental investigation of natural convection in discretely heated open-top two-dimensional cavities. The heat source was mounted on a vertical side wall. Conduction in the substrate was considered. Surface radiation was also included for some cases. It was found that inclusion of radiation did not enhance the total heat transfer coefficient in comparison to pure natural convection. The increased heat transfer due to radiation from the opening was accompanied by a reduction in convection due to the heating of enclosure walls. The incorporation of radiation was, however, necessary to accurately predict the thermal and flow fields.

The main objective of the present study is to investigate the role of conjugate transport processes in the cooling of a discrete heat source in a compact three-dimensional enclosure with a side opening. This configuration models many electronics enclosures where top venting may be undesirable due to greater potential of accidental liquid ingress into the enclosure through spillage. A single discrete heat source is flush-mounted on a vertical enclosure wall of finite thickness (substrate). This simulates the highest power component such as a microprocessor on a printed circuit board. The vent is centrally located on the wall facing the substrate. The

¹ Currently at CFD Research Corporation, 215 Wynn Drive, Huntsville, AL 35805.

Contributed by the Heat Transfer Division for publication in the JOURNAL OF HEAT TRANSFER and presented at 1996 ASME IMECE, Atlanta. Manuscript received by the Heat Transfer Division, Sept. 8, 1998; revision received, May 5, 1999. Keywords: Experimental, Heat Transfer, Interferometry, Radiation, Thin Films. Associate Technical Editor: P. Menguc.

enclosure is modeled by considering an extended computational domain. The interaction between radiation, natural convection, and conduction is examined for two Rayleigh numbers (input power levels) and a range of surface emissivities of the substrate. The relative contributions of radiation and convection to the overall heat transfer are determined for the vented enclosure. The computed results are compared with surface temperature measurements on the heater and substrate and flow visualizations.

Model

The side-vented enclosure examined in this study is seen in Fig. 1(a). Both the substrate and enclosure walls have finite thickness to allow heat transfer by conduction in the solid. Exploratory computations revealed that the boundary conditions prescribed on the opening in many two-dimensional studies (Lage et al., 1992; Balaji and Venkateshan, 1994a; Dehghan, 1994), do not accurately predict the three-dimensional flow and temperature patterns, especially in the proximity of the opening. The heat transfer coefficient variation on the component was found to be significantly different from extended domain simulations. An enlarged computational domain was therefore selected to handle the specifications of convection and radiation boundary conditions on the exterior enclosure walls and the opening. Only half of the physical domain, shown in Figs. 1(b) and 1(c), is employed for the computations to save on computing resources. Selected numerical runs showed that the results for the half domain were in very good agreement with those for the full domain, even at the highest Ra.

Solutions are obtained for normalized dimensions (based on enclosure height L) of $H = 0.325$, $H_s = H_w = 0.05$, $H_{cp} = 4.7 \times 10^{-4}$, $L_s = 0.9$, and $T_a = 25^\circ\text{C}$. The ratio of the enclosure dimensions in x , y , and z directions, $(h_b - 2h_s):(L - 2h_s):(L - 2h_s)$ is 1:4:4. The ratio of the square opening area to the internal side wall area ($l_s \times l_s$) is kept fixed at 0.4 for most runs, but has been varied in the range 0–1 for selected cases. The thickness of the substrate is the same as that of the enclosure walls. The thermal conductivity of all the solid materials is 0.197 W/m-K corresponding to plexiglass. All the surfaces of the vented enclosure are treated as black except the substrate whose emissivity is varied from 0 to 1. A substrate to fluid thermal conductivity ratio R_s of 7.3 corresponding to plexiglass and air is used in the following, unless

stated otherwise. Rayleigh numbers have two levels: 2.6×10^6 and 2.0×10^7 , corresponding to heat generation rates of 0.05 W and 0.5 W, respectively, in air.

Governing Equations. Combined natural convection in the air, conduction in the solid and radiation exchange between the different walls, and through the opening are investigated. The nondimensional steady-state equations under the Boussinesq approximation are as follows:

Continuity:

$$\frac{\partial U}{\partial X} + \frac{\partial V}{\partial Y} + \frac{\partial W}{\partial Z} = 0. \quad (1)$$

X-Momentum:

$$\begin{aligned} \frac{\partial(UU)}{\partial X} + \frac{\partial(VU)}{\partial Y} + \frac{\partial(WU)}{\partial Z} \\ = -\frac{\partial P}{\partial X} + (\text{Pr}/\text{Ra})^{1/2} \left(\frac{\partial^2 U}{\partial X^2} + \frac{\partial^2 U}{\partial Y^2} + \frac{\partial^2 U}{\partial Z^2} \right). \end{aligned} \quad (2)$$

Y-Momentum:

$$\begin{aligned} \frac{\partial(UV)}{\partial X} + \frac{\partial(VV)}{\partial Y} + \frac{\partial(WV)}{\partial Z} \\ = -\frac{\partial P}{\partial Y} + (\text{Pr}/\text{Ra})^{1/2} \left(\frac{\partial^2 V}{\partial X^2} + \frac{\partial^2 V}{\partial Y^2} + \frac{\partial^2 V}{\partial Z^2} \right) + \theta. \end{aligned} \quad (3)$$

Z-Momentum:

$$\begin{aligned} \frac{\partial(UW)}{\partial X} + \frac{\partial(VW)}{\partial Y} + \frac{\partial(WW)}{\partial Z} \\ = -\frac{\partial P}{\partial Z} + (\text{Pr}/\text{Ra})^{1/2} \left(\frac{\partial^2 W}{\partial X^2} + \frac{\partial^2 W}{\partial Y^2} + \frac{\partial^2 W}{\partial Z^2} \right). \end{aligned} \quad (4)$$

Energy for air:

Nomenclature

A_s = nondimensional surface area of substrate; $A_s = L_s^2 = (l_s/L)^2$
 F = view factor
 g = gravitational acceleration (m/s^2)
 G = irradiation (W/m^2)
 h_{cp} = thickness of component (m)
 h_s = thickness of substrate (m)
 h_b = height of enclosure (m)
 h = heat transfer coefficient ($\text{W/m}^2\text{-K}$)
 \bar{h} = average heat transfer coefficient ($\text{W/m}^2\text{-K}$)
 H = nondimensional height;
 H_{cp} = nondimensional component thickness; h_{cp}/L
 H_s = nondimensional substrate thickness; h_s/L
 J = radiosity (W/m^2)
 k = thermal conductivity (W/m-K)
 l_{cp} = length of component (m)
 l_s = length of substrate (m)
 L = length of enclosure (m)
 M_{out} = nondimensional mass outflow rate

Nu = Nusselt number: hL/k
 $\bar{\text{Nu}}$ = Average Nusselt number
 p = pressure (N/m^2)
 p_0 = reference pressure (N/m^2)
 P = nondimensional pressure $(p - p_0)/(\rho U_0^2)$
 Pr = Prandtl number: ν/α
 q'' = heat flux (W/m^2)
 Q = heat generation rate (W)
 Ra = Rayleigh number: $g\beta QL^2/(\alpha\nu k_f)$
 R_b = ratio of enclosure case thermal conductivity to fluid thermal conductivity
 R_{cp} = ratio of component thermal conductivity to fluid thermal conductivity
 R_s = ratio of substrate thermal conductivity to fluid thermal conductivity
 T = temperature (K)
 T_{ref} = reference temperature: $Q/(Lk_f)$
 u, v, w = velocity in x, y, z directions, respectively (m/s)
 x, y, z = Cartesian coordinate (m)

α = thermal diffusivity of fluid (m^2/s)
 β = coefficient of volumetric expansion (K^{-1})
 ϵ = surface emissivity
 ν = kinematic viscosity (m^2/s)
 θ = nondimensional temperature: $(T - T_a)/T_{\text{ref}}$
 ρ = density of fluid (kg/m^3)

Subscripts

a = ambient
 b = enclosure (box)
 c = convection
 cp = component
 f = fluid
 r = radiation
 s = substrate
 t = total
 v = vent
 w = wall of enclosure

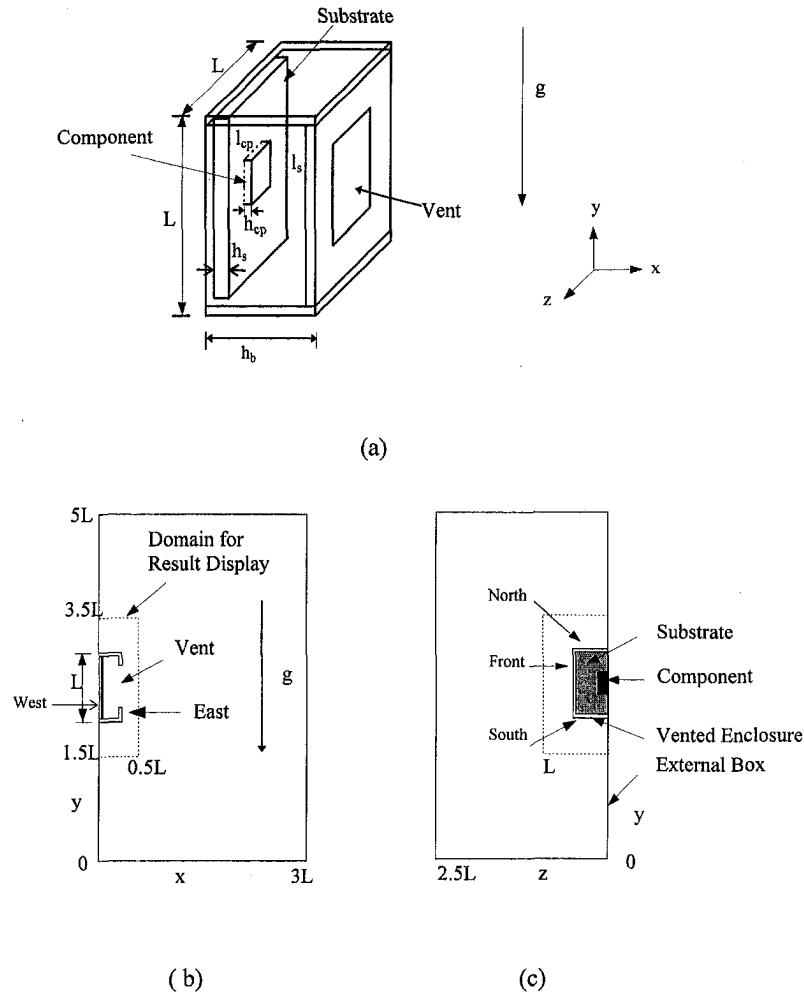


Fig. 1 (a) Schematic of the enclosure geometry with the component flush mounted on the substrate; (b) front view of calculation domain; (c) side view of calculation domain

$$\frac{\partial(U\theta)}{\partial X} + \frac{\partial(V\theta)}{\partial Y} + \frac{\partial(W\theta)}{\partial Z} = (1/\text{Pr Ra})^{1/2} \left(\frac{\partial^2 \theta}{\partial X^2} + \frac{\partial^2 \theta}{\partial Y^2} + \frac{\partial^2 \theta}{\partial Z^2} \right) \quad (5)$$

Energy for component ($0.045 \leq X \leq 0.05$, $2.4 \leq Y \leq 2.6$, $0 \leq Z \leq 0.1$):

$$\frac{\partial^2 \theta}{\partial X^2} + \frac{\partial^2 \theta}{\partial Y^2} + \frac{\partial^2 \theta}{\partial Z^2} + 1/(R_{cp} H_{cp}) = 0 \quad (6)$$

Energy for substrate and enclosure walls:

$$\frac{\partial^2 \theta}{\partial X^2} + \frac{\partial^2 \theta}{\partial Y^2} + \frac{\partial^2 \theta}{\partial Z^2} = 0 \quad (7)$$

The nondimensional parameters are defined below, based on the characteristic length L , the characteristic velocity $U_0 = (g\beta Q/k_f)^{1/2}$, and the heat generation rate Q .

The boundary conditions for the computational domain are as follows:

$$\frac{\partial \theta}{\partial X} = 0, \quad U = V = W = 0 \quad \text{at } X = 0 \quad (8)$$

$$\frac{\partial \theta}{\partial Z} = \frac{\partial U}{\partial Z} = \frac{\partial V}{\partial Z} = 0, \quad W = 0, \quad \text{at } Z = 0 \quad (9)$$

and

$$\theta = U = V = W = 0 \quad (10)$$

for the four remaining planes at $X = 3$, $Y = 0$, $Y = 5$, and $Z = 2.5$, respectively.

The boundary conditions at the interfaces of different materials are

$$R_i \left(\frac{\partial \theta}{\partial X_n} \right)_i = R_j \left(\frac{\partial \theta}{\partial X_n} \right)_j - \delta_{ij} Q_r \quad (11)$$

$$\theta_i = \theta_j \quad (12)$$

$$U = V = W = 0 \quad (13)$$

where X_n is the coordinate normal to the surface and i, j refer to the two different materials (s, cp, b, f). Also, $Q_r = (q''_r L^2)/Q$, $R_s = k_s/k_f$, $R_{cp} = k_{cp}/k_f$, $R_b = k_b/k_f$, $R_f = 1.0$, $\delta_{ij} = 1$ when i refers to solid and j to fluid, $\delta_{ij} = -1$ when i refers to fluid and j to solid, $\delta_{ij} = 0$ when both i and j refer to solid materials, and q''_r is the radiation flux.

Radiation Formulation. Radiation is incorporated based on the radiosity/irradiation formulation. The six interior surfaces of the enclosure are assumed to be opaque, diffuse, and gray. The opening is assumed to be black at the ambient temperature. The enclosure surfaces are divided into smaller regions called zones,

Table 1 Validation of numerical model. The results are for a side-heated cubic enclosure for $Ra = 10^3$ at mid x - y plane.

Author/year	Grid	U_{max}	V_{max}	$Nu_{overall}$
Fusegi et al. (1991)	32^3	3.5013	3.5170	1.085
Mallinson and de Vahl Davis (1977)	21^3	3.5890	3.6290	—
Present work	21^3	3.5690	3.5560	1.077
Present work	32^3	3.5440	3.5500	1.074

each assumed to be isothermal. The net rate, q_i , at which radiation leaves zone i is given by

$$q_i = \frac{\sigma T_i^4 - J_i}{(1 - \epsilon_i)/(\epsilon_i A_i)} \quad (14a)$$

When $\epsilon_i = 1$,

$$q_i = A_i(\sigma T_i^4 - G_i), \quad (14b)$$

where irradiation G_i is given by

$$G_i = \sum_{j=1}^N F_{ij} J_j \quad (15)$$

and the radiosity J_i is given by

$$J_i = \epsilon_i \sigma T_i^4 + (1 - \epsilon_i) \sum_{j=1}^N F_{ij} J_j \quad (16)$$

The view factors F_{ij} between two area elements on parallel surfaces and between those on perpendicular surfaces are calculated based on the formulas described by Howell (1982).

The radiation heat transfer rates on the external surfaces of the vented enclosure are determined by treating them as small surfaces in an infinite environment at the ambient temperature. The following equation is used to calculate the radiation flux at each such small surface:

$$q_i'' = \epsilon_i \sigma (T_i^4 - T_a^4) \quad (17)$$

Numerical Method. The governing equations for the conjugate heat transfer are solved using SIMPLER algorithm detailed by Patankar (1980). A power-law scheme is used for handling the convection-diffusion terms. A single-domain nonuniform mesh is employed for natural convection, conduction, and also for radiation on the external surfaces of the vented enclosure. The calculation of radiation within the vented enclosure is carried out using different coarser grids based on isothermal radiative zones to save on computing resources.

The numerical solution is considered to be converged when the ratio of the maximum temperature change to the maximum temperature at that iteration is within 1×10^{-5} , the ratio of the maximum velocity change to the maximum velocity at that iteration is within 1×10^{-4} , and the residual of the energy equation for the whole domain is within one percent. The natural convection model is validated for a cubic enclosure with vertical walls heated and cooled and four insulated walls. The results for maximum velocity and Nu were found to be within two percent and one percent, respectively of those reported by Fusegi et al. (1991) and Mallinson and de Vahl Davis (1977), as detailed in Table 1.

The radiation model is validated by suppressing the convection and conduction and solving radiation heat transfer. The results were within one percent of those from direct calculations. Radiation energy balance, reciprocity relations, summation of view factors to unity, and symmetric allocation of radiation rates are all satisfied. Grid testing for convection and radiation was carried out, and the results show that the $40 \times 52 \times 28$ grid is fine enough for

accurate results and used for most of the computations. For radiation grid testing, 68 isothermal zones were found sufficient for the present radiation calculations.

The discretization of grids for the internal walls was handled by considering conduction in the walls and boundary layers along the walls. Two grid cells have been used in the walls to resolve less strong wall conduction and six grid cells in the substrate to capture the strong heat spreading effects.

Experimental Validation of Model

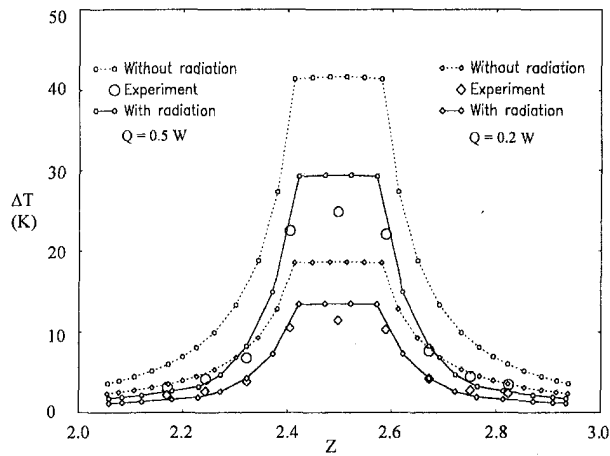
The experimental arrangement includes two enclosures. The external box shown as the outer enclosure in Fig. 1(b) is employed to simulate a well-defined boundary condition, damp-out stray circulation, and to create a natural convection environment. The internal box, i.e., the vented enclosure, is of actual interest. Plexiglass of known emissivity 0.83 serves as the wall. A single thermofoil heater was centrally mounted flush on a substrate made of plexiglass. The heat generation rate in the thermofoil heater was controlled by a regulated DC power supply. The signals from various thermocouples were sent to a data acquisition system (DAS) controlled by a personal computer. Temperatures of the substrate surface were measured at several locations along the horizontal and vertical midplanes using 0.0762-mm diameter Copper-Constantan thermocouples. The substrate and the heater were painted black using Krylon 1602 of known emissivity 0.95.

The temperature measuring system was calibrated using an ice-water bath and a precision mercury thermometer, with the resulting measurement uncertainty estimated as $\pm 0.1^\circ\text{C}$. In the thermocouple placement, the uncertainty was estimated as ± 0.5 mm. Surface emissivity of plexiglass was quoted at an uncertainty of ± 0.01 and that of Krylon 1602 was ± 0.05 by the vendor. Uncertainties in voltage and current measurements are ± 0.4 percent and ± 1.5 percent, respectively, resulting in an uncertainty of ± 1.6 percent for the power input of 0.5 W, based on the uncertainty analysis method described by Kline and McClintock (1953).

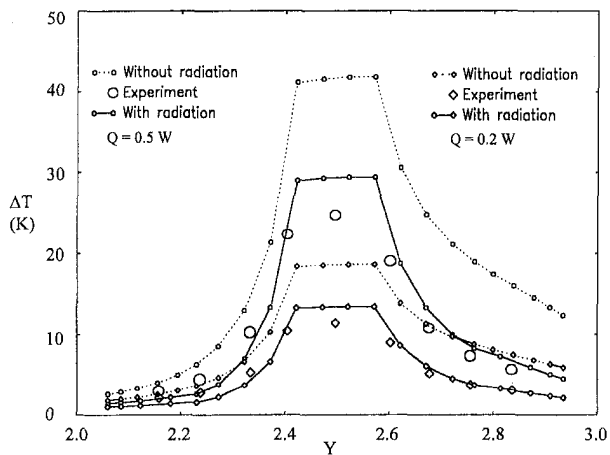
The results of the present numerical model for combined modes of heat transfer and the experiments are compared in Figs. 2(a) and (b). Figure 2(a) shows the symmetric temperature rise across the surface of the component and substrate in a horizontal centered plane. Figure 2(b) show the temperature rise in a centered vertical plane. The substrate heating by the convective flow above the component results in an asymmetric profile. The ratio of the discrepancy in temperature at the center of the component surface between computations and experiments is 21.1 percent for an input power of 0.2 W and 35.9 percent for 0.5 W power level, if radiation is not included, indicating the importance of surface radiation for prediction of the overall heat transfer. The corresponding ratios with radiation included are 6.7 percent and 10.7 percent.

These remaining differences are attributed collectively to uncertainties in thermal conductivity values and the heat loss from the back of the substrate. The heater element in the experiments consists of a foil network on a polymer substrate, which is modeled with a single effective thermal conductivity, k_{cp} . This is estimated based on the volume fraction content of the metal and polymer. A ten percent uncertainty in the value of k_{cp} results in a two percent change in the maximum temperature. Also, in the computations, the backside of the substrate is adiabatic. In the experiments, heat loss through the insulation will result in a drop in the maximum measured temperature, consistent with Fig. 2.

Flow Visualizations. Flow visualizations were conducted for qualitative assessment of the numerical simulations. A 20-mW Helium-Neon laser was used to generate a laser sheet passing through the transparent plexiglass enclosure. Both incense and cigarette smoke were tested. The results presented were obtained with cigarette smoke, which produced better photographs for the present configuration. The smoke was generated in the far corner of the external enclosure and entrained into the smaller enclosure, through its side opening. The laser sheet was projected through the



(a) Horizontal mid-ZX plane



(b) Vertical mid-XY plane

Fig. 2 Comparisons between experimental and numerical results for temperature rises on the surfaces of the component and substrate over the ambient

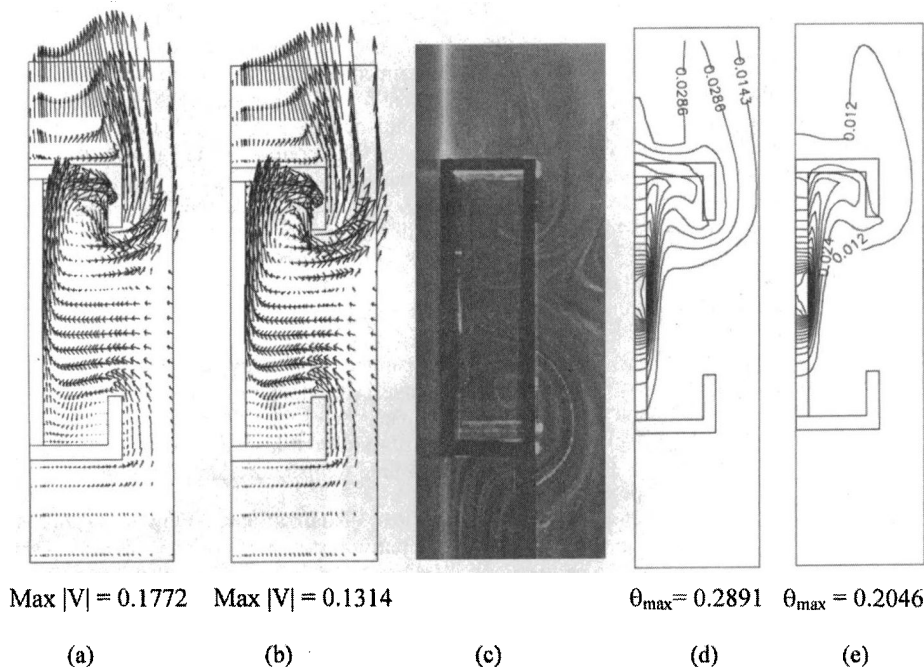


Fig. 3 Flow and temperature patterns in X-Y plane at Z = 0 for $S_v = 0.4$ and $Ra = 2.0 \times 10^7$; (a), (d) without radiation; (b), (e) with radiation; (c) experimental flow visualization (exposure time: 2 sec)

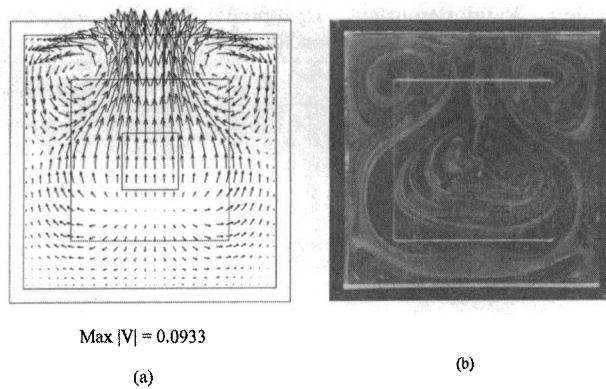


Fig. 4 Flow patterns in Y-Z plane at $X = 0.1125$ (mid-yz plane) for $S_v = 0.4$ and $Ra = 2.0 \times 10^7$ (a) computational result with radiation (b) experimental flow visualization (exposure time: 2 sec)

smaller enclosure after the cigarette was extinguished, in order to reduce the intrusiveness both from the laser and cigarettes. Typical exposure times ranged from 1 s to 2 s. A 35-mm camera was employed to capture the photographs of the flow patterns.

Figures 3(a), (b), and (c) exhibit the results of computations and flow visualization in two planes, for power input at 0.5 W ($Ra = 2.0 \times 10^7$). It is observed that the flow cell at the bottom of the enclosure in Fig. 3(c) is well simulated when radiation is considered in Fig. 3(b). The result from only natural convection and conduction models, Fig. 3(a), does not predict this feature. This cell arises due to the radiative heating of the right wall from the heat source. In the y-z plane, Fig. 4, the overall flow structure is also well predicted using the radiation model. Without inclusion of radiation, a similar flow pattern is obtained, however, the magnitudes of velocity vectors are much larger.

Based on these comparisons, it is concluded that the numerical model is able to adequately predict the temperature of the component and the overall flow patterns in the present compact enclosures.

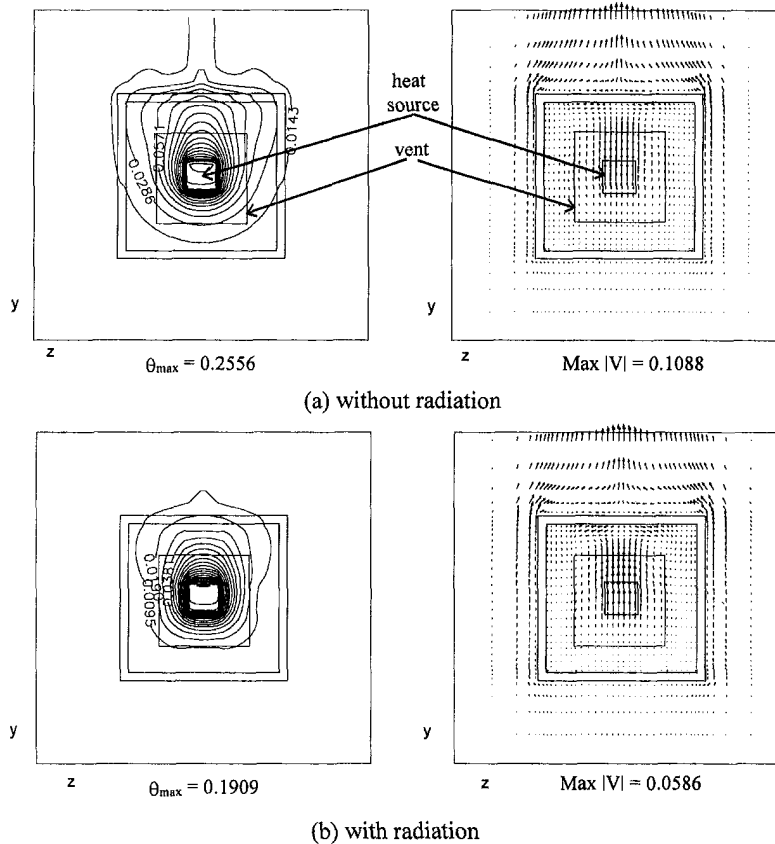


Fig. 5 Temperature contours and velocity vectors in Y-Z plane at $X = 0.054$ for $S_v = 0.4$ and $Ra = 2.0 \times 10^7$

Conjugate Transport

Computational results are obtained for $Ra = 2.0 \times 10^7$ and $Ra = 2.6 \times 10^6$, corresponding to the power inputs of 0.5 W and 0.05 W, respectively. Due to qualitative similarities, only the results for $Ra = 2.0 \times 10^7$ are discussed in detail. Contours of temperature and velocity vectors are displayed in Figs. 3–5 for three planes in a domain near the heat source identified in Fig. 1(b). The influence of radiation on flow patterns in selected planes, in Figs. 3 and 4, has already been presented.

The temperature fields in Figs. 3 and 5 account for the heat spreading in the substrate and convection in the air, with and without radiation. Reduced heat spreading on the substrate is observed in Fig. 5(b) due to the interaction of radiation between different walls, leading to their closer temperatures. Also, weaker plumes occur along the substrate when radiation is included, resulting from reduced convection. Unique thermal patterns are also observed external to the enclosure, including a weaker hot plume in Figs. 3(e) and 5(b). The weaker convection for Ra of 2×10^6 is characterized by thicker thermal and hydrodynamic regions along the substrate. The relative influence of radiation is more pronounced than for higher Ra .

In order to understand the effect of enclosure opening on radiation heat transfer, complete enclosures ($S_v = 0$), fully open enclosures ($S_v = 1$) and enclosures with $0 < S_v < 1$ are also examined. For complete enclosures, computational results are presented for $Ra = 2 \times 10^7$ (Figs. 6(a)–(d)) and are compared with the experimental flow visualization image (Fig. 6(e)). Inside the enclosure, a strong flow recirculation, also seen in Fig. 6(e), is created in the upper corner when radiation is included, which is not seen without radiation. When radiation is included, the interaction between the inertia of the descending flow along the right wall and the buoyancy induced by the right wall, which is radiatively heated by the heat source and other enclosure walls, results in the forma-

tion of the observed recirculation. External to the enclosure, a strong boundary layer flow along the right wall is in both Figs. 6(b) and (d). Inclusion of radiation produces a pronounced drop in the right and top wall temperatures. The resulting plume above the enclosure in Fig. 6(d) has a lower maximum velocity and larger spatial extent than in Fig. 6(b) when radiation is not included.

Effects of Substrate Thermal Conductivity. Substrate thermal conductivity ratio R_s has been demonstrated to play a significant role in conjugate heat transfer involving conduction and natural convection (e.g., Wroblewski and Joshi, 1993; Dehghan and Behnia, 1996). The role of R_s in the vented enclosures is examined by focusing on the heat transfer in Fig. 7. Two levels of R_s are employed: $R_s = 7.3$ and 667, corresponding to plexiglass and ceramic, respectively, for $S_v = 0.4$ and $Ra = 2 \times 10^7$. For $R_s = 7.3$, when radiation is neglected, Fig. 7(a), the highest Nu_c are seen around the component ($2.4 < Y < 2.6$). These values decrease rapidly away from the component in both Y and Z directions. Above the component, negative values of the convective Nusselt number Nu_c defined by

$$Nu_c = \frac{1}{\theta_{sur}} \left(-\frac{\partial \theta}{\partial X} \right)_{sur} \quad (18)$$

where

$$\theta_{sur} = \frac{(\delta X_s/R_s)\theta_f + (\delta X_f/R_f)\theta_s}{(\delta X_s/R_s) + (\delta X_f/R_f)} - \frac{Q_r}{R_s/\delta X_s + R_f/\delta X_f} \quad (19)$$

indicate substrate heating by the plume. When radiation is included, Fig. 7(b), the response is qualitatively similar, with reduced values of Nu_c . Above the heat source larger negative values of Nu_c are found due to the heating of the substrate by radiative interactions.

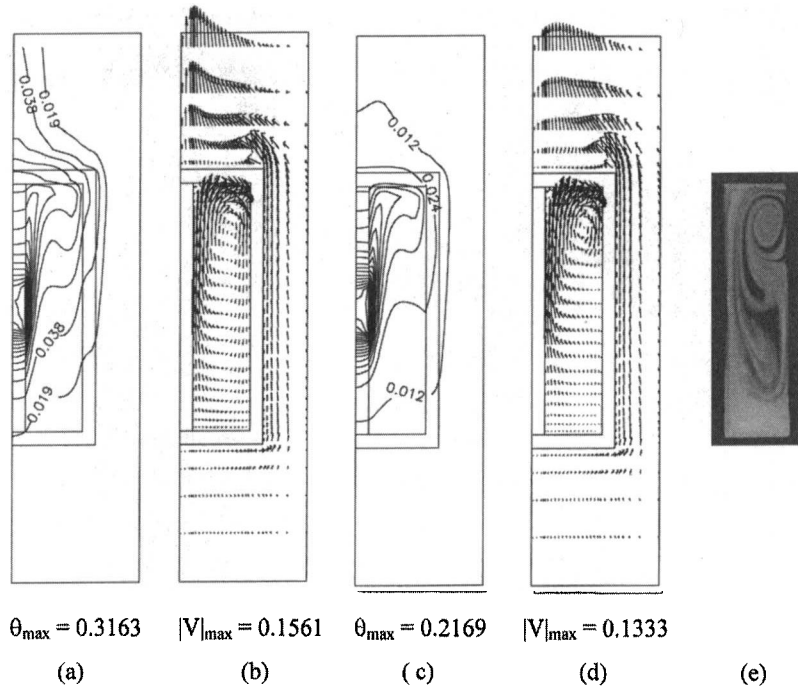


Fig. 6 Radiation effects on flow and temperature fields in a complete enclosure ($S_v = 0$) for $Ra = 2 \times 10^7$; (a), (b) without radiation; (c), (d) with radiation at $\epsilon = 1$; (e) flow visualization results with radiation (exposure time: 2 sec)

For $R_s = 667$, the substrate temperature is much more uniform (only about 20 percent drop across the region, compared to almost 100 percent drop for $R_s = 7.3$). The normalized maximum temperature for this R_s is only about $\frac{1}{5}$ of that for $R_s = 7.3$ (when radiation effects are included for both cases). In Figs. 7(c) and (d) the Nu_c values are seen to be positive even above the component due to the substrate conduction. The inclusion of radiation transport in Fig. 7(d) results in reduced values of Nu_c at all locations, compared to Fig. 7(c). The two peaks seen in Fig. 7(c) are a result

of surface temperature drops encountered near the substrate corners due to conduction into the adjoining colder walls. When radiative interactions are included, Fig. 7(d), the tendency is for the substrate to achieve a more uniform temperature. This causes a greater drop in the temperature near the top of the substrate, than at the bottom, compared to the no-radiation case. As a result, in Fig. 7(d) the peak in Nu_c remains near the bottom, but is considerably reduced near the top of the substrate.

Effect of Substrate Emissivity. The effect of substrate emissivity variation on the overall heat transfer is examined. Emissivities of all the remaining surfaces are kept fixed at $\epsilon = 1$. The results are presented in terms of average convection and radiation heat transfer coefficients, Nusselt numbers, surface temperatures, and mass outflow rates, defined as follows:

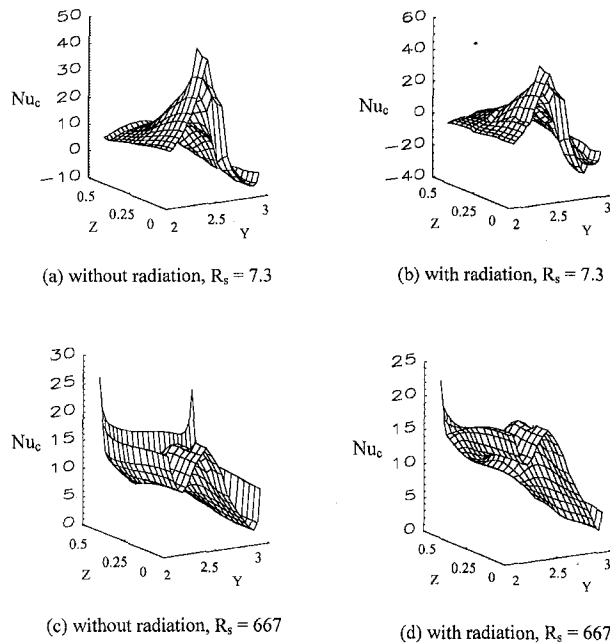


Fig. 7 Local convection Nu_c on the substrate for $S_v = 0.4$, $Ra = 2 \times 10^7$ and variable R_s with and without radiation. The component is defined by $0 \leq Z \leq 0.1$ and $2.4 \leq Y \leq 2.6$.

$$\bar{h}_c = \frac{k_f}{A_s \bar{\theta}_{sur} L} \iint_{A_s} \left(-\frac{\partial \theta}{\partial X} \right)_{sur} dYdZ \quad (20)$$

$$\bar{h}_r = \frac{1}{A_s \bar{\theta}_{sur} T_{ref}} \iint_{A_s} q_r'' dYdZ \quad (21)$$

$$\bar{h}_t = \bar{h}_c + \bar{h}_r \quad (22)$$

$$\overline{Nu}_c = \frac{1}{A_s \bar{\theta}_{sur}} \iint_{A_s} \left(-\frac{\partial \theta}{\partial X} \right)_{sur} dYdZ \quad (23)$$

$$\overline{Nu}_r = \frac{1}{A_s \bar{\theta}_{sur} T_{ref}} \iint_{A_s} \frac{q_r'' L}{k_f} dYdZ \quad (24)$$

$$\overline{Nu}_t = \overline{Nu}_c + \overline{Nu}_r \quad (25)$$

$$\begin{aligned} q_t &= q_r + q_c = \bar{h}_t A_s \bar{\theta}_{sur} L^2 T_{ref} \\ &= \bar{h}_r A_s \bar{\theta}_{sur} L^2 T_{ref} + \bar{h}_c A_s \bar{\theta}_{sur} L^2 T_{ref} \end{aligned} \quad (26)$$

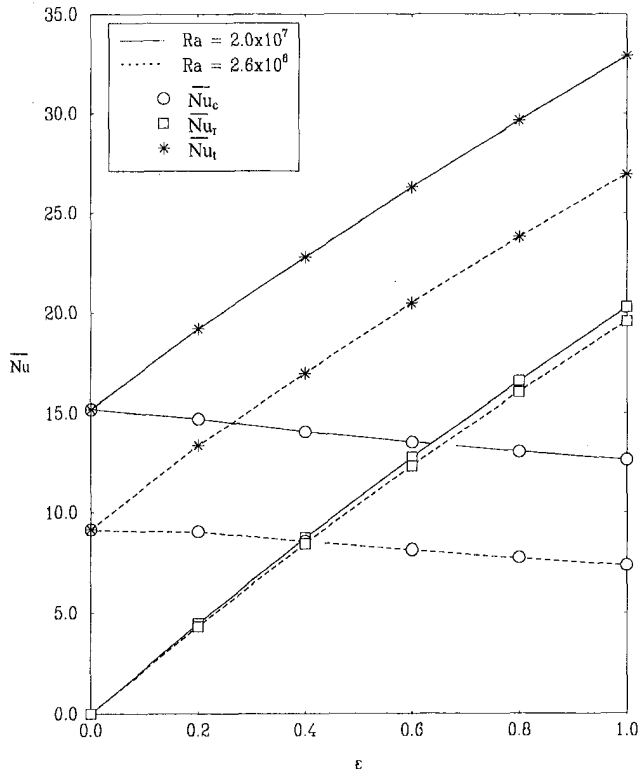


Fig. 8 Profiles of Nu at various ϵ for two Ra

$$\bar{\theta}_{\text{sur}} = \frac{1}{A_s} \iint_{A_s} \theta_{\text{sur}} dYdZ \quad (27)$$

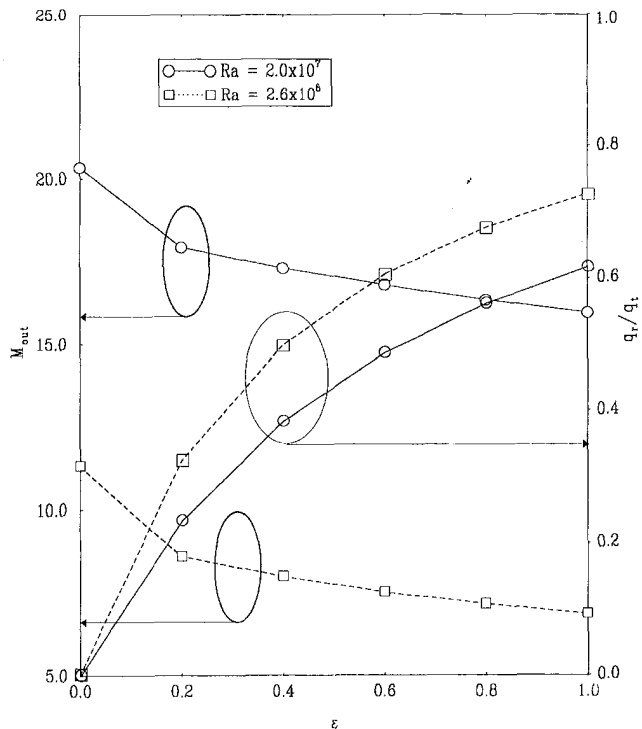


Fig. 9 Mass outflow rate M_{out} through the opening and relative radiation heat transfer rate q_r/q_t on the substrate at various ϵ for $S_v = 0.4$ and two Ra

$$M_{\text{out}} = \iint_{A_p} URa^{1/2} dYdZ \quad (28)$$

where

$$U = U_{x=H} \text{ for } U_{x=H} > 0$$

$$U = 0 \text{ for } U_{x=H} \leq 0.$$

In the definition of surface temperature θ_{sur} , θ_f and θ_s are the fluid and solid temperatures at the nodes closest to the interface, $R_f = 1$, and δX_s and δX_f are the respective distances normal to this interface. When the component is involved, the subscript "s" is replaced by "cp" and the corresponding values of the component are used.

Figure 8 shows the relative influences of convection and radiation on the average Nusselt numbers on the substrate. It can be seen that the convection Nusselt number \bar{Nu}_c is decreased when radiation is included. This is consistent with the weaker flow and resulting thickening of the boundary layer along the substrate when radiation is considered. As expected, with increase in ϵ , radiation Nusselt number \bar{Nu}_r is elevated. The total heat transfer is enhanced when ϵ increases, even though the convection contribution is reduced. This is true for both levels of Ra considered. This behavior is in contrast to that found by Dehghan and Behnia (1996) for a top-vented enclosure with insulated boundaries. There the incoming ambient flow through the opening was warmed up by the hotter enclosure walls, resulting in a larger reduction in convective heat transfer compared to the increase in heat transfer due to radiation.

It is found that \bar{Nu}_r is not dependent on Ra as significantly as \bar{Nu}_c . For example, when Ra changes from 2.0×10^7 to 2.6×10^6 for $\epsilon = 1$, \bar{Nu}_c drops 42 percent, while \bar{Nu}_r decreases only 3.5 percent. Also, it is observed that \bar{Nu}_r and \bar{Nu}_t increase in a similar fashion as ϵ changes from 0 to 1, emphasizing the significance of radiation in this combined heat transfer process.

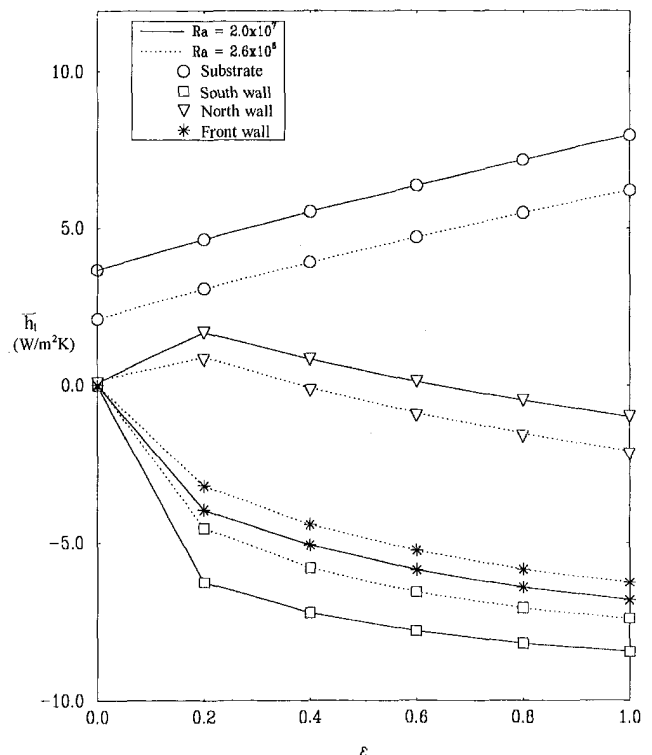


Fig. 10 Average heat transfer coefficient including radiation and natural convection on each wall for $S_v = 0.4$ and two Ra

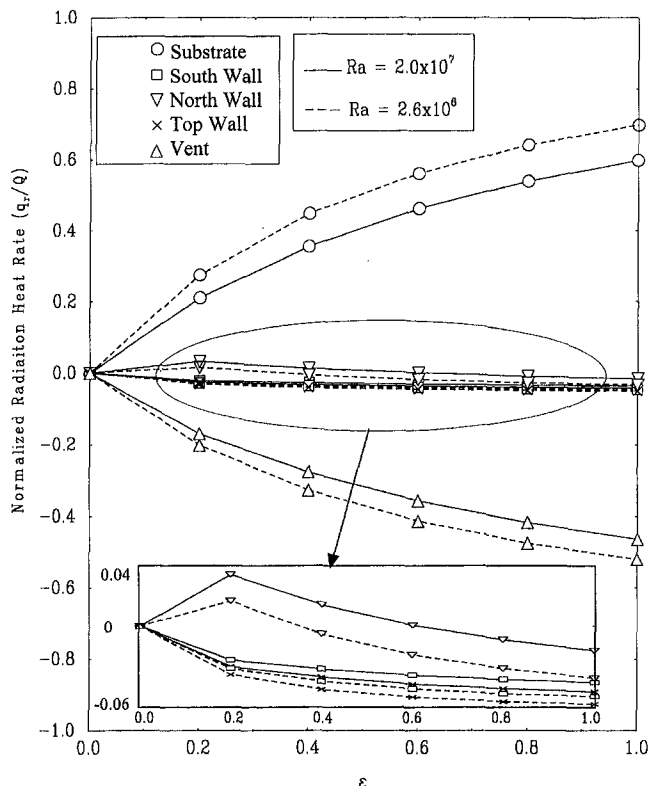


Fig. 11 Normalized radiation heat transfer rate on each wall at various ϵ for $S_v = 0.4$ and two Ra

The net mass outflow rate through the opening is presented in Fig. 9 as a function of substrate emissivity. For fixed Ra , M_{out} decreases when ϵ increases, as a result of the weakened convection. For fixed ϵ , M_{out} decreases when Ra decreases, due to the reduced buoyancy. Figure 9 also shows the relative contribution of radiation in the overall heat removal from the surface of the substrate. The fraction of heat loss as radiation, is increased from 0 to about 0.6 for $Ra = 2.0 \times 10^7$ and from 0 to 0.72 for $Ra = 2.6 \times 10^6$ when ϵ changes from 0 to 1. It is noticed that radiation is more important for lower Ra , evidenced by the change of the maximum component temperature. A 29 percent drop occurs in this for $Ra = 2.0 \times 10^7$, and 35 percent drop for $Ra = 2.6 \times 10^6$, when ϵ changes from 0 to 1.

The average heat transfer coefficient \bar{h}_i on each internal wall is displayed in Fig. 10. A negative value of \bar{h}_i implies a net heat inflow into the wall. On the substrate, south, and front walls, heat transfer is stronger compared to the north wall. The overall heat transfer intensity (either heating or cooling) is increased with the inclusion of radiation. It is seen that \bar{h}_i is close to 0 on all the walls except the substrate for pure convection and conduction. However, \bar{h}_i is well below 0 when $\epsilon = 1$, especially, on the south and top walls, indicating that radiation and convection heat up the other walls while the substrate is cooled down. It is also found that the north wall is cooled when ϵ is small and is heated for ϵ above about 0.5, as a result of the interaction between natural convection and radiation.

Figure 11 displays the normalized radiation heat transfer rate on each wall and through the vent. It is revealed that most of the heat emitted from the substrate escapes through the vent, while a small amount is absorbed by the other walls. This is to be expected for the low value of $R_s = 7.3$, for which the thermal spreading is relatively weak around the component footprint. In the zoomed view, it is seen that the normalized radiation heat rate follows a similar trend as the heat transfer coefficient displayed in Fig. 10, on the south, north, and front walls.

Conclusions

Combined conduction, natural convection and radiation in a three-dimensional vented enclosure is investigated. The results show that radiation-convection interactions are strongly dependent on venting configuration. For a side-vented arrangement, as in the present study, natural convection is weakened by radiation, however, the overall heat transfer is enhanced. The maximum increase of \bar{Nu} , is 194 percent for $Ra = 2.6 \times 10^6$ and 117 percent for $Ra = 2.0 \times 10^7$, accompanied by 35 percent and 29 percent decreases in component temperatures respectively. In comparison to the conjugate convection and conduction calculations, including radiation reduces the temperature differences between different walls and also leads to more uniform thermal distributions on them. Radiant heating of walls results in distinctive flow cells. The radiation from the substrate at $\epsilon = 1$ and $Ra = 2.6 \times 10^6$ accounts for 72 percent of the total heat transfer rate, showing the significant contribution of radiation to the overall heat transfer. It is also found that radiation plays a more critical role at lower Ra for the present system, by reducing temperatures more substantially. Radiative heat transfer to the north wall exhibits a maximum with substrate emissivity. In discretely heated configurations, the conductive spreading on the substrate is reduced when radiation is included. From a practical standpoint, unlike the top-vented configuration, side venting does provide a means to increase the overall heat transfer rate.

Acknowledgments

The authors acknowledge the support for this study by the Maryland Industrial Partnerships (MIPS) Program at the University of Maryland.

References

- Balaji, C., and Venkateshan, S. P., 1993, "Interaction of Surface Radiation With Free Convection in a Square Cavity," *International Journal of Heat and Fluid Flow*, Vol. 14, No. 3, pp. 260-267.
- Balaji, C., and Venkateshan, S. P., 1994a, "Correlation for Free Convection and Surface Radiation in a Square Cavity," *International Journal of Heat and Fluid Flow*, Vol. 15, No. 3, pp. 249-251.
- Balaji, C., and Venkateshan, S. P., 1994b, "Interaction of Radiation With Free Convection in an Open Cavity," *International Journal of Heat and Fluid Flow*, Vol. 15, No. 4, pp. 317-324.
- Beckermann, C., and Smith, T. F., and Pospichal, B., 1994, "Use of a Two-dimensional Simulation Model in the Thermal Analysis of a Multi-Board Electronic Module," *ASME JOURNAL OF HEAT TRANSFER*, Vol. 116, pp. 126-133.
- Dehghan, A. A., 1994, "Natural Convection in a Discretely Heated Open Cavities," Ph.D. thesis, The University of New South Wales.
- Dehghan, A. A., and Behnia, M., 1996, "Combined Natural Convection-Conduction and Radiation Heat Transfer in a Discretely Heated Open Cavity," *ASME JOURNAL OF HEAT TRANSFER*, Vol. 118, pp. 56-64.
- Fusegi, T., Hyun, J.M., Kuwahara, K., and Farouk, B., 1991, "A Numerical Study of Three Dimensional Natural Convection in Differentially Heated Cubic Enclosure," *Int. J. Heat Mass Transfer*, Vol. 34, pp. 1543-1557.
- Howell, J. R., 1982, *A Catalog of Radiation Configuration Factors*, McGraw-Hill, New York, pp. 96-99.
- Kassem, M., 1993, "Analysis of Radiation-Natural Convection Interactions in 1-g and low-g Environment Using the Discrete Exchange Factor Method," *International Journal of Heat and Mass Transfer*, Vol. 36, No. 1, pp. 4141-4149.
- Kline, S. J., and McClintock, F. A., 1953, "Describing Uncertainties in Single-Sample Experiments," *Mechanical Engineering*, Vol. 75, Jan., pp. 3-8.
- Lage, J. L., Lim, J. S., and Bejan, A., 1992, "Natural Convection With Radiation in a Cavity With Open Top End," *ASME JOURNAL OF HEAT TRANSFER*, Vol. 114, pp. 479-486.
- Lasance, C. J. M., and Joshi, Y., 1998, "Thermal Analysis of Natural Convection Electronic Systems-Status and Challenges," *Advances in Thermal Modeling of Electronic Components and Systems*, Vol. 4, A. Bar-Cohen and A. D. Kraus, eds., ASME, New York, Chapter 1, pp. 1-177.
- Mallinson, G. D., and de Vahl Davis, G., 1977, "Three-Dimensional Natural Convection in a Box, a Numerical Study," *J. Fluid Mech.*, Vol. 83, pp. 1-31.
- Moutsoglou, A., Rhee, J. H., and Wong, Y. H., 1992, "Natural Convection-Radiation Cooling of a Vented Channel," *International Journal of Heat and Mass Transfer*, Vol. 35, No. 11, pp. 2855-2863.
- Patankar, S. V., 1980, *Numerical Heat Transfer and Fluid Flow*, Hemisphere and McGraw-Hill, New York.
- Smith, T. F., Beckermann, C., and Weber, S. W., 1991, "Combined Conduction, Natural Convection, and Radiation Heat Transfer in an Electronic Chassis," *ASME JOURNAL OF HEAT TRANSFER*, Vol. 113, pp. 382-391.
- Wroblewski, D., and Joshi, Y., 1993, "Computations of Liquid Immersion Cooling for a Protruding Heat Source in a Cubic Enclosure," *Int. J. Heat Mass Transfer*, Vol. 36, No. 5, pp. 1201-1208.

Enhanced Heat Transfer Characteristics of Viscous Liquid Flows in a Chevron Plate Heat Exchanger

A. Muley¹
Assoc. Mem. ASME

R. M. Manglik²
e-mail: Raj.Manglik@uc.edu
Mem. ASME

H. M. Metwally

Department of Mechanical, Industrial
and Nuclear Engineering,
University of Cincinnati,
Cincinnati, OH 45221-0072

Steady-state heat transfer and pressure drop data for single-phase viscous fluid flows ($2 \leq Re \leq 400$) in a single-pass U-type counterflow plate heat exchanger (PHE) with chevron plates are presented. With vegetable oil as test fluid ($130 < Pr < 290$), three different plate arrangements are employed: two symmetric ($\beta = 30 \text{ deg}/30 \text{ deg}$ and $60 \text{ deg}/60 \text{ deg}$) and one mixed ($\beta = 30 \text{ deg}/60 \text{ deg}$). The effects of chevron angle β , corrugation aspect ratio γ , and flow conditions (Re , Pr , μ/μ_w) on Nu and f characteristics of the PHE are delineated. The results show a rather complex influence of plate surface corrugations on the enhanced thermal-hydraulic behavior. Relative to the performance of equivalent flat-plate packs, chevron plates sustain up to 2.9 times higher heat transfer rates on a fixed geometry and constant pumping power basis, and require up to 48 percent less surface area for the fixed heat load and pressure drop constraint.

Introduction

Thermal processing and manufacturing in the chemical, foods, pharmaceutical, hygiene products, and biochemical industries invariably involve heating and cooling of highly viscous fluid media. These fluids tend to flow in the low Reynolds number regime, inherently have relatively low heat transfer coefficients, and are often temperature sensitive and prone to thermal degradation in the presence of large temperature differences. In recent times, plate heat exchangers (PHEs) have found increasing usage in such applications, primarily due to their features that promote enhanced heat transfer, and provide for the flexibility in altering their unit thermal size with ease, close approach temperature operation, and mitigation of thermal degradation of the process fluid. The reviews by Shah and Focke (1988), Manglik and Muley (1993), and Manglik (1996) address some aspects of their construction, performance, and applications.

The thermal-hydraulic performance of PHEs is strongly influenced by the surface-corrugation geometry of the plates employed in them. Typical characteristics of the more commonly used chevron plates are illustrated in Fig. 1. The corrugation inclination angle β , wavelength λ , depth b , and profile of waviness are the primary determinants of their surface geometry's influence on the heat transfer and pressure drop (Gaiser and Kottke, 1998; Manglik, 1996; Focke et al., 1985). Plates with $\beta = 30 \text{ deg}$ or 60 deg are usually stacked together in either a symmetric or mixed arrangement as shown in Fig. 1(a). Generally, both heat transfer coefficients and flow friction losses increase with higher β chevron plates. The enhanced heat transfer performance is primarily due to the increased effective heat transfer area (area a-b-c-d-e-f-a in Fig. 1(a) that includes the main chevron area as well as the triangular distribution and collection areas), small-hydraulic-diameter flow channels, disruption and reattachment of boundary layers, and swirl or vortex-flow generation.

The literature on the performance of PHEs for viscous fluid flow

heat transfer applications is rather sparse (Manglik, 1996). For a limited range of laminar flow conditions, Nusselt number and isothermal friction factor results for chevron plates are reported by Savostin and Tikhonov (1970), Maslov and Kovalenko (1972), Focke et al. (1985), Talik et al. (1995), Wanniarachchi et al. (1995), and Thonon et al. (1995). In each of these studies, the chevron or corrugation inclination angle β is found to be the primary surface geometry variable that affects the thermal-hydraulic behavior; both Nu and f increase significantly with increasing β . The results, however, are seen to disagree considerably with each other and present a rather wide performance envelope for typical operating conditions (Manglik, 1996; Muley and Manglik, 1998). The effective usage of PHEs requires more reliable performance prediction tools with a larger database, and this is addressed in the present study.

In this paper, new experimental data for heat transfer and pressure drop in laminar flows in a PHE with two symmetric ($\beta = 30 \text{ deg}/30 \text{ deg}$, and $60 \text{ deg}/60 \text{ deg}$) and one mixed-plate ($\beta = 30 \text{ deg}/60 \text{ deg}$) arrangements are presented for the cooling of the test fluid (vegetable oil³). The influence of chevron angle β on Nu and f is delineated, the data are compared with previously reported results from the literature, and flow mechanisms that promote enhanced heat transfer are identified. Also, for the associated heat transfer enhancement, a quantitative evaluation is made for two different application constraints that are commonly employed for optimizing heat exchangers used in the process industry—fixed geometry and constant pumping power, and fixed heat duty and constant pressure drop.

Experimental Apparatus and Procedure

The experimental apparatus consists of two PHEs (a heat source and a heat sink) arranged in series in a closed loop, as shown in Fig. 2. A variable speed moyno pump (progressive cavity pump) circulates the process fluid—vegetable oil, a Newtonian fluid, in the present study—which was first heated in one PHE by condensing low-pressure steam and then cooled in second PHE (the test unit) by means of utility water supply. A micromotion flow meter, differential pressure transducers, copper-constantan (T-type, 30-gauge) thermocouples at locations indicated in Fig. 2, and a

¹ Present address: Aerospace Equipment Systems, Allied Signal, Inc., Torrance, CA 90504-6099.

² To whom correspondence should be addressed.

Contributed by the Heat Transfer Division for publication in the JOURNAL OF HEAT TRANSFER. Manuscript received by the Heat Transfer Division, Dec. 9, 1998; revision received, June 25, 1999. Keywords: Augmentation, Enhancement, Forced Convection, Heat Transfer, Heat Exchangers, Processing. Associate Technical Editor: C. Beckermann.

³ A Newtonian fluid, that is commonly processed in PHEs.

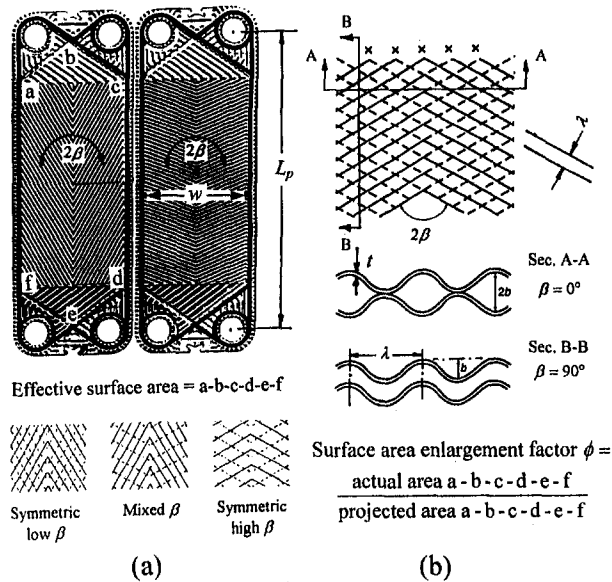


Fig. 1 Chevron plates: (a) different chevron angle plates and their stack arrangements, and (b) geometrical features of surface corrugations

rotameter for cooling-water flow rates provided the primary measurements. The PHEs and significant portions of the inlet/outlet piping were well insulated to reduce heat losses. Also, static mixers (Kenics fluid-mixing elements) were installed in the outlet ports upstream of the thermocouple probes to ensure accurate "mixed-mean" or bulk-fluid temperature measurements. The inlet/outlet thermocouple probes were placed close to the PHE ports in well-insulated pipe sections, and temperature measurements were periodically made by traversing them in the pipe cross section to check and confirm the accuracy of recorded bulk-mean values. All data were obtained under steady-state conditions (confirmed by the invariant fluid outlet temperatures over a 25~30 minutes period) with close energy balances (less than ± 5 percent difference between the measured Q for the two fluid streams), and were recorded on a computerized data-acquisition system. Extended details of the setup, instrumentation, and operating procedure can be found in Muley and Manglik (1998).

Nomenclature

A_c = channel flow cross section area, m^2
 A = effective or actual heat transfer surface area, m^2
 b = corrugation depth, Fig. 1(b), mm
 C = heat capacity rate, $=\dot{m}c_p$, W/K
 C^* = ratio of heat capacity rates, $=C_{min}/C_{max}$
 c_p = specific heat, J/kgK
 d_e = equivalent diameter, $=2b$, mm
 E = frictional pumping power, W/ m^2
 f = Fanning friction factor, Eq. (9)
 h = heat transfer coefficient, W/ m^2 K
 k = thermal conductivity, W/mK
 L = effective projected flow length of the corrugated plate surface, m
 L_p = plate length between ports, Fig. 1(a), m
 \dot{m} = mass flow rate, kg/s
 N = number of interplate channels for each fluid stream
 Nu = Nusselt number, $=hd_e/k$

NTU = number of transfer units, Eq. (4)
 Δp = pressure drop, N/ m^2
 Δp_{core} = pressure drop in the corrugated core section of PHE, N/ m^2
 Δp_{port} = pressure drop in the circular inlet/out ports of the plate pack, N/ m^2
 Pr = Prandtl number, $=\mu c_p/k$
 Q = heat load, Eqs. (2) and (6), W
 Re = Reynolds number, $=(\dot{m}d_e)/(NA_c\mu)$
 t = plate thickness, mm
 ΔT_{lm} = log mean temperature difference, Eq. (1b), K
 T = temperature, K
 U = overall heat transfer coefficient, Eqs. (4b)–(5), W/ m^2 K

Greek Symbols

β = corrugation inclination angle relative to flow direction, Fig. 1

γ = corrugation profile aspect ratio, $=2b/\lambda$
 ϵ = effectiveness of the heat exchanger, Eq. (3)
 λ = wavelength of surface corrugation, Fig. 1(b), mm
 μ = dynamic viscosity, kg/ms
 ρ = fluid density, kg/ m^3
 ϕ = ratio of effective to projected area of corrugated plate, Fig. 1

Subscripts

b = at bulk temperature
 c = cooling-water stream
 ch = pertaining to chevron plate
 h = hot process fluid stream
 i = inlet fluid condition
 o = outlet fluid condition
 pp = pertaining to parallel-plate
 $plate$ = of the plate material
 w = at plate wall conditions

The test PHE (cooling unit) was configured in a single-pass, U-type (inlet/outlet ports for the two fluid streams on the same end), counterflow arrangement with 12 to 24 chevron plates. Chevron plates made of stainless steel with $\beta = 30$ deg and 60 deg were used in two symmetric (30 deg/30 deg and 60 deg/60 deg) and one mixed (30 deg/60 deg, $\beta_{avg} = 45$ deg) arrangements. The measured plate-surface corrugation profiles and other geometrical details are given in Fig. 3.

The primary measurements consist of the flow rates of each fluid stream (hot vegetable oil and cooling utility water), their inlet and outlet temperatures, and the pressure drop in the process stream between the inlet and outlet of the heat exchanger. The channel flow Reynolds number is based on the equivalent diameter d_e ($=2b$), and all fluid properties were calculated at the bulk-mean temperature given by

$$T_{c,b} = (T_{c,i} + T_{c,o})/2, \quad \text{and} \quad T_{h,b} = (T_{c,b} + \Delta T_{lm}) \quad (1a)$$

where

$$\Delta T_{lm} = [(T_{h,i} - T_{c,o}) - (T_{h,o} - T_{c,i})] / \ln [(T_{h,i} - T_{c,o}) / (T_{h,o} - T_{c,i})] \quad (1b)$$

In all test runs, the cooling-water flow rates were maintained such that $C_c > C_h$ so as to ensure that the process stream provided the dominant thermal resistance. The values of C^* ($=C_h/C_c$ in this case) ranged from 0.11 to 0.60, and $T_{h,b}$ calculated by Eq. 1(a) thus takes into account nonlinear temperature variations of the hot process stream along the length of PHE. The steady-state energy balance on the process and cooling fluids,

$$Q = [\dot{m}c_p(T_i - T_o)]_h = [\dot{m}c_p(T_o - T_i)]_c \quad (2)$$

was maintained within ± 5 percent, after accounting for all heat losses, and the average of Q_h and Q_c was taken as the total heat load.

From the overall thermal effectiveness of the heat exchanger, based on the average heat load,

$$\epsilon = [Q/C_{min}(T_{h,i} - T_{c,i})] \quad (3)$$

the NTU for the pure counterflow arrangement was calculated as

$$NTU = [1/(1 - C^*)] \ln [(1 - \epsilon C^*) / (1 - \epsilon)] \quad (4a)$$

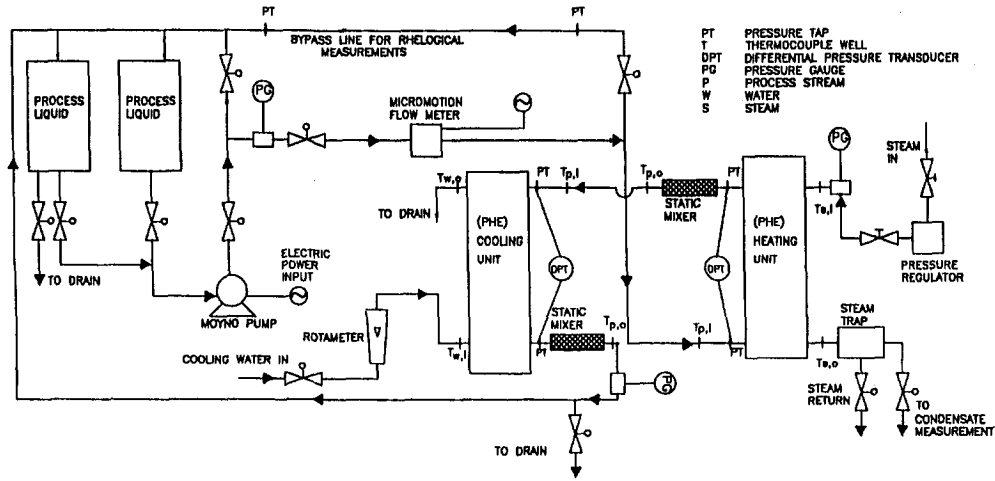


Fig. 2 Schematic of experimental test facility

where $C^* = C_{\min}/C_{\max}$; as noted above, for all the test runs in the present experiments, $C_h = C_{\min}$. Also, 12 to 24 plates were used in these experiments in order to cover a wide range of Re , and the influence of small number of thermal plates on NTU, as suggested by Shah and Focke (1988), was less than 0.5 percent. This was so because C^* , $(\epsilon \cdot C^*)$, and $(C^* \cdot NTU)$ values were relatively small in all data sets, and the plate effects are significant only when the converse is true (Manglik, 1999). The overall heat transfer coefficient was thus determined from

$$U = (C_{\min} NTU)/A \quad (4b)$$

and the heat transfer coefficient for the process fluid stream was then calculated from the thermal resistance summation

$$(1/h_h) = (1/U) - (t/k_{\text{plate}}) - (1/h_c) \quad (5)$$

Note that the heat transfer area A is the same on both sides of the plate. However, in order to calculate h_h from Eq. (5), the cooling-water-side heat transfer coefficient h_c is needed. This was determined from "calibration" equations that were devised on the basis of extended experiments employing the modified Wilson Plot

technique (Shah, 1990; Manglik and Bergles, 1991). This modification of the classical Wilson Plot method (Wilson, 1915) essentially incorporates and accounts for variable-fluid-property effects. The calibration results for calculating h_c for $\beta = 30$ deg/30 deg, 30 deg/60 deg, and 60 deg/60 deg chevron plate arrangements can be found in Muley and Manglik (1997, 1998), and are not presented here for brevity. In all subsequent experiments, the cooling-water-side conditions were always maintained within the range of Wilson plot data (turbulent flows with $Re > 1000$). Finally, the average wall temperature of the plate was determined iteratively from the heat-and-resistance balance

$$Q = h_h A (T_b - T_w)_h = (k_w A/t) (T_{w,h} - T_{w,c}) = h_c A (T_w - T_b)_c \quad (6)$$

From the measured overall pressure drop across the PHE in the process stream, the core pressure drop can be obtained from

$$\Delta p_{\text{core}} = \Delta p_{\text{measured}} - \Delta p_{\text{port}} - \Delta p_{\text{pipe}} \quad (7)$$

Here, based on an empirical equation (Shah and Focke, 1988; Kays, 1950) and the mean port velocity, port losses were estimated by

$$\Delta p_{\text{port}} = 1.5(\rho V_{\text{port}}^2/2) \quad (8)$$

The pressure loss in small inlet/outlet port-pipe sections of the PHE (Δp_{pipe}) was estimated on the basis of smooth tube friction factor and pipe flow velocity. Thus, for the shear loss within the corrugated passages (including the distribution and collection channels), the Fanning friction factor was calculated as

$$f = (\rho d_e \Delta p_{\text{core}}) / [2L(\dot{m}/NA_c)^2] \quad (9)$$

The measurements were made for isothermal conditions, with fluid properties calculated at the bulk-mean flow temperature.

Finally, for the measured and calculated data presented in this study, the experimental uncertainties were determined by the procedure outlined by Moffat (1988). The maximum errors in the primary measurements of \dot{m} , Δp , ΔT_{in} , and Q for the process flow stream were ± 2.3 percent, ± 7.6 percent, ± 3.5 percent, and ± 7.8 percent, respectively. For \dot{m} and Q measurements for the cooling water, these values were ± 7.5 percent and ± 7.6 percent, respectively. Based on this measurement uncertainty and the propagation of error analysis, the maximum uncertainties in Re , f , and Nu were, respectively, ± 7.6 percent, ± 8.6 percent, and ± 11.0 percent. Also, as mentioned earlier, the energy balance was within ± 5.0 percent for the majority of the heat transfer data. Extended

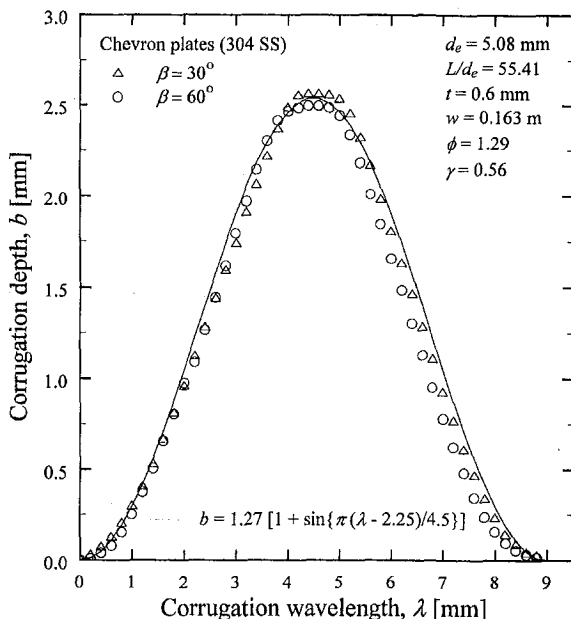


Fig. 3 Geometric details of plate surface corrugations

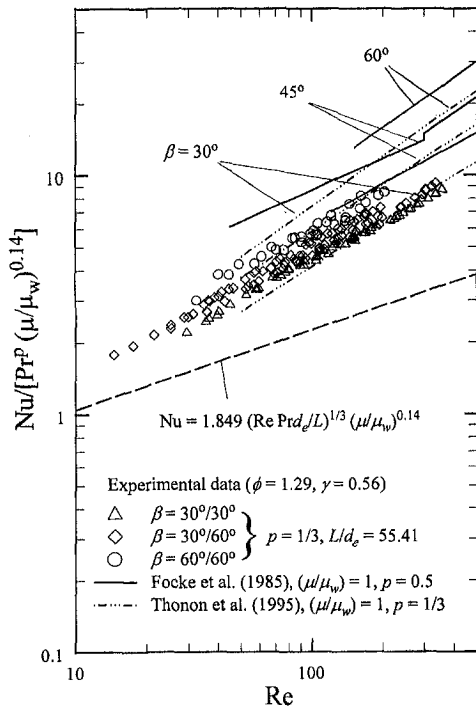


Fig. 4 Variation of Nusselt number with chevron angle β and comparison with results reported in the literature

details of the instrumentation precision, error estimation, and uncertainty analysis can be found in Muley and Manglik (1998).

Results and Discussion

The experimental data for Nu and isothermal f , for the three chevron-plate arrangements ($\beta = 30$ deg/30 deg, 30 deg/60 deg, and 60 deg/60 deg), presented in Figs. 4 and 5, respectively, for cooling of hot vegetable oil ($130 < \text{Re} < 290$, $0.118 < \mu/\mu_w < 0.393$), cover a wide laminar flow range ($2 < \text{Re} < 400$). In order to evaluate the heat transfer enhancement due to chevron plates, the performance of an equivalent (same d_e) flat-plate pack predicted by (Kakaç et al., 1987)

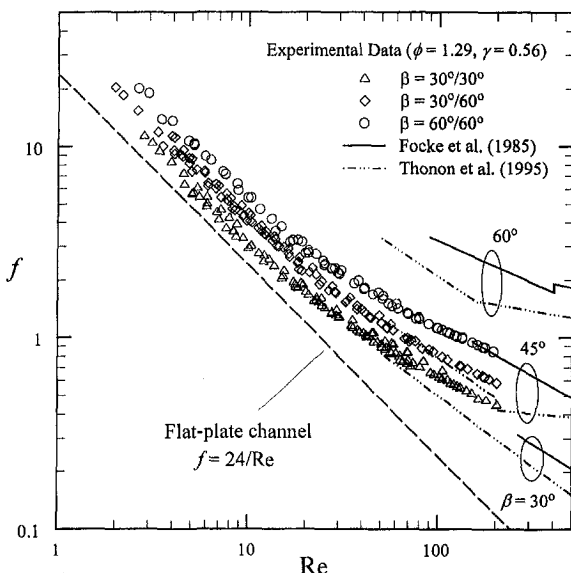


Fig. 5 Variation of isothermal friction factor with chevron angle β and comparison with results reported in the literature

$$\text{Nu} = 1.849[(d_e/L) \text{Re} \text{Pr}]^{1/3}(\mu/\mu_w)^{0.14}, \quad (L/d_e) = 55.41$$

$$f = (24/\text{Re}) \quad (10)$$

is also graphed in each figure. The enhanced performance is clearly evident with up to three times higher Nu in chevron-plate passages, and, for the same Re, higher Nu is obtained with increasing β . This reflects the increased intensity of swirl or secondary flows generated in the larger β chevron plates. However, there is a correspondingly higher pressure-drop penalty as well, with up to 6.6 times higher f than in an equivalent flat-plate duct.

The f -Re data of Fig. 5 provide some interesting evidence of the interplay between the flow conditions and plate surface corrugations on the enhancement mechanisms. With flows in the $15 < \text{Re} < 25$ region, the data show a distinct change in the log-linear slope for all three chevron plates. This is indicative of the onset and intensification of swirling flows that are induced by the wavy, crisscrossing flow passages (obtained from the mating of corrugated chevron plates) when $\text{Re} > 25$. The corresponding enhanced heat transfer data for this swirl-flow regime are presented in Fig. 4. In lower flow rates ($\text{Re} < 25$), however, there appears to be no swirl mixing, and the higher f in Fig. 5 are primarily due to the larger convoluted flow path; with $\phi = 1.29$, a 29 percent longer effective flow path is obtained. In this regime, the experimental f data exhibit the classical straight duct, fully developed laminar flow behavior.

A comparison of the Nu and f data with the rather sparse results of Thonon et al. (1995), and Focke et al. (1985) is also given in Figs. 4 and 5. Note that the latter are only for symmetric plate arrangements ($\beta = 30$ deg/30 deg, 45 deg/45 deg, and 60 deg/60 deg), whereas in the present study a mixed-plate arrangement is used for the second case ($\beta = 30$ deg/60 deg $\Rightarrow \beta_{\text{avg}} = 45$ deg). There is fair agreement between the new Nu and f data and those of Thonon et al. (1995) for $\beta = 30$ deg and 45 deg, but their results for $\beta = 60$ deg plates are considerably higher. The Nu and f results of Focke et al. (1985) that are based on mass transfer experiments with simulated scaled-up plate surfaces are significantly higher for all β cases. Given that neither of these two studies has compared their own data with any other results reported in the literature⁴, it is rather difficult to explain these differences. However, among several factors, the differences in the chevron-plate corrugation geometry in these studies might be primarily responsible (Muley and Manglik, 1999, 1997; Ding and Manglik, 1996; Gaiser and Kottke, 1990). For example, the surface enlargement factor $\phi = 1.464$ ($\gamma = 1$) in the mass transfer data of Focke et al. (1985) with scaled-up surfaces, as compared with $\phi = 1.29$ ($\gamma = 0.56$) in the present experiments. The deeper grooves ($\gamma = 1$) of the former would tend to induce greater swirl mixing, thereby producing higher Nu and f . Additionally, different Pr exponents (0.5 in the case of Focke et al. and $\frac{1}{3}$ in the present data), and absence of a viscosity-variation correction factor could account for part of the deviations. In the latter case, for typical viscous liquids ($\text{Pr} \sim 185$), a variation of $0.80 > (\mu/\mu_w) > 0.20$ could result in a 3 percent to 20 percent difference in Nu.

In order to obtain a clear picture of the β effects on the performance of a chevron-plate PHE, variations in $[\text{Nu}(\mu/\mu_w)^{-n} \text{Pr}^{-p}]$ and f for typical viscous flow condition of $\text{Re} = 200$ and corrugation aspect ratio γ , are shown in Figs. 6 and 7, respectively. The increase in Nu and f with increasing β is obvious from these figures. However, significant differences between the results of other investigators are once again evident. While the Focke et al. (1985) results indicate that both Nu and f peak when $\beta \approx 80$ deg, predictions from the Wanniarachchi et al. (1995) correlations suggest almost an exponentially increasing behavior with β . The

⁴ For example, Thonon et al. (1995) could have compared their data with those of Focke et al. (1985), and the latter could have considered comparing their results with those of Savostin and Tikhonov (1970), and Maslov and Kovalenko (1972). Manglik (1996) and Muley and Manglik (1998) have given composite comparisons, which show considerable differences between these results.

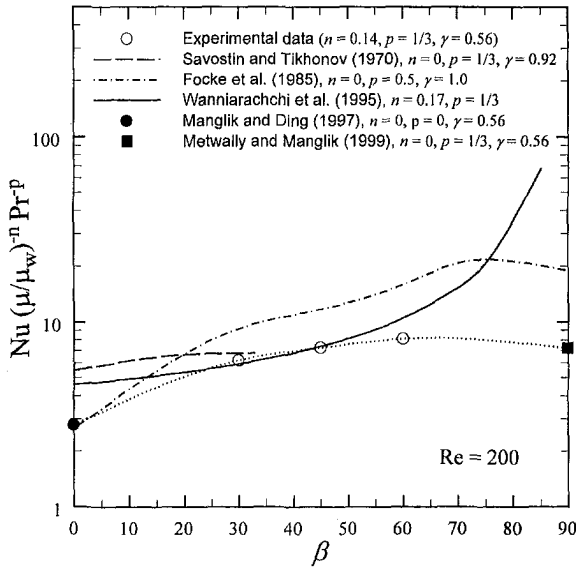


Fig. 6 Effect of chevron angle β on the Nusselt number

present data and results of Savostin and Tikhonov (1970), on the other hand, show fair agreement for Nu but not for f . Again, these variations are perhaps due to differences in the corrugation geometry (γ and ϕ). Also included in these figures are the analytical results from Manglik and Ding (1997), and Metwally and Manglik (1999) for fully developed laminar flows in double-sine and wavy-parallel-plate channels, respectively. These results for aspect ratio $\gamma = 0.56$, corresponding to the chevron plates used in this study, represent the two limiting cases of the chevron-plate geometry, i.e., $\beta = 0$ deg and 90 deg.

The influence of the aspect ratio γ (ratio of twice the corrugation depth and wavelength, $=2b/\lambda$) of the sinusoidal-plate corrugations in promoting swirl flows is shown in Fig. 8. Velocity vector results given by Metwally and Manglik (1999) for flows in $\beta = 90$ deg channels are graphed in this figure, and they depict the evolution of secondary circulation due to change in γ and Re . It is evident that with deeper grooves (large γ) and/or higher flow rates (higher Re), lateral vortices or recirculation zones develop in the channel troughs with higher core-flow peak velocities. When 0 deg $< \beta < 90$ deg, particularly for higher β , with crisscrossing

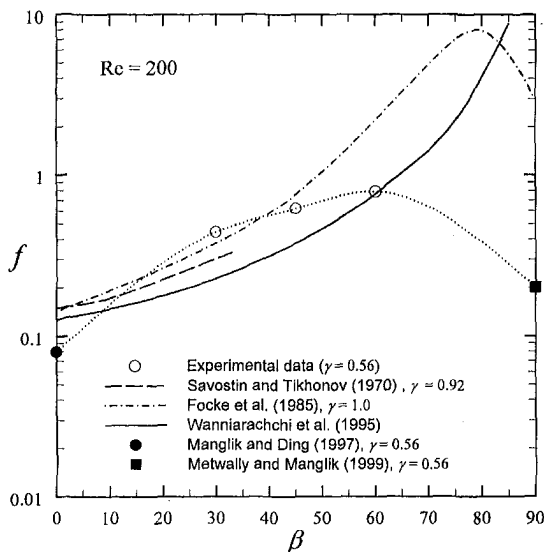


Fig. 7 Effect of chevron angle β on the isothermal friction factor

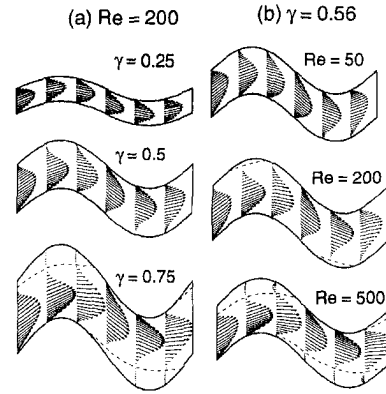


Fig. 8 The evolution of swirl flows in $\beta = 90$ deg corrugated plate flow passages (Metwally and Manglik, 1999): (a) effect of γ , and (b) effect of Re

flow streams, this lateral swirling fluid motion tends to be characterized by helical vortices (Focke and Knibbe, 1986). For $\beta = 0$ deg, straight flows in channels of double-sine cross section are obtained (Manglik and Ding, 1997). In any event, corrugations with deeper grooves and/or smaller wavelengths produce higher Nusselt numbers and friction factors. This is seen in Fig. 9 where the variation in Nu and f with γ for flows in $\beta = 90$ deg and 0 deg channels for $Re = 200$ are graphed (based on the results given by Metwally and Manglik (1999), and Manglik and Ding (1997), respectively). These results suggest that corrugations with $0.25 < \gamma < 0.75$ would perhaps give the better thermal-hydraulic performance, because the pressure drop penalty with $\gamma > 1$ grooves appears to outweigh the increase in heat transfer coefficients.

Clearly there are rather complex influences of plate-surface corrugation geometry variables such as β and γ (or ϕ) that contribute to the enhanced thermal-hydraulic behavior (this is also seen in turbulent flows, as reported in Muley and Manglik (1999)). Nevertheless, the new data can be predicted within ± 10 percent for both Nu and f by the following equations:

$$Nu = 1.6774(d_e/L)^{1/3}(\beta/30 \text{ deg})^{0.38} Re^{0.5} Pr^{1/3} (\mu/\mu_w)^{0.14}$$

$$30 \text{ deg} \leq \beta \leq 60 \text{ deg}, \quad \gamma = 0.56, \quad 30 \leq Re \leq 400 \quad (11)$$

$$f = [(30.20/Re)^5 + (6.28/Re^{0.5})^5]^{0.2} (\beta/30 \text{ deg})^{0.83}$$

$$30 \text{ deg} \leq \beta \leq 60 \text{ deg}, \quad \gamma = 0.56, \quad 2 \leq Re \leq 300 \quad (12)$$

It should be recognized that Eqs. (11) and (12) are perhaps best applicable for chevron plates with $\phi = 1.29$. Also, even though Pr was not a specific test variable, $Pr^{1/3}$ has been found to adequately describe its effects in viscous swirl flow heat transfer (Manglik and

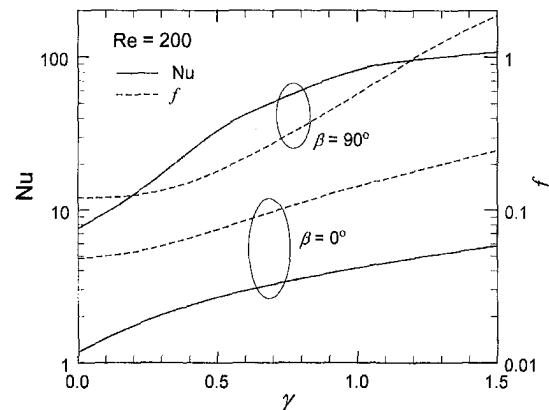


Fig. 9 Thermal-hydraulic performance of laminar periodically developed flows in $\beta = 90$ deg and $\beta = 0$ deg interplate channels

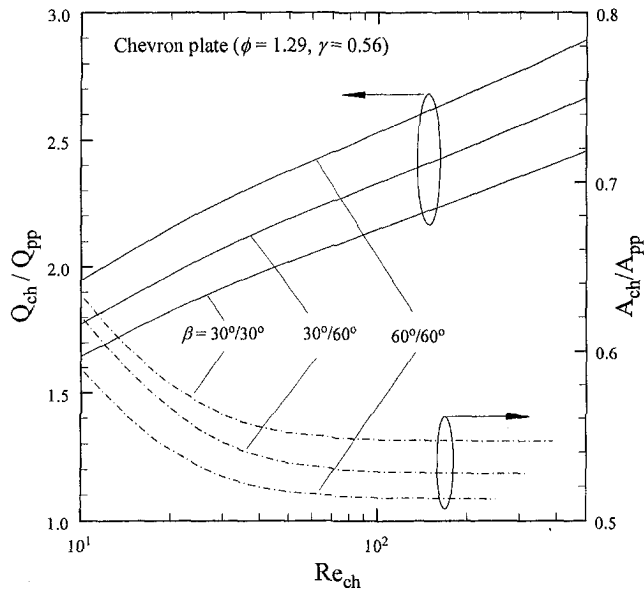


Fig. 10 Effect of β on heat transfer enhancement with (a) fixed surface geometry (b , λ , L , w , and ϕ) and constant pumping power (E), and (b) fixed heat load (Q) and constant pressure drop (Δp)

Bergles, 1993). This would extend the applicability of Eq. (11) to most viscous liquids, including water ($Pr \sim 5$). Furthermore, in conformity with much of the literature (Manglik, 1996; Manglik and Bergles, 1998), the classical Sieder and Tate (1936) viscosity-ratio correction is used in Eq. (11). Whether the complex interplate channel flow requires a different factor is unclear; though for many practical applications this is a second-order refinement. In any case, additional data over an extended range of plate-surface characteristics (b , λ , ϕ , and β) and flow conditions (Re , Pr , and Q) would be needed to develop more generalized Nu and f predictive correlations.

While the increased effective surface area and swirl flows generated in the interplate flow passages of chevron plates enhance the heat transfer, a large pressure drop penalty is also incurred. Bergles (1998), Webb (1994), and Kays and London (1984), among others, have outlined several figures of merit to evaluate the net enhancement in heat exchangers for different applications. A particularly useful criterion is to assess the heat transfer gains on the basis of equal pumping power and fixed surface geometry, relative to an equivalent flat-plate pack. This can be expressed as

$$(q_{ch}/q_{pp}) = [Nu_{ch}/Nu_{pp}]_{L,d_e,N,A,E,\Delta T} \quad (13)$$

where the chevron-plate and flat parallel-plate Reynolds numbers are linked by the equal pumping-power constraint as

$$(f Re^3)_{ch} = (f Re^3)_{pp} \quad (14)$$

Equation (14) requires that, for a given Re_{ch} , Re_{pp} must be higher, thereby accounting for the higher f in chevron-plate channels. The enhanced performance of chevron plates according to this criterion is shown in Fig. 10. Here, the Nu_{ch} data have been reduced to a projected area basis in order to account for enlargement factor ϕ , so that both chevron-plate and parallel-plate channels have the same heat transfer area. Inspection of this plot indicates that the heat transfer in corrugated chevron plates is enhanced by 1.5 to 2.9 times that in parallel-plate channels of same geometry at equal pumping power. Also, higher β and Re promote the better performance.

Another useful criterion is to evaluate the reduction of heat transfer surface area (or heat exchanger size), when compared with an equivalent flat-plate pack, based on the constraint of fixed heat duty and pressure drop, i.e.,

$$(A_{ch}/A_{pp}) = [Nu_{ch}/Nu_{pp}]_{q,d_e,\Delta T,\Delta p} \quad (15)$$

Once again, the specified Δp gives the interdependent Reynolds numbers in the chevron-plate and flat-plate channels according to

$$(f Re^2)_{ch} = (f Re^2)_{pp} \quad (16)$$

The consequent enhancement due to chevron plates in laminar flows, as measured by the criterion of Eq. (15), is also depicted in Fig. 10. The relatively less area requirement for same heat duty and pressure drop, which makes the PHE a more compact and economical heat exchanger, is clearly evident. Depending upon the flow rate and β , up to 48 percent reduction in heat transfer surface area is obtainable with chevron plates; the largest reduction, of course, is obtained with the higher chevron angle β . Furthermore, as seen in Fig. 10 for the performance criteria described by both Eqs. (13) and (15), there appears to be no significant advantage in using a mixed-plate arrangement over a symmetric arrangement. This is contrary to the previous observations of Marriott (1977) that mixed plates promote relatively higher heat transfer coefficients with a much smaller pressure-drop penalty. The results in Fig. 10 are further supported by those reported by Heaven et al. (1993), and Muley and Manglik (1997, 1999). Nevertheless, mixed-plate arrangements have the advantage of providing an intermediate performance (between the symmetric high and low- β plate arrangements) without requiring new plates for the intermediate value of β .

Conclusions

Experimental Nu and isothermal f data for cooling of hot vegetable oil ($130 < Pr < 290$) flows in the laminar regime ($2 < Re < 400$) in a single-pass PHE are presented. Three different chevron-plate arrangements were used (symmetric arrangements with $\beta = 30$ deg/30 deg and 60 deg/60 deg plates, and a mixed-plate arrangement with $\beta = 30$ deg/60 deg). Up to three times higher Nu is obtained with chevron plates when compared with an equivalent flat-plate pack at the same flow conditions, though the corresponding isothermal f is 6.6 times higher. The enhanced thermal-hydraulic performance is influenced by the chevron angle β , corrugation aspect ratio γ , and fluid flow parameters Re , Pr , and (μ/μ_w) . Specifically, increasing β (and/or γ) is seen to increase both Nu and f in chevron plate PHEs. The experimental data for $30 \text{ deg} \leq \beta \leq 60 \text{ deg}$, $\gamma = 0.56$ and $\phi = 1.29$ are represented within ± 10 percent by Eq. (11) for Nu and Eq. (12) for f . However, in order to develop more generalized Nu and f correlations, additional data for plates with different values of surface geometry variables such as γ or ϕ (b and λ) along with β would be needed. Furthermore, the heat transfer enhancement, that is produced primarily by the larger effective area of the corrugated surface and swirl flow mixing in the interplate passages, is quantified on the basis of two different criteria. For the constraint of fixed surface geometry and constant pumping power, and depending upon Re and β , the heat transfer is enhanced by up to 2.9 times that in flat-plate channels. Likewise, for the constraint of fixed heat duty and pressure drop, there is as much as 48 percent less heat transfer area required by using chevron plates instead of flat plates in a PHE.

Acknowledgment

This study was supported by the National Science Foundation (Grant # CTS-9502128) and The Procter & Gamble Company.

References

- Bergles, A. E., 1998, "Techniques to Enhance Heat Transfer," *Handbook of Heat Transfer*, 3rd Ed., W. M. Rohsenow et al., eds., McGraw-Hill, New York, Chapter 11.
- Ding, J., and Manglik, R. M., 1996, "Analytical Solutions for Laminar Fully Developed Flows in Double-Sine Shaped Ducts," *Heat and Mass Transfer*, Vol. 31, pp. 269–277.
- Focke, W. W., and Knibbe, P. G., 1986, "Flow Visualization in Parallel-Plate Ducts with Corrugated Walls," *Journal of Fluid Mechanics*, Vol. 165, pp. 73–77.
- Focke, W. W., Zachariades, J., and Olivier, I., 1985, "The Effect of the Corrugation

- Inclination Angle on the Thermohydraulic Performance of Plate Heat Exchangers," *International Journal of Heat and Mass Transfer*, Vol. 28, pp. 1469–1479.
- Gaiser, G., and Kottke, V., 1990, "Effects of Corrugation Parameters on Local and Integral Heat Transfer in Plate Heat Exchangers and Regenerators," *Heat Transfer 1990*, Vol. 5, G. Hetsroni, ed., Hemisphere, New York, pp. 85–90.
- Gaiser, G., and Kottke, V., 1998, "Effects of Wavelength and Inclination Angle on the Homogeneity of Local Heat Transfer Coefficients in Plate Heat Exchangers," *Heat Transfer 1998*, Vol. 6, J. S. Lee, ed., KSME, Seoul, Korea, pp. 203–208.
- Heavner, R. L., Kumar, H., and Wanniarachchi, A. S., 1993, "Performance of an Industrial Heat Exchanger: Effect of Chevron Angle," *AIChE Symposium Series*, No. 295, Vol. 89, pp. 262–267.
- Kakaç, S., Shah, R. K., and Aung, W., 1987, *Handbook of Single-Phase Convective Heat Transfer*, John Wiley and Sons, New York, Chapters 3 and 4.
- Kays, W. M., 1950, "Loss Coefficients for Abrupt Changes in Flow Cross Section with Low Reynolds Number Flow in Single and Multiple Tube Systems," *Transactions of ASME*, Vol. 72, pp. 1067–1074.
- Kays, W. M., and London, A. L., 1984, *Compact Heat Exchangers*, 3rd Ed., McGraw-Hill, New York.
- Manglik, R. M., 1996, "Plate Heat Exchangers for Process Industry Applications: Enhanced Thermal-Hydraulic Characteristics of Chevron Plates," *Process, Enhanced and Multiphase Heat Transfer*, R. M. Manglik and A. D. Kraus, eds., Begell House, New York, pp. 267–276.
- Manglik, R. M., 1999, "On the Influence of Number of Thermal Plates on the Performance of Plate Heat Exchangers," *International Communications in Heat and Mass Transfer*, being submitted.
- Manglik, R. M., and Bergles, A. E., 1991, "Heat Transfer Enhancement of Intube Flows in Process Heat Exchangers by Means of Twisted-Tape Inserts," Report No. HTL-18, Heat Transfer Laboratory, Rensselaer Polytechnic Institute, Troy, NY.
- Manglik, R. M., and Bergles, A. E., 1993, "Heat Transfer and Pressure Drop Correlations for Twisted-Tape Inserts in Isothermal Tubes: Part I—Laminar Flows," *ASME JOURNAL OF HEAT TRANSFER*, Vol. 115, pp. 881–889.
- Manglik, R. M., and Bergles, A. E., 1998, "Numerical Modeling and Analysis of Laminar Flow Heat Transfer in Non-Circular Compact Channels," *Computer Simulations in Compact Heat Exchangers*, B. Sundén and M. Faghri, eds., Computational Mechanics, Southampton, UK, Chapter 2.
- Manglik, R. M., and Ding, J., 1997, "Laminar Flow Heat Transfer to Viscous Power-Law Fluids in Double-Sine Ducts," *International Journal of Heat and Mass Transfer*, Vol. 40, pp. 1379–1390.
- Manglik, R. M., and Muley, A., 1993, "Heat Transfer and Pressure Drop Characteristics of Plate-and-Frame Heat Exchangers: A Literature Review," Report No. TFL-Int-1, Thermal-Fluids Laboratory, University of Cincinnati, Cincinnati, OH, Sept.
- Marriott, J., 1977, "Performance of an Alfaflex Plate Heat Exchanger," *Chemical Engineering Progress*, Vol. 73, No. 2, pp. 73–78.
- Maslov, A. M., and Kovalenko, L. M., 1972, "Hydraulic Resistance and Heat Transfer in Plate Heat Exchangers," *Molochnaya Promyshlennost*, No. 10, pp. 20–22.
- Metwally, H. M., and Manglik, R. M., 1999, "Numerical Predictions of Periodically Developed Laminar Flow and Heat Transfer in Sinusoidal Corrugated Plate Channels," Thermal-Fluids & Thermal Processing Laboratory Report No. TFTP-4, Department of Mechanical, Industrial and Nuclear Engineering, University of Cincinnati, Cincinnati, OH.
- Moffat, R. J., 1988, "Describing the Uncertainties in Experimental Results," *Experimental Thermal and Fluid Science*, Vol. 1, pp. 3–17.
- Muley, A., and Manglik, R. M., 1995, "Experimental Investigation of Heat Transfer Enhancement in a PHE with $\beta = 60^\circ$ Chevron plates," *Heat and Mass Transfer 95*, S. Srinivasa Murthy and Y. Jaluria, eds., Tata McGraw-Hill, New Delhi, pp. 737–744.
- Muley, A., and Manglik, R. M., 1997, "Enhanced Heat Transfer Characteristics of Single-Phase Flows in a Plate Heat Exchanger with Mixed Chevron Plates," *Journal of Enhanced Heat Transfer*, Vol. 4, pp. 187–201.
- Muley, A., and Manglik, R. M., 1998, "Heat Transfer and Pressure Drop in Plate Heat Exchangers," Thermal-Fluids Laboratory Report No. TFL-2, Department of Mechanical, Industrial and Nuclear Engineering, University of Cincinnati, Cincinnati, OH.
- Muley, A., and Manglik, R. M., 1999, "Experimental Study of Turbulent Flow Heat Transfer and Pressure Drop in a Plate Heat Exchanger With Chevron Plates," *ASME JOURNAL OF HEAT TRANSFER*, Vol. 121, pp. 110–117.
- Savostin, A. F., and Tikhonov, A. M., 1970, "Investigation of the Characteristics of the Plate Heating Surfaces," *Thermal Engineering*, Vol. 17, No. 9, pp. 75–78.
- Sieder, E. N., and Tate, G. E., 1936, "Heat Transfer and Pressure Drop of Liquids in Tubes," *Industrial and Engineering Chemistry*, Vol. 28, pp. 1429–1435.
- Shah, R. K., 1990, "Assessment of Modified Wilson Plot Techniques for Obtaining Heat Exchanger Design Data," *Heat Transfer 1990*, Vol. 5, G. Hetsroni, ed., Hemisphere, New York, pp. 51–56.
- Shah, R. K., and Focke, W. W., 1988, "Plate Heat Exchangers and Their Design Theory," *Heat Transfer Equipment Design*, R. K. Shah et al., eds., Hemisphere, Washington, pp. 227–254.
- Talik, A. C., Fletcher, L. S., Anand, N. K., and Swanson, L. W., 1995, "Heat Transfer and Pressure Drop Characteristics of a Plate Heat Exchanger Using a Propylene-Glycol/Water Mixture as the Working Fluid," *Proc. 1995 National Heat Transfer Conference*, Vol. 12, HTD-Vol. 314, ASME, New York, pp. 83–88.
- Thonon, B., Vidil, R., and Marvillet, C., 1995, "Recent Research and Developments in Plate Heat Exchangers," *Journal of Enhanced Heat Transfer*, Vol. 2, Nos. 1–2, pp. 149–155.
- Wanniarachchi, A. S., Ratnam, U., Tilton, B. E., Dutta-Roy, K., 1995, "Approximate Correlations for Chevron-Type Plate Heat Exchangers," *Proc. 1995 National Heat Transfer Conference*, Vol. 12, HTD-Vol. 314, ASME, New York, pp. 145–151.
- Webb, R. L., 1994, *Principles of Enhanced Heat Transfer*, John Wiley and Sons, New York.
- Wilson, E. E., 1915, "A Basis for Rational Design of Heat Transfer Apparatus," *Transactions of the ASME*, Vol. 37, pp. 47–82.

Performance of Dehumidifying Heat Exchangers With and Without Wetting Coatings

K. Hong

Development Engineer,
Daimler Chrysler Corporation,
14250 Plymouth Road,
Detroit, MI 48227
e-mail: kh39@daimlerchrysler.com

R. L. Webb

Department of Mechanical Engineering,
The Pennsylvania State University,
University Park, PA 16802
e-mail: rlwebb@psu.edu
Fellow ASME

Limited previous work has shown that use of special hydrophilic coatings will provide lower air pressure drop in finned tube heat exchangers operated under dehumidifying conditions. However, no detailed work has been reported on the effect of different coating types, or different fin surface geometries on the wet pressure drop. In this study, wind tunnel tests were performed on three different fin geometries (wavy, lanced, and lower) under wet and dry conditions. All dehumidification tests were done for fully wet surface conditions. For each geometry, the tests were performed on uncoated and coated heat exchangers. For all three fin geometries, the wet-to-dry pressure drop ratio was 1.2 at 2.5 m/s frontal air velocity. The coatings have no influence on the wet or dry heat transfer coefficient. However, the wet surface heat transfer coefficient was 10 to 30 percent less than the dry heat transfer coefficient, depending on the particular fin geometry. The effect of the fin press oil on wet pressure drop was also studied. If the oil contains a surfactant, good temporary wetting can be obtained on an uncoated surface; however, this effect is quickly degraded as the oil is washed from the surface during wet operation. This work also provides a critical assessment of data reduction methods for wet surface operation, including calculation of the fin efficiency.

Introduction

Most previous dehumidifying heat exchanger experiments on uncoated fins were primarily concerned with the air-side heat transfer coefficient and the pressure drop. The wet pressure drops under wet condition were reported as 1.5 to 2.0 times higher than that of the dry condition, depending upon the fin geometry and the condensation load. The only reported work on hydrophilic coated heat exchangers is that of Mimaki (1987). He found that the wet pressure drop of the coils was reduced up to 40 to 50 percent using hydrophilic coated fins. He also claimed that the air-side heat transfer coefficient of the coated core was increased by two to three percent. Mimaki (1987) did not describe the fin geometry tested, nor did he provide details of the operating conditions and data reduction method.

There is controversy regarding the reported air-side heat transfer coefficients under wet conditions. For instance, McQuiston (1978a) claimed that the air-side heat transfer under wet conditions was lower than that of the dry condition, while Eckels and Rabas (1987) came to the opposite conclusion. Careful study of the literature on operation with dehumidification suggests that the differing answers may be because: (1) incorrect equations were used to calculate the wet-surface fin efficiency, (2) the fins were not fully wet, or (3) steady state was not achieved during the test. Further, some authors have used the enthalpy driving potential and others have used the specific humidity driving potential to define the wet surface heat transfer coefficient. The enthalpy driving potential includes small approximations not involved in use of the specific humidity driving potential. Threlkeld (1970) justified that the approximations were negligible if the fins are fully wet.

Because of the differing methods used by the several authors reporting wet surface data, and the lack of detailed information, there is considerable uncertainty in the literature. This work seeks to perform the dehumidification tests under fully wet conditions, and uses the specific humidity driving potential for the data reduc-

tion. The purpose of this work was to assess the effect of hydrophilic coatings on the performance of three different enhanced fin geometries. The wet surface tests were run under fully wet surface conditions. Appendices A and B provide the detailed methodology for reducing wet surface heat transfer data. This description is provided for use of either the specific humidity or the enthalpy driving potentials.

Experimental Program

A wind tunnel test was conducted to assess the thermal performance of the coils having Aqua-Shed and Sama coated fins. Aqua-Shed and Sama are commercial hydrophilic coating brand names produced by Alcoa and Sama companies, respectively. The details on the coatings are described in Appendix B of Hong (1996). Heat exchangers having uncoated fins of the same geometry were also tested to provide a comparison base. The three-row coils have wavy or lanced fins 472 fins/m (12 fins/in.) on 9.5-mm tubes, while two-row coils have louver fins 670 fins/m (17 fins/in.) on 7-mm tubes. The three different fin geometries are shown in Figs. 1(a), 1(b), and 1(c). The heat exchangers tested are listed in Table 1.

The water circuiting pattern for three row coils and two row coils is shown in Figs. 2(a) and 2(b). Three row coils have four passes and the two row coils have two passes, respectively.

Wind Tunnel Apparatus Setup. The wind tunnel has a 305 mm \times 476 mm (12 in. \times 18 $\frac{3}{4}$ in.) cross section and is shown in Fig. 3(a). A humidifier was installed upstream from the extended duct (Fig. 3(b)) to humidify the incoming air. To remove nonuniformity in temperature and humidity, two of 2.44-m (8-ft) long ducts, having a 381 mm \times 559 mm (15 in. \times 22 in.) cross section (Fig. 3(b)), were placed upstream of the heat exchanger. Two steam bars were installed at the front of the extended duct in which a 305-mm (12-in.) diameter stationary propeller fan was installed. This fan helped mix the air with injected steam. The fan was framed with rectangular shaped plywood (381 mm \times 559 mm) whose center has a 305 mm hole for a fan installation. Also, two mixing devices were inserted between the extended ducts as shown in Fig. 3(b). These mixing devices were made by following ASHRAE 41.1 instructions as in Fig. 3(c). To have uniform flow

Contributed by the Heat Transfer Division for publication in the JOURNAL OF HEAT TRANSFER. Manuscript received by the Heat Transfer Division, June 16, 1998; revision received, Apr. 1, 1999. Keywords: Coatings, Convection, Dehumidification, Experimental, Heat Transfer, Heat Exchangers. Associate Technical Editor: M. Kaviany.

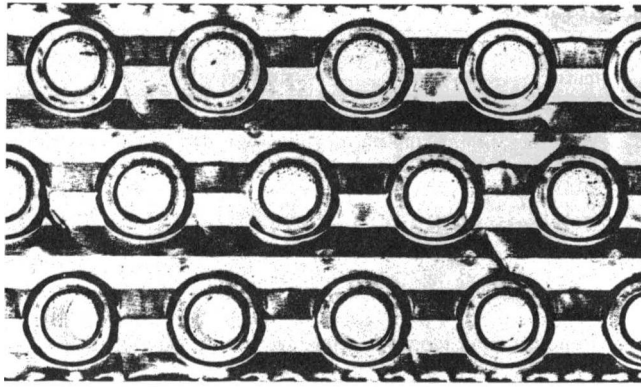


Fig. 1(a)

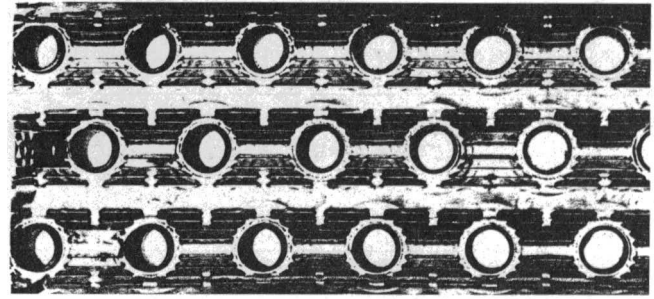


Fig. 1(b)

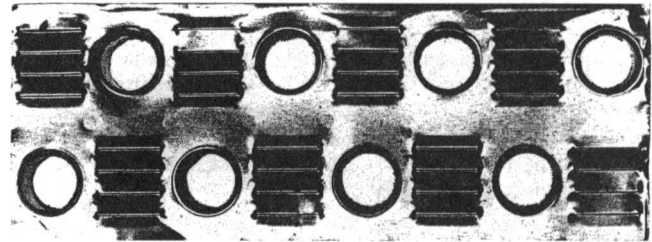


Fig. 1(c)

Fig. 1 Fin geometries; (a) wavy (b) lanced, and (c) louver

through the duct, different sizes of honey combs were positioned in the second duct. To overcome the cross section size difference between the extended ducts and the Plexiglas part of the wind tunnel, the linking box was made of smooth curved thin stainless steel panels. Two wire meshes were installed at each end of this box. An observation box was installed downstream from the test section (Fig. 3(a)); it was used to observe and measure the water carryover. A refrigeration system (Fig. 4) was installed to allow air cooling in the heat exchanger. This consists of a three-ton hermetic R-22 compressor, and a city water cooled condenser. This system cools the water circulating the heat exchanger.

Two thermocouples were placed upstream of the test section to measure the incoming air temperature and a grid array of 24 thermocouples were installed downstream of the test section for measuring the leaving air temperature. A Pitot tube, placed in the

plexiglass section of the wind tunnel as in Fig. 3(a) connected to the precision manometer measured the incoming air velocity.

To measure the cooled water mass flow rate, the volumetric flow meter (2.27 kg/s full-scale capacity) was set up before the cooled water goes to the heat exchanger. This flowmeter was calibrated by

Nomenclature

a = constant defined by Eq. (4)
 A = area, m^2
 A_{fr} = heat exchanger air side flow frontal area, m^2
 b_i = slope of the saturated air enthalpy versus temperature curve, $kJ/(kg \cdot K)$
 c_p = specific heat at constant pressure, J/kgK
 D = tube diameter, m
 D_h = hydraulic diameter, m
 f = fanning friction factor, dimensionless
 h = convection heat transfer coefficient, W/m^2K
 i = enthalpy of steam-air mixture, enthalpy of saturated air at tube wall temperature (i_{sat}), kJ/kg
 h_{fg} = latent heat of vaporization of steam, kJ/kg
 I_0 = modified Bessel function solution of the first kind, order 0
 I_1 = modified Bessel function solution of the first kind, order 1
 j = Colburn factor, dimensionless
 k = thermal conductivity, $W/m \cdot K$
 K_m = mass transfer coefficient, $kg/m^2 \cdot s$
 K_o = modified Bessel function solution of the second kind, order 0
 K_1 = modified Bessel function solution of the second kind, order 1
 \dot{m} = mass flow rate, kg/s

NTU = number of heat transfer units, dimensionless
 Nu = Nusselt number, dimensionless
 Pr = Prandtl number, dimensionless
 q = heat flux, W/m^2
 Q = heat transfer rate, W
 Re = Reynolds number, dimensionless
 Sc = Schmidt number, dimensionless
 t = tube wall thickness, m
 T = temperature, $^{\circ}C$
 U = overall heat transfer coefficient, $W/m^2 \cdot K$
 W = specific humidity at bulk air condition, specific humidity of saturated air at tube wall temperature (W_{sat}), kg/kg

Greek Letters

α = thermal diffusivity, m^2/s
 β = parameter defined as $\beta = Ci_{fg}/c_{p,a}$
 ΔP = pressure drop, Pa
 ΔT_{lm} = logarithmic mean temperature difference, K
 ϕ = parameter defined by Eq. (B5)
 η_f = fin efficiency of the fin, dimensionless
 η_o = surface efficiency for finned surface [$= 1 - (1 - \eta_f)A_f/A$], dimensionless
 μ = fluid dynamic viscosity coefficient, $Pa \cdot s$

ν = kinematic viscosity, m^2/s
 ρ = fluid density, kg/m^3

Subscripts

air = evaluated at local bulk air condition
 avg = average
 c = cross-sectional
 $conv$ = convection
 D = diameter
 dry = dry surface condition
 eff = effective
 f = fin
 fr = frontal
 h = hydraulic
 i = inside tube
 in = inlet condition
 lat = latent
 max = maximum
 ma = moist air
 o = outside
 out = outlet condition
 sen = sensible
 tot = total
 w = water
 wet = wet surface condition

Superscripts

m = constant defined by Eq. (4)
 n = constant defined by Eq. (4)

Table 1 Heat exchangers tested

Core number	Fins/m spacing	Fin type	Tube O.D. (mm)	S_i (mm)	S_o (mm)	Surface treatment	Tube type
1	472	Wavy	9.5	25.4	22.0	None	Smooth
2	472	Wavy	9.5	25.4	22.0	Aqua-Shed	Smooth
3	472	Lanced	9.5	25.4	22.0	None	Micro-fin
4	472	Lanced	9.5	25.4	22.0	Aqua-Shed	Micro-fin
5	670	Louver	7.0	25.4	22.0	None	Micro-fin
6	670	Louver	7.0	25.4	22.0	Sama	Micro-fin

weighing the mass collected during a given period. The relationship between the mass flow rate in kg/s units and the percentage scale was found and the scale calibration curve was prepared. To measure the entering and leaving cooled water, reliable thermometers (0.15°C accuracy) were installed 1.0 m away from the heat exchanger. The 1-m length of pipe, between the thermistors and the heat exchanger was well insulated. A container was located below the heat exchanger to catch the condensate when the incoming air was dehumidified.

The wet-bulb temperature was measured inside the wind tunnel duct by inserting high-accuracy mercury thermometers (0.05°C division), which are 0.61 meter away upstream and downstream from the test section. The wet bulb temperature was used to determine the relative humidity, and enthalpy of the incoming and leaving air. To make certain that the fins are fully wet, the relative humidity was kept above 82 percent for which the leading edge fin tip was below the dew point of the inlet air.

Heat Exchanger Preparation. Because the physical size of the testing heat exchangers was larger than the test section of the wind tunnel, the area outside the wind tunnel flow cross section was blocked by duct tape. The space between the fins was not filled. It is probable that a small amount of air bypassed into the fin region outside the wind tunnel cross section. The fin height outside the wind tunnel cross section is 14 percent of the total fin height. As discussed later, this may slightly increase the calculated heat transfer coefficient and reduce the pressure drop. However, this is not an important issue in the present work, because the issues of concern were the wet heat transfer and pressure drop of the coated coils, relative to the uncoated coils.

Heat Transfer Coefficient Measurement. For the dry condition, the heat transfer rate (Q) is calculated as the average of the air and water-side values. For the wet condition, the sensible heat transfer rate is calculated from the $Q_{sen} = Q_{tot} - Q_{lat}$. The UA value was calculated using the effectiveness-NTU equation for unmixed-unmixed cross flow. The air-side sensible heat transfer coefficient was calculated by subtracting the water-side and the wall resistance from the total thermal resistance, assuming zero water-side fouling resistance. Thus,

$$\frac{A_{fr}}{\eta_o h_o A_o} = \frac{A_{fr}}{UA} - \frac{A_{fr}}{h_i A_i} - \frac{A_{fr} t_w}{k_w A_w} \quad (1)$$

For smooth tubes, the Petukhov (1970) correlation for turbulent flow in tubes was used to calculate the tube-side heat transfer coefficient because the Reynolds number of this work fell in the turbulent region ($Re_{dh} > 10^4$). This equation is

$$Nu = \frac{\left[\frac{f}{2}\right] Re_D Pr}{1.07 + 12.7 \sqrt{\frac{f}{2}} (Pr^{2/3} - 1)} \quad (2)$$

the friction factor is given by

$$f = \frac{1}{(1.58 \ln Re_{dh} - 3.28)^2} \quad (3)$$

For micro-finned tubes, the Brognaux et al. (1997) correlation for single-phase flow was used. They developed a correlation for the water-side heat transfer coefficient for the different helix angles of micro-finned tubes. Their correlations are of the form

$$Nu_{De} = a Re_{De}^m Pr^n \quad (4)$$

where the constants "a," "m," and "n" were empirically determined for different geometries of the micro-finned tubes. The Re_{De} is based on the tube inside diameter if the fins are melted and the metal is returned to the tube wall.

The air-side sensible j factor is obtained using the following equation:

$$j = \frac{h}{\left[\frac{\dot{m}}{\sigma A_{fr}}\right] c_p} Pr^{2/3} \quad (5)$$

The wet sensible j -factor is obtained by using the wet sensible heat transfer coefficient h_{wet} , in place of h in Eq. (5). Appendix A shows the methodology to calculate the wet heat transfer coefficient.

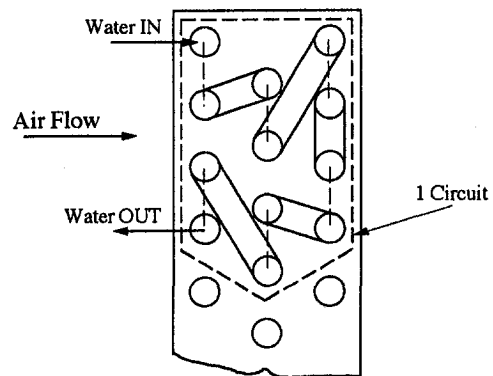


Fig. 2(a)

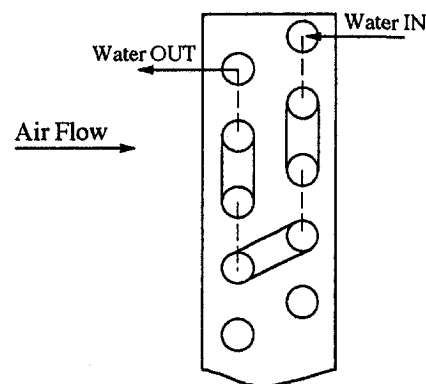


Fig. 2(b)

Fig. 2 Water circuiting of the heat exchangers; (a) three rows (b) two rows

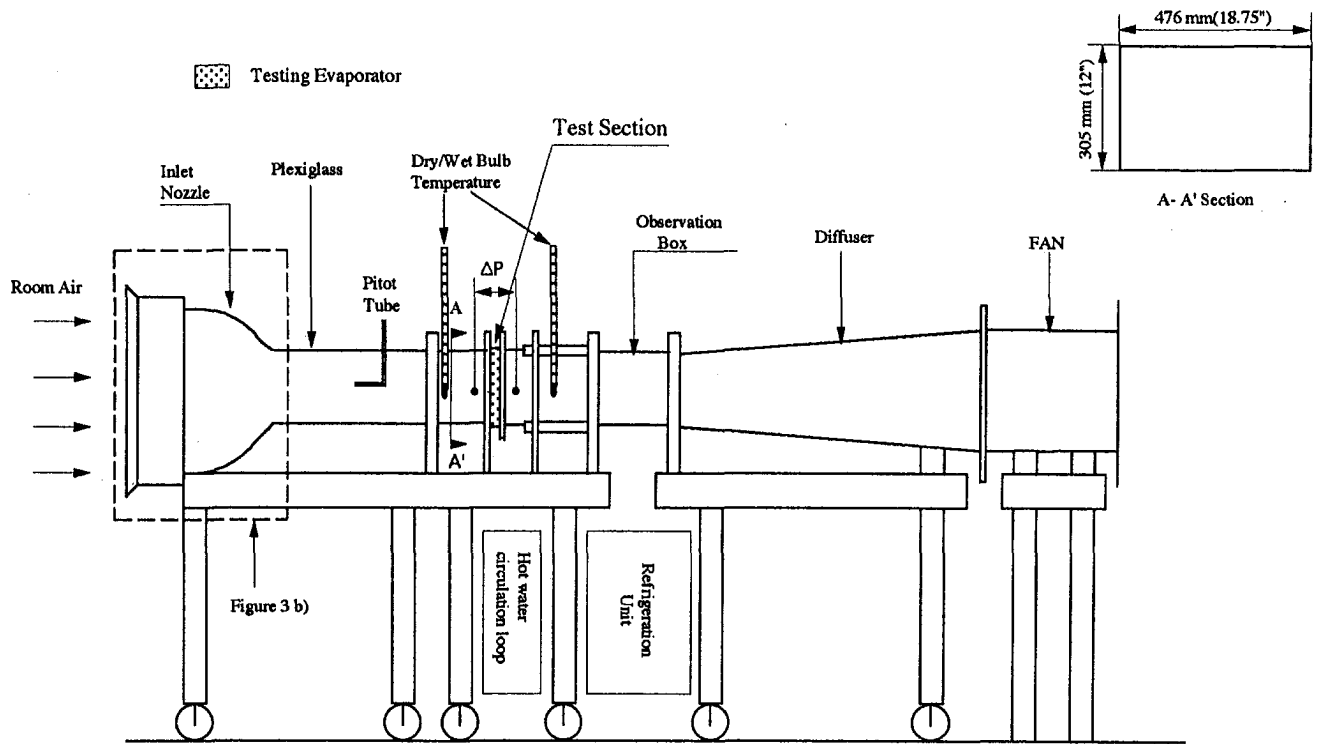


Fig. 3(a) Subsonic wind tunnel

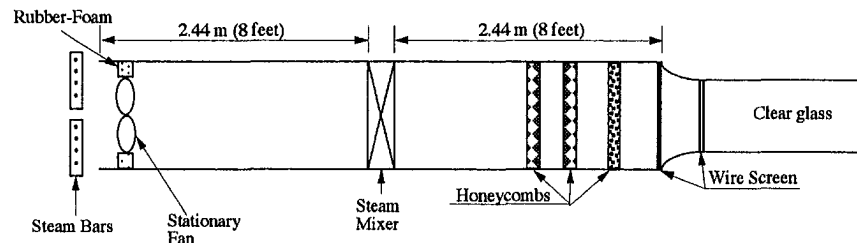


Fig. 3(b) Extended duct section of wind tunnel to accommodate the steam mixer

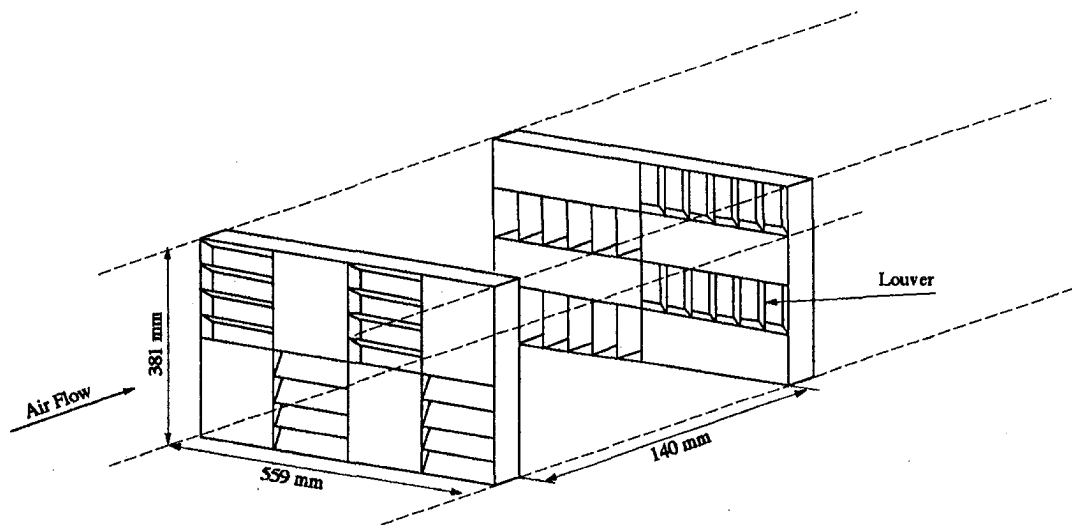


Fig. 3(c) Steam mixer

Fin Efficiency Calculation. To obtain the heat transfer coefficient, it is necessary to find the fin efficiency. The fin efficiency of wavy fins was calculated using Eq. (B4) of Appendix B, which is based on the sector method using the equivalent circular fin area. The fin length for the wavy fins was based on the total profile

length of the wave. This method probably overestimates the fin efficiency for the louver and lanced fins. This will result in underestimating the sensible heat transfer of louver and lanced fin heat exchangers.

For calculation of the wet surface fin efficiency, the C-parameter

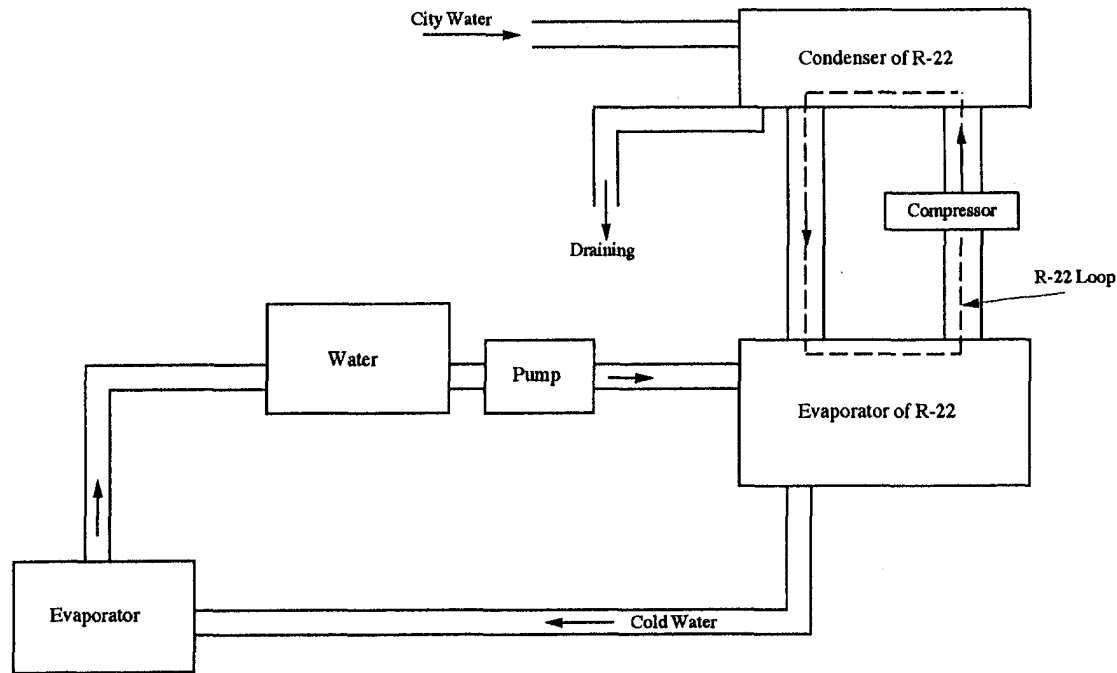


Fig. 4 Refrigeration system to provide the cold water on the tube-side

in the Hong and Webb equation is calculated as described by Wu and Bong (1994) as shown in Eq. (B3). Wu and Bong showed that the C-parameter defined by McQuiston and Parker (1994) is incorrect. More precisely, the McQuiston and Parker C-parameter is valid only for air in the bulk stream at 100 percent relative humidity. The authors have compared the calculated wet fin efficiency based on the Wu and Bong C-parameter with the equation proposed by Threlkeld (1970). Both methods give the same answer. However, the McQuiston and Parker (1994) method shows that wet fin efficiency is dependent on the air inlet humidity. We believe this incorrect calculation results from the erroneous definition of the C-parameter.

Air-Side Pressure Drop Measurement. A traveling well micro-manometer was used to measure the static pressure difference across the heat exchanger. Piezo-stating rings consisting of four small taps (one in each duct wall) are used for measuring the pressure upstream and downstream of the heat exchanger. Data were taken for a range of increasing frontal air velocities between 1 to 3 m/sec or up to a higher velocity at which carryover occurs.

The dry condition was accomplished by supplying hot water (46°C) to the tube-side of the heat exchangers. The wet condition was established by circulating cold water. The driving potential for the wet condition is defined by the enthalpy driving potential ($i_{air,in} - i_{sat,wat,in}$). To keep the driving potential constant, the entering water temperature was controlled to a fixed value. This was done by either controlling the R-22 temperature in the refrigeration system, or steam from the humidifier.

The pressure drop test for the wet condition was conducted using the following procedure:

- 1 Run the refrigeration system until the entering water temperature reaches 5°C.
- 2 Turn on the wind tunnel with humidification of the incoming air. Start with low air velocity and be sure to have the level of incoming air humidity greater than 82 percent.
- 3 Measure the air velocity and read the pressure drop across the heat exchanger after the steady state is reached. Here, steady state means that when the fluctuation of wet bulb temperature of the incoming air and the water entering temperature is within 0.1°C for two minutes.

- 4 Repeat the above procedures for each air velocity.

To confirm that the coated and uncoated core were identical geometries, the isothermal condition pressure test was performed. Because the bottom of the pressure tap downstream from the test section was clogged by condensate for the dehumidifying test, the isothermal condition pressure test was also conducted without using the bottom tap. No difference was found whether three or four taps were used.

Uncertainty Analysis. An uncertainty analysis was performed using the method of Kline (1965) and described in Holman (1989). Assuming accurate knowledge of the flow cross-sectional area, the results are given in Table 2.

It was previously noted that the oversize coil was sandwiched between flanges. This allowed air to expand in the fin region at the top of the coil. This "bypass" effect introduced additional uncertainty in the flow cross section, and in the actual heat transfer/friction surface area. It is expected that this acted to increase the heat transfer coefficient and reduce the pressure drop below the values that would exist if such bypass did not exist. In separate tests performed later, work was done to determine the magnitude of the error associated with this bypass effect. It was concluded that the additional error associated with the bypass are very small.

The key purpose of these tests was to determine the effect of coatings on the wet heat transfer coefficient. Although the bypass effect may have a small effect on the absolute error of the data, it should have no effect on the relative effect of the coating on the wet and dry pressure drop. This is the key issue addressed in this work.

Table 2 Results of uncertainty analysis

(Based on known flow area)			
Air velocity	ΔP (%)	h (dry)	h (wet)
Low	1.0	5.0	14.0
High	0.1	3.0	7.0

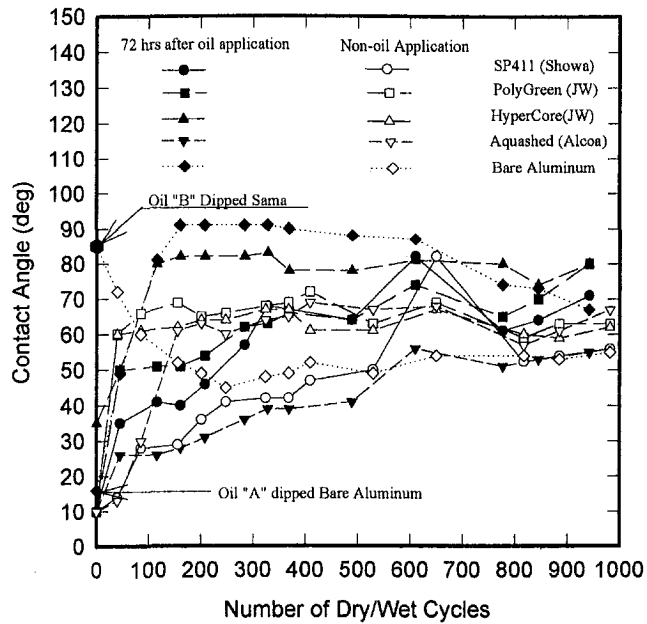


Fig. 5 Coating durability dry/wet cycle

Results and Discussion

The purpose of the wind tunnel test was to assess how the coating, and oil contamination, affected the wet surface heat transfer and pressure drop results. It was expected that the contact angle will influence the wet surface pressure drop results. The effect of coatings on contact angle is reported by Hong and Webb (1998).

The present wind tunnel test results should be indicative of the first dry/wet cycle. Hence, it is suggested that the wind tunnel test results are related to the contact angles shown in Fig. 5 (Hong and Webb, 1999) for the first dry/wet cycle. It is probable that test results presented here are not indicative of the contact angle effects that will result after 1000 dry/wet cycles.

Heat Transfer Coefficient and Pressure Drop.

Dry Coil Performance. The dry heat transfer coefficients and pressure drop results for 472 fins/m (12 fins/in.) wavy, lanced fins and 670 fins/m (17 fins/in.) louver fin cores are shown in Fig. 6. This figure shows no coating effect on the dry coil performance. This is expected because the thickness of the coating is so small

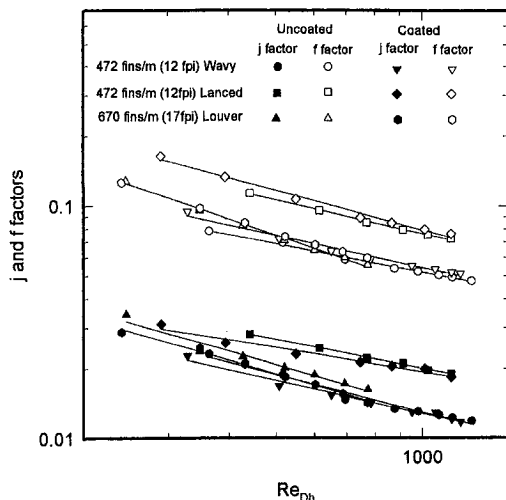


Fig. 6 Dry coil performance comparison

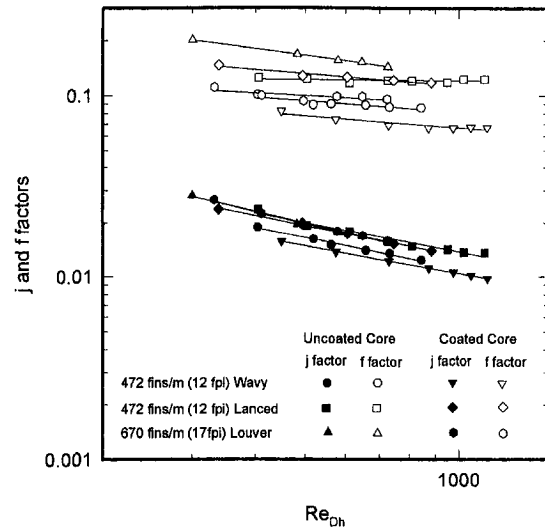


Fig. 7 Wet coil performance comparison

($1 \mu\text{m}$) that the thermal resistance of the coating can be negligible. The lanced fin heat exchanger has the best thermal performance among the three fin geometries as well as showing the highest pressure drop. Because the fin efficiency was overestimated for both louver and lanced fin heat exchangers, the heat transfer performance will be higher than shown in Fig. 6. It is noted that the wavy fin efficiency equation was used for lanced and louver fins.

Wet Coil Performance. The wet coil performance for 472 fins/m (12 fins/in.) wavy, lanced fin and 670 fins/m (17 fins/in.) louver fin cores are presented in Fig. 7. The thermal performance (heat transfer coefficient) of the tested cores was expressed by the j -factor as defined in Eq. (16) and the pressure drop characteristics by the friction factor. In general, the hydrophilic coating did not decrease the wet sensible heat transfer coefficients for three different fin geometries compared with the uncoated heat exchangers. However, the ratio of the wet-to-dry heat transfer coefficients were 0.8 to 0.9 for wavy and louver coils, and 0.7 for the lanced fin heat exchanger, respectively, as shown in Fig. 8. It is believed that the low value of the $h_{\text{wet}}/h_{\text{dry}}$ ratio for the lanced fins (Fig. 8) occurs because the wet fin efficiency is less than that for the dry fin. This implies that if the actual wet surface fin efficiency of lanced fins is

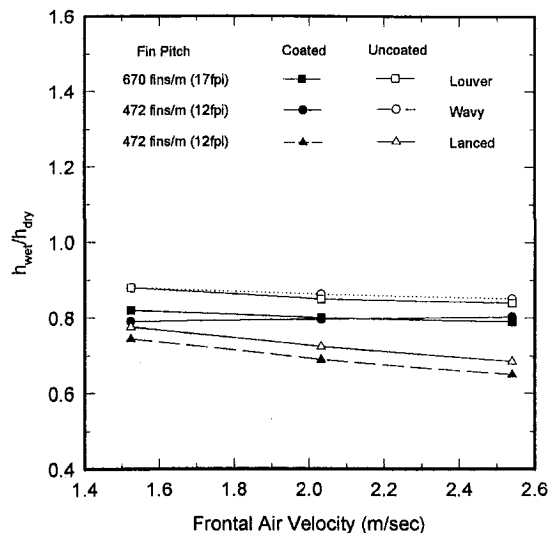


Fig. 8 Wet-to-dry heat transfer coefficient ratio of the tested cores

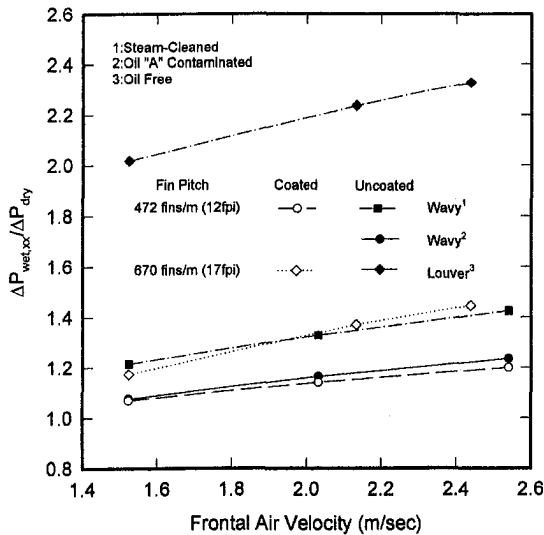


Fig. 9 Wet-to-dry pressure drop ratio of the tested cores

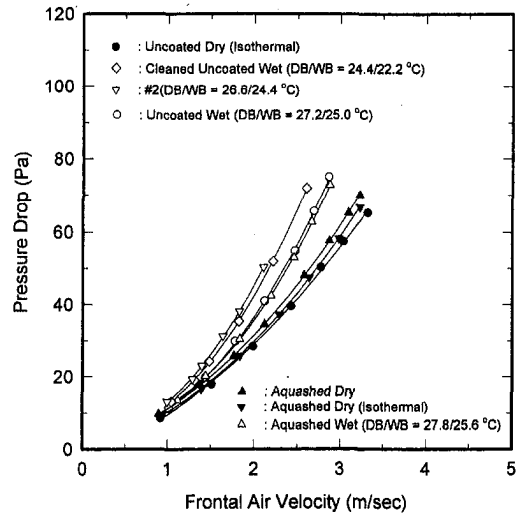


Fig. 10 Pressure drop of 472 fins/m (12 fins/in.) wavy core

used in calculation of the wet sensible heat transfer coefficient, the heat transfer ratio (h_{wet}/h_{dry}) would be higher.

The coating on the 670 fins/m (17 fins/in.) louver fin coil resulted in a 40 percent to 50 percent wet coil pressure drop reduction as in Fig. 9. This result is consistent with those shown by Mimaki (1987). He showed that the coated heat exchangers could provide a wet coil pressure drop reduction as large as 50 percent. It is believed that the contact angles of the uncoated and coated louver fins are 88 deg and 10 deg, respectively, as shown in Fig. 5 which was shown in Hong (1998). This is based on the measurement of the contact angles on the samples dipped in the type "B" oil and was heated with a torch for 30 seconds to evaporate the oil. This is the same procedure used in the manufacturing process of the louvered fin heat exchanger. This supports the postulate that the lower contact angle will provide lower wet coil pressure drop.

For 472 fins/m (12 fins/in.) wavy and lanced finned cores, type "A" fin press oil was used in the coil fabrication process. The characteristics of the fin press oil (Type "A") are totally different than that of the type "B" oil. Type "A" oil provided hydrophilicity on the surface because it contained a surfactant. However, type "B" oil, which did not contain a surfactant, did not enhance wetting, as shown in Fig. 5. The summary of the Fig. 5 is tabulated as shown in Table 3.

The contact angle of oil "A" dipped uncoated aluminum is 16 deg and that of oil "B" dipped coated one is 88 deg. This indicates that the oil "A" applied cores will provide wet pressure drop as low as the coated cores. However, this effect is believed to be temporary and will exist until the surfactant is washed away by repeated wet/dry cycling. This is shown in Fig. 10 and the 472 fins/m (12 fins/in.) lanced fin data in Fig. 9. Figure 10 demonstrated that the

wet coil pressure drop of oil "A" contaminated uncoated wavy core was the same as that of the coated one. To make oil free fin surfaces, the uncoated wavy core was steam cleaned with steam cleaning compound (1:20 volume ratio) for ten minutes. The cleaned cores were retested after the confirmation that the uncoated fin surface was oil free. This was done by observation that the sprayed water made bridges between the fins. The effect of the steam cleaning is to increase the wet surface pressure drop of the uncoated coil approximately 16 percent, relative to the uncleaned test. A dehumidification test for a cleaned, uncoated core was repeated and the original results were reproduced as in Fig. 10.

The hydrophilic coating on the 472 fins/m (12 fins/in.) wavy fin provides only 15 percent wet pressure drop reduction at 2.5 m/s frontal air velocity, whereas the coating on the 670 fins/m (17 fins/in.) louver fin gives 40 percent wet pressure drop reduction at the same air velocity. This is because of the difference in the wet to dry pressure drop ratio ($\Delta P_{wet}/\Delta P_{dry}$) of the uncoated cores and the fin spacing (12 fins/in. versus 17 fins/in.). At 2.5 m/s frontal velocity, the $\Delta P_{wet}/\Delta P_{dry}$ of the uncoated louver fin core was 2.4 as compared to 1.42 for the wavy fins and thus the coating had more impact on the louver fin core than the wavy fin core. However, the ratio of the wet to dry pressure drop ($\Delta P_{wet}/\Delta P_{dry}$) for the coated cores were both 1.2 at the same frontal air velocity.

For a coating having approximately 10-deg contact angle, the coating will provide only a 20 percent pressure drop increase (relative to the dry value) at 2.5 m/s frontal air velocity, regardless of the fin geometry, fin spacing, and tube layout. The associated wet pressure drop reductions, relative to the uncoated values, will be greatest when applied to high-density lanced or louver fin geometries; without the hydrophilic coating, these fins typically have 100 percent pressure drop increase under wet conditions.

We note that the present wind tunnel results do not prove durability of coatings in providing low wet pressure drop over many wet/dry cycles. Previous work of Hong and Webb (1999) has shown that the contact angle increases with number of wet/dry cycles. Hence, further work is desired to obtain wet pressure drop wind tunnel data on coils for increasing numbers of wet/dry cycles.

Table 3 Contact angle of the aluminum substrate

Condition	Initial contact angle	Contact angle after 1000 dry/wet cycles
Bare Aluminum	85 deg	55 deg
Hydrophilic Coated Aluminum w/o Oil Application	<15 deg	55-to-65 deg
Oil "A"		
Bare Aluminum	15 deg	65 deg
Coated Aluminum	<15 deg	55-to-80 deg
Oil "B"		
Bare Aluminum	Not Available	Not Available
Coated Aluminum	88 deg	Not Available

Conclusions

Hydrophilic coatings will reduce the wet pressure drop without decreasing the wet sensible heat transfer coefficient. The present test results do not establish that the wet pressure drop reduction will be maintained with increasing number of wet/dry cycles. Further testing is required to investigate this. The itemized conclusions obtained from this study are as follows:

1 For wet coils the hydrophilic coating applied on the louver and wavy fin reduces the wet pressure drop to 45 percent, and 15, respectively at 2.5 m/s frontal air velocity.

2 Fin press oil can influence the test results. If the oil contains a surfactant, it will provide temporary wet pressure drop reduction on uncoated coils. However, the surfactant is easily washed off.

3 The coating has no effect on the dry and wet sensible heat transfer coefficient for all fin geometries tested.

4 The ratio of the wet to dry sensible heat transfer coefficient was 0.85 to 0.90 for the wavy and louver fin heat exchangers. The apparent ratio was smaller for lanced fin exchangers. This is because the fin efficiency of the wet surface is overestimated.

5 Wet surface fin efficiency should be calculated using the Wu and Bong (1994) C-parameter (for specific humidity driving potential) or the Threlkeld (1970) equation for enthalpy driving potential. The McQuiston and Parker (1994) C-parameter will yield incorrect results for air humidity less than 100 percent and is not recommended.

References

- Brognaux, L. J., Webb, R. L., Chamra, L. M., and Chung, B. K., 1997, "Single-Phase Heat Transfer in Micro-Fin Tubes," *Int. Journal of Heat and Mass Transfer*, Vol. 40, pp. 4345–4358.
- Charters, W. W. S., and Theerakulpisut, S., 1989, "Efficiency Equations for Constant Thickness Annular Fins," *Int. Comm. Heat Mass Transfer*, Vol. 16, pp. 547–558.
- Eckels, P. W., and Rabas, T. J., 1987, "Dehumidification: On the Correlation of Wet and Dry Transport Processes in Plate Finned-Tube Heat Exchangers," *ASME JOURNAL OF HEAT TRANSFER*, Vol. 109, pp. 574–582.
- Holman, J. P., 1989, *Heat Transfer*, 7th Ed., McGraw-Hill, New York.
- Hong, K., 1996, "Fundamental Characteristics of the Dehumidifying Heat Exchangers With and Without the Wetting Coatings," Ph.D. thesis, The Pennsylvania State University, University Park, PA.
- Hong, K., and Webb, R. L., 1996, "Calculation of Fin Efficiency for Wet and Dry Fins," *Int. J. HVAC & R Research*, Vol. 2, No. 1, pp. 27–41.
- Hong, K. T., and Webb, R. L., 1999, "Wetting Coating Characteristics of Dehumidifying Heat Exchangers," *Int. Journal of HVAC&R*, in press.
- Kays, W. M., and London, A. L., 1984, *Compact Heat Exchangers*, McGraw-Hill, New York.
- Kim, G. R., and Webb, R. L., 1996, "Hydrophilic Treatment for Dehumidifying Heat Exchanger," technical report to LG Electronics.
- Kline, S. J., 1965, *Similitude and Approximation Theory*, McGraw-Hill, New York.
- McQuiston, F. C., and Parker, J. D., 1994, *Heating, Ventilating, and Air Conditioning*, John Wiley and Sons, New York.
- McQuiston F. C., 1975, "Fin Efficiency with Combined Heat and Mass Transfer," *ASHRAE Transactions*, Vol. 81, Part 1, pp. 350–355.
- McQuiston, F. C., 1978a, "Heat, Mass and Momentum Transfer Data For Five Plate-Fin-Tube Heat Transfer Surfaces," *ASHRAE Transactions*, Vol. 84, Part 1, pp. 266–293.
- Mimaki, M., 1987, "Effectiveness of Finned-Tube Heat Exchanger Coated Hydrophilic-Type Film," *ASHRAE Transactions*, Vol. 93, Part 1, pp. 62–71.
- Petukhov, B. S., 1970, *Advances in Heat Transfer*, Vol. 6, T. F. Irvine and J. P. Hartnett, eds., Academic Press, New York, 1970.
- Schmidt, T. E., 1945–1946, "La Production Calorifique des Surfaces Munies D'ailettes," *Annexe Du Bulletin De L'Institut International Du Froid*, Annexe G-5.
- Threlkeld, J. L., 1970, *Thermal Environmental Engineering*, Prentice-Hall, Englewood Cliffs, NJ.
- Wu, G., and Bong, T. Y., 1994, "Overall Efficiency of a Straight Fin with Combined Heat and Mass Transfer," *ASHRAE Transactions*, Vol. 100, No. 1, pp. 367–374.

APPENDIX A

Wet Surface Data Reduction

Data Reduction Methods With Dehumidification. Two different driving potentials have been used to define the wet, sensible heat transfer coefficient. These are specific humidity and enthalpy. It is important that the tests be run under fully wet conditions. Both methods are described below.

Specific Humidity Driving Potential. The heat transfer rate under wet conditions is the sum of the sensible heat and the latent heat transfer rate. The latent heat transfer rate is proportional to the mass transfer coefficient and the specific humidity change

$$q = \eta_{o,wet} [h_{wet}(T - T_{air}) + K_m h_{fg}(W_{air} - W_{sat})]. \quad (A1)$$

From the experimental measurement, the total heat transfer rate and the sensible heat transfer rate are computed using Eqs. (A.2) and (A.3).

$$Q_{tot} = \dot{m}_{air}(i_{air,in} - i_{air,out}) \quad (A2)$$

$$Q_{sen} = \dot{m}_{air} c_{p,air} \Delta T_{air} \quad (A3)$$

The Q_{sen} is also given by $Q_{sen} = UA \Delta T_{lm}$, where

$$\Delta T_{lm} = \frac{(T_{air,in} - T_{water,out}) - (T_{air,out} - T_{water,in})}{\ln \left(\frac{T_{air,in} - T_{water,out}}{T_{air,out} - T_{water,in}} \right)} \quad (A4)$$

and

$$\frac{1}{UA} = \frac{1}{\eta_o h_o A_o} + \frac{t}{k A_m} + \frac{1}{h_i A_i} \quad (A5)$$

The air-side thermal resistance is obtained from subtraction of the tube-side thermal resistance and the tube wall thermal resistance from the total thermal resistance. Thus, the wet sensible heat transfer coefficient is determined as

$$\frac{1}{\eta_{o,wet} h_{wet} A_o} = \frac{1}{UA} - \frac{t}{k A_m} - \frac{1}{h_i A_i} \quad (A6)$$

The wet surface fin efficiency ($\eta_{f,wet}$) is described in Appendix B.

Enthalpy Potential. Threlkeld (1970) has shown that Eq. (A1) can be approximated as an air enthalpy difference given by

$$q = \frac{\eta_{o,wet} h_{wet} dA}{c_{p,m}} (i_{air} - i_{sat}). \quad (A7)$$

When one uses Eq. (A7), the wet surface fin efficiency is defined by

$$\eta_{f,wet} = \frac{i_{f,avg} - i_{air}}{i_{f,base} - i_{air}} \quad (A8)$$

In this analysis, the water film thickness and temperature drop across the water film is assumed to be negligible.

APPENDIX B

Dry and Wet Surface Fin Efficiency Calculation

Various equations have been proposed for calculation of the fin efficiency of plate and circular fins for dry and wet operating conditions. These are summarized in Table B1.

Wet fin efficiency equations for different fin geometries were tabulated in Table B1.

For a continuous plate fin, the following three methods have been used in literature publications:

- Schmidt Eq. (1945),

Table B1 Summary of the fin efficiency equations

Fin geometry	Dry fin efficiency equation	Wet fin efficiency equation
Straight Fin	Threlkeld (1970)	Threlkeld (1970): I-Potential
	McQuiston (1975)	McQuiston (1975): W-Potential
	Wu and Bong (1994)	Wu and Bong (1994): W-Potential
Circular Fin	Schmidt (1945)	McQuiston and Parker (1994): W-Potential
	Hong and Webb (1996)	Hong and Webb (1996): W-Potential

- 2 sector method employing circular fin efficiency equation, and
- 3 equivalent circular method employing circular fin efficiency equation.

An analytical method to calculate the dry fin efficiency of lanced or louver fin geometries does not exist. Authors typically use the fin efficiency equation for a continuous plate fin equation. However, the fin efficiency of slit fins will be overestimated using the fin efficiency equation for continuous fins.

The fin efficiency of a wet fin is obtained using a modified form of the dry surface fin efficiency equation, where

$$\eta_{f,wet} = \frac{2r_i}{M(r_o^2 - r_i^2)} \left[\frac{K_1(Mr_i)I_1(Mr_o) - K_1(Mr_o)I_1(Mr_i)}{K_1(Mr_o)I_0(Mr_i) + K_0(Mr_i)I_1(Mr_o)} \right] \quad (B1)$$

where

$$M = \frac{hP}{kA_c} \left(1 + C \frac{i_{fg}}{c_{p,a}} \right)^{1/2} \quad (B2)$$

The C-parameter is defined here as

$$C = \frac{W_{f,tip} - W_{f,base}}{T_{f,tip} - T_{f,base}} \quad (B3)$$

Because the Bessel functions are tedious to evaluate, an empirical curve fit solution to Eq. (B1) was developed by Hong and Webb (1996). This is

$$\eta_{f,wet,e} = \frac{\tanh(Mr_i\phi) \cos(0.1Mr_i\phi)}{Mr_i\phi} \quad (B4)$$

where ϕ is defined as

$$\phi = \left(\frac{r_o}{r_i} - 1 \right) \left[1 + 0.35 \ln \left(\frac{r_o}{r_i} \right) \right] \quad (B5)$$

Schmidt (1945) defined an alternate empirical equation for fin efficiency, which is given by

$$\eta_f = \frac{\tanh(mr_i\phi)}{mr_i\phi} \quad (B6)$$

Equation (B6) may be used for wet surfaces if m is replaced by M as defined by Eq. (B2). Equation (B4) is accurate within nine percent, whereas Eq. (B6) is accurate within 18 percent, for $0 \leq m(r_o - r_i) \leq 2.5$.

Both Wu and Bong (1994) and McQuiston (1975) have defined the C-parameter to be used in the fin efficiency equation. Wu and Bong (1994) defined the C-parameter per Eq. (B3), which is based on the fact that the specific humidity of the saturated air on the wet surface is a linear function of the local fin temperature. However, the McQuiston (1975) definition for the C-parameter is valid only for saturated air. Therefore, the authors have recommended use Wu and Bong (1994) C-parameter.

One may also use Eq. (B4) to calculate the fin efficiency when using the enthalpy driving potential (Eq. (A7)). In this case, the parameter M is defined as

$$M = \frac{hP}{kA_c} \left(\frac{b_i}{c_p} \right)^{1/2} \quad (B7)$$

where b_i is the slope of the saturated air enthalpy, di_s/dT_s .

Note that the fins must be fully wet to use the wet surface fin efficiency equations.

Turbulent Convection in a Czochralski Silicon Melt

T. Zhang

F. Ladeinde
Mem. ASME

V. Prasad
Fellow ASME

Consortium for Crystal Growth Research,
State University of New York,
Stony Brook, NY 11794-2300

The individual and combined effects of buoyancy, crystal rotation, and crucible rotation are reported in this paper for axisymmetrically averaged melt convection in a large Czochralski crystal growth system for silicon. These body force effects are characterized by the respective parameters of Grashof number, Gr, rotational Reynolds number, Re_r, and the Marangoni number, Ma. The range investigated consists of $10^8 \leq Gr \leq 10^{10}$, $10^3 \leq Re_r \leq 3 \times 10^4$, and $10^3 \leq Ma \leq 10^4$, which is appropriate for the real Czochralski system. The studies are based on a multizone, adaptive, finite volume calculation. Validations of the numerical procedures are presented, including a grid convergence study. The effects of buoyancy and rotation on melt convection are discussed in detail. When the crystal and crucible both rotate at the same speed, but in opposite directions, without buoyancy, the effect of the crucible rotation is stronger. The rotation induces turbulence, contrary to what the literature suggests. For the combined effects, the intensity of turbulence and the average Nusselt number at the crucible wall are largest when buoyancy is slightly dominant over rotation. High rotation rates generate temperature oscillations in the presence of high Grashof numbers. Because of the consequence of oscillation for crystal quality, a dynamic adjustment of the rotation rate might be necessary in order to obtain desirable growth conditions.

1 Introduction

The problem of interest in this paper pertains to the melt convection in large-diameter silicon crystal growth, which plays a central role in the Czochralski (Cz) crystal growth process (Müller and Ostrogorsky, 1994; Prasad et al., 1997). Some important process features, such as the crystal-melt interface shape, temperature distribution, and the stress field are quite sensitive to the melt flow. The melt flow also determines the distribution of oxygen or rejected species at the growth interface and hence the composition of the crystal (Prasad et al., 1997). The melt flow in a Cz system is driven by buoyancy, crystal and crucible rotation, and surface tension. These effects are characterized by the respective nondimensional parameters: the Grashof number, Gr, rotational Reynolds number, Re_r, and the Marangoni number, Ma. The Cz technology has evolved from 25–50 mm (1–2 in.) diameter crystals to the current industry trend of 150–300 mm (6–12 in.) crystals. In systems with medium to large crystals (diameter ≥ 150 mm), Gr has values in the range $10^9 \leq Gr \leq 3 \times 10^{10}$, Re_r values of $10^4 \leq Re_r \leq 7 \times 10^5$, and Ma in the range $10^3 \leq Ma \leq 10^5$. The flow in these systems is known to be turbulent (Ristorcelli and Lumley, 1993; Zhang, T. et al., 1996). However, many numerical studies of crystal growth are set up for the laminar model. Kim and Langlois (1986), Anselmo et al. (1993), and Togawa et al. (1995) carried out time-dependent axisymmetric laminar simulations and showed multicellular flow structures that evolve in time. Mihelčič and Wingerath (1989) performed three-dimensional time-dependent simulations for the buoyancy-driven flow in a 120-mm diameter crucible and predicted a three-dimensional time-dependent convection. However, these simulations do not reproduce the high-frequency oscillations which have been observed in experiments on both the temperature fields and dopant striations (Elwell and Andersen, 1989; Iliev et al., 1991; Müller and Ostrogorsky, 1994). It has been observed by Kobayashi et al. (1991), Ono et al. (1993), and the current authors (Zhang, T., et al., 1996) that the numerical simulations for $Gr \geq 10^8$ will not converge if a laminar model is used, unless an unacceptably large amount of numerical dissipa-

tion is applied. The results obtained from laminar calculation also do not agree well with experimental observations (Kobayashi et al., 1991; Ono et al., 1993; Kinney and Brown, 1993).

In principle, one could apply the direct numerical simulation (DNS) technique to calculate the turbulence during crystal growth. However, DNS requires very fine mesh in space and time, as well as special numerical schemes, and is therefore limited to low Gr and Re values and relatively simple geometries and boundary conditions. Further, although significant progress has been made in recent years (Germano et al., 1991), the large eddy simulation procedure, LES, has not matured to a state where it can be routinely used for the calculation of realistic engineering systems. Therefore, the use of Reynolds-averaged Navier-Stokes equations (RANS) is perhaps the only feasible approach to analyze the Cz system, given the current state of turbulence and CFD technology. Kobayashi et al. (1991) and Kinney and Brown (1993) have calculated the Cz system with the standard kinetic energy-turbulence dissipation ($k-\epsilon$) model. Ristorcelli and Lumley (1993) used a more complicated model based on the second moments of turbulence fluctuations. Their approach, however, requires the simultaneous solution of 17 coupled partial differential equations and 23 nonlinear algebraic equations. This is computationally expensive and will not be a choice for simulating the flow in a real Cz system. In a recent comparison study (Zhang, T., et al., 1996), the present authors have shown that, in comparison to many variations of the $k-\epsilon$ model, the renormalization group (RNG) model, which is the one used to generate the results in this paper, gave the best overall performance for natural convection in a cavity. It does not introduce much complication or cost relative to the standard $k-\epsilon$ model. Further work by the authors has confirmed the suitability of the RNG model for melt convection.

Some interesting observations have been reported from the handful of studies on turbulent melt convection in crystal growth. Kobayashi et al. (1991) studied the effects of crucible rotation on the temperature fluctuation; Ristorcelli and Lumley (1993) reported on the effect of buoyancy and Kinney and Brown (1993) predicted temperature and interface shape, and the enhancement of heat and mass transfer with increasing crucible rotation. However, parametric studies of the crystal growth process that systematically investigate the individual and combined roles of the various driving forces are rare. The results from simple systems have often

Contributed by the Heat Transfer Division for publication in the JOURNAL OF HEAT TRANSFER. Manuscript received by the Heat Transfer Division, Nov. 10, 1997; revision received, Jan. 19, 1999. Keywords: Computational, Heat Transfer, Natural Convection, Rotating, Turbulence. Associate Technical Editor: A. Lavine.

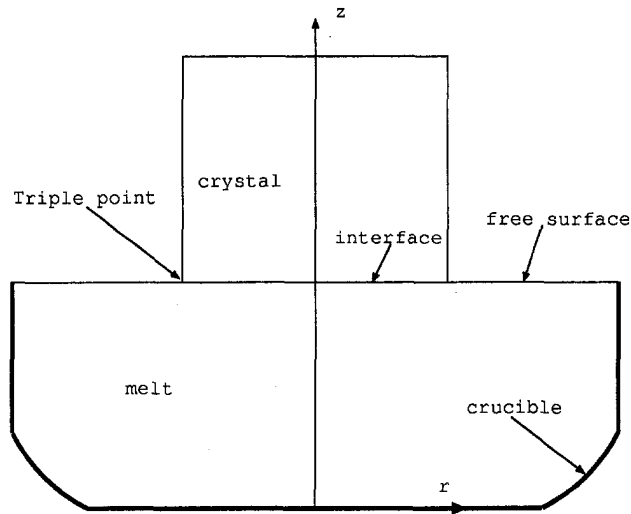


Fig. 1 Schematic of the Czochralski process for growing single silicon crystals

been used to explain the phenomena in the real, complicated system. For example, conclusions drawn from the studies of natural convection in a cavity and the rotation of a disk in an infinite fluid layer have been used to explain the melt convection phenomena in the Cz system (Müller and Ostrogorsky, 1994), which is not accurate. The present work has been undertaken to address the aforementioned shortcomings through numerical simulation. The studies by Hurle (1983), Jones (1988), Kobayashi (1995), and Prasad et al. (1997) on the effects of the driving forces in a Cz system are relevant, as useful information was reported regarding the dependence of the flow structure on various combinations of the driving forces. However, these studies are limited to small systems, with small nondimensional parameters: $Gr \leq 10^7$, $Re \leq 10^4$, $Ma \leq 10^3$. The convection is laminar, so that the effects of turbulence, which is important in industry-size Cz systems, were not taken into account. In addition, the important issue of the effect

of the various driving forces on heat transfer was not addressed by the foregoing studies, even though the growth process and the final crystal quality are known to depend on them. These and various other issues are addressed in this paper.

2 Mathematic Modeling

Figure 1 shows a schematic of the physical system. The silicon melt is contained in a quartz crucible, which is heated to keep the melt in a molten state, with the crystal being slowly pulled vertically upwards from the melt. This paper focuses on the flow and heat transfer characteristics of the melt as they are affected by the combination of buoyancy, rotation, and surface tension. The heat conduction equation is also solved in the solid crystal, in a conjugate thermal model.

The equations governing the melt flow in the Cz system are those stating the conservation of mass, momentum, and energy. The multidomain nature of the modeled system, together with the presence of multiple body force types necessitates that some simplifying assumptions be made. The Cz melt is modeled as a Newtonian, Boussinesq liquid with constant properties; the solid crystal is also assumed to have constant properties. The azimuthally averaged (Dupret et al., 1998) RANS equations are used, with the dimensional form:

$$\frac{\partial}{\partial r}(rv) + \frac{\partial}{\partial z}(ru) = 0 \quad (1)$$

$$\frac{\partial ru}{\partial t} + \frac{\partial rvu}{\partial r} + \frac{\partial ruu}{\partial z} = -\frac{r}{\rho} \frac{\partial p}{\partial x} + r\beta g(T - T_{ref}) + \frac{\partial}{\partial r} r\nu \frac{\partial u}{\partial r} + \frac{\partial}{\partial z} r\nu \frac{\partial u}{\partial z} - \left(\frac{\partial}{\partial z}(r\tau_{rz}) + \frac{\partial}{\partial r}(r\tau_{rz}) \right) \quad (2)$$

$$\frac{\partial rv}{\partial t} + \frac{\partial rvv}{\partial r} + \frac{\partial ruv}{\partial z} = -\frac{r}{\rho} \frac{\partial p}{\partial r} + \frac{\partial}{\partial r} r\nu \frac{\partial v}{\partial r} + \frac{\partial}{\partial z} r\nu \frac{\partial v}{\partial z} + w^2 - \nu \frac{v}{r} - \left(\frac{\partial}{\partial r}(r\tau_{rr}) + \frac{\partial}{\partial z}(r\tau_{rz}) - \tau_{\theta\theta} \right) \quad (3)$$

Nomenclature

b = radius of crucible, characteristic length (m)
 C = turbulence model constant
 g = acceleration due to gravity (m/s^2)
 P_b = production due to buoyancy ($kg/m \cdot s^3$)
 Gr = Grashof number with respect to crucible radius, $g\beta b^3(T_w - T_f)/\nu^2$
 Gr_h = Grashof number with respect to melt height, $g\beta h^3(T_w - T_f)/\nu^2$
 h = height of the melt (m)
 k = turbulence kinetic energy (m^2/s^2)
 Ma = Marangoni number, $d\sigma/dT(T_w - T_f)b/\rho\nu\alpha$
 Nu = Nusselt number, $(\partial\Theta/\partial n^*)|_{surface}$
 P = pressure (Pa)
 Pr = Prandtl number, ν/α
 P_k = production of turbulent kinetic energy ($kg/m \cdot s^3$)
 Q = heat input (KW)
 r = radial coordinate (m)
 Re = rotational Reynolds number, $\omega b^2/\nu$
 S_{ij} = strain rate tensor (s^{-1})
 T = mean temperature (K)

T' = temperature fluctuation (K)
 t = time (s)
 u = mean velocity in the axial direction (m/s)
 u' = fluctuating velocity in the axial direction (m/s)
 v = mean velocity in the radial direction (m/s)
 v' = fluctuating velocity in the radial direction (m/s)
 w = mean velocity in the azimuthal direction (m/s)
 w' = fluctuating of velocity in the azimuthal direction (m/s)
 z = vertical coordinate (m)

Greek Symbols

α = thermal diffusivity (m^2/s)
 β = volume expansion coefficient (K^{-1})
 ϵ = turbulence dissipation rate (m^2/s^3)
 η = irreducible invariants
 γ = thermal conductivity ($W/m \cdot K$)
 μ = viscosity ($kg/m \cdot s$)
 ν_i = turbulence kinematic viscosity (m^2/s)

ν = kinematic viscosity (m^2/s)
 ρ = density (kg/m^3)
 σ = turbulence model constant
 $d\sigma/dT$ = thermocapillary coefficient ($N/m \cdot K$)
 τ_{ij} = Reynolds stress tensor (N/m^2)
 Θ = dimensionless temperature, $(T - T_f)/(T_w - T_f)$
 θ = azimuthal coordinate (K)
 ω = angular velocity (s^{-1})

Subscripts

cry = crystal
 crb = crucible
 ϵ = turbulence dissipation rate
 μ = viscosity
 f = freezing temperature of silicon
 i = i th coordinate direction
 k = turbulence kinetic energy
 n = coordinate out-normal to a surface
 r = rotational
 t = turbulent
 w = crucible side wall

$$\frac{\partial rw}{\partial t} + \frac{\partial rvw}{\partial r} + \frac{\partial ruw}{\partial z} = \frac{\partial}{\partial r} r\nu \frac{\partial w}{\partial r} + \frac{\partial}{\partial z} r\nu \frac{\partial w}{\partial z} - vw - \frac{vw}{r} - \left(\frac{\partial}{\partial r} (r\tau_{r\theta}) + \frac{\partial}{\partial z} (r\tau_{z\theta}) + \tau_{r\theta} \right) \quad (4)$$

$$\frac{\partial rT}{\partial t} + \frac{\partial rvT}{\partial r} + \frac{\partial ruT}{\partial z} = \frac{\partial}{\partial r} r\alpha \frac{\partial T}{\partial r} + \frac{\partial}{\partial z} r\alpha \frac{\partial T}{\partial z} - \frac{\partial ru'T'}{\partial z} - \frac{\partial rv'T'}{\partial r}, \quad (5)$$

where u , v , p , T are the mean quantities as defined in the Nomenclature, and $\tau_{ij} \equiv \overline{u'_i u'_j}$ is the Reynolds stress tensor. An overbar indicates ensemble averaging and a prime indicates fluctuation relative to the averaging. The fluctuating temperature is denoted by T' . For the parameter values used, the flow is probably three-dimensional, with baroclinic waves inclined to the (r, θ) plane. However, the solutions to our model equations above represent azimuthal averaging and Reynolds time-averaging over short time intervals. This way, the model can predict oscillations superimposed on the turbulence fluctuations.

Concerning boundary conditions, constant temperature with a nondimensional value of 1 is assumed along the crucible side wall with a linear distribution decreasing to the value 0.7 on the bottom. No-slip velocity conditions are used at the solid walls: $u = v = 0$, $w = w_{\text{wall}}$. At the free surface (Fig. 1), the stress tangential to the surface must balance the surface tension, which leads to

$$\mu \left(\frac{\partial v}{\partial n} - \frac{\partial u}{\partial \tau} \right) = - \frac{\partial \sigma}{\partial T} \frac{\partial T}{\partial n}. \quad (6)$$

In this equation, n is the coordinate in the direction normal to the free surface, τ in the tangential direction, and $\partial \sigma / \partial T$ is the thermocapillary coefficient. Radiative effects are included via the gray diffusive model (Zhang and Prasad, 1995).

Note that the nondimensional form of the governing Eqs. (1) through (6) were computed by the computer program, with the scales for nondimensionalization: ν/b for velocity, b^2/ν for time, and b for length. The nondimensional temperature is $\Theta = (T - T_f)/(T_w - T_f)$. The scale for the Stoke's stream function is ν .

Details of the boundary conditions can be found in Zhang and Prasad (1995) and Zhang et al. (1996b).

3 Turbulence Models

The RANS equations contain the Reynolds stress tensor, $\tau_{ij} = \overline{u'_i u'_j}$, where u'_i is fluctuating velocity in the i th coordinate direction. The turbulence heat flux $\overline{u'_i T'}$ also appears, where T' is fluctuating temperature. Models are needed for these terms in order to close the RANS equations. Several turbulence models have been tested, including the standard $k-\epsilon$ model (SKM) (Jones and Lauder, 1972), the low Reynolds number model (LRM) of Abe and Kondoh (1995), algebraic stress model (ASM) (Gatski and Speziale, 1993), and the Renormalization Group (RNG) $k-\epsilon$ model (Yakhot et al., 1992). These models were used to calculate turbulent natural convection in a 5:1 cavity, using the conditions of the physical experiment by Cheesewright et al. (1986). Figure 2 shows the comparison of the predicted midplane velocity profiles with the measurements of Cheesewright (Zhang, T. et al., 1996). It can be seen that ASM and RNG yield very good predictions but the other two models do not. Studies by Noble (1993) have also reported a poor performance of the $k-\epsilon$ model for natural convection. We subjected ASM and RNG to further studies, using the Cz system, and ASM was found to have a poorer convergence. This is probably due to its nonlinearity with respect to the strain rate, which will tend to amplify errors. The RNG model has the same complexity as SKM in terms of implementation, its convergence rate is comparable to that of SKM, and it gives more accurate results. Hence the RNG $k-\epsilon$ model has been adopted for the present work.

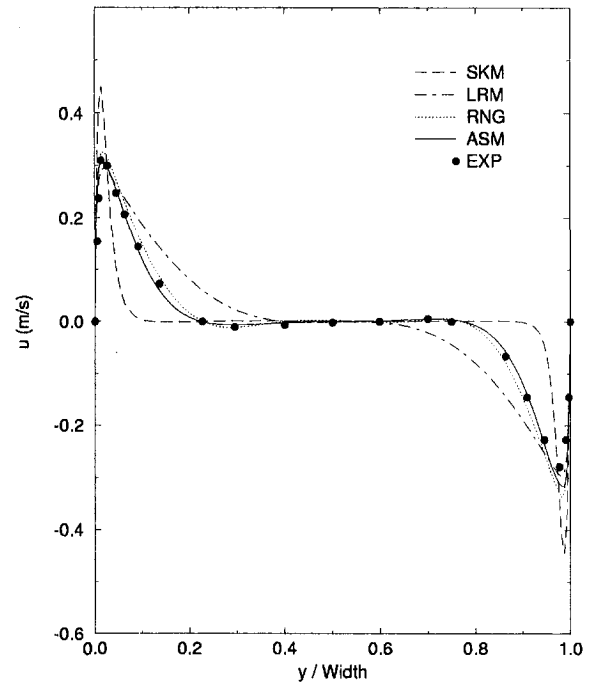


Fig. 2 Comparison with the experiment of Cheesewright et al. for natural convection in a 5:1 cavity: mean vertical velocity distribution at midheight

In the RNG model, the Reynolds stresses τ_{ij} are modeled using the eddy-viscosity concept:

$$\tau_{ij} = \frac{2}{3} k \delta_{ij} - 2\nu_t S_{ij}, \quad \nu_t = C_\mu \frac{k^2}{\epsilon}. \quad (7)$$

Gradient transport model is assumed for the turbulent heat flux:

$$\overline{u'_i T'} = - \frac{\nu_t}{Pr_t} \frac{\partial T}{\partial x_i}. \quad (8)$$

In these equations, k , ν_t , S_{ij} , and Pr_t are the turbulence kinetic energy, turbulence viscosity, the (i, j) component of strain rate tensor, and the turbulence Prandtl number, respectively (Pr_t is set at 0.9 for these calculations). We use the axisymmetric form of RNG equations:

$$\frac{\partial rk}{\partial t} + \frac{\partial rvk}{\partial r} + \frac{\partial ruk}{\partial z} = \frac{\partial}{\partial r} r \left(\nu + \frac{\nu_t}{\sigma_k} \right) \frac{\partial k}{\partial r} + \frac{\partial}{\partial z} r \left(\nu + \frac{\nu_t}{\sigma_k} \right) \frac{\partial k}{\partial z} + (rP_k + rP_B - r\epsilon) \quad (9)$$

$$\frac{\partial r\epsilon}{\partial t} + \frac{\partial rv\epsilon}{\partial r} + \frac{\partial ru\epsilon}{\partial z} = \frac{\partial}{\partial r} r \left(\nu + \frac{\nu_t}{\sigma_\epsilon} \right) \frac{\partial \epsilon}{\partial r} + \frac{\partial}{\partial z} r \left(\nu + \frac{\nu_t}{\sigma_\epsilon} \right) \frac{\partial \epsilon}{\partial z} + \frac{\epsilon}{k} (C_{1\epsilon} rP_k - C_{2\epsilon} r\epsilon) \quad (10)$$

where

$$P_k = -\tau_{ij} \frac{\partial u_i}{\partial x_j} = \nu_t \left[2 \left\{ \left(\frac{\partial v}{\partial r} \right)^2 + \left(\frac{v}{r} \right)^2 + \left(\frac{\partial u}{\partial z} \right)^2 \right\} + \left(\frac{\partial u}{\partial r} + \frac{\partial v}{\partial z} \right)^2 + \left(\frac{\partial w}{\partial z} \right)^2 + \left(\frac{\partial w}{\partial r} - \frac{w}{r} \right)^2 \right] \quad (11)$$

and

Table 1 Grid convergence study

	21 × 31	42 × 62	84 × 124
ψ_{max}	0.00	8.41	8.43
ψ_{min}	-795.33	-752.50	-752.70
ν_{tmax}	3.52	11.47	11.48
u_{max}	18041.90	19310.32	19309.83
u_{min}	-9220.99	-8748.89	-8749.92
v_{max}	10004.30	9774.65	9775.02
v_{min}	-21252.04	-20781.13	-20780.81

ψ is the stream function. All quantities are nondimensional.

$$P_B = -\beta g \frac{\nu_t}{\sigma_k} \frac{\partial T}{\partial z} \quad (12)$$

are the production of kinetic energy by shear and buoyancy, respectively. In Eq. (10),

$$C_{1\epsilon} = 1.42 - \frac{\eta(1 - \eta/\eta_0)}{1 + \beta\eta^3}, \quad \eta = Sk/\epsilon,$$

$$S = (2S_{ij}S_{ij})^{1/2}, \quad \eta_0 = 4.38, \quad \beta = 0.015,$$

and the coefficients C_μ , σ_k , σ_ϵ , $C_{2\epsilon}$ are 0.085, 0.7179, 0.7179, 1.68, respectively.

The present paper used the wall function approach for the k and ϵ equations. At crucible walls and melt-crystal interface, zero value is specified for k . The value of ϵ is specified at one grid point away from the solid walls:

$$\epsilon_p = C_d K^{3/2} / \kappa C_\mu^{1/4} y_p$$

where the subscript p stands for the point one grid away from the wall and $C_d = 1.0$, $\kappa = 0.4187$. The effective eddy-viscosity ($\nu_{eff} = \nu + \nu_T$) is calculated as follows:

$$\mu_{eff} = \mu \quad \text{if } y^+ \leq 11.63 \quad (13)$$

$$\mu_{eff} = \mu y^+ / 2.5 \log(Ey^+) \quad \text{if } y^+ > 11.63, \quad (14)$$

where

$$y^+ = C_\mu^{1/4} k^{1/2} y / \nu$$

and $E = 9.793$.

The wall treatment for the k - ϵ model does not calculate natural convection correctly (Noble, 1993), but it seems that the RNG version produces more accurate results, consistent with earlier studies (Zhang, T. et al., 1996).

It is pointed out that the chosen turbulence model in this paper might not be appropriate for a full three-dimensional model of the Cz system because of the complicated rotational effects. These effects originate from gyroscopic torques which are a consequence of the Coriolis force, $2\mathbf{\Omega} \times \mathbf{u}$, which exists only in three-

dimensional flows. Therefore, these effects are not relevant to the present work, in which axisymmetrically averaged equations are used. In fact, the turbulence modeling difficulties associated with rotation by virtually all modelers fail to distinguish between the role of the Coriolis force and that of the other effects when flows are examined in the astrophysical frame of reference. Furthermore, we are not aware of any rotating flow models that are based on the inertial frame. A rotating flow issue relevant to the present work is centrifugal buoyancy (Ladeinde and Torrance, 1991), which preliminary work shows is not significant for the parameters used in this work.

4 Numerical Procedure

The numerical scheme used in this study is based on the multizone adaptive grid generation (MAGG) and curvilinear finite volume (CFV) discretization program developed by Zhang and Prasad (1995, 1997). The MASTRAPP (multizone adaptive scheme for transport and phase-change problems) scheme efficiently handles the multidomain environment of a Cz system, where the melt and the solid crystal have very different thermophysical properties. An efficient scheme is contained in this code for fast and accurate prediction of interface movement caused by phase change and flow oscillations, as well as for clustering grids in the interface regions. A semi-implicit solution scheme is used to solve a generic convective-diffusion equation with the SIMPLER method for pressure correction, power law for convection terms, and the momentum interpolation method to prevent pressure oscillations. Details of the numerical schemes can be found in Zhang and Prasad (1995, 1997).

The simulation of the melt flow in a Cz system is a formidable task. A typical run with a 42×62 mesh requires 5–15 hours CPU time on a single processor of the multiprocessor IBM SP/2. In addition, high parameter calculations have to be carried out in an incremental fashion, i.e., via the continuation process.

5 Code Validation

Earlier work on the laminar version of our code has subjected the code to very stringent tests to generate confidence in the results (Zhang et al., 1995). However, the code has been modified by the procedures reported in this paper and hence requires further validation. As mentioned earlier, comparison with Cheesewright (Fig. 2) shows that our code is quite capable of generating accurate turbulence results. The convergence (grid-independence) property of our code is shown in Table 1. Here three grids, with different levels of refinement (21×31 , 42×62 , 84×124) are used to compute natural convection in a Cz melt for $Gr = 10^9$. The results in Table 1 clearly show grid independence beyond the 42×62 refinement. The reader should be aware that convergence issues are important for rotating flows, not because of the physics of the Coriolis force per se, but because of the centrifugal force field, $\mathbf{\Omega}$

Table 2 Experiments on laminar computations

	Ra							
	10^5				10^6			
	1	2	3	4	1	2	3	4
v_{max}	34.96	35.02	34.73	35.73	67.61	66.76	64.63	68.81
z ($y = 0.5$)	0.856	0.856	0.855	0.857	0.856	0.856	0.850	0.872
u_{max}	68.51	68.66	68.59	69.08	221.57	220.84	217.36	221.8
y ($z = 0.5$)	0.063	0.063	0.066	0.067	0.039	0.039	0.0379	0.0375
$\bar{N}u$	4.52	4.53	4.519	4.430	9.21	9.03	8.799	8.754
Nu_{max}	7.963	7.978	7.717	7.626	19.08	18.84	17.925	17.872
z ($y = 0$)	0.0793	0.0793	0.081	0.0825	0.0354	0.0354	0.0378	0.0375
Nu_{min}	0.735	0.739	0.729	0.824	1.070	1.052	0.989	1.232
z ($y = 0$)	0.9915	0.9915	1.0	0.9925	0.9915	0.9915	1.0	0.9925

Note: (1) Present solution with turbulence model; (2) present solution without turbulence model; (3) de Vahl Davis' solution (de Vahl Davis, 1983); Markatos' solution (Markatos and Pericleous, 1984). All velocities are nondimensionalized with κ/D , and lengths with D , where D is the cavity width, and κ is the thermal diffusivity of air.

Table 3 Parameter values used in simulation

Case	Subcase	Gr	Re_{cry}	Re_{crb}	Ma
I	(a)	10^8	0	0	0
	(b)	10^9	0	0	0
	(c)	10^{10}	0	0	0
II	(a)	0	10^3	0	0
	(b)	0	10^4	0	0
	(c)	0	3×10^4	0	0
III	(a)	0	0	10^3	0
	(b)	0	0	10^4	0
	(c)	0	0	3×10^4	0
IV	(a)	0	10^4	10^4	0
	(b)	0	10^4	10^4	0
	(c)	0	3×10^4	3×10^4	0
V	(a)	10^8	10^4	10^4	10^3
	(b)	10^9	10^4	10^4	10^4
	(c)	10^9	3×10^4	3×10^4	10^4

$\times \Omega \times r$. The effect depends explicitly on the spatial coordinates, so that grid independence is relatively more difficult to obtain compared to nonrotating systems. Furthermore, different numerical problems arise depending on whether a rotating flow problem is solved in the inertial or rotating frame of reference. Grid convergence may be better in the inertial frame. Finally, grid-independent studies were carried out to establish convergence for the present simulations, which use inertial frame, with and without rotation of the crucible and crystal.

A desirable feature of a turbulence code is that, when the averaged quantities, including the equations for k and ϵ , are solved for laminar flows, it should produce the accurate laminar results, even though the equations were developed for turbulent flows. This requirement is very important because, in application, we are not always certain that a flow is turbulent or laminar until after some preliminary work.

To demonstrate this interesting feature, which is absent in most commercial software packages, comparisons are made with the solutions of de Vahl Davis (1983) and Markatos and Pericleous (1984) for the laminar natural convection of air in a square cavity. Table 2 shows the results from the present work with and without RNG turbulence model, as well as the results of de Vahl Davis and Markatos. It can be seen that both our laminar and turbulence calculations agree very well with the other two solutions, indicating that our RNG model is capable of accurate calculations even when the flow is laminar.

6 Results and Discussion

The Cz system considered in this study has a crystal to crucible diameter ratio of 0.4 and the ratio of melt height to crucible radius is 0.6. No interface movement is calculated in this paper. Table 3 lists the set of parameter values used in our simulation, which have been grouped into five cases. Case I investigates the effects of buoyancy, assuming negligible effects of surface tension and rotation. This case provides a basis for evaluating the effects of rotation. The results for various Grashof number values are presented. Case II studies the effects of pure crystal rotation without buoyancy and crucible rotation, by varying the rotational Reynolds number of the crystal. Case III examines the effects of crucible rotation without buoyancy and crystal rotation, by varying the rotational Reynolds number. Case IV investigates the combined effects of both crystal and crucible rotation. Since the rotational Reynolds number is evaluated with respect to the crucible radius, equal crucible and crystal rotational Reynolds number indicates that the crystal and crucible are rotating at the same rate, although in opposite directions. In Cases II through IV, Gr and Ma are all set to zero so that the effect of pure rotation can be evaluated. Studying the individual driving forces provides a basis for interpreting results when all driving forces are present, as in a real process. Case V studies the combined effects of all the driving forces. The effects of the relative strength of rotation and buoyancy

are reported, with the focus mainly on the turbulent flow regime. All the results in the tables and figures are in nondimensional units except when otherwise indicated.

6.1 Natural Convection (Case I). In this section, the effect of buoyancy on melt flow and heat transfer across the melt is presented for the case without rotation. Note that Ma is set to zero when studying the individual effects but is set to its actual value when all the effects are combined to model the real process. Three subcases are studied: (a) $Gr = 10^8$; (b) $Gr = 10^9$; (c) $Gr = 10^{10}$, all for $Re_r = 0$ and $Ma = 0$. Figures 3(a) through 3(c) show the streamlines for the Stokes stream function, ψ , corresponding to these three subcases. It can be seen that, for different Grashof numbers, the basic flow pattern is similar in the sense that the hot fluid rises along the crucible side wall and the cold fluid descends at the center region of the system, forming a circulation within the crucible. However, the intensity of the flows increases as Grashof number increases. A similar single cell structure caused by buoyancy has also been reported by Kinney and Brown (1993). For the $Gr = 10^{10}$ case, streamlines with values less than -840 depart from the circular pattern. This shows an incipient separation of the vortex as the flow acquires larger kinetic energy with increasing Grashof number. The large values of turbulent viscosity results in Figs. 4(a) through 4(c) support this explanation. Note that when $Gr \leq 10^8$ (Fig. 4(a)), turbulence viscosity, which is an indicator of the extent of turbulence transport, is negligible compared to the physical viscosity of silicon melt, indicating that the flow is laminar. This result agrees with suggestions that the flow in silicon melt is laminar when $Gr < 10^8$ (Müller and Ostrogorsky, 1994).

When $Gr \geq 10^9$ (Figs. 4(b) and 4(c)), ν_t becomes significant compared to ν , indicating significant turbulence. The tendency toward separation at the highest Grashof number can be observed in the turbulence viscosity contour map for this case. Since silicon growth is being simulated, with an assumed temperature difference of 50 K, the Grashof number is proportional to the cube of the characteristic convection length scale (in our case, the radius of the crucible). Therefore, and as expected, our results show that laminar flow exists only in small systems (the crucible diameter would be less than 120 mm when $\Delta T = 50$ K to keep $Gr \leq 10^8$).

Figures 5(a) through 5(c) show that the shapes of the isotherms follow the convection pattern in Figs. 3(a) through 3(c), which implies that convective transport of heat is stronger than molecular transport. For silicon melt ($Pr = 0.015$), the effective diffusivity of temperature, α_{eff} , can be written as

$$\alpha_{eff} = \nu \left(66.7 + 1.1 \frac{\nu_t}{\nu} \right) \quad (15)$$

within our turbulence modeling framework. This shows enhanced thermal transport with increasing ν_t or Gr .

Solidification takes place at the interface, which has been kept flat in our simulation in order to focus on the melt convection. However, our code can calculate, and has been used to dynamically calculate, the actual interface shape.

Figure 6 shows the distribution of the effective local Nusselt number in terms of the nondimensional quantities:

$$Nu_{eff} = \frac{\partial \Theta}{\partial n^*} \Big|_{melt} - \frac{\kappa_{crystal}}{\kappa_{melt}} \frac{\partial \Theta}{\partial n^*} \Big|_{crystal} \quad (16)$$

along the interface for the three subcases, where n^* is the nondimensional coordinate normal to the interface, $\kappa_{crystal}$ is the crystal thermal conductivity and κ_{melt} is the melt thermal conductivity, the subscript "melt" and "crystal" imply the melt and crystal side of the interface, respectively. Note that $\kappa_{crystal}/\kappa_{melt} \approx 0.34$. It can be seen that at the outer edge of the crystal ($r > 0.3$), the effective heat flux is high (>100 for the case where $Gr = 10^{10}$), while close to the crystal center ($r < 0.1$), it is relatively small (about -3). The tri-junction position is governed by capillary effects (surface

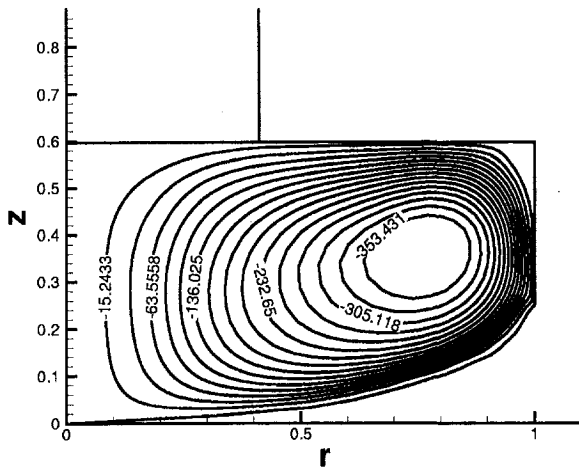


Fig. 3(a)

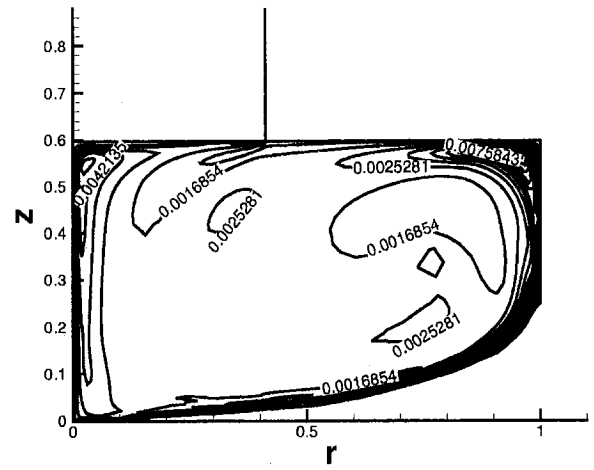


Fig. 4(a)

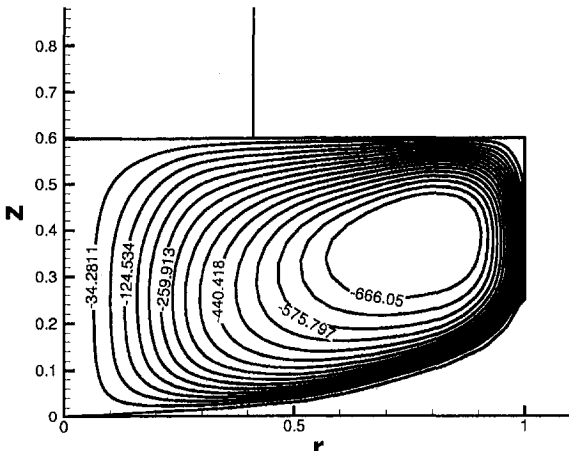


Fig. 3(b)

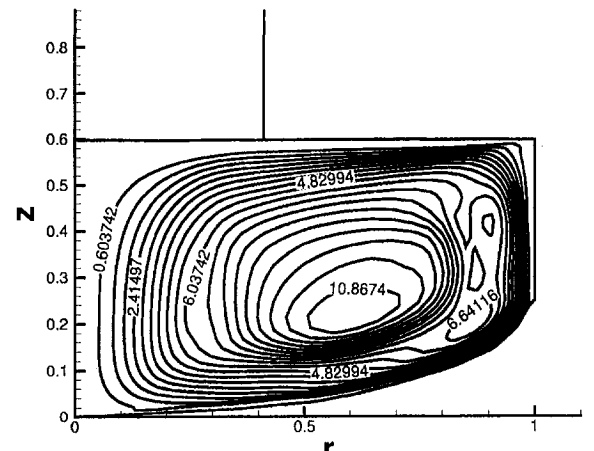


Fig. 4(b)

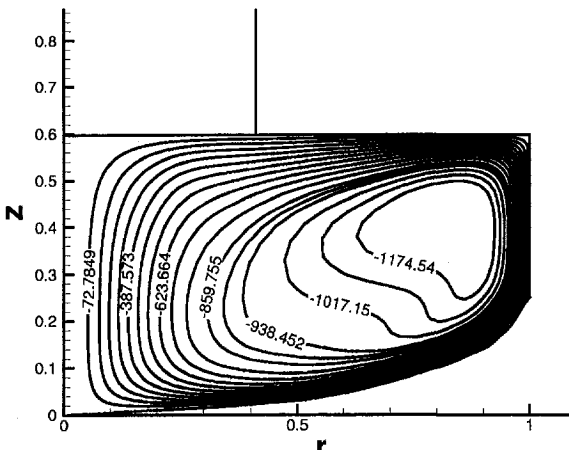


Fig. 3(c)

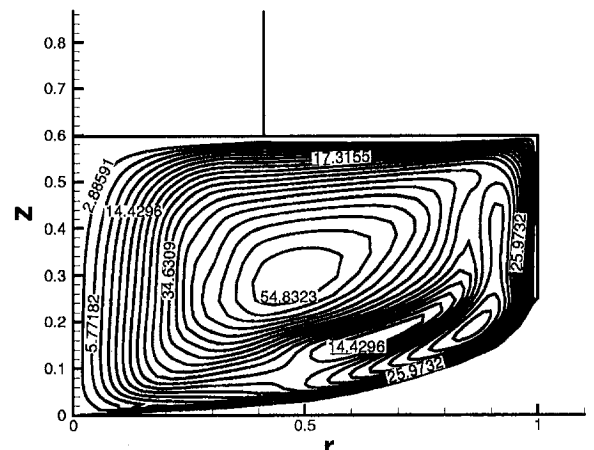


Fig. 4(c)

Fig. 3 Effect of Grashof number, Gr , on melt flow in a nonrotating Cz system, showing the nondimensional Stokes stream function plot for (a) $Gr = 10^8$; (b) $Gr = 10^9$; (c) $Gr = 10^{10}$. $Re_c = 0$ and $Ma = 0$.

Fig. 4 Effect of Grashof number, Gr , on melt flow in a nonrotating Cz system, showing the turbulent viscosity (ν_t/ν) for (a) $Gr = 10^8$; (b) $Gr = 10^9$; (c) $Gr = 10^{10}$. $Re_c = 0$ and $Ma = 0$.

tension and wetting angle). The position of the tri-junction with respect to the melt level (the free surface) has no real importance, while the position of the tri-junction with respect to the intersection of the interface and the axis governs the melt-crystal interface convexity. The sharp increase in local Nusselt number with Grashof number implies serious difficulty in growing large diameter silicon crystals.

The average Nusselt number (\bar{Nu}) on the crucible is also calculated as

$$\bar{Nu} = \frac{1}{A^*} \int_{A^*} -\frac{\partial \Theta}{\partial n^*} dA^* \quad (17)$$

where A^* is the total nondimensional area of the crucible wall, and n^* is the nondimensional coordinate normal to the wall; the

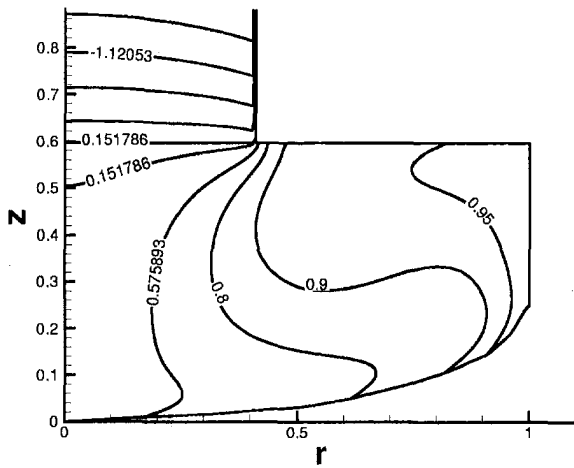


Fig. 5(a)

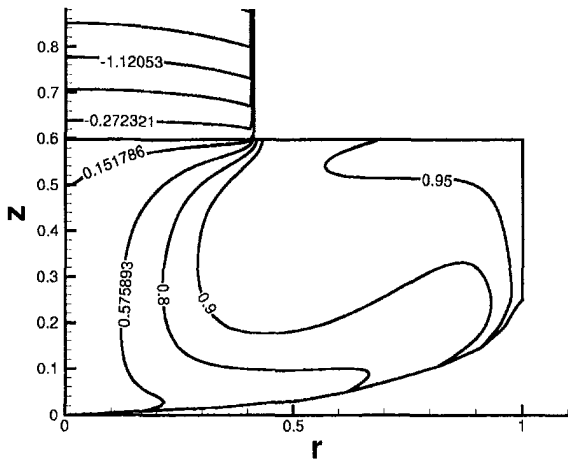


Fig. 5(b)

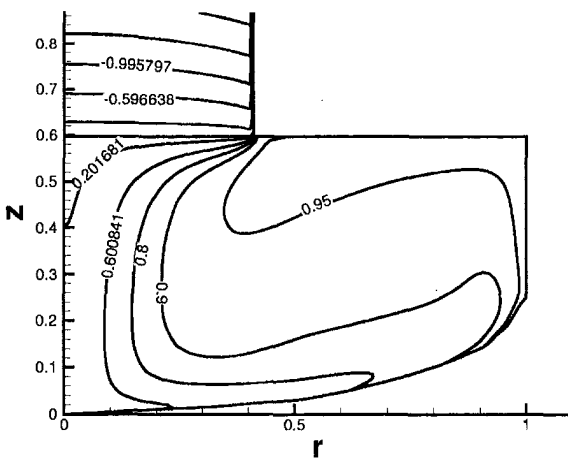


Fig. 5(c)

Fig. 5 Effect of Grashof number, Gr , on melt flow in a nonrotating Cz system, showing the nondimensional isotherms for (a) $Gr = 10^8$; (b) $Gr = 10^9$; (c) $Gr = 10^{10}$. $Re_c = 0$ and $Ma = 0$.

superscript “*” implies that the quantity is nondimensional. The heat flow rate from the crucible to the melt can then be estimated as

$$Q_{\text{ctb}} = \int_A -\kappa \frac{\partial T}{\partial n} dA$$

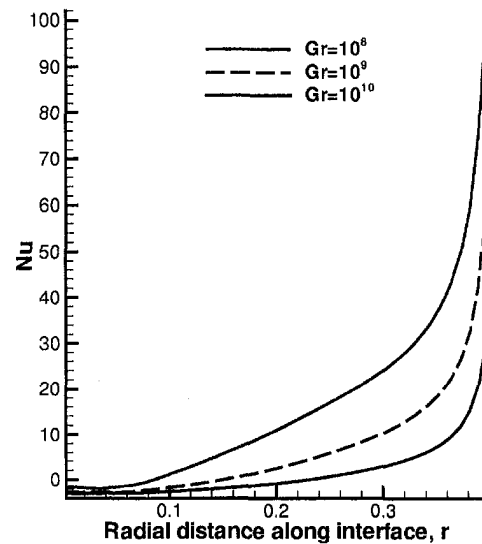


Fig. 6 Effect of Grashof number, Gr , on the effective Nusselt number for $Gr = 10^8$, 10^9 , and 10^{10} . $Re_c = 0$, $Ma = 0$. The uppermost curve is for $Gr = 10^{10}$.

$$\begin{aligned} &= \kappa \int_{A^*} -\frac{\partial \Theta}{\partial n^*} \frac{\Delta T}{b} b^2 dA^* \\ &= \kappa b \Delta T A^* \overline{Nu} \end{aligned} \quad (18)$$

where A is the area of the crucible surface, ΔT is the temperature difference across the melt, and κ is the thermal conductivity of silicon melt, which is $60 \text{ Wm}^{-1}\text{K}^{-1}$. The total heat flow rate to the system, Q_{total} , is estimated as $Q_{\text{ctb}}/0.3$. Table 4 gives estimates for Q for the various cases investigated.

6.2 Effects of Crystal and Crucible Rotation. During growth, the crystal and crucible are usually rotated to ensure thermal symmetry and uniformity. It has also been suggested that rotation could reduce the turbulence level and stabilize the flow. This section reports on the effects of crucible and crystal rotation on flow and heat transfer. Three cases are reported: (a) crystal rotation (Case II in Table 3), (b) crucible rotation (Case III in Table 3), and (c) combined crystal and crucible rotation (Case IV in Table 3). To appreciate our results, the reader needs to be aware that rotation could have dual effects. Relative to a non-rotating system, rotation will normally introduce some non-axisymmetric modes of instability, which usually have the amplitude and growth rate advantage to dominate other modes and cause instability (Ladeinde and Torrance, 1991). On the other hand, finite amplitude

Table 4 Maximum turbulent viscosity (ν_t/ν) and heat transfer data

Case	Subcase	Max ν_t/ν	Nu	Q_{total} (KW)
I	(a)	0.0076	0.91	2.2
	(b)	10.90	1.65	12.1
	(c)	54.80	2.9	42.5
II	(a)	9.0×10^{-6}	0.27	2.0
	(b)	0.0014	0.31	2.3
	(c)	1.72	0.35	2.6
III	(a)	0.003	0.27	2.0
	(b)	8.12	0.29	2.1
	(c)	25.32	0.36	2.7
IV	(a)	0.0096	0.27	2.0
	(b)	12.62	0.31	2.3
	(c)	36.62	0.39	2.9
V	(a)	21.75	0.42	3.1
	(b)	100.43	1.48	11.0
	(c)	62.35	0.47	3.4

$$\text{Re}_{cry} \equiv \frac{\omega_{cry} b^2}{\nu} \quad (19)$$

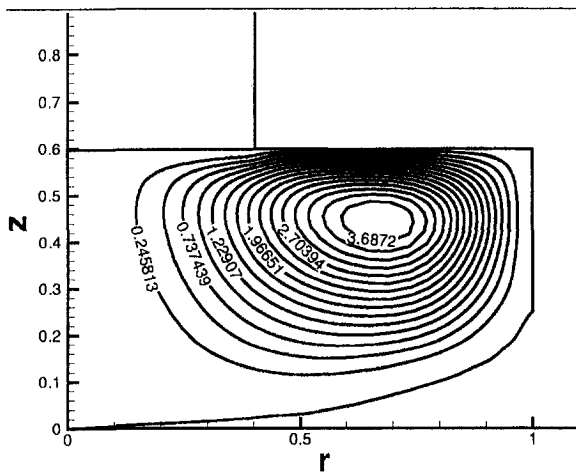


Fig. 7(a)

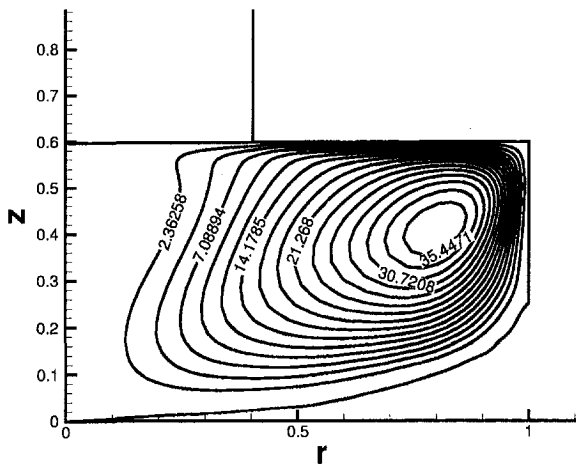


Fig. 7(b)

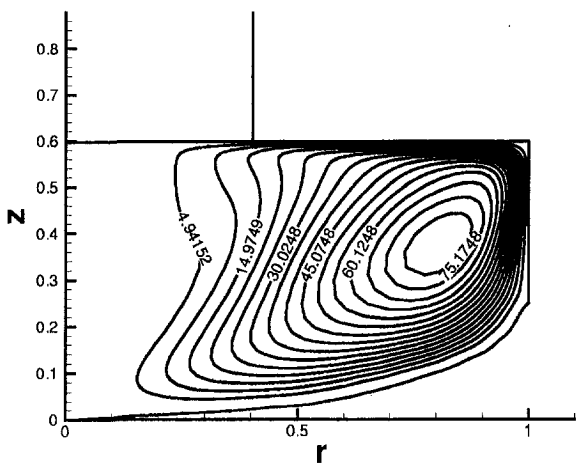


Fig. 7(c)

Fig. 7 Effect of crystal rotation on flow in a Cz melt, showing the nondimensional Stokes stream function plot for (a) $\text{Re}_{cry} = 10^3$; (b) $\text{Re}_{cry} = 10^4$; (c) $\text{Re}_{cry} = 3 \times 10^4$. $\text{Gr} = 0$, $\text{Ma} = 0$, and $\text{Re}_{crb} = 0$.

flows subjected to high levels of rotation are severely weakened in the direction of rotation, with wave-like manifestations. So the context is important.

(a) *Crystal Rotation (Case II)*. Figures 7(a) through 7(c) show the effects of crystal rotation on the stream function for $\text{Re}_{cry} = 10^3$, 10^4 , and 3×10^4 , where

denotes the rotational Reynolds number associated with the rotation of the crystal. In terms of rotation, we have used Re_r to denote the crystal and/or crucible rotational Reynolds number, when no distinction needs to be made between the two types of rotation. It can be seen that the flow forms a circulating pattern, which is necessary to conserve mass. This flow pattern is different from the pattern seen in a rotating disk in an infinite liquid (Zandbergen and Dijkstra, 1987). In that case, there will be no circulation as there is an infinite mass to compensate for the moved fluid mass. The confinement of the crucible causes the circulation observed in present system. It can be seen, by comparing the streamline values in Figs. 7(a) through 7(c), that the flow strength increases with increasing Re_{cry} . This is simply because higher rotation rates provide higher centrifugal forces to drive the fluid radially. Note, however, that Figures 7(a) through 7(c) and Figs. 3(a) through 3(c) show that the flow driven by crystal rotation is much weaker than that due to natural convection. This might be related to the fact that the rotational modes are mostly perpendicular to the (r, z) plane, with weak components in that plane. On the other hand, the gravitational buoyancy modes are parallel to the (r, z) plane, with a direct conversion of internal energy to meridional circulation in that plane. Another observable feature in Figs. 7(a) through 7(c) is that, as Re_{cry} increases, the convection cell becomes more distorted. The increase of centrifugal force with increasing Re_{cry} also causes the tendency for confinement of the flow towards the vertical wall, creating a more stagnant region at the center of the crucible. Note, however, that the cell center is approximately the same for $\text{Re}_{cry} = 10^4$ and 3×10^4 . The velocity gradient at the wall increases with increasing Re_{cry} , which is necessary, in Fig. 7(c), to compensate for the reduced size at the right of the cell center, since mass must be conserved.

The maximum values of turbulence viscosity (ν_t/ν) are reported in Table 4. Note that, for $\text{Re}_{cry} \leq 10^4$, the turbulence level is insignificant, while $\text{Re}_{cry} = 3 \times 10^4$ shows the tendency towards turbulence. However, for the parameters shown, crystal rotation alone does not lead to much turbulence. The distortion of the isotherms (not shown) is also consistent with the flow directions. Since the flow in the (r, z) plane generated by crystal rotation is very weak, the effect of increasing Re_{cry} on the isotherms is also weak. Nevertheless, these results do show that crystal rotation alone generates some motion of the melt under isothermal, non-buoyant, conditions.

(b) *Crucible Rotation (Case III)*. Figures 8(a) through 8(c) show the effects of crucible rotation on the streamlines for $\text{Re}_{crb} = 10^3$, 10^4 and 3×10^4 , from which it is evident that predominant circulation occurs under the crystal. The stagnation of the melt under the free surface indicates a flow close to rigid body rotation, which can be observed in the contour map of the azimuthal velocity in Figs. 9(a) through 9(c). The distortion of these contour lines under the crystal shows clearly that the presence of the solid crystal destroys rigid-body rotation. In fact, the boundary layer under the crystal and on the crucible bottom wall are manifestation of the Taylor-Proudman flow in the theory of rotating flows (Greenspan, 1969). The thickness of these layers can be observed to decrease with increasing angular velocity (or rotational Reynolds number), which is expected.

The effect of crucible rotation on the turbulent viscosity (ν_t/ν) is shown in Table 4. It can be seen that for $\text{Re}_{crb} \geq 10^4$, the flow is turbulent. Again, it is interesting to note the effect of the solid crystal: instead of a rigid body rotation mode, which has no motion in the (r, z) plane, a complicated turbulent flow is seen because of the presence of the solid crystal. Our results also show that the turbulence level increases with increasing crucible rotation. This means that the idea of using rotation to "damp" turbulence, as is widely accepted in the crystal growth community, needs to be re-evaluated. We will discuss more about this in section 6.3 below.

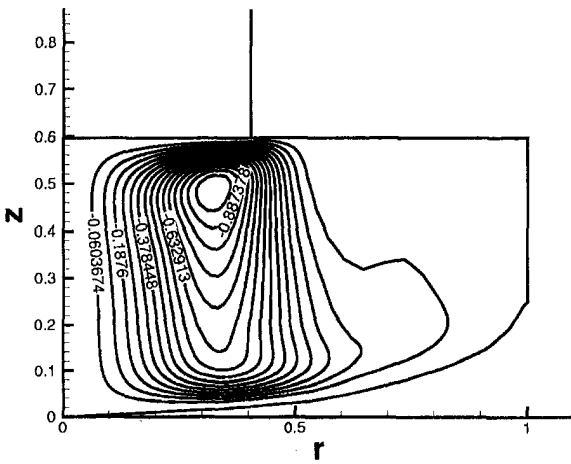


Fig. 8(a)

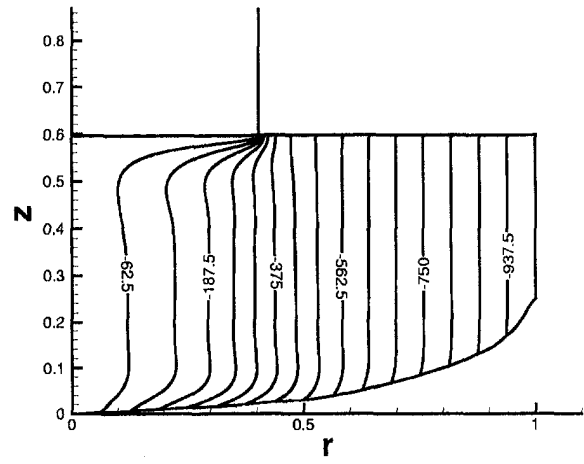


Fig. 9(a)

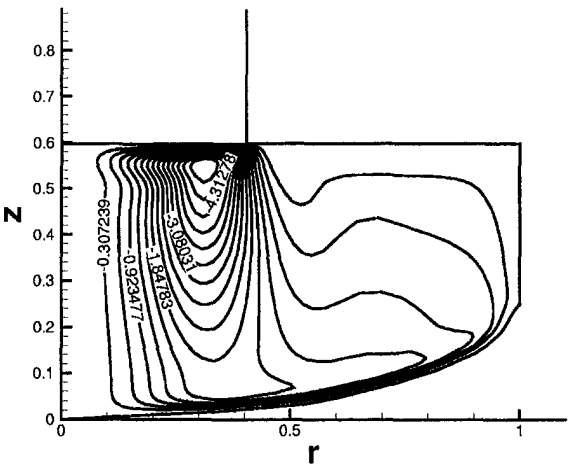


Fig. 8(b)

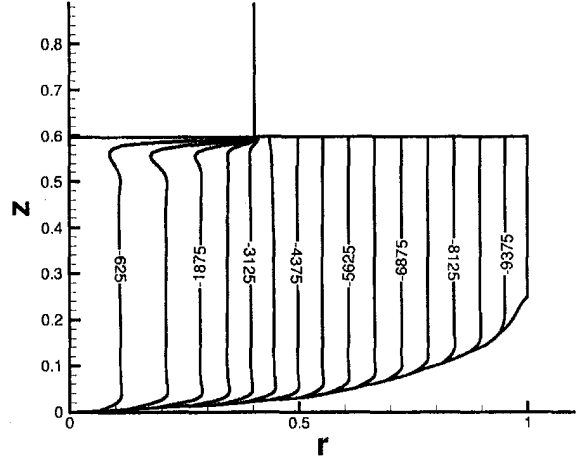


Fig. 9(b)

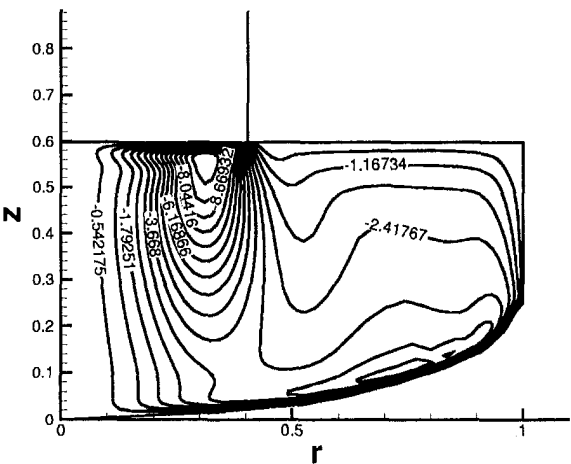


Fig. 8(c)

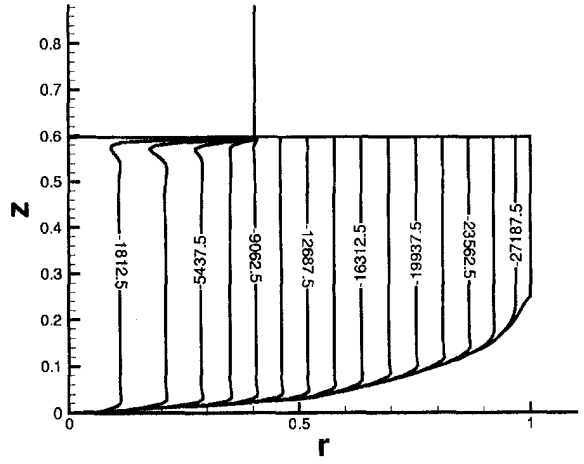


Fig. 9(c)

Fig. 8 Effect of crucible rotation on flow in a Cz melt, showing the nondimensional Stokes stream function plot for (a) $Re_{crb} = 10^3$; (b) $Re_{crb} = 10^4$; (c) $Re_{crb} = 3 \times 10^4$. $Gr = 0$, $Ma = 0$, and $Re_{crb} = 0$.

Fig. 9 Effect of crucible rotation on flow in a Cz melt. Results are shown in this figure for the contours of azimuthal velocity for (a) $Re_{crb} = 10^3$; (b) $Re_{crb} = 10^4$; (c) $Re_{crb} = 3 \times 10^4$. $Gr = 0$, $Ma = 0$, and $Re_{crb} = 0$.

Increasing Re_{crb} has little effect on the isotherms (not shown). This is because the rotation-induced flow in the r - z plane is very weak and the part under the free surface is very close to a rigid body rotation, so that heat transfer is mainly by conduction.

(c) *Combined Crystal and Crucible Rotation (Case IV)*. Figures 10(a) through 10(c) show the streamlines for the flow driven

by the combined rotations of the crystal and the crucible with values of the rotational Reynolds number of $Re_r = 10^3$, 10^4 , and 3×10^4 , for both the crystal and crucible which are rotated in opposite directions. The fixed ratio of crucible to crystal rotation makes sense from application standpoint. It can be seen that the flow pattern is similar to that for Case III, i.e., a large cell under the crystal and a flow under the free surface that is close to rigid body

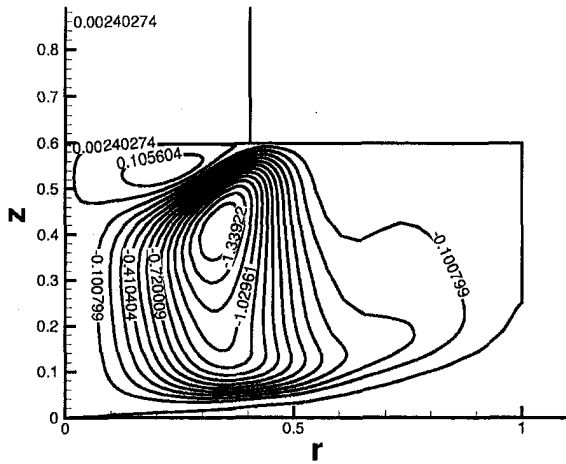


Fig. 10(a)

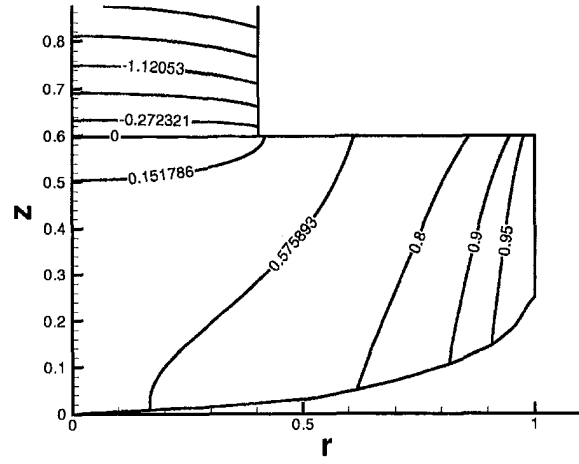


Fig. 11(a)

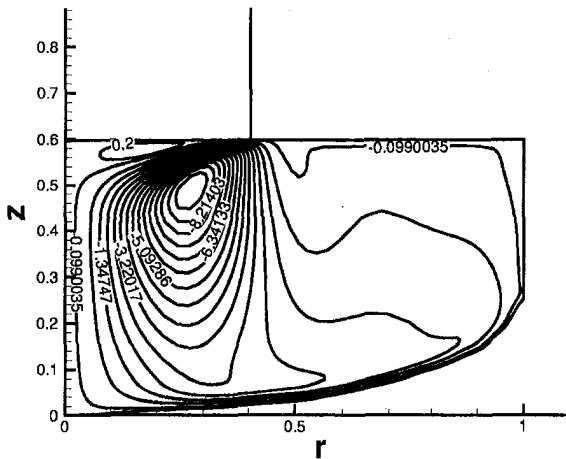


Fig. 10(b)

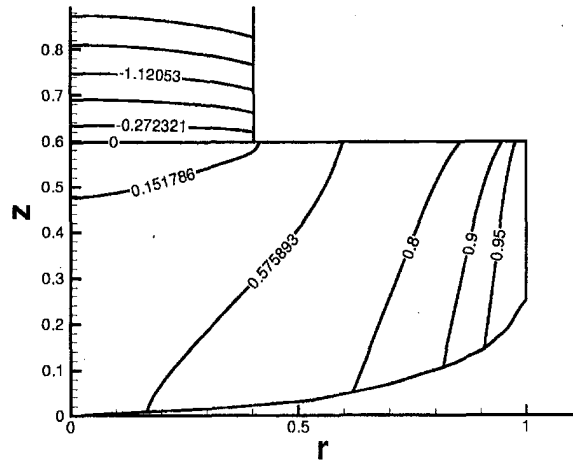


Fig. 11(b)

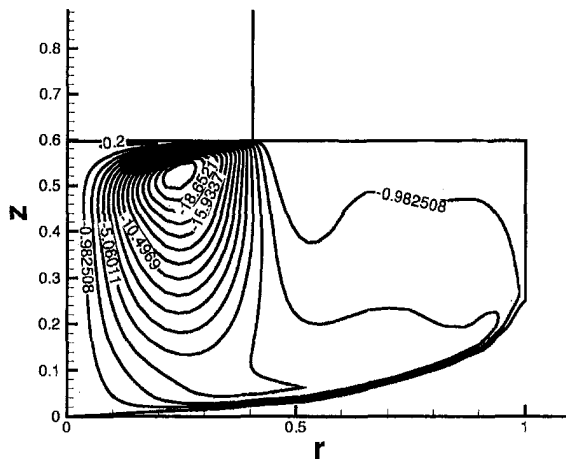


Fig. 10(c)

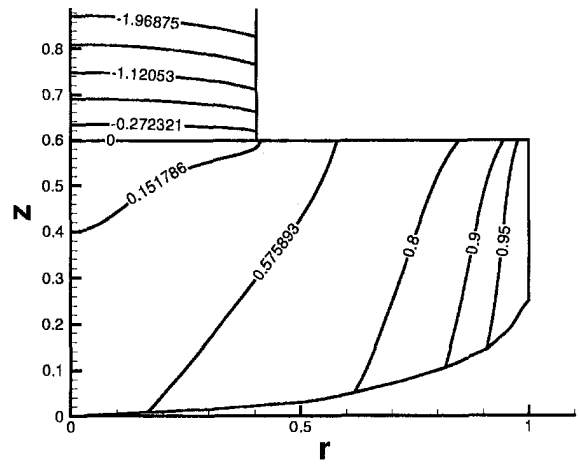


Fig. 11(c)

Fig. 10 Effect of combined crucible and crystal rotation on flow in a Cz melt, showing the nondimensional Stokes stream function for (a) $Re_r = 10^3$; (b) $Re_r = 10^4$; (c) $Re_r = 3 \times 10^4$. Crucible and crucible are rotating at the same speed but in opposite direction, and $Gr = 0$, $Ma = 0$.

Fig. 11 Effect of combined crucible and crystal rotation on flow in a Cz melt, showing the nondimensional isotherms for (a) $Re_r = 10^3$; (b) $Re_r = 10^4$; (c) $Re_r = 3 \times 10^4$. Crucible and crucible are rotating at the same speed but in opposite directions, and $Gr = 0$, $Ma = 0$.

rotation. However, a small convection cell appears right under the crystal, which is a consequence of the crystal rotation. As expected, the effect of the crucible rotation is more dominant when both the crystal and crucible have the same angular rotation rate. As Re_r increases, the size of the upper cell becomes smaller (Fig. 10(c)). The strength of the large cell is almost twice the value in

Case III. This is probably due to the stronger shear that results from rotating (shearing) the crystal and crucible in opposite directions. Note that the cellular flow structure under the crystal may not be desirable for crystal growth because it could trap solute particles, causing high solutal concentration at the crystal center. However, it might prevent too much oxygen from being incorporated into the grown crystal, which is desirable.

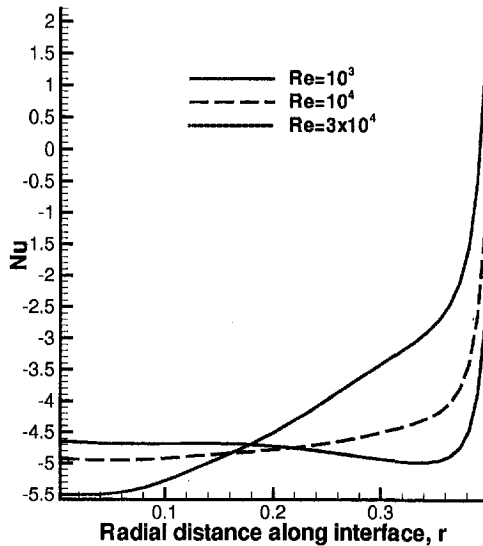


Fig. 12 Effect of combined crystal and crucible rotation on the effective local Nusselt number for $Re_r = 10^3$, 10^4 , and 3×10^4 . $Gr = 0$, $Ma = 0$. The uppermost curve at small r is for $Re_r = 10^3$.

The effect of the combined rotation on the turbulent viscosity (ν_t/ν) is shown in Table 4. The turbulence level increases with increasing Re_r , and, compared with Cases II and III, the melt flow in this case has a larger turbulence transport level. This may be attributed to the higher shear from the counter-rotation of the crystal and crucible, which obviously acts as a source of production of turbulence kinetic energy. Figures 11(a) through 11(c) show the effects on the isotherms. Similar to Case III, the effect of convection on isotherms is less obvious due to the weak flow in the meridional plane. Heat is transferred across the melt mainly by conduction.

Figure 12 shows the distribution of the Nusselt number along the interface. Compared to Case I, the spatial variation of the effective Nusselt number is more modest, which implies that the present case will result in a flatter interface shape.

6.3 Combined Effects of Surface Tension, Natural Convection, and Rotation (Case V). In this section, we study the combined effects of buoyancy, surface tension, and rotation. Three subcases are reported: (a) $Gr = 10^8$, $Ma = 10^3$ and $Re_r = 10^4$; (b) $Gr = 10^9$, $Ma = 10^4$ and $Re_r = 10^4$; and (c) $Gr = 10^9$, $Ma = 10^4$ and $Re_r = 3 \times 10^4$. Re_r denotes the rotational Reynolds number of both the crystal and crucible, although with rotations in opposite directions. Figures 13(a) through 13(c) show the streamlines for the three subcases. Generally, the flow pattern is different from the corresponding cases with only the individual driving forces, in that there are now multiple cells in the flow field. Similar multicellular flow structures can also be found in the results of Kinney and Brown (1993) and Ono et al. (1993). However, we do see a strong effect of crucible rotation in Fig. 13(a) in the large convection cell under the crystal and the relatively weak flow just beneath the free surface. The ratio Gr_h/Re_r^2 , which is the Burgers number, is a measure of the relative strengths of the gravitational buoyancy force and the rotational (centrifugal) force. The value is 0.22 for Case (a), indicating the relative dominance of rotation. Note that, in spite of this, the buoyancy effect is still very important. The direction of flow of the cell in the vicinity of the vertical wall is that of gravitational buoyancy, while the smaller cells are produced by the interaction of buoyancy and rotation. There is also boundary layer flow along the crucible bottom and vertical walls, which is mainly driven by buoyancy. These features enhance the strength of the large cell by a factor of two (compared with Fig. 10(b)) and move the cell center downward. When $Gr_h/Re_r^2 \cong 2.2$, as in Fig. 13(b), the buoyancy force shows a stronger effect. The large flow

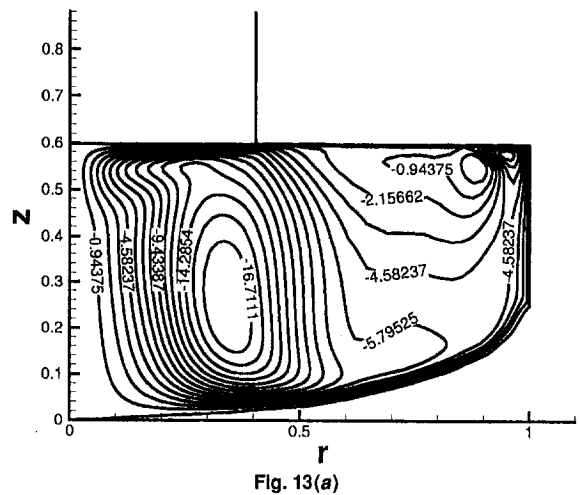


Fig. 13(a)

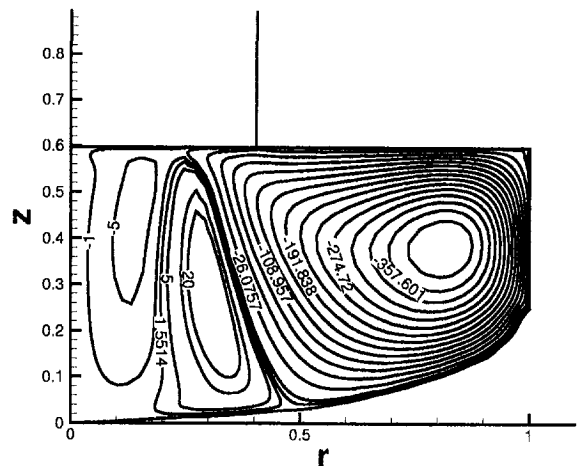


Fig. 13(b)

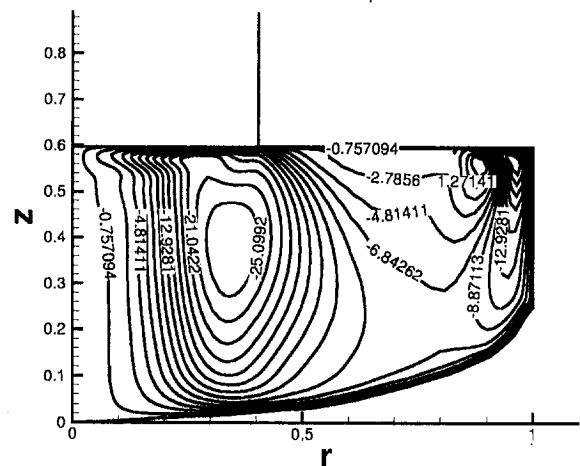


Fig. 13(c)

Fig. 13 Combined effect of Grashof number, Gr , Marangoni number, Ma , and rotational Reynolds number, Re_r , on the flow in a Cz melt, nondimensional Stokes stream function plot for (a) $Gr = 10^8$, $Re_r = 10^4$, and $Ma = 10^3$; (b) $Gr = 10^9$, $Re_r = 10^4$, and $Ma = 10^4$; (c) $Gr = 10^9$, $Re_r = 3 \times 10^4$, and $Ma = 10^4$

cell on the right is basically a natural convection pattern. This is the cell closest to the vertical wall in Fig. 13(a). With increasing Gr (thus Gr_h), this cell grows larger, forcing the other two cells to lie under the crystal. When the rotation rate is further increased to $Gr_h/Re_r^2 \cong 0.22$ (Fig. 13(c)), the rotation-driven cell grows larger, confining the other two cells to the vertical wall. However, in this

case we see a stronger boundary layer flow and a larger, buoyancy driven cell, than in Fig. 13(a). This is probably due to the fact that the Marangoni force is stronger (Ma is one order of magnitude higher), although we really do not have enough Ma cases to comment on its effect.

Compared to flow driven solely by buoyancy (Figs. 3(a) and 3(b)), weaker flows are observed in Figs. 13(a)–13(c). It can be seen that the turbulent viscosities in this case are higher than those due to pure rotation or buoyancy (Table 4), although the strength of the meridional flow is weaker. This may be attributed to the shear associated with the multicellular structures and the shear in the azimuthal direction. Note that, by comparing Subcase (a) with the pure buoyancy case with $Gr = 10^8$, it can be seen that adding rotation changes the flow from laminar to turbulent, in agreement with Ristorcelli and Lumley (1992) who suggested that large rotation rates could promote instability.

Another interesting observation is that a lower level of turbulent viscosity occurs in Subcase (c) in comparison to Subcase (b). This implies that the turbulence transport in the Cz melt is higher when the buoyancy dominates the rotation force. This coincides with the commonly adopted notion in the crystal growth community that rotation will “stabilize” the flow or “damp” the melt turbulence. To explain this, note that when the effect of rotation dominates, the strength of flow in the meridional plane is greatly reduced, in accordance with the well-known Taylor-Proudman phenomenon. The main source of turbulence kinetic energy comes from the shear in the azimuthal plane, which is inefficiently converted into meridional circulation. As observed in Subcase (a) of Case V and in Case IV, further increase in the rotation rate increases the turbulence level. Kobayashi and co-workers (1991) observed decreasing temperature fluctuations as the crucible rotation rate increased from 2 rpm to 5 rpm but increasing fluctuations when the crucible rotation was further increased to 10 rpm. This is consistent with the observation in the present work.

The manifestation of the combined driving forces on the temperature field is shown in Figs. 14(a) through 14(c), from which can be seen a pattern similar to that for the case where there are only crystal and crucible rotations (not shown). This shows rotation-induced, mostly conductive transport of heat in the bulk of melt under the free surface. However, Fig. 14(b) shows a relatively strong effect of convection. The large flow cell on the right (in Fig. 13(b)) causes a distortion of the isotherms between $\Theta = 0.8$ and $\Theta = 0.95$. The cell in the middle brings the hot fluid down to the crucible bottom and then drives it towards the crucible center region, causing the kind of distortion seen in the isotherm $\Theta = 0.5759$. This cell, together with the cell in the center region, are responsible for the distortion of the isotherm $\Theta = 0.1518$.

Figure 15 shows the variation of the effective Nusselt number along the interface. It can be seen that for Subcases (a) and (c), the variations along the interface are relatively small (6–15), implying that a flat interface shape is expected for the real process. The Nusselt number at the crystal outer edge is higher for Subcase (c), showing a stronger buoyancy effect. Subcase (b) shows a doubly curved profile (concave towards the crystal for $r < 0.25$ and convex towards the melt for $r > 0.25$) due to the effect of the two cells under the crystal (Fig. 13(b)), which may produce an interface with doubly curved shape as observed in some experiments (Prasad et al., 1997). Nu is high at the crystal edge because of the strong flow.

Figures 16(a) through 16(c) show the time evolution of the average Nusselt number on the crucible wall, \bar{Nu} . When rotation is dominant (Figs. 16(a) and 16(c)), \bar{Nu} has much lower values (0.415 and 0.467 for (a) and (b), respectively) compared to the case when buoyancy is more dominant (1.147). The reason for this is that heat is transferred mainly by conduction in the melt volume under the free surface. The magnitude of the fluctuations in Figs. 16(a) through 16(c) ranges from one to two percent of the mean value. The period of oscillation ranges from 150 sec for Subcase (a) to about 50 sec for Subcases (b) and (c), showing that increasing Gr increases the frequency of the oscillation.

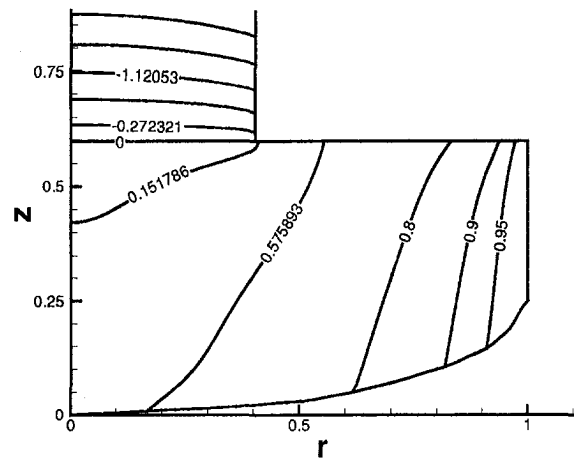


Fig. 14(a)

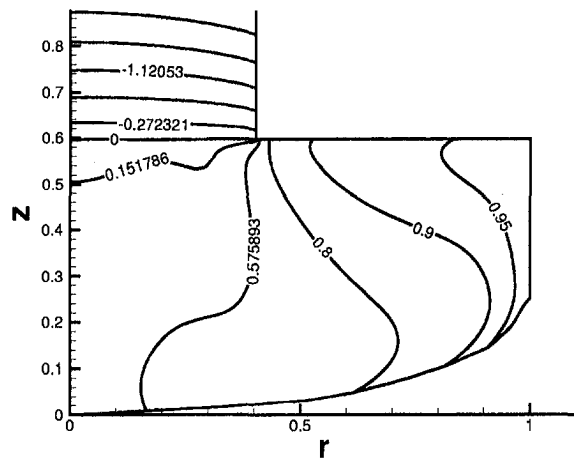


Fig. 14(b)

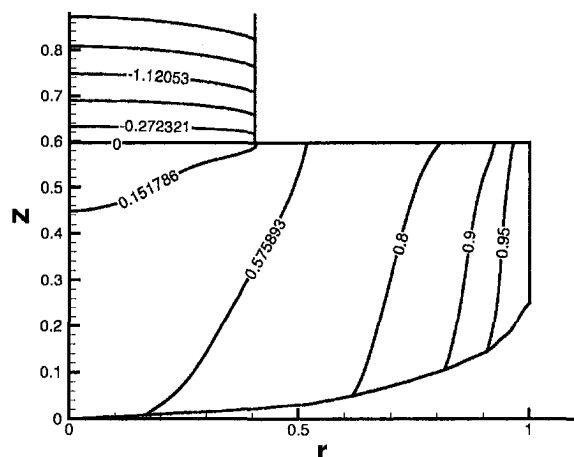


Fig. 14(c)

Fig. 14 Combined effect of Grashof number, Gr , Marangoni number, Ma , and rotational Reynolds number, Re_r , on the flow in a Cz melt, showing nondimensional isotherms for (a) $Gr = 10^8$, $Re_r = 10^4$, and $Ma = 10^3$; (b) $Gr = 10^9$, $Re_r = 10^4$, and $Ma = 10^4$; (c) $Gr = 10^9$, $Re_r = 3 \times 10^4$, and $Ma = 10^4$

Figures 17(a) through 17(c) show the temporal evolution of the temperature at $r = 0$ near the melt-crystal interface. Considering that we have a temperature difference of 50 K across the melt, the amplitudes of these oscillations are: 0.03 K, 0.3 K, and 0.4 K, respectively. Case (a) shows very little oscillation. For Cases (b)

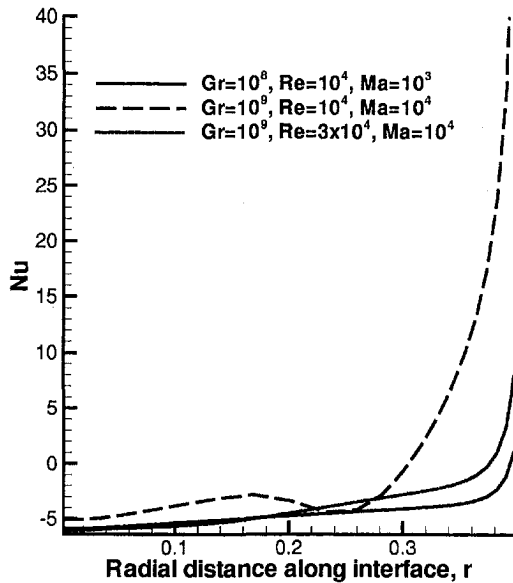


Fig. 15 Combined effect of Grashof number, Gr , Marangoni number, Ma , and rotation Reynolds number, Re_r , on the effective local Nusselt number at the interface. Results in this figure are shown for $Gr = 10^8$, $Ma = 10^3$, $Re_r = 10^4$; $Gr = 10^8$, $Re_r = 10^4$, $Ma = 10^4$; and $Gr = 10^9$, $Re_r = 3 \times 10^4$, $Ma = 10^4$ (upper solid curve).

and (c), where $Gr = 10^9$, increasing rotation rate raises the amplitude of the oscillation but decreases the mean.

The oscillations in Figs. 16 and 17 are physical and not an artifact of the numerical procedure. Grid refinement shows convergence of the results. Moreover, oscillations are a common part of high parameter natural convection systems, particularly when the systems also rotate. The results in the two figures show that the mean turbulence quantities are time-dependent. The flow oscillations, which are captured by the model and whose period ranges from 50s to 150s, are superimposed on the turbulence fluctuations from which only the average effect is considered. The implication is that the mean flow equations used do not come from straightforward time-averaging. Also, a spatial averaging procedure is inappropriate because of the inhomogeneous nature of the turbulence in crystal growth. Therefore, the only averaging procedure that makes sense is ensemble averaging or phase averaging. Obviously, this situation has to be considered in a posteriori sense, because the mean flow equations from different averaging procedures are similar, save the time-dependent terms. This similarity derives from the fact that the properties of the averaging process, such as fluctuating quantities having zero averages, commutativity of averaging and differentiation, etc., are usually assumed to be the same.

7 Conclusion

The individual and combined effects of buoyancy, crystal, and crucible rotations on the azimuthally averaged turbulent convection and heat transfer in the Czochralski silicon melt growth are presented in this paper. Parameters typical of the real physical system are used. The main findings are as follows:

1 The numerical results compare very well with Cheeswright turbulence measurements. The results also exhibit grid independence, as desired, and the numerical scheme is capable of calculating both laminar and turbulent flows with the RNG $k-\epsilon$ model turned on.

2 For the parameters used, buoyancy alone generates strong convection with large heat transfer rates across the melt and causes large local heat flux at the edge of the crystal, which may result in a very high triple-phase point. The intensity of turbulence increases with the melt Grashof number.

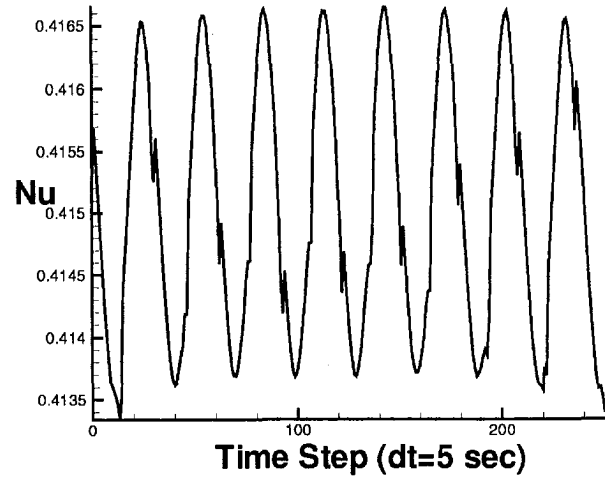


Fig. 16(a)

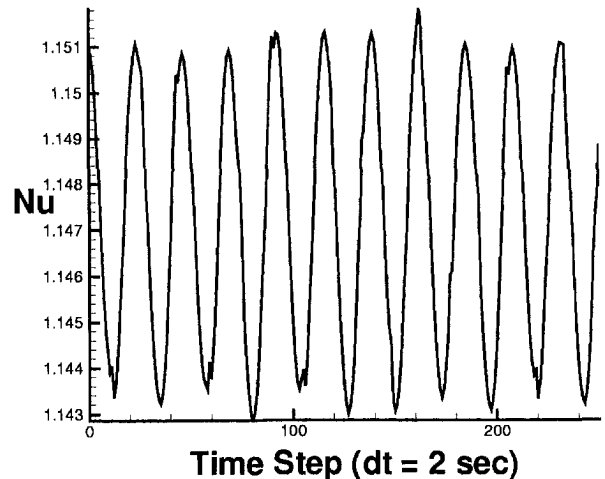


Fig. 16(b)

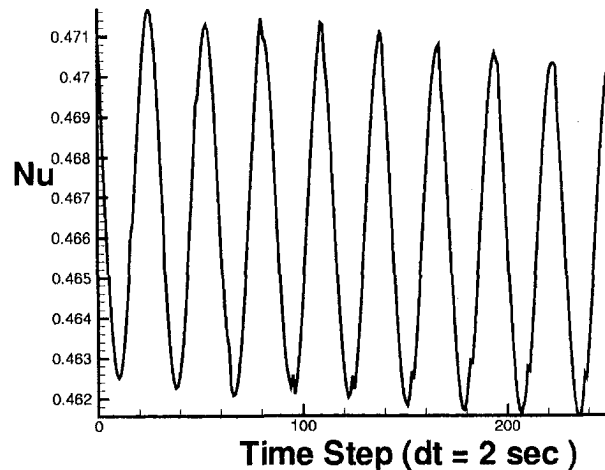


Fig. 16(c)

Fig. 16 Combined effect of Grashof number, Gr , Marangoni number, Ma , and rotational Reynolds number, Re_r , on the averaged Nusselt number of the crucible wall in a Cz melt. Results in this figure are shown for (a) $Gr = 10^8$; $Re_r = 10^4$, and $Ma = 10^3$; (b) $Gr = 10^8$, $Re_r = 10^4$, and $Ma = 10^4$; (c) $Gr = 10^9$, $Re_r = 3 \times 10^4$, and $Ma = 10^4$.

3 When both the crystal and the crucible rotate at the same speed without buoyancy, the effect of crucible rotation tends to dominate. A large but weak convection cell forms beneath the crystal and a flow close to rigid body rotation exists under the free

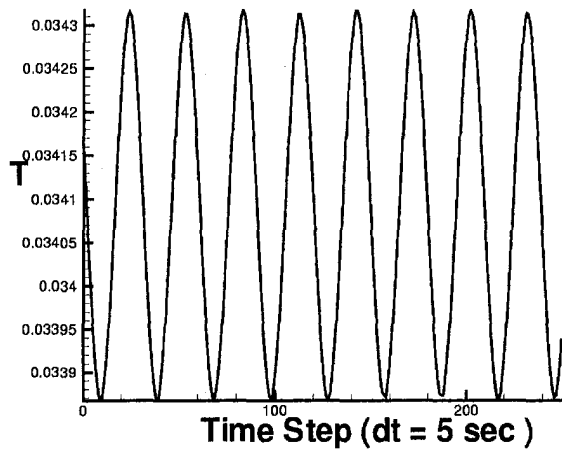


Fig. 17(a)

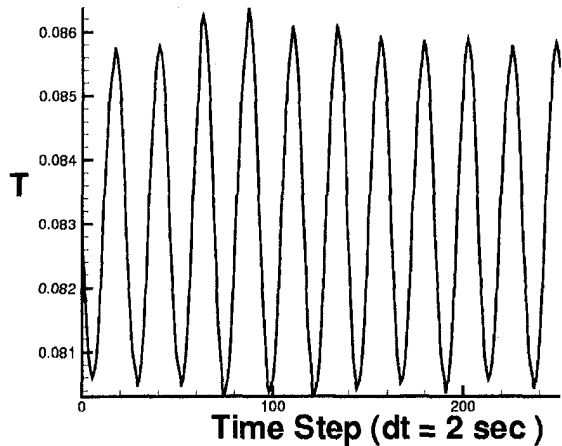


Fig. 17(b)

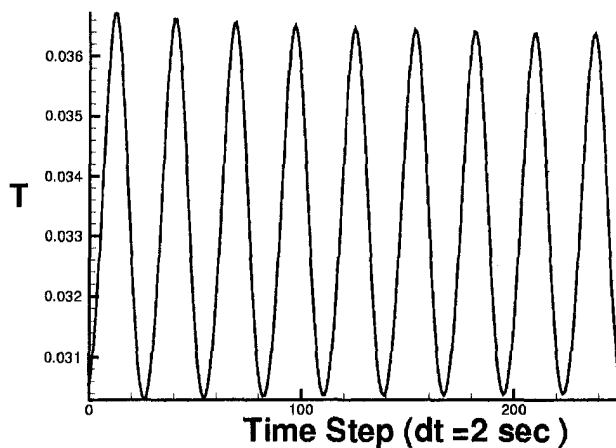


Fig. 17(c)

Fig. 17 Combined effect of Grashof number, Gr , Marangoni number, Ma , and rotation Reynolds number, Re_r , on the dimensionless temperature under the center of the crystal in a Cz melt. Results in this figure are shown for (a) $Gr = 10^8$, $Re_r = 10^4$, and $Ma = 10^3$; (b) $Gr = 10^9$, $Re_r = 10^4$, and $Ma = 10^4$; (c) $Gr = 10^9$, $Re_r = 3 \times 10^4$, and $Ma = 10^4$.

surface. This flow structure prevents heat and mass from being effectively transferred across the melt, which is desirable as it promotes the flattening of the interface shape and prevents the transportation of impurities or oxygen from the crucible wall to the interface. Some of these observations could have important consequence for the crystal growth process. For example, the weak flow under the crystal may favor the growth process as it provides

a "stable" condition in the vicinity of the solidification front. The small variation in the effective heat flux will enhance a flat interface, which is favorable as it reduces thermal stress and ensures radial uniformity. Turbulent transport is observed to increase with the rotation rate, contrary to what the literature suggests. Also note that the streamline and isotherm contours are based on the mean quantities. Since our results show that turbulence transport increases with increasing rotation rate, turbulence velocity and temperature fluctuations are also expected to increase, even if the mean quantities remain relatively constant. This situation is not a favorable one for crystal growth, because turbulence fluctuations lead to a higher increase in microdefect concentration (Kuroda et al., 1984). Finally, the small cell from crystal rotation could trap solutal particles, causing high concentrations at the crystal outer edge and radial segregation of impurity or oxygen.

4 When all the driving forces are combined, as in a real production system, turbulent viscosity and the average Nusselt number at the crucible wall are highest when buoyancy is slightly dominant over rotation. A decrease in ν , and \bar{Nu} is observed when rotation dominates. However, further increase in rotation rate increases the magnitude of the temperature oscillation and the turbulence level. Since the actual Grashof number of the system depends on the melt height and the temperature difference across the melt, which change with time in a real system, the rotation rate of the system might also need to be adjusted dynamically during the growth process in order to obtain a desirable process. The oscillations referred to in this paper are superposed on the turbulence fluctuations.

Acknowledgments

Acknowledgements are due to AFOSR and DARPA for the support of the research through the Consortium for Crystal Growth Research and to NSF Division of Design, Manufacturing, and Innovation. The authors also thank Prof. E. E. O'Brien, Dr. H. Zhang, and Dr. G.-X. Wang for their help in conducting this research.

References

- Abe, K., and Kondoh, T., 1995, "A New Turbulence Model for Predicting Fluid Flow and Heat Transfer in Separating and Reattaching Flows—I. Flow Field Calculations," *Int. J. Heat Mass Transfer*, Vol. 38, pp. 1467–1481.
- Anselmo, A., Prasad, V., Koziol, J., and Gupta, K. P., 1993, "Oscillatory Convection in Low Aspect Ratio Czochralski Melts," *J. Crystal Growth*, Vol. 134, pp. 116–139.
- Cheesewright, R., King, K. J., and Ziai, S., 1986, "Experimental Data for the Validation of Computer Codes for the Prediction of Two-Dimensional Buoyant Cavity Flows," *Significant Questions in Buoyancy Affected Enclosure or Cavity Flows*, ASME, New York, pp. 75–81.
- de Vahl Davis, G., 1983, "Natural Convection of Air in a Square Cavity: A Benchmark Numerical Solution," *Int. J. Heat Mass Transfer*, Vol. 3, pp. 249–264.
- Dupret, F., Van den Bogaert, N., Assaker, R., and Regnier, V., 1998, "Mathematical Modeling of the Growth of Large Diameter Czochralski Silicon Crystals Considering Melt Dynamics," *Proc. 8th Int. Symp. on Silicon Materials Sci. and Tech.*, H. R. Huff, U. Gösele, and H. Tsuya, eds., Electronic Division of the Electrochemical Society, Proc. Vol. 98–1, pp. 396–410.
- Elwell, D., and Andersen, E., 1989, "Temperature Oscillation in Silicon Melts," *J. Crystal Growth*, Vol. 98, pp. 667–678.
- Gatski, T. B., and Speziale, C. G., 1993, "On Explicit Algebraic Stress Models for Complex Turbulent Flows," *J. Fluid Mech.*, Vol. 254, pp. 59–78.
- Germano, M., Piomelli, U., Moin, P., and Cabot, W. H., 1991, "A Dynamic Subgrid-Scale Eddy Viscosity Model," *Phys. Fluids A*, Vol. 3, pp. 1760–1765.
- Greenspan, H. P., 1969, *The Theory of Rotating Flows*, Cambridge University Press, London.
- Hurle, D. T. J., 1983, "Convective Transport in Melt Growth Systems," *Journal Crystal Growth*, Vol. 65, pp. 124–132.
- Iliev, K., Berkowski, M., and Piekarczyk, W., 1991, "Conditions of Existence and Character of the Temperature Fluctuations During Czochralski Growth of Oxide Single Crystals," *J. Crystal Growth*, Vol. 108, pp. 219–224.
- Jones, A. D. W., 1988, "Scaling Analysis of the Flow of Low Prandtl Number Czochralski Melt," *J. Crystal Growth*, Vol. 88, pp. 465–476.
- Jones, W. P., and Launder, B. E., 1972, "The Prediction of Laminarization With a Two-Equation Model of Turbulence," *Int. J. Heat Mass Transfer*, Vol. 15, pp. 301–314.
- Kakimoto, K., Eguchi, M., Watanabe, H., and Hibiya, T., 1988, "Natural and Forced Convection of Molten Silicon During Czochralski Single Crystal Growth," *J. Crystal Growth*, Vol. 94, pp. 412–420.

- Kim, K. M., and Langlois, W. E., 1986, "Computer Simulation of Boron Transport in Magnetic Czochralski Growth of Silicon," *J. Electrochem. Soc.*, Vol. 133, No. 12, pp. 2586-2590.
- Kinney, T. A., and Brown, R. A., 1993, "Application of Turbulence Modeling to the Integrated Hydrodynamic Thermal-Capillary Model of Czochralski Crystal Growth of Silicon," *J. Crystal Growth*, Vol. 132, pp. 551-574.
- Kobayashi, N., 1995, "Steady State Flow in a Czochralski Crucible," *J. Crystal Growth*, Vol. 147, pp. 382-389.
- Kobayashi, S., Miyahara, S., Fujiwara, T., Kubo, T., and Fujiwara, H., 1991, "Turbulent Heat Transfer Through the Melt in Silicon Czochralski Growth," *J. Crystal Growth*, Vol. 109, pp. 149-154.
- Kuroda, E., Kozuka, H., and Takano, Y., 1984, "The Effect of Temperature Oscillations at the Growth Interface on Crystal Perfection," *J. Crystal Growth*, Vol. 68, pp. 613-623.
- Markatos, N. C., and Pericleous, K. A., 1984, "Laminar and Turbulent Natural Convection in an Enclosed Cavity," *Int. J. Heat Mass Transfer*, Vol. 27, No. 5, pp. 755-772.
- Ladeinde, F., and Torrance, K. E., 1991, "Convection in Rotating, Horizontal Cylinders With Radial and Normal Gravity Forces," *J. of Fluid Mech.*, Vol. 228, pp. 361-385.
- Mihelčić, M., and Wingerath, K., 1989, "Instability of the Buoyancy Driven Convection in Si Melts During Czochralski Crystal Growth," *J. Crystal Growth*, Vol. 97, pp. 42-49.
- Müller, G., and Ostrogorsky, A., 1994, "Convection in Melt Growth," *Handbook of Crystal Growth*, Vol. 2b, D. T. J. Hurle, ed., North-Holland, New York.
- Noble, E., 1993, "Comparison of Turbulence Models for Side-Heated Cavities," *Turbulent Natural Convection in Enclosures: A Computational and Experimental Benchmark Study*, R. A. W. M. Henkes and C. J. Hoogendoorn eds., Proc. Eurotherm Seminar No. 22, EETI, Paris, pp. 214-233.
- Ono, N., Kida, M., Arai, Y., and Sahira, K., 1993, "Thermal Analysis of the Double-Crucible Method in Continuous Silicon Czochralski Processing," *J. Electrochem. Soc.*, Vol. 140, No. 7, pp. 2106-2111.
- Prasad, V., Zhang, H., and Anselmo, A., 1997, "Transport Phenomena in Crystal Growth Process," *Adv. Heat Transfer*, Vol. 30, Academic Press, New York, pp. 313-435.
- Ristorcelli, J. R., and Lumley, J. L., 1992, "Instabilities, Transition, and Turbulence in the Czochralski Crystal Melt," *J. Crystal Growth*, Vol. 116, pp. 447-460.
- Ristorcelli, J. R., and Lumley, J. L., 1993, "A Second-Order Turbulence Simulation of the Czochralski Crystal Growth Melt: The Buoyancy Driven Flow," *J. Crystal Growth*, Vol. 129, pp. 249-265.
- Togawa, S., Huang, X., Izunome, K., Terashima, K., Kimura, S., 1995, "Oxygen Transport Analysis in Czochralski Silicon Melt by Considering the Oxygen Evaporation From the Melt Surface," *J. Crystal Growth*, Vol. 148, pp. 70-78.
- Yakhot, V., Orszag, S. A., Thangam, S., Gatski, T. B., and Speziale, C. G., 1992, "Development of Turbulence Models for Shear Flows by a Double Expansion Technique," *Phys. Fluids*, Vol. A4, No. 7, pp. 1510-1520.
- Zandbergen, P. J., and Dijkstra, D., 1987, "Von Karman Swirling Flows," *Annu. Rev. of Fluid Mech.*, Vol. 19, pp. 465-491.
- Zhang, H., and Prasad, V., 1995, "A Multizone Adaptive Process Model for Low and High Pressure Crystal Growth," *J. Crystal Growth*, Vol. 155, pp. 47-65.
- Zhang, H., Prasad, V., and Moallemi, M. K., 1996a, "A Numerical Algorithm Using Multi-Zone Grid Generation for Multiphase Transport Processes With Moving and Free Boundaries," *Numerical Heat Transfer, Part B*, Vol. 29, in press.
- Zhang, H., Prasad, V., and Bliss, D., 1996b, "Transport Phenomena in High Pressure Crystal Growth Systems for III-V Compounds," *J. Crystal Growth*, Vol. 169, pp. 250-260.
- Zhang, H., and Prasad, V., 1997, "An Advanced Numerical Scheme for Materials Process Modeling," *Computer Modeling and Simulation in Engr.*, Vol. 3, pp. 230-237.
- Zhang, T., Ladeinde, F., Zhang, H., and Prasad, V., 1996, "A Comparison of Turbulence Models for Natural Convection in Enclosures: Applications to Crystal Growth Processes," *Proc. 31st National Heat Transfer Conf.*, HTD-Vol. 323, ASME, New York, pp. 17-26.

Measurement of the Transient Glass Surface Deformation During Laser Heating

T.-R. Shiu

C. P. Grigoropoulos

e-mail: cgrigoro@newton.Berkeley.edu
Fellow ASME

R. Greif

Department of Mechanical Engineering,
University of California,
Berkeley, CA 94720-1740

The distinct transient geometry and material response of a deforming glass surface during CO₂ laser heating are related to the temperature history and the thermal regimes resulting from different energy deposition and heating rates. The transient deformation is measured using a probing system based on the photo thermal deflection technique. The variation with temperature of the optical constants yields a variable reflection signal which ultimately decreases, corresponding to a permanent volume expansion. The transient deflection signal associated with the variable deformation results from the distinct physical mechanisms in three thermal regimes, i.e., the elastic behavior, the glass transition, and the viscous flow regimes.

1 Introduction

This work is a study of the modification of glass surfaces resulting from CO₂ laser heating. An application of this process is the reduction of friction during magnetic head-disk interaction, which is achieved by variable surface features depending on the specific laser energy deposited (see, e.g., the recent works of Miller and Bhushan (1996), Teng et al. (1996), Tam et al. (1997), and Kuo et al. (1997)). Few attempts have been made to elucidate the physical mechanisms leading to the surface modification. Previous experiments by Teng et al. (1996) on glass substrates showed a volume increase, implying that thermal expansion of the material during and after heating is an important factor in the formation of the bump. Tam et al. (1997) related qualitatively the volume expansion to the maximum temperature increase, assuming laser energy deposition with heat transfer by diffusion only.

The present research proposes a mechanism to explain the formation of bumps caused by pulsed laser heating of glass. The semi-transparent characteristics of glass at the CO₂ laser wavelength (10.6 μm) requires a coupled radiation and diffusion energy transport analysis. In general, the geometry and the transient behavior of the surface deformation are related to the temperature history resulting from the energy deposition and heating rate. When the maximum temperature induced by the laser heating is below the glass transition temperature, the glass material is elastic and linear elasticity predicts no permanent deformation after the temperature field restored. However, when the temperature reaches or exceeds the glass transition temperature and then cools, the structure of glass changes, resulting in a permanent net volume increase. The phenomena can be studied based on glass forming processes as described in Scherer (1986) and Varshneya (1994). During the cooling of glass, the liquid deviates from its equilibrium state when the available thermal energy cannot provide atomic movements that are fast enough to attain equilibrium. The deviation from equilibrium can be characterized by the glass transition temperature. The beginning of the departure from equilibrium depends on the cooling rate. The faster the cooling, the less time available for structural rearrangement to attain equilibrium, and at higher temperatures, deviation from equilibrium occurs. During the pulsed laser heating of glass with a permanent deformation, the material is first brought to a temperature higher than the glass transition temperature. During the subsequent cooling the

characteristic cooling rate is about 10⁶°C/sec which is related to the time needed for thermal diffusion to carry the heat away. This high cooling rate (in contrast to the typical 0.1°C/sec cooling rate for the manufacture of glass in a furnace) gives the laser-treated glass a less compact structure resulting in a net volume increase. The glass transition temperature here refers to the fast cooling rate induced by laser heating which is higher than the transition temperature corresponding to furnace heating and subsequent cooling. For higher energy deposition the temperature increases above the glass transition region and viscous flow becomes more important; this results in larger deformation and different topography. In the present work, we focus on the transient response of the heated material and its temperature dependence. The distinct behavior among three different temperature regimes is also of interest.

In the current laser texturing process there is no provision to ensure the consistent quality of the generated surface features on-site. The probing system we developed, based on the photo-thermal deflection (PTD) technique, provides the transient information and also establishes a means for industry to in-situ monitor the glass modification process.

2 Experiment

2.1 Apparatus. A schematic of the experimental system is shown in Fig. 1(a). A continuous-wave CO₂ laser of wavelength $\lambda = 10.6 \mu\text{m}$ is used because the target material, glass, has a strong Si-O absorption band at this operating wavelength. An acousto-optic modulator, controlled by a pulse generator, deflects the continuous-wave laser beam emitted from the laser aperture. The pulse generator was operated in single-pulse mode (square wave with fixed pulse width). These three components, combined with a shutter, produce a single CO₂ laser pulse with adjustable power and pulse width. This laser beam was then expanded three times, reflected by a mirror, and focused by a ZnSe lens (focal length = 50 mm) on the surface of the target glass substrate with estimated 1/e² CO₂ beam diameter of 62 μm. Measuring the pulsed energy after the ZnSe lens, we found the fluctuation between pulses (defined as the ratio between their standard deviation and average) to be less than eight percent. A solid HgCdTe detector behind the ZnSe lens checked the transient characteristics of the CO₂ pulse arriving at the target. It was found that the pulse width remained the same as from the pulse generator, but with a delay of 200 ns. This delay was much smaller than the time scale of interest. Furthermore, a small portion (estimated less than seven percent) of the laser energy was delivered after the nominal end of the laser pulse.

In our probing system, a 5 mW/polarized HeNe laser was

Contributed by the Heat Transfer Division for publication in the JOURNAL OF HEAT TRANSFER. Manuscript received by the Heat Transfer Division, June 9, 1998; revision received, Jan. 22, 1999. Keywords: Heat Transfer, Laser, Manufacturing, Measurement Techniques, Nonintrusive Diagnostics, Participating Media. Associate Technical Editor: R. Mahajan.

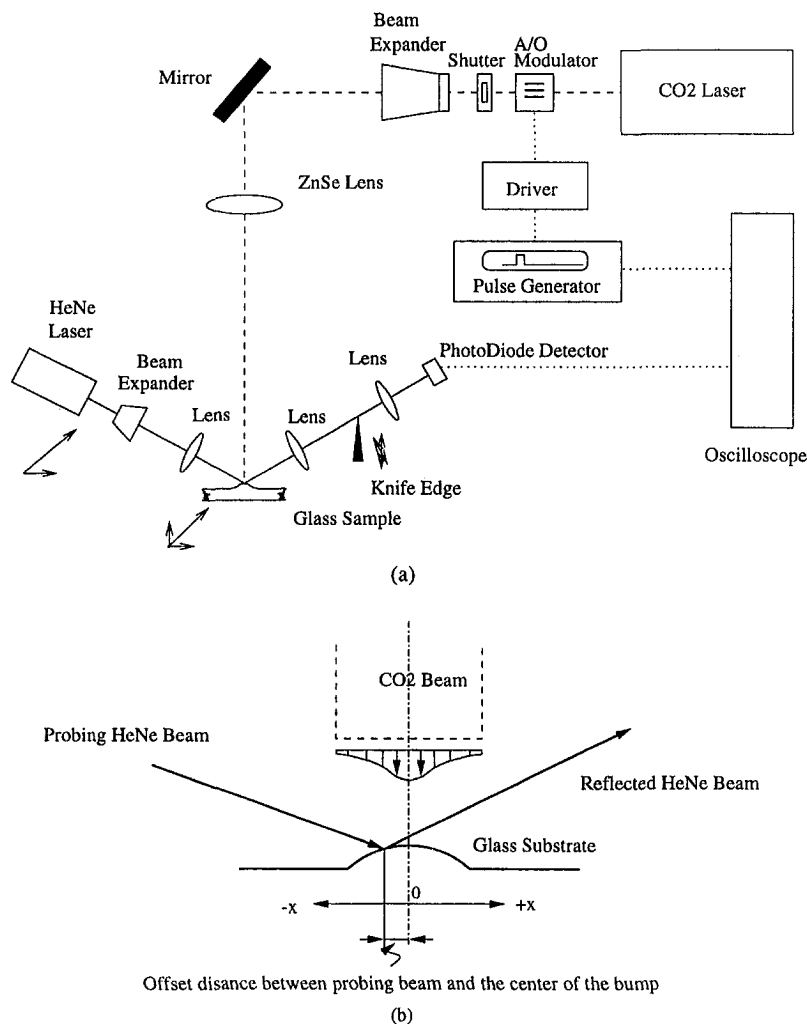


Fig. 1 (a) Schematic of CO₂ laser texturing and PTD measurement setup, (b) beam-target interaction

assembled with a 5–10× beam expander and a lens of 50 mm focal length. The outgoing laser beam from the assembly was focused with an incident angle of 27° on the region of the target surface illuminated by the focused CO₂ beam. The focused HeNe beam diameter was measured using knife-edge profiling and found to be 7.6 μm, with a 144 μm confocal length. From atomic force microscopy (AFM) images as shown in Fig. 2, all the bumps had diameters ranging from 32 to 48 μm and heights ranging from 27 to 156 nm, implying that their side slopes are less than 0.4°. These dimensions are small compared with the HeNe beam's confocal length so that the HeNe beam is always focused on the surface. The polarization orientation (p-type) and the incident angle of the HeNe laser were chosen to maximize the reflection signal from glass; this is necessary because, otherwise, the signal would be weak due to the low reflectivity of glass at the HeNe operating wavelength ($\lambda = 632.8$ nm). After reflection from the glass surface, the HeNe beam passed through two lenses to obtain a tight focus on the photodiode detector's effective detection area (1 mm × 1 mm). The signal received by the photodiode detector was recorded with a digital oscilloscope triggered by the same pulse-

generator signal that produced the CO₂ pulse. For the photothermal deflection measurement a knife edge was added in the reflected beam path to block half of the beam (in terms of energy). The HeNe laser/beam expander/lens assembly was mounted on a two-dimensional translation stage, with the x -probing direction parallel to the HeNe laser's incident plane and the y -probing direction normal to it. The focus was not lost in the scanning due to the small characteristic dimension of interest. Nevertheless, simpler one-dimensional probing (x -probing direction) through the central line of the bump was sufficient for the study since the pumping CO₂ beam is axisymmetric, and so is the generated deformation as confirmed by the AFM images, e.g., Fig. 2. This was done as follows; at a fixed x -location, the maximum deflection signal was recorded with the upper half of the reflected HeNe beam blocked as the probing beam was scanned along the y -direction. It was established that the deflection normal to the plane of incidence was minimized as the probing beam was scanned along a bump diameter and that it reversed signs at diametrically symmetric positions. The glass substrates used in this investigation were soda-lime glass (72.15 percent SiO₂, 14.25 percent Na₂O, 6.25 percent CaO)

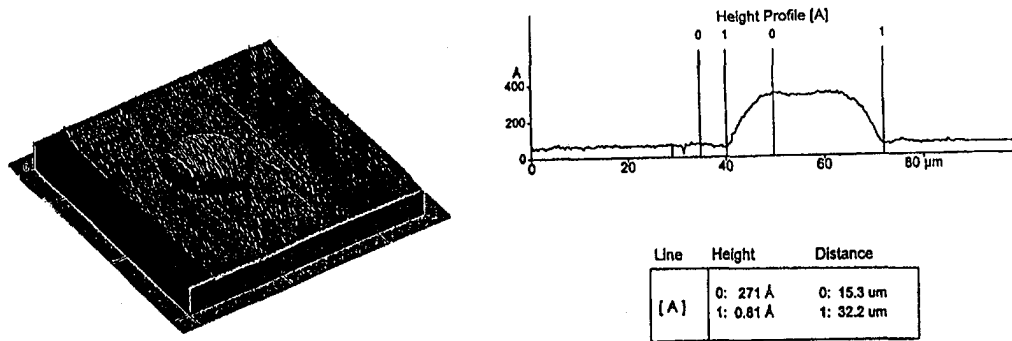
Nomenclature

λ = wavelength
 x = probing direction/parallel to the incident plane of the probing beam, μm

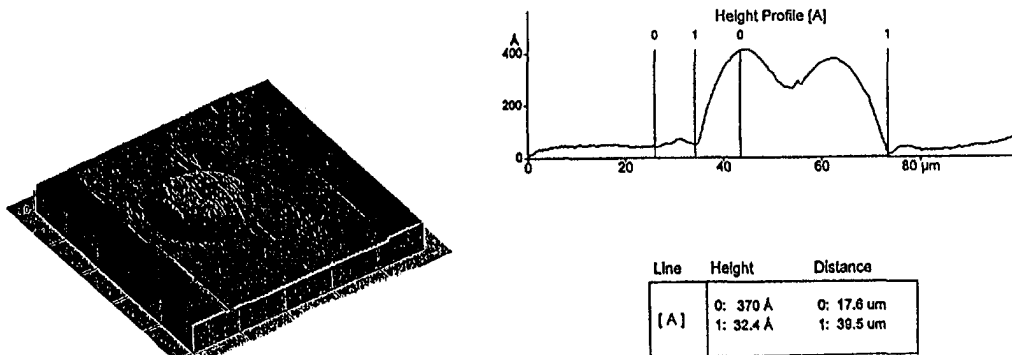
y = normal to the incident plane of the probing beam, μm

W = watts
 μs = micro second

(a) Laser Power = 3W, Pulse Width = 10 μ s



(b) Laser Power = 5W, Pulse Width = 6 μ s



(c) Laser Power = 5W, Pulse Width = 20 μ s

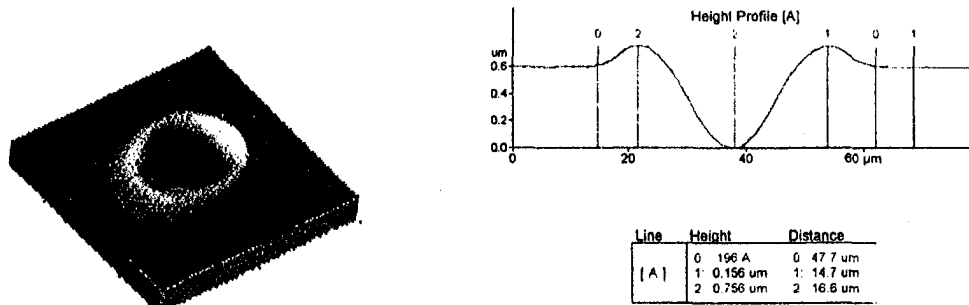


Fig. 2 AFM images showing different bump topography

of 1 mm thickness. The optical constants at room temperature and $\lambda = 10.6 \mu\text{m}$ are $n = 2.224$ and $k = 0.102$, respectively (Palik, 1985). Due to the low reflectivity of the glass at the HeNe wavelength, there were severe multiple internal reflection effects. This was alleviated by roughening the bottom side of the glass substrate.

3 Results and Discussion

Three different signals have been recorded at every position along a bump diameter; the total reflection, and two deflection signals with opposite knife edge blocking directions. The total reflection signal records transient temperature-affected changes of the optical constants. There is no contribution from geometry change to this signal because it is collected and focused on a

position-insensitive detector. The deflection signals, however, primarily show the transient geometrical change of the surface and are obtained by blocking, respectively, the top and the bottom half of the reflected HeNe beam before firing the CO₂ laser pulse. Any deflection either increases or decreases the energy received by the photodiode detector. These two signals are composed of one identical nongeometrically-induced part (half of the total reflection plus noise) and the other geometrically-induced part (pure deflection) which should be equal but of opposite sign; both components can be obtained by adding or subtracting the two recorded signals. However, our results show that the deflection signal is always one order of magnitude higher than the reflection signal. Although the above procedure was used to verify the results, it provides little additional information than that obtained from the direct measure-

Table 1 Measurements according to different laser parameters

Case	Laser Power (W)	Pulse Width (μ s)	Energy (μ J)	Maximum Temperature
A	3	10	30	between strain point and glass transition temperature
B	5	6	30	below glass transition range
C	5	2	10	above full melting
D	5	20	100	
E	5	50	250	

ments and therefore, in the following, we simply refer to reflection as the total reflection signal and to deflection as the signal obtained by blocking the top half of the reflected probing beam.

Tests have been conducted over a range of laser parameters to study the material response induced by different temperatures. The tests are listed in Table 1. A two-dimensional semi-infinite axisymmetric analysis has been made with coupled radiation and diffusion. Constant properties are assumed with no phase change and no heat loss from the surface. Predicted maximum surface temperature histories are shown in Fig. 3; A and B reach surface temperatures that are at least 200°C above the typical glass transition temperature of 525°C for the soda-lime glass. The value of the new glass transition temperature corresponding to the fast cooling following laser heating is unknown but is higher than the standard value for slow cooling. Case C corresponds to a small maximum temperature so that the glass material can be treated simply as an elastic solid. The last two cases, D and E, yield maximum temperatures in the full melting regime where the glass material is in viscous flow. Since the analysis omits viscous flow and assumes room-temperature properties, the predicted temperatures for these two cases should only be viewed as indications of the thermal region.

Figures 4(a),(b) show that the reflection signals are almost identical at diametrically symmetric positions on a dome-shaped bump (case A). This symmetry indicates that the signal is not related to geometry change but to temperature-affected property change. As given in Fig. 4(c), regardless of pulse width, the glass

reflectivity decreases rapidly during heating as the temperature increases, followed by a slow increase during cooling. Note that the reflectivity sustains a permanent decrease, indicating that the glass has experienced a change in optical properties accompanying the permanent volumetric expansion.

In conventional PTD investigations, such as the works by Olmstead et al. (1983), and Zimmerman and Welsch (1994), the deflection signals correspond to the elastic behavior of the material. The present work determines the transient behavior of bump formation induced by a single pulse with a resulting permanently modified surface. The measurements were repeated and averaged. As explained in previous PTD studies, the change in slope has the largest effect on the signals and is confirmed in our results presented in Fig. 5: The signal changes sign on opposite sides of the bumps (see Fig. 5(a, b, e, f) versus (c, d, g, h)). Also the signal increases (or decreases, depending on which side the signal was measured) rapidly during the pulse and reaches a maximum (or minimum) after the end of the pulse. There is some delay between the occurrence of the maximum (or minimum) and the end of the pulse for cases A and B. This can be explained from the characteristics of the laser pulse noted earlier: The surface temperature of the target continues to increase shortly after the nominal end of the pulse because there is still some diminishing laser energy incident on the surface that is greater than the energy losses and diffusion. During the cooling period, heat conduction is the dominant energy transport mechanism and the signal changes very slowly. After the signals become steady, a change exists in the magnitude of the

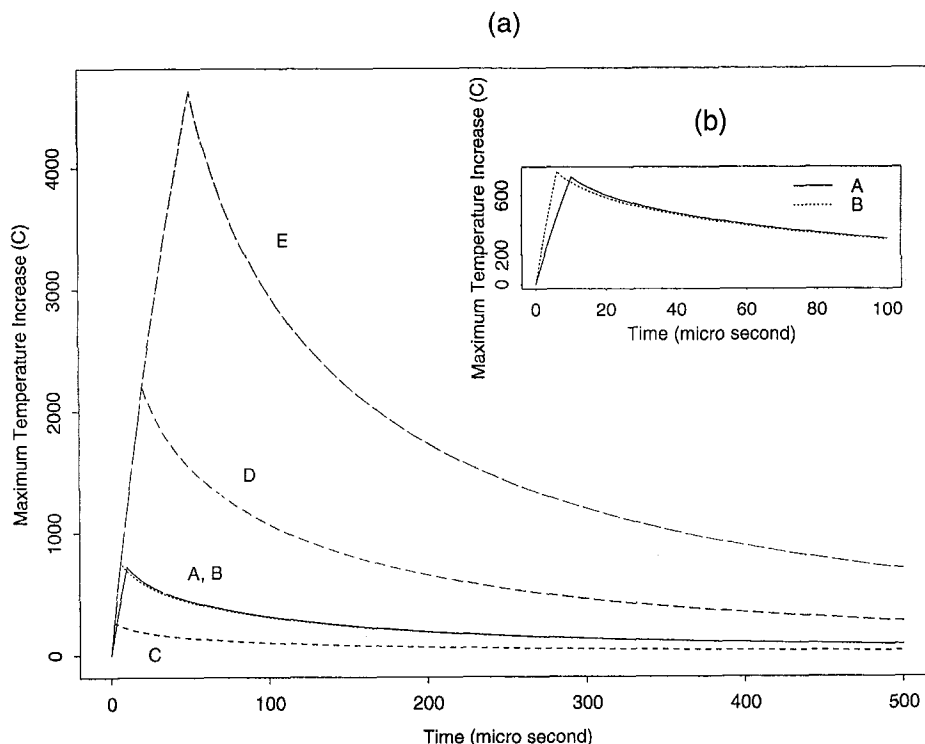


Fig. 3 (a) Calculated maximum surface temperature histories for the cases in Table 1; **(b)** Note the difference between cases (A) and (B) which have the same total deposited energy

signals, indicating the formation of permanent surface modification, except for case C. In the following, we discuss and compare the phenomena.

Cases A and B in Fig. 5(a)–(d) show smooth and clear deflection responses as expected for dome shaped bumps. In addition to the trends mentioned in the previous paragraph, larger changes in magnitude occur for a $\pm 15 \mu\text{m}$ offset (Fig. 5(a, d)) compared with those at $\pm 5 \mu\text{m}$ offset (Fig. 5(b, c)). This indicates that a steeper slope of the bump profile appears at $\pm 15 \mu\text{m}$ offset, while the slope becomes flatter closer to the center of the bump. Another obvious tendency is the larger change in magnitude of the signal with higher energy deposition. The energy incident for the two cases A and B can be viewed as the reasonable working range for dome-shaped bumps in the current system. The above results are directly confirmed from AFM images as shown in Fig. 2(a, b).

The difference in the transient behavior between cases A and B should be noted. Both cases have the same total deposited energy but different heating rates. The results show that both signals are comparable in magnitude, indicating a similar surface dimension. However, their growth rates are different and strongly related to the pulse width. A shallow dimple is formed at the center of the bump in case B, indicating the onset of the effect of viscous flow. The higher maximum temperature predicted in Fig. 3(b) and the change in the glass transition region due to the different heating rates may both contribute to this result.

Case C in Fig. 5(e)–(h), with only very small energy deposited, shows elastic material response; the deflection vanishes eventually even at the hottest spot. The signals presented record the life of these bumps as they grow, shrink, and then eventually disappear.

Cases D and E (Fig. 5(e)–(h)) represent high-energy depositions which change the surface deformation mechanism. The formation of a deep crater is clearly observed at the rear of these bumps (i.e., for positive x) and also confirmed in the AFM images in Fig. 2(c). For example, with a $+ 5 \mu\text{m}$ offset (Fig. 5(g)), the signal increases monotonically in the first $15 \mu\text{s}$, as also obtained in Fig. 5(c). However, after $15 \mu\text{s}$, the signal drops dramatically indicating that the geometry has changed from a bump to a crater. The corresponding time of the peak deflection signal can ideally be viewed

as an indication of the maximum threshold energy for the formation of the dome shaped bumps. The above is concluded from the observation that, regardless of pulse width, this characteristic time is fixed at about $15 \mu\text{s}$ for $75 \mu\text{J}$ laser pulse energy. However, the accuracy of this observation is effected by the resolution limitations of the system. A separate AFM measurement shows that with the same laser power, a crater is already formed for a $10 \mu\text{s}$ laser pulse (with the predicted maximum temperature = 900°C the glass transition temperature).

4 Conclusions

The photothermal deflection technique has been applied in this work to measure both the transient reflection and the deflection signals during the CO_2 laser heating of glass surfaces. In the reflection measurement, the change in the temperature-affected material, reflectivity in particular, is presented. It is concluded that the decrease in reflectivity follows the transient temperature increase and vice versa. Moreover, the steady-state offset indicates that in addition to the geometry change, the material may have also experienced a permanent change in phase and properties. For different total energy depositions and heating rates, three different material responses and/or surface features are detected. Small energy input imparts elastic behavior resulting in complete recovery of the surface. When the deposited energy was sufficiently high to raise the surface temperature to within the glass transition range, permanent dome-shaped bumps were detected. The dimensions of the bumps increase as the deposited energy increase. However, different heating rates affect the behavior of the material and also result in differences in the geometry of the bumps, even for the same total amount of laser energy deposited. At large laser pulse energy, transition occurs from dome-shaped bumps to cavities, which is attributed to the stronger effect of viscous flow. In addition to the fundamental study of the transient surface behavior, the present highly sensitive technique can be incorporated into the laser texturing process to monitor on-line both the growth of the desired surface features and the repeatability of the produced bumps.

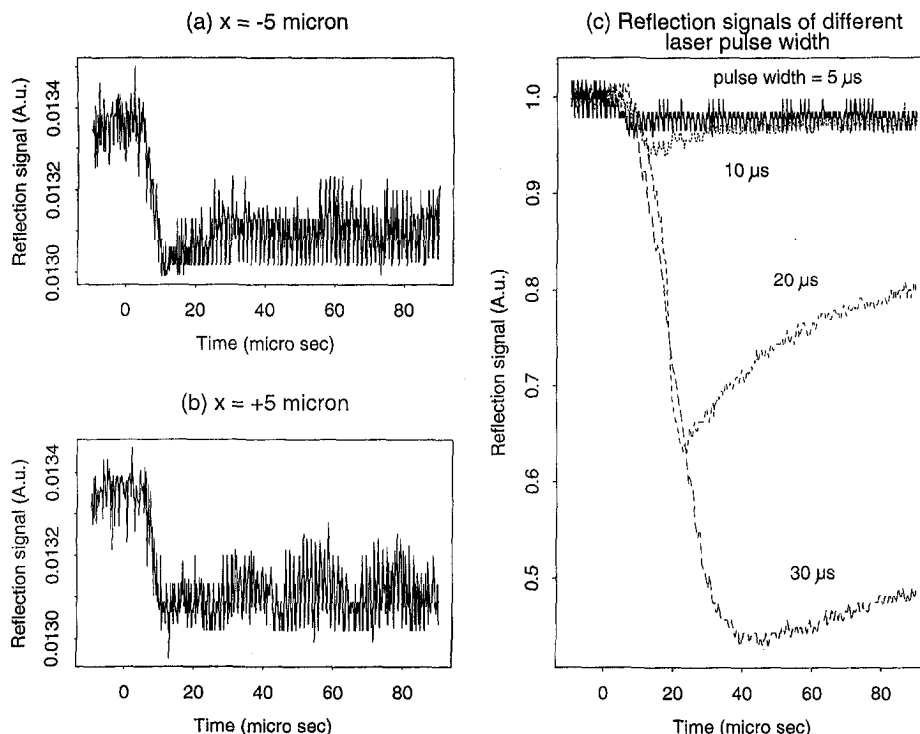


Fig. 4 (a) and (b) Reflection signals at $\pm 5 \mu\text{m}$ offset of a dome-shape bump, (c) reflection signals according to different laser pulse width at a fixed probing position

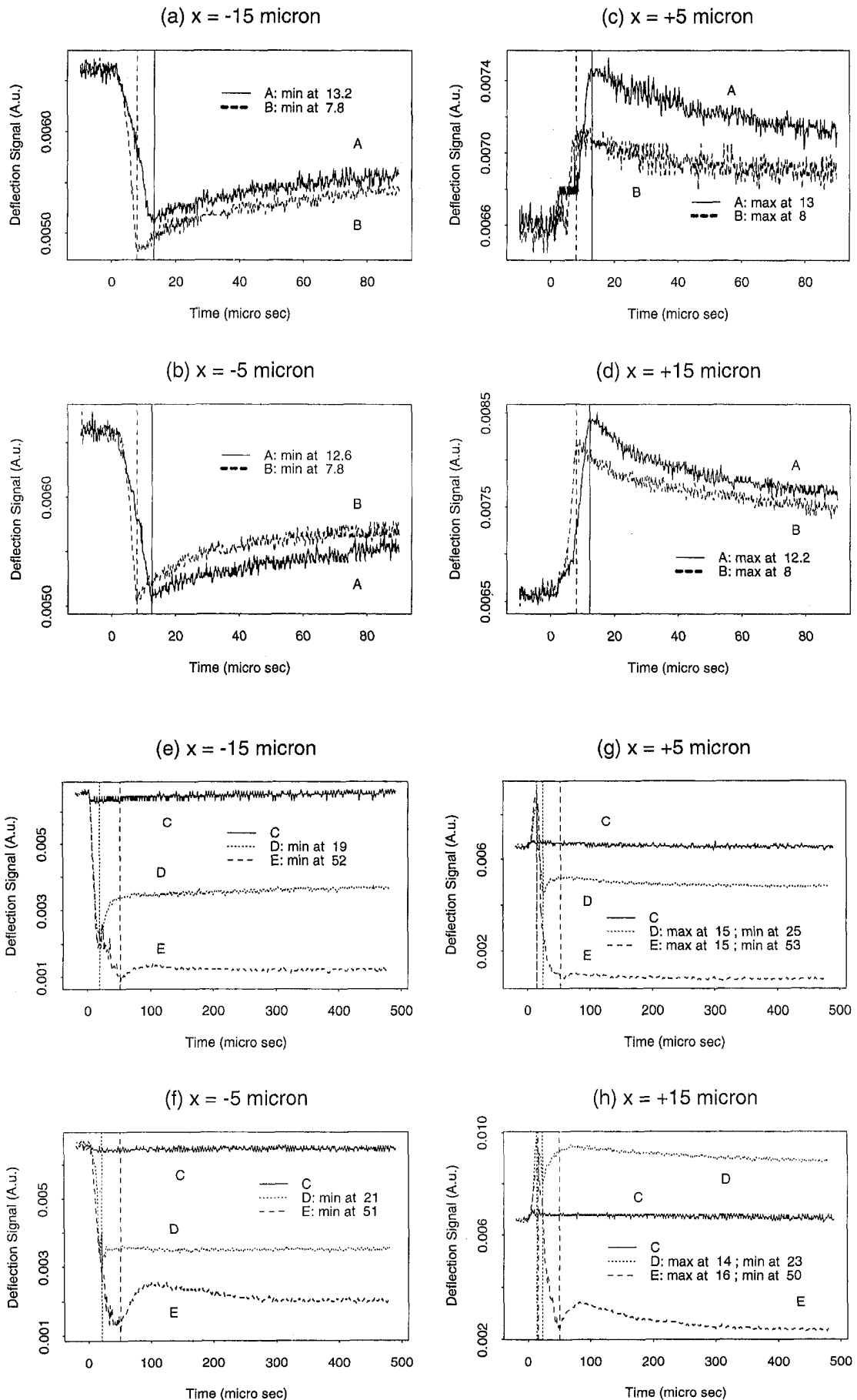


Fig. 5 Transient deflection signals at four different offset distance for case A and B: (a)–(d), and for case C, D, E: (e)–(h)

Acknowledgment

Support for this work by the National Science Foundation, under Grant CTS-9710502, and the Computer Mechanics Laboratory of the University of California at Berkeley is gratefully acknowledged.

References

- Kuo, D., Vierk, S. D., Rauch, O., and Polensky, D., 1997, "Laser zone texturing on glass and glass-ceramic substrates," *IEEE Transactions on Magnetics*, Vol. 33, No. 1, Pt. 2, pp. 94-99.
- Miller, R., and Bhushan, B., 1996, "Alternative substrates for gigabit recording," *Data Storage*, pp. 37-42.
- Olmstead, M. A., and Amer, N. M., and Kohn, S., 1983, "Photothermal displacement spectroscopy: An optical probe for solids and surfaces," *Appl. Phys. A*, Vol. 32, pp. 141-154.
- Palik, E. D., 1985, *Handbook of Optical Constants of Solids*, Academic Press, San Diego.
- Tam, A. C., Brannon, J., Baumgart, P., and Pour, I. K., 1997, "Laser texturing of glass disk substrates," *IEEE Transactions on Magnetics*, Vol. 33, No. 5, Pt. 1, pp. 3181-3183.
- Teng, E., Goh, W., and Eltoukhy, A., 1996, "Laser zone texture on the alternative substrate disks," *IEEE Transactions on Magnetics*, Vol. 32, No. 5, Pt. 1, pp. 3759-3761.
- Scherer, G. W., 1986, *Relaxation in glass and composites*, John Wiley and Sons, New York.
- Varshneya, A. K., 1994, *Fundamental of inorganic glasses*, Academic Press, San Diego.
- Zimmerman, P., and Welsch, E., 1994, "Modeling of signal detection by using the photothermal probe beam deflection technique," *Rev. Sci. Instrum.*, Vol. 65, No. 1, pp. 97-101.

Modeling of Fluid Flow and Heat Transfer in a Hydrothermal Crystal Growth System: Use of Fluid-Superposed Porous Layer Theory

Q.-S. Chen

V. Prasad
Fellow ASME

A. Chatterjee

Consortium for Crystal Growth Research,
State University of New York at Stony Brook,
Stony Brook, NY 11794-2300

Hydrothermal synthesis, which uses aqueous solvents under high pressure and relatively low temperature, is an important technique for difficult to grow crystalline materials. It is a replica of crystal growth under geological conditions. A hydrothermal growth system usually consists of finely divided particles of the nutrient, predetermined volume of a solvent and a suitably oriented crystal seed (Fig. 1) under very high pressures, generally several thousand bar. The nutrient dissolves at a higher temperature in the lower region, moves to the upper region due to buoyancy-induced convective flows, and deposits on the seed due to lower solubility if the seed region is maintained at a lower temperature. The system can be modeled as a composite fluid and porous layer using the Darcy-Brinkman-Forchheimer flow model in the porous bed. Since the growth process is very slow, the process is considered quasi-steady and the effect of dissolution and growth is neglected. This first study on transport phenomena in a hydrothermal system therefore focuses on the flow and temperature fields without the presence of the seed and mass transfer. A three-dimensional algorithm is used to simulate the flow and heat transfer in a typical autoclave system. An axisymmetric flow pattern at low Grashof numbers becomes three-dimensional at high Grashof numbers. A reduction in the porous bed height for fixed heated and cooled regions can result in oscillatory flows. These results, for the first time, depict the possible flow patterns in a hydrothermal system, that can have far reaching consequences on the growth process and crystal quality.

Introduction

The hydrothermal process, which imitates the crystal growth phenomena under geological conditions, has been widely used in crystal growth industry since the 1960s (Byrappa, 1994; Shternberg, 1971; Laudise and Nielsen, 1961; Laudise, 1970; James and Kell, 1975; Larkin et al., 1993). High-quality single crystals of many materials, such as quartz, berlinite, malachite, bismuth silicate, and many other oxides, can be obtained by this technique. Among the hydrothermally grown crystals, quartz is the most popular and technologically the most important material.

A typical hydrothermal system consists of finely divided particles of the nutrient at the bottom, predetermined volume of a solvent, a suitably oriented crystal seed in the upper portion, and a metal baffle with holes above the porous bed (Fig. 1). The system is highly pressurized, e.g., to about 1,379 bar in the case of quartz growth. Using strap heaters on the cylindrical autoclave sidewall, a higher temperature condition is produced in the lower portion of the autoclave and a lower temperature in the upper portion, typically 355–369°C and 350°C, respectively, for quartz. The polycrystalline quartz dissolves at this temperature in a mineralizer, e.g., about 1N NaOH or Na₂CO₃ solution, although the solubility is very low under these conditions, 2.30–2.35 wt% (Laudise and Nielsen, 1961). Due to the imposed temperature difference, a

buoyancy-induced flow is established and the aqueous solution moves to the upper portion of the autoclave. Since the temperature in the upper region is lower, the solubility goes down, about 2.28 wt%, and a part of dissolved nutrient is separated and deposited on the seed. The growth process is generally very slow and it takes several weeks to grow a full size crystal, say 38 mm in the transverse direction and 125–150 mm in the axial direction. The knowledge of growing crystals in a hydrothermal system is basically an “art” developed through extensive trial and error experiments.

In the absence of any good understanding of the flow pattern and temperature field, the height of the nutrient level, pressure inside the autoclave, and temperature differential on its wall are all prescribed based on the knowledge gained from experiments. It has been found that a porous baffle helps the growth process, although the mechanism by which it aids the hydrothermal synthesis is not clear. The presence of baffle, however, introduces several process control parameters. The present paper considers the flow and heat transfer in an autoclave system that is used for growing crystals which have positive temperature coefficient of solubility, such as quartz.

The buoyancy-induced convective circulation in a hydrothermal system will depend on Grashof number. At small Grashof numbers the flow will be laminar, but the flow can become oscillatory or even turbulent when the Grashof number is high. The inner diameter of the autoclave varies from a few centimeters to as high as 65 centimeters, indicating that the fluid Grashof number may change from 10⁴ to 10¹³. The reference length scale in defining Gr is also an issue and it is difficult to make a perfect choice between the

Contributed by the Heat Transfer Division for publication in the JOURNAL OF HEAT TRANSFER and presented at '98 IMECE, Anaheim. Manuscript received by the Heat Transfer Division, Aug. 2, 1998; revision received, Feb. 9, 1999. Keywords: Crystal Growth, Heat Transfer, Modeling, Natural Convection, Porous Media. Associate Technical Editor: C. Beckermann.

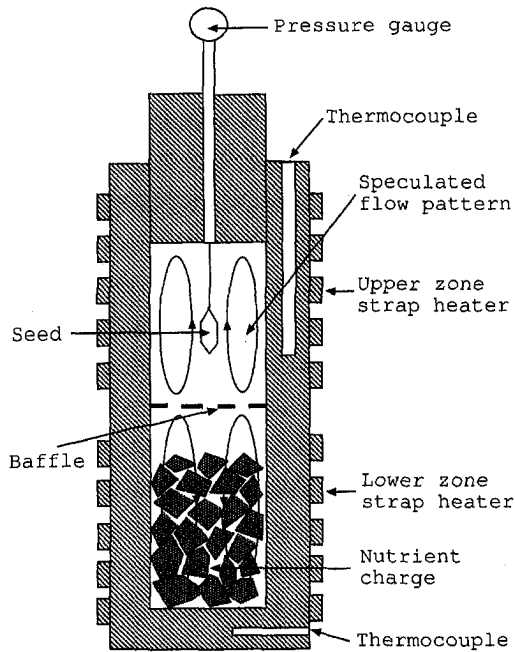


Fig. 1 A schematic of the autoclave with nutrient and seed plate, and speculated flow pattern as shown by Laudise and Nielsen (1961)

radius of the cylinder and its height. The value of Gr will increase substantially if the height is chosen to calculate Gr since the aspect ratio of these autoclaves is generally large, 2–20. In the present discussion, we ignore the buoyancy effect due to the variation in nutrient concentration since it is very low; although to predict the deposition rate it will be necessary to consider the concentration distribution.

It is evident that the buoyancy flow will strongly influence the temperature distribution in the nutrient and growth regions. Since the solubility is a strong function of temperature, the knowledge of temperature distribution can help in estimating the supersaturation of the solution, the rate of dissolving in the nutrient zone, and the rate of growth of the seed. The actual temperature difference between the growth zone and the nutrient zone is certainly far less than the temperature difference imposed on the side wall of the autoclave, due to thermal resistance of the wall and convective flow in the fluid (Byrappa, 1994). If the temperature and flow fields become oscillatory when the Grashof number is high, inhomogeneities will appear in the grown crystal. A baffle between the growth zone and the nutrient zone may help in reducing the flow

strength and thus suppress the oscillations when the Grashof number is high.

A suitable convective circulation is necessary to transfer material from the nutrient zone to the seed zone. (It cannot be accomplished by diffusion-controlled mass transfer.) However, the baffle can reduce the mass transfer between the nutrient zone and the growth zone, thus reducing the growth rate of the crystal. The baffle, therefore, plays a competing role between suppressing the flow strength and oscillations and reducing the mass transport. Its location, thickness, and porosity can all influence the process. Other parameters which can control the hydrothermal growth process are: the portions of the autoclave wall that are maintained at two different temperatures, height of the nutrient charge, aspect ratio of the autoclave, seed location, etc.

Since the hydrothermal process involves very high pressures, it is difficult, if not impossible, to measure the temperature and velocity fields in such a system. Currently, we neither have any data available on the velocity, temperature, and concentration distributions nor do we know the growth rate as a function of time. The only information that has been reported is the overall growth, the total time taken, and the quality of the crystal. The primary objective of this paper is, therefore, to develop a transport model that can provide insights into the physics of the hydrothermal process. To develop a basic understanding of the transport mechanisms, this study focuses on the flow and temperature fields in an autoclave without a baffle. Preliminary results are presented to analyze the flow pattern and temperature distribution.

Mathematical Model

It is evident that a hydrothermal system can be considered as a composite porous and fluid layer (Fig. 2). For modeling, the porous bed is considered homogeneous and isotropic, and saturated with a fluid which is in local thermodynamic equilibrium with the solid matrix. A higher temperature, T_H , is applied on the lower portion of the cylindrical wall, $0 < x^* < h_H$, and a lower temperature, T_C , is considered on the upper portion of the cylindrical wall, $h_H < x^* < H$. The ratio of the height of the wall at T_H and the overall height is defined as

$$A_T = h_H/H.$$

The height of the wall where the temperature changes from T_H to T_C is assumed as δ_T^* . (A real system will not allow a step change in temperature.) The top and bottom of the cylinder are considered adiabatic.

The Darcy-Brinkman-Forchheimer model is employed in the porous layer, while for the flow in the upper layer, Navier-Stokes equations are used with the assumption of incompressible flow and

Nomenclature

Ar = aspect ratio, H/R
 A_T = ratio of the wall height at T_H to the overall height of the system, h_H/H (Fig. 2)
 b = Forchheimer coefficient, $CK^{0.5}$, m
 c_p = specific heat, $J/kg \cdot K$
 C = inertia coefficient, $1.75/\sqrt{150} \epsilon^{-3/2}$
 D_e = diffusion term
 Da = Darcy number, K/R^2
 F_e = convection term
 Fs = Forchheimer number, $b/R = CDa^{0.5}$
 g = acceleration due to gravity, m^2/s
 Gr = Grashof number, $g\beta R^3(T_H - T_C)/\nu^2$
 Gr^* = modified Grashof number, $Gr \cdot Da$

h_H = heated portion of the wall at T_H , m
 h_p = porous bed height, m
 h_ξ, h_η, h_ζ = scales of covariant base vectors
 H = height of autoclave, m
 Ja = Jacobian of transformation
 K = permeability of porous matrix, m^2
 Nu = Nusselt number, $1/A_T \int_0^{A_T} R_k \partial T / \partial r|_{r=1} dx$
 p = dimensionless pressure
 p^* = pressure, Pa
 Pe = Peclet number, F_e/D_e
 Pr = Prandtl number, $(\nu/\alpha)_f$
 r = dimensionless coordinate

r^* = radial coordinate, m
 R = radius of cylindrical autoclave, m
 R_k = ratio of thermal conductivity, k_{eff}/k_f
 S_c, S_p = linear source terms for momentum equations and energy equation
 S_e = specific heat ratio, $(c_p)_{eff}/(c_p)_f$
 S_m = mass source term
 S_{NO} = curvature source term for the transformed continuity equation
 S_ϕ = curvature source term for the transformed momentum and energy equations
 T = temperature, K

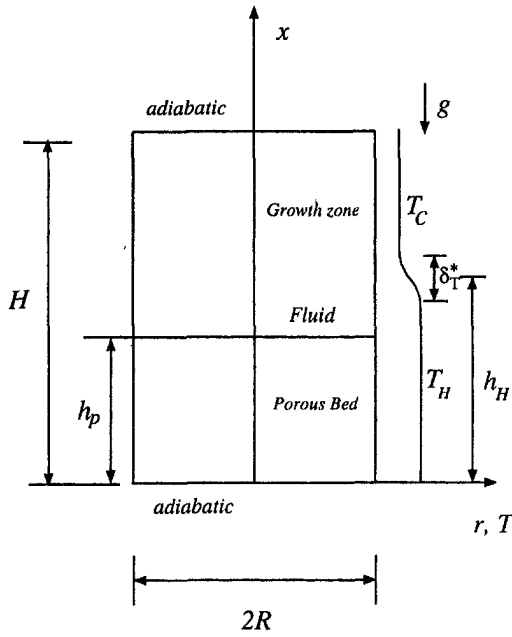


Fig. 2 Schematic of a hydrothermal system for transport modeling

the Boussinesq approximation (Bejan, 1984; Beckermann et al., 1987; Prasad, 1991). The governing equations in porous and fluid layers can be combined by defining a binary parameter B ,

$$B = \begin{cases} 0, & \text{in fluid layer} \\ 1, & \text{in porous layer} \end{cases} \quad (1a)$$

$$(1b)$$

and appropriately selecting the void fraction, $\epsilon = 1$ for the fluid layer and $0 < \epsilon < 1$ for the porous layer (Prasad, 1991), which leads to

$$\frac{\partial(\epsilon\rho_f)}{\partial t^*} + \nabla^* \cdot (\rho_f \mathbf{u}^*) = S_m^*, \quad (2)$$

$$\left[\frac{\rho_f}{\epsilon} \frac{\partial \mathbf{u}^*}{\partial t^*} + \frac{\rho_f}{\epsilon} (\mathbf{u}^* \cdot \nabla^*) \frac{\mathbf{u}^*}{\epsilon} \right] = -\nabla^* p^* - \rho_f g \mathbf{k} + \nabla^* \cdot (\mu_{\text{eff}} \nabla^* \mathbf{u}^*) - B \left[\left(\frac{\mu_f}{K} + \frac{\rho_f b}{K} |\mathbf{u}^*| \right) \mathbf{u}^* \right], \quad (3)$$

Nomenclature (cont.)

u, v, w = dimensionless velocities
 $|u|_{\text{max}}$ = maximum of u
 u^*, v^*, w^* = velocities, m/s
 u_ξ, u_η, u_ζ = dimensionless covariant velocities
 x, y, z = dimensionless coordinates
 x^*, y^*, z^* = cartesian coordinates, m

Greek Symbols

α = thermal diffusivity, m^2/s
 $\alpha_\xi, \eta_\xi, \zeta_\xi$ = primary area and secondary areas in ξ direction
 $\alpha_\eta, \eta_\eta, \zeta_\eta$ = primary area and secondary areas in η direction
 $\alpha_\zeta, \eta_\zeta, \zeta_\zeta$ = primary area and secondary areas in ζ direction
 β = isobaric coefficient of expansion, $1/\text{K}$

Γ_{eff} = effective coefficient of diffusivity
 δ_T^* = height of the wall where temperature changes from T_H to T_C , m (Fig. 2)
 Δt = time step
 ϵ = porosity
 θ = dimensionless temperature, $(T - T_C)/(T_H - T_C)$
 Λ = viscosity ratio, μ_{eff}/μ_f
 η = ratio of porous bed height and overall height, h_p/H
 μ = viscosity, $\text{kg}/\text{m} \cdot \text{s}$
 ν = kinematic viscosity, m^2/s
 ξ, η, ζ = dimensionless curvilinear coordinates
 ρ = density, kg/m^3

Subscripts and Superscripts

C = cold
 e, w, t, b, n, s = east, west, top, bottom, north, and south faces of a control volume
 eff = effective, porous medium property
 E, W, T, B, N, S = east, west, top, bottom, north, and south neighbors of the grid point P
 f = fluid
 H = hot
 P = grid point P
 ξ, η, ζ = along curvilinear coordinate directions
 0 = last time-step value
 $*$ = dimensional value

Table 1 Typical governing parameters for quartz-aqueous system

Parameter	Value
Aspect ratio, Ar	2 ~ 20
Initial dimensionless porous bed height, η	0.4 ~ 0.5
Prandtl number, Pr	1 ~ 2
Grashof number, Gr	$10^4 \sim 10^{13}$
Darcy number, Da	$10^{-13} \sim 10^{-3}$
Forchheimer number, Fs	$10^{-7} \sim 10^{-2}$
Viscosity ratio, Λ	1 ~ 2.5
Specific heat ratio, S_e	1 ~ 2
Conductivity ratio, R_k	1 ~ 1.4

$$(\rho c_p)_{\text{eff}} \frac{\partial T}{\partial t^*} + (\rho c_p)_f [(\mathbf{u}^* \cdot \nabla^*) T] = \nabla^* \cdot (k_{\text{eff}} \nabla^* T), \quad (4)$$

where \mathbf{k} is the unit vector in the x direction, b is the Forchheimer coefficient (Ergun, 1952), and K is the permeability of the nutrient bed.

The following scales are used to nondimensionalize the governing equations: length, R ; velocity, ν_f/R ; time, R^2/ν_f ; pressure, $\rho_f \nu_f^2/R^2$; and temperature, $T_H - T_C$. The dimensionless parameters that govern the flow and heat transfer in a hydrothermal system under the conditions described earlier and their typical values are shown in Table 1. The nondimensional form of Eqs. (2)–(4) are then obtained as

$$\frac{\partial \epsilon}{\partial t} + \nabla \cdot \mathbf{u} = S_m, \quad (5)$$

$$\frac{1}{\epsilon} \frac{\partial \mathbf{u}}{\partial t} + \frac{1}{\epsilon} (\mathbf{u} \cdot \nabla) \frac{\mathbf{u}}{\epsilon} = -\nabla p + Gr \theta \mathbf{k} + \nabla \cdot \Lambda \nabla \mathbf{u} - B \left(\frac{1}{Da} + \frac{Fs}{Da} |\mathbf{u}| \right) \mathbf{u}, \quad (6)$$

$$S_e \frac{\partial \theta}{\partial t} + (\mathbf{u} \cdot \nabla) \theta = \frac{1}{Pr} \nabla \cdot (R_k \nabla \theta). \quad (7)$$

In Eq. (6), the Brinkman and Forchheimer terms can be easily neglected, if desired, by considering $\Lambda = 0$ and $Fs = 0$, respectively. Equations (5)–(7) can be solved together with the following boundary conditions: No slip and constant temperature conditions are applied on the vertical wall of the autoclave,

$$\mathbf{u} = 0, \quad (8a)$$

$$\theta = \begin{cases} 0, & x \geq 0.5(A_T + \delta_T) \\ 1 + \cos \left[\frac{\pi(x - 0.5A_T + 0.5\delta_T)/\delta_T}{2} \right]^2, & 0.5(A_T - \delta_T) < x < 0.5(A_T + \delta_T), \\ 1, & x \leq 0.5(A_T - \delta_T) \end{cases} \quad (8b)$$

where δ_T is the dimensionless height of the wall where the temperature changes from 1 to 0 and chosen as $0.05 Ar$ for the present calculations. The top and bottom of the autoclave are considered adiabatic, and hence

$$\mathbf{u} = 0, \quad (9a)$$

$$\frac{\partial \theta}{\partial x} = 0, \quad \text{at } x = 0 \text{ and } Ar. \quad (9b)$$

In the azimuthal direction, periodic boundary conditions are used for both the velocity and temperature. At the fluid and porous layer interface, the continuity of temperature, velocity, pressure, stress, and heat flux is required which is automatically satisfied by solving the combined equations in a single domain (Prasad, 1991).

Three-Dimensional Finite Volume Solution Procedure

A three-dimensional numerical algorithm is developed using the curvilinear coordinates (Karki and Patankar, 1988). The discretized form of the continuity Eq. (5) is then written as (Zhang and Moallemi, 1995; Zhang et al., 1996; Chatterjee, 1998a, b):

$$\frac{(\epsilon)_P(\mathbf{J}\mathbf{a})_P - (\epsilon^0)_P(\mathbf{J}\mathbf{a}^0)_P}{\Delta t} \Delta \xi \Delta \eta \Delta \zeta + \{(\alpha_{\xi} u_{\xi})_e - (\alpha_{\xi} u_{\xi})_w\} \Delta \eta \Delta \zeta + \{(\alpha_{\eta} u_{\eta})_i - (\alpha_{\eta} u_{\eta})_b\} \Delta \xi \Delta \zeta + \{(\alpha_{\zeta} u_{\zeta})_n - (\alpha_{\zeta} u_{\zeta})_s\} \Delta \xi \Delta \eta = \{\mathbf{J}\mathbf{a}S_m + S_{NO}\}_P \Delta \xi \Delta \eta \Delta \zeta, \quad (10)$$

where the curvature source term S_{NO} has the following form:

$$S_{NO} = - \left[\frac{\partial}{\partial \xi} (\beta_{\xi} u_{\eta} + \gamma_{\xi} u_{\zeta}) + \frac{\partial}{\partial \eta} (\beta_{\eta} u_{\xi} + \gamma_{\eta} u_{\zeta}) + \frac{\partial}{\partial \zeta} (\beta_{\zeta} u_{\xi} + \gamma_{\zeta} u_{\eta}) \right]. \quad (11)$$

The momentum Eq. (6) and energy Eq. (7) can be discretized as follows:

$$\frac{(c\epsilon\mathbf{J}\mathbf{a})_P\phi_P - (c^0\epsilon^0\mathbf{J}\mathbf{a}^0)_P\phi_P^0}{\Delta t} \Delta \xi \Delta \eta \Delta \zeta + \{(\alpha_{\xi} J_{\xi})_e - (\alpha_{\xi} J_{\xi})_w\} \Delta \eta \Delta \zeta + \{(\alpha_{\eta} J_{\eta})_i - (\alpha_{\eta} J_{\eta})_b\} \Delta \xi \Delta \zeta + \{(\alpha_{\zeta} J_{\zeta})_n - (\alpha_{\zeta} J_{\zeta})_s\} \Delta \xi \Delta \eta = \{\mathbf{J}\mathbf{a}(S_c + S_p\phi) + S_{\phi}\}_P \Delta \xi \Delta \eta \Delta \zeta, \quad (12)$$

where

$$S_c = \begin{cases} \text{Gr}\theta - \frac{\partial p}{\partial x}, & \phi = u \\ -\frac{\partial p}{\partial y}, & \phi = v \\ -\frac{\partial p}{\partial z}, & \phi = w \\ 0, & \phi = \theta \end{cases}$$

$$S_p = \begin{cases} -B \left(\frac{1}{\text{Da}} + \frac{\text{Fs}}{\text{Da}} |\mathbf{u}| \right), & \phi = u, v, w \\ 0, & \phi = \theta. \end{cases}$$

We define, $c = 1/\epsilon^2$, $d = 1/\epsilon^2$, and $\Gamma_{\text{eff}} = \Lambda$ for momentum equations ($\phi = u, v, w$); $c = S_c/\epsilon$, $d = 1$, and $\Gamma_{\text{eff}} = R_k/\text{Pr}$ for

energy equation ($\phi = \theta$). The covariant total fluxes (convection and diffusion) are given by

$$J_{\xi} = du_{\xi}\phi - \frac{1}{h_{\xi}} \Gamma_{\text{eff}} \frac{\partial \phi}{\partial \xi},$$

$$J_{\eta} = du_{\eta}\phi - \frac{1}{h_{\eta}} \Gamma_{\text{eff}} \frac{\partial \phi}{\partial \eta},$$

$$J_{\zeta} = du_{\zeta}\phi - \frac{1}{h_{\zeta}} \Gamma_{\text{eff}} \frac{\partial \phi}{\partial \zeta},$$

The curvature source term S_{ϕ} arises from the nonorthogonal grids, and is given by

$$S_{\phi} = - \left[\frac{\partial}{\partial \xi} (\beta_{\xi} J_{\eta} + \gamma_{\xi} J_{\zeta}) + \frac{\partial}{\partial \eta} (\beta_{\eta} J_{\xi} + \gamma_{\eta} J_{\zeta}) + \frac{\partial}{\partial \zeta} (\beta_{\zeta} J_{\xi} + \gamma_{\zeta} J_{\eta}) \right]. \quad (13)$$

Multiplying Eq. (10) by $(d\phi)_P$ and subtracting it from Eq. (12) yields

$$\frac{\{d\epsilon^0\mathbf{J}\mathbf{a}^0 + (c-d)\epsilon\mathbf{J}\mathbf{a}\}_P}{\Delta t} \phi_P \Delta \xi \Delta \eta \Delta \zeta + (\alpha_{\xi})_e \{J_{\xi}\}_e - (u_{\xi})_e (d\phi)_P \Delta \eta \Delta \zeta - (\alpha_{\xi})_w \{J_{\xi}\}_w - (u_{\xi})_w (d\phi)_P \Delta \eta \Delta \zeta + (\alpha_{\eta})_i \{J_{\eta}\}_i - (u_{\eta})_i (d\phi)_P \Delta \xi \Delta \zeta - (\alpha_{\eta})_b \{J_{\eta}\}_b - (u_{\eta})_b (d\phi)_P \Delta \xi \Delta \zeta + (\alpha_{\zeta})_n \{J_{\zeta}\}_n - (u_{\zeta})_n (d\phi)_P \Delta \xi \Delta \eta - (\alpha_{\zeta})_s \{J_{\zeta}\}_s - (u_{\zeta})_s (d\phi)_P \Delta \xi \Delta \eta = \{\mathbf{J}\mathbf{a}(S_c + S_p\phi - dS_m\phi) + (S_{\phi} - dS_{NO}\phi)_P\} \Delta \xi \Delta \eta \Delta \zeta + \frac{(c^0\epsilon^0\mathbf{J}\mathbf{a}^0)_P}{\Delta t} \phi_P^0 \Delta \xi \Delta \eta \Delta \zeta. \quad (14)$$

The discretization of total flux J in each control-volume face is performed as in Patankar (1980),

$$(J_{\xi})_e - F_e \phi_P = \{D_e A(|P_e|) + \max[-F_e, 0]\} (\phi_P - \phi_E), \dots$$

where the convection term $F_e = (du_{\xi})_e \Delta \eta \Delta \zeta$, D_e is the diffusion term, P_e is the Peclet number, and function $A(|P_e|)$ is chosen by the power law scheme of differencing. The final discretized equation is then obtained as

$$a_P \phi_P = a_E \phi_E + a_W \phi_W + a_T \phi_T + a_B \phi_B + a_N \phi_N + a_S \phi_S + b, \quad (15)$$

with the coefficients a 's as described in Chatterjee (1998a) following Patankar (1980), and a should be different here,

$$a_P = a_E + a_W + a_T + a_B + a_N + a_S + \left\{ -\mathbf{J}\mathbf{a}S_p + \mathbf{J}\mathbf{a}dS_m + dS_{NO} + \frac{d\epsilon^0\mathbf{J}\mathbf{a}^0 + (c-d)\epsilon\mathbf{J}\mathbf{a}}{\Delta t} \right\}_P \Delta \xi \Delta \eta \Delta \zeta,$$

$$b = \left\{ \frac{(c^0\epsilon^0\mathbf{J}\mathbf{a}^0)_P}{\Delta t} \phi_P^0 + (\mathbf{J}\mathbf{a}S_c)_P + (S_{\phi})_P \right\} \Delta \xi \Delta \eta \Delta \zeta.$$

The power-law scheme is used for discretization and the solutions are obtained employing the SIMPLER method with pressure obtained on a nonstaggered grid system (Zhang et al., 1996; Chatterjee, 1998a, b). The numerical algorithm is verified by considering natural convection flow in a cubic enclosure with vertical fluid and porous layers. The two vertical sidewalls of the enclosure are applied constant but differential temperatures, and the vertical front and back walls and the horizontal walls are considered adiabatic. These boundary conditions reduce the problem to two dimensions at least in the midplane, $z = 0.5$, the

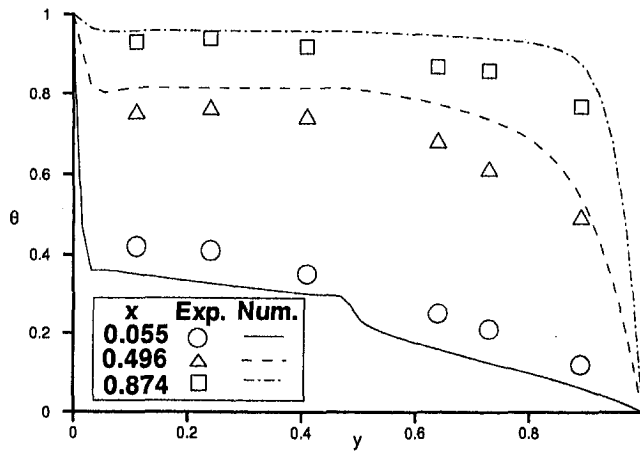


Fig. 3 Predicted and experimental temperature profiles for a composite vertical fluid and porous layer for $Ar = 1$, $\eta = 0.5$, $\epsilon = 0.4$, $Pr = 6.97$, $Da = 1.296 \times 10^{-5}$, $Gr = 4.344 \times 10^6$, $C = 0.5648$, $R_k = 1.383$ (Beckermann et al., 1987)

two-dimensional configuration considered by Beckermann et al. (1987). The parameters are also chosen as in Beckermann et al. (1987), $Ar = 1$, $\eta = 0.5$, $\epsilon = 0.4$, $Pr = 6.97$, $Da = 1.296 \times 10^{-5}$, $Gr = 4.344 \times 10^6$, $C = 0.5648$, $R_k = 1.383$. The temperature distribution and streamlines predicted here agree well with that reported by these authors (see Chen et al., 1998). In Fig. 3, the temperature profiles at different heights are compared with the experimental data presented by Beckermann et al. In general, the agreement between the present temperature profiles and Beckermann's predictions is within five percent although some discrepancies exist between the predictions and experiments (Fig. 3). As noted by Beckermann et al. (1987), the discrepancies between the predicted and measured temperature profiles are possible due to the inaccuracies in determining the exact position of the movable thermocouple probe. The present model has been successfully tested for many other natural convection problems (Chatterjee, 1998a, b; Chen et al., 1999).

A grid independence test for the present hydrothermal problem has been carried out by obtaining several solutions for $Ar = 3$, $\eta = 0.5$, $Da = 10^{-4}$, $Gr = 10^5$ (see Figs. 6(a) and 6(b)). Table 2 presents the Nusselt number

$$Nu = \frac{1}{A_T} \int_0^{A_T Ar} R_k \left. \frac{\partial T}{\partial r} \right|_{r=1} dx$$

for four different sets of grids. As can be seen, the Nusselt number changes by less than 2.5 percent when the mesh size changes. Based on a series of trial runs, a grid of $31 \times 20 \times 39$ nodal points in the axial, radial, and azimuthal directions, respectively, is used for the results presented in this paper. The nodal points are uniformly distributed in the radial and azimuthal directions, while in the axial direction they are densely distributed near the fluid/porous layer interface to ensure smooth changes of the properties across the interface. The grid overlaps in the azimuthal direction to implement the periodic boundary conditions and satisfy the continuity and flux conditions. Because of singularity, special treatment is needed at the central axis, $r = 0$. The properties in the $r = 0$ region are averaged as follows:

$$\phi|_{r=0} = \bar{\phi}|_{r=0^+}$$

Time steps used for the calculations strongly depend on the parameters being considered. For example, a time step of 10^{-3} is employed when $Gr = 10^5$, $Da = 10^{-3}$ and $\eta = 0.5$, which is reduced to 5×10^{-4} when η becomes 0.4.

Results and Discussion

Typical Flow Pattern in a Hydrothermal System and Growth Mechanism. Since it has been impossible to observe the flow field in an autoclave, only intuitive attempts have been made to speculate the flow pattern in a hydrothermal system, as shown in Fig. 1 (Laudise and Nielsen, 1961). Since the vertical wall is differentially heated and cooled, the flow pattern is assumed to have two counter-rotating cells (in one-half of the autoclave); one in the upper region and the other in the lower region as depicted in Fig. 1. However, there are too many parameters to influence the flow pattern, such as the aspect ratio of the autoclave, portions of the wall at T_H and T_C , porous bed height, Darcy number, Grashof number, etc. Here we present some typical numerical solutions to reveal the basic structure of the flow and temperature fields in an autoclave. The porosity is chosen as $\epsilon = 0.4$ with inertia coefficient C obtained as 0.5648, while other fixed parameters considered for this study are: Prandtl number, $Pr = 1$, viscosity ratio, $\Lambda = 2.5$, conductivity ratio, $R_k = 1$, and dimensionless height of the heated portion, $A_T = 0.5$.

Figure 4(a) shows a typical temperature field in a vertical cross section of the autoclave when $Ar = 3$, $\eta = 0.5$, $Da = 10^{-6}$, $Gr = 10^7$. It can be seen that the heat transfer in the porous bed is conduction-dominated while that in the fluid layer is strongly influenced by convection. Figure 4(b) shows the corresponding flow field. The flow is almost invisible in the porous layer while there is a strong vortex in the fluid layer. With respect to the hydrothermal growth, if the flow in the charge is too weak, the nutrient will not convect to the growth zone and the mass transfer in bottom region will be diffusion-dominated. From a review of porous media literature, one can conclude that if the modified Grashof number, $Gr^* = Gr \cdot Da$, is small, the temperature and flow fields will approach similar solutions regardless of the values of the Darcy number and fluid Grashof number because of almost negligible effects of the Brinkman and Forchheimer's terms—Darcy flow regime in the porous layer.

Figure 5(a) shows the temperature field in a vertical cross section of the autoclave when $Gr = 10^6$, $Gr^* = 10$, ($Da = 10^{-5}$), all other parameters remaining the same. The temperature field is slightly modified in both the fluid and porous regions. The recirculating fluid brings more heat from the porous bed and dissipates in the cold portion of the autoclave wall. The flow field is modified accordingly and the solution can be seen rising along the heated portion of the side wall. Under axisymmetric (two-dimensional) flow conditions, two recirculating cells exist in one-half of the vertical plane, one weak recirculation in the porous region and the other very strong cell in the fluid region. The convective roll in the lower region feeds quartz-aqueous solution to the cell in the seed region, upward flow concentrated in the central region. It should be noted that even though the flow seems to be very strong in the upper region, the nutrient to crystallize on the seed can be brought by the solution only through a weak convective interaction between the two cells directly under the seed and some diffusion along the fluid/porous layer interface.

Figure 5(b) demonstrates the basic mechanism of transport of nutrient from the charge to the seed. It establishes the common belief of the hydrothermal crystal grower that the convective flow is essential for the seeds to grow. Without this direct transport of saturated solution towards the seed, the crystal will not grow since the diffusion-dominated mass transport can not bring solute to the seed in any appreciable quantity. In addition, there will be no special incentive for the separated solute to deposit only on the crystal seed. In fact, it can deposit anywhere on the autoclave wall.

Table 2 Nusselt number as a function of mesh size for the case presented in Fig. 6

Grids	$31 \times 16 \times 39$	$31 \times 20 \times 39$	$41 \times 20 \times 39$	$51 \times 25 \times 39$
Nu	2.346	2.364	2.384	2.396

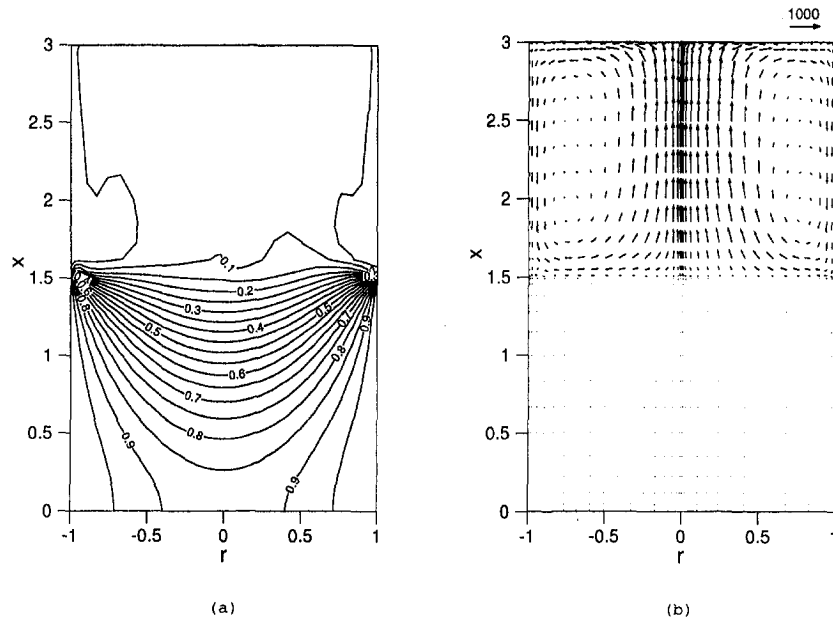


Fig. 4 Temperature distribution (a) and flow field (b) in a vertical cross section of the autoclave, $Ar = 3$, $\eta = 0.5$, $Pr = 1$, $Da = 10^{-6}$, and $Gr = 10^7$ ($Gr^* = 10$)

Another important point to note is that the temperature variation in the fluid region is small, $\theta \cong 0.15$ to $\theta = 0$, indicating that most of the separation because of the decreased solubility takes place directly under the seed, and in the upper layer of the porous bed, not while the solution is moving from the central portion of the autoclave towards the side wall.

There are a few other important features of this flow pattern that must be noted. First, the flow strength of the two vortices are very different, which cannot be understood clearly without conducting a thorough transport analysis of the system for a wide range of parameters. Secondly, the strong vertical flow directly under the seed can have negative effects on the growth process; it can wash away the solute from the seed surface. It is not surprising that the hydrothermal crystal growers have placed a porous baffle in the

autoclave. Clearly, this can reduce the vertical flow velocity in the central portion to improve the flow conditions for the growth, although the growth rate will be reduced. Another critical issue that will determine the rate of growth is the role of kinetics of deposition and bonding versus the flow velocity in the seed region.

Effect of Permeability of the Porous Bed. Figures 6(a) and 6(b) show the temperature and flow fields for a high permeability porous bed, $Da = 10^{-4}$, but for a lower Grashof number, $Gr = 10^5$ (compared to Fig. 5). All other parameters remain the same. There is no appreciable change in the flow pattern and its strength in the porous region since the Darcy-modified Grashof number Gr^* is identical in Figs. 5 and 6. However, the increased permeability changes the conditions near the fluid-porous layer interface. Also

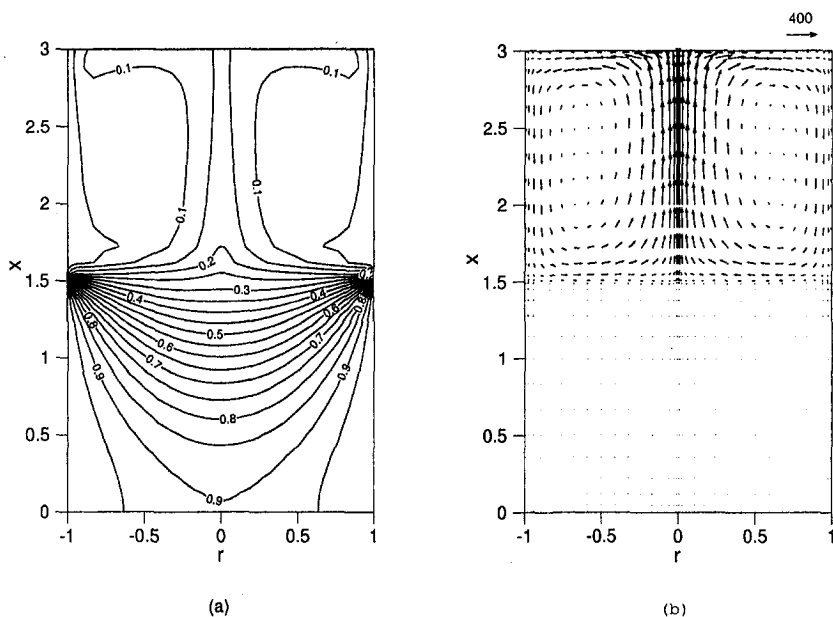


Fig. 5 Temperature distribution (a) and flow field (b) for $Ar = 3$, $\eta = 0.5$, $Pr = 1$, $Da = 10^{-5}$, and $Gr = 10^6$ ($Gr^* = 10$)

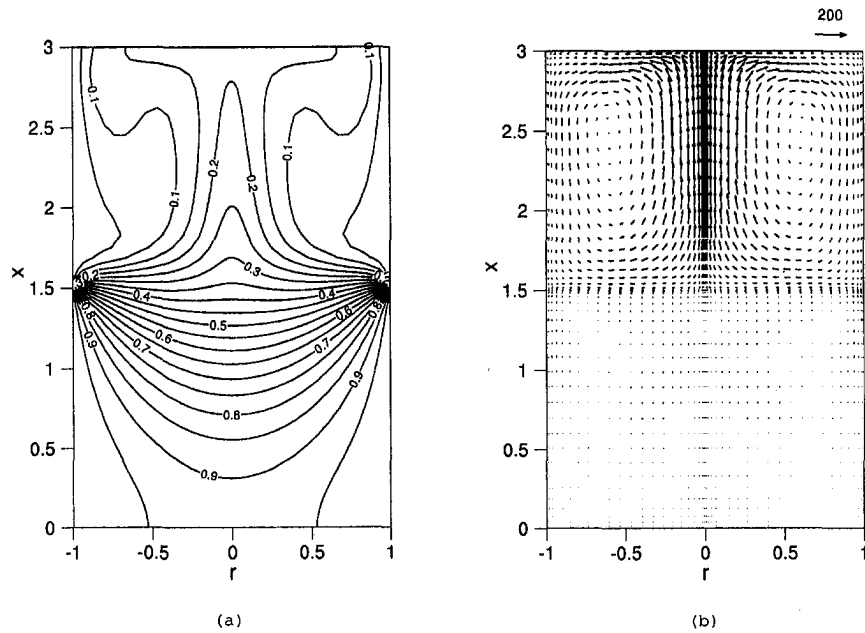


Fig. 6 Temperature distribution (a) and fluid flow (b) in a vertical cross section of the autoclave, $Ar = 3$, $\eta = 0.4$, $Pr = 1$, $Da = 10^{-4}$, and $Gr = 10^5$ ($Gr^* = 10$)

with a reduction in Gr from 10^6 to 10^5 (between Figs. 5 and 6), the convective effects in the fluid layer have become weaker but the flow penetrates easily in the porous layer resulting in a stronger temperature gradient in the fluid region.

Figures 7(a) and 7(b) present the temperature and flow fields for $Gr = 10^5$ and $Gr^* = 10^2$ with all other parameters as in Fig. 6. Again, there exist two recirculating cells. With an increase in the Darcy-modified Grashof number from 10 to 10^2 (Figs. 6 and 7), the flow in the porous layer has become much more stronger because of the increased permeability. The temperature field is modified accordingly and the isotherms in the lower region have become somewhat parallel to the vertical wall rather than normal as in Fig. 6(a). This represents a major shift in temperature field, and the temperature gradient in the central portion of the autoclave is now

much weaker than that near the wall. As shown in Fig. 7(b), the axisymmetric nature of the flow has been destroyed. This can have negative effect on the growth process. Although $Da = 10^{-3}$ may be too high to achieve in a hydrothermal system, this result shows an upper limit on the permeability of the nutrient charge.

The complex effect of the heating and cooling condition in a hydrothermal system also becomes evident at this point. Even though the temperature conditions in Figs. 4(a), 5(a), and 6(a) promote Bénard-type convection in the porous bed (heated bottom and cold top) because of the resulting temperature field, the flow remains symmetric and steady because of the low permeability of the porous media. On the other hand, when the permeability increases, the thermal interaction between the porous bed and fluid layer becomes very complex in the region where the temperature

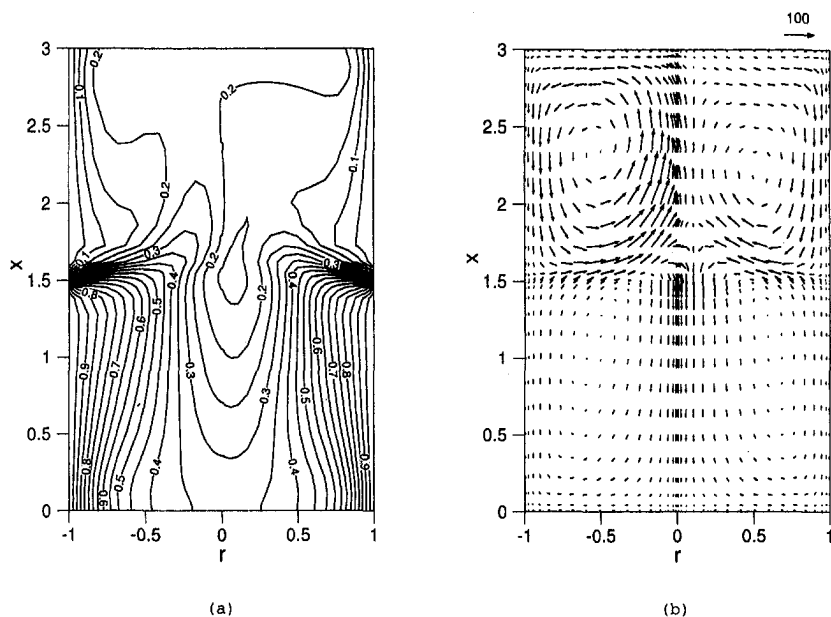


Fig. 7 Temperature distribution (a) and fluid flow (b) for $Ar = 3$, $\eta = 0.5$, $Pr = 1$, $Dr = 10^{-3}$, and $Gr = 10^5$ ($Gr^* = 100$, $\Delta t = 10^{-3}$)

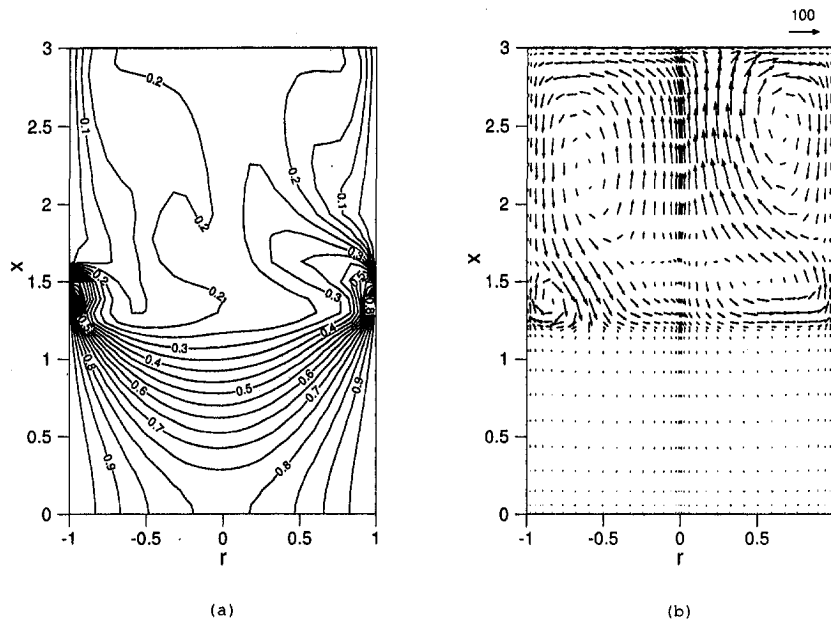


Fig. 8 Temperature distribution (a) and fluid flow (b) in a vertical cross section of the autoclave, $Ar = 3$, $\eta = 0.4$, $Pr = 1$, $Da = 10^{-4}$, and $Gr = 10^5$ ($Gr^* = 10$, $\Delta t = 5 \times 10^{-4}$)

decreases from 1 to 0, promoting stronger convective instability, which destroys the symmetry and two-dimensional nature of the flow and temperature fields. Probably, a much more gradual change in wall temperature is desirable.

Effect of Porous Bed Height on the Flow Pattern. The influence of the height of the porous bed on transport phenomena in a hydrothermal system is investigated next. Since the hydrothermal growth is a very slow process, we can consider it quasi-steady and analyze the flow and temperature fields for given porous bed height assuming steady-state condition. Note that the height of porous bed decreases as the polycrystalline charge dissolves and the solute moves up for deposition on the seed. Evidently the flow and temperature patterns will change with the porous bed height. To examine the effect of decreasing height, keeping all other parameters as in Fig. 6, we have considered a case for $\eta = 0.4$ (Fig. 8). It can be seen that the temperature and flow fields have changed significantly as compared to that in Fig. 6.

A small portion of the hot surface now lies in the fluid region, which promotes a local recirculation at the bottom of the fluid domain because of the increased buoyancy effect in this region. The isotherm pattern is distorted accordingly even though in the central region of the system, the temperature field remains similar to that depicted in Fig. 6. The small cell now acts as a buffer restricting the fluid moving from the porous region to the fluid region. It gains fluid from both of the stronger cells and feeds back to them. When the Grashof number is low, the flow may show an axisymmetric pattern with two strong convective rolls and one weak cell. However as shown in Fig. 8(b), the axisymmetric nature of the flow field is completely destroyed at a higher Grashof number. A convective roll may then appear in the central region directly above the porous bed, and depending on its location the large convective rolls in the fluid region may shift. As can be expected, this does not influence the flow and temperature fields in the porous region in any appreciable manner as long as the Darcy number or permeability is low. From growth considerations, a change in flow pattern in the porous bed will have less impact. However, a major shift in flow characteristics in the fluid region can significantly change the growth dynamics and quality of the crystal. These issues need to be further investigated.

To further elaborate on the effect of changing the porous bed height as the crystal grows, simulations have also been performed

for $\eta = 0.4$, $Gr = 10^5$, and $Gr^* = 10^2$ (Fig. 9). As can be expected, the flow in the porous layer strengthens with an increase in Gr^* . This gives rise to strong distortions in the temperature field (compare Figs. 8(a) and 9(a)). The effect of decreasing height on the flow field can be seen in 9(b). An additional recirculating layer (including porous and part of fluid layers) has clearly emerged near the fluid-porous layer interface. In comparison with Fig. 7, the flow and temperature fields are now very complex because of a small portion (20 percent) of the fluid layer being in direct contact with the heated wall. Not only the axisymmetric nature of the temperature and flow fields is destroyed but they have become quite irregular and strongly three-dimensional. The oscillations have set in, even in the central region. Figure 9(c) shows the flow field in a horizontal plane at $x = 1.5$.

Figure 9(d) shows the temperature fluctuations near the central axis ($r = 0$) at various vertical positions, $x = 0.4 Ar$, $0.6 Ar$, $0.8 Ar$, and Ar . These fluctuations will directly influence the solute transport and its rate of dissolving and separation. As a consequence, the growth rate and crystal quality will be greatly affected. Figure 9(e) shows the oscillation frequency domain of the temperature, a series of temperature at every time step $dt = 5 \times 10^{-4}$ from $t = 0$ to 5 was used for the FFT analysis.

Conclusions

In this paper, a transport model based on the fluid-superposed porous layer theory has been developed to simulate the hydrothermal crystal growth processes. The Darcy-Brinkman-Forchheimer formulation is used to model the flow in the nutrient bed. A three-dimensional algorithm based on curvilinear finite volume scheme is developed and verified by computing the flow and heat transfer in an enclosure consisting of vertical fluid and porous layers. The temperature and flow patterns for varying porous bed height, Darcy number (or permeability of the nutrient charge), and Grashof number are studied to examine the basic transport mechanisms of a hydrothermal system. Although this is a preliminary study and the governing parameters are selected somewhat arbitrarily, the numerical results show interesting features of the flow and heat transfer phenomena that can have direct influence on the solute transport, rates of nutrient dissolving and separation, growth kinetics, and crystal quality.

The basic flow structure consists of a buoyancy-induced recirculatory flow with one cell in the porous region and the other in the

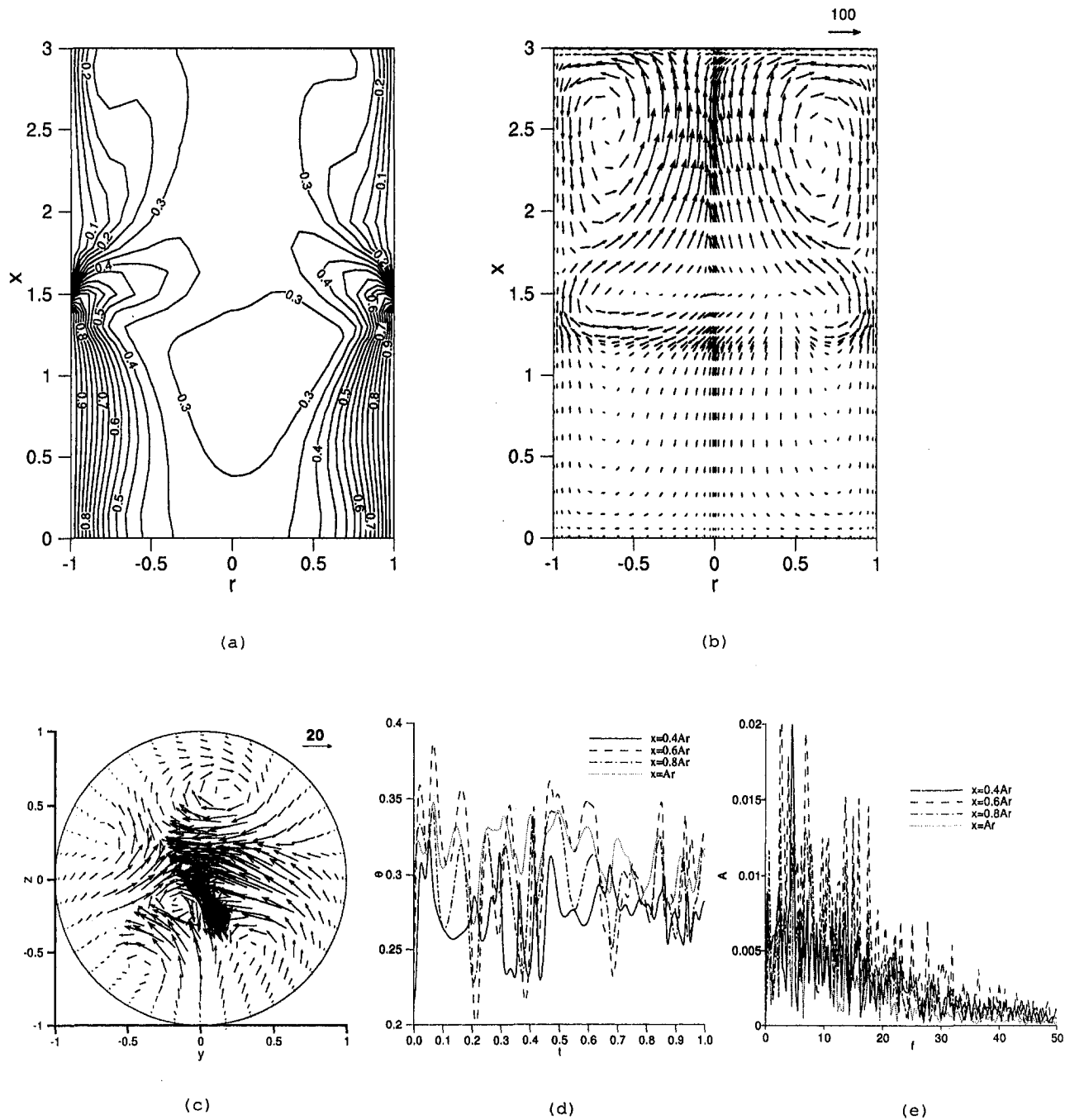


Fig. 9 Thermal and flow fields at $t = 1$ for $Ar = 3$, $\eta = 0.4$, $Pr = 1$, $Da = 10^{-3}$, and $Gr = 10^5$ ($Gr^* = 100$, $\Delta t = 5 \times 10^{-4}$): (a) temperature field; (b) flow field; (c) flow field in horizontal plan at $x = 1.5$; (d) temperature oscillations near the axis $r = 0$ at various vertical positions $x = 0.4 Ar$, $0.6 Ar$, $0.8 Ar$, and Ar ; (e) frequency analysis

fluid region. At low Darcy-modified Grashof number ($Gr \cdot Da$), the flow in the porous region is weak and temperature field is diffusion-dominated, indicating that the mass transfer of nutrient will be controlled by diffusion. Even though it is weak, the convective cell in the porous bed brings the solute to the interface region. The recirculation in the fluid region shows strong vertical flow along the axis and downward flow along the autoclave wall. The flow pattern therefore allows to carry the nutrient to the interface region, and deposit on the crystal seed.

An increase in permeability of the nutrient bed can significantly change the flow and temperature fields in the lower region. A very high permeability enhances the convective instability and destroys the axisymmetric nature of the flow. At high Darcy and/or Grashof number the flow becomes three-

dimensional and produces a layer of convective rolls sandwiched between the large recirculatory flows in the fluid and porous regions. A reduction in the height of the porous bed also complicates the flow structure and temperature field if the portions of the wall that are maintained at higher and lower temperatures are not changed. Again the flow and temperature fields become three-dimensional and oscillatory.

Although the present study has been conducted only for a small range of parameters, it successfully reveals the basic transport mechanism of the hydrothermal synthesis. Further investigations are necessary to examine the effect of other parameters. In particular, the effect of autoclave height and baffle can change the flow patterns and temperature field significantly (Chen et al., 1999).

Acknowledgments

Acknowledgments are due to AFOSR and DARPA for supporting this research through Consortium for Crystal Growth Research. The authors also appreciate the helpful discussions and contributions of A. Anselmo, D. F. Bliss, M. Harris, G. X. Wang, and H. Zhang to this work.

References

- Beckermann, C., Ramadhyani, S., and Viskanta, R., 1987, "Natural Convection Flow and Heat Transfer between a Fluid Layer and a Porous Layer Inside a Rectangular Enclosure," *ASME JOURNAL OF HEAT TRANSFER*, Vol. 109, pp. 363–370.
- Bejan, A., 1984, *Convection Heat Transfer*, John Wiley and Sons, New York, pp. 388–416.
- Byrappa, K., 1994, "Hydrothermal Growth of Crystals," *Handbook of Crystal Growth*, Vol. 2, D. T. J. Hurle, ed., Elsevier Science, pp. 465–562.
- Chatterjee, A., 1998a, "Three Dimensional Adaptive Finite Volume Scheme for Transport Phenomena in Materials Processing: Application to Czochralski Crystal Growth," Ph.D. dissertation, Department of Mechanical Engineering, SUNY at Stony Brook, Stony Brook, NY.
- Chatterjee, A., and Prasad, V., 1998b, "A Three-Dimensional Adaptive Finite Volume Scheme for Transport Phenomena in Phase Change Processes," *Num. Heat Transfer*, under preparation.
- Chen, Q.-S., Prasad, V., and Chatterjee, A., 1998, "Modeling of Fluid Flow and Heat Transfer in a Hydrothermal Crystal Growth System: Use of Fluid-Superposed Porous Layer Theory," *Proceedings of the ASME Heat Transfer Division—1998*, ASME, New York, pp. 119–129.
- Chen, Q.-S., Prasad, V., Chatterjee, A., and Larkin, J., 1999, "A Porous Media-Based Transport Model for Hydrothermal Growth," *J. Crystal Growth*, Vol. 198–199, pp. 710–715.
- Ergun, S., 1952, "Fluid Flow Through Packed Columns," *Chem. Eng. Prog.*, Vol. 48, pp. 89–94.
- James, J. A., and Kell, R. C., 1975, "Crystal Growth from Aqueous Solutions," *Crystal Growth*, B. R. Pamplin, ed., Pergamon Press, London, pp. 557–575.
- Karki, K. C., and Patankar, S. V., 1988, "Calculation Procedure for Viscous Incompressible Flows in Complex Geometries," *Num. Heat Transfer*, Vol. 14, pp. 295–307.
- Larkin, J., Harris, M., and Cormier, J. E., 1993, "Hydrothermal Growth of Bismuth Silicate (BSO)," *J. Crystal Growth*, Vol. 128, pp. 871–875.
- Laudise, R. A., and Nielsen, J. W., 1961, "Hydrothermal Crystal Growth," *Solid State Physics*, Vol. 12, F. Seitz and D. Turnbull, eds., Academic Press, San Diego, pp. 149–222.
- Laudise, R. A., 1970, *The Growth of Single Crystals*, Prentice-Hall, NJ, pp. 275–293.
- Patankar, S. V., 1980, *Numerical Heat Transfer and Fluid Flow*, Hemisphere, Washington, DC.
- Prasad, V., 1991, "Convective Flow Interaction and Heat Transfer Between Fluid and Porous Layers," *Convective Heat and Mass Transfer in Porous Media*, S. Kakaç, et al., eds., Kluwer, Netherlands, pp. 563–615.
- Shternberg, A. A., 1971, "Crystallization Processes in Autoclaves," *Hydrothermal Synthesis of Crystals*, A. N. Lobachev, ed., Consultants Bureau, New York, pp. 25–33.
- Zhang, H., and Moallemi, M. K., 1995, "A Multizone Adaptive Grid Generation Technique for Simulation of Moving and Free Boundary Problems," *Num. Heat Transfer*, Vol. 27, Part B, pp. 255–276.
- Zhang, H., Prasad, V., and Moallemi, M. K., 1996, "Numerical Algorithm Using Multi-Zone Adaptive Grid Generation for Multiphase Transport Processes with Moving and Free Boundaries," *Num. Heat Transfer*, Vol. 29, Part B, pp. 399–421.

G. D. Caplinger
Graduate Research Assistant

W. H. Sutton
Associate Professor
e-mail: sutton@ou.edu
Mem. ASME

R. Spindler
Research Assistant

School of Aerospace and
Mechanical Engineering,
The University of Oklahoma,
865 Asp Avenue, Room 212
Norman, OK 73019

H. Gohlke
Chief Engineer,
Rectorseal, Inc.,
2601 Spenwick Drive,
Houston, TX 77055-1035

Transient Heat Transfer for Layered Ceramic Insulation and Stainless Foil Fire Barriers

Time-varying flame boundaries to heat transfer applications is a common application in energy and safety related systems. Many such systems could be tested and analyzed; however, the number of thermophysical parameters involved and the possibilities of boundary conditions are endless. Many papers have justified numerical and analytical models based on computational efficiency, with the objective of eventually applying those efficient techniques to real problems. There are, however, a number of standard test situations related to such systems that may be readily studied. The purpose of this study is to be able to optimize a coarse numerical model and range of thermophysical parameters that represent the physics of the real problem in a standard test situation. The applied thermal problem involves fire barrier safety in the design of buildings, such as hospitals and schools. Public buildings are often primarily constructed of concrete with significant gaps between sections to allow the concrete to expand and contract, due to climate changes or transients. In seismically active regions of the world, gaps may be up to several meters across, requiring some type of thermal fire barrier designed to prevent a fire from spreading for some time. A radiative/conductive fire barrier is first tested with an ASTM standard fire. A numerical model is then applied, which is an optimally coarse finite difference/finite volume formulation applied to the standard transient conduction energy equation with radiative heat flux (Ozisik, 1973) and to the radiative transfer equation (Su, 1993). The numerical model is able to predict thermal performance of the test system, illustrating the utility of the coarse grid model in engineering applications.

Introduction

One standard test method used for transient temperature of concrete expansion joint fire barriers is specified in *ASTM Standard E 119*, "Standard Methods of Fire Tests of Building Construction and Materials" (1983). The test standard prescribes a fire of given severity and extent, but is written primarily for full, non-loadbearing walls. This standard gives a prescribed minimum ambient (fire side) temperature as a function of time outside the first boundary of the fire barrier. In a slab geometry, a thermal performance criteria is then established at the opposite unexposed boundary of the barrier. The barrier is then rated as satisfying the standard for some stated period of time. Standard prescribes a fire of given severity and extent, but is written primarily for full, non-load bearing walls. The specification is necessary to ensure that the fire-resistive properties of materials and assemblies are measured according to some common standard, and that it can be applied in a variety of cases.

One of the conditions of test acceptance is that the fire barrier not allow passage of the flame or hot gases, sufficient to ignite a cotton sample. A second condition is that the transmission of heat be limited so as not to allow the unexposed barrier surface temperature to be raised more than 139°C (250°F) above its initial temperature. Also, the sample must maintain its structural integrity throughout the experiment. A performance rating is then given as "½-h," "1-h," or "2-h" according to how long, in hours, the sample continues to meet all of the conditions of acceptance.

As in many high-temperature and combustion applications, ceramic fiber insulation is often used, because it can withstand the high temperatures involved in such situations. For structural sup-

port and for radiative shielding, thin layers of foil are placed on the outside of the ceramic fiber blanket and sometimes between layers of insulation. Aluminum foil would work very well for this purpose in terms of reflectivity, but it cannot withstand the high temperatures. Therefore, layers of stainless steel foil are used as a radiative shield. Since the primary modes of heat transfer in high-performance insulations are radiation and convection, the foil layers also serve the purpose of blocking bulk transport (and convection) of hot gases passing through the porous insulation in the barrier.

Once a candidate fire barrier has been proposed, a detailed heat transfer analysis is performed to calculate the transient temperatures within the barrier. In the analysis, one must look at all modes of heat transfer, including conduction, convection, and radiation. Even though the sample can be modeled as a one-dimensional slab, obtaining an analytical solution for even simplified cases is very difficult. Convection, conduction, and radiation are all considered at the outside boundaries, while only conduction and radiation are used within the slab; the boundary exposed to the fire is termed the exposed boundary, while the boundary opposite the fire is termed unexposed. To solve this problem numerically, accurate finite difference representations of transient conduction and radiative heat transfer must be determined. Then, an iteration between the radiation and the conduction at each time-step is converged at each grid location. Once the temperature calculations at one time-step are complete, new solutions are found for the next time-step. These steps are repeated for a specified amount of time. A coarse grid numerical technique (optimized for the minimum grid resolution) is incorporated here to model the conduction and radiation in a one-dimensional slab, built up of successive layers of foil and insulation, in which the variable direction is perpendicular to the plane of the slab boundaries (and the fire).

The ASTM Standard E 119 test setup was used as an experimental validation of the numerical analysis presented here. Although the standard was followed as closely as possible, some of

Contributed by the Heat Transfer Division for publication in the *JOURNAL OF HEAT TRANSFER*. Manuscript received by the Heat Transfer Division, Aug. 5, 1998; revision received, Apr. 20, 1999. Keywords: Conduction, Fire, Heat Transfer, Insulation, Radiation. Associate Technical Editor: P. Menguc.

the test conditions could not exactly match the standard. The actual furnace temperatures, while measured with relatively small uncertainty, could not be controlled exactly according to the standard. Therefore, the furnace temperature was controlled to always be greater than the standard, anywhere from 1 to 168 K (2 to 297 R). This led to a conservative analysis of the fire barrier temperatures, relative to the standard. A second variance is that the standard is based on testing a full wall (cross-sectional area not less than 9 m²); the actual test area exposed to the fire, however, was only 0.36 m², with dimensions 0.6 × 0.6 m. The aspect ratio (sample width to thickness) for the tests was greater than 20 for all tests; this is well within the one-dimensional slab assumption based on prior research (Saboonchi, 1988).

Literature Review

Many investigators have studied combined conduction and radiation heat transfer, especially as it applies to thermal insulation. King (1978) developed a model for the heat transfer through fibrous insulating materials that could be used to estimate the apparent thermal conductivity as well as heat losses and temperature profiles. Barker (1984, 1985) developed a numerical code, based on exact transient and steady-state solutions of the combined conduction and radiation heat transfer for a gray medium, heated by separate external sources; he also presented (1984) an extensive review of the related literature up to that time. His analysis showed that as the conduction to radiation ratio decreased, the medium reached steady state faster. Experimental and analytical results for transient total heat transfer through fiberglass insulation, applied to residential attics, were compared by Rish and Roux (1987). The results showed that the addition of a radiant foil barrier reduced the total heat transfer by up to 42 percent. Su (1993) also calculated the transient heat transfer through an electromagnetic window with varying system parameters. Using constant values for specific heat, thermal conductivity, and density proved to have little effect on the results, compared to temperature-dependent properties.

Since fibrous insulation material properties are affected by the size, distribution, and orientation of the fibers, Tong and Tien (1983) and Tong et al. (1983) performed analytical and experimental studies, respectively, on insulation heat transfer. In the analytical study, the mean fiber radius was found to have a greater effect than the type of size distribution or the chemical composition of the fibers. In the experimental analysis, extinction coefficients, radiant heat fluxes, and total heat fluxes were measured. The results agreed with the analytical study only qualitatively, due to the nongray and nonuniform characteristics of the insulation. Saboonchi et al. (1988) developed a technique for determining the scattering coefficient and mass extinction coefficient of insulation, and Kumar and White (1995) developed a simple model to account for the interaction between

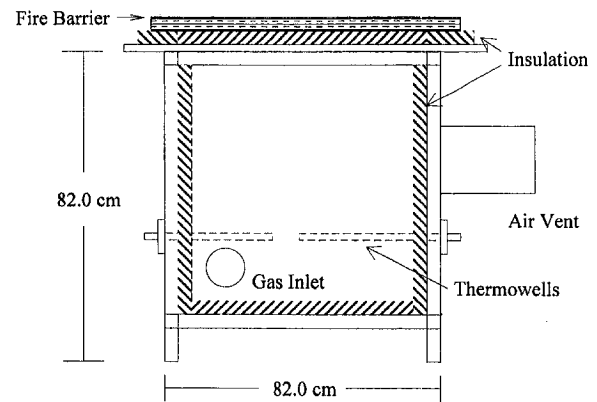


Fig. 1 Experimental setup

scattered radiation for the individual fibers. It was found that as the fiber separation decreased and the absorption index increased, the scattering efficiency increased.

The effects of natural and forced convection on the heat transfer in insulation materials have also been studied. Bankvall (1978) found that as the aspect ratio (height/depth of insulation) was increased, indicating a longer sample, the heat transfer decreased. Silberstein et al. (1991) related various experimental studies to find that the thermal properties of the insulation were not significantly affected by forced convection, except in cases where poor workmanship allowed multiple air entry paths.

The focus of this study is to analyze the combined conduction and radiation heat transfer of a one-dimensional gray medium, modeling an expansion joint fire barrier. A parametric study of time/temperature profiles was made for various thicknesses, numbers of layers, and material properties. For validation, the numerical results were compared with experimental data.

Experimental Apparatus

Experimental measurements of fire barrier temperature were obtained as a basis for validating the numerical results. The experimental apparatus can be divided into three major components. These include the test specimen or the fire barrier, the furnace which served to simulate the standard fire, and the temperature measurement and data acquisition equipment. Figure 1 shows an illustration of the apparatus used in this experiment. The experimental setup was built and tests performed at the University of Oklahoma, Aerospace and Mechanical Engineering, North campus test cell facility.

The test specimen was composed of seven thin layers (0.32 cm ea., uncompressed) of insulation with eight layers of foil placed between the insulation gaps and on the outer boundaries. Thermo-

Nomenclature

A = cross-sectional area of slab
 C_p = specific heat
 Fo = Fourier number
 h_1 = convective heat transfer coefficient at fire boundary
 h_2 = convective heat transfer coefficient at unexposed boundary
 I, I_i = radiative intensity and radiative intensity at node i , with n being the last node
 k = thermal conductivity
 L = slab thickness
 q_{cond} = conductive heat transfer

q^r, q_i^r = radiative heat transfer and radiative heat transfer at node i
 S, S_i = radiative source function
 t = time
 T_{avg} = control volume-averaged nodal temperature
 T_i, T_{O_i} = temperature and temperature from previous time-step at node i
 $T_{\infty 1}, T_{\infty 2}$ = fire temperature and unexposed side ambient temperature
 V = control volume

x = slab position
 α = thermal diffusivity
 β, ω = mass extinction coefficient and scattering albedo
 $\Delta t, \Delta x$ = time-step and control volume length increments
 μ = cosine of the radiative propagation angle, θ
 ρ = density (without subscript)
 ρ_1, ρ_2 = reflectivity at 1st, 2nd, and successive boundaries
 σ = Stefan-Boltzmann constant
 τ = optical thickness

couples were located on the outsides of the insulation, just inside the foil boundaries of layers, and as close as possible to the center (in the area dimension). The insulation material was a ceramic fiber blanket called Durablanket® S, manufactured by Carborundum Company. This material was selected specifically because of its ability to withstand the extreme fire temperatures, low heat capacity, and resistance to thermal shock.

As previously noted, layers of mirror finish, stainless steel foil were used between layers and on the outer boundary to reflect thermal radiation from the fire and to add structural stability to the fire barrier. The thickness of each layer of foil was 0.0076 cm.

The furnace to simulate the fire in a building, as given in *ASTM E 119*, was constructed of standard sheet steel and angle iron, with outer dimensions of 82.0 × 82.0 × 82.0 cm. The four side walls and bottom of the furnace were heavily insulated, leaving inside dimensions of 60.0 × 60.0 × 70.0 cm. A 60.0 × 60.0 cm exposed opening was left at the top, on which the test specimen could be fixed. Steel bars and fire bricks fixed the horizontal sample in place. Care was taken not to compress the insulation within the exposed area opening. In order to avoid secondary heat loss effects, no structural support, other than the foil, supported the sample from the lower (fire) side. However, in avoiding compression of the sample, some minor “bagging” expansion of the insulation may have occurred at higher temperatures. To account for this observed structural behavior, sensitivity calculations on the position of thermocouples in the thickness dimension were made. The associated systematic uncertainties to thermocouple position are estimated and discussed later.

The furnace of the test setup was manually controlled. An inlet on one side was used to pipe natural gas into the system. A blower forced combustion air was forced into the furnace. Combustion products were allowed to escape through a manually position flue vent. The gas was turned on, then a sparking device was used to ignite the flame. The gas was adjusted, manually, to best match the theoretical temperatures. Openings were also left for thermowells, to measure the flame temperature. The thermowells were extended 32.0 and 42.0 cm into the furnace so the flame temperature measurements could be taken at two locations and averaged. The thermowells were made of 1.8-cm diameter standard black steel piping and end caps.

Finally, temperature measurement and data acquisition equipment were used to obtain the temperatures of the oven and the sample. Twenty-gage, type K thermocouples from Omega were located within the thermowells. Data acquisition was done using a standard Dell 386 SX-16 computer, with a Keithley Metrabyte DAS-8 data acquisition card and a Keithley EXP-16 I/O expansion board. The thermocouples within the sample were 30-gage, type K, glass insulated, that were placed inside the sample and on the unexposed surface. In the following section, the uncertainties involved in the experiment and the experimental results will be discussed.

Experimental Results

Since the furnace system was controlled manually, a number of preliminary tests were made to give the proper static gas and air setting used; since this was set for the entire time, only the outlet vent damper was varied slowly in small increments to control the furnace temperature (quicker variation would not be compatible with the response of the thermowells). Thus the temperature of the fire was controlled to stay above that of ASTM Standard E 119 (1983). Since the control in varying the furnace temperature was purposely bounded below by the standard, the actual oven temperature remained from 1 to 168 K above the standard temperature throughout the experiment as shown in the results.

As discussed earlier, vertical thermocouple position in the horizontal unsupported sample was an area of uncertainty. Since 20-gage thermocouples were used for portions of the test, an assumed uncertainty for all measurement locations (even those

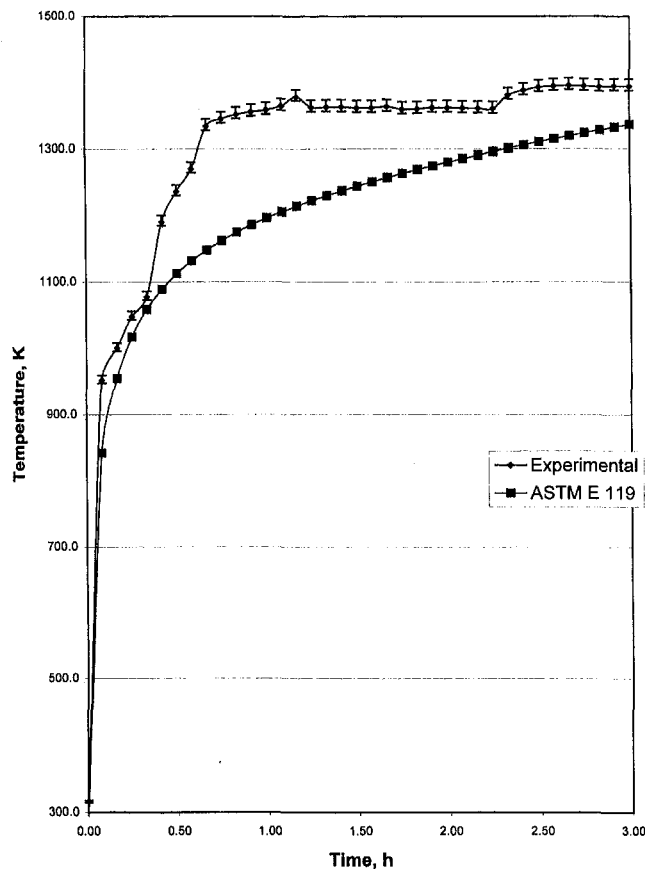


Fig. 2 Comparison of experimental flame temperature versus ASTM flame curve

with 30 gage) was taken as ± 0.089 cm, and sensitivity calculations performed within that range.

Finally, the experiment was performed only once for a given set of conditions with this level of instrumentation. The reported uncertainty therefore notes only the system bias (without random error) of the measurement system relative to fixed ice bath and boiling water standards.

The data acquisition system consisted of a DOS-based PC with a Keithley/Metrabyte DAS-08 A/D converter and a Keithley/Metrabyte EXP-16 MUX board. The EXP-16 was wired to a SMP plug harness by 183 cm of special limits of error, transmission grade, type K thermocouple wire (OMEGA). Individual internal sample measurements were by commercial SMP male terminated, 30-gage, glass insulated, type K thermocouples of the same manufacture, connected to the harness. Figure 2 illustrates the experimental flame temperature compared to the ASTM standard. Error bars on the measured temperature are estimated by linear extrapolation, point by point, based on the water standard noted above. For example, the plotted error bars are for uncertainty estimated to be +11.4 K and -6.1 K on a temperature of 1394.8 K after three hours of heating.

Another uncertainty, not accounted for in the model, was the thermal degradation by partial oxidation of the reflectivity of the outer stainless foil layer during the test. Also, the effective density used in the analysis was most likely too low, because it did not specifically take into account the foil density (although composite system was varied).

Again in Fig. 2, comparison of the experimental flame temperature and the ASTM standard flame curve as a function of time is given. For the first five minutes, the actual flame temperature matched the standard almost exactly, and stayed close for the first 20 minutes. The largest temperature difference occurred after about 40 minutes, with the measured flame temperature staying

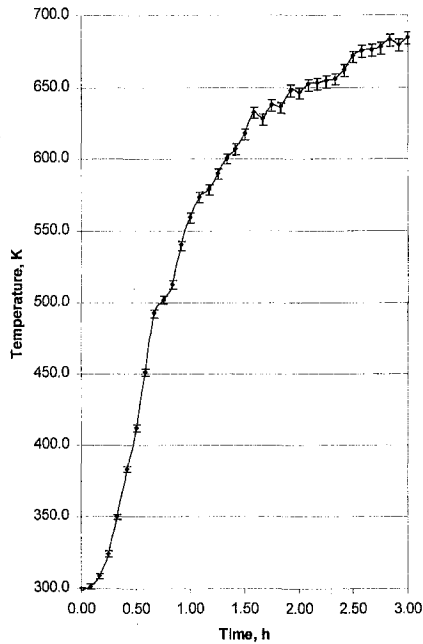


Fig. 3 Experimental temperatures at unexposed boundary, seven layer sample

close to 1350 K for the rest of the time. The temperature difference was 40 K after three hours.

The experimental temperatures at the unexposed boundary are given in Fig. 3. These are the values measured on the outer foil layer of the seven layer fire barrier sample. From the figure there appears to be a 10 to 15-minute time period before the outer boundary temperatures began to rise significantly. For the next 45 minutes, the temperature increase was close to linear, from 320 to 560 K. The temperature increased to 650 K after two hours and 685 K after three. Over the last one-half hour, the temperature increase was somewhat smaller.

Thermal Analysis

In order to determine the heat transmission and temperatures through the sample, a thermal analysis was performed. The ceramic fiber sample was considered a one-dimensional slab medium of thickness L . The one-dimensional assumption was taken since the cross-sectional dimensions were much larger than the thickness (24:1). The slab was assumed to be an isotropic, homogenous, absorbing, emitting, and scattering medium. Thermal, physical, and radiative properties of the materials involved were taken to be constant. Su (1993) showed that there was very little effect in the results of combined radiation and conduction analysis when the properties were allowed to change with temperature. The convective heat transfer coefficient was varied with temperature difference between the surface and the ambient air outside (model taken as a hot plate facing up, or cold plate facing down with $hL/k = c(\text{Gr}_L \text{Pr})^{1/3}$) through the Grashof number.

When using the energy equation and radiative transfer equation it is important that the boundary conditions be properly described. In this case, one boundary was heated by a flame, while the other boundary was exposed to a constant ambient temperature. The boundary nearest the flame will be referred to as the fire side boundary, and the boundary on the opposite side of the flame will be referred to as the unexposed boundary. For the fire side, natural convection, radiation, and conduction from the oven were considered. On the unexposed boundary, radiation, conduction, and convection were again considered. Within the barrier, only conduction and radiation were analyzed. Convection was neglected inside the porous slab since the fiber insulation (and foil layers when used) prevented air inside the barrier from moving freely. The foil layers,

located on both the fire side and unexposed boundaries, as well as between layers, were only considered for their reflective properties. Using a lumped system analysis, according to (Ozisik, 1985, p. 103), it was found that the entire layer of foil would reach 96.4 percent of the fire temperature within 0.01 hours (due to the small thickness). Therefore for the analysis, the foil was assumed to have the temperature of the adjacent insulation.

The energy equation was applied to this problem by dividing the slab into coarse grid multiple control volumes, using a finite difference approximation. For the cases in which only one layer of insulation was used, the thickness was divided into five control volumes and six equally spaced nodal locations. Five volumes was determined to give accuracy within thermocouple tolerances by successively reducing the number of control volume which would reproduce benchmark results with the model (approximately 20) when compared to published exact solutions (Barker). When multiple layers were used, each layer was again divided into five control volumes. Visual illustrations of the thermal energy balance on the fire side boundary, the interior nodes, and the unexposed boundary, from Caplinger (1997), are given in the Appendix, using simplified heat transfer coefficients for free convection on a horizontal plate (hot plate facing up or cold surface facing down, (Ozisik, 1985, p. 437).

The transient conduction energy equation includes conduction and radiation; the development of the analytical form of the equation may be found in Ozisik (1973, Chapter 12). The finite difference model derivation from the analytical statement of the problem used here may be found in Su (1993). Here, we simply state the physical basis of the control volume model. For the flame-side first finite difference volume, a half volume of the slab includes the flame side boundary. The sum of the rate heat transfer coming in from the left and right of the control volume equal the energy storage inside. The rate of heat being added from the left combines the convection and radiation from the fire. The rate of heat being added from the right side includes both internal conduction and radiation (no convection). The rate of energy storage is equal to the sum of these terms. This energy rate balance can be described mathematically as

$$h_1 A (T_{\infty 1} - T_1) + (1 - \rho_1) \sigma A (T_{\infty 1}^4 - T_1^4) + k A \frac{(T_2 - T_1)}{\Delta x} - \frac{(q_1^r + q_2^r)}{2} A = \rho C_p V \frac{(T_{\text{avg}} - T_{o_{\text{avg}}})}{\Delta t} \quad (1)$$

where $V = A \Delta x / 2$, and T and T_o refer to the temperatures at the present and previous time-steps.

To evaluate the energy storage term in this coarse grid, space-averaged temperatures were needed for the present and previous time-steps. This is essential for a coarse grid model. Therefore, the storage term was given as follows:

$$\rho C_p V \frac{(T_{\text{avg}} - T_{o_{\text{avg}}})}{\Delta t} = \rho C_p A \frac{\Delta x}{2} \frac{\left(\frac{3T_1 + T_2}{4} - \frac{3T_{o1} + T_{o2}}{4} \right)}{\Delta t} \quad (2)$$

The radiation term was given by the difference of the fourth powers of the fire temperature and boundary temperature. To use a tridiagonal matrix solver for the temperatures in the energy equation, it was necessary to linearize the radiation term as follows:

$$(T_{\infty 1}^4 - T_1^4) = (T_{o_{\infty 1}}^2 + T_{o_1}^2)(T_{o_{\infty 1}} + T_{o_1})(T_{\infty 1} - T_1) \quad (3)$$

Because of the number of time-steps taken (and resulting small temperature changes) and the successive iteration between radiation and temperature solutions, this linearization has negligible

effect on the results. The tridiagonal solver, however, greatly accelerates the computation speed.

The interior nodal equations are identical, except for the nodal references. The heat being added from the right and left both included conduction and radiation. The energy storage term was similar to that used in the first boundary, and the energy balance is best described by the following equation:

$$kA \frac{(T_{i-1} - T_i)}{\Delta x} + A \frac{(q_{i-1}^r + q_i^r)}{2} + kA \frac{(T_{i+1} - T_i)}{\Delta x} - A \frac{(q_{i+1}^r + q_i^r)}{2} = \rho C_p A \Delta x \frac{(T_i - T_{o_i})}{\Delta t} \quad (4)$$

After the interior and fire side boundary equations have been formulated, the unexposed boundary equation was determined. It was much the same as the fire-side boundary equation, except for the nodal designations and an ambient temperature that remains constant. An equation for the energy balance on the unexposed boundary is given as follows:

$$h_2 A (T_n - T_{\infty 2}) - (1 - \rho_2) \sigma A (T_{\infty 2}^4 - T_n^4) + kA \frac{(T_{n-1} - T_n)}{\Delta x} + \frac{(q_{n-1}^r + q_n^r)}{2} A = \rho C_p V \frac{(T_{\text{avg}} - T_{o_{\text{avg}}})}{\Delta t} \quad (5)$$

where n indicates the last node and T_{avg} was defined in a similar manner to the first boundary.

To calculate the radiative heat transfer values in the energy equation it was necessary to numerically determine the radiative heat transfer at each nodal location. For the radiation analysis a combination of finite difference and a variation of discrete ordinates was used. Radiative intensity was determined from the formulation of the radiative transfer equation, found in Ozisik (1973, Ch. 8), which is given as

$$\mu \frac{\partial I(\tau, \mu)}{\partial \tau} + I(\tau, \mu) = (1 - \omega) I_b[T] + \frac{\omega}{2} \int_{-1}^1 I(\tau, \mu') d\mu' \quad (6)$$

where $I_b[T] = n^2 \sigma T^4 / \pi$ (assuming refractive index $n = 1$), $\omega = \sigma / \beta$, $d\tau = \rho \beta dx$, $\mu = \cos \theta$, and θ is defined as the angle of radiation propagation with respect to the surface normal of the material. The right-hand side of the equation is called the source function $S(\tau)$. Therefore, the radiative transfer equation can be simplified to

$$\mu \frac{\partial I(\tau, \mu)}{\partial \tau} + I(\tau, \mu) = S(\tau) \quad (7)$$

where $\mu > 0$ for radiative intensity from the positive direction relative to planes perpendicular to τ ($\mu = 0$) and $\mu < 0$ for intensity from the negative direction.

The boundary intensities in the insulation are given physically by the effective emitted intensity plus reflected incident intensities from the stainless steel foil into that direction

$$I^+(0, \mu) = (1 - \rho_1) \frac{\sigma T_1^4}{\pi} + \rho_1 I^-(0, -\mu); \quad \mu > 0 \quad (8a)$$

$$I^-(\tau_0, -\mu) = (1 - \rho_2) \frac{\sigma T_n^4}{\pi} + \rho_2 I^+(\tau_0, \mu); \quad \mu > 0 \quad (8b)$$

where τ_0 is the optical thickness of the slab, and $-\mu$ has been used to make all directions $\mu > 0$.

The radiative transfer equation for the insulation was then put in discretized form, and a form of discrete ordinates, found in

Sutton and Kamath (1986), was used to calculate boundary intensities

$$\mu \frac{I_i^+ - I_{i-1}^+}{\Delta \tau} + \frac{I_i^+ + I_{i-1}^+}{2} = \frac{S_i + S_{i-1}}{2}; \quad \mu > 0 \quad (9a)$$

$$-\mu \frac{I_i^- - I_{i+1}^-}{\Delta \tau} + \frac{I_i^- + I_{i+1}^-}{2} = \frac{S_i + S_{i+1}}{2}; \quad \mu > 0. \quad (9b)$$

An initial guess was made for the source term that considers only the emission term

$$S_i = (1 - \omega) \frac{\sigma T_i^4}{\pi} \quad (10)$$

Then, after the intensity for the first iteration was calculated, the in-scattering integral could be evaluated. Both terms for the source function were then used for the following iterations:

$$S_i = (1 - \omega) \frac{\sigma T_i^4}{\pi} + \frac{\omega}{2} \int_{-1}^1 I d\mu \quad (11)$$

Once the intensities had been calculated, the radiative heat transfer could be determined. The radiative heat transfer perpendicular to the plane of the slab was defined as follows:

$$q^r = \int_{\theta=0}^{\pi} \int_{\phi=0}^{2\pi} I \cos \theta \sin \theta d\phi d\theta \quad (12)$$

where $\mu = \cos \theta$ and $-d\mu = \sin \theta d\theta$. This may be resolved in terms of positive and negative intensities as in Ozisik (1973)

$$q_i^r = 2\pi \left[\int_0^1 \mu I_i^+ d\mu - \int_0^1 \mu I_i^- d\mu \right] \quad (13)$$

Sensitivity Analysis and Results

The numerical computations were made for many different cases to determine how changing barrier characteristics and material properties affected the temperature distribution. Comparisons were made to published pure conduction, pure radiation, and combined results in Barker (1984) with agreement within the convergence tolerance. The two most important cases were for varying the thickness of insulation, to try to find an optimum thickness and changing the number of layers of foil between insulation layers. Other material properties that were varied include density, thermal conductivity, and specific heat. The convergence criteria used in the computer code was $\Delta T < 0.01$ (between iterations for conduction and radiation) and $\Delta S < 1.0 \times 10^{-5}$ (between iterations for radiation). The following is a list of default properties used in the numerical code, unless otherwise specified: $\Delta t = 0.01$ h, $\Delta x =$ thickness/number of control volumes, $\beta = 38$ m²/kg, $\tau = 4864$ * thickness, ρ_1 and $\rho_2 = 0.6$, $\rho = 128$ kg/m³, $k = 6.20 \times 10^{-2}$ W/(m °C), and $C_p = 1170$ J/(kg °C). Variations of this code have been used in a number of cases, such as Su (1993) and Barker (1984), in which the results agreed with published data.

The most critical factor that determines the effectiveness of a fire barrier is the thickness of insulation. In Fig. 4, a single-layer sample with foil only on the outer boundaries was examined. All of the material properties were held constant while the material thickness was varied from 0.318 to 5.08 cm by multiples of two. As expected, when the thickness was increased, the temperatures for the entire three-hour time period decreased. For the thinner material cases, the curves were not as steep over the first 1.5 hours, but then become close to parallel. One important fact from these curves is that as the insulation thickness was doubled, the benefits of decreased temperature became additive rather than doubling.

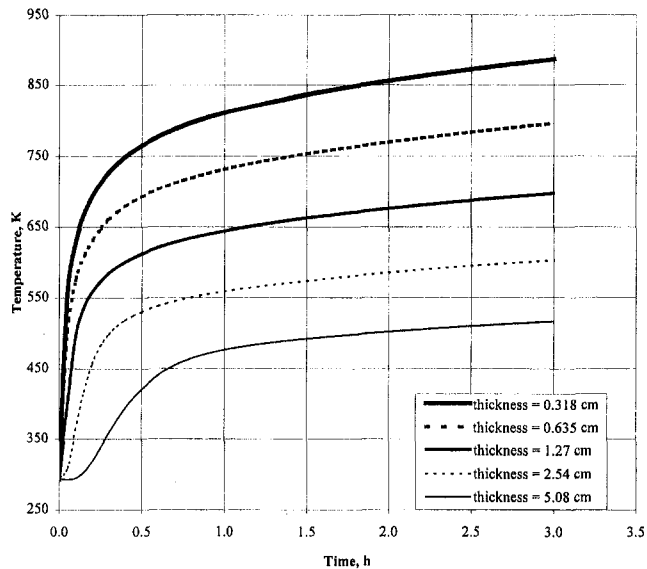


Fig. 4 Unexposed boundary temperatures for varying insulation thickness

The second factor examined was the number of foil layers between insulation layers. It is important to know how many layers of foil are necessary to provide the greatest benefit in blocking the thermal radiation. For this case, each sample was taken to be 2.54-cm thick with foil located on the outer boundaries in every case. The material properties were held constant and the sample was divided in halves, twice; giving one, two, and four-layer samples, with foil between each. Figure 5 shows the temperature distribution, in these cases, for the unexposed boundary. The difference between the two and four-layer cases was nearly indistinguishable, while the one-layer cases varied less than 5 K. The profiles show that the multiple foil layer cases did not perform much better than the single-layer case, indicating the need for foil only on the boundaries. Additional foil layers are only necessary if the outer layer were to break down over time or to physically preserve the model conditions (no convective flow through and dimensional stability).

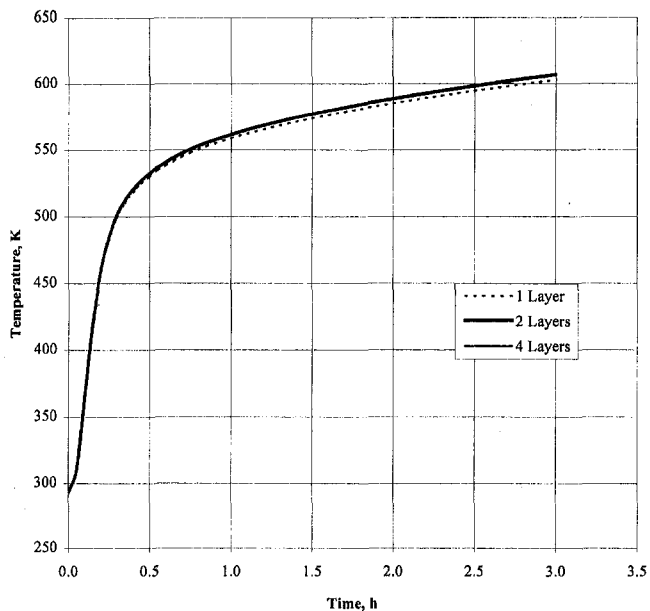


Fig. 5 Unexposed boundary temperatures for 2.54 cm sample

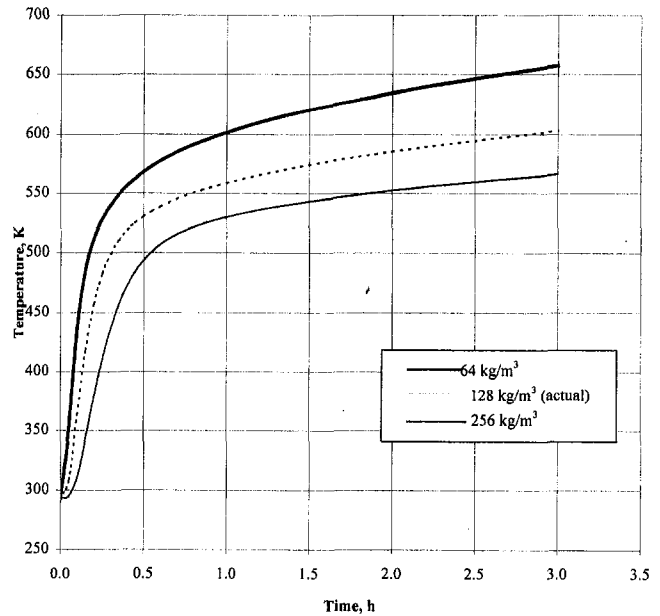


Fig. 6 Transient temperature chart for various densities

The next series of figures shows the effects of changing material properties while maintaining a constant thickness and number of layers. Three charts are given for variations in effective density, thermal conductivity, and specific heat, respectively, for a 2.54-cm thick slab with only one layer of insulation. These results track trends of the pure conduction case, except for density; this is due to the fact that density also changes the optical thickness for the radiation in a nonlinear fashion. Figure 6 shows temperature profiles for a three-hour time period with densities of 64, 128, and 256 kg/m³. The most significant trend evident in these curves is that as the density increased, the slope of the curve decreased. After 3.0 hours, the temperature of the 256 kg/m³ case was 35 K less than the 128 kg/m³ case and 85 K less than the 64 kg/m³ case. As density was increased, the heat transmission was less and it reached steady state earlier. The transient temperatures for thermal conductivities of 4.04×10^{-2} , 6.20×10^{-2} , and 8.36×10^{-2} W/(m K) are given in Fig. 7. From these curves it was determined that as thermal conductivity increased, the temperatures for the entire time period increased. As expected, higher thermal conductivity allowed more heat to pass through the barrier. In Fig. 8, temperature curves are given for three different specific heat values of 1.17, 2.01, and 2.85 kJ/(kg K). Specific heat appears to play a role only for the initial times. As it was increased, the heat transmission over the first hour was slower.

It was necessary to compare the numerical results with those obtained experimentally to determine a correlation. Since the experimental case contained seven layers of insulation separated by foil, this was used in the numerical computation. The material properties were optimized over a limited range to find the best fit to the experimental time-temperature curve. The optimization was done systematically, by holding two of the thermal properties constant and finding the best match for the other property. This was done until the best match was found for all three properties. The property values that brought about the best match to the experimental results were: density = 256 kg/m³, thermal conductivity = 7.93×10^{-2} W/(m K), and specific heat = 2.93×10^3 J/(kg K). The temperature position was offset by 0.089 cm inside the boundary to account for possible thermocouple position uncertainty that might be due to vertical "bagging" of the unsupported horizontal sample or due to the finite size of the thermocouple wire junction (single AWG 30 wire is 0.0254 cm in diameter).

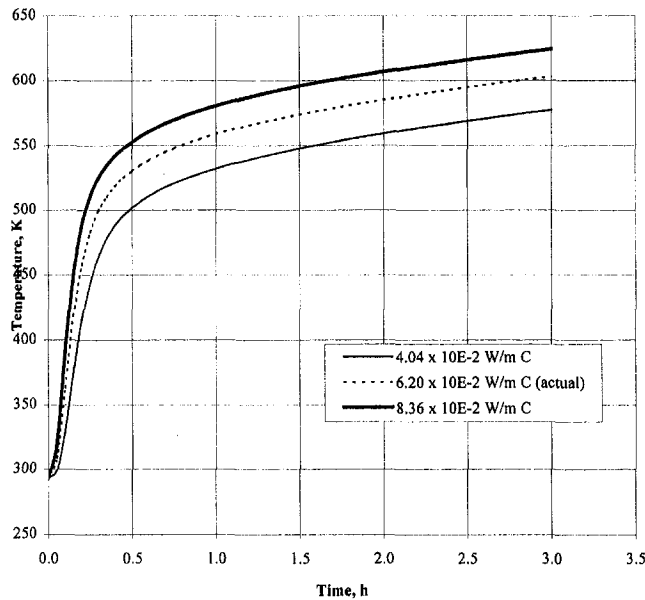


Fig. 7 Transient temperatures for various thermal conductivities

The plot of the experimental and computed temperature profiles at the unexposed boundary is given in Fig. 9. The experimental flame temperature curve (Fig. 2) was used as input data to the numerical model. The figure shows that for the first 1.5 hours the numerical solution matched the experimental data very closely, overestimating the temperatures from 2–50 K. The curves then cross, and for the next 1.5 hours the temperatures were underestimated. After 3.0 hours, the temperature difference was 27 K. The numerical solution came to a steadier upward trend faster than the measured temperatures. Note that as in many heavily insulated systems, with active heat rate addition, no steady state is achieved; the process ultimately would end in destruction of the sample.

The better experimental fit by increased density can be explained by the fact that the foil was not explicitly taken into account in the conduction energy equation. Including the foil would increase the effective density and thermal conductivity of the composite system. The conductivity was increased slightly to

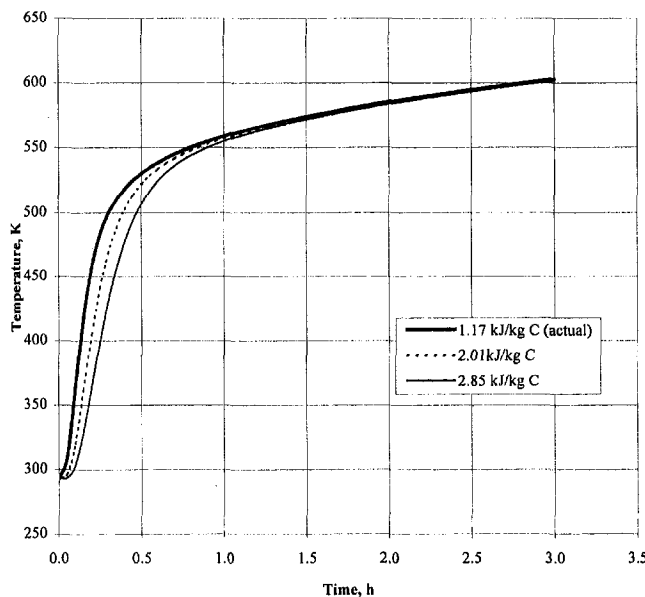


Fig. 8 Transient temperature chart for various specific heats

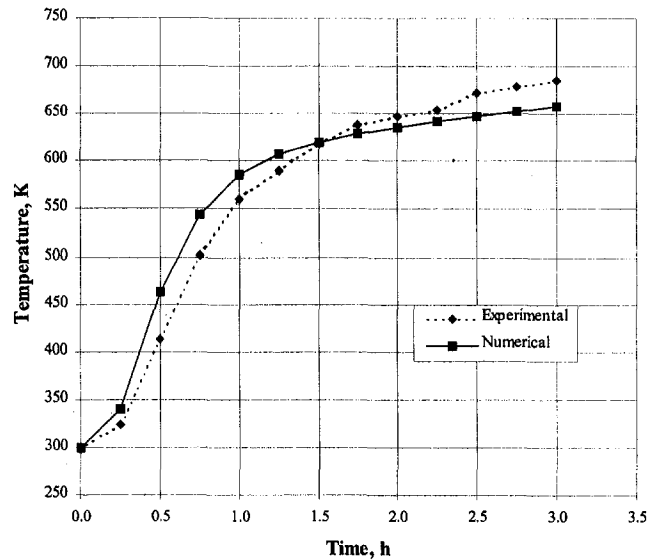


Fig. 9 Experimental versus best numerical approximate unexposed boundary temperatures

match the test data. Since there was such a large range of temperatures estimating a constant specific heat was difficult. The specific heat had to be increased significantly, which could also be due to a low mean temperature value, initial moisture in the sample, or transient response of the furnace walls.

Conclusions

In this study, transient thermal analysis was studied relative to an experiment for foil and insulation fire. The transient temperature profile of *ASTM E 119-1983* was used as a basis for the experiment and validation of the numerical code. The experimental fire barrier was composed of seven layers of ceramic fiber insulation material, with layers of stainless steel foil placed between each layer and at the outer boundaries. Interior sample and unexposed boundary temperature measurements were made in five-minute intervals (to match the standard) for a period of three hours at two locations within the furnace and on the outer boundary of the test sample. The furnace temperatures were found to be consistently higher than the standard curve, which was necessary for a conservative analysis. A numerical model was developed based on the transient conduction energy equation for the fire barrier. The one-dimensional slab was divided into six nodes per layer of insulation (including the boundaries), and temperatures were calculated for varying conditions over a three hour period, according to the standard ASTM fire. From these calculations, it was found that as the insulation thickness was doubled, there was an additive (but diminishing) benefit of decreased boundary temperatures. When the number of foil layers was varied, there was very little difference in the calculated temperature profiles. In order to get the best match of numerical to experimental values, the density, thermal conductivity, and specific heat were all increased.

With the small changes noted above (foil not being considered in the effective density, the use of constant properties, and other factors) the numerical model agreed well in predicting the experimental trend in temperature through a three-hour test of a real fire barrier.

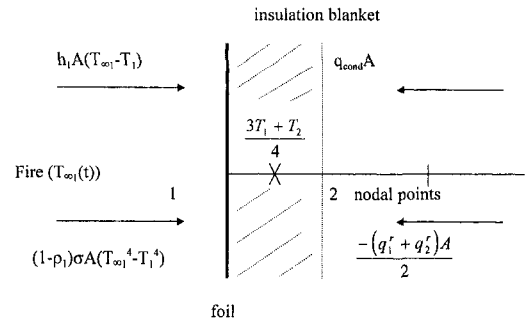
Acknowledgment

This work was sponsored in part by U.S. Department of Energy under contract DE-FG36-95GO101112.

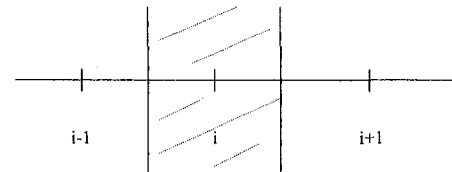
References

- ASTM Designation: E 119-83, 1983, "Standard Methods of Fire Tests of Building Construction and Materials," American Society for Testing and Materials, Philadelphia, PA.
- Bankvall, C. G., 1978, "Natural Convective Heat Transfer in Permeable Insulation," *Thermal Transmission Measurements of Insulation*, ASTM STP 660, American Society for Testing and Materials, Philadelphia, PA, pp. 73-81.
- Barker, C., 1984, "The Combined Radiation and Conduction Heat Transfer in a Participating Medium with Semitransparent Boundaries," M.S. thesis, University of Oklahoma, Norman, OK.
- Barker, C., and Sutton, W. H., 1985, "The Transient Radiation and Conduction Heat Transfer in a Gray Participating Medium with Semi-Transparent Boundaries," *Radiation Heat Transfer*, B. F. Arnaly and A. F. Emery, eds., HTD-Vol. 49, ASME, New York.
- Caplinger, G. D., 1997, "Stainless Foil and Ceramic Insulation Fire Barrier Analysis and Design," M.S. thesis, University of Oklahoma, Norman, OK.
- King, C. R., 1978, "Fibrous Insulation Heat-Transfer Model," *Thermal Transmission Measurements of Insulation*, ASTM STP 660, American Society for Testing and Materials, Philadelphia, PA, pp. 281-292.
- Kumar, K., and White, S. M., 1995, "Dependent Scattering Properties of Woven Fibrous Insulations for Normal Incidence," *ASME JOURNAL OF HEAT TRANSFER*, Vol. 117, pp. 160-166.
- Ozisik, M. N., 1985, *Heat Transfer: A Basic Approach*, McGraw-Hill, New York.
- Ozisik, M. N., 1973, *Radiative Transfer, and Interactions with Conduction and Convection*, Wiley-Interscience, New York.
- Rish, J. W., III, and Roux, J. A., 1987, "Heat Transfer Analysis of Fiberglass Insulations With and Without Foil Radiant Barriers," *Journal of Thermophysics and Heat Transfer*, Vol. 1, No. 1, pp. 43-49.
- Saboonchi, A., Sutton, W. H., and Love, T. J., 1988, "Direct Determination of Gray Participating Thermal Radiation Properties of Insulating Materials," *Journal of Thermophysics and Heat Transfer*, Vol. 2, No. 2, pp. 97-103.
- Silberstein, A., Arquis, E., and McCaa, D. J., 1991, "Forced Convection Effects in Fibrous Thermal Insulation," *Insulation Materials: Testing and Applications*, ASTM STP 1116, American Society for Testing and Materials, Philadelphia, PA, pp. 292-309.
- Su, M. H., 1993, "High Temperature Heat Transfer in Semitransparent Materials," Ph.D. dissertation, University of Oklahoma, Norman, OK.
- Sutton, W. H., and Kamath, R., 1986, "Participating Radiative Heat Transfer in a Three Dimensional Rectangular Medium with Layered Properties," Joint AIAA/ASME Thermophysics and Heat Transfer Conference, 86-HT-25.
- Tong, T. W., and Tien, C. L., 1983, "Radiative Heat Transfer in Fibrous Insulations—Part I: Analytical Study," *ASME JOURNAL OF HEAT TRANSFER*, Vol. 105, pp. 70-75.
- Tong, T. W., Yang, Q. S., and Tien, C. L., 1983, "Radiative Heat Transfer in Fibrous Insulations—Part II: Experimental Study," *ASME JOURNAL OF HEAT TRANSFER*, Vol. 105, pp. 76-81.

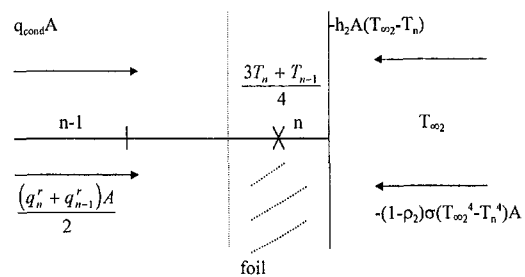
APPENDIX



Fire side boundary thermal energy balance



Interior nodal designations



Unexposed boundary energy balance

This section contains shorter technical papers. These shorter papers will be subjected to the same review process as that for full papers.

Hysteresis of Thermochromic Liquid Crystal Temperature Measurement Based on Hue

J. W. Baughn,^{1,4} M. R. Anderson,^{3,4}
J. E. Mayhew,^{2,5} and J. D. Wolf^{3,4}

Nomenclature

Bi = Biot number for copper plate ($h_c Lc/k$)
 H = hue matrix, Eqs. (1) or (2)
 h_c = heat transfer coefficient from copper plate
 k = thermal conductivity of copper plate
 Lc = thickness of copper plate

R , G , B = matrices of red, green, and blue components, respectively

S_h = standard deviation in hue
 S_T = precision limit in temperature
 SEE = standard error of estimate
 U_T = uncertainty in temperature
 ΔT = bandwidth of useful temperature range

Introduction

This paper presents detailed hue-temperature calibration data for a microencapsulated thermochromic liquid crystal (TLC) with a useful range of 26–31°C. A significant hysteresis is observed in the hue-calibration data (i.e., the data during cooling is different than that during heating). If heated to 55°C, the temperature for a particular hue during cooling may differ by as much as 1°C (20 percent of the useful range) from the heating value; however, if the temperature never exceeds 35°C the hysteresis is less than 0.1°C.

For more than two decades TLC's have proven to be a powerful tool for the investigation of convective heat transfer (e.g., see Cooper, 1975). When coated on a surface (usually in the form of

microcapsules) their reflected color can be calibrated to determine the surface temperature distribution. The first author was introduced to TLC's by the team under Prof. Terry Jones at Oxford University (e.g., see Jones and Ireland, 1985) more than a decade ago and collaborated with them on both transient and heated-coating methods (Baughn et al., 1989). This early work was done using a narrow-band TLC to measure a single isotherm on a surface (using yellow, which is an easy color to identify). Since then, we have used narrow-band TLC's extensively at UC Davis and at the USAF Academy (Baughn, 1994).

Many investigators have contributed to the development and application of TLC's for the study of heat transfer, and space does not allow adequate recognition of these investigators and their contributions. Some who have been particularly influential in studies which lead up to the present study include (in alphabetical order): Professor Camci and student Kim at Pennsylvania State University (e.g., Camci et al., 1992), Hippensteele and Poinsette at NASA Lewis Research Center (e.g., Hippensteele et al., 1983), Professor Hollingsworth and his students at the University of Houston (e.g., Hay and Hollingsworth, 1996), Professor Jones and his students at Oxford University including Ireland and Wang (e.g., Jones and Ireland, 1985; Wang et al., 1995), Professors Moffat and Eaton and their students at Stanford University including Simonich and Farina (e.g., Simonich and Moffat, 1985; Farina et al., 1993), and Professor Owen at the University of Bath (e.g., Wilson et al., 1993).

Recent work with TLC's has concentrated on methods for using broadband TLC's to determine multiple isotherms. These methods take advantage of the fact that the reflectivity of a TLC has a dominant peak, which occurs at a wavelength that varies with temperature. In one early study (Zharkova, 1980) the peak wavelength at one location was identified using a spectrometer to measure the spectral intensity of the scattered light from the TLC. Another method involves using a set of sharp band-pass optical filters, one for each peak wavelength and corresponding isotherm (Akino et al., 1989; Rau 1998). This method provides one isotherm for each filter. Akino (1989) used 18 interferential filters.

Currently the most common method for converting the TLC color (peak wavelength) into temperature is to use a hue technique (Camci et al., 1992). With this technique an image of a surface is captured (typically in 24-bit color) and image processing is used to convert the color into a hue-saturation-value domain. The hue is calibrated against temperature. Camci et al. (1992) do an initial investigation of the nature of this calibration curve including the effects of light source distance, effect of illumination angle, uniformity, and repeatability. Further investigations of hue-temperature calibrations were done by Farina et al. (1993) and by Hay and Hollingsworth (1996). Farina et al. (1993) suggest an on-axis lighting/viewing system with crossed-polarizers to eliminate the need for in-situ calibration. Hay and Hollingsworth (1996) do calibrations of three different TLC's using three different hue

¹ Professor. e-mail: jwbaughn@ucdavis.edu. Fellow ASME.

² Assistant Professor.

³ Graduate Student.

⁴ Department of Mechanical and Aeronautical Engineering, University of California, One Shields Avenue, Davis, CA 95616.

⁵ Department of Aeronautics, United States Air Force Academy, CO 80840.

Contributed by the Heat Transfer Division for publication in the JOURNAL OF HEAT TRANSFER. Manuscript received by the Heat Transfer Division, Nov. 1, 1998; revision received, June 15, 1999. Keywords: Heat Transfer, Image Processing, Instrumentation, Measurement Techniques, Temperature. Associate Technical Editor: D. Majumdar.

from the plate normal. Because the authors noted some variations in the light output during the first four to five minutes of operation, the light is allowed to warm up and reach steady state for five minutes prior to the start of data collection. The light remains on for the duration of a calibration run.

A thermistor was inserted 38 mm into the side of the plate (near the center of the plate). The hole was filled with silicone heat sink compound to aid in thermal contact between the thermistor and the copper. In this arrangement, the time constant was measured to be approximately 0.8 s. The thermistor was calibrated against a platinum resistance thermometer in the temperature range of the measurements (i.e., 20–60°C). The resistance is measured with a HP 3455A DVM driven by Labview. During a run, the temperature is read simultaneously with the capture of each digital image of the TLC coated surface. The thermistor/voltmeter combination provides a resolution in temperature measurement of 0.001°C.

A typical heating run begins with the plate at approximately 23°C and heated at a maximum rate of 0.005°C/sec. This ensures that the copper plate and thermistor remain within 0.01°C of each other. Images are captured at 0.2°C to 0.5°C intervals with the CCD camera and framegrabber. When the copper plate has been heated to the end of the useful color-play range, the variac is either turned off (to cool from 35°C) or output is increased to heat the plate to 45°C or 55°C in preparation for cool down runs from higher initial temperatures. During cooling, cool air is used on the backside of the plate to assist in bringing the plate down to the useful temperature range for data collection. Upon reaching 32°C, the rate of change of temperature is slowed to no more than 0.005°C/sec and data are collected down through 23°C.

Great care was taken to ensure that temperature variations, both across the plate and between the plate and the temperature sensor, were small. The transient response of the copper block, which had a Biot number of approximately 0.0063, was investigated. If the rate of change of plate temperature was kept below 0.005°C/sec, then the maximum difference in plate temperature between the top surface and bottom surface would be less than 0.01°C. The temperature sensors are located midway between the top and bottom of the plate and, therefore, the temperature difference between the liquid crystal surface and temperature sensor is less than 0.005°C. Plate uniformity was tested by using three different temperature sensors (two thermistors, and one PRT) located at three approximately equidistant points around the plate. Each sensor was coated with silicone heat sink compound and embedded approximately 40 mm into the plate. During a heating run at 0.005°C/sec, temperatures from the three sensors were recorded, yielding temperatures within 0.01°C of one another. Subsequent testing, therefore, required only a single thermistor for temperature measurement. With a time constant of 0.8 seconds the thermistor lag was approximately 0.004°C.

Image Capture

Positioned directly over the copper plate is a three-chip Sony XC003 CCD camera, which is connected to a Matrox Meteor RGB framegrabber card installed in a Micron 166 MHz PC with 128 MB of RAM. Each image is captured as a three-dimensional matrix of red, green, and blue values. The image size is 480 × 640 pixels, thus the matrix is 480 × 640 × 3 (approximately 0.9 MB).

A Macbeth ColorChecker color rendition chart was used to adjust the balance of the color rendition system used in these experiments. To perform this adjustment, several of the ColorChecker's gray squares were captured using the default settings on the RGB camera. Then, the red and blue gains were adjusted (green cannot be adjusted) so that the red and blue components (averaged) for each square were equal to the respective green component for each square (any true gray has equal amounts of *R*, *G*, and *B*). These settings, Red -22, Blue +26, were used throughout all test runs. The same light was also used for all measurements. Finally the overall gain of the camera was adjusted to produce peak *R*, *G*, or *B* values near 200 (255 is maximum for

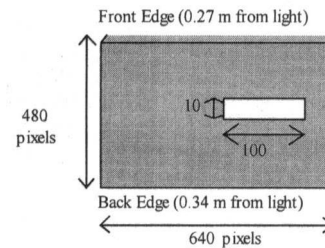


Fig. 2 Area of Interest

eight bits). This gain setting (+06) was also kept the same for all test runs.

Image Processing

Image processing was done using MATLAB 5.1 and its Image Processing Toolbox. Image processing begins with a captured image for the entire copper plate which is 480 × 640 pixels. Although the design of the apparatus produces a very uniform temperature throughout the copper plate the light angle and intensity vary slightly across the plate. Furthermore, the airbrushed TLC is not completely uniform across the plate. In order to eliminate these effects a small section on the plate was selected for processing (see Fig. 2).

The section used is a rectangular area of 10 × 100 pixels (providing a large population size of 1000 pixels), and is the same for all data presented here. This region was selected with the long edge parallel to the light source to minimize angle effects and to achieve relatively uniform illumination intensity throughout the region.

The data from the section is first processed using a 5 × 5 median filter (Medfilt2 in MATLAB) on each of the *R*, *G*, and *B* image components separately. This median filter replaces the value of *R*, *G*, and *B* in each pixel with the median of the values within the surrounding block. The resulting RGB image is then converted to a hue, saturation, and value (HSV) three-dimensional matrix. The hue, saturation, and value are then averaged over the 10 × 100-pixel area. Note that it is possible to do the median filter on the hue matrix instead of the *R*, *G*, and *B* matrices separately, but this requires care due to the discontinuity in hue values between 0 and 1.

Experimental Results and Discussion

Calibrations were performed on the liquid crystals by both heating them from below the useful color-play range and cooling them from above the useful color-play range.

Heating Results. Figure 3 shows the individual components of red, green, and blue versus temperature for three separate heating runs, all starting below the useful color-play range. Each data point is an area average (see Fig. 2) after using a 5 × 5 median filter. This shows that the heating data is highly repeatable. The fact that the bottom of each curve does not go to zero is due to the background reflection of the surface. Although not shown on these graphs, the blue component peaks at about 35°C and drops off to the background level at approximately 49°C.

Figure 4 shows the hue-temperature calibration curve for these three heating runs. The hues are determined in this figure by using a 5 × 5 median filter on the RGB data, calculating the hue matrix (using Eq. (2)), and then determining the mean value for the 1000 pixels. Figure 4 also shows the excellent repeatability of the hue versus temperature curves over the useful calibration range of 26°C to 31°C. It appears that when heating liquid crystals from below the start of their useful color-play temperature range, highly repeatable calibration data can be obtained. This figure has a fifth-order polynomial regression curve of the heating data along

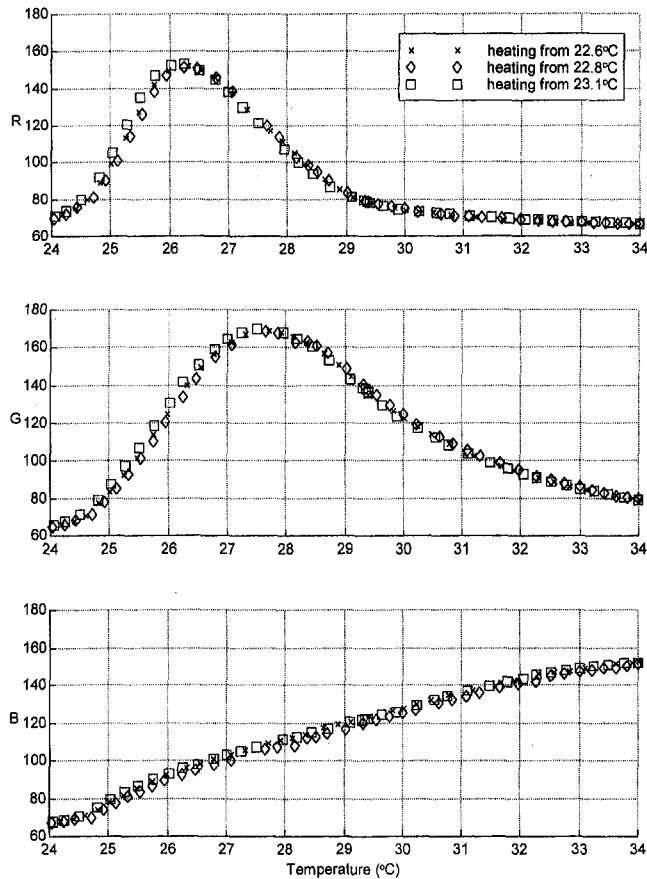


Fig. 3 RGB components of images from three different heating runs

with ± 2 SEE (standard error of estimate) bands superimposed (the SEE is 0.075°C).

Uncertainty. The uncertainty in the temperature using a hue calibration of this TLC can be determined by following the approach of Hay and Hollingsworth (1996). They suggest determining the uncertainty in temperature using a root-sum-square of the SEE for the calibration curve and the precision error associated with the standard deviation of the hue from pixel to pixel. Using a coverage factor of 2 (to provide a standard 95 percent confidence level) the uncertainty in temperature is given by

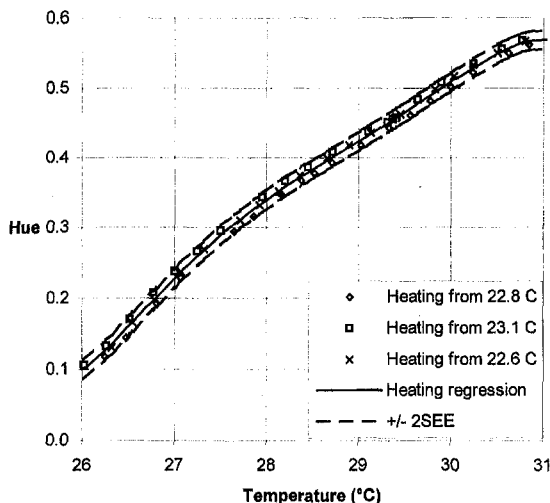


Fig. 4 Hue-temperature calibration with regression curve for three heating runs showing SEE

Table 1 Uncertainty summary for various regressions using 5×5 median filter

number of data points used in regressions	SEE ($^\circ\text{C}$)	S_T ($^\circ\text{C}$)	U_T ($^\circ\text{C}$)	$U_T/\Delta T$ (%)
58 heating	.075	.054	.19	3.7
58 heating and 23 cooling from 35°C	.082	"	.20	3.9
58 heating and 41 cooling from 45°C	.13	"	.28	5.7
58 heating and 37 cooling from 55°C	.48	"	.96	19

$$U_T = 2 \times (\text{SEE}^2 + S_T^2)^{1/2} \quad (5)$$

where the precision limit is determined by

$$S_T = S_h \times \frac{\partial T}{\partial h} \quad (6)$$

This method of calculating the uncertainty is not entirely rigorous since the SEE is the result of a regression and not necessarily a bias or precision error (Coleman and Steele, 1989; Coleman and Steele, 1995). However, if we view the source of the SEE as one elemental precision error and the pixel to pixel standard deviation as another elemental precision error, the root-sum-square should be a first approximation of the combined uncertainty. In the limit of one term (SEE or S_T) being much larger than the other the uncertainty given by Eq. (5) approaches either $2 \times \text{SEE}$ or $2 \times S_T$. The first limit suggests that $\pm 2 \times \text{SEE}$ is a 95 percent "confidence interval." Schenck (1979) proposes this viewpoint. However, Coleman and Steele (1989) point out that "this can be considered reasonable only for a case in which the bias contribution to the uncertainty is negligible." If the calibration curve is going to be used with an in-situ calibration (i.e., same lighting, camera, etc.) this is a valid viewpoint.

The bias error is already embodied in S_h and SEE. We are using eight-bit resolution for each of the R , G , and B components. The digital bias error in R , G , and B is $\frac{1}{2}$ part in 255.

Using the standard deviation in hue and the sensitivity coefficients from the fifth-order polynomial regression, the precision limit for the temperature due to the pixel to pixel variation in hue is calculated.

The uncertainty in temperature can now be found by combining this precision limit with the regression SEE using Eq. (5). The SEE for the heating data regression (shown in row 1 of Table 1) is 0.075°C . The average S_T is approximately 0.054°C . This results in an overall uncertainty of 0.186°C , which is 3.7 percent of the useful range of 5°C . This is approximately half the uncertainty that has been previously reported (Hay and Hollingsworth, 1996). This improvement is largely a consequence of using a median filter on the RGB data before calculating the hue.

Cooling (Hysteresis) Results. Figure 5 shows the red, green, and blue components versus temperature for liquid crystals when cooled from approximately 35, 45, and 55°C . A representative heating curve for each of the components is superimposed to show the differences in heating versus cooling (see Fig. 3). The values of the red, green, and blue components clearly decrease as the peak temperature prior to cooling increases (the incident light levels were the same). The blue component is relatively unchanged when cooled from the lower temperatures of 35°C and 45°C but shows a significant effect when cooling from 55°C . There also appears to be a variation in the temperature at which the peak values in R and G occur. As the crystals are cooled from higher temperatures, the peak initially shifts to a higher temperature. For higher initial heating temperatures it seems to shift back to lower temperatures.

The corresponding hue calibration for the cooling data is shown in Fig. 6. Again, a representative heating curve (from Fig. 4) is

superimposed to show the differences in heating versus cooling. The hysteresis in hue when cooled from temperatures above the color-play is clear. The most noticeable hysteresis is observed after heating to 55°C, which results in a temperature offset of up to 1.0°C. Cooling from 45°C and 35°C also show signs of hysteresis, although not as significant. Changing heating and cooling direction within the useful color-play temperature range did not show any significant hysteresis effect. This was established by reversing direction near the middle of the useful temperature range and is also evident in the cooling from 35°C (see Fig. 6). It is not known whether or not there is a rate dependence since the present measurements were all done relatively slowly to ensure uniform temperature and to minimize thermal lag.

The effect of the hysteresis on the uncertainty in temperature can be calculated by using a common regression for both the heating and cooling data. Table 1 shows the SEE for single curve regressions using various combinations of heating and cooling data. This, of course, is what one would do if unaware of the hysteresis. If aware of the hysteresis it would be far better to use separate regressions for heating and cooling. The S_T for each image remains approximately the same for both heating and cooling data. The uncertainty, U_T , is calculated using Eq. (5), and is summarized in Table 1 as well. $U_T/\Delta T$ represents the overall uncertainty over the useful range, $\Delta T = 5^\circ\text{C}$.

From Table 1 we see that if the cooling occurs from 35°C (just above the useful color-play) the effect on the SEE of a common heating and cooling curve is small as is the effect on uncertainty. However, when cooling data from 45°C is included the uncertainty increases to 5.7 percent. When data from 55°C is included the uncertainty increases to 19 percent. The actual SEE's and uncertainties will depend on how many data points

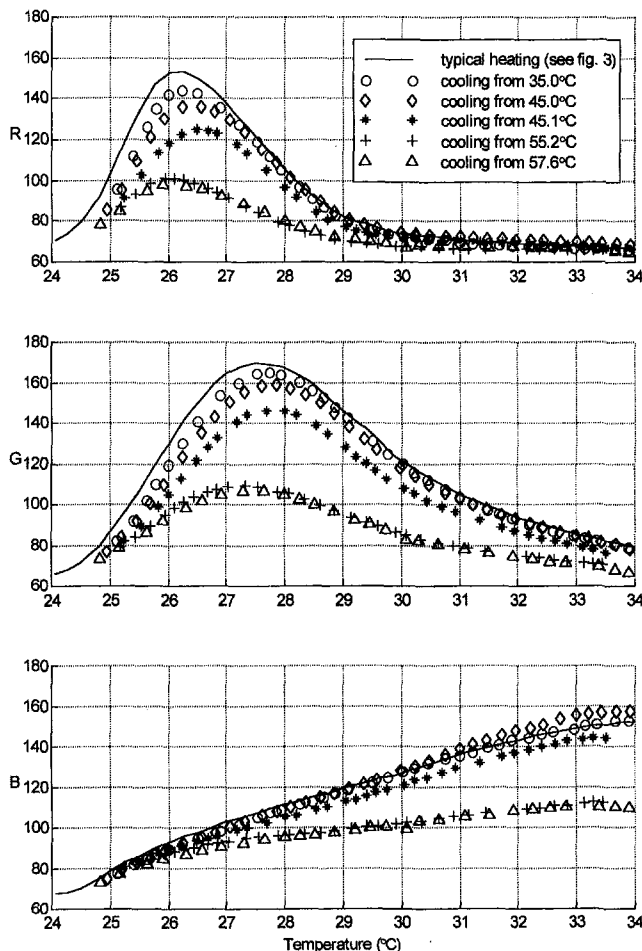


Fig. 5 RGB components for cooling data (showing hysteresis effect)

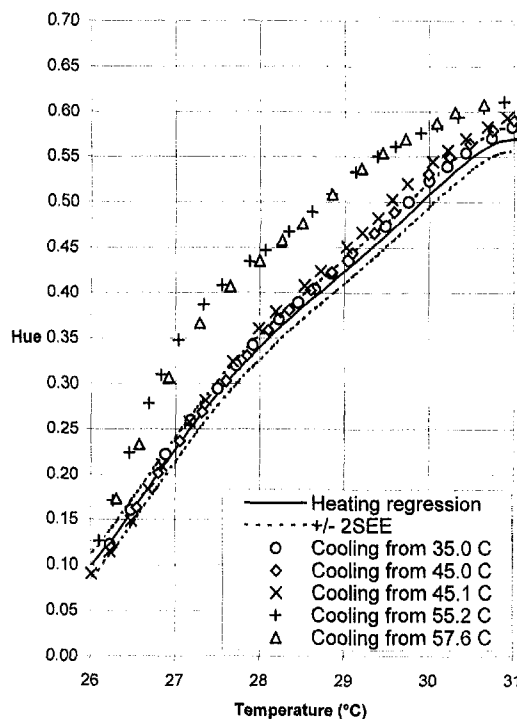


Fig. 6 Hue calibration with cooling data showing hysteresis effect

are used from each heating and cooling curve and the number of runs.

Conclusions

The hue-temperature behavior of one particular microencapsulated TLC has been examined in detail. The hue-temperature behavior was found to contain a significant hysteresis if the TLC was heated much above its useful color-play range (i.e., the hue-temperature behavior during cooling is significantly different than during heating). This hysteresis does not appear if the direction of heating and cooling is changed within the useful temperature range (the initial temperature sets the behavior). After cooling below the useful color-play start temperature the TLC seems to reset (i.e., the heating curve is repeatable even after a previous heating to 55°C). Since completion of this work, the authors have observed similar behavior in several other microencapsulated TLC's.

The authors have carefully examined the question of whether thermal lag or nonuniform temperature in the calibration block could have influenced these results. The hysteresis is far greater than the uncertainty caused by these effects. Furthermore, one of the characteristics of the observed hysteresis was a reduction in the R , G , and B values, which cannot be explained by thermal lag or other experimental errors.

Based on these observations the authors make the following recommendations:

- 1 If a single temperature-hue regression is to be used for both heating and cooling the maximum temperature of the TLC should be limited.
- 2 If the temperature of the TLC will exceed the useful color-play range it is best to use separate hue-temperature regressions for heating and cooling. This may be especially important for researchers doing transient experiments with preheated models. When using the regressions, it is important to recognize that, depending on the high and low temperatures used, there may be hysteresis effects.
- 3 The authors strongly suggest in-situ calibration (data not used in this report suggest that the hue-temperature calibration

regressions depend heavily on a great many factors, including reproducibility of the lighting, angles of lighting, and viewing, and even the time since application of the TLC). We further recommend hue-temperature calibrations of TLC's be done immediately before and after an experiment.

Acknowledgments

The support of the Air Force Office of Scientific Research, which provided a University Resident Researcher Program grant for the assignment of Professor Baughn to the USAF Academy, is gratefully acknowledged. We would also like to acknowledge the support and advice of Dr. Richard Rivir of the USAF Wright Laboratory, Aeropropulsion and Power Directorate. Captain John Jumper of USAFA provided invaluable help by writing the program to drive our frame grabber. Discussions with Prof. Terry Jones (Oxford University) and Prof. J. Michael Owen (University of Bath), who visited the USAF Academy under an EOARD WOS grant, were helpful and are greatly appreciated.

References

- Akino, N., Kunugi, T., Ichimiya, K., Mitsuhiro, K., and Ueda, M., 1989, "Improved Liquid-Crystal Thermometry Excluding Human Color Sensation," *ASME JOURNAL OF HEAT TRANSFER*, Vol. 111, pp. 558–565.
- Baughn, J. W., 1995, "Liquid Crystal Methods for Studying Turbulent Heat Transfer," *International Journal of Heat and Fluid Flow*, Vol. 16, pp. 365–375.
- Baughn, J. W., Ireland, P. T., Jones, T. V., Saniei, N., 1989, "A Comparison of the Transient and Heated-Coating Methods for the Measurement of Local Heat Transfer Coefficients on a Pin Fin," *ASME JOURNAL OF HEAT TRANSFER*, Vol. 111, pp. 877–881.
- Birrell, D. C., and Eaton, J. K., 1998, "Liquid Crystal Temperature Measurement for Real-Time Control," *Proceedings of the SPIE Conference on Applications of Digital Image Processing XXI*, Vol. 3460, pp. 58–66.
- Camci, C., Kim, K., and Hippensteele, S. A., 1992, "A New Hue Capturing Technique for the Quantitative Interpretation of Liquid Crystal Images Used in Convective Heat Transfer Studies," *ASME Journal of Turbomachinery*, Vol. 114, pp. 765–775.
- Coleman, H. W., and Steele, W. G., 1989, *Experimentation and Uncertainty Analysis for Engineers*, John Wiley and Sons, New York.
- Coleman, H. W., and Steele, W. G., 1995, "Engineering Application of Experimental Uncertainty Analysis," *AIAA Journal*, Vol. 33, No. 10.
- Cooper, T. E., Field, R. J., and Meyer, J. F., 1975, "Liquid Crystal Thermography and Its Application to the Study of Convective Heat Transfer," *ASME JOURNAL OF HEAT TRANSFER*, Vol. 97, pp. 442–450.
- Dixon, G. D., Scala, L. C., 1970, "Thermal hysteresis in cholesteric color responses," *Molecular Crystals and Liquid Crystals*, Vol. 10, pp. 317–325.
- Farina, D. J., Hacker, J. M., Moffat, R. J., and Eaton, J. K., 1993, "Illuminant Invariant Calibration of Thermochromic Liquid Crystals," J. J. Simonean and B. F. Armaly, eds., *ASME HTD-Vol. 252*, pp. 1–11.
- Hay, J. L., and Hollingsworth, D. K., 1996, "A Comparison of Trichromatic Systems for Use in the Calibration of Polymer-Dispersed Thermochromic Liquid Crystals," *Experimental Thermal and Fluid Science*, Vol. 12, pp. 1–12.
- Hippensteele, S. A., Russell, L. M., and Stepka, F. S., 1983, "Evaluation of a Method for Heat Transfer Measurement and Thermal Visualization Using a Composite of a Heater Element and Liquid Crystals," *ASME JOURNAL OF HEAT TRANSFER*, Vol. 105, pp. 184–189.
- Jains, A. K., 1989, *Fundamentals of Digital Image Processing*, Prentice-Hall, Englewood Cliffs, NJ.
- Jones, T. V., 1992, "The Use of Liquid Crystals in Aerodynamic and Heat Transfer Testing," *Proceedings of the Fourth International Symposium on Transport Phenomena in Heat and Mass Transfer*, pp. 1242–1273.
- Jones, T. V., Ireland, P. T., and Wang, Z., 1992, "Liquid Crystal Techniques," Keynote Paper, *Proceedings of the International Symposium on Heat Transfer in Turbomachinery*, Athens, Greece, Aug. 24–28.
- Kenning, D. B. R., and Yan, Y., 1996, "Pool Boiling Heat Transfer on a Thin Plate: Features Revealed by Liquid Crystal Thermography," *International Journal of Heat and Mass Transfer*, Vol. 39, Pergamon Press, Oxford, pp. 3117–3137.
- Rau, G., Cakan, M., Moeller, D., and Arts, T., 1998, "The Effect of Periodic Ribs on the Local Aerodynamic and Heat Transfer Performance of a Straight Cooling Channel," *ASME Journal of Turbomachinery*, Vol. 120, pp. 368–375.
- Shenck, H., 1979, *Theories of Engineering Experimentation*, 3rd Ed., McGraw-Hill, New York.
- Simonich, J. C., and Moffat, R. J., 1984, "Liquid Crystal Visualization of Surface Heat Transfer on a Concavely Curved Turbulent Boundary Layer," *ASME Journal of Engineering for Gas Turbines and Power*, Vol. 106, pp. 619–627.
- Wang, 1998, personal communication.
- Wang, Z., Ireland, P. T., Jones, T. V., 1995, "An Advanced Method of Processing Liquid Crystal Video Signals From Transient Heat Transfer Experiments," *ASME Journal of Turbomachinery*, Vol. 117, pp. 184–189.
- Wilson, M., Syson, B. J., and Owen, J. M., 1993, "Image Processing Techniques Applied to Wide-Band Liquid Crystals," *Heat Transfer in Single Phase Flow: Proceedings of Eurotherm Seminar 32*, July 5–7.

Zharkova, G. M., Khachatryan, V. M., Vostokov, L. A., and Alekseev, M. M., 1980, "Study of Liquid Thermoindicators," *Advances in Liquid Crystal Research and Applications*, Vol. 2, L. Bata, ed., Pergamon Press, Oxford, pp. 1221–1239.

The Time Delay for a Perceptible Thermal Disturbance in a Slab

M. G. Davies¹

If a thermal disturbance such as a step change in temperature is applied at each surface of a homogeneous slab of thickness $2L$, the effect of cooling at $x = +L$ at first has no effect at $x = -L$ but is clearly evident after a time described by a Fourier number $F_0 = \lambda t / (\rho c_p L^2)$ of around 0.2. To establish the time of a perceptible change the minimum value of $\phi_i - (\phi_1 + \phi_2)$ is sought, where ϕ_i is the flux into a semi-infinite solid and ϕ_1 and ϕ_2 are the first and second eigenfunction contributions to the solution for a slab of finite thickness. Cooling throughout the slab is determined virtually by the first eigenfunction alone after $F_0 = 0.22$. For a fluid-cooled slab these values are larger.

Nomenclature

- $Bi = \alpha L / \lambda$ (Biot number) nondimensional semi-thickness of the finite thickness slab
- $F_0 = \lambda t / (\rho c_p L^2)$, (Fourier number) time nondimensionalized to describe stages of cooling within the slab
- $F_1 = \alpha t / (\rho c_p L)$, time nondimensionalized to describe cooling of a core
- $F_2 = \alpha^2 t / (\lambda \rho c_p)$, time nondimensionalized to express cooling curves
- L = semi-thickness of the finite thickness slab
- t = time lapse following a step change in surface or fluid temperature at the exposed surface(s)
- T = temperature
- u_j = eigenvalue of eigen number j
- x = the distance from the central plane of a finite thickness slab
- λ, ρ, c_p = conductivity, density, and specific heat of the conducting material, supposed constant
- α = heat transfer coefficient between the slab surface and the fluid
- θ = nondimensionalized temperature
- θ_i = temperature at the surface of a semi-infinite slab
- θ_f = temperature at the surface of a finite slab
- θ_j = eigenfunction components of $\theta_j, j = 1, 2, \dots$
- $\phi, \phi_1, \phi_2, \phi_j$ = similarly nondimensionalized heat flows

Subscripts

- I = initial value
- i = value at the surface of an infinitely thick slab

¹ School of Architecture and Building Engineering, The University, Liverpool L69 3BX, UK.

Contributed by the Heat Transfer Division for publication in the *JOURNAL OF HEAT TRANSFER*. Manuscript received by the Heat Transfer Division, Sept. 25, 1998; revision received, May 2, 1999. Keywords: Building Heat Transfer, Conduction, Heat Transfer, Transient. Associate Technical Editor: A. Majumdar.

regressions depend heavily on a great many factors, including reproducibility of the lighting, angles of lighting, and viewing, and even the time since application of the TLC). We further recommend hue-temperature calibrations of TLC's be done immediately before and after an experiment.

Acknowledgments

The support of the Air Force Office of Scientific Research, which provided a University Resident Researcher Program grant for the assignment of Professor Baughn to the USAF Academy, is gratefully acknowledged. We would also like to acknowledge the support and advice of Dr. Richard Rivir of the USAF Wright Laboratory, Aeropropulsion and Power Directorate. Captain John Jumper of USAFA provided invaluable help by writing the program to drive our frame grabber. Discussions with Prof. Terry Jones (Oxford University) and Prof. J. Michael Owen (University of Bath), who visited the USAF Academy under an EOARD WOS grant, were helpful and are greatly appreciated.

References

- Akino, N., Kunugi, T., Ichimiya, K., Mitsuhiro, K., and Ueda, M., 1989, "Improved Liquid-Crystal Thermometry Excluding Human Color Sensation," *ASME JOURNAL OF HEAT TRANSFER*, Vol. 111, pp. 558–565.
- Baughn, J. W., 1995, "Liquid Crystal Methods for Studying Turbulent Heat Transfer," *International Journal of Heat and Fluid Flow*, Vol. 16, pp. 365–375.
- Baughn, J. W., Ireland, P. T., Jones, T. V., Saniei, N., 1989, "A Comparison of the Transient and Heated-Coating Methods for the Measurement of Local Heat Transfer Coefficients on a Pin Fin," *ASME JOURNAL OF HEAT TRANSFER*, Vol. 111, pp. 877–881.
- Birrell, D. C., and Eaton, J. K., 1998, "Liquid Crystal Temperature Measurement for Real-Time Control," *Proceedings of the SPIE Conference on Applications of Digital Image Processing XXI*, Vol. 3460, pp. 58–66.
- Camci, C., Kim, K., and Hippensteele, S. A., 1992, "A New Hue Capturing Technique for the Quantitative Interpretation of Liquid Crystal Images Used in Convective Heat Transfer Studies," *ASME Journal of Turbomachinery*, Vol. 114, pp. 765–775.
- Coleman, H. W., and Steele, W. G., 1989, *Experimentation and Uncertainty Analysis for Engineers*, John Wiley and Sons, New York.
- Coleman, H. W., and Steele, W. G., 1995, "Engineering Application of Experimental Uncertainty Analysis," *AIAA Journal*, Vol. 33, No. 10.
- Cooper, T. E., Field, R. J., and Meyer, J. F., 1975, "Liquid Crystal Thermography and Its Application to the Study of Convective Heat Transfer," *ASME JOURNAL OF HEAT TRANSFER*, Vol. 97, pp. 442–450.
- Dixon, G. D., Scala, L. C., 1970, "Thermal hysteresis in cholesteric color responses," *Molecular Crystals and Liquid Crystals*, Vol. 10, pp. 317–325.
- Farina, D. J., Hacker, J. M., Moffat, R. J., and Eaton, J. K., 1993, "Illuminant Invariant Calibration of Thermochromic Liquid Crystals," J. J. Simonean and B. F. Armaly, eds., *ASME HTD-Vol. 252*, pp. 1–11.
- Hay, J. L., and Hollingsworth, D. K., 1996, "A Comparison of Trichromic Systems for Use in the Calibration of Polymer-Dispersed Thermochromic Liquid Crystals," *Experimental Thermal and Fluid Science*, Vol. 12, pp. 1–12.
- Hippensteele, S. A., Russell, L. M., and Stepka, F. S., 1983, "Evaluation of a Method for Heat Transfer Measurement and Thermal Visualization Using a Composite of a Heater Element and Liquid Crystals," *ASME JOURNAL OF HEAT TRANSFER*, Vol. 105, pp. 184–189.
- Jains, A. K., 1989, *Fundamentals of Digital Image Processing*, Prentice-Hall, Englewood Cliffs, NJ.
- Jones, T. V., 1992, "The Use of Liquid Crystals in Aerodynamic and Heat Transfer Testing," *Proceedings of the Fourth International Symposium on Transport Phenomena in Heat and Mass Transfer*, pp. 1242–1273.
- Jones, T. V., Ireland, P. T., and Wang, Z., 1992, "Liquid Crystal Techniques," Keynote Paper, *Proceedings of the International Symposium on Heat Transfer in Turbomachinery*, Athens, Greece, Aug. 24–28.
- Kenning, D. B. R., and Yan, Y., 1996, "Pool Boiling Heat Transfer on a Thin Plate: Features Revealed by Liquid Crystal Thermography," *International Journal of Heat and Mass Transfer*, Vol. 39, Pergamon Press, Oxford, pp. 3117–3137.
- Rau, G., Cakan, M., Moeller, D., and Arts, T., 1998, "The Effect of Periodic Ribs on the Local Aerodynamic and Heat Transfer Performance of a Straight Cooling Channel," *ASME Journal of Turbomachinery*, Vol. 120, pp. 368–375.
- Shenck, H., 1979, *Theories of Engineering Experimentation*, 3rd Ed., McGraw-Hill, New York.
- Simonich, J. C., and Moffat, R. J., 1984, "Liquid Crystal Visualization of Surface Heat Transfer on a Concavely Curved Turbulent Boundary Layer," *ASME Journal of Engineering for Gas Turbines and Power*, Vol. 106, pp. 619–627.
- Wang, 1998, personal communication.
- Wang, Z., Ireland, P. T., Jones, T. V., 1995, "An Advanced Method of Processing Liquid Crystal Video Signals From Transient Heat Transfer Experiments," *ASME Journal of Turbomachinery*, Vol. 117, pp. 184–189.
- Wilson, M., Syson, B. J., and Owen, J. M., 1993, "Image Processing Techniques Applied to Wide-Band Liquid Crystals," *Heat Transfer in Single Phase Flow: Proceedings of Eurotherm Seminar 32*, July 5–7.

Zharkova, G. M., Khachatryan, V. M., Vostokov, L. A., and Alekseev, M. M., 1980, "Study of Liquid Thermoindicators," *Advances in Liquid Crystal Research and Applications*, Vol. 2, L. Bata, ed., Pergamon Press, Oxford, pp. 1221–1239.

The Time Delay for a Perceptible Thermal Disturbance in a Slab

M. G. Davies¹

If a thermal disturbance such as a step change in temperature is applied at each surface of a homogeneous slab of thickness $2L$, the effect of cooling at $x = +L$ at first has no effect at $x = -L$ but is clearly evident after a time described by a Fourier number $F_0 = \lambda t / (\rho c_p L^2)$ of around 0.2. To establish the time of a perceptible change the minimum value of $\phi_i - (\phi_1 + \phi_2)$ is sought, where ϕ_i is the flux into a semi-infinite solid and ϕ_1 and ϕ_2 are the first and second eigenfunction contributions to the solution for a slab of finite thickness. Cooling throughout the slab is determined virtually by the first eigenfunction alone after $F_0 = 0.22$. For a fluid-cooled slab these values are larger.

Nomenclature

- $Bi = \alpha L / \lambda$ (Biot number) nondimensional semi-thickness of the finite thickness slab
- $F_0 = \lambda t / (\rho c_p L^2)$, (Fourier number) time nondimensionalized to describe stages of cooling within the slab
- $F_1 = \alpha t / (\rho c_p L)$, time nondimensionalized to describe cooling of a core
- $F_2 = \alpha^2 t / (\lambda \rho c_p)$, time nondimensionalized to express cooling curves
- L = semi-thickness of the finite thickness slab
- t = time lapse following a step change in surface or fluid temperature at the exposed surface(s)
- T = temperature
- u_j = eigenvalue of eigen number j
- x = the distance from the central plane of a finite thickness slab
- λ, ρ, c_p = conductivity, density, and specific heat of the conducting material, supposed constant
- α = heat transfer coefficient between the slab surface and the fluid
- θ = nondimensionalized temperature
- θ_i = temperature at the surface of a semi-infinite slab
- θ_f = temperature at the surface of a finite slab
- θ_j = eigenfunction components of $\theta_j, j = 1, 2, \dots$
- $\phi, \phi_1, \phi_f, \phi_j$ = similarly nondimensionalized heat flows

Subscripts

- I = initial value
- i = value at the surface of an infinitely thick slab

¹ School of Architecture and Building Engineering, The University, Liverpool L69 3BX, UK.

Contributed by the Heat Transfer Division for publication in the *JOURNAL OF HEAT TRANSFER*. Manuscript received by the Heat Transfer Division, Sept. 25, 1998; revision received, May 2, 1999. Keywords: Building Heat Transfer, Conduction, Heat Transfer, Transient. Associate Technical Editor: A. Majumdar.

f = value at the surface of a finite thickness slab
 j = eigen number

1 Introduction

It is a matter of experience that, following excitation of some sort at the surface of a homogeneous slab, initially at uniform temperature say, there is some delay before any perceptible change, however defined, is apparent in the temperature at the other surface. The handle of a silver teaspoon when immersed in hot water warms up faster than that of a stainless steel teaspoon and it is commonly remarked that a diurnal temperature wave passes through a 30-cm masonry wall in about ten hours. It is to be shown that although no exact value for the delay can be stated, an approximation can be found through use of two solutions to the classical Fourier continuity equation,

$$\lambda \frac{\partial^2 T(x, t)}{\partial x^2} = \rho c_p \frac{\partial T(x, t)}{\partial t} \quad (1)$$

They are the solution when a step in temperature is applied at the surface of a semi-infinite slab, expressed in terms of an error function, and the solution for a finite thickness slab, which involves eigenfunctions.

2 The Surface-Cooled Slab

Consider a layer of material of thickness $2L$, ($-L < x < +L$), initially at the uniform temperature T_i and from $t = 0$ onward, $T(-L, t) = T(+L, t) = 0$. The solution $T(x, t)$ is given in Carslaw and Jaeger (1959a).

$$\frac{T(x, t)}{T_i} = \frac{4}{\pi} \sum \frac{(-1)^{j-1}}{2j-1} \cos\left(\frac{(2j-1)\pi x}{2L}\right) \times \exp\left(-\frac{\pi^2(2j-1)^2}{4} F_0\right) \quad j = 1, 2, \dots \infty \quad (2)$$

The heat flow q from the $x = -L$ surface is given in dimensionless form as

$$\phi_f = \frac{q(-L, t) \cdot L}{T_i \lambda} = \sum 2 \exp\left(-\frac{\pi^2(2j-1)^2}{4} F_0\right) = \phi_1 + \phi_2 + \phi_3 + \dots \phi_j + \quad (3)$$

where ϕ_j is the j th eigenfunction contribution to ϕ_f .

If the material is semi-infinite, the surface heat flux (Carslaw and Jaeger, 1959b), nondimensionalized, is

$$\phi_i = (\pi F_0)^{-1/2} \quad (4)$$

Now it is obvious on physical grounds that in the early stages of cooling, ϕ_f and ϕ_i should be nearly equal. This proves to be the case through $\phi_f - \phi_i$ is found to be finite, if vanishingly small, for small values of t .

However, the cooling imposed at the $x = +L$ slab surface leads to an additional loss of heat from the slab so that in due course the flux ϕ_f at $x = -L$ becomes substantially less than ϕ_i , Figure 1 shows in detail the development of ϕ_f ($= \phi_1 + \phi_2 + \phi_3 + \dots$) from its asymptotic value of ϕ_i during early cooling, through the period when ϕ_f values higher than ϕ_i are decaying rapidly with time, to its late cooling asymptotic value of ϕ_1 alone. (The contributions of ϕ_2 and higher terms for low values of F_0 are omitted from the figure so as not to complicate it. They total ϕ_i .)

It is clear that $\phi_f - \phi_1$ has a minimum value, readily found to fall at $F_0 = 0.2094$, when $\phi_i = 1.233$ and $\phi_1 = 1.193$, a difference of 0.040 or 3.2 percent. As a first approximation, cooling at $x = -L$ could be said to proceed unaffected by cooling at $x = +L$ for a time given by F_0 of about 0.2, that is, determined by Eq. (4), and thereafter by the first term in Eq. (3). (In building applications, the value of λ is strongly affected by water content and so is

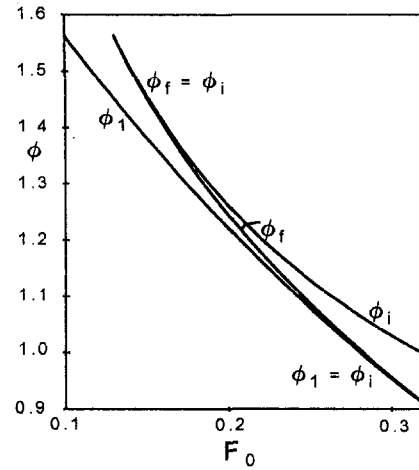


Fig. 1 Cooling curve for a double-sided slab, initially at uniform temperature whose surfaces themselves are at zero temperature from $t = 0$. Vertical axis: nondimensionalized heat flux $\phi = qL/T_i\lambda$; horizontal axis, nondimensionalized time $F_0 = \lambda t/\rho c_p L^2$. The figure shows the development of the surface flux ϕ_f from the value ϕ_i for a semi-infinite solid, to the value ϕ_1 , the first eigenvalue component.

uncertain. Further, quoted values c_p for concrete say vary between 800 and 1000 J/kgK. Thus the value of F_0 is uncertain and an error 3.2 percent would not be important here.)

The estimate is coarse, however, since by now ϕ_f is quite perceptibly less than ϕ_i . $d\phi_f/dF_0$ is correspondingly greater than $d\phi_i/dF_0$ and the difference in this region changes uniformly with F_0 . $d^2(\phi_i - \phi_f)/dF_0^2$, however, shows a weak maximum at $F_0 = 0.181$, which gives some qualitative measure of the region in which ϕ_f departs from ϕ_i . A more conservative estimate of the duration of early cooling is given by the time when $\phi_i - (\phi_1 + \phi_2)$ has its minimum. This is found at $F_0 = 0.124$, when $\phi_i = 1.602$ and $\phi_1 - (\phi_1 + \phi_2) = 0.0023$, a deviation now of only 0.14 percent.

At $F_0 = 0.2$, the second eigenfunction ϕ_2 still contributes significantly to ϕ_f as Fig. 1 shows, but in due course it becomes effectively zero. We cannot assign any nonarbitrary value to F_0 to indicate when this is so, since ϕ_2/ϕ_f never becomes strictly zero.

An estimate, however, can be arrived by noting that in steady-state conditions the heat flow in one dimension is everywhere constant, so $\partial^2 q/\partial t \partial x = 0$. Now $\partial^2 q/\partial t \partial x$ is proportional to $\partial^2 T/\partial t^2$, so $\partial^2 T/\partial t^2$ is a measure of departure from steady conditions, (though it is not a sufficient condition for steady state.) Within the slab under discussion, the amplitude of temperature of the second eigenfunction, T_2 say, is at all times less than T_1 but initially $\partial^2 T_2/\partial t^2$ is greater and latterly less than $\partial^2 T_1/\partial t^2$. When they are equal, their respective departures from steady conditions are equal. Thus this condition denotes a time after which T_2 and so ϕ_2 are becoming negligible compared with the first eigenvalue quantities.

The condition that $\partial^2 T_2/\partial t^2$ should equal $\partial^2 T_1/\partial t^2$ just within the surface of the slab readily gives a value of $F_0 = \ln(81)/2\pi^2 = 0.223$ so that we expect that shortly after this ϕ_2 will be negligible compared with ϕ_1 . In the late phase of cooling, the rate of cooling is fractionally speaking the same everywhere in the slab and is fastest at the centre.

Thus by taking account of the first two eigenfunction contributions to ϕ_f we should expect ϕ_f to depart from its early asymptotic form of ϕ_i some time after a value of F_0 of about 0.12 and to have assumed its late asymptotic form of ϕ_1 shortly after an F_0 value of 0.22. From Fig. 1 these values, estimated by eye, appear to be about 0.15 and 0.26. In the following section this analysis will be applied to the case where cooling takes place through a resistive layer.

3 The Fluid-Cooled Slab

If the slab is cooled through a film of transmittance α at both surfaces, two new variables are introduced: the Biot number

Table 1 Deviation of the θ_1 envelope from θ_i

θ_i	1.0	0.9	0.8	0.7	0.6	0.5	0.4	0.3	0.2	0.1
$\theta_i - \theta_{1e}$	0.0000	0.0022	0.0043	0.0060	0.0073	0.0081	0.0083	0.0075	0.0058	0.0032

$Bi = \alpha L / \lambda$, which is a nondimensional form of slab thickness, and $F_2 = \alpha^2 t / \lambda \rho c_p$, another form of dimensionless time, and unlike F_0 , independent of slab thickness.

Consider the problem: A slab of thickness $2L$ is initially at a constant temperature T_i throughout. At time $t = 0$, the temperature of the fluid is reduced to and thereafter held at zero. The initial condition, together with the boundary conditions that $\alpha T = \pm \lambda \partial T / \partial x$ at the two exposed surfaces and the Fourier equation, Eq. (1), lead to the temperature $T(x, t)$ at a distance x from the centreline and at time t (Carslaw and Jaeger 1959c):

$$\frac{T(x, t)}{T_i} = \theta(x/L, F_2) = \sum \frac{2 Bi}{Bi^2 + Bi + u_j^2} \cdot \frac{\cos(u_j x/L)}{\cos u_j} \cdot \exp\left(-\frac{u_j^2 F_2}{Bi^2}\right) \quad (5)$$

where the eigenvalues u_j satisfy the relation $u_j \tan u_j = Bi$, $j = 1, 2, \dots, \infty$. (They have the property that $\sum (1/u_j^2) = 1/Bi + \frac{1}{2}$.)

This relation, due to Groeber (1925), appears in many standard texts on heat transfer and might be regarded as the classical equation for transient response since it includes finite values of L , α and λ . (If $\lambda = \infty$, Eq. (5) reduces to $T(t)/T_i = \exp(-\alpha t / \rho c_p L) = \exp(-F_1)$, a well-known form. If $\alpha = \infty$ it reduces to Eq. (2). If $L = \infty$, numerical solutions are obtainable using Eq. (7) below and if both α and L are infinite, $T(x, t)/T_i = \text{erf}(\sqrt{(\rho c_p x^2 / 4\lambda t)})$; (see Carslaw and Jaeger, 1959d).) The expression provides cooling curves and the forms given by Groeber himself, by Heisler (1947) and by Bachmann (1938) are often quoted in texts.

It is commonly remarked that the contributions of the higher eigenfunctions die away quickly. As in the previous section, when consideration is taken of the first two eigenfunctions ($j = 1$ and 2) certain stages in the cooling at the surface can be distinguished.

Since the surface temperatures remain finite, it is more convenient to work in terms of temperature rather than of flux as previously. The temperature of the finite thickness slab at $x = -L$ is

$$\frac{T(-L, t)}{T_i} = \theta_f = \sum \frac{2 Bi}{Bi^2 + Bi + u_j^2} \cdot \exp\left(-\frac{u_j^2 F_2}{Bi^2}\right) = \theta_1 + \theta_2 + \theta_3 + \dots \quad (6)$$

This is to be compared with the temperature at the surface of a semi-infinite medium (Carslaw and Jaeger, 1959e):

$$\theta_i = \exp(F_2) \text{erfc}(\sqrt{F_2}). \quad (7)$$

As in the previous section, at some time during cooling the value of θ_1 is found to be very little less than θ_i . To demonstrate this, we first note that for a slab where Bi is small, θ_1 is initially almost unity, but falls rapidly with F_2 . For a slab having a larger value of Bi , θ_1 is initially less than unity but falls away less rapidly. Thus the θ_1, F_2 characteristic for Bi (moderate) must cross over that for Bi (small). In general, the θ_1, F_2 characteristics cross each other to form an envelope which is determined by the condition

$$\partial \theta_1 / \partial u_1 = 0. \quad (8)$$

This leads to a time F_0 (written as $[F_0]_e$, subscript e for envelope) when the first eigenfunction component θ_1 touches the envelope of θ_1 values, given by

$$[F_0]_e = \frac{1}{2u_1^2} \left(\frac{Bi^2 + Bi - u_1^2}{Bi^2 + Bi + u_1^2} \right). \quad (9)$$

Values are included in Table 2. The value of θ_1 itself at this time is

$$\theta_{1e} = \frac{2 Bi}{Bi^2 + Bi + u_1^2} \exp(-u_1^2 [F_0]_e). \quad (10)$$

Values of θ_{1e} in relation to θ_i values are shown in Table 1. (A value of Bi was selected and the value of $[F_0]_e$ found from Eq. (9), from which $F_2 = F_0 Bi^2$.) With this value of F_2 , θ_i was found from Eq. (7). The Bi values were so chosen as to give values of $\theta_i = 0.9, 0.8$, etc. θ_{1e} follows from Eq. (10); hence $\theta_i - \theta_{1e}$.

It will be seen that over the full range of dimensionless slab thicknesses, the envelope of the first eigenfunction characteristics lies only very little below the semi-infinite value θ_i . Since θ_f for some specific value of Bi must initially follow θ_i and latterly θ_1 this demonstrates that there can only be a small transitional range of θ_f between these asymptotic conditions.

The corresponding time $[F_0]_e$ could be taken as a crude measure of the transition from early to late cooling. Following the arguments of the last section, however, a more conservative estimate of time is that when $\theta_i - (\theta_1 + \theta_2)$ has its minimum value. Values are listed as $[F_0]_d$ in Table 2. (d denotes "departure" from early cooling at the surface of finite thickness slab.)

Again, following the argument of Section 2, an estimate can be made of the time $[F_0]_f$ after which the surface temperature θ_f is virtually determined as θ_1 alone. It is given by the condition that

$$\partial^2 \theta_2 / \partial t^2 = \partial^2 \theta_1 / \partial t^2 \quad (11)$$

and leads to a value

$$[F_0]_f = \frac{1}{u_2^2 - u_1^2} \ln \left(\frac{u_2^4 (Bi^2 + Bi + u_2^2)}{u_1^4 (Bi^2 + Bi + u_1^2)} \right). \quad (12)$$

See Table 2. It will be seen that although the Biot numbers cover a fractional range of 5000, the times describing the stages reached in cooling, expressed as a Fourier number, vary over quite a small range. It will be noted too that the values of F_0 for $Bi = \infty$ are those already found for the surface-cooled slab: A large value of Bi implies that in effect the surfaces themselves are brought to near zero at $t = 0$.

It is easy to write down a value for $[F_0]_f$ for the central plane of a double-sided slab. The values are similar to, though a little smaller than, the surface values. We cannot write down values for $[F_0]_d$ and $[F_0]_e$, however. Temperature at the central plane remains undisturbed for a while after excitation, but cooling eventually takes place due to excitation from both sides equally. Nor, it seems, can use be made of the eigenfunction contributions: Their

Table 2 Values of $F_0 = \lambda t / \rho c_p L^2$ at three stages of cooling

Bi	$[F_0]_d$	$[F_0]_e$	$[F_0]_f$
0.01	0.155	0.333	1.002
0.1	0.155	0.330	0.541
1	0.154	0.311	0.356
10	0.140	0.236	0.259
50	0.129	0.210	0.231
∞	0.124	0.203	0.223

Subscript definitions:

- d , the approximate time of departure from early cooling at the slab surface given by the minimum of $\theta_i - (\theta_1 + \theta_2)$
- e , the time at which the θ_1 characteristic for Bi touches the envelope of all θ_1 characteristics
- f , the time after which cooling is dominated by the first eigenfunction alone

Table 3 Surface cooling curve for a fluid-cooled slab, initially at unit temperature, Bi = 1

θ_f	1.0	0.9	0.8	0.7	0.6	0.5	0.4	0.3	0.2	0.1
F_2	0	9.27_{10}^{-3}	4.46_{10}^{-2}	1.24_{10}^{-1}	2.77_{10}^{-1}	5.12_{10}^{-1}	8.13_{10}^{-1}	1.20	1.75	2.68

values are alternatively positive and negative with increasing j . We may note, however, that in the initial stage of cooling, the cooling rate is largest at the surface and in the final stage it is largest at the midplane.

4 Applications

The foregoing argument leads to the conclusion that there will be a delay of about $F_0 = 0.2$ before a perceptible signal is propagated, that is a time of about $0.2\rho c_p L^2/\lambda$. Taking standard values for silver and steel the time to travel the 6 cm of a spoon are about 4 and 60 seconds, respectively, readily checked by a practical test. The rule of thumb in the building field—passage of a wave through a 30-cm brick wall in about 10 hours—is largely confirmed by this analysis: a step change in external excitation should be apparent after about eight hours.

The argument also confirms one of Bachmann's charts. Results for the fluid-cooled slab were first evaluated by Groeber but the curves are difficult to interpret. He encouraged Bachmann (1938) to replot them with nondimensionalized temperature θ as ordinate (as previously) but with $F_2 = \alpha^2 t/\lambda\rho c_p$ (independent of slab thickness) as abscissa and with $\text{Bi} = \alpha L/\lambda$ (independent of time) as parameter, thereby separating time and thickness. The results for the surface of a plane slab show an envelope of curves, (given in fact by Eq. (7)), from which curves for $\text{Bi} = 0.05, 0.1, 0.2 \dots 5$, etc., diverge. The points of divergence are not easy to judge by eye but are mostly between $F_0 = 0.1$ and 0.3 (for $\text{Bi} = 0.2, F_0 = 0.5$) while F_2 varies by a factor of 5000. These roughly accord with the $[F_0]_d$ values in Table 2.

The author once witnessed a test to find how long it would take before the heat generated by failure of a gland on a rapidly rotating steel shaft would be felt at the roller bearing some distance from the gland. It involved the destruction of some expensive and laboriously assembled equipment. No one responsible for the tests at the time had any real idea of what time delay might be expected and knowledge of the above simple relation would have gone some way to allay fears.

The principal application of these ideas, however, relates to cooling curves for surface temperatures. Consider the case for example for $\text{Bi} = 1.0$. For this choice, F_0 and F_2 are numerically the same so according to Table 2, early cooling should proceed up to $F_2 = 0.154$ and late or exponential cooling should proceed after $F_2 = 0.356$. Direct calculation of θ_f using Eq. (6) gives the values in Table 3.

It is easily checked that the values of (F_2, θ_f) down to $\theta_f = 0.7$ are in fact given by the relation for a semi-infinite slab (Eq. (7)) and those from $\theta_f = 0.5$ derive from the first term of Eq. (6) alone; only the values of $\theta_f = 0.65$ and 0.60 lie in the transitional range; they could be found by interpolation between the limiting relations. It will be found that for slabs where Bi is less than about 0.05, virtually the whole cooling process takes place in a state of late (exponential) cooling and so can be estimated in a simple way without summation of series. Further, for slabs where Bi is greater than about 50, the surface temperature (of more general importance than at locations within the slab) is determined down to a value of θ_f of 0.05 by the semi-infinite value of $\theta_i = \exp(F_2) \cdot \text{erfc}(\sqrt{F_2})$ (Davies, 1978). Table 4 of that paper presents a set of values structured to show the ranges of early and late cooling for Bi between 0.001 and 1000.

The "response time," "decay time," or "time constant," t_r is defined as the time taken for a system, initially in steady-state conditions, to complete $(1 - 1/e)$ or 63.2 percent of its total change to a new steady state, following some step excitation. In the present case, t_r is the time taken for T_f/T_i to equal $1/e = 0.368$. Since u_1 is near enough equal to $\sqrt{\text{Bi}}$ for thin slabs, it readily follows that the response time F_{2r} is equal to Bi itself. This necessarily holds up to a value of Bi of about 0.05, and it continues to hold (to about two percent) up to $\text{Bi} = 0.5$. (This is useful in a building connection.) From $\text{Bi} = 3.2$ upward, the condition that T_f/T_i should equal $1/e$ is reached in early cooling and $F_{2r} = 1.562$.

Conventionally, α denotes a single physical process—convection (or radiation in Carslaw and Jaeger, 1959). It can be generalized, however, to comprise a number of physical processes together with step changes either at the surface itself or at any of the intermediate nodes. The author has used it in this way to estimate the response to the switching on and off of the classroom lights in a passive solar-heated school, and in this application α was made up of internal convective and radiative exchanges, together with the effect of ventilation and an external mixed convection/radiation loss, five links in all, variously acting in series and parallel. Furthermore, a step in heat input rather than of temperature can be taken to be input at any of the temperature nodes between that of the slab surface, which is the real dependent variable, and ambient temperature T_0 which is assumed constant. This could be for example at the node representing the room mean air temperature, where the convective component of the heat input acts. The matrix formulation needed to handle the thermal circuit is presented in Davies (1986), Section 3.12.

According to solutions to the parabolic Fourier continuity equation (which assumes a continuous distribution of matter), the effect of a thermal signal applied in a solid is instantaneously transmitted to finite distances though with vanishingly small effect. In recent years the continuity equation has been extended to take account of the atomic structure of materials (Tzou, 1997) and this leads to propagation of a signal at a speed of order of sound velocity. These developments have no bearing on the process discussed here, where time delays for perceptible changes through building walls are of order hours, not milliseconds.

References

- Bachmann, H., 1938, *Tafeln über Abkühlungsvorgänge Einfacher Körper*, Verlag Julius Springer, Berlin.
- Carslaw, H. S., and Jaeger, J. C., 1959, *Conduction of Heat in Solids*, Clarendon Press, Oxford, a: p. 97, Eq. (8); b: p. 61, Eq. (11); c: p. 122, Eq. (12); d: p. 59, Eq. (3); e: p. 71, Eq. (2).
- Davies, M. G., 1978, "Structure of the Transient Cooling of a Slab," *Applied Energy*, Vol. 4, pp. 87–126.
- Davies, M. G., 1986, "The Passive Solar Heated School in Wallasey: III—Model Studies of the Thermal Response of a Passive School Building," *Energy Research*, Vol. 10, pp. 203–234.
- Groeber, H., 1925, "Die Erwärmung und Abkühlung Einfacher Geometrischer Körper," *Z. Vereines deut. Ingenieure*, Vol. 69, pp. 705–711.
- Heisler, P. M., 1947, "Temperature Charts for Induction and Constant Temperature Heating," *Transactions of the ASME*, Vol. 69, pp. 227–236.
- Tzou, D. Y., 1997, *Macro-to-Microscale Heat Transfer—The Lagging Behavior*, Taylor & Francis, Washington DC.

A Residual-Based Fuzzy Logic Algorithm for Control of Convergence in a Computational Fluid Dynamic Simulation

J. Ryoo,¹ D. Kaminski,¹ and Z. Dragojlovic¹

Introduction

In heat transfer and fluid dynamic simulations, stabilizing the computation and achieving convergence can be very difficult, especially in highly nonlinear cases. In an attempt to promote convergence, user-specified parameters such as relaxation factor have often been used. However, specifying these values can be difficult. The user chooses them from experience and adjusts them when the simulation diverges or fails to converge in a reasonable amount of time. In this work, a rule-based fuzzy logic algorithm was applied to control the relaxation factors of a common CFD algorithm. Relaxation factors were adjusted automatically during code execution based on the behavior of residuals.

There have been efforts to accelerate convergence in CFD analysis via multigrid acceleration (Brandt, 1977), generalized minimum residual algorithms (Saad and Schultz, 1986), or various preconditionings. While these are mainly focused on solving a system of linear equations iteratively, the current work is focused on how to linearize nonlinear equations to be solved by such methods.

Little work has been reported in using soft computing methods such as fuzzy logic to aid in CFD simulations. Cort et al. (1982) performed a one-dimensional finite element heat transfer simulation with radiative boundary conditions. They used a simple feedback control method to adjust the relaxation factors. Iida et al. (1994) recently published a study in which wobbling adaptive control was applied to a CFD simulation of the Benard problem.

Ryoo et al. (1998) developed a fuzzy algorithm to control an under-relaxed CFD computation. The algorithm used the behavior of the dependent variables and their iterative errors as inputs. However, the values of the dependent variables are not necessarily the best indicators of convergence. In the present work, residuals were chosen as the input variables, resulting in a simpler rule set and faster convergence.

The well-known SIMPLER algorithm (Patankar, 1980) was used in the present work. Three different benchmark problems were simulated and the same rule set was applied to all three benchmark cases to test the generality of the control algorithm.

Analysis

In all cases, the flow was assumed to be Newtonian, incompressible laminar, and two-dimensional. Viscous dissipation was neglected. All thermophysical properties were assumed constant, except for the density, which was treated using the Boussinesq approximation. The conservation equations for mass, momentum, and energy are given in Patankar (1980).

The conservation equations were discretized by a finite volume approach as

$$a_p \phi_p = \sum a_{nb} \phi_{nb} + b \quad (1)$$

¹ Department of Mechanical Engineering, Aeronautical Engineering and Mechanics, Rensselaer Polytechnic Institute, Troy, NY 12180.

Contributed by the Heat Transfer Division for publication in the JOURNAL OF HEAT TRANSFER. Manuscript received by the Heat Transfer Division, Dec. 1, 1998; revision received, May 3, 1999. Keywords: Artificial Intelligence, Computational, Fluids, Heat Transfer, Laminar, Numerical Methods. Associate Technical Editor: Y. Jaluria.

Table 1 Relaxation factor control rules

Local	ρ_l	NB	NM	LU	GU	PM	PB
control	$\Delta\alpha$	NB	NS	PS	PS	NS	NB
Global	ρ_g	PB	PM	PS			
control	$\Delta\alpha$	NB	NS	PS			

where a_p is a coefficient for the point P under consideration, a_{nb} 's are the coefficients of neighboring grid points, ϕ_p is the value of the dependent variable for the equation under consideration, ϕ_{nb} 's are the values of the neighboring grid points and b is the source term. The generic variable ϕ is used to represent u , v , and T .

On each iteration, the assumed values of the solution vector were updated with under-relaxed values according to

$$\phi_n^* = \phi_{n-1} + \alpha(\phi_n - \phi_{n-1}) \quad (2)$$

where α is a relaxation factor. The relaxation factor can be varied from iteration to iteration and from point to point in the solution domain without affecting the final converged solution. The goal of the current work is to design a controller that will adjust values of α to enable or accelerate convergence.

Most control systems are designed to reach target values of the controlled variables. In this work, the target values for the residuals are zero, so the residuals themselves are useful inputs. The discretized equation for the residual is given by

$$r = \sum a_{nb} \phi_{nb} + b - a_p \phi_p \quad (3)$$

The residual was normalized by the value of the coefficient a_p in the discretized equation to obtain the displacement, d , which is defined as

$$d = \frac{\sum a_{nb} \phi_{nb} + b - a_p \phi_p}{a_p} \quad (4)$$

The goal of the controller is, then, to force the displacement to zero.

Two different control strategies were developed. One, a local controller, adjusted the relaxation factor at every control volume in the domain on every iteration. The second strategy used a global controller, which picked a representative value for relaxation factor on each iteration.

In the current work, a local tuning index similar to one used by Bare et al. (1990) was defined as

$$\rho_l = \frac{d_{n+1}}{d_n} \quad (5)$$

where d_{n+1} and d_n are displacements on two consecutive iterations. The tuning index was used to indicate whether the convergence is linear and to moderate the rate of convergence. If $|\rho_l|$ was much bigger than one, then the controller decreased the relaxation factor and if $|\rho_l|$ was near one, the relaxation factor was increased.

For the global controller, the 2-norm of the displacement was used as a representative value.

$$\|d\| = \sqrt{\sum d^2} \quad (6)$$

A tuning index based on this quantity was defined as

$$\rho_g = \frac{\|d\|_{n+1}}{\|d\|_n} \quad (7)$$

Control Rules and Membership Functions. Fuzzy logic (Zade, 1965) was applied to control the relaxation factors. The relaxation factor control rules are presented in Table 1. For the ρ_l input in the local control algorithm, six membership functions were used to fuzzify, and for the global control algorithm, three

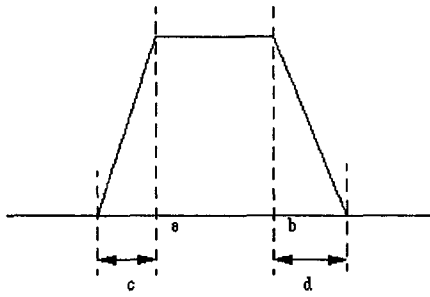


Fig. 1 Trapezoidal membership function model

membership functions were used. Defuzzification of the relaxation factors used three consequent membership functions.

If the tuning index, ρ_i , is large in magnitude, i.e., either negative big (NB) or positive big (PB), then the current displacement is bigger in absolute value than the previous displacement. Since this is an indicator of possible divergence, the rule set acts to reduce α by invoking the negative big (NB) rule for $\Delta\alpha$. This is shown in Table 1. If ρ_i is near one, greater than unity (GU) or less than unity (LU), the positive small (PS) rule in the consequent is invoked to speed up the computation. The attempt to increase the relaxation factor by a large amount was abandoned because it usually destabilizes the iteration. The same line of reasoning was applied to the global controller, except that there is no need for a rule to monitor negative values.

Usual triangle or trapezoidal shape membership functions were used for the antecedent, and right triangle membership functions were used for the consequent. The membership functions can be generalized by a trapezoidal model as shown in Fig. 1. Tables 2 and 3 specify the geometric parameters for each membership function. A center of gravity method was used for defuzzification. After defuzzification, the relaxation factors were updated as follows:

$$\alpha_{n+1} = (1 + \Delta\alpha)\alpha_n \quad (8)$$

The relaxation factors were restricted to take on values between zero and one.

Application to Benchmark Problems. Three benchmark problems were examined to test the utility of the controller. In each case, fluid properties were assumed constant and the no-slip condition was applied to all surfaces. The convergence criterion was given by

$$\frac{\max |\phi_n - \phi_{n-1}|}{\max |\phi_n| \cdot \alpha_n} \leq 10^{-5} \quad (9)$$

Here, the maximum error in the domain was divided by the maximum function value in the domain. The maximum value was multiplied by the relaxation factor to avoid the illusion of convergence from heavy relaxation factors.

The controller was used to relax the two components of velocity and the temperature field. The relaxation factor for each variable was independently controlled. The pressure and pressure correction were not under-relaxed, since little benefit resulted for the cases examined.

Two different methods of applying the control algorithm to the benchmark problems were used, a local method and a global

Table 2 Membership functions for local control antecedent

ρ_l	NB	NM	LU	GU	PM	PB
a	$-\infty$	-2	0.7	1	4	5
b	-3	-2	1	1	4	∞
c	0	2	0.3	0	2.5	2
d	2	2	0	0.3	2.5	0

Table 3 (a) Membership functions for global control antecedent, (b) membership function for local and global consequent

ρ_g	PS	PM	PB
a	0	1.5	2.5
b	0	1.5	∞
c	0	0.4	1
d	1	0.4	0

(a)

$\Delta\alpha$	NB	NS	PS
a	-0.4	-0.25	0.2
b	-0.4	-0.25	0.2
c	0	0	0.4
d	0.5	0.5	0

(b)

method. In the local method, every control volume in the domain was controlled separately, and therefore every control volume was assigned a different relaxation factor. In the global method, the 2-norm of the displacements from the domain was used as a representative value to select a relaxation factor for the entire domain. In the global approach, there were only three different relaxation factors, one for the horizontal velocity, one for the vertical velocity, and the third for the temperature. For comparison, fixed relaxation factor cases were also tested.

The first case is a two-dimensional steady state buoyancy driven flow in a square cavity (Elder, 1965). The cavity is closed and filled with a constant property fluid. The left and right sides are isothermal at two different temperatures and the horizontal sides are insulated. Because of heat transfer from the hot wall, a buoyancy-driven recirculation pattern appears in the cavity. The problem is nondimensionalized and characterized by a Rayleigh number, $Ra = \rho^2 g \beta \Delta T L^3 Pr / \mu^2$.

As a second model problem, a cavity with a lid which moves horizontally with constant velocity U was simulated (Schreiber and Keller, 1983). The energy equation was not solved since the flow is assumed isothermal. The problem was nondimensionalized and characterized by a Reynolds number which is based on the lid speed.

The third case involves a two-dimensional flow in a channel with a sudden expansion (Blackwell and Armaly, 1993). The inlet flow temperature is the same as the temperature of the left straight wall. The step in the right part of the channel is insulated and the straight part of the right wall is at a higher temperature than the inlet. The inlet flow enters the domain in parabolic profile (Blackwell and Armaly, 1993). The Reynolds number, $Re = \bar{u}s/n$, was set at 100 and the Peclet number, $Pe = \bar{u}s/a$, was set at 70. The problem was nondimensionalized and simulated as a mixed convection flow as well as a forced convection flow with $Gr = 0$ and $Gr = 1000$.

Table 4 Iterations required to converge for various fixed relaxation factor and controlled cases

Buoyancy-driven Cavity						
Ra	0.2	0.4	0.6	0.8	Local	Global
10^2	3024	1301	683	328	301	252
10^3	5704	2278	1101	477	280	289
10^4	4009	1583	754	322	202	136
10^5	3407	1323	627	275	261	141
10^6	2482	1034	521	238	489	270
Lid-driven Cavity						
Re	0.2	0.4	0.6	0.8	Local	Global
10^2	2346	921	437	187	250	143
10^3	1641	640	300	120	206	285
Backward Facing Step Channel						
Gr	0.2	0.4	0.6	0.8	Local	Global
0	4123	1598	743	304	379	292
10^3	3158	1235	582	244	397	253

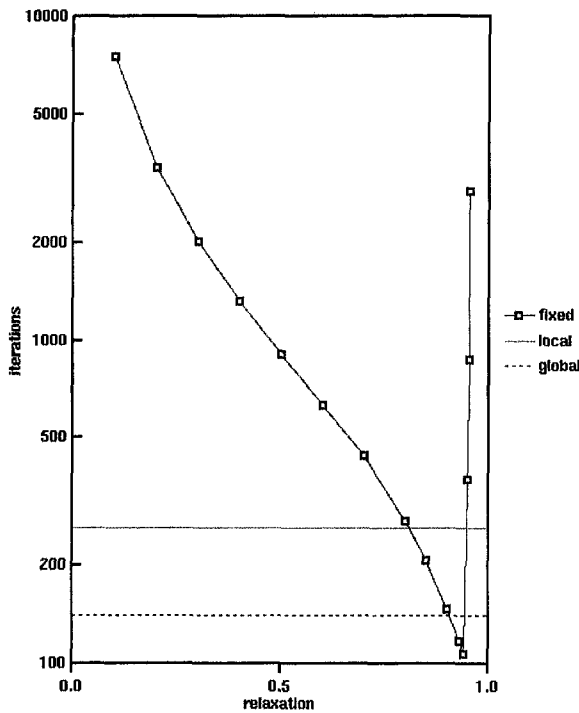


Fig. 2 Iterations required in buoyancy-driven cavity at $Ra = 10^5$

Results and Discussion

The solutions from the relaxation-factor-controlled computation and the fixed relaxation factor computation were compared with published results (Blackwell and Armaly, 1993; Elder, 1965; Schreiber and Keller, 1983). The results from the controlled and the uncontrolled cases are almost identically the same and match the published results well.

The controller achieved convergence for all cases tested. A summary of the number of iterations required for convergence using various constant relaxation factors is compared to that required using fuzzy control in Table 4. In general, the number of iterations using the controller was lower than that for most of the constant relaxation factor cases. A plot of the iterations required for convergence vs. the relaxation factor for a Rayleigh number of 10^5 is shown in Fig. 2.

Although it is possible for the user to select a constant relaxation factor that will outperform the controlled algorithm, it is generally not easy to do so especially in highly nonlinear cases. Furthermore, the danger of divergence is always present if relaxation factors are set too high, and the user may need to manually restart the code more than once with new lower relaxation factors. The results show that the locally-controlled case is sometimes better and sometimes worse than the globally controlled case.

There is a major disadvantage of the local controller in that it requires a substantial amount of CPU time to apply the rule set to every node on every iteration. Table 5 gives the CPU times for the buoyancy-driven case with $Gr = 10^6$. The local controller requires

Table 5 CPU time in $Gr = 10^6$ buoyancy-driven case

relaxation factor	CPU time
0.2	857.13
0.4	357.69
0.6	180.89
0.8	82.76
Global	54.45
Local	2643.95

more than ten times the CPU time for the global case is thus not practical.

This work can potentially be extended to the simulation of turbulence, radiation, or two-phase flow. Also, further study is needed to design a more optimal controller such as a neuro-fuzzy algorithm or a fuzzy controller optimized by a genetic algorithm.

References

- Bare, W. H., Mullholland, R. J., and Sofer, S. S., 1990, "Design of a Self-Tuning Rule Based Controller for a Gasoline Refinery Catalytic Reformer," *IEEE Trans Automat. Control*, Vol. 35, No. 2, pp. 156-164.
- Blackwell, B. F., and Armaly, B. F., 1993, "Benchmark Problem Definition and Summary of Computational Results for Mixed Convection Over a Backward Facing Step," HTD-Vol. 258, ASME, New York, pp. 1-10.
- Brandt, A., 1997, "Multi-Level Adaptive Solutions to Boundary-Value Problem," *Math. Comput.*, Vol. 31, No. 138, pp. 333-390.
- Cort, G. E., Graham, A. L., and Johnson, N. L., 1982, "Comparison of Methods for Solving Nonlinear Finite-Element Equations in Heat Transfer," ASME Paper No. 82-HT-40.
- Elder, J. W., 1965, "Laminar Free Convection in a Vertical Slot," *Journal of Fluid Mechanics*, Vol. 23, pp. 77-98.
- Iida, S., Ogawara, K., Furusawa, S., and Ohata, N., 1994, "A Fast Converging Method Using Wobbling Adaptive Control of SOR Relaxation Factor for 2D Benard Convection," *J. of Mechanical Engineering Society of Japan*, Vol. 7, pp. 168-174.
- Patankar, S. V., 1980, *Numerical Heat Transfer and Fluid Flow*, McGraw-Hill, New York.
- Ryoo, J., Kaminski, D., and Dragojlovic, Z., 1998, "Automatic Convergence in a Computational Fluid Dynamics Algorithm Using Fuzzy Logic," The Sixth Annual Conference of the Computational Fluid Dynamics Society of Canada, VIII.
- Saad, Y., and Schultz, M. H., 1986, "GMRES: A Generalized Minimum Residual Algorithm for Solving Nonsymmetric Linear Systems," *SIAM J. Sci. Stat. Comp.*, Vol. 7, No. 3, pp. 856-869.
- Schreiber, R., and Keller, H. B., 1983, "Driven Cavity Flows by Efficient Numerical Techniques," *J. of Computational Physics*, Vol. 49, pp. 310-333.
- Zade, L., 1965, "Fuzzy Sets," *Information and Control*, Vol. 8, pp. 338-358.

Analytical Solution of the Graetz Problem With Axial Conduction

J. Lahjomri¹ and A. Oubarra²

1 Introduction

The present investigation is concerned with a new method of an analysis and improved solution for the extended Graetz problem of heat transfer in a conduit. It is well known that the extended Graetz problem is defined when the axial heat conduction is included in the analysis and its effect becomes important at small Peclet numbers. For example, heat transfer in liquid metals: in general, the Graetz problem with axial conduction is treated by separating the domain of the conduit into two semi-infinite regions, an upstream region ($-\infty < x \leq 0$) and downstream region ($0 \leq x < +\infty$). The temperature field is then determined in both regions and the two solutions are matched at $x = 0$ where heating (or cooling) starts. Previous studies dealing with the extended Graetz problem have clearly shown that this type of problem is related to the

¹ To whom correspondence should be addressed. Assistant Professor, Département de Physique, groupe d'Energétique, Faculté des Sciences Ain Chock, Université Hassan II, Km 8 route El jadida, Maarif B. P. 5366, Casablanca, Morocco. e-mail: Lahjomri@facsc-achok.ac.ma.

² Professor, Département de Physique, groupe d'Energétique, Faculté des Sciences Ain Chock, Université Hassan II, Km 8 route El jadida, Maarif B. P. 5366, Casablanca, Morocco.

Contributed by the Heat Transfer Division for publication in the JOURNAL OF HEAT TRANSFER. Manuscript received by the Heat Transfer Division, Aug. 24, 1998; revision received, July 1, 1999. Keywords: Analytical, Entrance, Forced Convection, Heat Transfer, Laminar. Associate Technical Editor: R. Mahajan.

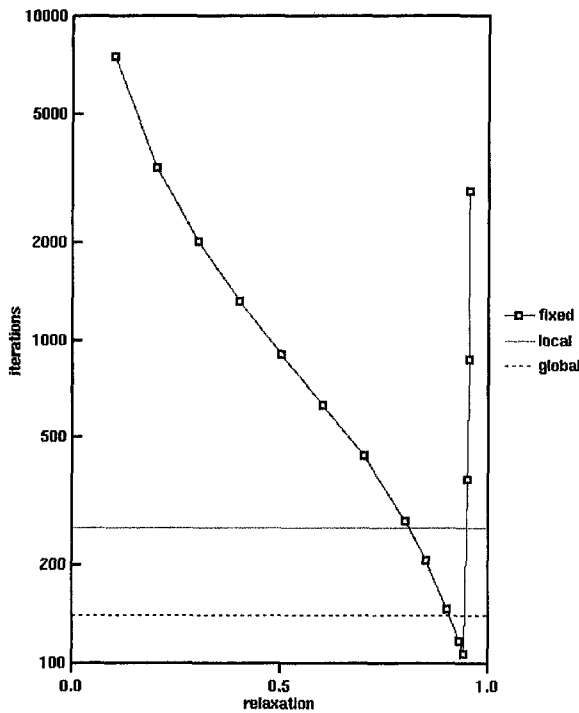


Fig. 2 Iterations required in buoyancy-driven cavity at $Ra = 10^5$

Results and Discussion

The solutions from the relaxation-factor-controlled computation and the fixed relaxation factor computation were compared with published results (Blackwell and Armaly, 1993; Elder, 1965; Schreiber and Keller, 1983). The results from the controlled and the uncontrolled cases are almost identically the same and match the published results well.

The controller achieved convergence for all cases tested. A summary of the number of iterations required for convergence using various constant relaxation factors is compared to that required using fuzzy control in Table 4. In general, the number of iterations using the controller was lower than that for most of the constant relaxation factor cases. A plot of the iterations required for convergence vs. the relaxation factor for a Rayleigh number of 10^5 is shown in Fig. 2.

Although it is possible for the user to select a constant relaxation factor that will outperform the controlled algorithm, it is generally not easy to do so especially in highly nonlinear cases. Furthermore, the danger of divergence is always present if relaxation factors are set too high, and the user may need to manually restart the code more than once with new lower relaxation factors. The results show that the locally-controlled case is sometimes better and sometimes worse than the globally controlled case.

There is a major disadvantage of the local controller in that it requires a substantial amount of CPU time to apply the rule set to every node on every iteration. Table 5 gives the CPU times for the buoyancy-driven case with $Gr = 10^6$. The local controller requires

Table 5 CPU time in $Gr = 10^6$ buoyancy-driven case

relaxation factor	CPU time
0.2	857.13
0.4	357.69
0.6	180.89
0.8	82.76
Global	54.45
Local	2643.95

more than ten times the CPU time for the global case is thus not practical.

This work can potentially be extended to the simulation of turbulence, radiation, or two-phase flow. Also, further study is needed to design a more optimal controller such as a neuro-fuzzy algorithm or a fuzzy controller optimized by a genetic algorithm.

References

- Bare, W. H., Mullholland, R. J., and Sofer, S. S., 1990, "Design of a Self-Tuning Rule Based Controller for a Gasoline Refinery Catalytic Reformer," *IEEE Trans Automat. Control*, Vol. 35, No. 2, pp. 156-164.
- Blackwell, B. F., and Armaly, B. F., 1993, "Benchmark Problem Definition and Summary of Computational Results for Mixed Convection Over a Backward Facing Step," HTD-Vol. 258, ASME, New York, pp. 1-10.
- Brandt, A., 1997, "Multi-Level Adaptive Solutions to Boundary-Value Problem," *Math. Comput.*, Vol. 31, No. 138, pp. 333-390.
- Cort, G. E., Graham, A. L., and Johnson, N. L., 1982, "Comparison of Methods for Solving Nonlinear Finite-Element Equations in Heat Transfer," ASME Paper No. 82-HT-40.
- Elder, J. W., 1965, "Laminar Free Convection in a Vertical Slot," *Journal of Fluid Mechanics*, Vol. 23, pp. 77-98.
- Iida, S., Ogawara, K., Furusawa, S., and Ohata, N., 1994, "A Fast Converging Method Using Wobbling Adaptive Control of SOR Relaxation Factor for 2D Benard Convection," *J. of Mechanical Engineering Society of Japan*, Vol. 7, pp. 168-174.
- Patankar, S. V., 1980, *Numerical Heat Transfer and Fluid Flow*, McGraw-Hill, New York.
- Ryoo, J., Kaminski, D., and Dragojlovic, Z., 1998, "Automatic Convergence in a Computational Fluid Dynamics Algorithm Using Fuzzy Logic," The Sixth Annual Conference of the Computational Fluid Dynamics Society of Canada, VIII.
- Saad, Y., and Schultz, M. H., 1986, "GMRES: A Generalized Minimum Residual Algorithm for Solving Nonsymmetric Linear Systems," *SIAM J. Sci. Stat. Comp.*, Vol. 7, No. 3, pp. 856-869.
- Schreiber, R., and Keller, H. B., 1983, "Driven Cavity Flows by Efficient Numerical Techniques," *J. of Computational Physics*, Vol. 49, pp. 310-333.
- Zade, L., 1965, "Fuzzy Sets," *Information and Control*, Vol. 8, pp. 338-358.

Analytical Solution of the Graetz Problem With Axial Conduction

J. Lahjomri¹ and A. Oubarra²

1 Introduction

The present investigation is concerned with a new method of an analysis and improved solution for the extended Graetz problem of heat transfer in a conduit. It is well known that the extended Graetz problem is defined when the axial heat conduction is included in the analysis and its effect becomes important at small Peclet numbers. For example, heat transfer in liquid metals: in general, the Graetz problem with axial conduction is treated by separating the domain of the conduit into two semi-infinite regions, an upstream region ($-\infty < x \leq 0$) and downstream region ($0 \leq x < +\infty$). The temperature field is then determined in both regions and the two solutions are matched at $x = 0$ where heating (or cooling) starts. Previous studies dealing with the extended Graetz problem have clearly shown that this type of problem is related to the

¹ To whom correspondence should be addressed. Assistant Professor, Département de Physique, groupe d'Energétique, Faculté des Sciences Ain Chock, Université Hassan II, Km 8 route El jadida, Maarif B. P. 5366, Casablanca, Morocco. e-mail: Lahjomri@facsc-achok.ac.ma.

² Professor, Département de Physique, groupe d'Energétique, Faculté des Sciences Ain Chock, Université Hassan II, Km 8 route El jadida, Maarif B. P. 5366, Casablanca, Morocco.

Contributed by the Heat Transfer Division for publication in the JOURNAL OF HEAT TRANSFER. Manuscript received by the Heat Transfer Division, Aug. 24, 1998; revision received, July 1, 1999. Keywords: Analytical, Entrance, Forced Convection, Heat Transfer, Laminar. Associate Technical Editor: R. Mahajan.

determination of the eigenvalues and the eigenfunctions of a Sturm-Liouville non-self-adjoint operator. So, the eigenfunctions are not orthogonal and are difficult to obtain. Consequently, a simple determination of the related expansion coefficients of the solution by classical methods fails. In order to remedy these difficulties, various elaborate mathematical techniques have been used to analyze the extended Graetz problem, such as Gram-Schmidt orthogonalization, asymptotic approach methods, collocation and variational methods, numerical methods, and the functional analysis method. An extensive list of contributions related to this problem may be found in the papers of Papoutsakis et al. (1980) and Liou and Wang (1990).

However, none of these previous studies give any explicit form of the exact nonorthogonal eigenfunctions and the related expansion coefficients. Furthermore, even for laminar conditions, no precise solution has hitherto been reported on the values of the local Nusselt number in the important thermal entrance region, precisely in the immediate neighborhood of $x = 0$. The main difficulty in the analysis comes from a singularity which exists for the conduit wall temperature at $x = 0$, which in general cause a problem for the numerical modelers. So, an analytical solution near the entrance is required to resolve the singularity.

In this paper we give the solution to the Graetz problem with axial conduction by the method of separation of variables with Dirichlet wall boundary conditions. Although the eigenfunctions are not orthogonal, we present a new general procedure for the direct determination of the expansion coefficients in their explicit forms and in terms of eigenfunctions with an arbitrary given fully developed velocity profile. The solution will be made for a cylindrical conduit and a parallel-plate channel and the results are obtained for the two geometries in the case of Hagen-Poiseuille flow. In this case, the eigenfunctions correspond to a confluent hypergeometric functions, which can be represented successfully by Tricomi's formula (1953). In addition, we show that the analytical solution proposed efficiently resolves the singularity and this methodology allows extension to other problems such as the Hartmann flow (Lahjomri et al., 1999), conjugated problems (Fithen and Anand, 1988) and other boundary conditions.

2 Mathematical Formulation and General Form of the Solution for Given Developed Velocity Profile

Consider a long cylindrical conduit and/or parallel-plate channel, and more precisely the part of the conduit for which the flow is laminar and fully developed with arbitrary velocity $u_x(r)$ (r transverse coordinate from center of conduit). The physical properties of the fluid are supposed to be constant. Viscous dissipation and free convection are negligible. The fluid enters with uniform temperature profile T_0 at abscissa $x = -\infty$ and attains a uniform temperature T_f at $x = +\infty$. The wall temperature is T_0 for $x \leq 0$ and T_f for $x > 0$. The dimensionless energy equation governing the field temperature is given by

$$\text{Pe } u(\eta) \frac{\partial \theta_i}{\partial X} = \frac{1}{\eta^p} \frac{\partial}{\partial \eta} \left(\eta^p \frac{\partial \theta_i}{\partial \eta} \right) + \frac{\partial^2 \theta_i}{\partial X^2}$$

for $\begin{cases} (i = 1, -\infty < X < 0) \\ (i = 2, 0 < X < +\infty) \end{cases}$ and $(0 < \eta < 1)$, (1)

in which the dimensionless variables and parameters are defined as follows:

$$X = \frac{x}{R}, \quad \eta = \frac{r}{R}, \quad \theta_i = \frac{T_i - T_f}{T_0 - T_f},$$

$$u(\eta) = \frac{u_x(r)}{U_{\max}}, \quad \text{Pe} = \frac{U_{\max} R}{\alpha}$$

where p denotes the plane ($p = 0$) or cylindrical ($p = 1$) geometry of a conduit and U_{\max} is the velocity in the center of the conduit. R is a radius of cylindrical or half-thickness between parallel-plate channels; Pe is the Peclet number, where α is the thermal diffusivity. The boundary conditions associated with (1) are well known:

$$\frac{\partial \theta_i}{\partial \eta} = 0 \quad \text{if } \eta = 0 \quad (i = 1, 2) \quad (2)$$

$$\theta_1 = 1 \quad \text{if } \eta = 1 \quad \forall X \leq 0 \quad (3)$$

$$\theta_2 = 0 \quad \text{if } \eta = 1 \quad \forall X > 0 \quad (4)$$

$$\theta_1 = 1 \quad \text{if } X \rightarrow -\infty \quad \forall 0 \leq \eta < 1 \quad (5)$$

$$\theta_2 = 0 \quad \text{if } X \rightarrow +\infty \quad \forall 0 \leq \eta < 1 \quad (6)$$

$$\theta_1 = \theta_2 \quad \text{and} \quad \frac{\partial \theta_1}{\partial X} = \frac{\partial \theta_2}{\partial X} \quad \text{if } X = 0 \quad \forall 0 \leq \eta < 1. \quad (7)$$

The general solution of elliptic Eq. (1) in the upstream and downstream region verifying the conditions (3), (4) and (5), (6), respectively, at the wall and at $X \rightarrow -\infty$ or $X \rightarrow +\infty$ can be represented by an infinite series of eigenfunctions given by

$$\theta_1(X, \eta) = 1 + \sum_{n=1}^{\infty} A_n f_n(\eta) \exp\left(\lambda_n^2 \frac{X}{\text{Pe}}\right) \quad \text{for } X \leq 0 \quad (8a)$$

$$\theta_2(X, \eta) = \sum_{n=1}^{\infty} B_n g_n(\eta) \exp\left(-\beta_n^2 \frac{X}{\text{Pe}}\right) \quad \text{for } X > 0, \quad (8b)$$

where λ_n and β_n designate the real eigenvalues associated with, respectively, the eigenfunctions f_n and g_n . A_n and B_n are the constants of integration. The eigenfunctions f_n and g_n are solutions of the following differential equations:

$$\frac{d}{d\eta} \left(\eta^p \frac{df_n}{d\eta} \right) + \lambda_n^2 \left[\frac{\lambda_n^2}{\text{Pe}^2} - u(\eta) \right] \eta^p f_n = 0 \quad (9)$$

$$\frac{d}{d\eta} \left(\eta^p \frac{dg_n}{d\eta} \right) + \beta_n^2 \left[\frac{\beta_n^2}{\text{Pe}^2} + u(\eta) \right] \eta^p g_n = 0, \quad (10)$$

satisfying the boundary conditions

$$f_n'(0) = 0 \quad \text{and} \quad f_n(1) = 0 \quad (11a)$$

$$g_n'(0) = 0 \quad \text{and} \quad g_n(1) = 0. \quad (11b)$$

The fundamental problem is then to determine the eigenvalues λ_n , β_n and the coefficients A_n , B_n . From the boundary condition (11) the eigenvalues λ_n and β_n must be roots of the characteristics equations $f_n(1) = 0$ and $g_n(1) = 0$. Substituting the solutions (8a), (8b) into Eqs. (7), which represent the continuity of temperature and its first derivative at the junction $X = 0$, we obtain the following equations, with unknown constants A_n and B_n :

$$1 + \sum_{n=1}^{\infty} A_n f_n(\eta) = \sum_{n=1}^{\infty} B_n g_n(\eta) \quad (12a)$$

$$\sum_{n=1}^{\infty} \lambda_n^2 A_n f_n(\eta) = - \sum_{n=1}^{\infty} \beta_n^2 B_n g_n(\eta). \quad (12b)$$

The eigenfunctions f_n and g_n defined by the Eqs. (9)–(11) are not mutually orthogonal by referring to the standard Sturm-Liouville problem since the eigenvalues occur nonlinearly in (9) and (10). However, if Eq. (12a) is multiplied by $[(\beta_n^2/\text{Pe}^2) + u(\eta)] \eta^p g_m$ and integrated from 0 to 1 with respect to η , then

$$\int_0^1 \left[\frac{\beta_m^2}{\text{Pe}^2} + u(\eta) \right] \eta^p g_m d\eta = B_m \int_0^1 \left[\frac{\beta_m^2}{\text{Pe}^2} + u(\eta) \right] \eta^p g_m^2 d\eta$$

$$+ \sum_{n=1}^{\infty} A_n \int_0^1 \left[-\frac{\beta_m^2}{\text{Pe}^2} - u(\eta) \right] \eta^p g_m f_n d\eta$$

$$+ \sum_{(n \neq m)}^{\infty} B_n \int_0^1 \left[\frac{\beta_m^2}{\text{Pe}^2} + u(\eta) \right] \eta^p g_m g_n d\eta. \quad (13)$$

Using the fact that the function g_n satisfies the following property:

$$\int_0^1 \left[\frac{\beta_n^2 + \beta_m^2}{\text{Pe}^2} + u(\eta) \right] \eta^p g_m g_n d\eta \begin{cases} = 0 & \text{if } \beta_m \neq \beta_n \\ \neq 0 & \text{if } \beta_m = \beta_n, \end{cases} \quad (14)$$

obtained easily from the differential Eq. (10) and boundary condition. (11b), the integral in the last term of second member of Eq. (13) can be rewritten and Eq. (13) becomes

$$\int_0^1 \left[\frac{\beta_m^2}{\text{Pe}^2} + u(\eta) \right] \eta^p g_m d\eta = B_m \int_0^1 \left[\frac{\beta_m^2}{\text{Pe}^2} + u(\eta) \right] \eta^p g_m^2 d\eta$$

$$+ \sum_{n=1}^{\infty} A_n \int_0^1 \left[-\frac{\beta_m^2}{\text{Pe}^2} - u(\eta) \right] \eta^p g_m f_n d\eta$$

$$- \sum_{(n \neq m)}^{\infty} B_n \frac{\beta_n^2}{\text{Pe}^2} \int_0^1 \eta^p g_m g_n d\eta. \quad (15)$$

And from Eq. (12b), by multiplying both terms by $(\eta^p g_m / \text{Pe}^2)$ and integrating from 0 to 1 with respect to η we have

$$- \sum_{n=1}^{\infty} B_n \frac{\beta_n^2}{\text{Pe}^2} \int_0^1 \eta^p g_m g_n d\eta = \sum_{n=1}^{\infty} A_n \frac{\lambda_n^2}{\text{Pe}^2} \int_0^1 \eta^p g_m f_n d\eta. \quad (16)$$

After some manipulation, Eq. (15) takes the following form by using (16):

$$\int_0^1 \left[\frac{\beta_m^2}{\text{Pe}^2} + u(\eta) \right] \eta^p g_m d\eta = B_m \int_0^1 \left[\frac{2\beta_m^2}{\text{Pe}^2} + u(\eta) \right] \eta^p g_m^2 d\eta$$

$$+ \sum_{n=1}^{\infty} A_n F_{n,m}, \quad (17)$$

with $F_{n,m} = \int_0^1 [(\lambda_n^2 - \beta_m^2) / \text{Pe}^2 - u(\eta)] \eta^p g_m f_n d\eta$. The previous technique can be used, by multiplying this time Eq. (12a) by $[(\lambda_m^2 / \text{Pe}^2) - u(\eta)] \eta^p f_m$ and also using the similar property to (14) verified by the functions f_n . We can obtain a second equation in A_m and B_n :

$$\int_0^1 \left[\frac{\lambda_m^2}{\text{Pe}^2} - u(\eta) \right] \eta^p f_m d\eta = -A_m \int_0^1 \left[\frac{2\lambda_m^2}{\text{Pe}^2} - u(\eta) \right] \eta^p f_m^2 d\eta$$

$$+ \sum_{n=1}^{\infty} B_n F_{m,n}. \quad (18)$$

It is easy to show that the integrals $F_{n,m}$ and $F_{m,n}$ are zero for any m and n . Indeed, if we consider two solutions f_n and g_m of the Eqs. (9) and (10) and multiply the first by g_m and the second by f_n , and then subtracting and integrating by parts, we obtain

$$g_m(1)f_n'(1) - f_n(1)g_m'(1) + (\lambda_n^2 + \beta_m^2)F_{n,m} = 0, \quad (19)$$

and in the same way, we can show that

$$g_n(1)f_m'(1) - f_m(1)g_n'(1) + (\lambda_m^2 + \beta_n^2)F_{m,n} = 0. \quad (20)$$

All of this shows that by using the boundary conditions (11a) and (11b), the integrals $F_{n,m}$ and $F_{m,n}$ vanish for any n and m . Finally, from (17) and (18) we obtain the expressions of the constants A_n and B_n as ratios of two integrals:

$$A_n = - \frac{\int_0^1 \left[\frac{\lambda_n^2}{\text{Pe}^2} - u(\eta) \right] \eta^p f_n d\eta}{\int_0^1 \left[\frac{2\lambda_n^2}{\text{Pe}^2} - u(\eta) \right] \eta^p f_n^2 d\eta} = - \frac{2}{\lambda_n \left. \frac{\partial f_n(1)}{\partial \lambda} \right|_{\lambda=\lambda_n}} \quad (21a)$$

$$B_n = \frac{\int_0^1 \left[\frac{\beta_n^2}{\text{Pe}^2} + u(\eta) \right] \eta^p g_n d\eta}{\int_0^1 \left[\frac{2\beta_n^2}{\text{Pe}^2} + u(\eta) \right] \eta^p g_n^2 d\eta} = - \frac{2}{\beta_n \left. \frac{\partial g_n(1)}{\partial \beta} \right|_{\beta=\beta_n}}. \quad (21b)$$

The dimensionless bulk temperature $\theta_{b,i}(X)$ and the local Nusselt number $\text{Nu}_i(X)$ (constructed by hydraulic radius) can now be defined and obtained:

$$\theta_{b,i}(X) = \frac{\int_0^1 \eta^p u(\eta) \theta_i d\eta}{\int_0^1 \eta^p u(\eta) d\eta},$$

$$\text{Nu}_i = - \frac{2^{2-p} \left. \frac{\partial \theta_i}{\partial \eta} \right|_{\eta=1}}{\theta_{b,i} - \theta_i(\eta=1)} \quad (i = 1, 2). \quad (22)$$

Substituting Eq. (8b) into Eqs. (22) by using Eq. (10), we can deduct the expression of the local Nusselt number $\text{Nu}_2(X) = \text{Nu}(X)$ in the downstream region for the two geometries:

$$\text{Nu}(X) = \frac{2^{3-p} \sum_{n=1}^{\infty} B_n g_n'(1) \exp\left(-\beta_n^2 \frac{X}{\text{Pe}}\right)}{(p+1)(p+3) \sum_{n=1}^{\infty} B_n \exp\left(-\beta_n^2 \frac{X}{\text{Pe}}\right) \left[\frac{g_n'(1)}{\beta_n^2} + \frac{\beta_n^2}{\text{Pe}^2} \int_0^1 \eta^p g_n(\eta) d\eta \right]} \quad \text{if } X > 0. \quad (23)$$

3 Application to Hagen-Poiseuille Flow

In the case of Hagen-Poiseuille flow, the velocity profile is parabolic, $u(\eta) = 1 - \eta^2$. The eigenfunctions f_n and g_n solutions of Eqs. (9), (10) can be expressed in terms of the confluent hypergeometric functions $\Phi(a, b; z)$ as follows:

$$g_n(\eta) = \exp\left(-\frac{\beta_n \eta^2}{2}\right) \Phi(\alpha_n, c; \beta_n \eta^2), \quad (24a)$$

$$f_n(\eta) = \exp\left(-\frac{i\lambda_n \eta^2}{2}\right) \Phi(a_n, c; i\lambda_n \eta^2), \quad (24b)$$

with $\alpha_n = (c/2) - (\beta_n/4) - (\beta_n^3/4Pe^2)$, $a_n = (c/2) - (i\lambda_n/4) + (i\lambda_n^3/4Pe^2)$ and $c = (1 + p)/2$; ($i^2 = -1$). Using Tricomi's formula each of the eigenfunctions f_n and g_n can be represented explicitly in the entire complex plane by a uniformly convergent infinite series expansions in terms of Bessel functions:

$$f_n(\eta) = \begin{cases} \Gamma(c)(h_n \lambda_n)^{(1-c)/2} \sum_{m=0}^{\infty} E_m \eta^{m+1-c} \left(\frac{\lambda_n}{4h_n}\right)^{(m/2)} J_{c-1+m}[2\sqrt{h_n \lambda_n} \eta] & \text{if } |\lambda_n| > Pe \\ \Gamma(c)(-h_n \lambda_n)^{(1-c)/2} \sum_{m=0}^{\infty} E_m \eta^{m+1-c} \left(-\frac{\lambda_n}{4h_n}\right)^{(m/2)} I_{c-1+m}[2\sqrt{-h_n \lambda_n} \eta] & \text{if } |\lambda_n| < Pe \\ 2^{c-1} \Gamma\left(\frac{c+1}{2}\right) \lambda_n^{(1-c)/2} \eta^{1-c} J_{(c-1)/2}\left(\frac{\lambda_n \eta^2}{2}\right) & \text{if } |\lambda_n| = Pe \end{cases} \quad (25)$$

$$g_n(\eta) = \Gamma(c)(k_n \beta_n)^{(1-c)/2} \sum_{m=0}^{\infty} D_m \eta^{m+1-c} \left(\frac{\beta_n}{4k_n}\right)^{(m/2)} \times J_{c-1+m}[2\sqrt{k_n \beta_n} \eta] \quad \forall \beta_n \quad (26)$$

with $h_n = i((c/2) - a_n)$, $k_n = (c/2) - \alpha_n$, where $\Gamma(x)$ is the gamma function, J_ν and I_ν are, respectively, the Bessel function and modified Bessel function of the first kind. The coefficients E_m and D_m verify the following recurrence relations:

$$\begin{cases} E_0 = 1, E_1 = 0, E_2 = -\frac{c}{2} \\ (m+1)E_{m+1} = -(m+c-1)E_{m-1} + 2h_n E_{m-2} \quad (m=2, 3, 4, \dots) \end{cases} \quad (27a)$$

$$\begin{cases} D_0 = 1, D_1 = 0, D_2 = \frac{c}{2} \\ (m+1)D_{m+1} = (m+c-1)D_{m-1} - 2k_n D_{m-2} \quad (m=2, 3, 4, \dots) \end{cases} \quad (27b)$$

Note that for sufficiently large values of the eigenvalues, the asymptotic eigenfunctions and the temperature derivative at the wall also exist as in the classical Graetz problem and may be given

by the so-called WKB approximations which give good results for $n \geq 5$. However, the asymptotic eigenvalues could not be obtained explicitly as in the case of no axial conduction because the characteristic Eqs. (11a), (11b) remain transcendental for the finite value of the Peclet number. Such asymptotic formulas were not used in this present study, since computation times needed for evaluating the more general expressions were reasonably small.

4 Results and Discussion

The eigenvalues λ_n , β_n and the important constants have been numerically computed with very high accuracy. Note that the infinite series (8a) and (8b) converge very slowly near $X = 0$ and require a very high number of terms, especially for low values of Peclet number. This difficulty is due to a slow decrease of the expansion coefficients A_n and B_n of the series. In this study, we have calculated the temperature profiles and the local Nusselt number using 1000 terms in Eqs. (8a), (8b), and (23). This allows a satisfactory convergence and a good matching at $X = 0$ for the temperature and its longitudinal gradient between upstream and

downstream region where their comparison can be used as convergence verification. For example, for a parallel-plate channel at $X = 0$, the relative error between temperature in the upstream and downstream region is of the order of 0.04 percent at $\eta = 0; 0.24$

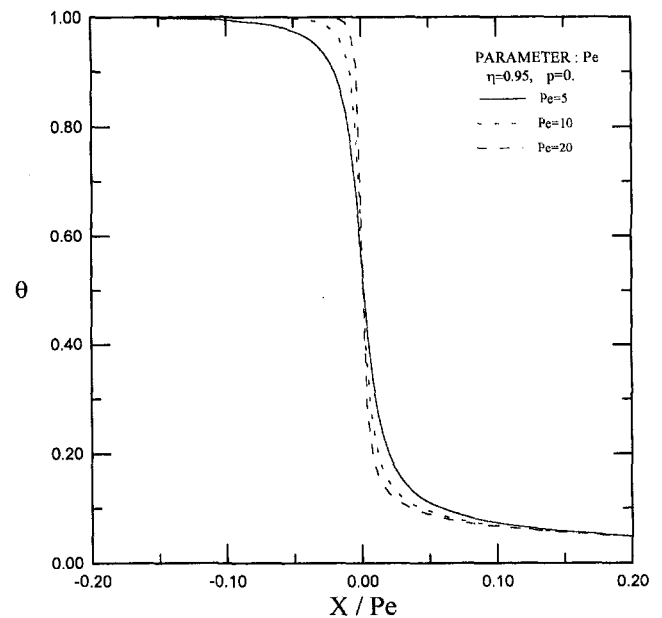


Fig. 1 Axial profiles of dimensionless temperature for various values of Peclet number in the case of a parallel-plate channel ($p = 0$) at radial position $\eta = 0.95$

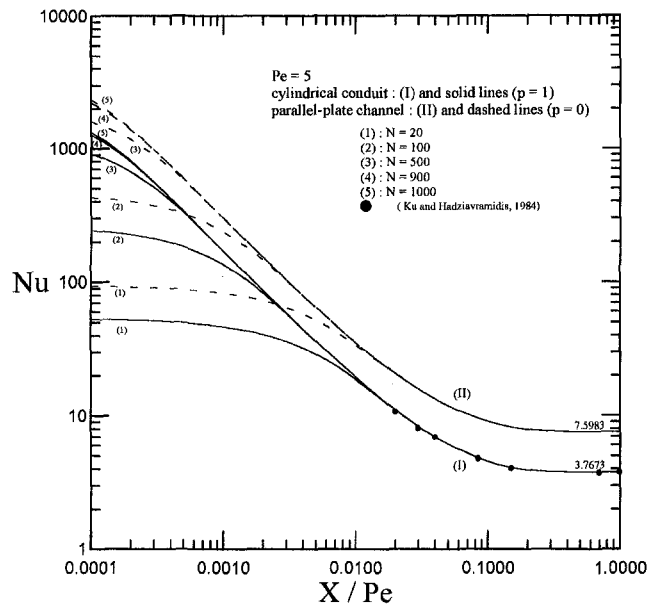


Fig. 2 Effect of different truncation orders N on the accuracy of a local Nusselt number for $Pe = 5$, in the case of a cylindrical conduit ($p = 1$) and a parallel-plate channel ($p = 0$) and comparison with the results of Ku and Hadziavramidis (1984)

percent at $\eta = 0.5$ and 0.8 percent at $\eta = 0.95$ for $Pe = 5$, with 1000 eigenvalues. These relative errors increase markedly and show poor matching if only a few terms are considered (e.g., for 20 terms, relative errors are: 1.68 percent at $\eta = 0$; 2.6 percent at $\eta = 0.5$, and 28 percent at $\eta = 0.95$). Note that when Peclet number increases the relative errors decrease more and more, and the matching processes improved with the same number of terms. Therefore, to obtain an improved solution, we must take into account a higher number of eigenvalues, especially for the lower Peclet numbers. Figure 1 represents the axial dimensionless temperature profiles (computed with 1000 eigenvalues) for a parallel-plate channel at $\eta = 0.95$ close to a discontinuity of the temperature at the wall, for three values of the Peclet number $Pe = 5, 10$, and 20. It clearly shows that the profiles in the upstream and downstream regions match each other very well at $X = 0$ (near singularity) and our analytical solution proves to be efficient in resolving singularity. Figure 2 shows the evolution of the local Nusselt number versus the axial distance X/Pe , for a cylindrical conduit ($p = 1$) and for a parallel-plate channel ($p = 0$) and $Pe = 5$. This figure illustrates the effect of different truncation orders N of the series in Eq. (23) on the accuracy of local Nusselt number. The curves of different values of N indicate the improved convergence level of the local Nusselt number. Clearly, the accuracy or relative error of Nusselt number is improved and convergence is achieved with a very high number of terms and requiring an increasing in N as X/Pe is decreased (i.e., $N \approx 950$ terms around $X/Pe = 10^{-4}$ for $Pe = 5$). Relative errors (between curve 5 and curves 1–4) are, for example, for the cylindrical conduit, around $X/Pe = 10^{-4}$, of the order of four percent for $N = 900$, 31 percent for $N = 500$, and 96 percent for the choice of $N = 20$ terms. Similar trends can be observed for the parallel-plate channel. The choice of 20 terms, for example, in evaluating the Graetz series, causes considerable error and yields erroneous results in the prediction of local Nusselt number near $X = 0$, and this choice is therefore recommended only for axial distance great than 10^{-2} . For increasing X/Pe the error drops down markedly and all curves merge together for $X/Pe > 10^{-2}$. Figure 2 also shows a comparison of the local Nusselt number, obtained in the present work with results of Ku and Hadziavramidis (1984), for the cylindrical conduit, obtained numerically from Chebyshev element method and given only for $X/Pe > 10^{-2}$. Clearly our results are in agreement

with data of these authors in this region of axial distances. The data of the literature were given only for $X/Pe > 10^{-2}$, (for example, Verhoff and Fisher (1973) and others).

Notice that for very large values of the Peclet number, recently Housiadas et al. (1999) treated the particular case of the problem without axial conduction (classical Graetz problem) for the cylindrical conduit. These authors used a combination of two formulas for evaluating the eigenfunctions nonasymptotically in the interval $0 < \eta < 1$, up to order $N = 40$: series expansions in terms of Bessel functions over the interval $0 < \eta \leq 0.863$; series expansions in terms of the power of η over the interval $0.863 < \eta < 1$ and used the asymptotic formula for large values of N ($40 < N \leq 125$). The series expansions in terms of Bessel functions used by Housiadas et al. correspond to a particular case ($p = 1$ or $c = 1$ and $Pe \rightarrow \infty$) of Tricomi's formula given by Eq. (26). The numerical experiment shows that this formula becomes inaccurate, especially for large values of order N ($N \geq 25$). This is in agreement with Housiadas et al.

However, there exists another (second) Tricomi's formula (1953) which is more appropriate for a large Peclet number and large N . This formula has the advantage to represent the eigenfunctions in the whole interval $0 \leq \eta \leq 1$ without using the asymptotic formula, while Housiadas et al. used a combination of three formulas for evaluating their eigenfunctions in this interval.

The results obtained for the local Nusselt number computed from the second Tricomi's formula in the case of the Graetz problem without axial conduction (for cylindrical conduit), are given in Fig. 3. This figure shows the effect of different truncation orders ($N = 20, 50, 100$, and 200) of the series on the accuracy of the local Nusselt number. It is clear that with increasing N the accuracy of the calculation increases, and only 50 terms are required for attaining convergence around $X/Pe = 10^{-4}$ and 100 terms around 10^{-3} (curves 3 and 4). In Fig. 3 the local Nusselt numbers are compared with those of Kays and Crawford (1980) and are in agreement in the interval given by these authors ($X/Pe \geq 10^{-3}$).

5 Conclusion

The solution presented here has the advantage over numerical methods by efficiently resolving singularity. This is clearly demonstrated by our results obtained in the neighborhood of $X = 0$

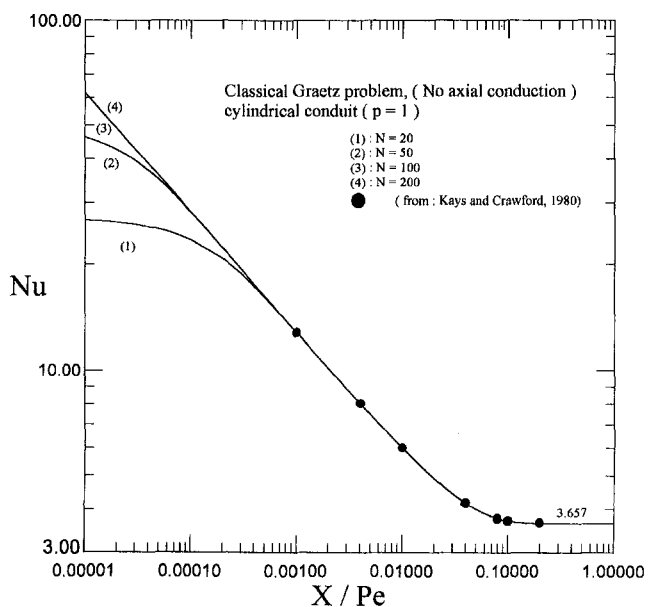


Fig. 3 Effect of different truncation orders N on the accuracy of a local Nusselt number for a cylindrical conduit in the case of a classical Graetz problem and comparison with the data of Kays and Crawford (1980)

(Figs. 1–3) where singularity causes a big problem (Gibbs oscillations) for numerical modelers when evaluating the axial temperature derivatives (Ku and Hatzivramidis, 1984). Furthermore, the method can be applied to other problems, such as the Hartmann flow of liquid metal in magnetohydrodynamics with a prescribed external uniform magnetic field. In this situation the eigenfunctions correspond to Mathieu's functions (Lahjomri et al., 1999). The treatment is given here for the Dirichlet wall boundary condition, but it can be extended easily to other boundary conditions, such as the Neumann or Robin boundary conditions. In these cases the explicit form of the expansion coefficients can be also obtained.

References

- Fithen, R. M., and Anand, N. K., 1988, "Finite Element Analysis of Conjugate Heat Transfer in Axisymmetric Pipe Flows," *Numerical Heat Transfer*, Vol. 13, pp. 189–203.
- Housiadas, C., Larrodé, F. E., and Drosinos, Y., 1999, "Numerical Evaluation of the Graetz Series," *Int. Journal Heat Mass Transfer*, Vol. 42, pp. 3013–3017.
- Kays, W. M., and Crawford, M. E., 1980, *Convective Heat and Mass Transfer*, 2nd Ed., McGraw-Hill, New York, p. 111.
- Ku, H. C., and Hatzivramidis, D., 1984, "Chebyshev Expansion Methods for the Solution of the Extended Graetz Problem," *Journal of Comput. Physics*, Vol. 56, pp. 495–512.
- Lahjomri, J., Oubarra, A., and Alemany, A., 1999, "Solution of the Extended Graetz Problem With Applied Magnetic Field," to be submitted.
- Liou, C. T., and Wang, F. S., 1990, "A Computation for the Boundary Value Problem of a Double Tube Heat Exchanger," *Numerical Heat Transfer*, Part A, Vol. 17, pp. 109–125.
- Magnus, W., Oberhettinger, F., and Tricomi, F. G., 1953, *Higher Transcendental Functions*, Vol. 1, A. Erdelyi, ed., McGraw-Hill, New York, Chapter 6, pp. 276–277.
- Papoutsakis, E., Damkrishna, D., and Lim, H. C., 1980, "The Extended Graetz Problem With Dirichlet Wall Boundary Conditions," *Appl. Sci. Research*, Vol. 36, pp. 13–34.
- Verhoff, F. H., and Fisher, D. P., 1973, "A Numerical Solution of the Graetz Problem With Axial Conduction," *ASME JOURNAL OF HEAT TRANSFER*, Vol. 95, pp. 132–134.

Nusselt Numbers in Rectangular Ducts With Laminar Viscous Dissipation

G. L. Morini¹ and M. Spiga²

In this paper, the steady temperature distribution and the Nusselt numbers are analytically determined for a Newtonian incompressible fluid in a rectangular duct, in fully developed laminar flow with viscous dissipation, for any combination of heated and adiabatic sides of the duct, in H1 boundary condition, and neglecting the axial heat conduction in the fluid. The Navier-Stokes and the energy balance equations are solved using the technique of the finite integral transforms. For a duct with four uniformly heated sides (4 version), the temperature distribution and the Nusselt numbers are obtained as a function of the aspect ratio and of the Brinkman number and presented in graphs and tables. Finally it is proved that the temperature field in a fully developed T boundary condition can be obtained as a particular case of the H1 problem

¹ Dipartimento di Ingegneria, Facoltà di Ingegneria, Università di Ferrara, Via Saragat 1, 44100 Ferrara, Italy.

² DIENCA, Facoltà di Ingegneria, Università di Bologna, Viale Risorgimento 2, 40136, Bologna, Italy.

Contributed by the Heat Transfer Division for publication in the JOURNAL OF HEAT TRANSFER. Manuscript received by the Heat Transfer Division, Oct. 10, 1998; revision received, May 26, 1999. Keywords: Channel Flow, Forced Convection, Heat Transfer, Laminar, Viscous. Associate Technical Editor: D. Kaminski.

and that the corresponding Nusselt numbers do not depend on the Brinkman number.

Nomenclature

- a, b = longer and shorter sides, respectively, of the rectangular cross section, m
- Br = Brinkman number referred to the wall linear power $\mu W^2/q_w$
- c_p = specific heat, J/kgK
- D_h = hydraulic diameter of the duct $2ab/(a + b)$, m
- h = heat transfer coefficient, W/m²K
- k = fluid thermal conductivity, W/mK
- m, n = summation integer indices
- Nu = Nusselt number hD/k
- p = pressure, Pa
- P = dimensionless heated perimeter
- Pe = Peclet number WD/α
- q = total thermal power per unit length, W/m
- q_s = thermal power per unit length generated by viscous dissipation, W/m
- q_w = thermal power per unit length transferred to the walls, W/m
- $T(\cdot)$ = dimensionless fluid temperature
- $u(\cdot)$ = fluid velocity, m/s
- $V(\cdot)$ = dimensionless fluid velocity
- W = fluid average velocity, m/s
- x, y, z = dimensionless Cartesian coordinate

Greek Symbols

- α = fluid thermal diffusivity, m²/s
- β = aspect ratio $b/a < 1$
- λ = eigenvalue
- Φ^* = dimensionless function defined by Eq. (5)
- μ = fluid viscosity, Pa s
- Ψ = eigenfunction
- ρ = fluid density, kg/m³
- $\theta(\cdot)$ = fluid temperature, K
- ξ, η, ζ = Cartesian coordinate, m

Subscripts

- b = bulk quantity
- w = evaluated to the wall

Introduction

The need for high thermal performance has stimulated the use of rectangular ducts in a wide variety of compact heat exchangers, mainly in tube-fin and plate-fin exchangers, in order to obtain an enhancement in heat transfer, with the same cross-sectional area of the duct. The small hydraulic diameter and the use of viscous liquids make the flow laminar and fully developed in many industrial applications. Laminar fully developed flow through rectangular ducts has been extensively investigated in the last decades as reviewed by Shah and London (1978). Compared to the circular pipe flow, the theoretical analysis of rectangular geometry requires a complicated two-dimensional approach. The thermal boundary conditions, too, are complex, because there are many combinations for imposing different temperatures or heat fluxes on the four wetted sides (Shah and London, 1974). The most common boundary conditions, for practical applications, are the well-known T and H1 conditions. For the former, the wall temperature is constant both peripherally and axially. This situation occurs in many practical applications, such as condensers, evaporators, and automotive radiators with high liquid flow rates, with negligible wall thermal resistance. On the other hand, in heated ducts with highly conductive materials (e.g., copper, aluminium) it is more appropriate to consider the H1 condition (constant axial wall heat flux and constant wall temperature on the cross section). Moreover, many

(Figs. 1–3) where singularity causes a big problem (Gibbs oscillations) for numerical modelers when evaluating the axial temperature derivatives (Ku and Hatzivramidis, 1984). Furthermore, the method can be applied to other problems, such as the Hartmann flow of liquid metal in magnetohydrodynamics with a prescribed an external uniform magnetic field. In this situation the eigenfunctions correspond to Mathieu's functions (Lahjomri et al., 1999). The treatment is given here for the Dirichlet wall boundary condition, but it can be extended easily to other boundary conditions, such as the Neumann or Robin boundary conditions. In these cases the explicit form of the expansion coefficients can be also obtained.

References

- Fithen, R. M., and Anand, N. K., 1988, "Finite Element Analysis of Conjugate Heat Transfer in Axisymmetric Pipe Flows," *Numerical Heat Transfer*, Vol. 13, pp. 189–203.
- Housiadas, C., Larrodé, F. E., and Drosinos, Y., 1999, "Numerical Evaluation of the Graetz Series," *Int. Journal Heat Mass Transfer*, Vol. 42, pp. 3013–3017.
- Kays, W. M., and Crawford, M. E., 1980, *Convective Heat and Mass Transfer*, 2nd Ed., McGraw-Hill, New York, p. 111.
- Ku, H. C., and Hatzivramidis, D., 1984, "Chebyshev Expansion Methods for the Solution of the Extended Graetz Problem," *Journal of Comput. Physics*, Vol. 56, pp. 495–512.
- Lahjomri, J., Oubarra, A., and Alemany, A., 1999, "Solution of the Extended Graetz Problem With Applied Magnetic Field," to be submitted.
- Liou, C. T., and Wang, F. S., 1990, "A Computation for the Boundary Value Problem of a Double Tube Heat Exchanger," *Numerical Heat Transfer*, Part A, Vol. 17, pp. 109–125.
- Magnus, W., Oberhettinger, F., and Tricomi, F. G., 1953, *Higher Transcendental Functions*, Vol. 1, A. Erdelyi, ed., McGraw-Hill, New York, Chapter 6, pp. 276–277.
- Papoutsakis, E., Damkrishna, D., and Lim, H. C., 1980, "The Extended Graetz Problem With Dirichlet Wall Boundary Conditions," *Appl. Sci. Research*, Vol. 36, pp. 13–34.
- Verhoff, F. H., and Fisher, D. P., 1973, "A Numerical Solution of the Graetz Problem With Axial Conduction," *ASME JOURNAL OF HEAT TRANSFER*, Vol. 95, pp. 132–134.

Nusselt Numbers in Rectangular Ducts With Laminar Viscous Dissipation

G. L. Morini¹ and M. Spiga²

In this paper, the steady temperature distribution and the Nusselt numbers are analytically determined for a Newtonian incompressible fluid in a rectangular duct, in fully developed laminar flow with viscous dissipation, for any combination of heated and adiabatic sides of the duct, in H1 boundary condition, and neglecting the axial heat conduction in the fluid. The Navier-Stokes and the energy balance equations are solved using the technique of the finite integral transforms. For a duct with four uniformly heated sides (4 version), the temperature distribution and the Nusselt numbers are obtained as a function of the aspect ratio and of the Brinkman number and presented in graphs and tables. Finally it is proved that the temperature field in a fully developed T boundary condition can be obtained as a particular case of the H1 problem

¹ Dipartimento di Ingegneria, Facoltà di Ingegneria, Università di Ferrara, Via Saragat 1, 44100 Ferrara, Italy.

² DIENCA, Facoltà di Ingegneria, Università di Bologna, Viale Risorgimento 2, 40136, Bologna, Italy.

Contributed by the Heat Transfer Division for publication in the JOURNAL OF HEAT TRANSFER. Manuscript received by the Heat Transfer Division, Oct. 10, 1998; revision received, May 26, 1999. Keywords: Channel Flow, Forced Convection, Heat Transfer, Laminar, Viscous. Associate Technical Editor: D. Kaminski.

and that the corresponding Nusselt numbers do not depend on the Brinkman number.

Nomenclature

- a, b = longer and shorter sides, respectively, of the rectangular cross section, m
- Br = Brinkman number referred to the wall linear power $\mu W^2/q_w$
- c_p = specific heat, J/kgK
- D_h = hydraulic diameter of the duct $2ab/(a + b)$, m
- h = heat transfer coefficient, W/m²K
- k = fluid thermal conductivity, W/mK
- m, n = summation integer indices
- Nu = Nusselt number hD/k
- p = pressure, Pa
- P = dimensionless heated perimeter
- Pe = Peclet number WD/α
- q = total thermal power per unit length, W/m
- q_s = thermal power per unit length generated by viscous dissipation, W/m
- q_w = thermal power per unit length transferred to the walls, W/m
- $T(\cdot)$ = dimensionless fluid temperature
- $u(\cdot)$ = fluid velocity, m/s
- $V(\cdot)$ = dimensionless fluid velocity
- W = fluid average velocity, m/s
- x, y, z = dimensionless Cartesian coordinate

Greek Symbols

- α = fluid thermal diffusivity, m²/s
- β = aspect ratio $b/a < 1$
- λ = eigenvalue
- Φ^* = dimensionless function defined by Eq. (5)
- μ = fluid viscosity, Pa s
- Ψ = eigenfunction
- ρ = fluid density, kg/m³
- $\theta(\cdot)$ = fluid temperature, K
- ξ, η, ζ = Cartesian coordinate, m

Subscripts

- b = bulk quantity
- w = evaluated to the wall

Introduction

The need for high thermal performance has stimulated the use of rectangular ducts in a wide variety of compact heat exchangers, mainly in tube-fin and plate-fin exchangers, in order to obtain an enhancement in heat transfer, with the same cross-sectional area of the duct. The small hydraulic diameter and the use of viscous liquids make the flow laminar and fully developed in many industrial applications. Laminar fully developed flow through rectangular ducts has been extensively investigated in the last decades as reviewed by Shah and London (1978). Compared to the circular pipe flow, the theoretical analysis of rectangular geometry requires a complicated two-dimensional approach. The thermal boundary conditions, too, are complex, because there are many combinations for imposing different temperatures or heat fluxes on the four wetted sides (Shah and London, 1974). The most common boundary conditions, for practical applications, are the well-known T and H1 conditions. For the former, the wall temperature is constant both peripherally and axially. This situation occurs in many practical applications, such as condensers, evaporators, and automotive radiators with high liquid flow rates, with negligible wall thermal resistance. On the other hand, in heated ducts with highly conductive materials (e.g., copper, aluminium) it is more appropriate to consider the H1 condition (constant axial wall heat flux and constant wall temperature on the cross section). Moreover, many

Table 1 Eigenvalues and eigenfunctions for any version of the H1 problem

Version	$\lambda_{x,n}^2$	$\lambda_{y,m}^2$	$\psi_{x,n}$	$\psi_{y,m}$
1L	$n^2\pi^2$	$(2m-1)^2 \frac{\pi^2}{4\beta^2}$	$\cos(\lambda_{x,n}x)$	$\sin(\lambda_{y,m}y)$
1S	$(2n-1)^2 \frac{\pi^2}{4}$	$\frac{m^2\pi^2}{\beta^2}$	$\sin(\lambda_{x,n}x)$	$\cos(\lambda_{y,m}y)$
2L	$n^2\pi^2$	$\frac{m^2\pi^2}{\beta^2}$	$\cos(\lambda_{x,n}x)$	$\sin(\lambda_{y,m}y)$
2S	$n^2\pi^2$	$\frac{m^2\pi^2}{\beta^2}$	$\sin(\lambda_{x,n}x)$	$\cos(\lambda_{y,m}y)$
2C	$(2n-1)^2 \frac{\pi^2}{4}$	$(2m-1)^2 \frac{\pi^2}{4\beta^2}$	$\sin(\lambda_{x,n}x)$	$\sin(\lambda_{y,m}y)$
3L	$(2n-1)^2 \frac{\pi^2}{4}$	$\frac{m^2\pi^2}{\beta^2}$	$\sin(\lambda_{x,n}x)$	$\sin(\lambda_{y,m}y)$
3S	$n^2\pi^2$	$(2m-1)^2 \frac{\pi^2}{4\beta^2}$	$\sin(\lambda_{x,n}x)$	$\sin(\lambda_{y,m}y)$
4	$n^2\pi^2$	$\frac{m^2\pi^2}{\beta^2}$	$\sin(\lambda_{x,n}x)$	$\sin(\lambda_{y,m}y)$

different situations can be considered, assuming different conditions for every side of the rectangle; in the literature, eight classic thermal versions are proposed for the T, H1 problems. For any boundary condition, extensive numerical, analytical, and experimental studies have been carried out by many authors (Chandrupatla et al., 1977; Schmidt and Newell, 1967; Marco and Han, 1955) but always neglecting the effect of the viscous dissipation. In fact, the shear stresses can induce a relevant power generation due to viscous dissipation. This phenomenon is particularly important in flows in microtubes in the polymer industry (in extrusion and injection processes), and also in radiator design where the working fluid are highly viscous oils. The effects of viscous dissipation in laminar flows have not yet been deeply investigated; some papers analyse T and H1 boundary conditions for circular ducts (Basu and Roy, 1985; Ou and Cheng, 1973; Zanchini, 1997) and cylindrical tubes with elliptic, rectangular, and triangular cross-section (Tyagi, 1966; Ikryannikov, 1966). In a recent work, Morini et al. (1998) obtained the fluid temperature distribution in the presence of energy dissipation for a rectangular duct with four sides uniformly heated with H1 boundary conditions. The aim of

the present paper is to determine the temperature field and the Nusselt numbers in a rectangular duct in H1 boundary conditions for any combination of heated and adiabatic sides with viscous dissipation. In particular, the present work points out cases in which the effect of viscous dissipation on the fully developed temperature distribution cannot be neglected. The general solution for the H1 boundary condition allows us to obtain, as a particular case, the solution to the same problem with T conditions. The solution in the T boundary condition case offers the opportunity to extend to rectangular ducts some interesting conclusions recently published for circular ducts. In fact, for circular tubes, some authors have proved that, with T boundary conditions, the fully developed Nusselt number is dependent on neither the thermophysical properties nor the mean velocity of the fluid. The asymptotic value assumed by the Nusselt number in a circular duct is very different if one considers or neglects the effect of the viscous dissipation in the energy equation. Neglecting the viscous dissipation the fully developed Nusselt number should assume the well-known value of 3.6567935; however, it assumes the value $48/9 = 9.6$ if the viscous dissipation is accounted for (Basu and Roy, 1985; Zanchini, 1997). Hence, for a circular duct in T boundary condition, the hypothesis of negligible viscous dissipation effects leads to incorrect results, for any value of the fluid viscosity. The present analysis will confirm the same result for rectangular ducts and will provide the Nusselt numbers for any aspect ratio, in T boundary condition.

Table 2 Φ^* as function of the duct aspect ratio

β	Φ^*	β	Φ^*
1	28.40	0.5	34.94
0.9	28.55	0.4	40.13
0.8	29.06	0.3	49.32
0.7	30.12	0.2	68.60
0.6	31.95	0.1	127.97

Theoretical Model, H1 Boundary Condition

Consider a Newtonian incompressible fluid in hydrodynamically developed laminar flow in a rectangular duct with constant peripheral wall temperature on the cross section and constant axial heat transfer rate (H1 condition). The origin of the ξ, η, ζ Cartesian coordinate system is the bottom left corner of the duct, with the

Table 3 Test of convergence of the proposed procedure to calculate the Nusselt numbers under T boundary condition

N	Nu _T			
	β=1	β=0.75	β=0.5	β=0.25
3	7.952	8.141	8.994	11.498
5	7.940	8.128	8.973	11.439
7	7.939	8.126	8.970	11.425
9	7.938	8.125	8.969	11.420
11	7.938	8.125	8.968	11.418
13	7.938	8.125	8.968	11.417
15	7.938	8.125	8.968	11.416

flow direction along the ζ -axis. The following dimensionless variables and the Brinkman number are introduced:

$$x = \frac{\xi}{a}, \quad y = \frac{\eta}{a}, \quad z = \frac{\zeta}{D_h Pe},$$

$$V = \frac{u}{W}, \quad T = \frac{\theta - \theta_w}{q_w/k}, \quad Br = \frac{\mu W^2}{q_w} \quad (1)$$

The fluid in the duct receives a linear power q_s (generated by viscous dissipation) and q_w (transferred at the walls). Under the usual no-slip condition, the Navier-Stokes equation has been solved by using the finite Fourier transform by Spiga and Morini (1994), as a sum of trigonometric functions

$$V(x, y) = \left[\sum_{n=1, \text{odd}}^{\infty} \sum_{m=1, \text{odd}}^{\infty} \frac{4}{(\pi n m)^2 (\beta^2 n^2 + m^2)} \right]^{-1}$$

$$\times \left[\sum_{n=1, \text{odd}}^{\infty} \sum_{m=1, \text{odd}}^{\infty} \frac{\sin(n\pi x) \sin(m\pi y/\beta)}{mn(\beta^2 n^2 + m^2)} \right] \quad (2)$$

while the temperature distribution is the solution to the energy balance equation

$$\frac{\partial^2 \theta}{\partial \xi^2} + \frac{\partial^2 \theta}{\partial \eta^2} + \frac{\mu}{k} \left[\left(\frac{\partial u}{\partial \xi} \right)^2 + \left(\frac{\partial u}{\partial \eta} \right)^2 \right] = \frac{1}{\alpha} \frac{\partial \theta}{\partial \zeta} u(\xi, \eta). \quad (3)$$

In dimensionless form the Eq. (3) can be written as

$$\frac{\partial^2 T}{\partial x^2} + \frac{\partial^2 T}{\partial y^2} + Br \left[\left(\frac{\partial V}{\partial x} \right)^2 + \left(\frac{\partial V}{\partial y} \right)^2 \right] = \frac{V(x, y)}{\beta} (1 + Br \Phi^*(\beta)) \quad (4)$$

where the dimensionless viscous-energy-dissipation function is defined as

$$\Phi^*(\beta) = \int_0^1 \int_0^\beta \left[\left(\frac{\partial V}{\partial x} \right)^2 + \left(\frac{\partial V}{\partial y} \right)^2 \right] dx dy. \quad (5)$$

An energy balance along the ζ -axis provides the well-known H1 condition

$$\frac{\partial \theta}{\partial \zeta} = \frac{\partial \theta_b}{\partial \zeta} = \frac{\partial \theta_w}{\partial \zeta} = \frac{q}{\rho ab W c_p} \quad (6)$$

Table 4 Coefficients of the Eq. (22) to determine the Nusselt numbers in rectangular ducts (4 version)

	g ₁	g ₂	g ₃
β=1	0.1281	0.5501	0.0355
β=0.75	0.1277	0.5548	0.0345
β=0.5	0.1249	0.5717	0.0303
β=0.25	0.1003	0.5704	0.0188

which implies $\partial T / \partial z = 0$. By applying the Gauss theorem to the energy Eq. (4), the relation between the total linear heat flux (q), the power transferred to the wall (q_w), and the power due by viscous dissipation (q_s) is obtained:

$$q = q_w + q_s = q_w + \mu W^2 \int_0^1 \int_0^\beta \left[\left(\frac{\partial V}{\partial x} \right)^2 + \left(\frac{\partial V}{\partial y} \right)^2 \right] dx dy$$

$$= q_w (1 + Br \Phi^*(\beta)). \quad (7)$$

When the temperature distribution is known, the fluid bulk temperature is easily obtained as

$$T_b(\beta) = \frac{1}{\beta} \int_0^1 \int_0^\beta T(x, y) V(x, y) dx dy \quad (8)$$

and the Nusselt number is equal to

$$Nu = - \frac{2\beta}{(1 + \beta)} \frac{1}{PT_b(\beta)}. \quad (9)$$

The value assumed by the heated perimeter P depends on the heated sides of the duct.

A general solution is achieved considering any of the eight versions proposed in literature for the H1 condition in rectangular ducts, namely 4 (four constant wall temperature), 3L (three constant wall temperature and one adiabatic short side), 3S (three constant wall temperature and one adiabatic long side), 2L (two constant wall temperature and two adiabatic short sides), 2S (two constant wall temperature and two adiabatic long sides), 2C or corner version (one short and one long constant wall temperature), 1L (one constant wall temperature long side), and 1S (one constant wall temperature short side).

The differential problem defined by Eq. (4) is linear and its solution can be tackled by the finite-integral transform technique (Tranter, 1962). The appropriate eigenvalue problem is

$$\begin{cases} \frac{d\psi_{i,n}}{di} + \lambda_{i,n}^2 \psi_{i,n} = 0 \\ d_{1i} \psi_{i,n}(0) + d_{2i} \frac{d\psi_{i,n}}{di} \Big|_0 = 0 \\ d_{3i} \psi_{i,n}(\delta) + d_{4i} \frac{d\psi_{i,n}}{di} \Big|_\delta = 0 \end{cases} \quad \text{with } \delta = \begin{cases} 1 & \text{if } i = x \\ \beta & \text{if } i = y \end{cases} \quad (10)$$

where i is equal to x or y and n is the order of the general eigenvalue (λ) and of the general eigenfunction (ψ) that fulfills the Sturm-Liouville problem (10).

The coefficients d_{Ni} can assume the values 0 or ± 1 and depend on the specified combination of heated and adiabatic walls, imposed by the boundary conditions. In heat conduction problems the infinite series of eigenvalues $\lambda_{i,n}$ and the related eigenfunctions $\psi_{i,n}$ are frequently used and they can be found in several textbooks on heat conduction (Ozisik, 1989). For the sake of completeness,

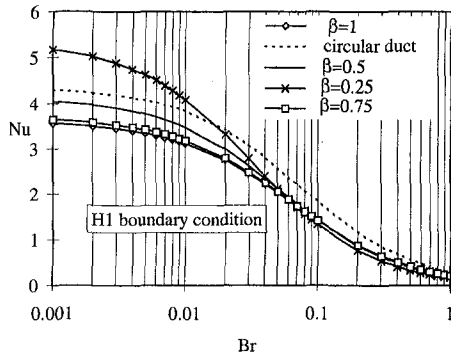


Fig. 1 Nusselt numbers in H1 boundary conditions versus the Brinkman number, 4 version, for the circular duct and different aspect ratios

Table 1 shows the eigenvalues and the eigenfunctions generated by Eq. (10) for the eight versions considered in the H1 problems.

Using the appropriate eigenfunctions, the unknown temperature field is sought as the sum of a linear function in z and a double series in x and y :

$$T(x, y) = \sum_{n=1}^{\infty} \sum_{m=1}^{\infty} B_{n,m} \psi_{x,n} \psi_{y,m} \quad (11)$$

In fact, the H1 boundary condition states that the wall temperature $\theta_w(z)$ is uniform on the heated length of a rectangular perimeter and that it increases linearly with the longitudinal coordinate z (Marco and Han, 1955). Hence, the temperature distribution T is defined apart from the additive constant $T_w(z)$. It is suitable to define the twofold transformed temperature:

$$T_{n,m} = \int_0^1 \int_0^\beta T(x, y) \psi_{x,n} \psi_{y,m} dx dy \quad (12)$$

By multiplying each term of the Eq. (4) by $\psi_{x,n}$, $\psi_{y,m}$ and integrating over x and y , in the range $[0, 1]$ and $[0, \beta]$, respectively, an algebraic equation is obtained, whose the solution is

$$T_{n,m} = -\frac{1}{(\lambda_{x,n}^2 + \lambda_{y,m}^2)} \left[\frac{V_{n,m}}{\beta} + \text{Br} \left(\frac{\Phi^*(\beta) V_{n,m}}{\beta} - [a_{n,m} + b_{n,m}] \right) \right] \quad (13)$$

where the coefficients $a_{n,m}$, $b_{n,m}$, and $V_{n,m}$ are

$$a_{n,m} = \int_0^\beta dy \int_0^1 dx \left(\frac{\partial V}{\partial x} \right)^2 \psi_{x,n} \psi_{y,m}$$

$$b_{n,m} = \int_0^\beta dy \int_0^1 dx \left(\frac{\partial V}{\partial y} \right)^2 \psi_{x,n} \psi_{y,m}$$

$$V_{n,m} = \int_0^\beta dy \int_0^1 dx V(x, y) \psi_{x,n} \psi_{y,m} \quad (14)$$

The integrals appearing in this procedure can be easily solved exactly, because the eigenfunctions are simple trigonometric functions and also the velocity profile is expressed as a sum of trigonometric functions. The final step in the solution procedure consists of the inversion of the transformed temperature $T_{n,m}$

$$T(x, y) = \sum_n \sum_m \frac{T_{n,m}}{N_{x,n} N_{y,m}} \psi_{x,n} \psi_{y,m} \quad (15)$$

where $N_{i,n}$ is the normalization coefficient





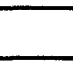
$$N_{i,n}^2 = \int_0^\delta \psi_{i,n}^2 di \quad (16)$$

Using the proposed procedure, the temperature field is univocally determined for any thermal version considered of the H1 problem.

The T Boundary Condition

In this section the temperature distribution in a rectangular duct under the T boundary condition is obtained as a particular case of

Table 5 The Nusselt numbers in T boundary condition for the 4 version: with viscous dissipation (Nu_T) and without viscous dissipation (Nu_T^*)

	Nu_T	Nu_T^*	Δ (%)
 Circular duct	9.6	3.656	+162.6
 Square duct ($\beta=1$)	7.938	2.976	+166.7
 Rectangular duct ($\beta=0.75$)	8.125	3.042	+167.1
 Rectangular duct ($\beta=0.5$)	8.968	3.391	+164.5
 Rectangular duct ($\beta=0.25$)	11.415	4.439	+157.2

the solution for the H1 boundary condition. A similar procedure has been carried out by Zanchini (1997) to determine the asymptotic behavior of the temperature distribution in circular ducts. Considering a hydrodynamically developed flow, the governing equations are the Navier-Stokes (which solution is quoted in Eq. (2)) and the energy balance (Eq. (3)). Integrating any term of Eq. (3) over the cross section of the rectangular duct, the following equation is obtained:

$$q_w(\zeta) + \mu W^2 \Phi^*(\beta) = \rho c_p W \frac{D_h^2}{\beta} \left(\frac{1 + \beta}{2} \right)^2 \frac{d\theta_b}{d\zeta} \quad (17)$$

where the heat flux at the wall, in the T boundary condition, is

$$q_w = hD_h \left(\frac{1 + \beta}{2\beta} \right) P(\theta_w - \theta_b). \quad (18)$$

Under the hypothesis of constant wall temperature (T boundary condition), Eqs. (17) and (18) give

$$-\left[\frac{1}{\text{Br}(z)} + \Phi^*(\beta) \right] = \left(\frac{1 + \beta}{2P} \right) \frac{d}{dz} \left[\frac{1}{\text{Nu Br}} \right]. \quad (19)$$

In the fully developed region the local Nusselt number tends to a constant value Nu_T and hence Eq. (19) allows one to obtain the Brinkman number variation along the thermally fully developed region of the duct

$$\text{Br}(z) = \frac{1}{C \exp\left(-\frac{2P \text{Nu}_T}{1 + \beta} z\right) - \Phi^*(\beta)} \quad (20)$$

where C is an integration constant. The asymptotic value that the Brinkman number assumes in the fully developed region for T boundary condition is obtained with a passage to limit of $z \rightarrow \infty$:

$$\text{Br}_T = \lim_{z \rightarrow \infty} \text{Br}(z) = -\frac{1}{\Phi^*(\beta)}. \quad (21)$$

This is consistent with the conclusions of Zanchini (1997) for circular tubes, where $\Phi^* = 8\pi$. For rectangular ducts, the fully developed Nusselt number in the T boundary condition is therefore given by Eq. (9) with $\text{Br} = -1/\Phi^*(\beta)$.

In Table 2 the values of Φ^* are shown as function of the aspect ratio of the rectangular duct.

Results and Conclusions

The proposed solution gives the temperature distribution and the Nusselt numbers in rectangular ducts, for any version of the H1 boundary condition. In this method the Nusselt number and the temperature distribution are obtained as a series; only a few terms of these series are permitted to obtain a high precision on the Nusselt number; this fact is underlined by the results quoted in Table 3. It is interesting to note that, if the aspect ratio of the rectangular duct decreases, the numerical convergence is slower. The expression of the Nusselt number for the H1 boundary condition can be easily simplified in a numerical form, more attractive for designers,

$$\text{Nu}_{H1} = \frac{g_1}{g_2 \text{Br} + g_3}, \quad (22)$$

where the coefficients g_i depend on the version and the aspect ratio. Table 4 shows the coefficients g_i for some aspect ratios, in the 4 version. For the sake of brevity, only the Nusselt numbers in this version are presented in Fig. 1, as function of the Brinkman number, for different aspect ratios of the ducts. The dotted line related to the circular duct is used as a benchmark. For any geometry, the Nusselt number decreases with the Brinkman number. For inviscid fluids in rectangular geometry it is well known that the highest Nusselt numbers are obtained in ducts with small aspect ratios. The graphs in Fig. 1 confirm this result, but they show a new interesting feature. For large Brinkman numbers (approximately $\text{Br} > 0.1$) the square duct presents higher Nusselt numbers than for rectangular ducts. In the T boundary condition, the results can be obtained by the general solution, imposing $\text{Br} = -1/\Phi^*(\beta)$. The temperature distribution for the square duct is quite close to the profile presented by Ikryannikov (1966), the Nusselt numbers depend only on the aspect ratio (do not depend on the fluid viscosity) and are very much larger than the Nusselt numbers of inviscid flows in rectangular ducts, for any geometry the increase is approximately 160 percent. In Table 5 the Nusselt numbers in T boundary conditions are presented for the circular duct and for some aspect ratios of rectangular ducts, for viscous and inviscid flows.

References

- Basu, T., and Roy, D. N., 1985, "Laminar Heat Transfer in a Tube with Viscous Dissipation," *Int. J. Heat Mass Transfer*, Vol. 28, pp. 699–701.
- Chandrupatla, A. R., and Sastri, V. M. K., 1977, "Laminar Forced Convection Heat Transfer of a Non-Newtonian Fluid in a Square Duct," *Int. J. Heat Mass Transfer*, Vol. 20, pp. 1315–1324.
- Ikryannikov, N. P., 1966, "Temperature Distribution in Laminar Flow of an Incompressible Fluid in a Rectangular Channel Allowing for Energy Dissipation," *Inzhenerno-Fizicheskii Zhurnal*, Vol. 10, pp. 306–310.
- Marco, S. M., and Han, L. S., 1955, "A Note on Limiting Laminar Nusselt Number in Ducts With Constant Temperature Gradient by Analogy to Thin-Plate Theory," *Transactions of the ASME*, Vol. 77, pp. 625–628.
- Morini, G. L., Spiga, M., and Tartarini, P., 1998, "Laminar Viscous Dissipation in Rectangular Duct," *Int. Comm. Heat and Mass Transfer*, Vol. 25, pp. 551–560.
- Morini, G. L., Spiga, M., and Tartarini, P., 1996, "A Solution for Slug and Fully Developed Newtonian Flows in H1 Boundary Conditions," *Proc. of 2nd European Thermal-Sciences and 14th UIT National Heat Transfer Conference*, Rome, pp. 655–660.
- Ou, W. J., and Cheng, K. C., 1973, "Viscous Dissipation Effects on Thermal Entrance Region Heat Transfer in Pipes With Uniform Heat Flux," *Appl. Sci. Res.*, Vol. 28, pp. 289–301.
- Ozsisik, M. N., 1989, *Boundary Value Problems of Heat Conduction*, Dover, New York.
- Schmidt, F. W., and Newell, M. E., 1967, "Heat Transfer in Fully Developed Laminar Flow Through Rectangular and Isosceles Triangular Ducts," *Int. J. Heat Mass Transfer*, Vol. 10, pp. 1121–1123.
- Shah, R. K., and London, A. L., 1974, "Thermal Boundary Conditions and Some Solutions for Laminar Duct Flow Forced Convection," *ASME JOURNAL OF HEAT TRANSFER*, Vol. 96, pp. 159–165.
- Shah, R. K., and London, A. L., 1978, "Laminar Flow Forced Convection in Ducts," *Adv. Heat Transfer* (Suppl. 1), Vol. 14, p. 169.
- Spiga, M., and Morini, G. L., 1994, "A Symmetric Solution for Velocity Profile in Laminar Flow Through Rectangular Ducts," *Int. Comm. Heat Mass Transfer*, Vol. 21, pp. 469–475.
- Tranter, C. J., 1962, *Integral Transform in Mathematical Physics*, John Wiley and Sons, New York.
- Tyagi, V. P., 1966, "Laminar Forced Convection of a Dissipative Fluid in a Channel," *ASME JOURNAL OF HEAT TRANSFER*, Vol. 88, pp. 161–169.
- Zanchini, E., 1997, "Effect of Viscous Dissipation on the Asymptotic Behaviour of Laminar Forced Convection in Circular Tubes," *Int. J. Heat Mass Transfer*, Vol. 40, pp. 169–178.

Experimental Investigation of Marangoni Convection in Aqueous LiBr Solution With Additives

Y. T. Kang,^{1,2} A. Akisawa,¹ and T. Kashiwagi¹

Nomenclature

add = additive
 D = Decanol
 O = Octanol
 T = temperature (°C)
 w = with
 w/o = without
 x = concentration (percent)
 σ = surface tension (mN/m)
 σ_1 = surface tension of aqueous LiBr solution with additive (mN/m)
 σ_2 = surface tension of additive (mN/m)
 σ_3 = interfacial tension between aqueous LiBr solution and additive (mN/m)

Introduction

The most crucial and expensive component in commercial absorption machines is the absorber where the refrigerant vapor is absorbed into the absorbent solution. The absorption performance can be improved by mechanical or chemical means. As the mechanical means, efficient heat transfer mechanisms, such as falling film or bubble-type modes, are suggested by using enhanced surfaces (Kang et al., 1999). As the chemical means, the performance of heat and mass transfer has been significantly enhanced by adding heat transfer additives to the working solution pairs. A small addition of heat transfer additives causes interfacial turbulence by the Marangoni effect, leading to a higher heat and mass transfer performance. It is generally known that Marangoni convection is caused by the surface tension gradient that is originated from the concentration and temperature dependence of the surface tension. Some literature has been found on mechanism of Marangoni convection. Kashiwagi (1988) suggested that the inducement of Marangoni convection be strongly affected not only by the presence of additive droplets on the surface but also by the magnitude of the interfacial tension. However, Hozawa et al. (1991) reported that the presence of additive droplets is not a necessary condition to initiate Marangoni convection. They suggested that Marangoni convection be initiated by the "salting-out" phenomenon, which is explained in the next subsection. Hihara and Saito (1993) adopted the hypothesis of the salting-out phenomenon to explain the inducement of Marangoni convection. Kim et al. (1996) reported that Marangoni convection was initiated by the surface tension gradients by not only LiBr concentration but also additive concentration and solution temperature. Recently Daiguji et al. (1997) investigated Marangoni convection using a linear stability analysis based on the salting-out effect. They reported that it was difficult to explain the Marangoni instability only by the

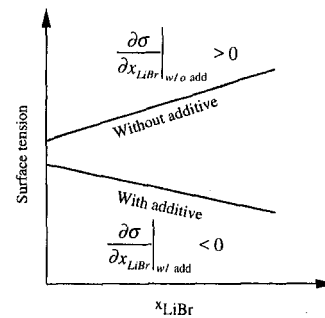


Fig. 1 Typical surface tension gradient of LiBr aqueous solution with respect to LiBr concentration

salting-out effect after the solubility limit. As described above, the criterion for inducement of Marangoni convection differs with each model. Therefore, it is desirable to establish a general model which can be applied for the best heat transfer additive selection in aqueous LiBr solution.

The primary objective of this paper is to establish a general model on the onset of Marangoni convection based on experimental results. The experimental data of the surface tension and interfacial tension of aqueous LiBr solution with heat transfer additives are provided. The effects of the LiBr concentration, the additive concentration, and the solution temperature on the surface tension and interfacial tension gradients are studied and compared quantitatively.

Models

Kashiwagi Model (Kashiwagi, 1988). This model proposed that the presence of droplets on the surface is required for inducement of Marangoni convection, and the imbalance of surface tensions be the initial cause of violent Marangoni convection. The droplets of heat transfer additives appear on the solution surface after the solubility. Before water vapor absorption, three tension forces σ_1 , σ_2 , and σ_3 are balanced well on the surface. After water vapor absorption starts, imbalance of the surface tension and the interfacial tension occurs due to the rapid increase of the surface tension near the droplets. As a result, Marangoni convection occurs on the solution surface.

Salting-Out Model (Hozawa et al., 1991; Kim et al., 1996; Daiguji et al., 1997). When the heat transfer additives are introduced, a part of the additive molecules is dissolved in the bulk solution, and the other molecules are adsorbed on the surface. If the LiBr molecules are added to the solution, water molecules are to bind electrolyte ions, Li^+ and Br^- because the hydration force with electrolyte ions is stronger than the bonding force with additives. As a result, some additive molecules are segregated from the bulk solution and move to the solution surface. This phenomenon is so called "salting-out." The surface tension of the solution decreases by the salting-out effect in surface-active materials such as LiBr. In the surface-active materials, the surface tension gradient with respect to its concentration is negative in the case with additives while the gradient is positive in the case without additives as shown in Fig. 1. This model proposed that the salting-out effect be the initial cause of Marangoni convection.

Experimental Apparatus and Procedures. Experiments were conducted to measure the surface tension and the interfacial tension for various heat transfer additives such as n-Octanol, 2-Octanol, 3-Octanol, 4-Octanol, n-Decanol, 2-Decanol, 3-Decanol and 2-ethyl-1-hexanol (2E1H). Figure 2 shows the experimental apparatus for the surface tension and the interfacial tension measurements. The experimental setup consists of a sample stage, a detecting platinum plate, a balance rod, a sensor, a motor, a temperature controller, a central processing unit (CPU), and a terminal printer. The solution temperature was controlled by the temperature controller with the PID control method. The surface tension was measured by the high-performance

¹ Department of Mechanical Systems Engineering, Tokyo University of Agriculture and Technology, 2-24-16, Nakasho, Koganei, Tokyo 184, Japan.

² To whom correspondence should be addressed. e-mail: ytkang@cc.tuat.ac.jp.

Contributed by the Heat Transfer Division for publication in the JOURNAL OF HEAT TRANSFER. Manuscript received by the Heat Transfer Division, Mar. 13, 1998; revision received, June 29, 1999. Keywords: Additives, Aqueous LiBr Solution, Interfacial Tension, Marangoni Convection, Surface Tension. Associate Technical Editor: R. Mahajan.

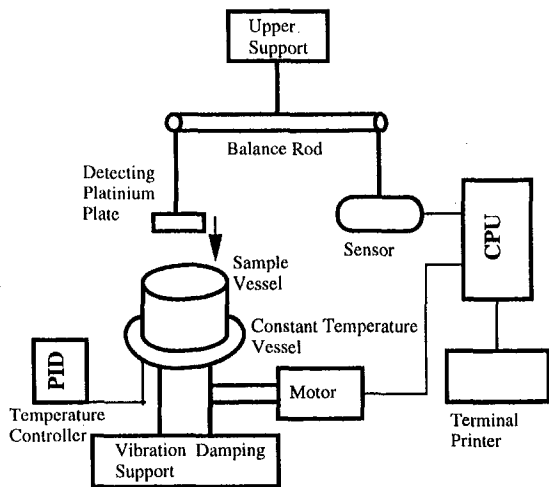


Fig. 2 Schematic diagram of the experimental apparatus

Wilhelmy plate method (Chavepeyer et al., 1995) with a microcomputer. The surface tension could be measured in fully automatic operation to minimize the human error. As the detecting platinum plate is slowly contacted with the liquid surface, the surface tension of the solution takes the detecting plate into the solution, and the balance rod gets the stress by the surface tension. The stress is detected in the sensor, and converted into the surface tension or the interfacial tension in the CPU. The surface tension is then displayed in digital at real time and printed out. Initially, aqueous LiBr solution was made from distilled water and LiBr with LiBr concentration of 40, 50, 55, and 60 percent in mass. The solution was carefully prepared to avoid the effect of the hand oil which would give a crucial effect on the experimental results. A digital micro pipette was used to make the solution with additives in the ranges between 0 and 1000 ppm. Prior to every measurement, the platinum plate was cleaned at a high temperature of 700°C with an alcohol lamp to remove the experimental error by the impurities of the plate. The cleaned plate was prewetted with the solution to remove the liquid repelling problem with a dried surface. The cleaned prewetted plate was then slowly contacted with the surface and dipped into the solution in automatic operation. Finally, the surface tension was measured by the principle of the Wilhelmy plate method. The measurement ranges of the surface tension were from 0 to 199.9 mN/m. The surface tension and the interfacial tension could be measured in the solution temperature ranges between 10°C and 100°C. The additive amount could be measured in the ranges of 2 to 10 μ l. Experimental errors in the

measurements of the solution temperature and the additive amount were $\pm 0.1^\circ\text{C}$ and $\pm 0.01 \mu\text{l}$, respectively. The experimental error was $\pm 0.2 \text{ mN/m}$ in measurements of the surface tension and the interfacial tension. Experimental uncertainties were estimated as 2.5 percent, 0.5 percent, 0.7 percent, and 2.41 percent in measurements of additive concentration, solution temperature, surface tension, and interfacial tension, respectively.

Results and Discussion

Figure 3 shows the effects of the LiBr concentration on the surface tension (σ_1) for the cases with and without the additives. The surface tensions were measured at 100 ppm of each additive concentration. In Fig. 3, Y and N represent "observation" and "no-observation" of Marangoni convection from the visualization tests, respectively. In the cases without the heat transfer additives, the surface tension of aqueous LiBr solution increased with increasing the LiBr concentration. Yao et al. (1991) and Uemura and Hasaba (1964) also obtained the same results from their experiments. In the cases with heat transfer additives, the surface tension of aqueous LiBr solution decreased with increasing the LiBr concentration for 2E1H, n-Octanol, 2-Octanol, and 2-Decanol. However, the surface tension gradient was not decreased with increasing the LiBr concentration for 3-Octanol, 4-Octanol, n-Decanol, and 3-Decanol. The experimental results show that the salting-out model agreed with the results from Kashiwagi model except n-Decanol. Marangoni convection was observed for n-Decanol by experiments (Beutler et al., 1996) even if n-Decanol has not the negative surface tension gradient. Violent Marangoni convection was also observed for n-Decanol after the solubility limit by Kashiwagi (1988). From the experimental results, it was concluded that the salting-out model could not be a general criterion for inducement of Marangoni convection. Based on the instability analysis, Daiguji et al. (1997) also reported that it was difficult to explain the Marangoni instability only by the salting-out effect when the additive concentration exceeds the solubility limit.

Figure 4 shows the effects of LiBr concentration on the interfacial tension (σ_3) for the cases of n-Octanol, 2-Octanol, 3-Octanol, n-Decanol, and 3-Decanol. As can be seen clearly, the same trend of concentration gradients of the interfacial tension was found for all cases (except n-Decanol) even though Marangoni convection was not observed for 3-Octanol and 3-Decanol. Therefore, it should be concluded that the concentration gradient of the interfacial tension is not a trigger to induce Marangoni convection. It could be noted from Fig. 4 that the magnitude of the interfacial tension played an important role for Marangoni convection inducement. Marangoni convection was observed for low values of the interfacial tension (σ_3 for n-Octanol, 2-Octanol, and n-Decanol)

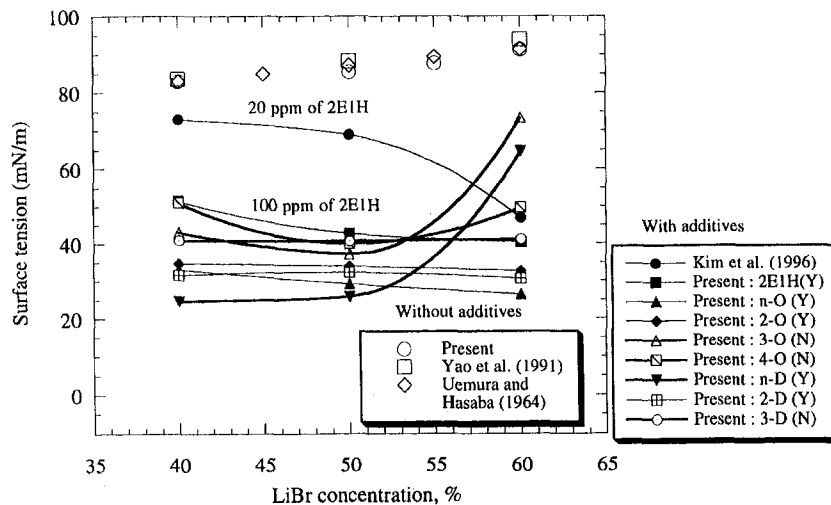


Fig. 3 The effect of LiBr concentration on the surface tension

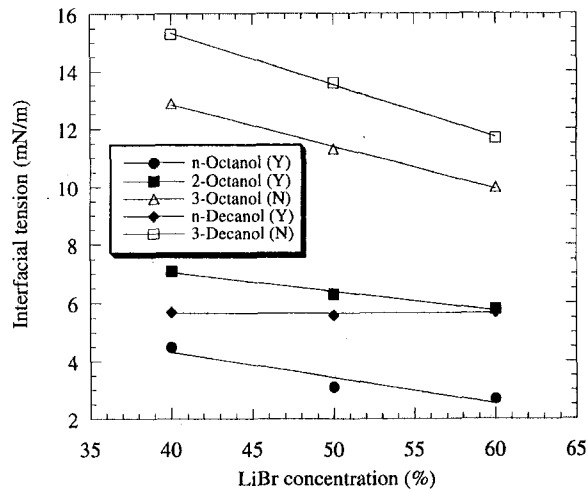


Fig. 4 The interfacial tension between aqueous LiBr solution (50 percent of LiBr) and additives

after the solubility while it was not for high values (for 3-Octanol and 3-Decanol). Therefore, recognizing that surface tensions of Octanol and Decanol isomers (σ_2) are nearly same (about 25 mN/m), it could be concluded that the imbalance of the surface tension and the interfacial tension ($\sigma_1 > \sigma_2 + \sigma_3$) is a criterion for inducement of Marangoni convection after the additive solubility.

Comparisons of Experimental Results With Existing Model. Table 1 shows the summary of the experimental results from the present paper. The surface tension and the interfacial tension gradients with respect to LiBr concentration and solution temperature were presented for eight different heat transfer additives. The experimental results show that the salting-out model gives different result from the Kashiwagi model for the n-Decanol case. Marangoni convection was experimentally observed for n-Decanol which has not a negative

gradient of the surface tension (criterion by the salting-out model). Based on the comparisons, a new model is proposed here: Marangoni convection occurs before (for example, n-Octanol) or after (for example, n-Decanol) the solubility. The negative concentration gradient of the surface tension is a trigger for inducement of Marangoni convection before the additive solubility while the imbalance of the surface tension and the interfacial tension is a trigger after the solubility limit. The new model is called "solubility model" in this paper. A promising additive in aqueous LiBr solution can be selected by checking the inducement criterion of the solubility model which is summarized in Table 2. An additive candidate with the negative concentration gradient of the surface tension is considered promising by the criterion of the salting-out model. However, an additive candidate without the negative gradient is also considered promising if it has the criterion of the surface tension imbalance ($\sigma_1 > \sigma_2 + \sigma_3$). The solubility model includes both criteria of the negative concentration gradient and the imbalance of the tension forces. In other words, the salting-out model is not a sufficient condition but a necessary condition for Marangoni convection inducement, while the solubility model is a necessary and sufficient condition, which is a general model in aqueous LiBr solution. Table 1 also show that the temperature gradients of the surface tension and the interfacial tension cannot be an initial cause for inducement of Marangoni convection. Regardless of the trend of temperature gradients of the surface tension and the interfacial tension, Marangoni convection was observed for 2E1H, n-Octanol, and n-Decanol while it was not for 3-Octanol.

Conclusions

This paper proposed a new model for inducement of Marangoni convection in an aqueous LiBr solution, called the solubility model. It was found first by the experiments that the salting-out model could not be a general criterion for inducement of Marangoni convection. It was also found that the temperature gradients of the surface tension and the interfacial tension could not be an initial cause for inducement of Marangoni convection. However, the magnitude of the interfacial tension played an important role for inducement of Marangoni con-

Table 1 Summary of experimental results

Additives	$\frac{\partial \sigma}{\partial x_{LiBr}} \Big _{w/ add} < 0$	$\frac{\partial \sigma}{\partial T} \Big _{w/ add} > 0$	$\frac{\partial \sigma_3}{\partial x_{LiBr}} \Big _{w/ add} < 0$	$\frac{\partial \sigma_3}{\partial T} \Big _{w/ add} > 0$	$\sigma_1 > \sigma_2 + \sigma_3$
2E1H	Yes	Yes	Yes	Yes	Yes
n-Octanol	Yes	Yes	Yes	Yes	Yes
2-Octanol	Yes	-	-	-	Yes
3-Octanol	No	Yes	Yes	Yes	No
4-Octanol	No	-	-	-	No
n-Decanol	No	Yes	No	Yes	Yes
2-Decanol	Yes	-	-	-	Yes
3-Decanol	No	-	-	-	No

Table 2 Comparisons of each model for inducement of Marangoni convection

Models	Kashiwagi model	Salting-out model	Solubility Model
Onset condition	Additive droplets	Salting-out effect by surface tension gradient	Negative concentration gradient of surface tension before solubility limit Imbalance of tension forces after solubility limit
Valid ranges	After solubility	Before solubility	Whole ranges
Criterion	$\sigma_1 > \sigma_2 + \sigma_3$	$\frac{\partial \sigma}{\partial x_{LiBr}} \Big _{w/ o add} > 0$ $\frac{\partial \sigma}{\partial x_{LiBr}} \Big _{w/ add} < 0$	$\frac{\partial \sigma}{\partial x_{LiBr}} \Big _{w/ o add} > 0$ $\frac{\partial \sigma}{\partial x_{LiBr}} \Big _{w/ add} < 0$ and $\sigma_1 > \sigma_2 + \sigma_3$

vection. The main conclusion from this study is that the negative concentration gradient of the surface tension is a trigger for induction of Marangoni convection before the additive solubility, while the imbalance of the surface tension and the interfacial tension is a trigger after the solubility limit.

Acknowledgment

The authors thank Mr. K. Iizuka, Tokyo University of Agriculture and Technology, for his experimental assistance. The authors acknowledge that this work has been partially funded by the Japan Science and Technology Corporation (JST).

References

- Beutler, A., Greiter, I., Wagner, A., Hohmann, L., Schreier, S., and Alefeld, G., 1996, "Surfactants and Fluid Properties," *Int. J. Refrigeration*, Vol. 19, No. 5, pp. 342–346.
- Chavepeyer, G., Salajan, M., Platten, J. K., and Smet, P., 1995, "Interfacial Tension and Surface Adsorption in *n*-Heptanol/Water Systems," *Journal of Colloid and Interface Science*, Vol. 174, pp. 112–116.
- Daiguji, H., Hihara, E., and Saito, T., 1997, "Mechanism of Absorption Enhancement by Surfactant," *Int. J. Heat and Mass Transfer*, Vol. 40, No. 8, pp. 1743–1752.
- Fujita, T., 1993, "Falling Liquid Films in Absorption Machines," *Int. J. Refrigeration*, Vol. 16, No. 4, pp. 282–294.
- Hihara, E., and Saito, T., 1993, "Effects of Surfactant on Falling Film Absorption," *Int. J. Refrigeration*, Vol. 16, No. 5, pp. 339–346.
- Hozawa, M., Inoue, M., Sato, J., and Tsukada, T., 1991, "Marangoni Convection During Steam Absorption into Aqueous LiBr Solution With Surfactant," *J. of Chemical Engineering of Japan*, Vol. 24, No. 2, pp. 209–214.
- Kang, Y. T., Akisawa, A., and Kashiwagi, T., 1999, "Experimental Correlation of Combined Heat and Mass Transfer for $\text{NH}_3\text{-H}_2\text{O}$ falling film absorption," *International Journal of Refrigeration*, Vol. 22, No. 4, pp. 250–262.
- Kashiwagi, T., 1988, "Basic Mechanism of Absorption Heat and Mass Transfer Enhancement by the Marangoni Effect," *Newsletter, IEA Heat Pump Center*, Vol. 6, No. 4, pp. 2–6.
- Kim, K. J., Berman, N. S., and Wood, B. D., 1996, "The Interfacial Turbulence in Falling Film Absorption: Effects of Additives," *Int. J. Refrigeration*, Vol. 19, No. 5, pp. 322–330.
- Uemura, T., and Hasaba, S., 1964, "Studies on the Lithium Bromide-Water Absorption Refrigeration Machine," Technical Report of Kansai University, Vol. 6, pp. 31–55.
- Yao, W., Bjurstrom, H., and Setterwall, F., 1991, "Surface Tension of Lithium Bromide Solutions With Heat Transfer Additives," *J. Chem. Eng. Data*, Vol. 36, pp. 96–98.

Transient Free Convection Flow Past an Infinite Vertical Plate With Periodic Temperature Variation

U. N. Das,¹ R. K. Deka,¹ and V. M. Soundalgekar²

Nomenclature

- C_p = specific heat at constant pressure
 g = gravitational acceleration
 K = thermal conductivity
 L_R = reference length
 Pr = Prandtl number
 T' = temperature of the fluid near the plate

¹ Department of Mathematics, Gauhati University, Guwahati 781 014, India.

² 31A-12 Brindavan Society, Thane 400 601, India.

Contributed by the Heat Transfer Division for publication in the JOURNAL OF HEAT TRANSFER. Manuscript received by the Heat Transfer Division, June 9, 1998; revision received, July 23, 1999. Keywords: Computational, Finite Element, Heat Transfer, Inverse, Nonintrusive Diagnostics, Stress. Associate Technical Editor: P. Ayyaswamy.

- T'_∞ = temperature of the fluid far away from the plate
 t' = time
 t_R = reference time
 u = velocity of the fluid
 U_R = reference velocity
 ω' = frequency
 X_p = distance of the transition point from the leading edge
 β = coefficient of volume expansion
 ρ = density
 ϵ = amplitude (constant)
 θ = nondimensional temperature
 θ = nondimensional velocity
 $i = \sqrt{-1}$

1 Introduction

Transient laminar-free convection flow past an infinite vertical plate under different plate conditions was studied by many researchers. The first closed-form solutions for Prandtl number $Pr = 1.0$ in case of a step change in wall temperature with time was derived by Illingworth (1950) and for $Pr \neq 1.0$, he derived the solution in integral form. Siegel (1958) studied the unsteady free-convection flow past a semi-infinite vertical plate under step-change in wall temperature or surface heat flux by employing the momentum integral method. Experimental evidence for such a situation was presented by Goldstein and Eckert (1960). For a semi-infinite vertical plate, unsteady free-convection flow was studied analytically by Chung and Anderson (1961), Sparrow and Gregg (1960), and Hellums and Churchill (1961, 1962) under boundary layer assumptions. Siegel (1958) first pointed out that the initial behavior of the temperature and velocity fields for a semi-infinite vertical flat plate is the same for the doubly infinite vertical flat plate, i.e., in the case of a temperature field it is the same as a solution of an unsteady one-dimensional heat conduction problem. The transition from conduction to convection begins only when some effect from the leading edge has propagated up the plate as a wave, to the particular point in question. Before this time, the fluid in this region effectively does not know that the plate has a leading edge. Hence, Goldstein and Briggs (1964) studied analytically the problem of transient free-convection flow past an infinite isothermal plate and introduced the idea of leading edge effect. Because of the importance of these problems, Gebhart et al. (1988) discussed this problem in their book. Jaluria and Gebhart (1974) also studied the transition mechanisms of vertical natural convection flow.

In all these papers, the plate was assumed to be maintained at a constant temperature T'_∞ , which is also the temperature of the surrounding stationary fluid. But in industrial applications, quite often the plate temperature starts oscillating about a nonzero mean temperature. Under these physical conditions, how transient free-convection past an infinite vertical plate is affected? This has not been studied in the literature. Hence, it is now proposed to study the behavior of transient free-convective flow when the mean plate temperature is superposed by periodic plate temperature with frequency ω' . In many engineering applications, transient free-convection flow occurs as such a flow acts as a cooling device. However, free-convection flow is enhanced by superimposing oscillatory temperature on the mean plate temperature. Again transient natural convection is of interest in the early stages of melting adjacent to a heated surface or in transient heating of insulating air gaps by heat input at the start-up of furnaces. In Section 2 the mathematical formulation of the problem is presented, along with its solution by the Laplace transform technique and in Section 3 the conclusions are summarized.

2 Mathematical Analysis

Consider the infinite vertical plate held in infinite mass of fluid, the temperature of both being assumed at T'_∞ initially. At time $t' > 0$, the plate temperature is raised to T'_w and a periodic temperature

vection. The main conclusion from this study is that the negative concentration gradient of the surface tension is a trigger for induction of Marangoni convection before the additive solubility, while the imbalance of the surface tension and the interfacial tension is a trigger after the solubility limit.

Acknowledgment

The authors thank Mr. K. Iizuka, Tokyo University of Agriculture and Technology, for his experimental assistance. The authors acknowledge that this work has been partially funded by the Japan Science and Technology Corporation (JST).

References

- Beutler, A., Greiter, I., Wagner, A., Hohmann, L., Schreier, S., and Alefeld, G., 1996, "Surfactants and Fluid Properties," *Int. J. Refrigeration*, Vol. 19, No. 5, pp. 342–346.
- Chavepeyer, G., Salajan, M., Platten, J. K., and Smet, P., 1995, "Interfacial Tension and Surface Adsorption in *n*-Heptanol/Water Systems," *Journal of Colloid and Interface Science*, Vol. 174, pp. 112–116.
- Daiguji, H., Hihara, E., and Saito, T., 1997, "Mechanism of Absorption Enhancement by Surfactant," *Int. J. Heat and Mass Transfer*, Vol. 40, No. 8, pp. 1743–1752.
- Fujita, T., 1993, "Falling Liquid Films in Absorption Machines," *Int. J. Refrigeration*, Vol. 16, No. 4, pp. 282–294.
- Hihara, E., and Saito, T., 1993, "Effects of Surfactant on Falling Film Absorption," *Int. J. Refrigeration*, Vol. 16, No. 5, pp. 339–346.
- Hozawa, M., Inoue, M., Sato, J., and Tsukada, T., 1991, "Marangoni Convection During Steam Absorption into Aqueous LiBr Solution With Surfactant," *J. of Chemical Engineering of Japan*, Vol. 24, No. 2, pp. 209–214.
- Kang, Y. T., Akisawa, A., and Kashiwagi, T., 1999, "Experimental Correlation of Combined Heat and Mass Transfer for $\text{NH}_3\text{-H}_2\text{O}$ falling film absorption," *International Journal of Refrigeration*, Vol. 22, No. 4, pp. 250–262.
- Kashiwagi, T., 1988, "Basic Mechanism of Absorption Heat and Mass Transfer Enhancement by the Marangoni Effect," *Newsletter, IEA Heat Pump Center*, Vol. 6, No. 4, pp. 2–6.
- Kim, K. J., Berman, N. S., and Wood, B. D., 1996, "The Interfacial Turbulence in Falling Film Absorption: Effects of Additives," *Int. J. Refrigeration*, Vol. 19, No. 5, pp. 322–330.
- Uemura, T., and Hasaba, S., 1964, "Studies on the Lithium Bromide-Water Absorption Refrigeration Machine," Technical Report of Kansai University, Vol. 6, pp. 31–55.
- Yao, W., Bjurstrom, H., and Setterwall, F., 1991, "Surface Tension of Lithium Bromide Solutions With Heat Transfer Additives," *J. Chem. Eng. Data*, Vol. 36, pp. 96–98.

Transient Free Convection Flow Past an Infinite Vertical Plate With Periodic Temperature Variation

U. N. Das,¹ R. K. Deka,¹ and V. M. Soundalgekar²

Nomenclature

- C_p = specific heat at constant pressure
 g = gravitational acceleration
 K = thermal conductivity
 L_R = reference length
 Pr = Prandtl number
 T' = temperature of the fluid near the plate

- T'_∞ = temperature of the fluid far away from the plate
 t' = time
 t_R = reference time
 u = velocity of the fluid
 U_R = reference velocity
 ω' = frequency
 X_p = distance of the transition point from the leading edge
 β = coefficient of volume expansion
 ρ = density
 ϵ = amplitude (constant)
 θ = nondimensional temperature
 θ = nondimensional velocity
 $i = \sqrt{-1}$

1 Introduction

Transient laminar-free convection flow past an infinite vertical plate under different plate conditions was studied by many researchers. The first closed-form solutions for Prandtl number $Pr = 1.0$ in case of a step change in wall temperature with time was derived by Illingworth (1950) and for $Pr \neq 1.0$, he derived the solution in integral form. Siegel (1958) studied the unsteady free-convection flow past a semi-infinite vertical plate under step-change in wall temperature or surface heat flux by employing the momentum integral method. Experimental evidence for such a situation was presented by Goldstein and Eckert (1960). For a semi-infinite vertical plate, unsteady free-convection flow was studied analytically by Chung and Anderson (1961), Sparrow and Gregg (1960), and Hellums and Churchill (1961, 1962) under boundary layer assumptions. Siegel (1958) first pointed out that the initial behavior of the temperature and velocity fields for a semi-infinite vertical flat plate is the same for the doubly infinite vertical flat plate, i.e., in the case of a temperature field it is the same as a solution of an unsteady one-dimensional heat conduction problem. The transition from conduction to convection begins only when some effect from the leading edge has propagated up the plate as a wave, to the particular point in question. Before this time, the fluid in this region effectively does not know that the plate has a leading edge. Hence, Goldstein and Briggs (1964) studied analytically the problem of transient free-convection flow past an infinite isothermal plate and introduced the idea of leading edge effect. Because of the importance of these problems, Gebhart et al. (1988) discussed this problem in their book. Jaluria and Gebhart (1974) also studied the transition mechanisms of vertical natural convection flow.

In all these papers, the plate was assumed to be maintained at a constant temperature T'_∞ , which is also the temperature of the surrounding stationary fluid. But in industrial applications, quite often the plate temperature starts oscillating about a nonzero mean temperature. Under these physical conditions, how transient free-convection past an infinite vertical plate is affected? This has not been studied in the literature. Hence, it is now proposed to study the behavior of transient free-convective flow when the mean plate temperature is superposed by periodic plate temperature with frequency ω' . In many engineering applications, transient free-convection flow occurs as such a flow acts as a cooling device. However, free-convection flow is enhanced by superimposing oscillatory temperature on the mean plate temperature. Again transient natural convection is of interest in the early stages of melting adjacent to a heated surface or in transient heating of insulating air gaps by heat input at the start-up of furnaces. In Section 2 the mathematical formulation of the problem is presented, along with its solution by the Laplace transform technique and in Section 3 the conclusions are summarized.

2 Mathematical Analysis

Consider the infinite vertical plate held in infinite mass of fluid, the temperature of both being assumed at T'_∞ initially. At time $t' > 0$, the plate temperature is raised to T'_w and a periodic temperature

¹ Department of Mathematics, Gauhati University, Guwahati 781 014, India.

² 31A-12 Brindavan Society, Thane 400 601, India.

Contributed by the Heat Transfer Division for publication in the JOURNAL OF HEAT TRANSFER. Manuscript received by the Heat Transfer Division, June 9, 1998; revision received, July 23, 1999. Keywords: Computational, Finite Element, Heat Transfer, Inverse, Nonintrusive Diagnostics, Stress. Associate Technical Editor: P. Ayyaswamy.

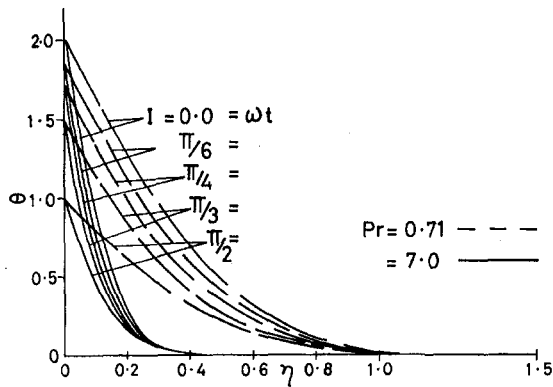


Fig. 1 Temperature profiles

is assumed to be superimposed on this mean constant temperature of the plate. Then neglecting viscous dissipation and assuming variation of density in the body force term (Boussinesq's approximation), the problem can be shown to be governed by the following set of equations:

$$\frac{\partial u'}{\partial t'} = \nu \frac{\partial^2 u'}{\partial y'^2} + g\beta(T' - T'_\infty) \quad (1)$$

$$\rho C_p \frac{\partial T'}{\partial t'} = K \frac{\partial^2 T'}{\partial y'^2} \quad (2)$$

with following initial and boundary conditions:

$$u' = 0, \quad T' = T'_\infty \quad \text{for all } y', t' \leq 0$$

$$u' = 0, \quad T' = T'_\infty + \epsilon(T'_w - T'_\infty) \cos \omega t' \quad \text{at } y' = 0, t' > 0$$

$$u' \rightarrow 0, \quad T' \rightarrow T'_\infty \quad \text{as } y' \rightarrow \infty, t' > 0. \quad (3)$$

The temperature distribution is independent of the flow and heat transfer is by conduction alone. This is true for fluids in the initial stage due to absence of convective heat transfer or at small Grashof number Gr flow ($Gr \ll 1$).

All the physical variables are defined in the Nomenclature. Because the plate is infinite in nature, the physical variables are functions of y' and t' only as the flow is fully developed.

We now introduce the following nondimensional quantities in Eqs. (1)–(3).

$$Pr = \mu C_p / K, \quad t = t' / t_R, \quad \omega = t_R \omega', \quad y = y' / L_R,$$

$$u = u' / U_R, \quad \theta = (T' - T'_\infty) / (T'_w - T'_\infty), \quad \Delta T = T'_w - T'_\infty,$$

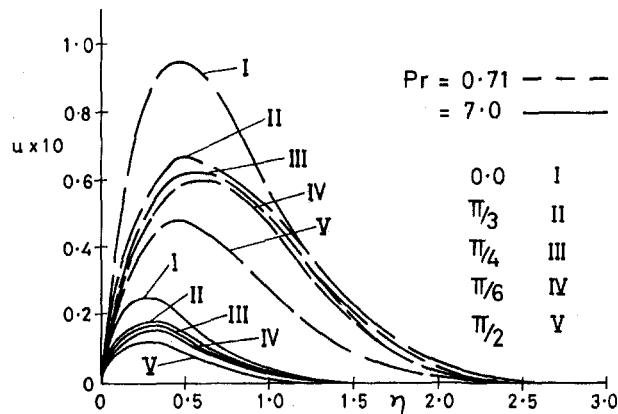


Fig. 2 Velocity profiles $\omega = 10.0, \epsilon = 0.2$

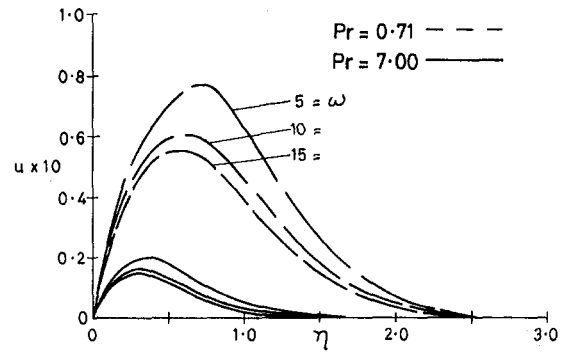


Fig. 3 Velocity profiles $\omega t = \pi/6, t = 0.2$

$$U_R = (\nu g \beta \Delta T)^{1/3}, \quad L_R = (g \beta \Delta T / \nu^2)^{1/3},$$

$$t_R = (g \beta \Delta T)^{-2/3} \nu^{1/3} \quad (4)$$

Then Eqs. (1)–(3) reduce to following nondimensional form:

$$\frac{\partial u}{\partial t} = \frac{\partial^2 u}{\partial y^2} + \theta \quad (5)$$

$$Pr \frac{\partial \theta}{\partial t} = \frac{\partial^2 \theta}{\partial y^2} \quad (6)$$

with following initial and boundary conditions:

$$u = 0, \quad \theta = 0 \quad \text{for all } y, t \leq 0$$

$$u = 0, \quad \theta = 1 + \epsilon \cos \omega t \quad \text{at } y = 0, t > 0$$

$$u \rightarrow 0, \quad \theta \rightarrow 0 \quad \text{as } y \rightarrow \infty, t > 0. \quad (7)$$

The solutions of these coupled linear Eqs. (5) and (6) satisfying the initial and boundary conditions (7) are derived by the Laplace transform technique and are as follows:

$$\theta = \text{erfc}(\eta / Pr) + \frac{\epsilon}{2} \{g(\eta / Pr, \omega i) + g(\eta / Pr, -\omega i)\} \quad (8)$$

$$u = \frac{1}{(Pr - 1)} \{f(\eta) - f(\eta / Pr)\} - \frac{i\epsilon}{2\omega(Pr - 1)} \{g(\eta, \omega i)$$

$$- g(\eta, -\omega i)\} + \frac{i\epsilon}{2\omega(Pr - 1)} \{g(\eta / Pr, \omega i)$$

$$- g(\eta / Pr, -\omega i)\}. \quad (9)$$

When $t = \pi/2$, the plate is isothermal and the solutions reduce to

$$\theta = \text{erfc}(\eta / Pr) \quad (10)$$

$$u = \frac{1}{Pr - 1} \{f(\eta) - f(\eta / Pr)\}. \quad (11)$$

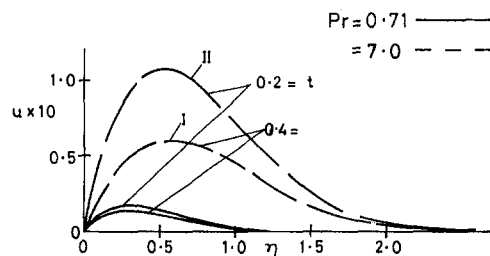


Fig. 4 Velocity profiles $\omega t = \pi/6, \omega = 10$

In order to gain physical insight into the problem, we have computed numerical values of θ and u for $\epsilon = 1.0$ and these are shown graphically. However, the argument of the complementary error function is imaginary. So during computation, we have separated the real and imaginary parts by using the formula

$$\operatorname{erf}(a + ib) = \operatorname{erf}(a) + \frac{e^{-a^2}}{2\pi a} \{1 - \cos 2ab + i \sin 2ab\} + \frac{2e^{-a^2}}{\pi} \sum_{n=1}^{\infty} \frac{e^{-n^2/4}}{n^2 + 4a^2} \{f_n(a, b) + ig_n(a, b)\} + \epsilon(a, b)$$

where

$$f_n(a, b) = 2a - 2a \cosh(nb) \cos 2ab + n \sinh(nb) \sin 2ab$$

$$g_n(a, b) = 2a \cosh(nb) \sin 2ab + n \sinh(nb) \cos 2ab$$

$$|\epsilon(a, b)| \ll 10^{-16} |\operatorname{erf}(a + ib)|. \quad (12)$$

The temperature profiles for $Pr = 0.71$ (air) and 7.0 (water) are shown on Fig. 1 and we observe that there is a fall in temperature due to an increase in the Prandtl number of the fluid. Temperature also falls owing to an increase in the value of ωt . The effect of ωt on the velocity profiles for $\omega = 10.0$ are shown on Fig. 2 for both air and water. In case of both air and water, the velocity is found to decrease with increasing ωt and the Prandtl number Pr . Velocity profiles are shown for different values of the frequency ω on Fig. 3 for both air and water when $\omega t = \pi/6$ and $t = 0.2$. It is interesting to note that the transient velocity is observed to decrease with increasing the frequency ω . The effect of time on the transient velocity can be seen on Fig. 4 and it is found that the transient velocity increases with increasing time.

Initially, the heat is transferred through the plate by conduction. But at a little later stage, convection currents start flowing near the plate. Hence it is necessary to know the position of a point on the plate where conduction mechanism changes to convection mechanism. In scientific literature, this is studied as a leading edge effect. The distance of this point of transition from conduction to convection is given by

$$X_p = \int_0^t u(y, t) dt \quad (13)$$

or in terms of the Laplace transform and its inverse, we have

$$X_p = L^{-1} \left[\frac{1}{s} L\{u(y, t)\} \right]. \quad (14)$$

Substituting for $L\{u(y, t)\}$ from (9) and carrying out the simplification we have

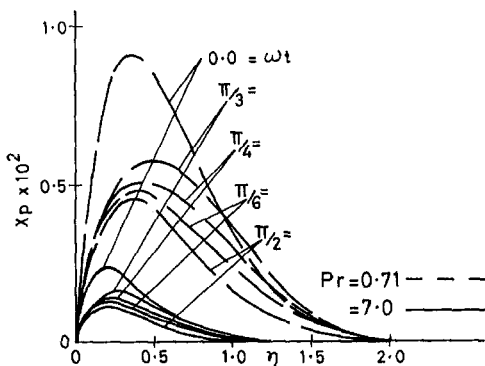


Fig. 5 Penetration distance $\omega = 10.0, t = 0.2$

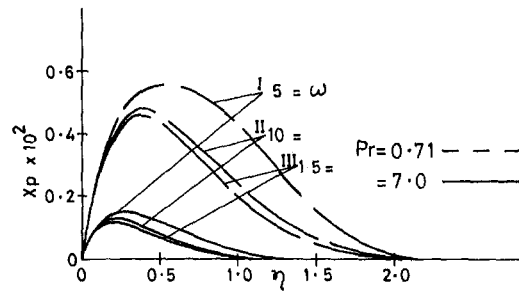


Fig. 6 Penetration distance $\omega t = \pi/6, t = 0.2$

$$X_p = \frac{1}{Pr - 1} \left[h(\eta) - \frac{\epsilon}{2\omega^2} \{g(\eta, i\omega) + g(\eta, -i\omega)\} - h(\eta/\sqrt{Pr}) + \frac{\epsilon}{2\omega^2} \{g(\eta/\sqrt{Pr}, i\omega) + g(\eta/\sqrt{Pr}, -i\omega)\} - \frac{\epsilon}{2\omega^2} \operatorname{erfc}(\eta/\sqrt{Pr}) \right] \quad (15)$$

where

$$f(a) = t \left\{ (1 + 2a^2) \operatorname{erfc}(a) - 2 \frac{ae^{-a^2}}{\sqrt{\pi}} \right\}$$

$$g(a, b) = \frac{e^{bt}}{2} \{e^{2a/bt} \operatorname{erfc}(a + \sqrt{bt}) + e^{-2a/bt} \operatorname{erfc}(a - \sqrt{bt})\}$$

$$h(a) = \frac{t}{2} f(a) - \frac{at^{3/2}}{3} \left\{ \frac{a^2 e^{-a^2}}{\sqrt{\pi}} - a(1 + 2a^2) + \frac{2e^{-a^2}}{\sqrt{\pi}} - 2a \operatorname{erfc}(a) \right\},$$

where $a = \eta$ or $a = \eta/\sqrt{Pr}$ and $b = i\omega$ or $b = -i\omega$.

Numerical values of X_p are computed by using (15) and are plotted on Figs. 5 to 7. On Fig. 5 the effects of ωt on X_p are shown

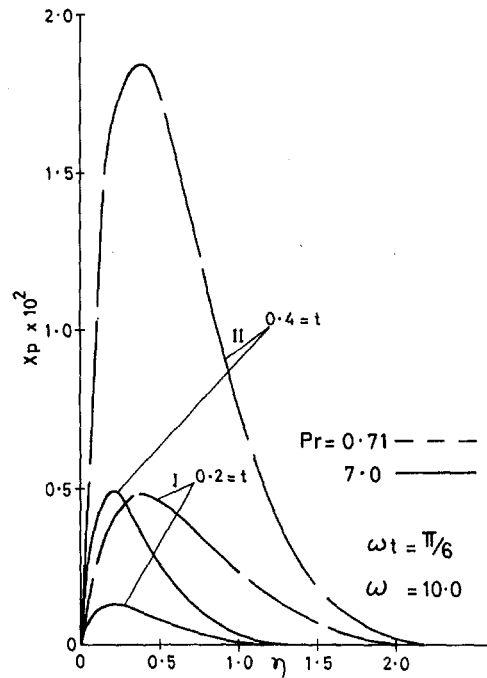


Fig. 7 Penetration distance

and we observe that the penetration distance is more for $Pr = 0.71$ (air) as compared to that in case for $Pr = 7.0$ (water), but it decreases with an increase in ωt . On Fig. 6, the penetration distance is shown for different values of the frequency ω . It is seen from this figure that the penetration distance decreases with increasing the frequency ω for both air and water. However, the decrease in X_p is more prominent when ω increases from 5 to 10 and X_p is less affected when ω increases from 10 onwards or at large values of ω . Hence we conclude that the penetration distance is more influenced at small values of the frequency ω and less influenced at large values of frequency ω . On Fig. 7, the penetration distance is shown for different values of time t when ωt and ω are held constant and it is seen that the penetration distance decreases with increasing the Prandtl number Pr .

3 Conclusion

1. Transient velocity decreases with increasing ωt , ω , or Pr .
2. The penetration distance is also found to decrease with increasing ωt , ω , or Pr , but the penetration distance is more affected in case of fluids with small Prandtl number.

References

- Chung, P. M., and Anderson, A. D., 1961, "Unsteady Laminar Free Convection," *ASME JOURNAL OF HEAT TRANSFER*, Vol. 83, pp. 474-478.
- Gebhart, B., Jaluria, Y., Mahajan, R. L., and Sammakia, B., 1988, *Buoyancy induced flows and transport*, Hemisphere Publishing Corporation, New York, p. 731.
- Goldstein, R. J., and Briggs, D. G., 1964, "Transient free convection about vertical plates and circular cylinders," *ASME JOURNAL OF HEAT TRANSFER*, Vol. 86, pp. 490-500.
- Hellums, J. D., and Churchill, S. W., 1962, "Transient and steady state free and natural convection," *Numerical solutions, Pt. 1, Amer. Inst. Chem. Engg. Journal*, Vol. 8, pp. 690-695.
- Hellums, J. D., and Churchill, S. W., 1961, "Computation of natural convection by finite difference methods," *International Development in Heat Transfer*, Part V, Sec. B, ASME, New York, pp. 985-994.
- Illingworth, C. R., 1950, "Unsteady laminar flow of gas near an infinite plate," *Proc. Camb. Phil. Soc.*, Vol. 46, pp. 603-613.
- Jaluria, Y., and Gebhart, B., 1974, "On transition mechanisms in vertical natural convection flow," *Journal of Fluid Mechanics*, Vol. 66, pp. 309-337.
- Siegel, R., 1958, "Transient free convection from a vertical flat plate," *Transactions of the ASME*, Vol. 30, pp. 347-359.
- Sparrow, E. M., and Gregg, J. L., 1960, "Nearly Quasi-Steady Free Convection Heat Transfer in Gases," *ASME JOURNAL OF HEAT TRANSFER*, Vol. 82, pp. 258-260.

Onset of Convection in a Fluid Saturated Porous Layer Overlying a Solid Layer Which is Heated by Constant Flux

C. Y. Wang¹

The thermoconvective stability of a porous layer overlying a solid layer is important in seafloor hydrothermal systems and thermal insulation problems. The case for constant flux bottom heating is considered. The critical Rayleigh number for the porous layer is found to increase with the thickness of the solid layer, a result opposite to constant temperature heating.

¹ Departments of Mathematics and Mechanical Engineering, Michigan State University, East Lansing, MI 48824. Mem. ASME.

Contributed by the Heat Transfer Division for publication in the *JOURNAL OF HEAT TRANSFER*. Manuscript received by the Heat Transfer Division, Dec. 1, 1998; revision received, May 11, 1999. Keywords: Geophysical, Heat Transfer, Instability, Natural Convection, Porous Media. Associate Technical Editor: T. Tong.

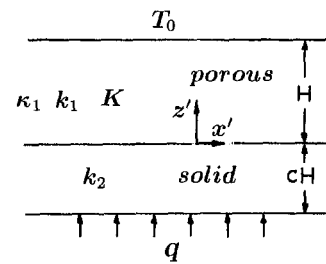


Fig. 1 Constant flux heating of a porous layer overlying a solid layer

1 Introduction

Thermoconvective stability of a porous medium is important in thermal insulation problems and geothermal energy problems. For a porous layer heated from below, heat transfer is through conduction only until a critical Rayleigh number R_c is reached. Above this critical value convection starts and the heat transfer is increased dramatically. See, e.g., Cheng (1978) and Gebhart et al. (1988) for a review.

For a homogeneous unbounded porous layer under isothermal conditions, Horton and Rogers (1945) found R_c to be $4\pi^2$. The case of two different porous layers was studied by Gheorghitza (1961) and Masuoka et al. (1978) who found incipient convection may be confined to a specific layer. The multiple porous layers case was considered by McKibbin and O'Sullivan (1980). They concluded that large permeability differences are required to alter the basic homogeneous incipient mode. The case of one porous layer overlying a solid layer is important in seafloor hydrothermal systems (Rosenberg et al., 1993). The first analysis of the effect of the solid layer was done by Donaldson (1962) and extended by McKibbin (1983).

All the above references considered constant temperature bottom heating. Few papers addressed the constant flux bottom heating. This situation occurs, for example, when the heat source is an exothermic chemical reaction. In thermal insulation problems, the heat source may be electric heating elements. Nield (1968) and Ribando and Torrance (1976) considered the constant flux heating of an infinite porous layer, and concluded the critical Rayleigh number is lowered to 27.1. Wang (1998) studied case where the porous layer is constrained by a cylindrical enclosure, showing R_c is increased from 27.0976, but not monotonically, as the radius is decreased. The present paper considers the case of a porous layer overlying a solid layer which is bottom heated by constant flux. The results would complement those of McKibbin (1983) which is bottom heated by constant temperature.

2 Formulation

Figure 1 shows a porous layer of thickness H overlying a solid layer of thickness cH . Let the bottom of the system be heated with constant flux q and the top be kept at constant temperature T_0 . The Darcy-Boussinesq equation for the porous layer is

$$u' = -\frac{K}{\mu} p'_{x'} \quad (1)$$

$$w' = -\frac{K}{\mu} \{p'_{z'} + \rho_0 g [1 - \delta(T'_1 - T_0)]\}. \quad (2)$$

Here (u', w') are velocity components in the directions (x', z') , respectively, K is the permeability, μ is the viscosity, p' is the pressure, g is the gravitational acceleration, δ is the fluid coefficient of thermal expansion, T'_1 is the temperature of the porous layer, and ρ_0 is the fluid density at the top temperature T_0 . The energy equation is

$$u' T'_{1x'} + w' T'_{1z'} = \kappa_1 (T'_{1x'x'} + T'_{1z'z'}) \quad (3)$$

and we observe that the penetration distance is more for $Pr = 0.71$ (air) as compared to that in case for $Pr = 7.0$ (water), but it decreases with an increase in ωt . On Fig. 6, the penetration distance is shown for different values of the frequency ω . It is seen from this figure that the penetration distance decreases with increasing the frequency ω for both air and water. However, the decrease in X_p is more prominent when ω increases from 5 to 10 and X_p is less affected when ω increases from 10 onwards or at large values of ω . Hence we conclude that the penetration distance is more influenced at small values of the frequency ω and less influenced at large values of frequency ω . On Fig. 7, the penetration distance is shown for different values of time t when ωt and ω are held constant and it is seen that the penetration distance decreases with increasing the Prandtl number Pr .

3 Conclusion

1. Transient velocity decreases with increasing ωt , ω , or Pr .
2. The penetration distance is also found to decrease with increasing ωt , ω , or Pr , but the penetration distance is more affected in case of fluids with small Prandtl number.

References

- Chung, P. M., and Anderson, A. D., 1961, "Unsteady Laminar Free Convection," *ASME JOURNAL OF HEAT TRANSFER*, Vol. 83, pp. 474-478.
- Gebhart, B., Jaluria, Y., Mahajan, R. L., and Sammakia, B., 1988, *Buoyancy induced flows and transport*, Hemisphere Publishing Corporation, New York, p. 731.
- Goldstein, R. J., and Briggs, D. G., 1964, "Transient free convection about vertical plates and circular cylinders," *ASME JOURNAL OF HEAT TRANSFER*, Vol. 86, pp. 490-500.
- Hellums, J. D., and Churchill, S. W., 1962, "Transient and steady state free and natural convection," *Numerical solutions, Pt. 1, Amer. Inst. Chem. Engg. Journal*, Vol. 8, pp. 690-695.
- Hellums, J. D., and Churchill, S. W., 1961, "Computation of natural convection by finite difference methods," *International Development in Heat Transfer*, Part V, Sec. B, ASME, New York, pp. 985-994.
- Illingworth, C. R., 1950, "Unsteady laminar flow of gas near an infinite plate," *Proc. Camb. Phil. Soc.*, Vol. 46, pp. 603-613.
- Jaluria, Y., and Gebhart, B., 1974, "On transition mechanisms in vertical natural convection flow," *Journal of Fluid Mechanics*, Vol. 66, pp. 309-337.
- Siegel, R., 1958, "Transient free convection from a vertical flat plate," *Transactions of the ASME*, Vol. 30, pp. 347-359.
- Sparrow, E. M., and Gregg, J. L., 1960, "Nearly Quasi-Steady Free Convection Heat Transfer in Gases," *ASME JOURNAL OF HEAT TRANSFER*, Vol. 82, pp. 258-260.

Onset of Convection in a Fluid Saturated Porous Layer Overlying a Solid Layer Which is Heated by Constant Flux

C. Y. Wang¹

The thermoconvective stability of a porous layer overlying a solid layer is important in seafloor hydrothermal systems and thermal insulation problems. The case for constant flux bottom heating is considered. The critical Rayleigh number for the porous layer is found to increase with the thickness of the solid layer, a result opposite to constant temperature heating.

¹ Departments of Mathematics and Mechanical Engineering, Michigan State University, East Lansing, MI 48824. Mem. ASME.

Contributed by the Heat Transfer Division for publication in the *JOURNAL OF HEAT TRANSFER*. Manuscript received by the Heat Transfer Division, Dec. 1, 1998; revision received, May 11, 1999. Keywords: Geophysical, Heat Transfer, Instability, Natural Convection, Porous Media. Associate Technical Editor: T. Tong.

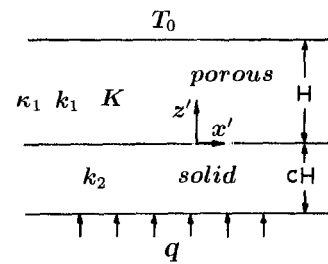


Fig. 1 Constant flux heating of a porous layer overlying a solid layer

1 Introduction

Thermoconvective stability of a porous medium is important in thermal insulation problems and geothermal energy problems. For a porous layer heated from below, heat transfer is through conduction only until a critical Rayleigh number R_c is reached. Above this critical value convection starts and the heat transfer is increased dramatically. See, e.g., Cheng (1978) and Gebhart et al. (1988) for a review.

For a homogeneous unbounded porous layer under isothermal conditions, Horton and Rogers (1945) found R_c to be $4\pi^2$. The case of two different porous layers was studied by Gheorghitza (1961) and Masuoka et al. (1978) who found incipient convection may be confined to a specific layer. The multiple porous layers case was considered by McKibbin and O'Sullivan (1980). They concluded that large permeability differences are required to alter the basic homogeneous incipient mode. The case of one porous layer overlying a solid layer is important in seafloor hydrothermal systems (Rosenberg et al., 1993). The first analysis of the effect of the solid layer was done by Donaldson (1962) and extended by McKibbin (1983).

All the above references considered constant temperature bottom heating. Few papers addressed the constant flux bottom heating. This situation occurs, for example, when the heat source is an exothermic chemical reaction. In thermal insulation problems, the heat source may be electric heating elements. Nield (1968) and Ribando and Torrance (1976) considered the constant flux heating of an infinite porous layer, and concluded the critical Rayleigh number is lowered to 27.1. Wang (1998) studied case where the porous layer is constrained by a cylindrical enclosure, showing R_c is increased from 27.0976, but not monotonically, as the radius is decreased. The present paper considers the case of a porous layer overlying a solid layer which is bottom heated by constant flux. The results would complement those of McKibbin (1983) which is bottom heated by constant temperature.

2 Formulation

Figure 1 shows a porous layer of thickness H overlying a solid layer of thickness cH . Let the bottom of the system be heated with constant flux q and the top be kept at constant temperature T_0 . The Darcy-Boussinesq equation for the porous layer is

$$u' = -\frac{K}{\mu} p'_{x'} \quad (1)$$

$$w' = -\frac{K}{\mu} \{p'_{z'} + \rho_0 g [1 - \delta(T'_1 - T_0)]\}. \quad (2)$$

Here (u', w') are velocity components in the directions (x', z') , respectively, K is the permeability, μ is the viscosity, p' is the pressure, g is the gravitational acceleration, δ is the fluid coefficient of thermal expansion, T'_1 is the temperature of the porous layer, and ρ_0 is the fluid density at the top temperature T_0 . The energy equation is

$$u' T'_{1x'} + w' T'_{1z'} = \kappa_1 (T'_{1x'x'} + T'_{1z'z'}) \quad (3)$$

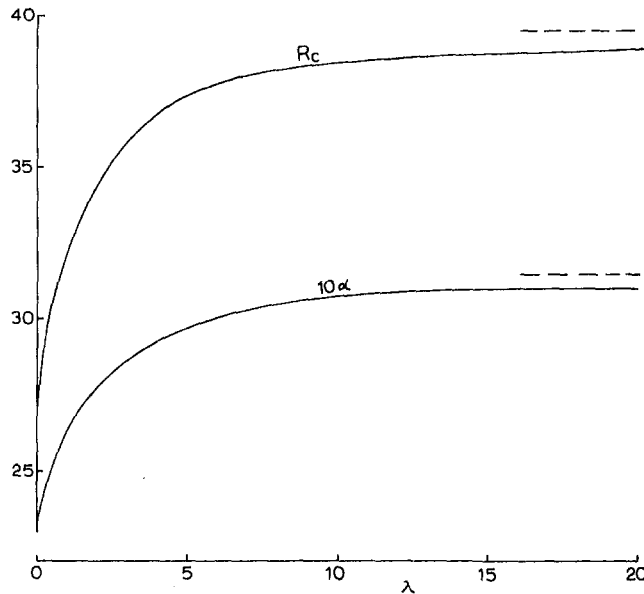


Fig. 2 Critical Rayleigh number R_c and corresponding frequency α versus λ , impermeable top; $c = \infty$

where κ_1 is the thermal diffusivity of the matrix. Continuity gives

$$u'_x + w'_z = 0. \quad (4)$$

For the solid layer of the heat conduction equation is

$$T'_{2x'x'} + T'_{2z'z'} = 0 \quad (5)$$

where T'_2 is the temperature. In the absence of convection the heat flux q is uniform everywhere. We perturb from this state

$$T'_1 = T_0 - \frac{qH}{k_1} (z - 1 - T_1) \quad (6)$$

$$T'_2 = T_0 - \frac{qH}{k_1} \left(\frac{z}{\lambda} - 1 - T_2 \right). \quad (7)$$

Here all lengths are normalized by H , k_1 , k_2 are the thermal conductivities of the two layers, $\lambda \equiv k_2/k_1$, and T_1 , T_2 are the perturbation temperatures normalized by qH/k_1 . Linearization of Eq. (3) gives

$$w = -\nabla^2 T_1 = -(T_{1xx} + T_{1zz}) \quad (8)$$

where velocities are normalized by κ_1/H . Eliminating pressure from Eqs. (1), (2) and using Eq. (4) give

$$\nabla^2 w = RT_{1xx} \quad (9)$$

where R is the Rayleigh number for the porous layer $qK\rho_0q\delta H^2/\mu\kappa_1k_1$. Thus the governing equations are

$$\nabla^4 T_1 + RT_{1xx} = 0 \quad (10)$$

$$\nabla^2 T_2 = 0 \quad (11)$$

with the following boundary conditions. On the bottom the perturbation flux is zero

$$T_{2z}(x, -c) = 0; \quad (12)$$

on the interface temperature, heat flux, and mass flux match.

$$T_2(x, 0) = T_1(x, 0) \quad (13)$$

$$\lambda T_{2z}(x, 0) = T_{1z}(x, 0) \quad (14)$$

$$T_{1xx}(x, 0) + T_{1zz}(x, 0) = 0 \quad (15)$$

On the top the temperature perturbation is zero

$$T_1(x, 1) = 0 \quad (16)$$

plus either zero flow or constant pressure on the top. For the zero flow case, Eqs. (8), (16) give

$$T_{1zz}(x, 1) = 0. \quad (17)$$

For constant pressure Eqs. (1), (4), (8) give $u_x = 0$ or

$$T_{1xx}(x, 1) + T_{1zz}(x, 1) = 0. \quad (18)$$

We seek minimum R such that Eqs. (10)–(18) yield nontrivial solutions.

3 The Case of Impermeable Top

In this case convection is prevented to leave the porous layer due to an impermeable top surface. Periodic solutions in x are sought. The general solution satisfying Eqs. (10), (16), (17) is

$$T_1(x, z) = \sin(\alpha x) \left\{ A_1 \sinh[b_1(z-1)] + A_2 \begin{cases} \sinh[b_2(z-1)], & \alpha > \sqrt{R} \\ \sin[b_2(z-1)], & \alpha < \sqrt{R} \end{cases} \right\}. \quad (19)$$

Here α , A_1 , A_2 are constants and

$$b_1 \equiv \sqrt{\alpha(\alpha + \sqrt{R})}, \quad b_2 \equiv \sqrt{|\alpha(\alpha - \sqrt{R})|}. \quad (20)$$

Equation (15) then yields

$$A_2 \begin{pmatrix} \sinh b_2 \\ \sin b_2 \end{pmatrix} = A_1 \sinh b_1. \quad (21)$$

The solution to Eqs. (11), (12) is

$$T_2(x, z) = \sin(\alpha x) A_3 \cosh[\alpha(z+c)]. \quad (22)$$

Then Eqs. (13), (14) yield the characteristic equation

$$F(\alpha, R) = 2\lambda\alpha \tanh(\alpha c) + b_1 \coth b_1 + b_2 \left(\frac{\coth b_2}{\cot b_2} \right) = 0. \quad (23)$$

For given λ , c , the minimum R with respect to all α is sought. In general, we find $\alpha < \sqrt{R}$ and the lower form is used.

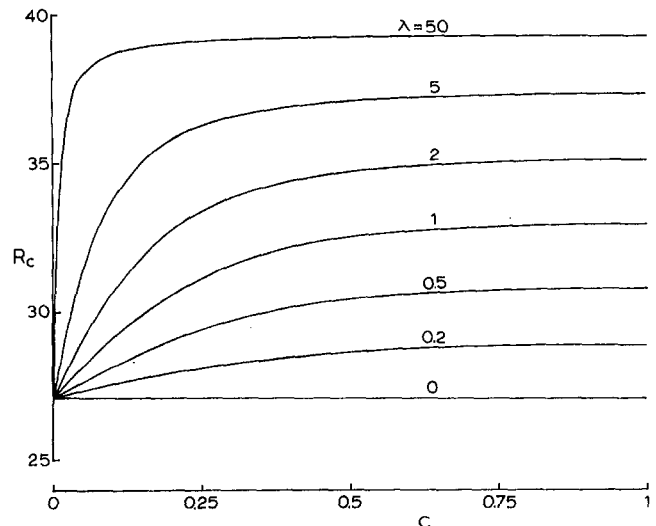


Fig. 3 R_c versus c for various λ , impermeable top

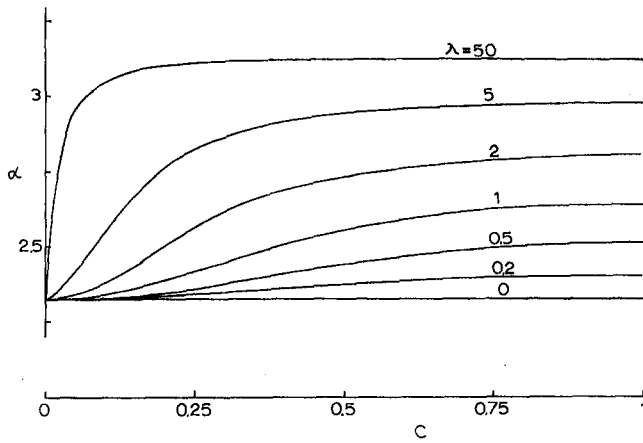


Fig. 4 α versus c for various λ , Impermeable top

When $c = 0$ the solid layer is absent. Equation (23) reduces to

$$b_1 \coth b_1 + b_2 \cot b_2 = 0. \quad (24)$$

The numerical solution is $\alpha = 2.326$ with a critical Rayleigh number of 27.098. The latter agrees with the result of Ribando and

Torrance (1976). When $c = \infty$ the solid layer is infinite. From Eq. (23)

$$F_1(\alpha, R) \equiv 2\lambda\alpha + b_1 \coth b_1 + b_2 \cot b_2 = 0. \quad (25)$$

Figure 2 shows the critical Rayleigh number R_c as a function of λ for the infinite solid thickness case. The corresponding optimum periodicity α is also shown. We see that R_c increases with conductivity ratio λ , starting with 27.098 at $\lambda = 0$. The solution of Eq. (25) as $\lambda \rightarrow \infty$ can be obtained as follows. Notice that the first and last terms of Eq. (25) are most important, giving $b_2 \approx \pi$. Another condition is $dR/d\alpha = 0$ or $F_{1\alpha} = 0$. Equation (25) yields

$$2\lambda + \frac{d}{db_2}(b_2 \cot b_2) \frac{\partial b_2}{\partial \alpha} = 0 \quad (26)$$

or $\sqrt{R} \approx 2\alpha$. Therefore as $\lambda \rightarrow \infty$, $R_c \rightarrow 4\pi^2$ and $\alpha \rightarrow \pi$.

For general c and λ , Eq. (23) is solved for minimum R . The results are shown in Figs. (3) and (4). Having obtained R_c and α , one can solve for the eigenvector (A_1, A_2, A_3) and the temperature profile is given by Eqs. (19), (22).

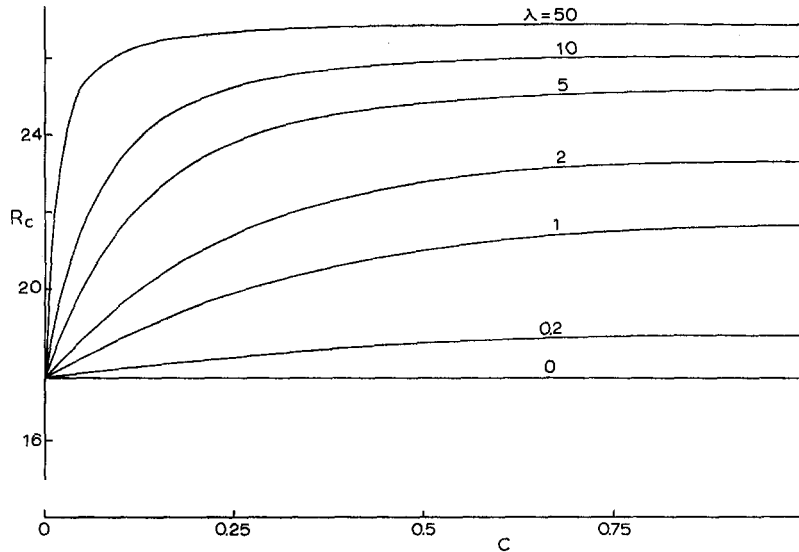


Fig. 5 R_c versus c for various λ , constant pressure top

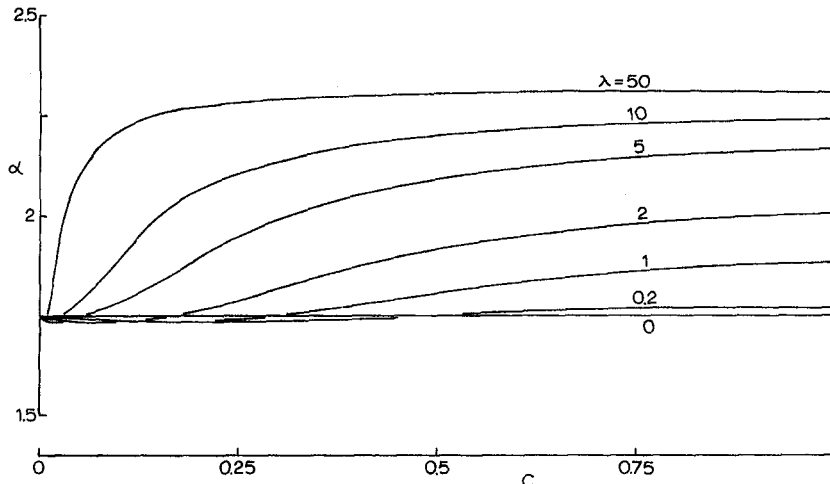


Fig. 6 α versus c for various λ , constant pressure top

4 The Case of Constant Pressure Top

In this case fluid is free to leave and enter the top surface of the porous layer. The temperature distribution for the solid layer is same as Eq. (22). For the porous layer we set

$$T_1(x, z) = \sin(\alpha x) \left\{ A_1 \sinh [b_1(z-1)] + A_2 \left(\frac{\sinh [b_2(z-1)]}{\sin [b_2(z-1)]} \right) + A_4 \left(\frac{\cosh [b_1(z-1)]}{\cos [b_2(z-1)]} \right) \right\}. \quad (27)$$

Again the top form is used if $\alpha > \sqrt{R}$. The pressure condition, Eq. (18) yields

$$A_1 b_1 - A_2 b_2 = 0 \quad (28)$$

while the impermeable condition Eq. (15) gives

$$-A_1 \sinh b_1 + A_2 \left(\frac{\sinh b_2}{\sin b_2} \right) + A_4 \left[\cosh b_1 + \left(\frac{\cosh b_2}{\cos b_2} \right) \right] = 0. \quad (29)$$

The matching conditions Eqs. (13), (14) yield the characteristic equation

$$\lambda \alpha \tanh(\alpha c) \left[\left(\frac{\sinh b_2}{\sin b_2} \right) + \frac{b_2}{b_1} \tanh b_1 \left(\frac{\cosh b_2}{\cos b_2} \right) \right] + \frac{b_2}{\cosh b_1} + b_2 \left(\frac{\cosh b_2}{\cos b_2} \right) + \frac{\alpha^2}{b_1} \tanh b_1 \left(\frac{\sinh b_2}{\sin b_2} \right) = 0. \quad (30)$$

Again we find $\sqrt{R} > \alpha$ and the lower form should be used. For $c = 0$ (or $\lambda = 0$) the numerical solution is $R_c = 17.654$ at $\alpha = 1.75$. The critical Rayleigh numbers and corresponding frequencies for arbitrary c are shown in Figs. 5 and 6. Note that α dips slightly below 1.75 at small c .

5 Discussions

In this paper we studied the constant flux heating of a porous layer supported by a solid layer. The results complements those of the constant temperature heating investigated by McKibbin (1983). Although the definitions of the Rayleigh numbers for constant flux and constant temperature are different, they are equivalent at subcritical Rayleigh numbers and thus can be compared. For the infinite solid layers ($c = \infty$) the two cases are identical, and our numerical results are within three percent lower than those obtained by McKibbin (1983). However, for finite solid layer thicknesses the results differ completely. For example, at zero solid thickness c and impermeable top, $R_c = 27.098$ for constant flux bottom heating while $R_c = 4\pi^2$ for

constant temperature bottom heating. In the present case R_c increases with c while the constant temperature case is opposite, i.e., R_c decreases with thickness c . Similarly the trend is also opposite in the constant pressure top cases. Since heating in practice is somewhere between constant temperature and constant flux, we are not able to predict how R_c changes with thickness of the solid layer. However, we can say for certainty that the smallest R_c , i.e., 27.098 for the impermeable top and 17.65 for the constant pressure top, is the value below which no convection would occur.

In both impermeable top and constant pressure top cases the frequency α in general increases with λ and c , again opposite to the constant temperature heating of McKibbin (1983). We find the constant pressure case has smaller α or larger period. The incipient streamlines, confined to the porous layer, are in alternate two-dimensional rolls for the impermeable top and half rolls for the constant pressure top. This is similar to the constant temperature heating. The perturbation temperature, however, is quite different. While the constant temperature case would show closed isotherms spanning the two layers, the constant flux case shows isotherms ending at the bottom boundary. This, added to the linear unperturbed temperature gradient, gives a local temperature maximum (hot spots) at periodic locations on the bottom surface.

Lastly, we mention that although other boundary conditions may be considered (e.g., Nield, 1968), the cases studied here are the most natural for seafloor and insulation systems.

References

- Cheng, P., 1978, "Heat Transfer in Geothermal Systems," *Advances in Heat Transfer*, Vol. 14, pp. 1-105.
- Donaldson, I. G., 1962, "Temperature Gradients in the Upper Layers of the Earth's Crust due to Convective Water Flows," *J. Geophys. Res.*, Vol. 67, pp. 3449-3459.
- Gebhart, B., Jaluria, Y., Mahajan, P. L., and Sammakia, B., 1988, *Buoyancy-Induced Flows and Transport*, Hemisphere, New York, Chapter 15.
- Gheorghitza, S. I., 1961, "The Marginal Stability in Porous Inhomogeneous Media," *Proc. Camb. Philo. Soc.*, Vol. 57, pp. 871-877.
- Horton, C. W., and Rogers, F. T., 1945, "Convective Currents in a Porous Medium," *J. Appl. Phys.*, Vol. 16, pp. 367-370.
- Masuoka, T., Katsuhara, T., Nakazono, Y., and Isozaki, S., 1978, "Onset of Convection and Flow Patterns in a Porous Layer of Two Different Media," *Heat Trans.—Japanese Res.*, Vol. 7, pp. 39-52.
- McKibbin, R., 1983, "Convection in an Aquifer above a Layer of Heated Impermeable Bedrock," *New Zeal. J. Sci.*, Vol. 26, pp. 49-64.
- McKibbin, R., and O'Sullivan, M. J., 1980, "Onset of Convection in a Layered Porous Medium Heated From Below," *J. Fluid Mech.*, Vol. 96, pp. 375-393.
- Nield, D. A., 1968, "Onset of Thermohaline Convection in a Porous Medium," *Water Resources Res.*, Vol. 4, pp. 553-560.
- Ribando, R. J., and Torrance, K. E., 1976, "Natural Convection in a Porous Medium: Effects of Confinement, Variable Permeability, and Thermal Boundary Conditions," *ASME JOURNAL OF HEAT TRANSFER*, Vol. 98, pp. 42-48.
- Rosenberg, N. D., Spera, F. J., and Haymon, R. M., 1993, "The Relationship Between Flow and Permeability Field in Seafloor Hydrothermal Systems," *Earth Planetary Sci. Lett.*, Vol. 116, pp. 135-153.
- Wang, C. Y., 1998, "Onset of Natural Convection in a Fluid-Saturated Porous Medium Inside a Cylindrical Enclosure Bottom Heated by Constant Flux," *Int. Comm. Heat Mass Trans.*, Vol. 25, pp. 593-598.